



PHYSICAL CHEMISTRY 2006

Proceedings

*of the 8th International Conference
on Fundamental and Applied Aspects of
Physical Chemistry*

September 26-29,
Belgrade, Serbia

ISBN 86-82139-26-X
Title: Physical Chemistry 2006. (Proceedings)
Editors Prof. dr A. Antić-Jovanović
Published by: The Society of Physical Chemists of Serbia, Studentski trg 12-16, P.O.Box 137, 11001 Belgrade, Serbia
Publisher: Society of Physical Chemists of Serbia
For publisher: Prof. dr S. Anić, president of the Society of Physical Chemists of Serbia
Printed by: "Jovan" Printing and Published Comp;
250 Copies; Number of Pages: x + 442; Format B5;
Printing finished in September 2006.
Text and Layout: Aleksandar Nikolić
250 – copy printing

The Conference is organized by
the Society of Physical Chemists of Serbia

in cooperation with
Institute of Catalysis, Bulgarian Academy of Sciences

Boreskov Institute of Catalysis,
Siberian Branch of the Russian Academy of Sciences

Faculty of Physical Chemistry, University of Belgrade

Institute of Chemistry, Technology and Metallurgy, Belgrade

Institute of General and Physical Chemistry, Belgrade

* * *

The Conference is held under the auspices of the
Ministry of Sciences and Environmental Protection
of the Republic of Serbia

Organizing Committee

Chairman: S. Anić (Serbia)
Vice-chairmans: S. Damyanova (Bulgaria),
V.A. Sobyenin (Russia)
B. Adnađević (Serbia)

Members:

V. I. Elokhin (Russia), T. Grozdić (Serbia), D. Jovanović (SCG), M. Koleva (Bulgaria), M. Lalić (BiH), P. Manojlović (Serbia), D. Marković (Serbia), Z. Marković (Serbia), B. Milosavljević (USA), N. Miljević (Serbia), I. Mitev (Bulgary), T. Nenadović (Serbia), N. Ostrovski (Serbia), C. Pona (I), B. Simonović (Serbia), N. Vukelić (Serbia), V. Vukojević (SWE)

Scientific Committee

Chairman: A. Antić-Jovanović (Serbia)
Vice-chairmans: V. N. Parmon (Rus)
O. Nešković (Serbia)
L. Petrov (Bulgaria)

Members:

P. Allen (GBR), C. Bonev (Bulgaria), R. Cervellati (I), Ž. Čupić (Serbia), V. Dondur (Serbia), V. Gáspár (Hungary), P. Graae Sørensen (Denmark), M. Jeremić (Serbia), A. L. Kawczyński (Poland), Lj. Kolar-Anić (Serbia), R. Leblanc (USA), S. Mentus (Serbia), S. Milonjić (Serbia), Z. Noszticzius (Hungary), M. Perić (Serbia), V. Petruševski (Makedonija), M. Plavšić (Serbia), M. Ristić (Serbia), G. Schmitz (Belgium), I. Schreiber (CSc), P. Sevcik (Slovakia), N. F. Stepanov (Rus), A. Terlecki-Baričević (Serbia), M. Trtica (Serbia), D. Veselinović (Serbia),

Local Executive Committee

Chairman: B. Adnađević
Vice-chairmans: Ž. Čupić

Members:

N. Begović, S. N. Blagojević, I. Cekić, N. Cvjetičanin, M. Daković, Lj. Damjanović, V. Drobnjak, A. Đerić, N. Gavrilov, A. Ignjatović, Lj. Ignjatović, S. Kuprešak, D. Lončarević, M. Mojović, N. Pejić, N. Potkonjak, D. Ranković, D. Stanisavljev

Honorary Committee

Aleksandar Popović, Serbian Minister of Science and Environment

Nikola Hajdin, President of Serbian Academy of Sciences and Arts

Dejan Popović, Rector, University of Belgrade

Paula Putanov, Member of Serbian Academy of Sciences and Arts

Momčilo Ristić, Member of Serbian Academy of Sciences and Arts

Ivan Draganić, Honorary Member of Society of Physical Chemists of Serbia

Bratislav Đorđević, Ambassador, Ministry of Foreign Affairs of Republic of Serbia

SPONSORS

Ministry of Science and Environmental Protection of Republic of Serbia

The Faculty of Physical Chemistry, University of Belgrade

Institute for Chemistry, Technology and Metallurgy, University of Belgrade

Organisation for the Prohibition of Chemical Weapons

Donau Lab, Belgrade

MOL, Belgrade

WARTA Microbattery GmbH, Ellwangen

Institute of General and Physical Chemistry, Belgrade

ENOLOŠKA STANICA dp, Society Company for Agricultural Products
and Foodstuffs Control, Vršac

Gradski zavod za zaštitu zdravlja, Beograd

This book contains the scientific contributions of about 500 authors from twenty-four different countries. Besides six plenary and twenty section lectures, it includes approximately 200 contributions given as either oral or poster presentations. All received papers were reviewed but without language revision, for which the authors bore the responsibility.

Organizers of the conference “Physical Chemistry 2006” wish to extend thanks to all of the authors that made the effort to provide us with their papers and take part in the conference. We hope that the experiences gathered at this meeting along with the remarkable collection of papers, will make the effort well worthwhile.

Organizers also wish to thank the Ministry of Science and Environmental Protection of the Republic of Serbia as well as our other sponsors for helping to make this conference a success.

Belgrade, 2006

Contents at a Glance

Plenary Lectures (PL)	1
Chemical Thermodynamics (A).....	47
Spectroscopy, Molecular Structures and Physical Chemistry of Plasma (B)	65
Kinetics, Catalysis (C)	121
Nonlinear Dynamics(D).....	217
Electrochemistry (E)	283
Biophysical Chemistry, Photochemistry and Radiation Chemistry (F)	339
Radiochemistry and Nuclear Chemistry (G).....	443
Materials Science (H)	467
Solid State Physical Chemistry (I).....	559
Macromolecular Physical Chemistry (J).....	577
Environmental Protection (K).....	597
Phase Boundaries (L).....	669
Complex Compounds (M)	687
General Physical Chemistry (N)	725
Education (O).....	761
Author Index	767
Participating Institutions	775

TABLE OF CONTENTS

PL – Plenary Lecture	1
Masamori Endo, Tokai University, Japan CHEMICAL OXYGEN-IODINE LASER: RECENT ADVANCES AS A CHEMICAL DEVICE	3
Roger M. Leblanc, University of Miami, U. S. A. BIOMOLECULAR RECOGNITION AND IMAGING USING QUANTUM DOTS	11
Andrzej L. Kawczyński, Polish Academy of Sciences, Poland PATTERN FORMATION IN REACTION-DIFFUSION SYSTEMS	15
L. Morozova-Roche, Umeå University, Sweden STRUCTURAL MECHANISMS AND PATHWAYS OF AMYLOID FORMATION. ITS IMPLICATION IN CONFORMATIONAL DISEASES	23
G. Smulevich (University of Florence, Italy) RESONANCE RAMAN SPECTROSCOPY AND SITE DIRECTED MUTAGENESIS TO PROBE HEME PROTEIN STRUCTURE	31
Andrzej G. Chmielewski (University of Technology, Warsaw, Poland) PRACTICAL APPLICATIONS OF RADIATION CHEMISTRY	38
A – Chemical Thermodynamics	47
D. M. Minić, Z. Nedić, I. Cekić and R. Marković THERMAL ISOMERIZATION OF PUSH-PULL 5-SUBSTITUTED-4- OXOTHIAZOLIDINES	49
L. Gomidželović and D. Živković CALCULATION OF MIXING ENTHALPIES FOR TERNARY Au-IN-Sb LIQUID ALLOYS	52
D. Manasijević, D. Minić, D. Živković and Ž. Živković PHASE EQUILIBRIA OF THE In-Sb-Bi SYSTEM	55
I. Cvijović, M. Spiegel and I. Parezanović GAS CORROSION DAMAGE IN Ti-STABILIZED INTERSTITIAL FREE STEEL	58
S. Ostojić, M. Kićanović, S. Zlatanović, M. Pavlović and Z. Marković THERMAL ANALYSIS OF WHEY MAYONNAISE	61

B – Spectroscopy, Molecular Structures, Physical Chemistry of Plasma	65
Lj. Pejov and K. Hermansson THE NATURE OF UNCONVENTIONAL BLUE-SHIFTING HYDROGEN BONDS – A THEORETICAL INSIGHT	67
R. Meckenstock MICROWAVE SPECTROSCOPY FOR NANO STRUCTURED MAGNETIC AND ELECTRONIC SYSTEMS	75
J. J. Savović, M. M. Kuzmanović, M. S. Pavlović, M. Stoiljković and M. Marinković AN EXPERIMENTAL STUDY OF RADIAL SYMMETRY DEVIATION IN DC ARGON ARC PLASMA BY CURRENT MODULATION TECHNIQUE	81
D. M. Marković, I. Novović and D. Vilotić DETERMINATION OF Fe, Mn AND Pb IN TREE-RINGS IN POPLAR (<i>Populus alba</i> L.) BY U-SHAPED DC ARC	84
G. Vasile, A. Moise and E. Mihaila THE OPTIMIZATION OF COLD VAPOR AAS TECHNIQUE FOR MERCURY ANALYSIS IN INDUSTRIAL WATER EFFLUENTS	87
I. Novović, V. Nikolić and D. M. Marković THE POSSIBILITY OF APPLICATION OF THE ATOMIC EMISSION SPECTROMETRY IN THE ECOLOGY	90
M. Kuzmanović, V. Bojović and A. Antić-Jovanović FRANCK-CONDON FACTORS FOR CERTAIN BANDS OF THE Ag ₂ MOLECULE	93
V. Bojović and A. Antić-Jovanović r-CENTROIDS FOR THE E-X BANDS OF Ag ₂ MOLECULE	96
J. M. Dimitrić-Marković, J. M. Baranac and M. L. Dašić SPECTROSCOPIC AND THEORETICAL INVESTIGATION OF DELPHINIDIN-ALUMINIUM (III) and CYANIDIN-ALUMINIUM (III) COMPLEXES IN AQUEOUS AND NON-AQUEOUS MEDIA	99
J. M. Dimitrić-Marković, J. M. Baranac and T. P. Brdarić THE INFLUENCE OF THE MEDIUM AND THE SUBSTITUTION PATTERN ON THE COMPLEXING ABILITIES OF SOME HYDROXYFLAVONES: A SPECTROSCOPIC AND THEORETICAL TREATMENT	102
D. Đikanović, A. J. Kalauzi, K. Radotić, C. Lapierre and M. Jeremić COMPARISON OF DIFFERENT MATHEMATICAL MODELS IN DECONVOLUTION OF LIGNIN FLUORESCENCE SPECTRA	105

S. M. Melnikov, E. K. L.Yeow, H. Uji-i, F. C. De Schryver and J. Hofkens SINGLE MOLECULE STUDY OF TWO-COLOR EMISSION IN PERY- LENEIMIDE-TERRYLENEDIIMIDE DENRIMERS	108
D. Bajuk-Bogdanović, I. Holclajtner-Antunović, M. Todorović, U. Mioč and J. Zakrzewska SPECTROSCOPIC INVESTIGATION OF AQUEOUS 12- TUNGSTOPHOSPHORIC ACID SPECIATION	111
S. M. Sunarić and S. S. Mitić SPECTROPHOTOMETRIC INVESTIGATION OF THE OXYTETRACY- CLINE DEGRADATION WITH Cu(II)/H ₂ O ₂ SYSTEM IN AQUEOUS SOLUTIONS	114
S. Veličković, M. Veljković, V. Đorđević, J. Cvetičanin J. Đustebek and O. Nešković SURFACE IONIZATION STUDY OF THE NON- STOICHIOMETRIC LinFn-1 (n = 4 – 6) CLUSTERS	117
C – Kinetics Catalysis	121
J. Keranen, C. Guimon and A. Auroux A MULTITECHNIQUE APPROACH OF THE DETERMINATION OF THE SURFACE ACTIVE SITES OF CATALYSTS	123
N. F. Stepanov, A. A. Kubasov, and Ya. V. Tikhii SIMPLE MOLECULES ON ACCEPTOR CENTERS OF ZEOLITES: QUANTUM CHEMICAL SIMULATION	132
N. M. Ostrovskii CATALYTIC REACTION DYNAMICS CAUSED BY IONS MOBILITY IN SOLIDS	138
V. A. Sadykov, T. G. Kuznetsova, V. A. Matyshak, A. Ya. Rozovskii, V. V. Lunin and J. R. H. Ross NO _x SELECTIVE REDUCTION BY HYDROCARBONS IN THE EX- CESS OF OXYGEN ON ZR-PILLARED CLAYS: MAIN FEATURES OF THE REACTION MECHANISM AND PERFORMANCE IN REALISTIC FEEDS	144
S. Marković, D. Milenković and Z. Marković COMPUTATIONAL INVESTIGATION OF A NUCLEOPHILIC ADDI- TION REACTION	147
Z. Marković, S. Marković and N. Begović MECHANISM OF THE KOLBE-SCHMITT REACTION WITH DIFFER- ENT ALKALI METAL PHENOXIDES	150

G. Munteanu and N. Stănică MONTE CARLO SIMULATIONS OF THE MAGNETIC PROPERTIES OF SOME HARD-SOFT COMPOZITES	153
T. Novaković, Lj. Rožić, S. Petrović and Z. Vuković THE FRACTAL DIMENSIONS OF BENTONITE CLAY DETERMINED BY MAHNKE AND MÖGEL METHOD	156
J. Kiurski, D. Obadović and R. Marinković-Nedučín ENERGIES OF ELECTRONIC STATES OF NI(II) ION IN NiO-Al ₂ O ₃ CATALYST PREPARED BY MECHANICAL POWDER MIXING	159
D. Lončarević, J. Krstić, P. Banković, V. Drobnjak and Ž. Čupić TEMPERATURE DEPENDANCE OF CYCLOHEXANE PARTIAL OXI- DATION IN PTFE REACTOR	162
M. Gabrovska, D. Nikolova, M. Stanković, R. Edreva-Kardjieva and D. Jovanović TEXTURE OF THE Ag-Ni/DIATOMITE PRECURSORS OF EDIBLE OIL HYDROGENATION CATALYSTS	165
M. Stanković, Z. Vuković and P. Banković CHARACTERIZATION OF PROMOTED Ni CATALYSTS SUPPORTED ON MAGNESIA BY CHEMISORPTION. EFFECTS OF PROMOTER ON Ni-CRYSTALLITE SIZE	168
Z. Cherkezova-Zheleva, M. Shopska, J. Krstić, I. Mitov and G. Kadinov STUDY OF THE DISPERSITY OF FE AND FEME (ME=PD, PT) SUP- PORTED SYSTEMS	171
M. Milojević, V. Dondur, Lj. Damjanović, V. Rakić, D. Arandelović, D. Đorđević and S. Nikolić-Mandić THE IMPROVED IRON-EXCHANGED ZEOLITIC MATERIALS AC- TIVE FOR H ₂ O ₂ DEGRADATION	174
S. M. Sunarić and S. S. Mitić KINETIC INVESTIGATION OF THE REACTION BETWEEN NEOMY- CIN, HYDROGEN PEROXIDE AND Cu(II) IN AQUEOUS SOLUTIONS	177
A. Milutinović-Nikolić, Z. Mojović, P. Banković and A. Rosić PILLARED INTERLAYERED CLAYS AS CATALYST IN THE PRES- ENCE OF HYDROGEN PEROXIDE	180
C. Blanco, V. Krstic, P. Carranceja, C. Pesquera and F.González MESOPOROUS MATERIALS AS SUPPORTS OF Rh CATA- LYSTS. CATALYTIC APPLICATION	183
B. Adnađević, J. Jovanović and M. Sindić KINETICS OF ACID CATALYZED SUCROSE HYDROLYSES IN THE MICROWAVE FIELD	186

A. Kostić, J. Jovanović, B. Adnađević and A. Popović KINETICS OF Cu^{2+} BINDING TO THE POLY(ACRYLIC ACID) HYDROGEL	189
L. Izrael-Živković, I. Karadžić and M.M.Vrvić SYNTHESIS OF METHYL-ESTHERS BY LIPASE-CATALYZED TRANSESTERIFICATION IN METHANOL	192
F. T. Pastor, G. A. Milovanović and M. Todorović KINETIC DETERMINATION OF THYROXINE TRACES BASED ON THE MANGANESE(III) METAPHOSPHATE-ARSENIC(III) REACTION IN THE PRESENCE OF ORTHOPHOSPHORIC ACID	195
St. Christoskova, M. Stoyanova, E. Manova, Z. Zheleva, D. Paneva, B. Kunev and I. Mitov MONO - AND BIMETALLIC SPINELS. PART II: CATALYTIC BEHAVIOUR IN H_2O_2 DECOMPOSITION REACTION	198
D.Vučinić and P. Lazić KINETICS OF ETHYLXANTHATE ADSORPTION ON Pb(II)-MODIFIED GALENA AND SPHALERITE	201
D.Ranković, N.Radić, B.Grbić, Z.Arsenijević and Ž.Grbavčić REMOVAL OF VOLATILE ORGANIC COMPOUNDS (VOCs) FROM ACTIVATED CARBON BY THERMAL DESORPTION AND CATALYTIC COMBUSTION	204
M. Gabrovska, Ts. Tzacheva, D. Lončarević, R. Edreva-Kardjjeva and D. Jovanović MORPHOLOGY STUDY OF THE Ni-Mg/SiO ₂ MATERIALS AS CATALYST PRECURSORS	207
J. Krstić, M. Gabrovska, D. Nikolova, N. Gavrilov, R. Edreva-Kardjjeva and D. Jovanović TEXTURE PROPERTIES OF Ni-Mg/SiO ₂ PRECURSORS AS EDIBLE OIL HYDROGENATION CATALYSTS	210
M. Stanković, L. Pezo, B. Kovacević, S. Stanojlović, M. Jovanović and D. Debeljković DISSOLUTION OF SiO ₂ IN NaOH AQUEOUS SOLUTION – KINETICS MODELS I –	213
D – Nonlinear Dynamics	217
G. Schmitz COMPLEX OSCILLATIONS AND CHAOS IN SPACES WITH MORE THAN THREE DIMENSIONS	219

M. K. Koleva and L. A. Petrov BOUNDEDNESS: THE ONTOLOGICAL CONCEPT BEHIND THE DETERMINISTIC CHAOS	230
I. Schreiber, O. Pešek, P. Špás, M. Voslař and L. Schreiberová STOICHIOMETRIC NETWORK ANALYSIS AND CLASSIFICATION OF A pH-OSCILLATOR	238
D. Bakeš, L. Schreiberová and I. Schreiber COMPLEX OSCILLATIONS OF A pH-OSCILLATOR	246
L. Schreiberová, O. Pešek and I. Schreiber DYNAMICAL PATTERNS OF A pH-OSCILLATOR IN MASS-COUPLED CELLS	249
S. Blagojević, N. Pejić, S. Blagojević, Ž. Čupić, S. Anić and Lj. Kolar-Anić ROLE OF Br_2O SPECIES IN THE MODEL OF BELOUSOV-ZHABOTINSKY REACTION	252
R. Cervellati and S. D. Furrow PRACTICAL APPLICATION OF AN OSCILLATING CHEMICAL SYSTEM	255
N. Pejić, S. Blagojević, S. Anić and V. Vukojević OPTIMIZATION OF CONDITIONS FOR QUANTITATIVE DETERMINATION OF MORPHINE USING NUMERICAL SIMULATIONS	258
N. I. Potkonjak, T. N. Potkonjak and S. N. Blagojević SOME NEW DETAILS OF ELECTROCHEMICAL OSCILLATIONS DURING THE PASSIVITY BREAKDOWN OF COPPER IN TRIFLUOROACETIC ACID	261
S. Jelić, Ž. Čupić and Lj. Kolar-Anić INFLUENCE OF THE FORM OF THE PERIODIC FUNCTION THAT DESCRIBES THE CIRCADIAN RHYTHM OF THE HPA SYSTEM ACTIVITY	264
S. Jelić SINGULARITY THEORY APPROACH APPLIED TO FOUR-DIMENSIONAL MODEL OF THE HYPOTHALAMIC-PITUITARY-ADRENAL SYSTEM ACTIVITY	267
A. L. Kawczyński, M. Leda and B. Legawiec BREAKING OF TRANSLATIONAL SYMMETRY OF A TRAVELING PLANAR IMPULSE IN A 2D TWO-VARIABLE REACTION-DIFFUSION MODEL	270

J. Čejková, Ch. Hilgardt and H. Ševčíková TIMING OF DYNAMIC REGIMES IN DICTYOSTELIUM DISCOIDEUM (Dd) UNDER EFFECTS OF EXTERNAL CAMP	273
Č. N. Radenović, M. V. Beljanski, N. Maksimova and G. V. Maksimov CHARACTERISTICS OF LITHIUM OSCILLATORY TRANSPORT TROUGH EXCITED BIOMEMBRANE	276
P. M. Mitrašinić SYSTEMS BIOLOGY STUDIES OF REACTIVE OXYGEN SPECIES (ROS)-MEDIATED APOPTOSIS	279
E – Electrochemistry	283
J. Barek NEW ELECTRODE MATERIALS FOR VOLTAMMETRY AND AMPEROMETRY	285
Lj. Jovanović ELECTROCHEMISTRY OF VITAMIN B6 VITAMERS, THEIR DERIVATIVES AND METAL COMPLEXES	290
B. N. Grgur ZINC-POLYANILINE BATTERIES BASED ON CHLORIDE/CITRATE ELECTROLYTES	296
G. Papakonstantinou, K.S.Nagabhushana, H. Bönnemann, M. M. Jakšić and S.G. Neophytides INTERFACING SURFACE CATALYSIS AND ELECTROCATALYSIS FOR THE SUCCESSFUL IMPLEMENTATION OF PEM FUEL CELLS: THE CASE OF PtMo CATALYSTS	304
D. Ilić NANOMATERIALS FOR ELECTROCHEMICAL SYSTEMS WITH LITHIUM INTERCALATION-ANODES	311
B. Šljukić, C. E. Banks and R. G. Compton COMPOSITES OF MULTI-WALLED CARBON NANOTUBES AND ELECTROCHEMICALLY POLYMERIZED POLY(VINYLFERROCENE) AND THEIR APPLICATION	314
S. Mentus and A. Abu Rabi HYDROXIDE ION OXIDATION ON BARE AND NAFION COVERED NOBLE METAL SURFACES	317
Z. Mojović, S. Mentus, I. Krstić and A. Rosić THIN LAYER OF NIO-MODIFIED 13 X ZEOLITE ON GLASSY CARBON SUPPORT AS AN ELECTRODE MATERIAL IN AQUEOUS SOLUTIONS	320

D. Todorović, Z. Dražić-Janković, Lj. M. Ignjatović and D. A. Marković DETERMINATION OF THE OPTIMAL GELATIN SOLUTION FOR INHIBITION OF Cu CORROSION	323
K. R. Kumrić, T. M. Trtić-Petrović and J. J. Čomor VOLTAMMETRIC DETERMINATION OF LUTETIUM	326
B. Jocić, M. M. Aleksić, M. Zečević and V. Kapetanović VOLTAMMETRIC AND HPLC MONITORING OF CEFOTAXIME AND ITS MAIN METABOLYTE DESACETYLCEFOTAXIME IN REAL URINE SAMPLE	329
I. Cekić, D. M. Minić, V. Jovanović and R. Marković ELECTROCHEMICAL BEHAVIOUR OF 5-SUBSTITUTED 2-ALKYLIDENE-4-OXO-THIAZOLIDINE DERIVATIVES	332
N. I. Potkonjak, V. M. Nikolić, S. N. Blagojević, B. R. Simonović, T. N. Potkonjak, M. P. Marčeta-Kaninski and D. Ž. Sužnjević ENHANCEMENT OF THE ELECTROCATALYTIC ACTIVITY OF Ni ELECTRODE FOR HYDROGEN EVOLUTION BY ELECTRODEPOSITED V AND Co ON ITS SURFACE	335
F – Biophysical Chemistry, Photochemistry, Radiation Chemistry	339
S. Radaković, I. Spasojević and G. Bačić CAN CHANGES OF ERYTHROCYTE MEMBRANE RHEOLOGY ACCOUNT FOR CARDIOTOXICITY OF CYTOSTATIC DRUGS? A CISPLATIN STUDY.	341
A. Nićiforović, M. Adžić, B. Zarić, V. Vučić and M. B. Radojčić ADJUVANT ANTIPROLIFERATIVE AND CYTOTOXIC EFFECT OF ALOIN IN IRRADIATED HeLaS ₃ CELLS	344
M. Zloh, S. Balan, S. Shaunak and S. Brocchini THE EFFECT OF HYDROGEN BONDING INTERACTIONS ON THE REACTIVITY OF A NOVEL DISULFIDE-SPECIFIC PEGYLATION REAGENT	347
A. Popović-Bijelić, G. Bijelić, Lj. Kolar-Anić and V. Vukojević MODELING THE TEMPERATURE DEPENDENCE OF CATALASE-LIKE ACTIVITY OF HORSERADISH PEROXIDASE	350
O. Čudina, S. Vladimirov, M. Čomor and I. Janković PARTITIONING OF QUINAPRIL ANION BETWEEN CETYLTRIMETHYLAMMONIUM BROMIDE MICELLES AND WATER	353
T. Momić, J. Savić and N. Miljević PROTOLYTIC EQUILIBRIA AND STABILITY OF QUERCETIN IN AQUEOUS SOLUTIONS	356

T. Momić, Z. Vujčić and V. Vasić INHIBITION OF MYELOPEROXIDASE BY QUERCETIN	359
A. Rakić and P.M. Mitrašinović APPLICATIONS OF THE STATE-OF-THE-ART COMPUTATIONAL METHODS IN THE MODELING OF rRNA STRUCTURE	362
G. V. Maksimov, C. N. Radenovic, A. A. Churin and V. V. Volkov APPLICATION OF RESONANCE RAMAN SPECTRA OF CAROTENE FOR PROBING O ₂ ACTION ON NERVE CELL	365
S. Stojanović, V. B. Medaković and G. Predović NON-CONVENTIONAL INTERACTIONS IN PROTEINS CONTAINING PORPHYRINE	368
S. Gorjanović and R. Gorjanović IDENTIFICATION OF β-GLUCOSIDASE AND PEROXIDASE FROM DOMESTIC BARLEY GRAIN	371
V. Pavelkić, K. Gopčević, D. Krstić and M. Ilić TEMPERATURE AND Al ³⁺ INFLUENCE ON ELECTROPHORETIC MOBILITY OF PORCINE PEPsin	374
S. Gorjanović, M. V. Beljanski, M. Gavrović-Jankulović and F. Bejosano ISOLATION AND IDENTIFICATION OF THAUMATIN LIKE PRO- TEINS FROM DOMESTIC BARLEY GRAIN	377
S. Ostojić, V. Dragutinović, M. Kićanović and B. R. Simonović ZINC BINDING AND THERMOSTABILIZATION OF BOVINE SERUM ALBUMIN (BSA) STUDIED BY DSC	380
S. O. Podunavac-Kuzmanović and D. M. Cvetković ANTIBACTERIAL SCREENING OF NICKEL(II) AND ZINC(II) COM- PLEXES WITH SOME 2-METHYLBENZIMIDAZOLES	383
S. O. Podunavac-Kuzmanović and D. M. Cvetković ANTIBACTERIAL INVESTIGATION OF COBALT(II) AND ZINC(II) COMPLEXES WITH N-1-SUBSTITUTED BENZIMIDAZOLES	386
S. O. Podunavac-Kuzmanović and S.L. Markov ANTIMICROBIAL EVALUATION OF COPPER(II) COMPLEXES WITH SOME 2-AMINOBENZIMIDAZOLES	389
S. Gorjanović, M. V. Beljanski, R. Gorjanović and G. Gojgić-Cvijanović ANTIMICROBIAL ACTIVITY OF BARLEY GRAIN THAUMATIN LIKE PROTEINS	392
M. Milošević, M. Demajo and A. Horvat EFFECT OF EDTA ON THE INHIBITION OF RAT MYOMETRIAL ecto- ATPase ACTIVITY IN THE PRESENCE OF HEAVY METAL IONS I. MERCURY	395

M. Milošević, A. Banjac, M. Demajo and A. Horvat EFFECT OF EDTA ON THE INHIBITION OF RAT MYOMETRIAL ecto-ATPase ACTIVITY IN THE PRESENCE OF HEAVY METAL IONS II. CADMIUM	398
D. Krstić, M. Bavcon-Kralj, P. Trebše, M. Čolović, K. Krinulović and V. Vasić INHIBITION OF AChE BY MALATHION AND SOME STRUCTURALLY SIMILAR COMPOUNDS	401
S. S. Konstantinović, D. Z. Marković and B. C. Stojčeva-Radovanović PHOTODEGRADATION OF ISATIN-3-THIOSEMICARBAZONE	404
D. Cvetković and D. Marković UV-EFFECTS ON ANTIOXIDANT CAPACITIES OF β -CAROTENE AND LYCOPENE IN THE PRESENCE OF LECITHIN	407
J. Zvezdanović and D. Marković UV-IRRADIATION INDUCED CHLOROPHYLLS BLEACHING IN PIGMENTS EXTRACTS	410
N. Veličković, A. D. Đorđević and N. Popović LOW DOSE GAMMA-IRRADIATION ALTERS THE EXPRESSION OF P53 PROTEIN IN THE RAT HIPPOCAMPUS	413
M. Adžić, B. Zarić, A. Nićiforović and M. B. Radojčić REDOX-SENSITIVE TRANSCRIPTION FACTOR NF κ B IN BRAIN OF STRESSED WISTAR RATS	416
I. Stanojević, A. D. Đorđević, A. Banjac and A. Horvat LOW-DOSE IONIZING IRRADIATION AFFECTS NTPDase ACTIVITY IN NEURONAL CELLS OF YOUNG FEMALE RATS	419
J. Prokopović, M. Adžić, A. Nićiforović, V. Vučić, B. Zarić and M. B. Radojčić SUPEROXIDE DISMUTASES IN RADIORESISTANT PC-3 HUMAN PROSTATE CARCINOMA CELLS	422
N. Veličković, A. D. Đorđević, N. Popović and M. Demajo DIFFERENT INDUCTION OF DUAL CORTICOSTEROID RECEPTOR SYSTEM IN THE RAT HIPPOCAMPUS FOLLOWING GAMMA RADIATION	425
J. Požega, L. Korićanac, I. Petrović and A. Ristić-Fira EFFECTS OF SHORT TIME EXPOSURE OF HTB140 MELANOMA CELLS TO FOTEMUSTINE AND DACARBAZINE	428

N. S. Nikolic, M. D. Mirkovic, S. D. Vranješ-Đuric and D. D. Đokic EVALAUTION OF RADIOIODINATION OF SYNTHESISED meta- IODOBENZYLGUANIDINE CATALYZED BY in situ GENERATED Cu(I)	431
D. Đokić, D. Janković, Lj. Stamenković, N. Nikolić, M. D. Mirković and I. Pirmettis ^{99m} Tc-HEXAKIS-(2-METOXY-ISOBUTYL-ISONITRILE) (^{99m} Tc-MIBI) A NEW MYOCARDIAL IMAGING agent: SYNTHESIS OF MIBI, OPTI- MISING CONDITIONS FOR RADIOLABELLING WITH ^{99m} Tc AT HIGH RADIOCHEMICAL PURITY AND IN VIVO BEHAVIOR	434
D. Filipović THE LEVEL OF CUZN SUPEROXIDE DISMUTASE IN LIVER OF RATS EXPOSED TO ACUTE, CHRONIC OR COMBINED STRESS	437
M. Simonović, B. R. Simonović, S. Zlatanovic-Milošević, E. Spillner and R. Bredehorst DETECTION OF TNT-ANALOG TNP-TRIS IN IMMUNOASSAY WITH TWO RECOMBINANT SCFV-ANTIBODIES	440
G – Radiochemistry and Nuclear Chemistry	443
S. Vranješ, N. Nikolić, M. D. Mirković, D. Janković and G. J. Bayer FACTORS AFFECTING LABELLING YIELD OF ¹¹¹ In-DTPA-BSA	445
D. Todorović, I. Petrović, G. Cuttone and A. Ristić-Fira PROLIFERATION CAPACITY AND p53 EXPRESSION OF HTB140 CELLS AFTER PROTON IRRADIATION	448
L. Korićanac, I. Petrović, G. Privitera, G. Cuttone and A. Ristić-Fira SENSITIVITY OF HTB140 CELL EXPOSED TO PROTONS AND AL- KYLATING AGENTS	451
S. Dragović and A. Onjia PATTERN RECOGNITION METHODS FOR CLASSIFICATION OF SOILS BASED ON THEIR RADIONUCLIDE CONTENT	454
J. Vučina, D. Lukić, S. Milonjić and M. Stoiljković PREPARATION OF CONCENTRATED RHENIUM SOLUTIONS	457
D. Janković, I. Pirmettis, Lj. Matović, D. Đokić and S.Vranješ TRICARBONYLTECHNETIUM (I) LABELLED LIGANDS WITH NSO DONOR ATOM SET: In vitro and in vivo evaluation	460
B. Šećerov, M. Daković, M. Sarić, G. Bačić and N. Borojević DOSIMETRY USING HS GafChromic FILMS THE INFLUENCE OF READOUT LIGHT ON SENSITIVITY OF DOSIMETRY	463

H – Materials Science	467
D. Batani, H. Stabile, M. Tomasini, G. Lucchini, F. Canova, M. Koenig, A. Benuzzi, H. Nishimura, Y. Ochi, J. Ullschmied, J. Skala, B. Kralikova, M. Pfeifer, T. Mocek, A. Präg, T. Hall, P. Milani, E. Barborini and P. Piseri	469
HIGH PRESSURE BEHAVIOUR OF CARBON BY LASER-GENERATED SHOCKS	
J. M. Nedeljković, M. Marinović-Cincović and J. Kuljanin-Jakovljević	472
POLYMER BASED NANOCOMPOSITES	
S. T. Wellinghoff, D. P. Hanson, P. M. Thompson, S. M. Crumlett, B. R. Furman, B. K. Norling and H. R. Rawls,	479
ADVANCED DENTAL RESTORATIVE COMPOSITES UTILIZING LOW POLYMERIZATION SHRINKAGE LIQUID CRYSTALLINE MONOMERS	
A. M. Spasić	486
CLASSIFICATION OF FINELY DISPERSED SYSTEMS: PHYLOSOPHICAL BREAKPOINTS	
Z. S. Nikolic and M. Yoshimura	489
THEORETICAL STUDY OF SOLIDIFIED SAMPLE INFLUENCED BY MELT SUPERHEAT	
Z. S. Nikolic and M. Yoshimura	492
NUMERICAL PREDICTION OF HEAT TRANSFER BETWEEN SAMPLE AND SUBSTRATE DURING RAPID SOLIDIFICATION	
Z. S. Nikolić	495
MODELING PORE GROWTH BY COALESCENCE FOR COMPUTER STUDY OF LIQUID PHASE SINTERING	
M. Stevanović, N. Ignjatović, D. Miličević and D. Uskoković	498
PREPARATION OF COMPOSITE MATERIAL BCP/DLPLG WITH A DIFFERENT CONTENT OF CERAMIC AND POLYMER COMPONENT	
T. Brdarić, J. Grbović-Novaković, N. Novaković and S. Mentus	501
THE STUDY OF NANODISPERSED COMPOSITE MgH ₂ -Ti: EXPERIMENT AND THEORY	
J. Đustebek., J. Cvetičanin, V. Đorđević, S. Veličković, M. Veljković and O. Nešković	504
TIMS AND MALDI TOF OF ENDOHEDRAL ^{99m} Tc@C ₆₀ METALLO-FULLERENE	

N. Časić, M. Stoiljković, M. M. Kuzmanović, M. Novaković and M. Popović AN SIMPLE TECHNIQUE FOR SYNTHESIS OF CARBON NANOTUBES BY UNDERWATER ARC PLASMA	507
J. Krstić, O. Terzić, N. Vukelić and M. Mitrić INFLUENCE OF SILVER ADDITION ON TEXTURAL PROPERTIES OF NEW SYNTHETIC ACTIVATED CARBON	510
E. Manova, D. Paneva, Z. Zheleva, B. Kunev, I. Mitov, M. Stoyanova and St. Christoskova MONO- AND BIMETALLIC SPINELS. PART I: MECHANOCHEMICAL SYNTHESIS	513
D. Jugović, M. Mitrić, N. Cvjetičanin, M. Miljković, and D. Uskoković SYNTHESIS AND STRUCTURE OF $\text{LiMn}_{2-x}\text{Zn}_x\text{O}_4$ THROUGH ULTRASONIC SPRAY PYROLYSIS	516
S. Marković, Lj. Kandić, M. Mitrić, G. Starčević and D. Uskoković ULTRASOUND MODIFICATIONS OF PHYSICAL PROPERTIES OF BaTiO_3 POWDERS	519
O. A. Kovačević, B. T. Kovačević, D. Arandelović, N. L. Lazić, L. Pezo and Ž. Lj. Tešić CHANGES OF NANO PARTICLE SIZES IN THERMALY TREATED PRECIPITATED SILICA	522
A. Devečerski, M. Logar, M. Pošarac, T. Brdarić, D. Božić and B. Matović, SYNTHESIS OF FIBROUS SiC FROM NATURAL PRECURSOR	525
Z. Jakšić, D. Vasiljević-Radović and M. Sarajlić ANALYTE-TARGETED PATTERNING OF SUBWAVELENGTH APERTURE ARRAYS WITH EXTRAORDINARY OPTICAL TRANSMISSION FOR ENHANCED BIOSENSING	528
B. Nedić, V. Dondur, A. Kremenović and R. Dimitrijević Yb^{3+} DOPED DYPHILLOSILICATES PREPARED BY THERMALY INDUCED PHASE TRANSFORMATION OF ZEOLITES	531
M. Pošarac, S. Bošković, A. Devečerski, T. Husović and B. Matović PHASE EVOLUTION OF Si_3N_4 WITH Mg -EXCHANGED ZEOLITE ADDITIVE	534
M. S. Trtica and B. M. Gaković SURFACE MODIFICATIONS OF TiN COATING BY PULSED TEA CO_2 LASER	537

A. Egelja, J. Dukić, S. Bošković, A. Radosavljević-Mihajlović and B. Matović	540
SYNTHESIS OF CRYSTALLINE SILICON OXYNITRIDE COMPOSITES	
D. M. Minić, A. M. Maričić and R. Z. Dimitrijević,	543
PHASE TRANSFORMATION OF $\text{Co}_{70}\text{Fe}_5\text{Si}_{10}\text{B}_{15}$ AMORPHOUS ALLOY INDUCED BY HEATING	
S. R. Grujić, N. S. Blagojević, M. B. Tošić, V. D. Živanović and J. D. Nikolić	546
NUCLEATION BEHAVIOR OF POTASSIUM TITANIUM GERMANATE GLASS STUDIED BY DIFFERENTIAL THERMAL ANALYSIS	
M. B. Tošić, S. R. Grujić, N. S. Blagojević, V. D. Živanović and J. D. Nikolić	549
THE EFFECT OF THE FREE ENERGY CHANGE ON CRYSTALLIZATION IN GERMANATE GLASS	
D. M. Todorović and T. Grozdić	552
PLASMAELASTIC WAVES IN SEMI-INFINITE SEMICONDUCTOR	
S. Despotović, D. Babić and M. Isaković	555
INVESTIGATION OF MINERALOGICAL CHANGES IN BRICK CLAY ZORKA OF LOCALITY DONJE CRNILJEVO DEPENDING ON FIRING TEMPERATURE	
I – Solid State Physical Chemistry	559
Z. Miladinović and J. Zakrzewska	561
KINETIC APPROACH TO THE ZEOLITE A CRYSTALLIZATION USING IN SITU ^{27}Al NMR SPECTROSCOPY	
S. Damyanova, K. Arishtirova, B. Pawelec, J. L. G. Fierro and L. Petrov	564
SURFACE CHARACTERIZATION OF Ni-BASED CATALYSTS FOR DRY REFORMING	
A. Predoeva, E. Gaigneaux, S. Damyanova and L. Petrov	567
STRUCTURAL TRANSFORMATION OF MIXED WV AND MoV HETEROPOLY COMPOUNDS UPON HEATING	
M. Milić, V. M. Matić and N.Đ.Lazarov	570
CVM STUDY OF CHARGE TRANSFER IN $\text{YBa}_2\text{Cu}_3\text{O}_{6+x}$ MATERIAL	
V. Kusigerski, N. Cvjetičanin, D. Marković, V. Spasojević and J. Blanuša	573
RE-ENTRANT SPIN GLASS TRANSITION IN $\text{LiCr}_{0.175}\text{Mn}_{1.825}\text{O}_4$ SPINEL	

J – Macromolecular Physical Chemistry	577
G. Ćirić-Marjanović, Z. Jovanović, B. Marjanović and I. Juranić SYNTHESIS OF CONDUCTIVE POLYANILINE NANOPARTICLES BY OXIDATION OF ANILINE WITH CERIUM(IV) SULFATE	579
G. Ćirić-Marjanović, A. Janošević, B. Marjanović, M. Trehová, J. Stejskal and P. Holler CHEMICAL OXIDATIVE POLYMERIZATION OF DI-ANILINIUM 5- SULFOSALICYLATE	582
A. Nastasović, Z. Sandić, Lj. Malović, D. Jakovljević and J. Marković STUDY OF COPPER ADSORPTION ON AMINOFUNCTIONALIZED MACROPOROUS POLY(GMA-co-EGDMA)	585
A. Nastasović, S. Kljajević, D. Jakovljević, Z. Vuković and J. Marković KINETICS OF HEAVY METAL SORPTION ON MACROPOROUS VI- NYLPYRIDINE BASED COPOLYMER	588
S. Lukić, A. Milutinović-Nikolić, K. Asanović and G. Popović HEALTHCARE AND HYGIENE PRODUCTS MADE OF NONWOVEN TEXTILE MATERIALS	591
G. Marković, M. Marinović-Cincović and B. Radovanović, CURE CHARACTERISTICS OF RECYCLED RUBBER POWDER FILLED STYRENE BUTADIENE /CHLOROSULPHONATED POLY- ETHYLENE RUBBER BLENDS	594
K – Environmental Protection	597
A. Stamatović INSTRUMENTAL ASPECTS OF THE ENVIRONMENTAL PROTEC- TION	599
N. Miljević ENVIRONMENTAL ISOTOPE INVESTIGATION OF THE RIVER CATCHMENTS	607
P. Manojlović CHEMICAL THREATS	615
M. Tomašević, Z. Vukmirović, S. Rajšić, M. Tasić and B. Stevanović ACCUMULATION OF TRACE ELEMENTS IN TREE LEAVES IN RE- LATION TO ATMOSPHERIC CONCENTRATIONS	621
S. Rajšić, Z. Mijić, M. Tasić, D. Đorđević, M. Radenković and J. Joksić HEAVY METAL CONTENT OF PM10 AND PM2.5 WITHIN URBAN AREA OF BELGRADE	624

M. Aničić, M.V. Frontasyeva, M. Tomašević and A. Popović ASSESSMENT OF TRACE ELEMENT ATMOSPHERIC DEPOSITION IN BELGRADE AND SOURCE APPORIONMENT USING MOSS AND INAA	627
V. Ž. Jovanović, P. A. Pfenđt and A. J. Jovanović CHARACTERISTICS OF WINTERTIME POLYCYCLIC AROMATIC HYDROCARBON ASSEMBLAGE IN THE SUBURBAN ADRIATIC ATMOSPHERE	630
D. Golobočanin, A. Žujić and N. Miljević PRECIPITATION CHEMISTRY IN THE VELIKA MORAVA CATCH- MENT	633
A. Moise, E. Mihaila and I. Ciurcanu A SPECTROMETRIC METHOD FOR BROMATE ANALYSIS IN DRINKING WATER	636
A. Čučulović, M. S. Pavlović, D. Veselinović and Š. S. Miljanić THE EFFECT OF SIMULATED ACID RAIN ON METAL DESORPTION FROM CETRARIA ISLANDICA	639
D. Veselinović, D. A. Marković, A. Savin, S. Filip and D. Bengin THE CORRELATION BETWEEN THE AMOUNTS OF CADMIUM IN WATER AND IN SOIL	642
S. Matijašević, A. Daković, M. Stojanović and D. Ileš URANIUM(VI) ADSORPTION ON ACID MODIFIED CLINOPTILOLITE / HEULANDITE RICH TUFF	645
V. Jovanović, G. Jordanov, V. Dondur, Lj. Damjanović and V. Rakić REMOVAL OF PESTICIDES FROM AQUEOUS SOLUTION BY FUNC- TIONALIZED ZEOLITES	648
Lj. Janković, S. Dragović and G. Bačić ESTIMATION OF EXTERNAL GAMMA EXPOSURE FROM SURFACE SOILS IN SERBIA	651
M. Radenković, A. Kandić, I. Vukanac J. Joksić and D. Đorđević CHEMICAL AND RADIOCHEMICAL FRACTIONATION OF DE- PLETED URANIUM IN CONTAMINATED SOILS	654
D. V. Šojić, N. D. Abazović, V. B. Anderluh, B. F. Abramović and M. I. Čomor VISIBLE-LIGHT PHOTOCATALYTIC DEGRADATION OF HERBICIDE MECOPROP IN N-DOPED TiO ₂ SUSPENSIONS	657
V. Batas, S. Janković, S. Stefanović, R. Petronijević, T. Radičević and A. Spirić DETERMINATION OF FENICOLS IN MILK BY LC-MS/MS	660

S. S. Milovanović, M. A. Lješević and B. M. Babić IMPACT OF THE PROCESS OF POLYMERIZATION OF POLYOL AND TOLUEN DIISOCYANATE ON THE ENVIRONMENT	663
A.M. Žujić, Z.J. Gršić, and B.B. Radak SPATIAL DISTRIBUTION OF BELGRADE AIR POLLUTION	666
L – Phase Boundaries	669
Z. Jakšić, Z. Đurić, O. Jakšić, I. Jokić and M. Frantlović ADSORPTION-DESORPTION NOISE IN SURFACE PLASMON RESO- NANCE SENSORS	671
D. A. Pichugina, A. F. Shestakov and N. E. Kuz'menko OXYGEN CHEMISORPTION ON GOLD NANOCUSTER: QUANTUM- CHEMICAL STUDY	674
B. Janković and B. Adnađević NON-ISOTHERMAL THERMOGRAVIMETRIC ANALYSIS OF THE PARTIAL REDUCTION OF NICKEL OXIDE BY HYDROGEN	677
V. Rac, R. Hercigonja, V. Rakić and A. Auroux THE ADSORPTION PROPERTIES OF Mn-EXCHANGED ZSM-5 ZEO- LITES	680
D. Todorović, Z. Dražić-Janković, Lj.M. Ignjatović and D.A. Marković THE DETERMINATION OF THE GELATIN ADSORPTION DEGREE ON THE COPPER AND BRASS	683
M – Complex Compounds	687
G. V. Janjić, M. K. Milčić, S. D. Zarić STUDY ON INTERACTIONS OF COORDINATED WATER WITH PHENYL GROUP IN CRYSTAL STRUCTURES OF METAL COM- PLEXES	689
D. N. Sredojević, Z. D. Tomić and S. D. Zarić STACKING INTERACTIONS BETWEEN CHELATE AND PHENYL RINGS IN SQUARE-PLANAR COMPLEXES OF Cu, Ni, Pt AND Pd	692
A. Vujačić, V. Vasić, J. Savić and S. Sovilj MECHANISM OF COMPLEX FORMATION BETWEEN [AuCl ₄] ⁻ AND L-METHIONINE	695
V. M. Jovanović, K. Babić-Samardžija and S. P. Sovilj CORRELATION BETWEEN STRUCTURAL PROPERTIES AND INHI- BITION EFFICIENCY OF SOME COBALT(III) COMPLEXES USING MOLECULAR MODELING CALCULATIONS	698

V. B. Medaković, M. K. Milčić and G. A. Bogdanović STUDY OF C–H... π INTERACTIONS WITH PYRROLE AND CHELATE RINGS IN METAL-PORPHYRIN COMPLEXES	701
M. K. Milčić, V. B. Medaković and S. D. Zarić THE NATURE OF CH/ π INTERACTIONS IN TRANSITION METAL COMPLEXES	704
L. Molnár-Hamvas, E. Börcsök, R. Csonka-Rákosa, J. Molnár and K. Németh INVESTIGATION OF ALUMINIUM COMPLEXES OF FLAVONOLS	707
N. R. Filipović, M. B. Rajković, T. R. Todorović, D. M. Sladić, I. T. Novaković and K. K. Anđelković SYNTHESIS, CHARACTERIZATION AND BIOLOGICAL ACTIVITY EVALUATION OF Zn(II), Pd(II) AND Pt(II) COMPLEXES WITH HETEROCYCLIC HYDRAZONE LIGANDS	710
G. Vučković, S. B. Tanasković, M. Antonijević-Nikolić and D. D. Radanović SYNTHESIS AND STUDY OF THE COMPLEX $[\text{Co}_2(\text{Cl})_2\text{tpmc}](\text{BF}_4)_2$	713
B. B. Krajčinović, G. N. Kaluđerović, D. Steinborn, Ch. Wagner, K. Merzweiler, S. R. Trifunović, Z. M. Miodragović and T. J. Sabo COMPLEX COMPOUNDS OF Pd(II) AND O ₃ O'-DIISOPROPYL-(S,S)-ETHYLENEDIAMINE-N,N'-DI-2-PROPANOATO LIGAND	716
G. S. Nikolić, Ž. Mitić, M. Cakić and Lj. Ilić STUDY OF COPPER(II)-DEXTRAN COMPLEXES STABILITY BY CONDUCTOMETRY METHOD	719
G. S. Nikolić, M. Cakić, Ž. Mitić and Lj. Ilić COPPER(II) COMPLEXES OF REDUCED LOW-MOLAR DEXTRAN: A DECONVOLUTED LNT-FTIR STUDY	722
N – General Physical Chemistry	725
P. I. Premović Geochemistry of “Impact Layer” of the Cretaceous-Tertiary Boundary (KT) Fish Clay At Højerup (Stevns Klint, Denmark)	727
R. Ninković, J. A. Rard, J. Miladinović, M. Todorović and S. Grujić THE FORMATION OF $\text{ZnCl}^+(\text{aq})$ ION-PAIRS IN SOLUTIONS OF $\text{ZnCl}_2(\text{aq})$ AT $T = 298.15 \text{ K}$	730
D. Stanisavljev, T. Grozdić, M. Marčeta-Kaninski, A. Đorđević and D. Stojić MICROWAVE ASSISTED ELECTROLYSIS OF ALKALINE WATER SOLUTION	733

A.V. Dremetsika, P. A. Siskos and N. A. Katsanos EXPERIMENTAL DETERMINATION OF ADSORPTION ENERGIES, LOCAL MONOLAYER CAPACITIES AND LOCAL ADSORPTION ISO- THERMS FOR ORGANIC ACID-COPPER SYSTEMS	736
G. Popović and M. Čakar STUDY ON PROTOLYTIC EQUILIBRIA OF LORATADINE AND DE- SLORATADINE	739
Z. Vujić, V. Kuntić, B. Ivković and K. Ilić STATISTICAL OPTIMIZATION APPLIED TO SIMULTANEOUS DE- TERMINATION OF MAPROTILINE, DESIPRAMINE AND MO- CLOBEMIDE BY RP-HPLC	742
D. Tošković, M. B. Rajković, D. Stanojević and Lj. Vasiljević GALLIUM EXTRACTION FROM DECOMPOSED BAYER'S ALKA- LINE SOLUTIONS	745
M. M. Krsmanović, B. Z. Veličković, N. N. Mišković and P. I. Premović Ni AND Co IN THE SMECTITE FRACTION OF THE CRETACEOUS- TERTIARY (KT) BOUNDARY FISH CLAY NEAR RØDVIG (STEVNS KLINT, DENMARK)	748
N. D. Nikolić, B. Ž. Todorović, P. I. Premović and M. S. Pavlović THE CRETACEOUS-TERTIARY BOUNDARY FISH CLAY AT HØJE- RUP (STEVNS KLINT, DENMARK): Ni IN THE BIOGENIC CALCITE- RICH FRACTION	751
G. M. Nikolić, R. S. Nikolić and J. M. Perović THE INFLUENCE OF ortho-EFFECT ON THE EXTRACTION OF CRE- SOLS AND DIHYDROXYBENZENES BY ETHERS	754
M. B. Rajković, Č. Lacnjevac, D. Tošković and D. Stanojević THE CONCEPT OF THE PILOT-PLANT IN THE AIM TO THE WET- PROCESS DERIVED H ₃ PO ₄ FOR COMMERCIAL PRODUCTION OF PHOSPHATE SALTS	757
O – Education	761
T. Halaši CONTRIBUTION TO THE BIOGRAPHY OF THE FIRST NOBEL PRIZE WINNER AND PHYSICAL CHEMIST Jacobus Henricus Van't Hoff	763

Plenary Lectures

(PL)

CHEMICAL OXYGEN-IODINE LASER: RECENT ADVANCES AS A CHEMICAL DEVICE

Masamori Endo

*Department of Physics, School of Science, Tokai University,
1117 Kitakaname, Hiratsuka 259-1292, Japan.*

Abstract

Recent advances of Chemical Oxygen-Iodine Laser (COIL) are reviewed. In this paper, developments of COIL as a unique chemical device, whose product is not chemical substance, but coherent photons, is emphasized. The key component of COIL is singlet oxygen generator (SOG). Unique principles of modern SOG are reviewed. For high-efficiency operation, rapid mixing of oxygen and iodine is of primarily important. Latest mixing enhancement techniques are reviewed. Applications of ultra high-power COIL are presented.

Introduction

Chemical oxygen-iodine laser (COIL) is an unusual chemical device. Although it comprises of series of chemical reaction chambers, the output of COIL is not a chemical substance. Instead, it produces extremely high-power, coherent photon flux in near-infrared region, at 1.315 μm . As a chemical laser, COIL is unique because it is the only electronic transition chemical laser. In other chemical lasers, population inversion is attained between vibrational levels of active molecule, thus the wavelength is in the range of mid-infrared. Because the operating wavelength is in the minimum loss band of silica optical fiber, long-distance fiber delivery of the laser output is possible and that makes COIL promising for unique applications.

Figure 1 shows the schematic drawing of typical modern supersonic COIL. It comprises of Singlet Oxygen Generator (SOG), iodine injector, supersonic expansion nozzle, laser cavity and vacuum pump. The energy source of the COIL is aqueous basic hydrogen peroxide (BHP). The gas-liquid surface reaction between BHP and gaseous chlorine produces electronically excited oxygen molecules, $\text{O}_2(^1\Delta)$ by the following overall reaction,



The $\text{O}_2(^1\Delta)$ is mixed with inert buffer gas such as nitrogen or helium, and transferred to the laser cavity under a low partial pressure (less than 2 kPa) to avoid col-

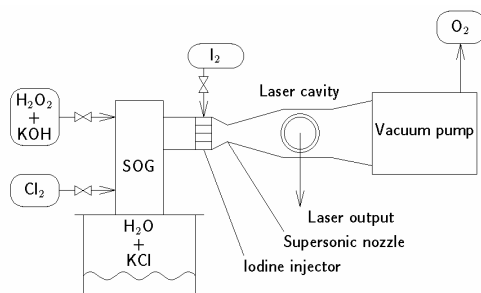
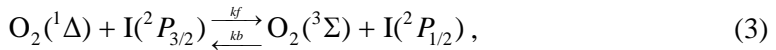


Fig. 1. Schematic drawing of a supersonic COIL device.

lisional deactivation. Then molecular iodine carried with inert gas is injected into the main flow, and the mixture is supersonically expanded. The iodine is dissociated by a complex, collisional process involving $O_2(^1\Delta)$ [1] described as



where $O_2(^3\Sigma)$ is a ground-state oxygen and n is believed to be 6 to 10. In the typical COIL operation, the ratio of I_2 to O_2 is approximately 2%. As shown above, part of the energy contained in $O_2(^1\Delta)$ is used to dissociate the iodine, and the rest is used to excite iodine atoms via the near-resonant energy transfer reaction



where the equilibrium constant $k_f/k_b = 0.75\exp[403/T]$. Population inversion is established between excited $I(^2P_{1/2})$ and ground-state $I(^2P_{3/2})$ to stimulate laser action,



Supersonic expansion of the laser medium is employed mainly to achieve a high efficiency since the gasdynamic cooling of the medium shifts the equilibrium condition of Eq. (3) to the right-hand side as indicated by

$$K_e = \frac{[O_2(^3\Sigma)][I(^2P_{1/2})]}{[O_2(^1\Delta)][I(^2P_{3/2})]} = 0.75\exp\left[\frac{403}{T}\right], \quad (5)$$

a change that results in a higher gain and more complete energy extraction from $O_2(^1\Delta)$. The figure-of-merit of COIL is measured by ‘‘Chemical Efficiency’’. It is defined as the number of emitted photons divided by the number of chlorine molecules input. Chemical efficiency of typical COIL is on the order of 20%.

The first COIL was demonstrated in 1977 by McDermott *et al.* at the U. S. Weapons Laboratory[2]. Figure 2 shows the photograph of the first COIL. Because he was a chemist, the first COIL apparatus looks quite familiar to them, but it does not resemble to any other lasers. Since the operational parameter was not optimized, the output power of the first COIL was merely 4 mW. In the first 10 years, COIL was scaled-up by simply increasing the size of the apparatus, and finally a 4.6 kW output was reported by an apparatus with a 4 m-width laser duct[3]. Further scale up by simply increase the size of the apparatus was prohibitive.

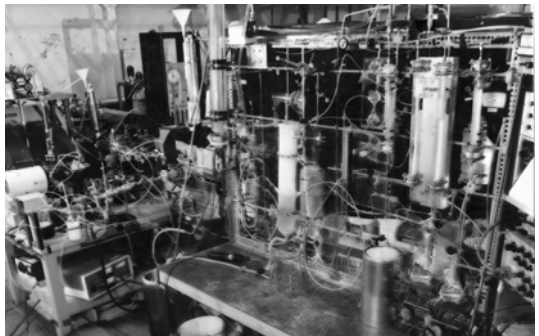


Fig. 2. The first COIL experimental apparatus[2].

In the mid 80’s a breakthrough technology, supersonic expansion was introduced. The merit of supersonic expansion was twofold. The gasdynamic cooling of the laser medium shifted the equilibrium of oxygen-iodine energy transfer more

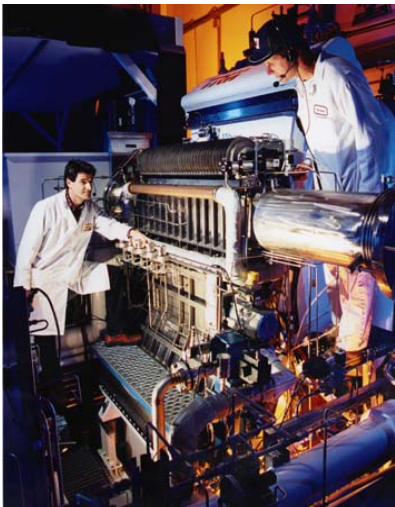


Fig. 3. A flight-weight, multi hundred-kW laser module.

favorable to energy extraction, and the energy flow density through gas transport duct was increased tenfold. A 1.6 kW apparatus was developed in the mid 80's[3], but the width of the flow duct was only 25 cm.

Another breakthrough in SOG technology boosts the output of the COIL tenfold. In the ancient SOG, the density of oxygen generation was restricted by the surface area of the gas-liquid interface. The bottleneck was broken by the advent of "Jet SOG" and it is currently employed most of the COIL devices around the world.

As of 2006, an output of several hundreds kW is demonstrated by a single COIL device, and multi-MW device is being developed by operating those devices in series. Figure 3 shows the multi hundred-kW COIL module

developed by TRW[4]. Its size is surprisingly compact compared to other ultra high-power lasers.

SOG Technology

Singlet oxygen is generated by the gas-liquid surface reaction between HO_2^- ion in the BHP and gaseous chlorine. The reaction cross section is so large that Cl_2 molecule could penetrate into the liquid phase only a few molecular layers if the surface HO_2^- ion is not depleted. Therefore, the technical challenges of SOG is summarized as:

1. Making as large surface area as possible in a unit volume of reaction chamber
2. Prevention of HO_2^- ion depletion by constant renewal of the gas-liquid interface

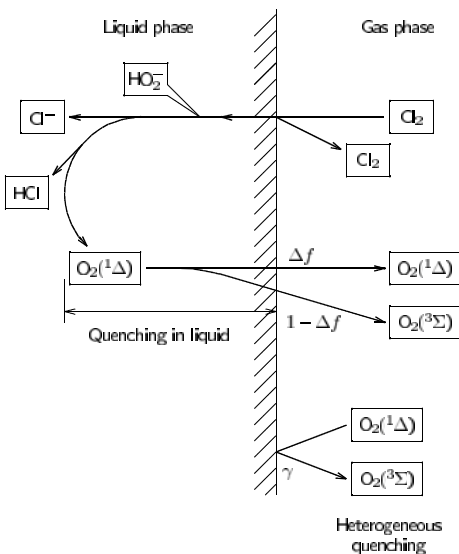


Fig. 4. Schematic drawing of the gas-liquid surface reaction of $\text{O}_2(^1\Delta)$ generation.

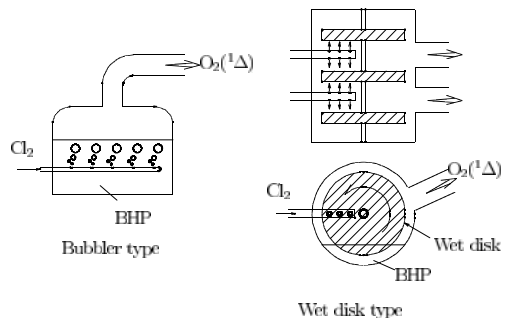
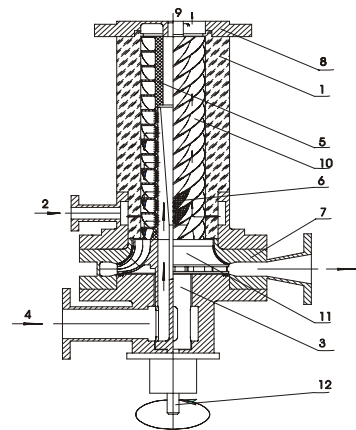


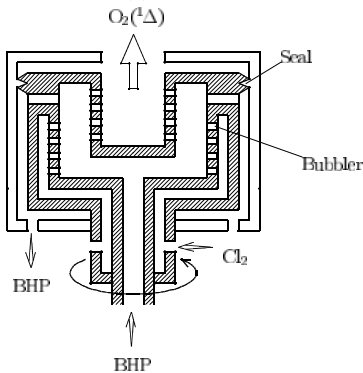
Fig. 5. Singlet oxygen generator of the early age.

3. Detachment of generated $O_2(^1\Delta)$ as fast as possible to prevent heterogeneous quenching at the gas-liquid interface

SOG technology has been evolved over the years from a very simple sparger to modern sophisticated chemical devices. Figure 5 shows the schematic drawing of early SOGs. The first successful SOG was based on simple sparger, in which bubbler is located near the liquid surface to prevent heterogeneous deactivation of $O_2(^1\Delta)$. Then variety of



(a) TA-SOG



(b) Centrifugal bubbler SOG

Fig. 7. Advanced SOGs. 1: reactor body; 2: chlorine source; 3: BHP injection unit; 4: BHP source; 5: hollow rotor; 6: holes in rotor’s wall; 7: BHP collector; 8: singlet oxygen output unit; 9: singlet oxygen; 10: multiple-thread screw; 11: liquid pump; 12: rotor’s shaft.

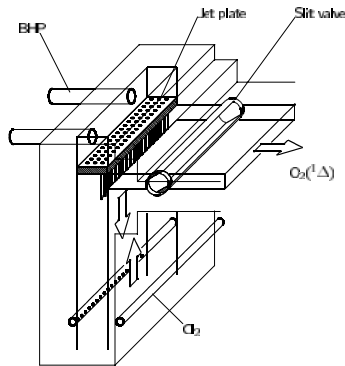


Fig. 6. Schematic drawing of a jet SOG.

“wet surface” type SOGs shown in Fig. 5 has been developed. In those types, thin layer of BHP is generated on the vertically held plates so that they could pack much more surface area per unit volume than bubbler type.

In 1991, Zagidullin *et al.* developed revolutionary “Jet SOG”[5]. The principle was very simple, but quite effective. Figure 6 shows the schematic drawing of the Jet SOG. Dense row of holes are punched at the jet plate and mounted on the top of the SOG. BHP jet shower fills the reaction volume and Cl_2 gas flows from bottom of the reaction volume. More than 90% of Cl_2 is converted to oxygen within 10 cm of interaction length. The properties of Jet SOG are characterized by its large surface-to-volume ratio and fast renewal of the liquid surface. The Jet SOG is so successful that almost all the COIL research sites in the world are now employing this type SOG. In Tokai University, a Jet SOG is operating with the following specifications: Reaction zone cross section = 10 cm², Cl_2 input molar flow rate = 20 mmol/s, pressure = 20 Torr, O_2/Cl_2 yield = 90%, $O_2(^1\Delta)/O_2$ yield = 60%.

Today’s challenge for SOG is higher operational pressure and higher throughput per reaction volume without degradation of the yield. To achieve these requirements, modern SOGs use centrifugal force to maintain gas-liquid interface under very high flow of Cl_2 gas. Figure 7(a) shows the schematic drawing of the “TA-SOG”[6]. In this SOG, BHP jet flows from the hub of the screw

perpendicularly to its axis. Cl_2 gas is forced to go up by the rotating vane, and reacts with BHP droplets. Due to the strong centrifugal force, droplets are not entrained by the gas flow, thus high throughput is possible. Figure 7(b) shows the schematic of the centrifugal bubbler SOG[7]. The principle of this SOG is same as the ancient bubbler SOG, except that the liquid surface is held vertically under the strong centrifugal force. The maximum operation pressure thus throughput is boosted considerably by the false gravitational force.

Mixing of Oxygen/Iodine

Rapid mixing of oxygen and iodine is critical to the performance of supersonic COIL. During the first 15 years of supersonic COIL developments, the shape of the expansion nozzle was simple Laval nozzle with holes of iodine injectors. The optimization of the iodine holes was achieved mainly by the cut-and-try basis experiments. Since the late 1990's, evolution of the personal computers changed the situation. Three-dimensional Computational Fluid Dynamics (CFD) became available for COIL researchers who were not specialized in fluid dynamics. Since then, number of unique mixing concepts has been proposed.

We have developed so-called "X-wing" mixing nozzle[8]. Figure 8 shows the schematic drawing. Thin wedges are set in an alternating fashion across the flow duct. Because those wedges resemble the letter "X" viewed from the side, we call this component the "X-wing". The assembly of wedges primarily functions as the supersonic expansion nozzle, but also doubles as a streamwise vortex generator. The secondary flow is injected at the nozzle exit plane (NEP) perpendicularly to the main flow. The contact surface between the primary and secondary flows is immediately enlarged by the streamwise vortices, a change that should lead to rapid completion of iodine dissociation. Notably, the streamwise vortex has a much longer life than the transverse vortex in the supersonic flow, and it is the most effective factor in enhancing the mixing in the supersonic stream. By employing this mixing nozzle, we have achieved record chemical efficiency of 33%.

Another trend of oxygen/iodine mixing is so-called "Ejector COIL"[9-11]. Ejector COIL is motivated to overcome the drawback of the conventional supersonic COIL. Because of the collisional deactivation, cavity pressure of COIL is limited at less than 1 kPa. Vacuum pumps to evacuate the active medium to atmospheric pressure is rather large and that limits the mobility of COIL. In ejector COILs, supersonic expansion of the active medium is done by the ejector effect of hypersonic nitrogen flow injected into the flow channel. Mixing of iodine into the supersonic flow of oxygen ejected by the nitrogen in a limited period is a very in-

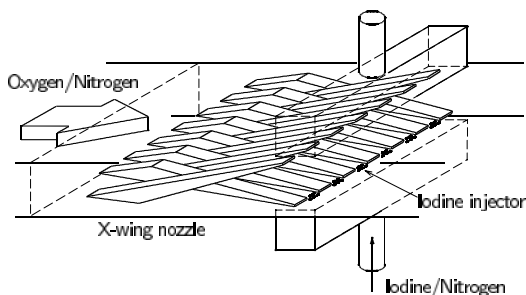


Fig. 8. Schematic drawing of X-wing supersonic mixing nozzle.

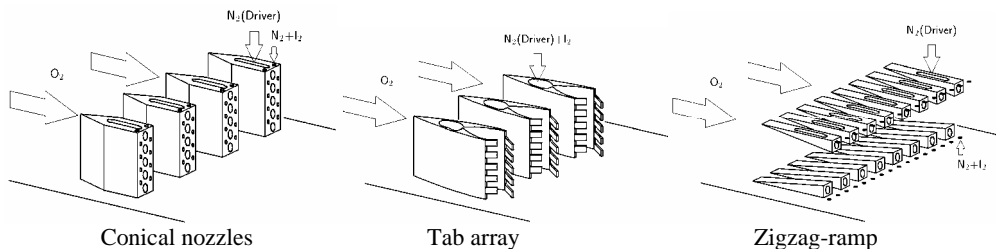


Fig. 9. Various nozzle configurations of "Ejector COIL".

interesting problem. A number of nozzles are developed by the aid of CFD as shown in Fig. 9. Typically, 25% of chemical efficiency are achieved and pressure at downstream of the supersonic diffuser reaches at 13 kPa.

Electrochemical BHP Regeneration

In every COIL system, singlet oxygen generator (SOG) is operated with a predetermined quantity of dense BHP solution (approx. 6M) that is continuously recirculated within the system and reacts with Cl_2 . During a batch operation of COIL, the molarity of HO_2^- in the BHP decreases. Since the absorbability of the gaseous Cl_2 depends on the HO_2^- ion concentration at the gas-liquid interface, the efficiency of the $\text{O}_2(^1\Delta)$ production depends on the HO_2^- molarity. When HO_2^- molarity is decreased to a point (approx. 3M), residual BHP is drained and replaced with fresh one. Continuous regeneration of the BHP with an electrochemical reaction may extend the continuous operation period of COIL outstandingly, and leads to a drastic reduction of the operational costs.

Motivated by those facts, we have been studying the electrochemical regeneration of BHP[12]. Figure 10 shows the schematic drawing of the electrochemical BHP regenerator. BHP is refreshed by the following three-phase contact reaction on the carbon-felt cathode,



The key for successful regeneration of high molarity BHP is the control of decomposition of BHP on the carbon-felt surface. We have found that adding caffeine is effective to prevent decomposition. Currently, positive gain of molarity is achieved up to 3.6M of BHP with electric current efficiency of 67%.

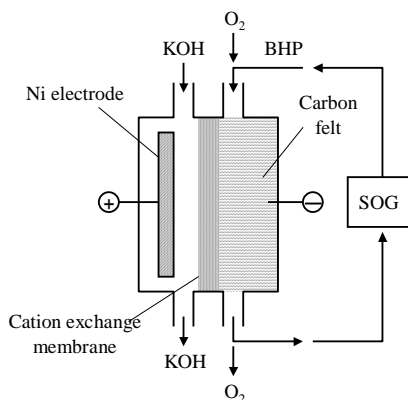


Fig. 10. Electrochemical BHP regeneration.

Applications

COIL is a highly scalable laser operating at the lowest loss band of silica optical fiber. Moreover, it is independent of electrical input to pump the active medium. Various applications are projected to exploit the characteristics of this unique laser. The most distinctive COIL application should be the “Airborne Laser”[13]. A multi-megawatt COIL system is carried on the modified B-747 aircraft, and kill the hostile ballistic missiles at the boost phase from a few hundreds km away. The laser module and platform are already completed and it will be deployed in 2011.

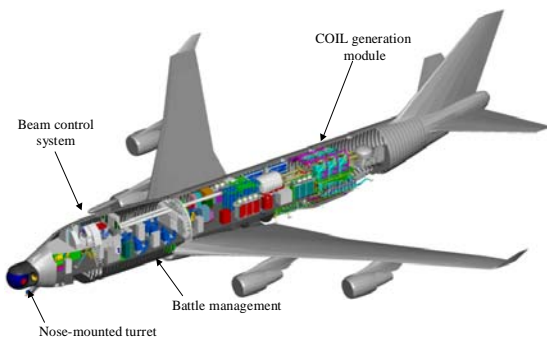


Fig. 11. The “Airborne Laser” concept.

The mobility and optical fiber deliverability of COIL could be used for decommission and dismantlement of the ceased nuclear plants. There was an extensive research done by Kawasaki Heavy Industries in 1990’s[14].

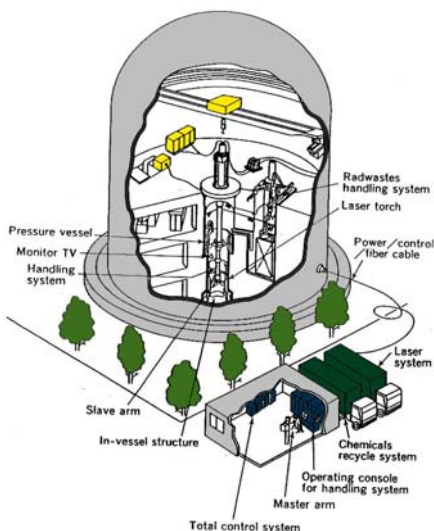


Fig. 12. Nuclear facility D&D by COIL.

COIL, an open-cycle chemical laser, is a drawback for continuous operation. The motivation of the electrochemical regeneration of BHP comes partly from our proposal.

In addition to those applications, excavation of the underwater natural resource[17] and space debris removal[18] by COIL are proposed.

We have proposed “Optical Power Network” concept on the basis of ultra high-power COIL facility[15]. It is like today’s electric power network, a supplier generates coherent photons and users buy them through optical fiber delivery. The initial and running costs of high-power laser for general industrial uses would be greatly reduced due to the scale merit. A 1kW, 1km delivery of COIL output is already demonstrated[16]. In this concept, the nature of

Optical power network concept is shown in Fig. 13. An optical power station (top) is connected via optical fibers to a laser system (middle) which is connected via optical fibers to a laser system (bottom) which is connected via optical fibers to a laser system (bottom right).

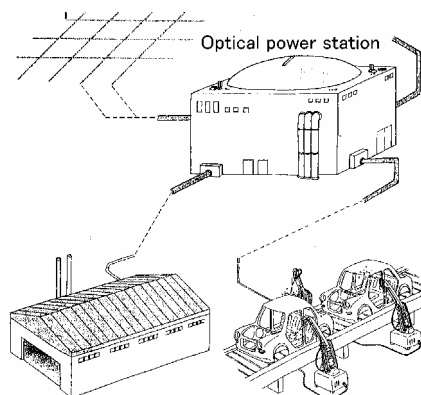


Fig. 13. Concept of “Optical Power Network”.

Summary

The paper has been aimed at introducing the unique features of chemical oxygen-iodine laser (COIL) as a chemical device, and presenting latest achievements. Trends of singlet oxygen generator (SOG) developments and oxygen-iodine mixing concepts are highlighted. Some briefly described projects of COIL applications demonstrate the unique characteristics of this chemical device.

References

- [1] R. F. Heidner III, C. E. Gardner, G. I. Segal and T. M. El-Sayed, *J. Phys. Chem.*, 1983, **87**, 2348-2360.
- [2] W. E. McDermott, N. R. Pchelkin, D. J. Benard and R. R. Bousek, *Appl. Phys. Lett.*, 1978, **32**, 469.
- [3] K. A. Truesdell, C. A. Helms and G. D. Hager, *Proc.*, SPIE 2502, 1994, 217-237.
- [4] G. Koop, J. Hartlove, C. Clendening, P. Lohn, C. C. Shih, J. Rothenflue, K. Hulick, K. Truesdell and R. Walter, AIAA-00-2421, 2000, 31st Plasmadynamics and Lasers Conference, Denver CO.
- [5] M. V. Zagidullin, A. Yu. Kurov, N. L. Kupriyanov, V. D. Nikolaev, M. I. Svistun and N. V. Erasov, *Sov. J. Quant. Electern.*, 1991, **21**, 747-753.
- [6] F. Wani, M. Endo, B. Vyskubenko, S. Ilyn, I. Krukovsky, S. Takeda and T. Fujioka, *IEEE J. Quant. Electron.*, 1998, **34**, 2130-2137.
- [7] V. D. Nikolaev, M. I. Svistun, M. V. Zagidullin and G. D. Hager, *Appl. Phys. Lett.*, 2005, **86**, 231102 (2p).
- [8] M. Endo, T. Masuda and T. Uchiyama, *IEEE J. Quant. Electron.*, 2006, 71-77.
- [9] V. D. Nikolaev, M. V. Zagidullin, T. J. Madden and G. D. Hager, AIAA2000-2427, 2000.
- [10] T. T. Yang, R. A. Dickerson, L. F. Moon and Y. S. Hsia, AIAA-2000-2425, 2000.
- [11] M. Endo, H. Nagaoka, T. Osaka, T. Dabamoto, S. Takeda and F. Wani, AIAA2003-3618, 2003.
- [12] M. Endo, M. Hano, S. Wakita, M. Uno and S. Takeda, *Proc. SPIE 5777*, 2004, 66-69.
- [13] S. J. Thornton, *Proc. SPIE 5777*, 2004, 1008-1010.
- [14] J. Adachi, N. Takahashi, K. Yasuda and T. Atsuta, *Progress in Nuclear Energy* 1998, **32**, 517-523.
- [15] M. Endo, S. Nagatomo, S. Takeda, F. Wani, K. Nanri and T. Fujioka, *Proc. SPIE 3268*, 1998, 106-114.
- [16] N. Takeuchi, K. Tei, D. Sugimoto, O. Vyskubenko and T. Fujioka, *Proc. SPIE 5777*, 2004, 298-301.
- [17] K. Josui, T. Fujioka, K. Tei and D. Sugimoto, *Proc. SPIE 5777*, 2004, 302-306.
- [18] W. L. Bohn, *Proc. SPIE 3612*, 1999, 79-84.

BIOMOLECULAR RECOGNITION AND IMAGING USING QUANTUM DOTS

Roger M. Leblanc

*University of Miami, Department of Chemistry, 1301 Memorial Drive,
Cox Science Center, Coral Gables, FL 33146, U.S.A.*

Abstract

Development of bioanalytical applications of quantum dots has been in the focus of the researchers in the latest years. We are focusing in developing assemblies that can be used for sensing. The advantage of using quantum dots over the organic fluorophores is the absence of photobleaching upon extended exposure to light, broad UV-Vis absorbance, narrow emission band and very high extinction coefficient.

We used Layer-by-Layer (LbL) deposition technique, which is based on electrostatic interaction, to build multilayers of organophosphorus hydrolase (OPH) enzyme and quantum dots, in order to detect the presence of p-nitrophenol which is the hydrolysis product of paraoxon in presence of OPH.

As a different approach we directly attached OPH on the surface of the QDs and a similar effect was determined as in the case of LbL assembly, which is the QDs emission quenching probably due to the presence of diethyl phosphoric acid which is released together with p-nitrophenol during hydrolysis.

Towards a different goal we were able to control the interparticle distance using different surfactants which could be used to consolidate QDs particle arrays with applications in memory storage or non-linear optics.

Introduction

Quantum dots-based nanostructures may be utilized as building blocks for photonic, electronic, and magnetic devices.¹⁻³ As a result, periodic arrays of semiconductor or other nanoparticles in all three dimensions are of current research interest. "Top-down" techniques (e.g., photo- and electron-beam lithography), several building supports including bioconjugation, and self-assemblies are being used to construct such nanostructures.^{4,5} The self-assembly fabrication methods have shown great potentiality for directing the organization of nanoparticles.⁶ This "bottom-up" methodology consists of inorganic/organic hybrid systems in which the nanoparticles assemble or co-assemble into superlattices.

Langmuir films of QDs as a function of particle size or nature of surface stabilizer have been previously studied. However, a greater understanding of the QD monolayer properties as well as the 2D arrangement and luminescence properties of QDs in these systems is of broad interest. Hence, the aims of this study were to characterize and manipulate the self-assembly of CdSe quantum dot monolayers at the air-water interface. The factors studied include particle size, nature of surfactant, surface pressure, and mixed monolayer systems. Characterization of the QDs or monolayer films was performed by UV-vis spectroscopy, surface pressure-area (π -A) isotherms, and trans-

mission electron microscopy (TEM). Additionally, the luminescence properties of the QD Langmuir films together with the epifluorescence microscope were used to image the film topographies directly at the interface. Langmuir-Blodgett (LB) films of QDs on hydrophilic or hydrophobic solid substrates were also studied.

Hybrid systems consisting of semiconductor QDs coupled to biomaterials find growing interest in the developing research area of both biotechnology and nanotechnology. The bioconjugation of QDs yields hybrid materials, processes, and devices that can utilize both the unique optical and magnetic properties of QDs and highly selective binding to oligonucleotides and proteins. In particular, the attachment of proteins to QDs has recently received much attention for their applications in constructing more complex structures and in new sensing and imaging technologies.

Considering the fact that the quantum dots (also known as semiconductor nanocrystals) have generated great interest for high sensitivity fluorescence microscopic imaging of biological samples^{7,8}, we rationalized that the synthetic peptides of amyloid fragments coated on the surface of quantum dots may open a new approach for studying the morphology of amyloid fibrils.

Results and Discussion

In this study, the stepwise synthesis procedure was adopted, and the UV-vis spectroscopy of QD solutions was used to calculate the size of the QDs. The amounts of $\text{Zn}(\text{Et})_2$ and $(\text{TMS})_2\text{S}$ were then calculated for deposition of a 0.5 nm thick ZnS shell on the QDs. The QD size and the thickness of the TOPO surface cap helped to explain the limiting nanoparticle area of the QDs as derived from the surface pressure-area isotherm.

Surface-ligand exchange of $(\text{CdSe})\text{ZnS}/\text{TOPO}$ QDs with 2-mercaptoacetic acid made the QDs water soluble in basic aqueous solution and it was used for the bioconjugation of QDs with organophosphorus hydrolase (OPH).

For Langmuir film properties, UV-vis spectroscopy, epifluorescence microscopy, and transmission electron microscopy were used to study CdSe quantum dots (QDs) in 2D. By combining these results, it was possible to determine the molar absorptivity, limiting nanoparticle area, luminescence property, and arrangement of the QDs in the monolayer films at the air-water interface. Either trioctylphosphine oxide (TOPO) or 1-octadecanethiol (ODT) stabilized the QDs. The data collected reveal that TOPO forms close-packed monolayers on the surface of the QDs and that ODT-stabilized QDs undergo alkyl chains interdigitation. It was also found that varying the nanoparticle size, nature of surfactant, surface pressure, and mixed monolayers could help engineer the 2D self-assembly of the QDs at the air-water interface.⁹ Of practical importance is the transfer of these monolayer films onto hydrophilic or hydrophobic solid substrates, which could be successfully accomplished via the Langmuir-Blodgett film deposition technique.

For $(\text{CdSe})\text{ZnS}$ QDs the surface pressure-area isotherm of the Langmuir film of the QDs gave an average diameter of 4.4 nm, which matched very well with the value determined by transmission electron microscopy (TEM) measurements if the thickness of the TOPO cap was counted. The stability of the Langmuir film of the QDs was

tested by two different methods, compression/decompression cycling and kinetic measurements, both of which indicated that TOPO-capped (CdSe)ZnS QDs can form stable Langmuir films at the air-water interface. Epifluorescence microscopy revealed the two-dimensional aggregation of the QDs in Langmuir films during the early stage of the compression process. However, at high surface pressures, the Langmuir film of QDs was more homogeneous and was capable of being deposited on a hydrophobic quartz slide by the Langmuir-Blodgett (LB) film technique. Photoluminescence (PL) spectroscopy was utilized to characterize the LB films.¹⁰ The PL intensity of the LB film of QDs at the first emission maximum was found to increase linearly with increasing number of layers deposited onto the hydrophobic quartz slide, which implied a homogeneous deposition of the Langmuir film of QDs at surface pressures greater than $20 \text{ mN}\cdot\text{m}^{-1}$.

Regarding the bioncojugation, the organophosphorus hydrolase (OPH) was coupled to (CdSe)ZnS core-shell QDs through electrostatic interaction between negatively charged QDs surfaces and the positively charged protein side chain and ending groups ($-\text{NH}_2$). Circular dichroism (CD) spectroscopy showed no significant change in the secondary structure of OPH after the bioconjugation, which indicates that the activity of OPH was preserved. Detectable secondary structure changes were observed by CD spectroscopy when the OPH/QDs bioconjugate was exposed to organophosphorus compounds such as paraoxon. Photoluminescence (PL) spectroscopic study showed that the PL intensity of the OPH/QDs bioconjugate was quenched in the presence of paraoxon. The overall quenching percentage as a function of paraoxon concentration matched very well with the Michaelis-Menten equation. This result indicated that the quenching of PL intensity was caused by the conformational change in the enzyme, which is confirmed by CD measurements. The detection limit of paraoxon concentration using OPH/QDs bioconjugate was about 10^{-8} M . Although increasing the OPH molar ratio in the bioconjugates will slightly increase the sensitivity of biosensor, no further increase of sensitivity was achieved when the molar ratio of OPH to QDs was greater than 20 because the surface of QDs was saturated by OPH. These properties make the OPH/QDs bioconjugate a promising biosensor for the detection of organophosphorus compounds.¹¹

For the imaging of fibril formation related to Alzheimer's disease, A β (31-35) peptide and control peptides as well as full length A β (1-40) and A β (1-42) peptides were labelled with luminescent CdSe/ZnS quantum dots (QDs) to observe the morphology of amyloid fibers. A comparison was made between QDs and an organic dye, namely Dansyl group, which showed that the QDs present a much better contrast for imaging than the organic dye.¹²

Conclusions

Quantum dots can assemble in 2D and the interparticle distance can be controlled using Langmuir films. Langmuir-Blodgett films can form arrays of QDs with controlled distance between QDs and different number of layers. QDs can replace successfully the use of organic fluorophores in detection of paraoxon with a detection limit of 10^{-8}

M. Imaging of amyloid peptides was successful and the aggregation patterns are completely different compared to control peptides.

References

- [1] I. S. Nandhakumar, T. Gabriel, X. Li, G. S. Attard, M. Markham, D. C. Smith, J. J. Baumberg, *Chem. Commun.*, 2004, **12**, 1374.
- [2] Y. Lin, H. Skaff, T. Emrick, A. D. Dinsmore, T. P. Russell, *Science*, 2003, **299**, 226.
- [3] D. M. Guldi, I. Zilbermann, G. Anderson, N. A. Kotov, N. Tagmatarchis, M. Prato, *J. Am. Chem. Soc.*, 2004, **126**, 14340.
- [4] X. Huang, J. Li, Y. Zhang, A. Mascarenhas, *J. Am. Chem. Soc.*, 2003, **125**, 7049.
- [5] J. Liang, H. Luo, R. Beresford, J. Xu, *Appl. Phys. Lett.*, 2004, **85**, 5974.
- [6] R. Shenhar, V. M. Rotello, *Acc. Chem. Res.*, 2003, **36**, 549.
- [7] X. Michalet, F. Pinaud, T. D. Lacoste, M. Dahan, M. P. Bruchez, A. P. Alivisatos, S. Weiss, *Single Mol.*, 2001, **2**, 261.
- [8] W. C. Chan, D. Maxwell, X. Gao, R. Bailey, M. Han, S. Nie, *Curr. Opin. Biotechnol.*, 2002, **13**, 40.
- [9] K. M. Gattas-Asfura, C. A. Constantine, M. J. Lynn, D. A. Thimann, X. Ji, R. M. Leblanc, *J. Am. Chem. Soc.*, 2005, **127**, 14640.
- [10] X. Ji, C. Wang, J. Xu, J. Zheng, K. M. Gattas-Asfura, R. M. Leblanc, *Langmuir*, 2005, **21**, 5377.
- [11] X. Ji, J. Zheng, J. Xu, V. K. Rastogi, T.-C. Cheng, J. J. DeFrank, R. M. Leblanc, *J. Phys. Chem. B.*, 2005, **109**, 3793.
- [12] X. Ji, D. Naistat, C. Li, J. Orbulescu, R. M. Leblanc, *Colloids and Surfaces B: Bio-interfaces*, 2006, in press.

PATTERN FORMATION IN REACTION-DIFFUSION SYSTEMS

Andrzej L. Kawczyński

*Institute of Physical Chemistry, Polish Academy of Sciences
Kasprzaka 44/52, 01-224 Warsaw, Poland
e-mail: alk@ichf.edu.pl*

Abstract

Two problems with reaction-diffusion systems are discussed. They illustrate examples of pattern formation in rather simple systems. One of them is still open problem of kinds and a number of possible asymptotic solutions in one-variable, one-dimensional (1D), infinite multistable system. Besides well known simple trigger fronts, non-monotonic multiple traveling fronts not mentioned in literature are shown. Another one is the problem of all possible types of asymptotic solutions to two-variable, 1D excitable system with three stationary states. Unknown types of asymptotic solutions for infinite and bounded systems are presented. The solution of the second problem is summarized by two-parametric diagrams for infinite and bounded systems.

Introduction

Our visible world is composed of various shapes (patterns). Some of them are very regular (symmetrical), like crystals. Others are not regular but easy to distinguish, like children's faces for their patterns. Still others are irregular, like shapes of clouds. All these patterns are spontaneously generated by nature. Our knowledge about generation of patterns in equilibrium systems is not far to be completed. Completely different situation is in far-from-equilibrium systems. There is a fundamental question concerning processes involved in pattern formation. Simple far-from-equilibrium systems in which spatial patterns are well understood are the Rayleigh-Benard convection and the Taylor-Couette flows in hydrodynamics. We have also some knowledge about the pattern formation in reaction-diffusion (RD) systems. They can be treated as minimal models which can describe the pattern formation in physical, chemical, biological and other systems. One of the most fascinating problems is morphogenesis in biological systems. Real nonlinear reaction-diffusion systems can be treated as useful caricatures of many biological systems. For example, running impulses can be easily observed experimentally in a thin layer of the reaction mixture in which the Belousov-Zhabotinsky (B-Z) reaction occurs. Qualitative properties of such waves are similar to the spreading of electrical excitations along axons in neurons as well as to waves in the Purkinje fibers in heart. It is much easier to investigate qualitative properties of such waves in chemical systems than in biological ones. Solutions to reaction-diffusion systems are determined by configurations of attractors and repellers of chemical dynamics. Chemical reactions are described by corresponding kinetic equations describing dynamics of reagents which appear in chemical schemes. For one- and two-variable systems the situation is simple. Stable stationary states and stable limit cycles are possible attractors and unstable stationary states and unstable limit cycles are possible repellers. Changes of parameters can cause bifurcations which are separated in a parameter

space. However, for three- and more variable systems besides stable stationary states and stable limit cycles, strange attractors (deterministic chaos) appear. Moreover, one can meet the situation when small changes of values of a parameter can induce infinite number of bifurcations. It makes the situation much more difficult. It is noteworthy that problems with one- and two-variable systems can have sufficiently rich variety of asymptotic solutions.

In the present lecture two problems concerning unknown kinds of asymptotic solutions to simple nonlinear RD systems are discussed. The existence of various possible types of traveling fronts as well as their numbers in multistable, one-variable, one dimensional (1D) infinite RD systems is the first problem. Complete two parametric diagrams of all possible asymptotic solutions to excitable, two-variable 1D infinite and bounded RD system with three stationary states is another problem.

One-variable systems

Unfortunately, exact solutions to initial value problems for far from bifurcations chemical systems are available only for one-variable infinite systems with two or three stationary states. Asymptotic solutions in such systems have the form of traveling fronts which may propagate from an unstable stationary state to stable stationary state or from a stable stationary state to another stable stationary state. In the first case, according to the Kolmogorov-Petrovsky-Piskunov theorem [1], the absolute values of front velocities are bounded from below and may depend on the initial conditions. In bistable systems traveling fronts are attractive solutions for appropriate initial conditions and have unique velocity as follows from the Kanel and Fife-McLeod theorems [2]. Trigger fronts connecting different stable stationary states in one-variable 1D infinite reaction-diffusion systems are described by:

$$\frac{\partial S}{\partial t} - \frac{\partial^2 S}{\partial x^2} = f(S) \quad (1)$$

with appropriate initial conditions. In multistable systems the kinetic term has $2n+1$ ($n = 1, 2, \dots$) positive ($0 < S_1 < S_2 < \dots < S_{2n+1}$) stationary states among which $n+1$ odd ones are attractive and the remaining even ones are repulsive. The diffusion coefficient D is set equal to 1 due to the proper scaling of the spatial coordinate $x' = xD^{1/2}$ where x' is the physical coordinate. We consider the family of initial condition problems (Cauchy problems) for all values of parameters which specify $f(S)$. Initial conditions have the form

$$0 < S(x,0), \limsup_{x \rightarrow -\infty} S(x,0) < S_{2i} < \liminf_{x \rightarrow \infty} S(x,0) < \infty \quad (2)$$

for at least one value of $i=1, 2, \dots, n$. Such initial conditions ensure the existence of at least one traveling front joining two different stable stationary states as an asymptotic solution to Eq. (1) because S_{2i} are repulsive stationary states. According to the theorems by Kanel and Fife-McLeod in bistable systems ($n = 1$) non-trivial asymptotic solution to the Eq (1) has the form of the traveling impulse $\lim_{t \rightarrow \infty} s(t,x) = s(\zeta)$

where $\zeta = x + ct + x_0$, and c is the velocity of the traveling impulse. The uniqueness of the velocity of the traveling front connecting the attracting zeros is the result of the structural instability of the heteroclinic orbit.

Let us mention that the system (3) is invariable with respect to transformation

$$\zeta \rightarrow -\zeta + \zeta_0, c \rightarrow -c, \zeta_0 \in \mathbf{R} \tag{3}$$

This symmetry means that if a traveling front exists for given initial conditions, then also its mirror reflection exists for symmetrical initial conditions.

Examples of possible traveling fronts are shown schematically in following figures

where $F_{i,j} = \int_{S_i}^{S_j} f(S) dS$.

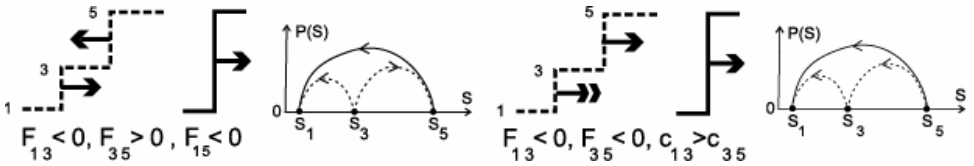


Fig. 1. Single traveling fronts (solid) connecting states S_1 and S_5 in the tristable system, initial conditions (dashed) and corresponding trajectories are shown schematically. Numbers denote stable stationary states.

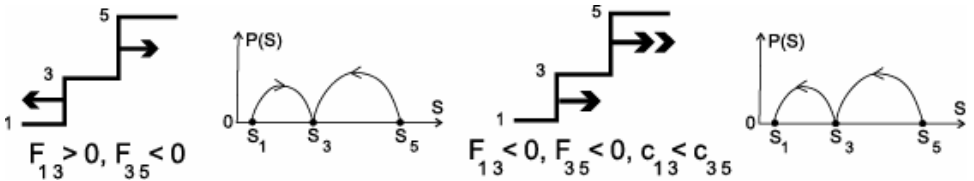


Fig. 2. Multiple monotonic fronts and corresponding trajectories on "the compound phase plane" (S, P) for the tristable system are shown schematically.

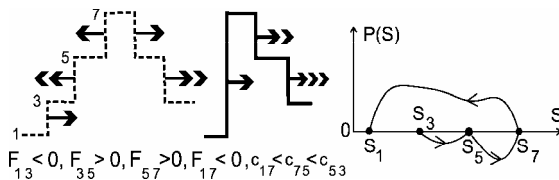


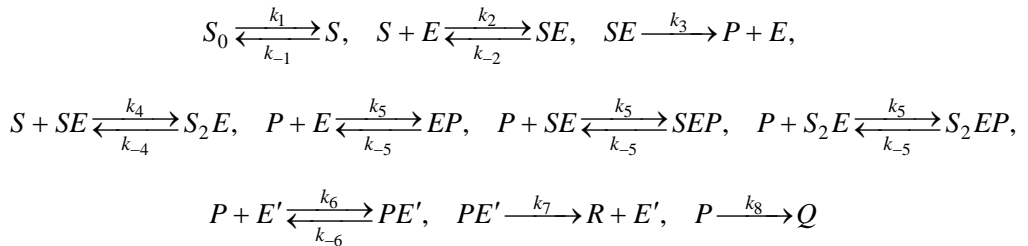
Fig. 3. Nonmonotonic front in the system with four stable stationary states ($n=3$).

Numbers of possible traveling fronts connecting two different stable stationary states are given in the table:

Type of the solution	Number of solutions	$2n+1$			
		3	5	7	9
Single fronts connecting adjacent states	$4n$	4	8	12	16
Single fronts connecting nonadjacent states	$2n(n-1)$	0	4	12	24
Multiple fronts travelling in the same direction	$2^{n+3} - 2(n+1)(n+2) - 4$	0	4	20	64
Multiple fronts travelling in the opposite directions	$2((n-3)2^n + n + 3)$	0	2	12	46
Nonmonotonic solutions	$3^{n+1} - 2^{n+3} + 2n + 5$	0	4	28	128

Two-variable systems

In two variable models, besides traveling fronts, traveling impulses, stationary periodic structures and solutions periodic in space and time are known as asymptotic solutions. The list of possible asymptotic solutions to these systems is still incomplete. New types of asymptotic solutions are obtained in a model presented below. The model describes an open chemical system, in which two catalytic (enzymatic) reactions occur.



We assume that the total concentrations of catalysts (enzymes) E and E' are much smaller than the concentrations of the reactant S and the product P . On the basis of the Tikhonov theorem [3] the concentrations of both catalysts (enzymes) and their complexes may be eliminated as fast variables, and the dynamics of the system may be described by the two kinetic equations for the reactant S and the product P only. Its space-time behavior in dimensionless variables is described by the following equations:

$$\frac{\partial s}{\partial t} - \frac{\partial^2 s}{\partial x^2} = A_1 - A_2 s - \frac{s}{(1 + s + A_3 s^2)(1 + p)} \quad (4a)$$

$$\frac{\partial p}{\partial t} - D \frac{\partial^2 p}{\partial x^2} = B \left(\frac{s}{(1 + s + A_3 s^2)(1 + p)} - B_1 - B_2 p \right) \quad (4b)$$

where $x = \sqrt{k_3 E_0 / (D_s K_m)} x'$ is dimensionless space coordinate, $t = k_3 E_0 / K_m t'$ is dimensionless time, $s = S / K_m$ and $p = K_5 P$ are dimensionless concentrations of the reactant S and the product P , $D = D_p / D_s$ is the ratio of the diffusion coefficients for the product D_p and the reactant D_s , $K_5 = k_5 / k_{-5}$, and $K_m = (k_{-2} + k_3) / k_2$, $K_m' = (k_{-6} + k_7) / k_6$ are the Michaelis constants. $A_1 = k_1 S_0 / (k_3 E_0)$, $A_2 = k_{-1} K_m / (k_3 E_0)$, $A_3 = k_4 / k_{-4} K_m$, $B = K_m K_5$, $B_1 = k_7 E_0' / (k_3 E_0)$ and $B_2 = k_8 / (k_3 E_0 K_5)$ are dimensionless parameters. The assumption that the second catalytic (enzymatic) reaction occurs in its saturation regime means that K_m' is much smaller than p . Therefore, the rate of this reaction is constant and equal to B_1 .

Initial and initial-boundary value problems are considered for a 1D system. For the initial value problem following initial conditions are assumed:

$$\begin{aligned} s(x, 0) &= s^*, p(x, 0) = p^* \text{ for } x \in [0, l^*]; \\ s(x, 0) &= s_0, p(x, 0) = p_0 \text{ for } x \in (l^*, \infty] \end{aligned} \quad (5)$$

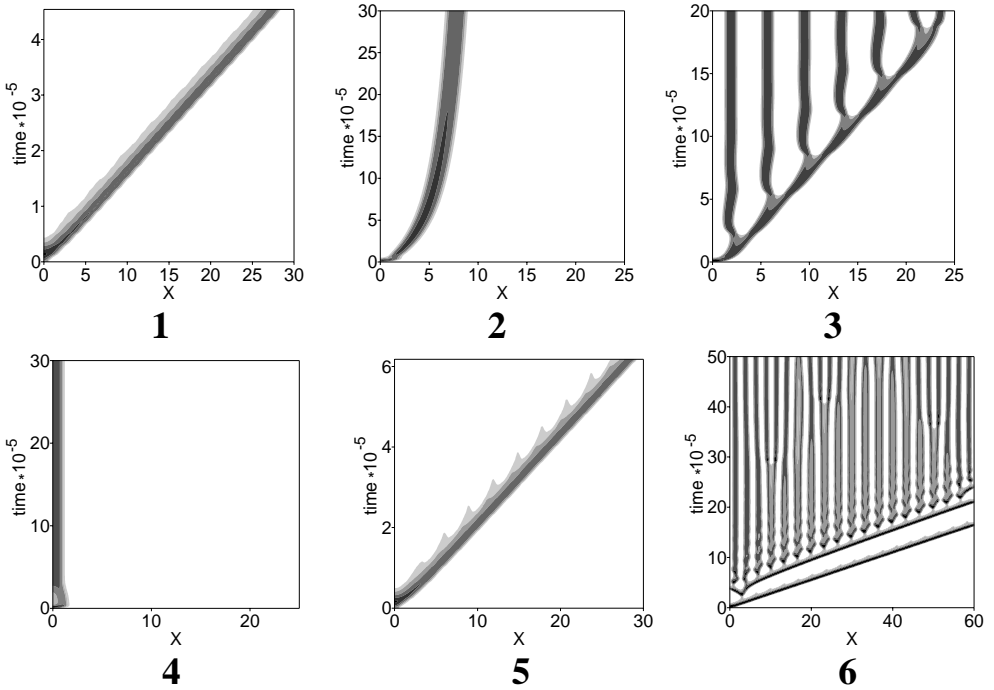
For the initial-boundary value problem we assume that

$$\begin{aligned} s(x, 0) &= s^*, p(x, 0) = p^* \text{ for } x \in [0, l^*]; \\ s(x, 0) &= s_0, p(x, 0) = p_0 \text{ for } x \in (l^*, L] \end{aligned} \quad (6)$$

where s^* and p^* are perturbations of the stationary state s_0 , and p_0 and the boundary conditions:

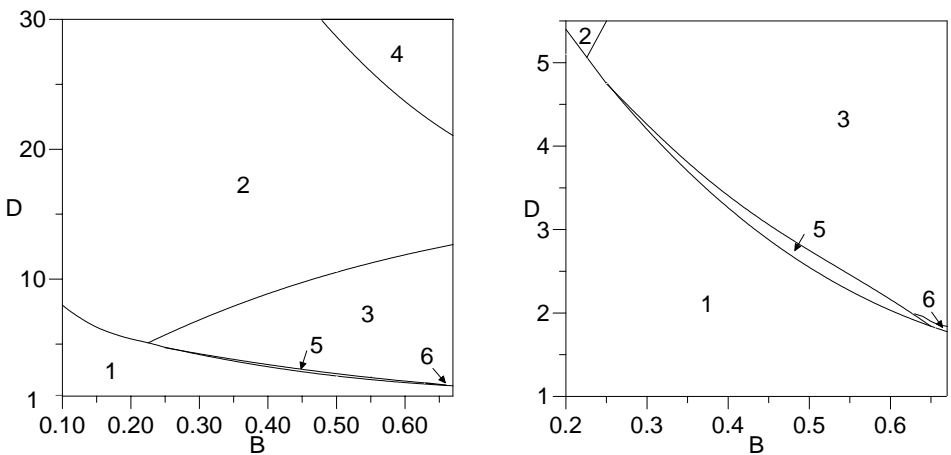
$$\frac{\partial s}{\partial x}(0, t) = \frac{\partial s}{\partial x}(L, t) = \frac{\partial p}{\partial x}(0, t) = \frac{\partial p}{\partial x}(L, t) = 0 \quad (7)$$

We assume the following values of the parameters: $A_1 = 0.01$, $A_2 = 0.0001$, $A_3 = 0.505$, $B_1 = 7.99 \times 10^{-3}$, $B_2 = 4.65 \times 10^{-5}$. At these values of the parameters the system without the diffusion terms has three stationary states: the stable node, the saddle point and the unstable focus. B and $D = D_p / D_s$ play the role of bifurcation parameters. The following types of patterns appear in the infinite system.



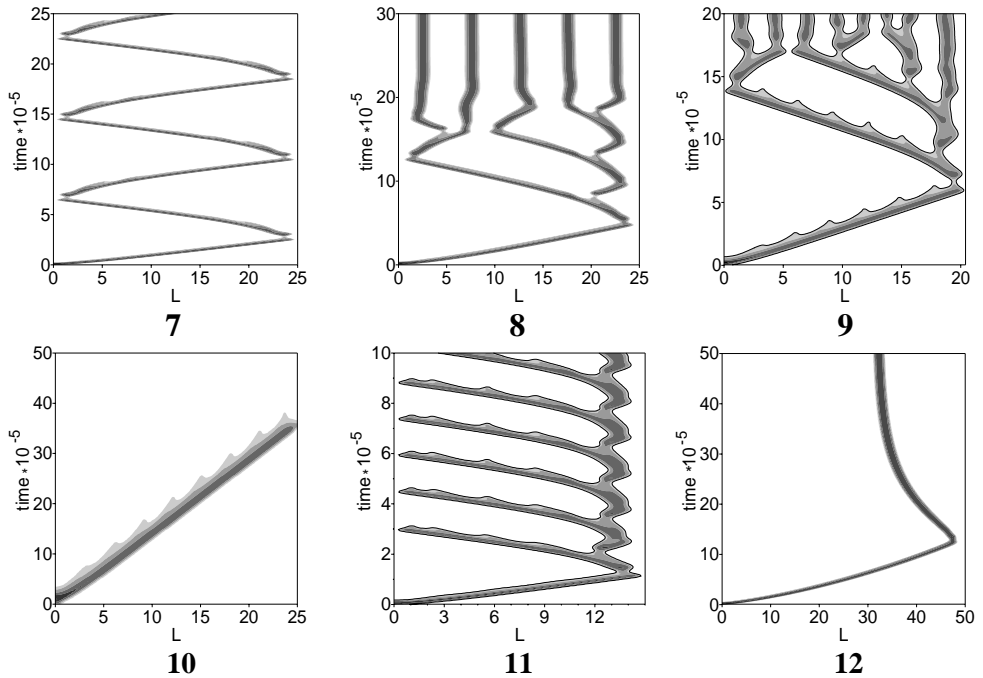
The topographic plots of the patterns observed in the infinite system. The patterns 1 - 4 are well known, but the patterns 5 and 6 have been never mentioned in literature.

Results of our numerical calculations for infinite system are summarized in the following two-parametric diagram and its detail. The numbers shown in the diagrams correspond to the patterns notation.

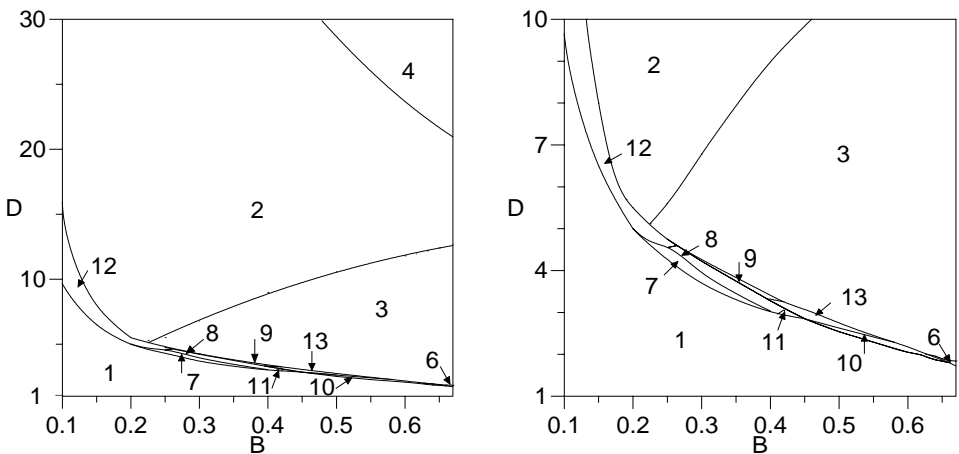


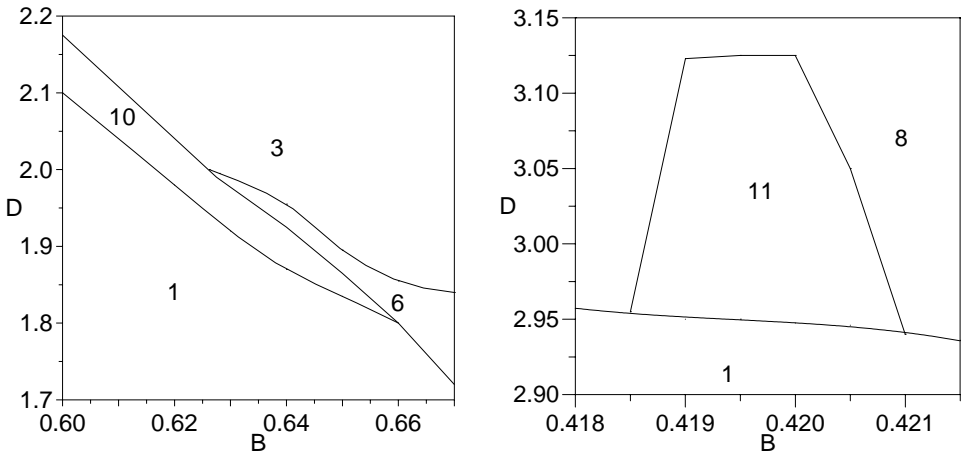
In bounded systems, the simple traveling impulse shown as pattern 1 vanishes at the right boundary and asymptotically the system becomes homogenous. Besides the patterns 2, 3, 4 and 6 the following patterns shown as topographic plots appear. The reflect-

ing impulse (pattern 7) and the meandering impulse (pattern 12) are well known. The traveling impulse with periodically decaying pulses shown as the pattern 10 vanishes before the right boundary and the system becomes homogenous. The remaining patterns have never been mentioned in literature.



The results of numerical calculations showing regions of the parameters plane where the corresponding patterns have been observed are presented in the following diagram and its details. The numbers in the diagram correspond to the pattern notation.





The region marked as 13 corresponds to the periodical survival or decay of the traveling impulse with periodically decaying pulses. Continuous increase of the size of the system causes periodical repetition of surviving and decay of the impulse [4]. The survival and decay of the impulse are shown as the patterns 9 and 10, respectively.

Conclusions

The still open problem of the variety of possible traveling fronts in multistable one-variable, 1D infinite RD system is solved. Multiple monotonic as well as unmentioned earlier nonmonotonic traveling fronts can exist for appropriate initial conditions. The number of various traveling fronts increases dramatically with the number of stable stationary states.

The complete list of the asymptotic solutions to two-variable, excitable 1D system is presented. Besides the well known solutions like the simple traveling impulse or stationary periodical structure, the unknown earlier solutions like the traveling impulse with periodically decaying pulses and the patterns 6 and 11 are shown. In the two-parameter space there is also the region where periodical survival or decay of the impulse is observed.

The results presented in this paper increase our knowledge about the possible solutions to nonlinear reaction-diffusion systems, which are minimal models for pattern formation. One may imagine that such models are able to describe many patterns observed in nature.

References

- [1] A.N. Kolmogorov, I.G. Petrovsky and N.S. Piskunov, *Moscow Univ. Bull.*, 1937, **17**, 1.
- [2] P.C. Fife, *Mathematical Aspects of Reacting and Diffusing Systems*, Springer-Verlag, 1979.
- [3] A.N. Tikhonov, *Mat. Sborn.*, 1952, **31**, 575.
- [4] A.L. Kawczyński and B. Legawiec, *Phys. Rev. E*, 2006, **64**, 026112.

STRUCTURAL MECHANISMS AND PATHWAYS OF AMYLOID FORMATION. ITS IMPLICATION IN CONFORMATIONAL DISEASES

L. Morozova-Roche

*Department of Medical Biochemistry and Biophysics,
Umeå University, Umeå, 90781 Sweden*

Abstract

Mechanisms and pathways of amyloid formation by hen and equine lysozymes as well as by *de novo* protein albebetin were analysed. These examples highlight a universality of amyloid self-assembly which can be prompted by varying environmental conditions. The amyloid-prone conditions are those which induce molten globule state of protein or destabilise its structure enhancing hydrophobic interactions at protein interfaces and favouring ion pairing in order to provide the directionality of this process versus unstructured aggregation. Polymorphism is a distinctive feature of amyloid which can also be governed by solution conditions, including basic ones as pH, temperature, ionic strength and calcium ions. Using lysozymes and albebetin as model proteins, we showed that their cross- β -sheet containing amyloid oligomers are cytotoxic inducing apoptosis, while hen lysozyme fibrils cause necrosis cell death. Cytotoxicity is not a property of particular type of amyloid species but rather of their continuum, though cellular mechanism involved can be different for each amyloid type.

Introduction

Protein misfolding and amyloid aggregation play crucial role in a wide range of human disorders, including Alzheimer's, Parkinson's, prion diseases, type II diabetes, systemic amyloidoses and even normal aging. All amyloid disorders have a common pathological feature such as extra- or intra-cellular protein deposits. About 20 polypeptides with unrelated sequences and tertiary structures are known to be involved in amyloidoses. When they assemble into amyloid fibrils, the latter share a common cross β -sheet core which serves as a distinctive marker of amyloid. This indicates that proteins can undergo dramatical conformational conversions in order to adopt uniform β -sheet-based structure within the amyloid fibrils, as some of them such as lysozyme and insulin contain α -helices in their monomeric forms. The mechanisms of structural rearrangement occurring upon amyloid polymerization still remain largely unresolved. Another common feature of amyloid is that its deposits are associated with cellular pathology. They commonly cause cell death and tissue degradation leading subsequently to the failure of the affected organ. A wide variety of cellular types can be affected depending on the location of amyloid in the body, among them neuronal cell death associated with neurodegenerative diseases, hepatocytes die in systemic lysozyme amyloidoses, pancreatic β -cells - in type II diabetes. In recent years an increasing number of non-disease related polypeptides have been shown to form amyloid under *in vitro* conditions. As a result of these observations it has been envisaged

that amyloidogenicity is a common property of a polypeptide chain as it is stabilized by the hydrogen bonding between polypeptide backbones, while the sequence specificity determines the propensity to form amyloid [1]. It was also suggested that due to the common structure of amyloid, its cellular toxicity is also a generic phenomenon which can be attributed to aggregates formed by many, if not all, polypeptides [2].

However, in spite of large experimental evidence accumulated today on the role of protein self-assembly in amyloid-related diseases, there is neither a definite structural description of the toxic amyloid species nor a unified view on the mechanisms involved in the cell death processes caused by amyloid. As amyloid is naturally constituted by highly heterogeneous and polymorphic species even within the same sample, this fact also contributes to the complexity of its structural characterisation.

Multiple pathways of amyloid assembly

We used *de novo* protein albebetin and well structurally characterized in our previous studies equine lysozyme as model systems to study the molecular mechanisms of their amyloid assemblies under changing environment. As amyloid possesses common structural properties, the information on the self-assembly of one particular protein has a general implication for understanding the amyloid phenomenon as a whole. Albebetin is a 72 amino acid residue protein composed of two $\alpha\beta\beta$ motives forming four stranded β -sheet covered by two α -helices and characterized by a mobile molten globule type conformation at neutral pH. It was designed as an immunologically inert carrier protein for drug delivery. However, albebetin appeared to be highly amyloidogenic protein, which was completely unforeseen by the initial design. Indeed, protein needs to be destabilised in order to undergo alternative arrangement and integrate into fibrils. Molten globule conformation is a good candidate for an amyloid precursor state. Upon incubation of albebetin and its constructs with the biologically active peptides from interferon- α_2 , LKEKKYSP, and differentiation factor, TGENHR, under physiological conditions we have produced a hierarchy of their amyloid structures. These structures were characterised in detail by using atomic force microscopy (AFM) as a monitoring technique.

We demonstrated that the depending on the environmental conditions such as temperature, ionic strength or the presence of additional charged groups in the solution albebetin can undergo the multiple fibrillation pathways [3,4] as shown in Fig.1. The amyloid types formed from albebetin include oligomers, single stranded polymers- protofilaments and the lateral assemblies of the latter into thicker fibrillar branches. Screening the structures deposited in the imaging field and using the AFM height and volume measurements we have identified two distinct types of oligomers. First kind is "pivotal" oligomers with ca. 1.2 nm height which are comprised of 10 to 12 monomers; they serve as an initial building block for multiple amyloid assemblies. If they are not converted further into larger structures, they are able to assemble into chains and rings with "bead-on-string morphology", in which "beads" corresponds to individual oligomers. These assemblies are rather stable in solution, once formed both the rings and chains remain concomitantly to fibrils. The proportion of the rings versus the

chains increases with incubation time indicating that circularisation stabilises these structures. Second type, on-pathway to fibrillation “amyloid-prone” oligomers with ca. 2 nm height are constituted of 26 to 30 molecules. They give rise to protofilaments and fibrils and their formation is concomitant to increased binding of amyloid specific dyes such as thioflavin T and Congo red indicative of the cross- β -sheet structure formation within the oligomers. The amyloid nature of filamentous structures was confirmed also by the β -sheet rich far-UV circular dichroism spectra. Transformation of the “pivotal” oligomers into the “amyloid-prone” ones is suggested to be a limiting stage in amyloid assembly. Amyloid formation proceeds by fusing oligomers together into polymeric strands (Fig.1) given that at least one of them is “amyloid-prone” oligomer. This type of self-assembly is consistent with the polymerization model based on nucleation-conformational conversion.

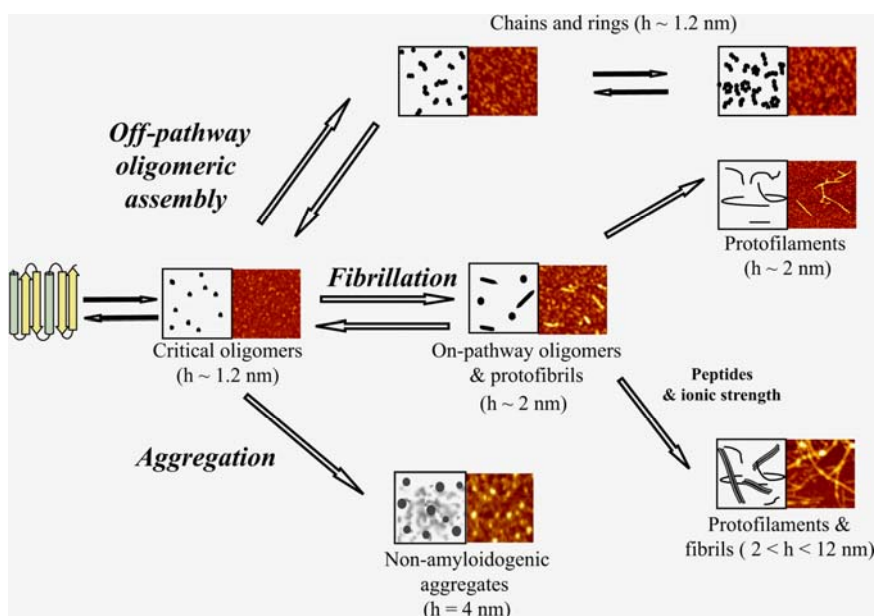


Fig. 1. Multiple amyloid structures and fibrillation pathway of albebetin [3]. The schematic presentations are shown in the left images and the corresponding AFM images in the right ones. This scheme demonstrates that the self-assembly of typical amyloidogenic protein involves a partitioning between the amyloid fibrillation, non-specific aggregation and off-pathway oligomerisation.

Albebetin is a very soluble protein due to a high net charge -12 under neutral pH. Electrostatic repulsions prevent it from stochastic non-structured aggregation upon incubation at neutral pH. Our results demonstrate that balancing the electrostatic repulsions by an increased ionic strength or charged peptides, either fused to N-terminus of albebetin or added into the solution, significantly enhances amyloidogenicity of

albebetin, promoting its further fibrillation into network of micron-long, thick, unbranched fibrils. Increasing temperature to 37 °C or even 57 °C also promotes the polymerization of albebetin which does not undergo conversion into fibrils at room temperature, even though the “pivotal” oligomers are formed under these conditions. This indicates that it requires overcoming a significant free-energy barrier to transform these structures into β -sheet containing types. An increase of temperature effectively lowers the energy barrier, facilitating transformation of the smaller oligomers into the “amyloid-prone” ones and their subsequent assembly into fibrils.

The circularisation of amyloid into rings or pores were viewed as major pathogenic course in Alzheimer’s and Parkinson’s diseases [5]. We studied equine lysozyme as a model protein to address this problem and evaluate the conditions which affect the amyloid ring formation. Equine lysozyme forms molten globule states under a variety of destabilising conditions and during its kinetic of refolding [6,7]. This state is characterised by an extended hydrophobic core stabilised by tertiary interactions of its three major α -helices. Incubating equine lysozyme at pH 4.5 and 57 °C we have produced its single-stranded rather short filamentous structures with 2 nm width [8]. They did not grow till micron length, neither assemble into thicker threads. We propose that the presence of the stable core in equine lysozyme molten globule affects its fibrillation; though the amino acid sequences which are most likely form the cross- β -sheet fibrillar structure correspond to the β -sheet region in the native protein, stable α -helical core forms unsticky fibrillar interface preventing further fibrillar grow. These results highlight that not only the propensity to form β -sheet structure governs the amyloid formation but the overall destabilisation of protein molecule.

We have shown that calcium-binding equine lysozyme depleted of calcium ions forms massive ring-shaped amyloid structures both at pH 4.5 and pH 2 and elevated temperatures [8]. At pH 4.5 the rings are 45-50 nm in diameters, while at pH 2 – of 70-80 nm diameters and also being less populated. They bind amyloid dyes Congo red and thioflavin T similar to the disease-related ring structures of A β peptide and α -synuclein. Their formation is largely governed by calcium binding and pH but can be also a consequence of stochastic process. We propose that amyloid rings are not limited to disease-involved polypeptides but represent a second generic type of amyloid in addition to more common linear filaments.

Thus, our results demonstrated the polymorphism of amyloid structures of equine and hen lysozymes as well as albebetin, which raises the next question- which of them, if not all, are cytotoxic.

Relating Amyloid Structure and Cytotoxicity

Cellular toxicity is a major known today property gained by proteins as a result of their self-assembly into amyloid. Currently, among various amyloid types the prefibrillar amyloid structures rather than mature polymeric fibrils most commonly viewed as a cytotoxic source. This class encompasses a wide variety of structures ranging from misfolded monomers or hexamers of transthyretin to amyloid rings as well as spherical oligomers of all dimensions from a few to hundred nanometers large and

formed by A β peptide, α -synuclein, lysozyme, PI3-SH3 domain and other polypeptides. Knowing in detail the amyloid pathways of albebetin, we examined its cytotoxic properties [9]. Another advantage of using albebetin lies in its ability to convert into amyloid under conditions closely resembling those of the cytotoxicity assays and therefore little perturbation of toxic species occurs in the course of the experiment. Subjecting its amyloid splices to cerebellar granular neurons and SH-SY5Y neuroblastoma cells and measuring their mitochondrial activity by the tetrasolium MTT salt reduction assay we have shown its “pivotal” oligomers were not toxic to cells. Monomers and protofilaments of albebetin were also non-toxic. The cytotoxicity is a property of larger “amyloid-prone” oligomers which are characterised by the development of cross- β -sheet structure able to bind amyloid specific dyes and displaying also characteristic β -sheet far-UV circular dichroism spectrum. When these oligomers were populated in the amyloid samples the cell viability decreased upon their addition by ca. 20-30%. We suggest that oligomeric size is important for stabilising their cross- β -sheet core. It appeared, however, that the rings populated in the specimen did not increase noticeably its cellular toxicity.

Amyloid species of equine lysozyme described above were also subjected to the cytotoxicity assays such as the MTT reduction by mitochondrial enzymes, the ethidium bromide staining sensitive to cellular membrane permeability and the TUNNEL assay labelling free DNA ends upon its fragmentation during apoptotic death [10,11]. In all these tests neither monomers, nor amyloid protofilaments displayed cytotoxicity. However, soluble amyloid oligomers of tetra- and octamer size formed both under the pH 2 and 4.5 conditions appeared to be cytotoxic on three cell types used in these experiments including primary neuronal cells, primary fibroblasts and neuroblastoma cell line IMR-32. Even higher toxicity yielding in the death of a half of neuroblastoma cells was induced by the larger oligomers of 20-mer range as it was estimated by the AFM particle volume measurements. We suggested that these dimensions of soluble oligomers are optimal for stabilisation of their cross- β -sheet structure. Similar to albebetin amyloid, there was no correlation between the population of the amyloid rings and cytotoxic properties of the specimen. This indicates that the rings are not the primary source of cytotoxicity by themselves but rather constituting them oligomers, their dimensions and the structural properties determine the toxicity of amyloid sample.

Hen egg white lysozyme is another protein which readily assembles into amyloid under the pH 2 and elevated temperatures condition which proved to be a universal one promoting amyloid formation. Examining the cytotoxicity of hen lysozyme amyloid by the mitochondrial assay based on the inhibition of WST-1 reduction in dieing cells, we have found that the SH-SY5Y neuroblastoma cell viability decreases progressively with the accumulation of cross- β -sheet amyloid structures irrespectively whether their morphology is oligomeric or fibrillar (Fig. 2).

Then the comparative analysis of toxic properties of both oligomers and fibrils of hen lysozyme were undertaken subjecting the SH-SY5Y cells treated with amyloid to a range of cell viability tests. We revealed that the amyloid oligomers and fibrils act via different cellular mechanisms. The fibrils induce a rapid cell death due to mem-

brane damage shown by lactate dehydrogenase release and propidium iodide intake. By contrast, the oligomers rapidly activate caspases but exert slow apoptotic death only after 48 hours co-incubation with cells which manifested in phosphatidylserine externalization, lactate dehydrogenase release and propidium iodide DNA staining. We conclude that oligomers induce apoptotic-like cascades, while the fibrils act more rapidly and less specifically via necrosis-like pathways.

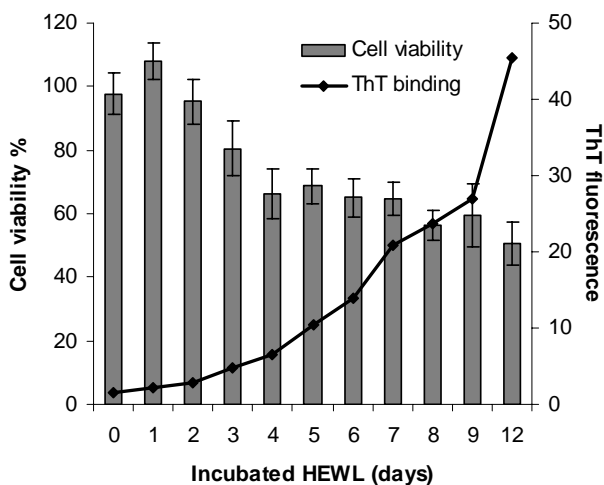


Figure 2. Kinetics of hen lysozyme amyloid formation and cell viability in the presence of amyloid.

Time dependence of amyloid formation was monitored by thioflavin-T binding to cross- β -sheet containing amyloid; fluorescence intensity of thioflavin-T dye is shown in the right y-axes. The SH-SY5Y cell viability in the presence of amyloid was measured by WST-1 assay after 24 hour of their co-incubation; the percent of cell viability compared to untreated controls is shown in the left axes.

Discussion

Ability to form amyloid by *de novo* protein albebetin and its constructs with biologically active peptide as well as by ubiquitous lysozymes, which are present in many tissues and body fluids of all mammals, demonstrates a universality of amyloid self-assembly process. If initially the amyloid was discovered as deposits involved in human and animal diseases (prions), it become increasingly evident that any protein under destabilising or specially designed conditions can undergo amyloid self-assembly [1,3,4,12]. The amyloid prompting conditions are those which induce the molten globule state of protein or destabilisation of its structure that would enhance hydrophobic interactions at protein interfaces and favour ion pairing in order to provide the directionality of this process versus spontaneous unstructured aggregation. Albebetin was designed to be a highly soluble protein under physiological conditions;

however, its molten globule conformation appeared to be highly amyloidogenic leading to formation of variety of amyloid structures even after a few hours of incubation under neutral pH.

As in the molten globule state the hydrophobic side chains can be easily accessible due to conformational fluctuation and mobility of the polypeptide chain, the initial nucleation of monomeric molecules can easily be prompted. Therefore, the overall stabilisation of protein structure is a most general strategy in preventing amyloid formation. This extends not only on the region of the primary structure most likely involved in the cross- β -sheet formation, but also on the structures which do not undergo the conversion into β -sheet but involved in the packing of the surrounding amyloid core areas. Compared to the core structure of amyloid fibrils the information on the molecular arrangement at the fibrillar interfaces is very limited if not absent. In the case of equine lysozyme, the far UV circular dichroism spectra of the fibrillar material show always some contribution from the α -helical structures. This indicates that its stable α -helical core, while being distorted within the fibrils, can retain its residual structure. The stability of this core can be a major structural feature preventing the significant growth and lateral assembly of equine lysozyme protofilaments compared to the long and thick mature fibrils of its structural homologous hen and human lysozymes [12].

The polymorphisms of amyloid species is another common property of amyloid emerging as a result of its multiple fibrillation pathways [3,4,8]. Due to conformational plasticity of amyloid precursor state and uncooperative nature of protein aggregation, the proteins can assemble into amyloid complexes in different registers of their cross- β -sheets and with different complexity and dimensions of their species. Ongoing inter-conversion of smaller oligomers into larger ones and their subsequent assembly into filamentous structures contributes to the intrinsic heterogeneity of amyloid specimen. Environmental conditions may govern the population of the certain species. Indeed, in the case of equine lysozyme we have observed that its circular protofilaments are populated in the absence of calcium ions, while long fibrils of albebetin can be induced by increasing ionic strength. The effect of solution conditions on amyloid formation can be explored in order to design amyloid structures with desired properties.

Among newly gained properties of the amyloid assemblies compared to their monomeric precursors the cellular toxicity plays a central role. In recent years, the pre-fibrillar structures were in the focus of research as a major cytotoxic source. It is clear, however, that they are represented not by a single uniform species but rather by a continuum of structures. The oligomers of equine lysozyme and albebetin which have not developed cross- β -sheet core appeared to be non-toxic, indicating that the stabilisation of this structural pattern is critical for the induced toxicity. The formation of cross- β -sheet core may be important in stabilising the oligomers from dissociation upon penetration through cellular membrane and within the cellular environment. The studies of cytotoxicity of hen lysozyme amyloid demonstrated that not only amyloid oligomers but also fibrils can exert toxic effect, though they act via different mechanisms. If the oligomers induce more specific and slow evolving apoptotic cascades, the fibrils act

faster killing cells via necrosis-like pathways. These results highlight that lysozyme amyloid is harmful for the cells and neither its form can be viewed as a neutral or inert material. In a view of heterogeneity of fibrillar types and the fact that protofilaments from some other proteins such as equine lysozyme and albebetin are not toxic, the toxicity of amyloid can depend on its fibrillar morphology, the problem which requires further detail studies. Given that lysozyme is an abundant protein which is present in many food and biological products as well as albebetin was designed initially for biomedical applications, the toxicological studies of amyloid species are of paramount importance. Indeed, amyloid can possess newly gained hazardous properties which need to be foreseen and prevented.

Acknowledgments

We acknowledge the support of our research by Swedish Medical Research Council, Swedish Royal Academy of Sciences and Kempe Foundation.

References

- [1] C.M. Dobson, *Nature*, 2003, **426**, 884-890.
- [2] M. Bucciantini et al, *Nature*, 2002, **416**, 507-511.
- [3] L.A. Morozova-Roche et al, 2004, *Biochemistry*, **43**, 9610-9619.
- [4] M. Lavrikova et al., *Biochem (Mosc)*, 2006, **71**, 306-314.
- [5] H.A. Lasual et al., *Nature*, 2002, **418**, 291.
- [6] L.A. Morozova-Roche et al, *J. Mol. Biol.*, 1997, **268**, 903-21.
- [7] L.A. Morozova-Roche et al, *J. Mol. Biol.*, 1999, **289**, 1055-1073.
- [8] M. Malisauskas et al., *J. Mol. Biol.*, 2003, **330**, 879-890.
- [9] V. Zamotin et al., *FEBS Lett*, 2006, **580**, 2451-2457.
- [10] M. Malisauskas et al., *J. Biol. Chem*, 2005, **280**, 6269-6275.
- [11] M. Malisauskas et al., *Biochem (Mosc)*, 2006, **71**, 505-512.
- [12] L.A. Morozova-Roche et al., *J. Struct Biol.*, 2000, **130**, 339-351.

RESONANCE RAMAN SPECTROSCOPY AND SITE DIRECTED MUTAGENESIS TO PROBE HEME PROTEIN STRUCTURE

G. Smulevich,

*Dipartimento di Chimica, Università di Firenze, Via della Lastruccia 3,
50019 Sesto Fiorentino (FI), Italy, E.mail: giulietta.smulevich@unifi.it*

Abstract

The combined analysis of electronic absorption and resonance Raman spectroscopies has been fundamental to the comprehension of heme protein function under physiological conditions. The electronic absorption spectra of heme proteins are characterized by the presence of intense bands due to π - π transitions of the heme group. The analysis of these spectra allows one to establish the coordination of the heme iron atom on the basis of the correlation with structurally characterized proteins and model compounds. However, the presence of a number of species in equilibrium, solvent effects and other factors necessitate the use of other techniques. Resonance Raman (RR) spectroscopy has been extensively applied to study heme proteins in general [1] since it provides a more complete characterization, being capable of giving specific structural information with regard to ligation and spin state of the heme. The enhancement mechanism of the Raman scattering by hemoproteins has been reported in many reviews. Upon excitation in the Soret region, the totally symmetric modes (A_{1g}) of the porphyrin ring (pseudo-symmetry D_{4h}) give rise to very intense polarized bands, whereas the depolarized non-totally symmetric modes (B_{1g} or B_{2g}) are weakly enhanced due to the Jahn-Teller effect [1]. The high frequency region (1300 - 1700 cm^{-1}) of the RR spectrum is characterized by the skeletal modes which give rise to intense bands known as “core-size marker bands”. Their name derives from the correlation of the RR frequency with the size of the porphyrin core and, therefore, to the spin (high and low spin) and coordination (5- and 6-) states of the Fe atom. For planar metal porphyrins, increasing the core size lowers the Raman frequencies: a change of only 0.01 \AA in the size of the core produces a change of 5 - 6 cm^{-1} in the frequency of these bands. The Fe-ligands give rise to intense bands in the low-frequency region 150 - 600 cm^{-1} .

A comprehensive analysis of the information presently available from electronic absorption (UV-Vis) and resonance Raman (RR) spectra, and X-ray crystallography of wild-type peroxidases and site directed mutants involving residues close to the heme will be presented. In particular, the present lecture will examine the contribution to our understanding of heme peroxidases provided by electronic and resonance Raman spectroscopies in conjunction with site-directed mutagenesis. Moreover, the finding of novel spectroscopic markers, enables some general conclusions to be reached concerning peroxidase active sites, which can also be extended to other heme proteins [2].

Heme containing peroxidases

The “plant peroxidase superfamily I” is a large group of intra- and extracellular heme containing peroxidases evolutionarily related. Sequence alignment of various peroxidases has revealed the existence of three well separated classes within this superfamily [3,4]. Peroxidases catalyze the two-electron oxidation of a variety of substrates at the expense of H_2O_2 via the formation of oxy-ferryl catalytic species [5, 6]. These enzymes are involved in a wide range of biological functions, such as defence against stress (class I), metabolism of lignin (class II and III), developmental processes, and defence against environmental changes (class III).

The three classes show less than 20% amino acid sequence identity, however, they contain invariant residues in the heme cavity which are catalytically relevant. On the proximal side of the heme (below the heme) the His axial ligand of the heme iron is hydrogen-bonded to a buried carboxylate group of an aspartic (Asp) residue, and on the distal side of the heme (above the heme) a distal histidine (His) together with an arginine (Arg) residue, render the heme cavity of peroxidases very polar. Moreover, common to all peroxidases there is an extended hydrogen-bond network involving the proximal and the distal conserved catalytic residues and water molecules (Figure 1).

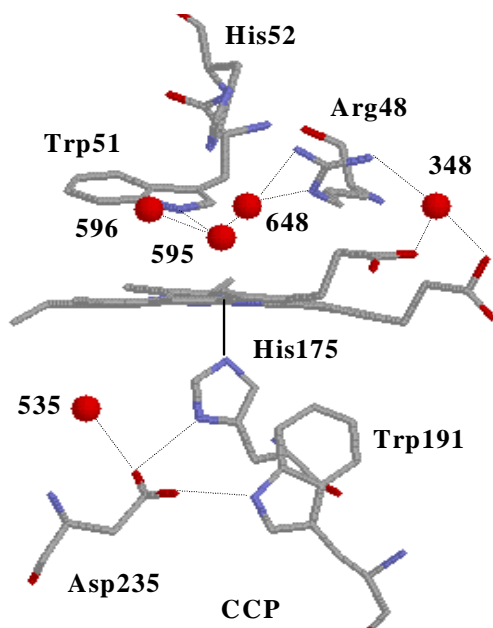


Fig. 1. Active site residues of yeast Cytochrome C Peroxidase (CCP) The figure was constructed using the coordinates deposited in the PDB data bank (1CCA).

Dotted lines indicate the inferred hydrogen-bonds, on the basis of distance criteria. Water molecules are also shown.

In addition to the peroxidases in plants, in humans there are several peroxidases that play an important role in the non-specific immune defence system. These enzymes are

structurally and functionally related and form the homologous mammalian heme-containing peroxidase superfamily II, to be distinguished from the peroxidase superfamily I.

Spectroscopic Results

The combination of resonance Raman and electronic absorption spectroscopy, at different pH and temperature, in the presence of various exogenous ligands, in solution and single crystal forms, has enabled the role of the key residues in the heme cavity to be defined and their structure-function properties to be elucidated. The combination of resonance Raman and electronic absorption spectroscopy, especially when applied to a study incorporating native, recombinant and mutant proteins of key residues, gives detailed information at the molecular level of the active site.

Roles of the conserved residues in the heme cavity and the hydrogen bonding network lining the proximal and distal sides of the heme.

The most fascinating result is the finding that both proximal and distal side chains have a profound influence on heme ligation due to an extensive network of hydrogen-bonds coupling the distal and proximal sides which is a common feature of heme peroxidases. In fact, the coordination state of peroxidases can be dramatically affected by the physical and chemical conditions as a consequence of the high polarity of the distal cavity and the extended hydrogen-bond network involving water molecules and conserved distal and proximal amino acids. Mutation of the distal His and Arg residues modifies the heme coordination and perturbs the proximal Fe-His bond strength, as a consequence of pH-dependent changes, charge distribution, size, and hydrogen-bonding acceptor/donor properties of the substituting amino acid.[7-10]. Based on the RR studies of model compounds which demonstrated the sensitivity of the Fe-His frequency to hydrogen-bonding [11, 12], RR spectra of several site directed mutants of many heme peroxidases clearly indicated that the proximal His-Asp hydrogen-bond is a critical interaction, modulating the Fe-His bond strength and restraining the Fe from moving into the heme plane and binding a distal water [2, 7, 9, 13, 14].

Recently catalase-peroxidases (KatGs) have raised considerable interest, since, despite their striking sequence homologies to the members of class I of the plant peroxidase superfamily [4], they are the only members of the plant peroxidase superfamily exhibiting peroxidase and substantial catalase activities similar to monofunctional catalases. To gain insight into their structure-function properties, many variants were produced and extensive RR studies have been performed to understand their dual enzymatic activity [14-22]. Spectroscopic studies revealed marked differences in the structural role of conserved amino acids and hydrogen-bond networks in KatG with respect to the other plant peroxidases [15]. The proximal amino acids play a major role in the stability of the protein architecture, since disruption of the proximal hydrogen-bond by mutation weakens the heme binding to the protein [14]. Furthermore, RR spectroscopy allowed us to identify a novel link between the proximal and distal sides of the heme cavity important for the stability of the heme pocket and for maintaining the proximal hydrogen-bond strength [14]. The results suggested that small structural

perturbations and disruption of the hydrogen-bond networks have only a small impact for both catalytic and peroxidatic activity, but a defined extended hydrogen-bond network is crucial for the catalytic activity [14, 15]

Factors influencing the stabilization of exogenous ligands (OH, F, CO) and their spectroscopic markers.

Heme pocket proximal and distal amino acid residues control ligand binding in hemo-proteins. Peroxidases are characterized by a high polarity of the distal cavity due to the presence of the His and Arg (Figure 1) which play a concerted role in the catalytic mechanism through direct hydrogen bonds and charge stabilization fundamental for the heterolytic cleavage of the peroxy group of hydrogen peroxide [23]. RR and electronic absorption spectra of site directed mutants of the distal residues provided evidence that the cavity characteristics of peroxidases are also reflected in the binding of other exogenous ligands.

Fluoride and Hydroxide Anionic Ligands: the Arg is determinant in controlling the ligand binding via a strong hydrogen bond between the positively charged guanidinium group and the anion. The distal His plays a minor but important role by accepting a proton from HF and hydrogen-bonding probably through a water molecule with the anion. Replacing arginine with leucine inhibits fluoride and hydroxyl binding [24-28]. We found that a sensitive indicator of axial ligand interactions with the distal amino acids is the wavelength of the porphyrin to iron charge-transfer transition (CT1) in the 600-630 nm region. It blue-shifts when the ligand acts as a hydrogen-bond donor. The stronger the hydrogen-bond and charge donation to the iron atom, the lower is the charge-transfer transition wavelength [26, 27].

Carbon Monoxide. Carbon monoxide is a sensitive probe for investigating both proximal ligand properties and distal environmental effects in the heme cavity of heme proteins. In particular, hydrogen-bonding and, more generally, polar interactions between the bound CO and the distal residues increase the extent of back-donation from the Fe $d\pi$ to the CO π^* orbitals. As a consequence, the Fe-C bond strengthens while the CO bond weakens, thereby increasing the $\nu(\text{FeC})$ stretching frequency and decreasing the $\nu(\text{CO})$ stretching frequency [29, 30].

The comparison of the RR and IR spectra of CO complexes of different peroxidases and their distal mutants indicate that in these peroxidases the oxygen atom of the bound CO is involved in hydrogen-bond interactions with the distal amino acids. We have identified different types of conformers [31-33]. One form is hydrogen-bonded with the distal arginine, another with the distal histidine, and the third, in CCP, is characterized by the CO, whose oxygen atom, according to the X-ray structure [34], is hydrogen-bonded to the distal arginine via a water molecule.

Protein interactions which modulate i) the heme conformation and ii) the orientation of the vinyl groups.

i) RR spectroscopy has proved to be one of the best probes of the conformation of the porphyrin due structure-sensitive porphyrin modes which are activated differentially,

according to whether the conformation of the heme is planar or non-planar. Many Raman studies have been devoted to the quantification of the type and magnitude of the porphyrin distortion [35, 36]. Recently RR spectra of human myeloperoxidase (MPO), and its Met243Thr and Asp94Val mutants with different excitation wavelengths and in polarized light have been obtained [37]. The crystal structure [38] of MPO shows that the heme is covalently attached to the protein via two ester linkages with the Glu242 and Asp94 residue, and a sulfonium linkage with the sulfur atom of Met243. Because of the covalent bonds, the heme ring assumes a bow-shaped structure. Despite the spectral crowding, we proposed an almost complete assignment of the RR bands of MPO. The data allowed us to conclude that the RR spectra of MPO were very rich because of the activation of almost all the in-plane skeletal modes observed for the Ni-octaethylporphyrin model compound, induced by the distortion of the heme imposed by the covalent links with the protein. The two mutants, which lost at least one of the covalent links between the protein and the heme group, were useful to determine the effect of the symmetry lowering of the heme group.

ii) The heme porphyrin ring of the plant peroxidases contains two vinyl substituents in positions 2 and 4, which, based on the X-ray structures, differ mainly in the orientation of vinyl 2 as a consequence of different steric hindrances imposed by the protein matrix. Accordingly, the corresponding RR vinyl stretching frequencies markedly differ [39]. As the constraint on the 2-vinyl diminishes, the conjugation between the vinyl and the porphyrin decreases, therefore, the 2-vinyl $\nu(\text{C}=\text{C})$ stretching frequency increases, and a large frequency separation is observed between the two $\nu(\text{C}=\text{C})$ stretching modes in the RR spectra. When the protein matrix exerts weak or no constraints on the 2-vinyl group, two distinct $\nu(\text{C}=\text{C})$ stretching modes are found in the RR spectra.

The combined analysis of the x-ray diffraction data, the resonance Raman frequency of the vinyl modes and electronic absorption spectra of several plant peroxidases, together with selected mutants and their complexes with imidazole and fluoride, has enabled us to establish a direct relationship between the $\nu(\text{C}=\text{C})$ stretching frequencies and the orientations of the vinyl groups, as induced by specific protein interactions. Therefore, the $\nu(\text{C}=\text{C})$ vinyl stretching frequency is a sensitive probe of the degree of electronic conjugation [40]

Acknowledgements

The author gratefully acknowledges the contributions of collaborators whose names are listed in appropriate references.

References

- [1] T. G. Spiro, *Biological Applications of Raman Spectroscopy*; John Wiley & Sons, New York, 1988; Vol. 3.
- [2] G. Smulevich, A. Feis, G. Smulevich *Acc. Chem. Res.* 2005, **38**, 433-440
- [3] K. G. Welinder, "The plant peroxidase superfamily," in *Biochemical, Molecular, and Physiological Aspects of Plant Peroxidases*, Ed. by J. Lobarzewski, H. Greppin, C. Penel, and Th. Greppin, University of Geneva, Geneva, Switzerland, 1991, 1-13.

- [4] K.G. Welinder, *Curr. Opin. Struct. Biol.*, 1992, **2**, 383–393.
- [5] A.T. Smith, N.C. Veitch, *Curr. Opin. Struct. Biol.* 1992, **2**, 269-278.
- [6] A.M. English, G. Tsaprailis, *Adv. Inorg. Chem.* 1995, **34**, 79-125.
- [7] G. Smulevich, J.M. Mauro, L.A. Fishel, A. English, J. Kraut, T.G. Spiro, *Biochemistry*, 1988, **27**, 5477-5485.
- [8] G. Smulevich, M.A. Miller, J. Kraut, T.G. Spiro, *Biochemistry*, 1991, **30**, 9546-9558.
- [9] G. Smulevich, M. Paoli, J.F. Burke, S.A. Sanders, R.N.F. Thorneley, A.T. Smith, *Biochemistry*, 1994, **33**, 7398-7407.
- [10] F. Neri, C. Indiani, K.G. Welinder, G. Smulevich, *Eur. J. Biochem.* **1998**, 251, 830-838.
- [11] P. Stein, T.G. Spiro, *J. Am. Chem. Soc.*, 1980, **102**, 7795-7797.
- [12] H. Hori, T. Kitagawa, *J. Am. Chem. Soc.*, 1980, **102**, 3608-3613.
- [13] G. Smulevich, A. Feis, C. Focardi, K.G. Welinder, *Biochemistry*, 1994, **33**, 15425-15432.
- [14] E. Santoni, E. C. Jakopitsch, C. Obinger, G. Smulevich, *Biochemistry*, 2004, **43**, 5792-5802.
- [15] G. Smulevich, C. Jakopitsch, E. Droghetti, C. Obinger, *J. Inorg. Biochem.* 2006, **100**, 568–585.
- [16] A.H. Heering, C. Indiani, G. Regelsberger, C. Jakopitsch, C. Obinger, G. Smulevich, *Biochemistry*, 2002, **41**, 9237–9247.
- [17] C. Jakopitsch, E. Droghetti, F. Smuckenschlager, P.G. Furtmüller, G. Smulevich, C. Obinger, *J. Biol. Chem.*, 2005, **280**, 42411–42422.
- [18] G.S. Lukat-Rodgers, N.L. Wengenack, F. Rusnak, K.R. Rodgers, *Biochemistry*, 2000, **39**, 9984–9993.
- [19] E. Santoni, C. Jakopitsch, C. Obinger, G. Smulevich, *Biopolymers*, 2004, **74**, 46–50.
- [20] S. Kapetanaki, S. Chouchane, S. Giroto, S. Yu, R.S. Magliozzo, *Biochemistry*, 2003, **42**, 3835–3845.
- [21] S. Chouchane, S. Giroto, S. Kapetanaki, J.P.M. Schelvis, S. Yu, R.S. Magliozzo, *J. Biol. Chem.*, 2003, **278**, 8154–8162.
- [22] S. Kapetanaki, S. Chouchane, S. Yu, X. Zhao, R.S. Magliozzo, J.P. Schelvis, *Biochemistry*, 2005, **44**, 243–252.
- [23] J.H. Dawson, *Science*, 1988, **240**, 433-439.
- [24] A. Feis, M.P. Marzocchi, M. Paoli, G. Smulevich, *Biochemistry*, 1994, **33**, 4577-4583.
- [25] B.D. Howes, J.N. Rodriguez-Lopez, A.T. Smith, G. Smulevich, *Biochemistry*, 1997, **36**, 1532-1543.
- [26] F. Neri, D. Kok, M.A. Miller, G. Smulevich, *Biochemistry*, **1997**, 36, 8947-8953.
- [27] F. Neri, C. Indiani, B. Baldi, J. Vind, K.G. Welinder, *Biochemistry*, 1999, **38**, 7819-7827.
- [28] M. Nissum, F. Neri, D. Mandelman, T.L. Poulos, G. Smulevich, *Biochemistry* 1998, **37**, 8080-8087.
- [29] G.M.J. Phillips, M.L. Teodoro, B. Smith, B., J.S. Olson, *J. Phys. Chem.*, 1999, **B 103**, 8817-8829.
- [30] G.B. Ray, X.-Y. Li, J.A. Ibers, J.L. Sessler, T.G. Spiro, *J. Am. Chem. Soc.*, 1994, **116**, 162-176.
- [31] G. Smulevich, J.M. Mauro, L.A. Fishel, A. English, J. Kraut, T.G. Spiro, *Biochemistry*, 1988, **27**, 5486-5492.
- [32] A. Feis, J.N. Rodriguez-Lopez, R.N.F. Thorneley, G. Smulevich, *Biochemistry*, 1998, **37**, 13575-13581.

- [33] A. Feis, E. Santoni, F. Neri, C. Ciaccio, G. De Sanctis, M. Coletta, K.G. Welinder, G. Smulevich, *Biochemistry*, 2002, **41**, 13264-13273.
- [34] S.L. Edwards, T.L. Poulos, *J. Biol. Chem.*, 1990, **265**, 2588-2595.
- [35] J.A. Shelnutt, X.-Z. Song, J.-G. Ma, S.-L. Jia, W. Jentzen, C.J. Medforth, *Chem. Soc. Rev.*, 1998, **27**, 31-42
- [36] J.A. Shelnutt, In *The Porphyrins Handbook*, vol. 7, Ed by C.M. Kadish, K.M. Smith, R. Guilard. Academic Press: San Diego, CA, USA, 2000, 167-224.
- [37] S. Brogioni, A. Feis, M. P. Marzocchi, M. Zederbauer, P.G. Furtmüller, C. Obinger, G. Smulevich, *J. Raman Spectrosc.*, 2006, **37**, 263-276.
- [38] T.J. Fiedler, C.A. Davey, R.E. Fenna, *J. Biol. Chem.*, 2000, **275**, 11964-11971.
- [39] G. Smulevich *G. Biospectroscopy* 1998; **4**, S3-S17 and references therein.
- [40] M. Marzocchi, G. Smulevich, *J. Raman Spectrosc.*, 2003, **34**, 725-736.

PRACTICAL APPLICATIONS OF RADIATION CHEMISTRY

Andrzej G. Chmielewski

Institute of Nuclear Chemistry and Technology

&

Department of Chemical and Process Engineering, University of Technology

Warsaw, Poland

Introduction

Radiation chemistry is a part of the physical chemistry like photo-chemistry, plasma-chemistry, ultrasonic-chemistry etc. Shortwave high energy electromagnetic (gamma radiation or X-rays) or high penetration corpuscular (electrons) radiation (Fig.1) transfer the energy into the continuous, even high density matter.

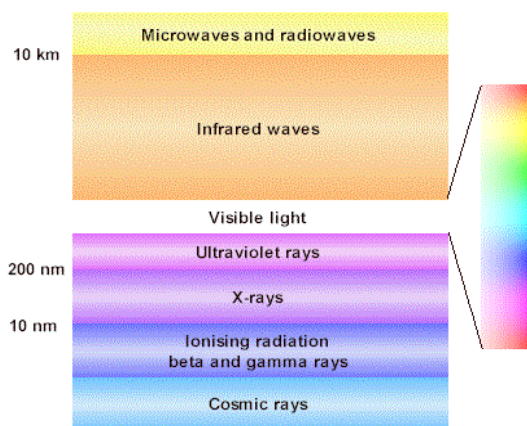


Fig.1. Electromagnetic radiation wavelengths.

Fundamentals

Ionizing radiation, X-rays, gamma radiation, high energy electrons produce abundant secondary electrons. The collision of a photon with a molecule usually causes an electron to be ejected via Compton effect. Thus, nearly all of the physical and chemical changes in the system are produced by the energetic electron and not by the initial photon. The kinetics of reactions induced by high-energy photons are therefore similar to those obtained if high-energy electrons are used as the primary radiation. Therefore there is not a big difference in the effects caused by these different forms of radiation. Depending to the energy transferred, molecules can undergo ionization, excitation or thermal transfer. The interaction with the matter can be divided in the time scale in the following stages; initial physical processes, pre-chemical reactions, chemical reactions and finally radical diffusion. The time scale for the physical stage is on the order of 10^{-16} seconds. The electron excitation occurs in the range shorter than $\sim 10^{-10}$ s and vibrational excitation in the range of 10^{-14} to 10^{-11} . Molecular dissociation takes place

in the range of 10^{-14} to 10^{-6} centered to 10^{-10} s. Reactions governed by diffusion take place in the range of $\sim 10^{-10}$ to $\sim 10^{-6}$ s. In a liquid systems, it takes an ion pair about 10^{-5} s to separate and become free ions. Following these primary events, the ions, secondary electrons and excited molecules undergo further transformations, exchanging charges and energy and reacting with surrounding molecules, thereby producing free radicals and other reactive species which finally evolve into new stable products.

Radiation Sources

Three main sources of radiation are applied for radiation processing. These are electron accelerators, gamma sources and X-ray unit based on e^-/X conversion process. Accelerators are available supplying electron beams in the energy range up to 10 MeV [1] and sources of the radionuclides Co-60 and Cs-137 emitting gamma rays 1.17/1.33 and 0.662 MeV respectively [2]. The introduction of new X-ray (Bremsstrahlung) powerful radiation sources opens new, until now unexplored fields as well [3]. Electron beams are corpuscular radiation and are characterized by limited penetration. The whole energy of high-energy electrons is deposited in relatively thin layers of material. In the case of X-rays and gamma rays, ionizing radiation is provided by photons which have no mass and are thus able to penetrate deeper into materials [4]. The cobalt-60 emitted gamma rays penetrate ~ 300 mm of unit density material on an equal entrance-equal exit basis. In contrast, the highest electron energy used in commercial applications, 10 MeV, penetrates ~ 38 mm only. Dose rates are for gamma and X-rays 4 to 5 orders of magnitude lower as compared to EB. Therefore throughput efficiencies of gamma and X-rays are significantly lower than those of e-beams, electron beams are capable of delivering 100 kGy per second, whereas typical dose rate for gamma rays is 2.8×10^{-3} kGy per second or ~ 10 kGy per hour. The radiation dose rate generated by the electron accelerator of 15 kW power is approximately equal to that generated by 1 MCi of the cobalt source. X-ray target conversion efficiencies vary with the atomic number of the metal used, they are typically no higher than 5-8%. In practice this means that in order for an X-ray to process products with the same speed as a 10 MeV, 50 kW e-beam, it will need to have 625 kW of power.

Polymers

Radiation processing was used early on for polymer modification [5]. The irradiation of polymeric materials with ionizing radiation (gamma rays, X-rays, accelerated electrons, ion beams) leads to the formation of very reactive intermediates, free radicals, ions and excited states. These intermediates can follow several reaction paths that result in disproportion, hydrogen abstraction, rearrangements and/or the formation of new bonds. The degree of these transformations depends on the structure of the polymer and the conditions of treatment before, during and after irradiation. Thorough control of all of these factors facilitates the modification of polymers by radiation processing. Nowadays, the modification of polymers covers radiation cross-linking, radiation-induced polymerization (graft polymerization and curing) and the degradation of polymers. The success of radiation technology for the processing of synthetic polymers can be attributed to two reasons, namely the easiness of processing

in various shapes and sizes and, secondly, most of these polymers undergo cross-linking reaction upon exposure to radiation. On the other hand, naturally occurring polymers were difficult to process and degraded when exposed to high-energy radiation. In recent years, natural polymers are being looked at again with renewed interest because of their unique characteristics like inherent biocompatibility, biodegradability and easy availability. A further progress in natural polymers' processing is foreseen. Many processes of radiation treatment of natural polymers, though known for a long time, have not yet been commercialized, either because of the high cost of irradiation (high dose) or because of the reluctance on part of the industry to adapt to the radiation technology. It is therefore of importance to consider combining the beneficial effects of conventional technology along with radiation technology to overcome such problems. Recently, some products based on radiation processed cellulose derivatives or chitosan have been developed and introduced to the market. A significant difference exists between electron beam and gamma processing of polymers, which is related to dose rate and often to oxidative degradation of material at or near the surface for reactions conducted at low dose-rates. The introduction of new X-ray (Bremsstrahlung) powerful radiation sources opens new, until now unexplored fields of polymer processing as well[6]. New applications are foreseen in the field of nanotechnology [7].

Sterilization

Radiation sterilization of a product means destruction of all viable organisms present on that product (mainly microorganisms) by using ionizing radiation. Both types of ionizing radiation, i.e. gamma radiation from isotopic sources and electron beams from accelerators are used for radiation sterilization. It is now universally accepted that the deoxyribonucleic acid (DNA) in the chromosomes represents the most critical 'target' for ionizing radiation. Effect on the cytoplasmic membrane appears to play an additional role in some circumstances.

The destruction of microorganisms by physical or chemical agents follows an exponential law. Accordingly, one can calculate a finite probability of a surviving organism regardless of the magnitude of the delivered sterilization dose or treatment. The probability of survival is a function of the number and types (species) of microorganisms present on the product (bioburden), the sterilization process lethality, and, in some instances, the environment in which the organisms exist during treatment. It follows that the sterility of an individual item in a population of products sterilized cannot be ensured in the absolute sense. A sterility assurance level (SAL) is derived mathematically and it defines the probability of a viable microorganism being present on an individual product unit after sterilization. SAL is normally expressed as 10^{-n} .

Commercial radiation sterilization has been used for more than 50 years. Over the decades, there has been enormous growth in the disposable medical products market. With this, there has been significant growth in the use of ionizing radiation as a method for sterilization. At present, 40% to 50% of all disposable medical products manufactured in North America are radiation-sterilized. Worldwide, there

are now some 160 commercial cobalt-60 irradiators for radiation sterilization operating in 47 countries containing approximately 240 to 260 million curies ($8.9\text{--}9.6 \times 10^{18}$ Bq) of the gamma emitting cobalt-60. Included in this are service type facilities operated in R&D centres. Because of the ability to down-scale cobalt-60 units, there are many R&D and pilot-scale small facilities as well, almost equal in number (~150). When other uses are taken into account, there are in total over 300 gamma irradiators being operated for a variety of purposes in 55 different countries. Syringes, surgical gloves, gowns, masks, band aids, dressings, medical tetra packs, bottle teats for premature babies, artificial joints, food packaging, raw materials for pharmaceuticals and cosmetics, and even wine corks are gamma sterilized. An increasing number of electron beam (EB) accelerators are also being used, but at present EB is used for only a minority of radiation sterilized product [8].

Food Irradiation

Joint FAO/IAEA/WHO Expert Committee approved the use of radiation treatment of foods up to 10 kGy dose in 1980 [9]. After 1980, new regulations allowed the irradiation of foods, which were not approved for this process before in the US. Approval of irradiation for treatment of packaged fresh or frozen uncooked poultry in 1990 and for treatment of fruits, vegetables and grains in 1986 are some of the examples for these new regulations. Today, more than 40 countries permitted the use of irradiation of over 60 food products. Moreover, the use of irradiation is becoming a common treatment to sterilize packages in aseptic processing of foods and pharmaceuticals. The biggest amount of food product treated are spices [10].

Environmental Applications

Over the last few decades, extensive work has been carried out for utilizing electron beam technology for environmental remediation. This includes application of this technology for flue gas treatment, purification of drinking water and wastewater and hygienization of sewage sludge for use in agriculture [11].

Flue gas treatment

Fossil fuels, which include coal, natural gas, petroleum, shale oil and bitumen, are the main primary source of heat and electrical energy production, are responsible for emitting a large number of pollutants into the atmosphere with off-gases from industries, power stations, residential heating systems and vehicles. All these fuels contain major constituents (carbon, hydrogen, oxygen) as well as other materials, such as metal, sulphur and nitrogen compounds. During the combustion process different pollutants like fly ash, sulphur oxides (SO_2 and SO_3), nitrogen oxides ($\text{NO}_x = \text{NO}_2 + \text{NO}$) and volatile organic compounds are emitted. Wet and dry deposition of inorganic pollutants leads to acidification of environment. These phenomena affect human health, increase corrosion, and destroy plants and forests.

Wet flue gas desulfurization (FGD) and selective catalytic reduction (SCR) can be applied for flue gas treatment and SO_2 and NO_x emission control. All these technolo-

gies are complex chemical processes and waste, like wastewater, gypsum and used catalyst are generated..

Electron beam flue gas treatment technology (EBFGT) is a dry-scrubbing process of simultaneous SO_2 and NO_x removal, where no waste except the by-product are generated. Studies show that irradiation of flue gases with an electron beam can bring about chemical changes that make removal of sulfur and nitrogen oxides easier. The main components of flue gases are N_2 , O_2 , H_2O , and CO_2 , with much lower concentration of SO_x and NO_x . NH_3 may be present as an additive to aid removal of the sulfur and nitrogen oxides. Radiation energy is absorbed by gas components in proportion to their mass fraction in the mixture. The fast electrons slow down and secondary electrons are formed which play important role in overall energy transfer. After irradiation, fast electrons interact with gas creating various ions and radicals, the primary species formed include e^- , N_2^+ , N^+ , O_2^+ , O^+ , H_2O^+ , OH^+ , H^+ , CO_2^+ , CO^+ , N_2^* , O_2^* , N , O , H , OH , and CO . In the case of high water vapour concentration the oxidising radicals OH^\cdot and HO_2^\cdot and excited ions as $\text{O}(^3\text{P})$ are the most important products. These species take part in a variety of ion-molecule reactions, neutralization reactions, dimerization. The SO_2 , NO , NO_2 , and NH_3 present cannot compete with the reactions because of very low concentrations, but react with N , O , OH , and HO_2 radicals. After humidification and lowering its temperature, flue gases are guided to reaction chamber, where irradiation by electron beam takes place. Ammonia is injected upstream the irradiation chamber. Partly NO is reduced to atmospheric nitrogen. The byproduct formed in the process is a mixture of ammonium sulfate and nitrate which is a good fertilizer component.. The electron beam flue gas treatment industrial plants are also operating in the coal-fired plants in China and Poland. The power of accelerators installed at the Polish plant is bigger than 1 MW, therefore it is the largest plasma flue gas treatment facility ever built. The plant treats approx. 270,000 Nm^3/h of flue gases. The installation consists of four main, separated systems: flue gas conditioning unit, ammonia storage and injection unit, process vessels and by-product collecting and storage unit.

The scheme of installation is presented in Fig 2.

The tests carried on the industrial installation showed, that the way of ammonia adding affects the pollutants (especially, SO_2) removal efficiency. The by-product aerosol is collected by the electrostatic precipitator and after granulation and storage is shipped to the NPK fertilizers production plant. The by-product consists mainly of ammonium sulfate and ammonium nitrate. The high efficiency of SO_x and NO_x removal was achieved (up to 95% for SO_x and up to 70% for NO_x) and by-product is a high quality fertilizer [12]. The other possibility is application of the process for VOC removal. Coal combustion is one of the biggest sources of VOCs, which are emitted with various concentrations, polynuclear aromatic hydrocarbons (PAH) are known as the most dangerous, and among them, e.g. benzo(a)pyrene $\text{C}_{20}\text{H}_{12}$, benzo(g,h,i)perylene $\text{C}_{22}\text{H}_{12}$ or dibenzo(a,h)anthracene $\text{C}_{22}\text{H}_{14}$ are the most toxic according to EPA.

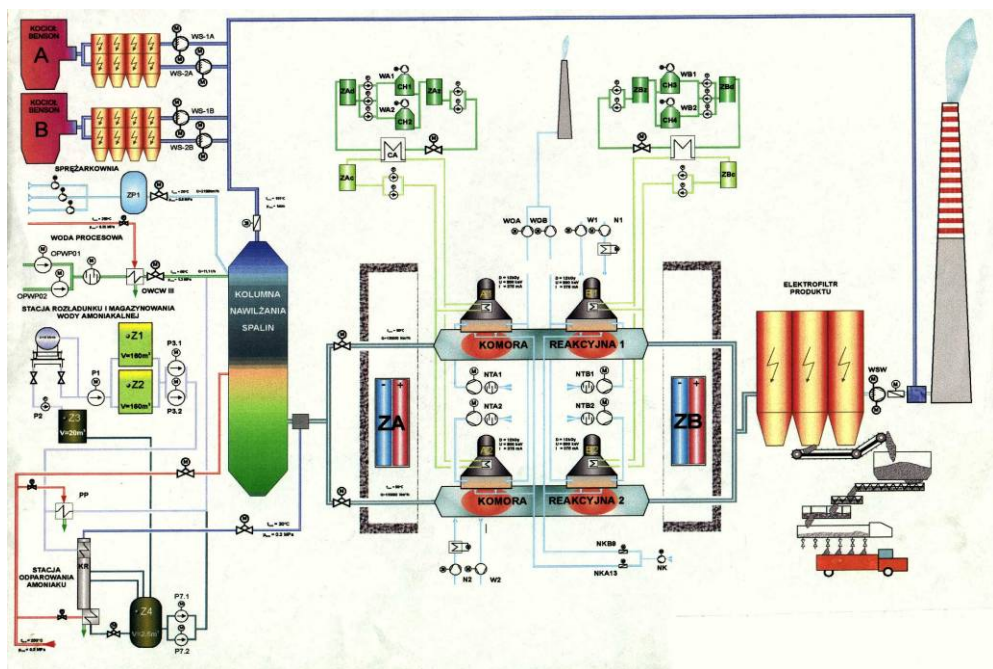


Fig.2. Scheme of industrial plant constructed at EPS Pomorzany, Poland.

Recent years have brought new regulations concerning PAH emission, and European countries have signed an international treaty, covering PAH emission. Tests at the pilot plant constructed at a coal-fired power station were performed with the purpose of estimating the influence of electron beam on VOCs present in flue gas, during SO₂ and NO_x removal. The influence of electron beam on the global toxicity factor of flue gas has been analysed. The removal efficiencies have been ranged from 40% up to 98% [13]. The chlorocarbons may be removed with the high efficiency as well [14].

Wastewater treatment

Increasing urbanization in the last two centuries has been accompanied by expansion of sewerage collection systems without any or adequate treatment. Liquid waste loads have become so large that the self-purification capacity of receiving streams downstream of large populations can no longer prevent adverse effects on water quality. These wastes now constitute significant sources of water pollution. The industrial effluents carry chemical contaminations such as heavy metals, organic pollutants, petrochemicals, pesticides and dyes, while discharge of sewage and sludge gives rise to microbiological contamination of water bodies. The discharge of such materials into water bodies is responsible for risk of infection, health effects caused by contaminated drinking water and offensive odours. Therefore all these industrial and municipal wastewater need adequate treatment. Radiation processing of wastewater treatment is non-chemical, and uses fast formation of short-lived reactive species that can interact with a wide range of pollutants [15]. High-energy irradiation produces instantaneous

radiolytic transformations by energy transfer from high energy photons or accelerated electrons to orbital electrons of water molecules. Absorbed energy disturbs the electron system of the molecule and results in breakage of inter-atomic bonds. the most important products of the fragmentation and primary interactions (radiolytic products).



with yields (G value) of $0.28(\text{e}_{\text{aq}}^-)$, $0.062(\text{H})$; $0.28(\text{OH})$, $0.072(\text{H}_2\text{O}_2)$, in units of $\mu\text{mol}/\text{J}$. High reactivity is characteristic of water radiolysis products. Typical time of their reactions with the impurities in water is, as the rule, less than 1 micro second. At the same time, reactivity of radiolytic products has quite different characteristics. Hydrogen peroxide, H_2O_2 , radicals $\cdot\text{OH}$ and $\text{HO}_2\cdot$ are oxidizing species, while H atom and e_{aq}^- - are reducing in nature. Simultaneous existence of strong oxidants and strong reductants within wastewater under treatment is remarkable and one of the important characteristics of radiation processing. Such reactive radicals are strong oxidizing or reducing agents that can transform the pollutants in the liquids wastes [16]. A large number of substances such as hard surfactants, lignin, pesticides cannot be degraded by conventional biochemical methods and thus escape from decomposition in biological treatment. Biodegradation quality of wastewater depends on oxidation level and structure of pollutants and preliminary oxidation and fragmentation of biologically resistant molecules contribute to improvement of their biodegradability. Above mentioned mechanism of radiolytical oxidation shows possibility for the just required transformation of various pollutants. Research and industrial treatments testify significant improvement of pollutant biodegradability after radiation-oxidation in aerated wastewater. Usually a dose of about 1~2 kGy is necessary for complete transformation of pollutants by biological resistant to a biodegradable state. In December 2005 EB TECH Co, DYETEC, and KAERI finished the installation of high power accelerator (1MeV 400kW) and wastewater treatment system in Daegu Dyeing Industrial Complex (DDIC), Korea, and started operation of the plant. This plant treats up to $10,000\text{m}^3$ of textile dyeing wastewater (from the total of $80,000\text{m}^3$) per day and shows good removal of non-degradable organic impurities. This is a breakthrough in the technology implementation worldwide and the biggest wastewater treatment plant based on electron emission unit ever built [17].

Sludge hygenization and biohazards

Research has shown that sewage sludge can be disinfected successfully by exposure to high-energy radiation. At a plant near Munich, doses of 2-3 kGy destroy more than 99.9% of bacteria present in sewage sludge, and at a plant near Boston a slightly higher dose (4 kGy) was used. Higher doses (up to 10 kGy) are required to inactivate more radiation resistant organisms at plants in Albuquerque and Ukraine. Both gamma sources (Co-60, Cs-137) and electron accelerators can be used for the irradiation of sewage sludge.

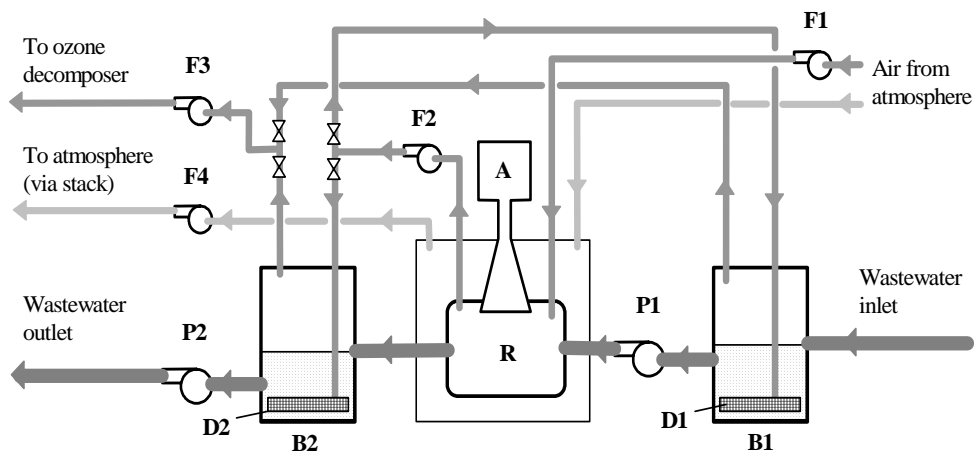


Fig. 3. Simplified technological scheme of the industrial plant in Daegu, Korea.
F1-F4 – Air fans, **P1-P2** – Water pumps, **D1** and **D2** – Diffusers,
A – Accelerator, **R** – Reactor, **B1** and **B2** – Primary and secondary basins.

Gamma sources have better penetration allowing thicker layers of sludge to be irradiated [18], although they are less powerful and take longer irradiation time than electron sources [19]. The pilot plant using gamma source is operated in India. The irradiator system can be easily integrated with conventional treatment plant with flexibility of operation. Various dose treatment can be imparted to sludge with addition of sensitizing agents such as oxygen, air, ozone etc. About 3 kGy of absorbed dose in sewage sludge removes 99.99% of pathogenic bacteria consistently and reliably in a simple fashion. The irradiated sludge being pathogen free can be beneficially used as manure in the agricultural fields as it is rich in nutrients required for the soil. Since the irradiated sludge is free from bacteria, this can also be used as a medium for growing soil useful bacteria like rhizobium and azetobactor to produce bio-fertilizers, which can be used to enhance the crop yields

Special applications regards biohazards combat. Anthrax that was sent in mail in October 2001 caused several deaths and big economical losses in the USA. Radiation proved to be very effective for mail decontamination. About 4000 tons of letter mail and 200 tons of parcels had been sanitized by the end of 2003[20], the units are in operation nowadays as well.

Conclusions

Physical, chemical and biological effects of ionizing radiation on the matter are the basis of many practical applications. The number of applications is growing and radiation sources; gamma, eb and X are becoming an industrial equipment operated in the harsh, demanding environment. They play important role in the economical development of many countries.

References

- [1] Zimek, Z. and Chmielewski, A.G., Electron accelerators for radiation processing, *Nukleonika*, 1993, **38**(2), 3-19.
- [2] IAEA, 2005, Gamma irradiators for radiation processing, Vienna, ISBN 83-909690-6-8.
- [3] Stichelbaut, S., F., Bol, J-L., Cleland, M.R., Gregoire, O., Herer, A.S., Jongen, Y., Mullier, B., The Pallettron™: a high-dose uniformity pallet irradiator with X-rays, *Radiat. Phys. Chem.* 2004, **71** (1-2), 291-295.
- [4] Mehta, K., Radiation: Basics principles, *J.Vascular Surgery*, 2005, 1237-1238.
- [5] Zaman Haji Mohd Dahlan, K., 2004, Radiation processing, Physical Sciences, Engineering and Technology Resources, in *Encyclopedia of Life Support Systems (EOLSS)*, Developed under the Auspices of the UNESCO, Eolss Publishers, Oxford, UK, [<http://www.eolss.net>].
- [6] Chmielewski, A.G., Haji-Saeid, M., Shamshad, A., Progress in radiation processing of polymers, *Nucl. Instr. Meth. in Phys. Res. B*, 2005, **226**, 44-54.
- [7] Chmielewski, A.G., Michalik, J., Buczkowski, M. Chmielewska, D.K, Ionizing radiation in nanotechnology, *Nucl. Instr.Meth.Phys.Res.* 2005, **B236**, 329-332.
- [8] Chmielewski, A.G., Haji-Saeid, M., Radiation technologies: past, present and future, *Radiat. Phys. Chem.*, 2004, **71** (1-2) 17-21.
- [9] FAO/IAEA/WHO, 1999, High-dose irradiation: wholesomeness of food irradiated with doses above 10 kGy, WHO Technical Reports Series no 890, Geneva, Switzerland.
- [10] Chmielewski, A.G., Migdał, W., Radiation decontamination of herbs and species, *Nukleonika*, 2005, **50**(4), 179-184.
- [11] Chmielewski, A.G., Application of ionizing radiation to environment protection, *Nukleonika* , 2005, **50** (suppl. 3), S17-S22.
- [12] Chmielewski, A. G., Licki, J., Pawelec, A., Tymiński, B., Zimek, Z., *Radiat. Phys. Chem.*, 2004, **71** (1-2), 441-444.
- [13] Chmielewski, A.G., Ostapczuk, A., Licki, J., Zimek, Z., Kubica, K., Reduction of VOCs in flue gas from coal combustion by electron beam treatment , *Radiat. Phys. Chem.*, 2002, **63** (3-6), 653-655.
- [14] Sun, Y, Chmielewski, A.G., 1,2-Dichloroethylene decomposition in air mixture by using ionization technology, *Radiat. Phys. Chem.*, 2004, **71**(1-2), 433-436.
- [15] Getoff N., Radiation-induced degradation of water pollutants--state of the art, *Radiat. Phys. Chem.*, 1996, **47**(4), 581-593.
- [16] Wasiewicz M., Chmielewski, A.G., Getoff, N., Radiation-induced degradation of aqueous 2,3-dihydroxynaphthalene, *Radiat. Phys. Chem.*, 2006, **75**(2), 201-209.
- [17] Han, B., Kim, Y.R, Kim, R.A., Salimov, R.A., Kuksanov, N.K, Nemytov, P.I., Electron beam treatment of textile dyeing wastewater: Operation of pilot plant and industrial plant construction, in *TECDOC-1473*, IAEA, Vienna, 2005, 101-110.
- [18] Sabharwal, S., Shah, M.R., Kumar, N., Patel, J.B., Technical and economic aspects of radiation hygenization of municipal sewage sludge using gamma irradiator, in *TECDOC-1473*, IAEA, Vienna, 2005, 111-118.
- [19] Chmielewski A.G., Zimek, Z., Bryl-Sandalewska, T., Kosmal, W., Kalisz, L, Kazimierczuk, M., Disinfection of municipal sludges in installation equipped with electron accelerator, *Radiat.Phys.Chem.*, 1995, **46**, 1071-1074.
- [20] Desrosiers, M.F., Irradiation applications for homeland security, *Radiat.Phys.Chem.*, 2004, **71**(1-2), 479-482.

Chemical Thermodynamics

(A)

THERMAL ISOMERIZATION OF *PUSH-PULL* 5-SUBSTITUTED-4-OXOTHIAZOLIDINES

D.M. Minić¹, Z. Nedić¹, I. Cekić¹ and R. Marković²

¹*Faculty of Physical Chemistry, University of Belgrade, Belgrade, Serbia*

²*Faculty of Chemistry, University of Belgrade, Belgrade, Serbia, dminic@ffh.bg.ac.yu*

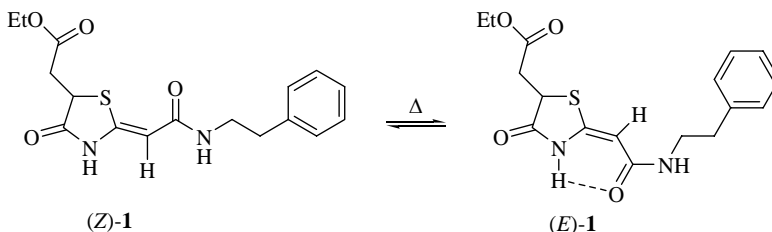
Abstract

Thermal *Z* → *E* isomerization of push-pull 5-substituted-4-oxothiazolidines was studied. It was shown that irreversible isomerization with simultaneous crystal structure cleavage, occurs at 145 °C. The rate constant and activation energy, as well as the activation parameters of this process, were determined.

Introduction

The series of stereodefined 4-oxothiazolidines attracted our attention due to their potential biological activity and as precursors for the synthesis of *push-pull* polyenes[1]. We have shown that the equilibrated mixtures of structurally related 4-oxothiazolidines consist of the intramolecularly H-bonded (*E*)-isomer and intermolecularly H-bonded (*Z*)-isomer in varying proportions, which depend on the solvent polarity and temperature [2-4].

Herein, we report the first kinetic and thermodynamic studies of thermal *Z/E* isomerization of 5-substituted 4-oxothiazolidine derivative, i.e. ethyl (*Z*)-(5-ethoxycarbonylmethyl-4-oxothiazolidin-2-ylidene)-*N*-(2-phenylethyl)ethanamide (**1**) in solid state, taking place according to following reaction scheme:



Experimental

IR spectra in the ν 4000-400 cm^{-1} range were measured on a Perkin Elmer 983GxFT-IR spectrophotometer, using KBr discs. Spectra at higher temperature were recorded in an adapted variable-temperature cell model VLT.2 (RIIC London).

The thermal stability and structural transformations were investigated by non-isothermal thermal analysis (DSC) using a Du Pont Thermal Analyzer (model 1090).

Results and Discussion

Investigation of thermal behaviour in the temperature interval of 20-200 °C, shows that solid (*Z*)-5-ethoxycarbonylmethyl-4-oxothiazolidin-2-ylidene)-*N*-(2-phenylethyl)-ethanamide was stable up to approximately 136 °C. Upon heating above this temperature, the *Z*-isomer first melted ($T_m=145.1\text{ °C}$), then resolidified without crystallization, remelted at slightly lower temperature ($T_m=130.9\text{ °C}$) and finally resolidified without crystallization. The change of the melting point can be ascribed to the irreversible *Z* → *E* phase transformation of the sample after melting.

IR spectrum of the starting *Z*-isomer **1** at room temperature (Fig. 1) significantly differs from the corresponding spectrum of the *E*-isomer **1** at 150 and 170 °C (Figs. 1b and 1c). The greatest differences in IR spectra of *Z*- and *E*-forms are noted within the regions of NH group vibrations (at about 3300 cm^{-1}) and these of the exo C=O group at the vinyl position and lactam group (at about 1700 cm^{-1}), whereby the strong band which appears at 1733 cm^{-1} , attributed to C=O ester group of the ethoxycarbonylmethyl substituent at the C-5 position, is present in the spectra of both isomers.

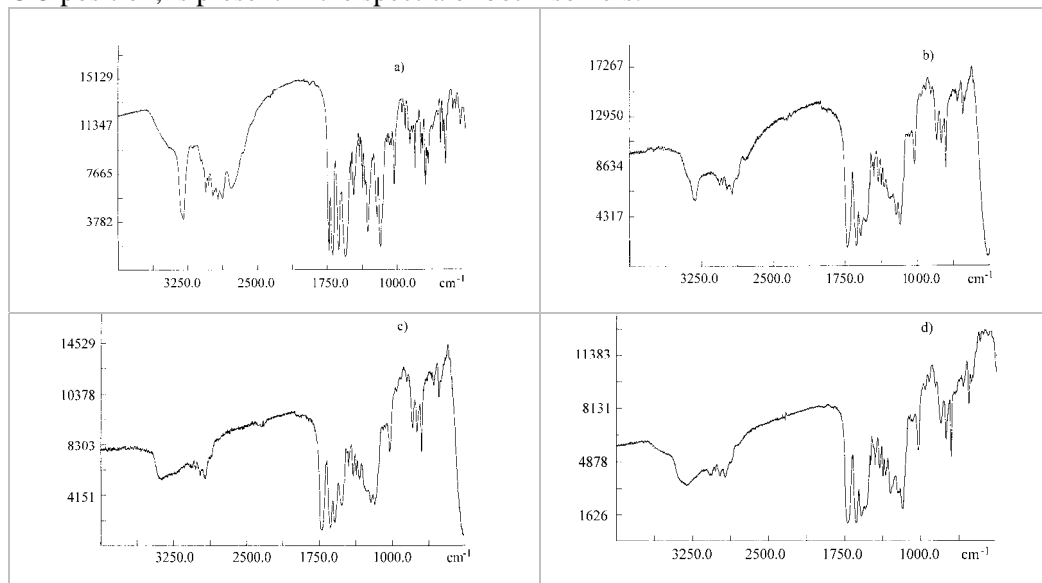


Figure 1. IR spectra of (*Z*)-5-ethoxycarbonylmethyl-4-oxothiazolidin-2-ylidene)-*N*-(2-phenylethyl)ethanamide (**1**) in the ν 4000-250 cm^{-1} range: a) at room temperature before heating; b) at room temperature after melting; c) at 150 °C and d) at room temperature after 24 h.

Thus the central band of the strong intensity at 3320 cm^{-1} belonging to the amide functional group in the *Z*-isomer is shifted in the *E*-isomer to higher frequency (3355 cm^{-1}). The band at 3296 cm^{-1} corresponding to the expanding vibration of the NH lactam group

present in the *Z*-isomer is not present in the *E*-isomer, while the bending vibration of the NH lactam group giving rise to the band at 1532 cm^{-1} in the *Z*-isomer, appears in the case of the *E*-isomer at 1515 cm^{-1} . Furthermore, the band at 1719 cm^{-1} of the C=O lactam group is shifted to 1726 cm^{-1} in the *E*-isomer. The band at 1695 attributed to the C=O amide group participating in the formation of intermolecular bonds with neighboring molecules disappears in the *E*-isomer. However, the IR spectrum of this isomer contains a new band at 1639 cm^{-1} characteristic of the *E*-isomer stabilized by an intramolecular hydrogen bond formed between the C=O and NH lactam groups. It should be noted that rather strong enamine band at around 1526 cm^{-1} appears in the spectra of the both isomers as one of the most typical in the IR spectra of the push-pull 4-oxothiazolidine derivatives.

Table 1. Kinetic and thermodynamic parameters of phase transformation of *Z*- and *E*-isomers of compound **1**

Isomer	T_m (°C)	ΔH (J/g)	k (s ⁻¹)	$t_{1/2}$ (s)	n
<i>Z</i> -form	145.1	434.0	4.48	0.15	0.90
<i>E</i> -form	130.9	134.0	9.75	0.07	1.05

Activation energy was determined as $E_a = 351.6\text{ kJ/mol}$ [5,6]. Thus, the kinetic parameters, based on the Arrhenius-like equation, $k = Z \exp(-E_a/RT)$, can be then evaluated and used to provide a valid description of the thermal behavior of ethyl (*Z*)- and (*E*)-(5-ethoxycarbonylmethyl-4-oxothiazolidin-2-ylidene)-*N*-(2-phenylethyl)-ethanamide (**1**) (Table 1).

Conclusion

The variable-temperature IR data recorded for 5-substituted 4-oxothiazolidine **1** were analyzed and discussed in terms of the *Z* → *E* isomerization.

References

- [1] R. Marković, M. Baranac, J. Serb. Chem. Soc., 1998, **63**, 165.
- [2] R. Marković, Z. Džambaski, M. Baranac, Tetrahedron, 2001, **57**, 5833.
- [3] R. Marković, M. Baranac, Heterocycles, 1998, **48**, 893.
- [4] R. Marković, M. Baranac, S. Jovetić, Tetrahedron Lett., 2003, **44**, 7087.
- [5] J.H. Borchardt, F.Danniels, J. Am.Chem. Soc., 1957, **79**, 41.
- [6] E.H. Kissinger, J. Res. Nat. Bur. Stand., 1956, **57**, 217.

CALCULATION OF MIXING ENTHALPIES FOR TERNARY Au-IN-Sb LIQUID ALLOYS

L. Gomidželović¹ and D. Živković²

¹ *Copper Institute, Zeleni bulevar 35, 19210 Bor, Serbia (lgomidzelovic@yahoo.com)*

² *University of Belgrade, Technical Faculty, VJ 12, 19210 Bor, Serbia*

Abstract

The results of calculation of mixing enthalpies for ternary Au-In-Sb liquid alloys using derived form of the Gibbs-Helmholtz equation in temperature interval 300 - 1000K are presented in this paper. Also, values of mixing enthalpies at 1000K were compared with the results of calculation using the Redlich-Kister-Muggianu expression.

Introduction

Indium-based lead-free alloys belong to a group of solders considered as a possible alternative to conventional Pb-bearing solders in step soldering, which are required for high density packaging of multi-chip modules demanding a number of solders with melting points over a wide temperature range [1, 2]. Also, the phase diagram of ternary Au-In-Sb system is important in predicting the interface reactions between In-based solders and Au-substrate, which can provide a tool for design a potential interface [2]. Literature thermodynamic data for constitutive binary systems, Au-In, In-Sb and Au-Sb can be found in the COST 531 Database for Lead Free Solders [3]. So far, only phase equilibria investigations of this system was given by Kubiak and Schubert [4] and Tsai and Williams [5].

Results and Discussion

For the purpose of thermodynamic calculation three sections were chosen with molar ratios 1:3, 1:1, 3:1, from each corner of ternary Au-In-Sb system, respectively, and with molar content of 0-0.9 for third component. The enthalpy of mixing was determined using derived form of the Gibbs-Helmholtz equation, as follows:

$$\left[\frac{\partial(\Delta G^E/T)}{\partial(1/T)} \right]_P = \Delta H^M \quad (1)$$

Basic data for this calculation were the results for the integral excess Gibbs energies for chosen alloys, obtained by application of Redlich-Kister polynomials, known for three constitutive binary systems [3] and given in Table 1.

Table 1. Redlich-Kister parameters for the investigated systems

System <i>ij</i>	L_{ij}^0 (T)	L_{ij}^1 (T)	L_{ij}^2 (T)
<i>AU-IN</i> [3]	-80027.7+89.7173262T- 9.57049TlnT	-34977.3+117.293782T- 13.0337TlnT	0
<i>In-Sb</i> [3]	-25631.2+102.9324T- 13.45816TlnT	-2115.4-1.31907T	2908.9
<i>Au-Sb</i> [3]	-15437.35-4.63455T	-18854.1+15.64707T	-4271.85

Final derived expression used in the calculation of mixing enthalpies for liquid ternary Au-In-Sb alloys is given as follows:

$$\Delta H^M = -T^2 \left[\left(\frac{1}{T} \right) \left(x_{Au} x_{In} (-9.57 - 13.03(x_{Au} - x_{In})) - 13.46 x_{In} x_{Sb} \right) + \left(\frac{1}{T^2} \right) \left(x_{Au} x_{In} (80027 + 34977(x_{Au} - x_{In})) + x_{In} x_{Sb} (25631 + 2115(x_{In} - x_{Sb}) - 2909 \dots (2) \right. \right. \\ \left. \left. (x_{In} - x_{Sb})^2 \right) + x_{Au} x_{Sb} (15437 + 18854(x_{Au} - x_{In}) + 4272(x_{Au} - x_{Sb})^2) \right] \right]$$

The values of mixing enthalpies of chosen liquid ternary alloys were defined at 1000K, also, using data from Ref [7-9] and Redlich-Kister-Muggianu expression, given as:

$$\Delta H^M = x_1 x_2 \Delta H^M_{12} + x_2 x_3 \Delta H^M_{23} + x_1 x_3 \Delta H^M_{31} \quad \dots (3)$$

where:

$$\Delta H^M_{ij} = X_i X_j (A^0_{ij} + A^1_{ij} (X_i - X_j) + A^2_{ij} (X_i + X_j)^2 + \dots + A^n_{ij} (X_i - X_j)^n) \quad \dots (4)$$

and shown for the sections from antimony corner in Table 2.

Table 2. The results of ΔH^M for liquid Au-In-Sb alloys at 1000 K (section from antimony corner) obtained from (3)

Au:In	xSb										
	0	0.1	0.2	0.3	0.4	0.5	0.6	0.7	0.8	0.9	1
1:1	-21290	-21034	-19755	-17604	-14774	-11504	-8076	-4819	-2102	-343	0
ΔH^M 1:3	-11793	-12508	-12558	-11912	-10609	-8758	-6539	-4200	-2059	-507	0
3:1	-14132	-16494	-16911	-15782	-13517	-10531	-7250	-4110	-1553	-29	0

Because of the lack of experimental data for the investigated system, the comparison was done only for the results attained from Eq. (2) and (3), and shown in Fig.1. This comparison reveals reasonable agreement between the values of integral mixing enthalpies calculated using derived Gibbs-Helmholtz equation (2) and Redlich-Kister-Muggianu expression (3), especially for the higher content of antimony. In both cases, strong negative values for integral mixing enthalpies were obtained in whole concentration range, which indicates that considerable attraction exists between constitutive components.

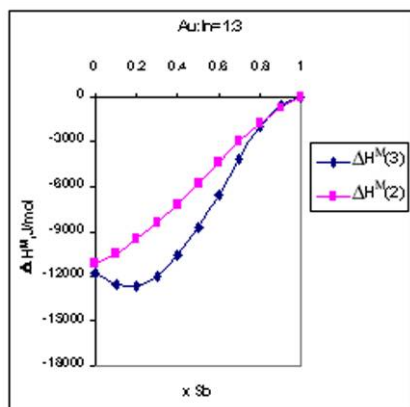


Fig.1. The comparison of ΔH^M at $T=1000$ K calculated using derived Gibbs-Helmholtz equation (2) and Redlich-Kister-Muggianu expression (3)

Conclusion

It's widely acknowledged that information about thermodynamic properties such as enthalpies of mixing is irreplaceable for the thermodynamic optimization of phase diagrams and the estimation of several physical properties like surface tension and wettability. Therefore, data presented in this paper can be very useful in further investigation of ternary Au-In-Sb system, like a possible lead-free solder.

Acknowledgement

The authors are grateful to the Ministry of Science and Environmental Protection of the Republic of Serbia (Project N^o142043) for financial support.

References

- [1] J. S. Hwang, Environment-friendly electronics: Lead-free technology, Electrochemical Publications Ltd., Port Erin, 2001, 97.
- [2] H. S. Liu, C. L. Liu, C. Wang, Z. P. Jin, K. Ishida, J. Electron. Mater., 2003, **32**, 81.
- [3] Version 1.1 of the COST 531 Database for Lead-Free Solders (<http://www.ap.univie.ac.at/users/www.cost531>).
- [4] R. Kubiak and K. Schubert, Z. Metallkd., 1980, **71**, 635.
- [5] C. T. Tsai and R. S. Williams, J. Mater. Res., 1986, **1**, 352.
- [6] Y. K. Rao, Stoichiometry and Thermodynamics of Metallurgical Processes, Cambridge University Press, New York, 1985, 307.
- [7] R. C. Sharma, T. L. Nagai, Y. A. Chang, Bull. Alloy Phase Diagrams, 1989, **10**, 657.
- [8] R. Castanet, W. Ditz, K. L. Komarek, E. Reiffenstein, Z. Metallkde., 1981, **72**, 176.
- [9] H. Okamoto, T. B. Massalski, Bull. Alloy Phase Diagrams, 1984, **5**, 166.

PHASE EQUILIBRIA OF THE IN-Sb-Bi SYSTEM

D. Manasijević¹, D. Minić², D. Živković¹ and Ž. Živković¹

¹University of Belgrade, Technical Faculty, VJ 12, 19210 Bor, Serbia (dmanasijevic@tf.bor.ac.yu)

²University of Pristina, Mining and Metallurgy Faculty, 38220 Kosovska Mitrovica, Serbia

Abstract

Binary thermodynamic data, successfully used for phase diagram calculations of binary systems In-Sb, Bi-Sb and In-Bi, were used for prediction of phase equilibria in ternary system In-Sb-Bi. Predicted equilibrium phase diagrams were compared with the results of SEM-EDX and DTA.

Introduction

The knowledge of phase equilibria in the ternary systems of the corresponding metals with the elements of III-V compound semiconductor is an important step toward a better understanding of contact formation and presents a basis for the development of new and improved contact materials.

The aim of this study is to calculate some characteristic equilibrium phase diagrams of the In-Sb-Bi system according to CALPHAD approach [1] and to compare obtained results with experimental results based on SEM-EDX and DTA.

Thermodynamic Modelling

The pure solid elements at 298.15 K and 1 bar in their stable form were chosen as the reference state for the systems (SER). The Version 4.4 of the SGTE Unary Database (Scientific Group Thermodata Europe) of phase stabilities for stable and metastable states of pure elements was used [2]. The thermodynamic descriptions of binary systems were taken from literature [3]. Calculation was performed using Thermo-Calc software (TC4A version).

Experimental

Alloys of the In-Sb-Bi system were prepared from pure metals (99.99 %) by induction melting of weighted amounts of indium, antimony and bismuth under argon atmosphere.

After melting, alloys were subjected to a homogenizing annealing in evacuated quartz glass capsules. Annealing was done in a resistance furnace at 300 °C for 100 hours with subsequent quenching into ice water (for SEM-EDX measurements) and cooling inside the furnace to the room temperature (for DTA measurements).

The equilibrium compositions of samples were determined using JEOL scanning electron microscope with accelerating voltage 20kV and EDX analyzer.

DTA measurements were carried out with the Derivatograph 1500 (MOM Budapest) apparatus under following conditions: air atmosphere, heating rate 10 K/min.

Results and Discussion

Phase diagram of the isothermal section at 300 °C, was calculated only on the base of binary thermodynamic data using Redlich-Kister-Muggianu model for ternary thermodynamic functions. The SEM (scanning electron microprobe) with EDX (energy dispersive X-ray) analysis can give us very important information of composition of searching phases. Reasonable agreement between the experimental data and binary-based prediction was found as it is shown in Fig. 1.

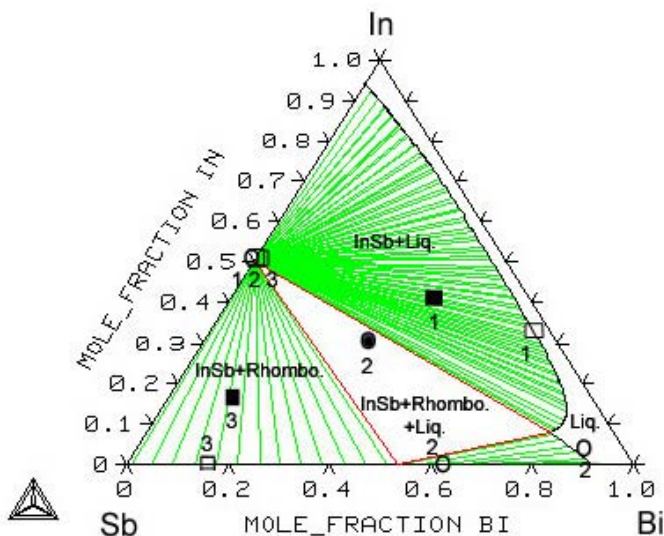


Fig. 1. Results of SEM analysis, comparison with prediction at 300 °C. Full symbols – overall composition, empty symbols – compositions of phases.

Isothermal section of the In-Sb-Bi ternary system at 300 °C includes one three-phase region (InSb+Rhomb+Liquid), three two-phase regions (InSb+Rhomb; InSb+Liquid; Rhomb+Liquid) and one single-phase region (Liquid).

Figure 2 shows predicted phase diagram of the isoconcentration section with the DTA results.

Conclusion

Binary-based thermodynamic prediction of the In-Sb-Bi system equilibria was performed using optimized thermodynamic parameters for the constitutive binaries from literature. Estimated phase diagram at 300 °C was compared with experimental results obtained by SEM analysis. Experimentally determined liquid and rhombo phases for the In_{0.31}Sb_{0.38}Sn_{0.31} sample contain higher contents of bismuth comparing to prediction, which suggests the need for introduction of ternary interaction parameters for rhombo and liquid phase. In spite of experimental results presented in this work, more thermodynamic and phase equilibrium data at various temperatures are required for detailed assessment.

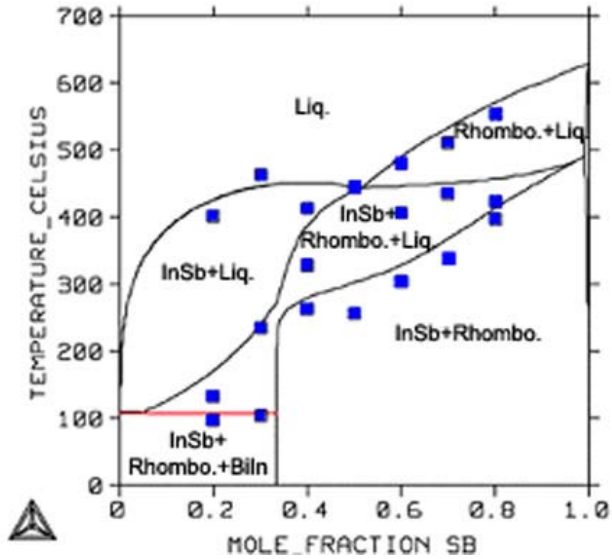


Fig. 2. Predicted isoconcentration cross section in ratio $x_{\text{In}} : x_{\text{Bi}} = 1:1$ with DTA results from this work

Acknowledgments

The authors are grateful to the Ministry of Science and Environmental Protection of the Republic of Serbia (Project No. 142043) for financial support and to Dr. Jan Vrestal, Masaryk University, Brno, Czech Republic.

References

- [1] N. Saunders, A. P. Miodownik, CALPHAD (CALculation of PHase Diagrams): A comprehensive guide, Pergamon, New York, 1998.
- [2] Version 4.4 of the SGTE Unary Database.
- [3] Version 1.1 of the COST 531 Database for Lead Free Solders.

GAS CORROSION DAMAGE IN Ti-STABILIZED INTERSTITIAL FREE STEEL

I. Cvijović¹, M. Spiegel², and I. Parezanović²

¹*Institute of Nuclear Sciences »Vinča«, P.O. Box 522, 11001 Belgrade, Serbia. (ivanac@vin.bg.ac.yu)*

²*Max-Planck Institute for Iron Research, Max-Planck Str. 1, 40237 Düsseldorf, Germany.*

Abstract

The selective oxidation damage in the Ti-stabilized interstitial free steel during 60 s of recrystallization annealing at 820 °C under the different compositions of protective H₂-N₂ atmosphere at low dew point (-40 °C) was investigated using various experimental techniques. It was found that Mn, Al and Si oxide particles are the main products of external and internal oxidation. Increase of the H₂ content in gas atmosphere favors external oxidation and leads to appearance of greater nonwetted surface areas.

Introduction

The surface segregation and selective oxidation during recrystallization annealing of high strength steels used in automotive industry can cause the poor wettability of the steel surface by molten baths during hot-dip galvanizing [1], reducing the quality of corrosion-protective coatings [2]. The external presence and appearance of nonwettable Mn-oxides have the main influence on the coatings coverage. Since it is impossible to prevent external oxidation [3], it is very important to determine the annealing conditions and surface state which would improve the wetting and spreading of the coating melts, changing the nature, morphology and distribution of oxide particles. In this work, the effects of protective H₂-N₂ atmosphere composition on the selective oxidation mode and external/internal particle characteristics were investigated in the case of Ti-stabilized interstitial free steel (Ti-IF).

Experimental Procedure

The investigated steel with the chemical composition: Fe-0.0028C-0.0033N-0.085Mn-0.006Si-0.044Al-0.0001B-0.016Cr-0.006P-0.006S-0.073Ti (in wt.%) was supplied in the form of 0.8mm thick cold-rolled sheets. Metallographically prepared samples were annealed for 60 s at 820 °C under the 5 vol.% H₂-N₂ and 15 vol.% H₂-N₂ protective atmosphere with traces of water (dew point of -40 °C). The characterization of sheet surface composition before and after annealing was carried out using a LEO 1550 VP field emission scanning electron microscope (FE-SEM) equipped with energy dispersive spectrometer (EDS) at a 15 kV voltage and PHI Quantum 2000 X-ray photoelectron spectrometer (XPS). The XPS depth profiles were recorded with a sputter rate of 2.67 nm/min.

Results and Discussion

The XPS analysis of cold rolled sheet surface showed that it is covered with 38.9 nm thick oxide layer, mainly containing Fe_2O_3 and Fe_3O_4 . The presence of these oxides is confirmed with appearance of O 1s and Fe 2p peaks on XPS spectrum shown in Fig. 1a. A weak Si 2p peak indicates that SiO_2 is also present, while an appreciable amount of C may only be present as a contaminant.

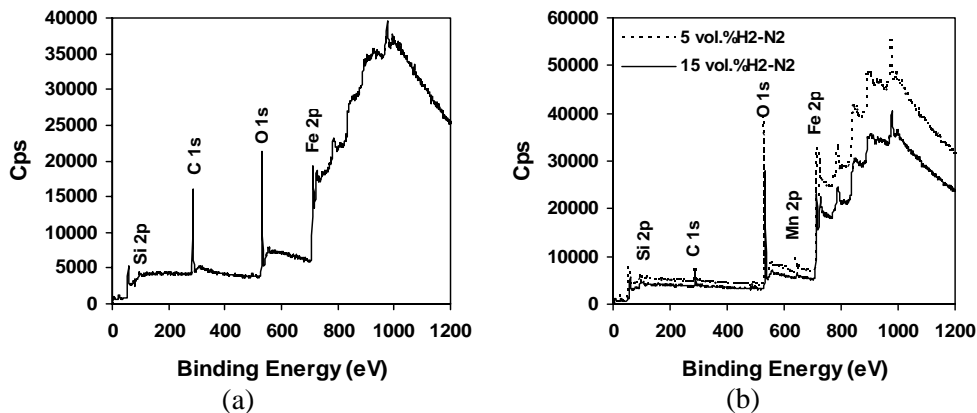


Fig. 1. XPS spectra recorded on as-cold rolled sheet surface of Ti-IF steel (a) before and (b) after annealing under $\text{H}_2\text{-N}_2$ protective gas atmosphere for 60 s.

During annealing at 820 °C the native Fe-oxides are reduced which is confirmed with the shift of the Fe 2p peak towards lower binding energy, Fig. 1b. Simultaneously, the external and internal oxidation of alloying elements is progressive, Fig. 2. The Mn oxides growing at the sheet surface are the main product of selective oxidation. Double Mn 2p and Si 2p peak, Fig. 1b, at the position which does not correspond to the formation of SiO_2 , indicate that different types of external Mn oxides are present, Fig. 3. Nodular MnO islands formed inside the grain are found only after annealing under 15 vol.% $\text{H}_2\text{-N}_2$ atmosphere, Fig. 3b. Another Mn oxide detected as complex MnSiO_3 oxide is precipitated at the grain boundaries during annealing under both conditions. Since the partial pressure of oxygen is decreased with increased H_2 content in the gas atmosphere, segregating elements have enough time to diffuse to the surface. As a result, the outer oxide layer is thicker than on the sheet surface annealed under 5 vol.% $\text{H}_2\text{-N}_2$ atmosphere. The formation of 39.2 nm thick oxide layer is primarily consequence of the expressive external oxidation. Large surface coverage with external oxides limits the oxygen penetration into the steel and decreases the internal oxidation as shown in Fig. 2b. As can be seen, the concentration of Al increases slightly with depth indicating the presence of a small amount of internal Al_2O_3 oxide. The behavior of Ti-IF steel during annealing under 5 vol.% $\text{H}_2\text{-N}_2$ atmosphere is quite different. The smaller surface coverage is observed. Except separate MnSiO_3 islands, Fig. 3a, the particles of other oxides are not present. Moreover, the beneficial TiN particles are sporadically present at the surface. Intensive internal oxidation and deeper presence of Al_2O_3 oxide led to formation of 50.4 nm thick oxide layer.

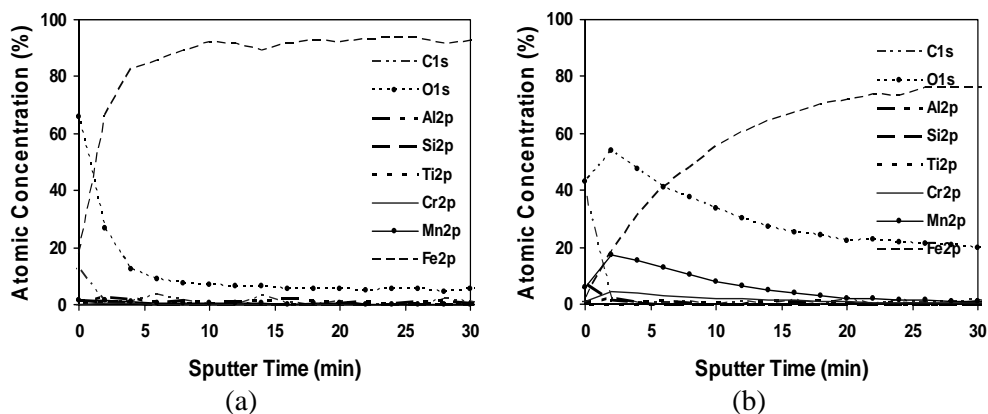


Fig. 2. XPS in-depth profiles on Ti-IF steel after annealing under (a) 5 vol.% H₂-N₂ and (b) 15 vol.% H₂-N₂ atmosphere for 60 s.

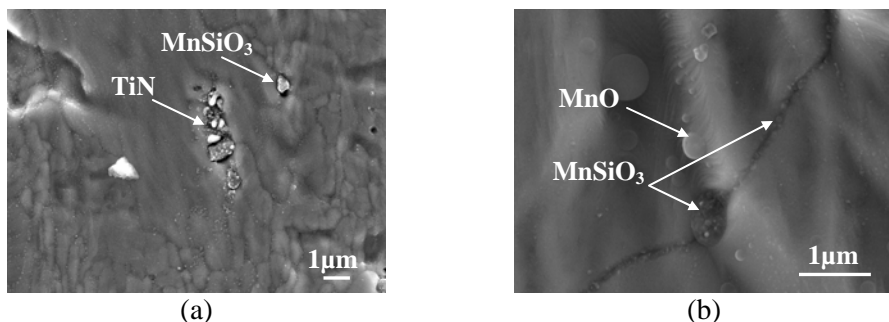


Fig. 3. FE-SEM micrographs of Ti-IF steel surface after annealing under (a) 5 vol.% H₂-N₂ and (b) 15 vol.% H₂-N₂ atmosphere for 60 s.

Conclusion

The selective oxidation of Ti-IF steel, occurring externally and internally during annealing at 820 °C, is strongly dependent on the H₂-N₂ protective atmosphere composition. External formation of MnO and MnSiO₃ islands is predominant. Internal appearance of Al₂O₃ oxide contributes to the overall thickness of oxide layer. As the H₂ content increases from 5 to 15 vol.% the surface coverage with nonwetable oxides increases. On the other hand, decrease in the H₂ content favors internal oxidation and leads to increase of oxide layer thickness for 11.2 nm.

Acknowledgements

Authors are grateful to the Ministry of Science and Environmental Protection of the Republic of Serbia for the financial support.

References:

[1] M. Lamberigts, J.P. Servais, Applied Surface Science, 1999, **144-145**, 334-338.
 [2] K. Hulka, Mater. Sci. Forum, 2005, **473-474**, 91-102.
 [3] J.P. Servais, H. Graas, V. Leroy, Metall. Rep. CRM, 1975, **44**, 29-38.

THERMAL ANALYSIS OF WHEY MAYONNAISE

S. Ostojić, M. Kićanović, S. Zlatanović, M. Pavlović and Z. Marković

*Holding Institute of General and Physical Chemistry,
Studentski trg 12/V, Belgrade, Serbia*

Abstract

Thermal stability of whey mayonnaise has been analyzed by Differential Scanning Calorimetry (DSC). The objective of the present study was to investigate the thermostability of mayonnaise emulsions based on partially denaturated whey protein concentrates. Information on thermal stability of sample, valuable for technological process, was obtained.

Introduction

Whey proteins are of high nutritional and bioregulatory value, rich in essential amino acids and cystein, and are widely used in food industry because of their emulgating, gelling, fat-mimetic and antioxidative properties [1-4]. Because of their excellent emulgating and gelling properties, whey protein concentrates could be a good replacement of egg yolk in mayonnaise, with up to 70 times lowered concentration of cholesterol. The objective of the present study was to investigate the thermostability of mayonnaise emulsions based on partially denaturated whey protein concentrates.

Experimental

Sample preparation: Mayonnaise was produced in 0.7 kg batches composed of 39.8 % (w/w) sunflower oil, 11.23 % (w/w) of row whey protein concentrate of with 2.5% (w/w) pure whey protein, 0.7% NaCl (w/w) 1.5 % vinegar, 0.073 % (v/w) citric acid, 5% (w/w) mustard, 0.1% (w/w) conservans potassium sorbate, and 0.3% stabilisator Grinsted FF5103 (Danisco, Denmark). Antioxidant α -tokoferol (240 mg/kg) was added to the oil phase before mayonnaise production. Mayonnaise was produced by mixing oil with aqueous phase containing whey protein concentrate, preheated 20 min at 70 °C and cooled to 30 °C. The acid phase containing vinegar, citric acid, salt, mustard and conservans was added after emulsion was obtained. The coarse emulsion was prepared by homogenizing oil and aqueous phase using a high-speed blender at setting 2 for 2 minutes.

Thermal analysis: DSC scans of obtained whey mayonnaise were performed by TA Instrument DSC Q1000 with RCS cooling system. TA Universal Analysis: TA2000, TA Instruments, software was used for DSC data analysis. Sample was prepared by carefully weighing of 2.6 mg of mayonnaise in aluminum hermetic DSC pan, closed with hermetic sealing. The sample of whey mayonnaise was subjected to cyclic cooling and heating described above. Cycle I: cooling from 313 K to 193 K, with cooling rate 5K/min. Cycle II: hating from 193 K to 313 K with heating rate 5 K/min. Cycle III: cooling from 313K to 193K with cooling rate 2.5 K/min. Cycle IV: heating from 193 K to 313K with heating rate 5 K/min. Cycle V: cooling from 313 K to 193 K with cooling rate 1.25 K/min. Cycle VI: heating from 193 K to 313 K.

Results and Discussion

The crystallization and melting DSC curves of the whey mayonnaise, oil and water emulsion of 39.8 % sunflower oil are shown in Figure 1. Crystallization DSC curves are presented on Figure 1. a) c) e) and melting DSC curves on Figure 1. b) d) f).

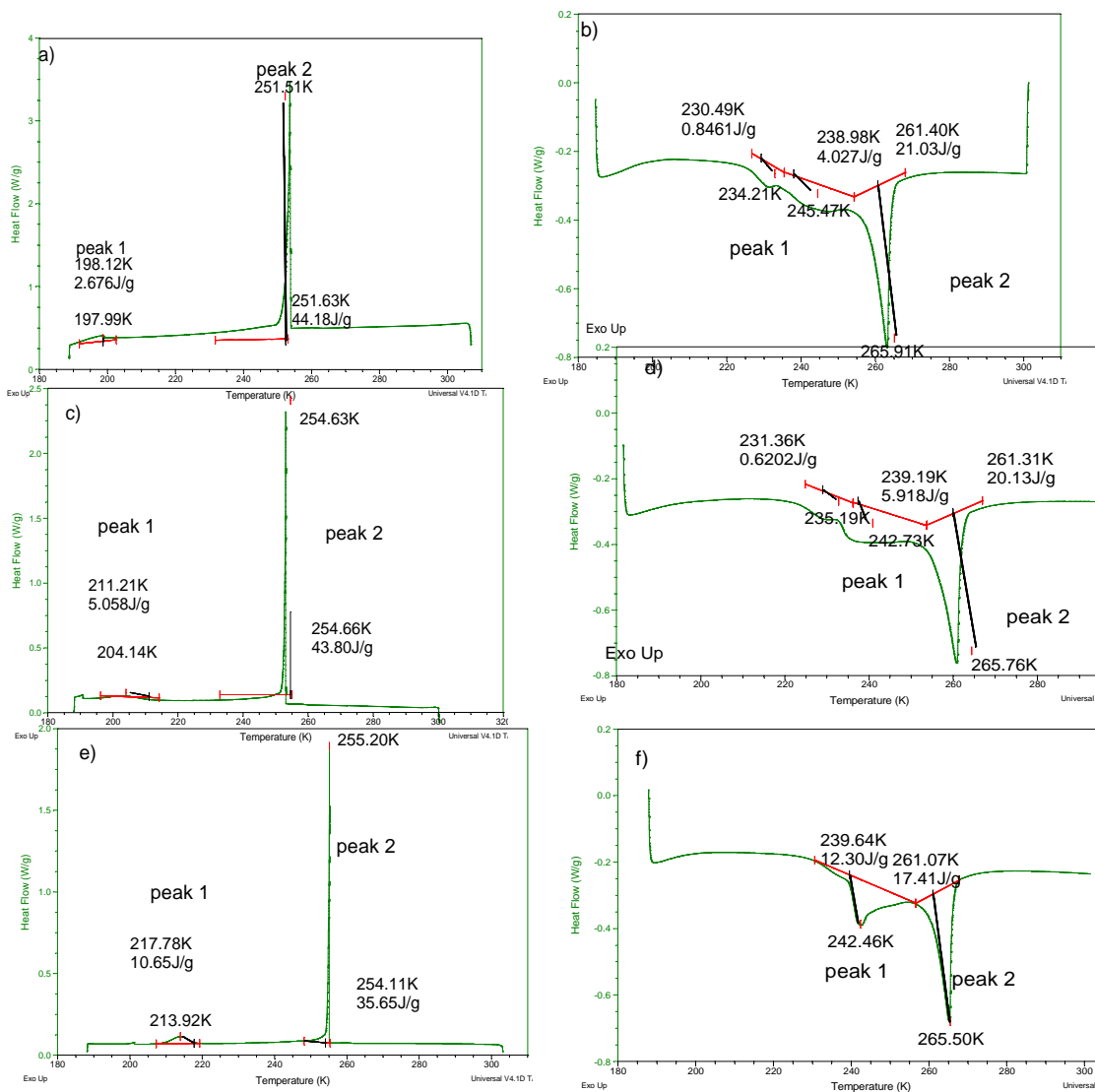


Fig. 1. DSC curve of whey mayonnaise **a)** Cycle I: cooling from 313 K to 193 K, with cooling rate 5K/min (crystallization); **b)** Cycle II: heating from 193 K to 313 K with heating rate 5K/min (melting); **c)** Cycle III: cooling from 313K to 193 K with cooling rate 2.5 K/min (crystallization); **d)** Cycle IV: heating from 193K to 313K with heating rate 5 K/min (melting); **e)** Cycle V: cooling from 313 K to 193 K with cooling rate 1.25 K/min (crystallization); **f)** Cycle VI: heating from 193 K to 313 K (melting).

All cooling and heating DSC curves showed the presence of two distinct peaks, which can be associated with phase transition of the oil (peak 1) and water (peak 2) [5]

Presence of whey proteins, and other whey mayonnaise components did not seem to influence significantly the melting behavior of sunflower oil in water emulsion, compared to literature data [5]. It can be seen that melting temperature of water is shifted to lower temperature (266 K) due to the presence of whey mayonnaise components in the water phase. Peak 2 in the, Figure 1. b) d) e), become complex, compared to results of Caligaris et al [5] as the consequence of presence of other whey mayonnaise components. Temperature shift of peak 2 is due of different cooling rates.

Conclusion

Presence of whey proteins, and other whey mayonnaise components did not seem to influence significantly the melting behavior of sunflower oil in water emulsion. Partial characterization of prepared product and information on thermal stability of sample, valuable for technological process, was obtained.

Acknowledgment

The present investigations are partially supported by Ministry of Science Technologies and development of Serbia, project number: BTN-371013B:

References

- [1] S. Damodaran & A. Paraf, Food proteins and their applications, Marcell Dekker, Inc., New York Basel, 1997.
- [2] T. Hakkak,., Cancer Epidemiology, Biomarkers & Prevention, 2001, **10**, 555-558.
- [3] D. Đorđević, D.J. McClements, E.A. Decker, JFS, 2004, **69**, C356-361.
- [4] C.C. Akoh, Food Technol., 1998, **52**, 25-37.
- [5] S. Calligaris, L. Manazocco, M. C. Nicoli, Food Chemistry, 2006, *in press*

Spectroscopy
Molecular Structures
Physical Chemistry of Plasma

(B)

THE NATURE OF UNCONVENTIONAL BLUE-SHIFTING HYDROGEN BONDS – A THEORETICAL INSIGHT

Lj. Pejov¹ and K. Hermansson²

¹*Institute of Chemistry, Faculty of Science, POBox 162, 1001 Skopje, Macedonia;
ljupcop@iunona.pmf.ukim.edu.mk*

²*Materials Chemistry, The Ångström Laboratory, Uppsala University, Box 538,
S-751 21 Uppsala, Sweden; kersti@mkem.uu.se*

Abstract

A theoretical insight into the main driving forces leading to unconventional blue-shifting hydrogen bonds is proposed on the basis of high-level *ab initio* and density functional theory calculations. For that purpose, several 1:1 fluoroform complexes (with acetonitrile, ethyleneoxide, formaldehyde and water) were explored at the HF, MP2 and B3LYP/6-311++G(*d,p*) levels of theory. Anharmonic C-H stretching vibrational frequency shifts were calculated for all the local minima on the studied potential energy hypersurfaces (PESs). The lowest-energy minima in all studied cases occurred for a C-H...O(N) hydrogen-bonded arrangement, and are characterized by a significant C-H frequency blue shift. On the other hand, the additional minima (for “reversed” orientations in which there is no direct C-H...O(N) contact) show only small C-H frequency upshifts. The Kitaura-Morokuma and RVS-SCF energy decomposition analyses, along with the charge field perturbational (CFP) approach were employed to explore the proton-acceptor influence on the C-H stretching potential. The electronic exchange interaction appeared to be the main reason for *large blue shifts found for the hydrogen-bonded arrangements*, while the purely electrostatic + polarization interaction leads to C-H frequency redshifts. However, the large net blue-shifting effect of the exchange contribution is only possible thanks to the smallness of the red-shifting electrostatic + polarization contribution. This, in turn, is a consequence of the fact that $d\mu^{(0)}/dr_{\text{CH}}$ is negative for the fluoroform molecule. In all cases the charge transfer as well as the dispersion energy contributions lead to frequency redshifts. The *small C-H blue shifts for the “reversed” orientations* are almost completely governed by the electrostatic interaction.

Introduction

Among all non-covalent intermolecular interactions, the hydrogen bonding ones appear to be particularly important in various fields of science and technology. Although the basic (*i.e.* conventional) type of h-bond has been well-known long ago, in recent years some peculiar examples of the phenomenon have been noted, with respect to both the nature of possible proton-acceptor and the manifestations of the interaction. Among the unconventional h-bonds, the blue-shifting ones, which make the hydrogen-bond-donating molecule internally *stronger* and not *weaker*, are particularly relevant in the context of biomolecular interactions, as they mostly involve C-H proton donors. In fact, blue shifts of X-H frequencies were detected

experimentally several decades ago [1], and discussed theoretically somewhat later [2]. However, it is only recently that they have received much attention in the literature [3-5]. Blue-shifting hydrogen bonds manifest themselves in a shortening of the X-H distance upon bonding, an upshift (blueshift) of the $\omega(X-H)$ stretching vibrational frequency, and an IR intensity decrease of the X-H stretching vibration. All these features are opposite to the behavior of traditional hydrogen bonds, although both types are stabilizing. Despite the rather large number of papers devoted to the phenomenon of blue-shifting hydrogen bonds, it was very recently that a consistent model for the theoretical understanding of this interaction was proposed [6]. In this paper, we briefly review our previous work in the field [7], the main aim of which was to provide a unifying theoretical basis for the spectroscopic and structural manifestations of this peculiar interaction.

Computational Details

Explorations of the PESs of the studied CF_3H complexes were performed at the HF, MP2 and B3-LYP levels of theory, using standard 6-311++G(*d,p*) basis set for orbital expansion in solving the HF or Kohn-Sham equations. In most cases, searches for stationary points on the PESs were performed using an initial guess of the Hessian matrix. However, in particular cases also the Hessian was analytically calculated in the first optimization step. All geometry optimizations were performed using Schlegel's gradient optimization algorithm (the second derivatives of the energy with respect to nuclear coordinates were computed analytically). The character of each located stationary point was tested by a harmonic vibrational analysis, the absence of negative eigenvalues of the Hessian matrices indicating a true minimum. In all DFT calculations, the "ultrafine" (99,590) grid was used for the numerical integration.

Geometry optimizations, harmonic vibrational analyses, and the anharmonic vibrational potential calculations were performed with the Gaussian 98 suite of programs. The Kitaura-Morokuma (KM) and the Reduced variational space SCF (RVS SCF) calculations were done with the latest version of the GAMESS code.

The (full) function counterpoise-corrected interaction energies for the located minima on the studied PESs of the four complexes were computed by the standard Boys-Bernardi procedure. Adopting the notation of Xantheas [8]:

$$\Delta E(\text{fCP}) = E_{AB}^{\alpha\cup\beta}(AB) - E_{AB}^{\alpha\cup\beta}(A) - E_{AB}^{\alpha\cup\beta}(B) \quad (1)$$

where the superscripts denote the basis set and the subscripts refer to the geometry used for energy calculation. The BSSE itself is calculated as the difference between $\Delta E(\text{fCP})$ and the uncorrected interaction energy:

$$\Delta E = E_{AB}^{\alpha\cup\beta}(AB) - E_{AB}^{\alpha}(A) - E_{AB}^{\beta}(B) \quad (2)$$

Anharmonic vibrational frequencies for the various C-H oscillators were calculated from one-dimensional (1D) HF, MP2 and DFT vibrational potentials, as explained in ref. [7]. In each case, the resulting vibrational potential energy curve was least-squares

fitted to a fifth-order polynomial in r_{CH} , subsequently cut after the fourth order and transformed into Simons-Parr-Finlan (SPF) coordinates: $\rho = 1 - r_{\text{CH,e}}/r_{\text{CH}}$. The resulting vibrational Schrödinger equation was solved variationally, using 15 harmonic oscillator eigenfunctions as a basis. The fundamental anharmonic vibrational frequency was calculated from the energy difference between the ground and first excited vibrational levels.

The charge-field perturbation (CFP) approach was employed to distinguish between various intermolecular bonding contributions (electrostatics + polarization vs. the rest, namely charge transfer and exchange) influencing the anharmonic C-H stretching frequency shift. This approach consists of the following [7]. *The proton-accepting monomeric unit* is represented by a set of point charges placed at its nuclear positions and with values chosen such as to best reproduce its electrostatic potential at series of points generated by the three most widely employed point-selection schemes: CHelp, CHelpG and MK. The C-H stretching vibrational potential energy curve was then calculated for the “isolated” fluoroform molecule exposed to the inhomogeneous electrostatic field generated by the CFP approach, as just described, and subsequently the corresponding *anharmonic* vibrational frequency was calculated. By this procedure, one considers *only* the electrostatic + polarization influence on the C-H oscillator exhibited by the neighboring monomeric unit. The full wavefunction representation including both units, on the other hand, accounts for both the electrostatic and polarization effects, as well as the charge-transfer and exchange effects (and, at the MP2 and B3-LYP levels, also some of the dispersion effects).

Moreover, as mentioned above, as a second approach, the Kitaura-Morokuma (KM) interaction energy decomposition analysis scheme was used to calculate the different contributions to the C-H frequency shift (electrostatic, polarisation, charge transfer, exchange and mix).

Results and Discussion

The main insights into the physics of this peculiar intermolecular interaction will be illustrated through the example of the $\text{CF}_3\text{H}\dots\text{acetonitrile}$ complex. More details concerning also other studied complexes are given in Ref. [7].

Explorations of all PESs considered in the present study for the $\text{CF}_3\text{H}\dots\text{acetonitrile}$ complex confirmed the existence of two minima. One of them is characterized by a hydrogen-bonded C-H \dots N contact (the $\text{F}_3\text{CH}\dots\text{NCCH}_3$ minimum; Fig. 1), while at the second minimum the fluoroform and acetonitrile subunits are in a reversed orientation as compared to the first one ($\text{NCCH}_3\dots\text{F}_3\text{CH}$; Fig. 2). Small conformational structural differences between minima located at various theoretical levels will not be discussed in the present paper, as they are irrelevant to the main point stated in the introduction. The interaction energies (Table 1) show that the global minimum on all three PESs corresponds to the $\text{F}_3\text{CH}\dots\text{NCCH}_3$ orientation. The BSSE accounts for only $\approx 5\%$ of the overall $\Delta E(\text{fCP})$ for this case, except at the MP2 level, where it is more significant and accounts for $\approx 15\%$. For the reversed minima, the BSSE is much more signifi-

cant, accounting for $\approx 10\%$ of the total $\Delta E(\text{fCP})$ at the HF level to more than 50% at the MP2 level.

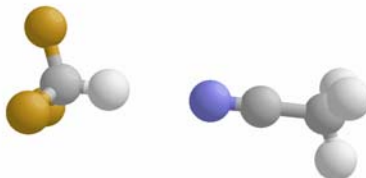


Fig. 1. The hydrogen-bonded minimum (with a direct C-H \cdots N contact) on B3LYP/6-311++G(*d,p*) fluoroform-acetonitrile PESs.



Fig. 2. The “reversed” minima (with no direct C-H \cdots N contact) on B3LYP/6-311++G(*d,p*) fluoroform-acetonitrile PESs.

Both the hydrogen-bonded and the reversed minima represent stabilizing orientations of the dipole moment vectors of the two molecular subunits (favorable dipole-dipole interaction). The CF_3H molecule is characterized by dipole moment enhancement upon C-H bond shortening, *i.e.* it has a negative $d\mu^{(0)} / dr_{\text{CH}}$ derivative (unlike most other molecules); therefore a shortening of the C-H bond enhances the intermolecular dipole-dipole interaction. If an enhancement of the dipole-dipole interaction energy is the main reason for the blue-shifting character of this H-bonding interaction, then one would expect almost equally pronounced manifestations of this interaction (C-H frequency upshifts) for the hydrogen-bonded and the reversed minima. This is, however, not the case. Several important conclusions concerning the character of this interaction may be derived from Tables 2 and 3, where anharmonic C-H stretching frequencies for the free CF_3H molecule and for the hydrogen-bonded (Table 2) and reversed (Table 3) fluoroform-acetonitrile minima are given at the HF, MP2 and B3LYP levels, both within the full wavefunction approach and with the CFP methodology. As can be seen from Table 2, in the case of the hydrogen-bonded $\text{F}_3\text{CH}\cdots\text{NCCH}_3$ minimum, the purely electrostatic + polarization interaction of CF_3H with the proton-accepting unit leads to C-H frequency red shift, instead of a blue shift. Therefore, obviously, some other factors must be responsible for the blue shift in this case. For the reversed $\text{NCCH}_3\cdots\text{F}_3\text{CH}$ minimum (Table 3), the (significantly smaller) C-H frequency blue shift can be almost fully attributed to the inhomogeneous electro-

static field generated by the acetonitrile unit. Here, the frequency blue shift is due to the relatively modest field strength influencing the C-H oscillator, combined with a negative $d\mu^{(0)} / dr_{\text{CH}}$ dipole moment derivative, as elaborated in Ref. [6]. The CFP approach for modeling the electrostatic + polarization influence on the C-H vibrational frequencies accounts completely for all terms in the perturbation-theory expansion of the energy as a function of the field:

$$-\Delta E(\vec{F}) = \vec{\mu}^0 \cdot \vec{F} + \frac{1}{2!} \overline{\Theta} \cdot \nabla \vec{F} + \frac{1}{3!} \overline{\Omega} \cdot \nabla^2 \vec{F} + \frac{1}{4!} \overline{\Phi} \cdot \nabla^3 \vec{F} + \dots + \frac{1}{2!} \overline{\alpha} \cdot \vec{F} + \dots \quad (3)$$

(where $\overline{\Theta}, \overline{\Omega}, \overline{\Phi}, \dots$ are the quadrupole, octupole, hexadecapole tensor functions of second, third, fourth etc. order, while $\vec{\mu}^0$ and $\overline{\alpha}$ are the dipole moment vector of the free molecule and the dipole polarizability function, respectively, the last quantity being a second order tensor).

Table 1. Interaction energies for the two minima located on B3LYP, MP2 and HF/6-311++G(d,p) fluoroform – acetonitrile PES-s.

	$\Delta E' / \text{kcal mol}^{-1}$	$\Delta E (\text{fCP}) / \text{kcal mol}^{-1}$	BSSE / kcal mol^{-1}
B3LYP			
direct min.	-4.03	-3.83	0.20
reversed min.	-0.73	-0.50	0.23
MP2			
direct min.	-4.50	-3.75	0.75
reversed min.	-1.76	-0.77	0.99
HF			
direct min.	-3.84	-3.59	0.25
reversed min.	-0.90	-0.82	0.08

The small differences between the full wavefunction representation results and the CFP ones for the reversed minima are due to the fact that the “real” interaction (described by the full wavefunction approach) includes interaction of CF_3H with every volume element of the (continuous) charge distribution in CH_3CN , and, moreover, the polarisation of the CH_3CN molecule is not taken into account in our CFP calculations. (Charge transfer and exchange energy contributions are also ignored in the CFP approach, but they are significantly smaller here, compared to the H-bonded minima, as demonstrated by the KM analysis). Besides this, the point charges representing the proton-accepting unit have been obtained by fitting to the molecular electrostatic potential, a procedure which inherently includes errors since it is a least-squares fitting procedure.

Table 2. Anharmonic C-H stretching frequencies and r_e values for free CF_3H and $\text{CF}_3\text{H}\cdots\text{NCCH}_3$ “direct” minimum at B3LYP, HF and MP2/6-311++G(d,p) levels obtained by pointwise energy calculations

Level	Methodology	System	$r_e(\text{C-H})/\text{\AA}$	$\nu(\text{CH})/\text{cm}^{-1}$
B3LYP	full wavefunction	$\text{CF}_3\text{H-free}$	1.0890	3022
			1.0877	3040
	CHelp	$\text{CF}_3\text{H}\cdots\text{NCCH}_3$	1.0914	2991
	CHelpG		1.0914	2990
	MK		1.0914	2989
MP2	full wavefunction	$\text{CF}_3\text{H-free}$	1.0870	3109
			1.0849	3140
	CHelp	$\text{CF}_3\text{H}\cdots\text{NCCH}_3$	1.0890	3081
	CHelpG		1.0891	3080
	MK		1.0891	3079
HF	full wavefunction	$\text{CF}_3\text{H-free}$	1.0758	3247
			1.0733	3288
	CHelp	$\text{CF}_3\text{H}\cdots\text{NCCH}_3$	1.0777	3218
	CHelpG		1.0776	3220
	MK		1.0776	3220

In order to further check the conclusions implied by the CFP analyses for the direct and reversed minima, we performed interaction energy decomposition analyses according to the Kitaura-Morokuma (KM) scheme for several points along the C-H vibrational potential curves. At present the KM analysis has only been implemented for HF wavefunctions and here we have chosen to present only the results obtained with the HF/6-311++G(d,p)/B3LYP/6-311++G(d,p) density matrices (*i.e.* decomposition analyses performed at the HF level for the minima found on the B3LYP PES). For the $\text{F}_3\text{CH}\cdots\text{NCCH}_3$ arrangement (as well as for the other hydrogen-bonded complexes), the electrostatic (ΔE_{ES}), polarization (ΔE_{POL}), electrostatic+polarization ($\Delta E_{\text{ES+POL}}$) and the charge-transfer (ΔE_{CT}) terms are seen to all give negative contributions to the external force constant of the C-H mode, $k_{\text{ext}} (k_{\text{ext}} = \sum_i k_{\text{ext},i}; k_{\text{ext},i} = d\Delta E_i(r)/dr)$ where

ΔE_i is the corresponding component of the total interaction energy, as partitioned by the KM algorithm) [7]. These contributions all lead to red shifts of the C-H vibrational frequency (in agreement with the CFP predictions). Only the exchange contribution ΔE_{EX} (as well as the mixed terms, ΔE_{MIX} , which are, however, of minor importance) gives rise to a positive contribution to k_{ext} , *i.e.* a blue shift in the C-H stretching frequency. The last conclusion is fully in agreement with the conclusions reached in Ref. [6].

Table 3. Anharmonic C-H stretching frequencies and r_e values for free CF_3H and $\text{NCCH}_3\cdots\text{CF}_3\text{H}$ “reversed” minimum at B3LYP, HF and MP2/6-311++G(*d,p*) levels obtained by pointwise energy calculations

Level	Methodology	System	$r_e(\text{C-H})/\text{\AA}$	$\nu(\text{CH})/\text{cm}^{-1}$
B3LYP		$\text{CF}_3\text{H-free}$	1.0890	3022
	full wavefunction		1.0886	3029
	CHelp	$\text{NCCH}_3\cdots\text{CF}_3\text{H}$	1.0885	3030
	CHelpG		1.0885	3029
	MK		1.0885	3029
MP2		$\text{CF}_3\text{H-free}$	1.0870	3109
	full wavefunction		1.0866	3115
	CHelp	$\text{NCCH}_3\cdots\text{CF}_3\text{H}$	1.0865	3117
	CHelpG		1.0865	3117
	MK		1.0865	3117
HF		$\text{CF}_3\text{H-free}$	1.0758	3247
	full wavefunction		1.0754	3253
	CHelp	$\text{NCCH}_3\cdots\text{CF}_3\text{H}$	1.0753	3254
	CHelpG		1.0753	3254
	MK		1.0753	3254

The purely electrostatic contribution (ΔE_{ES}) (i.e. when the charge distributions of the donor and acceptor molecules are not allowed to polarise each other, nor to be rearranged due to exchange interaction) gives rise to a blue-shift at long H...Y hydrogen-bond distances. This blue-shifting (X-H bond shortening) contribution is due to the negative free-molecule dipole moment derivative, $d\mu^0/dr_{\text{XH}}$. At intermediate and shorter hydrogen-bond distances, the perturbational approach is no longer applicable, and the purely electrostatic interaction gives rise to a redshift, perhaps because of stabilizing electron density piling up in the H...N region between the H and N nuclei; more electron density the longer the X-H bond. ΔE_{POL} also gives a red-shifting contribution and the resulting $\Delta E_{\text{ES}} + \Delta E_{\text{POL}}$ interaction is then of course also red-shifting; this is true both for traditional H-bonds and for the blue-shifting ones, but – for the same H-bond acceptor – the red-shift is much more modest for H-bond donors with $d\mu^0/dr_{\text{XH}} < 0$, compared to those for which $d\mu^0/dr_{\text{XH}} > 0$ (cf. the dashed CFP “frequency vs. field” curves in Fig. 4 in Ref. [6]).

Regarding the role of the dispersion contribution to the interaction energy on the C-H frequency shift, it can be estimated from a comparison of the HF and MP2 data (although, of course, it is clear that the dispersion energy cannot be the main cause of the vibrational frequency blue shifts since a blue shift is obtained already at the HF level). From the slopes of $\Delta E(r)$ vs. $r(\text{C-H})$ curves at the HF and MP2 levels for the H-bonded $\text{F}_3\text{CH}\cdots\text{NCCH}_3$ minimum on the MP2 PES (which are seen to be very similar

at the HF and MP2 levels), it may be concluded that the dispersion giving rise to only a small red shift in C-H vibrational frequency ($[d\Delta E(r)/dr]_{\text{HF}} > [d\Delta E(r)/dr]_{\text{MP2}}$, and $d(\Delta E_{\text{MP2}}(r) - \Delta E_{\text{HF}}(r))/dr = k_{\text{ext,DISP}} < 0$). The dispersion interaction is thus not responsible for the blue shift at all.

From variations of the KM interaction energy components with the C-H bond stretching coordinate for the “reversed” minimum on the B3LYP/6-311++G(*d,p*) fluoroform-acetonitrile PES it is concluded that, fully in line with the CFP predictions, the electrostatic energy makes a positive contribution to k_{ext} , *i.e.* here the main cause for the blue shift is the electrostatic interaction with the acetonitrile subunit. The other interaction energy components for this minimum add a negative contribution to k_{ext} , but their change upon C-H bond stretching is far smaller than the change in E_{ES} . The dispersion energy leads to frequency downshift even for this arrangement ($[d\Delta E(r)/dr]_{\text{HF}} > [d\Delta E(r)/dr]_{\text{MP2}}$).

Conclusion

A quantum theoretical model that allows for explanation of various peculiar properties of blue-shifting h-bonds is proposed and illustrated via particular examples.

References

- [1] H.D. Lutz, W. Eckers, G. Schneider and H. Haeuseler, *Spectrochim. Acta*, 1981, **37A**, 561.
- [2] K. Hermansson, *J. Chem. Phys.*, 1991, **95**, 3578.
- [3] I.E. Boldeskul, I.F. Tsybal, E.V. Ryltsev, Z. Latajka and A.J. Barnes, *J. Mol. Struct.*, 1997, **436**, 167.
- [4] P. Hobza, V. Spirko, H.L. Selzle and E.W. Schlag, *J. Phys. Chem.*, 1998 **102**, 2501.
- [5] P. Hobza, V. Spirko, Z. Havlas, K. Buchhold, B. Reimann, H.-D. Barth, B. Brutschy, *Chem. Phys. Lett.*, 1999, **299**, 180.
- [6] K. Hermansson, *J. Phys. Chem. A*, 2002, **106**, 4695.
- [7] Lj. Pejov, K. Hermansson, *J. Chem. Phys.*, 2003, **119**, 313.
- [8] S. S. Xantheas, *J. Chem. Phys.*, 1996, **104**, 8821.

MICROWAVE SPECTROSCOPY FOR NANO STRUCTURED MAGNETIC AND ELECTRONIC SYSTEMS

R. Meckenstock

AG Festkörperspektroskopie, Ruhr-Universität-Bochum, Germany

Abstract

In the last few years the development of magnetic devices has opened new perspective in electronics and mass storage technology. Tailored nano-structured magnetic materials and metal semiconductor heterostructures allow high storage density and fast magnetic switching processes.

Microwave spectroscopy has proven to be an extremely sensitive tool to characterize the magnetism of those devices. It permits to investigate the static magnetic properties and the spin dynamics even with local resolution on nm-scale due to the combination of ferromagnetic resonance FMR with thermal near field microscopy.

Introduction

Measurement of the thermal response in course of the microwave resonance absorption especially ferromagnetic resonance (FMR) allows locally resolved detection of the microwave spectroscopy down to the nano scale when a scanning thermal near field microscope (SThM) is used in combination with the microwave spectrometer.

This method provides a lateral resolution of less than 100 nm and is sensitive to structures with less than 10^6 spins. The spatial resolution is only limited by the contact area and the thermal sensitivity of the thermal nano probe. This thermal detection provides a strict separation of photon excitation and phonon detection but exhibits an exact correlation of the SThM-FMR image and the simultaneously taken AFM-topography.

In this paper the experimental setup and the signal generation processes of SThM-FMR are described. To demonstrate the potential of the new technique for the determination of local magnetic properties of single magnetic nano-structures SThM-FMR measurements are presented, showing non uniform FMR excitations in a Co stripe structure of $(100 \times 1.2 \times 0.024)\mu\text{m}$ (length x width x heights).

Other approaches to achieve spatial resolution for FMR which had been developed in recent years are the photothermally modulated ferromagnetic resonance (PM-FMR) and the time-resolved magneto optical Kerr effect (TRMOKE), relying on the ability to focus a laser onto the sample. Thus their optimum of resolution is given by the refraction limit of the used laser light [1,2]. A further non-optical approach is a magnetic force resonant microscope (MFRM) using the stray field of a magnetic tip to selectively meet the resonance condition in bowl shaped slices of the sample. While exhibiting exceptional sensitivity, this method is restricted in its spatial resolution to an optimum of about $1\mu\text{m}$ [3].

Microwave Spectroscopy

Microwaves are widely used in radio transmission technology, and for heating purposes. Due to the frequency range in the GHz range microwaves are suitable to investigate fast relaxation processes in field of molecule rotation and magnetization precession.

Microwave spectroscopy can be grouped into three main branches of investigation fields: electron spin resonance (EPR), ferromagnetic resonance (FMR) and non resonant EM absorption. This paper will specially focus on FMR:

FMR is classically seen the precession of the collective spin system around the direction of an effective magnetic field and is described by the Landau-Lifshitz equation of motion [4]:

$$\frac{d\vec{M}}{dt} = -\gamma (\vec{M} \times \vec{B}_{eff}) + \frac{\alpha}{M} \left(\vec{M} \times \frac{d\vec{M}}{dt} \right),$$

$$\vec{B}_{eff} = \vec{B}_{ext} + \vec{b}_{microw.} \cdot e^{i\omega t} + \vec{B}_{dem} + \vec{B}_{ani} \quad (1)$$

where M_s is the saturation magnetization, γ the gyro magnetic ratio, α the damping parameter, B_{ext} the external, B_{dem} the demagnetizing and B_{ani} the anisotropy magnetic field. As the sample comprises of polycrystalline Co stripes on Si substrate with a random distribution in the sample plane and a [111] texture perpendicular to the sample plane e.g. [5], the main influence for the FMR-line position for the Co stripes is the shape anisotropy or the demagnetizing field given by $\vec{B}_{dem} = -\underline{\underline{N}} \cdot \mu_0 \vec{M}$, where $\underline{\underline{N}}$ is the demagnetizing tensor. For an arbitrary sample shape the electromagnetic problem can only be solved numerically [6]. For the here shown rectangular shape there exists a uniaxial anisotropy in the film plane. Due to the specific size of the stripe there exists a non uniform FMR excitation for an applied field perpendicular to the stripe [7]. An explanation of the principle conventional FMR setup is given e.g. in [1].

Detection of Microwave Absorption by Scanning Thermal Microscopy (Methodology)

Because of the microwave wavelength of at least a view mm microwave spectroscopy and especially FMR in a cavity setup lag of focussing abilities for modern nano scale materials. The spatial resolution can be considerably improved by application of thermal near field techniques [8].

For the present investigations on magnetic nano stripes a SThM is used as passive detector of the dissipated heat while the sample is absorbing microwaves during FMR.

Fig. 1 provides a scheme of the combined SThM-FMR setup. The SThM part consists of a conventional AFM with a thermal nano probe as tip. Thus topography and resistivity change in the tip due to heat flow can be detected simultaneously.

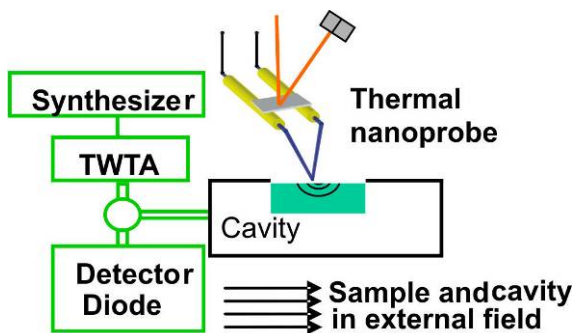


Fig. 1. Scheme of STh-FMR setup

As shown in Fig. 1, the foundation of the SThM-FMR set-up is a cavity based FMR spectrometer capable of frequencies from 5 to 12 GHz and microwave powers up to 10 W. The self build cavity is integrated into the magnet, which provides a maximum field of 0.12 T. Cavity and magnet form a flat surface onto which the SThM is placed. The sample is mounted at the top of the cavity and is electrically isolated from it. Due to the TE₁₀₁ mode of the cavity the sample is positioned in the linearly polarized high frequency magnetic field, which is oriented perpendicular to the external field. The AFM probe used to detect the heat is based on an etched platinum wire with a contact area of 100 nm diameter with the sample. The temperature resolution achieved by the lock-in technique is of the order of 1 mK.

In this application field the determination of absolute values of the temperature or other thermo-physical parameters is of minor importance. Since the important parameter is the thermal contrast for imaging the magnetic resonance excitation. However, to overcome the influence of different thermal contact between tip and Co and Si respectively the sample under investigation is coated with amorphous carbon.

Fig. 2 shows the calculated distribution for a Co stripe of 300nm width perpendicular to the stripe. The theoretical model calculates the amplitude and phase of the modulated temperature rise in the metal, as well as in the backing Si substrate and adjacent atmosphere by solving the three-dimensional heat conduction equation see e.g. [9].

It turns out that the heat distribution is governed by the size of the heat source and not by the modulation frequency if the heat source is smaller than the heat diffusion length of the material. The upper line in Fig. 2 for 100Hz modulation frequency provides only a small difference to the lower line at 100kHz modulation frequency. The important message is that 100nm away from the heat source you have a significant reduction of the heat of about 30% which is important for a high local thermal contrast.

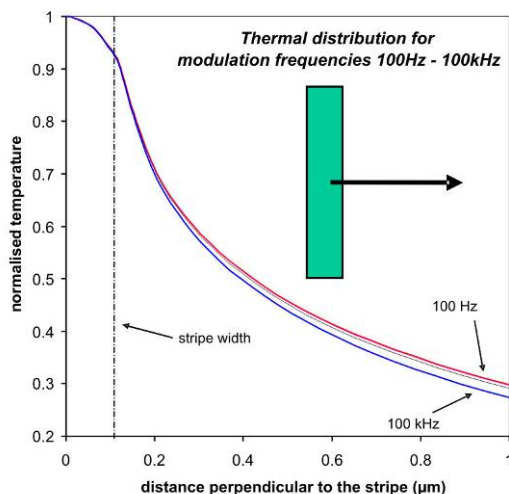


Fig. 2. Thermal heat distribution calculated for a 300nm wide heated metal on Si

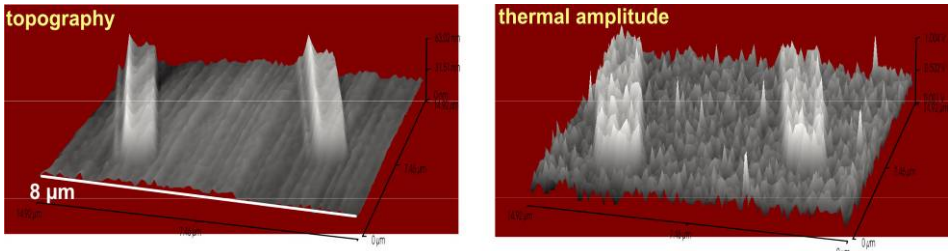


Fig. 4. Topography and thermal amplitude of the SThM-FMR measurements with external field along the Co stripes

The thermal contrast represents a change of $0.5 \mu\text{V}$ at the Lock-in and thus a temperature rise of at least 10 mK in the tip taking into account the guaranteed specification of the tip manufacturer VEECO ($4 \text{ mA} / 1 \text{ K}$) and the preamplification. In order to obtain an exact correlation of lock-in voltage and heat, finite element calculations are in progress, taking into account the complete tip geometry.

Fig. 5 is the illustration of the first lateral thermal detection of a non uniform FMR excitation in Co-strips with a lateral resolution of 100nm. The thermal amplitude clearly show that the heat generation in the Co stripe for this resonance with 90mT magnetic field applied perpendicular to the stripe is located in the rim of the stripe only. This is supported by the thermal phase image. The phase signal is only stable in areas where the heat is generated. From the topography one can see that the heated areas are slightly larger than the fold over areas of the Co stripe. This is due to the heat distribution as shown in Fig. 3 and the fact that the non uniform FMR excitation is only supported by the fold over areas but is originated from the size distribution of the Co stripes. The formation of the rim mode is due to the ratio of width to height and the magnetization value of the stripe. The fold over structure was necessary to reduce the field value of the perpendicular resonance position to match the field area accessible to our locally resolved setup. Other angle dependent measurements show the same line splitting at fields above 120mT for non fold over Co-strips.

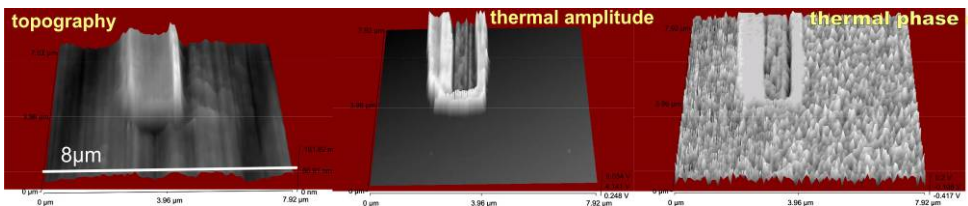


Fig. 5. Topography and thermal amplitude and phase of the SThM-FMR measurements with external field perpendicular to the Co stripes

Conclusion

In conclusion, these measurements point out the high potential of the SThM-FMR investigating the local magnetic properties of nano tailored magnetic heterostructures. A further potential of SThM-FMR is its strong increasing sensitivity towards decreasing

temperatures and its high flexibility in the experimental setup, which allows investigation in in-situ vacuum conditions or ex-situ lab conditions.

Acknowledgment

This work is carried out in the frame of the German SFB 491 magnetic heterostructures: spin structure and spin transport.

References

- [1] R. Meckenstock, K. Harms, O. von Geisau, and J. Pelzl, *J. Appl. Phys.*, 1995, **79**, 81007
- [2] M. J. Pechan, C. Yu, R. L. Compton, J. P. Park, and P. A. Crowell, *J. Appl. Phys.*, 2005, **97**, 10J903
- [3] D. Rugar, R. Budakian, H. J. Mamin and B. W. Chui, *Nature*, 2004, **430**, 329.
- [4] G.V. Skrotskii, L.V. Kurbatov, in: S.V. Vonsovskii (Ed.), *Ferromagnetic Resonance*, Pergamon, New York, 1966.
- [5] B. Hausmanns, T. P. Krome, G. Dumpich, E. F. Wassermann, D. Hinzke, U. Nowak, and K. D. Usadel, *J. Magn. Magn. Mater.*, 2002, **240**, 297.
- [6] R. I. Joseph and E. Schlömann, *J. Appl. Phys.*, 1965, **36**, 1579.
- [7] B. B. Maranville, R. D. McMichael, S. A. Kim, W. L. Johnson, C. A. Ross, Joy Y. Cheng, *J. Appl. Phys.* 2006, **99**, 08C703.
- [8] J. Pelzl, R. Meckenstock, D. Spoddig, F. Schreiber, J. Pflaum, Z. Frait; *J. Phys.: Condens. Matter*, 2003, **15**, 451-463.
- [9] M. Reichling and H. Grönbeck, *J. Appl. Phys.*, 1994, **75**, 1914.

AN EXPERIMENTAL STUDY OF RADIAL SYMMETRY DEVIATION IN DC ARGON ARC PLASMA BY CURRENT MODULATION TECHNIQUE

J. J. Savović¹, M. M. Kuzmanović², M. S. Pavlović¹,
M. Stoiljković¹ and M. Marinković¹

¹Laboratory of Physical Chemistry, The Vinča Institute, P.O. Box 522,
Belgrade, Serbia

²Faculty of Physical Chemistry, University of Belgrade, P.O. Box 137,
Belgrade, Serbia

Abstract

A current square modulation technique is used to investigate radial asymmetry of plasma column of argon stabilized direct current U-shaped arc. By monitoring the temporal behavior of spectral line intensities (in a millisecond domain) for various elements, it was observed that nonhomogeneous emission was much more pronounced for current modulated arc plasma compared to the stationary regime plasma. The reason for such behavior, for this as well as for other arc sources, lies in a mode the stream of argon with aerosol is introduced into the arc plasma.

Introduction

For many applications, particularly in plasma diagnostics, detailed knowledge of symmetry in radial distribution of plasma parameters, especially in a direction perpendicular to viewing direction, is important. Radial plasma symmetry for one of the plasma parameters does not necessarily mean that the plasma is symmetric related to other plasma parameters. Also, different plasma parameters respond with different sensitivity to plasma asymmetry. It was shown in ICP that radial distribution of analyte emission intensity is not a sensitive tool for investigation of asymmetry [1]. On the other hand, instant responses to power modulation of spectral line intensities proved to be much more reliable tool for investigation of asymmetry distribution of important plasma parameters such as electron density and temperature.

The objective of this work was to investigate a radial symmetry of argon stabilized U-shaped dc arc, operating at atmospheric pressure [2]. For that purpose, we studied the temporal evolution of spectral line intensities for various elements with different ionization energies. Also, we investigated the influence of easily ionized elements (EIE) addition on the arc discharge symmetry. Because greatest influence of asymmetry is expected on transport processes in plasma (due to asymmetric analyte introduction) a special attention was paid to delayed responses, as they may give us a more detailed insight into these processes.

Experimental

A detailed description of the U-shaped arc device used in this work is given in previous publication [2]. The analyte water solutions were introduced into the plasma as

aerosol obtained with glass concentric nebulizer and double-pass cloud chamber. Emission from a horizontal part of arc plasma was "end on" observed. Radial distributions of emission were monitored by moving the arc device perpendicular to the optical axis of the monochromator, taking care that it remained parallel to the arc axis.

The horizontal part of the arc column plasma was projected with acromatic lenses on the entrance slit of a Zeiss SPM-2 monochromator (dispersion 4 nm/mm in the first diffraction order). The argon stream carrying the analyte particles was introduced into the central segment cavity of the arc device (diameter 68 mm, height 8 mm) providing a gas vortex that additionally stabilizes the arc column. In Figures 1 and 2, parts of distribution curves from the side where the aerosol is introduced are marked with (+) sign, and those from the opposite side are marked with (-) sign.

The arc current was square modulated between 9 and 3 A with the aid of electronic switch circuit based on fast MOS-FET transistors. The current transition time was better than 5 μ s. The lower current period was 50 ms with a repetition period of 250 ms. In order to minimize a signal noise, photomultiplier current was first amplified by a factor of 50 with a fast preamplifier and then via coaxial connection carried to a digital storage oscilloscope. The oscilloscope was PC controlled via GPIB interface. The oscilloscope traces are 32 times averaged, and subsequently transferred to a PC.

Results and Discussion

The asymmetry in response of H_{α} spectral line intensity, on current jump, is seen in Figure 1. Similar effects are obtained for argon lines as well as for recombination continuum. The similarity between temporal responses for lines with high ionization energies and for recombination continuum is expected because in both cases intensity is a quadratic function of electron number density. Temporal responses presented in Figure 1. are hard to explain, but they certainly correspond to the plasma asymmetry which is a consequence of asymmetrical introduction of the argon stream carrying the aerosol.

Also, in stationary regime, asymmetrical radial distribution of spectral line intensities is obtained, but it is less pronounced than in Figure 1. Line intensities on a minus (-) side of plasma are a bit smaller and they show a steeper dependence of radial position.

Temporal responses of Mg I line, as a representative for elements with medium ionization energies, are presented in Figure 2. Temporal responses, of line intensities related to arc current drop and jump, show a pronounced asymmetry. The intensity increase during the arc current drop may be a consequence of a decreased barrier imposed by radial electric field [3]. Explanation of such behaviour by the increase of ground state atoms concentration due to recombination must be discarded because of a similar behaviour of ionic line intensities (e.g. Mg II, Ba II, Ca II...). Asymmetrical response at the arc current drop indicates a large asymmetry of radial electric field induced by ambipolar diffusion. The fact that the large addition of EIE reduces asymmetry in temporal responses of line intensities at arc current drop (since introduction of EIE decreases the radial electric field) is in accordance with the previous conclusion [3].

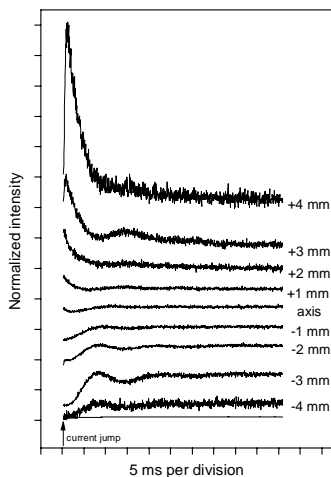


Fig. 1. Temporal responses for H_{α} 656.3 nm line intensity after the current jump, at different displacement from the arc axis.

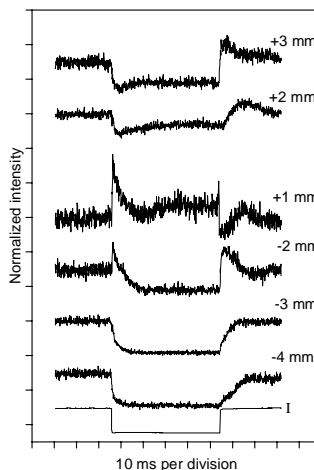


Fig. 2. Temporal responses of Mg I 285.21 nm line intensity in presence of 0.3% KCl, at different displacement from the arc axis.

Conclusion

By comparing the radial distribution of spectral line intensities and their temporal responses to arc power modulation, it was shown that delayed responses are more sensitive to asymmetry in plasma parameters compared to intensities in a stationary regime. Pronounced asymmetry in argon U-shaped arc is a consequence of asymmetry in the aerosol introduction in a discharge.

Acknowledgments

This work has been financially supported by Ministry of Science and Environmental Protection, Republic of Serbia, under Project No. 142065.

References

- [1] L.E. Bydder and G. P. Miller, *Spectrochim. Acta* 1988, **43B**, 1431-42.
- [2] M. S. Pavlović, N.Z. Pavlović and M. Marinković, *Spectrochim. Acta*, 1991, **46B**, 1487-1498.
- [3] M. M. Kuzmanović, M. S. Pavlović, J. Savović, M. Marinković, *Spectrochim. Acta*, 2003, **58B**, 239-248.

DETERMINATION OF FE, MN AND PB IN TREE-RINGS IN POPLAR (*POPULUS ALBA L.*) BY U-SHAPED DC ARC

D. M. Marković¹, I. Novović¹ and D. Vilotić²

¹*Institute of Physics, P.O. Box 57, Pregrevica 118, Belgrade, Serbia (markovic@phy.bg.ac.yu)*

²*Faculty of Forestry, University of Belgrade, Kneza Višeslava 1, Belgrade, Serbia*

Abstract

The U-shaped DC arc with aerosol supply was applied for determination of Fe, Mn and Pb in poplar (*Populus alba L.*) tree-rings. By optimization of the operating parameters and by selection of the most appropriate signal integration time (20s), the obtained limits of detection for Fe, Mn and Pb are 5.8 ng/ml, 1.6 ng/ml and 2.0 ng/ml, respectively.

Introduction

Current demands required from control and protection of the environment are strict. Therefore, the methods enabling the detection of low element concentration are very useful. The spectrochemical method applied in this study is a simple method for determination of low concentrations. It may be applied for Fe, Mn and Pb concentration determination in tree-rings. Tree-rings represent a unique, widely available, cheap and simple source of long-term data for monitoring trace metal levels in the atmosphere.

An U-shaped low current (7.5 A) argon DC arc with aerosol supply was applied as excitation source. A laboratory modified spectrograph PGS-2 with holographic grating (Spectrogon, 2100 grooves/mm) was used as spectrometer. The intensity of the analyte spectral line was recorded by photomultiplier (Hamammatsu R-3788) and AD conversion card (ED-300) connected with PC. The recorded signal intensities were accumulated during the integration time of 20s, by application of the appropriate computer program. The slit width was 0.15 mm. Spectral lines intensities are measured for Fe I ($\lambda = 371.99$ nm), Mn I ($\lambda = 403.08$ nm) and Pb I ($\lambda = 405.78$ nm) at 4 mm from the axis of the arc.

A series of reference solutions (Fe, Mn and Pb) were prepared in the range from 5 ng/ml to 5000 ng/ml, by appropriate dilution of the stock solutions (1 mg/ml Merck). Each of the solutions contained 0.5 % potassium chloride as spectroscopic buffer. The nebulization of the solution was performed by a Meinhard nebulizer (TR 30 K2) connected with a double-pass spray chamber.

Tree-rings samples (3 years segments) were placed in pre-washed (15% H₂SO₄) 50ml borosilicate glass tube, dried at 70 °C for 48h and weighed. Samples were suspended in 10 ml of 70 % HNO₃ at 80 °C for 24h. The cold solution was filtered through acid washed (10 % HNO₃) Whatmam No. 42 filter paper and diluted to 50 ml with bidistilled water [1].

Results and Discussion

Tree-rings are a unique source of long-term data and have often been used in studies for understanding and quantifying of air pollution on forests [2]. The concentrations of Fe, Mn and Pb in poplar tree-rings from locations Obrenovac and Novi Sad, were determined in this paper. Each poplar tree was divided into 3 years segments starting from 1979 for poplar from Obrenovac and from 1985 for the locatin of Novi Sad. Obtained results of the concentrations of Fe, Mn and Pb are presented in Figs. 1,2 and 3.

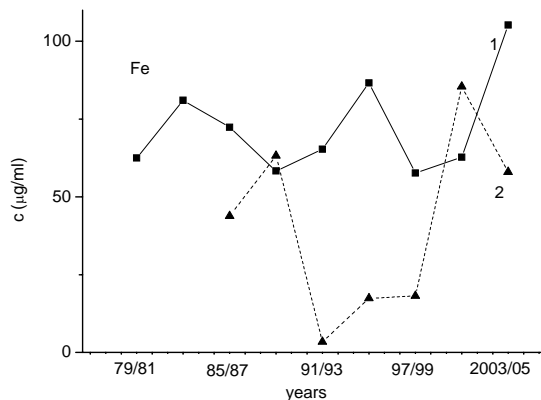


Fig. 1. Fe mean concentration in poplar (*Populus alba L.*) tree-rings for the location Obrenovac from 1979. (1) and for the location Novi Sad from 1985. to 2005. (2).

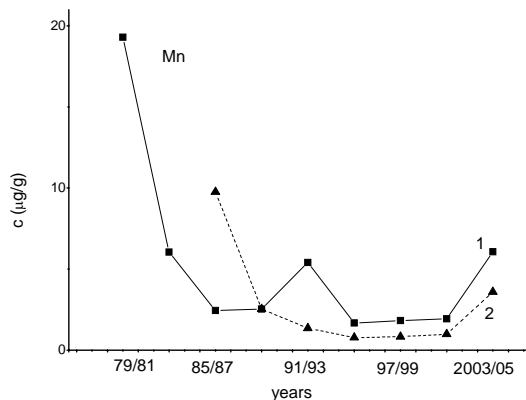


Fig. 2. Mn mean concentration in poplar (*Populus alba L.*) tree-rings for the location Obrenovac from 1979. (1) and for the location Novi Sad from 1985. to 2005. (2).

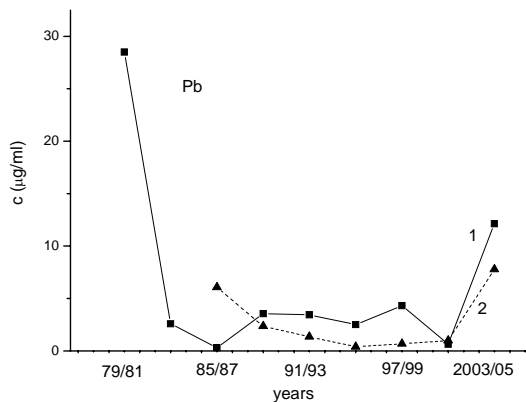


Fig. 3. Pb mean concentration in poplar (*Populus alba L.*) tree-rings for the location Obrenovac from 1979. (1) and for the location Novi Sad from 1985. to 2005. (2).

Increased concentrations of Fe, Mn and Pb have been recorded in tree-rings of poplar samples from the location Obrenovac. The pH of the soil has considerable influence on concentration of the metals in tree-rings [3,4, 5].

Conclusion

Increased concentration of Fe, Mn and Pb have been recorded in tree-rings of poplar (*Populus alba L.*) from the location Obrenovac formed during periods of high activity of 'Nikola Tesla A' power plant in Obrenovac.

References

- [1] M. Orlandi, M. Pelfini, M. Pavan, M. Santilli and M. P. Colombini, *Microchemical Journal*, 2002, **73**, 237-244.
- [2] M. Forretti, J. L. Innes, R. Jalkanen, M. Saurer, J. Schaffer, H. Spiecker, K. von Wilpert, *Dendrochronologia*, 2002, **20**, 159-174.
- [3] S. A. Watmough, T. C. Hutchinson, *Environmental pollution*, 1996, **93**, 93-102.
- [4] K.L. Padilla, K. A. Anderson, *Chemosphere*, 2002, **49**, 575-585.
- [5] S. A. Watmough, N. M. Dickinson, *Environmental pollution*, 1995, **90**, 135-142.

THE OPTIMIZATION OF COLD VAPOR AAS TECHNIQUE FOR MERCURY ANALYSIS IN INDUSTRIAL WATER EFFLUENTS

G. Vasile, A. Moise and E. Mihaila

*National Research and Development Institute for Industrial Ecology-ECOIND,
90-92 Panduri St., 050663 Bucharest – 5, Romania*

Abstract

The cold vapor AAS (Atomic Absorption Spectrometry) technique for mercury was optimized for analysis of water samples.

The analytical parameters, like sodium borohydride and nitric acid concentrations, sample volume and equipment settings (position of the fused silica cell in the lamp beam, slit width), have been adjusted to obtain maximum sensibility and reproducibility for mercury determination in waste water sample analysis.

For the proposed, optimized, method the main quality performance parameters (linearity range, regression coefficients, S_y , S_{x_0} , CV) have been fully evaluated.

The recovery rates of the mercury from some matrixes like mine water and surface water have been in the range 101.3 – 112 %.

The performance parameters of the proposed optimized method make it suitable for the application in mercury analysis in surface water moderately contaminated spent waters.

Introduction

Mercury is a unique element due to its tendency to form health hazard compounds, unusually toxic, at trace levels in the environment. Mercury toxicity is highly dependent upon the chemical species of this metal: generally, the organic compounds are more toxic than inorganic ones. Quicksilver and mercury sulfide, which are insoluble, are much less toxic than other compounds. Fish accumulate mercury in their body, mainly in the form of methyl mercury, a compound which is highly toxic [1].

Monitoring mercury concentration in the environment samples, especially in unpolluted areas, needs a reliable technology, suitable to measure the very low concentrations levels (up to at least a few tenth of a microgram/liter), stated by existing legal regulations [2].

Maximum accepted limits of mercury in water samples, according to the Romanian legislation, which corresponds with European provisions, are in ppb range:

- 0,05 mg/l, for effluent spent waters flowed over in natural water sources
- 1 μg / l for drinking water and for surface water used in drinking-water treatment plants

The aim of this study was the optimization of the cold vapor AAS technique for mercury determination and the evaluation of its method suitability for mercury analysis in real spent effluents samples.

Results and Discussion

The following analytical parameters have been evaluated in order to attain the best performance of the analytical system for mercury quantitation: sodium borohydride concentration, nitric acid concentration, sample volume taken for analysis, slit width, fused silica cell position.

The best results have been obtained with the 3% sodium borohydride solution, which is in accord with the equipment producer's recommendations (Analytik Jena - Germany).

In Table 1 we present the optimal parameters found during the study and the operating settings used for the AAS equipment and hydride system.

Table 1. The operating parameters for Atomic Absorption Spectrometer and Hydride System module

<i>- Mercury vapor generator</i>	
NaBH ₄ concentration	3 % (m/v), stabilized with 1 % NaOH (m/v)
Argon (99,99%) flow	18 l/h
Sample volume	10 ml / 25 ml
Sample load time	7 sec.
Reaction time	8 sec
Wash time	20 sec
<i>- Atomic Absorbtion Spectrometer</i>	
Wavelength	253,7 nm
Slit width	0,8 nm / 1,2 nm
Lamp current	3 mA

Using linear regression, the calibration curve was plotted, and the most relevant performance features of the method have been evaluated (regression quotients a and b, linearity range, S_y , S_{x_0} , CV_{x_0}) [3].

The method has been validated "in house" and its reliability in analysis of mercury in surface waters and in spent effluents has been tested. The results are presented in Table 2.

Table 2. Performance parameters of the mercury quantitation method which has been validated "in house"

No.	Parameter	Mercury – AAS Cold Vapor Technique
1	Exactitude	87,93%
2	Fidelity	CV% = 2,96%
3	Repeatability	$r = 0,06297 \mu\text{g/l}$
4	Reproducibility	$R_L = 0,155 \mu\text{g/l}$
5	Sensibility	$b = 0,158$
6	Detection limit	$\text{LoD} = 0,1737 \mu\text{g/l}$
7	Quantitation limit	$\text{LoQ} = 0,289 \mu\text{g/l}$
8	Concentration range	$0,2 \mu\text{g/l} - 1,5 \mu\text{g/l}$
9	Average recovery rate	112 %

Conclusions

The most relevant analytical parameters and equipment settings have been evaluated and optimized for the analysis of mercury by cold vapor technique: sodium borohydride and nitric acid concentrations, sample volume, slit width, quartz cell position in lamp beam.

The method for mercury analysis has been validated "in house" by evaluating the relevant method's parameters: exactitude, fidelity, repeatability, reproducibility, sensibility, detection limit, quantitation limit, concentration range, recovery rate [3].

The proposed method can be used for quantitative determination of mercury in surface waters and spent effluents.

References

- [1] M. Morita, J. Yoshinaga, J. Edmonds, *Pure&Appl.Chem.*, 1998, **70**, 1585-1615.
- [2] 98/83/EC: Council Directive of 3 November 1998 on the quality of water intended for human consumption.
- [3] W. Funk, V. Dammann, G. Donnevert, *Quality Assurance in Analytical Chemistry*, VCH, Weinheim, New York Basel Cambridge Tokyo, (1995).

THE POSSIBILITY OF APPLICATION OF THE ATOMIC EMISSION SPECTROMETRY IN THE ECOLOGY

I. Novović¹, V. Nikolić² and D. M. Marković¹

¹*Institute of Physics, P.O. Box 57, Pregrevica 118, Belgrade, novovic@phy.bg.ac.yu,*

²*Institute of general and physical chemistry, P.O. Box 551, Studentski trg 12-16, Belgrade, Serbia*

Abstract

Argon-stabilized U-shaped DC arc with the system for aerosol introduction was used for uranium determination. By optimizing the operation conditions of U-shaped arc plasma and by applying of appropriate computer program that performs temporal integration of recorded signals, the measurement precision as well as the concentration sensitivity are improved, and the detection limit is lowered. The detection limit achieved by this method is comparable with the detection limits obtained by such methods as ICP-AES, DCP-AES and MIP-AES.

Introduction

High uranium toxicity suggests the necessity to develop as sensitive methods as possible for uranium detection on various natural samples and complex matrices. Therefore, the methods enabling the detection of low element concentrations are very useful. In this paper a very simple method for determination of uranium is suggested. The main characteristics of this arc plasma are high emission stability, construction simplicity and low running cost [1, 2].

As a very sensitive and simple spectrochemical source, low current (7.5 A) argon-stabilized U-shaped DC arc with the system for aerosol introduction was used. The main characteristics of the arc are presented in the paper [1]. Emission is observed from the horizontal part of the arc column in the direction parallel to the arc axis. A PGS-2 spectrograph with holographic grating (Spectrogon 2100 grooves/mm) was used as spectrometer. The intensity of the analyte spectral line was recorded by photomultiplier (Hamamatsu R-3788) and AD conversion card (ED-300) connected with a computer. The recorded signal was integrated in several different time intervals, by applying the appropriate computer program. The slit width was 0.15 mm. From the lateral relative emission intensity distribution the peak position (relative to the arc axis) was determined. Spectral line intensity is measured for U II 385,958 nm at 3.5 mm from the axis of the arc. Under these conditions all subsequent measurements were performed.

Concentrated standard uranium solution (1 mg/mL) was prepared by uranium oxide U₃O₈ (Johnson Matthey Chemicals Limited). By appropriate dilution of the concentrated solutions by bidistilled water, a series of standard water solutions of uranium within the range of 0.1 to 10 µg/mL was prepared. Each of the solutions contained 0.5% KCl as the spectroscopic buffer. The nebulization of the solution was performed by a Meinhard nebulizer (TR 30 K2) connected with a double-pass spray chamber.

Results and Discussion

After the optimization of operating conditions, a series of standard water solutions of uranium in 0.5% KCl were recorded during varying integration times. On the basis of the obtained results the calibration curves were formed (Fig. 1).

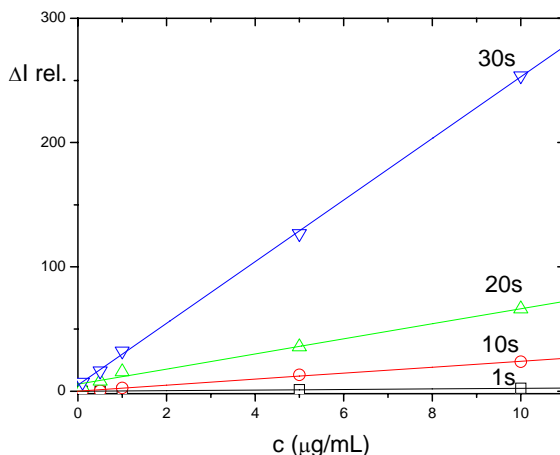


Fig. 1. Calibration curves of uranium ($\lambda = 385.958$ nm) for different integration time

From Fig. 1 linearity of the calibration curves is clearly noticed within two orders of magnitude. The increase in the curve slope with the integration time can also be noticed. The calculated values of relative standard deviations (RSD), concentration sensitivities ($\Delta I/\Delta c$) and detection limits (C_L) for different integration times are represented in Table 1. The dependence of the detection limit on integration time can be applied for the estimation of the optimum integration time for the applied experimental set up. The detection limit of 70 ng/mL was obtained for optimum integration time of 30 s.

Table 1. The obtained values of relative standard deviation, concentration sensitivity and detection limit for different integration intervals

Integration interval (s)	RSD (%)	$\Delta I/\Delta c$	Detection limit ($\mu\text{g/mL}$)
1	2.59	0.24	2.60
10	1.72	2.41	1.50
20	0.67	6.08	0.20
30	0.44	24.79	0.07

With the increase in integration time, the relative standard deviation is decreased and concentration sensitivity (Table 1.), that contribute to the increase of determination precision [3], is increased.

The detection limits achieved by the varying spectrochemical methods: ICP-AES, DCP-AES and MIP-AES, are presented in Table 2.

Table 2. Detection limits (ng/mL) achieved by various spectroscopic methods

U-shaped DC arc	ICP-AES [4]	ICP-MS [5]	DCP-AES [4]	MIP-AES [6]
70	40	0.001	40	400

On the basis of the results presented in Table 2., the detection limit achieved by applying the argon-stabilized U-shaped DC arc is of the same order as the detection limits achieved by ICP-AES and DCP-AES methods, while it is significantly lower than the detection limit achieved by MIP-AES method. The detection limit achieved by ICP-MS is several orders of magnitude lower than all the mentioned methods.

Conclusion

By applying the argon-stabilized U-shaped DC arc the detection limit for uranium is decreased by increasing integration time. The lowest detection limit amounts to 70 ng/mL and it is achieved during 30s integration time. The improved method of atomic emission spectrometry may be very successfully applied in the control and protection of the environment.

References

- [1] M. Marinković, V. Antonijević, *Spectrochimica Acta* 1980, **35B**, 129-138.
- [2] M. Kuzmanović, M. S. Pavlović, M. Marinković, *Spectroscopy letters*, 1996, **29**, 205-215.
- [3] M. Tripković, I. Holclajtner-Antunović, M. Marinković, D. Marković, *Journal of the Serbian Chemical Society*, 2001, **66**, 249-258.
- [4] L. H. J. Lajunen, *Spectrochemical Analysis by Atomic Absorption and Emission*, Cambridge, Royal Society of Chemistry, 1992.
- [5] A. Seubert, *Trends in analytical chemistry*, 2001, **20**, 274-287.
- [6] Z. Duan, S. Scherrer, S.P. Koirola, C. Wang, C. B. Winstead, *Analytica Chimica Acta*, 2005, **532**, 47-54.

FRANCK-CONDON FACTORS FOR CERTAIN BANDS OF THE Ag₂ MOLECULE

M. Kuzmanović, V. Bojović and A. Antić-Jovanović

Faculty of Physical Chemistry, University of Belgrade, P.O.Box 137, Belgrade, Serbia

Abstract

The arrays of Franck Condon factors for the bands of $D^1\Sigma_u^+ - X^1\Sigma_g^+$ and $E^1\Pi_u - X^1\Sigma_g^+$ transitions of gaseous $^{107}\text{Ag}^{109}\text{Ag}$ molecule are presented. Calculation has been performed employing Morse potential function. Obtained values are compared with intensity distribution of the bands in experimental spectrum.

Introduction

Franck-Condon factors (FCFs) have a central role in the studies of radiative and nonradiative transitions of molecules. Among a number applications, a knowledge of FCFs is essential for prediction of relative intensity distribution in the band systems, that is for prediction which bands can be observable in the sources where the molecules are expected to be present under favorable physical conditions.

In this work we report the FCFs for $D^1\Sigma_u^+ - X^1\Sigma_g^+$ and $E^1\Pi_u - X^1\Sigma_g^+$ bands of $^{107}\text{Ag}^{109}\text{Ag}$ molecule which, to our knowledge, are not available in the literature. This is not surprising, because calculation of FCFs requires a precise knowledge of vibrational and rotational constants of the molecule in the states involved in observed transition. The $D - X$ and $E - X$ bands, situated in the UV regions 256 – 261 nm and 247 – 256 nm, respectively, are known since 1959 [1]. However, the limited resolution in the conventional absorption techniques, used up to 1990, allowed only determination of vibrational constants ω_e and $\omega_e x_e$ in the analysis of the bands [2, 3, 4]. The rotational constant B_e for the X state, which authors applied in evaluation of B_e constants of the D and E states, could only be estimated from Morse-Clark rule [5].

Modern laser spectroscopic techniques applied to Ag_2 molecule allowed resolution of the rotational structure of the bands and thus direct determination of the rotational constants. These results showed that the Morse-Clark rule for Ag_2 molecule represents only a crude estimation.

Calculation of FCFs in the present work was performed using very accurate r_e values, evaluated from a new B_e constants of the $X^1\Sigma_u^+$ and $E^1\Sigma_u^+$ states, derived from high resolution spectra [6, 7], and from revised B_e for the $D^1\Sigma_u^+$ state, calculated from energy separation between bandheads and bandorigins in partly rotationally resolved bands, using new ground-state constant B_e . From high resolved spectra, improved vibrational constants of the $E^1\Sigma_u^+$ state have been derived and included in calculation of FCFs.

Method of Calculation

The FCFs, $q_{\nu', \nu''}$, associated with the ν' , ν'' band in diatomic band system are defined by:

$$q_{\nu', \nu''} = \left[\int \psi_{\nu'} \psi_{\nu''} dr \right]^2$$

where $\psi_{\nu'}$ and $\psi_{\nu''}$ are the vibrational wave functions of the upper and lower states, respectively.

In the absence of exact expression for ψ_{ν} , the method of calculating of FCFs depends on the choice of approximate functions ψ_{ν} , which are obtained by solving vibrational Schrödinger equation with the same approximate potential function.

Good agreement between experimental values of distortion constants D_e and those calculated using Kratzer relation

$$D_e = 4B_e^3/\omega_e^2$$

suggested that lower part of three states involved, X , D and E , can be well described by a Morse potential

Since only bands with low ν' and ν'' quantum numbers have been observed in absorption spectrum, we have used Morse approximation in a formalism developed by Fraser and Jerman [8].

The program of Felenbok, modified by us to be compatible with PC, has been used to compute the eigenfunctions and overlap integrals. The impute parameters were molecular constants ω_e , $\omega_e x_e$ and r_e , collected from Refs. [2] and [6], and reduced mass $\mu_{107Ag109Ag}$ (= 53.94783 a.m.u.). The lower limit, upper limit and interval integration were 2.200, 2.950 and 0.003 Å, respectively.

Results and Discussion

The 6 x 6 arrays of calculated FCFs for the $D - X$ and $E - X$ bands are given in Table 1. The factors smaller than 10^{-4} are refrained from presentation.

Similar equilibrium geometries for the D and X states lead to small Δr_e (< 0.01 Å) and, thus, a narrow Franck-Condon envelope: the most prominent FCFs in Table 1 (i.e. the most intense bands) fall on the diagonal axis and descend in value in the $\Delta \nu = 0$ sequence with increasing ν . This is in good agreement with the intensity distribution of observed bands, estimated visually [2-4] and serve as a check for reliability of calculation method of FCFs for transition between low ν -levels.

In the case of $E - X$ band system ($\Delta r_e > 0.01$ Å), FCFs indicate that the strongest bands have to form broader Franck-Condon envelope, as really observed in experimental spectrum.

Table 1. Franck-Condon factors for *D-X* and *E-X* bands of $^{107}\text{Ag}^{109}\text{Ag}$

$\nu' \setminus \nu''$	0	1	2	3	4	5	6
0	0.9929	0.0049	0.0022				
	0.7387	0.2044	0.0461	0.0090	0.0016	0.0003	
1	0.0057	0.9693	0.0174	0.0074	0.0002		
	0.2290	0.3157	0.2867	0.1207	0.0365	0.0090	0.0019
2	0.0013	0.0226	0.9197	0.0387	0.0166	0.0009	0.0001
	0.0304	0.3630	0.0619	0.2393	0.1833	0.0835	0.0282
3		0.0027	0.0562	0.8385	0.0680	0.3133	0.0027
	0.0019	0.1030	0.3533	0.0014	0.1199	0.1916	0.1341
4		0.0005	0.0031	0.1104	0.7245	0.1012	0.0523
		0.0132	0.2003	0.2256	0.0643	0.0208	0.1348
5			0.0014	0.0019	0.1851	0.5825	0.1322
		0.0007	0.0463	0.2714	0.0748	0.1304	0.0046
6				0.0030	0.1369	0.2744	0.4246
			0.0052	0.1086	0.2625	0.0014	0.1187

First row: FCFs for *D-X* bands; second row row: FCFs for *E-X* bands

Conclusion

Reasonable agreement between calculated FCFs and estimated intensity distribution in both band systems proves that the Morse potential yields accurate FCFs, especially for vibrational transitions involving low ν -levels.

Acknowledgement

This work was supported by the Ministry of Science and Environmental Protection of the Republic of Serbia, Project No 142065.

References

- [1] J. Ruamps, Ann. Phys. 1959, **4**, 1111-1131.
- [2] C. M. Brown and M. L. Ginter, J. Mol. Spectrosc., 1978, **69**, 25-36.
- [3] V. I. Srdanov and D. S. Pesic, Bull. Soc. Chim. Belgrade, 1979, **44**, 281-289
- [4] V. I. Srdanov and D. S. Pesic, J. Mol. Spectrosc., 1981, **90**, 27-32.
- [5] G. Herzberg, "Spectra od diatomic molecules", 2nd. Ed., 1951, Van Nostrand, Princeton.
- [6] B. Simmard, A. Hackett, A. James, Chem. Phys Letters, 1991, **186**, 415-422.
- [7] V. Beutel, H. G. Kramer, G. L. Bhale, M. Kuhn, K. Weyers and W. Demtroder, J. Chem. Phys., 1993, **98**, 2699-2708.
- [8] P. A. Fraser and W. R. Jerman, Proc. Phys. Soc., 1953, **A66**, 1145-1152

***r*-CENTROIDS FOR THE *E-X* BANDS OF Ag₂ MOLECULE**

V. Bojović and A. Antić-Jovanović

*Faculty of Physical Chemistry, University of Belgrade, P.O.Box 137,
Belgrade, Serbia*

Abstract

The *r*-centroids, which are very closely related to relative vibrational transition probabilities, have been computed under a Morse model for the *E-X* band system of 107Ag109Ag molecule. The computed values indicate that the potentials are neither anharmonic nor so wide.

Introduction

It is well known that the Franck-Condon factors control values of the relative vibrational transition probabilities in a given electronic transition, if the electronic transition moment $Re(r)$ is substantially independent of internuclear separations r [1]. However, if $Re(r)$ is not independent of r in the range of r encountered in the transition, its effect must be taken into account. In order to find the variation of $Re(r)$ with internuclear separation, one has to know the value of *r*-centroids.

The *r*-centroid of the ν', ν'' band, $r_{\nu', \nu''}$, is defined as:

$$r_{\nu', \nu''} = \frac{\int \psi_{\nu'} r \psi_{\nu''} dr}{\int \psi_{\nu'} \psi_{\nu''} dr} \quad (1)$$

and represents a unique value of internuclear separation which may be associated with the $\nu' - \nu''$ transitions in a diatomic molecular band system. $\psi_{\nu'}$ and $\psi_{\nu''}$ are vibrational wave functions of the upper and lower states involved in transition, which satisfy the time independent vibrational Schrödinger equation:

$$[(-\hbar^2/2\mu_M)(d^2/dr^2) + U(r)] \psi_\nu = E_\nu \psi_\nu \quad (2)$$

where μ is reduced mass, E_ν - the vibrational energy and $U(r)$ - the potential energy. The accuracy of results and, therefore, the accuracy of eigen functions $\psi_{\nu'}$ and $\psi_{\nu''}$ and their overlap integrals, i. e. the *r*-centroids, depends on the choice of approximate potential energy function.

Expression (1) is valid if (i) $\mu_M \omega_e \sim 10^4$ for the molecule under consideration (μ_M - reduced mass of the molecule in a.m.u; ω_e - vibrational constant in cm^{-1}); (ii) $0.25 \text{ \AA} > |r_{e1} - r_{e2}| > 0.01 \text{ \AA}$ (r_{e1} and r_{e2} are the two equilibrium internuclear separations concerned in transition); (iii) ν' and ν'' do not exceed about 10.

To our knowledge, there has been no report on the *r*-centroids for the *E-X* system of Ag_2 in the literature. Therefore, the reliable values of the *r*-centroids for this band system have been determined in this work for the first time.

Method of Calculation

Calculation was performed using a modified computer program developed by Felembok [2] and Morse approximation for potential function. In the program, the molecular constants, listed in Table 1, were used as the input data. Numerical integration was done in step of 0.003A for the range of r from 2.200 A to 2.950 A and resulting eigen functions were used to calculate r -centroids.

Table 1. Molecular constants used as input data

State	ω_e (cm ⁻¹)	$\omega_e x_e$ (cm ⁻¹)	μ_M (amu)	r_e (A)	Ref.
$X^1\Sigma_g^+$	192.0	0.580	53.94783	0.25303	[3]
$E^1\Pi_u$	146.41	1.595	53.94783	0.25738	[4]

Results and Discussion

Table 2 contains computed values of r -centroids for investigated system together with the wavenumbers of the corresponding bands.

Table 2. r -Centroids and wavenumbers of observed $E - X$ bands

$v' \setminus v''$	0	1	2	3	4	5	6
0	2.5545 40136.4	2.6437 39945.7	2.6916 39756.1	-	-	-	-
1	2.4878 40279.4	2.5588 40088.6	2.6528 39899.0	2.7008 39710.7	-	-	-
2	2.3919 40419.0	2.5071 40228.1	2.5390 40039.6	2.6612 39850.4	2.7100 39663.7	2.7499 39474.1	-
3	-	2.4293 40364.4	2.5226 40175.4	-	2.6675 39798.1	2.7190 39611.9	2.7583 39427.4
4	-	-	2.4601 40308.5	-	-	-	2.7275 39562.1
5	-	-	-	2.4855 40251.2	2.5210 40062.4	2.6664 39876.6	-
6	-	-	-	2.4121 40378.6	2.5051 40228.1	-	2.6688 39820.0

First row: r -centroids (in A); second row: wavenumbers (in cm⁻¹)

The r -centroid value varies systematically from band to band of a system following the extension in r of $\psi_{v'}$, $\psi_{v''}$. Generally, it may be an increasing or decreasing function of wavelength according as $r_{e1} > r_{e2}$ or $r_{e1} < r_{e2}$. For the $E-X$ band system, computed

values of r -centroid for v',v'' bands (Table 2) increase smoothly with decrease of corresponding wavenumbers $\nu_{v',v''}$ (increase of wavelengths $\lambda_{v',v''}$), as has been observed by Nicholls and Jermain [5] in the case of red-degraded band system. Any small scatter about a smooth curve which is noted may possibly be attributed to the band-head wavenumbers instead of wavenumbers of band origins. The smooth relationship between r -centroid and band wavenumbers (or wavelengths) provides a useful bridge between experimental measurements, which are often expressed as a function of wavelength, and theoretical studies, which are often expressed in terms of internuclear separation.

As can be seen in Tables 1 and 2, the r -centroid value for 0,0 band is slightly greater than $(r_e' + r_e'')/2$ that proves that the potentials are not very anharmonic in the lower part. Further, the sequence differences $\Delta r = (r_{v'+1, v''+1} - r_{v', v''})$ are found to be constant for a given sequence and varying from about 0.005 to 0.03 Å, suggesting that the potentials of the system are not so wide.

Conclusion

In the present work the arrays of r -centroids for the $E-X$ bands of Ag_2 molecule are reported for the first time. They should be undoubtedly help in the studies of variation of electronic transition moment with internuclear separation as well as in the search of other molecular properties as a function of r .

Acknowledgment.

This work was supported by the Ministry of Science and Environmental Protection of the Republic of Serbia, project No 142065.

References

- [1] G. Herzberg, "*Spectra of Diatomic Molecules*", 2nd ed., 1951, Van Nostrand Comp., Princeton.
- [2] P. Felenbok, C. R. Acad. Sc., 1963, **256**, 2334-2346.
- [3] C. M. Brown and M. L. Ginter, J. Mol. Spectrosc., 1978, **69**, 25-32.
- [4] V. Beutel, H. G. Kramer, G. L. Bhale, M. Kuhn, K. Weyers and W. Demtroder, J. Chem Phys., 1993, **98**, 2699-2708
- [5] R. W. Nicholls and W. R. Jermain, Proc. Phys. Soc., 1956, LXIX, 3-A, 253 -260

SPECTROSCOPIC AND THEORETICAL INVESTIGATION OF DELPHINIDIN-ALUMINIUM (III) AND CYANIDIN-ALUMINIUM (III) COMPLEXES IN AQUEOUS AND NON-AQUEOUS MEDIA

J. M. Dimitrić-Marković, J. M. Baranac and M.L. Dašić

*Faculty of Physical Chemistry University of Belgrade Studentski trg 12-16,
Belgrade, Serbia, markovich@fjh.bg.ac.yu*

Abstract

A natural anthocyanidin molecules, delphinidin and cyanidin, have been used as model compounds for the study of the influence of the medium on the complexation abilities of these organic ligands towards aluminium (III). The complexation was monitored in acidic aqueous buffered solutions of pH 3.0 and pH 3.8 and in methanol. Electronic absorption spectroscopy was performed to characterize the stoichiometry and stability of the complexes formed.

Semi empirical *in vacuo* calculations, performed in the AM1 parameterization, enabled the determination of the structural features of free compounds as well as complex structural modifications caused by chelated Al (III) ions.

Introduction

Anthocyanidins and anthocyanins, as well as some other classes of flavonoids, possess one or more structural features that can be involved in complexation reactions with metal ions [1-5]. This molecular property plays non negligible role in biological systems. *In vivo* complex formation is one of the mechanisms which enable metal accumulation in peripheral tissues and reduces the possibility of their migration to eco systems. At the same time metal complexation is very efficient mechanism of protecting plants from pathogens and plant eaters. Moreover, metal complexation reactions are also very sensitive and powerful color stabilization mechanism developed in higher plants under *in vivo* conditions. The aim was to determine the stoichiometric composition and stability constants of the complexes formed and to investigate the influence of the complexing medium on complexation abilities of the investigated molecules and structural modifications caused by complex formation.

Results and Discussion

Earlier investigations of the anthocyanidin (anthocyanin) complexation reactions [1, 2] assumed that pigment molecules have to adopt some of the deprotonated, neutral or anionic anhydrobase structural forms characteristic to neutral and weakly alkaline or alkaline pH domains, to be able to enter metal complexation reactions in aqueous solutions. The obtained spectroscopic results confirmed the complexation ability of delphinidin and cyanidin in acidic aqueous, pH 3.0 and pH 3.8, solutions as well as in methanol. Chosen pH values are close to an average physiological pH value of the

natural media [2, 3] so the obtained results could give insight into the processes of biological relevance under *in vivo*. On the other hand, the higher pH values could not be used because of the strong hydrolytic properties of aluminium ion, which at higher concentrations, can form various types of hydroxo and acetate complexes, with some of them strongly precipitating at pH values higher than $\text{pH} > 4.5$ [3].

At pH 3.0 and pH 3.8 pure delphinidin and cyanidin exhibit, in a visible range of the spectrum, absorption bands of cationic transformation forms. Addition of aluminium to the pigment solutions results in important spectral modifications with the appearance of new bands bathochromically shifted up to $\Delta\lambda = 40 \text{ nm}$ (Fig. 1). Absorption bands of the complexes formed in the investigated acidic buffered solutions corresponded to some of the anhydrobase transformation forms of delphinidin and cyanidin molecules. This fact confirmed the ability of the small, hard, charged aluminium (III) ion to remove phenolic protons of the flavylum chromophore, even in acidic buffered solutions, and make the molecules adopt some of their anhydrobase forms.

The stability constant values obtained by molar ratio method are in a good agreement with the results obtained for the complexation of some of the delphinidin and cyanidin glyco- and acyl- analogs [3]. The values point to greater stability of the complexes formed at pH 3.8 compared to the complexes formed at pH 3.0. Complexes formed in methanol (Fig. 3) show even greater stability, probably as a consequence of the stronger electrostatic interactions in methanol than in the water. The molar ratio plots indicated different stoichiometries depending on the aluminium concentration.

Semi empirical *in vacuo* calculations, performed in the Austin Model 1 (AM1) parameterization [6], enabled the determination of the structural features of free delphinidin and cyanidin as well as complex structural modifications caused by Al (III) ions. Molecular features like bond lengths, bond orders, valence angles and some of the dihedral angles of the geometry optimized complex structures, indicated that the structural modifications of free pigments, caused by the chelation of Al (III) ions, are mainly localized on the C rings and on the chelating sites of the B rings of the pigments. The main changes occur on C(3)-C(4), C(4)-C(10) and C(9)-C(10) bonds in the C rings. The changes are also evident on possible chelating sites, C(3')-C(4'), C(4')-C(5') and on the C(2)-C(1') bonds which decrease upon complexation indicating the delocalization of the π bonds between two plains. Figure 2 presents geometry optimized chelate complex structures (of the optimal conformation), in the AM1 parameterization, involving C(3')-C(4') cyanidin chelating sites.

Utilizing electronic spectra combined with semi empirical calculations it is possible to conclude that delphinidin and cyanidin complexation with Al(III) generate chelate complexes of similar stabilities and same stoichiometries in the investigated media with most probable participation of the C(3')-C(4') chelating sites of both pigments.

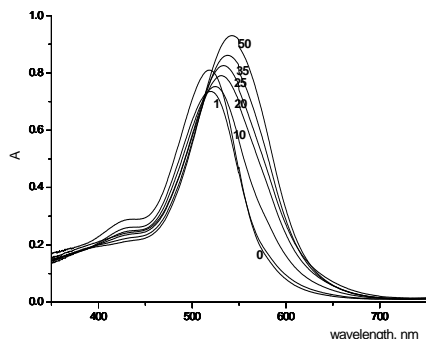


Fig. 1. Electronic spectra of equilibrated solutions of cyanidin at pH 3.8 at different aluminium-pigment molar ratios

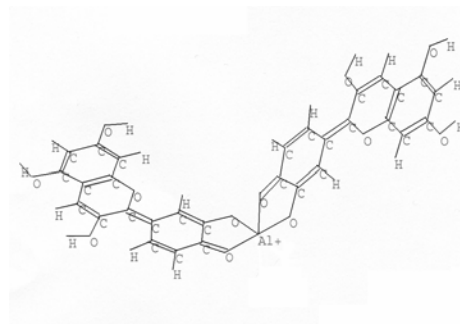


Fig. 2. Geometry optimized structure of the $(\text{Cy}_2\text{Al})^+$ chelate complex

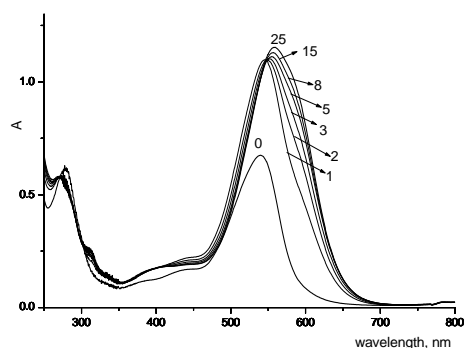
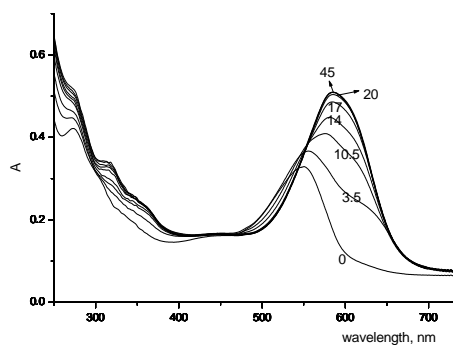


Fig. 3. Electronic spectra of equilibrated solutions of delphinidin and cyanidin in methanol at different aluminium-pigment molar ratios

References

- [1] E. Bayer, H. Egeter, A. Fink, K. Nether, K. Wegmann, *Angew. Chem. Int. Ed. Engl.*, 1966, **5**, 791-797.
- [2] J. B. Harborne, R. Grayer, *The Flavonoids - Advances In Research since 1980*, Chapman and Hall: London, 1988, 1-20.
- [3] P. Figureido, K. Toki, N. Saito, R. Brouillard, *J. Soc. Perkin Trans.* 1997, **2**, 355-361.
- [4] A. C. Boudet, J. P. Cornard, J. C. Merlin, *Spectrochimica Acta*, 2000, **56**, 829-839.
- [5] J. P. Cornard, A. C. Boudet, J. C. Merlin, *Spectrochimica Acta*, 2001, **57**, 591-597.
- [6] M. J. S. Dewar, E. G. Zoebisch, E. F. Healey, J. J. Stewart, *J. Am. Chem. Soc.*, 1985, **107**, 3902-3909.

THE INFLUENCE OF THE MEDIUM AND THE SUBSTITUTION PATTERN ON THE COMPLEXING ABILITIES OF SOME HYDROXYFLAVONES: A SPECTROSCOPIC AND THEORETICAL TREATMENT

J. M. Dimitrić-Marković*, J. M. Baranac and T. P. Brdarić

*Faculty of Physical Chemistry, University of Belgrade
Studentski trg 12-16, Belgrade, Serbia
markovich@ffh.bg.ac.yu*

Abstract

A series of hydroxyflavones, luteolin, morin and quercetin, widely occurring in nature, have been used as model compounds for the study of the influence of the medium and the substitution patterns on the complexation abilities of these multi-site ligands towards Mg (II). The chelating powers of the investigated compounds have been compared in different media, pure methanol, and pure ethanol and in these alcohols containing AcO⁻. Electronic absorption spectroscopy was performed to characterize the stoichiometry and stability of the complexes formed. Semi empirical *in vacuo* calculations, performed in the AM1 parameterization, enabled the determination of the structural features of free compounds as well as complex structural modifications caused by Mg (II) ions.

Introduction

The flavone molecules belong to the class of flavonoid compounds, or, in a more general sense, to the class of polyphenols. As plant pigments these compounds have a prominent role in the phytochemical processes *in vivo*.

Because of the remarkable array of pharmacological and biological activities of flavones, especially those referring to their high activity in oxidative processes with air oxygen, these molecules have attracted the attention of many researchers during the last decade [1-7]. Flavones possess one or more structural features that can be involved in complexation reactions with metal ions. *In vivo* flavone complexation is an important factor of their bioactivity as carriers of metals and regulators of their accumulation in plant tissues. This molecular property is a very efficient mechanism of protecting plants from pathogens and plant eaters and is also very often used for colorimetric purposes in the detection of metal traces in solutions.

The aim of the present paper was to determine the stoichiometric composition and stability constants of the complexes formed in different complexing medium and structural modifications caused by chelation of one or more Mg (II) ions.

Results and Discussion

The spectroscopic results confirm the selective ability of investigated flavones towards complexation with Mg (II) in different medium. Complexation abilities depend on complexing medium and available chelating sites. All investigated molecules

possess several chelating sites in competition: 5-OH-4 keto and 4' 5' ortho dixydroxyl groups in luteolin, 3-OH-4 keto, 5-OH-4 keto and 3' 4' ortho dixydroxyl groups in quercetin, 3-OH-4 keto and 5-OH-4 keto groups in morin (Fig.1).

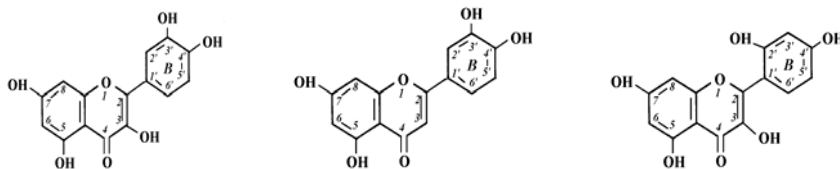


Fig. 1. Structural formulas of quercetin, luteolin and morin

The addition of magnesium (II) to flavone solutions (methanolic, ethanolic and alkaline containing sodium methanoate) resulted in important spectral modifications with the apparition of the new bands bathochromically or hypsochromically shifted (Fig. 2). Results imply that in methanol and ethanol 3-OH-4-keto and 5-OH-4-keto groups exhibit the greatest chelating power towards Mg (II). The 3' 4' ortho dixydroxyl group does not form complex with Mg (II) in pure alcohols even for important concentrations of Mg. In alkaline medium, methanol and ethanol containing AcO^- , the catechol structural unit exhibits the greatest complexing power. The stoichiometric composition of the complexes is also influenced by the medium i.e. consequently by the ligand chelating sites involved in complexes formation. The determination of the structural features of free compounds and their structural modifications caused by the chelation of Mg (II) ions was enabled by semi empirical *in vacuo* calculations, performed in the AM1 parameterization.

Conclusion

Metal complexation abilities of the differently substituted flavones, bearing a catechol moiety, towards Mg (II) are moderate and dependent upon substitution pattern of the B ring as well as on the composition of the complexing medium.

Molecular modelling of free and complexed molecules, performed by semiempirical AM1 method, indicated significant structural changes of the investigated molecules upon complexation involving the carbonyl structural unit.

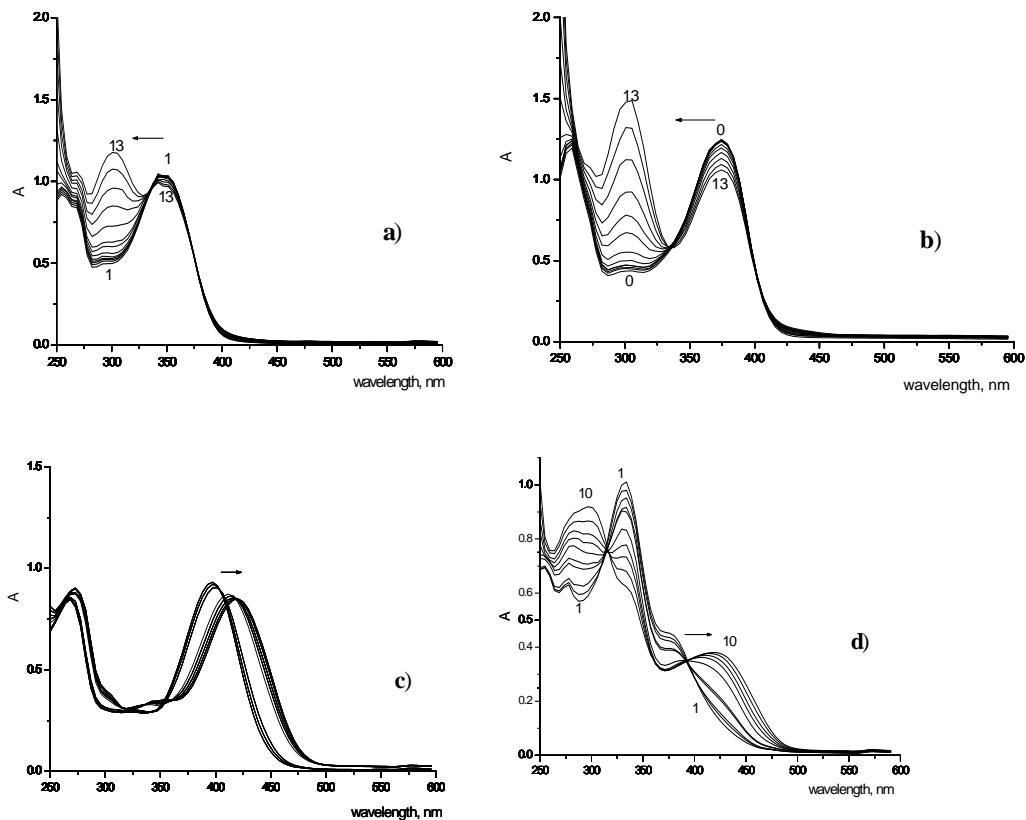


Fig. 2. Absorption spectra of flavones at different pigment: magnesium mole ratios: a) luteolin in methanol b) quercetin in ethanol c) morin in ethanol containing AcO^- and d) quercetin in methanol containing AcO^-

References

- [1] A. C. Boudet, J. P. Cornard, J. C. Merlin, *Spectrochimica Acta*, 2000, **56** 829-839.
- [2] J. P. Cornard, A. C. Boudet, J. C. Merlin, *Spectrochimica Acta*, 2001, **57**, 591- 602.
- [3] P. Figureido, K. Toki, N. Saito, R. Brouillard, *J. Soc. Perkin Trans. 2*, (1997) 355-361.
- [4] J. P. Cornard, J. C. Merlin, *J. Mol. Struct.* 2001, **569**, 129-138.
- [5] J. P. Cornard, J. C. Merlin, *Polyhedron*, 2002, **21**, 2801-2810.
- [6] J. P. Cornard, J. C. Merlin, *J. Inorg. Biochem.*, 2002, **92**, 19-27.
- [7] J. P. Cornard, J. C. Merlin, *J. Mol. Struct.*, 2003, **651**, 381-387.

COMPARISON OF DIFFERENT MATHEMATICAL MODELS IN DECONVOLUTION OF LIGNIN FLUORESCENCE SPECTRA

D. Đikanović¹, A. J. Kalauzi¹, K. Radotić¹, C. Lapierre² and M. Jeremić³

¹Centre for Multidisciplinary Studies, Laboratory of biophysics, University of Belgrade,
29. Novembra 142, Belgrade, Serbia;

²Institut National Agronomique, 78850 Thiverval-Grignon, France;

³Faculty of Physical Chemistry, University of Belgrade, Belgrade, Serbia

Abstract

We analysed fluorescence spectra of poplar lignin and lignin model compound, using gaussian, log-normal and exponential power model. Asymmetric models show wavelength positions of components in a complex molecule. Gaussian model indicates only discrete origin of the emission, but fails in defining component positions.

Introduction

Fluorescence spectroscopy is a sensitive tool for structural and kinetic studies of macromolecules. The analysis of fluorescent spectra of polymeric molecules is especially complex, since they may contain different fluorophores or a fluorophore in various microenvironments. Therefore, it is necessary to use computer methods for numerical deconvolution of complex emission spectra into individual components.

In this work we analyzed fluorescence spectra of lignin and lignin model compound, using three different mathematical models. The aim of the study was to see which of them best fits the original spectra, as well as to find out which model is most suitable for analytic application. Lignin, as a major structural polymer in the plant cell walls, is the second most abundant polymer on Earth. Fluorescence is an intrinsic property of lignin. The structural complexity of lignin makes its fluorescence spectra difficult to interpret. We also aimed to obtain the new data on the structural characteristics of lignin as a complex molecule and, on the basis of this approach, we hope to be able to distinguish lignins of different origin.

Materials and Methods

Lignin model dehydrogenative polymer (DHP) was synthesized from coniferyl alcohol, using horseradish peroxidase as an enzymatic catalyst [1].

Lignins from poplar (*Populus tremuloides*, clone 1214) and spruce (*Picea abies* (L.)) were obtained from wood mill using method of thyoacidolysis [2].

Fluorescence spectra were collected using a Fluorolog-3 spectrofluorimeter (Jobin Yvon Horiba, Paris, France) equipped with a 450 W xenon lamp and a photomultiplier tube. The spectra were corrected for the dark counts. In each measurement seven scans were averaged. The emission spectrum of the solvent (dioxane/water, 9/1 v/v) was subtracted. All measurements were performed at controlled temperature of 25 °C by means of a Peltier element.

A total of $N_{\text{DHP}} = N_{\text{poplar}} = N_{\text{spruce}} = 22$ emission spectra were collected for each sample (DHP, lignin from poplar and spruce) by excitation at different wavelengths, starting from excitation maximum at 360 up to 465 nm, with a 5 nm-step. Nonlinear fitting of each of the 66 spectra was performed using the Nelder-Mead algorithm implemented in Matlab, version 6. All spectra were deconvoluted by gaussian, log-normal and exponential-power model:

$$I(\lambda) = \sum_{i=1}^n A_i \frac{1}{\sqrt{2\pi}\sigma_i} \exp\left[-\frac{(\lambda - \lambda_{0i})^2}{2\sigma_i^2}\right] \quad \text{Gaussian model}$$

$$\left\{ \begin{array}{l} F_\lambda = F_m \exp\left\{-\left(\ln 2 / \ln^2 \rho\right) \ln^2 \left[(1/a' - 1/\lambda) / (1/a' - 1/\lambda_m) \right]\right\}, \quad \text{for } \lambda > a' \\ F_\lambda = 0, \quad \text{for } \lambda \leq a' \end{array} \right. \quad \text{Log-normal model}$$

$$F_\lambda = \frac{a}{\exp(b\lambda) \exp(c(\lambda^d)) - 1} \quad \text{Exponential-power model}$$

Results and Discussion

A set of fluorescence spectra, recorded by excitation of spruce lignin at different wavelengths (λ_{ex}), starting from excitation maximum at 360 nm, with 5 nm-step, is shown in Fig. 1 (left panel). A typical result of component Gaussian deconvolution of the emission spectra of spruce lignin, obtained by excitation at 405 nm, is shown in Figure 1 (right panel).

In order to acquire a distribution profile for all the positions of the components, we constructed corresponding histograms of their positions. Histogram profiles indicate that there are intervals of grouping for the position of the components. However, since positions and relative amplitudes of histogram maxima depended on the number of histogram abscissa intervals, we calculated approximate probability distribution (APD) for position components by weighed averaging histogram values for a set of histograms, where interval number varied from 2 to 30. Results of overlaid APDs for the poplar lignin, obtained using different mathematical models, are presented in Fig. 2. The presence of several peaks in APD in case of all lignin samples indicates that its fluorescence originates from several distinct fluorophores, which may be distinct molecular species or the same species in different microenvironments. We can note that there is a high compatibility between APD results obtained by the two asymmetric models.

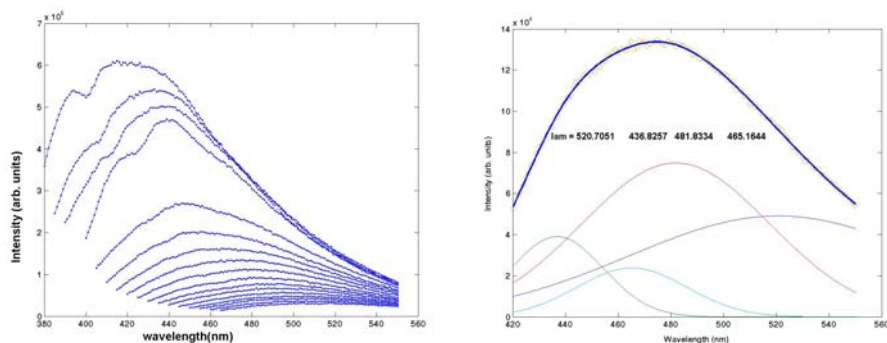


Fig. 1. Left panel: Emission spectra of poplar lignin dissolved in dioxane/water (9:1, v/v), for excitation wavelengths in the range 360 - 465 nm with 5 nm step. Right panel: Example of emission spectra deconvoluted into four Gaussian components; excitation wavelength was 405 nm; Circles – measured spectra, solid lines - separate components and their sum fitted to the experimental data.

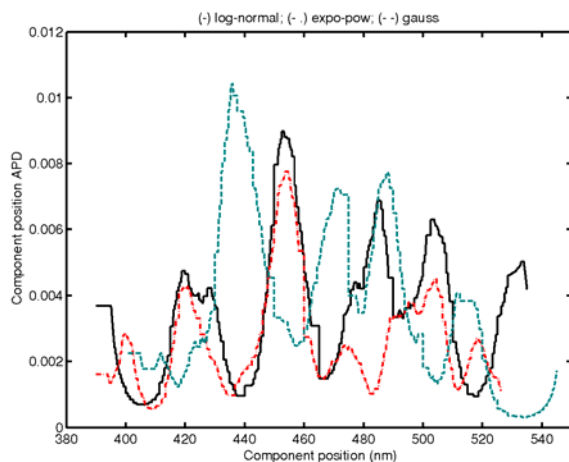


Fig. 2. Approximate distribution of the probability that a fitted Gaussian (---), exponential-power (-.-) and log-normal (—) component of all poplar emission spectra occupies a position on the λ_0 -axis (reconstructed from the histograms). In all cases, APD is multimodal, indicating that component positions are not equally probable.

The obtained results show that asymmetric models, as more precise description of the emission spectrum of a fluorophore, show wavelength positions of components in a complex molecule. Gaussian model, however, indicates only discrete origin of the emission, but fails in defining component positions.

References

- [1] K. Radotić, J. Simić-Krstić, M. Jeremić, M. Trifunović, A study of lignin formation at the molecular level by scanning tunneling microscopy, *Biophys. J.*, 1994, **66**, 1763-1767.
- [2] C. Lapierre, B. Monties, C. Rolando, Thiocidolysis of poplar lignins, *Holzforschung*, 1986, **40**, 113-118.

SINGLE MOLECULE STUDY OF TWO-COLOR EMISSION IN PERYLENEIMIDE-TERRYLENEDIIMIDE DENRIMERS

S.M. Melnikov¹, E.K.L. Yeow², H. Uji-i¹, F.C. De Schryver¹ and J. Hofkens¹

¹*Department of Chemistry, Katholieke Universiteit Leuven, Celestijnenlaan 200 F, 3001 Heverlee, Belgium (sergey.melnikov@chem.kuleuven.be)*

²*Division of Chemistry and Biological Chemistry, Nanyang Technological University, 1 Nanyang Walk, Block 5, Level 3, Singapore 637616*

Abstract

Förster resonance energy transfer (FRET) in donor-acceptor peryleneimide-terrylenediimide dendrimers has been examined at the single molecule level. Very fast Förster-type energy transfer in these donor-acceptor systems means that the donor emission is not detectable in principle. However, a fraction of the molecules (about 10-15% of the total number studied) showed simultaneous emission from both donor and acceptor chromophores. Single molecule detection techniques, photon-correlation measurements, and mathematical simulations were used to reveal the origin of this two-color emission. It is found that the two-color emission arises from unfavorable spatial orientation between a donor molecule and the other chromophores. The effect becomes apparent mostly after photobleaching of the majority of donors.

Introduction

Intensive research directed at understanding the photophysical properties of multi-chromophoric dendrimers has been carried out in the past decade. Recently, rapid and very efficient energy transfer in individual donor-acceptor peryleneimide-terrylenediimide rigid dendrimers has been reported [1, 2]. The result is that every excited donor chromophore transfers its energy to the acceptor chromophore without any donor emission. However, when more than one excited donor molecule is present simultaneously within a dendrimer, the observation of donor fluorescence may be expected under some conditions. Indeed, at high excitation power, single molecules of peryleneimide-terrylenediimide dendrimers display two-color emission [2]. This was attributed to a so-called “exciton blockade” arising from the presence of multiple excitations. In this study, we focus our attention on individual dendrimers showing simultaneous donor and acceptor emission. Two-color single molecule detection by confocal and defocused wide-field microscopy techniques, and Monte-Carlo simulations were applied to obtain a thorough comprehension of the mechanism responsible for this effect.

Results and Discussion

Two generations of peryleneimide-terrylenediimide dendrimers consisting of a terrylenediimide energy acceptor as a core, and eight (**T2P₈**) or four (**T1P₄**) perylenemonoimide donor molecules located at the edge of the polyphenylene branches were studied. The molecular structure of **T2P₈** is depicted in Fig. 1.

Fluorescence traces of 110 single molecules of **T1P₄** and 339 single molecules of **T2P₈** under pulse excitation were analyzed. Furthermore, fluorescence traces of 66 single molecules of **T1P₄** and 95 single molecules of **T2P₈** were recorded using CW excitation. The measured single molecules are divided into three groups as follows: 1) molecules showing only red emission, 2) molecules showing red followed by blue emission, and 3) molecules displaying two-color (*i.e.*, red and blue) emission. The majority of molecules fall into the first two groups as expected because of the efficient energy transfer occurring in these systems. The relative proportions of each group are nearly equal for both dendrimer generations, and for different excitation conditions. A typical fluorescence trace of a single molecule displaying monochromatic emission is displayed in Figure 2A. An example of a two-color fluorescence trace is displayed in Figure 2B. The dual-color fluorescence is registered mostly after significant decrease of acceptor emission from initial level. This decrease in the acceptor emission intensity is attributed to sequential bleaching of donor chromophores. Fluorescence decay time measurements, performed in the blue detection channel, resulted in one decay component equal to the decay time of the unquenched donor emission.

The percentage of dual-color fluorescence for different dendrimer generations and excitation regimes, and photon-correlation measurements strongly suggest that multiple excitation as a main source for two-color emission is unlikely. As mentioned before, the fluorescence decay time of the blue emission is equivalent to the life time of the unquenched donor. This means that the emitting donor chromophore does not interact with the acceptor, and directional FRET does not take place. The orientation factor might play a role, however, its influence is minimal in intact dendrimers containing 4 or 8 interacting donor chromophores. The orientation of donor chromophore can become important when the ones with a favorable orientation are bleached.

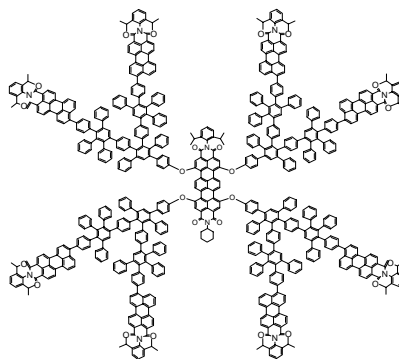


Fig. 1. The structure of **T2P₈**

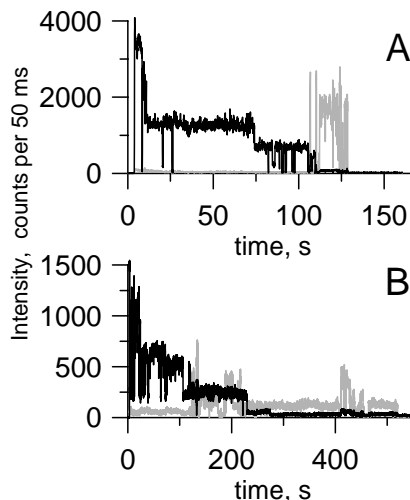


Fig. 2. Fluorescence transients of single molecules. The black color and the grey color curves denote the acceptor and the donor emission trajectories correspondingly.

Indeed, two-color emission emerges only after significant reduction in the acceptor irradiance for most of the traces.

Defocused imaging of single molecules has been used to examine the angular distribution of their emission dipole moments [3]. We applied this technique to determine the orientation of emitting chromophores. Defocused wide-field image sequences of 45 single **T1P₄** molecules and 268 single **T2P₈** molecules were recorded. Fig. 3 shows the defocused wide-field images of a single molecule which exhibits simultaneous donor-acceptor emission. Assuming that the absorption and emission transition dipoles of the acceptor are oriented in the same direction, the calculated orientation factor (κ^2) is approximately 0 for this example. The molecule exhibits both in-plane emission dipoles for the acceptor (Fig. 3A) and the donor (Fig. 3B) chromophores, respectively, however, they are both oriented perpendicular to each other.

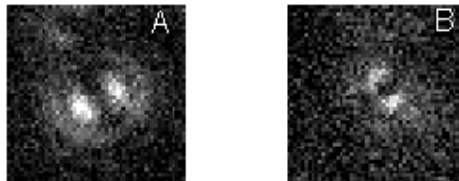


Fig. 3. Defocused wide-field images of single molecule which showed the dual-color fluorescence. (A) displays the acceptor detection channel, (B) - the donor one.

Conclusion

We have argued that an exciton blockade is not the main source for two-color emission. We attribute this observed two-color emission to the presence of some unfavorable oriented donor chromophores. The importance of spatial orientation for energy transfer process has been clearly illustrated by two-color defocused wide-field imaging.

Efficient annihilation processes and strong coupling among different donors prevent the dual-color fluorescence from occurring when there exist more than two to three donors. Therefore, two-color emission appears mostly after significant decrease of initial acceptor fluorescence intensity.

References

- [1] S. Jordens, G. De Belder, M. Lor, G. Schweitzer, M. Van der Auweraer, T. Weil, E. Reuther, K. Mullen, and F.C. De Schryver. *Photochem. Photobiol. Sci.*, 2003, **2**, 177-186.
- [2] M. Cotlet, R. Gronheid, S. Habuchi, A. Stefan, A. Barbafina, K. Müllen, J. Hofkens, F.C. De Schryver. *J. Am. Chem. Soc.* 2003, **125**, 13609-13617.
- [3] H. Uji-i, S.M. Melnikov, A. Deres, G. Bergamini, F.C. De Schryver, A. Herrmann, K. Müllen, J. Enderlein, and J. Hofkens. *Polymer* 2006, **47**, 2511-2518.

SPECTROSCOPIC INVESTIGATION OF AQUEOUS 12-TUNGSTOPHOSPHORIC ACID SPECIATION

D. Bajuk-Bogdanović¹, I. Holclajtner-Antunović^{1*}, M. Todorović²,
U. Mioč¹ and J. Zakrzewska³

¹Faculty of Physical Chemistry, P.O.Box 137, Belgrade,

²Faculty of Chemistry, P.O.Box 157, Belgrade

³Institute of General and Physical Chemistry, P.O.Box 551, Belgrade, Serbia

Abstract

The speciation during base decomposition of 12-tungstophosphoric acid (WPA) has been determined by UV, IR and ³¹P NMR spectrometry over the pH range 1-11.5. The results have shown that Keggin structure of WPA is present only at pH 1; at pH about 2.0, species with 2 phosphorus atoms are present. Under the physiological conditions, WPA is present as lacunary Keggin anion, which is, with further increase in pH, progressively decomposed to tungstate and phosphate.

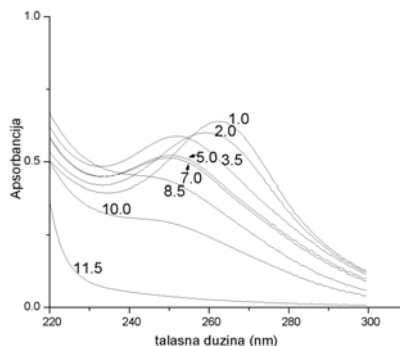
Introduction

Polyoxometalates (POMs) of various types are interesting compounds with unusual behavior: they are analytical reagents, good catalysts, superionic proton conductors and biochemical active species too. The properties of POMs in solid state are extensively studied and well established, while their behavior in solution state is not well understood and explained. In this paper, the aqueous solutions of WPA were investigated in dependence of pH, buffer type and ageing of solution.

Experimental

The pH of WPA aqueous solutions was adjusted with addition of NaOH or HCl. UV/VIS spectra of solutions were obtained by Cintra 10e (GBS) spectrophotometer. The IR spectra were recorded on a Perkin-Elmer 983G spectrophotometer using KBr pellets technique. Solid samples were obtained by evaporation of water from solutions of different pH. The NMR experiments were carried out with Bruker MSL 400 spectrometer at 80.98 MHz.

Results and Discussion



The UV spectrum of WPA solution of pH=1 has intense absorption maximum at 263 nm, corresponding to electron transition $O_b/O_c \rightarrow M$ (Fig.1). When the solution's pH is increased (1-3.5), the band maximum is shifted towards lower wavelengths and its intensity is decreased.

Fig. 1. UV spectra of WPA solutions of various pH

In the pH region of 3.5-7 the band maximum is at the same position but its intensity is decreased. The further increase in pH up to 11.5 causes disappearance of this band confirming the total degradation of parent Keggin structure.

IR spectra of dry residua of WPA solutions of different pH make easier consideration of WPA stability (Fig 2.). Spectrum of WPA solution of pH=1 is equivalent to the spectra of solid WPA with vibration bands characteristic for Keggin anion: 1080, 990, 890 and 810 cm^{-1} , corresponding to vibrations $\nu_{\text{as}}(\text{P-O}_a)$, $\nu_{\text{as}}(\text{W-O}_d)$, $\nu_{\text{as}}(\text{W-O}_b\text{-W})$ and $\nu_{\text{as}}(\text{W-O}_c\text{-W})$ respectively [1]. Already at pH=2 these bands are modified, some bands are disappeared while new bands are appeared and remained up to pH=7. It can be noticed that stretching P-O vibration at the 1080 cm^{-1} is splitted into bands at the 1100 and 1050 cm^{-1} . This indicates the existence of new anion identified as $\text{PW}_{11}\text{O}_{39}^{7-}$ or as $\text{P}_2\text{W}_{18}\text{O}_{62}^{6-}$. Comparing the characteristic bands of the mentioned two structures with spectra in Fig. 2. it is difficult to ascribe the obtained spectrum to the particular structure, especially because both of them have similar IR spectra. The IR spectra at higher pH values indicate the total degradation of parent anion to tungstate and phosphate.

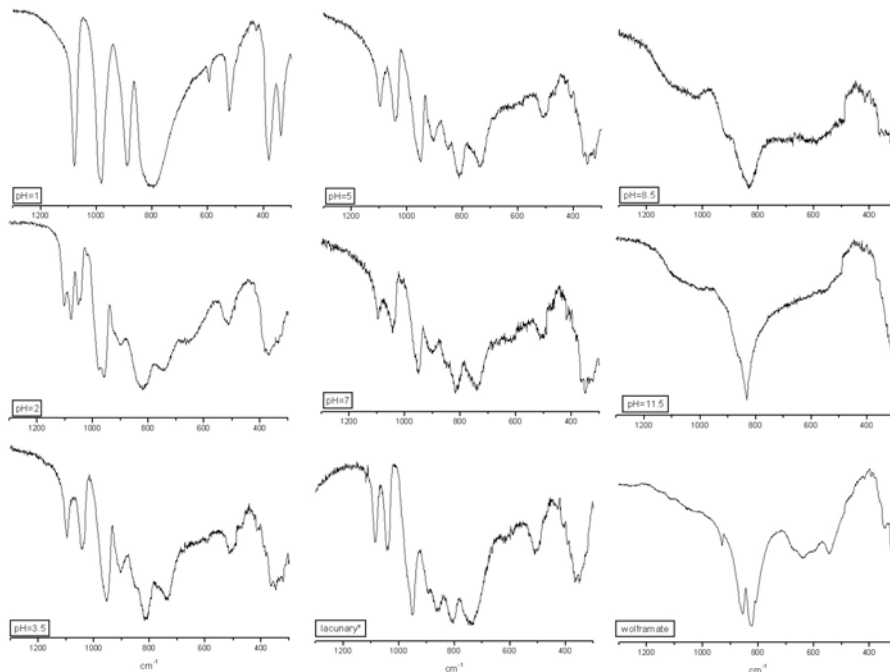


Fig. 2. IR spectra of evaporated WPA solutions of various pH

The ^{31}P NMR spectra of WPA solutions, recorded for the same pH range show more evidently Keggin anion transformations (Fig. 3a.). The literature values of chemical shifts were used for identification of the formed ions in solutions [2].

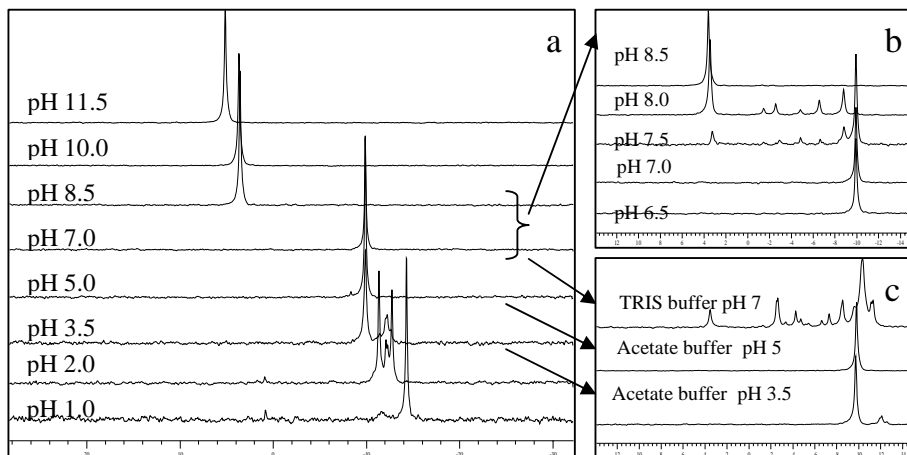


Fig. 3. ^{31}P NMR spectra of WPA solutions of different pH values

It can be seen that the parent Keggin $\text{PW}_{12}\text{O}_{40}^{3-}$ anion can be easily recognized through its intense single signal at -14.3 ppm. At $\text{pH}=2$ there appear few peaks about -12 ppm, assigned to the structures with 2 phosphorus atoms from Dawson series, such as $\text{P}_2\text{W}_{21}\text{O}_{71}^{6-}$, $\text{P}_2\text{W}_{18}\text{O}_{62}^{6-}$ and $\text{P}_2\text{W}_{20}\text{O}_{70}^{10-}$. These peaks are present also at $\text{pH}=3.5$; the intensities of these peaks decrease and besides them appear a dominant peak at about -9.9 ppm which corresponds to the lacunary Keggin $\text{PW}_{11}\text{O}_{39}^{7-}$ anion. Due to the importance of this pH region in biomedical investigations, the NMR spectra are recorded for the pH values between 6.5 and 8.5, which is presented in Fig. 3b. It is evident that up to pH 7, lacunary anion is the only structure present in the solution. At pH 7.5, which almost corresponds the physiological condition, besides the dominant lacunary anion, there appear some other products. The change in pH from 7.5 to 8.0 causes complete destruction of lacunary anion to the phosphate anion. The spectra recorded in longer time period (up to 14 days) showed no change and equilibrium was established shortly after solutions preparation (up to 10 min). ^{31}P NMR spectra recorded for WPA solutions buffered with acetate and tris buffers showed that acetate buffer is very convenient for pH maintaining while in tris buffer at pH 7, formation of some other polytungstophosphates besides lacunary Keggin anion is observed (Fig. 3c).

Conclusion

All spectroscopic methods used indicate the instability of WPA in aqueous solutions, with complex decomposition scheme of Keggin anion. The obtained results are of importance for biomedical and catalytic applications of these compounds and for better understanding of mechanism of their activities.

References

- [1] M. T. Pope, *Heteropoly and Isopoly Oxometalates*, 1983, Springer, Berlin.
- [2] B. Smith and V. Patrick, *Aust. J. Chem.*, 2004, **57**, 261-268.

SPECTROPHOTOMETRIC INVESTIGATION OF THE OXYTETRACYCLINE DEGRADATION WITH Cu(II)/H₂O₂ SYSTEM IN AQUEOUS SOLUTIONS

S. M. Sunarić¹ and S. S. Mitić²

¹Faculty of Medicine, Department of Pharmacy, University of Niš, Bulevar dr Zorana Djindjica 81, 18000 Niš, Serbia, (ssunaric@medfak.ni.ac.yu)

²Faculty of Natural Sciences and Mathematics, Department of Chemistry, University of Niš, Višegradska 33, P.O.Box 224, 18000 Niš, Serbia

Abstract

The reaction between oxytetracycline, hydrogen peroxide and Cu(II) ions was investigated spectrophotometrically. It was found that in weak alkaline aqueous solutions degradation of antibiotic drug occurred. The product of degradation has absorption maximum at 366 nm. The influence of pH was studied and pH 8.2 was found as the alkalinity which enables maximum value of reaction rate.

Introduction

Oxytetracycline is an antibiotic substance isolated from the elaboration products of the *Streptomyces rimosus*. It is a member of the tetracycline family of the antibiotics that are derivatives of an octahydronaphthacene [1].

Decomposition of H₂O₂ in the presence of Cu(II) ions leads to production of oxygen-derived active species such as hydroxyl radicals in Fenton-like reactions [2]:



in which Mⁿ⁺ is a metal ion.

The kinetic data so far available on the Cu(II)-dependent breakdown of hydrogen peroxide, indicate that this reaction follows a complex mechanism, which includes formation of hydroxocopper(III) ion [3], or Cu(II)-H₂O₂ reactive complex [4].

In consideration to intracellular decomposition of hydrogen peroxide in the presence of Cu(II) ions [5], the aim of this work was investigation of the reaction conditions and reaction which proceeds between oxytetracycline, hydrogen peroxide and Cu(II) ions.

Experimental

Pure oxytetracycline-hydrochloride, C₂₂H₂₄N₂O₉·HCl, was kindly provided by Zdravlje-Leskovac. A stock solution of oxytetracycline (1.00 x 10⁻³ mol/dm³) was freshly prepared by dissolving the required amount of oxytetracycline-hydrochloride in deionised water. A solution of Cu(II) (1.00 x 10⁻⁴ mol/dm³) was prepared by dissolving CuCl₂·2H₂O (Merck) in deionised water. A hydrogen peroxide solution (1.00 mol/dm³) was prepared just before use from a 35% commercial reagent (Merck).

The reaction rate was followed spectrophotometrically by Perkin-Elmer Lambda 15 UV/VIS spectrophotometer, connected to a thermocirculating bath. The vessel was thermostated at $20 \pm 0.1^\circ\text{C}$ and the reaction was initiated by mixing.

Results and Discussion

The absorption spectra of the system containing oxytetracycline, hydrogen peroxide, tris-HCl buffer (pH 8.2) and Cu(II) was recorded in the time interval of 2-7 min after the reaction was started (Figure 1, curve 2). A volume of 0.3 cm^3 H_2O_2 solution was stored in one compartment of a special vessel, intended for kinetics measurements; 5 cm^3 of a Cu(II) solution was placed in the second compartment, 0.3 cm^3 of the buffer solution in the third, and 0.1 cm^3 of the doxycycline stock solution in the fourth compartment. Deionised water was added up to the total volume of the reaction mixture of 15 cm^3 . The vessel was thermostated at $20 \pm 0.1^\circ\text{C}$ and the reaction was initiated by mixing.

The absorption maximum at 366 nm appeared and decreased with time. The absorption spectra shows that in the Cu(II)/ H_2O_2 system in aqueous solution degradation of oxytetracycline is occurred. Assuming the radical-chain mechanism given in Eq. 1, which is well studied by many authors [6], [7], it can be conclude that highly reactive species attack the molecule of oxytetracycline forming a degradation product of drug with absorption maximum at 366 nm.

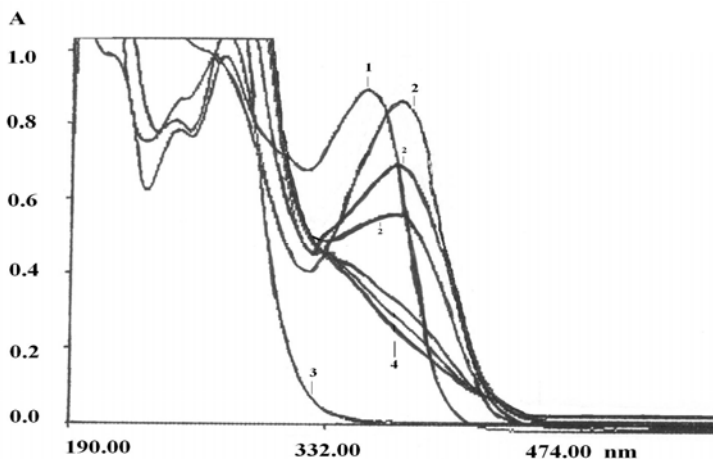


Fig. 1. The absorption spectra of the mixtures: 1) aqueous solution of oxytetracycline; 2) oxytetracycline-Cu(II)-hydrogen peroxide-buffer in the time interval 2-7 min after mixing of reagents; 3) Cu(II)-hydrogen peroxide-buffer; 4) oxytetracycline-Cu(II)-hydrogen peroxide-buffer 20 min after mixing.

Because of pH is one of the variables that strongly influences on the chemical forms and reaction of drugs, dependence of the reaction rate on the pH was investigated at $20 \pm 0.1^\circ\text{C}$. The phosphate buffer was used for the pH range between 6.0 and

7.8, tris (hydroxymethyl)aminomethane - HCl buffer for pH 8.0 - 9.0, and bicarbonate buffer for pH 9.0 – 11.0. The rate of change of absorbance at 366 nm was measured during 2-7 min after mixing. The initial rates of the reaction were determined by measuring the slopes of the initial tangents to the absorbance-time curves, dA/dt . Figure 2 shows the influence of pH on the reaction rate. As can be seen the reaction rate has maximum value at pH 8.2. The reaction is slower, but also takes place at physiologically pH 7.4.

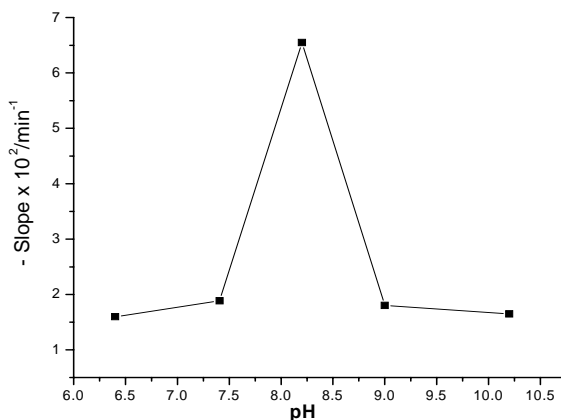


Figure 2. Correlation between the reaction rate and pH.

Acknowledgement

This research was supported by grant 142015 from the Ministry of Science and Environmental Protection of the Republic of Serbia.

References

- [1] J. N. Delgado, W. A. Remers, "Wilson and Gisvold's Textbook of Organic Medicinal and Pharmaceutical Chemistry", 10th ed., 1998, Lippincott Williams & Wilkins, pp. 299.
- [2] J. Ueda, Y. Shimazu, T. Ozawa, *Free Radic. Biol. Med.*, 1995, **18** (5) 929-933.
- [3] J. F. Perez-Benito, *Monatsh. Chem.*, 2001, **132**, 1477.
- [4] T. Tomiyasu, S. Aikou, K. Anazawa, H. Sakamoto, *Anal. Sci.*, 2005, **21**, 917.
- [5] B. Halliwell, J. M. C. Gutteridge, *Methods Enzymol.*, 1990, **186**, 1.
- [6] B. Halliwell, M. C. J. Gutteridge, *Biochem. J.*, 1984, **219**, 1.
- [7] J. A. Simpson, K.H. Cheeseman, S.E. Smith, R.T. Dean, *Biochem. J.*, 1988, **254**, 519.

SURFACE IONIZATION STUDY OF THE NON- STOICHIOMETRIC $\text{Li}_n\text{F}_{n-1}$ ($N = 4 - 6$) CLUSTERS

S. Veličković, M. Veljković, V. Đorđević, J. Cvetičanin
J. Đustebeć and O. Nešković

*Laboratory for Physical Chemistry, The Vinca Institute of Nuclear Sciences,
P.O. box 522, Belgrade, Serbia
vsuzana@vin.bg.ac.yu*

Abstract

In this study we are presenting the results of the surface ionization of $\text{Li}_n\text{F}_{n-1}$ ($n=4-6$) clusters on rhenium surface impregnated with fullerenes using the magnetic mass spectrometer. The Li_5F_4 nanocubic cluster was detected for the first time. We determined values of ionization energies for Li_4F_3 and Li_6F_5 , they are $4,3 \pm 0,2$ eV, $4,0 \pm 0,2$ eV, respectively. The ionization energies agreed with theoretical ionization energies obtained by *ab initio* method, which indicates the excess electron localized in a specific site for non-stoichiometric clusters. The first ionization energy value for the Li_4F_3 was in accordance with earlier results obtained experimentally using photoionization time-of-flight mass spectrometer. There are currently no reliable experimental data for the ionization energy of Li_6F_5 cluster.

Introduction

Electronic structure of metal-rich nonstoichiometric binary clusters has been widely studied to obtain better understanding of the metal-insulator transition mechanisms depending on the variations of cluster size and their chemical composition[1]. Based on observed abundances and ionization threshold Honea et al. classified of $\text{Li}_n\text{F}_{n-1}$ clusters as follows: cubic clusters of a filled cubic lattice of ion with the extra electron occupying a weakly bound surface state; F-center clusters consist of a nearly filled cubic lattice with an electron localized in an anion vacancy; and nonocubic clusters have the excess electron bound to single cation [2].

For the $\text{Li}_n\text{F}_{n-1}$ ($n = 4-6$) cluster system, the electronic structure was often found to be segregated into a metallic part and an ionic part. The most stable isomer of Li_4F_3 has a C_{3v} symmetry with a cuboidal structure with a vacancy of one missing fluorine. The odd electron localizes around this vacancy, so that this cluster has a typical F-center structure. Cluster Li_4F_3 segregated into the metallic Li_3^{2+} moiety and the ionic LiF_3^{2-} . The most stable isomer of Li_5F_4 has a C_{3v} symmetry with a cuboidal $(\text{LiF})_4$ structure with a terminal lithium attached to one of the fluorine atoms. The odd electron localized around the terminal lithium implicates the low abundances of Li_5F_4 nanocubic cluster. Cluster Li_6F_5 have F-center structure[3].

Here we are reporting the results of a mass spectrometric study of the surface ionization clusters $\text{Li}_n\text{F}_{n-1}$ ($n = 4-6$).

Results and Discussion

The ionization energies of the non-stoichiometric $\text{Li}_n\text{F}_{n-1}$ clusters were studied experimentally using a triple thermal ionization source and magnetic mass spectrometer. The mass spectrometer used in this investigation was a 12-inch radius, 90° sector magnetic instrument of local design. Pressures in the analyzer region were maintained below 10^{-8} Torr and operating pressures in the source region below 5×10^{-7} Torr. In these experiments for ionization of samples we used Re filament impregnated with fullerenes. The $\text{LiF/LiI/BiF}_3/\text{C}_2\text{H}_5\text{OH}$ solution was first deposited on the evaporation filaments (Re) and then dried under a heat lamp. The beam of clusters to be investigated was produced by heating the LiF+LiI+BiF_3 sample in the Re canoe, where a certain fractions of the neutrals are ionized. The filaments are heated with an electric current and the temperature was determined with an optical pyrometer. Identification of the gaseous species formed in the ion source was achieved from their mass-to-charge ratio, isotopic abundance and ionization energy. Figure 1 present obtained mass spectrum of ions Li_4F_3^+ , Li_5F_4^+ and Li_6F_5^+ . The mechanism of the formation of $\text{Li}_n\text{F}_{n-1}$ clusters from the alkali halide is not fully elucidated.

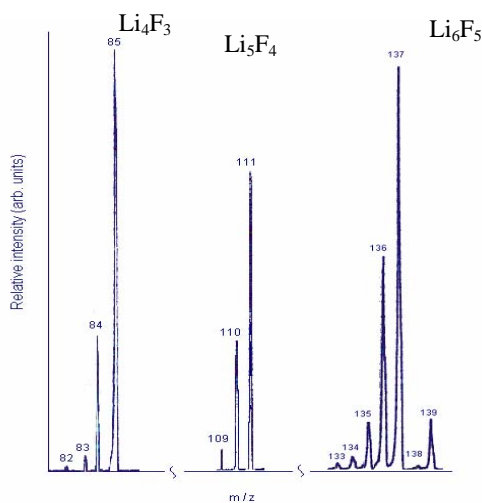


Fig. 1. Mass spectrum of non-stoichiometric clusters Li_4F_3 , Li_5F_4 and Li_6F_5 produced by surface ionization technique

Surface ionization or thermal ionization is a method for generating ions at a hot metal surface. The values of the ionization energy of Li_4F_3 and Li_6F_5 were obtained from the Saha-Langmuir equation:

$$\alpha^+ = \frac{g^+}{g} e^{\frac{\Phi - IE}{kT}} \quad (1)$$

where α^+ are the ionization coefficients; g^+ and g are the statistical

weights of the ions and neutrals; IE is the ionization energy of clusters; k is Boltzmann's constant; T is the temperature of the surface; Φ is the work function of the surface. The value of work function of the surface shows dependence on the adsorption of the sample, fullerenes and residual gas in the working temperature range. Therefore, the work function was determined for each surface and experimental conditions rather than using literature data. The ion intensities of Li_4F_3 and Li_6F_5 clusters increased exponentially with increasing temperature of filament and the canoe. Figure 2 shows the logarithm of ion intensity of Li_4F_3^+ and Li_6F_5^+ ions as a function of temperature.

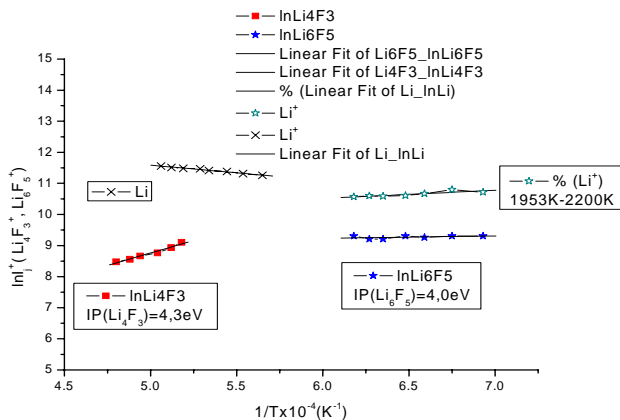


Fig. 2. Ionization of Li_4F_3 and Li_6F_5 on Re impregnated with fullerenes.

The values of the ionization energies obtained from the Saha-Langmuir equation where $4.3 \pm 0.2 eV$ for Li_4F_3 and $4.0 \pm 0.2 eV$ for Li_6F_5 .

Conclusions

The surface ionization method offers the possibility of measuring ionization energies of clusters type F-center Li_4F_3 and Li_6F_5 . Comparing these ionization energies values with those obtained by the *ab initio* MO calculations it has been concluded that the Li_4F_3 and Li_6F_5 clusters have "superalkaly" configuration in which the odd electron localization is in a specific site, characteristic for F-center clusters. The Li_5F_4 nanocubic cluster was detected for the first time by surface ionization method, but his low abundance prevents the measuring of its ionization energy.

Acknowledgments

This work was financially supported by the Ministry of Science and Environmental Protection, Republic of Serbia, under Project No. 142001.

References

- [1] K. Yokoyama, N. Haketa, H. Tanaka, K. Furukawa, H. Kudo, Chem. Phys. Lett., 2000, **330**, 339-346.
- [2] N. Haketa, K. Yokoyama, H. Tanaka, H. Kudo, J. Mol. Struc., 2002, **577**, 55-67.
- [3] E. C. Honea, M. L. Homer, P. Labastie, R. L. Whetten, Phys. Rev. Lett., 1989, **63**, 394.

Kinetics Catalysis

(C)

A MULTITECHNIQUE APPROACH OF THE DETERMINATION OF THE SURFACE ACTIVE SITES OF CATALYSTS

J. Keranen¹, C. Guimon² and A. Auroux¹

¹*Institut de Recherches sur la Catalyse, CNRS, 2, Av. Einstein, 69626 Villeurbanne Cedex, France*

²*Laboratoire de Physico-Chimie Moléculaire, Université de Pau et des Pays de l'Adour, 2, Av. P. Angot, 64053 Pau Cedex 9, France*

Abstract

The determination of the active surface sites of solid catalysts requires the use of complementary methods. Most of them are based on acid-base reactions between a gas and the solid under study, i.e. on chemisorption experiments. Usually, the adsorption or thermo-desorption of probe (acidic or basic) molecule is monitored by thermal or spectroscopic techniques. This paper deals with the use of adsorption microcalorimetry and X-ray photoelectron spectroscopy for the evaluation of the amount and the strength of the active sites (microcalorimetry) and the determination of the nature of these sites (XPS and FTIR). Several examples will be given concerning the acidity of zeolites and supported oxides.

Introduction

Many industrial processes are based on acid or/and base-catalyzed reactions. The majority of these processes use heterogeneous catalysts, particularly mixed or supported oxides possessing both hydroxyl groups (Brønsted acid or basic sites) and coordinatively unsaturated metallic cations (Lewis acid sites) and anions (Lewis basic sites as O²⁻ ions). A good description and knowledge of the surface active sites is essential for a better understanding of the relationships between their physico-chemical properties and their catalytic performances (activity, selectivity, stability...). The acidity and the basicity of solids is much more complex to determine than that of solutions because of their heterogeneity in terms of composition (particularly between the bulk and the surface), nature (Brønsted, Lewis), strength, concentration and distribution of sites. Moreover, the hydrophilic/hydrophobic character of the surface is also an important parameter which has to be known.

The acid-base properties of solids can be analyzed with a number of thermal or spectroscopic methods, based on gas-phase adsorption of basic or acidic probes. The most important and widely used techniques are microcalorimetry [1-6], continuous or intermittent temperature-programmed desorption [7,8], thermogravimetry [9] and Fourier-transform IR spectroscopy [7,10-12]. However, we lack of an ideal technique able to provide an exhaustive knowledge of acid-base character of solids and we have to use a combination of complementary techniques. Moreover, these techniques analyze mainly the bulk while the surface of solids, essential in catalysis, often presents different compositions and properties. Among the various analysis techniques, X-ray photoelectron spectroscopy (XPS) and adsorption calorimetry are certainly techniques hav-

ing found the widest applications in the study of catalytic materials. They give not only qualitative but also quantitative data about the surface under study.

Like the other techniques mentioned above, XPS can be used in conjunction with the adsorption and the thermodesorption of gaseous bases or acids. Measuring the binding energy of the main element (heteroatom) of probe molecules chemisorbed on solid surface can provide the identification and the quantitative determination of Brønsted and Lewis site concentration. XPS is thus a good complement to adsorption microcalorimetry. This latter technique permits an accurate determination of the strength and the strength distribution of the sites with the help of the differential heat of adsorption vs coverage curve, but cannot generally distinguish between sites of different nature. For that purpose, FTIR of adsorbed probes is essential to give a complete picture of the solid surface.

This short revue reports several examples investigated by our research groups, using these three techniques to examine the surface acidity and basicity of different classes of catalysts, zeolites and supported or mixed oxides. In some cases, the informations obtained can be related to the catalytic activity of the solids under study.

Experimental

Calorimetry

The heats of adsorption were measured in a heat flow microcalorimeter of Tian-Calvet type (C80 from Setaram) linked to a volumetric line allowing the introduction of small doses of reactive gas (ammonia or sulfur dioxide). Successive doses were sent onto the sample until a final equilibrium pressure of 67 Pa is obtained. Before adsorption, the samples were activated overnight at 673 K. The adsorption temperature was maintained at 393 K (zeolites) or 353 K (mixed oxides) in order to limit physisorption.

X-ray Photoelectron Spectroscopy

After adsorption of base (ammonia) or acid (sulfur dioxide) in the same conditions than those chosen for the microcalorimetry experiments, the samples were introduced, without air exposure, in the XP spectrometer, a SSI 301 model using monochromatic and focused (spot diameter of 600 μm , 100 W) $\text{AlK}\alpha$ radiation. The analyses were carried out at room temperature under a residual pressure of 10^{-7} Pa. Quantitative analyses were performed using appropriate intensity (Scofield) factors [13]. Binding energies (BE) were determined by reference to main element of the catalysts (Si2p for zeolites for example) [14].

FTIR Spectroscopy

FTIR spectra were recorded using FTIR Bruker spectrometer. A self-supported pellet was placed in an IR cell with CaF_2 windows; the activation was done in situ in oxygen flow from 298 K up to 673 K, and the sample was held at 673K for 4 h. Subsequently, the sample was evacuated in vacuum (10^{-3} Pa) during 2 h. The adsorption of H_2O was done after cooling up to room temperature and the collections of 100 scans spectra at 2 cm^{-1} resolution were recorded.

Results and Discussions

Acidity of Zeolites

The adsorption of nitrogen containing bases, such as ammonia, is widely used for the analysis of acidity of solid surfaces. In this case, the binding energy N1s of the nitrogen atom is a function of its neighborhood. When the base reacts with a Brønsted site to form a cation (ammonium), the value of BE (N1s) is generally between 401.5 and 402.8 eV. When it forms a complex with a Lewis site, BE is in the 399-401.5 eV range depending on the base chosen and the resulting charge transfer which is related to the acid strength of the site. Of course, given the natural width of XPS peaks, the experimental signal corresponds to a more or less asymmetrical band that needs to undergo deconvolution.

Together with ZSM-5 zeolites, dealuminated HY (ultra-stable Y or USY) are the most widely used in petrochemistry (FCC processes). The active centers are Brønsted acid sites carried by the zeolites framework. USY comes from synthetic Y faujasites dealuminated by chemical or, more commonly, hydrothermal treatments. These treatments partially remove aluminium from the crystal framework, improving their thermal stability, decreasing the number of Brønsted sites that is a function of the concentration of Al atoms, but generating extra-framework aluminium and framework defects which generally are associated to Lewis acidity. The Lewis sites may have their own catalytic activity and also may interact with Brønsted sites, increasing their strength [14,15].

The effect of the dealumination can be observed in a series of commercial Y faujasites LZ-Y62, (Si/Al atomic ratio equal to 2.6), CBV712 (Si/Al = 5.8), CBV720 (Si/Al = 12.8), CBV760 (Si/Al = 24). The modification of the acidity resulting from the dealumination is illustrated by the curves of the heat of ammonia adsorption (Figure 1).

The initial heats, in the range of 180-230 kJ.mol⁻¹, correspond to particularly strong sites. With the exception of the most dealuminated zeolite, the curves present a quasi plateau around 140 kJ.mol⁻¹, then they decrease to about 70 kJ.mol⁻¹, a value often considered as the chemisorption - physisorption limit for ammonia. These curves evidence the existence of three populations of sites: the strong sites (Q above 150 kJ.mol⁻¹), the medium (Q between 150 and 120 kJ.mol⁻¹) and the weak acid sites (Q between 70 and 120 kJ.mol⁻¹). In terms of relative site population, the two most dealuminated zeolites present fewer weak sites (between 25 and 35%) than the two others zeolites (about 50%), but a higher number of very strong sites (30% and 15% respectively).

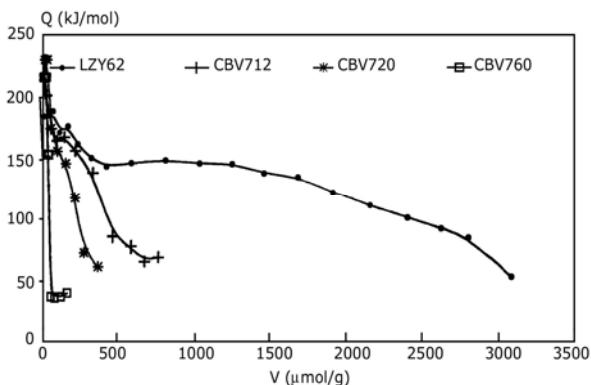


Fig. 1. Differential heats of ammonia adsorption vs. coverage for HY zeolites.

This information on strength distribution must be completed by the determination of the nature of the acid sites. It is possible to study by XPS the ammonia adsorption as a function of the NH_3 volume sent over the zeolite. Figure 2 reports the example of LZ-Y62. The Brönsted/Lewis ratio observed by XPS depends on the amount of adsorbed ammonia. The first dose of base (0.35 mmol g^{-1}) reacts with about half of the Lewis sites which correspond thus to the strongest sites. Afterwards, the adsorption mainly occurs over the Brönsted sites until the fourth dose (1.4 mmol g^{-1}). Figure 2 highlights that the strong and the weak acidity is due in a large part to Lewis sites and the intermediate acidity to Brönsted sites [14].

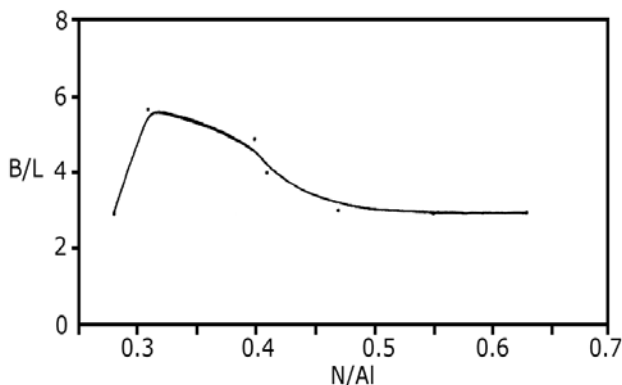


Fig. 2. Brönsted/Lewis ratio (XPS) vs NH_3 adsorbed amount at 393K on LZ-Y62.

Acidity of supported oxides ($\text{TiO}_2/\text{SiO}_2$)

Highly dispersed titania supported on silica is a material of great interest either as a catalyst [16,17] or as a support for active species [16,18]. Atomic layer deposition (ALD) was applied to prepare highly dispersed titania/silica support materials by chemisorption of volatilized titanium(IV) isopropoxide on silica followed by an oxygen treatment. In the present study, ALD technique was applied to modify silica sur-

faces with increasing amounts of highly dispersed titania. The ultimate goal of the study was to prepare high performance titania/silica support materials for metal oxides with interesting surface properties. Firstly, the suitability of a wide reaction temperature range for the isopropoxide precursor was investigated by elemental analyses and inert diffuse reflectance infrared spectroscopy (DRIFTS) measurements. Secondly, in order to achieve a titania monolayer coverage, the deposited amounts were increased by applying several consecutive precursor – oxygen cycles. The texture and dispersion of the TiO₂/SiO₂ samples were examined in detail as a function of the number of ALD reaction cycles by BET surface area/porosity measurements, X-ray diffraction (XRD), and UV-Vis diffuse reflectance (DRS) and X-ray photoelectron spectroscopies (XPS).

Table 1. Physico-chemical properties of TiO₂/SiO₂ samples, bulk silica and titania.

Sample	Titanium amount		N ₂ adsorption		
	(wt-%)	(atoms/ nm ² _{support})	S _{BET} (m ² /g)	Pore volume (cm ³ /g)	Pore diameter (Å)
SiO ₂	-	-	301	1.20	195
TiO ₂	-	-	101	0.35	95
1TiSi	2.7	1.2	323	1.25	210
3TiSi	6.5	3.1	305	1.15	205
5TiSi	10.2	5.1	297	1.05	200
7TiSi	13.1	7.0	284	0.95	190

The acidity of these materials was examined by microcalorimetry and XPS of ammonia adsorption at 353 K, and the basicity using SO₂ at the same temperature. The calorimetry results are presented in Figure 3, which displays the differential heats of NH₃ and SO₂ as a function of coverage. Besides, Figure 4 shows the relative contributions of acid sites (Lewis and Bronsted) together with the surface atomic ratio N/Ti, as calculated from XPS spectra.

Figure 3 shows that the acidity of the TiO₂/SiO₂ samples as given by the differential heats of NH₃ adsorption increases gradually with the amount of titania. The deposition of TiO₂ by ALD created strong surface acid sites (120<Q<150 kJ/mol) through the forming of strong Ti-O-Si bonding, even at low titania coverage (1.2-3.2 atoms Ti/nm²). The increasing of silica coating by titania until the monolayer was achieved (~ 5.1 atom Ti/nm²) resulted in weak and medium acid strength sites (40<Q<120 kJ/mol). We can observe that after three ALD cycles of deposition, a good coating of silica was already achieved. Similarly, the basicity of the samples increased gradually with the amount of Ti deposited on the surface; however, it did not reach that of pure TiO₂.

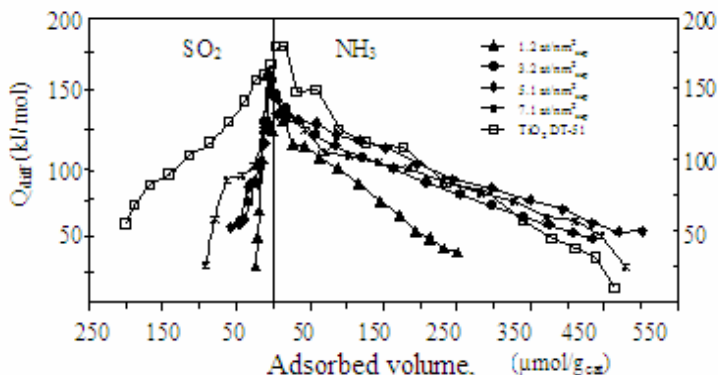


Fig. 3. Differential heats of adsorption of NH₃ et SO₂ as a function of coverage on TiO₂ and TiO₂/SiO₂ samples prepared by ALD.

The XPS data of ammonia adsorption (Figure 4) confirmed the good dispersion of superficial species of titanium at a sub-mono or monolayer. A relative increase of the Lewis acid sites (linearly from 65 to 80%) as a function of Ti coverage was also observed.

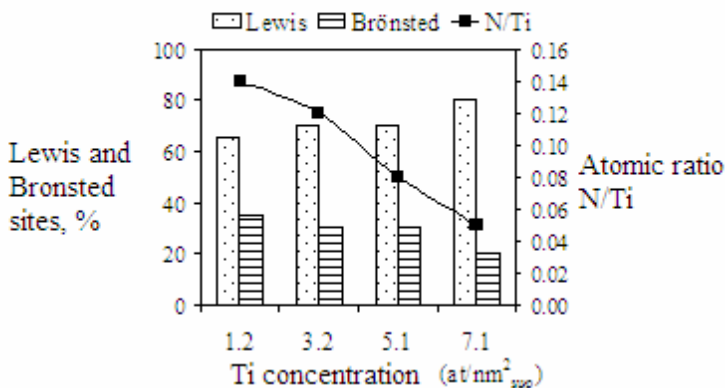


Fig. 4. Relative amounts of acid sites components (B and L) and N/Ti surface atomic ratios of samples TiO₂/SiO₂.

Figure 5 shows that TiO₂/SiO₂ samples present very similar ammonia adsorption uptakes, obtained by calorimetry and XPS, which confirms the homogeneous distribution and broad dispersion of titania species in these materials. On this figure, the bell shape curve shows a maximum for the monolayer coverage (5.1 atoms Ti/nm²). Above this value, the decreasing illustrates a lower dispersion and the formation of small TiO₂ crystallites.

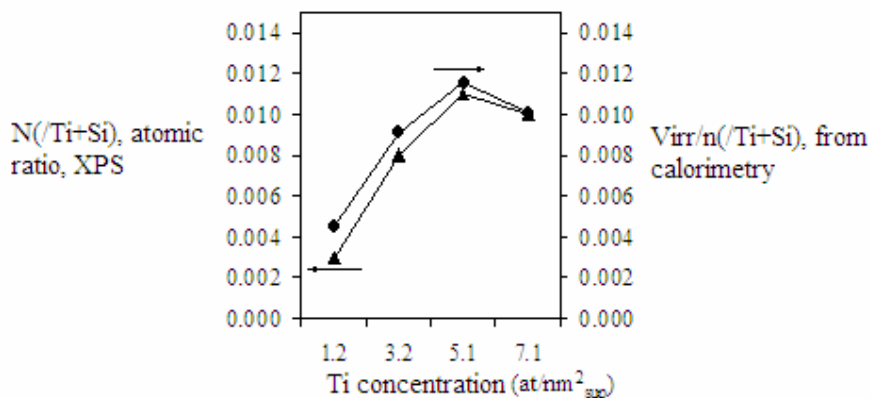


Fig. 5. Comparison of the acidity of medium and strong sites, as determined by microcalorimetry and XPS of ammonia adsorption.

Hydrophilic/hydrophobic character (Ga_2O_3/ZrO_2)

Zirconia supported gallia samples were prepared by wet impregnation of ZrO_2 using gallium nitrate. The samples were fully characterized by various physico-chemical techniques, including calorimetry and FTIR [19]. Among the various properties studied, we focused on the estimation of their hydrophilic/hydrophobic character. Table 2 presents the amount of water adsorbed by pure zirconia, pure gallia and on the sample Ga12-Zr which has 12.7 % wt of Ga_2O_3 (close to the monolayer).

Table 2. Amount of total and irreversibly adsorbed water on Ga_2O_3/ZrO_2 samples under an equilibrium pressure of 27 Pa, and the corresponding integral heat.

Sample	$V_{total}/\mu\text{mol.m}^{-2}$	$V_{irreversible}/\mu\text{mol.m}^{-2}$	$Q_{integral}/\text{J.m}^{-2}$
ZrO_2	4.33	1.96	0.53
Ga12-Zr	3.86	1.85	0.34
Ga_2O_3	3.68	2.38	0.36

Figure 6 represents the differential heats of water adsorption vs coverage at 353 K on the investigated samples. The deposition of Ga_2O_3 on zirconia decreased considerably the strength of water interaction with the surface.

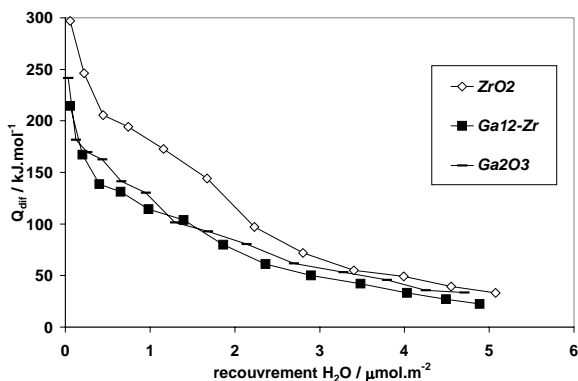


Fig. 6. Differential heats of water adsorption at 353 K vs. coverage.

The IR spectra of water adsorption at 298 K and successive desorption at 298 K, 373 K, 473 K, 573 K and 673 K on ZrO_2 and Ga12-Zr evidenced higher hydrophobicity of the gallia surface. Molecular water (band at 1625 cm^{-1}) which can be observed until 573 K on the surface of the support can be removed at 373 K from $\text{Ga}_2\text{O}_3/\text{ZrO}_2$.

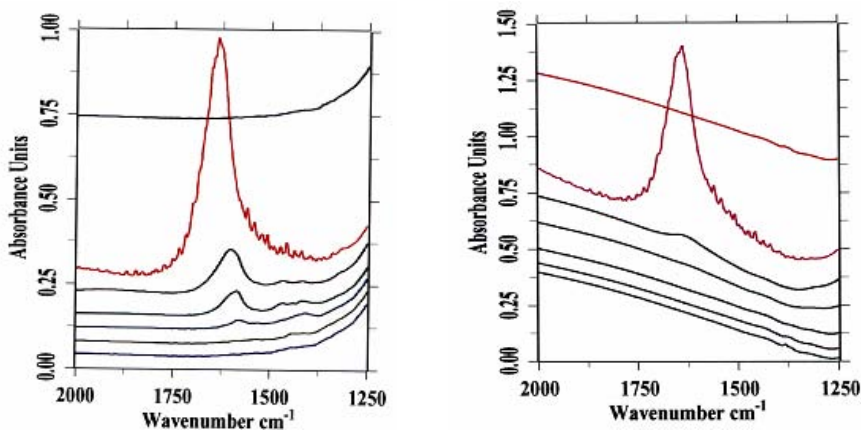


Fig. 7. FTIR spectra of water adsorption at 298 K and desorption at 298 K, 373 K, 473 K, 573 K and 673 K on zirconia (left) and Ga12-Zr (right).

References

- [1] N. Cardona-Martinez, J. A. Dumesic, *Adv. Catal.*, 1992, **38**, 149.
- [2] A. Auroux, *Physical Techniques for Solid Materials*, B. Imelik, J. C. Vedrine, (Eds), Plenum Press, New York, 1994, 611.
- [3] W. E. Farneth, R. J. Gorte, *Chem. Res.*, 1995, **95**, 615.
- [4] A. Auroux, *Top. Catal.*, 1997, **4**, 71 and 2002, **19**, 205.
- [5] P.J. Andersen, H. H. Kung, *Catalysis*, 1995, **11**, 441.
- [6] V. Solinas, I. Ferino, *Catal. Today*, 1998, **41**, 179.
- [7] H. G. Karge, *Catalysis and Adsorption by Zeolites*, Ohlmann (Ed), Elsevier, Amsterdam, 1991, 133.
- [8] D. B. Akolekar, V. R. Choudhary, *J. Catal.*, 1987, **105**, 416.
- [9] S. L. Soled, G. B. Mc Vicker, L. L. Murrell, L. G. Sherman, N. C. Dispenziere Jr, S. L. Hsu, D. Waldman, *J. Catal.*, 1988, **111**, 286.
- [10] A. Corna, *Chem. Rev.*, 1995, **95**, 559.
- [11] L. M. Kustov, *Top Catal.*, 1997, **4**, 131.
- [12] G. Busca, *Catal. Today*, 1998, **41**, 191.
- [13] J. H. Scofield, *J. Elect. Spectrosc. Relat. Phenom.*, 1976, **8**, 129.
- [14] C. Guimon, H. Martinez, *Recent Res. Devel. Catalysis*, 2003, **2**, 81.
- [15] Y. Yong, V. Gruver, J. J. Fripiat, *J. Catal.*, 1994, **150**, 421.
- [16] X. Gao, I. Wachs, *Catal. Today*, 1999, **51**, 233.
- [17] J. Keranen, E. Iiskola, C. Guimon, A. Auroux, L. Niinisto, *Stud. Surf. Sci. Catal.* 2002, **143**, 777.
- [18] J. Keranen, C. Guimon, E. Iiskola, A. Auroux, L. Niinisto, *Catal. Today*, 2003, **78**, 149.
- [19] A. L. Petre, A. Auroux, A. Gervasini, M. Caldararu, N.I. Ionescu, *J. Therm. Anal. Cal.* 2001, **64**, 253.

SIMPLE MOLECULES ON ACCEPTOR CENTERS OF ZEOLITES: QUANTUM CHEMICAL SIMULATION

N. F. Stepanov, A. A. Kubasov, and Ya. V. Tikhii

Faculty of Chemistry, Moscow State University, Moscow 119899, Russia

Abstract

The results of the nonempirical quantum chemical calculations provide the ground for understanding the basic and specific features of adsorption complexes formed by model zeolite structure fragments which include aluminum atom as an active center and one or several molecules of water, ammonia, carbon oxide, ethylene, and methanol

Introduction

Studies of the molecular system behavior in their interactions with clusters (associates) of other molecules were actively developing for the last years. Such systems can include simple molecules interacting with oligomers of the other similarly simple molecules or comprise the rather complicated systems the structure of which is now an object of the supramolecular chemistry. The important problem of these studies is the search and understanding of the regularities which govern the system formation, i. e. lead to the preferable formation of comparatively small number of stable structures which successfully gain the competition with other structures approximately equivalent in energy. The most important applied fields of these studies belong to the molecular biology and to the heterogeneous catalysis where the active centers providing the chemical transformations can often be simulated by a surface of a small rigid cluster cut out of solid state body.

Two problems should be solved for such catalytic systems, the simulation of initial fragment with the corresponding active center and analysis of the interactions of some other molecule (or molecules) with the active center. For the last several years we have studied complexes of some simple molecules (e. g. ozone and nitrogen dioxide) with water clusters composed of 2 to 100 water molecules and complexes of water, ammonia, methanol, and other molecules with zeolite structure fragments, i. e. fragments of catalysts which are widely used in technology. The structures of zeolites are rather diverse. Nevertheless, all of them are characterized by highly developed ordering and self-organization. We have believed that in studying the active centers of catalytic transformations on zeolites we should start with complexes of molecules with fragments, which do not contain many atoms and on the other hand can be considered as incorporating the active centers. The results of quantum chemical consideration of such complexes are presented in the lecture.

Till now the attention was mainly paid to protonic acid centers in studying deca-tionized zeolites. The acceptor centers, formed by some zeolite structure defects at the thermal catalyst activation and complexes produced at the interaction of molecules with these centers were investigated to much lesser degree. What is more, the opinion

that such centers do not manifest any activity and are not noteworthy was widespread. This opinion was in contradiction to the experimental results obtained in 60-ies, which evidence the influence of these centers on the zeolite catalytic activity. The necessity to understand the role plaid by such centers turned us to the systematic quantum chemical consideration of molecular models of the complexes arising at interactions of simple molecules with acceptor centers and to the simulation of active centers themselves as a natural first step (see e.g. [1-3]).

Calculation Techniques and Active Center Models

Quantum chemical calculations proceeded with the following techniques: semiempirical approach PM3 (program package MOPAC93), restricted Hartree – Fock approach, second order Møller – Plesset perturbation theory (MP2 and LMP2, PC GAMESS), and density functional theory with the nonlocal functional BLYP and hybrid functional B3LYP (program package JAGUAR). The majority of problems were considered using the BLYP functional which provided an optimal ratio of accuracy and efficiency. Semiempirical approach was only applied in preliminary test calculations. The other nonempirical techniques were used to check the reliability of the results obtained in BLYP approximation. The basis set was of 6-31G** quality, the proton detachment energy was calculated with the 6-31++G** basis set. The selection of basis sets was done after preliminary tests of several possible basis sets. All calculations except for the proton detachment energy were carried out with the complete geometry optimization of the nuclear subsystem.

The acceptor center models included an aluminum atom, coordinated by three oxygen atoms in cyclic fragments of the zeolite framework. These fragments which included also from 2 to 7 silicon atoms were denoted as 3Z – 8Z. Their remarkable feature is the combination of small sizes and structural rigidity which should be assured for the solid body fragments. The preliminary analysis showed that the fragment 3Z is sufficient for the consideration of single molecule binding by the fragment though the fragment 8Z is in need for more complicated systems. Both fragments are actually the zeolite regular structure fragments: fragment 3Z is in the structure of ZSM-18 and fragment 8Z is in the structure of faujasite. The fragments 3Z and 8Z as well as corresponding structural types MEI and FAU are shown in Fig. 1.

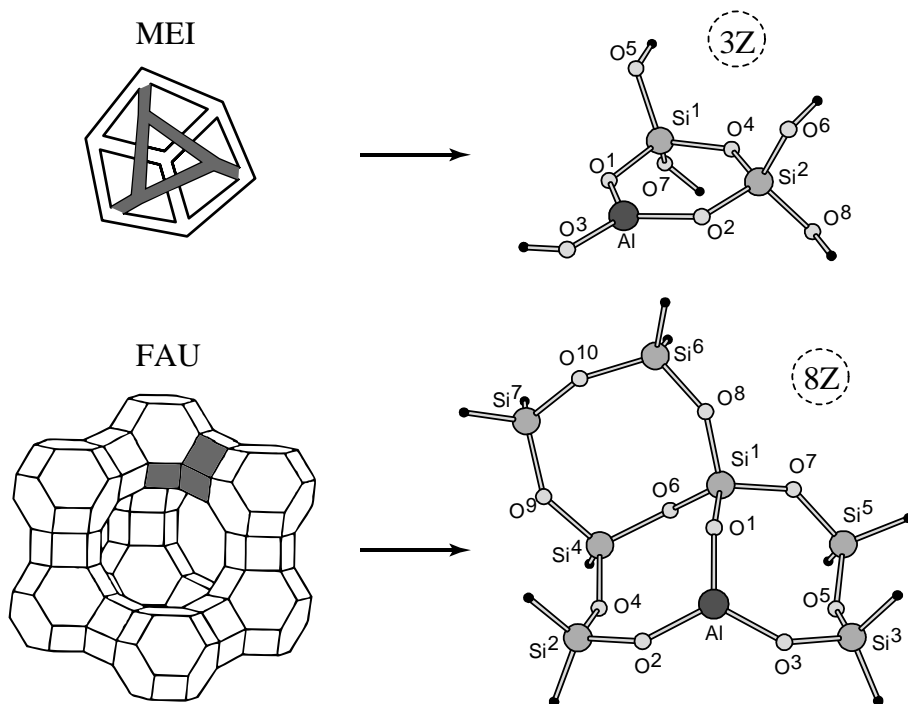


Fig. 1. Fragments 3Z and 8Z of the zeolite structures.

One should note that the models of acceptor centers and centers with single adsorbed molecules were earlier considered in the literature which opened the possibility to compare our results with the literature ones in order to gain some additional evidence of reliability of results obtained.

Results and Discussion

A single adsorbed molecule. The calculation results agreed quantitatively with the experimental literature data for all systems that included only one adsorbed molecule and the zeolite fragment. For the carbon oxide molecule, widely used as a probe for acid center detection with the help of IR spectroscopy, the heat of adsorption (50 – 60 kJ/mole) and blue shift of the IR band are reproduced with a confidence. The essential transfer of the electron density from the CO molecule to an acceptor center is also in correspondence with the conclusion made on the basis of experimental results. The complex formation by CO molecule and active catalytic center is achieved through the Al...C coordination (not through Al...O bonding) which is also in accord with the experimental conclusions.

The ammonia coordination by the acceptor center entails an increase of its proton donor ability. The ammonia dissociation on the Al–O pair of the acceptor center leads to the formation of stronger protonic center than on ammonia coordination. Nevertheless the coordination with the following dissociation is energetically less efficient (by 130 kJ/mole) than the energy gain at coordination only (161 – 162 kJ/mole). Calculation results reproduce well the experimental value of coordination (adsorption) energy and the blue shift of the frequency of ammonia δ_s vibrations (140 – 160 cm^{-1}).

The ethylene molecule prefers to form a stable π -complex with the acceptor center, in this state proton splits off easier than in free molecule. That means that the proton acidity of R–H type molecules is increased in the zeolite acceptor center field. Methanol molecule interacting with 3Z and 8Z fragments favors coordination not the dissociation. The influence of the acceptor center facilitates the proton detachment from the hydroxyl group. This group in the coordinated methanol demonstrates the features of proton donor center and approaches the bridge OH zeolite group in its strength. Methoxy group CH_3O of the methanol molecule is activated and approaches the bridge methoxy group in bond lengths, valence angles, and harmonic vibrational frequencies. Hence, the methanol interaction with zeolite acceptor centers can manifest itself in formation of surface compounds which are analogues to the systems with the bridge methoxy group in their reactivity.

The zeolite fragment transformations induced by adsorption touch mainly the AlO_3 group and in essentially lesser degree the atoms nearest to it. This notion supports the possibility of using local models for simulation of adsorption and catalytic processes on zeolites. The acceptor center gives also rise to strengthening of the proton donor ability in R–H molecules which explains the experimental data on the activity rising of zeolite catalysts absorbing small water amounts.

Two and three adsorbed molecules. The presence of several molecules that enter the influence area of the zeolite fragment leads to the appearance of ordered structures mainly of cyclic type with the chains of the adsorbed molecules. If there are two or three water molecules the proton of the molecule directly bonded to acceptor center demonstrates the features closely resembling the properties of hydrated proton. As a consequence the proton transfer from the coordination bonded water molecule to the other molecules can happen along the chain of H-bonds. This effect is very like to the mechanism of proton transfer in hydrated shell of amino acid molecules and some other compounds.

The acceptor center field action results in the ability of the bound one or two water molecules to protonate an ammonia molecule and give rise to stable complexes which include the bound ammonium ion (Fig. 2). This ion can serve as an attraction center for the other water and ammonia molecules. Other words, the adsorption with several water and ammonia molecules (instead of monomeric adsorption) is quite probable for the zeolite catalysts.

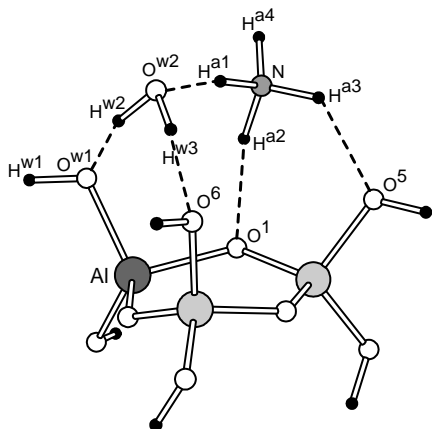


Fig. 2. The complex $3Z-2H_2O-NH_3$.

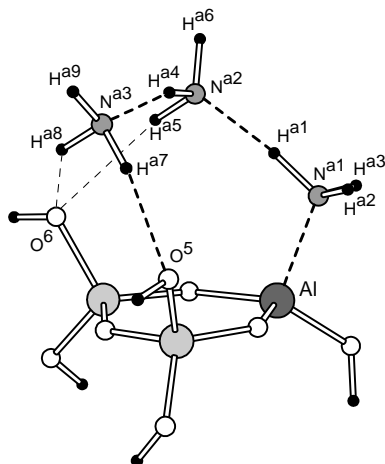


Fig. 3. The complex of the 3Z fragment with 3 ammonia molecules.

Complexes of the CO and C_2H_4 molecules with the coordinatively bound water molecule are very like in their characteristics to the complexes of these molecules with the zeolite hydroxyl group. The water molecule directly bound to the adsorption center is like to such group in its ability to proton donating.

The proton donor ability increases also for ammonia molecule directly bound to the acceptor center which reflects in comparatively high energetic stability of associates $(NH_3)_n$ at $n = 2$ and 3. The stepwise detachment of one ammonia molecule and then the second one from the complex $3Z-(NH_3)_3$ (Fig. 3) needs energy consumption of 36 and 71 kJ/mole as compared with the dissociation energy of the free ammonia dimer equal 17 kJ/mole. The coordinated ammonia molecule gets the ability to H-bonding formation with one or several water molecules, the situation which is quite unrealistic in the gas phase. It also binds carbon oxide and ethylene molecules though the strength of chemical bonds is not very high in these cases (~ 29 and 25 kJ/mole respectively) in contrast to the coordinated water molecule. The transfer of the influence of acceptor center along the self-organized chain is like to corresponding effects in enzymatic catalysis.

In a case of two methanol molecules (complexes with the Z8 fragment) the stepwise coordination is also more preferable. Though the second methanol molecule is not directly bound to the acceptor center its geometry and charge distribution parameters are markedly changing. Here the acceptor center plays the decisive role in ordering and strengthening the interaction between the molecules attached to the zeolite fragment though the interactions themselves with the acceptor center can not be strong.

The interaction of ammonia molecule with the bound methanol molecule in the adsorption complex does not lead to the proton transfer to the ammonia molecule in contrast to the analogues situation with the water molecule. In spite of this, the interaction

between the methanol and ammonia molecules in the complex is strong enough (~ 100 kJ/mole), the effect also related to the model fragment influence.

It seems to be reasonable to mention as an example the useful employment of the results obtained. The thermo programmed desorption (TPD) curves for ammonia demonstrate peaks in low-temperature region that are usually related to ammonia desorption from hypothetical weak adsorption centers existing on the zeolite surface. Our results show distinctly another reason of their appearance, i. e. the desorption of molecules produced in destruction of the associates such as $(\text{NH}_3)_n$ or $[\text{NH}_4^+ \cdot n\text{NH}_3]$.

There was also offered a mechanism of associate destruction under the water action followed by forcing out ammonia by water molecules in spite of higher ammonia adsorption energy for such centers. The forcing out of this type was observed experimentally when the zeolite species were treated with water vapor directly before the TPD experiments. As a result of the treatment, only one peak survives on the TPD curve which corresponds to ammonia desorption from the strong proton donor centers. The peaks in the low temperature region and the desorption peak of acceptor centers virtually disappear. The final product of this mechanism is the hydrated ammonium ion which as a rule, experimentalists refer to strong proton donor centers. The hydrated shell formed during this process provides the ammonia forcing out to be an energetically efficient process.

Conclusion

The acceptor zeolite center interacts not only with the adsorbed molecule directly bound to it, but its influence stretches along the relatively flexible chain of simple molecule self-organized during the adsorption. On the other hand, the local character of the simple molecule interaction with the acceptor center opens the possibility to apply a cluster approach to the quantum chemical simulations of the main features of catalytic transformations on the zeolite catalysts.

The second important result of the carried out study is as follows. The model of the adsorbed R-H molecule polarization under the defect active center influence in zeolites which was offered earlier on the basis of experimental catalytic investigations and the IR spectra of adsorbed molecules is substantiated by quantum chemical calculations. The molecules of this type can act as proton donor centers that are able to interact with hydrocarbon and alcohol molecules and provide the chemical transformations of them.

Literature

- [1] T. M. Domracheva, Yu. V. Novakovskaya, A. A. Kubasov, N. F. Stepanov, Russ. J. Phys. Chem., 1999, **73**, 1115.
- [2] Ya. V. Tikhii, A. A. Kubasov, N. F. Stepanov, Russ. J. Phys. Chem., 2003, **77**, 1455.
- [3] Ya. V. Tikhii, A. A. Kubasov, N. F. Stepanov, Int. J. Quantum Chem. 2005, **104**, 214.

CATALYTIC REACTION DYNAMICS CAUSED BY IONS MOBILITY IN SOLIDS

N.M. Ostrovskii

Chemical Industry HIPOL, 25250 Odžaci, Serbia

Introduction

The mobility of ions and atoms in solid catalysts is widely observed and can influence the catalytic reaction significantly. First of all, it concerns the mobility of oxygen ions in metal oxides. It happens when reagents oxidize or reduce the surface layer of the catalyst. The solid bulk tends “to lick its wound” by diffusion of oxygen ions from the bulk to surface (in reducing medium) or in opposite direction (in oxidizing medium). Certainly, oxygen mobility is marked only in oxides of variable level of metal oxidation (V, Cr, Mn, Fe, Mo, Ce) in contrast to Al_2O_3 or SiO_2 . For example, in propylene oxidation over bismuth molybdate catalyst, approximately 500 layers of oxide ions from the catalyst participate in product formation [1].

Similarly, the mobility of hydrogen in hydride catalysts or hydrogen storage alloys is known [2]. Finally, the diffusion of carbon in metal carbides (Fe, Ni) is considered as a key stage in catalytic formation of carbon nano-tubes [3].

Since ions diffusion in bulk is caused by reaction on the surface, it affects the state of surface, and consequently affects the reaction dynamics. Because the capacity of bulk is much higher than that of the surface, ions mobility increases the working period of the catalyst. It makes acceptable the non-stationary cyclic regime of the process with reaction and catalyst recovery periods. In oxidation processes such a regime provides usually higher selectivity than the stationary one.

Model of ions mobility (oxygen in oxides)

Let us define the “oxidation level” of catalyst (σ) as the ratio of oxygen concentration in crystalline lattice to its maximum value: $\sigma = [\text{O}] / [\text{O}]_{\text{max}}$. Then oxidation level of catalyst surface (σ_s) is determined by diffusion of oxygen ions in catalyst bulk, and by reduction of the surface. Thus, for (σ) and (σ_s) the diffusion model can be used [4-8]:

$$\frac{\partial \sigma}{\partial \tau} = \frac{1}{\Psi_L^2} \frac{\partial^2 \sigma}{\partial \xi^2}, \quad \Psi_L^2 = L^2 k_s / D_L, \quad (1)$$

with the initial [$t=0$: $\sigma(\xi) = \sigma_o$] and boundary conditions:

$$\underline{\xi=0}: \frac{d\sigma}{d\xi} = 0, \quad \underline{\xi=1}: \frac{d\sigma}{d\xi} = -\Psi_L^2 \sigma_s \varphi(\bar{\theta}, \bar{y}). \quad (2)$$

Ions diffusivity D_L , thickness of active component crystallites L , and rate constant of surface–bulk interaction k_s are main parameters that influence the level and dynamics of surface oxidability σ_s . The function $\varphi(\theta, y)$ represents the influence of reaction mixture on surface–bulk interaction.

Possible influence on reaction dynamics

The region in which the diffusion of oxygen in catalyst bulk affects the transient regime of catalytic reaction can be estimated by solving (1, 2) at $\varphi = 1$. It gives the left boundary (min Ψ_L): $1 - \cos \Psi_L < \varepsilon$ [4, 6]. At $\varepsilon < 0.1$, $\Psi_L < 0.5$.

More precise estimations were made in [8] using model reactions of partial oxidation $A + nO_2 = B$, having rate $r_p = k_p (b_o y_O)^{1/2} y_A \Theta_Z$. It was supposed that active sites Z can be reduced to inactive state Z_R :



Sites Z_R can be re-oxidized by oxygen from gas phase:



or by lattice oxygen from the bulk of catalyst:



Then in (2) $\varphi(\theta, y) = \Theta_R$, $\Theta_R = 1 - \Theta_Z / \Theta_Z^o$, and in gradientless reactor:

$$\frac{d\Theta_Z}{dt} = (k_s \sigma_s + k_o y_O) \Theta_R - k_r y_A^o (1 - X) \Theta_Z, \tag{3}$$

$$X = Da \Theta_Z / (1 + Da \Theta_Z), \quad Da = k_p (b_o y_O)^{1/2} \tau_r.$$

It is seen from Fig. 1, that there are two regions of Ψ_L in which the oxygen mobility does not affect the transient regime in catalyst crystallite. The first region is at $\Psi_L < 0.7$, where the oxygen mobility is faster in comparison to the rate of catalyst reduction. The second region is $\Psi_L > 7$, corresponding to low oxygen mobility. In other words, the region in which the diffusion of oxygen in solid catalyst affects the transient regime of catalytic reaction is $\Psi_L \in [0.7 \div 7]$.

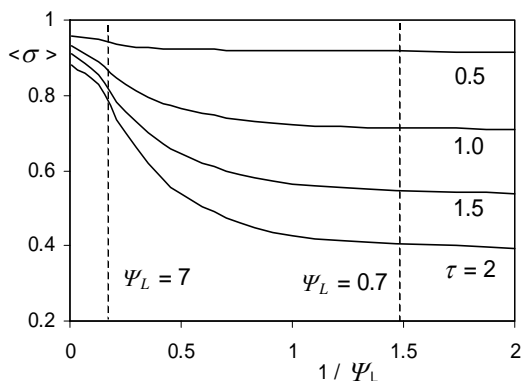


Fig. 1. Dependence of average catalyst oxidation level on crystallite Thiele modulus [8].
 At $L = 2 \div 30$ nm,
 $D_L = 10^{-17} \div 10^{-13}$ cm²/s.

Ions diffusion in bulk and reagents diffusion in pores

In order to examine this complex effect, a single first order reaction was considered: $r_p = k_p y_A^o (1-X) \sigma_s$. Equations (1, 2) were supplemented with diffusion equation in catalyst pellet having slab geometry [4, 6]:

$$\frac{d^2 X}{d\rho^2} = -\Psi_R^2 \sigma_s(\rho) (1-X), \quad \Psi_R^2 = R^2 k_p / D_R, \quad (4)$$

$$\underline{t=0}: \sigma_s^o(\rho) = 1, \quad \underline{\rho=0}: dX/d\rho = 0, \quad \underline{\rho=1}: X = 0.$$

The overall process in this case is characterized by four rates of reaction:

- $W_K^o = k_p y_A^o$ – initial rate in kinetic region,
- $W_K = k_p y_A^o \sigma_s(1)$ – current rate in kinetic region,
- $W_D^o = k_p y_A^o \int [1-X(\rho)] d\rho$ – initial rate in diffusion region,
- $W_D = k_p y_A^o \int \sigma_s(\rho) [1-X(\rho)] d\rho$ – current rate in diffusion region.

Consequently, four parameters of pellet effectivity are formulated [6]:

- $\eta_o = W_D^o / W_K^o = \int [1-X(\rho)] d\rho$ – initial effectiveness factor,
- $\eta = W_D / W_K = \int \sigma_s(\rho) [1-X(\rho)] d\rho / \sigma_s(1)$ – current effectiveness factor,
- $\chi = W_D / W_K^o = \eta \sigma_s(1)$ – overall pellet effectivity,
- $\langle \sigma_s \rangle = W_D / W_D^o = \chi / \eta_o$ – average oxidability (activity) of surface.

It was shown that pellet effectivity (χ) in kinetic region (low Ψ_R) is considerably affected by ions diffusion in catalyst bulk (Ψ_L). On the contrary, in diffusion region (high Ψ_R) pellet effectivity only slightly depends on ions diffusion (Fig. 2).

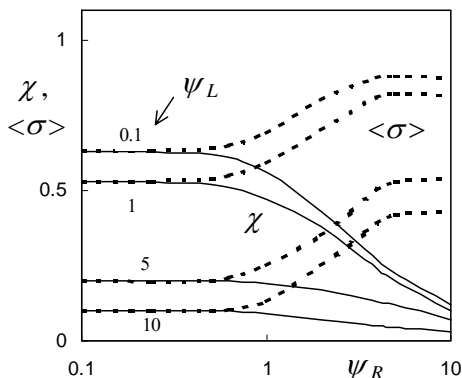


Fig. 2. Domains of influence of diffusions in catalyst bulk ($D_L = L^2 k_s / \Psi_L^2$) and in pores ($D_R = R^2 k_p / \Psi_R^2$) on the overall pellet effectivity (χ) and average pellet activity ($\langle \sigma \rangle$) [6].

Ions Diffusion in Bulk and Particles Diffusion in Fluidized Bed

Considered problem of ions diffusion in catalyst bulk takes on special significance in the case of fluidized bed reactor. First, a fluidized bed with internal or external circulation of catalyst is the most convenient option for cycle periodic regime of process. Second, due to the chaotic motion of particles in fluidized bed, they work in continuously changing conditions, i.e. in non-stationary regime.

The following model was derived [5, 6] for corresponding analysis:

$$\frac{\partial \sigma}{\partial z} = \frac{1}{Pe_k} \frac{\partial^2 \sigma}{\partial z^2} + \frac{\tau_k}{\Psi_L^2} \frac{\partial^2 \sigma}{\partial \xi^2}, \quad Pe_k = H u_k / D_k, \quad (5)$$

$$\frac{\partial x_A}{\partial z} = Nu (y_A - x_A), \quad Nu (y_A - x_A) = \tau_r k_p y_A \sigma_s(z), \quad (6)$$

$$\underline{z=0}: \frac{d\sigma}{dz} = Pe_k (\sigma - \sigma_o(\xi)), \quad \underline{z=1}: \frac{d\sigma}{dz} = 0. \quad (7)$$

$$\underline{\xi=0}: \frac{d\sigma}{d\xi} = 0, \quad \underline{\xi=1}: \frac{d\sigma}{d\xi} = -\Psi_L^2 \sigma_s y_A. \quad (8)$$

Eq. (5) represents oxidability profiles $\sigma(z, \xi)$ along the bed height (z) and crystallite depth (ξ), and Eqs. (6) represent reagent concentrations in bubble (x_A) and in dense (y_A) phases.

Analytical analysis and numerical calculations using this model confirmed the above estimations. The limiting value of Ψ_L was evaluated as $\Psi_L < (3\div 5)\varepsilon$. It means that in this case $D_L \leq L k_s y_A / (3\div 5)\varepsilon$.

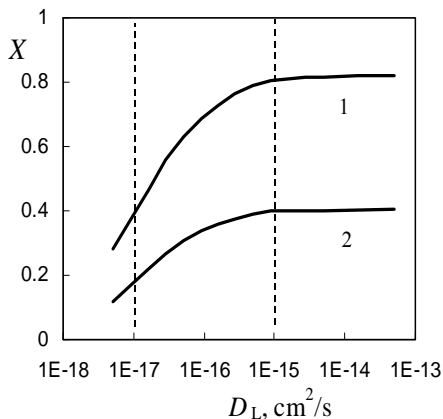


Fig. 3. Conversion vs. ions diffusivity [6].
 1 - $L = 4 \cdot 10^{-7}$ cm, $k_s y_A = 1 \cdot 10^{-9}$ cm/s;
 2 - $L = 2 \cdot 10^{-7}$ cm, $k_s y_A = 2 \cdot 10^{-9}$ cm/s.

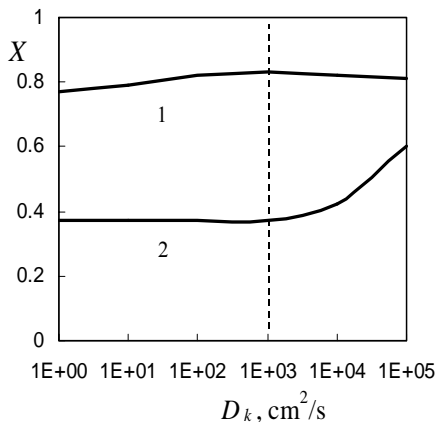


Fig. 4. Conversion vs. particles diffusivity [6].
 1 - $D_L = 5 \cdot 10^{-15}$ cm²/s, Nu = 6;
 2 - $D_L = 5 \cdot 10^{-17}$ cm²/s, Nu = 1.2.

The interval of ions diffusivity that affects total conversion in reactor (fig. 3) and average oxidability of catalyst (fig. 1) is practically the same $D_L = 10^{-17} \div 10^{-15} \text{ cm}^2/\text{s}$. This interval of diffusivity is characteristic for many oxides, such as V_2O_5 , CoO , CeO_2 , MoO_3 , Cr_2O_3 [8]. At relatively high ions mobility ($D_L \geq 10^{-15} \text{ cm}^2/\text{s}$) the intensity of particle diffusion in bed (D_k) do not affect the process effectivity (fig. 4, line 1). At lower mobility ($D_L \leq 10^{-17} \text{ cm}^2/\text{s}$), a good mixing of catalyst in bed ($D_k \geq 10^3 \text{ cm}^2/\text{s}$) is necessary (fig. 4, line 2).

Examples

Similarly to oxides, some chlorides are characterized by chlorine mobility [9]. In order to explain the dynamics of propylene polymerization on $\text{TiCl}_3 + \text{AlEt}_2\text{Cl}$, the model like (1, 2) was applied [7]. Fig. 5 indicates that the reaction rate dynamics ($R_p = k_p \sigma_s C_{\text{mon}}$) can be controlled by diffusion of chloride ions with interval of diffusivity $D_L = 4 \cdot (10^{-17} \div 10^{-15}) \text{ cm}^2/\text{s}$.

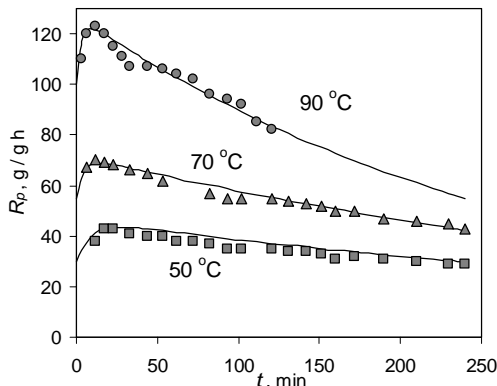


Fig. 5. Dynamics of propylene polymerization rate on catalyst $\text{TiCl}_3 + \text{AlEt}_2\text{Cl}$. Points – experiments of [10]; lines – model prediction [7]. At $L = 10 \text{ nm}$, $D_L = 4 \cdot 10^{-17} - 17 \text{ cm}^2/\text{s}$; at $L = 100 \text{ nm}$, $D_L = 4 \cdot 10^{-17} - 15 \text{ cm}^2/\text{s}$.

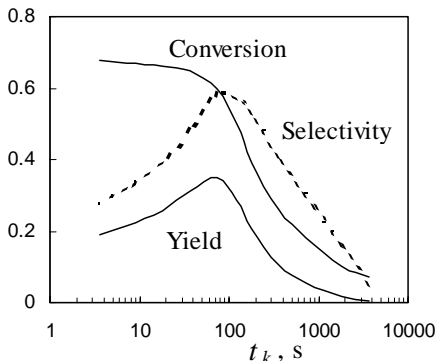


Fig. 6. Effect of catalyst residence time in oxidative dehydrogenation of C_4H_{10} [11].

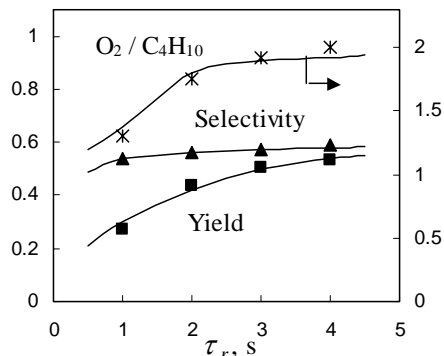


Fig. 7. Effect of feed contact time in oxidative dehydrogenation of C_4H_{10} [6].

Oxidative dehydrogenation of butane $C_4H_{10} + O_2 = C_4H_6 + 2H_2O$ is one of the processes in which oxygen mobility in Mg-Mo-oxide catalyst provides the increasing of selectivity in non-stationary regime. Selective dehydrogenation occurs by lattice oxygen in reaction zone of fluidized bed reactor, and catalyst re-oxidation takes place in regeneration zone.

The process selectivity is regulated by catalyst residence time, the optimum of which depends on capacity of bulk oxygen in the catalyst (fig. 6). Additional regulation of selectivity is carried out by ratio $\lambda = O_2/C_4H_{10}$ (fig. 7).

Nomenclature

$\sigma(\xi)$ – oxidability inside crystallite; σ_s – oxidability of crystallite surface;
 Ψ_L, Ψ_R – Thiele moduli; D_L, D_R, D_k – diffusion coefficients of ions in catalyst crystallite, reagents in pellet and catalyst particles in fluidized bed;
 L – half-thickness of catalyst crystallite; R – radius of pellet; H – height of bed;
 $\xi = l/L, \rho = r/R, z = h/H$ – dimensionless coordinates; k_p – reaction rate constant;
 k_s – rate constant of surface–bulk interaction; $\tau = k_s t$ – dimensionless time;
 τ_r – contact time in reactor; $\tau_k = k_s H/u_k$ – dimensionless catalyst residence time in reactor; u_k – catalyst velocity; b_o – adsorption equilibrium constant;
 X – conversion of reagent; y_A, y_O – molar fractions of A and O_2 ;
 Θ_Z, Θ_R – fraction of oxidized (Z) and reduced (Z_R) active sites;
 Da – Damkohler number; Pe – Peclet number; $Nu = \beta \tau_r$ – Nusselt number;
 β – mass transfer coefficient; $\langle \sigma \rangle = \int \sigma(t, \xi) d\xi$ – average level.

References

- [1] G.W. Keulks, Journal of Catalysis, 1970, **19**, 232.
- [2] V.M. Azambuja, D.S. dos Santos, J. of Alloys and Compounds, 2004, **383**, 219-223.
- [3] J.W. Snoeck, G.F. Froment, M. Fowles, Journal of Catalysis, 1997, **169**, 240-246.
- [4] N.M. Ostrovskii, In "Unsteady-state processes in chemical reactors", Novosibirsk, 1982, 167-170.
- [5] O.A. Mahotkin, N.M. Ostrovskii, Yu.I. Kuznetsov, M.G. Slin'ko, Dokl. AN SSSR, 1979, **249**, 403-406.
- [6] N.M. Ostrovskii, Catalyst deactivation kinetics, Moscow, Nauka, 2001, 334 p.
- [7] N.M. Ostrovskii, F. Kenig, Chem. Eng. Journ., 2005, **107**, 73-77.
- [8] N.M. Ostrovskii, S.I. Reshetnikov, Chem. Eng. Journ., 2005, **107**, 141-146.
- [9] E. Magni, G.A. Somorjai, Surface Science, 1996, **345**, 1-16.
- [10] K.Y. Choi, W.H. Ray, Journ. Appl. Polym. Sci., 1985, **30**, 1065-1081.
- [11] S.I. Reshetnikov, N.M. Ostrovskii, E.A. Ivanov, Theor. Found. Chem. Eng., 2002, **36**, 80-85.

NO_x SELECTIVE REDUCTION BY HYDROCARBONS IN THE EXCESS OF OXYGEN ON ZR-PILLARED CLAYS: MAIN FEATURES OF THE REACTION MECHANISM AND PERFORMANCE IN REALISTIC FEEDS

V. A. Sadykov¹, T. G. Kuznetsova¹, V. A. Matyshak², A. Ya. Rozovskii³,
V. V. Lunin⁴ and J. R. H. Ross⁵

¹Boreshov Institute of Catalysis SB RAS, pr. Lavrentieva, 5, Novosibirsk, 630090, Russia, sadykov@catalysis.ru; ²Semenov Institute of Chemical Physics RAS, Moscow, Russia; ³Topchiev Institute of Petrochemical Synthesis RAS, Moscow, Russia; ⁴Chemical Department of Lomonosov Moscow State University, Moscow, Russia; ⁵Limerick University, Limerick, Ireland

Abstract

The progress in design of efficient and stable catalysts for selective catalytic reduction of NO_x by hydrocarbons in the oxygen excess (NO_x HC-SCR) depends upon elucidation of the reaction mechanism as well as upon design of new nanostructured systems stable to action of water and sulfur dioxide in the exhausts. Zirconia-pillared clays (ZrPILC) loaded with Pt+Cu appear to meet demands of hydrothermal stability, sulfur tolerance and good low-temperature performance at high GHSV in realistic feeds [1-3]. This work overviews result of the mechanistic studies of NO_x propylene SCR for those systems by using combination of FTIRS *in situ* and unsteady-state (TPD/TPR, pulse titration, relaxation experiments) kinetics methods [3-6].

Experimental

Procedures for the catalysts preparation and detailed characterization of their structural, catalytic and adsorption properties are described elsewhere [1-3, 7-9].

The FTIR spectra *in situ* in the course of components adsorption, temperature programmed desorption and /or reaction were recorded in the transmission mode using a Perkin Elmer "Spectrum RX I FT-IR System" spectrometer in specially designed flow cell.

Results and Discussion

Mechanistic features. Nanosized zirconia pillars in ZrPILC are mainly comprised of isolated tetrameric Zr₄(OH)_n(H₂O)_m complexes, where Zr cations are strongly bound with terminal and bridging hydroxyls, while Lewis acid sites are absent. In contrary, the surface of bulk ZrO₂ contains basic on-top oxygen forms along with rather weak Lewis acid sites – coordinatively unsaturated Zr⁴⁺ cations. As a result, for nano-zirconia, activation of propylene on acidic hydroxyls easily proceeds at ~150 °C giving in the presence of O₂ or NO + O₂ isopropoxide species along with coordinatively bound acetone. Bridging and bidentate nitrates located on those nanoparticles appear to increase acidity of hydroxyls, thus accelerating activation of propylene and increasing the surface coverage by selective oxidation products.

For bulk ZrO_2 , activation of hydrocarbons proceeds with participation of Lewis acid sites which requires higher (~ 250 °C) temperatures yielding in the presence of O_2 acetate species. Nitrates are not directly involved in activation of propylene or other hydrocarbons. Monodentate nitrates observed only for bulk ZrO_2 interact with acetate species yielding nitromethane-like intermediate further transformed into SCR products by interaction with nitrates or NO_2 . For nano-zirconia, more efficient low-temperature route includes interaction of isopropoxide with bridging nitrates forming (di)nitropropane-like species, which are either thermally decomposed into NH_3 and acetate species or interact nitrates yielding reaction products via sequence of fast acid-catalyzed steps.

Different structure of bulk ZrO_2 and Zr_4 tetrameric species is reflected also in different local coordination and reactivity of supported Cu (Cu+Pt) active components. For bulk ZrO_2 , clusters of Cu^{2+} cations appear even at a low loading. Terminal oxygen forms bound with these cations are very reactive easily combusting hydrocarbons even at moderate temperatures, which is further accelerated by supporting Pt. As the result, maximum NO_x conversion for Cu/(Cu+Pt)-supported bulk zirconia is low due to domination of combustion route.

Supported Cu cations and Pt strongly interact with the bridging hydroxyls on nanosized zirconia pillars and with each other which ensures their rather low oxidizing ability preventing undesirable combustion of hydrocarbons. They do not participate in activation of propylene so its activation proceeds on acid sites yielding isopropoxides. Loading of nano-zirconia with Pt+ CuO_x increases the rate of NO transformation onto nitrate complexes as well as their coverage and reactivity, while decreases their bonding strength, which suggests their location on Cu and Pt cations. The surface coverage by C,N,O-containing intermediates at ~ 200 °C is increased due to Pt+Cu supporting, thus ensuring a higher performance in SCR. Pt+ CuO_x facilitate deep oxidation of oxygenates and make possible a high-temperature route via the acetate-nitromethane sequence. This ensures a high performance of these catalysts in a broad temperature range.

For all studied systems, the rates of nitrates and nitroorganic species transformation under $NO + O_2$ action and their activation energies are close to those of the overall SCR reaction thus confirming their role as key intermediates. Pulse titration experiments revealed that N_2 along with the admixture ($\sim 10\%$) of N_2O are formed through reactions of strongly bound intermediates with $NO+O_2$ or nitrates, a share of direct NO decomposition route even on reduced Pt+Cu-promoted nanozirconia surface covered by oxygenates being negligible.

Catalytic performance. For both reductants-propylene and decane, the increase of O_2 and H_2O content in the feed improves performance of Pt+Cu/ZrPILC. For feeds with a high O_2 and H_2O content, both pre-sulfation of catalysts and addition of SO_2 (up to 300 ppm) to the feed increase both decane and NO_x conversion, which is rather unique feature for NO_x HC SCR catalysts. Next factors could be responsible for this specificity:

- 1) Weakening of key intermediates - nitrate complexes bonding with the surface due to sulfation and hydroxylation which increases their reactivity.

- 2) Sulfation of pillars increases acidity of bridging hydroxyls, and, hence, enhancing the rate of propylene activation. For decane, combined effect of Pt and acid hydroxyls facilitates its cracking and dehydrogenation thus producing reactive olefins easily converted further into oxygenates.
- 3) Suppression of coking/oligomers accumulation.
- 4) A developed supermicroporosity along with a high share of mesopores formed due to defects in clay sheets stacking allows a free access of bulky decane molecules and their easy migration within pillared clays galleries. At low (~ 150 °C) temperatures, condensation of decane films on the hydrophobic surfaces of clay sheets might favor interaction between dissolved olefins and NO_2 forming C,N,O-containing species transformed on Pt+Cu-loaded pillars.

All these factors allow to achieve in realistic feeds with a high content of oxygen, water and admixture of SO_2 up to 50% of NO_x conversion into N_2 already at ~ 150 °C and GHSV $\sim 90,000/\text{h}$ without any N_2O formation. In the same conditions, Pt/ Al_2O_3 catalyst converts less than 20% of NO with N_2O selectivity up to 50%. Similarly, in those feeds, Pt+Cu/ bulk mesoporous zirconia catalyst is much less active in NO_x selective reduction by propylene or decane. Hence, a high performance of Zr-PILC-based catalysts appears to stem from the specificity of zirconia nanopillars structure.

Conclusions

A specificity of the NO_x C_3H_6 SCR reaction mechanism on Zr-PILC based catalysts revealed by spectrokinetic method is associated with the ability of acidic hydroxyls bound with nanosized zirconia pillars to activate propylene into isopropoxide, which is further transferred into dinitropane intermediate by interaction with strongly bound nitrate species. Loading of Pt+Cu mixed clusters on pillars accelerates the rate of nitrates accumulation and transformation of intermediates via red-ox stages. Participation of strongly bound intermediates in key stages of reaction mechanism and acid-catalysed HC activation route are main factors ensuring a high performance of Pt+Cu/ZrPILC in C_3H_6 or $\text{C}_{10}\text{H}_{22}$ NO_x SCR in realistic feeds with a high content of O_2 , H_2O and SO_2 .

References

- [1] V. Sadykov, T. Kuznetsova, et al., Topics in Catalysis, 2005, **32**, 29-38.
- [2] V. Sadykov, T. Kuznetsova, et al., Chem. Sustain. Developm., 2003, **11**, 249.
- [3] V. Sadykov, T. Kuznetsova, et al., Catal. Today, 2006, 114, 13.
- [4] V. Sadykov, V. Lunin, V. Matyshak, et al., Kinetika i Kataliz, 2003, **44**, 412.
- [5] V. Matyshak, O. Krylov, Catal. Today, 1995, **25**, 1.
- [6] S.A. Beloshapkin, E.A. Paukshtis, V.A. Sadykov et al., J. Molec. Catal. A: Chem., 2000, **158**, 355.
- [7] D. Efremov, T. Kuznetsova, V. Sadykov, J. Phys. Chem., 2005, **B 109**, 7451.
- [8] V.A. Sadykov et al., J. Catal., 2001, 200, 117, 131.
- [9] V.A. Sadykov, V. I. Zaikovskii, et al., Mater. Res. Soc. Symp. Proc. 878E (2005) Y4.8.

COMPUTATIONAL INVESTIGATION OF A NUCLEOPHILIC ADDITION REACTION

S. Marković¹, D. Milenković¹ and Z. Marković²

¹*Faculty of Science, University of Kragujevac, Serbia*

²*Faculty of Agronomy, University of Kragujevac, Serbia*

Abstract

All reaction paths for the nucleophilic addition of enolate anion of ethyl acetate to ethyl acetate are constructed and corresponding activation energies are calculated. There is exponential correlation between energy barrier and HOMO-LUMO gap of the reactants. Conformations and mutual positions of the reactants in energetically favorable reaction paths are determined.

Introduction

This work deals with the reaction of nucleophilic addition of enolate anion of ethyl acetate to ethyl acetate (a phase of the Claisen condensation) [1].

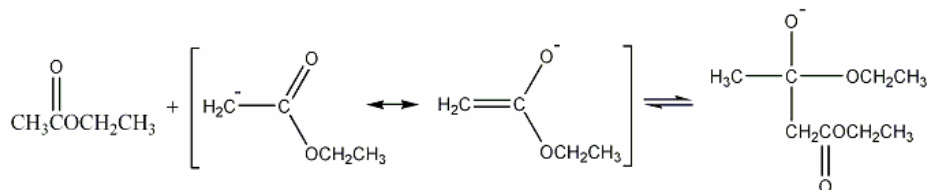


Fig. 1. Reaction scheme for nucleophilic addition of enolate anion of ethyl acetate to ethyl acetate.

It will be shown later that the addition of enolate anion of ethyl acetate to ethyl acetate can conform various reaction paths, depending on the reactants conformations and their mutual positions. Each of these paths requires different energy barrier.

This reaction involves movement of electrons from the anion (electron donor) to the ester molecule (electron acceptor). This electron movement can be considered as electron movement from the HOMO of the anion to the LUMO of the ester molecule [2]. Following this consideration an assumption can be put forward according to which activation energies of different reaction paths will depend on HOMO-LUMO gaps of corresponding reactants. It is reasonable to expect that the fastest reaction path should involve the reactants combination that has the smallest HOMO-LUMO energy gap.

The goal of this work is to confirm or negate the assumption given above, and to determine which combination of reactants requires the lowest energy barrier.

Results and Discussion

Both molecule and enolate anion of ethyl acetate exist in 4 stable conformations. These conformations will be denoted M_x , $x=1-4$, and A_y , $y=1-4$, where M and A stand for conformations of ester molecule and anion, respectively. This implies that there are

16 combinations of the reactants conformations, i.e. 16 reaction paths for addition of enolate anion to ethyl acetate. These paths are denoted M_xA_y . If an arbitrary M_xA_y is inspected it can be concluded that the reactants can take different positions to each other. This implies that this M_xA_y further branches, thus increasing the number of possible reaction paths. In order not to miss any of numerous paths, Newman projections are used to construct different positions of reactants within a certain combination of reactants conformations. This is illustrated with Fig. 2.

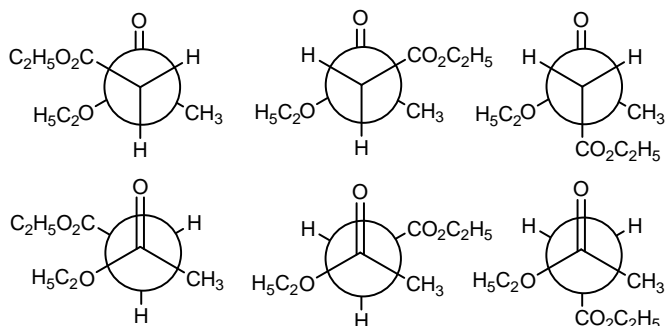


Fig. 2. Newman projections of mutual positions between the ester molecule M_1 and anion A_2 . Note that a projection represents conformations of two separate species, and the front and back carbons are not bonded.

It can be shown that there are in total 108 structures of the reactants in the reaction considered. In other words there are 108 reaction paths that need to be examined. Taking into account the scope of the task and corresponding computational effort, HF/3-21G* is selected for the calculations. It is expected that this level of theory will provide preliminary results that will serve as input for the calculations at higher level of theory.

By means of the program package Gaussian 98 [3], the geometries of activated complexes and activated intermediates are optimized. 16 reaction paths are selected,

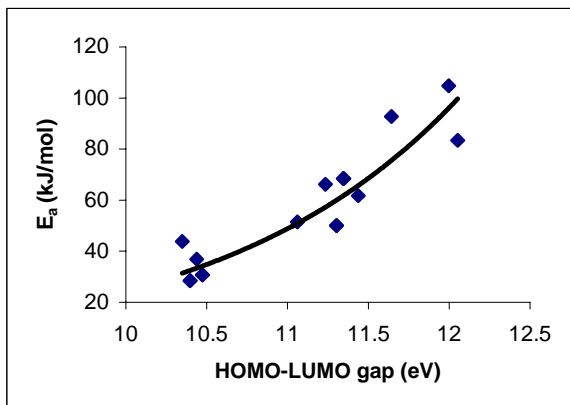


Fig. 3. Activation energy of investigated reaction versus HOMO-LUMO gap.

each of them exhibiting the lowest activation energy within its group of reaction paths. Fig. 3 represents the plot of activation energies versus HOMO-LUMO gaps for these reaction paths. There is exponential correlation between these two quantities, with the correlation coefficient of 0.93.

By inspecting activation energies of different reaction paths, one can conclude that M_1A_4 , M_2A_3 (28.5 kJ/mol),

and M_2A_1 , M_4A_2 (30.7 kJ/mol) are energetically most favorable. Most unfavorable paths are M_3A_3 (104.7 kJ/mol) and M_3A_4 (101.0 kJ/mol). Optimized geometries for the activated intermediate and activated complex for the M_1A_4 reaction path are given in Fig. 4.

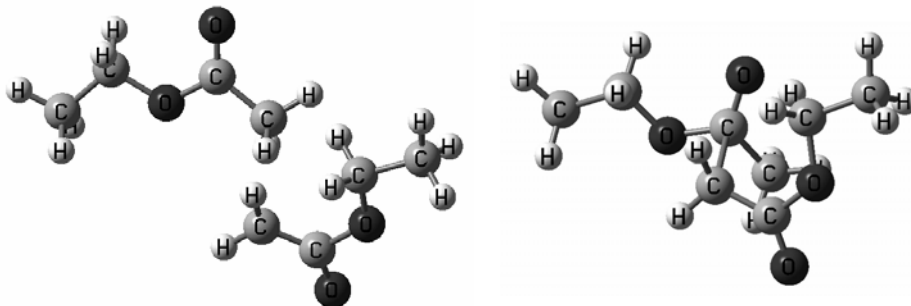


Fig. 4. Reactants (left) and transition state (right) for the most favorable reaction path.

Conclusion

Activation energies of different reaction paths for the reaction under investigation are dependent on HOMO-LUMO gaps of corresponding reactants. HOMO-LUMO gap is not the only factor that makes influence to the energy barrier. Steric factors also play significant role in the energetics of the reaction considered.

Acknowledgement

This work is supported by the Ministry of Science and Environment of Serbia, project N^o 142025.

References

- [1] K. P. C. Vollhardt, N. E. Schore: Organic Chemistry, Freeman, New York, 1994.
- [2] W. J. Hehre, Practical Strategies for Electronic Structure Calculations, Wavefunction, Irvine, 1995.
- [3] *Gaussian 98, Revision A.9*; Gaussian, Inc.: Pittsburgh, PA, 1998.

MECHANISM OF THE KOLBE-SCHMITT REACTION WITH DIFFERENT ALKALI METAL PHENOXIDES

Z. Marković¹, S. Marković² and N. Begović³

¹*Faculty of Agronomy, University of Kragujevac, Serbia*

²*Faculty of Science, University of Kragujevac, Serbia*

³*Holding Institute of General and Physical Chemistry, Belgrade, Serbia*

Abstract

The mechanisms of the carboxylations of lithium, potassium, rubidium and cesium phenoxides are investigated by means of Density Functional Theory method with LANL2DZ basis set. It is shown that the reactions of all alkali metal phenoxides with carbon dioxide occur via very similar reaction mechanisms. The reactions can proceed in the ortho and para positions. The exception is lithium phenoxide, which yields only salicylic acid in the Kolbe-Schmitt reaction. It is found that the yield of the para substituted product increases with increasing ionic radius of the alkali metal used. An explanation for this experimental and theoretical observation is proposed.

Introduction

The Kolbe-Schmitt reaction is a carboxylation reaction of alkali metal phenoxides with carbon dioxide where hydroxybenzoic acids are formed [1,2]. It is a classical example of a reaction where the nature of the reaction products is dependent on the alkali metal cation.

There are controversial discussions concerning the mechanism of the Kolbe-Schmitt reaction. The existence of the intermediate NaOPh-CO₂ complex was confirmed experimentally [3,4]. A Density Functional Theory (DFT) study on the mechanism of the reaction between sodium phenoxide and carbon dioxide was performed at the B3LYP/LANL2DZ level of theory [5]. This mechanism was confirmed by Stane-scu and Achenie who investigated solvent effects on the Kolbe-Schmitt reaction kinetics [6].

The aim of this work is to investigate the dependence of the distribution of products of the Kolbe-Schmitt reaction on the alkali metal cation. For this purpose, the reaction mechanism is investigated for different alkali metal phenoxides (i.e. lithium, potassium, rubidium and cesium phenoxides) by means of DFT method.

Results and Discussion

Geometrical parameters of all stationary points and transition states are optimized in vacuum, at the B3LYP/LANL2DZ level of theory, using GAUSSIAN98 program package [7].

Before we present our results we need to introduce some symbols. M denotes any alkali metal under the consideration (i.e. lithium, potassium, rubidium and cesium). PhO-M, B-M, C-M, D-M and E-M stand for alkali metal phenoxide, first, second and third intermediates, and alkali metal salt of hydroxybenzoic acid, respectively.

Analogously, the symbols TS1-M, TS2-M and TS3-M denote the first, second and third transition states. Prefixes o and p denote ortho and para routes of the Kolbe-Schmitt reaction.

The reactions of all PhO-Ms with carbon dioxide occur via very similar reaction mechanisms with similar energy profiles (Fig. 1 and Table 1). All reactions are exothermic. The reactions can proceed in the ortho and para positions. The exception is PhO-Li which yields only salicylic acid in the Kolbe-Schmitt reaction. The reaction in both ortho and para positions proceeds via three transition states and three intermediates. The intermediates that appear in the ortho and para routes of the Kolbe-Schmitt reaction are presented in Fig. 2.

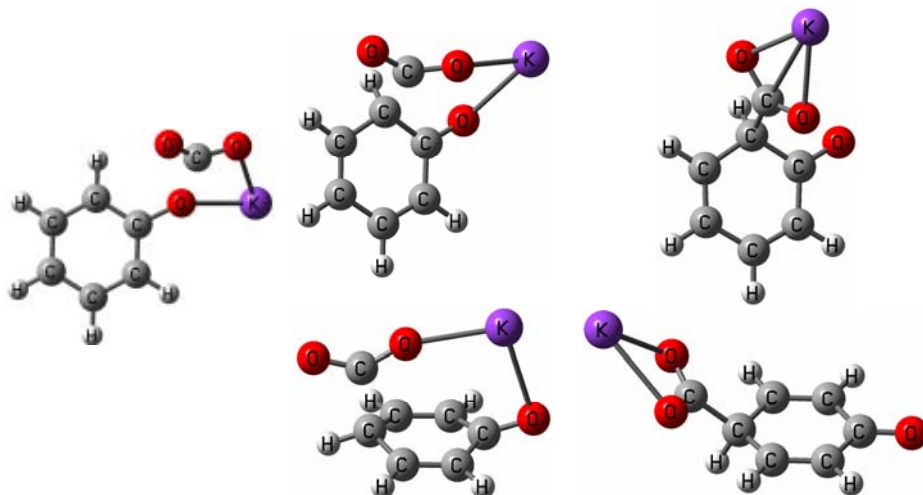


Fig. 1. Intermediates in the carboxylation reaction of potassium phenoxide and carbon dioxide: left – first intermediate responsible for branching to ortho and para routes; top - ortho route; bottom - para route.

Table 1. Experimental and calculated ratios between the concentrations of the ortho and para products.

M		Li	K	Rb	Cs
Ortho/para ratio	Exp.	1 : 0	1: 0.03	1 : 1.29	1 : 2.32
	Calc.	1 : 0	1 : 0.09	1 : 0.55	1 : 2.07

It is clear that the intramolecular conversion of the B-M complex is the most responsible for the products distribution in the Kolbe-Schmitt reaction. The free energy differences between the two transition states for the conversions of B-Ms are calculated, in agreement with the Curtin-Hammond principle. The resulting ratios between the concentrations of ortho and para products are given in Table 1.

Conclusion

The intramolecular conversion of the intermediate B is most responsible for the product distribution of the Kolbe-Schmitt reaction, since it determines the ortho and para routes of the reaction. The yield of para substituted product increases with increasing ionic radius of the alkali metal used, which is in accord with experimental findings. The O-M bond lengths in TS1 also increase with increasing ionic radius of alkali metals. This is of great importance for the geometry of pTS1-M. Since these bonds form a bridge that enables the bonding of C7 to the para carbon, the geometry of pTS1-M becomes more relaxed as the O-M bond lengths increase.

The ionic radius of lithium is only 0.60, so that a possible geometry of pTS1-Li would require significant deformations of benzene ring. For this reason pTS1-Li does not form. The ionic radius of sodium enables the formation of pTS1-Na, but at very low yield. As the ionic radius of alkali metals increases the formation of pTS1-M is more facilitated, and in the case of TS1-Ce the formation of pTS1-Ce is more favorable than that of oTS1-Ce. These computational findings are generally in agreement with experimental results.

Acknowledgement

This work is supported by the Ministry of Science and Environment of Serbia, project N° 142025.

References

- [1] H. Kolbe, *Ann.*, 1860, **113**, 125-127.
- [2] R. Schmitt, *J. Prakt. Chem.*, 1885, **31**, 397.
- [3] M. Kunert, E. Dinjus, M. Nauck, J. Sieler, *Chem. Ber./Recueil*, 1997, **130**, 1461-1465.
- [4] Y. Kosugi, Y. Imaoka, F. Gotoh, M. A. Rahim, Y. Matsui, K. Sakanishi, *Org. Biomol. Chem.*, 2003, **1**, 817-821.
- [5] Z. Marković, J. P. Engelbrecht, S. Z. Marković, *Naturforsch.*, 2002, **57a**, 812-818.
- [6] I. Stanescu, L. E. K. Achenie, to appear in *Chemical Engineering Science*.
- [7] *Gaussian 98, Revision A.9*; Gaussian, Inc.: Pittsburgh, PA, 1998.

MONTE CARLO SIMULATIONS OF THE MAGNETIC PROPERTIES OF SOME HARD-SOFT COMPOZITES

G. Munteanu and N. Stănică

“Ilie Murgulescu” Institute of Physical Chemistry, Bucharest, Romania, (gmunteau@icf.ro)

Abstract

Monte Carlo Metropolis calculations were performed to simulate hard-soft magnetic composites. The composites were mixtures of 1 and 5/2 spin phases, having cubic structures, with well defined magnetic properties. Four basic structures, for which the ratios between the two phases were 1:7, 1:3, 1:1 (layered structure) and, again 1:1 (mozaical structure), were taken into account. The exchange integral that characterize the interaction between the phases was taken as parameter. There were computed the spontaneous magnetization, magnetic specific heat, as well as the hysteresis curves. It was considered a temperature range between 50 and 700 K and external magnetic fields up to 10 T. Both quantic and classical models were considered. The properties of the composites depends not only on the strength of the exchange interaction and proportion between the two components. They also depends on the contact surface area. The structural anisotropy is reflected the magnetic properties anisotropy.

Introduction

It is known that the magnetic properties of the bi-component composite materials, especially the hard-soft combinations, are different than the sum of their individual properties [1,2]. Along the time there were various trials to explain the observed phenomena. For the beginning the influence of the mean grain size on the magnetic properties of isotropic nanocrystalline FeNdB/ α -Fe composite magnets has been investigated [3]. Very soon it was understood that the composite materials have unexpected magnetic properties due to the interactions that exist at the interface between the two phases [4].

Recently, Han and colaborators showed that both the exchange interaction between the hard/soft grains and the effective anizotropy constant depend on the ratio of magnetically soft and hard grain sizes [5].

Schrefl and Fidler [6] revealed, using the finite-element method, the correlation between the local arrangement of the magnetic moments on a length scale of several nanometers and the magnetic properties of nanocomposite permanent magnets.

Results and Procedures

In this paper we present the results of some Monte Carlo Metropolis [8] simulations regarding the the magnetic properties of the four hard-soft cubic systems presented in Figure 1. Any of those four large cubes of Figure 1 have an edge of 16 u (lattice units). The embeded cube of Figure 1a has the edge of 8 u and, consequently, the proportion between the two phases is 1:7. The dimension of similar part of Figure 1b is 8x16x8, the proportion between the two phases being 1:3 in this case. The proportions be-

tween the two phases is 1:1 both in case of Figure 1c and 1d, the dimensions of the embedded parts being 16x16x8 and 8x8x8.

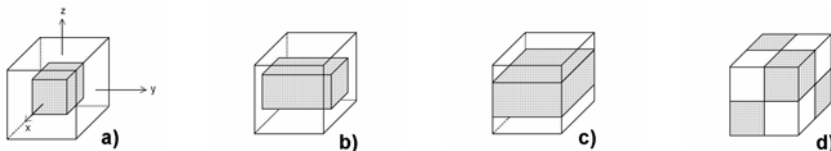


Fig. 1. The four structures used in the Monte Carlo simulations. The pixelated part represent in the all cases the "hard" component. The proportion hard:soft are: a) 1:7, b) 1:3, c) 1:1 and d) 1:1.

The two magnetic materials, having the same lattice constant, consist of 1 and 5/2 spins, being characterized by well defined exchange interactions and, consequently, by well defined Curie points (see Figure 2).

In our simulations we considered three parameters: the exchange interaction between the two magnetic phases, that exists along their border, the proportion between the components, and the area of the common surface. As one may note in Figure 1 the common surface areas in the four cases are: $384 u^2$, $512 u^2$, $512 u^2$ and $1536 u^2$.

We considered for any spin of the structure an interaction Hamiltonian:

$$\hat{H} = g\mu_B \vec{H} \vec{S} - 2S_z \sum_{i=1}^6 J_i S_{iz}$$

where g is the giromagnetic factor, μ_B - the Bohr magneton, \vec{H} - the applied external magnetic field, \vec{S} - the spin, S_z - the projection of the spin on the direction Oz , J - the exchange integral characteristic to the interaction with the i^{th} neighbour and S_{iz} - the projection of the spin on the direction Oz characteristic to the i th neighbour.

For all the composites showed in Figure 1 there were computed the spontaneous magnetization curves and magnetic specific heat for temperatures between 50 and 700 K as well as the hysterezis curves.

In Figure 2 we present only a part of the results: both magnetization curves for the two basic materials and for composites materials having the structure like in Figure 1c, with various interaction strengts between the components (from 0 up to 100 cm^{-1}). In Fig. 2 one may note that the magnetization curve reveals, in this case when the components are in the ratio 1:1, even when the interaction between components is large (100 cm^{-1}), especially at temperatures located between the two Curie points, the presence of both components. At low tempetarures the magnetization is the weighted average of the components. The magnetizations of the compozite, when no interaction exists between the components, may be equal, at low temperatures, to the difference of the individual saturation magnetizations.

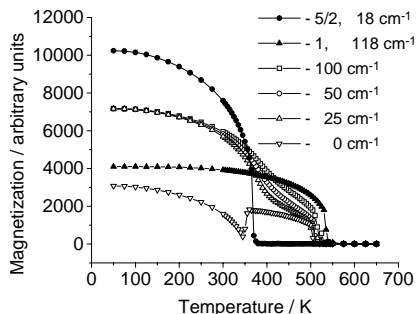


Fig. 2. Spontaneous magnetization of pure materials as well as the *c* type composite with various spin exchange interaction between components.

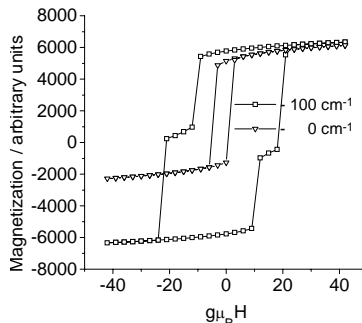


Fig. 3. Hysteresis curves, at 300 K, for the *c* type composite characterized by two extreme values of the spin exchange interaction between components.

In Figure 3 we note that a similar phenomenon may take place when the hysteresis curves are measured. In case of no interaction between components the hysteresis curve is asymmetric. This is because reversing the applied magnetic field the 5/2 spins firstly flip without any correlation with the others.

Conclusion

The properties of the composites depends not only on the strength of the exchange interaction and proportion between the two components. They also depends on the contact surface area.

The structural anisotropy is reflected the magnetic properties anisotropy.

References:

- [1] O. Jarjayes, P.H. Fries, G. Bidan, *J. Magn. Magn. Mater.*, 1994, **137**, 205-218.
- [2] Z. Chen, H. Okumura, G.C. Hadjipanayis, Q. Chen, *J. Appl. Phys.*, 2001, **89**, 2299-2303.
- [3] O.V. Billoni, S.E. Urreta, L.M. Fabietti, H.R. Bertorello, *J. Magn. Magn. Mater.*, 1998, **187**, 371-380.
- [4] S.Y. Zhang, H.W. Zhang, Z.G. Sun, B.S. Han, B.G. Shen, T. Zhao, F.R. Deboer, K.H.J. Buschow, *J. Alloys Compounds*, 1999, **292**, 253-257.
- [5] G.B. Han, R.W. Gao, S. Fu, H.Q. Liu, W.C. Feng, W. Chen, *J. Rare Earth*, 2004, **22**, 790-793.
- [6] T. Schrefl, J. Fidler, *J. Magn. Magn. Mater.*, 1998, **177**, 970-975.
- [7] N. Metropolis, A.W. Rosenbluth, M.N. Rosenbluth, A.H. Teller, E. Teller, *J. Chem. Phys.*, 1953, **21**, 1087.

THE FRACTAL DIMENSIONS OF BENTONITE CLAY DETERMINED BY MAHNKE AND MÖGEL METHOD

T. Novaković, Lj. Rožić, S. Petrović and Z. Vuković

IChTM- Department of Catalysis and Chemical Engineering, Belgrade, Serbia

Abstract

Raw bentonite from southern Serbia was chemically activated using various concentrations of HCl solutions in order to determine the influence of this chemical treatment on textural properties of activated samples. On the basis of the sorption-structure analysis, the fractal dimension of the bentonite surfaces was determined by Mahnke and Mögel method. As expected, the values of the fractal dimension of activated bentonites decreases with the increase of the concentrations of hydrochloric acid, indicating that the irregularities of their surfaces become smaller.

Introduction

Physical, chemical and adsorption properties of natural adsorbents depend on the crystal structure of their constituent clay minerals. The adsorption properties of adsorbents based on bentonite are a function of the content of smectite and the nature and number of interlayer cations. In order to remove impurities and various exchangeable cations from bentonite clay and produce homogeneous, well-defined materials with a high specific surface area, suitable to be used as adsorbents and catalysts, different treatments are used, mostly those with inorganic acids.

Gas adsorption is a method frequently used to determine the surface fractal dimension of porous media. Several different theories have been developed to analyze gas adsorption data and obtain the surface fractal dimension [1,2,3].

Fripiat, Gatineau and Van Damme [4] extended the BET-formalism, which originally was designed for perfectly flat surfaces. Besides being non-applicable for the case of irregular surfaces, their formula exhibits inconsistent behavior in the limiting case of the surface fractal dimension $d = 3$. Mahnke and Mögel developed a generalized BET-formula, which solves the inconsistency problem. An approximate version of this formula offers an easy method for calculating the fractal dimension from adsorption data [5].

This version is applied to determine the fractal dimension of surfaces of chemically activated bentonite samples.

Experimental

Bentonite with particle size below $0.74\mu\text{m}$ was used for acid treatment. The chemical composition of the bentonite samples was : SiO_2 -69.12%, Al_2O_3 -14.01%, Fe_2O_3 -5.43, MgO -2.57%, CaO -1.62%, Na_2O -1.33%, K_2O -0.66%, H_2O -4.69%.

Chemical activation of bentonite was carried out in a glass reactor at 90 °C, during 2h with solid-liquid ratio 1:4, with concentrations of HCl 3M (sample AB₃) and 4.5M (sample AB_{4.5}).

Nitrogen adsorption-desorption isotherms were determined in a high vacuum volumetric apparatus at -196 °C. Prior to adsorption measurement the samples were out-gassed at 200 °C at pressure of 1mPa, for 3h. The monolayer capacity and the specific surface area of the adsorbents were evaluated by the BET method. The values of S_{BET} of starting and activated samples were 63m²/g, 236m²/g and 279m²/g, respectively.

Results and Discussion

The monolayer volume V_m and C_{BET} were calculated from nitrogen adsorption isotherms of activated bentonite samples AB₃ and AB_{4.5}, using data up to p=0.3. For the purpose of fractal analysis only the adsorption part of the isotherm was used. The plot (Fig.1.) adapted from Eq. 1 is nearly linear.

$$\log \left(\frac{V}{V_m} \frac{1-p+Cp}{Cp} \right) \text{ vs. } -\log(1-p) \tag{1}$$

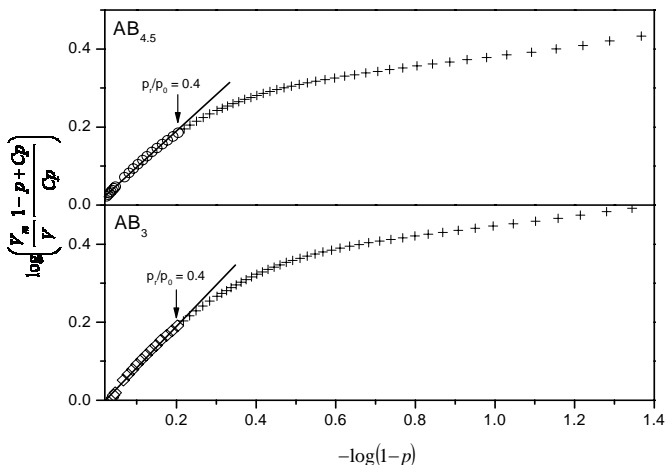


Fig. 1. Estimation of d according to equation (1)

The straight line fitted for 0.05 < p < 0.42 using values of C and V_m measured directly from the BET approximation, give a slope α = 0.89 for AB₃ and 1.06 for AB_{4.5} which points to a surface fractal dimension d = 2.11 and d = 1.94, respectively.

The isotherms calculated from Eq. 2 with these parameters are shown in Fig. 2.

$$V = \frac{V_m}{1-p+Cp} \frac{Cp}{(1-p)^\alpha} \tag{2}$$

As can be seen from Fig.2. the line fits the dependence equally well for values of p up to 0.55 (for AB_3) and up to 0.45 (for $AB_{4.5}$). In the low pressure region the estimated fractal dimension is near 2, which indicates that irregularities of the surface are larger than the size of the adsorbate.

The surface behaves as a flat one on that scale. In this pressure range only one or at most two layers participate adsorption. For high pressures newly build layers lie outside the fractal regime of the surface and the omitted lateral interactions tend to smooth the interface surface. This again leads to underestimation of the fractal dimension.

Conclusion

The approximate version of Mahnke-Mögel isotherm was used to estimate the fractal dimension of the surface of porous bentonite clay. The fractal dimension evaluated by this method was 2.11 for AB_3 and 1.94 for $AB_{4.5}$ sample. The isotherm has been successfully fitted to N_2 adsorption data of activated bentonite samples, in the region of the relative pressures 0.05-0.55 for AB_3 sample and 0.05-0.45 for $AB_{4.5}$ sample.

The values of the fractal dimension of activated bentonites decreases with the increase of the concentrations of hydrochloric acid, indicating that the irregularities of their surfaces are smaller.

Acknowledgement:

This work was supported by the Ministry of Science and Environmental Protection of the Republic of Serbia (Projects number TR 6712B and ON 142019)

References

- [1] P. Pfeifer, D. Avnir, Fractal theory of heterogeneous surfaces, *J. Chem. Phys.*, 1983, **79**, 3558
- [2] D. Avnir, D. Farin, Fractal surfaces of adsorbents, *J. Chem. Phys.*, 1983, **79**, 3566
- [3] P. Pfeifer, M. Olbert, M.W.Cole, *Proc. R. Soc. Lond. Ser. A*, 1989, **423**, 169
- [4] J.J. Fripiat, L. Gataineau, H. Van Damme, *Langmuir*, 1986, **2**, 562
- [5] M. Mahne, H.J. Mögel, *Colloids and Surfaces A: Physicochem. Eng. Aspects*, 2003, **216**, 215

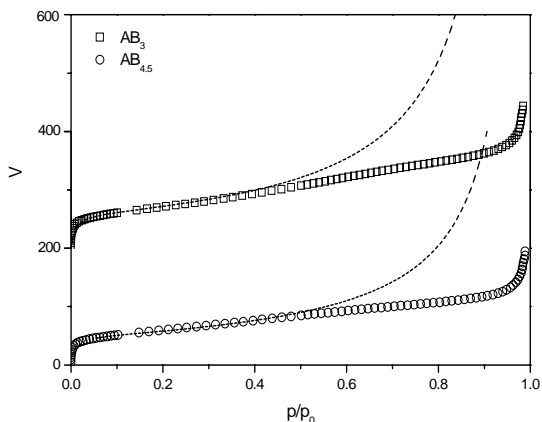


Fig. 2 Estimated isotherms according to equation (2)

ENERGIES OF ELECTRONIC STATES OF Ni(II) ION IN NiO-AL₂O₃ CATALYST PREPARED BY MECHANICAL POWDER MIXING

J. Kiurski¹, D. Obadović² and R. Marinković-Nedučini³

¹ Faculty of Technical Sciences, 21000 Novi Sad, Serbia

² Faculty of Sciences, Department of Physics, Trg Dositeja Obradovića 4, 21000 Novi Sad, Serbia (obadovic@im.ns.ac.yu)

³ Faculty of Technology, 21000 Novi Sad, Serbia

Abstract

In the present work we investigated the influences of Ni(II) ion on NiO-Al₂O₃ catalysts properties due to the preparation by powder mixing method. Based on experimental diffuse reflectance spectroscopy (DRS) data of electronic d-d transitions of Ni(II) promoter ion, the energies of electronic states in spinel-like structure were calculated, and the most probable scheme of molecular orbital has been proposed.

Introduction

Designing of a new catalyst structure depends on the design of active sites in the molecule/atom range, catalysts multifunctionality and a new nanostructure application [1]. However, the catalysts structure formed in the process of its synthesis is susceptible to other changes during the catalyst activation and operation in the regeneration processes. Every change in the bulk or on the catalyst surface has an influence on the catalyst properties.

This has led to several relationships between the catalytic activity and other significant parameters such as elemental electronic configuration, methods and heats of formation of the corresponding compounds. The insight into electronic configuration of active centers and bond strengths in a complex structure formed during the interaction with alumina as catalyst support is the basis of contemporary catalyst design. Investigation of d-electron configuration in active structure and the changes that proceed during the catalyst preparation contribute to establishing the correlation between the catalyst structure and its performances [1].

This work represents a continuation of our previous studies [2-4] and deals with the calculation of the energies of electronic states of Ni(II) ion in NiO-Al₂O₃ catalyst due to the preparation by powder mixing method, because of its differences toward catalysts prepared by impregnation, precipitation or some other methods.

Experimental

The NiO-Al₂O₃ catalysts were prepared with mechanical powder mixing with 5.0; 10.0 and 20.0 wt% of metallic nickel calculated on dried metal oxides. The homogenization of metal oxide powders was carried out in a rotational mixer for one hour. All the samples were treated at temperature 400°, 700° and 1100 °C in static air atmosphere during 6 hours.

The structural investigations were performed by X-ray diffraction (XRD; Philips, PW 1050 CuK α) and diffuse reflectance spectroscopy (DRS; SPM-2 monochromator Veb Zeiss, Jena with a reflection cell of R-45/0 type) [4]. The textural investigation was performed by low-temperature nitrogen adsorption (LTNA; Micromeritics, ASAP 2000) method.

Results and Discussion

Reflection spectroscopy was used to establish the coordination of the central Ni(II) ion in the investigated samples, contents of spinels formed, as well as the occupation degree of T_d and O_h centers with Ni(II) ions [4]. In view of its outer orbital, Ni(II) ion belongs to the d⁸ system, and on the basis of the Tanabe–Sugano diagram for the d⁸ system it was found that the samples prepared by mechanical mixing at 400 and 700 °C have an octahedral structure (Fig. 1).

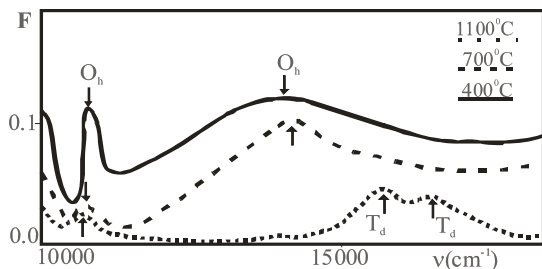


Fig. 1 Kubelka-Munk functions of catalysts with 5wt% of nickel treated in air

It was found that the spinel structure was formed only at the treatment temperature of 1100 °C, for all nickel concentrations, with the simultaneous transformation of alumina from the γ - to an α -modification and the presence of unreacted nickel oxide (Fig.1). It was also observed, that irrespective of the nickel concentration, specific surface area of binary

catalyst systems essentially change, but not before the heat treatment temperature of 1100 °C [4]. In view of the fact that this temperature corresponds to the transformation of alumina from the γ - to α -modification, it is obvious that this phase transformation plays a key role in the textural changes taking place in the system.

An indication of this is also the appearance of maxima of the Kubelka-Munk function at $\sim 15,600$ and $\sim 16,000$ cm⁻¹, which correspond to the transitions ³T₁(F)→¹E(D) and ³T₁(F)→³T₁(P) of the tetrahedral symmetry of the Ni(II) ion, (Fig.1), as well as the results of X-ray diffraction analysis [4].

The calculation and experimental values of the electronic spectrum maxima

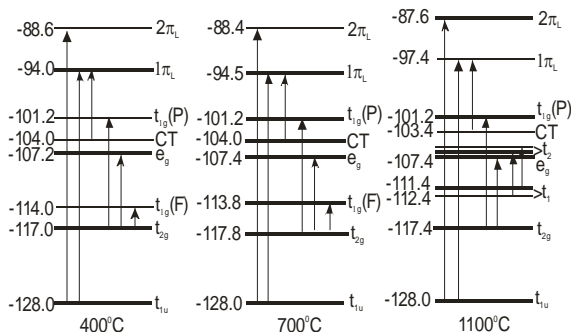


Fig. 2 Most probable scheme of molecular orbitals: 400, 700 and 1100 °C

of NiO-Al₂O₃ catalyst prepared by mechanical powder mixing served as the basis for forming a most probable scheme of MO (Fig.2), which is one more confirmation of the disturbance, occurring un the initial promoter structure.

Conclusion

On the basis of the presented results of studying the system models it can be concluded that the type of contact between the starting phases has a decisive influence on the coordination of Ni(II) ions. In the case of applying powder mixing method, spinel structure was registered only at the highest heat treatment temperature (1100 °C). The fact that the nickel concentration in the starting system does not influence the formation of spinel structure, along with the above observations, confirms the pronounced effect of the nature of the contact and temperature on the kinetics of this solid-phase reaction. Formation of spinels suggests the rise of fine microstructural changes in the system, which, depending on the preparation method begins at significantly higher temperatures.

Acknowledgements

This work was supported by research Grant No. 141020 and No. 142024 from the Ministry of Science, Technologies and Development of the Republic of Serbia.

References

- [1] H.Topsøe, *Studies in Surface Science and Catalysis*, 2000, **130**, 1.
- [2] D. Ž. Obadović, J.Kiurski, R.Marinković-Nedučin, *Polyhedron*, 1996, **15**, 3631-3634.
- [3] E. Kiš, R. Marinković-Nedučin, G. Lomić, G. Bošković, D.Ž. Obadović, J. Kiurski and P. Putanov, *Polyhedron*, 1998, **17**, 27-34.
- [4] J.S.Kiurski, Ph.D.Thesis, University of Novi Sad, Faculty of technology, Yugoslavia 1997.

TEMPERATURE DEPENDANCE OF CYCLOHEXANE PARTIAL OXIDATION IN PTFE REACTOR

D. Lončarević, P. Banković, V. Drobňjak and Ž. Čupić

*Institute of Chemistry, Technology and Metallurgy,
Department of Catalysis and Chemical Engineering, Njegoševa 12, Belgrade, Serbia
zcupic@nanosys.ihm.bg.ac.yu*

Abstract

Polymer-supported Co(II) catalyst was prepared and its activity and selectivity in the partial oxidation of cyclohexane was determined at several temperatures, in polytetrafluoroethylen reactor. Activation energies were determined for the net production of the cyclohexanone and of the cyclohexanol.

Introduction

The system, currently in use for partial oxidation of cyclohexane (Ch) to the mixture of cyclohexyl hydroperoxide (Chhp), cyclohexanol (Chl) and cyclohexanone (Chn), employs 0.3-3 ppm of a soluble cobalt catalyst, at temperature value of 150-175 °C and pressure value of 0.8-1.0 MPa [1].

Investigations are extensively performed in the heterogenization of batch reactions, on various solid supports (inorganic oxides, zeolites etc.) [2, 3]. Metal ion acts as an initiator of free radical auto-oxidation which proceeds further via radical chain reaction [3]. Our previous results in stainless steel reactor show that polymer-supported Co(II) catalyst, catalyze cyclohexane partial oxidation at 170 °C and 2.8 MPa, with high conversion and good selectivity towards desired products [4, 5]. The goal of present work was to investigate the temperature influence on the cyclohexane oxidation at several temperatures in isothermal regime in polytetrafluoroethylene (PTFE) reactor.

Experimental

The support used was macroreticular copolymer of poly-4-vinylpyridine with divinylbenzene (REILLEX-425), produced by Reilly Tarr & Chemical Corporation. Catalyst was prepared from the ethanol solutions of the $\text{Co}(\text{NO}_3)_2$.

Activity tests were performed in stainless steel, laboratory scale (100 cm³), stirred autoclave with PTFE liner. In all catalytic runs the following conditions were used: polymer fraction in reaction mixture equal to wt. 1.43% with respect to cyclohexane (35g Ch, 0.5g cat.), air pressure 2.8 MPa, stirrer speed 350 rpm. Air-flow rate was maintained at about 100 cm³min⁻¹. Gas and liquid samples were analyzed by gas chromatography.

The activity tests were performed under the isothermal conditions: after an initial fast heating up to the working temperature, and the system was kept at this temperature for 120 min before the reaction was stopped. In each experiment, the fresh charge of the catalyst was used.

Composition of the liquid samples was analyzed by gas chromatography using stainless steel column packed with 10% Carbowax 20M on Chromosorb WAW, coupled to a flame ionization detector, isothermally at 150 °C. The Chhp concentration was determined by iodometric titration and indirectly by reduction with triphenylphosphine [6].

Results and Discussion

The concentration profiles of the Chl and Chn are presented in the Fig. 1, with respect to reaction time. The higher yields were obtained for both Chn and Chl, with increasing reaction temperature.

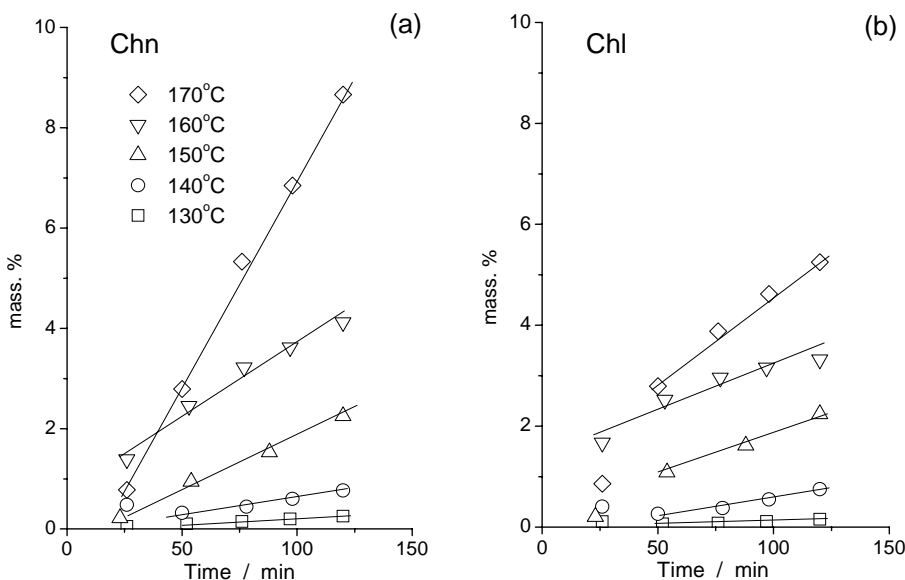


Fig. 1. Concentration profiles for Chn (a) and Chl (b) production

Rate of the production of both products is proportional to concentration of cyclohexylperoxy radical $[ChOO^*]$: $\frac{d[P]}{dt} = k \cdot [Ch] \cdot [ChOO^*]$, where P is any of products Chl or Chn, and rate constant k depends on the product. After some initial time, the concentrations of both products increase with approximately constant rate in used temperature interval and reaction time interval. Constant rate is a consequence of constant free radical intermediary concentrations in steady state and small changes of the $[Ch]$ value due to low conversion levels. Therefore, it was possible to evaluate activation energies of the steady state overall production, for both, Chl and Chn. Arrhenius plots are shown at Fig. 2 for both products. Obtained value for the activation energy of the Chl production process (1.01 kJ/mol) is lower than for the Chn production process (1.36 kJ/mol).

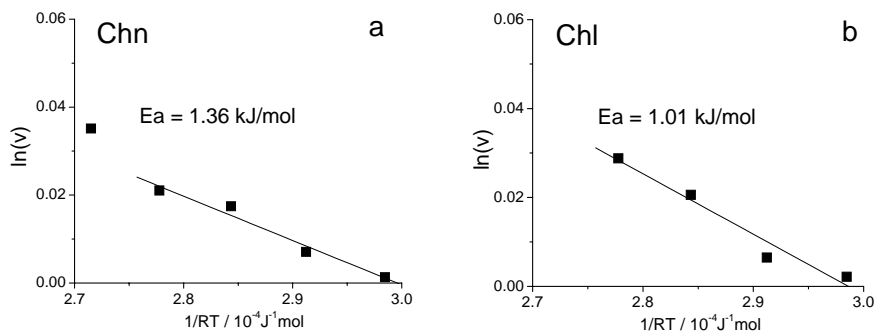


Fig. 2. Arrhenius plots for Chn and Chl production

Both obtained values for the activation energy of investigated catalytic processes are lower than reported values for any of the reactions in the model of non-catalytic reaction mechanism.

Conclusion

Results obtained in cyclohexane partial oxidation over the macroporous polymer supported Co catalysts, confirmed once more that reaction proceeds selectively to Chn and Chl, with very low extent of deep oxidation.

Influence of the temperature was characterized through the Arrhenius type behavior and activation energies were evaluated for Chl and Chn overall production processes.

Acknowledgement:

The authors gratefully acknowledge the partial support of the Fund for Science and Technologies and Development of Serbia. Proj. 142019B

References:

- [1] D. E. Danley, C. R. Campbell, in Kirk Othmer Encyclopedia of Chemical Technology, (3rd Ed.) John Wiley & Sons; New York, 1978, **1**, 514.
- [2] G. L. Goe, C. R. Marston, E. F. V. Scriven, E. E. Sowers in 'Catalysis of Organic Reactions', Ed. D. W. Blackburn, Marcel Dekker, Inc., New York, 1989, p. 275.
- [3] I. W. C. E. Arends, R. A. Sheldon, Appl. Catal., 2001, **A 212**, 175.
- [4] Ž. Čupić, A. Terlečki-Baričević, M. Stanković, Activity of the Polymer Catalyst for the partial oxidation of Cyclohexane, 4th World Congress on Oxidation Catalysis, Berlin, 2001, Extended Abstracts, p.p.155-158.
- [5] D. Lončarević, Ž. Čupić: "Characterization and Catalytic Activity of Poly(4-Vinylpyridine-co-Divinylbenzene)-Co²⁺ Complex", Material Sciences Forum, 2005, **494**, 363-368.
- [6] G. B. Shul'pin, J. Mol. Cat. A: Chemical 2002, **189**, 36-66.

TEXTURE OF THE AG-NI/DIATOMITE PRECURSORS OF EDIBLE OIL HYDROGENATION CATALYSTS

M. Gabrovska¹, D. Nikolova¹, M. Stanković²,
R. Edreva-Kardjieva¹, D. Jovanović²

¹*Institute of Catalysis, BAS, 1113 Sofia, Bulgaria (dimi@ic.bas.bg)*

²*ICTM, Department of Catalysis and Chemical Engineering, 11000 Belgrade, Serbia*

Abstract

Silver modified Ni/diatomite materials with ratios of SiO₂/Ni=1.0 and Mg/Ni=0.1 were prepared by precipitation-deposition technique. Two Ag/Ni ratios (Ag/Ni=0.025 and 0.1, respectively) were chosen to investigate the effect of the silver presence and content on the texture of the catalyst precursors. The silver additionally modified the texture of the Ni/diatomite precursor. The sample with the higher silver content seems to be more suitable catalyst precursor for edible oil hydrogenation because of its higher total intrusion pore volume, total porosity and monodisperse macroporous type of pore size distribution.

Introduction

Nickel supported on diatomite is the most commonly used catalyst for partial hydrogenation of vegetable oils [1]. However, metal Ni catalysts work at high temperatures favouring *cis*- to *trans*-isomerization [2]. It is known that the metallic silver, as a member of the IB group, decreases the reduction temperature of the transition metal ions. It may be supposed that the addition of silver to the nickel/diatomite material will provoke lower temperature of the hydrogenation process, thus hampering the *cis*- to *trans*-isomerization reaction.

The aim of the present work is to study the effect of the silver presence and content on the textural properties of the nickel/diatomite catalyst precursors for edible oil hydrogenation. The precursor texture characteristics are essential factor for the mass transport of the great triglyceride molecules to the active surface as well as the re-transport of the reaction products.

Experimental

Sample preparation

The catalyst precursors with the same SiO₂/Ni=1.0 and Mg/Ni=0.1 ratios were prepared by the precipitation-deposition method from aqueous solutions of Ni(NO₃)₂·6H₂O, Mg(NO₃)₂·6H₂O, AgNO₃, Na₂CO₃ and an aqueous suspension, containing 2.0 wt. % diatomite (D). A nickel/diatomite sample (Ni/D) and two Ag-containing samples with the ratios of Ag/Ni=0.025 (1Ag-Ni/D sample) and Ag/Ni=0.1 (2Ag-Ni/D sample) were obtained. The precipitation was performed at 90°C under vigorous stirring and constant value of pH=9.0±0.05. The resulting materials were filtered and thoroughly washed with hot distilled water until the absence of NO₃⁻ and Na⁺ ions was achieved. The precursors were dried for 24 h in an oven at 120 °C and ground to a powder.

Sample characterization

The texture characterization of the support and precursors were estimated using N_2 sorption at $-196\text{ }^\circ\text{C}$ (Sorptomatic 1990 Thermo Finnigan) and Mercury porosimetry (Porosimeter 2000, Fisons).

Results and Discussion

The N_2 sorption results show that the S_{BET} of the diatomite increases from 17 to $185\text{ m}^2\text{ g}^{-1}$ in the Ni/D sample (Table 1). This effect may be explained by the interaction between Ni- and Si-containing species, leading to the formation of the nickel hydrosilicate-type linkages ($-\text{Si}-\text{O}-\text{Ni}-$) [3]. It is observed, that the addition of silver to Ni/D precursor diminishes its S_{BET} to $167\text{ m}^2\text{ g}^{-1}$ and $124\text{ m}^2\text{ g}^{-1}$ in the case of 1Ag-Ni/D and 2Ag-Ni/D precursors, respectively (Table 1).

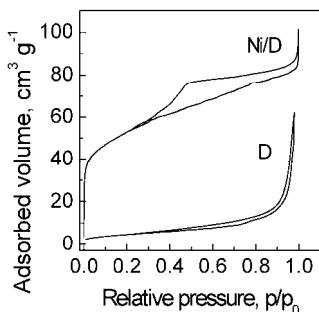


Fig. 1. The isotherms of the support (D) and precursor Ni/D

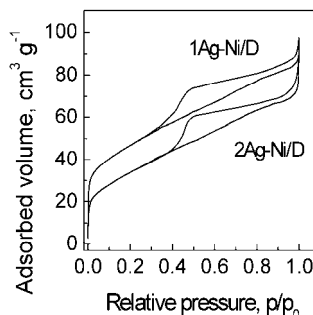


Fig. 2. The isotherms of the 1Ag-Ni/D and 2Ag-Ni/D precursors

The diatomite isotherm (Fig. 1) is close to type II, characteristic for macroporous adsorbents [4]. The isotherms of Ni/D, 1Ag-Ni/D and 2Ag-Ni/D precursors change in shape, transforming into IV-like type, typical for mesoporous materials (Figs. 1 and 2). The hysteresis loops in the isotherms of the precursors are complex ones and they may be assigned to a combination of H2 and H4 types.

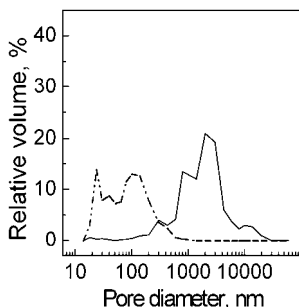


Fig. 3. PSD curves of : (—) diatomite and (---) Ni/D precursor

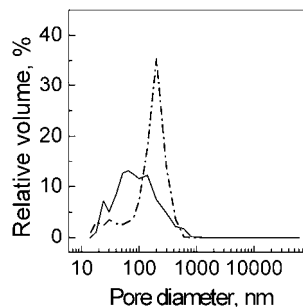


Fig. 4. PSD curves of precursors: (—) 1Ag-Ni/D and (---) 2Ag-Ni/D

The H4 type loop is associated with the presence of micropores, while the H2 type loop is related to the interconnected network of pores, different in size and shape [4].

The pore size distribution (PSD) of the samples cannot be correctly estimated by N₂ sorption because of the macroporous character of diatomite. The PSD curve of the support, obtained by mercury porosimetry, demonstrates a polydisperse type of distribution in the range of 200–30000 nm (Fig. 3). The mean part of macropores is situated at maximum pore diameter (d_{\max}) of about 980 and 2350 nm. The nickel introduction (Ni/D sample) provokes shifting of the PSD maxima to the mesoporous region with d_{\max} at about 25 and 120 nm (Fig. 3). The presence of silver modified the texture causing pore size redistribution. The maxima for the 1Ag-Ni/D sample were registered at 25, 70, 140 and 510 nm (Fig. 4) while only one maximum at 205 nm was observed in the case of the 2Ag-Ni/D precursor.

Table 1. Texture characterization of the support and precursors

Sample	Mercury porosimetry		N ₂ sorption
	V_{total} (cm ³ g ⁻¹)	Total porosity (%)	S_{BET} (m ² g ⁻¹)
D	1.45	66.6	17
Ni/D	0.67	13.3	185
1Ag-Ni/D	0.92	16.4	167
2Ag-Ni/D	1.11	20.5	124

The support modification with nickel and silver is also demonstrated by the changes in the total intrusion pore volume and total sample porosity (Table 1).

Conclusions

The texture of the polydisperse macroporous diatomite is modified by nickel introduction towards the mesoporous region. The presence of silver additionally modified the texture of the Ni/D precursor depending on the Ag/Ni ratio. The sample with the higher silver content seems to be more suitable catalyst precursor for edible oil hydrogenation because of its higher cumulative intrusion pore volume, total porosity and monodisperse macroporous type of PSD.

Acknowledgements

The authors (M.G., D.N. and R.K.) are grateful to the National Science Fund at the Ministry of Education and Science of Bulgaria, for the partial financial support (Project X-1411). The authors (M.S., J.K. and D.J.) greatly acknowledge the support of the Serbian Ministry of Science and Environmental Protection through the Project - TR 6712 B.

References

- [1] E. Draguez de Hault, A. Demoulin, *JAOCS*, 1984, **61**, 195-200.
- [2] A. Wright, A. Wong, L. Diosady, *Food Res. Int.*, 2003, **36**, 1069-1072.
- [3] K. Ghuge, A. Bhat and G. Babu, *Appl. Catal. A: General*, 1993, **103**, 183-204.
- [4] F. Rouquerol, J. Rouquerol and K. Sing, in *Adsorption by Powders and Porous Solids, Principle, Methodology and Applications*, Academic Press, 1999.

CHARACTERIZATION OF PROMOTED Ni CATALYSTS SUPPORTED ON MAGNESIA BY CHEMISORPTION. EFFECTS OF PROMOTER ON Ni-CRYSTALLITE SIZE

M. Stanković, Z. Vuković and P. Banković

ICTM, Department of Catalysis and Chemical Engineering, 11000 Belgrade, Serbia

Abstract

The chemisorption of oxygen on three different promoted magnesia supported nickel catalysts was studied. The results of chemisorption experiments show that promotion of magnesia supported nickel catalyst with nonreducible metal oxide differing in acido-basic properties Al_2O_3 , CaO or Cr_2O_3 leads to different oxygen uptakes. The surface chemical distribution characteristics - nickel surface area and Ni-crystallite size of the promoted catalyst samples were determined and related to each other. In the presence of the promoter used, the nickel surface area increases and the mean Ni-crystallite size decreases according to the following order: $\text{Cr}_2\text{O}_3 < \text{CaO} < \text{Al}_2\text{O}_3$.

Introduction

Supported nickel catalysts are widely used in many industrial high temperature processes such as reforming of light hydrocarbon with carbon dioxide to synthesis gas (CO/H_2) [1], steam reforming of methane [2], methanation [3], and partial oxidation [4]. The promotion by nonreducible metal oxides is known to increase the lifetime of these catalysts due to reduced deactivation by coking [5]. Several suggestions have been made to explain the effect of added oxides as promoters such as increased dispersion due to promoter acting as a spacer, formation of ensembles of a favorable size, etc. [6]. It has also been established that the non-reducible metal oxides as structural promoters are capable of going into solid solution with active metallic nickel [7], similar to the reaction that occurs between nickel and magnesia support [8]. A suitable size of active metal or its clusters and higher dispersion for a given metal loading are preferred for the activity [9]. Both activity and rate of deactivation were found to decrease with increasing metal particle size. However, the degree of these dependences was found to be largely affected by the nature of the support, suggesting that the dependence of activity and rate of deactivation on metal particle size is likely to be related to metal-support interactions.

The preparation of supported metal catalysts with deployment dispersion and narrow size distribution of metal particles becomes particularly desirable for the improvement of catalytic activity and the understanding of the mechanism of some size-dependent or structure-sensitive reactions. This is accomplished by selective chemisorption measurements where the chemisorbed gas adsorbs with a specific stoichiometry on the surface metal atoms but does not adsorb on the support [10].

In the present work, the effects of nonreducible oxides with different acido-basic characteristics on the oxygen chemisorption of magnesia supported nickel catalyst applied in partial oxidation of light hydrocarbons were studied.

Experimental

Three samples of promoted magnesia supported nickel catalyst were prepared. Al₂O₃ promoted magnesia supported Ni sample containing 3.13 wt% of Ni was prepared by successive impregnations of the macroporous low area MgO support ($S_{\text{BET}} = 0.3 \text{ m}^2 \text{ g}^{-1}$; $V_p = 0.145 \text{ cm}^3 \text{ g}^{-1}$) using Ni(NO₃)₂·6H₂O and Al(NO₃)₃·9H₂O as precursors of Ni and Al₂O₃ (atomic ratio of Al/Ni = 0.1). After each impregnation step the sample was dried at 120 °C and calcined at 400 °C to convert nitrates to oxides. The same procedure was performed in the case of CaO (Ca(NO₃)₂·4H₂O) and Cr₂O₃ (Cr(NO₃)₃·9H₂O) promoted catalyst samples containing 3.12 and 3.08 wt% of Ni, respectively.

The specific surface areas of the nonreduced samples were measured by the BET method from the N₂ adsorption isotherms at -196 °C (Sorptomatic 1990). The total intrusion pore volume of the nonreduced samples was measured by mercury porosimetry (Macropore unit 120, Porosimeter 2000).

Prior to the chemisorption experiments the catalysts were activated according to the following procedure: H₂ flow -60 cm³/min, heating rate -5 °C/min up to 500 °C, dwell time 2h, and finally cooling to 0 °C when the chemisorption experiments were started. The oxygen chemisorption experiments were conducted using pulse gas chromatographic method reported by Buyanova et al. [11].

Results and Discussion

Chemical and textural characteristics are summarized in Table 1.

Table 1. Chemical and textural characteristics of the studied samples

Sample code	Ni content (wt%)	Promoter (wt%)	S_{BET} (m ² g ⁻¹)	V_{total} (cm ³ g ⁻¹)	$d_{\text{pore}}^{\text{a}}$ (nm)
Al ₂ O ₃ -Ni/MgO	3.13	0.27	1.6 ± 0.2	0.136	340
CaO-Ni/MgO	3.08	0.28	1.3 ± 0.2	0.125	385
Cr ₂ O ₃ -Ni/MgO	3.12	0.30	1.4 ± 0.2	0.116	330

^aaverage pore diameter ($4V_{\text{total}}/S_{\text{BET}}$).

The textural properties of promoted samples slightly differed from each other. In comparison with MgO support, the increase of S_{BET} and the decrease of the total intrusion pore volume of nonreduced promoted catalyst samples can be explained by the secondary porosity of NiO deposits within the MgO support.

Table 2 lists the chemisorption characteristics of the prepared catalyst samples.

Table 2. Chemisorption results (at 0 °C) for the studied samples

Sample code	^b Adsorption O ₂ (μmole g ⁻¹)	Ni x 10 ⁻¹⁸ (atoms g ⁻¹)	^c S_{Ni} (m ² g _{Ni} ⁻¹)	^d d_{Ni} (nm)
Al ₂ O ₃ -Ni/MgO	10.9	7.77	15.7	35
CaO-Ni/MgO	7.5	5.31	11.1	51
Cr ₂ O ₃ -Ni/MgO	5.4	3.79	7.7	73

^bcorrected for 0.05 μmole g⁻¹ O₂ uptake on the pure support; ^cnickel surface area was calculated assuming chemisorption stoichiometry O/Ni = 1; ^dmean Ni-crystallite size was derived according to the relation: $d_{\text{Ni}} = 5 \times 10^3 / \gamma_{\text{Ni}} x S_{\text{Ni}}$ (nm).

The chemisorption experiments showed that the amount of oxygen adsorbed by nickel is increased in the presence of Al_2O_3 , which indicates that Al_2O_3 promotion increases the dispersion of the surface nickel particles. On the other hand, oxygen chemisorption uptakes for the CaO and Cr_2O_3 catalyst samples were much lower than those observed for $\text{Al}_2\text{O}_3\text{-Ni/MgO}$, suggesting that nickel cannot be stabilized by dividing the surface into small ensembles of Ni atoms. As a consequence the calculated surface characteristics of Ni are considerably distinguished depending on the promoter applied. From the data present in Table 2 the following order for the increase of surface Ni area and the decrease of Ni-crystallite size was established: $\text{Cr}_2\text{O}_3 < \text{CaO} < \text{Al}_2\text{O}_3$.

The obtained results suggest an inhibiting effect of CaO and particularly Cr_2O_3 on the oxygen chemisorption. The inhibiting effect of these oxides may be ascribed to the change in the electronic properties of nickel particles either by formation of a solid solution with Ca (II) and Cr (III) ions, or by intense interaction with MgO support as a result of the presence of Ca and Cr oxides.

Conclusion

Chemisorption of O_2 was utilized to characterize magnesia supported nickel catalyst promoted with nonreducible oxides of Al, Ca and Cr. The presence of different oxides strongly affects the chemisorptive properties of nickel.

The surface chemical distribution characteristics - nickel surface area increases and the mean Ni-crystallite size decreases according to the following order:



Acknowledgments

This work was supported by the Ministry of Science and Environmental Protection of the Republic of Serbia (Project TR 6712.B).

References

- [1] M. C. J. Bradford, M. A. Vannice, *Appl. Catal. A*, 1996, **142**, 97-122.
- [2] H. S. Roh, K. W. Jun, W. S. Dong, S. E. Park, Y. S. Baek, *Catal. Lett.*, 2001, **74**, 31-36.
- [3] M. Agnelli, C. Mirodatos, *J. Catal.*, 2000, **192**, 204-214.
- [4] W. J. M. Vermeiren, E. Blomsma, P. A. Jacobs, *Catal. Today*, 1992, **13**, 427-436.
- [5] C. H. Bartholomew, *Appl. Catal. A*, 2001, **212**, 17-60.
- [6] R. Burch, *J. Catal.*, 1981, **71**, 348-359.
- [7] M. E. Dry, L. C. Ferreira, *J. Catal.*, 1967, **7**, 352-358.
- [8] W. C. Hahn, Jr and A. Muan, *J. Phys. Chem. Solids*, 1961, **19**, 338-348.
- [9] Z. L. Zhang, V. A. Tsipouriari, A. M. Efstathiou, X. E. Verykos, *J. Catal.*, 1996, **158**, 51-63.
- [10] R. P. H. Gasser in: *An introduction to chemisorption and catalysis by metals*, Clarendon Press, Oxford, 1985.
- [11] N. E. Buyanova, A. P. Karnaukhov, L. M. Kefeli, I. D. Ratner, O. N. Cernyavskaya, *Kinet. Katal.*, 1967, **8**, 868-877.

STUDY OF THE DISPERSITY OF FE AND FEME (ME=PD, PT) SUPPORTED SYSTEMS

Z. Cherkezova-Zheleva¹, M. Shopska¹, J. Krstić²,
I. Mitov¹ and G. Kadinov¹

¹*Institute of Catalysis, Bulgarian Academy of Sciences,
Acad. G. Bonchev St., Block 11, 1113 Sofia, Bulgaria, zzhel@ic.bas.bg*

²*ChTM-Center of Catalysis and Chemical Engineering,
Njegoševa 12, Belgrade, Serbia*

Abstract

Samples of one (Fe) and two-component (Fe-Pd and Fe-Pt) catalysts were prepared by incipient wetness impregnation of four different supports: TiO₂ (anatase), γ -Al₂O₃, activated carbon and diatomite. The different texture of the used supports, as well as their chemical composition resulted in formation of nearly bidisperse (ultra- and high-disperse) hematite-like α -Fe₂O₃ supported particles.

Introduction

The emission levels of volatile and semi-volatile organic compounds such as benzene, formaldehyde and polycyclic aromatic hydrocarbons in the air are under strict legislation and control in many countries. Therefore the complete hydrocarbon oxidation is of great importance for the environmental protection. The investigation of transition metal-noble metal supported catalysts is a question of theoretical and practical interest, because of the expected synergetic effect between the components and improvement of their catalytic performance in the hydrocarbon oxidation due to formation of nanosize metal/metal oxide supported particles. The formation of highly active sites is associated with the formation of highly dispersed iron oxide because of the strong iron-support interaction [1].

The aim of the present study was to investigate the influence of support and preparation conditions on the active phase dispersity and its catalytic properties.

Experimental

Four different supports were used - TiO₂ (anatase, BDH Chemical Ltd., England), γ -Al₂O₃ (type 20-1/83P, G-3, Poland), activated carbon (10-30 mm, NORIT PKDA, The Netherlands) and diatomite. The used diatomite support is a natural substance (Baroševac, the "Kolubara" Coal Basin – field B, Lazarevac, Serbia). The crude diatomite has relatively high humidity level and is preliminary ground, chemically (with an aqueous solution of HCl) and thermally (at 1073 K) treated in order to obtain an activated support before catalyst synthesis. After activation the chemical composition (wt %) of the diatomite was 93.07% SiO₂, 3.87% Al₂O₃, 0.56% Fe₂O₃, 0.59% CaO, 0.80% MgO, 0.05% Na₂O, and 0.56% K₂O.

The metal loading of Fe and noble metals in studied catalyst systems is 8 and 0.7%, respectively. The detailed preparation of catalysts and the used instruments (Moessbauer spec-

trosopy, XRD, XPS and -196°C N_2 sorption), for characterization of the carriers and the samples of catalysts before and after the calcination and catalytic test, as well as the very catalytic test, are described elsewhere [2 - 4].

Results and Discussion

Nitrogen adsorption/desorption measurements show certain difference of the S_{BET} , the total pore volume and the pore diameters distribution for the studied catalysts. The

Table 1. Supports textural characteristics

Support	S_{BET} , m^2/g	Total pore volume, cm^3/g	Predominant pore size, nm
$\gamma\text{-Al}_2\text{O}_3$,	303.9	0.627	3-6nm (69.5%) 6-10nm (21.4%)
TiO_2	11.9	0.023	Uniform distri- bution
activated carbon	923.4	0.618	0-3nm (47.0%) 3-6nm (34.8%)
Diatomite	16.8	0.250	2-4nm (33.6%) 4-6nm (14.2%)

corresponding calculated values for the used supports are presented in Table 1. The results show predominantly mesoporous character of the studied sup-ports (about 50-70% of pores are of mesosize) besides of differences among them. One of the supports, activated carbon, has a large amount of micropores. There are macropores in the diatomite and the activated carbon also. The impregnation process and the chemical nature of the precursors affect insignificantly the dispersity of support characteristics. The results show incorporation of iron and palladium (platinum) salts into the pore structure, parallel to the deposition of salts on the walls of meso- and macropores. There are no evidences for the pore closing.

The obtained Moessbauer spectra of the samples at various stages of thermal pretreatment and after the catalytic test show the presence of doublet and sextet part [2 - 4]. They are typical for the high spin Fe^{3+} ions in an octahedral oxygen co-ordination. The doublet part of the spectra was computer processed according to the "core-shell" model [5]. According to this model, the mean particle size is D about 3–4 nm. The appearance of sextet component in the spectra after thermal treatment and catalytic test shows partial agglomeration of iron oxide-like particles. The relatively narrow lines of the components (low values of FWHM) show nearly bi-disperse particle size distribution. Along with the particles of $D \approx 3\text{--}4$ nm, particles with size about 10–20 nm exist, too. The crystallite size of Fe_2O_3 samples decrease in the following order: Fe sample > Fe-Pt sample > Fe-Pd sample for all studied supports. The agglomeration degree in studied samples decreases in the same order. This mode of distribution could be explained with presence of hematite-like ultradisperse particles in the pores and on the surface. The latter part could agglomerate with increase of the temperature. The hematite-like particles in Fe and Fe-Pt samples are both in the pores and on the surface of the support, whereas in Fe-Pd samples they are predominantly in the pores. The other reason for the different ratio between ultradisperse and high disperse particles in the samples can be ascribed with the presence of the noble metal (Pd and Pt) and/or with the nature of the used noble metal precursors [6]. These results are confirmed by cal-

culations of mean effective particle size from the XRD pattern (Sheerer equation) and the detailed XPS spectra (Kirchoff-Moulijne model [7]). The particle sizes of α -Fe₂O₃ were about 3–9 nm. From the detail XPS spectra noble metal particle sizes are calculated also: for platinum - about 1.2–1.8 nm and about 0.7–1.4 nm for the palladium particles. In the course of thermal treatment and the catalytic tests the initial high dispersity of the samples slightly decreased in the case of TiO₂, activated carbon and diatomite, but it was not significantly changed in the case of Al₂O₃ support.

With the two-component samples thus obtained supported active phases revealed nearly 100% benzene oxidation at 573 K. We suppose that the catalytic activity is due to the noble metals, mainly. The thermal pretreatment procedure has not significant influence on the catalyst activity. This feature can be assigned to the mutual stabilizing effect of both the nanosize iron(III) oxide and the noble metal.

Conclusions

Predominantly meso-porous character of the studied supports was not significantly changed after impregnation with active phases. Catalysts containing nanosize iron(III) oxide particles and noble metal (Pt or Pd) particles were synthesized. Appearance of mixed phases between the active phase and the support is not exactly evidenced, but the influence of the chemical composition and dispersity of used support on the dispersity and catalytic behavior of synthesized active phase have been obtained.

Acknowledgments

The authors are grateful to the National Science Fund at the Ministry of Education and Science of Bulgaria (Project MU-1301/2003) and to the Ministry of Science and Environmental Protection of Serbia for the support (TR 6712 B).

References

- [1] L. Guczi, G. Pető, A. Beck, and Z. Pászti, *Topics in Catalysis*, 2004, **29**(3–4), 129-138.
- [2] Z. Cherkezova-Zheleva, M. Shopska, B. Kunev, I. Mitov, G. Kadinov and L. Petrov, in: *Physical Chemistry 2004*, Ed. S. Anic, Society of Physical Chemists of Serbia, Belgrade, 2004, **2**, 478-483.
- [3] Z. Cherkezova-Zheleva, M. Shopska, G. Gouliev, I. Donchev, I. Mitov, G. Kadinov, L. Petrov, 'Nanoscience & Nanotechnology', Issue 5, Eds. E. Balabanova, I. Dragieva, Heron Press, Sofia 2005, p. 148-151.
- [4] M. Shopska, Z. Cherkezova-Zheleva, B. Kunev, I. Shtereva, D. Jovanović, J. Krstić, G. Kadinov, I. Mitov, L. Petrov, *Bull. Chem. Commun.*, 2005, **37**/3, 178-184.
- [5] J. Niemantsverdriet, A. Van der Kraan, *J. Phys. Chem.*, 1985, **89**, 67-72.
- [6] A. Lecloux, J. P. Pirard, *J. Colloid Interface Sci.*, 1979, **70**/2, 265-275.
- [7] V. Leon, *Surf. Sci*, 1995, **339**, L931-L934.

THE IMPROVED IRON-EXCHANGED ZEOLITIC MATERIALS ACTIVE FOR H₂O₂ DEGRADATION

M. Milojević¹, V. Dondur¹, Lj. Damjanović¹, V. Rakić², D. Arandelović³,
D. Đorđević⁴ and S. Nikolić-Mandić⁵

¹*Faculty of Physical Chemistry, Studentski trg 12-16, Belgrade (maja@ffh.bg.ac.yu)*

²*Faculty of Agriculture, Nemanjina 6, Belgrade-Zemun; Serbia*

³*Institute of General and Physical Chemistry, Studentski trg 12-16, Belgrade*

⁴*Institute for Chemistry, Technology and Metallurgy, Center for Chemistry, Njegoševa 12, Belgrade*

⁵*Faculty of Chemistry, Studentski trg 12-16, Belgrade*

Abstract

The system comprising heterogeneous iron ions and H₂O₂ is an efficient oxidant of various organic substances in aqueous solutions. In this work FeZSM-5 catalysts were obtained by ion-exchange procedure using Fe-citrate and Fe-oxalate solutions. The activity of synthesized samples for H₂O₂ decomposition is investigated and the influence of synthetic route on the rate of the decomposition is reported. The results presented here indicate that catalyst obtained from Fe-citrate solutions show higher activity for H₂O₂ decomposition than those prepared from Fe-oxalate solutions. Also, the relationship between obtained Fe content in the samples and the half life of H₂O₂ is established.

Introduction

Iron-containing solid materials are catalysts for H₂O₂ decomposition and oxidation reactions of different compounds in the presence of H₂O₂ [1]. Among these materials, iron-containing zeolites are very significant. In zeolitic structures iron can exist as extraframework or framework cation. Iron-containing zeolitic materials have high catalytic activity in the presence of H₂O₂ for the removal of phenol [2] and other organic compounds (dimethylhydrazine [3], methylene blue [4], carboxylic acids [5]). FeZSM-5 catalysts have attracted a lot of attention due to their extraordinary activity for oxidation of benzene to phenol, selective catalytic reduction of NO_x, and the fact that FeZSM-5 could be a promising material for N₂O abatement [6]. In this work, FeZSM-5 catalyst has been synthesized by ion-exchange of ZSM-5 zeolite using Fe-citrate and Fe-oxalate solutions. The influence of this synthetic procedure on the activity of synthesized materials for H₂O₂ decomposition has been studied.

Experimental

FeZSM-5 catalysts have been obtained from a hydrogen form of the zeolite ZSM-5, with Si/Al=15, provided by Zeolyst International. The samples synthesized by aqueous ion-exchange procedure with Fe-citrate solutions are denoted FeZSM-5/cit(1-5), and those synthesized using Fe-oxalate solutions are denoted FeZSM-5/ox(1-5). In both cases, samples 1-3 underwent several cycles while samples 4 and 5 have been obtained by one exchange cycle. For the purpose of comparison, one

sample of FeZSM-5 catalyst was prepared by one ion-exchange cycle using Fe-nitrate solution and is denoted FeZSM-5/nit. The analysis of Fe content in the samples was performed by Atomic Absorption Spectrometry on Varian Spectra AA55. The influence of synthetic route on the structure of ion-exchanged zeolites was analyzed by X-Ray Powder Diffraction (XRPD) method using Philips PW 1729 automated diffractometer in $4 - 65^\circ 2\theta$ range counting at every 0.02° for 0.25 s. The activity of synthesized samples for H_2O_2 decomposition was analyzed spectrophotometrically using UV-VIS Spectrometer GRC CiUltra 10e. The concentration of H_2O_2 was monitored by measuring the decrease in absorbance of the $C_4K_2O_9Ti \cdot 2H_2O$ complex with H_2O_2 at the maximum absorption wavelength of 392 nm.

Results and Discussion

Obtained Fe content in the investigated samples is presented in Table 1.

Table 1. Fe content in the samples

sample	$c_{Fe} \cdot 10^{-4} \text{ mol g}^{-1}$	Fe wt %	$t_{1/2} / \text{min}$
FeZSM-5/cit1	0.13	0.074	165.0
FeZSM-5/cit2	0.28	0.158	77.9
FeZSM-5/cit3	0.48	0.267	38.5
FeZSM-5/cit4	0.23	0.127	120.3
FeZSM-5/cit5	0.28	0.158	77.0
FeZSM-5/ox1	0.04	0.024	308.0
FeZSM-5/ox2	0.16	0.091	194.7
FeZSM-5/ox3	0.14	0.078	216.6
FeZSM-5/ox4	0.11	0.060	203.2
FeZSM-5/ox5	0.28	0.154	192.0
FeZSM-5/nit	0.02	0.012	761.7

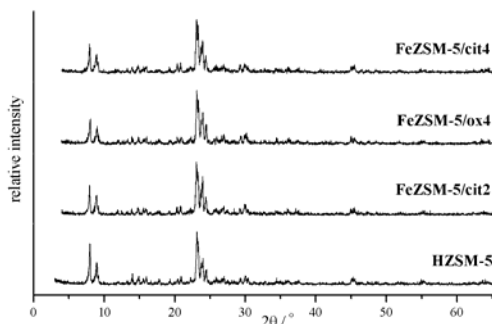


Fig. 1. XRPD results of initial ZSM-5 zeolite and selected FeZSM-5 samples.

The results of XRPD analysis of the initial HZSM-5 zeolite and selected FeZSM-5 samples are presented in Fig.1. It can be seen that crystal structure of ion-exchanged samples does not differ from that of initial zeolite. In this work, the activity of different iron containing catalysts for H_2O_2 decomposition at the room temperature has been compared and evaluated.

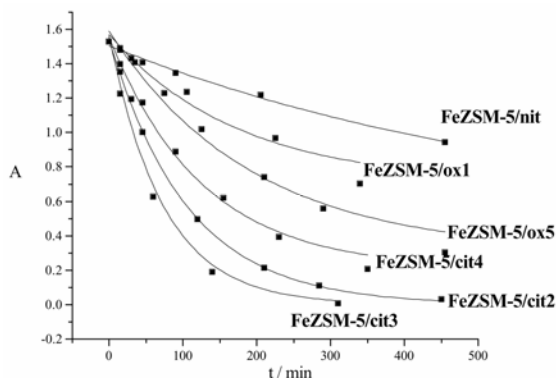


Fig. 2. H_2O_2 decomposition in the presence of FeZSM-5/ox1, FeZSM-5/ox5, FeZSM-5/cit2, FeZSM-5/cit3 and FeZSM-5/cit4 samples.

It is apparent that higher catalytic activity of investigated materials, represented by H_2O_2 decomposition, corresponds to the higher iron content. This effect can be seen for both series of samples - those synthesized from Fe-citrate and from Fe-oxalate solutions.

Acknowledgment

The authors would like to thank Ministry of Science and Environment Protection of Republic of Serbia for financial support within the framework of the project 142055.

References

- [1] N.R.E.Radwana, E.A.El-Sharkawy, A.M.Youssef, *App.Catal.A: General*, 2005, **281**, 93–106.
- [2] A.L.Villa, C.A.Caro, C.M.de Correa, *J. Mol.Catal.A: Chemical*, 2005, **228**, 233–240.
- [3] O.P.Pestunova, G.L.Elizarova, Z.R.Ismagilov, M.A.Kerzhentsev, V.N. Parmon, *Catal. Today*, 2002, **75**, 219–225.
- [4] I.A.Salem,M.S.El-Maazawi, *Chemosphere*, 2000, **41**, 1173-1180.
- [5] G.Centi, S.Perathoner, T.Torre, M.G.Verduna, *Catal.Today*, 2000, **55**, 61–69.
- [6] V.Rakić, V.Rac, V.Dondur, A.Auroux, *Catal. Today*, 2005, **110**, 272–280.
- [7] M.Milojević, Lj.Damjanović, V.Dondur, V.Rakić, *TEHNIKA-Novi Materijali*, 2006, **1**, 7-13.

It has been reported recently, that the ion exchange procedure has an influence on the active sites of the FeZSM-5 catalysts [7]. The ion-exchanged ZSM-5 zeolites obtained from Fe-citrate solutions are more active for H_2O_2 decomposition than those prepared with Fe-oxalate solutions, as shown in Fig.2. The useful indication of the rate of H_2O_2 decomposition is its half life ($t_{1/2}$ of reaction). The calculated half lives for H_2O_2 decomposition in the presence of synthesized materials are presented in Table 1.

KINETIC INVESTIGATION OF THE REACTION BETWEEN NEOMYCIN, HYDROGEN PEROXIDE AND Cu(II) IN AQUEOUS SOLUTIONS

S. M. Sunarić¹ and S. S. Mitić²

¹Faculty of Medicine, Department of Pharmacy, University of Niš, Bulevar dr Zorana Đinđića 81, 18000 Niš, Serbia (ssunaric@medfak.ni.ac.yu)

²Faculty of Natural Sciences and Mathematics, Department of Chemistry, University of Niš, Višegradska 33, P.O.Box 224, 18000 Niš, Serbia

Abstract

The kinetics of neomycin degradation by hydrogen peroxide in the presence of Cu(II) at pH 9.0 was investigated. The influences of temperature, pH and reagents concentration on the reaction were studied. The absorbance of degradation product was measured at 364 nm and the initial-rate method was applied. The pseudo-first order kinetic of antibiotic degradation with hydrogen peroxide and Cu(II) was observed and relative rate constant k_r was calculated at 298 K, 303 K and 308 K.

Introduction

Neomycin is a water-soluble aminoglycoside antibiotic drug, that has been used in the treatment of gastrointestinal and dermatologic infections. It is an antibiotic complex composed of neomycin B, neomycin C and neamine (neomycin A), produced by *Streptomyces fradiae*. Neomycin as the sulfate salt is very soluble in water, hygroscopic and photosensitive, but stable over a wide pH range [1].

The objective of our study was investigation of the behavior of neomycin in the Cu(II)/H₂O₂ system. Catalytic decomposition of H₂O₂ in the presence of Cu(II) ions leads to production of reactive oxygen species (ROS) in Fenton-like reactions [2]. Hydrogen peroxide and ROS, such as superoxide radical O₂^{•-} and hydroxyl radicals OH[•], are also generated in the human body [3]. For that reason, it was interesting to investigate the reaction between neomycin, Cu(II) ion and hydrogen peroxide at physiologically pH and in weak alkaline aqueous solutions.

Experimental

Pure neomycin-sulfate, C₂₃H₄₆N₆O₁₃·3H₂SO₄, was kindly provided by Zdravlje-Leskovac. A stock solution of neomycin (1.00 x 10⁻³ mol/dm³) was freshly prepared by dissolving the required amount of neomycin-sulfate in deionised water; it was stable for 24 h. A solution of Cu(II) (1.00 x 10⁻⁴ mol/dm³) was prepared by dissolving CuCl₂·2H₂O (Merck) in deionised water. A hydrogen peroxide solution (1.00 mol/dm³) was prepared just before use from a 35% commercial reagent (Merck). The bicarbonate buffer, pH 9.0, was obtained from the solutions of NaHCO₃ (1.00 mol/dm³) and Na₂CO₃ (1.00 mol/dm³).

The reaction rate was monitored spectrophotometrically by Perkin Elmer

Lambda 15 UV/VIS spectrophotometer, connected to a thermocirculating bath. The absorbance at 364 nm was measured every 30 s over a period of 1-6 min after mixing of reagents.

Results and Discussion

We found that in the Cu(II)/H₂O₂ system in aqueous solution degradation of neomycin is occurred. This degradation gave rise to the formation of a yellow-color product, having an absorption maximum at 364 nm.

The influence of temperature, pH, hydrogen peroxide and Cu(II) concentration on the reaction of the degradation of neomycin were studied. The initial-rate method was used to determine partial orders [4]. The rate of increase of absorbance of degradation product at 364 nm was measured. The initial rates of the reaction were determined by measuring the slopes of the initial tangents to the absorbance-time curves, dA/dt. The *pseudo*-order with respect to one reactant was determined by arranging that the initial concentrations of the others were held at fixed values.

The reaction was investigated in the interval between pH 6.0 and pH 11. The reaction rate has maximum value at pH 9.0 and it was chosen for experiments. The reaction is *pseudo*-first order with respect to Cu(II) in the concentration range between 0.67-4.00 x 10⁻⁵ mol/dm³, and *pseudo*-first order with respect to H₂O₂ in the concentration range between 0.20-1.33 x 10⁻² mol/dm³ (Table 1). The reaction rate has maximum value at C_{Cu(II)} = 4.00 x 10⁻⁵ mol/dm³ and C_{H₂O₂} = 1.33 x 10⁻² mol/dm³, therefore this concentration were selected for further study.

Table 1. Dependence of the initial rate on the initial concentration of Cu (a), H₂O₂ (b) and neomycin (c).

C _{Cu} x 10 ⁵ (mol dm ⁻³) (a)	Slope x 10 ² (min ⁻¹) (a)	C _{H₂O₂} x 10 ² (mol dm ⁻³) (b)	Slope x 10 ² (min ⁻¹) (b)	C _{Neomyc.} x 10 ⁵ (mol dm ⁻³) (c)	Slope x 10 ² (min ⁻¹) (c)
0.67	0.05	0.20	0.40	1.00	2.10
1.34	0.53	0.33	0.85	1.33	2.40
2.00	1.33	0.40	1.00	1.67	2.70
2.67	1.80	0.67	1.86	2.33	3.35
3.34	2.60	0.80	2.25	3.00	3.75
3.67	2.90	1.00	2.65	3.67	4.35
4.00	2.98	1.33	3.40	4.67	5.05

a) C_{H₂O₂} = 2.00 x 10⁻² moldm⁻³, C_{Neomycin} = 2.33 x 10⁻⁵ moldm⁻³

b) C_{Cu} = 4.00 x 10⁻⁵ moldm⁻³, C_{Neomycin} = 2.33 x 10⁻⁵ moldm⁻³

c) C_{Cu} = 4.00 x 10⁻⁵ moldm⁻³, C_{H₂O₂} = 1.33 x 10⁻² moldm⁻³

Under selected and constant initial concentration of $C_{\text{Cu(II)}} = 4.00 \times 10^{-5}$ mol/dm³, $C_{\text{H}_2\text{O}_2} = 1.33 \times 10^{-2}$ mol/dm³ and pH = 9.0, the rate of the reaction is dependent only on neomycin concentration. The slope of the line obtained as a dependence of reaction rate on neomycin concentration, indicates a *pseudo*-first order reaction with respect to neomycin (Table 1), therefore the proposed kinetic equation is:

$$dA/dt = k_r \cdot C_{\text{Neomycin}} \quad (1)$$

where k_r is a relative rate constant.

The effect of temperature on the reaction rate was investigated over the range 25-35 °C. Decreasing of reaction rate was observed as the temperature increased. The relative rate constant k_r was calculated as the ratio of reaction rate and neomycin concentration at given temperature. In Table 2, k_r is presented as the average value for 3 different concentrations of neomycin at indicated temperature.

Table 2. Constant k_r at three temperatures

T/ K	$k_r \times 10^{-3} \pm \text{SD}^a / \text{dm}^3 \text{mol}^{-1} \text{min}^{-1}$
298	1.50 ± 0.07
303	1.33 ± 0.09
308	1.10 ± 0.12

a. SD, standard deviation of k_r determination for 3 different neomycin concentrations.

Acknowledgement

This research was supported by grant 142015 from the Ministry of Science and Environmental Protection of the Republic of Serbia.

References

- [1] J. N. Delgado and W. A. Remers, Wilson and Gisvold's Textbook of Organic Medicinal and Pharmaceutical Chemistry, 10th ed., Lippincott Williams&Wilkins, 1998.
- [2] J. F. Perez-Benito, Monatsh. Chem., 2001, **132**, 1477.
- [3] I. Fridovich, Annu. Rev. Biochem., 1995, **64**, 97.
- [4] J. M. Mermet, M. Otto, and M. Valcarcel, Analytical Chemistry, 2nd ed., Wiley-VCH, 2004.

PILLARED INTERLAYERED CLAYS AS CATALYST IN THE PRESENCE OF HYDROGEN PEROXIDE

A. Milutinović-Nikolić¹, Z. Mojović¹, P. Banković¹ and A. Rosić²

¹*Institute of Chemistry, Technology and Metallurgy, Department of Catalysis and Chemical Engineering, Njegoševa 12, Belgrade, Serbia. (snikolic@nanosys.ihtm.bg.ac.yu)*

²*Faculty of Mining and Geology, Dušina 7, Belgrade, Serbia.*

Abstract

The metal oxide pillared interlayered clays (PILCs) exhibit high activity in numerous catalytic reactions, among them the catalytic oxidative degradation in the presence of H₂O₂ is getting more attention as alternative water purification method. The Al and Al-Cu PILCs were synthesized from domestic clay, characterized by XRD and the latter tested as a catalyst in the degradation of toluene in the presence of H₂O₂. The decrease of toluene concentration within experimental conditions was observed.

Introduction

PILCs represent a new class of microporous solids that have found a wide range of potential applications in catalytic, adsorption and separation processes. Typically, the preparation of PILCs involves the introduction of bulky inorganic or organic clusters into the interlayer region of clays. When the intercalated species are metal polyoxycations, they are converted after heating at elevated temperatures into the corresponding metal oxide clusters that are rigid enough not only to prevent the interlayer spaces from collapsing, but also to generate micropores larger than those of conventional zeolites [1].

The metal oxide PILCs exhibit high activity in numerous catalytic reactions, among them the catalytic oxidative degradation in the presence of H₂O₂ as a generator of HO• radicals is gaining in importance [2-7]. It is possible to use this reaction as a good alternative water purification method. Therefore in this paper the PILC was synthesized from domestic clay source in order to be tested as a catalyst in the presence of H₂O₂.

Experimental

The starting material was clay, mainly containing smectite with a particle size $\leq 2 \mu\text{m}$. The chemical composition of starting clay employed in the present study given in mass percents was: SiO₂ 57.51; Al₂O₃ 17.13; Fe₂O₃ 7.67; MgO 2.35; CaO 1.81; Na₂O 0.75; K₂O 1.18 and CO₂ 0.5 and ignition loss 11.10 mass % [8]. The pillaring solution was prepared by titrating 0.2M Al(NO₃)₃ solution with 0.2M NaOH at 60 °C for 3 h and left overnight at room temperature in order to obtain oligomeric solutions with OH/Al = 2.0. In the next step the appropriate amount of pillaring solutions, required for the Al/clay ratio to be 10, was slowly added into clay dispersion in distilled water. The final suspension was rigorously stirred at 80 °C for 3 h, followed by stirring at room temperature

overnight, recovered by filtration, washed repeatedly with water, and then dried in air overnight at 110 °C. The obtained sample was calcined at 500 °C for 2 h [9] and referred to as Al PILC. The same procedure was applied in the synthesis of Al-Cu PILC sample only that the part of $\text{Al}(\text{NO}_3)_3$ pillaring solutions was substituted with 0.1 M $\text{Cu}(\text{NO}_3)_2$ solution. Solution volumes were adjusted to have an atomic ratio $\text{Cu}/(\text{Al}+\text{Cu})$ of 10 %.

Philips PW 1710 X-ray powder diffraction spectrometer ($\lambda=0.154178$ nm) was used to identify phases present in investigated samples. The change in d_{001} values of clay caused by pillaring process was investigated on previously oriented samples.

0.5g of the solid catalyst was added to 100 ml of an aqueous toluene solution (2×10^{-3} M) at the atmospheric pressure, ambient temperature and under continuous stirring. The same suspension was prepared and left to settle without stirring. After 15 min, 160 μl of an aqueous H_2O_2 solution (3 M) was added to the initial suspensions, which was regarded as a starting point of the reaction. 5 ml aliquots were taken at pre-determined periods of time (2, 4, 6, 8 and 24 h) and, after having the phases separated by centrifugation (5000 rpm, 60 min), analyzed using Thermo Electron Nicolet Evolution 500 UV-VIS spectrophotometer in the wavelength range from 190-300 nm. Toluene absorption peak at 268 nm was chosen for the further toluene degradation analysis.

Results and Discussion

According to XRD the following phases were identified in investigated samples: smectite, quartz, calcite, feldspar, illite and a small amount of amorphous phase [10]. It was observed that all the characteristic peaks of smectite gradually decrease during the pillaring procedure. The peak (001) shifts during different stages of the pillaring process. The Na-exchanging process lowered d_{001} from 1.53 (for starting clay) to 1.28 nm, but clay retained its swelling properties.

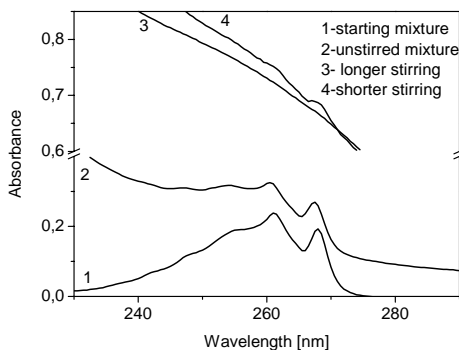


Fig. 1. UV spectra

The 261 and 268 nm UV absorption peaks characteristic for toluene are clearly distinct in curves 1 (starting mixture of toluene and H_2O_2) and 2 (spectra of the unstirred mixture). The toluene degradation could be deduced from the continuous disappearance of the 268 nm UV absorption peak characteristic for toluene in the case of the stirred

The pillaring process enlarged and fixed the basal spacing of the clay, $d_{001}=1.70$ nm and $d_{001}=1.80$ nm for Al PILC and Al-Cu PILC, respectively.

Mild H_2O_2 and Al-Cu PILC catalyst absorption occurs at the chosen wavelength interfering with the toluene peak, making it inappropriate for a more profound quantitative analysis. As illustration, the UV spectra of different mixtures are given in Fig. 1.

mixture. This is obvious from curves 3 (spectra of the stirred mixture after 24 h) and 4 (spectra of stirred mixture after 4 h), while the unstirred one didn't show any change in its UV spectra with time. In the future work other methods of physical-chemical analysis, such as TOC and HPLC, are found to be necessary in order to obtain more accurate toluene degradation information.

Conclusion

The Al and mixed Al-Cu pillared interlayered clays were synthesized from domestic clay and characterized by XRD. The efficiency of obtained Al-Cu PILC was tested as catalysts in the catalytic oxidative degradation of toluene in the presence of H₂O₂. It was observed that stirring evidently increases the number of the reactive species collisions, which makes it crucial for the progress of the reaction. This type of degradation appears to be slower in the case of toluene than when phenol was subjected to it in similar experimental procedures carried out by other researchers [3, 5, 6]. Nevertheless, the obtained results suggested that further investigation should be performed in order to have optimal catalytic conditions determined.

Acknowledgements:

This work was supported by the Ministry of Science & Environmental Protection of the Republic of Serbia (Projects TR6712B, TD7057B and 142019B).

References

- [1] H.J. Chae, I.-S. Nam, S.W. Ham, S.B. Hong, *Catal. Today*, 2001, **68**, 31–40.
- [2] H. Debellefontaine, M. Chakchouk, J. N. Foussard, D. Tissot, P. Striolo, *Environ. Pollut.*, 1996, **92**(2), 155-164.
- [3] J. Barrault, C. Bouchoule, K. Echachoui, N. Frini-Srasra, M. Trabelsi, F. Bergaya, *Appl. Catal. B: Environ.*, 1998, **15**, 269-274.
- [4] J. Barrault, M. Abdellaoui, C. Bouchoule, A. Majesté, J.M. Tatibouët, A. Louloudi, N. Papayannakos, N.H. Gangas, *Appl. Catal. B: Environ.*, 2000, **27**, L225–L230
- [5] J. Barrault, J.-M. Tatibouët, N. Papayannakos, *C.R. Acad. Sci., Ser. IIC: Chim.*, 2000, **3**, 777–783.
- [6] J.G. Carriazo, E. Guelou, J. Barrault, J.M. Tatibouët, S. Moreno, *Appl. Clay Sci.*, 2003, **22**, 303– 308.
- [7] S.-C. Kim, D.-K. Lee, *Catal. Today*, 2004, **97**, 153–158.
- [8] Z. Vuković, A. Milutinović-Nikolić, J. Krstić, A. Abu-Rabi, T. Novaković, D. Jovanović, *Mater. Sci. Forum*, 2005, **494**, 339-44.
- [9] P. Faralas, F. Lezov, P. Pomonis, A. Ladauos, *J. Electroanal. Chem.*, 2000, **486**, 156-165.
- [10] International Center for Diffraction Data, Joint Committee on Powder Diffraction Standards (JCPDS) 1990, Swarthmore, USA.

MESOPOROUS MATERIALS AS SUPPORTS OF RH CATALYSTS. CATALYTIC APPLICATION

C. Blanco, V. Krstić, P. Carranceja, C. Pesquera and F. González

*Group of Inorganic Chemistry, University of Cantabria, E-39005 Santander, Spain.
blancoc@unican.es*

Abstract

Mesoporous materials like MCM-41 and SBA-15 have been synthesised and used as supports to prepare Rh and Rh-Sn catalysts by adsorption in solution. These catalysts were applied in the hydrogenation of acetone. The catalytic reaction was carried out at atmospheric pressure and mild conditions. We found that a conversion and selectivity to methyl isobutyl ketone (MIBK) with Rh1.7Sn/SBA-15 catalyst is better than the same catalyst support on MCM-41.

Introduction

Silica mesoporous materials, MCM-41 and SBA-15, which have a hexagonal ordering, have great interest in adsorption and catalysis [1]. These materials have physico-chemical properties potentially suitable for its use as supports of catalysts: high specific surface, high, regular and controlled porosity, high thermal stability, capacity of adsorption and the distribution homogeneity of centres. For this reason, they offer a wide range of possibilities for the design and synthesis of supported metal-catalysts [2], materials in which can be incorporated active metallic phase in the network or as supports of catalyst, in supported metal-catalysts. On the other hand, a great dependency exists between surface properties and the incorporation of the catalytic active phase, metallic dispersion for some heterogeneous catalysts or adsorbents.

Therefore, the objective of this work is to synthesis, characterise and to study the surface properties of systems of Rh supported (only or promoted with Sn) in mesoporous materials (MCM-41 and SBA-15). Also, it will be analysed the effect of the support in the incorporation of the active phase and in the activity/selectivity in the hydrogenation of acetone in gas phase and atmospheric pressure, as well as the influence of different work variables and the addition of different percent of Sn. In order to carry out this objective it will be used diverse techniques of adsorption, as much in the characterization of the used supports, as in the preparation of the catalysts of Rh or Rh/Sn supported.

Experimental Section

Mesoporous materials: MCM-41 and SBA-15 were synthesized in the laboratory. In order to carry out the synthesis of the MCM-41 an aqueous solution of silica, tetramethylammonium hydroxide (TAMOH) and cetyltrimethylammonium bromide (CTABr) were used. The molar compositions of the gel were: $1\text{SiO}_2/0.25\text{CTABr}/0.1\text{TMAOH}/100\text{H}_2\text{O}$. This mixture was subjected to hydrothermal treatment during 48 h. In the synthesis of material SBA-15 it was used the tetraethyl

orthosilicate (TEOS) as silicon source and mixed with a polymer in acid medium. The resultant gel was transferred to a static teflon-lined stainless steel autoclave under autogeneous pressure and heated to 100 °C for 24 hours. After that, both solid were filtered, dried at 60 °C overnight and finally calcined at 550°C during 6h in air.

The incorporation of the metallic phase (1%Rh) on the supports was made in ce-tonic medium by adsorption in organometallic solution of Rh at room temperature [3]. The percentages of Sn were aggregate, in its case, previous incorporation to the Rh, and were carried out by adsorption in solution through acetate of Sn, with loads of 1 and 1.7%.

The synthesized MCM-41 and SBA-15 materials and the prepared systems of Rh (precursor and catalyst) were characterized by different physico-chemical techniques: XRD, IR, adsorption-desorption of N₂, adsorption-desorption of NH₃, thermal analysis, UV-Vis Spectroscopy and chemisorption of O₂-H₂.

The catalytic behaviour was studied in the reaction of hydrogenation of acetone in gas phase and atmospheric pressure at temperatures between 120 and 180°C. All the systems of Rh/support and Rh promoted with Sn/support were reduced in situ at 300°C under flow of hydrogen. The products of the reaction of the hydrogenation of acetone were analyzed by GC.

Results and Discussion

In Table 1 the textural parameters of the supports synthesized are gathered, which have been obtained from the adsorption-desorption isotherms of nitrogen. From these data it is observed that the specific surface of both materials is similar, while there is a great difference in the average pore radius, being the value of material SBA-15 higher than that of MCM-41 support. This data is in agreement with the type of reagents used for the synthesis of each material.

Table 1. Acidity and textural parameters of the samples: MCM-41 and SBA-15.

Sample	S _{BET} (m ² /g)	Rp (nm)	NH ₃ (cc/g)	N ^o acid centres /g
MCM41	784	1.54	0.38	1.02×10 ¹⁹
SBA-15	676	5.05	0.32	0.86×10 ¹⁹

Also, in Table 1 are the data of volume of ammonia adsorbed and from them it can be obtained the number of acid centres per gram for each material. The results that present acidity of both materials are very small, because for the synthesis of these samples has been used only silicon.

From the data of Table 2, we can said, that the incorporation and dispersion of the Rh without the presence of tin are similar for both supports, MCM-41 and SBA-15. The presence of tin and its proportion follow different behaviour (incorporated percentage of Rh and dispersion) for the different supports used.

The catalytic behaviour of the catalysts depends on the textural properties of the different supports used on the preparation of catalysts. In the mild conditions used, the

Rh1.7Sn/SBA-15 catalyst is, in general, much more selective towards the metil isobutyl ketone (MIBK), whereas the rest of the catalysts are more selective towards isopropanol. These facts are probably due to the greater size of pores that has SBA-15 support than MCM-41, and, of course, the promoter effect that perform the Sn on the Rh.

Table 2. Data of Rh (%) incorporated, metallic dispersion (D %), average size of particle (d), conversion of acetone (C %) and selectivity of MIBK (S %).

Catalyst	Rh %	D %	C%	S%
Rh/MCM-41	0.45	2.48	-	-
Rh1Sn/MCM-41	0.77	31.00	-	-
Rh1.7Sn /MCM-41	0.95	45.00	10.5	0.0
Rh/SBA-15	0.43	2.86	0.7	0.0
Rh1Sn/SBA-15	0.75	7.21	13.0	0.0
Rh1.7Sn/SBA-15	0.64	3.42	8.2	18.8

Conclusion

It is possible to conclude that synthesized material SBA-15, has resulted a better support to prepare systems of Rh and Rh promoted with Sn; existing a clear dependency of the selectivity of the reaction (to obtain MIBK), with presence and percent of Sn like promoter, the temperature of reaction and the characteristics of the material used like support.

Acknowledgments

Our acknowledgments to D. G. I. of M.C. y T. for financial support of this work under projects: MAT2005-04924 and MAT2005-03914.

References

- [1] J.S. Beck, J.C. Vartuli, W.J. Roth, M.E. Leonowicz, C.T. Kresge, K.D. Schmitt, C.T.-W. Chu, D.H. Olson, E.W. Sheppard, S.B. McCullen, J.B. Higgins, J.L. Schlenker, *J. Am. Chem. Soc.*, 1992, **114**, 10834.
- [2] G. Calleja, J. Aguado, A. Carrero, J. Moreno, *Catal. Commun.*, 2005, **6**, 153.
- [3] C. Blanco, R. Ruiz, C. Pesquera, F. González, *Current Topics Catal.*, 2005, **4**, 113.

KINETICS OF ACID CATALYZED SUCROSE HYDROLYSES IN THE MICROWAVE FIELD

B. Adnađević, J. Jovanović and M. Sindić

Faculty of Physical Chemistry, Studentski Trg 12-16, Belgrade, Serbia

Abstract

The influence of microwave field at isothermal acid catalyzed sucrose hydrolyses was investigated. By applying "model fitting" method it was confirmed that kinetics of the acid catalyzed sucrose hydrolyses in the microwave field obeys to the kinetics of the pseudo-first order chemical reaction. It was found that under the influence of the microwave field the kinetics parameters of the acid catalyzed sucrose hydrolysis are significantly changed compared to the conventional isothermal conditions.

Introduction

Sucrose is used in the food industry as a precursor of invert sugar through its partial or total hydrolysis and in in the non-food industry. The efficiency of sugar factory and refinery processes as well as the end product quality is affected by degradation of sucrose under industrial processing conditions.

In the papers of Bucheman [1], Vukov [2] and Pinter[3] kinetics of isothermal acid catalyzed sucrose hydrolyses under the conventional conditions (thermal activation) is investigated in details. The values of the kinetics parameters of that process are determined to be as follows: $E_a = 108-109$ kJ/mol and $\ln A = 33.47$.

Bearing in mind that microwave field leads to the significant enhancement of the chemical reaction [4], in this work the influence of microwave field at isothermal acid catalyzed sucrose hydrolyses was investigated.

Experimental

Acid catalyzed sucrose hydrolyses is undertaken in the microwave reactor CEM Discover, produced by CEM Co., Matthews, USA. The hydrolyses conditions was as follows: starting sucrose concentration $C_0 = 100$ g/l, acid type: sulfuric acid; molar ratio acid/sucrose=3; reaction temperature was in the interval $T = 25-45$ °C; reacting time: $t = 0-12$ minutes; microwave power untill predetrmined tempreature was reached $P_1 = 70$ W and after that $P_2 = 10$ W. Degree of sucrose conversion (α) was determined

according to equation (1):
$$\alpha = \frac{c_i}{c_{max}} \quad (1)$$

where c_i is glucose concentration at time interval t , and c_{max} is maximal achieved glucose concentration during reaction. Glucose concentration was determined by applying advanced Milers spectrophotometry method (5) on a Cintra 10e, UV-Visible Spectrometer, Serial No. V 3163, U.K

Results and Discussion

Figure 1 presents kinetics conversion curve of isothermal acid catalyzed sucrose hydrolyses undertaken in the microwave field.

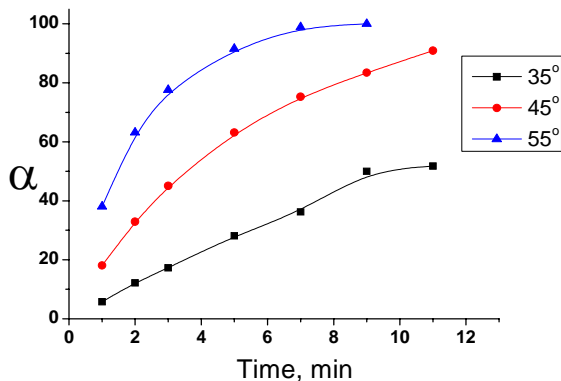


Fig. 1. Kinetics curve of isothermal acid catalyzed sucrose hydrolyses in the microwave field (power $P_1=70\text{W}$ and $P_2=10\text{W}$)

At the conversion curve of isothermal acid catalyzed sucrose hydrolyses in the microwave field clearly are distinguished two characteristic shapes of changes of degree of sucrose conversion (α) with the interacting time: a linear and a non-linear. The interacting temperature increase leads to the increase of maximal degree of hydrolyses and shortness to the duration of the linear changes of degree of sucrose conversion with time.

By applying “model fitting” method [6] it was confirmed that kinetics of the acid catalyzed sucrose hydrolyses in the microwave field obeys to the kinetics of the pseudo-first order chemical reaction. Isothermal dependences $-\ln(1-\alpha) = kt$ is presented at Figure 2.

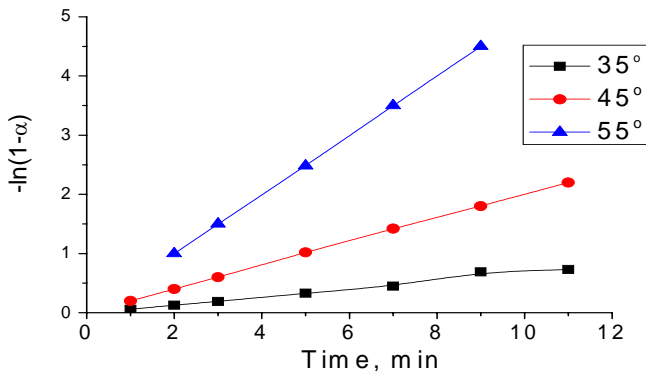


Fig. 2. A plot of isothermal dependences $-\ln(1-\alpha)$ from time

The changes of the model constants of the sucrose hydrolysis rate with temperature are presented at Table 1.

Table 1. Model constant of the sucrose hydrolysis rate

Temperature, °C	k, min ⁻¹	Ea, kJ/mol	lnA
35	0.067		
45	0.199	85.47	30.71
55	0.527		

The kinetic parameters (activation energy (Ea) and pre-exponential factor-(lnA)) of the investigated process of the acid catalyzed sucrose hydrolysis are determined by applying Arrhenius equation. The values of the calculated kinetics parameters are presented at Table 1, column 3 and 4. Under the influence of the microwave field, compared to the conventional isothermal conditions comes to the significant changes of the kinetics parameters of the acid catalyzed sucrose hydrolysis. Actually, activation energy lowers for 22% and pre-exponential factor lnA drops down for 9% compared to conventional conditions. The established decrease of the kinetic parameters of the sucrose hydrolyses process in the microwave field is a consequence of the changes of a reaction pathway of the reaction which occurs because H⁺ absorbed energy of microwave field.

Conclusion

The influence of microwave field at isothermal acid catalyzed sucrose hydrolyses is investigated. It was found that under the influence of the microwave field, compared to the conventional isothermal conditions comes to the significant changes of the kinetics parameters of the acid catalyzed sucrose hydrolysis. For this process the activation energy was lowered for 22% and pre-exponential factor lnA for 9% compared to conventional conditions.

References

- [1] S.Buchaman, G.Kubler, C.Meigs, M.Owens, A.Tallman, *Int.J.Chem.Kinet.*, 1983, **15**, 1229.
- [2] K.Vukov, *Int.Sugar J.*, 1967, **67**, 172.
- [3] A.Pintar, J.Batista, J.Levac, *Analyst*, 2002, **127**, 1535-1540.
- [4] K.D. Raner, C.R. Strauns, *J.Org.Chem*, 1992, **57**, 6231.
- [5] G.L.Miller, *Anal.Chem.*, 1959, **31**, 426-428.
- [6] M.E. Brown, D.E.Dollimore, A.K. Galwey, *Reactions in the solid state*, Comprehensive chemical kinetics, Elsevier 1980, **22**, 87-91.

KINETICS OF Cu^{2+} BINDING TO THE POLY(ACRYLIC ACID) HYDROGEL

A. Kostić¹, J. Jovanović², B. Adnađević² and A. Popović³

¹ Faculty of Agriculture, Nemanjina 6, Zemun, Belgrade, Serbia

² Faculty of Physical Chemistry, Studentski Trg 12-16, Belgrade, Serbia

³ Faculty of Chemistry, Studentski Trg 12-16, Belgrade, Serbia

Abstract

Isothermal kinetics of binding of copper to the poly(acrylic acid) hydrogel were investigated. The new model of kinetics for investigated process was established and kinetic parameters are determined. It was found that process has been controlled by diffusion or kinetically controlled depending on temperature.

Introduction

Polymer materials are widely used type of materials and the most popular in present time are so called "hydrogels". Hydrogels based on acrylic acid are known as specific materials because of their biocompatibility, nontoxicity, hydrophilicity, etc. Due to this properties they have been used in medicine and pharmacy [1, 2], environmental protection, agriculture. In recent time environmental protection has been confronted with increased contamination of waste water by heavy metals ions. They are metabolic poisons and enzyme inhibitors. Several ways of releasing of heavy metals ions have been known. For removal of heavy metals ions as pollutant different polymeric materials have been applied. To that effect absorption of copper has become an object of many testing. Kaşgöz *et al* in several works used modified polyacrylamide for removal of copper [3, 4]. Some authors suggested that copolymer of a polyacrylamide and polyacrylic acid should be of use for the recovery of copper from environment [5]. Aim of this work was to investigate kinetics of Cu^{2+} binding to the poly(acrylic acid) hydrogel.

Experimental

Materials: Acrylic acid (AA) was supplied by Merck A. G., Germany. N,N-methylene bisacrylamide (MBA) was purchased from Aldrich Chemical Co., Milwaukee, USA. Initiator, 2,2-Azobis-[2-(2-imidazolin-2-il)-propan]Dihydrochlorid, (AIPD) was supplied by Wako Pure Chemicals Industries, Ltd, USA. Copper-sulfate pentahydrate, $\text{CuSO}_4 \cdot 5\text{H}_2\text{O}$ was purchased from Zorka Pharma, Sabac, SCG. All substances were used as received without further purification. *Poly(acrylic acid) hydrogels (PAA):* were synthesized by simultaneous radical polymerization and crosslinking using AIPD as an initiator and MBA as a cross-linking agent, in general using experimental procedure previously described [6]. *Binding of copper to the PAA hydrogel:* Pre-weighed dry samples, with average weight of 0.1g, were immersed in solution of 0.01M CuSO_4 at different temperature. Aliquots of solution were taken at predetermined time intervals. The amount of copper was determined by atomic absorption

spectrometry using Varian SpectrAA 55 atomic absorption spectrometer. Specific quantity of binded Cu^{2+} (X) was determined according to (1):

$$X = \frac{C_o - C_i}{m} \cdot V \quad (1)$$

where C_o is Cu^{2+} concentration of the starting copper solution and C_i is Cu^{2+} -concentration at time t , V - volume of the Cu^{2+} solution, and m - hydrogel sample mass. Degree of binded Cu^{2+} was determined as:

$$\alpha = X/X_{max} \quad (2)$$

where X_{max} - is maximal quantity of binded Cu^{2+} .

Results and Discussion

Figure 1 presents kinetics curves of isothermal binding of Cu^{2+} to the PAA hydrogel. Kinetics of the investigated process of Cu^{2+} binding to the PAA was investigated by applying “model fitting” method [7]. This method is based on the graphical and analytical comparison of the determined reduced kinetics curves ($\alpha = f(t)$) with the model reduced kinetics curves.

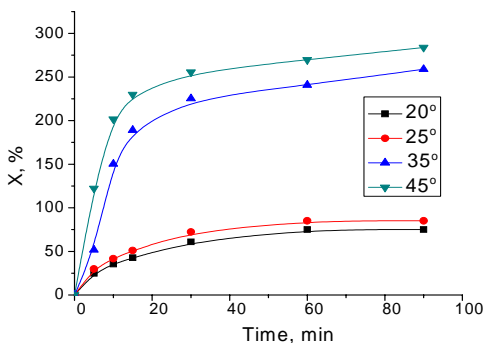


Fig 1. Kinetics curves of isothermal binding of Cu^{2+} to the PAA hydrogel

the process is kinetically controlled. The changes of the model constants of Cu^{2+} binding rate with temperature are presented at Table 1.

Table 1. Model constants of the Cu^{2+} binding rate

Temperature, °C	k , min^{-1}	E_a , kJ/mol	$\ln A$
20	0.022	10.45	0.48
25	0.024	10.45	0.48
30	0.250	25.67	8.65
35	0.350	25.67	8.65

Figures 2 and 3 presents dependence of α^2 on interacting time (for temperatures below 30 °C) and $1/(1-\alpha)$ on interacting time (for temperatures above 35 °C), respectively. Based on the results presented on Figures 2 and 3 one may conclude that the investigated process of Cu^{2+} binding to PAA at temperatures below 30 °C is a process that is controlled by diffusion, while at temperatures higher than 35 °C the process is kinetically controlled.

values are presented at column 3 and 4. At temperatures $T < 30\text{ }^{\circ}\text{C}$ kinetics of Cu^{2+} binding is limited with kinetics of Cu^{2+} diffusion to the active centers of the PAA hydrogel and E_a of that process is predetermined with the E_a for diffusion of Cu^{2+} ions in the solution. On the contrary to that, at temperatures $T > 35\text{ }^{\circ}\text{C}$ kinetics of binding is determined with kinetics of interaction of Cu^{2+} with active centers of the PAA and activation energy is defined with energy which is necessary to Cu^{2+} leave the hydrated complex.

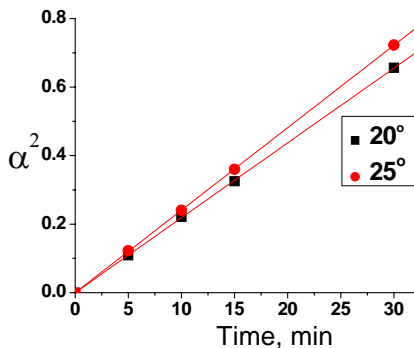


Fig. 2. A plot of α^2 from time

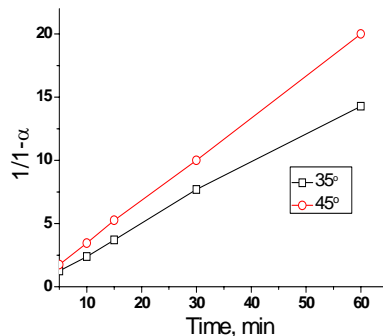


Fig. 3. A plot of $1/(1-\alpha)$ from time

Conclusion

Poly(acrylic acid) hydrogel has been synthesized. Kinetics of isothermal binding of Cu^{2+} was investigated. It was found that the investigated process of Cu^{2+} binding to PAA hydrogel at temperatures below $30\text{ }^{\circ}\text{C}$ is a process that is controlled by diffusion, while at temperatures higher than $35\text{ }^{\circ}\text{C}$ that process is kinetically controlled.

References

- [1] N. A. Peppas; A. G. Mikos, "Hydrogels in Medicine i Pharmacy", Vol. I: Fundamentals, CRC Press, Boca Raton, Florida, 1986, p. 2-23.
- [2] B. D. Ratner; A. S. Hoffman, in "Hydrogels for Medical and Related Applications", Andrade and Andrade, eds., American Chemical Society, Washington DC, 1976, p. 1-36.
- [3] H. Kaşgöz; S. Özgümüş; M. Orbay, Polymer, 2001, **42**, 7497-7502.
- [4] H. Kaşgöz; S. Özgümüş; M. Orbay, Polymer, 2003, **44**, 1785-1793.
- [5] W. Li; H. Zhao; P. R. Teasdale; R. John; S. Zhang, Reactive & Functional Polymer, 2002, **52**, 31-41.
- [6] J. Jovanović, B. Adnadević, S. Ostojčić, M. Kićanović, Mater. Sci. Forum, 2004, **453-454**, 543-548.
- [7] M.E. Brown, D.E. Dollimore, A.K. Galwey, Reactions in the solid state, Comprehensive chemical kinetics, Elsevier 1980, **22**, 87-91.

SYNTHESIS OF METHYL-ESTHERS BY LIPASE-CATALYZED TRANSESTERIFICATION IN METHANOL

L. Izrael-Živković¹, I. Karadžić¹ and M.M.Vrvić²

¹ School of Medicine, Department of Chemistry, University of Belgrade, Visegradska 26, Belgrade

² Faculty of Chemistry, University of Belgrad, Studentski trg 16, 11001 Belgrade, Serbia

Abstract

Lipases are among the most promising and important biocatalysts for carrying out reactions in both aqueous and non-aqueous media. Although the natural lipolytic reaction in water solutions is hydrolysis of carboxylic esters, lipases can also catalyze reactions in organic solvents (or water restricted medium).

Lipase from *P. aeruginosa* san-ai catalyses synthesis of methyl-esters in pure methanol. The reaction can be described by the Michaelis-Menten model with kinetic parameters of transesterification in non-solvent conditions on four *p*-nitrophenyl-esters (*p*-NP-esters) as substrates. Values of V_{\max} and k_{cat} for *p*-NP-laurate and *p*-NP-butyrate are significantly higher than for *p*-NP-palmitate and *p*-NP-caprylate, as well as the comparison of K_m values shows that the affinity of enzyme for *p*-NP-butyrate is very low, while for *p*-NP-caprylate is relatively high, suggesting that preferable substrates are middle and long chain esters.

Introduction

The tremendous potential of enzymes as catalysts in water solutions is well known, but their remarkable stability and capacity to work in water-restricted environments, including anhydrous organic solvents, have been recognized recently [1]. Moreover substrate, stereo-, regio- and chemoselectivity of the enzymes become markedly different in non-aqueous solutions [1]. Even though bioconversions by enzymes must often be carried out in the presence of organic solvents, only a few enzymes naturally stable in organic solvents have been reported [2]. Microbial enzymes, particularly those produced by extremophiles, are very often naturally stable and active in non-aqueous solvents. The phenomenon of enzymatic catalysis in organic solvent appears to be due to the structural rigidity of proteins in organic solvents resulting in high kinetic barriers that prevent native-like conformation from unfolding. Stability and activity of enzymes in mixtures of water and organic solvents are of special importance for bioconversion of substrates that are moderately soluble, or even insoluble, in water.

Lipases are among the most promising and important biocatalysts for carrying out reactions in both aqueous and non-aqueous media. This is primarily due to their ability to utilize a broad spectrum of substrates [3] having high chemo-, regio- and enantioselectivity in the synthesis or hydrolysis of lipid compounds, as well as their stability under a wide range of conditions.

Strain *Pseudomonas aeruginosa* san-ai was isolated from putrid mineral cutting oil used as metalworking fluid (MWF) in the metal industry [4] in Japan and provided from Osaka TRI, group of enzyme engineering. In medium containing fats, mineral oil and surfactants as a sole source of carbon, only microorganisms which secrete a lipase with specific properties can survive and grow. Strain *P. aeruginosa* san-ai secrete the unique lipases, which has been characterized [5].

From a biotechnological point of view, there may be remarkable advantages in employing lipases for enzymatic conversions in organic solvents, *e.g.* better solubility of substrates in organic solvents, the ability to carry out a reaction impossible in water because of kinetic restrictions, improved stability of these enzymes accompanied with their insolubility in organic solvents, that allows for their recovery and reuse [6]. Lipase, as an enzyme which functions in organic solvent, present a new opportunity in the area of applied enzyme catalysis.

Materials and Methods

Materials *p*-nitrophenyl-palmitate, *p*-nitrophenyl-laurate, *p*-nitrophenyl-caprylate and *p*-nitrophenyl-butyrate were purchased from Sigma Chemical (St. Louis, Mo, USA). Methanol was purchased from Merck (Darmstadt, Germany).

Lipase powder preparation After submerge growth of *P. aeruginosa* san-ai in LB medium for 72h, culture broth was collected and centrifuged at 10000 rpm for 20 min, and the supernatant was then lyophilized. The resulting dry powder was used as the crude enzyme preparation for reactions in the organic solvents.

Protein concentration determination The protein concentration was determined by the Bradford method [7] using crystalline BSA as a standard.

Transesterification (Methanolysis of *p*-nitrophenyl-esters) Enzymatic reaction was initiated by addition of crude lipase powder to solution of substrate in methanol. The lipase activity was measured spectrophotometrically. The enzyme reaction mixture was incubated at 37 °C and absorbance measured at 410 nm for the first 3 min. of reaction. Aliquots were analyzed by gas chromatography on HP 5890 s.

Results and Discussion

The natural reaction of lipase is hydrolysis of carboxylic esters. Enzymatic hydrolysis involves water as a substrate (nucleophile). As it was previously found that lipase from *P. aeruginosa* san-ai is stable in different organic solvents including methanol, we assumed that the lipase can also utilize methanol as a nucleophile, thus replacing hydrolysis with transesterification.

Enzymatic reaction was carried out in methanol, by lipase powder using of *p*-NP-esters, as substrate. Gas chromatography analysis confirmed the formation of methyl-esters as products of enzyme reaction in methanol.

On the basis of classical mechanism of lipase catalysis in water, the kinetic scheme of lipase-catalyzed transesterification in non-water environments is likely to involve formation of noncovalent enzyme-ester complex, formation of intermediate which

then interacts with nucleophile (methanol). This complex yields to the new ester and the free lipase.

In the contrast to kinetic of hydrolysis of lipase in water which cannot be described with Michaelis-Menten model, reaction of transesterification catalyzed by lipase from *P. aeruginosa* san-ai in methanol obey Michaelis-Menten kinetics. For the enzyme kinetic analysis the rate of methyl-esters formation was measured at different substrate concentration and the data were fit to the Michaelis-Menten equation using EZ-FIT software package [8]. As it is shown in table 1., values of V_{max} and k_{cat} for *p*-NP-laurate and *p*-NP-butyrate are significantly higher than for *p*-NP-palmitate and caprylate, and the value of K_m for *p*-NP-butyrate is significantly higher then for the other *p*-NP-esters, meaning that the affinity of enzyme for *p*-NP-butyrate is the lowest and for *p*-NP-caprylate is the highest. Previously reported kinetic parameters for the comparison to another lipase-catalyzed methanolysis were not found to date.

Table 1. Kinetic parameters of transesterification catalyzed by *P. aeruginosa* san-ai lipase in methanol

Substrate	v_{max} (mol/L min)	$x10^{-3}$	$K_m \times 10^{-3}$ (mol/L)	k_{cat} (1/s)	k_{cat}/K_m (mol/L $\times s)^{-1}$
<i>p</i> NP-palmitate	0.242		4.22	10.9	2583
<i>p</i> NP-laurate	0.358		6.39	16.13	2524
<i>p</i> NP-caprylate	0.238		4.01	10.7	2668
<i>p</i> NP-butyrate	0.387		19.11	17.43	910

Conclusion

The study has shown that extracellular lipase from *P. aeruginosa* san-ai successfully catalyses transesterification in methanol. The catalytic efficiency of the enzyme in methanol is high, and its action can be described by conventional Michaelis-Menten kinetics. It seems as quite possible that many enzymes can function in organic solvent but the challenge is finding the appropriate conditions, what could create new opportunities in the area of applied enzyme catalysis, particularly in methanolysis of vegetable oils using lipase, for the production of biodiesel.

References

- [1] A. Klibanov, Nature, 2001, **409**, 241-246.
- [2] H. Ogino and H. Ishikawa, J. Biosci. Bioenerg., 2001, **91**, 106-116.
- [3] A. Pandey, C. Benjamin Soccol, P. Nigam, N. Krieger and V. Soccol, Biotechnol. Appl. Biochem., 1999, **29**, 119-131.
- [4] I. Karadzic, A. Masui and N. Fujiwara, J. Biosci. Bioenerg., 2004, **98**, 145-152.
- [5] I. Karadzic, A. Masui, L. Izrael Zivkovic and N. Fujiwara, J. Biosci. Bioenerg., 2004 in press
- [6] A. Zaks and A. Klibanov, Proc. Natl. Acad. Sci. USA, 1985, **82**, 3192-3196.
- [7] M. M Bradford, Anal. Biochem., 1976, **72**, 248-254.
- [8] F. Perella, Anal. Biochem., 1988, **174**, 437

KINETIC DETERMINATION OF THYROXINE TRACES BASED ON THE MANGANESE(III) METAPHOSPHATE-ARSENIC(III) REACTION IN THE PRESENCE OF ORTHOPHOSPHORIC ACID

F. T. Pastor, G. A. Milovanović and M. Todorović

Faculty of Chemistry, University of Belgrade, P.O. Box 158, Belgrade, Studentski trg 12-16, Serbia

Abstract

The kinetics of the thyroxine-catalyzed Mn(III) metaphosphate - As(III) reaction was studied in the presence of orthophosphoric acid. The reaction rate was followed spectrophotometrically at 516 nm. It was established that orthophosphoric acid increased the reaction rate and that the extent of the non-catalytic reaction was extremely small. A kinetic equation was postulated and the apparent rate constant calculated. The dependence of the reaction rate on temperature was investigated and the energy of activation and other kinetic parameters determined.

Thyroxine was determined under the optimal experimental conditions in the range 5.5 - 23 ng mL⁻¹ with a relative standard deviation up to 6.7 % and a detection limit of 2.1 ng mL⁻¹.

Introduction

Thyroxine is a thyroid hormone which regulates the rate of cellular oxidative processes in human body. A deficient or excessive production of thyroid hormones result clinical disorders in thyroid function in man, hypothyroidism and hyperthyroidism. In the case of hypothyroidism thyroxine preparations are favoured for therapeutic use. It is the reason why it is a great need for sensitive analytical methods for trace determination of thyroxine.

In order to propose a sensitive, simple and inexpensive method for the determination of thyroxine traces we studied kinetics of the thyroxine catalyzed manganese(III)-metaphosphate-arsenic(III) reaction in the presence of orthophosphoric acid.

Experimental

Mn(III) solution in 3.1 mol L⁻¹ metaphosphoric acid was prepared as in our previous paper [1]. The stock (1.00 × 10⁻³ mol L⁻¹) solution of thyroxine was prepared by dissolving L-thyroxine Sigma T2376 (≥98%, HPLC), in 0.020 mol L⁻¹ HCl in ethanol.

The reaction was carried out in a special three-compartment vessel [2]. The solution of Mn(III) metaphosphate and orthophosphoric acid were placed in the first, thyroxine solution in the second, and As(III) and water, to a total volume of 12 mL, in the third compartment of the vessel. After the vessel was thermostated to 25±0.1 °C, the reaction was started by mixing the reactants. The absorbance of the solution was then measured at 516 nm every 15 s during the first five minutes of the reaction. All measurements were performed at constant ionic strength $I = 1$ (KNO₃).

Results and Discussion

The absorption spectra of Mn(III) metaphosphate solution ($7.0 \times 10^{-3} \text{ mol L}^{-1}$) (a), Mn(III) metaphosphate solution in the presence of orthophosphoric acid (2.0 mol L^{-1}) (b), Mn(III) metaphosphate solution in the presence of orthophosphoric acid and As(III) ($2.5 \times 10^{-2} \text{ mol L}^{-1}$) (c), as well as in the presence of orthophosphoric acid, As(III) and thyroxine ($3.0 \times 10^{-8} \text{ mol L}^{-1}$) (d) are presented in Fig. 1. It may be seen that the maximum absorbance of the Mn(III) metaphosphate solution was detected at 516 nm. The absorbance increases in the presence of orthophosphoric acid due to the reaction of Mn(III) with this acid. Mn(III) is reduced to Mn(II) in the reaction with As(III) and the solution is discolored. Thyroxine catalyze this reaction.

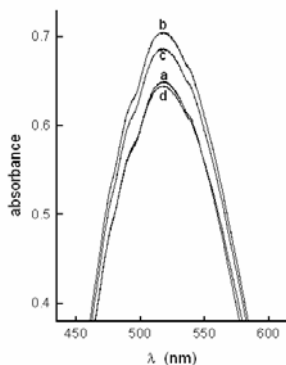


Fig. 1. Effect of thyroxine on the Mn(III) metaphosphate-As(III) reaction in the presence of orthophosphoric acid. Spectra recorded 5 min after start of the reaction.

It was found that the rate of the non-catalytic reaction was very small which indicated a sensitive indicator reaction. A linear relationship was established between the reaction rate and the thyroxine (T_4) concentration in the range from 5.0×10^{-9} to $1.0 \times 10^{-7} \text{ mol L}^{-1}$: $\tan \alpha = -5.27 \times 10^3 [T_4] + 6.6 \times 10^{-6}$; ($r = -0.9985$).

The effects of all components of the reaction mixture on the catalytic reaction rate were investigated (Table 1.).

The kinetic equation of the thyroxine-catalyzed Mn(III) metaphosphate-As(III) reaction in the presence of orthophosphoric acid was postulated and the apparent rate constant determined:

$$-dx/dt = k [\text{Mn(III)}]^{1.2} [\text{As(III)}]^{1/3} [\text{HPO}_3]^{-1} [\text{H}_3\text{PO}_4]^{0.8} [T_4]$$

$$k = (1.84 \pm 0.17) \times 10^4 \text{ L}^4 \cdot \text{mol}^{-4/3} \text{ s}^{-1}$$

Table 1. Summary of the kinetic data for the manganese(III) metaphosphate-arsenic(III) reaction in orthophosphoric acid solution, in the presence of thyroxine

Variable	Concentration range (mol L ⁻¹)	Partial order
As(III)	$1.0 \times 10^{-3} - 2.5 \times 10^{-2}$	1/3
As(V)	$0 - 1.0 \times 10^{-2}$	0.0
Mn(II)	$1.7 \times 10^{-4} - 2.0 \times 10^{-3}$	0.0
Mn(III)	$1.0 \times 10^{-3} - 1.5 \times 10^{-2}$	1.2
H ₃ PO ₄	0.10 – 2.0	0.8
PO ₃ ⁻	0.11 – 0.50	-1.0
PO ₃ ⁻	0.50 – 1.35	-1/4
T ₄	$0 - 1.0 \times 10^{-7}$	1.0
H ₃ O ⁺	0.05 – 0.80	0.5

The effect of temperature on the rate of the proposed reaction was also investigated. It was found that the reaction rate increased with increasing temperature. The activation energy and other kinetic parameters were calculated and the following results obtained: $E = 24.63$ kJ/mol, $\Delta H^\ddagger = 22.15$ kJ/mol, $\Delta S^\ddagger = -91.65$ J/K mol, $\Delta G^\ddagger = 49.48$ kJ/mol, $pK^\ddagger = 8.68$.

In order to test the sensitivity of the reaction studied, thyroxine was determined using the tangent method [3] under the following optimal conditions: Mn(III) metaphosphate, 7.0×10^{-3} mol·L⁻¹; As(III), 2.5×10^{-2} mol·L⁻¹; orthophosphoric acid, 2.0 mol·L⁻¹, in the concentration range $7.0 \times 10^{-9} - 3.0 \times 10^{-8}$ mol·L⁻¹ with a relative standard deviation up to 6.7 %. The detection limit was 2.1 ng mL⁻¹ and the limit of the determination was 3.3 ng mL⁻¹.

Conclusion

It can be concluded that the proposed method is one of the most sensitive methods for the determination of thyroxine.

Acknowledgement

The authors are grateful to the Ministry of Science and Environmental Protection of Serbia for financial support (Project 142037G).

References

- [1] G. A. Milovanovic, F.T. Pastor, Goran M. Petković and Marija Todorović, *Microchim Acta*, 2004, **144**, 51-56.
- [2] Yatsimirskii, K. B. *Kinetic Methods of Analysis*, Pergamon, Oxford, 1966, pp. 28-30.
- [3] Yatsimirski, K. B. *Kinetic Methods of Analysis*, Pergamon, Oxford, 1966, p. 39.

MONO- AND BIMETALLIC SPINELS. PART II: CATALYTIC BEHAVIOUR IN H₂O₂ DECOMPOSITION REACTION

St. Christoskova¹, M. Stoyanova¹, E. Manova², Z. Zheleva², D. Paneva²,
B. Kunev² and I. Mitov²

¹*Department of Physical Chemistry, University of Plovdiv, 4000 Plovdiv, Bulgaria*

²*Institute of Catalysis, Bulgarian Academy of Sciences, 1113 Sofia, Bulgaria*

Abstract

The catalytic behaviour of CoFe₂O₄, Co₂FeO₄, NiFe₂O₄, Ni₂FeO₄ and Fe₃O₄ prepared by mechanochemical synthesis has been studied in reaction of H₂O₂ decomposition. The results obtained reveal that the rate of reaction is strongly affected by the chemical composition of the samples. The most active catalysts in decomposition of H₂O₂ were found to be iron-cobalt spinel oxides, while the pure magnetite did not exhibit measurable activity at studied conditions.

Introduction

Recently iron oxides have been used as catalysts for oxidizing organic contaminants with hydrogen peroxide [1-3]. The results obtained indicate that the removal of contaminants is related to the decomposition of H₂O₂ by iron containing catalysts. Due to this important role, the catalytic decomposition of H₂O₂ deserves further investigation. Therefore, the kinetics of H₂O₂ decomposition on mechanochemically synthesized nickel and cobalt iron oxides and magnetite has been studied in this work.

Experimental

Mechanochemical synthesis of the catalysts and their characterization by means of XRD analysis and Mössbauer spectroscopy is described in Part 1 of the present study. The catalytic decomposition of H₂O₂ was carried out isothermally at 20°C in a batch reactor, using 100 ml 5 mM aqueous H₂O₂ solution (initial pH=6.0) and a known mass of the tested catalyst. The reaction kinetics were followed by taking aliquots from the reacting mixture at appropriate intervals and titrating them with KMnO₄ (0.01 M) in the presence of excess sulfuric acid.

Results and Discussion

The change in the concentration of H₂O₂ as a function of the reaction time in the presence of the studied samples (catalyst concentration 0.9 g/L) is presented in Fig.1. It can be seen that H₂O₂ is decomposed in quite different extent depending on the chemical composition of the catalyst used. The highest and in the same time the very similar activity exhibit CoFe₂O₄ and Co₂FeO₄ samples- a degree of H₂O₂ conversion of approx. 98 % is attained in 10 minute under the studied conditions. In contrast, decomposition of hydrogen peroxide proceeds considerably slower when NiFe₂O₄ and Ni₂FeO₄ samples are used- the decomposition efficiency is only 6 % in 10 minute. Interestingly, Fe₃O₄ exhibits no measurable catalytic activity in H₂O₂ decomposition at studied conditions. Furthermore, it was ascertained that the dissolved iron

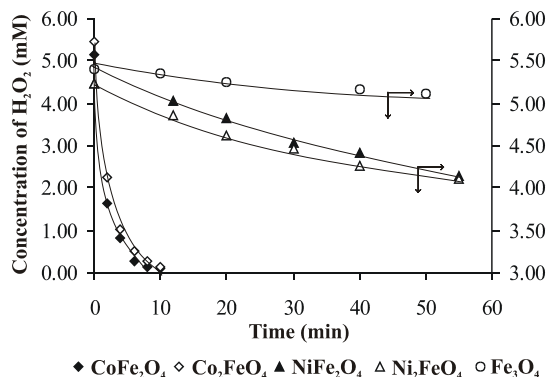


Fig. 1. Kinetic curves of H₂O₂ decomposition

more reactive than Co which in turn should be more reactive than Ni. For Fe and Co the observed trend is the reverse.

The decomposition behavior was clarified with the consideration of the effect of H₂O₂ concentration and catalyst dosage. In Fig. 2, the H₂O₂ concentration is plotted on a log scale against the reaction time for the experiment carried out in the presence of 0.6 g/L CoFe₂O₄ sample and at different initial concentration of H₂O₂.

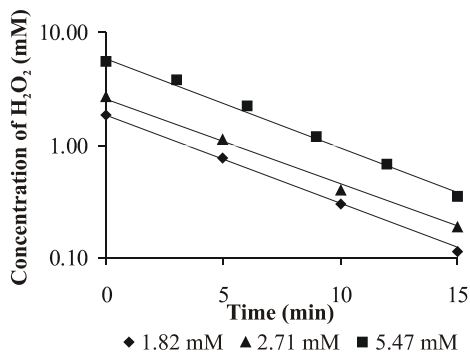


Fig. 2. First-order fit of reaction for different initial H₂O₂ concentration

concentration was always low (less than 0.5 mg/L) thus implying that the decomposition of H₂O₂ could not be affected by homogeneous Fenton chemistry. The trend in the reactivity for the catalysts studied in this work is somewhat unexpected, as has been also established by other authors [4]. From the ionization potentials of the divalent metals in the oxides one would expect Fe to be

Table 1. First-order rate constants (k) for H₂O₂ decomposition over studied catalysts (catalyst concentration: 0.9 g/L)

Catalyst	k (min ⁻¹)
CoFe ₂ O ₄	0.410
Co ₂ FeO ₄	0.378
NiFe ₂ O ₄	0.005
Ni ₂ FeO ₄	0.006

Evidently, the data obtained fit well to straight lines thus indicating that the decomposition of H₂O₂ over CoFe₂O₄ follows a first-order kinetic rate law. No significant difference was observed for the rate constant in these experiments implying that the number of sites on catalyst surface available to adsorption of H₂O₂ was still not limited under the range of H₂O₂ concentration in this study. The first order pattern was also observed for the experiments performed with all the rest catalysts prepared as indicated by the plots ln[H₂O₂]⁰/[H₂O₂] versus time (not shown). The slope of the straight lines thus obtained allows ready determination of the rate constant, measured for a certain catalyst sample and given in Table 1.

To determine the role of catalyst in the decomposition of H_2O_2 the experiments with various catalyst concentration were carried out. Since CoFe_2O_4 exhibited the highest activity in this reaction, it was selected for further study. The experimental observation is presented in Fig. 3 and show that decomposition rate is directly proportional to the catalyst concentration.

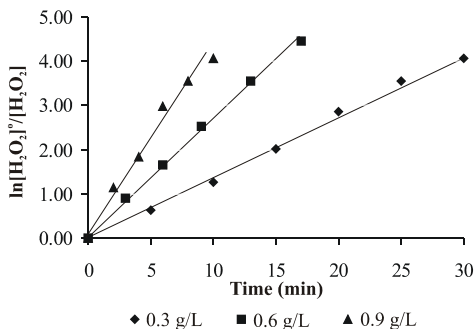


Fig. 3. First-order fit of H_2O_2 decomposition for different CoFe_2O_4 concentration

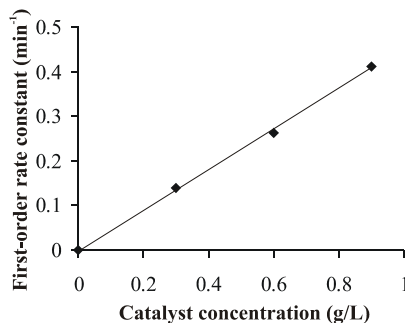


Fig. 4. First-order rate constant as a function of CoFe_2O_4 concentration

A plot of the observed first-order rate constants (calculated from the slopes of the kinetic plots in Fig. 3) against CoFe_2O_4 concentration was found to be a straight line passing through the origin (Fig. 4). Based on the established linear relationship between the rate constant and catalyst concentration, the rate expression for the H_2O_2 decomposition can be modified as:

$$-d[\text{H}_2\text{O}_2]/dt = k_1 [\text{CoFe}_2\text{O}_4] [\text{H}_2\text{O}_2]$$

where $k_1 = 0.452 \text{ min}^{-1} (\text{g/L})^{-1}$ is the second order rate constant.

Conclusion

The established high activity of mechanothesized CoFe_2O_4 and Co_2FeO_4 samples in H_2O_2 catalytic decomposition is a reason to expect good activity of the catalysts in liquid-phase oxidation of organic contaminants using H_2O_2 as oxidant, which is the object of our further investigations.

Acknowledgments

Authors gratefully acknowledge the financial support (Project VUX-1105) by the National Science Fund at the Ministry of Education and Science of Bulgaria.

References

- [1] G.Calleja, J. Melero, F. Martínez, R. Molina, *Wat. Res.*, 2005, **39**, 1741-1750
- [2] E. Guélou, J. Barrault, J. Fournier, *Appl. Catal. B: Environ.*, 2003, **44**, 1-8.
- [3] H. Huang, M. Lu, J. Chen, *Wat. Res.*, 2001, **35**, 2291-2299.
- [4] M. Nejad, M. Jonsson, *J. Nucl. Mater.*, 2004, **334**, 28-34.

KINETICS OF ETHYLXANTHATE ADSORPTION ON PB(II)-MODIFIED GALENA AND SPHALERITE

D. Vučinić and P. Lazić

*Department of mineral processing, Faculty of Mining and Geology, 7 Džušina St., Belgrade, Serbia
(dvcinic@rgf.bg.ac.yu)*

Abstract

The main surface reaction between ethyl xanthate anions ($\text{CH}_3\text{CH}_2\text{OCS}_2^-$) and Pb(II)-treated galena (PbS) and sphalerite (ZnS) in the flotation condition (pH range 8–9.5) is probably the ion-exchange reaction $\text{M-Pb-OH} + (\text{EX})^- = \text{M-Pb-EX} + (\text{OH})^-$ (M – mineral), which contributes to the chemical adsorption of $(\text{EX})^-$ on the surface of either mineral. The reaction between Pb(II)-treated mineral and $(\text{EX})^-$ ion is a reaction of pseudo-first order with respect to ethyl xanthate (on Pb(II)-modified galena the rate constant is $k_1 = 0.711 \text{ min}^{-1}$; on Pb(II)-modified sphalerite $k_1 = 0.1014 \text{ min}^{-1}$).

Introduction

Much of the research was focused on the action of hydrophobic xanthate-type surfactants (ROCS_2M) on sulphide minerals. Galena is known to float well with xanthates [1,2], but the short-chain xanthate homologues have a low ability to collect sphalerite [3]. The effects of Pb(II) on flotation and surface characteristics of sphalerite [4,5] or synthetic ZnS [6] and on galena [7,8] were reported earlier, but the mechanisms have not been completely understood. The purpose of this work was to study the effect of lead dissolved in a solution on ethyl xanthate ($(\text{EX})^-$) adsorption kinetics on galena and sphalerite surfaces in the flotation condition. As Pb(II) may be present in the pulp during Pb–Zn flotation, derived from most Pb-minerals including galena due to galvanic contact with more noble metal sulphides, added reagent (Pb-acetate), or in the recycled flotation water, it is very important to know how lead reacts with mineral surfaces and whether it influences the Zn- or Pb-concentrate qualities.

Results and Discussion

The specific areas of natural minerals were determined on a Culter Counter Model D Industrial (galena $4.00 \text{ m}^2/\text{g}$, sphalerite $2.97 \text{ m}^2/\text{g}$). Kinetic studies of ethyl xanthate adsorption ($3 \times 10^{-4} \text{ M KEX}$) on 15 minutes lead treated minerals ($7 \times 10^{-5} \text{ M Pb-acetate}$) were carried out. The solution of Pb-acetate was decanted before adding KEX solution. The suspensions of Pb(II)-treated mineral/KEX solution ($0.250 \text{ g of solid}/0.025 \text{ dm}^3$ of KEX solution) were shaken at 298 K from one to 15 min (the collection time). After shaking, they were filtered and the filtrates were UV analyzed ($\lambda_{\text{EX}} = 301 \text{ nm}$).

According to the distribution diagram for lead [6] the dominant lead species in alkaline medium (pH=7–10) are monohydroxy complex $\text{Pb}(\text{OH})^+$ and less Pb^{2+} ions ($\text{Pb(II)} < 50 \text{ ppm}$).

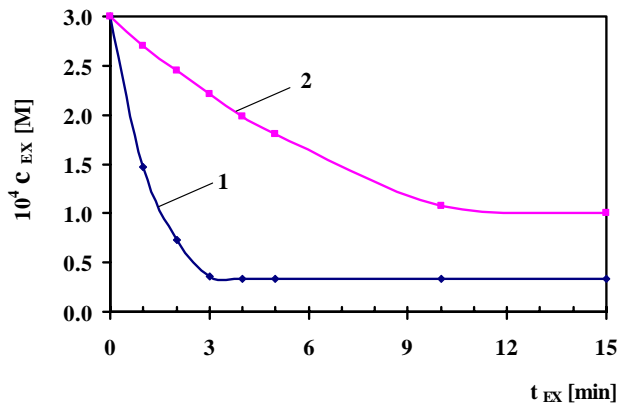


Fig. 1. Ethyl xanthate concentration as a function of KEX collection time for: (◆) Pb(II)-treated galena, (■) Pb(II)-treated sphalerite (t_{Pb}=15 min, c_{Pb}= 7×10⁻⁵ M, c_{oKEX}=3×10⁻⁴ M, pH_{act}= pH_{coll}= 8-9).

The obtained results showed that the interaction between Pb(II)-modified galena and (EX)⁻ ions was faster than between Pb(II)-modified sphalerite and (EX)⁻ (Fig.1). The rate expression for disappearance of ethyl xanthate from the solution can be written as [9]:

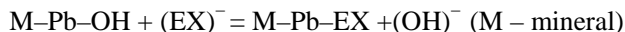
$$-\frac{dc_{(EX)^-}}{dt} = kc_{(EX)^-}^\alpha \prod_{i=0}^n c_{iPb(II)_{surf}}^{\alpha_i} \tag{1}$$

where are: c_{(EX)⁻} -concentration of ethyl xanthate at the collection time *t* with KEX solution; α - reaction order with respect to ethyl xanthate; c_{iPb(II)_{surf}} -surface concentration of the relevant surface Pb(II) site on minerals; α_i -reaction order with respect to the relevant surface Pb(II) site on minerals; n-number of different surface Pb(II) sites on minerals; k -reaction rate constant. Supposing that under the defined conditions the surface concentration of Pb(II) sites on Pb(II)-treated minerals is constant, the above expression can be written as:

$$-\frac{dc_{(EX)^-}}{dt} = k_1 c_{(EX)^-}^\alpha \tag{2}$$

The value of the rate constant $k_1 = k \prod_{i=0}^n c_{iPb(II)_{surf}}^{\alpha_i}$ is governed by several variables, some of which include: active surface area, pH, reaction temperature, mineral composition, particle size, Pb(II) solution concentration, solid/liquid ratio, time of Pb(II) activation. The equation (2) was tested for the pseudo-first reaction order (α=1). For Pb(II)-treated galena the KEX concentration in the solution decreased according to exponential expression of the collection time with KEX solution, *t*, which is the integration result of equation (2) for α=1, $c_{(EX)^-} = c_{o(EX)^-} e^{-0.711t}$ for *t* ≤ 3 minutes (Fig. 1, curve 1). The same type of curve was obtained for Pb(II)-treated sphalerite,

$c_{(EX)^-} = c_{o_{(EX)^-}} e^{-0.1014t}$, only for $t \leq 10$ minutes (Fig.1, curve 2). It means that the dominant reaction between Pb(II)-treated mineral (galena or sphalerite) and ethyl xanthate ion under the flotation conditions is pseudo-first order, probably the ion-exchange reaction:



which contributes to the increase of the amount of chemically adsorbed $(EX)^-$, i.e. monolayer $-Pb-EX$ on the surface of either mineral, needed for good mineral floatability. Near-equilibrium $(EX)^-$ adsorption on Pb(II)-modified galena was obtained within 3 minutes, with the rate constant $k_1 = 0.711 \text{ min}^{-1}$, and for Pb(II)-modified sphalerite in 10 minutes, with $k_1 = 0.1014 \text{ min}^{-1}$.

Conclusion

The dominant reaction between Pb(II)-treated minerals (galena or sphalerite) and $(EX)^-$ is probably the ion-exchange reaction $M-Pb-OH + (EX)^- = M-Pb-EX + (OH)^-$ of pseudo-first order in relation to ethyl xanthate. It is faster on Pb(II)-modified galena surface ($k_1 = 0.711 \text{ min}^{-1}$, $t \leq 3$ minutes) than on Pb(II)-modified sphalerite ($k_1 = 0.1014 \text{ min}^{-1}$, $t \leq 10$ minutes). The activation effect of lead on ethyl xanthate adsorption on sphalerite leads to the conclusion that recycled water which contains dissolved lead may be used in the process of selective galena/sphalerite flotation after galena has been floated, i.e. during the Zn-flotation.

Acknowledgment

The authors are indebted to the Research Fund of the Republic of Serbia for financial support (projects: no.146020; no. 232026).

References

- [1] R. Woods, J. Phys. Chem., 1971, **75**, 354.
- [2] M.C. Fuerstenau, in R. P. King (Ed.), Principles of Flotation, Inst. Min. Metall., Johannesburg, 1982, p. 91.
- [3] J. A. Mielczarski, Int. J. Miner. Process., 1986, **16**, 179.
- [4] W.J. Trahar, G.D. Senior, G.W. Heyes, M.D. Creed, Int. J. Miner. Process., 1997, **49**, 121.
- [5] F. Rashchi, C. Sui, J.A. Finch, Int. J. Miner. Process., 2002, **67**, 43.
- [6] J. Ralston, T. W. Healy, Int. J. Miner. Process., 1980, **7**, 175.
- [7] S. Popov, D. Vučinić, Colloids Surfaces, 1988, **30**, 387.
- [8] D. Vučinić, Ph.D. Thesis, Faculty of Mining and Geology, Belgrade, 1992.
- [9] H. Kuopanportti, T. Suorsa, E. Pöllänen, Minerals Engineering, 1997, **10**, 1193.

REMOVAL OF VOLATILE ORGANIC COMPOUNDS (VOCs) FROM ACTIVATED CARBON BY THERMAL DESORPTION AND CATALYTIC COMBUSTION

D.Ranković¹, N.Radić², B.Grbić², Z.Arsenijević² and Ž.Grbavčić³

¹Faculty of Physical Chemistry, University of Belgrade, Studentski trg 12-16, Belgrade

²ICHTM-Center for Catalysis and Chemical Engineering, Njegoševa 12, Belgrade

³Faculty of Technology and Metallurgy, University of Belgrade, Karnegijeva 4, Belgrade

Abstract

Within this work, thermal desorption by the air of saturated activated carbon discharged from industrial adsorber and catalytic oxidation of desorbed products over Pt/Al₂O₃ catalyst, have been investigated. The activated carbon are almost completely regenerated by flushing with air at 200 °C during 30 min. Desorbed products are fully oxidized over Pt/Al₂O₃ catalyst above the temperature of 275 °C.

Introduction

The removal of volatile organic compounds (VOCs) from numerous emission sources is of crucial importance for more rigorous demands on air quality. One of the major technologies for the removal of low concentrations of VOCs from the air is based on adsorption by activated carbon (AC), either in the powdered or in granular form. The saturated AC, however, must be regenerated before reuse. The regeneration methods are based either on desorption, induced by increasing temperature or by displacement with a suitable solvent. Desorbed products must be further removed by thermal or catalytic oxidation or by appropriate chemical, electrochemical or microbial processes.

Our previous work have been directed to development of combined adsorber – desorber – catalytic reactor system, nominal capacity 3.5 m³/h, using modified spouted bed with draft tube loaded with activated carbon for removal of xylene [1]. Combustion of adsorbed organics was conducted in separate catalytic reactor loaded with platinum catalyst.

Within this work investigation of thermal desorption by the air of spent activated carbon discharged from industrial adsorber and catalytic oxidation of desorbed products over Pt/Al₂O₃ catalyst, have been presented.

Experimental

Activated carbon, type K81/B Trayal Corporation, Kruševac, in the form of granulate, with mean size of 2 mm, was used as sorbent for removal of pollutants from industrial waste gasses. Samples for laboratory investigation were discharged from commercial adsorption unit.

Catalyst 0.12%Pt/Al₂O₃, grain size of 0.1 to 0.2 mm [2] was used for catalytic combustion of desorbed products from AC.

Apparatus is made of two independently heated reactors, connected in series. Both reactors are situated within Gas Chromatograph Shimadzu 14-A. The first, desorption reactor consisted of stainless steel tube, OD 6 mm, ID 4 mm and 115 mm in length, was placed in the oven that is originally designed for commercial on-column injector OCI-14. Oven is capable of being temperature programmed from other heated sections of gas chromatograph. Samples of AC ($0.12 \text{ g} - 0.23 \text{ cm}^3$) were placed in the middle of desorber on quartz wool holder, with thermocouple on the top of the bed. Air stream was used as desorption fluid. Flow of the air corresponded to the space velocity of $12\,000 \text{ h}^{-1}$. The second, catalytic reactor was also made of stainless steel tube, same dimensions as desorption reactor. Catalytic reactor was situated in the column oven of the gas chromatograph. Reactor was loaded with 0.15 g of $\text{Pt}/\text{Al}_2\text{O}_3$ catalyst and applied flow rates through bed corresponded to the space velocity of $13\,500 \text{ h}^{-1}$. Temperature programmed desorption of organics from AC was investigated in the temperature range from 50 to 300 °C with programmed temperature rise of 5, 10, 20 and 50 °C/min. Quantitative and qualitative analysis of desorption products were performed by means of FID detector, using stainless steel column, 6.5 ft. long and 1/8 in. in diameter, containing 23% SP 1700 on chromosorb PAW. Taking into account that catalytic reactor was placed in the column oven, analysis of unreacted organic products was restricted only to the total organic content. Therefore, in order to determine catalytic activity desorption products (inlet of catalytic reactor) were analyzed using the same method.

Results and Discussion

Investigated samples of AC were discharged from commercial adsorption unit.

Analysis of desorption products from AC in the temperature range from 120 to 300 °C with programmed temperature rise of 10 °C/min revealed that major constituent of adsorbed organics is xylene (about 90%). Rest of desorbed organics belong Solvesso 100 and their concentrations increase with temperatures. Solvesso 100 is commercial name for industrial solvent that consist primarily of C9-10 dialkyl and trialkyl-benzenes. In temperature range from 120 to 260 °C

with temperature rise of 10 °C/min AC mass losses gradually increase from 5 to 19 %. Further temperature rise does not affect loss of the AC mass. Also, maximal mass loss of 19 % was obtained at lower temperatures (200 °C) with same rate of heating but

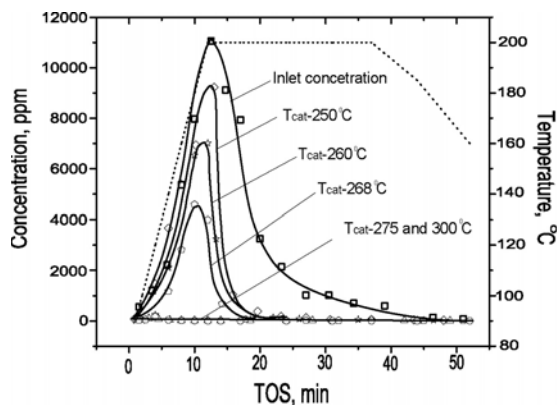


Fig. 1. Conversion of VOCs as a function of temperature

with increased hold time of desorber for 30 min. Therefore these temperature regimes have been chosen for catalytic activity tests.

Catalytic activity test are presented on Fig. 1, showing that catalysts temperatures of 275 °C is sufficient to combust all desorbed organics. It was noticed that concentrations of organics influenced conversions that is presented on Fig. 2. Increase of concentration of organics decrease catalyst efficiency. These results could indicate possible mechanism of catalytic reaction. Probably, surface concentrations of organics remain constant regardless the organics concentrations in the gas phase. This should be basis for further research about kinetics of xylene oxidation over Pt/Al₂O₃ catalysts employing gradientless reactor.

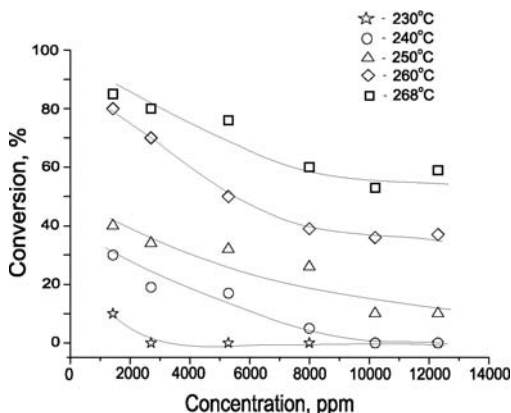


Fig. 2. Conversion of VOCs as a function of concentration

Conclusion

Thermal desorption of organics by the air from AC discharged from commercial adsorber enables satisfactory regeneration of AC. The AC saturated mainly by xylene and partly by SOLVESSO 100 are almost completely regenerated by flushing with air at 200 °C during 30 min.

Desorbed products are fully oxidized over Pt/Al₂O₃ catalyst above the temperature of 275 °C.

These results shows that removal of low concentrations of organic compounds by adsorption on AC, thermal regeneration of AC and post-treatment of desorbed products from AC over Pt/Al₂O₃ catalyst can be successfully applied for removal of organic pollutants from waste gases.

References:

- [1] Ž. Grbavčić, D. Ranković, Z. Arsenijević, Low concentration volatile organic pollutants removal in combined sorbent/catalytic reactor system, Physical chemistry 2004, Volume II, 2004, 709-711.
- [2] N. Radic, B. Grbic, A. Terlecki-Baricevic, Applied Catalysis B: Env., 2004, **50**, 153-159.

MORPHOLOGY STUDY OF THE Ni-Mg/SiO₂ MATERIALS AS CATALYST PRECURSORS

M. Gabrovska¹, Ts. Tzacheva³, D. Lončarević²,
R. Edreva-Kardjieva¹ and D. Jovanović²

¹*Institute of Catalysis, BAS, 1113 Sofia, Bulgaria (margo@ic.bas.bg)*

²*ICTM, Department of Catalysis and Chemical Engineering, Belgrade, Serbia*

³*Institute of Physical Chemistry, BAS, Sofia, Bulgaria*

Abstract

The morphological properties of the co-precipitated Ni-Mg/SiO₂ samples are studied by scanning electron microscopy. The materials are prepared with the same composition changing the order and rate of addition of the support and precipitation agent to the Ni-Mg solution. The results suggest the sample division in two groups. The surface of the *first* group unreduced and reduced materials is composed of well-formed fine mono-disperse particles about 5 times smaller than the precursor particles of *second* group. It may be a precondition for a high dispersion of the active components in the *first* group of materials.

Introduction

Scanning electron microscopy is very useful tool for an investigation of the morphology as well as the uniformity of the particle shape and size from macroscopic to nano-scales. The surface state of the studied materials could be very different, depending on the method of synthesis [1]. Considering that the reaction takes place on the catalyst surface, the surface morphology is a fundamental characteristic in the achievement of good performance.

The aim of this work is to study the effect of preparation variety on the morphological properties of Ni-Mg/SiO₂ materials as catalyst precursors for edible oil hydrogenation.

Experimental Procedures

Sample preparation

The samples of identical composition (SiO₂/Ni = 1.15 and Ni/Mg = 0.1), denoted as A, B, C, D, E and F, are prepared by co-precipitation method applying six preparation procedures. They differ by the order and mode of addition of the support (water glass) and the precipitation agent (Na₂CO₃) to the mixed Ni-Mg nitrate solutions. Detailed procedure of samples preparation is given previously [2].

Sample characterization

The Scanning electron microscopy (SEM) observations are carried out on a JEOL Superprobe 733 microscope with a 25 kV beams.

The reduction of the precursors with hydrogen is performed in a laboratory set-up for 5 h in gas mixture of H₂/N₂ (1/1 v/v) at a flow rate of 5 l h⁻¹ at 430 °C [3]. After cooling down to room temperature, the reduced precursors, are passivated with a mixture of 350 ppm O₂.

Results and Discussion

The SEM image of the support water glass (Fig. 1) reveals very well pronounced habit of the identical in shape angulated particles, randomly distributed on the surface, ranging in effective diameter from 8 to 170 μm . Their large smooth surfaces are mechanically covered with numerous fine particles.

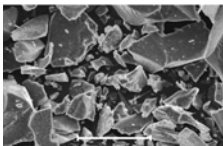


Fig. 1. SEM image of the support; bar = 150 μm

The SEM images of all precursors (Fig. 2 and 3) illustrate a drastic change in the morphology of the original support. The results show that both unreduced and reduced precursors B, C and E display different images than the A, D and F ones.

This phenomenon allows the distinguishing of the samples in two groups as a result of the preparation steps. The samples from *first* group (Fig. 2) are obtained when the precipitant is added drop-wise (flow 1.0=ml/min) before (B1 and E1) or mixed with the support (C1). The surface of the unreduced precursors from *first* group appear to be composed of fine mono-disperse particles with effective diameter $d_{\text{eff}} \sim 0.25\text{--}1.40 \mu\text{m}$. It must be noted that the surface of precursor E1 consists of identical, smallest and randomly distributed fine-grained particles forming porous structure ($d_{\text{eff}} \sim 0.20\text{--}0.50 \mu\text{m}$).

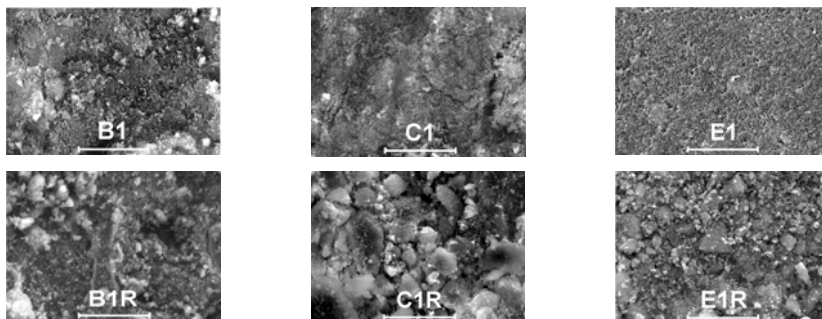


Fig. 2. SEM images of the precursors from I group, before and after reduction and passivation (R), bar = 15 μm

The SEM images of *first* group precursors demonstrate visible changes in their morphology after reduction and passivation. The samples undergo significant packing in result of water and CO_2 removing. A part of the fine particles preserved their size after reduction, but others formed agglomerates of great size from $\sim 2.0 \times 2.0$ up to $\sim 13.0 \times 7.0 \mu\text{m}$. Their surface is covered with fine-grained particles with $d_{\text{eff}} \sim 0.20\text{--}0.50 \mu\text{m}$.

The precursors from *second* group are prepared either by the introduction of the support before the precipitation agent (A2 and D2) or at once with the precipitant (F2). The samples demonstrated close surface structure and manifested well-pronounced habit (Fig. 3). They possess smooth walls with well-formed edges. The surface consist of larger independent fragments with size from $\sim 5.0 \times 7.0$ up to $\sim 12.0 \times 20.0 \mu\text{m}$, mixed or covered with particles with $d_{\text{eff}} \sim 3.0\text{--}6.0 \mu\text{m}$.

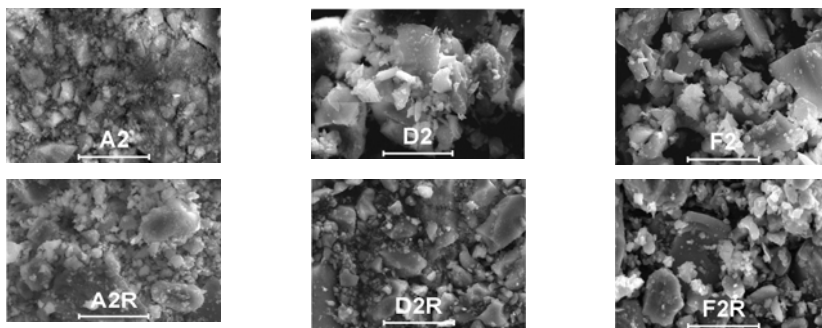


Fig. 3. SEM images of the precursors from II group, before and after reduction and passivation (R), bar = 15 μm

The particle morphology of *second* group of precursors resembles the parent support structure even after reduction and passivation procedure. The large aggregates (from $\sim 4.0 \times 4.0$ up to $\sim 12.0 \times 8.0$ μm) are mixed or covered with smaller particles of similar size and shape ($d_{\text{eff}} \sim 0.40\text{--}1.00$ μm).

A fine-grained material is registered for both groups of reduced precursors. It is obvious that the variation in the preparation procedure leads to formation of precursors with different morphological properties and surface particle size.

Conclusion

It may be concluded that varying the manner and order of introduction of the support and the precipitation agent significantly affects the morphology of the synthesized materials. All precursors demonstrated smaller surface particles than the support. The morphological properties of both unreduced and reduced Ni-Mg/SiO₂ catalyst precursors suggest their division in two groups. The surface of *first* group materials is composed of well-formed fine mono-disperse particles smaller than precursors of the *second* group. It may be a precondition for a high dispersion of the active components in the *first* group of materials.

Acknowledgements:

The authors (M. G., Ts. T. and R. K.) are grateful to the National Science Fund at the Ministry of Education and Science of Bulgaria, for the partial financial support (Project X-1411). The authors (J. K., D. L. and D. J.) greatly acknowledge the support of the Serbian Ministry of Science and Environmental Protection through the Project - TR 6712 B.

References:

- [1] G. Coudurier, J.C. Védrine, *Catal. Today* 2000, **56**, 415–430.
- [2] M. Gabrovska, M. Shopska, I. Shtereva, R. Edreva-Kardjieva, P. Zvetkov, J. Krstić, D. Jovanović, *IWON 2005*, Belgrade, Serbia and Montenegro, 56-59.
- [3] M. Gabrovska, J. Krstić, R. Edreva-Kardjieva, M. Stanković, D. Jovanović, *Appl. Catal. A: General*, 2006, **299**, 73-83.

TEXTURE PROPERTIES OF Ni-Mg/SiO₂ PRECURSORS AS EDIBLE OIL HYDROGENATION CATALYSTS

J. Krstić¹, M. Gabrovska², D. Nikolova², N. Gavrilov¹,
R. Edreva-Kardjieva² and D. Jovanović¹

¹ICTM, Department of Catalysis and Chemical Engineering, Belgrade, Serbia
(jkrstic@nanosys.ihtm.bg.ac.yu)

²Institute of Catalysis, BAS, Sofia, Bulgaria

Abstract

Six co-precipitated Ni-Mg/SiO₂ materials, with the same composition, are obtained by changing the order and mode of addition of the support and precipitation agent to the Ni-Mg solution. The data from N₂ sorption experiments suggest that both synthesized and reduced precursors can be distinguished in two groups as a result of applied preparation procedures. The *first* group of precursors demonstrates developed surface area and pore system of monodisperse character of distribution, which are significantly preserved even after reduction, on contrary to the *second* precursor group. The drop-wise addition of the precipitant to the Ni-Mg solution before the support (*first* group) leads to the formation of the most promising catalyst precursor. Its texture properties would enable the mass transport of the great triglyceride molecules to the active surface and the re-transport of the products out of the pore system.

Introduction

Nickel supported on natural and synthetic silicates is the most widely used catalyst in the industrial hydrogenation of edible oils. The choice and preparation of the support, the technique of nickel and promoter deposition is known to be important for the catalyst texture formation. Considering that reaction takes place on the catalyst surface, a large surface area and appropriate pore dimension are essential for achieving of good catalyst performance [1].

The aim of this study is to follow the effect of preparation variety on the texture properties of Ni-Mg/SiO₂ materials as a base to select the most suitable precursors of the edible oil hydrogenation catalysts.

Experimental Procedures

Sample preparation

The six precursors with identical composition (SiO₂/Ni = 1.15 and Ni/Mg = 0.1) denoted as A, B, C, D, E and F, are obtained by co-precipitation method, employing different preparation steps. The differences consist in the order and mode of addition of the water glass, used as source of SiO₂ support, and the precipitation agent (Na₂CO₃) to the mixed Ni-Mg nitrate solutions [2].

Sample characterization

The texture characteristics of the precursors are estimated using N_2 adsorption at $-196\text{ }^\circ\text{C}$ (Sorpomatic 1990 Thermo Finnigan) [3]. The reduction of the precursors with hydrogen is performed in a laboratory set-up for 5 h at $430\text{ }^\circ\text{C}$ [3].

Results and Discussion

The results from N_2 sorption measurements manifest that the isotherms of unreduced B, C and E precursors are close to type IV with hysteresis loops close to H3 type, characteristic for mesoporous materials [4]. The type of isotherms and hysteresis loops are illustrated by the E sample (Fig. 1). The isotherms of A, D and F precursors may be classified as type I, characteristic for microporous solids [4].

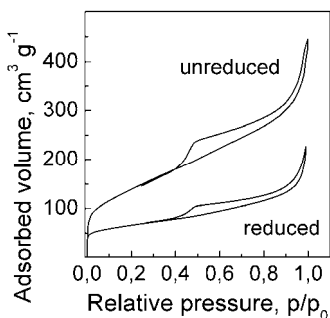


Fig. 1. N_2 sorption of the precursor E.

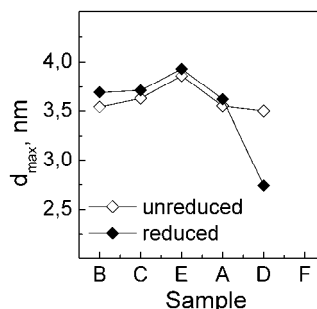


Fig. 2. Maximum pore diameter of the precursors.

The pore size distribution (PSD) curves of unreduced A, B, C, D and E precursors reveal the monodisperse character of the distribution with maximum pore diameter (d_{\max}) in the range of 3.5–4 nm (Fig. 2). The PSD curve of F precursor decreases strongly in the range of 2–10 nm without clearly pronounced d_{\max} .

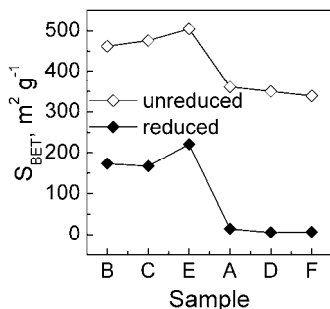


Fig. 3. S_{BET} of the precursors

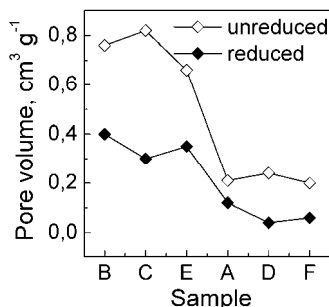


Fig. 4. Pore volume of the precursors

The unreduced B, C and E samples possess higher specific surface area (Fig. 3) and total pore volume (Fig. 4) than the rest of materials.

The observed textural differences allow two groups to be distinguished in the samples under study, as a result of the preparation variety.

The precursors from the *first* group are obtained when the precipitant is added drop-wise before (B1 and E1) or mixed with the support (C1). The precursors from the *second* group are prepared either by the introduction of the support before the precipitation agent (A2 and D2) or at once with the precipitant (F2).

The reduction of the *first* group materials slightly change the isotherm type (Fig. 1), decreasing S_{BET} with 55–65 % (Fig. 3) and pore volume with 45–65 % (Fig. 4). The monodisperse character of PSD remains unchanged a weakly growing of d_{max} being observed (Fig. 2).

The isotherm type of the reduced precursors from the *second* group changes in type II (A2 and D2), characteristic for non-porous materials and in type III (F2) typical for weak adsorbate-adsorbent interactions [4]. This is associated with drastic losses of S_{BET} (96–98 %) and diminution of pore volume with 43–80 %. The PSD curves demonstrate a transformation of mono- to polydisperse character of distribution. The range of d_{max} for A sample remains unchanged, while the range of the d_{max} for D sample is shifted to 2–3 nm. The PSD curve of reduced F sample shows that porous structure still exists only in the range of 16–20 nm without clearly pronounced d_{max} .

Conclusion

It may be concluded, that the texture of the obtained materials is significantly affected by the mode and the introduction order of the support and the precipitation agent.

The *first* group of precursors demonstrates developed surface area and pore system of monodisperse character of distribution, which are significantly preserved even after reduction, on contrary to the *second* precursor group.

The drop-wise addition of the precipitant to the Ni-Mg solution before the support leads to the formation of the most promising catalyst precursor (E sample) from the *first* group of materials. Its texture properties would enable the mass transport of the great triglyceride molecules to the active surface and the re-transport of the products out of the pore system.

Acknowledgements

The authors (M. G., D. N. and R. K.) are grateful to the National Science Fund at the Ministry of Education and Science of Bulgaria, for the partial financial support (Project X-1411). The authors (J. K., N. G. and D. J.) greatly acknowledge the support of the Serbian Ministry of Science and Environmental Protection through the Project - TR 6712 B.

References:

- [1] M. Balakos, E. Hernandez, *Cat. Today*, 1997, **35**, 415-425.
- [2] M. Gabrovska, M. Shopska, I. Shtereva, R. Edreva-Kardjieva, P. Zvetkov, J. Krstić, D. Jovanović, *Proc. 1st International Workshop on Nanoscience & Nanotechnology IWON 2005*, Belgrade, Serbia and Montenegro, 56-59.
- [3] M. Gabrovska, J. Krstić, R. Edreva-Kardjieva, M. Stanković, D. Jovanović, *Appl. Catal. A: General*, 2006, **299**, 73-83.
- [4] F. Rouquerol, J. Rouquerol and K. Sing, in *Adsorption by Powders and Porous Solids, Principle, Methodology and Applications*, Academic Press, 1999.

DISSOLUTION OF SiO₂ IN NaOH AQUEOUS SOLUTION – KINETICS MODELS I –

M. Stanković¹, L. Pezo¹, B. Kovačević¹, S. Stanojlović¹,
M. Jovanović² and D. Debeljković³

¹ Eng. Dept. Holding Institute of General and Physical Chemistry, Studentski trg 12/V, Belgrade, Serbia (inzenjer@eunet.yu)

² Faculty of Technology and Metallurgy, Karnegijeva 4, Belgrade, Serbia

³ Faculty of Mechanical Eng., 27. marta 80, Belgrade, Serbia

Abstract

Silica dissolution in aqueous NaOH, corresponding to the ratio SiO₂/Na₂O=2, is a complex process at elevated temperatures and high pressure. It is of extreme importance to develop adequate mathematical model, using which it is possible to predict the dynamical response of process parameters. In this article several kinetics models were developed, and compared with experimental results. Silica was assumed to be smooth spheres, which decreased in size, as dissolution proceeds. The influence of the particle size, the operating temperature and the hydroxide ion molality on the kinetic rate were studied. It is concluded that developed models are sufficiently correct, in engineering sense, and can be used for dynamical prediction of process parameters. It is certain that these models can be used to correlate the experimental data on dissolution.

Introduction

Production of sodium silicate in a pressure reactor, i. e. wet process, according to the following reaction: $y\text{SiO}_{2(\text{sd})} + \text{NaOH} \rightarrow \text{Na}_2\text{Si}_y\text{O}_{3+y}$ has increased over the last ten years, [1,2]. The compound corresponding to $y=2$, i. e. SiO₂/Na₂O=2 (silicate module), is used as a supplement in detergent manufacture, because of the good buffering action of silicates, and raw material for detergent zeolite 4A production. For the optimization of the process, kinetic data obtained from experimental data are of great importance, as well as reaction temperature and the size of sand particles. Chemical process model of SiO₂ dissolution in NaOH aqueous solution, is used for better understanding of steps by which process is been carried out, which parameters are more important, and how many parameters are present in the system. Confirmation of the model, as well as the mechanism should be done by experimental results. Within this article a few kinetics models are presented.

Experimental

Experiments were carried out with sand (average particle size 250 μm), and minimum SiO₂ content of 97%. The sodium hydroxide solution of 12.5 mol/kg were used, prepared from pure reagent-grade sodium hydroxide dissolved into distilled water. For the sand used in this work, the specific surface area was evaluated at approximately 200 cm²/g, which indicate low porosity. Amounts of sand (m_0), and NaOH solution, corresponding to the molar ratio SiO₂/Na₂O=2 were introduced into a 2l autoclave

(Parr). The temperature was regulated at 220 °C, and checked with thermocouple. The autoclave is equipped with agitator. At the end of each experiment, the autoclave was quenched into water. The mixture was filtered and the un-reacted sand was washed with hot water until the filtrate became non – basic. The remaining solid (m) was dried and weighed. Measured parameters (m_o , m , T , R) are used for evaluation of calculated parameters ($\alpha(t)$, $r(t)$, S). The influence of molality, temperature and particle size has been determined during data processing.

Mathematical Model

In the case of mathematical modeling of SiO₂ dissolving in NaOH solution, under high pressure and temperature, a few different approach can be presented: empirical model, shrinking core model using diffusion expression of kinetics, shrinking core model using assumption that at the beginning of reaction the system is controlled by chemical reaction, modified shrinking core model and variable activation energy shrinking core model.

The experimental results can be described by different empirical functions. Using the mean standard deviation between model predictions and experimental data as test, the following expression can be used to predict kinetic data, [1,2]:

$$\alpha(t) = 1,05 \cdot A_{MOL} \cdot [1 - \exp(-B_{MOL} \cdot t)] \cdot A_T \cdot [1 - \exp(-B_T \cdot t)] \cdot A_d \cdot [1 - \exp(-B_d \cdot t)], \quad (1)$$

where: A , B are adjustable parameters, which are calculated from experimental values, where influence of molality, temperature and particle size were determined and $\alpha = \frac{m_o - m}{m_o}$ - degree of conversion, m_o – initial mass of silica, m is the mass of un-

reacted silica at time t . Using experimental results, diagram on Fig. 1, continuous line, was plotted, and adjustable parameters were found.

Using geometrical equation for particle radius in time t :

$$r(t) = R \cdot \sqrt[3]{1 - \alpha}, \quad (2)$$

it is possible to plot the radius change diagram, Fig. 2, continuous line. This diagram shows that a large radius of particle remains even when degree of conversation reaches 99%, which does not represent the real nature of this process.

The experimental results can be described by different analytical functions. Using the modification of standard diffuse model, the following expression can be used to predict kinetic data, [1,2]:

$$\frac{dC_{SiO_2}(t)}{dt} \cdot V = k_2 \cdot S(t) \cdot (C_{SiO_2}^{area}(t) - C_{SiO_2}(t)). \quad (3)$$

Considering the variable activation energy term the kinetic expression of the sand dissolution can be written as, [2]:

$$\frac{d\alpha}{dt} = \frac{a_1}{R_p} \cdot \exp \left[- \left(\frac{E_a}{R} \cdot \left(\frac{1}{T} - \frac{1}{T'} \right) + \frac{a_2 \cdot \alpha^{a_3}}{R \cdot T} \right) \right] \cdot (C_{OH^-}^0 - \alpha \cdot C_{OH^-}^{st})^b (1 - \alpha)^{2/3}, \quad (4)$$

Variable activation energy shrinking core model take into account the change of the activation energy as the reaction proceeds.

Using experimental results, diagram shown on Fig. 3, thick continuous line was plotted, and adjustable parameters were found. Using equations (2) and (4) it is possible to plot the radius change diagram, Fig. 4, dashed line. This diagram shows that after approx. 70 minute dissolution process ends, and diameter of sand particles becomes zero, which represents the real nature of this process.

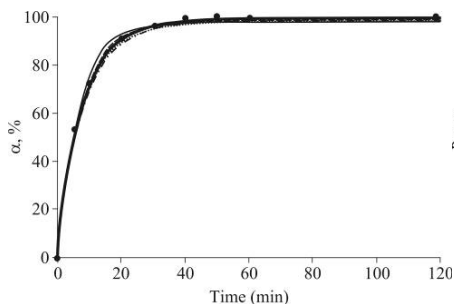


Fig. 1. Degree of conversion

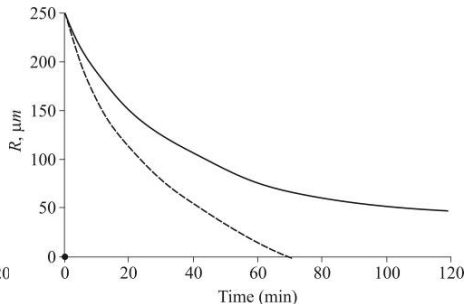


Fig. 2. Mean particle size decreasing during the dissolution process

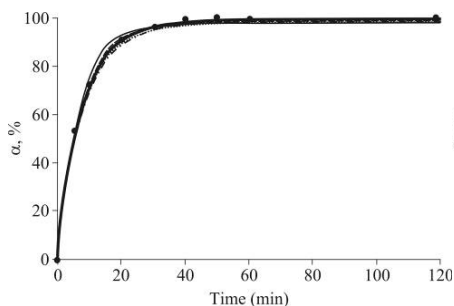


Fig. 3. Degree of conversion

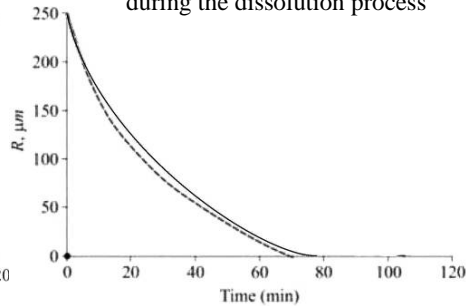


Fig. 4. Mean particle size decreasing during the dissolution process

Conclusion

Here presented study shows that silica and sodium hydroxide react rapidly at high pressure and temperature. Obtained curves seem to be a good representation of dissolution process. On the basis of acquired data, using geometrical resembles, an analytical expressions of kinetic model for shrinking core models was written, which describes the system well enough.

Reference

- [1] F. Jendoubi, A. Mgaidi, M. El Maaoui, The Canadian Journal of Chemical Engineering, 1998, **76**, 233-238.
- [2] A. Mgaidi, F. Jendoubi, D. Oulahna, M. El Maaoui, J. A. Dodds, Hydrometallurgy, 2004, **71**, 435-446.

Nonlinear Dynamics

(D)

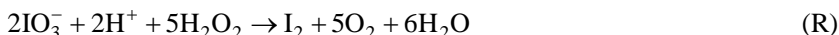
COMPLEX OSCILLATIONS AND CHAOS IN SPACES WITH MORE THAN THREE DIMENSIONS

G. Schmitz

*Université Libre de Bruxelles, Faculté des Sciences Appliquées,
CP165/63, Av. F. Roosevelt 50, 1050 Bruxelles, Belgium*

Introduction

The oscillatory decomposition of hydrogen peroxide in the presence of hydrogen and iodate ions, known as the Bray-Liebhafsky reaction [1-3], is the result of two complex pathways in which hydrogen peroxide acts either as a Reducing (R) or Oxidizing (O) agent.



The model we have proposed [3-6] to explain the kinetics of this reaction in a batch reactor can also simulate complex oscillations and chaos in a CSTR [7-10]. Figure 1 gives examples of calculated behaviours at different specific flow rates j_0 (total volume flow divided by the reactor volume). The model is given in Table I and its dynamics is described by the following six differential equations. Iodate and acid are in large excess and their concentrations are assumed to be constant. Adding two differential equations to account for their temporal evolution does not alter the dynamics of the system, but only slightly the position of the bifurcation points [9].

$$\begin{aligned} d[\text{H}_2\text{O}_2]/dt &= -r_5 - r_6 - r_7 - r_8 + j_0 ([\text{H}_2\text{O}_2]_{\text{in}} - [\text{H}_2\text{O}_2]) \\ d[\text{I}_2]/dt &= r_4 - j_0 [\text{I}_2] \\ d[\text{I}^-]/dt &= -r_1 - r_2 - r_4 + r_5 - j_0 [\text{I}^-] \\ d[\text{HIO}]/dt &= r_1 + 2r_3 - r_4 - r_5 + r_6 - j_0 [\text{HIO}] \\ d[\text{HIO}_2]/dt &= r_1 - r_2 + r_6 - r_7 + r_8 - j_0 [\text{HIO}_2] \\ d[\text{I}_2\text{O}]/dt &= r_2 - r_3 - r_6 - j_0 [\text{I}_2\text{O}] \end{aligned} \quad (1)$$

where $[\text{H}_2\text{O}_2]_{\text{in}}$ is the hydrogen peroxide concentration in the input flow and

$$\begin{aligned} r_1 &= k_1 [\text{IO}_3^-][\text{I}^-][\text{H}^+]^2 - k_{-1} [\text{HIO}][\text{HIO}_2] & r_5 &= k_5 [\text{HIO}][\text{H}_2\text{O}_2] \\ r_2 &= k_2 [\text{HIO}_2][\text{I}^-][\text{H}^+] & r_6 &= k_6 [\text{I}_2\text{O}][\text{H}_2\text{O}_2] \\ r_3 &= k_3 [\text{I}_2\text{O}] - k_{-3} [\text{HIO}]^2 & r_7 &= k_7 [\text{HIO}_2][\text{H}_2\text{O}_2] \\ r_4 &= k_4 [\text{HIO}][\text{I}^-] - k_{-4} [\text{I}_2]/[\text{H}^+] & r_8 &= k_8 [\text{IO}_3^-][\text{H}^+][\text{H}_2\text{O}_2]. \end{aligned}$$

Time series, like those in Figure 1, give only a very limited view of the features of the calculated behaviours, simple oscillations, mixed-mode oscillations or chaos. In order to obtain more information, identify fundamental properties and compare them with other known systems, we have to use other representations and different tools. This work discusses 3D views, calculations of the correlation dimension and Poincaré maps.

The composition of a system can be represented as a point in the space of the concentrations, called the state space, and its evolution with time as the trajectories of this point. Periodic oscillations give closed curves and aperiodic oscillations give unclosed curves known as chaotic attractors. Such representations help in analysing the structure of the state space, identifying attracting and repelling regions in transient regime, revealing common properties of sets of trajectories, and visualizing the shape of attractors. Figure 2 shows trajectories corresponding to the time series in Figure 1. For $j_0 = 4.825 \times 10^{-3} \text{ min}^{-1}$, Figure 1.a. suggests that we have simple oscillations but Figure 2.a. reveals that, instead of a limit cycle, we have a chaotic attractor discussed in details later. Figures 2.b. and 2.d. show two examples of mixed-mode oscillations, several large amplitude oscillations separated by one small amplitude oscillation or several small ones separated by a large one. Figure 2.c. illustrates a chaotic window in the region of mixed-mode oscillations. These 3D views are more informative than the time series but still insufficient to understand the dynamics of the system. A problem is the dimension of the state space: as they are six concentrations, the state space has six dimensions and Figure 2 shows only projections of the trajectories into a 3D subspace. We will try to give the answer to two questions: Do these projections give correct pictures of the real trajectories? Do we have reasons to prefer a special subspace?

Correlation dimension

Periodic trajectories are 1D objects and their projections from a 6D state space into a 3D subspace don't raise special problems. This is not so for chaotic attractors like those in Figures 2.a. and 2.c. To characterize them we have calculated their fractal dimension, or more precisely one of their fractal dimensions [11], that is the correlation dimension introduced by Grassberger and Procaccia [12]. They take N trajectory points and count the fraction $p_i(R) = N_i / (N - 1)$ of these points within a distance R of a given point i . (The expression is divided by $N - 1$ since there are at most $N - 1$ other points in the neighbourhood of the point i .) Then, they calculate the correlation sum defined as

$$C(R) = \frac{1}{N} \sum_{i=1}^N p_i(R)$$

$C(R)$ would be proportional to R if the trajectory points were located on a line and proportional to R^2 if they were located on a surface. This suggests the definition of the correlation dimension as the number D_c that satisfies

$$C(r) = \lim_{r \rightarrow 0} kR^{D_c}$$

In practice, it is impossible to calculate the limit for $R \rightarrow 0$ because the number of points used to calculate $C(R)$ is finite and there is some minimum distance between them. When R is less than this minimum $C(R)$ is equal to zero. The best that can be done is to plot $\log(C(R))$ as a function of $\log(R)$, look for a linear relation at small R values and take the slope as D_c . Figure 3 shows a typical example of the correlation sums calculated for chaotic attractors obtained with our model. To avoid scaling problems, these calculations use the dimensionless form of the kinetic equations discussed later and in annex A. When R is not much smaller than the size of the attractor, the slope of the plot is just a little larger than one. When R decreases, it increases and tends to about two. These results, obtained in the 6D state space, support the geometrical picture given by the 3D projections. The trajectory remains close to the periodic orbits obtained at slightly different j_0 values, which is one-dimensional, and the correlation sums at the higher R values are not very different from the correlation sums for these periodic orbits. The fractal dimension can only be obtained when R is much smaller than the thickness of the attractor. Then, $C(R)$ is small and the number of pairs of points in the calculation of D_c is significant only if N is very large. The precision becomes limited by the calculation times but the obtained information is nevertheless very enlightening: the dimension of the chaotic attractor is close to two. It is a thin band in the 6D state space and its projection in 3D subspaces could distort it but preserve this fundamental property.

Poincaré Sections

We, poor humans, have a great problem: we would like to see properties of the systems we study but are unable to imagine something with more than three dimensions. Even the so-called 3D views in Figure 2 are 2D views from which we try to reconstruct 3D objects in our mind. To characterize trajectories in 3D state spaces it is useful to make Poincaré sections, i.e. to study their intersections with a half plane. If the Poincaré plane is correctly selected, a simple limit cycle gives just an intersection point, complex oscillations give a finite number of points, quasi-periodic oscillations on a torus give a closed curve and a chaotic attractor gives more or less complicated structures of points in the plane. However, in our 6D state space, the Poincaré "plane" has five dimensions and we can only see projections of the Poincaré sections. They are nevertheless useful. Figure 4.a. shows sections of the attractor in Figure 2.a. for $[I] = 4.5 \times 10^{-8}$ M projected in the subspace $[H_2O_2] - [I_2]$. Such projections are identical to sections in Figure 2.a. They reveal a feature of the attractor not observable in this figure, the attractor has the shape of a folded strip and its Poincaré sections are nearly lines. As the intersection of an attractor of dimension D_a with a Poincaré "plane" has a dimension $D_a - 1$, the Poincaré sections in Figure 4.a. indicate that D_a is close to two, in accordance with the correlation dimension calculations. Actually, for any chaotic attractor D_a must be larger than two and zooms on other projections of the Poincaré section reveal that it is a "thick" line.

Poincaré sections don't only help to build geometrical representations of attractors; they also give representations of the motion on it through return maps. The values of

$[\text{H}_2\text{O}_2]$ at the intersections points in Figure 4.a. are plotted in Figure 4.b. in function of the preceding values giving the first return map $[\text{H}_2\text{O}_2]_{n+1} = F_{\text{H}_2\text{O}_2}([\text{H}_2\text{O}_2]_n)$. In the general case of j concentrations, they are j functions represented in vectorial form by $\mathbf{X}_{n+1} = \mathbf{F}(\mathbf{X}_n)$ where $\mathbf{X} = \{X_1 \dots X_j\}$. The theorem of existence and uniqueness of the trajectories imply the existence of these functions. They simplify greatly the description of the system's dynamics and still contain important information about it [11]. The example in Figure 4.b shows a surprising simplification: $[\text{H}_2\text{O}_2]_{n+1}$ depends only on $[\text{H}_2\text{O}_2]_n$ and not on the other concentrations allowing comparisons of the behaviour of this complicated system with well known one-dimensional maps. At the crossing point between the return map and the diagonal line $[\text{H}_2\text{O}_2]_{n+1}$ is equal to $[\text{H}_2\text{O}_2]_n$. This point is the intersection with the Poincaré plane of a period-one closed orbit, which must be unstable. Actually, a chaotic attractor is associated with an infinite number of closed orbits of any order. Important properties of the attractor can be extracted from these orbits [13-16]. The return map for $[\text{I}_2]$ in Figure 4.c seems also one-dimensional but with two branches giving two $[\text{I}_2]_{n+1}$ values for one $[\text{I}_2]_n$ value, which seems to be in contradiction with the uniqueness of the solutions of the differential equations. A closer look at the results shows that there is no contradiction because the $[\text{H}_2\text{O}_2]$ values are different on the two branches. The period-one unstable orbit crosses the Poincaré plane at point O near $[\text{I}_2]_{n+1} = [\text{I}_2]_n = 1.20644 \times 10^{-4}$ and $[\text{H}_2\text{O}_2]_{n+1} = [\text{H}_2\text{O}_2]_n = 0.041778$. At the other crossing point with the diagonal line, near $[\text{I}_2]_n = 1.20639 \times 10^{-4}$, $[\text{H}_2\text{O}_2]_{n+1}$ and $[\text{H}_2\text{O}_2]_n$ have different values and it is not a periodic orbit. In conclusion, Poincaré sections and return maps reduce the study of the main features of our 6D system to the study of 2D maps for $[\text{H}_2\text{O}_2]$ and $[\text{I}_2]$. We now show why and when this reduction is possible.

Dimensionless kinetic equations

The kinetic equations (1) describing the dynamics of our model can be transformed into the useful dimensionless form (2) as explained in the annex.

$$\begin{aligned}
 c_1 \, dy_1/d\tau &= -\rho_5 - \rho_6 - \rho_7 - \rho_8 + c_1 (1 - y_1) + c_2 \\
 dy_2/d\tau &= \rho_4 - y_2 \\
 c_3 \, dy_3/d\tau &= -\rho_1 - \rho_2 - \rho_4 + \rho_5 - c_3 y_3 \\
 c_4 \, dy_4/d\tau &= \rho_1 + 2 \rho_3 - \rho_4 - \rho_5 + \rho_6 - c_4 y_4 \\
 c_5 \, dy_5/d\tau &= \rho_1 - \rho_2 + \rho_6 - \rho_7 + \rho_8 - c_5 y_5 \\
 c_6 \, dy_6/d\tau &= \rho_2 - \rho_3 - \rho_6 - c_6 y_6
 \end{aligned} \tag{2}$$

The y_i are the ratios between the concentrations $[\text{H}_2\text{O}_2]$, $[\text{I}_2]$, $[\text{I}^\cdot]$, $[\text{IOH}^\cdot]$, $[\text{IO}_2\text{H}^\cdot]$ and $[\text{I}_2\text{O}^\cdot]$ and their values at the steady state, the ρ_i are dimensionless forms of the rates r_i and the c_i are dimensionless parameters. Beside the advantages pointed out in the annex of this dimensionless form of the kinetic equations, we show here that they throw light on the behaviour of the trajectories. The values of the parameters c_3 , c_4 , c_5 and c_6

calculated with the rate constants in Table I are smaller than 10^{-2} . One consequence of this smallness can be understood considering the simpler system (3). ε is a small parameter and we suppose that the surface $F_3 = 0$, called the slow manifold, has the folded shape represented in Figure 5. Its upper and lower part are stable, its middle part is unstable.

$$\begin{aligned} dx_1/dt &= F_1(x_1, x_2, x_3) \\ dx_2/dt &= F_2(x_1, x_2, x_3) \\ \varepsilon dx_3/dt &= F_3(x_1, x_2, x_3) \end{aligned} \quad (3)$$

As ε is small, dx_3/dt remains large until x_3 takes a value such that $F_3(x_1, x_2, x_3)$ is also small. The trajectories approach quickly the slow manifold and then move slowly on it. When they eventually reach a point at the borderline between its stable and unstable folds, as points A and C in Figure 5.a, they jump onto the other stable fold at points B and D. This motion gives normally simple or mixed-mode oscillations. It is also possible that the successive transition points are all different, which gives a chaotic attractor sketched in Figure 5.b. The no-intersection theorem [ref. 11, p.77] is not violated because the trajectories do not follow exactly the 2D slow manifold. However, a consequence of the smallness of ε is that they remain very close to it and the dimension of the chaotic attractor is close to two. The solution of the system (3) is nearly always close to the solution of the simpler system $dx_1/dt = F_1(x_1, x_2, x_3)$, $dx_2/dt = F_2(x_1, x_2, x_3)$ and $F_3(x_1, x_2, x_3) = 0$. The last equation gives the so-called "fast" variable x_3 in function of to the "slow" variables x_1 and x_2 . If it is written $x_3 = G(x_1, x_2)$, the approximate equations take the form $dx_1/dt = F_1(x_1, x_2, G(x_1, x_2))$, $dx_2/dt = F_2(x_1, x_2, G(x_1, x_2))$, showing that the main features of the motion are given by the behaviour of x_1 and x_2 .

Our system is more complicated but the simplification is similar. They are six variables but only two of them are slow, $[H_2O_2]$ and $[I_2]$. The slow manifold is two-dimensional and the correlation dimension of the chaotic attractor is close to two because c_3 , c_4 , c_5 and c_6 are small. This reduces the effective dimension of the motion but, of course, still in a 6D state space. Let us underline that the slow variables are the concentrations of species appearing in the stoichiometric equations (R) and (O). If we look at the definitions of the small parameters, we see that this is not fortuitous. The return maps for $[H_2O_2]$ and $[I_2]$ are two-dimensional because the motion remains close to the two-dimensional slow manifold. This could help to identify specific properties of our chaotic attractors. However, if many theoretical results have been obtained for one-dimensional maps, bi-dimensional maps are less known, with the noticeable exception of the Hénon map. Further theoretical works would be useful.

As a final comment, we mention that if we use the values of the parameters giving chaos but replace the first equation of our differential system with the "pool approximation" $[H_2O_2] = \text{constant}$, the solutions are simply stable steady states or limit cycles, depending on $[H_2O_2]$. This suggests that at least two slow variables are needed to get chaos and shows the danger of the pool approximation.

Conclusion

A previous work [10] showed that the model we had proposed for the Bray-Liebhaftsky reaction can simulate mixed-mode oscillations and chaos in a CSTR. In this work, we analyse the characteristics of the trajectories. The model involve six concentrations, $[\text{H}_2\text{O}_2]$, $[\text{I}_2]$, $[\text{I}^-]$, $[\text{IOH}]$, $[\text{IO}_2\text{H}]$ and $[\text{I}_2\text{O}]$, and the trajectories are located in a 6D state space. However, correlation dimensions calculations and Poincaré sections reveal that the chaotic attractors remain close to 2D surfaces. The return maps for $[\text{H}_2\text{O}_2]$ and $[\text{I}_2]$ are bi-dimensional. The dimensionless form of the kinetic equations explains this reduction of the number of effective dimensions. The four variables $[\text{I}^-]$, $[\text{IOH}]$, $[\text{IO}_2\text{H}]$ and $[\text{I}_2\text{O}]$ are "fast" variables and the trajectories are strongly attracted by a 2D slow manifold. The main features of the dynamics are found out in the behaviour of the "slow" variables, $[\text{H}_2\text{O}_2]$ and $[\text{I}_2]$, and we do have reasons to prefer subspaces including these variables. Models in chemical kinetics often lead to this particular kind of differential equations systems, autonomous equations with several "fast" variables and only a few "slow" variables. Writing them in a dimensionless form should reveal the distinction between these two kinds of variables and the associated simplifications. We suggest a link with the chemical intuition: the slow variables are those appearing in the stoichiometric equations.

References

- [1] Bray, W. C. J. Am. Chem. Soc., 1921, **43**, 1262.
- [2] Bray, W. C.; Liebhaftsky, H. A. J. Am. Chem. Soc., 1931, **53**, 38.
- [3] Schmitz, G.; J. Chim. Phys., 1987, **84**, 957.
- [4] Kolar-Anić, Lj.; Schmitz, G. J. Chem. Soc. Faraday. Trans., 1992, **88**, 2343.
- [5] Kolar-Anić, Lj.; Mišljenović, Đ.; Anić, S.; Nicolis, G. React. Kinet. Catal. Lett., 1995, **54**, 35.
- [6] Kolar-Anić, Lj.; Čupić, Ž.; Anić S.; Schmitz, G. J. Chem. Soc. Faraday Trans., 1997, **93**, 2147.
- [7] Vukojević, V.; Anić, S.; Kolar-Anić, Lj. J. Phys. Chem. A, 2000, **104**, 10731.
- [8] Vukojević, V.; Anić, S.; Kolar-Anić, Lj. Phys. Chem. Chem. Phys., 2002, **4**, 1276.
- [9] Kolar-Anić, Lj.; Grozdić, T.; Vukojević, V.; Schmitz, G.; Anić, S. In Selforganization in nonequilibrium systems; Anić, S., Čupić, Ž., Kolar-Anić, Lj., Eds.; Society of Physical Chemists of Serbia: Belgrade, 2004. pp 115.
- [10] Schmitz, G.; Kolar-Anić, Lj.; Anić, S.; Grozdić, T.; Vukojević, V. J. Phys. Chem. A, 2006, in press.
- [11] Hilborn, R. C. Chaos and Nonlinear Dynamics; Second edition; Oxford University Press: Oxford, 2000.
- [12] Grassberger, P.; Procaccia, I. Phys.Rev.Lett., 1983, **50**, 346.
- [13] Auerbach, D.; Cvitanovic, P.; Eckmann, J.P.; Gunarante, G.; Procaccia, I. Phys.Rev.Lett., 1987, **58**, 2387.
- [14] Cvitanovic, P. Phys.Rev.Lett., 1988, **61**, 2729.
- [15] Lai, Y-C.; Nagai, Y.; Grebogi, C. Phys.Rev.Lett., 1997, **79**, 649.
- [16] Gilmore, R.; Lefranc, M. The Topology of Chaos, Wiley, New York, 2002.

Annex: Dimensionless form of the kinetic equations.

A convenient form of the kinetic equations (1) is obtained replacing the actual concentrations by the ratios between their actual values and their values at the steady state, noted [...]_{ss}.

$$y_1 = [\text{H}_2\text{O}_2]/[\text{H}_2\text{O}_2]_{ss}; y_2 = [\text{I}_2]/[\text{I}_2]_{ss}; y_3 = [\text{I}]/[\text{I}]_{ss};$$

$$y_4 = [\text{HIO}]/[\text{HIO}]_{ss}; y_5 = [\text{HIO}_2]/[\text{HIO}_2]_{ss}; y_6 = [\text{I}_2\text{O}]/[\text{I}_2\text{O}]_{ss}$$

The concentrations at the steady state are solutions of the following equations derived from the six equations $d[\dots]_{ss}/dt = 0$.

$$j_o ([\text{H}_2\text{O}_2]_{in} - [\text{H}_2\text{O}_2]_{ss}) = (k_5 [\text{HIO}]_{ss} + k_6 [\text{I}_2\text{O}]_{ss} + k_7 [\text{HIO}_2]_{ss} + k_8 [\text{IO}_3^-][\text{H}^+]) [\text{H}_2\text{O}_2]_{ss}$$

$$j_o [\text{I}_2]_{ss} = k_4 [\text{HIO}]_{ss}[\text{I}]_{ss}[\text{H}^+] - k_{-4} [\text{I}_2]_{ss}$$

$$j_o (2 [\text{I}_2]_{ss} + [\text{I}]_{ss} + [\text{HIO}]_{ss} + [\text{I}_2\text{O}]_{ss}) = k_3 [\text{I}_2\text{O}]_{ss} - k_{-3} [\text{HIO}]_{ss}^2$$

$$j_o (2 [\text{I}_2]_{ss} + [\text{I}]_{ss} + [\text{HIO}]_{ss} + 2 [\text{I}_2\text{O}]_{ss}) = k_2 [\text{HIO}_2]_{ss}[\text{I}]_{ss}[\text{H}^+] - k_6 [\text{I}_2\text{O}]_{ss}[\text{H}_2\text{O}_2]_{ss}$$

$$j_o (2 [\text{I}_2]_{ss} + [\text{I}]_{ss} + [\text{HIO}]_{ss} + [\text{HIO}_2]_{ss} + 2 [\text{I}_2\text{O}]_{ss}) =$$

$$k_1 [\text{IO}_3^-][\text{I}]_{ss}[\text{H}^+]^2 - k_{-1}[\text{HIO}]_{ss}[\text{HIO}_2]_{ss} - k_7 [\text{HIO}_2]_{ss}[\text{H}_2\text{O}_2]_{ss} +$$

$$k_8 [\text{IO}_3^-][\text{H}^+][\text{H}_2\text{O}_2]_{ss}$$

$$j_o (5 [\text{I}_2]_{ss} + 3 [\text{I}]_{ss} + 2 [\text{HIO}]_{ss} + [\text{HIO}_2]_{ss} + 4 [\text{I}_2\text{O}]_{ss}) =$$

$$(k_5 [\text{HIO}]_{ss} - k_6 [\text{I}_2\text{O}]_{ss} - k_7 [\text{HIO}_2]_{ss} + k_8 [\text{IO}_3^-][\text{H}^+]) [\text{H}_2\text{O}_2]_{ss}$$

These equations have no explicit solution but can be solved by an iterative method. Beside the used solution in the region of the state space where we get the oscillations, there is another solution, always unstable, given by

$$[\text{I}_2]'_{ss} = [\text{I}]'_{ss} = [\text{HIO}]'_{ss} = [\text{I}_2\text{O}]'_{ss} = 0$$

$$j_o ([\text{H}_2\text{O}_2]_{in} - [\text{H}_2\text{O}_2]'_{ss}) = (k_7 [\text{HIO}_2]'_{ss} + k_8 [\text{IO}_3^-][\text{H}^+]) [\text{H}_2\text{O}_2]'_{ss}$$

$$j_o [\text{HIO}_2]'_{ss} = (-k_7 [\text{HIO}_2]'_{ss} + k_8 [\text{IO}_3^-][\text{H}^+]) [\text{H}_2\text{O}_2]'_{ss}$$

This steady state is not directly related to the oscillations but could be important for the analysis of the structure of the state space. To put the kinetic equations in a dimensionless form the eleven kinetic constants are replaced with eleven dimensionless parameters. Taking j_o as the unit of time and $[\text{I}_2]_{ss}$ as the unit of concentrations, they are

$$c_1 = [\text{H}_2\text{O}_2]_{ss}/[\text{I}_2]_{ss}; c_2 = ([\text{H}_2\text{O}_2]_{in} - [\text{H}_2\text{O}_2]_{ss})/[\text{I}_2]_{ss}; c_3 = [\text{I}]_{ss}/[\text{I}_2]_{ss};$$

$$c_4 = [\text{HIO}]_{ss}/[\text{I}_2]_{ss}; c_5 = [\text{HIO}_2]_{ss}/[\text{I}_2]_{ss}; c_6 = [\text{I}_2\text{O}]_{ss}/[\text{I}_2]_{ss};$$

$$a_1 = k_{-1} [\text{HIO}]_{ss}[\text{HIO}_2]_{ss} / (j_o \times [\text{I}_2]_{ss}); a_2 = k_{-3} [\text{HIO}]_{ss}^2 / (j_o \times [\text{I}_2]_{ss}); a_3 = k_{-4} / j_o;$$

$$a_4 = k_7 [\text{HIO}_2]_{ss}[\text{H}_2\text{O}_2]_{ss} / (j_o \times [\text{I}_2]_{ss}); a_5 = k_8 [\text{IO}_3^-][\text{H}^+][\text{H}_2\text{O}_2]_{ss} / (j_o \times [\text{I}_2]_{ss})$$

Introducing the dimensionless time $\tau = j_o \times t$ and dimensionless rates of reactions $\rho_i = r_i / (j_o \times [\text{I}_2]_{ss})$, the kinetic equations become

$$c_1 dy_1/d\tau = -\rho_5 - \rho_6 - \rho_7 - \rho_8 + c_1 (1 - y_1) + c_2$$

$$dy_2/d\tau = \rho_4 - y_2$$

$$c_3 dy_3/d\tau = -\rho_1 - \rho_2 - \rho_4 + \rho_5 - c_3 y_3$$

$$c_4 dy_4/d\tau = \rho_1 + 2\rho_3 - \rho_4 - \rho_5 + \rho_6 - c_4 y_4$$

$$c_5 dy_5/d\tau = \rho_1 - \rho_2 + \rho_6 - \rho_7 + \rho_8 - c_5 y_5$$

$$c_6 dy_6/d\tau = \rho_2 - \rho_3 - \rho_6 - c_6 y_6$$

where

$$\rho_1 = (2 + c_3 + c_4 + c_5 + 2c_6 + a_1 + a_4 - a_5)y_3 - a_1y_4y_5$$

$$\rho_2 = 0.5 (c_2 - 1 - c_3 - c_5 - 2a_4)y_3y_5$$

$$\rho_3 = (2 + c_3 + c_4 + c_6 + a_2)y_6 - a_2 y_4^2$$

$$\rho_4 = (1 + a_3)y_3y_4 - a_3y_2$$

$$\rho_5 = 0.5 (5 + c_2 + 3c_3 + 2c_4 + c_5 + 4c_6 - 2a_5)y_1y_4$$

$$\rho_6 = 0.5 (c_2 - 5 - 3c_3 - 2c_4 - c_5 - 4c_6 - 2a_4)y_1y_6$$

$$\rho_7 = a_4y_1y_5$$

$$\rho_8 = a_5y_1$$

This form of the kinetic equations gives convenient representations of the state space with unit concentrations at the steady state and uses parameters with a direct chemical meaning: the c_i are ratios of concentrations and a_1 to a_3 are characteristics of the reversibility of reactions (1), (3) and (4). The superiority of these equations is also a result of the smallness of the parameters c_3 , c_4 , c_5 and c_6 calculated with the rate constants in Table I. As long as they remain small, the permanent trajectories are nearly independent on their values. The original system depends on 13 parameters, j_0 , $[\text{H}_2\text{O}_2]_{\text{in}}$ and eleven kinetic constants but we don't need to know exactly all these constants. The dynamics of the system depends only on c_1 , c_2 and the five a_i . The dimensionless equations show which values, or ratios of values, are important and which are not. Moreover, they reduce some numerical problems associated with the stiffness of the classical equations.

Table I: Model of the Bray-Liebafsky reaction.

Reactions	Rate constants ^(a)	no.
$\text{IO}_3^- + \text{I}^- + 2\text{H}^+ \rightleftharpoons \text{HIO} + \text{HIO}_2$	$k_1 = 3.18 \times 10^5$; $k_{-1} = 7.91 \times 10^7$	(R1, R-1)
$\text{HIO}_2 + \text{I}^- + \text{H}^+ \rightarrow \text{I}_2\text{O} + \text{H}_2\text{O}$	$k_2 = 5.0 \times 10^{11}$	(R2)
$\text{I}_2\text{O} + \text{H}_2\text{O} \rightleftharpoons 2\text{HIO}$	$k_3 = 5.0 \times 10^3$; $k_{-3} = 3.15 \times 10^8$	(R3, R-3)
$\text{HIO} + \text{I}^- + \text{H}^+ \rightleftharpoons \text{I}_2 + \text{H}_2\text{O}$	$k_4 = 3.0 \times 10^{11}$; $k_{-4} = 4.5$	(R4, R-4)
$\text{HIO} + \text{H}_2\text{O}_2 \rightarrow \text{I}^- + \text{H}^+ + \text{O}_2 + \text{H}_2\text{O}$	$k_5 = 1.20 \times 10^4 + 3.0 \times 10^4 * [\text{H}^+]$	(R5)
$\text{I}_2\text{O} + \text{H}_2\text{O}_2 \rightarrow \text{HIO} + \text{HIO}_2$	$k_6 = 5.0 \times 10^5$	(R6)
$\text{HIO}_2 + \text{H}_2\text{O}_2 \rightarrow \text{IO}_3^- + \text{H}^+ + \text{H}_2\text{O}$	$k_7 = 2.0 \times 10^3$	(R7)
$\text{IO}_3^- + \text{H}^+ + \text{H}_2\text{O}_2 \rightarrow \text{HIO}_2 + \text{O}_2 + \text{H}_2\text{O}$	$k_8 = 9.5 \times 10^4 + 3.92 \times 10^{-2} * [\text{H}^+]$	(R8)

^(a) We keep the units $\text{mol} \times \text{dm}^{-3}$ and min used in the previous papers [3-6].

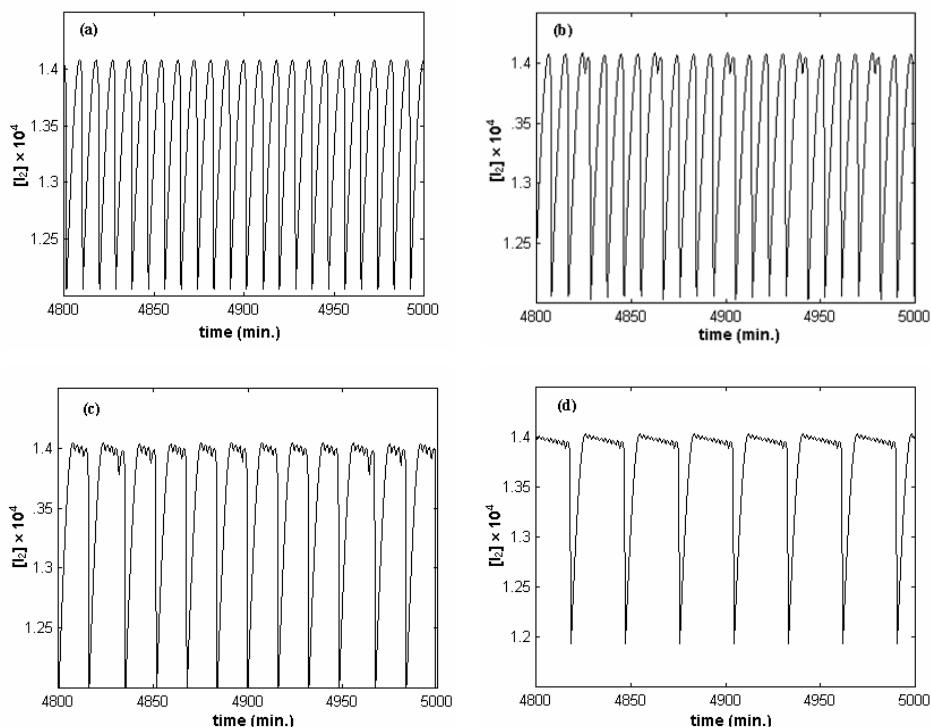


Fig. 1. Time series for $j_0 = 4.825 \times 10^{-3}$ (a), 4.828×10^{-3} (b), 4.9466×10^{-3} (c) and $5.02 \times 10^{-3} \text{ min}^{-1}$ (d).

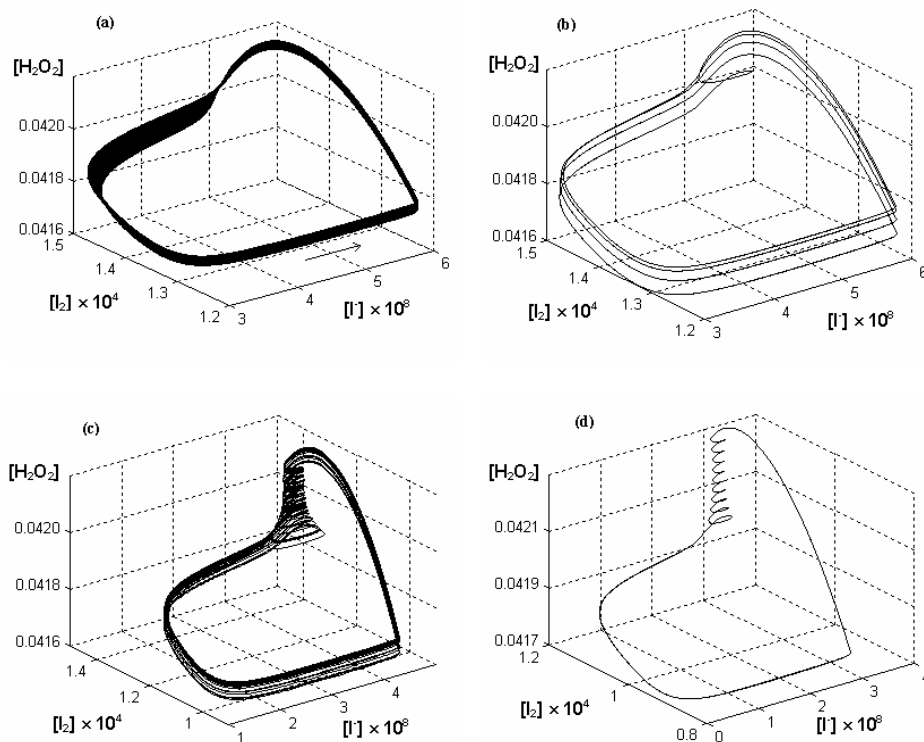


Fig. 2. 3D projections of the trajectories in the 6D state space for the same j_0 values as in Figure 1.

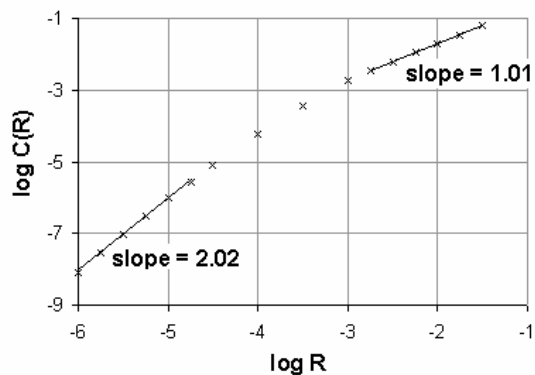


Fig. 3. Correlation sum and correlation dimension for the chaotic attractor of Figure 2.a.

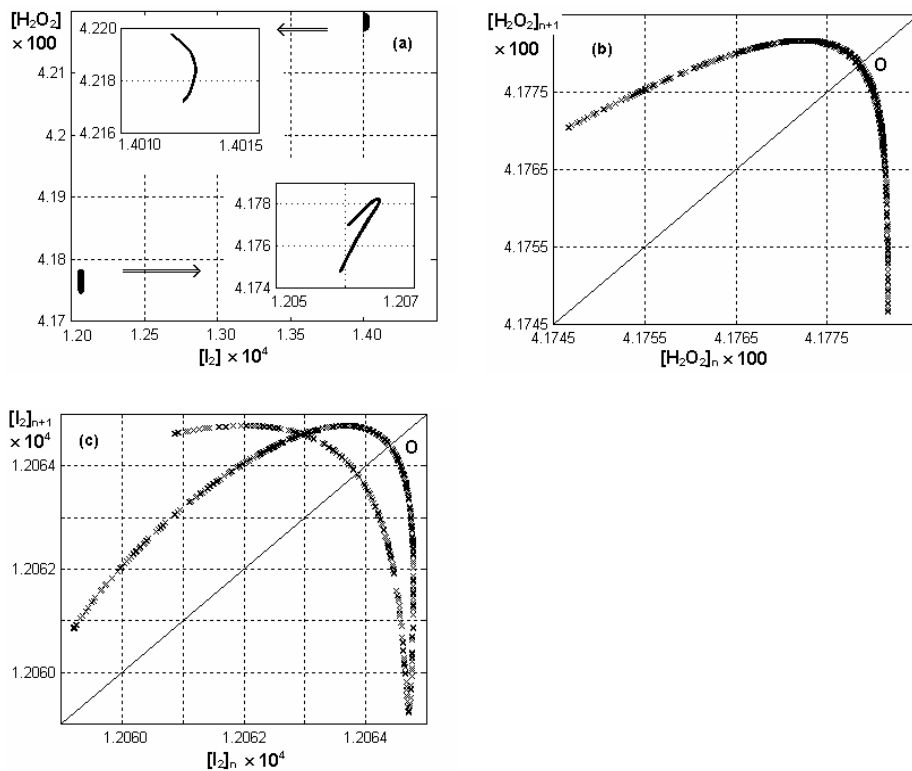


Fig. 4. Poincaré sections for $[I] = 4.5 \times 10^{-8}$ and $d[I]/dt < 0$ (upper part) or $d[I]/dt > 0$ (lower part) in the chaotic attractor of Figure 2.a. (a); First return maps for $d[I]/dt > 0$ (b and c).

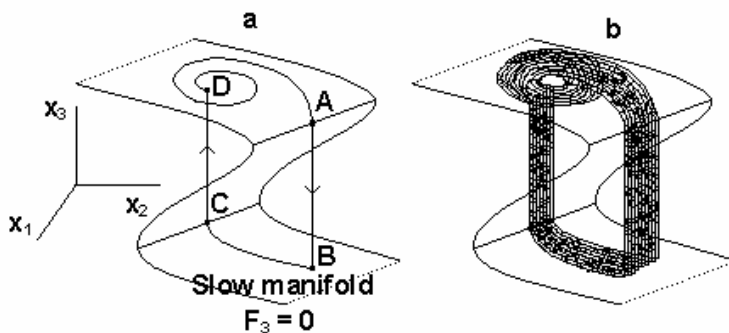


Fig. 5. Mixed-mode oscillations (a) and chaos (b) near a slow manifold.

BOUNDEDNESS: THE ONTOLOGICAL CONCEPT BEHIND THE DETERMINISTIC CHAOS

M. K. Koleva and L. A. Petrov

*Institute of Catalysis, Bulgarian Academy of Sciences, Sofia, Bulgaria
(mkoleva@bas.bg)*

Abstract

We present a new concept, that of the boundedness, which makes the chaotic properties insensitive to the mathematical origin of the corresponding time series. In result, they are not anymore hallmark of a special type “determinism” associated only with certain type of ordinary and partial differential equations but become properties related to the novel ontological concept of the boundedness.

Introduction

Deterministic chaos is one of the most attracting and still enigmatic conjectures in the science. It gains its popularity after the pioneering work of Lorentz who has studied numerically the solution of a system of 3 ordinary differential equations. He has established that at certain values of the control parameters the solution behaves in a highly non-trivial way: it widely varies and exhibits strong sensitivity towards initial conditions – any small perturbation of the initial values is rapidly amplified to a finite deviation of the perturbed solution from the unperturbed one. This behavior initiated an avalanche of works because it opens two questions of fundamental importance: (i) since the chaotic properties are established at wide variety of natural systems, is there a general enough concept that is able to associate the evolution of that broad spectrum of natural systems with single mathematical structure, that of the systems of differential equations; if so, how the Nature drives the irregularities of the chaotic time series in every particular system; (ii) though the properties of the chaotic solutions are well established now, the relation between the determinism of the differential equations and the statistical properties of their chaotic solutions is still open; moreover, the puzzling increases because it has been found out that the chaotic properties are insensitive to the statistics of the chaotic time series. Hence, we face a crucial question: what type of statistics brings about the insensitivity of chaotic properties and how it is related to the determinism of the differential equations. Going a step further, this question opens the door to challenging the very idea of deterministic chaos, namely: focusing attention on the type of statistics that provides properties insensitive to its particularities makes the matter about the mathematical origin of the irregularities irrelevant. In other words, we put the idea of deterministic chaos upside down: we ask whether there is an ontological concept that renders some properties of the natural time series independent of their statistics. This paraphrase is not only of particular interest for the mathematicians but it has deep epistemological sense as well. Indeed, our knowledge about the Nature is built on the idea that we are able to extract a genuine for the system signal

from the “noise” that inevitably accompanies its recording. Furthermore, the nonlinearities of the recording due to effects like local averaging, inertia, resolution, filtering etc. distort the genuine signal. However, the distortion is crucial for an irregular, “noisy” signal, chaotic ones included, because it “transforms” the original time series into a new one. This immediately illuminates the importance of the issue about the existence of such properties of the time series that are independent of their statistics. Furthermore, the ubiquity of the matter prompts to look for a general ontological concept that selects the appropriate statistical properties. We have demonstrated [1] that such ontological concept does exist and it is the concept of the boundedness. Furthermore, we proved that time series subject to that concept exhibit properties insensitive to the particularities of their statistics – to the most surprise, those properties are identical to the corresponding ones of the chaotic time series. Now we are going to do more: in §3 we will demonstrate that the numerical simulation of chaotic dynamical systems appears as an aspect of the boundedness ansatz. Yet, prior to that we will present the concept of the boundedness and will briefly illustrate its straightforward relation to the major chaotic properties.

1. Boundedness. Scaling Invariance

The above considerations give priority to the issue about the general properties of the fluctuating systems. Exerting fluctuations is a part of our daily life: chemical systems, currency exchange rate, rivers, quasars, they all permanently fluctuate. But is there any general rule that dictates the behavior of fluctuations at such broad spectrum of systems? We assert that such rules do exist and they are manifestations of the boundedness concept. It has 3-fold specifications that are: (i) every system has its thresholds of stability so that their exceeding destroys the system. Applied to fluctuations, the existence of thresholds of stability puts limits on the amplitude of fluctuations, namely – a system that exerts fluctuations stays stable if only the amplitude of fluctuations permanently stays within margins dictated by the threshold of stability. (ii) The second aspect of the boundedness concept concerns the rate of developing of the fluctuations. This confinement is imposed by one of the most fundamental conjectures in the science: that about the finite velocity of transmitting substance/energy through space-time - it imposes limitation over the rate of development of the fluctuations. (iii) The third specification of the boundedness concept concerns extended many-body systems with short-range interactions. We have proved [2] that the interplay between the short-range interactions and the boundedness of velocity of transmitting substance/energy through space-time yields amplification of the local fluctuations. In turn, if not suppressed, the latter would give rise to local destabilization that rapidly brings about collapse of the system. Therefore, there should exist mechanism that couples distant fluctuations so that their further behavior to be coherent. It turns out [1] that the operational protocol of coherence does exist and is interrelated to the above aspects of the boundedness concept, namely: in a natural way it puts limits both on the amplitude and the rate of development of the macroscopic fluctuations. The above interplay of all 3 aspects of the boundedness concept renders possible executing of “U-turns” on

reaching the thresholds of stability without involving any additional process. In turn, the latter immediately provides scaling invariance of the corresponding time series.

The boundedness along with the scaling invariance prompts the anticipation that the specific to the system properties are concentrated on the time scales smaller than the duration of the largest fluctuations, i.e. the duration of the fluctuations that reach the thresholds of stability; above that time scale it is expected that the properties of the time series are insensitive to the particularities of their statistics. Note, however, that the boundedness concept must be available for all time scales. This makes the target insensitivity to be expressed in parameter-free form because the latter is the only possible one that does not entangle the rate of development of the fluctuations with a specific time scale. Note that if opposite, i.e. if the form is exponential for example, the rate of development of fluctuations can reach arbitrary value through appropriate choice of the units of the specific parameters.

2. Major Chaotic Properties and Boundedness

The task of the present section is to illustrate how the chaotic properties emerge from the boundedness concept. Let us first focus our attention how the concept of the boundedness is incorporated in the structure of the time series. Obviously, that boundedness imposes two general constraints on every time series: the first one is that the amplitude of its terms is bounded so that the margins of their variations are dictated by the thresholds of stability; the second one is that the boundedness of the rate of development of the fluctuations renders interrelation between the size of a fluctuation and its duration. Now we must prove that these constraints are enough to ensure the target insensitivity of the chaotic properties from the statistics of a zero-mean time series subject to boundedness; we call hereafter such time series BIS (bounded irregular sequence).

We start with a very important characteristic of every irregular sequence, namely its autocorrelation function whose definition reads:

$$G(\eta) = \lim_{T \rightarrow \infty} \frac{1}{T} \int_0^{T-\eta} (X(t+\eta) - \langle x \rangle)(X(t) - \langle x \rangle) dt \quad (1)$$

The autocorrelation function is a measure of the average correlation between any two points in the sequence separated by a time interval $\eta \leq T$. An intriguing interplay of the boundedness and the scaling invariance is developed. On the one hand, the uniform contribution of all time scales restrains persistence extent without signaling out any specific one. On the other hand, the boundedness limitates the persistence because every deviation inevitably “turns back”. Note that the uniform contribution of all time scales is very different from random contributions. The latter is characterized by the lack of any systematic correlations whilst the former is characterized by persistent but parameter-free correlations. But how far away is the persistence spread? And how the

boundedness affects its extent? In §1.3 of [1] we found out that the autocorrelation function of BIS of arbitrary but finite length T reads:

$$G(x) = \sigma \left(1 - (x)^{\nu(x)}\right) \quad (2)$$

where $x = \frac{\eta}{T}$, $x \in [0,1]$; σ is the variance of the BIS and $\nu(x) = 1 - x$. It is obvious that the shape of $G(x)$ meets the requirement that the autocorrelation function is parameter-free. It should be stressed that the derivation of the above shape involves only constraints imposed by the boundedness. In turn, this immediately implies that the shape of the autocorrelation function is insensitive to the statistics of the time series.

Another important characteristic of every time series is its power spectrum. Though it is Fourier transformation of the autocorrelation function, it has its own role among the properties of the time series. It turns out that the shape of the power spectrum of every BIS is also insensitive to its statistics and uniformly fits the shape:

$$S(f) \propto 1/f^{\alpha(f)} \quad \text{for } f \geq \frac{1}{T} \quad (3a)$$

$$S(f) \equiv 0 \quad \text{for } f < \frac{1}{T} \quad (3b)$$

where $\alpha(f) = 1 + \kappa \left(f - \frac{1}{T}\right)$; T is the length of the time series and κ is a parameter set on the thresholds of stability.

The insensitivity of the shape of the power spectrum to the statistics of the time series opens the door to separation of genuine for the system information from the inevitable internal and external noises and their distortion by the recording. Note that the long-range correlations due to a genuine for the system process appear as discrete lines (bands) in the power spectra. Thus, the insensitivity of the “noise” power spectrum shape from the statistics lets unambiguous and reproducible separation of the discrete bands (genuine signal) from whatever noise on the only condition that the latter is to be bounded.

So far we have established that the power spectrum and the autocorrelation function of the BIS exhibit remarkable universality - their shape and characteristics are free from any specification of the fluctuation dynamics. Though this ubiquitous insensitivity has been rigorously proven, our intuition remains unsatisfied and we are strongly tempted to suggest that the power spectrum and the autocorrelation function are too “coarsen” characteristics to take into account the particularities of the fluctuations dynamics. Indeed, the dynamics of the fluctuations comes out from specific for every system processes associated with their development. Yet, now we shall show that the fluctuation dynamics is also subject to certain universality.

The usual way to reveal the dynamics of the correlations in a stochastic sequence is to study the properties of its phase space. The procedure involves dividing of the phase space volume into small size cells and counting the points at which the trajectory intersects each of them. It is certain that this elaborate operation helps much in the examination of the correlation dynamics. Alongside, it is to be expected that the obtained information is highly specific. However, the general aim of this section is to illuminate the universal properties of the BIS and their relation to the chaoticity. Our major goal is the systematic derivation of all chaotic properties from the boundedness. That is why now we focus the attention on the question whether the boundedness gives rise to some universality of the fluctuation dynamics. In §1.6 of [1] we proved that the interrelation between the size and the duration of a fluctuations drives a mechanism of stretching and folding in the phase space. This along with the presence of thresholds of stability makes the fine structure of the attractor very different from the coarse-grained one. The correlation dimension of the attractor vs. cell size at 3 different topological dimensions is plotted in Fig.1. Though we do not specify the actual topological dimension n , the plot is made so that to leave the dynamical rate intact. The plot exhibits the following characteristic properties of the population behavior:

(i) at every topological dimension the plot manifests nearly linear part. Accordingly the population behaves as l^{-D_n} where D_n decreases on n increasing.

(ii) at every topological dimension the population reaches saturation;

(iii) the saturation value is insensitive to the value of the topological dimension.

The linear part of the plot is apparently associated with the prevailing role of the stretching. Further, since the folding shrinks the distance between the points, it effectively weakens the correlations necessary for stretching. In other words it acts towards stochastisation of the phase space points. Thus the population tends to remain constant and insensitive to any further growth of the cell size. This immediately renders the saturation value insensitive to the topological dimension.

It is worth noting that the above plot is pronounced illumination in favor of the boundedness concept because the above behavior of the correlation dimension is one of the most pronounced chaotic properties. Furthermore, it is a not only a property related to the chaos but it turns out to be insensitive to the statistics of the time series as well. So, we again experience the remarkable universality that the boundedness brings about.

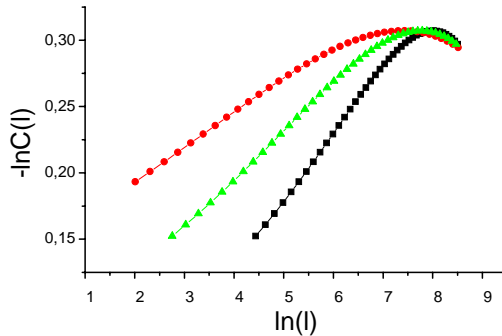


Figure 1: Phase space population vs. cell size

Another highly specific for the deterministic chaos characteristics is the so called K – entropy. It is a measure of the average information necessary for precise setting of the motion in the phase space. The value of K -entropy is definitive for the chaos since it is zero for the deterministic motion infinite for the stochastic one and finite for the deterministic chaos. So, what is its value for the BIS? In §1.7 of [1] we established that the behavior of K – entropy is straightforwardly related to the stretching and folding. The explication of that relation becomes evident by setting $K(u)$ through $(1 - P(u))$, where $P(u)$ is the probability for participation to the stretching and folding; u is the phase space angle. Then the plot of $K(u)$ vs. u presented in Fig.2 has the following meaning: the increase of the probability for stretching at small u requires more information for setting the distance between the initial and the final point of any trajectory. Further, the stretching reaches its maximum and turns to folding which, however, shrinks the distance between the initial and the final point of the trajectory. Thus the folding contributes to better precision of the position of the motion. In turn, the better precision needs less information for specifying the characteristics of the trajectory. As a result, the K -entropy turns to decrease.

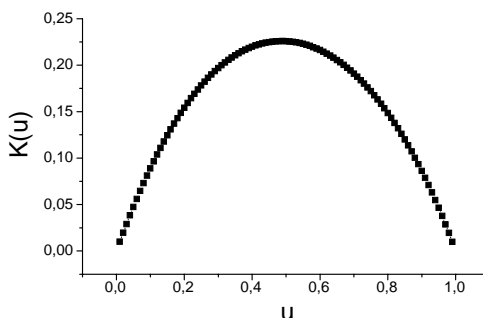


Figure 2: K -entropy of a BIS

A vital property of K – entropy is that it presents the stretching and folding in power type form. Let us outline that the power type form is the only possible parameter-free form that meets the interplay of the requirements about the lack of entanglement between any specific time scale and the boundedness of transmitting substance through space-time (dynamical boundedness).

Summarizing, let us mention once again that all the properties of BIS presented above are derived without involving any information about the statistics of the time series. At the same time, however, the derivation explicitly exploits the idea of boundedness and the scaling invariance. These circumstances let us to conclude that time series subject to boundedness concept manifest major chaotic properties regardless to the origin of the fluctuations. In turn, the latter gives priority to the boundedness concept as the onset of the chaoticity since it is not anymore related to a single mathematical structure (deterministic differential equations). Yet, the crucial test for the boundedness concept is whether the deterministic chaos that appears from the simulation of some dynamical systems can be put in the frame of the boundedness concept. If so, this result would justify an undisputable superiority and would ensure an enormous ubiquity of the boundedness concept. We will discuss this issue in the next section.

3. Deterministic Chaos and Boundedness

The low dimensional chaos is associated with the dynamical systems of the type:

$$\frac{d\bar{x}}{dt} = \bar{\alpha}\hat{A}(\bar{x}) - \bar{\beta}\hat{R}(\bar{x}) \quad (4)$$

where $\bar{\alpha}$ and $\bar{\beta}$ are control parameters. Eqs.(4) are a system of ordinary differential equations that fulfill Lipschitz conditions. Then its solution should be smooth line whose course is predetermined by the initial conditions in an arbitrarily long span both back and forward in the time. However, it turns out that numerical solution of some dynamical systems behaves differently at certain values of the control parameters $\bar{\alpha}$ and $\bar{\beta}$: it is highly irregular and exhibits strong sensitivity to the initial conditions. It has been established that this behavior arises around unstable solution(s). But what drives the solution to behave rather as a solution of stochastic than of deterministic equations? It is to the point to mention that the name deterministic chaos comes namely from the following vicious circle: though eqs.(4) are deterministic, i.e. they do not involve any stochastic functions, their solution behaves as a stochastic function that exhibits chaotic properties. It has been established that its power spectrum is a continuous band; its embedding dimension is finite and fractal. However, the great mystery remains: why the solution behaves as an irregular function?

To reveal the mystery let us remind that the numerical simulation involves inevitable round-off at every step. When the solution is stable the round-off is negligible. However, at unstable solutions the round-off is amplified and rapidly becomes compatible to the values of the smooth part. Further, it appears as multi-valued function since the round-off around 0.5 is executed as a random choice among two selections: the round-off to the lower value and the round-off to the higher value. Then, the amplification of the round-off causes "transformation" of the deterministic equations (3.17) into the following stochastic ones:

$$\frac{d\bar{x}}{dt} = \bar{\alpha}\hat{A}(\bar{x}) - \bar{\beta}\hat{R}(\bar{x}) + \bar{\alpha}\hat{\eta}_{ai}(\bar{x}) + \bar{\beta}\hat{\eta}_{rj}(\bar{x}) \quad (5)$$

where $\hat{\eta}_{ai}(\bar{x})$ and $\hat{\eta}_{rj}(\bar{x})$ are the stochastic terms that come from the amplification of the round-off. Moreover, the stochastic terms in (5) are bounded since it is well established that the solution of the chaotic dynamical systems is confined to the so called strange attractor that has finite volume. Thus, the solution of a simulated dynamical system (5) is BIS unlike the solution of (4) that is smooth function the course of which is predetermined by the initial conditions.

Note that the stochastic terms in (5) are pronounced only at those values of the control parameters where the solution is unstable. Thus, the chaoticity is manifested only at particular control parameters choice. It should be stressed that the association of the chaoticity with specific control parameters is a property generic only for the simulated

dynamical systems. Unlikely, the manifestation of the chaoticity at the natural systems is free from any general specification of the control parameter choice since the boundedness provides independence of the chaoticity from origin of the fluctuations and from the mathematical structure that describes them.

Summarizing, the boundedness concept manages to explain in a very natural way the greatest mystery of the deterministic chaos: the origin of the irregularities of the solution. The key point is that simulation transforms the deterministic equations into stochastic ones whose solutions are BIS.

Conclusion

We have demonstrated that the boundedness is a concept that gives credible fundament of the ubiquity of the chaoticity releasing that phenomenon from the confinement of a specific mathematical structure. Alongside, its vital advantage is that it ensures the insensitivity of the chaotic properties to the statistics of time series which in turn makes the separation of genuine for the system information from the internal and external noises unambiguous and reproducible.

References

- [1] M. K. Koleva, (2005), e-print <http://arXiv.org/physics/0512078>
- [2] M. K. Koleva, (2006), e-print <http://arXiv.org/nlin.AO/0601048>

STOICHIOMETRIC NETWORK ANALYSIS AND CLASSIFICATION OF A pH-OSCILLATOR

I. Schreiber, O. Pešek, P. Špás, M. Voslař and L. Schreiberová

*Department of Chemical Engineering, Institute of Chemical Technology, Prague,
Technická 5, 166 28 Prague 6, Czech Republic (Igor.Schreiber@vscht.cz).*

Abstract

Mechanisms of reactions displaying multiple steady states and/or oscillations can be categorized according to characteristic types of positive and negative feedback loops involved. These loops as well as conditions for the associated oscillatory instability are identified by using stoichiometric network analysis. Several types of experiments can be performed to classify reaction mechanisms and the role of species. Subsequently, main features of the mechanism can be deduced. A pH-oscillatory reaction of hydrogen peroxide with thiosulfate catalyzed by cupric ions (HPTCu) is taken as an example of this kind of analysis.

Introduction

Oscillating chemical reactions have the distinct property of periodic or aperiodic oscillatory course of concentrations of reacting chemical species as well as temperature. This behavior is due to interplay of positive and negative feedback with alternating dominance of these two dynamic effects. For example, an exothermic reaction produces heat that increases temperature, which in turn increases reaction rate and thus produces more heat. Such a thermokinetic effect is thus autocatalytic and represents a positive feedback. When run in a flow-through reactor with a cooling jacket, the autocatalysis is eventually suppressed if the reactant is consumed faster than it is supplied. At the same time, the excess heat is being removed via the jacket, which tends to quench the system. The latter two processes are inhibitory and represent a negative feedback. If the heat removal is slow enough to not suppress entirely the autocatalysis, but fast enough for temperature to drop before there is enough of reactant available via the feed to restore autocatalysis, then there are oscillations in both temperature and concentration of the reactant.

Autocatalysis and oscillations occur also in reactions where thermal effects are negligible, or the system is maintained at constant temperature, as is the case with homogeneous chemical reactions taking place in a thermostated flow-through reactor, as well as biochemical reactions in living cells and organisms. Autocatalysis can easily be realized in isothermal systems, where instead of a heat producing reaction there will typically be a closed reaction pathway, such that species involved are produced faster by reactions along the pathway than they are consumed by removal reactions. A classical example is provided by the well-known Belousov-Zhabotinsky (BZ) reaction [1].

We focus here on strategies of analysis for reaction mechanisms of oscillatory chemical reactions in open (flow-through) homogeneous systems with no spatial gra-

dients (stirred systems). In particular, we focus on pH-oscillators [2] – oscillating reactions with an autocatalytic effect involving protons. The hydrogen peroxide-thiosulfate-Cu(II) (HPTCu) reaction [3, 4] in a single continuous-flow stirred tank reactor (CSTR) provides nonlinear dynamical behavior including different types of steady states, spontaneous oscillations, bistability between steady states or between a steady state and oscillations, and hysteretic loops. In addition, there exist conditions under which the system is excitable.

Theory

A homogeneous oscillatory chemical reaction in a closed system is described by a set of ordinary differential equations

$$\frac{dX_i}{dt} = F_i(X_1, \dots, X_n) = R_i(X_1, \dots, X_n) + k_0(X_i^0 - X_i), \quad (1)$$

Here X_i is the concentration of species i and the net reaction rate R_i for species i is obtained as a sum over contributing rates from a reaction mechanism consisting of elementary steps by use of mass action kinetics. In an open system [a continuous-flow stirred tank reactor (CSTR)], $k_0(X_i^0 - X_i)$ is the term due to inflow and outflow of the i th species; k_0 is the reciprocal residence time (or flow rate) and X_i^0 is the input concentration of the i th species.

Stoichiometric Network Analysis (SNA). We introduce some of the concepts set out by Clarke [5] in his development of the SNA in order to discuss the categorization of oscillators set forth by Eiswirth et al. [6].

Assume that there are n reacting species taking part in r chemical reactions. Let \bar{S} be the $(n \times r)$ corresponding stoichiometric matrix, and $\bar{v}(X) = (\bar{v}_1(X), \dots, \bar{v}_r(X))$ the vector of reaction rates. The matrix \bar{S} together with the vector function $\bar{v}(X)$ define the mechanism of the reaction, also called a stoichiometric network. The time evolution of X in a flow-through system at constant temperature in a well-stirred reaction cell of constant reaction volume can be, according to Eqs. (1), rewritten in vector notation as

$$\frac{dX}{dt} = F(X) = \bar{S}\bar{v}(X) + k_0(X_0 - X) = Sv(X), \quad (4)$$

where $X_0 = (X_{01}, \dots, X_{0n})$ is the vector of feed concentrations for each species and k_0 is the flow rate (or reciprocal residence time). The inflow and outflow terms can be formally treated as zeroth and first order pseudoreactions, respectively, and are con-

veniently included in an extended reaction rate vector $v(X) = (\bar{v}, k_0 X_0, k_0 X)$ having nonnegative components. Accordingly, an extended stoichiometric matrix is $S = [\bar{S}, I, -I]$, where I is identity matrix. Then $F(X)$ is simply expressed as $Sv(x)$.

A stationary state X_s satisfies the equation $Sv(X) = 0$. Hence $v_s = v(X_s)$ is contained in the null space of S . Moreover, all components of v must be nonnegative numbers which narrows the set of all possible stationary reaction rate vectors v_s (the currents in SNA terminology) to an open, convex, d_r -dimensional cone, $d_r = r - \text{rank}(S)$, in the space of all v 's. The edges of this steady state cone represent sets of steady states that have minimum possible nonzero v_j 's admitted by (4), and uniquely define a set of major subnetworks (or extreme currents) e_k of the mechanism. In general, the number K of such subnetworks equals at least the dimension of the cone, $K \geq d_r$ and v_s is a linear combination of extreme subnetworks with nonnegative coefficients.

The Jacobian matrix J of Eq. (4) at X_s is

$$J = \left. \frac{dF}{dX} \right|_{X=X_s} = S(\text{diag } v_s) \kappa^T (\text{diag } X_s)^{-1} = -V(\text{diag } X_s)^{-1} \quad (5)$$

where the matrix of effective reaction orders $\kappa = \{\kappa_{ij}\} = \left\{ \frac{\partial \ln v_j(X_s)}{\partial \ln X_i} \right\}$ is called the kinetic matrix. If power law kinetics is in effect κ is constant and the stability of the current v_s is indicated by principal subdeterminants β_l of order $l = 1, \dots, n$ of the matrix V . There are different β_l 's related to all permutations of l species. If at least one of them is negative then at least one eigenvalue of J is unstable, provided that the values of the steady state concentrations of the corresponding l species are sufficiently small [5]. The stability of the network's steady states thus depends on the stability of the extreme subnetworks. An unstable e_k may induce instability of the entire network.

A network diagram is a convenient graphical representation of mass action networks. Any elementary reaction is drawn as a multi-headed multi-tailed arrow oriented from the species entering the reaction to those produced by the reaction: the number of feathers (barbs) at each tail (head) represents the stoichiometric coefficient of the reactant (product); the order of the reaction is the number of left feathers (for examples of network diagrams see Figure 2 discussed in the next section). A graph theoretical approach allows for checking the stability of a (small enough) network by inspection of the graph [5]. Typically, a cycle in this graph may be associated with autocatalysis and oscillatory instabilities if the corresponding β_l is either positive (strong cycle) or zero (critical cycle).

Role of Species in Oscillatory Reactions. Eiswirth et al. [6] proposed a categorization of chemical oscillators. First, a distinction is made between nonessential and essential species. If the concentration of a nonessential species is held constant, oscillations continue. In contrast, if the concentration of an essential species is fixed, oscillations cease. In analyzing the core mechanism of a chemical oscillator, nonessential species may be neglected or considered as parameters, which simplifies the problem under consideration. The categorization is based on a set of experimental tests that

lead to identification of essential chemical species and their roles in producing the instability leading to oscillatory behavior.

The roles of essential species in mechanisms of chemical oscillators are defined as: 1) *autocatalytic* or *cycle species* (those involved in a reaction in which an increase in the concentration of a species increases the rate of production of that species), denoted X; 2) *exit species* (those exerting direct inhibitory effect on the cycle species by reacting with it to produce nonessential species or essential species other than X), denoted Y; 3) *feedback species* (those exerting indirect inhibitory effect on the cycle species by providing negative feedback on the autocatalytic cycle), denoted Z; and 4) *recovery species* (those that take part in reactions allowing the autocatalysis to recover), denoted W. Not all of these roles are necessary in every category of oscillator.

Categorization of Oscillatory Reactions. The categories of oscillators discussed in Eiswirth et al. [6] contain topologically different connectivity between the species, that is, the relations among the species in a system, as products and reactants in elementary mechanistic steps, which can produce oscillatory behavior. Two main categories of oscillators are based on the autocatalytic cycle present in the mechanism.

Category 1 is the group of oscillators with a critical cycle that is combined with an exit reaction; this implies that type Y species is always involved, in addition to type X and Z.

Category 2 is a group of oscillators with a strong cycle; here a direct removal of a cyclic species instead of an exit reaction is sufficient, and thus type Y is absent.

Further classification of mechanisms leads to subcategories 1B, 1C (further subdivided into 1CX and 1CW) and 2B, 2C. In category 1, the order of the autocatalytic species in the cycle reaction is equal to one (and equal to the order of X in the exit reaction). Category 2 oscillators include mechanisms with autocatalytic reaction of a higher (effective) order in X than the order of X in the removal reaction, and the type X species need not necessarily be chemical species. Rather, they may include vacant surface sites in heterogeneous catalysis, or temperature in thermokinetic oscillations.

Subcategories within this classification scheme are distinguished according to the kind of negative feedback involving type Z species.

Input negative feedback: type Z species is flowed into the reactor and controls the autocatalytic process by reacting with the type X species; this feature may occur in both category 1 and 2. Additionally, in category 1 type Z species may also be produced by an exit reaction (i.e., $X + Y \rightarrow Z$) rather than provided via feed.

Output negative feedback: type Z species is a product of a cycle reaction (such a reaction is termed tangent) and controls the autocatalysis indirectly by producing type Y species that inhibits the type X species (tangent feedback); in another variant of this kind of indirect control the type Z species is produced by exit rather than tangent reaction, and then produces type Y species (exit feedback). For category 2, Z is also produced an autocatalytic cycle reaction but in the next step Z reacts directly with X in an exit reaction thereby leaving out type Y species. This represents tangent feedback, but exit feedback may occur as well (e.g., via $Z + X \rightarrow 2Z$).

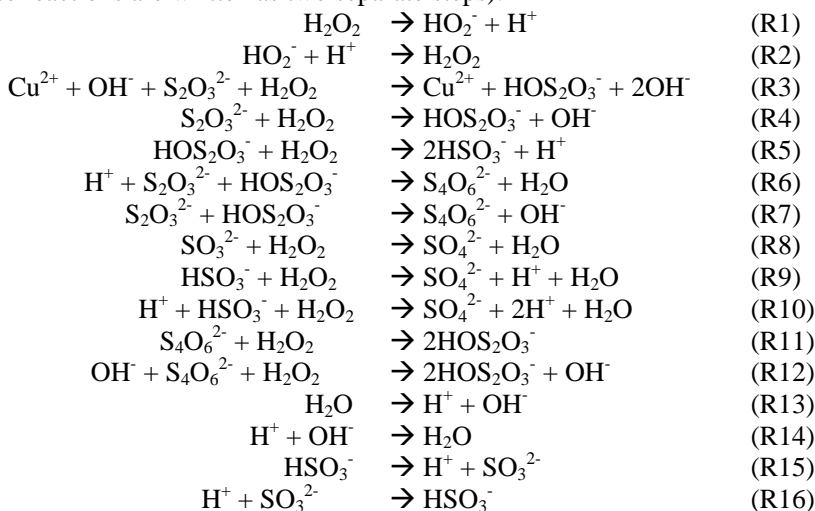
The subcategories 1C and 2C involve mechanisms with input feedback; either Z or Y (or both) has to be provided by feed and thus the C subcategory is crucially de-

pendent on inflow (C stands for continuous). The subcategories 1B and 2B involve mechanisms with output feedback, tangent or exit. Here the autocatalytic process is driven by a nonessential species present in surplus and thus all essential species are generated by reactions rather than inflow. Consequently, reactions in the B subcategory provide sustained oscillations even in a closed system until the nonessential species is exhausted (B stands for batch).

Experimental tests. Here a list of methods is provided from which we can deduce the essential and nonessential species in a given oscillatory system, the connectivity of the essential species producing the oscillations, and the category of the oscillatory system; these steps help to a formulation of the core of the reaction mechanism. The methods include: amplitude and phase relations, concentration shift regulation, concentration shift destabilization, bifurcation diagrams, pulsed species response, delay experiments, quenching, phase response experiments, external periodic perturbation, and others, see [7] and references therein for details.

Application to the HPTCu Reaction

The mechanism of the HPTCu reaction is as follows (for the purpose of the SNA reverse reactions are written as two separate steps):



In addition, inflow of Cu^{2+} , $(\text{S}_2\text{O}_3)^{2-}$, H_2O_2 , H^+ and outflow of every species (flow-through reactor) is considered.

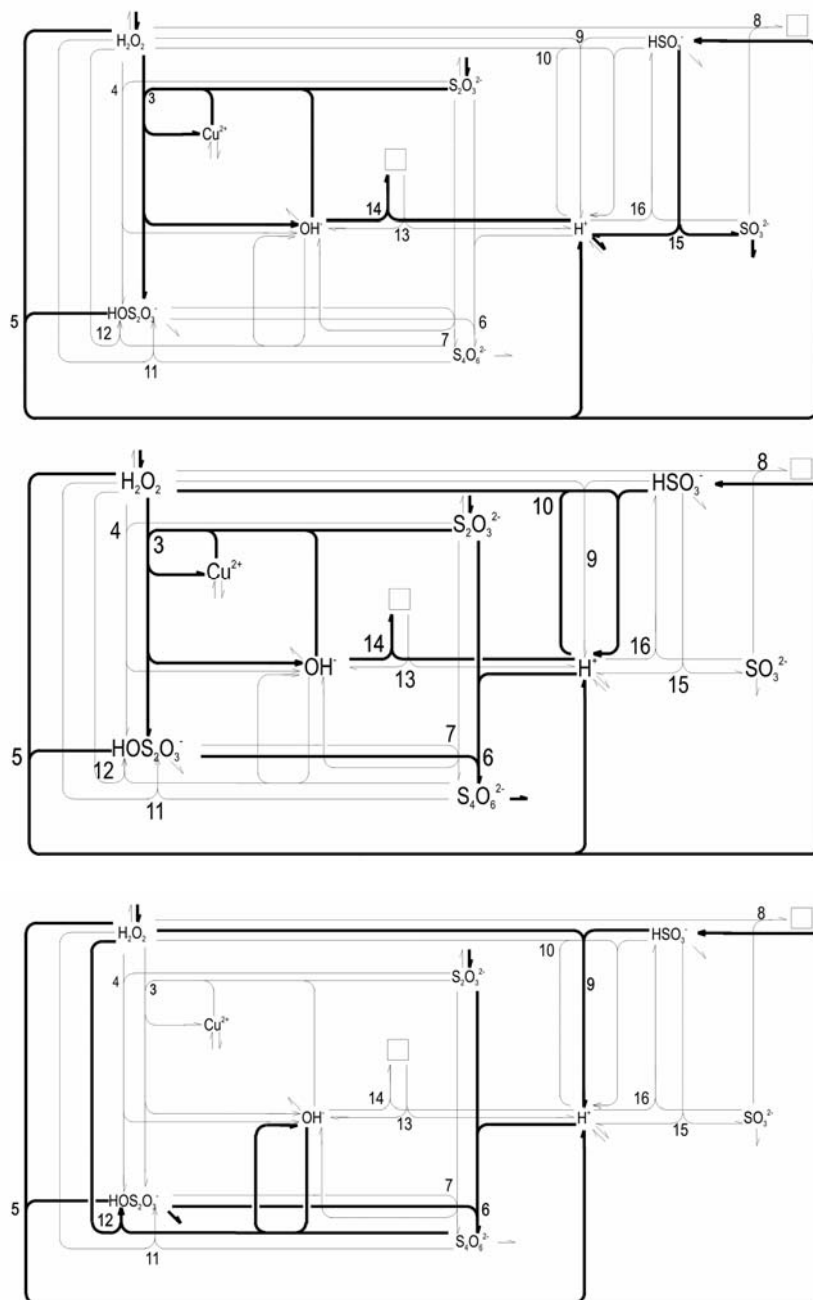
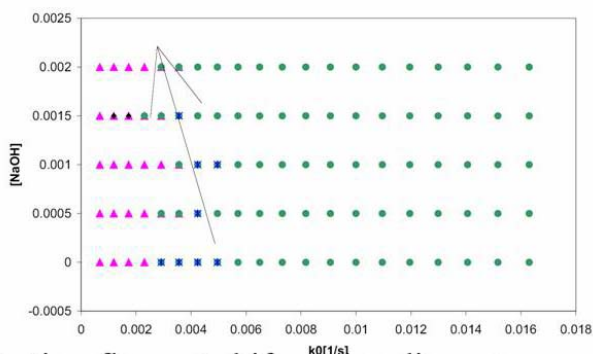


Fig. 1. Top – unstable subnetwork based on OH^- autocatalysis, middle – unstable subnetwork combining OH^- autocatalysis and H^+ autocatalysis, bottom – unstable subnetwork based on $HOS_2O_3^- - S_4O_6^{2-}$ autocatalytic loop.

In Fig. 1, basic subnetworks leading to oscillations are shown in thick lines within the framework of the whole network. There are three major autocatalytic cycles which may lead to oscillations: i) the OH^- based cycle (reaction R3) runs only in the presence of cupric ions, ii) the H^+ based cycle (reaction R9) is driven by HSO_3^- , iii) the $\text{HOS}_2\text{O}_3^- - \text{S}_4\text{O}_6^{2-}$ cycle (reactions 6 and 12). The cycles ii) and iii) can lead to oscillations independent of any other unstable subnetwork, while the cycle i) occurs only in combination with either the cycle ii) or the cycle iii) (not shown in the Figure). The OH^- autocatalysis assisted by Cu^{2+} is assumed to be the basis of experimentally observed oscillations, while the combination of the OH^- and H^+ cycles may provide an explanation for experimental observations of oscillations with a mix of large and small peaks of pH (mixed mode oscillations). The $\text{HOS}_2\text{O}_3^- - \text{S}_4\text{O}_6^{2-}$ cycle, however, does not correspond to experimental observations since no oscillations are observed in the absence of cupric ions.

We examined the role of species in the oscillatory behavior by using the method of bifurcation diagrams. These diagrams can be constructed both experimentally and from the model, examples are shown in Figs. 2 and 3, respectively.



- ▲ Oscillations
- Steady state I pH ~ 7-9
- ✕ Steady state II pH ~ 5
- Steady state III pH ~ 3,5

Fig. 2. Experimental bifurcation diagram in the plane of the inflow concentration of NaOH and the flow rate k_0 . The arrow shows the tilt of the region of coexisting steady states indicating type Y behavior.

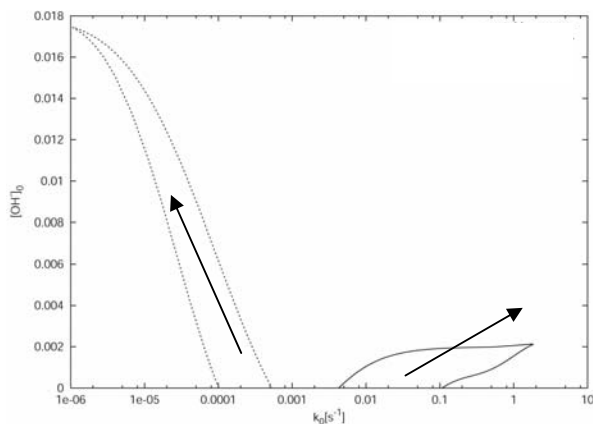


Fig. 3. Calculated bifurcation diagram corresponding to the experiments in Fig. 2. The tilt of the region of multiple steady state (enclosed by full lines) is diagonal (type X), the tilt of oscillatory region (enclosed by dashed lines) is antidiagonal (type Y).

The tilt of the region of multiple steady states is characteristic of the role of the species with varying inflow. The experiments show that the OH^- should be of type Y whereas the calculations indicate type X behavior for higher flow rates in agreement with the model assumption of operating OH^- autocatalysis. This contradiction suggests that the OH^- based autocatalysis is incorrect. At low flow rates the model suggests the H^+ autocatalysis, experiments do not contradict this suggestion. Further experiments and calculations are summarized as follows:

Model:

1) at higher flow rates:

OH^- type X (autocatalytic)
 $\text{S}_2\text{O}_3^{2-}$ type Z (negative feedback)
 H^+ type Y (exit)
 H_2O_2 nonessential

2) at low flow rates:

OH^- type Y (exit)
 HSO_3^- type Z (negative feedback)
 H^+ type X (autocatalytic)
 H_2O_2 nonessential

Experiments:

1) at higher flow rates:

OH^- type Y (exit)
 $\text{S}_2\text{O}_3^{2-}$ type Y (exit)
 H^+ type X (autocatalytic)
 H_2O_2 type Z (negative feedback) or
 nonessential

2) at low flow rates:

no contradiction with the model

Conclusions

The proposed mechanism suggests OH^- as the autocatalytic species which is contradicted by the role determining experiments. Rather, OH^- is an exit species, and H^+ seems to be the autocatalytic species. This observation prompts for a redesign of the model.

Acknowledgements

This work was supported by the project MSM6046137306 from the Ministry of Education of the Czech Republic and by the grants 203/06/1269 and 104/03/H141 from the Czech Science Foundation.

References

- [1] B. P. Belousov, In: Sbornik referatov po radiatsionnoj medicine za 1958 g. (conference proceedings); Medgiz: Moscow, 1959, p. 145; A. M. Zhabotinsky, *Biofizika* 1964, **9**, 306-311.
- [2] Y. Luo, I. R. Epstein, *J. Am. Chem. Soc.*, 1991, **113**, 1518-1522.
- [3] M. Orbán, I. R. Epstein, *J. Am. Soc.*, 1987, **109**, 101-106.
- [4] K. Kurin-Csörgei, M. Orbán, G. Rábai, I. R. Epstein, *J. Chem. Soc., Faraday Trans.*, 1996, **92**, 2851-2855.
- [5] B. L. Clarke, *Adv. Chem. Phys.* 1980, **43**, 1-278.
- [6] Eiswirth, M.; Freund, A.; Ross, J. *Adv. Chem. Phys.* 1991, **90**, 127-199.
- [7] J. Ross, I. Schreiber, M. O. Vlad, *Determination of Complex Reaction Mechanisms*, Oxford University Press, New York, 2006.

COMPLEX OSCILLATIONS OF A pH-OSCILLATOR

D. Bakeš, L. Schreiberová and I. Schreiber

*Department of Chemical Engineering, Institute of Chemical Technology, Prague,
Technická 5, 166 28 Prague 6, Czech Republic (Daniel.Bakes@vscht.cz).*

Abstract

The oxidation of thiosulphate by hydrogen peroxide catalyzed by cupric ions in acidic solution of sulphuric acid is studied. The reaction exhibits a large variety of nonlinear dynamical behaviour (oscillations, bistability and excitability). This reaction belongs to the group of so-called pH-oscillators. An experimental study is presented and the character of oscillations is studied in dependence on the flow rate. The system exhibits a rich variety of oscillatory patterns: simple and complex oscillations, and quasiperiodicity.

Introduction

The reaction of thiosulphate with hydrogen peroxide catalyzed by cupric ions in sulphuric acid solution (HPTCu reaction) displays highly nonlinear dynamics (oscillations, bistability and excitability can be observed). This reaction belongs to the group of so-called pH-oscillators, because of significant changes in the pH value in time. To explain such complex nonlinear behaviour, the mechanism of the reaction is needed. To improve existing mechanistic model [1] more experimental data are needed. In this paper an experimental study of the HPTCu reaction is presented. It is known, that HPTCu reaction exhibits different types of oscillations. But no detailed study of oscillatory regimes has been published except for work of Orbán and Epstein [2]. Therefore the focus of this contribution is on oscillatory behaviour of the HPTCu reaction carried out in a continuous stirred tank reactor (CSTR) at constant temperature. The pH time series are measured, results are evaluated and one-parameter bifurcation diagram is constructed. It is found that the HPTCu reaction provides a large variety of oscillatory regimes. Among them are simple and complex periodic regimes, and also quasiperiodic as well as chaotic oscillations.

Experiments

Experiments are carried out in a CSTR. The cylindrical reactor cell is thermostated at 25 °C. The volume of the reactor is 12.5 mL. Water solutions of hydrogen peroxide, sodium thiosulphate and mixture of cupric sulphate with sulphuric acid are fed to the reactor by a high precision syringe pump. The syringe pump is used to avoid any hydrodynamic perturbations (for example pulsation of the flow) at the entry to the reactor. The inlet concentrations of the reactants are $\text{H}_2\text{O}_2 = 0.1 \text{ mol/L}$, $\text{Na}_2\text{S}_2\text{O}_3 \cdot 5\text{H}_2\text{O} = 0.008 \text{ mol/L}$, $\text{CuSO}_4 = 5.0 \times 10^{-5} \text{ mol/L}$ and $\text{H}_2\text{SO}_4 = 0.001 \text{ mol/L}$. The experiments are carried out with syringes of volume 50 mL. At low flow rates, the volume of syringes suffice for about 10 hours long experiments (depending on a given flow rate k_0). At high flow rates ($k_0 \approx 0.02 \text{ s}^{-1}$) the duration of one experiment is lowered to three hours.

The pH value is measured in the reactor by using a pH-microelectrode. The pH value data are stored in a computer. The sampling frequency is 3 Hz.

Results

A rich variety of oscillatory regimes is observed, when the flow rate is varied. Also the onset of oscillations is studied. pH time series are measured for different values of k_0 . The asymptotic dynamics can be divided into three different regimes. These are simple oscillations, mixed-mode and complex oscillations, and low-amplitude oscillations. One-parameter bifurcation diagram (asymptotic dynamical behaviour in dependence on the flow rate k_0) is constructed as follows. The pH time series is measured for a chosen value of the flow rate k_0 . After sufficiently long time (a few hours) it is assumed that the system reaches its asymptotic regime. This regime can be a steady state, periodic or aperiodic oscillations. Maxima and minima of pH for major observed periodic regimes are plotted against the flow rate in Fig. 1. For a steady state, only one point is plotted (maximum and minimum coincide). Period one oscillations have one maximum and one minimum, period two oscillations possess two maxima and two minima, points for higher periodic regimes as well as for aperiodic regimes are not plotted.

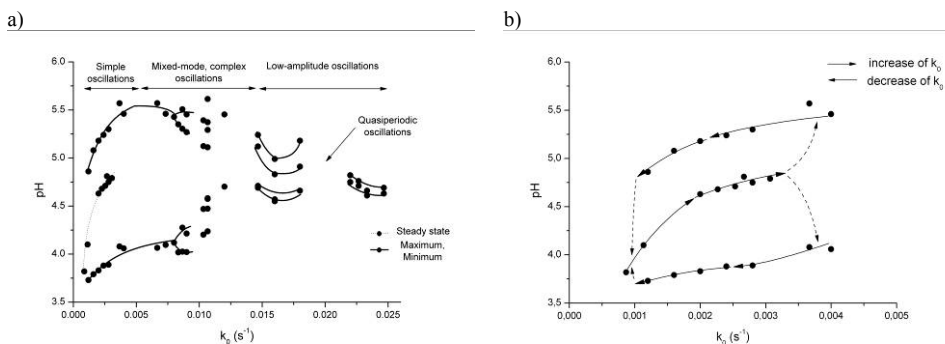


Fig. 1. (a) One parameter experimental bifurcation diagram of asymptotic dynamics of the HPTCu reaction, (b) a detail of the bifurcation diagram illustrating the hysteretic behaviour.

Discussion

The dynamical behaviour of the HPTCu reaction is highly nonlinear. The system can oscillate in many different dynamical regimes. The onset of simple oscillations is due to a subcritical Hopf-bifurcation. Fig. 1b shows that the system exhibits hysteresis – a steady state (focus) coexists with periodic oscillations. The two branches were obtained by stepwise increase and decrease of k_0 . The range of k_0 values where the system exhibits coexistence of two stable regimes is not fully determined, because the syringe pump does not allow for long-time experiments. Nonetheless, above $k_0 = 0.0032$ the steady state seems to lose stability via a subcritical Hopf bifurcation, leaving the large-amplitude oscillations as the only attractor above the bifurcation point.

Following the oscillatory branch to the low flow rates, the amplitude of oscillations drops suddenly to the steady state. This point seems to delimit the interval of hysteresis.

Simple oscillations are replaced with mixed-mode oscillations for $k_0 > 0.006\text{s}^{-1}$. That is, the smooth pattern of high-amplitude low-frequency (pH range ≈ 1.5 , period ≈ 350 s) oscillations is combined with a pattern of high-frequency low-amplitude (pH range ≈ 0.2 , period ≈ 50 s) oscillations creating a shoulder after every sudden drop of pH value at about pH = 4.5. This points to a secondary autocatalytic loop in the reaction scheme. The onset of mixed mode oscillations is smooth as the parameter k_0 is changed, the duration of high-frequency low-amplitude oscillatory shoulder varies with k_0 . Complex dynamics related to the high-amplitude mode seems to appear via a period-doubling bifurcation sequence starting at $k_0 \approx 0.008\text{ s}^{-1}$, although the low-amplitude oscillations are present as well. Period two regime is found in a relatively wide interval, but we do not see a subsequent period four regime before highly irregular pH oscillations occur. The dynamics seems to be chaotic but no complete period doubling sequence was observed. In addition, narrow windows of period two, period four and period one regimes were found within the region of complex behaviour (Fig. 1a). The system is extremely sensitive to external conditions and thus it is difficult to reproduce these periodic patterns.

As k_0 is increased, the amplitude of oscillations decreases. There is no sudden onset of low-amplitude oscillations (0.012s^{-1} to 0.014s^{-1}). The amplitude is about $\Delta\text{pH} = 0.6$ or less. The region of low-amplitude oscillations contains simple, period two and quasiperiodic oscillations. The origin of quasiperiodic oscillations seems to point to two different autocatalytic loops in the mechanism.

In future experiments longer time series should be recorded to analyse more thoroughly both large- and low-amplitude complex oscillations. The pH time series will be used for calculation of a measure determining chaotic dynamics, such as Ljapunov exponents or a reconstructed chaotic attractor. More experiments are also needed to determine the critical value of k_0 corresponding to a subcritical Hopf bifurcation at the low flow rates. Finally, the bifurcation scenario for the onset of quasiperiodicity prompts for further experiments.

Acknowledgements

This work was supported by the project MSM6046137306 from the Ministry of Education of the Czech Republic and by the grants 203/06/1269 and 104/03/H141 from the Czech Science Foundation.

References

- [1] K. Kurin-Csörgei, M. Orbán, G. Rábai, I. R. Epstein, *J. Chem. Soc., Faraday Trans.*, 1996, **92**, 2851-2855.
- [2] M. Orbán, I. R. Epstein, *J. Am. Chem. Soc.*, 1987, **109**, 101-106.

DYNAMICAL PATTERNS OF A pH-OSCILLATOR IN MASS-COUPLED CELLS

L. Schreiberová, O. Pešek and I. Schreiber

*Department of Chemical Engineering, Institute of Chemical Technology, Prague,
Technická 5, 166 28 Prague 6, Czech Republic (Lenka.Schreiberova@vscht.cz)*

Abstract

Dynamics of the reaction between hydrogen peroxide and thiosulfate catalyzed by Cu^{2+} in the solution of H_2SO_4 (HPTCu) in two coupled reaction cells are studied. The coupling is mediated by a membrane allowing for mass transfer. We studied effects of varying flow rate and the coupling strength on the system. Dynamical behavior includes inhomogeneous steady states, synchronized periodic as well as non-periodic behaviour. Also effects of external pulse perturbations under excitable conditions were studied.

Introduction

Oscillating reactions with an autocatalytic effect involving protons are called pH-oscillators [1]. The HPTCu reaction [2,3] in a single continuous-flow stirred tank reactor (CSTR) provides nonlinear dynamical behavior including different types of steady states, spontaneous oscillations, bistability between steady states or between a steady state and oscillations, and hysteretic loops. In addition, there exist conditions under which the system is excitable [4]. When two reaction cells are coupled by diffusion-like mass transfer, dynamical behavior may become quite complex as shown in this work.

Experiments

The two cells were made of plexiglass, equipped with a pH electrode and a magnetic stirrer. Operating conditions were as follows: the volume of both reaction cells was 19 mL, stirring rate 25 Hz, temperature was thermostated at 25 °C. Stock solutions were prepared from 30% H_2O_2 , $\text{Na}_2\text{S}_2\text{O}_3 \cdot 5\text{H}_2\text{O}$, 96% H_2SO_4 , $\text{CuSO}_4 \cdot 5\text{H}_2\text{O}$, actual inlet concentrations are shown in figure captions. At the start of an experiment without external pulses, the selected coupling strength and initial flow rate were set. The flow rate delivered by the peristaltic pump feeding the first reactor was controlled by a computer program and successively varied after a chosen time interval. The flow rate of the pump feeding the second reactor was kept constant at the value where the single reactor would oscillate spontaneously.

In experiments with external pulses, the flow rate of reactants was kept fixed for both of the reaction cells at the value where the steady state is excitable. External pulses were made via a syringe pump, the timing of the syringe pump was controlled to define the amount (amplitude) of the perturbant added. System was perturbed by addition of 0.5 mol/L H_2SO_4 or 0.5 mol/L NaOH. The perturbation was repeated with a sufficiently long period so that the excitatory response subsided

and the steady state reappeared. At the next pulse, the amount of perturbant was increased in search of conditions under which the system either responds by pulse propagation or under which the propagation fails.

When external constraints are varied, bifurcations give rise to several dynamical regimes. The constraints are: the inflow reactant concentrations, the flow rate, temperature in the reactor and the frequency of stirring. In a single cell, measured pH of the system indicates one of the following distinct regimes: steady state I (pH ~ 8) (may be excitable), steady state II (pH ~ 5) (may be excitable), steady state III (pH ~ 3), oscillations (periodic or mixed-mode). In the coupled system these regimes combine and in certain cases new dynamical modes emerge due to coupling. A typical experiment is shown in Fig. 1.

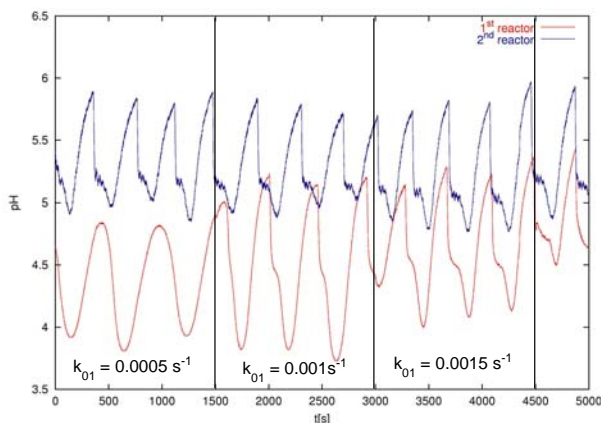


Fig. 1 Time series of pH in both reactors, the flow rate k_0 is stepwise varied; $[H_2O_2]_{01} = [H_2O_2]_{02} = 0.1 \text{ mol/l}$, $[S_2O_3^{2-}]_{01} = [S_2O_3^{2-}]_{02} = 0.008 \text{ mol/l}$, $[H_2SO_4]_{01} = [H_2SO_4]_{02} = 0.001 \text{ mol/l}$, $[Cu^{2+}]_{01} = [Cu^{2+}]_{02} = 2.5 \cdot 10^{-5} \text{ mol/l}$, $k_{02} = 0.003 \text{ s}^{-1}$, coupling strength $K = 0.00015 \text{ s}^{-1}$

All experiments are summarized in a bifurcation diagram, which is plotted in the parameter plane of the flow rate (reciprocal residence time) k_{01} in the first reactor and the mass transfer coefficient K . The region of oscillations contains various synchronized periodic regimes, there is coexistence of oscillations and the steady state SSII, as well as overlap between SSI and SSII.

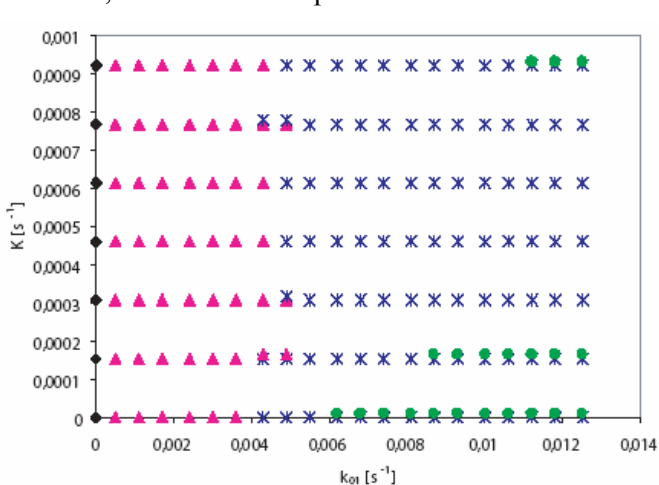


Fig. 2 Bifurcation diagram showing various dynamical regimes in the parameter plane k_{01} vs K , other parameters as in Fig. 1.

Fig. 3 shows experiments with pulse forcing of the system in an excitable steady state SSII. This figure shows how the pulse from the first reactor is propagated to the other. The perturbant is 0.5 M H₂SO₄ and the volume of additions is increased stepwise. The response always elicits an excitation in the first reactor, the transfer to the second cell occurs in all cases, but the second perturbation is the most effective.

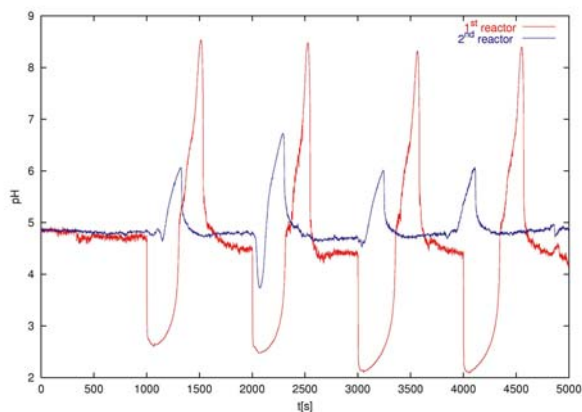


Fig. 3 Pulse experiments at $k_{01} = 0.005 \text{ s}^{-1}$, $k_{02} = 0.005 \text{ s}^{-1}$, $K = 0.00047 \text{ s}^{-1}$, all other parameters as in Fig. 1. The perturbation is applied every 1000 s.

Conclusions

By coupling two non-identical reactors, combination patterns as well as new dynamical modes appear. Bifurcation diagrams in the plane flow rate vs coupling strength display different dynamical regions including resonance patterns and disappearance of oscillations. External pulses can propagate as excitations. Chemical systems coupled by diffusion were examined in the past with some of the results similar to those found here. However, the HPTCu system has an extraordinarily rich dynamical behaviour including different modes of excitability, which will be studied in future work. The studied system serves as a qualitative model for more complex biochemical and biological systems that can be represented as coupled subsystems.

Acknowledgements

This work was supported by the project MSM6046137306 from the Ministry of Education of the Czech Republic and by the grants 203/06/1269 and 104/03/H141 from the Czech Science Foundation.

References

- [1] Y. Luo, I. R. Epstein, *J. Am. Chem. Soc.*, 1991, **113**, 1518-1522.
- [2] M. Orbán, I. R. Epstein, *J. Am. Soc.*, 1987, **109**, 101-106.
- [3] K. Kurin-Csörgei, M. Orbán, G. Rábai, I. R. Epstein, *J. Chem. Soc., Faraday Trans.*, 1996, **92**, 2851-2855.
- [4] O. Pešek, L. Schreiberová, I. Schreiber, in preparation.

ROLE OF Br₂O SPECIES IN THE MODEL OF BELOUSOV-ZHABOTINSKY REACTION

S. M. Blagojević¹, N. Pejić¹, S. N. Blagojević², Ž. Čupić³,
S. Anić⁴ and Lj. Kolar-Anić⁴

¹Faculty of Pharmacy, University of Belgrade, Vojvode Stepe 450, Belgrade

²Institute of General and Physical Chemistry, POB 551, Belgrade, Serbia

³ICHTM – Department of Catalysis and Chemical Engineering, Belgrade, Njegoševa 12

⁴Faculty of Physical Chemistry, University of Belgrade, Studentski trg 12, Serbia

Abstract

The model of the Belousov-Zhabotinsky (BZ) reaction was accomplished with Br₂O species. Experimental results are compared with the numerical obtained ones.

Introduction

The most studied Belousov-Zhabotinsky reaction consists of bromate ions, malonic acid and Ce(III) or (CeIV) as a catalyst in sulfuric acid solution [1]. Various kinetic schemes were proposed to describe experimentally observed evolutions of this reaction [1-6]. The first explanation of the mechanism was given by Field, Körös and Noyes [1].

Here, the kinetic scheme for the numerical simulation for the experimentally observed oscillations is mostly based on the previously proposed models [4-5]. Introduction of Br₂O species is given in analogy manner to the I₂O one existing in the Bray-Liebhafsky oscillatory reaction scheme [7]

Experimental

The BZ reaction was realized in the isothermal stationary well-stirred reactor. The reaction volume is 51 ml. The evolution of the BZ reaction was followed potentiometrically by bromide ion-sensitive electrode connected with Ag/AgCl reference electrode by the sulphate bridge. All experiments were carried out under the constant values of the initial concentrations of the components (in mol dm⁻³): [H₂SO₄]=1.00, [CH₂(COOH)₂] = 3.20 × 10⁻², [KBrO₃] = 6.20 × 10⁻², [KBr] = 1.50 × 10⁻⁵, [Ce₂(SO₄)₃] = 2.50 × 10⁻³. The measurements were carried out at two temperatures (30 and 40 °C, Figure 1).

Results and Discussion

We have simulated the experimentally observed time series by the reaction scheme shown in Table 1. The results of numerical calculations with the conditions as in experimental are given in Figure 2.

The calculated evolutions based on the proposed model have same type and structures as the experimental ones. Also, preoscillatory period, the time elapsed between the start of the reaction and the termination of the oscillatory phase τ_{end} and

number of oscillations n are in accordance with the experimentally obtained ones (Figures 3 and 4).

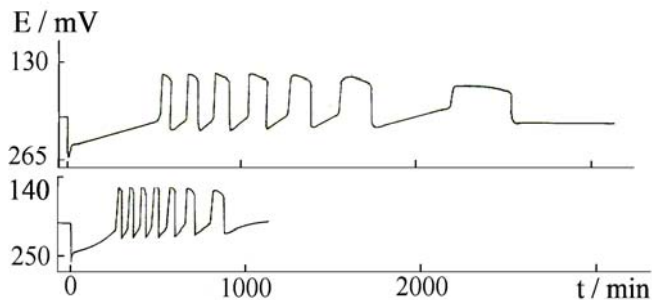


Fig. 1. The potentiometric traces of the BZ reaction obtained by the bromide ion sensitive electrode at 30 °C (up), and 40 °C (down). $[H^+]_0 = 1.29 \text{ mol dm}^{-3}$ and $[HOBr]_0 = 1.50 \times 10^{-8} \text{ mol dm}^{-3}$

Table 1. Reaction and rate constant used in the numerical simulations

Reaction	Rate constants ^{a,b}	
	30 °C	40 °C
$Br^- + HOBr + H^+ \leftrightarrow Br_2 + H_2O$	k_1 2.55E9	3.07E9
	k_{-1} 3.18	7.61
$HBrO_2 + Br^- + H^+ \rightarrow Br_2O + H_2O$	k_2 6.71E6	1.09E7
$Br_2O + H_2O \leftrightarrow 2HOBr$	k_3 3.22E3	7.75E3
	k_{-3} 3.22E8	7.78E8
$Br^- + BrO_3^- + 2H^+ \rightarrow HOBr + HBrO_2$	k_4 3.20	7.74
$2HBrO_2 \rightarrow BrO_3^- + HOBr + H^+$	k_5 3.49E3	4.62E3
$BrO_3^- + HBrO_2 + H^+ \leftrightarrow 2BrO_2 + H_2O$	k_6 44.70	78.76
	k_{-6} 6.72E7	1.62E8
$Ce^{3+} + BrO_2 + H^+ \leftrightarrow Ce^{4+} + HBrO_2$	k_7 3.20E4	7.74E4
	k_{-7} 1.12E4	2.71E4
$MA + Br_2 \rightarrow BrMA + Br^- + H^+$	k_8 4.23	10.48
$MA + Ce^{4+} \rightarrow Ce^{3+} + P + H^+$	k_9 0.36	0.84
$BrMA + Ce^{4+} \rightarrow Ce^{3+} + Br^- + P$	k_{10} 47.17	109.89

^a $[H_2O] = 55 \text{ mol dm}^{-3}$ including in the rate constant)

^bThe rate constant k_{-1} and k_3 are in units of s^{-1} ; the rate constant k_1, k_2, k_6, k_7 are in units of $dm^6 \text{ mol}^{-2} s^{-1}$. The rate constant k_4 are in units of $dm^9 \text{ mol}^{-3} s^{-1}$. The other rate constant in units $dm^3 \text{ mol}^{-1} s^{-1}$.

It is well known that the time evolution of the BZ oscillatory reaction depends on all intermediate species and between them the HOBr. We have demonstrated, here, that the reactions with Br_2O species as new intermediate, would be appropriate ones for the fine regulation of the HOBr concentration in the reaction system. This can be important since we expect that Br_2O react with malonic acid resulting to brommalonic acid and HOBr.

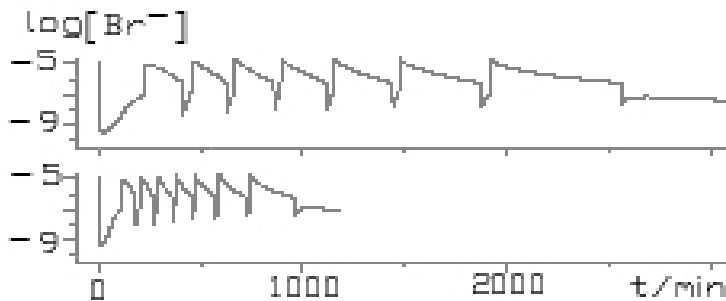


Fig. 2. Numerical simulations of the bromide concentration during the BZ oscillatory reaction.

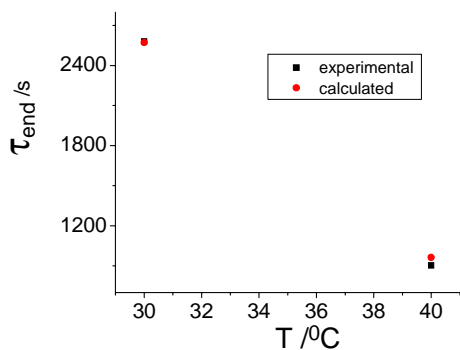


Fig. 3. The dependence of τ_{end} on the temperature.

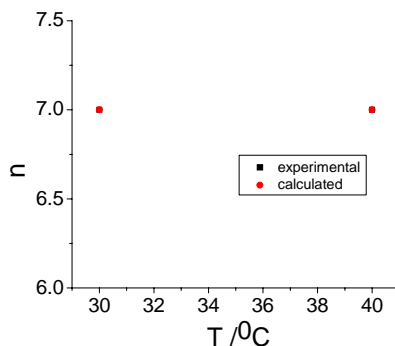


Fig. 4. The dependence of n on the temperature.

Conclusion

There is relatively high agreement between experimentally and numerically obtained results. However, it must be underlined that the duration of oxidized and reduced states in the experimental oscillations are rather close, while in the model calculations the oxidized state is much shorter than the reduced one.

Acknowledgment

We gratefully acknowledge the partial financial support in grants no. 142025 and 142019 of the Ministry for Science and Environmental protection of the Republic of Serbia.

References

- [1] R.Field, E.Körös, R.Noyes, *J. Am. Chem. Soc.*, 1972, **94**, 8649-8664.
- [2] R.Field, R.Noyes, *J. Chem. Phys.*, 1974, **60**, 1877.
- [3] L.Györgyi, R.Field, *J. Phys. Chem.*, 1991, **95**, 6594-6602.
- [4] T.Turanyi, L.Györgyi, R.Field, *J. Phys. Chem.*, 1993, **97**, 1931-1941.
- [5] П.Стрижак, Детермінований хаос в хімії, Академперіодіка, 2002.
- [6] L. Hegedus, M. Wittmann, Z. Nosztizsius, S. Yan, A. Sirimungkala, H-D. Forsterling, R.J. Field, *Faraday Discuss*, 2001, 120.21.
- [7] G. Schmitz, *J.Chim.Phys.*, 1987, **84**, 957-965.

PRACTICAL APPLICATION OF AN OSCILLATING CHEMICAL SYSTEM

R. Cervellati¹ and S. D. Furrow²

¹*Dipartimento di Chimica 'G. Ciamician', Università di Bologna, Via Selmi, 2, Bologna, Italy*

²*Penn State Berks, Reading, PA 19610, U.S.A.*

Abstract

A practical application of the Briggs-Rauscher oscillating reaction to the determination of the antioxidant activity of catechins is described and discussed.

Introduction

Oscillations of the *Briggs and Rauscher* (BR) oscillating reaction [1] in batch conditions are perturbed by the addition of compounds with free-radical scavenging activity (antioxidants). Perturbations consist of an immediate quenching of oscillations, an inhibition time that linearly depends on the concentration of the compound added, and subsequent regeneration of oscillations [2]. These inhibitory effects were ascribed to scavenging of HOO^\bullet radicals by the antioxidants [2,3], since hydroperoxyl radical was among the main intermediates for which concentrations oscillate in the BR system [4]. Decisive indirect evidence of involvement and important role played by HOO^\bullet radicals in the onset of oscillations was given by *Cervellati et al.* [5]. A method to determine the relative antioxidant capacity of free-radical scavengers was then implemented [2,6]. Indeed, the true antioxidant power is given by the value of the kinetic constant of the reaction between the scavenger and the radical. A mechanism able to reproduce inhibition times very well has been recently proposed [3], leading to the evaluation of this kinetic constant. The aim of this work is to compare the ranking order of relative antioxidant capacity measured with the BR method for six catechins with that obtained on the basis of the calculated kinetic constant of the inhibitory step. Catechin (C), Epicatechin (EC), Catechingallate (CG), Epicatechingallate (ECG), Epigallocatechin (EGC) and Epigallocatechingallate (EGCG) are among the main polyphenolics contained in the green tea and there are considerable epidemiological evidences that these polyphenols contribute to reduce the risk of cardiovascular and other diseases [7,8].

Experimental

Oscillations in the BR mixture were followed potentiometrically by recording the potential of a bright-platinum electrode coupled with a double junction $\text{Ag}/\text{AgCl}/\text{Cl}^- (\text{KNO}_3)$ reference electrode. Electrodes were connected to a pH multimeter controlled by an IBM-compatible PC. A suitable data-acquisition program was used. More details have been reported elsewhere [2,6].

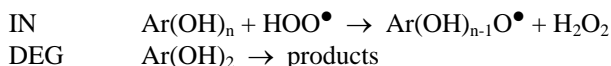
Typical recordings are shown in Fig. 1.

The dependence of the inhibition time on the concentration of the antioxidant added was found to be linear for all catechins in the range 1.09 – 13.76 μM .

Mechanistic Calculations

Furrow et al. [9] reported a 13-step new model for the BR reaction that takes into account the important role played by HOO^\bullet radicals in its oscillatory behavior.

To simulate the perturbations by a free-radical scavenger on the oscillations, the following steps were added to the model, where $\text{Ar}(\text{OH})_n$ indicates a generic polyphenol, as a catechin:



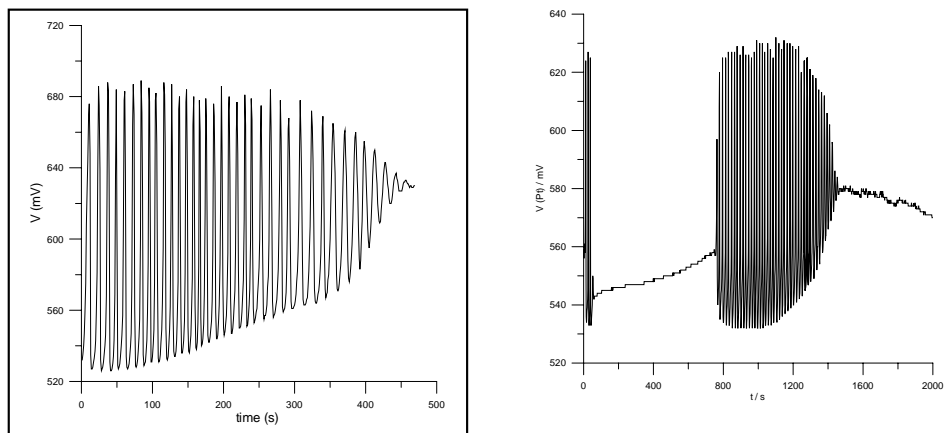


Fig. 1 Recording of the potential of the bright-platinum electrode vs. time. left) Reference mixture, initial conditions: $[MA] = 0.05 \text{ M}$, $[Mn^{2+}] = 6.67 \times 10^{-3} \text{ M}$, $[IO_3^-] = 6.67 \times 10^{-2} \text{ M}$, $[HClO_4] = 2.66 \times 10^{-2} \text{ M}$, $[H_2O_2] = 1.20 \text{ M}$; right) Oscillator perturbed by the addition of 1.0 ml epicatechin solution, initial concentration in mixture = $1.63 \mu\text{M}$. Temp. = $25.0 \pm 0.1 \text{ }^\circ\text{C}$.

The step IN represents the typical way of subtraction of a radical by an antioxidant: an H atom transfer from a phenolic OH group to the radical. In the simulations $Ar(OH)_{n-1}O^\bullet$ was considered an end product. The 1st order step DEG represents the possible parallel degradation of the inhibitor to unspecified products. The degradation may be due to oxidation or iodination of $Ar(OH)_n$. The kinetics of these reactions were recently studied in detail [3]: the results showed that for simulation purposes they can be summarized by step DEG.

The kinetic constants of the model steps were kept fixed to those reported in [9], while k_{IN} and k_{DEG} were allowed to vary for the best fit to experimental behaviors.

Experimental and simulated behaviors of $V(\text{Pt})$ and $[I^-]$ respectively vs. time for a typical BR mixture perturbed by epicatechin are reported in Fig. 2.

The very good agreement between the experimental and calculated inhibition time can be noted. A similar agreement was obtained in all the performed simulations.

Results and Discussion

Relative antioxidant activity (rac) of catechins was determined as the ratio $[\text{std}]/[\text{smp}]$, where $[\text{smp}]$ is the concentration of the sample added to the BR mixture giving a certain inhibition time and $[\text{std}]$ is the concentration of the standard (resorcinol) that should give the same inhibition time [2,6]. An average rac value, $(rac)_{av}$, was then calculated in an interval of inhibition times. Results are reported in Table 1.

Table 1 Experimental antioxidant activity of catechins

Compd.	C	EC	CG	ECG	EGC	EGCG
$(rac)_{av} \pm \sigma$	2.2 ± 0.2	2.6 ± 0.3	1.4 ± 0.4	0.8 ± 0.2	0.9 ± 0.2	1.0 ± 0.2

Simulations were carried out for two concentrations of each catechin finding unique values for the rate constants k_{IN} and k_{DEG} . Results are shown in Table 2.

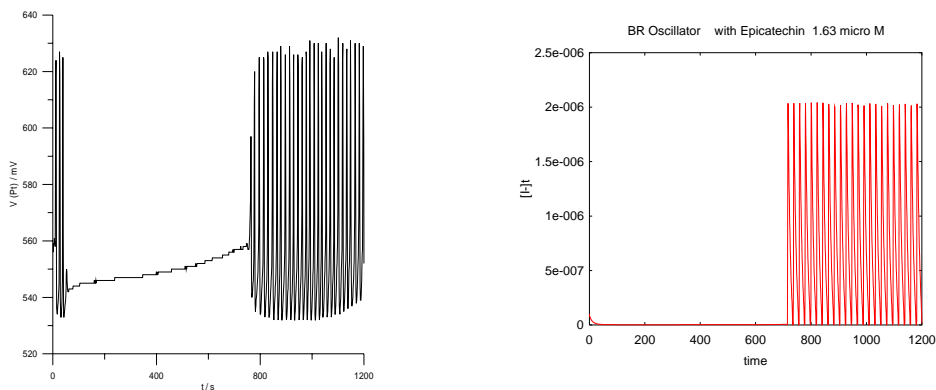


Fig. 2 left) Experimental behavior of $V(\text{Pt})$ vs. time; right) Simulated behavior of $[\text{I}^-]$ vs time. Initial conditions see Fig. 1

Table 2 Calculated rate constants $k_{\text{IN}}(\times 10^{-7} \text{ M}^{-1} \text{ s}^{-1})$ and $k_{\text{DEG}}(\times 10^4 \text{ s}^{-1})$

Compd.	C	EC	CG	ECG	EGC	EGCG
k_{IN}	3.95	10.4	6.0	3.9	3.4	4.3
k_{DEG}	1.0	7.9	15.	6.8	11.5	10.5

The experimental ranking order of $(\text{rac})_{\text{av}}$ for the six catechins (Table 1) is:



By using only the k_{IN} values, the relative activities (ra) of the catechins compared to resorcinol as a standard ($k_{\text{IN}}(\text{Re}) = 1.2 \times 10^7 \text{ M}^{-1} \text{ s}^{-1}$ [3]): $\text{ra} = k_{\text{IN}}(\text{catechin})/k_{\text{IN}}(\text{Re})$, fall in the order:



Taking into account the experimental errors, the two orders are in satisfactory agreement. It is not unexpected that the order of relative values of k_{IN} shows some correlation with the experimental one since k_{IN} is more important in the simulations than k_{DEG} , although, of course, both play a role.

References

- [1] T.S. Briggs, W.C. Rauscher, *J. Chem. Educ.*, 1973, **50**, 496.
- [2] R. Cervellati, K. Höner, S.D. Furrow, C. Neddens, S. Costa, *Helv. Chim. Acta*, 2001, **84**, 3533-3547.
- [3] R. Cervellati, K. Höner, S.D. Furrow, F. Mazzanti, S. Costa, *Helv. Chim. Acta*, 2004, **87**, 133-155.
- [4] R.M. Noyes, S.D. Furrow, *J. Am. Chem. Soc.*, 1982, **104**, 45-48.
- [5] R. Cervellati, N. Crespi-Perellino, S. D. Furrow, A. Minghetti, *Helv. Chim. Acta*, 2000, **83**, 3179-3189.
- [6] R. Cervellati, C. Renzulli, M.C. Guerra, E. Speroni, *J. Agric. Food Chem.*, 2002, **50**, 7504-7509.
- [7] C.A. Rice-Evans, N.J. Miller, G. Paganga, *Free Radic. Biol. Med.*, 1996, **20**, 933-956.
- [8] A. Scalbert, C. Manach, C. Morand, C. Rémésy, L. Jimenez, *Crit. Rev. Food Sci. Nut.*, 2005, **45**, 207-306.
- [9] S.D. Furrow, R. Cervellati, G. Amadori, *J. Phys. Chem. A*, 2002, **106**, 5841-5850.

OPTIMIZATION OF CONDITIONS FOR QUANTITATIVE DETERMINATION OF MORPHINE USING NUMERICAL SIMULATIONS

N. Pejić¹, S. M. Blagojević¹, S. Anić² and V. Vukojević³

¹*Faculty of Pharmacy, Department of Physical Chemistry, University of Belgrade, Vojvode Stepe 450, Belgrade, Serbia (bimesel@eunet.yu)*

²*Faculty of Physical Chemistry, University of Belgrade, Studentski trg 12-16, P.O. Box 137, Belgrade, Serbia*

³*Department of Clinical Neuroscience, Karolinska Institute, Stockholm, Sweden*

Abstract

An ultrasensitive kinetic method for quantitative determination of analytes, based on perturbing the Bray-Liebhaufsky (BL) reaction matrix in the vicinity of a bifurcation point, was applied for quantitative morphine (MH) determination. A mechanism of morphine interaction with the BL reaction matrix is proposed and evaluated numerically. Optimization of experimental conditions by using numerical simulations is discussed.

Introduction

A kinetic method for quantitative determination of analytes, based on perturbing the dynamics of the BL reaction matrix in the vicinity of a bifurcation point, was developed and successfully applied for quantitative determination of several analytes [1]. The method relies on disturbing the matrix reaction by altering the ratio between concentrations of intermediates that is established in a nonequilibrium stationary state close to a bifurcation point realized in a Continuously-fed well Stirred Tank Reactor (CSTR). The proximal bifurcation point separates the parameter space into domains characterized by qualitatively different dynamics, acting as an amplifier for the initial perturbation. In this study, we report on the application of this method for quantitative determination of the alkaloid morphine, propose a model of the mechanism of interaction of morphine with the matrix BL reaction, use numeric simulations to evaluate the validity of the proposed model and discuss the utility of numerical simulations in optimizing experimental conditions, in order to reach the highest sensitivity.

Results and Discussion

Three distinct nonequilibrium stationary states attained in the BL reaction matrix in an open reactor (Table 1) were evaluated in respect to sensitivity for morphine. Obtained results are summarized in Table 2.

Table 1. Experimental conditions under which stable stationary states existing in the vicinity of bifurcation points were realized in the BL reaction matrix.

Experimental conditions	[KIO ₃] ₀ (M)	[H ₂ SO ₄] ₀ (M)	[H ₂ O ₂] ₀ (M)	T (°C)	j ₀ (min ⁻¹)
A	7.5×10 ⁻²	6.0×10 ⁻²	7.0×10 ⁻³	39.0	4.5×10 ⁻³
B	5.9×10 ⁻²	5.5×10 ⁻²	2.0×10 ⁻¹	42.9	2.95×10 ⁻²
C	4.7 ×10 ⁻²	4.8×10 ⁻²	1.6×10 ⁻¹	60.0	2.80×10 ⁻²

To model the morphine interactions with the BL reaction matrix we assumed that in the acidic environment of the BL matrix iodination of MH occurs through the phenolic hydroxyl group by interaction with HIO [2]. Validity of this proposal is tested by numerical simulations, using a model of the BL reaction mechanism (1-8) [3] expanded by one additional reaction (9):

1. $\text{IO}_3^- + \text{I}^- + 2\text{H}^+ \rightleftharpoons \text{HIO} + \text{HIO}_2$
2. $\text{HIO}_2 + \text{I}^- + \text{H}^+ \rightarrow \text{I}_2\text{O} + \text{H}_2\text{O}$
3. $\text{I}_2\text{O} + \text{H}_2\text{O} \rightleftharpoons 2\text{HIO}$
4. $\text{HIO} + \text{I}^- + \text{H}^+ \rightleftharpoons \text{I}_2 + \text{H}_2\text{O}$
5. $\text{HIO} + \text{H}_2\text{O}_2 \rightarrow \text{I}^- + \text{O}_2 + \text{H}^+ + \text{H}_2\text{O}$
6. $\text{I}_2\text{O} + \text{H}_2\text{O}_2 \rightarrow \text{HIO} + \text{HIO}_2$
7. $\text{HIO}_2 + \text{H}_2\text{O}_2 \rightarrow \text{IO}_3^- + \text{H}^+ + \text{H}_2\text{O}$
8. $\text{IO}_3^- + \text{H}^+ + \text{H}_2\text{O}_2 \rightleftharpoons \text{HIO}_2 + \text{O}_2 + \text{H}_2\text{O}$
9. Morphine + HIO → Iodo-Morphine + H₂O

Table 2. Comparison of the results of numerical predictions with experimentally obtained ones and rate constants for morphine iodination used in the numerical simulations.

k ₉ / M ⁻² min ⁻¹	Linearity range / μmol		Regression coefficient	
	Experimental*	Numeric	Experimental*	Numeric
A 3.50 × 10 ⁷	0.087–0.58	0.16–0.60	0.9993	0.9871
B 1.43 × 10 ⁸	0.004–0.18	0.008–0.22	0.9998	0.9899
C 4.03 × 10 ¹⁰	0.040–0.50	0.060–0.50	0.9985	0.9747

*The reaction dynamics was followed potentiometrically, using a Pt electrode as the monitoring sensor.

In the simulations, concentrations of all species were treated as dynamical variables. A perturbation in the numerical simulation is performed by instantly changing the morphine concentration in the course of integration of the kinetic equations (Fig. 1). Rate constants for the reactions in the BL matrix were taken from the literature [3]. Concentrations of the reactants and the flow rate values used in numeric simulations are given in Table 1. Rate constants for morphine iodination (k₉) at different tempera-

tures are given in Table 2, together with a summary of the experimentally and numerically obtained results.

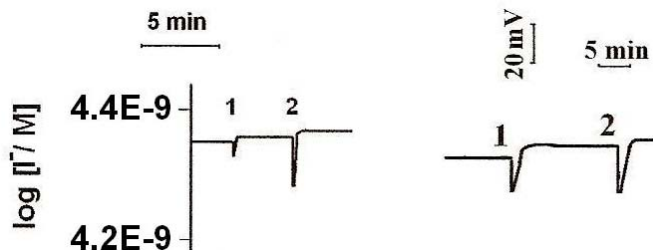


Fig. 1. (left) Potentiometrically recorded response of the BL matrix (exp. conditions A) and (right) numerically simulated temporal evolution of $[I^-]$ after perturbing the stationary state by adding morphine. In both cases, the intensity of perturbations was $[MH] = 0.094 \mu\text{mol}$ (1) and $[MH] = 0.165 \mu\text{mol}$ (2).

Conclusion

Sensitivity of a previously proposed kinetic method for quantitative determination of morphine was evaluated under different experimental conditions. A model that can account for the experimentally observed features was formulated and tested using numerical simulations. Given the high accordance between the model predictions and the experimental results we propose that mathematical modeling can be used for systematic search of conditions under which highest sensitivity of the proposed method for quantitative morphine determination can be reached. We underline the obvious advantage of using reliable mathematical models for systematic search of favorable experimental conditions, in particular appropriate types of bifurcations or excitability, instead of a laborious tuning of the conditions in actual experiments.

Acknowledgment

We acknowledge the financial support in grant no. 142025 of the Ministry for Science and Environmental Protection of the Republic of Serbia.

References

- [1] (a) V. Vukojević, N. Pejić, D. Stanisavljev, S. Anić, Lj. Kolar-Anić, *The Analyst*, 1999, **124**, 147-153; (b) N. Pejić, S. Blagojević, S. Anić, V. Vukojević, Lj. Kolar-Anić, *Anal. Bioanal. Chem.*, 2005, **381**, 775.
- [2]. (a) R. Davis, J. Feidhaus, J. Heveran, R. Wicks, M. Peckham, *Clin. Chem.*, 1975, **21** 1498; (b) Y. R. Cervellati, K. Höner, S. Furrow, F. Mazzanti and S. Costa, *Helvetica Chim. Acta*, 2004, **87**, 133.
- [3] (a) Lj. Kolar-Anić, Đ. Mišljenović, S. Anić, G. Nicolis, *React. Kinet. Catal. Lett.*, 1995, **54**, 35; (b) Lj. Kolar-Anić, Ž. Čupić, S. Anić, G. Schmitz, *J. Chem. Soc. Faraday Trans*, 1997, **93**, 2147.

SOME NEW DETAILS OF ELECTROCHEMICAL OSCILLATIONS DURING THE PASSIVITY BREAKDOWN OF COPPER IN TRIFLUOROACETIC ACID

N.I.Potkonjak¹, T.N. Potkonjak² and S.N. Blagojević¹

¹*Institute of General and Physical Chemistry, Studentski trg 12-16, Belgrade, Serbia*

²*Faculty of Physical Chemistry, Studentski trg 12-16, Belgrade, Serbia*

Abstract

Current oscillations were observed during anodic polarization of the copper stationary electrode in trifluoroacetic acid by applying potentiodynamic technique. Controllable parameters, the trifluoroacetic acid concentration and the temperature of electrochemical system, were varied. It was established that both of these parameters were important for oscillatory behavior of Cu/CF₃COOH electrochemical oscillator.

Introduction

Current oscillations have been observed during the anodic electrodisolution/passivation of various metals in corrosive media such as the acidic aqueous solution [1]. It is supposed, that generation of these oscillations is closely related to the processes involving surface chemistry reactions as well as mass-transport of ions in electrolyte. Numerous electrochemical oscillator involving copper as metal electrode have been reported [2-5].

In this paper, we present further experimental results concerning electrodisolution/passivation dynamics of the copper-trifluoroacetic acid oscillator [6].

Experimental

The preparation of stationary copper electrode as working one and experimental set up was described in the previous paper [6]. The potential of working electrode was measured versus saturated calomel electrode (SCE). The electrolyte was trifluoroacetic acid aqueous solution. Stationary copper electrode was anodically polarized by means of potential sweep. The dynamical response of system was investigated throughout variety of trifluoroacetic acid concentrations 0.125, 0.250, 0.500 and 1.00 mol dm⁻³. Furthermore oscillatory behavior of investigated electrochemical system was examined on four different temperatures 25, 30, 35 and 40 °C.

Results and Discussion

Figure 1 shows j-E polarization curves obtained by cyclic voltammetric measurements of the Cu / n mol dm⁻³ CF₃COOH system for n = 0.125, 0.250, 0.500 and 1.000. It appears that current oscillations exist in a certain potential region (495-630 mV vs. SCE). The current oscillations emerge during the potential sweep in both directions (forward and backward). As it is shown, (Fig. 1) increase of amplitude and frequency of current oscillations is directly influenced by trifluoroacetic acid concentration.

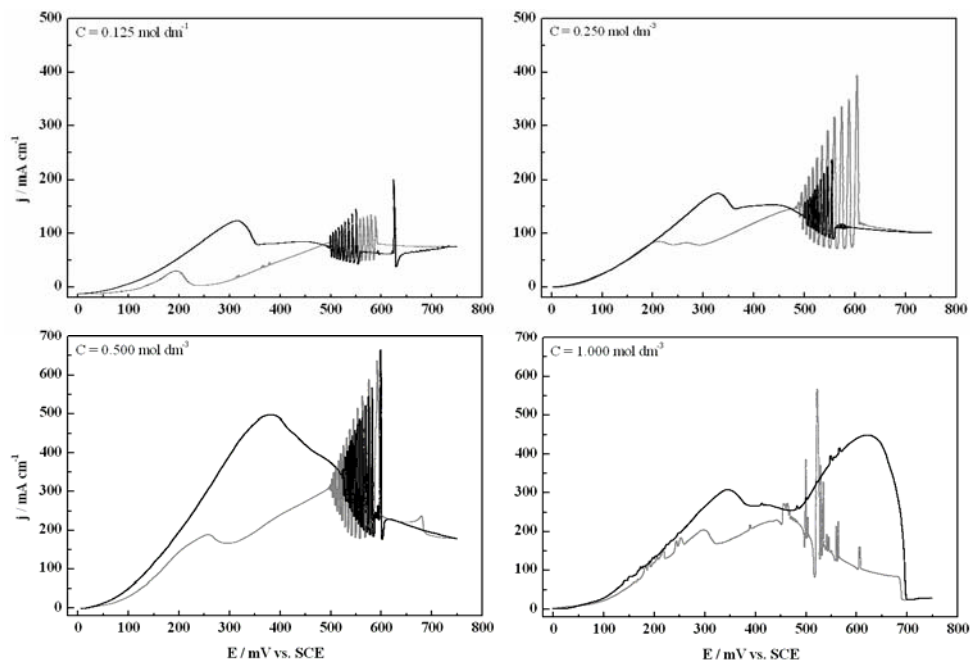


Fig. 1. j - E polarization curves of anodic dissolution/passivation of copper electrode in four different concentrations of trifluoroacetic acid aqueous solution. Sweep rate $dE/dt = 10 \text{ mV s}^{-1}$. Black line-forward direction sweep, gray line backward direction sweep, regarding more positively potentials.

In this non-linear dynamical system, the increase of current oscillation amplitudes with increase of acid concentration from 0.125 to $0.500 \text{ mol dm}^{-3}$ was observed. In the case of $1.000 \text{ mol dm}^{-3}$ electrolyte solution, electrochemical system shows chaotic small oscillations in the forward direction and chaotic large oscillations in backward one. Furthermore, from the obtained j - E polarization curves it is observed the existence of hysteresis loop in all cases (Fig. 1).

An insert of j - E polarization curves swept in forward direction on several temperatures are presented in Figure 2; electrolyte solution was 0.5 M . Result implies that processes related to current oscillations in the electrode interface are temperature depended. The largest amplitudes and maximal frequency of current oscillations are accomplished at $30 \text{ }^\circ\text{C}$. Below the mentioned temperature the passivation process is more promoted than electrodisolution. On the other hand, at temperature above $30 \text{ }^\circ\text{C}$ electrodisolution is favourable.

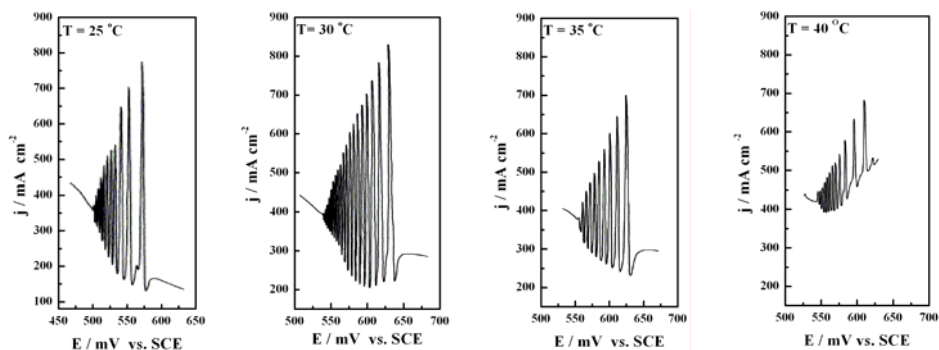


Fig. 2. Oscillatory domain of anodic polarization curve of copper in 0.5 mol dm^{-3} trifluoroacetic acid solution at various temperatures. Scan rate, 10 mV s^{-1}

Conclusion

The Cu / CF_3COOH electrochemical oscillator is examined by influence of trifluoroacetic acid concentration and temperature on potential region of current oscillations, their amplitudes and frequencies. It was found that investigated system have its maximum response with respect to current amplitudes and frequencies when electrolyte concentration is $C_{\text{CF}_3\text{COOH}} = 0.5 \text{ mol dm}^{-3}$ and temperature of electrolyte solution is $T = 30 \text{ }^\circ\text{C}$.

Acknowledgement

Present investigations are partially supported by The Ministry of Sciences and Environmental Protection of Serbia, under the Project 142025.

References

- [1] J. Wojtowicz in *Modern Aspects of Electrochemistry* (Edited by J. O'M. Bockris and B. E. Conway), Plenum Press, New York, 1972, **8**, 47-120.
- [2] F. N. Albahadily, M. Schell, *J. Chem. Phys.*, 1988, **88**, 4312-4319.
- [3] L. Li, S. Chen, H. Wu, H. Cui, *J. Serb. Chem. Soc.* 2004, **69**, 33-42.
- [4] Q. Cui, H. D. Dewald, *Electrocim. Acta*, 2005, **50**, 2423-2429.
- [5] H. Cui, S. Chen, S. Zhao, C. Wang, *J. Serb. Chem. Soc.* 2001, **66**, 881-886.
- [6] N. Potkonjak, Lj. Kolar-Anić, T. Potkonjak, S. N. Blagojević, S. Anić, *Matter. Sci. Forum*, 2006, **518**, 301-306.

INFLUENCE OF THE FORM OF THE PERIODIC FUNCTION THAT DESCRIBES THE CIRCADIAN RHYTHM OF THE HPA SYSTEM ACTIVITY

S. Jelić¹, Ž. Čupić² and Lj. Kolar-Anić³

¹*Department of Theoretical Physics and Physics of Condensed Matter 020/2, Vinča institute of Nuclear Sciences, P. O. Box 522, Belgrade (jelic@vin.bg.ac.yu)*

²*Institute of Chemistry, Technology and Metallurgy, Departement of Catalysis and Chemical Engineering, Njegoševa 12, Belgrade (zcupic@nanosys.ihm.bg.ac.yu)*

³*Faculty of Physical Chemistry, University of Belgrade, Studentski trg 12-16, P. O. Box 137, Beograd (lkolar@ffh.bg.ac.yu)*

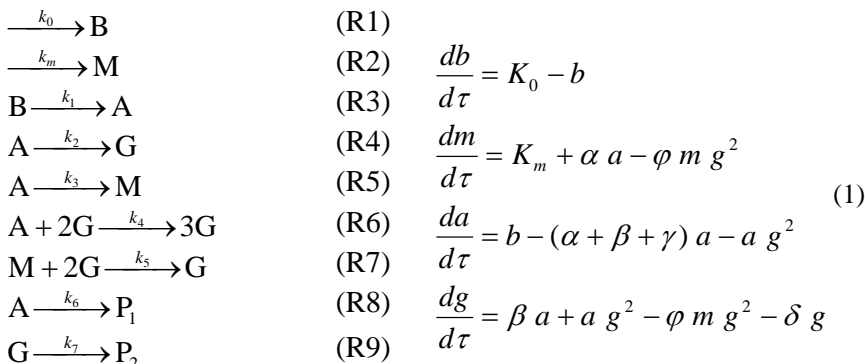
Abstract

The influence of the form of the periodic function that describes the circadian rhythm on the hypothalamic-pituitary-adrenal (HPA) system self-regulatory activity in humans is discussed. It was found that the HPA system is very sensitive to the choice of this function since it moderates the concentration of all species that are included in the model, as well as the form of ultradian pulses.

Introduction

We have proposed recently [1], [2] an initial model of the hypothalamic-pituitary-adrenal (HPA) system self-regulatory activity in humans. This model is here additionally elaborated in respect to the HPA system activity under stress conditions, with particular attention on the influence of the periodic function that was chosen to describe the daily rhythm.

The proposed model presents simplified picture of complex mechanism of the HPA system activity, with four crucial variables included in it. The species selected for the model are corticotrophin-releasing hormone (CRH), adrenocorticotropin (ACTH), mineralocorticoid aldosterone (M) and glucocorticoid cortisol (G). Analyzing experimental investigations of the mechanism of the HPA system activity, one can conclude that the model ought to take into account the positive feedback effect of cortisol exerted at the level of hippocampal glucocorticoid receptors (GR), where cortisol stimulates CRH gene expression, thus stimulating ACTH and its own production, besides its well known, classical, negative feedback effects at the level of hippocampal mineralocorticoid receptors (MR), and hypothalamic and pituitary GR, and, also, the influence of aldosterone on these feedforward and feedback pathways. Hence, denoting by B, A, G and M the species CRH, ACTH, cortisol and aldosterone, respectively, and by P_1 and P_2 the products of ACTH and cortisol elimination, the proposed model has the form



The first equation describes basal CRH production, the second one describes aldosterone production under the renin-angiotensin system control, the third describes CRH stimulated ACTH production from the pituitary, and the following two are simplified descriptions of the ACTH stimulated cortisol and aldosterone production from adrenal cortex. The sixth equation describes positive feedback of the cortisol, and the next equation represents cortisol negative feedback, acting through hippocampal MR (where aldosterone and cortisol “fight for” the same receptors), as well as hypothalamic and pituitary GR. Cortisol, as represent of the HPA system activity, has double periodic evolution [3]: daily rhythm (of 24 h period), dictated by the internal biological clock (part of the hypothalamus, called the suprachiasmatic nucleus (SCN)), and the other one is the intrinsic hormone oscillatory evolution, with the period of 20-30 minutes (ultradian rhythm). The amplitudes of ultradian oscillations depend on the daily rhythm. They are lower during the night. The HPA system stress reaction depends of both functions: $f(\text{intrinsic})$ and $f(\text{daily})$. We shall discuss only the influence of the mathematical form of the function that describes daily rhythm on the HPA system response to an acute stressor. This function can be simple sinusoidal function, or combination of sinusoidal one and others that help in obtaining the asymmetric form of a period that is more closed to the human being daily rhythm. Such function can also be the one proposed in our previous paper [2] given as $P = 0.8095 + 0.061248 \times \sin(2\pi t/1440) + 0.11484 \times \text{abs}(\sin(\pi t/1440))$ (where the constant 1440 is expressed in minutes) or any similar [2]. In that case, the rate of inflow of CRH into the system is changed, such that new rate of inflow is $K_p = K_0 \times P$.

Results and Discussion

The sensitivity of the model to the selection of the function that describes daily rhythm is analyzed for different functions. In Figure 1, we can see two very similar basal functions (A) and (B) and one sinusoidal (C). Perturbations were performed during the day, in downward inflection point of one cortisol pulse.

Conclusion

Numerical simulations performed, for two different functions chosen to describe daily rhythm of the HPA system, show that the form of these functions clearly influences

the systems response to stressful stimuli. This is in accordance with known fact that the same stressful situation can cause different stress responses in different subjects. Between humans significant differences in daily rhythm of the HPA system exist, whilst it is quite stable for one person during life.

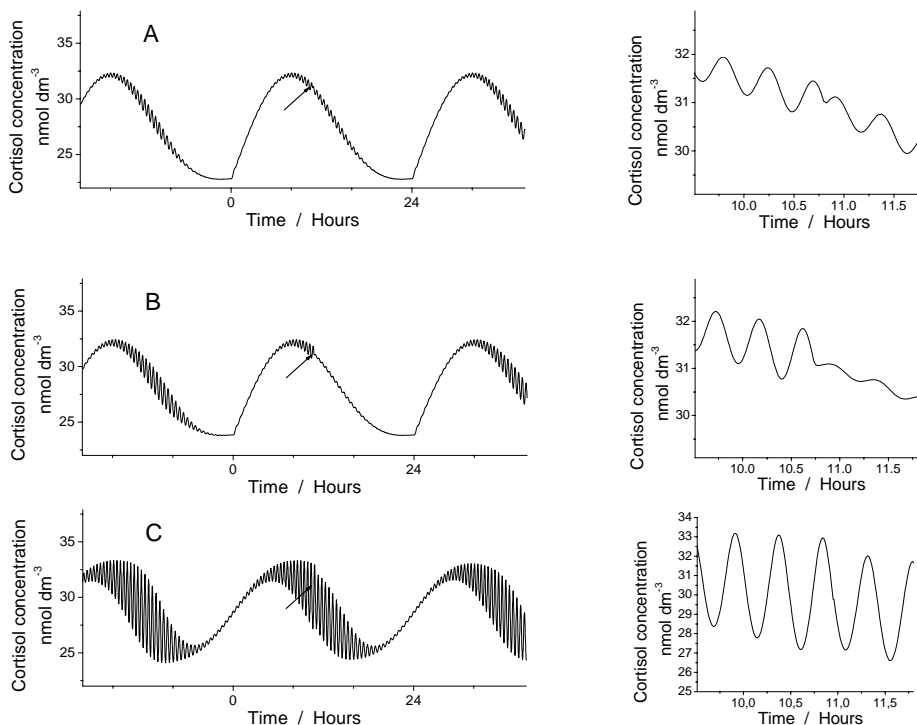


Fig. 1. Perturbations of the HPA system with two different functions of daily rhythm. The augmented segments, where perturbations in CRH concentration equal to $1 \times 10^{-9} \text{ mol dm}^{-3}$ was performed, are presented on the right side: $G(0) = 2.76 \times 10^{-8} \text{ mol dm}^{-3}$; $K_0 = 0.0831$; $K_m = 2.7693 \times 10^{-4}$; $\alpha = 1.5776 \times 10^{-4}$; $\beta = 0.0197$; $\gamma = 0.0293$; $\delta = 0.2245$; $\varphi = 0.0560$; (A) $P = 0.7904 + 0.0689 \times \sin(2\pi t/1440) + 0.1292 \times \text{abs}[\sin(\pi t/1440)]$; (B) $P = 0.8095 + 0.0612 \times \sin(2\pi t/1440) + 0.1148 \times \text{abs}[\sin(\pi t/1440)]$; (C) $P = 0.8980 + 0.0640 \times \sin(2\pi t/1440)$

Acknowledgement

Present investigations are partially supported by the Ministry of Sciences and Environmental Protection of Serbia under the project no. 142025 and 142019.

References:

- [1] S. Jelić, Ž. Čupić, Lj. Kolar-Anić, in: Selforganization in nonequilibrium systems, S. Anić, Ž. Čupić, Lj. Kolar-Anić (Eds.), SPCS, Belgrade, 2004.
- [2] S. Jelić, Ž. Čupić, Lj. Kolar-Anić, *Math. Biosci.*, 2005, **197**, 173-187.
- [3] C. Tsigos, G.P. Chrousos, *J. Psychosom. Res.*, 2002, **53**, 865-871.

SINGULARITY THEORY APPROACH APPLIED TO FOUR-DIMENSIONAL MODEL OF THE HYPOTHALAMIC-PITUITARY-ADRENAL SYSTEM ACTIVITY

S. Jelić

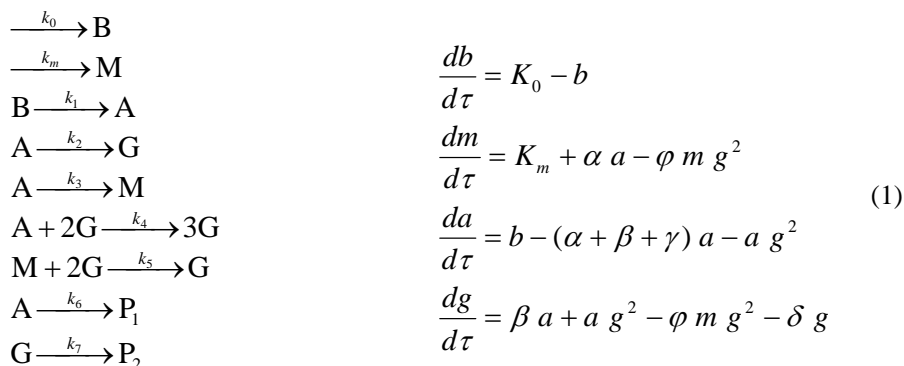
*Department of Theoretical Physics and Physics of Condensed Matter 020/2,
Vinča Institute of Nuclear Sciences, P. O. Box 522, Belgrade, Serbia*

Abstract

The HPA system is a complex neuroendocrine system whose main purpose is to regulate wide variety of bodily processes, under basal physiological conditions and during stress, by regulating the plasma levels of corticosteroids secreted from adrenal glands. In this paper, we apply the singularity theory approach to an initial model of this system, which we have previously published.

Introduction

The paraventricular nucleus (PVN) is a part of the hypothalamus which controls the secretion of corticotrophin-releasing-hormone (CRH) and arginin-vasopressin (AVP), which cause pituitary release of adrenocorticotropin (ACTH) and consequential adrenal gland stimulation, with release of corticosteroids (glucocorticoids, whose main representative in humans is cortisol (CORT), and corticosterone in rodents, and mineralocorticoids, whose main representative is aldosterone (ALDO)) from appropriate adrenal cortex zones [1]. In our previous paper, the HPA system was described by the following model [2]:



Here letters b , m , a and g represent dimensionless plasma concentrations of CRH, ACTH, cortisol and aldosterone, respectively. If we find the stationary state equation for dimensionless cortisol concentration

$$F(g_{ss}, K_0; \alpha, \beta, \gamma, \delta, K_m) = (g_{ss}^2 + \alpha + \beta + \gamma) \left(g_{ss} - \frac{K_0 - K_m}{\delta} \right) + \frac{K_0(2\alpha + \gamma)}{\delta} \tag{2}$$

then the condition for appearance/disappearance of a hysteresis loop (bistability) [3] can be written as

$$F(g_{ss}, K_0; \alpha, \beta, \gamma, \delta, K_m) = F_g(g_{ss}, K_0; \alpha, \beta, \gamma, \delta, K_m) = F_{gg}(g_{ss}, K_0; \alpha, \beta, \gamma, \delta, K_m) = 0$$

with $F_{ggg}(g_{ss}, K_0; \alpha, \beta, \gamma, \delta, K_m) \neq 0$. (3)

Here, K_0 is the bifurcation parameter, and F_g , F_{gg} , and F_{ggg} are corresponding partial derivatives of F with respect to g_{ss} (other higher partial derivatives of F , with respect to g_{ss} and bifurcation parameter K_0 , must all be non-zero). In our case

$$F(g_{ss}, K_0; \alpha, \beta, \gamma, \delta, K_m) = (g_{ss}^2 + \alpha + \beta + \gamma)(g_{ss} - \frac{K_0 - K_m}{\delta}) + \frac{K_0(2\alpha + \gamma)}{\delta} = 0 \quad (4)$$

$$F_g(g_{ss}, K_0; \alpha, \beta, \gamma, \delta, K_m) = g_{ss}^2 + \alpha + \beta + \gamma + 2g_{ss}(g_{ss} - \frac{K_0 - K_m}{\delta}) = 0 \quad (5)$$

$$F_{gg}(g_{ss}, K_0; \alpha, \beta, \gamma, \delta, K_m) = 2(3g_{ss} - \frac{K_0 - K_m}{\delta}) = 0 \quad (6)$$

When all three right hand sides of equations (4)-(6) equal zero simultaneously they fix the values of three quantities. For the selected α , β , γ and K_m , the values of g_{ss} , K_0 and δ can be determined at the point where the hysteresis loop just unfolds (uniquely). Solving the equation (6) we have the vertical inflection point value

$$g_{ss,V} = \frac{K_0 - K_m}{3\delta} \quad (7)$$

Again, as in the case of two-dimensional system, since only positive values of g_{ss} are realistic, we see that K_0 value must be larger than K_m . In the case of four dimensional system, vertical inflection point value does not depend on parameters α , β and γ . The region of multiple solutions is determined by the equations

$$F(g_{ss}, K_0; \alpha, \beta, \gamma, \delta, K_m) = F_g(g_{ss}, K_0; \alpha, \beta, \gamma, \delta, K_m) = 0,$$

with $F_{gg}(g_{ss}, K_0; \alpha, \beta, \gamma, \delta, K_m) \neq 0$ (8)

thus, we have the ignition and extinction point (or turning points) in the g - K_0 locus:

$$g_{ss,1,2} = \frac{K_0 - K_m \pm \sqrt{(K_0 - K_m)^2 - 3(\alpha + \beta + \gamma)\delta^2}}{3\delta} \quad (9)$$

and the following inequality $(K_0 - K_m)^2 - 3(\alpha + \beta + \gamma)\delta^2 > 0$ must be satisfied for bistability of the system to exist, if not, $F_{gg}(g_{ss}, K_0; \alpha, \beta, \gamma, \delta, K_m) = 0$ when $F_g(g_{ss}, K_0; \alpha, \beta, \gamma, \delta, K_m)$ vanishes, and two turning points (9) merge into the point of inflection (7).

Taking into account discussion about region of multistability given above, we performed further analysis of considered system numerically. Since the HPA system daily rhythm is dictated by one part of the hypothalamus, called the suprachiasmatic nucleus (SCN) [4], in numerical simulations made, we have described the HPA system daily rhythm by introducing one 24-h periodic function (P), and thus following result was obtained (Figure 1):

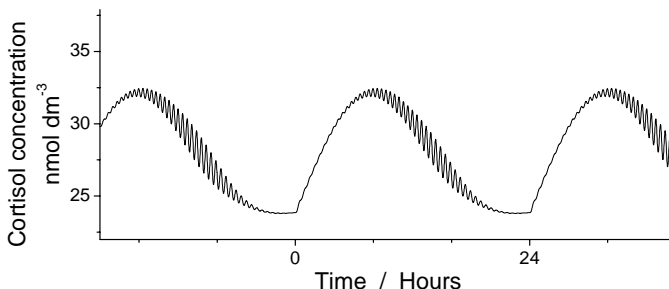


Fig. 1. Numerical simulations of the time evolution of cortisol concentrations with daily rhythm described by function $P = 0.8095 + 0.061248 \times \sin(2\pi t/1440) + 0.11484 \times \text{abs}(\sin(\pi t/1440))$. $G(0) = 2.76 \times 10^{-8} \text{ mol dm}^{-3}$, $K_0 = 0.0831$, $K_m = 2.7693 \times 10^{-4}$, $\alpha = 1.5776 \times 10^{-4}$, $\beta = 0.0197$, $\gamma = 0.0293$, $\delta = 0.2245$, $\varphi = 0.0560$, $k_p = k_0 \times P$.

Conclusion

Analytical analysis performed, show that, for certain set of systems parameters, bistability of considered system exists. Numerical simulations give the HPA system daily rhythm in accordance with medical literature. Further improvements of considered model are possible, by taking into account influences of other hormones (such as AVP, progesterone, or testosterone for example), that are able to modulate the HPA system activity.

Acknowledgement

Present investigations are supported by the Ministry of Sciences and Environmental Protection of Serbia under the project no. 142025.

References:

- [1] C. Tsigos, G.P. Chrousos, J. Psychosom. Res., 2002, **53**, 865-871.
- [2] S. Jelić, Ž. Čupić, Lj. Kolar-Anić, Math. Biosci., 2005, **197**, 173-187.
- [3] P. Gray, S. K. Scott. 1990, Chemical oscillations and Instabilities-Non-linear Chemical Kinetics. Clarendon Press, Oxford.
- [4] A. Balsalobre, S.A. Brown, L. Marcacci, F. Tronche, C. Kellendonk, H.M. Reichardt, G. Scuty, U. Schibler. Science, 2000, **289**, 2344-2349.

BREAKING OF TRANSLATIONAL SYMMETRY OF A TRAVELING PLANAR IMPULSE IN A 2D TWO-VARIABLE REACTION-DIFFUSION MODEL

A. L. Kawczyński, M. Leda and B. Legawiec

*Institute of Physical Chemistry
Polish Academy of Sciences, Warsaw, Poland
alk@ichf.edu.pl, leda@ichf.edu.pl, leg@ichf.edu.pl*

Abstract

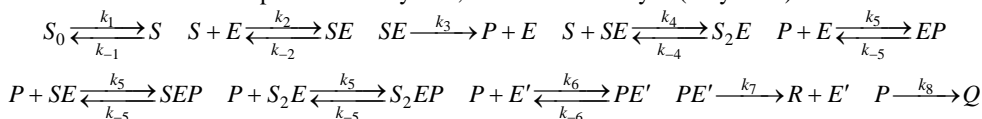
The stability of a planar impulse in rectangular spatial domains for a two-variable, excitable reaction-diffusion system is numerically studied. The dependence of the stability on the size of the domain perpendicular to the direction of the propagation of the impulse is shown. The instability results in asymptotic stable curved impulses or an asymptotic spatio-temporal structure, which is generated similarly to the 1D backfiring phenomenon.

Introduction

Each solution to an one-dimensional (1D) reaction-diffusion (RD) system is also the solution to the two-dimensional (2D) system, if initial conditions depend only on one coordinate. However, the stability of the solution to the 1D RD system does not imply the stability of this solution in the 2D system. The instabilities of 1D (planar or circular) travelling fronts has been studied in one- and two-variable RD systems with one stable and one unstable stationary state [1,2] and in real chemical systems [3,4] systems. Planar or circular traveling impulses in two-variable excitable activator-inhibitor systems may be unstable if the diffusion coefficient of the inhibitor is sufficiently greater than the diffusion coefficient of the activator [5].

Model

The model describes an open chemical system, in which two catalytic (enzymatic) reactions occur.



On the basis of the Tikhonov theorem [6] the concentrations of both catalysts and their complexes may be eliminated as fast variables. We consider the initial-boundary value problem for a 2D system $(x,y) \in [0,L_x] \times [0,L_y]$ whose the dynamics is described in dimensionless variables by the following equations:

$$\frac{\partial s(x,y,t)}{\partial t} - \frac{\partial^2 s(x,y,t)}{\partial x^2} - \frac{\partial^2 s(x,y,t)}{\partial y^2} = A_1 - A_2 s - \frac{s}{(1+s+A_3 s^2)(1+p)} \quad (1a)$$

$$\frac{\partial p(x,y,t)}{\partial t} - D \left(\frac{\partial^2 p(x,y,t)}{\partial x^2} + \frac{\partial^2 p(x,y,t)}{\partial y^2} \right) = B \left(\frac{s}{(1+s+A_3 s^2)(1+p)} - B_1 - B_2 p \right) \quad (1b)$$

where: s, p are dimensionless concentrations of S and P, dimensionless parameters are functions of rate constants and the total concentrations of the catalysts and $D=DP/DS$ is the ratio of the diffusion coefficients for the product and the reactant.

In order to define the problem the following initial conditions are assumed:

$$s(x,y,0) = s(x,t_0) + pert(x,y), \quad p(x,y,0) = p(x,t_0) \quad (x,y) \in [0, L_x] \times [0, L_y] \quad (2)$$

where: $s(x,t_0)$ and $p(x,t_0)$ are profiles of the 1D impulses at $t=t_0$, and the zero-flux boundary conditions. For the following values of the parameters: $A_1=0.01, A_2=0.0001, A_3=0.505,$

$B_1=7.99 \times 10^{-3}$, $B_2=4.65 \times 10^{-5}$, $B=0.3$ and $D=3.9$, the system (1) without the diffusion terms has three stationary states: the stable node, the saddle point and the unstable focus.

Results

Eqs (1-3) are solved numerically using the Cranck-Nicholson scheme and the Runge-Kutta algorithm. In a finite 1D system the traveling impulse reflects from the boundaries and spreads periodically from one wall to the other (**Fig. 1**). For $B=0.3$ the 1D traveling impulse is the structurally stable asymptotic solution for $D \in (1.0, 4.2)$. For values of $D > 4.2$ the backfiring phenomenon is observed.

The planar traveling impulse is the stable asymptotic solution in the 2D system for L_y smaller than some critical value $L_{y,cr} \approx 1.4$. However, if L_y grows above the critical value $L_{y,cr}$, the planar traveling impulse loses its stability and the curved traveling impulse becomes the stable asymptotic solution. This situation is shown in **Fig. 2(a)** and **2(b)** for $L_y = 1.5$. The velocity of the curved traveling impulse is greater than the velocity of the planar traveling impulse. Moreover, the curved traveling impulse vanishes at the wall, whereas the planar traveling impulse reflects from the boundaries. Due to the zero-flux boundary conditions the traveling impulse, which is a mirror reflection of the impulse shown in **Fig. 2(b)**, is the asymptotic solution for $L_y=3.0$ (**Fig.2(c)**). It should be stressed that if the diffusion coefficient of the inhibitor is equal or close to the diffusion coefficient of the activator ($D \cong 1$), then the planar traveling impulse is stable for all values of the size perpendicular to the direction of its propagation.

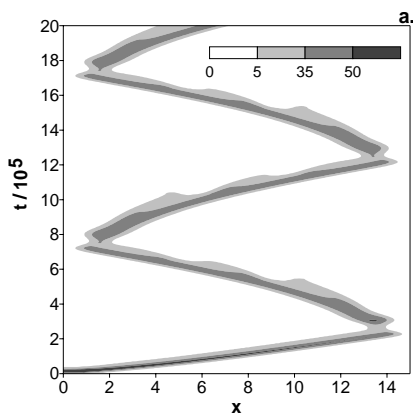


Fig.1. 1D solution to Eqs. (1-3) in the form of reflecting impulse.

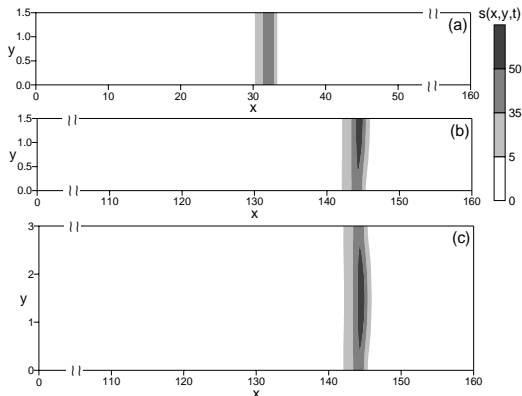


Fig.2. Solutions to Eqs. (1-3) for $pert(x,y)=\{5$ if $(x,y)=(32.18,1.49)$ and 0 for all other points} (a,b) and $pert(x,y)=\{5$ if $(x,y)=(32.18,1.49), (32.18,1.51)$ and 0 for all other points} (c) at $t = 0$ (a) and $t = 2 \cdot 10^6$ (b),(c).

The curved traveling impulse shown in **Fig. 2(c)** may coexist with the solution whose evolution is shown in **Fig. 3**. After perturbation the planar traveling impulse splits into a curved and a small excited region (**Fig. 3(b)**). In further evolution a curved traveling impulse spreading in the opposite direction is generated (**Fig. 3(c,d)**), leaving behind the excited region. The region splits producing a pair of next-generation curved traveling impulses behind which a periodic pattern is

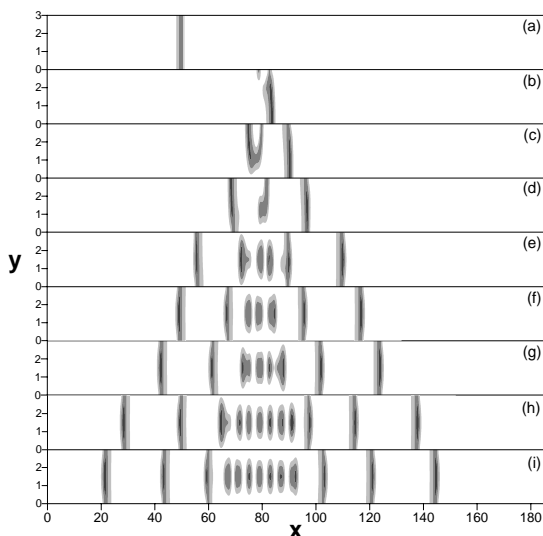


Fig.3. Solutions to Eqs. (1-3) for $pert(x,y)=\{5$ at $(x,y)=(32.18,1.49)$ and 0 on all other points) for $t =:$ 0 (a), $0.67 \cdot 10^6$ (b), $0.77 \cdot 10^6$ (c), $0.87 \cdot 10^6$ (d), $1.07 \cdot 10^6$ (e), $1.17 \cdot 10^6$ (f), $1.3 \cdot 10^6$ (g), $1.47 \cdot 10^6$ (h), $1.57 \cdot 10^6$ (i).

generated (**Fig. 3(e,f)**). The creation of the stationary periodic pattern is similar to the backfiring phenomenon observed in the 1D systems (**Fig. 3(g-i)**). In a finite system the subsequent curved traveling impulses vanish at the boundaries, and finally the stationary periodic structure occupies the whole system. In an infinite system an infinite series of curved traveling impulses is produced, leaving behind the stationary periodical structure which is generated step by step.

Conclusions

The planar traveling impulse is stable in the 2D systems with a small size (L_y) perpendicular to the direction of the propagation. Two types of stable asymptotic solutions appear for sufficiently large values of L_y . One of them is a single curved traveling impulse. The other one consists of an infinite series of curved traveling impulses which leaves behind the stationary periodical structure. The selection of one of these asymptotic solutions depends on the initial conditions. This type of instability may be another possibility of explaining the appearance of dissipative structures in experiments in which the diffusion coefficient of the inhibitor is greater than the diffusion coefficient of the activator. Chlorite-tetrathionate in polyacrylamide gel [7] and chlorite dioxide-iodine-malonic acid (CDIMA) in polyvinyl alcohol [8] are examples of such real chemical systems.

References

- [1] D. Horvath, V. Petrov, S. K. Scott, and K. Showalter, *J.Chem. Phys.*, 1993, **98**(8), 6332.
- [2] R. A. Milton, and S. K. Scott, *Proc. R. Soc. Lond.*, 1996, **A 452**, 391.
- [3] D. Horvath, and K. Showalter, *J.Chem. Phys.*, 1995, **102**(6), 2471.
- [4] D. Horvath, and A. Toth, *J.Chem. Phys.*, 1998, **108**(4), 1447.
- [5] M. Mimura, and M. Nagayama, *Chaos*, 1997, **7**(4), 817.
- [6] A. N. Tikhonov, *Mat. Sborn.*, 1952, **31**, 575.
- [7] A. Toth, I. Lagzi, and D. Horvath, *J. Phys. Chem.*, 1996, **100**(36), 14837.
- [8] P.W. Davies, P. Blanchedeau, E. Dulos, and P. De Kepper, *J. Phys. Chem.*, 1998, **102**(43), 8236.

TIMING OF DYNAMIC REGIMES IN *DICTYOSTELIUM DISCOIDEUM* (*DD*) UNDER EFFECTS OF EXTERNAL cAMP

J. Čejková¹, Ch. Hilgardt² and H. Ševčíková¹

¹Center for Nonlinear Dynamics of Chemical and Biological Systems, Institute of Chemical Technology, Prague, Technická 5, 166 28 Prague 6, Czech Republic; (Hana.Sevcikova@vscht.cz)

²Otto-von-Guericke University, Universitätsplatz 2, 39106 Magdeburg, Germany;

Abstract

Subcritical levels of external cAMP cause delays in the onset of both oscillatory production of cAMP and wave patterns in populations of starving *DD* cells. Number of oscillating wave centers increases with the cAMP level. At supercritical levels of cAMP the aggregation occurs without cAMP waves. At all levels of cAMP a global wave passes through the cell layer before the aggregation sets in.

Introduction

Production and degradation of a signalling substance cAMP (cyclic adenosin 3',5'-monophosphate) in starving cells of a slime mold *DD* during the aggregation stage adopts four consecutive dynamical regimes: i) a stable steady state with a low concentration of cAMP, ii) an excitable regime, iii) stable oscillations, and iv) a stable stationary state with a high cAMP concentration [1]. In a population of cells, timing of the regimes described above slightly differs from cell to cell depending on the cell's age at the onset of starvation [2]. The unsynchronized timing is necessary for cells to aggregate in response to propagating waves of cAMP. These waves are elicited by the cells that reached the oscillatory regime and are relayed by neighbouring cells still dwelling in an excitable state. Chemotaxis of cells against the propagating cAMP waves makes all the cells to gather in large aggregates (cf. Fig.1.)

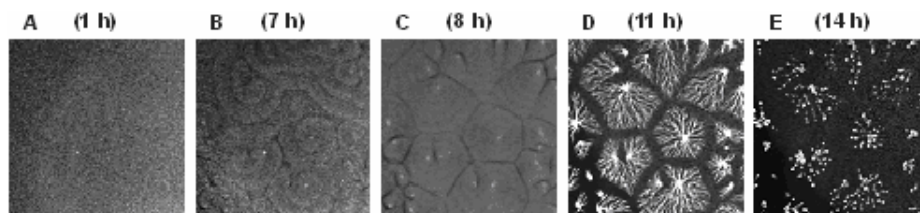


Fig. 1. Aggregation process on cAMP-free agar. A - quiescent layer; **B** - cAMP wave patterns; **C** - formation of aggregation territories; **D** - cell streams; **E** - tight aggregates.

Image size 1.9×1.9 cm.

The dynamics of cAMP synthesis and degradation is known to change under the influence of external substances, however, little attention has been devoted to investigation how these changes are projected to the aggregation process [3]. This paper investigates the aggregation characteristics in cell populations exposed to the long term influence of cAMP present in the supporting agar.

Experimental

Starving cells of AX2 strain of *DD* prepared by the standard way [4] were spread at the cell density 6.17×10^5 cells/cm² on nutrient-free agars loaded with different concentrations of cAMP. The aggregation process was monitored in the dark field at 21 °C by digital camera, recorded on PC and evaluated with the SW LUCIA [5].

Results and Discussion

The first important difference in the course of aggregation in cells on agars with cAMP is the emergence of a global wave (GW) during the pre-wave phase (Fig. 2A). The GW, initiated spontaneously in an arbitrary location, spreads fast within tens of minutes through the layer. The propagation of the GW slows down during its propagation and it is slower at higher levels of cAMP in agar (Fig. 2B). The propagation velocities range from $v = 3.6$ mm/min (the initial velocity at 0.125 mM cAMP) to $v = 0.05$ mm/min (the terminal velocity at 2.0 mM cAMP). The time of GW emergence increases with the increasing level of cAMP (cf. TABLE 1).

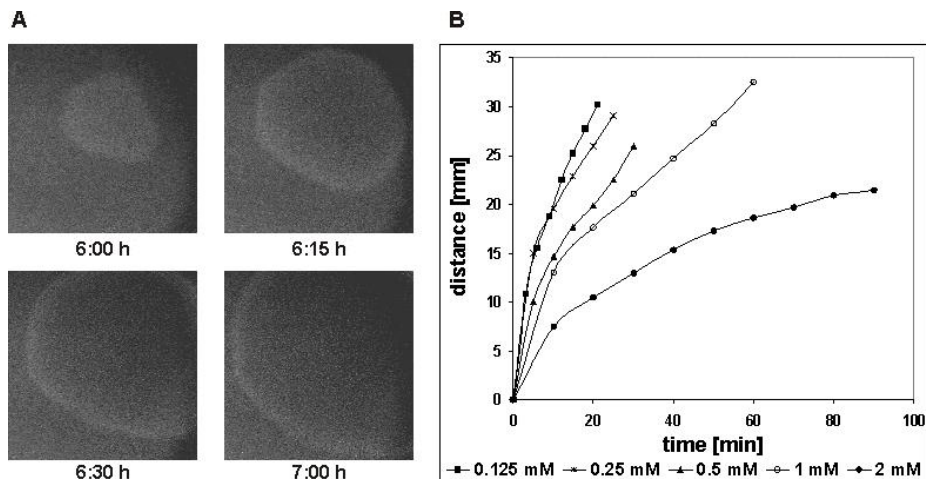


Fig. 2. Global wave. A – Dark field images. 2 mM cAMP in agar. Image size 2.5×2.5 cm. B – Track of the position of a global wave in time.

Effects of external cAMP on the aggregation characteristics are summarized in TABLE 1. At concentrations of cAMP up to 1mM, wave patterns emerge at some time after GW. The wave patterns look similar to those on cAMP-free agar, however, the size of aggregation territories decreases with the increasing concentration of cAMP. It indicates larger number of self-oscillating wave centers arise on agar with cAMP. The duration of the wave patterning is somewhat shorter but the wave velocities, periods, and their development in time are the same as on the cAMP-free agar.

Table 1. Characteristics of aggregation process in dependence on the cAMP concentration in agar. (NA – non applicable; * - time from the beginning of starvation)

		Concentration of cAMP in agar [mM]					
		0	0.125	0.25	0.5	1.0	2.0
Emergence of a Global Wave *	[h]	NA	1:40	3:00	4:00	4:40	6:00
Onset of wave patterning *	[h]	5:30	7:00	7:00	10:30	12:00	NA
Duration of wave patterning	[h]	3:30	3:00	3:00	2:30	NA	NA
Average size of agg. territories	[cm ²]	0.40	0.10	0.07	0.06	NA	NA
Number of wave centers	[1/cm ²]	2.5	10.3	15.2	17.7	NA	NA

On the 2 mM cAMP agar no wave patterns arise. Four hours after the GW, the cell layer disintegrates into tiny groups of loosely connected cells. The groups slowly merge together on forming tight aggregates in the end. On the 1 mM cAMP agar hazy, short lived, wave patterns arise only in some places; otherwise the development is similar to that on the 2mM cAMP agar.

Conclusions

The delay of onset of the oscillatory regime of *DD* cells observed at lower levels of cAMP can be explained by the time needed for cell-produced phosphodiesterase to degrade excess of external cAMP [3], however, the aggregation without cAMP waves at high levels of cAMP and the appearance of the global wave in the pre-wave period are the new phenomena open to further research.

Acknowledgement

This work has been supported by the grants No.: 204/04/1421 and 104/03/H141 of GACR and by the Research Project MSM 6046137306.

References

- [1] A. Goldbeter, „Biochemical Oscillations and Cellular Rhythms“, Cambridge University Press, Cambridge (1996).
- [2] M. Wang, J.R.Aerts, W. Spek, P. Schaap, *Dev. Biol.*, 1988, **125**, 410.
- [3] Kessin, R.H. *Dictyostelium: Evolution, Cell Biology, and the Development of Multicellularity*. Cambridge Univ. Press. 2001.
- [4] J.A. Spudich (Ed.), *Methods in Cell Biology*, vol. Academic Press, London, 1987, **28**, 26.
- [5] LUCIA – A System for Image Analysis, (www.lim.cz).

CHARACTERISTICS OF LITHIUM OSCILLATORY TRANSPORT THROUGH EXCITED BIOMEMBRANE

Č. N. Radenović^{1, 2}, M. V. Beljanski³, N. Maksimova⁴ and G. V. Maksimov⁴,

¹Maize Institute "Zemun Polje" Laboratory of Biophysics, Belgrade, Serbia

²Faculty of Physical Chemistry Belgrade University, Belgrade, Serbia

³Institute of General and Physical Chemistry, Belgrade, Serbia

⁴Lomonosov State University, Moscow, Russia

Abstract

Membrane biopotential oscillations influenced by Lithium ion were followed on fresh water alga *Nittela* cells using microelectrode technique. Addition and removal of Lithium ion into and from medium induces oscillations with different parameters.

Introduction

Lithium (Li) the lightest alkali metal, although not a normal constituent of soils, is not toxic to the plants and is readily absorbed and accumulated in them in detectable quantities. Due to its similarity with other alkaline ions, Li may interfere with cellular metabolic and regulatory mechanisms. Generally, two well characterized Li targets on molecular level are known: Inositol monophosphatase and Glycogen synthase kinase-3. In plants Li interferes with ion fluxes mechanisms mediated by the plasmallema [1, 3].

Experimental

Oscillations of membrane biopotential have been followed on fresh water alga *Nittela* cells using microelectrode technique [3]. Solitary (main and local) as well as complete impulses of membrane oscillations caused by different Li⁺ concentrations were registered [2-4]. Membrane potential oscillations were registered due to substitution of Standard solution (SS; 0.1 M KCl, 1.0 mM NaCl, SS) and Li solution (10 mM LiCl) as indicated by arrows on Fig. 1.

Results and Discussion

Bioelectrical measurements prior to oscillations of membrane biopotential. *Nittela* cells were cultivated as described previously. Prior to treatment cells were stabilized in standard solution for 1 h and bioelectrical parameters of algal cell state are given in Tab. 1.

In all experiments oscillations of membrane biopotential were reiterated with 50% probability. Generally, oscillations of membrane biopotential appeared in two solutions (with 30% probability), and after replacement of LiCl solution with SS (with 20% probability).

Table 1. Bioelectrical parameters of *Nittela* cell state prior to inducement of membrane potential oscillations.

Membrane stationary level (ψ_m , mV)	Cyclosis ($\mu \text{ sec}^{-1}$)	Standard solution for initial bioelectrical measurements
Standard levels:		
-90	45	0.1 mM KCl + 1.0 mM NaCl
-120	50	
-150	52	

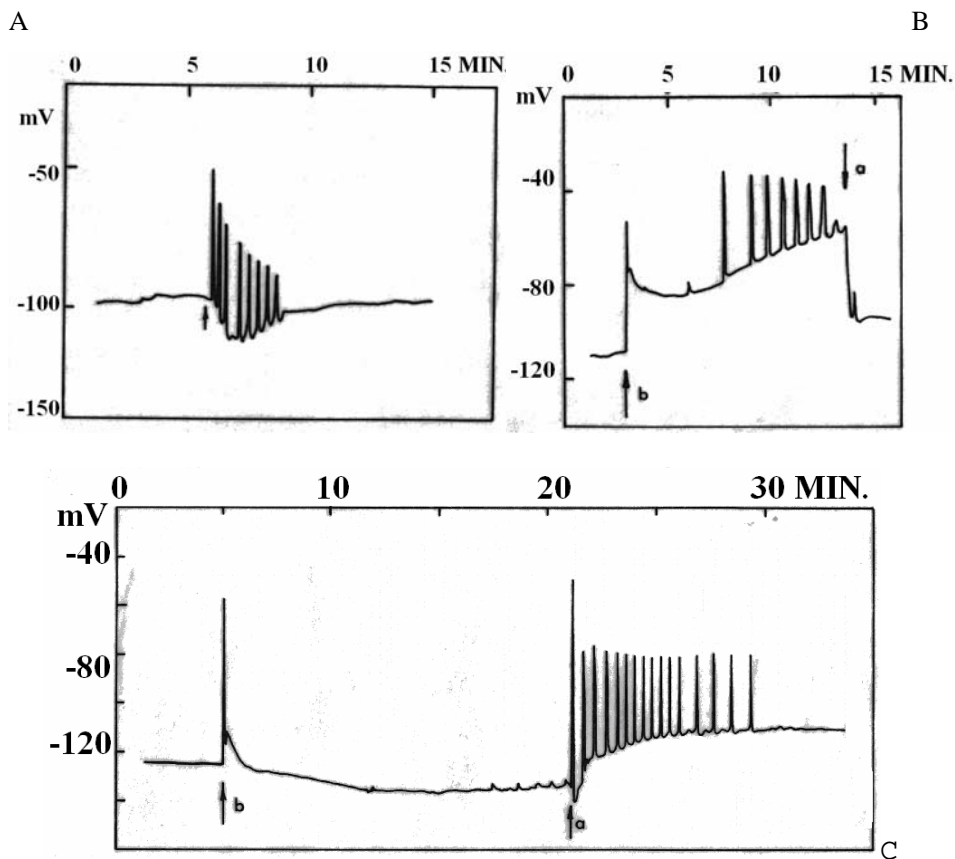


Fig. 1. (A, B and C) Oscillations of membrane biopotential caused by addition or removal of LiCl solutions into medium. Arrows point to change of medium contents, i.e. SS vs. LiCl solution. cases: after replacement of SS with LiCl

By analysing results of 27 experiments, following parameters were obtained: 27 oscillations were observed, number and average amplitude of impulses in oscillation were 13 ± 6 and 38.9 ± 13.7 respectively, oscillation duration and frequency were 12.4 ± 6.3 min and 1.44 ± 0.6 respectively and quenching factor was 1.265 ± 0.5 . Examples of representative oscillations are presented in Fig 1: oscillations of membrane biopotential caused by addition of 10 mM LiCl solution (arrow, Fig. 1 A). Oscillations are relatively short having quenching tendency. Addition of 10 mM LiCl (arrow, b, Fig. 1 B) causes appearance of individual impulse that is followed by oscillations with quenching tendency. Addition of SS (arrow, a) stops oscillations and leads to previous membrane potential. Fig. 1. C shows more complicated behaviour: after addition of 10 mM LiCl (arrow, b) and appearance of individual impulse, there is tendency for new but unstable membrane potential. Addition of SS (arrow, a) causes appearance of oscillations with smaller quenching tendency.

As may be seen from results presented, oscillations of membrane biopotential caused by Li shows complicated behaviour pointing to complex regulatory mechanism that adjust cell membrane transport.

Acknowledgement

This research was supported by the Ministry of Sciences and Environmental Protection of Republic of Serbia, Grant No. 1448.

References

- [1] T. Kondo, *Plant Physiol.*, 1984, **75**, 1071-1074.
- [2] Č. Radenović, et al., *Biofizika ANSSSR*, 1968, **13**, 270-281.
- [3] Č. Radenović, et al., in: *Plant membrane transport. Current conceptual issues*, R. M. Spanswick et al., (Eds.), Elsevier and North-Holland biomed. Press, Amsterdam, 1980.
- [4] Č. Radenović, *Proc. Nat. Sci. Matica Srpska*, 2001, **100**, 94-101.

SYSTEMS BIOLOGY STUDIES OF REACTIVE OXYGEN SPECIES (ROS)-MEDIATED APOPTOSIS

P. M. Mitrašinović

*Center for Multidisciplinary Studies, University of Belgrade, Kneza Visislava 1, Belgrade, Serbia
(pmitrasinovic@yahoo.ca)*

Abstract

ROS-mediated NF- κ B/JNK cross-talk is modeled using 36 species and 77 unidirectional reactions. A possible division of all molecular components into functional modules is proposed. Cell survival (transient JNK activation) and cell death (sustained JNK activation) are rationalized by determining the “JNK concentration vs. time” plots. The phase plane interpretation of the model indicates that a much lower-dimensional representation of the system of 77 kinetic equations could narrow down the range of possible instabilities that the oscillatory signaling can exhibit.

Introduction

Transcription factors acting on gene promoters are able to trigger several possible mechanisms leading to different outcomes in various biological contexts. The key issue is to elucidate fundamental background of the ability of cells to interpret a signal action in distinct fashions, e.g., survival vs. death signal transduction. To achieve the goal, applications of the state-of-the-art systems biology methods, derived from synthetic sciences such as engineering and computer science, may be quite relevant.

Objectives

Cells contain efficient strategies to antagonize ROS, e.g., by synthesizing superoxide dismutases (SODs), catalase, and glutathione peroxidases (Gpxs) from the family of enzymes capable of converting ROS into less-reactive species. Both suppressing the accumulation of ROS and controlling the activation of the JNK cascade can account for the antiapoptotic activity of NF- κ B. The mechanisms responsible for inhibition of the ROS proliferation by NF- κ B are still unclear. Whether JNK is an intrinsic component or a modulator of the death pathway, influenced by other signaling pathways such as NF- κ B pathway, is the question of vital importance [1].

Model and Method

TNF α -induced ROS generation can either be suppressed by NF- κ B targets or lead to programmed cell death (PCD) by inactivating JNK phosphatase from the mitogen-activated protein kinase (MAPK) phosphatase family (MKP). NF- κ B therefore acts as a modulator of the TNF α -induced death

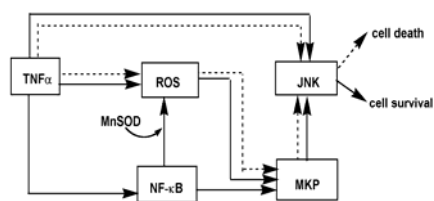


Fig. 1. NF-κB/JNK cross-talk

line in Fig. 1). A possible mechanism for the TNF α -induced ROS generation is unknown [2].

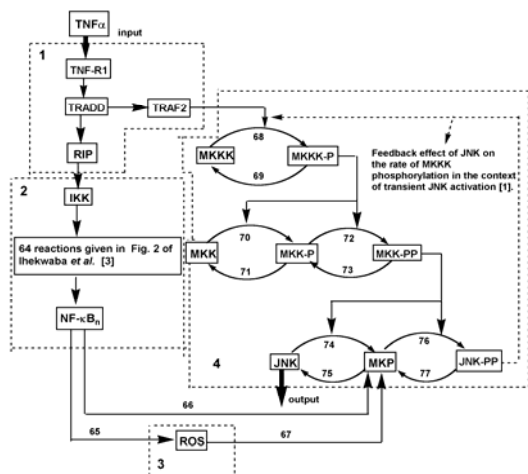


Fig. 2. Kinetic scheme. Numbering gives the order of reactions. Functional modules are: **1** – system, **2** – controller, **3** – disturbance, and **4** – object [1]

$I\kappa B\beta_n$ -NF- κB_n , $I\kappa B\epsilon_n$, $I\kappa B\epsilon_n$ -NF- κB_n , *Source*, $I\kappa B\alpha$ -t, *Sink*, $I\kappa B\beta$ -t, $I\kappa B\epsilon$ -t, ROS, MKP, JNK, JNK-PP, MKK, MKK-P, MKK-PP, MKKK, MKKK-P, TRAF2) participating in a series of 77 reactions are given in Fig. 2. All kinetic details are given in [1]. Simulations were performed by GEPASI 3.3 [5].

response by controlling both ROS accumulation and MKP activity. This means that transient JNK activation is observed in cells with a negative regulator of PCD such as NF- κB (solid line in Fig. 1), while sustained JNK activation is observed in NF- κB -deficient cells (dashed

unknown [2]. The NF- κB pathway is based on the model of Ihekwa *et al.* [3], while the JNK pathway is formally the MAPK cascade of Kholodenko [4]. The two signaling routes are linked by three additional connections 65, 66 and 67, being between NF- κB and ROS, NF- κB and MKP, and ROS and MKP, respectively. Thus, 36 molecules ($I\kappa B\alpha$, NF- κB , $I\kappa B\alpha$ -NF- κB , $I\kappa B\beta$, $I\kappa B\beta$ -NF- κB , $I\kappa B\epsilon$, $I\kappa B\epsilon$ -NF- κB , IKK, IKK $I\kappa B\beta$, IKK $I\kappa B\beta$ -NF- κB , IKK $I\kappa B\epsilon$, IKK $I\kappa B\epsilon$ -NF- κB , NF- κB_n , $I\kappa B\alpha_n$, $I\kappa B\alpha_n$ -NF- κB_n , $I\kappa B\beta_n$,

Results

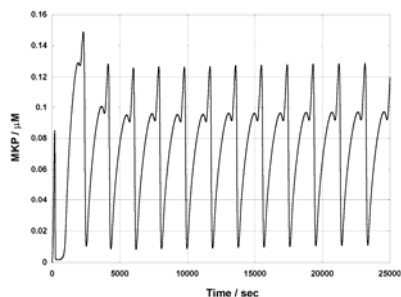


Fig. 3. [MKP] vs. time. Initial [ROS] is 0.3 μM

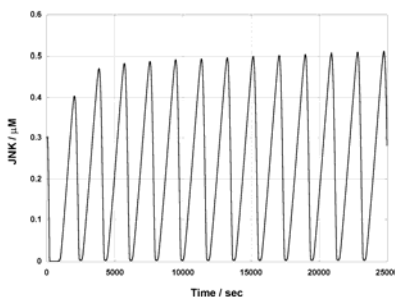


Fig. 4. Transient activation of JNK. Initial [ROS] is 0.3 μM

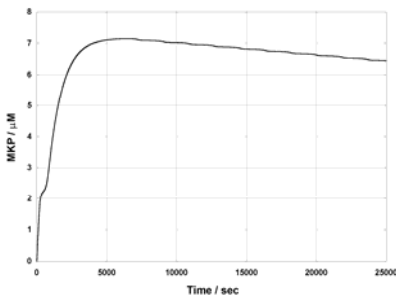


Fig. 5. [MKP] vs. time. Initial [ROS] is 10 μM

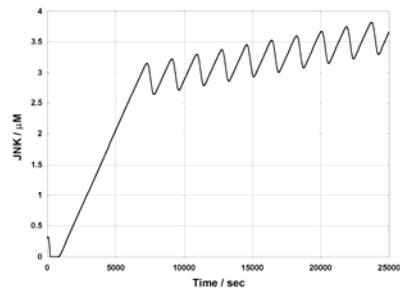


Fig. 6. Transient activation of JNK. Initial [ROS] is 10 μM

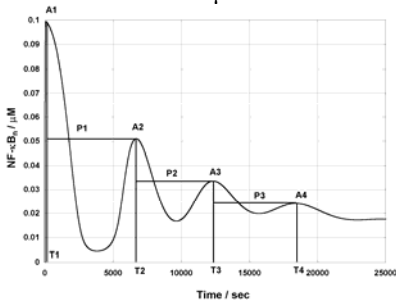


Fig. 7. Nuclear [NF- κB] vs. time for any initial [ROS]

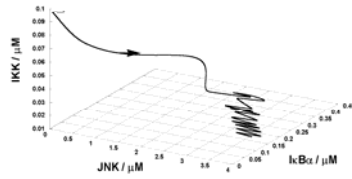


Fig. 8. Phase plane plot between [IKK], [I $\kappa\text{B}\alpha$] and [JNK]. Initial [ROS] is 10 μM

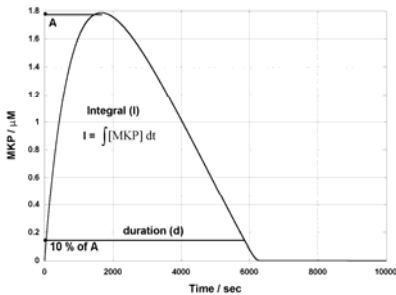


Fig. 9. [MKP] vs. time for sustained activation of JNK

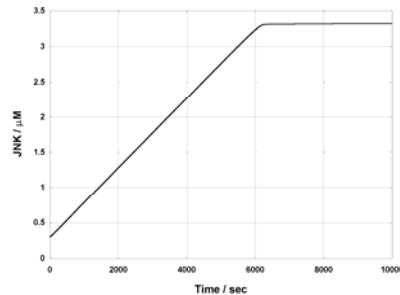


Fig. 10. Sustained activation of JNK. Initial [ROS] is 3 μM

References

- [1] P. M. Mitrasinovic, O. Mitrasinovic, GESTS Int'l Trans. Computer Science and Engr., 2006, **27**, 41-52.
- [2] H. Kamata, S. Honda, S. Maeda, L. Chang, H. Hirata, M. Karin, Cell, 2005, **120**, 649-661.
- [3] A. E. C. Ihekweba, D. S. Broomhead, R. L. Grimley, N. Benson, D. B. Kell, Systems Biology, 2004, **1**, 93-103.
- [4] B. N. Kholodenko, Eur. J. Biochem., 2000, **267**, 1583-1588.
- [5] P. Mendes, D. Kell, Bioinformatics, 1998, **14**, 869-883.

Electrochemistry

(E)

NEW ELECTRODE MATERIALS FOR VOLTAMMETRY AND AMPEROMETRY

Jiří Barek

Charles University in Prague, Department of Analytical Chemistry, UNESCO Laboratory of Environmental Electrochemistry., 128 43 Prague 2, Czech Republic (Barek@natur.cuni.cz)

Abstract

The application of new electrodes based either on non-toxic silver solid amalgam for voltammetric or amperometric determination of electrochemically reducible analytes or on boron doped diamond films for the determination of both reducible and oxidizable analytes will be discussed.

Introduction

The most important factor influencing the analytical parameters of voltammetric and amperometric determinations is the quality of the electrode, the electrode material playing the crucial role. Therefore, our research is oriented on systematic development of extremely sensitive electrochemical methods suitable for the determination of sub-micromolar concentrations of various biologically active organic compounds using different electrode materials and arrangements. Non-toxic and environmentally friendly silver solid amalgam electrode [1,2] is a suitable replacement of classical mercury electrodes, which are gradually phased-out because of unsubstantiated fears of mercury toxicity. Some examples on the use of these electrodes for the determination of micromolar and submicromolar concentrations of various pesticides, dyes and chemical carcinogens will be shown. Boron doped diamond film electrodes [3,4] are very promising electrode material for the determination of electrochemically reducible substances such as genotoxic nitrated polycyclic aromatic hydrocarbons or electrochemically oxidizable substances such as amino derivatives of polycyclic aromatic hydrocarbons.

Results and Discussion

Meniscus modified silver solid amalgam electrode (m-AgSAE) [1]

m-AgSAE consists of a drawn-out glass tube, the bore of which near the tip is filled with a fine silver powder, amalgamated by liquid mercury and connected to an electric contact (see Fig. 1). Afterwards, it is immersed into a small volume of liquid mercury and agitated for 15 seconds. Before starting the work, as well as after every pause longer than one hour the electrochemical activation of m-AgSAE should be carried out in 0.2 mol L^{-1} KCl at -2200 mV under stirring of the solution for 300 seconds followed by rinsing with distilled water. The m-AgSAE could be used for several weeks without major changes, only its amalgamation through mechanical contact with mercury is recommended to be repeated every week.

The pretreatment of m-AgSAE electrode is relatively simple and consists of three steps depending on the type of the electrode and the nature of the passivation.

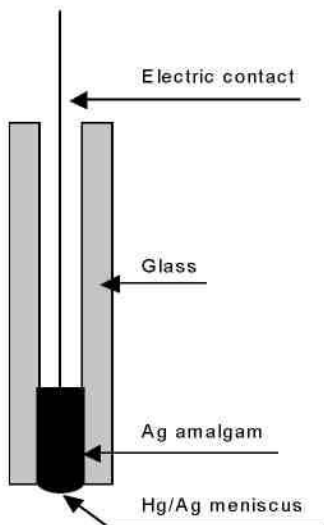


Fig. 1. Meniscus-modified silver solid amalgam electrode (m-AgSAE).

In the case of m-AgSAE the three steps are amalgamation, regeneration, and activation.

- Amalgamation is carried out once a week or when the performance of the electrode obviously deteriorates. The tip of freshly mechanically polished AgSAE is immersed into a small volume of liquid mercury and agitated for 15 seconds.
- Activation of m-AgSAE is carried out in 0.2 mol L^{-1} KCl without deaeration at -2.2 V in stirred solution for 300 seconds followed by rinsing with distilled water. The procedure is repeated after amalgamation, before starting the work after every pause longer than one hour or when the performance of the electrode deteriorates.
- Regeneration is carried out usually by periodical switching every 0.1 s between potentials 100 mV more negative than the potential of amalgam dissolution (E_{in}) and 100 mV more positive than the potential of hydrogen evolution (E_{fin}) in the used base electrolyte. Regeneration always ends at more negative potential. However, in cases of extremely severe passivation, the optimum values of E_{in} and E_{fin} must be found experimentally as the values leading to most stable signal values in repeated measurements. The appropriate values of the potential and the time of regeneration can be inserted in the program of the used computer-controlled instrumentation so that the regeneration of m-AgSAE is always carried out automatically.

The practical application of m-AgSAE can be demonstrated on the recently developed determination of submicromolar concentrations of genotoxic dinitronaphthalenes [5] (see Fig.2).

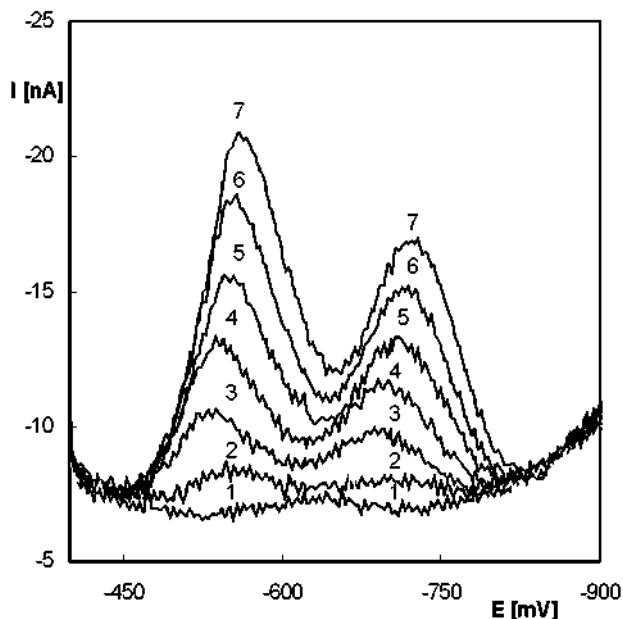


Fig. 2. DP voltammograms of 1,5-dinitronaphthalene (1,5-DNN) at m-AgSAE in MeOH-BR buffer (1:1) pH 10,4; $c(1,5\text{-DNN})$ ($\text{mol}\cdot\text{L}^{-1}$): (1) 0-base electrolyte; (2) $1\cdot 10^{-6}$; (3) $2\cdot 10^{-6}$; (4) $4\cdot 10^{-6}$; (5) $6\cdot 10^{-6}$; (6) $8\cdot 10^{-6}$; (7) $10\cdot 10^{-6}$; $E_{\text{in}} -100\text{mV}$; $E_{\text{fin}} -1800\text{mV}$

Another example is the determination of nitrated phenols [6] (see Fig.3). Several other recent applications of m-AgSAE for the determination of trace amounts of other biologically active organic substances will be given.

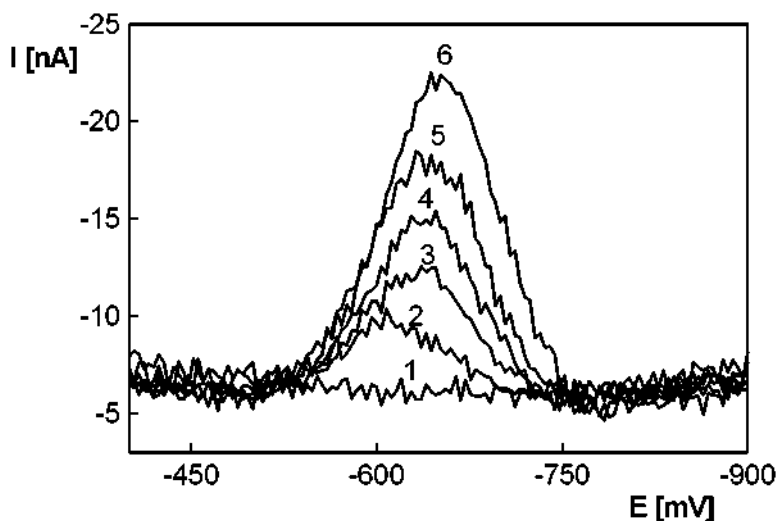


Fig. 3. DP voltammograms of 2-nitrophenol (2-NF) at m-AgSAE in Britton-Robinson buffer pH 8. $c(2\text{-NF})$: 0 (1); $2\cdot 10^{-6}$ (2); $4\cdot 10^{-6}$ (3); $6\cdot 10^{-6}$ (4); $8\cdot 10^{-6}$ (5); $1\cdot 10^{-5}$ (6) $\text{mol}\cdot\text{L}^{-1}$. $E_{\text{in}} = -100\text{mV}$; $E_{\text{fin}} = -1300\text{mV}$.

Boron doped diamond film electrode (BDDFE)

BDDFE consists of a Teflon body into which a boron doped microcrystalline film on a silica support is incorporated (see Fig. 4).

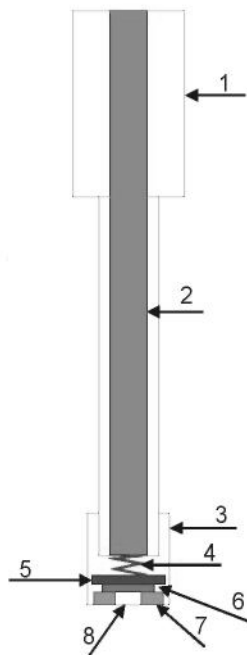


Fig. 4. Boron doped diamond film electrode

1. Electrode body
2. Screw contact
3. Screw attachment
4. Small metal spring
5. Brassy sheet
6. DFE on Si (1,1,1)
7. Silicone seal
8. Access for solution

The practical application of BDDFE can be demonstrated on the recently developed determination of submicromolar concentrations of genotoxic aminofluoranthene [7] (see Fig. 5).

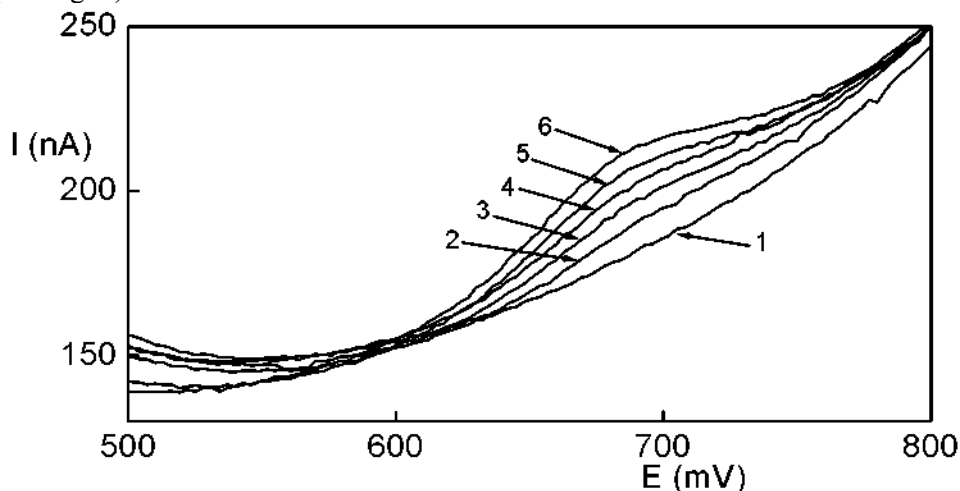


Fig. 5. DPV at BDDE 3-aminofluoranthene in MeOH-BR buffer (1:1), pH 4. c ($\mu\text{mol}\cdot\text{l}^{-1}$): 0 (1), 0.2 (2), 0.4 (3), 0.6 (4), 0.8 (5), 1.0 (6).

Conclusion

Both silver solid amalgam and boron doped diamond are very promising electrode materials. At the moment, many other applications of both silver solid amalgam electrodes and boron doped diamond film electrodes for the determination of trace amounts biologically active organic compounds both in batch analysis and in flowing systems are under development.

References

- [1] B. Yosypchuk, L. Novotná, Crit. Rev. Anal. Chem. , 2002, **32**, 141-151.
- [2] J. Barek, J. Fischer, T. Navrátil, K. Pecková, B. Yosipchuk, Sensors, 2006, **6**, 445-452.
- [3] V. Mocko, PhD Thesis. Charles University, Faculty of Science, Prague 2004.
- [4] A. E. Fischer, Y. Show, G.M. Swain, Anal. Chem., 2004, **76**, 2553-2560.
- [5] A. Daňhel, Diploma Thesis. Charles University, Faculty of Science, Prague 2006.
- [6] L. Vaňourková, Diploma Thesis. Charles University, Faculty of Science, Prague 2006.
- [7] K. Cizek, J. Barek, J. Zima, ChemZi, 2005, **1**, 127.

ELECTROCHEMISTRY OF VITAMIN B6 VITAMERS, THEIR DERIVATIVES AND METAL COMPLEXES

Lj. S. Jovanović

Department of Chemistry, Faculty of Sciences, 21000 Novi Sad, Serbia

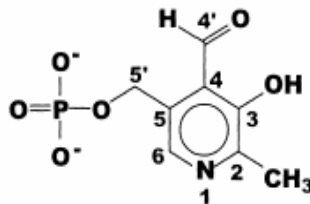
Abstract

The aim of this paper is to present the state of art in the electrochemistry of biologically important molecules such as vitamin B6 and the related substances, their derivatives and metal complexes. Since in the most of the enzyme catalysed reactions involving vitamin B6 vitamers pyridoxal 5'-phosphate acts as co-enzyme, it was the subject of a number of studies on chemical and redox reactions simulating some important biological processes. Rather complex chemical equilibria involving some other vitamers and their derivatives were the issue of electrochemical and spectrophotometric studies in aqueous and aprotic media with a special emphasis on the tautomeric and self-protonation reactions. Finally, some metal complexes of these and related substances, besides their potential biological activities, proved to be catalytically efficient in certain biochemically important redox reactions.

Introduction

Vitamin B6 consists of three related pyrimidine vitamer derivatives: pyridoxine (PO), pyridoxamine (PA) and pyridoxal (PL), the first two being its major constituents, and their phosphate esters (see below). The metabolically active coenzyme form of vitamin B6 is pyridoxal 5'-phosphate (PLP). B6 vitamers are first oxidized to pyridoxal, and rapidly phosphorylated to PLP in the liver. PLP is the main circulating form exported from the liver and it is considered the most relevant direct measure of vitamin B6 status.

4 = CH₂OH, 5' = OH (**PO**);
4 = CH₂NH₂, 5' = OH (**PA**);
4 = CHO, 5' = OH (**PL**);



PLP

These substances are well soluble in water and relatively stable in heat but not in light. Their chemistry, rich in proton and hydration involving equilibria, resulting in tautomeric forms of relative substances which additionally may be also susceptible to redox processes, has been the subject of numerous physicochemical studies on vitamin B6 vitamers [1], especially spectrophotometric ones. In addi-

tion, their proved biochemical and pharmacological significance was the main issue of a large number of investigations reported by now [1, 2]. Contrary to this, not very abundant electrochemical research data have been collected in studies performed either to describe important redox characteristics *per se* or, more often, to simulate some biochemically important processes. In addition, some reports on catalytic properties of PO have been published recently [3, 4].

Electrochemistry

PLP participates in transaminations, decarboxylations, racemizations, and numerous modifications of amino acids side-chains. The most important catalytic feature of the coenzyme is the electrophilic nitrogen of the pyridine ring, which acts as an electron sink, drawing electrons away from the amino acid and stabilizing a carbanion intermediate.

Electrochemistry of vitamin B6 vitamers has been investigated in several directions: first, to study their basic characteristics in aqueous solutions of a wide pH range [5-8]. These investigations were performed on the example of PL and PLP as the representatives of other relevant substances. Since some enzymatic reactions proceed after PLP was bound to enzymes in a hydrophobic pocket of protein, it was interesting to study its behaviour in aprotic or low polarity medium, such as: DMF and DMSO [7]. Another direction of the voltammetric investigations concerns the role in transamination processes which are simulated by the reaction of PL or PLP and hexylamine as a representative Schiff base [9,10]. Finally, there are some reports on reduction products of PLP [11] and 4-pyridoxic acid [12] as the final product of vitamin B6 catabolism. This very particular substance was the object of a study of electrooxidation of PL on a polycrystalline gold electrode [13].

First polarographic results on PL behaviour in aqueous media [5,6] showed the dependence of polarographic process on pH of the medium. Namely, both the values of $E_{1/2}$ (-0.87 V, pH 9) and the current intensity varied with pH (2-10) from residual value to practically $2e^-$ reaction. Since PLP under the same conditions behaves similarly, the authors [6] developed a polarographic procedure for simultaneous determination of both substances in their mixture. They found that the polarographic wave height for PLP does not alter with pH, so the decrease in current in acid solution (pH 2) (as compared to pH 9) was ascribed to PL. The other method was developed based on conversion of both substances to the corresponding oximes whose half-wave potentials differ sufficiently (by 80 mV) at pH 9.

The redox behaviour of PLP in aqueous and non-aqueous media (DMSO, water-DMF mixtures) was studied [7,8] at d.m.e. The main redox reaction is reduction of the aldehyde group in the overall conditions used. The total wave height corresponds to a two-electron process, which, depending on pH, can be carried out in 1-3 steps. In rather complex proton-involving equilibria in non-aqueous media a self-protonation effect was presumed. But, in a further study [8] the authors claimed the equilibria being even more complex. Namely, in acidic ethanolic solution PLP reduces in two one-electron steps, with the formation of an intermediate

which can dimerize, like the classical reduction mechanism of aromatic aldehydes and ketones. Evidence of the absence of phenolic group ionization was obtained.

In order to study a rather complicated mechanism of transamination reaction, simple models using Schiff bases were proposed, among them PL and/or PLP with hexylamine [9,10]. The bases formed in this way have similar behaviour but with some important differences. Thus, the polarographic total limiting current is pH-dependent for PL base, but not for the PLP one. The reason is fast dehydration reaction in PLP base which leads to unstable hydrated or hemiacetal forms. The whole process corresponds to a reversible two-electron transfer coupled with two or three protons. These results indicate the reduction of the protonated imine, in agreement with the general behaviour accepted for the electroreduction of a Schiff base [9].

Extension of the investigations of voltammetric behaviour of PLP Schiff base with hexylamine to aprotic media (DMF, methanol) and comparison with aqueous solutions resulted in a conclusion that ketoenamine is a dominant species in water and enolimine in DMF; methanol being intermediate situation with a ratio of approximately 3:1 in favour of the enolimine [10]. As in some other studies, a good support to the results of electrochemical investigations was obtained by the spectrophotometric method which served for identification of characteristic tautomeric forms either in solution or after the exhaustive electrolysis at specific reduction potentials. Since these equilibria involve protons, the presence of protonated electroactive centres in aprotic medium (DMF) is a direct proof that the Schiff base served as their source. Thus, once more self-protonation is supposed for the mechanisms postulated in DMF and partially in methanol.

Elimination of vitamin B6 metabolites *in vivo* proceeds through a mechanism not yet well understood. In order to contribute to its solution, electrochemical study of pyridoxic acid (PA) as the final product of vitamin B6 catabolism was performed, supported by spectroscopic characterization of the reduced products [12]. The 4-electron reduction of PA resulted in a two-component mixture of 2-methyl-3-hydroxy-pyridine derivatives (ratio 2:1). The results suggest an electroreduction involving hemiacetal ring cleavage in place of aldehyde group as an intermediate step in the four-electron process. This means a significant difference from the other activated monocarboxylic acids and may involve no formation of PL and PO. The formation of pyridoxal hydrate from PA by a two-electron transfer and its further transformation into hemiacetal seems to play an essential role at the electrode surface.

The investigation of transition metal complexes with Schiff bases derived from PL, amines and amino acids, has received much attention in view of their significance as models for a wide variety of biological reactions, catalyzed by enzymes, in which the PLP is an essential component. It has been shown that free PL, in the presence of polyvalent metal ions, can catalyze most of the known enzymatic reactions in which the PLP acts as a co-enzyme [14]. In order to explain the models of catalysis it seemed to be useful to study electrochemical characteristics of metal

complexes with Schiff-base ligands. However, the data on these investigations are scarce [2].

A detailed study of electrochemistry of the ligand N-[2-(3-ethylindole)] pyridoxalimine and its Mn(II), Mn(III), Ni(II) and Cu(II) complexes in DMSO at a Pt disc electrode has been published recently [15]. This NO bidentate ligand in a monoanionic form binds to a metal ion and forms several *bis*(ligand)complexes. The ligand alone was thoroughly studied in respect to its reduction and oxidation processes. The reduction proceeds *via* one-electron irreversible process ascribed to the imino-group electronation which is, as it is known for such reactions, followed by chemical complications. On the other hand, oxidation is carried out in two one-electron steps followed by irreversible chemical reactions, as is common with similar Schiff bases. The processes are supposed to involve monoanionic and neutral species, although their localization on the ligand moiety remain somewhat obscured. On the other hand, the redox processes of the complexes in this respect seem to be more clear. Generally, the complexes are reduced or oxidized in 1-3 peaks and the overall redox processes are connected with the M(III)/M(II) or M(II)/M(I) redox couples and the ligand. Although the processes alone are rich in chemical complications, some regularities were found, such as that the metal centered redox processes follow the order of the corresponding ionization potentials of the gaseous metal ions.

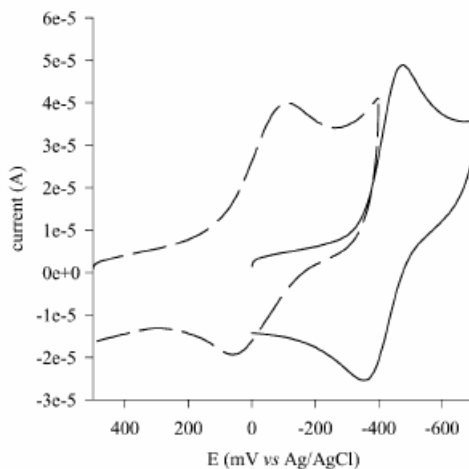


Fig. 1. Redox processes for $[\text{Fe}(\text{HIPH})_2]^+$ (pH 4, ---) and $[\text{Fe}(\text{IPH})(\text{HIPH})]$ (pH 9, —). Scan rate 400 mV s^{-1} ; $0.1 \text{ mol dm}^{-3} \text{ NaCl}$ [16].

Very efficient Fe chelators (aimed for treatments of Fe overload diseases) appeared to be diacylhydrazine ligands, among them those based on pyridoxal isonicotinoyl-hydrazone (PIH), luckily found as claimed by the authors [16]. The Fe(III) complexes with these ligands are electroactive and sensitive to pH (Fig. 1).

Redox process based on Fe(III)/Fe(II) couple is one-electron quasireversible as it is common with these metal ions. In the absence of Fe(III), the parent hydrazone ligand does not oxidize in aerobic aqueous solutions. But, a mixture of Fe(III) and HPCIH through putative $[\text{Fe}(\text{PCIH})_2]^+$ (not isolated) rapidly leads to $[\text{Fe}(\text{IPH})(\text{HIPH})]$ in which an intramolecular oxidation proceeds: the amino-ligand is oxidized in a dehydrogenation process on account of Fe(III) reduced to Fe(II). Finally, such reduced species in an electrochemical reaction is oxidized again to Fe(III) complex. A very good feature of this complex is its relatively low redox potential for Fe(III)/Fe(II) (-0.42 V vs. Ag/AgCl), which is pretty close to the reference potential (-0.60 V) for DFO complex (DFO - desferrioxamine, the most efficient Fe chelator for treating Fe overload diseases).

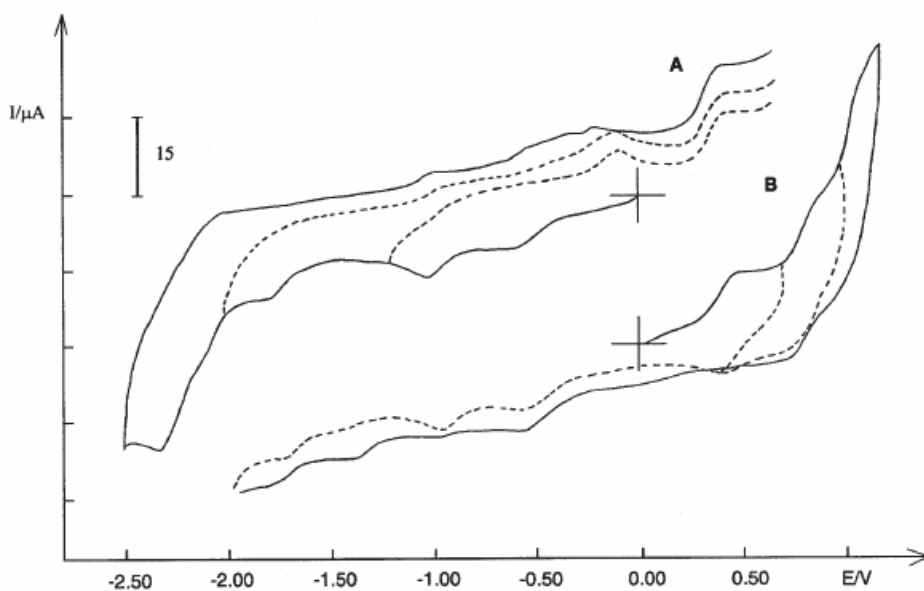


Fig. 2. Cyclic voltammograms for $[\text{Fe}(\text{HL})\text{L}]$ in 0.1 M TBAP: reduction (A) and oxidation (B) processes; scan rate 0.20 V s^{-1} [18].

Our recent papers on electrochemistry of Fe(III) complexes thiosemi-, semi- and isothiosemicarbazones [17,18] in DMF show their sensitivity on solution composition (i.e. supporting electrolyte, presence of acid/base, etc.). Several different-type complexes with some of the three ligands appear to be relatively unstable in solutions containing excess of Cl^- , especially the monoligand ones. In solutions of these complexes rapid ligand replacement occurs, leading to formation of $[\text{FeCl}_4]^-$, which easily reduces at -0.08 V (vs. SCE). The PL ligand reduction proceeds through one or two separated processes complicated with chemical reactions and usually adsorption [17]. However, more stable PL complexes with deprotonated ligands (HL^- , L^{2-}) result in a more complex electrochemical behaviour as can be

seen from Fig. 2 [18]. The first two one-electron reduction processes belong to Fe(III)-centered reactions, while the other three at more negative potentials are ligand-based. Similarly, the oxidation processes occur prevailingly at the ligand moieties. Both reduction and oxidation processes are followed with chemical complications, as can be seen from Fig. 2. Such a behaviour was observed previously at various Fe(III) complexes with several thiosemicarbazone-based ligands [19]. It should be point out the importance of these ligands and complexes is their potential biological activities but not only from the PL moiety. Namely, the thiosemicarbazone ligands alone are generally known by their antitumor, fungicidal, antiviral, antibacterial and antimicrobial activities [2,20,21].

Conclusion

In conclusion, the knowledge of electrochemical characteristics of vitamin B6 related compounds with their numerous complex chemical equilibria, proved to be a useful tool in the attempts to elucidate the mechanisms of a wide spectrum of enzymatic reactions, especially those in which PLP acts as co-enzyme.

References

- [1] D. Dolphin, R. Poulson, O. Avramovic (Eds.), Vitamin B6 pyridoxal phosphate. Chemical, Biochemical and Medical Aspects, Wiley, New York, 1986.
- [2] V.M. Leovac, V.S. Jevtović, Lj.S. Jovanović, G.A. Bogdanović, J. Serb. Chem. Soc., 2005, **70**, 393.
- [3] J.-M. Zen, J.-Ch. Chen, A. S. Kumar, Tamkang Journ. of Science and Engineer Engineering, 2002, **5**, 219.
- [4] Z. Cao, Q. Xie, M. Li, S. Yao, J. Electroanal. Chem., 2004, **568**, 343.
- [5] J. Volke, Z. physikal. Chem., (1958) 268.
- [6] O. Manousek, P. Zuman, J. Electroanal. Chem., 1960, **1**,324.
- [7] J. Llor, E.Lopez-Cantarero, M. Cortijo, Bioelectrochem.Bioenerg.,1978, **5**, 276.
- [8] R.Izquierdo, M. Blázquez, M. Dominguez, F.G. Blanco, Bioelectrochem. Bioenerg., 1984, **12**, 25.
- [9] T. Pineda, J.M. Sevilla, M. Blázquez, J. Electroanal. Chem., 1991, **304**, 53.
- [10] J.M. Sevilla, G. Cambron, T. Pineda, M. Blázquez, J. Electroanal. Chem. 1995, **381**, 179.
- [11] J.M. Sevilla, T. Pineda, A.J. Román, M. Blázquez, J.Electroanal. Chem., 1997, **428**, 91.
- [12] T. Pineda, M.I. Lopez-Cozar, J.M. Sevilla, M. Blázquez, J.Electroanal. Chem., 1996, **403**, 101.
- [13] T.Pineda, J.M. Sevilla, A.J. Román, M. Blázquez, J. Electroanal. Chem., 2000, **492**, 38.
- [14] E.H. Abott, A.E. Martell, J. Am. Chem. Soc., 1970, **92**, 5845.
- [15] P. Gilli, M.G. Martin Reyes, P. Martin Zarza, M.F.C. Guedes da Silva, Y.-Y. Tong, A.J.L. Pombeiro, Inorg. Chim. Acta, 1997, **255**, 279.
- [16] P.V. Bernhardt, P. Chin, D.R. Richardson, J. Biol. Inorg. Chem., 2001, **6**, 801.
- [17] V.S. Jevtović, Lj S. Jovanović, V.M. Leovac, L.J. Bjelica, J. Serb. Chem. Soc. 2003, **68**, 929.
- [18] Lj.S. Jovanović, V.S. Jevtović, V.M. Leovac, L.J. Bjelica, J. Serb. Chem.Soc. 2005, **70**, 187.
- [19] Lj. Jovanović, Ph.D. thesis, Faculty of Sciences, University of Novi Sad,1986.
- [20] H. Beraldo, D. Gambino, Mini Rev. Med. Chem., 2004, **4**, 159.
- [21] H. Beraldo, Quim. Nova, 2004, **27**, 461.

ZINC-POLYANILINE BATTERIES BASED ON CHLORIDE/CITRATE ELECTROLYTES

B. N. Grgur

Faculty of Technology and Metallurgy, Karnegijeva 4, Belgrade, Serbia

Abstract

Electrochemical behavior of zinc and polyaniline (PANI) electrode polymerized from 0.1 M HCl and 0.1 M aniline on graphite electrode, in 0.2 M ZnCl₂ and 0.50 M NH₄Cl (chloride electrolyte) and with addition of 0.33 M Na-citrate (chloride/citrate electrolyte) were investigated. In the chloride/citrate comparing with chloride containing electrolyte for the zinc electrode negative shift of the open circuit potential of 150 mV, decreases of exchange current density for more than order of magnitude and increase of cathodic Tafel slope, due to the zinc ions complexation, were observed. In citrate/chloride electrolyte zinc dendrite formation were completely suppressed. PANI electrodes show better discharge characteristic in chloride/citrate electrolyte with determined maximum discharge capacity of 164 mAh g⁻¹.

Introduction

Zinc-polyaniline (PANI) secondary cells have some advantages, in comparison with classical battery types (Cd|NiOOH, Pb|PbO₂, Zn|Ag₂O, MH|NiOOH) and aprotic cells (Li|C and Li|polymer). First advantage is ecological acceptability comparing with Cd|NiOOH or Pb|PbO₂, second is relatively low price (Zn|Ag₂O and MH|NiOOH), and third is uses of water based electrolytes (mainly ammonium chloride + zinc chloride) [1], that makes such cells much easier to manufacture than Li based one.

Up to now zinc-PANI batteries has not been commercialized from few main reasons. First reason is degradation process of PANI at potentials more positive than ~0.5 V [2, 3], and second is zinc passivation, which is possibly related to the formation of the solid phases ZnCl₂·3NH₄Cl and ZnCl₂·2NH₄Cl on the anode surface [4]. On the other hand, in chloride containing electrolytes Zn electrodes form dendrites during charge-discharge cycles [5, 6]. It results in decreased coulombic efficiency of batteries and charge life. Main reason for that are sort circuit provoked by penetration of dendrites through separator to cathode or formation of the anodic slime.

It is well known that some organic anions can form complexes with the metal ions, that results much better quality of the metal deposits and suppress dendrite formation [7]. Probably, the best choice will be oxalic anions, due to the small ionic radius, good PANI doping-dedoping characteristics, etc [8]. Unfortunately, zinc oxalate is an insoluble salt.

So, in this paper we investigated behavior of zinc and PANI electrodes in chloride containing electrolytes with addition of citrate anions, which at pH~5 form an soluble zinc citrate [ZnCit]⁻ complex with pK_s value of 4.8.

Experimental

Polyaniline was obtained from hydrochloric acid solution (0.1 M) with addition of 0.1 M aniline monomer (p.a. Merck, distilled in argon atmosphere), at constant current density of 1 mA cm^{-2} on graphite electrode. Electrolytes containing 0.5 M NH_4Cl , 0.20 M ZnCl_2 and with addition of 0.33 M Na-citrate were prepared from p.a. grade chemicals (Merck) and bidistilled water. For all experiments three compartment electrochemical cell, with platinum foil ($S=2 \text{ cm}^2$) as a counter and saturated calomel electrode as a reference electrode at room temperature was used.

The working electrodes, graphite ($S=0.64 \text{ cm}^2$) and zinc ($S=2 \text{ cm}^2$), were mechanically polished with fine emery papers (2/0, 3/0 and 4/0, respectively) and then with polishing alumina of $1 \mu\text{m}$ (Banner Scientific Ltd.) on the polishing cloths (Buehler Ltd.). After mechanical polishing the traces of polishing alumina were removed from the electrode surface in an ultra-sonic bath during 5 min. The electrochemical measurements were carried using a PAR 273A potentiostat controlled by a computer through a GPBI PC2A interface.

Results and discussion

On Fig. 1. comparison of zinc deposition-dissolution on graphite electrode from chloride and chloride/citrate containing electrolytes are shown. As it can be seen from chloride electrolyte, deposition processes starts at potentials around -1 V , thought one well defined peak, at -1.17 V , after at potentials more negative than -1.4 V proceed simultaneous zinc deposition and hydrogen evolution reactions. In anodic direction, zinc dissolution occurs at potentials more positive than -1 V through one peak and one shoulder. In citrate/chloride electrolyte deposition-dissolution reaction is shifted for $\sim 0.15 \text{ V}$ in negative direction and diffusion limited peak is two times smaller, than in chloride electrolytes. This behavior could be explained by zinc ions complexation and lowering of the free zinc ions activity, as well as diffusivity of zinc citrate complex comparing with chloride electrolyte.

Slow potentiodynamic ($v=1 \text{ mV s}^{-1}$) polarization curves in chloride and chloride/citrate electrolyte on solid zinc electrode are shown on Fig. 2. Open circuit potential, E_{ocp} , of zinc electrode in chloride electrolyte where -0.997 V which was $\sim 130 \text{ mV}$ more positive than in chloride/citrate electrolyte, $E_{\text{ocp}} = -1.125 \text{ V}$. In ideal case without corrosion, E_{ocp} can be attributed to reversible electrode potentials.

Determined Tafel slopes for the chloride electrolyte were $\pm 33 \text{ mV dec}^{-1}$, and exchange current density, extrapolated from intercept of Tafel lines with open circuit potentials was 1.02 mA cm^{-2} . Those kinetic parameters suggest diffusion control of deposition and dissolution reaction. In the chloride/citrate electrolyte anodic Tafel slope was 33 mV dec^{-1} , while cathodic Tafel slope was -30 mV dec^{-1} , at low current densities and not well define slope of -125 mV dec^{-1} at high current density, respectively. Determined exchange current density of 0.076 mA cm^{-2} , was more than one order of magnitude smaller than in chloride electrolyte. Hence, it should be expected that in chloride/citrate electrolyte corrosion of zinc electrode should be smaller than in chloride electrolyte.

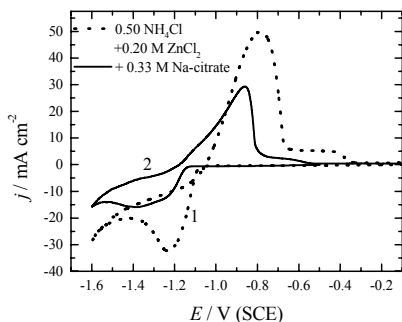


Fig. 1. Cyclic voltammograms of graphite electrode in 1) 0.50 M NH_4Cl + 0.20 M ZnCl_2 and 2) with addition of 0.33 M Na-citrate. Sweep rate 20 mV s^{-1} .

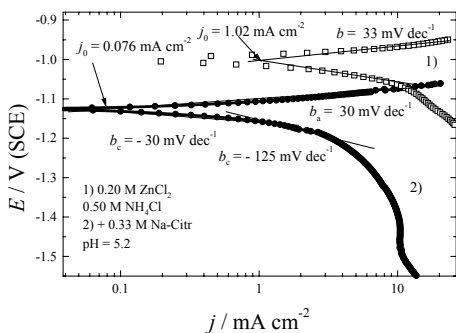


Fig. 2. Slow potentiostatic polarization curve ($v=1 \text{ mV s}^{-1}$) in chloride (1) and chloride/citrate (2) containing solution on solid zinc electrode.

In Fig. 3 micrographs of zinc deposits obtained from chloride and chloride/citrate electrolytes at a constant current density of 3.5 mA cm^{-2} and with deposition charges of $10.5 \text{ mA h cm}^{-2}$ are shown.

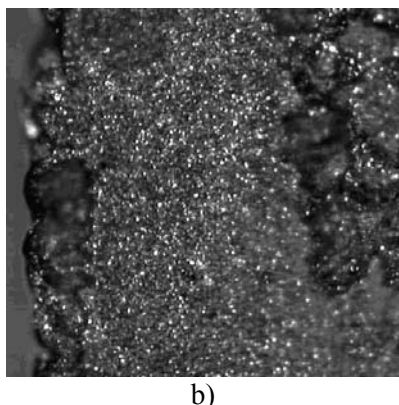
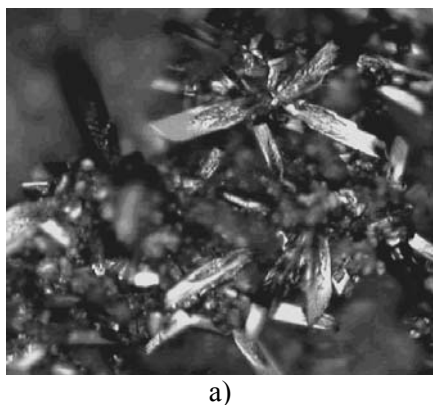


Fig. 3. Micrographs of the zinc deposits from a) 0.20 M ZnCl_2 + 0.50 M NH_4Cl and b) with addition of 0.33 M Na-citrate. Deposition current density 3.5 mA cm^{-2} , deposition time 3 h, magnification 200 x.

In chloride electrolyte, Fig. 3a, obtained deposits are practically completely dendritic, so potential risk of fast dendrite growth through separator, during the longer charging times, and formation of short circuits with cathode is permanently present. On the other hand in chloride/citrate electrolyte, Fig. 3b, deposit is smooth without irregularities even in the edges where local current density due to the current distribution phenomena is higher than at the central surface. Such differences can be explained in the following way.

The classical expression for the steady state nucleation rate, J , is given by [7]:

$$J = K_1 \exp\left(\frac{K_2}{\eta^2}\right) \quad (1)$$

where K_1 and K_2 are overpotential, η , ($\eta = E - E_{ocp}$) independent constants. Equation (1) is valid for a number of systems regardless of the value of the exchange current density for the deposition process. At one and the same deposition current density, j , decreasing j_0 leads to an increasing nucleation rate and decreasing nucleation exclusion zones radii [7]. The saturation nucleus density, i.e., the exchange current density of the deposition process, strongly affects the morphology of metal deposits. At high exchange current densities, the radii of the screening zones are large and the saturation nucleus density is low. This permits the formation of large, well-defined crystal grains and granular (dendrite) growth of the deposit. At low exchange current densities, the screening zones radii are low, or equal to zero, the nucleation rate is large and a smooth surface film can be easily formed.

The overpotential and the current density in activation-controlled deposition inside the Tafel region are related by:

$$\eta = \frac{b_c}{2.3} \ln \frac{j}{j_0} \quad (2)$$

Therefore, increasing b_c and decreasing j_0 leads to an increase in the deposition overpotential at the constant current density. It follows from all available data that the former effect is more pronounced resulting in deposits with a finer grain size with decreasing value of the exchange current density.

This analysis explain differences in deposit morphology for chloride and chloride/citrate electrolytes taking into account that Tafel slopes are -35 and -108 mV dec⁻¹, and exchange current densities are 0.38 and 0.027 mA cm⁻², respectively. Hence, in chloride electrolyte at 3.5 mA cm⁻² deposition overpotential is only -30 V, while in chloride/citrate electrolyte is -220 mV.

Insert of Fig. 4. shows the galvanostatic curve for polymerization of aniline from solution containing 0.10 M HCl and 0.10 M aniline monomer on graphite electrode at current density of 1 mA cm⁻² with polymerization charge of 0.3 mA h cm⁻². Polymerization starts at potential of 0.75 V and proceed in the potential range between 0.75 and 0.7 V. After polymerization, electrode was washed with bidistilled water and transferred in the three compartment electrochemical cell with chloride or chloride/citrate electrolyte. After transfer, electrode was conditioned at potential of -0.8 V for 600 s and cyclic voltammograms in the potential range between -0.8 and 0.4 V were taken as shown in Fig. 4. In anodic direction doping of the anions occur at potentials more positive than -0.2 V, with pronounced peak at 0.15 V. In cathodic direction dedoping of anions occur through one shoulder in the potential range of 0.4 to 0.05 V and one well defined peak with the maximum at -0.1 V. Dedoping of anions is finished at po-

tentials of -0.4 V. Small differences in the shapes of cyclic voltammograms between chloride and chloride/citrate electrolytes, could indicate that only chloride anions are involved in doping/dedoping reaction.

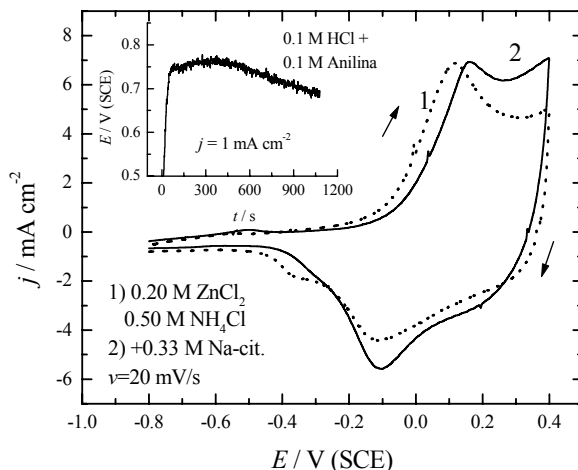
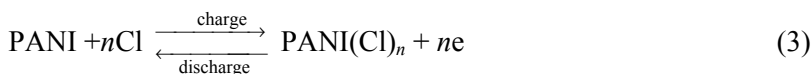


Fig. 4. Cyclic voltammograms of PANI electrode in 1) chloride and 2) chloride/citrate electrolyte ($v=20$ mV s^{-1}). Insert: galvanostatic curve for aniline polymerization from 0.1 M HCl and 0.1 M aniline at 1 mA cm^{-2} on graphite electrode.

Figure 5. shows charge-discharge curves in chloride and chloride/citrate electrolytes at current density of 0.25 mA cm^{-2} . Charging curves in both solutions are practically identical, but discharging curve in chloride/citrate solution have higher discharge potentials and longer discharge time. Up to now we do not have explanation for that kind of behavior.

Dependences of the potential for different charge/discharge current density for PANI electrode in chloride/citrate electrolyte are shown on Fig. 6. Charging/discharging reaction, assuming that only chloride anions are involved, can be given with following scheme [9]:



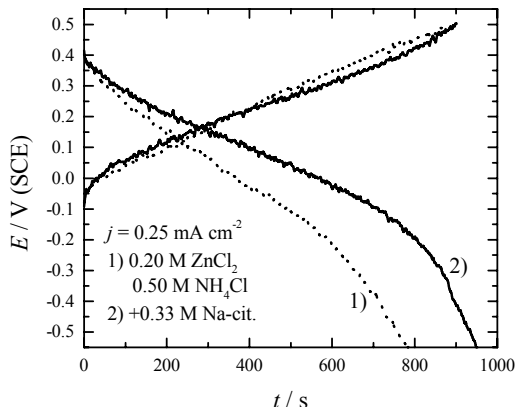


Fig.5. Charge-discharge curve for 1) chloride and 2) chloride/citrate electrolyte at current density of 0.25 mA cm^{-2} .

Charging reaction occur in the potential range between 0 and 0.5 V (upper potential limit is taken to avoid degradation of PANI film) with constant increase of the potential. Discharge of the electrode occurs in the potential region between 0.35 and ~ -0.2 V with average discharge potential of ~ 0.15 V. After potentials more negative than -0.2 V diffusion limitations provoke the sharp decrease of the potential. Tacking into account that average discharge potential for zinc electrode is ~ -1.1 V, it can be calculated that average discharge voltage for the zinc-PANI cell with chloride/citrate electrolyte will be 1.25 V. This value is higher than open circuit potentials for Cd|NiOOH or MH|NiOOH cells, and comparable with alkaline Zn|MnO₂ cell.

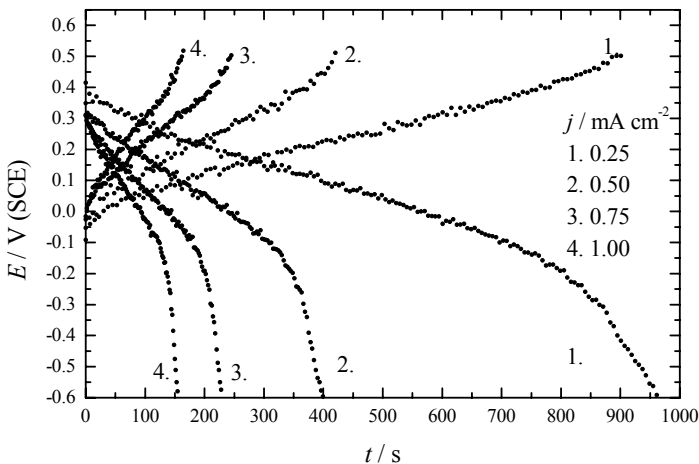


Fig. 6. Dependencies of the potential for different charge/discharge current density in chloride/citrate electrolyte for PANI electrode.

Charging/discharging characteristics of PANI film electrode are affected with applied current density, mainly because chloride anions diffusion limitation through

PANI film. On Fig. 7 dependence of capacity during discharge processes for different discharging current densities are shown.

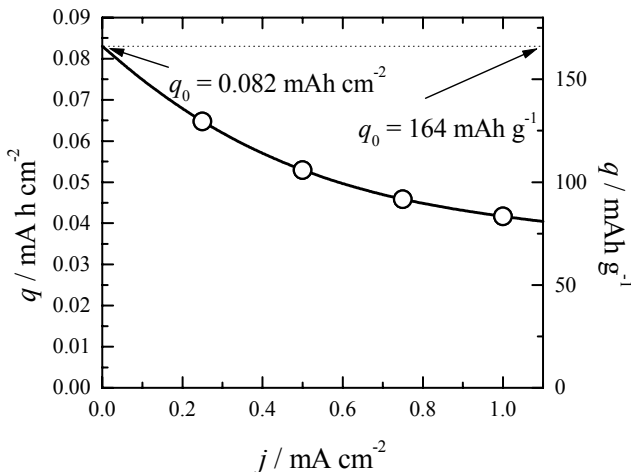


Fig. 7. Dependence of charge (left) and specific charge (right) at different discharge current density for PANI electrode in chloride/citrate electrolyte.

Discharge capacity increase with decreasing applied current density and for the limiting case when $j_d \rightarrow 0$, discharge capacity has a value of $0.082 \text{ mA h cm}^{-2}$.

Assuming the 100% current efficiency during the polymerization of aniline and using the equations [10, 11]:

$$m = \frac{jt(M_m + yM_a)}{(2 + y)F} \tag{4}$$

where m is the mass of the polyaniline polymerized with current density j during the time, t , M_m and M_a are molar mass of aniline monomer and inserted, chlorine, anions, and $y = 0.5$ is doping degree for emeraldine salt, it could be calculated that mass of the PANI on graphite electrode was approximately 0.5 mg. Hence, for the limiting case with discharge capacity of $0.082 \text{ mA h cm}^{-2}$ specific discharge capacity could be estimate on 165 mAh g^{-1} . In the range of investigated current densities of 0.25 to 1 mA cm^{-2} , specific discharge capacity was in the range of 130 to 85 mAh g^{-1} , respectively.

Acknowledgment

This work is financially supported by the Ministry of Science and Environmental protection, Republic of Serbia, contract No. 142044.

References

[1] M. Sima a, T. Visan b, M. Buda, J. Pow. Sourc., 1995, **56**, 133-136.
 [2] Arsov LD, Plieth W, Kossmehl G., J. Solid State Electrochem., 1998 **6**, 355-.

-
- [3] H. N. Dinh, J. Ding, S.J. Xia, V. I. Birss, *J. Electroanal. Chem.*, 1998, **459**, 45-56.
- [4] M.S. Rahmanifar, M.F. Mousavi, M. Shamsipur, M. Ghaemia, *J. Pow. Sources.*, 2004, **132**, 296-301.
- [5] J. Kan, H. Xue, S. Mu . *J. Pow. Sources.* 1998, **74**, 113-116.
- [6] G. Mengoli, M.M. Musiani, D. Pletcher, S. Valcher, *J. Appl. Electrochem.*, 1987, **17**, 525-531.
- [7] K. I. Popov, S. S. Djokić, B. N. Grgur, *Fundamental Aspects of Electrometallurgy*, Kluwer Academic/Plenum Publishers, New York, 2002.
- [8] E. Erdem, M. Saçak, M. Karakişla, *Polymer International*, 1996, **39**, 153-159.
- [9] A. Mirmohseni, R. Solhjo, *European Polymer Journal*, 2003, **39**, 219-223.
- [10] J. Kankare, in: D. Wise, G.E. Wnek, D.J. Trantolo, T.M. Cooper, J.D. Gresser (Eds.), *Electrical and Optical Polymer Systems: Fundamentals, Methods, and Applications*, Marcel Dekker, New York, 1998, Ch.6.
- [12] M.M. Popović, B.N. Grgur, *Synthetic Metals*, 1996, **143**, 191-195.

INTERFACING SURFACE CATALYSIS AND ELECTROCATALYSIS FOR THE SUCCESSFUL IMPLEMENTATION OF PEM FUEL CELLS: THE CASE OF PtMo CATALYSTS

G. Papakonstantinou¹, K.S. Nagabhushana², H. Bönnemann²,
M.M. Jakšić¹ and S.G. Neophytides¹

¹*Foundation of Research and Technology Hellas, Institute of Chemical Engineering and High Temperature Processes, FORTH-ICE/HT, PO Box 1414, GR-26504 Rion, Achaïas, Patras, Greece*
²*Max-Planck Institut für kohlenforschung, Kaiser-Wilhelm Platz-1, Mülheim an der Ruhr, Germany*

Abstract

In present study, Pt₄-Mo supported on C electrocatalyst was prepared by a colloidal nanoparticles synthesis route. PtCl₂ and Mo₂(OAc)₄ were the metal precursors and trimethylaluminum was used as reducing agent and stabilizer. The catalyst's chemical state was characterized ex situ in UHV conditions by XPS, while the electrocatalytic testing was performed in a single and half-cell arrangement, with the electrocatalyst being interfaced with NAFION 115 membrane. CO adsorption and oxidation experiments were conducted under He and H₂ atmospheres, followed by cyclic voltammetry under He flow.

It was found that Mo is present on the catalyst's surface in oxide form and in intimate contact with Pt, while a possible formation of solid solution could not be excluded. Thus, Mo not only modifies the electronic properties of the Pt, leading to suppression of the CO coverage on the Pt surface, but also enhances the CO oxidation in the potential window where a PEMFC anode is operating. This is true when Mo is in the oxy-hydroxide form with an oxidation state lower than +VI, thus promoting the CO oxidation, even under open-circuit conditions, through the water gas shift catalytic reaction, while CO electrooxidation takes place even at cell potentials very close to zero vs. RHE. At potentials higher than 0.2V vs. RHE, MoO₃ is the main chemical state, which is inactive for CO oxidation, and the electrocatalyst functions like monometallic Pt. In this respect the stability of the aforementioned lower oxidation state of Mo is the main prerequisite for the high CO tolerance of the PtMo anodes.

Introduction

Electrocatalysis plays a major role for the successful implementation of the fuel cell technology, towards an alternative, renewable and environmentally friendly energy production.

It is well known that the use of Pt as electrocatalyst in low temperature PEM Fuel Cells gives rise to a major problem. The Pt metal surface is easily poisoned by trace amounts of CO [1]. Binary (alloys or segregated metal particles) Pt-M catalysts (with M=Ru, Sn, Re, Rh and Mo) have received considerable attention as promising catalysts to increase the efficiency of CO oxidation on Pt [2]. Besides, the most important issues in contemporary fuel cell electrocatalysis are related to developing a material

that either oxidizes CO or that adsorbs a limited amount of CO while still being capable of oxidizing hydrogen at an acceptable rate.

Among the Pt-M binary systems Pt-Ru has been studied in the greatest detail, as this is still one of the most stable and active CO tolerant catalyst under practical conditions. The origin of the role of Ru is not yet completely understood, however it is now widely accepted that the mechanism by which CO is removed from the PtRu surface is the so-called “bifunctional mechanism” [3,4] or “Ligand effect” where M is influencing the Pt-CO bonding [5,6].

Molybdenum seems to be one of these potentially interesting additives since it is inexpensive and largely available. Furthermore recent experimental and theoretical studies suggested that Pt-Mo could be a better catalyst for CO oxidation than Pt-Ru [7,8,9].

In the present communication the electrocatalytic oxidation of CO on Pt₄Mo/C will be presented and discussed and by the use of combined FTIR-TPD experiments the chemisorptive features of CO and the catalytic reactivity of PtMo for the CO oxidation will be presented.

Experimental

Preparation methods

Pt-Mo/TiO₂ catalysts were prepared via wet impregnation of Pt and MoO₂ acetylacetonates (Aldrich Chem. Co) on TiO₂, anatase (Hombikat Sachtleben; surface area = 200 m²/g). The preparation procedure is described in detail in [10].

The Pt₄Mo/C catalyst was generated from the trialkylaluminum reductive stabilizer route as a bulk composition. In a 1L two neck round bottom flask fitted with a vacuum adapter and a dropping funnel, 1.57 g of PtCl₂, 0.22 g of Mo₂(OAc)₄ dispersed in 500 ml of toluene were placed with heavy stirring under argon atmosphere. To this well stirred solution, 2.5 ml of trimethylaluminum in 25 ml of toluene was dripped over 2 hours and the resulting solution was stirred overnight. The yellow solution had turned into a black solution and there were no visible precipitates. To this solution, 3.0 g of Vulcan XC 72 was added at once and stirred overnight, solvent evaporated, digested the precipitate with 150 ml of 0.1 M NaOH solution at 80° for 3 hours. The solution was allowed to stand, supernatant drained, washed with 2X100 ml of UHQ water, conditioned at 250°C using Ar, O₂/Ar, H₂. The Pt₄Mo loading was 20wt% on Vulcan carbon.

Electrocatalytic experiment

The Pt₄Mo/C catalyst was formulated into Gas diffusion electrode so that the Pt loading on the electrode was 0.3 mg/cm².

Electrocatalytic measurements were performed in a homemade PEMFC of 4 cm² geometric surface area. The cell was constructed so that single and half-cell polarization measurements could be carried out.

The reaction gases were analysed on line by means of gas chromatography (GC) CP 3800 and mass spectrometry (QMS) OMNISTAR in order to monitor the composition of the reactor outlet. For the half-cell polarization measurements 10%H₂/He flow

was fed in the counter and reference electrodes' compartment. The electrochemical measurements were carried out using an EG&G 263A potentiostat/galvanostat in communication with a PC using Powersuite software for the data acquisition/control. Potentiodynamic measurements were carried out under CO/He gas mixtures ranging from 100-6000ppm CO.

Temperature Programmed DRIFTS Studies

Diffuse reflectance infrared Fourier transform spectroscopy (DRIFTS) measurements were performed in a Bruker (Equinox 55) FTIR spectrometer. The powdered catalysts were placed on the sample holder of a small internal volume ($\sim 2 \text{ cm}^3$) homemade diffuse reflectance IR cell reactor sealed with ZnSe window. The cell allowed continuous gas flow through the catalyst bed during spectra acquisition while the sample could be heated linearly up to 673 K with a ramp rate of 60 degrees/min. The detailed experimental procedure is describe elsewhere [**Error! Bookmark not defined.**].

Results and Discussion

Electrocatalytic measurements of MoPt/C electrocatalysts

The effect of CO on the electrocatalytic activity of the MoPt/C electrode has been studied under continuous CO/He flow. Prior to CO exposure the electrode was treated at constant voltage equal to 0 V under He flow. Figs 1a and 1b depict the continuous CO flow experiment, where CO/He mixture containing 220ppm CO was fed to the anode. The CO and CO₂ molar fractions were recorded by the QMS. Two clearly distinguished CO oxidation regions are observed at low (labeled as I in Fig. 1) and high potential (labeled as II in Fig. 1) regions. It is worth noticing that in region I CO starts being oxidized at electrode voltage very close to 0V with rate maximum located around 0.22V while the CO oxidation rate is on the same order of magnitude with the corresponding CO oxidation in region II indicating that the two regions exhibit comparable reactivity. By scanning the voltage from 0.8V towards 0V surprisingly we observe that the CO oxidation rate in region I completely vanishes and the catalyst continues to be completely inactive even during the second cycle while region II shows repeatedly the same behavior (Fig. 1b).

Although region I was completely deactivated the exposure of the electrode under He flow at 0 V resulted in the regeneration of the Pt₄Mo/C electrocatalyst. It is worth noticing that the catalyst could not be regenerated under CO/He flow.

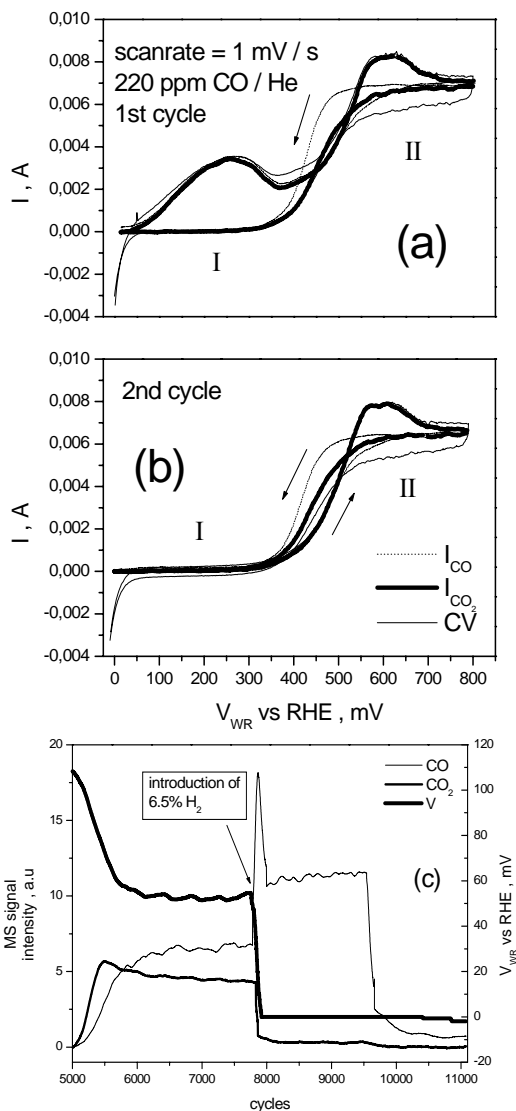


Fig. 1. Cyclic voltamograms (1mV/s) and Mass spectrometry under 220ppm CO/He flow at 60 °C in a three electrode PEM electrochemical reactor. Reference and Counter electrodes are exposed in 5% H₂/He mixture. (a) first cycle, (b) second cycle. (c) catalytic conversion of CO into CO₂ on Pt₄Mo/C under OC at 250 ppm CO/ He (dry) and subsequent H₂ introduction. The signals of CO and CO₂ correspond to arbitrary values recorder by mass spectrometer.

According to the above experimental observations the most attractive feature of the Pt₄Mo/C electrocatalyst is its ability to oxidize CO at voltages very close to the H₂ oxidation voltage. However, the low voltage active sites (region I of Fig. 1) are not stable at more positive potentials, becoming completely inactive at voltages higher

than 0.3-0.4V. This can be attributed to the oxidation of the Mo^{x+} ($x=4$ and 5) species into MoO_3 according to reaction (1) [11]:



The ability of the reduced Mo^{x+} to activate CO oxidation, at electrode voltages as low as 0.05V, should be related to its enhanced catalytic and electrocatalytic activity to activate the dissociation of water. This is also confirmed by the spontaneous catalytic CO_2 formation upon introduction of CO/He/ H_2O mixture over the catalyst just after the reduction/reactivation of the electrode (Fig. 1c). Upon introduction of gaseous H_2 or negative current application (not shown), thus implying H_2 production, CO_2 formation rate is inhibited.

Combined FTIR and Temperature programmed desorption of CO under He and H_2 flow on PtMo/TiO₂

Similar conclusions have been derived by carrying out combined FTIR-TPD experiments on MoPt/TiO₂ catalyst. In the case of monometallic Pt catalyst CO coverage goes through a maximum at 360 K and declines monotonically thereafter approaching zero at 500 K. The derivative of the CO coverage curve represents simulated temperature programmed desorption curves. Following this procedure the maximum CO_L desorption rate on Pt/TiO₂ is located at 420 K (see inset of Fig. 2a). On the other hand, Pt-Mo/TiO₂ catalysts exhibit significantly different curve profiles, which correspond to a much faster CO_L depletion rate. In particular the CO_L area decreases steadily without exhibiting any initial increasing stage or any inflection point, while complete desorption of CO is observed already at 370 K.

The exposure of CO_L adsorbed species in H_2 affects its desorption temperature. The evolution of the relative CO_L coverage upon sample annealing with 20 K/min under hydrogen flow is depicted in Fig. 2b. CO_L species desorbs at higher temperatures than the Pt/TiO₂ sample followed by Pt-Mo/TiO₂ and Pt₄-Mo/TiO₂ respectively. The maximum desorption rates of the CO_L species, being proportional to the derivative of $1-I_{\text{rel}}$ with respect to temperature (similar to the inset in Fig. 1b), are located at 460 K, 412 ± 5 K and 390 ± 5 K for the Pt/TiO₂, Pt-Mo/TiO₂ and Pt₄-Mo/TiO₂ samples respectively.

By comparing Figs 2a and 2b, i.e. TPD experiments under He and H_2 flows it is easily concluded that CO desorbs in all cases at higher temperatures under H_2 flow than under He flow. In the case of Pt_x-Mo catalysts the effect of hydrogen is significantly more prominent.

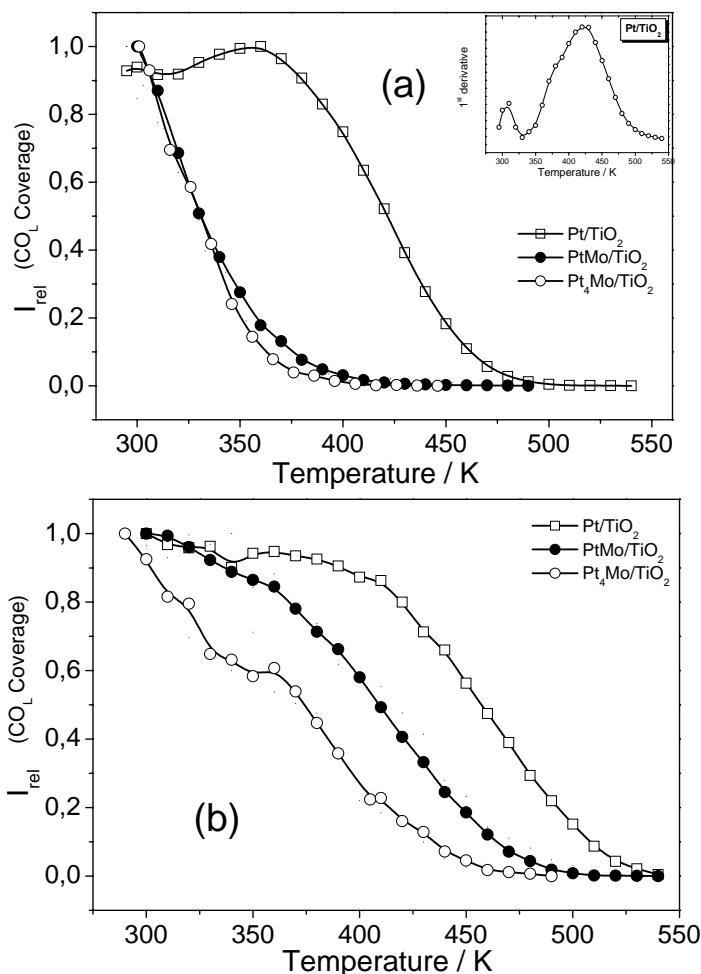


Fig. 2. Combined TPD-FTIR experiments on various Pt_x/Mo samples. (a) under He flow, (b) under H₂ flow. Initially the sample was exposed to 7% CO/He for 30 min and then annealing was carried out under He flow over the catalyst. Inset : The peak area derivative of Pt/TiO₂ TPD curve.

Several researchers in the past proposed that the promoting role of Mo on Pt for its high CO tolerance is due to its oxygenic nature which especially in the form of MoO(OH)₃ can easily supply OH species which can readily oxidize CO adsorbed species on Pt [7,12,13]. Based on this conclusion it is quite reasonable to assume that the complete depletion of CO_L species even below 370 K for the case of Pt_x-Mo samples (Fig. 2a) can be due to its oxidation by the highly active OH species supplied by MoO(OH)₃ at the boundaries of the MoO_x clusters which are decorating the Pt surface.

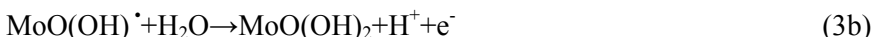
In order to realize the different behavior under H₂ flow (Fig. 2b) it is rational to consider that the interaction of the exposed samples in H₂ atmosphere is expected to result either in the reduction of the catalysts surface. In this respect, it is more likely to correlate the effect of H₂ with the reduction of the Pt surface. Considering that H₂ is

competitively reacting with the same oxidic species that react and oxidize CO_L it can be easily understood why CO_L species desorbs at significantly higher temperatures as depicted in Fig. 2b.

The effect of Mo oxide species on the modification of the chemisorptive properties of Pt can be deduced by the fact that CO desorption from Pt₄-Mo/TiO₂ sample under H₂ flow takes place at approximately 70 K below the corresponding desorption temperature on the Pt/TiO₂ sample (Fig. 2b). Thus in the case of Pt₄-Mo/TiO₂ sample CO_L species are less strongly bonded on the Pt surface atoms.

Conclusions

Taking into account the aforementioned considerations it can be proposed that CO species which can be either adsorbed on adjacent Pt atoms to Mo or directly from the gas phase react easily with the OH species of the MoO(OH)₂ towards the formation of CO₂ and H₂. Subsequently the empty space created on the Mo^{x+} species facilitate the dissociative adsorption of water and the regeneration of MoO(OH)₂. The application of positive potential not higher than 0.2V results in the partial oxidation of MoO(OH)₂ by removing H⁺ thus facilitating the formation of OH species.



The operating voltage, so that the stability of the reaction scheme presented by reactions (3) is secured, should not be above 0.2V. Above this voltage the average oxidation state of Mo^{x+} is expected to be larger than 5+ thus resulting in the deactivation of the Mo species due to the formation of MoO₃.

References

- [1] C. Song, *Catal. Today*, 2002, **77**, 17.
- [2] N.M. Markovic, P.N. Ross Jr, *Surf. Sci. Rep.*, 2002, **45**, 117.
- [3] M. Watanabe, S. Motoo, *J. Electroanal. Chem.*, 1975, **60**, 275.
- [4] J.C. Davies, B.E. Hayden, D.J. Pegg, *Surf. Sci.*, 2000, **467**, 118.
- [5] M.M.P. Janssen, J. Moolhuysen, *J. Catal.*, 1977, **46**, 289.
- [6] T. Frelink, W. Visscher, J.A.R. Vanveen, *Surf. Sci.*, 1995, **335**, 353.
- [7] B.N Grgur, N.M. Markovic, and P.N. Ross Jr, *J. Phys. Chem.*, 1998, **B 102**, 2494.
- [8] Y. Ishikawa, M.S. Liao, C.R. Cabrera, *Surf. Sci.*, 2002, **513**, 98.
- [9] B.N. Grgur, N.M. Markovic, and P.N. Ross Jr, *J. Electrochem. Soc.*, 1999, **146**(5), 1613-1619.
- [10] S. Zafeiratos, G. Papakonstantinou, M.M. Jacksic, S.G. Neophytides, *J. Cat.*, 2005, **232**, 127-136.
- [11] W. S. Li, L. P. Tian, Q. M. Huang, H. Li, H. Y. Chen and X. P. Lian, *J. Power Sources*, 2002, **104**, 281.
- [12] B.N Grgur, G. Zhuang, N.M. Markovic, and P.N. Ross, Jr., *J. Phys. Chem.*, 1997, **B 101**, 3910.
- [13] S. Mukerjee, R.C.Urian, *Electrochim.Acta*, 2002, **47**, 3219.

NANOMATERIALS FOR ELECTROCHEMICAL SYSTEMS WITH LITHIUM-INTERCALATION-ANODES

D. Ilić

*Varta Microbattery GmbH, Daimlerstrasse 1, 73479 Ellwangen, Germany
dejan.ilic@varta-microbattery.com*

Abstract

In this lecture a survey was made on the recent development of advanced batteries in Varta–Microbattery, involving nanodispersed materials, like carbon materials for negative electrodes, doped spherical Li-metal oxide for cathode materials, and new polymer materials for electrolytes and separators.

The principles of Lithium–Polymer batteries

Polymer batteries are now applied in a wide range of portable electronic devices such as Laptop, Digital frame, Wristphone, Camcorder, Camera, Cellular phones, Server, Organizer, PDA, Fingerprint-Scanner etc. Fig.1 shows how a Li-polymer battery works.

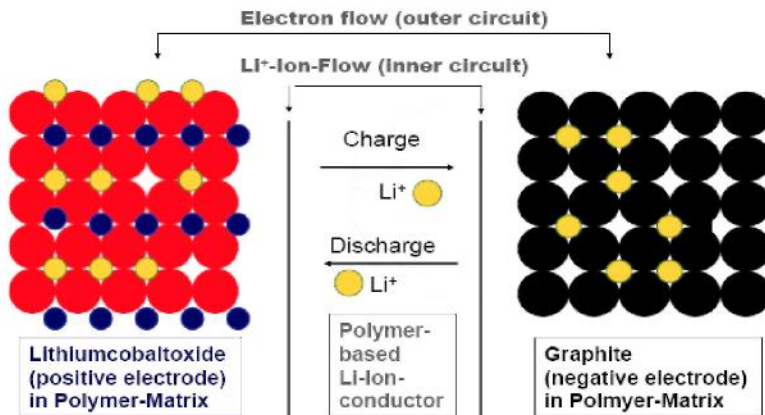


Fig. 1. The scheme of the processes in a lithium-polymer battery with (PoLiFlex™) [1].

Graphite in polymer-matrix presents anode (negative electrode), Lithium-cobalt-oxide in Polymer-Matrix presents cathode (positive electrode), and pure Li-ion conductive polymer works as the electrolyte. Inner circuit assumes Li⁺-ion- charge flow between anode and cathode through polymer-based Li-ion-conductor, and outer circuit involves flow of electrons.

The mechanism is in principle analogous to those of Li-ion and Li gel-polymer battery. A comparative survey of all of them, involving also possible production advantages and disadvantages, is summarized in Table 1.

Table 1. Comparison of production advantages/disadvantages of different Lithium batteries with various types of electrolytes.

Li-Ion	Li-Gel-Polymer	Li-Polymer (PoLiFlex [®])
– Excess of liquid electrolyte ▶ danger of leakage	– Gel-electrolyte ▶ difficult to implement in production	– Electrolyte in Polymer-Matrix ▶ no leakage
– Electrode porosity low ▶ long electrolyte soaking time	– Electrode porosity low, electrolyte viscous ▶ difficult to bring into cell	– high electrode porosity ▶ fast, efficient electrolyte soaking, low production costs
– Wound-Technology ▶ limited In height and form factor	– Wound-Technology ▶ limited in height and form factor	– Stack-/Lamination-Technology ▶ flexibility in height and form ▶ excellent separator-electrode-contact
– Rigid housing: stainless steel, aluminium	– Housing: Al-multilayer-foil	– Housing: Al-multilayer-foil

The development of new materials, particularly nanosized ones [2], and its application in batteries, have severe impact in battery performances, as shown in continuation:

Materials for negative electrodes: Nanocarbon

Carbon nanotubes present possible high capacity intercalation host for Lithium. Carbon nanotubes are also useful as conductive aid and host in hybride electrodes with Li-Si-Sn alloys, where capacity increase of more than 30 % is possible.

Materials for positive electrodes: LiCoO₂ versus LiNi_{0.33}Co_{0.33}Mn_{0.33}O₂

LiCoO₂ is well known cathodic material with good electrochemical properties. However, recently Cobalt is becoming more and more expensive, while exothermal decomposition of Li_{0.5}CoO₂ leads to poor safety of batteries. Recently developed material, LiNi_{0.33}Co_{0.33}Mn_{0.33}O₂, shows lower tap density, lower C-rate capability, higher irreversible formation losses, but it is much cheaper than LiCoO₂ and shows better stability during cycling and safety tests. The tap density of Li-Ni-Co-Mn-Oxides may be efficiently enhanced using nanoshaped spherical particles. In addition this effect is enhanced by combining larger ($d_{50} \sim 10 \mu\text{m}$) and smaller ($d_{50} \sim 3 \mu\text{m}$) particles in a ratio about 7:3. Optimized surface on nanoscale may additionally lower irreversible formation losses and enhance C-rate capability. Inorganic ceramic nano-coating over spherically shaped particles of cathode materials enables an excellent electrolyte soaking, also those of highly viscous high boiling point mixtures.

With ceramic material as flame protecting agent also significant overcharge protection is achieved. Inner nanostructure of cathodic material may be achieved by special preparation process. By such a structure an effect of catcher of parasitic gaseous de-

composition products, e.g. under long term high temperature storage conditions (4.2V@80°C) can be observed. Avoiding the degassing step after formation (advantage in production) is possible.

Polymer materials for electrolytes and separators:

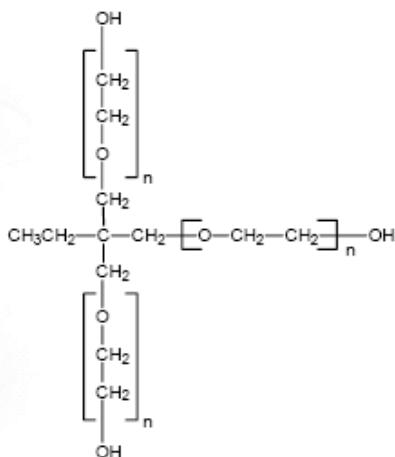


Fig. 2. The structure of oligo-(ethylene glycol)ether plasticizer

Battery performance depends on the use of advanced separators, flourine-free binder and star shape plasticizer for functional electrolytes. Star shape plasticizer (e.g. the class of Oligo-(ethylene glycol)ethers) may offer an effective replacement of established liquid electrolyte solvents: they show a large operating temperature regime [3] and can be part of a functional separator by light (UV) induced gelification or hardening, respectively. The oxidation stability is still to be improved but seems to be enhanced in combination by the lithium-conducting salt.

Conclusion

After introducing VARTA's development and design of a polymer battery, various examples have been given where nanotechnological aspects may be implemented in modern advanced battery systems. It has been shown that not the battery itself but the consequent aspect angle to nanomaterials used in these batteries may be the motor to drastically improve various cell properties and to reach new orders of magnitude in performance data.

References:

- [1] D. Ilić, K. Holl, P. Birke, T. Wührle, F. Birke-Salam, A. Perner, P. Haug J. Power Sources, 2006, **155**, 72-76.
- [2] D. Ilić, A. Perner, T. Wührle, P. Haug, C. Wurm, M. Pompetzki, NanoTrends 2005, Munich, June 6th-8th 2005
- [3] D. Ilić, P. Birke, P. Haug, A. Perner, M. Pompetzki, T. Wührle, C. Wurm, 6th Int. Symp. on New. Mat. for Electrochem. Systems, 10-13 July 2005, Quebec City, Canada, *in press*.

COMPOSITES OF MULTI-WALLED CARBON NANOTUBES AND ELECTROCHEMICALLY POLYMERIZED POLY(VINYLFERROCENE) AND THEIR APPLICATION

B. Šljukić, C.E. Banks, and R. G. Compton

*Physical and Theoretical Chemistry, University of Oxford,
South Parks Road, Oxford OX1 3QZ, United Kingdom.*

Abstract

Composites of multi-walled carbon nanotubes (MWCNTs) with poly(vinylferrocene) (PVF) supported on glassy carbon (GC) substrates were prepared electrochemically and characterized using cyclic voltammetry. The application of the composite for glucose determination in aqueous solutions was investigated using linear sweep voltammetry with the composite supported on GC substrates demonstrated superior performance to bare GC electrodes polymerised with PVF.

Introduction

The modification of electrodes by polymer films, in particular organometallic redox polymers such as poly-vinylferrocene, has long been an important area of research due to their interesting redox characteristics and applications for electrocatalysis [1]. Different methods have been used for the fabrication of PVF modified electrodes; however, the electrochemical polymerisation of VF has not been often employed, though this method is frequently used for polymerisation of other vinyl monomers and fabrication of redox polymer modified electrodes.

Ferrocene – modified electrodes are often used as mediators for glucose oxidation [2] as this reaction usually requires high overpotentials. The determination of glucose concentrations is very important in clinical, biological and chemical samples, as well as food processing and fermentation. Various carbon materials such as glassy carbon, graphite, carbon paste, carbon fibers, porous carbon, and carbon spheres are commonly employed as electrode materials in amperometric sensors. Carbon nanotubes are a new type of carbon material [3] that has only recently been demonstrated as sensors for glucose with much superior performance to those of other carbon electrodes in terms of reaction rate, reversibility, and detection limit.

Results and Discussion

The MWCNT–GC electrode prepared by evaporation procedure was coated with poly(vinylferrocene) by electrochemical polymerisation. The procedure involves scanning between -1.2 and + 1.0 V (vs. Ag wire) in a 3 M vinylferrocene solution in acetonitrile with 0.1 M TBAP as supporting electrolyte at scan rate of 100 mVs⁻¹ for 15 scans, followed by holding the potential at + 0.7 V (vs. Ag) for a period of up to 2 hrs. For comparison, a bare GC electrode was coated with a PVF film by the same procedure.

The stability of PVF-MWCNT modified GC electrode and surface coverage of PVF were examined using cyclic voltammetry in a solution of acetonitrile containing 0.1 M TBAP. Cyclic voltammograms showed a pair of well – defined redox peaks for ferrocene oxidation and reduction at *ca.* + 0.40 V (*vs.* Ag wire). With continuous scanning between - 0.5 and + 1.0 V (*vs.* Ag wire) of the modified electrode in the acetonitrile solution, the peak currents initially decreased *ca.* 70 %, possibly due to loss of soluble monomer and oligomer from the film, before giving stable currents. The surface coverage, Γ , of the poly (vinylferrocene) on the MWCNT modified GC electrode after stabilisation was calculated from the charge obtained from integration of the cathodic peak, Q , using the following equation:

$$\Gamma = \frac{Q}{nFA} \quad (1)$$

where A is the area of the GC electrode supporting the MWCNTs, n is the number of electrons per reactant molecule and F is the Faraday constant. The obtained coverages correspond to few monolayers of ferrocene groups with a limiting coverage of *ca.* 1.5×10^{-8} mol cm⁻² obtained after 20 min. Hence electrodes were subjected to polymerisation for 20 min in further experiments. Note that applying initial cycling regime before holding potential at constant value produced larger coverages than the ones acquired without cycling. The formed films exhibited characteristic electrochemical behaviour of thin layer – modified electrodes, with anodic to cathodic peak current ratio, I_{pa}/I_{pc} , close to 1 and both the redox peak currents and the peak-to-peak separations increased with increasing scan rate in the range from 10 to 250 mVs⁻¹.

For comparison, a bare GC electrode was subjected to electrochemical polymerisation from a vinylferrocene solution by the same procedure as used for the MWCNT modified GC electrode. In the case of PVF – GC electrode, a maximum coverage of *ca.* 1.0×10^{-9} mol cm⁻² was obtained which is more than 10 times less in comparison to the MWCNT modified GC electrode. This clearly demonstrates the advantages of using the MWCNTs where increased catalyst coverage is achievable with MWCNT modified electrodes as com-

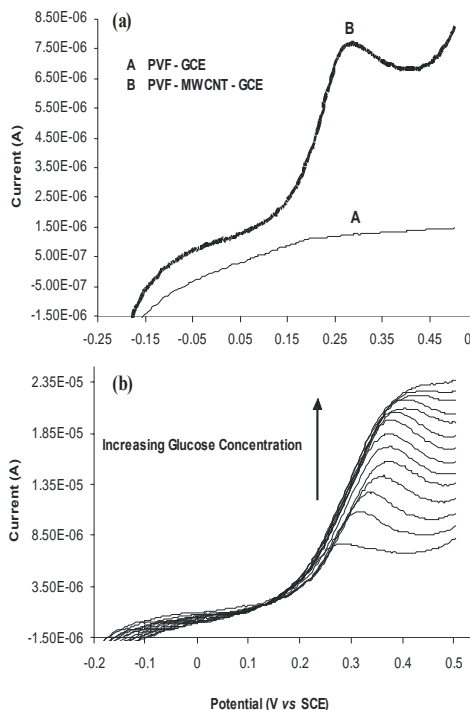


Fig. 1. (a) LSVs at PVF – GC (A) and PVF – MWCNT – GC (B) electrode in 1 mM glucose solution (b) LSVs of PVF-MWCNT-GC electrode with increasing glucose concentration in the range 0.5 - 10 mM

pared with a modified GC electrode indicating that greatly enhanced catalytic effects are attainable.

Therefore the application of the PVF-coated MWCNT modified GC electrode for the determination of glucose in aqueous solutions was investigated. PVF-MWCNT-GC electrode and PVF-GC electrode were characterized in pH 7.4 phosphate buffer using cyclic voltammetry. Linear sweep voltammetry (LSV) was used to determine level of glucose in aqueous solutions as the oxidation current increases with increasing the concentration of glucose. **Figure 1** shows comparison of the response of PVF-GC (A) and PVF-MWCNT modified GC (B) electrode in glucose solution where clear and distinct peak can be seen at *ca.* +0.3 V *vs.* SCE for the PVF-MWCNT modified GC electrode. The peak current at the PVF-MWCNT modified GC electrode was *ca.* 7.65 μA , significantly higher than the response of PVF-GC electrode of *ca.* 1.23 μA . The PVF-MWCNT modified GC electrode superiority to the PVF-GC electrode is possibly due to the higher coverage of polymer and hence more electrocatalytic centres. For PVF-MWCNT-GC electrode, the peak current showed a strong linear correlation with glucose concentration in a range from 0.4 to 8 mM with a limit of detection for glucose of 41 μM with a sensitivity of $9.5 \times 10^{-3} \text{ A M}^{-1}$.

Conclusions

The first study of the electrochemical polymerisation of vinylferrocene on MWCNT-carbon modified electrodes is presented. The new polymeric architecture has been characterized by electrochemical methods where the coverage of the formed PVF can be controlled by time of applying a constant potential of +0.7 V *vs.* Ag, which is advantageous over bulk polymerisation techniques. The resulting films exhibited characteristic electrochemical behaviour of redox polymer-modified electrodes. The application of PVF-modified MWCNT-GC electrodes for glucose detection in aqueous solutions was established. This method offers a promising, fairly easy generic procedure for the preparation of amperometric sensors.

References

- [1] A. D. Clegg, N. V. Rees, O. V. Klymenko, B. A. Coles, R. G. Compton, *J. Electroanal. Chem.* 2005, **580** (1), 78-86.
- [2] A. S. N. Murthy, J. Sharma, *Anal. Chim. Acta* 1998, **363**, 215-220.
- [3] G. G. Wildgoose, C. E. Banks, H. C. Leventis, R. G. Compton, *Microchim. Acta* 2006, **152**, 187.

HYDROXIDE ION OXIDATION ON BARE AND NAFION COVERED NOBLE METAL SURFACES

S.Mentus¹ and A. Abu Rabi²

¹*Faculty of Physical Chemistry, Belgrade University, Studentski Trg 12, Belgrade,*

²*IChTM-Center of Catalysis and Chemical Engineering, Njegoševa 12, Belgrade*

Abstract

The electrochemical oxidation of hydroxide ions on gold and platinum disc electrode, bare and covered with nafion, was studied. Under steady-state conditions well-defined wave due to direct oxidation of hydroxide, according to the equation: $\text{OH}^- = \frac{1}{4} \text{O}_2 + \text{H}_2\text{O} + \text{e}^-$ was registered. The nature of the OH^- ion oxidation wave was tested by varying the electrode rotation speed and concentration of OH^- ion in the solution. The influence of thickness of nafion film on the kinetics of hydroxide ions oxidation was investigated.

Introduction

In any aqueous alkaline solutions, oxygen evolution reaction commences on the basis of hydroxide ion oxidation reaction:



having standard electrode potential $E_0 = 0.401 \text{ V}$ vs. standard hydrogen electrode (SHE). For a reasonable small concentrations of hydroxide ions, in the presence of supporting electrolyte, the voltammograms of hydroxide ion oxidation after reaction (I) display a clear diffusion limitation [1-4]. A series of papers by Daniele et al. [2-4] was devoted to the voltammetric determination of hydroxide ions in aqueous solutions. The concentration of hydroxide ion in strong [2-4] alkaline solutions has been measured by means of both gold microelectrode [2-4], and gold rotating disc electrode [4]. For the same purpose, the gold microelectrode was used also in total absence of supporting electrolyte [3]. The influence of the nature of microelectrode material, i.e. gold, nickel and platinum [3], on the shape of voltammograms were investigated too, and defined wave attributed to the oxidation of OH^- ions has always been noticed.

It is known from literature that nafion film, covering metal surfaces, is permeable to electroactive species (for instance, oxygen molecules[5], hydrogen molecules [6]) and does not attenuate the electrochemical processes. The aim of this work was to examine the influence of Nafion film thickness on hydroxide ion oxidation on Nafion covered gold and platinum electrodes. For the sake of comparison, the same process was examined on bare metal surfaces.

Experimental

757 VA Computrace (Metrohm) was used to perform the voltammetric investigations. All the experiments were performed in thermostated three electrode electrolytic cell at

25 °C. Commercial Metrohm polycrystalline gold and platinum disc (2 mm in diameter) electrodes were used as working electrodes. Pt foil served as an auxiliary electrode and reference electrode was Ag/AgCl. To minimize possibility of electrolyte contamination by chloride ions, reference electrode was bridged by a Luggin capillary filled with the investigated electrolyte. After each set of measurements, the working electrode was polished with dry α -alumina powder ($\sim 1 \mu\text{m}$) on a polishing cloth. Nafion solution (1 wt%) was used for electrode preparation. The thickness of the nafion layer was calculated on the basis of solution volume applied on metal surface. Unless otherwise stated, the solutions, prepared from analytical grade of reagents and twice distilled water, were deoxygenated by bubbling the oxygen-free nitrogen during the experiments.

Results and Discussion

The voltammograms of oxidation of OH^- ions in 5 mM NaOH in 0.5 M Na_2SO_4 supporting solution on bare and Nafion coated rotating gold disk electrode (RDE) are presented in Figure 1. In order to maintain the clarity of presentation, immediately after achieving final anodic polarization, the recording of voltammetric curves was broken. These voltammograms show a plateau between 1.3 and 1.5 V, which agrees with literature data. According to the literature [7], in an alkaline solution, the monolayer of AuO forms itself between 0.17 and 0.9 v vs. SCE.

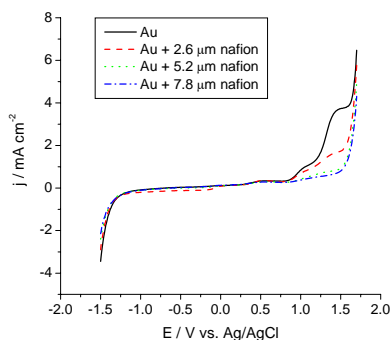


Fig. 1 The voltammograms of OH^- ion oxidation in 5 mM NaOH + 0.5 M Na_2SO_4 solution on rotating gold disc, bare and covered with nafion layer of various thickness

At potentials above 1 V vs. SCE, Au(III) oxide layer is formed over Au(II) oxide monolayer, so the current waves appearing in Fig.1, we attribute to OH^- ion oxidation on gold covered by Au(III) oxide layer.

It is obvious from Fig. 1 that Nafion coating suppress the OH^- oxidation wave and that the increase of the Nafion coating thickness leads to the decrease of limiting current. By analogy, voltammograms in Fig.2 show the highest limiting current for OH^- oxidation on bare platinum electrode.

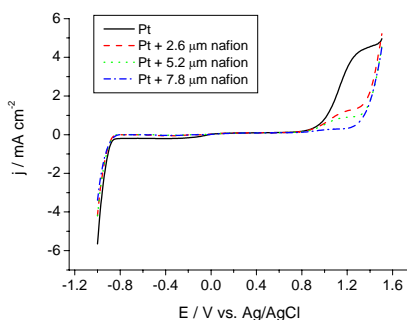


Fig. 2 The voltammograms of OH^- ion oxidation in 5 mM NaOH + 0.5 M Na_2SO_4 solution on rotating platinum disc, bare and covered with nafion layer of various thickness

The presumed diffusion nature of the plateaus of voltammograms both in Fig. 1 and Fig. 2 was tested by varying both the electrode rotation speed and the concentration of OH⁻ ions, with respect to the Levich equation:

$$j_l = 0.62nFD^{2/3}\nu^{-1/6}\omega^{1/2}C \quad (1)$$

where ν presents the kinematic viscosity and ω is angular rotation frequency. The plot of the limiting current corresponding to OH⁻ ions oxidation against the square root of the rotation speed gave a straight line, indicating that the limiting current is controlled by the diffusion of hydroxide ions. Similarly, at a fixed rotation rate, the limiting current was found to be proportional to the concentration of hydroxide ions. However, since the wave height decreases with the Nafion layer thickness, it seems that this layer blocks the electrode, and blocked fraction is proportional to the layer thickness.

Conclusion

Both gold and platinum show well-defined plateaus of voltammetric curves due to hydroxide ion oxidation. The influence of Nafion film thickness on kinetics of hydroxide ion oxidation on Nafion covered gold and platinum electrode was investigated and it was shown that the highest signal was obtained for bare electrodes. Nafion coating causes partial blockage of the surface available to the OH⁻ oxidation, thus the increase of the Nafion coating thickness leads to decrease of the limiting diffusion current.

Acknowledgements

This work was supported by the Ministry of Science and Environmental Protection of the Republic of Serbia (Project No.TR6712B).

References

- [1] E.L.Littauer, K.C.Tsai, *Electrochim. Acta*, 1979, **24**, 351.
- [2] M. E. Abdelsalam, G. Denuault, M. A. Baldo, S. Daniele, *J. Electroanal. Chem.*, 1998, **449**, 5.
- [3] S. Daniele, M. A. Baldo, C. Bragato, *Anal. Chem.*, 1999, **71**, 811
- [4] M. E. Abdelsalam, G. Denuault, M. A. Baldo, C. Bragato, S. Daniele, *Electroanalysis*, 2001, **13**, 289
- [5] J.-P. Diard, B.Le Gorrec, C. Montella, *J.Electrochem. Soc.*, 1998, **145**(9), 3308.
- [6] J. Maruyama, M. Inaba, K.Katakura, Z.Ogumi, Zen-ichiro Takehara, *J. Electroanal. Chem.*, 1998, **447**, 201.
- [7] G.Tremiliosi-Filho, L.H.Dall'Antonia, G.Jerkiewicz, *J.Electroanal.Chem.*, 1997, **422**, 149

THIN LAYER OF NiO-MODIFIED 13X ZEOLITE ON GLASSY CARBON SUPPORT AS AN ELECTRODE MATERIAL IN AQUEOUS SOLUTIONS

Z. Mojović², S. Mentus¹, I. Krstić³ and A. Rosić⁴

¹*Faculty of Physical Chemistry, Belgrade University, Studentski Trg 12, Belgrade,*

²*IChTM-Center of Catalysis and Chemical Engineering, Njegoševa 12, Belgrade*

³*Faculty of Chemistry, Belgrade University, Studentski Trg 12, Belgrade*

⁴*Faculty of Mining and Geology, Belgrade University, Đušina 7, Belgrade*

Abstract

Nickel oxide clusters were incorporated into 13X zeolite cavities by multiple impregnation with Ni-acetylacetonate and its thermal degradation in air. Procedure was repeated until Ni/13X mass ratio of 0.4 was achieved. Modified zeolite sample was characterized by x-ray diffractometry. This material, homogenized with 20 wt. % of carbon black, was applied in a form of thin layer to glassy carbon disc, and used as electrode material in an aqueous 0.1MNaOH. solution within the voltage window of water splitting.

Introduction

Zeolites, with their cavities of nanometer dimensions, present a specific support for metal or metal oxide clusters incorporation. The dimensions of cavities limit the dimensions of incorporated cluster to nanometer ones. The methods to modify zeolites by cluster incorporation [1] are either ion exchange followed by reduction, or impregnation by thermodegradable salt solution [2,3], followed by drying and thermal degradation. Such obtained modified zeolites may be used as thin-layer electrodes, after addition of carbon black which provides its electronic conductivity [3].

In this paper, the technique of zeolite impregnation by Ni-acetylacetonate dissolved in acetone was used to incorporate nickel oxide within the zeolite cavities. [2,3] NiO-modified zeolite was investigated as electrode material in an aqueous electrolyte solution.

Experimental

Ni-acetylacetonate was dissolved in acetone. Zeolite 13X was soaked by the solution, dried to evaporate acetone and heated to 350 °C in air in order to decompose the complex compounds and desorb the decomposition products. In this way nanodispersed NiO clusters were incorporated into the zeolite cages. Procedure was repeated until Ni/zeolite weight ratio of 0.4 was reached. XRD diagrams of original and modified zeolites were taken by means of Philips PW 1710 diffractometer using CuK α radiation. Modified zeolite was applied on rotating glassy carbon disc in three different manners: 1) 20 wt.% carbon black Vulcan XC72 (Carbot Corp.) was added to NiO-modified zeolite sample and together homogeneously suspended in ethanol. A droplet of the suspension was applied on glassy carbon disc, dried to evaporate ethanol and then covered by a droplet of 5wt % Nafion solution in ethanol. 2) Powdered mixture of the sample and 20 % carbon black, was homogeneously dispersed in a solution of

Nafion (5 wt.%), at Nafion solution/powder wt. ratio 2.5, and a droplet of the suspension was applied on rotating glassy carbon disc; 3) the same as in p. 2, but the Nafion solution/powder wt. ratio was 2.0.

Solvent evaporation resulted in a thin film of modified zeolite bonded, by a Nafion film, to glassy carbon support. The electrochemical performance of this material was investigated in 0.1M NaOH solution using rotating disc technique.

Results and Discussion

The x-ray diffractograms of pure 13X zeolite and NiO-modified zeolite (13X-Ni₄₀) are presented in Fig. 1. The lines characteristic of original zeolite appear, with the same intensity ratios, in the diffractogram of modified zeolite, too. This indicates that procedure did not destroy original crystal structure of zeolite 13 X. The new reflections appearing in the diffractograms of modified zeolite at $d = 0.209$, $d = 0.148$ and $d = 0.126$ nm, according to JCPDS (Joint Committee on Powder Diffraction Standards) belong to NiO. This means that Ni(acac)₂ decomposes in air, yielding nickel oxide. The diffraction lines are relatively narrow, indicating crystal structure of incorporated nickel oxide.

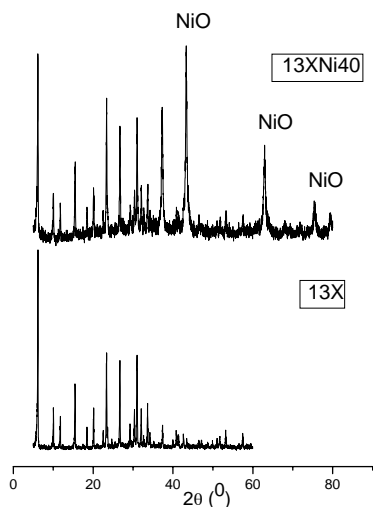


Fig. 1. The X-ray diffractograms of original 13X zeolite and modified zeolite, 13X-Ni₄₀

Cyclic voltammograms were recorded using the GC-supported, NiO-13X thin-layer electrode, in an aqueous 0.1M NaOH solution, at a scan rate 50mV/s and rotation rate 10 s⁻¹. The steady state voltammograms, obtained after 20-30 polarization cycles, are shown in Fig 2.

The shape of the voltammograms are characteristic of all samples, but the sizes of peak current were changeable during prolonged potential cycling. In the anodic sweep in the region between -1.0 and 0.0 V, the formation of Ni(OH)₂ takes place. Oxidation of Ni(OH)₂ to NiOOH takes place in the potential region 0.0-0.6V, followed by oxygen evolution reaction at higher anodic potentials. According to de Souza [4], NiOOH is actually mixture of Ni(OH)₂ and NiOOH with superficial layer of NiOOH. The reverse cathodic peak corresponds to the reduction of NiOOH to Ni(OH)₂. Reduction of residual oxygen in the zeolites cages is visible at the potentials lower than -0.4V. A lot of papers describe the nafion influence on the kinetics at bare electrodes, indicating that kinetics should not be attenuated by nafion film. [5,6] In this paper, the influence of nafion serving as a binder was considered, too and it was found that the final shape of voltammograms was greatly influenced by the way of electrode preparation. The lowest values of current densities were obtained for the electrode prepared by homogenising powder mixture in ethanol and then covered with one drop of Nafion solution. Better results were achieved starting

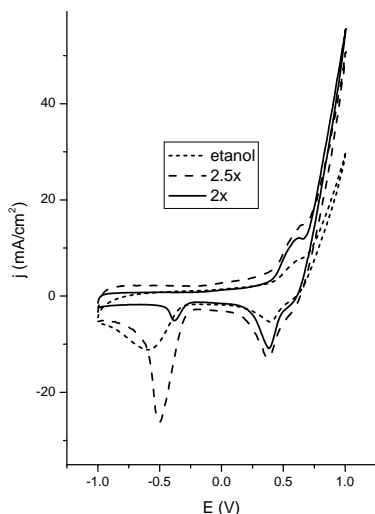


Fig. 2. Cyclic voltammograms of 13X-Ni₄₀ + 20 % C thin-layer, arranged as a rotating disc electrode: 1. applied as such, and bonded with ethanol/5% Nafion droplet, (dotted line); applied as suspension with Nafion/powder ratio either 2.5 (dashed line) (2), or 2 (solid line) (3), in an aqueous 0.1M NaOH solution, at a sweep rate 50 mVs⁻¹ and rotation rate 10 s⁻¹

application to glassy carbon support. The best results were achieved by applying the suspension of NiO-modified zeolite and 20 wt% carbon black in 5wt% Nafion solution, with Nafion/solid mixture wt ratio of 2.0.

References

- [1] A. Walcarius, *Anal.Chim.Acta*, 1999, **384**, 1-16.
- [2] M. Okumura, K. Tanaka, A. Ueda, M. Haruta, *Solid State Ionics*, 1997, **95**, 143.
- [3] S. Mentus, Z. Mojović, N. Cvjetičanin, Z. Tešić, *Fuell Cells – From Fundamentals to Systems*, 2003, **3**, 1.
- [4] L.M.M. de Souza et al, *Electrochim. Acta*, 1997, **42**, 1253-1267.
- [5] S.K. Zečević, J.S. Wainright, M.H. Litt, S.Lj. Gojković, R.F. Savinell, *J. Electrochem. Soc.*, 1997, **144**, 2973-2982.
- [6] R.M.Q. Mallo, E.A. Ticianelli, *Electrochim. Acta*, 1997, **42**, 1031-1039.

with the suspension of NiO-13X powder and Nafion solution. Electrode with nafion/powder wt. ratio of 2.5 displayed higher current densities, but in the region of OER, slightly slower kinetic is visible in comparison with the electrode Nafion/powder wt. ratio of 2.0. Oxygen reduction peak starting at -0.4V is the strongest in this case, what confirms that oxygen diffuses well through nafion membrane, although this peak is not reproducible in shape. If this peak is very high, other peaks may not be clearly resolved. Suspensions prepared with nafion/powder wt. ratio lower than 2.0 did not provide stable electrode layer. During cycling this layer occasionally came off the electrode surface or experiences degradation.

Conclusions

Modification of 13X zeolite by impregnation with Ni-acetylacetonate, and its thermal degradation, resulted in NiO nanoclusters incorporated into zeolite cavities. XRD analysis evidenced that the incorporation do not destroy the original crystal 13 X zeolite structure. The electrochemical performace of this material is influenced by the way of its appli-

DETERMINATION OF THE OPTIMAL GELATIN SOLUTION FOR INHIBITION OF Cu CORROSION

D. Todorović¹, Z. Dražić-Janković², Lj.M. Ignjatović² and D.A. Marković²

¹ *High School of Technics and Technology, Kosančićeva 22, Kruševac*

² *Faculty of Physical Chemistry, University of Belgrade, Studentski trg 12-16, Beograd*

Abstract

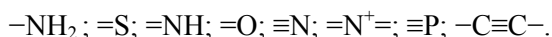
Electrochemical corrosion occurs in electrolyte solutions and presents metal devastation by electrochemical reaction with electrolyte. In terms to stop or to slow down corrosion, inhibitors should obstruct anodic, cathodic or both processes in metal-electrolyte system. In this work we examined the influence of gelatin as inhibitor in acid electrolytes in purpose to determine its optimal concentration for deposition as adsorptive protector on Cu sheets. We used relatively high concentrations of strong electrolytes within pH range 0-1.6. The mentioned pH values belong to the active Cu corrosion region according to Purber's diagram.

Introduction

Corrosion inhibitors are the substances that make physical, chemical (mostly coordinative) or both kinds of bonds, with the metal surface. The formed thin layer is usually monomolecular and successfully obstructs the corrosion. In order to be a good inhibitor, a compound must contain atoms with one or more free electron pairs.

Inhibitor efficiency depends also of characteristics and steric positions of these centers [1] (free electron pairs). It is convenient that the inhibition centers are located near the center of the molecule, so the other parts of the molecule could be able to cover the metal surface lobelikelly.

Some active centers are shown in decline order of inhibition efficiency [2]:



Gelatin could be achieved by partial hydrolysis of collagen, the principal protein of the intercellular substance in the animal tissue. Relatively insoluble in cold water, gelatin easily hydrates in warm water. Swollen gelatin particles dissolve on 40°C, forming solution which reaches a point of gelification when cools off. The degree of solubility could be changed by changing the temperature, concentration and size of the particles. Gelatin forms thermo-reversible gels which warmed on 30-35°C turn to solution. When reaches the point of gelification, gelatin solution forms the gel which has a different structure. Like the other proteins, due to the presence of the aminoacid groups, gelatin has amphoteric properties.

There are a few theories concerning the inhibition mechanism: theory of electric resistance, theory of layers, and theory of adsorptive exchange. Gelatin is one of the adsorptive inhibitors.

According to the theory of adsorptive exchange, the inhibitors push out adsorptive ions and molecules, like Cl^- , SO_4^{2-} and O_2 , from the corrosion area and as the final result of this process the bond between the metal (which is electron-acceptor) and the inhibitor (which is electron-donor) is formed.

Inhibitor efficiency, expressed in percents, is determined by the speed of corrosion on areas which are and which are not protected with the inhibitor [3]:

$$\omega = [(a_0 - a_1) / a_0] \times 100$$

where are: a_0 – the speed of corrosion on specimens without inhibitor;

a_1 – the speed of corrosion on specimens with inhibitor;

ω – efficiency of the inhibitor.

Experimental

The examinations were performed using 90 specimens of Cu-plates which dimensions were 30 x 50 x 0.5 mm. As inhibitors the solutions of following concentrations of gelatin were used: 1, 2, 4 and 8 %. The corrosion was followed in the solution of the following acids: 10%, 20% and 30% citric acid, 5% and 15% sulfuric acid, 5% and 15% hydrochloric acid. Cu plates were immersed in gelatin solutions on 30 °C for 10 min., and then dried up and put into protective foils, until it was time for immersing into electrolyte solutions. Immersing times were: 48, 96 and 192 hours. After treatment the plates were rinsed out with distilled water dried up with fan, and put again into protective foils. Tracking the corrosion of the specimens was performed on the basis of [4]: the mass loss (Δm (g)) speed of the specimen's corrosion (a ($\text{g}/\text{m}^2\text{day}$)), corrosion degree (I (%)) and the degree of inhibitor efficiency (ω (%)).

In addition, the corrosion of the unprotected and protected Cu specimens is followed by cyclovoltammetry using the solutions of citric acid as the corrosion medium and supporting electrolyte.

Results and Discussion

The goal of this experiment was determination of the optimal gelatin concentration in order to inhibit the corrosion. Because of a great number of experimental data, here we will show only the results obtained by experiments with 20 % citric acid (Table 1).

Presented results, as well as results for 10 % and 30% citric acid as corrosion electrolyte, besides certain deviations show that optimal concentration of the inhibitor was 2 % solution.

It must be emphasized that electrolytes used in this experiment were of high concentration and intensive corrosion environment for Cu was achieved, when long chains of gelatin molecules break and molecules of electrolytes come to direct contact with metal surface. Examinations showed, particularly when hydrochloric acid was used, that thicker deposits of gelatin partially dissolved producing cathodic and anodic areas which especially intensified the corrosion. Therefore values obtained for inhibitor efficiency in 15 % sulphuric and hydrochloric acid were negative.

Table 1. The results of the examination of Cu corrosion in 20 % citric acid

inhibitor	t (h)	Δm (g)	a(g/m ² day)	I (%)	ω (%)
without	48	0.0456	15.20	0.615	
without	96	0.0735	12.25	1.000	
without	192	0.0963	8.02	1.286	
1% gelatin	48	0.0237	7.90	0.316	48.02
1% gelatin	96	0.0313	5.22	0.422	47.39
1% gelatin	192	0.0581	4.84	0.782	39.65
2% gelatin	48	0.0220	7.33	0.300	51.78
2% gelatin	96	0.0295	4.92	0.395	59.84
2% gelatin	192	0.0492	4.10	0.662	48.88
4% gelatin	48	0.0392	13.07	0.517	14.18
4% gelatin	96	0.0398	6.63	0.532	45.88
4% gelatin	192	0.0410	3.42	0.548	57.36
8% gelatin	48	0.0423	14.10	0.572	7.23
8% gelatin	96	0.0621	10.35	0.831	15.51
8% gelatin	192	0.0922	7.68	1.237	4.24

The results of electrochemical measurements of the investigated corrosion are in good agreement with the above mentioned and will be presented in the full version of the work.

Conclusion

The results of experiment lead to the following conclusions: 1) The most protective effect was achieved with 2 % solution of gelatin as inhibitor. 2) Gelatin as inhibitor is not recommended in electrolyte solutions which pH values are lower than 2. 3) The presence of =NH group in the structure of gelatin molecule recommends gelatin as inhibitor, but it's long chain brakes in strong acids creating conditions not only for ceasing protective activity but also for speeding corrosion, as experiment with 15 % solutions of hydrochloric and sulphuric acid shows.

References

- [1] I.L.Rozental: Inhibitori korozii, Khimia, Moskva, 1977.
- [2] L.I. Antropov, E.M. Makušin: Inhibitori korozii metalov, Tehnika, Kiev, 1981.
- [3] S. Mladenović: Korozija metala, TMF, Beograd, 1978.
- [4] F. Sebenji, L. Hakl: Korozija metala, Tehnička knjiga, Beograd, 1980.

VOLTAMMETRIC DETERMINATION OF LUTETIUM

K. R. Kumrić, T. M. Trtić-Petrović and J. J. Čomor

Vinča Institute of Nuclear Sciences, Laboratory of Physics, P.O. Box 522, Belgrade, Serbia

Abstract

Half wave potential of lutetium was determined by anodic stripping voltammetry using various electrolyte solutions at the mercury electrode. The influence of electrolyte pH on the value of peak current was also observed. The results show that the choice of the supporting electrolyte and the electrolyte pH strongly influence the voltammetric behaviour of lutetium.

Introduction

Various voltammetric techniques, especially stripping voltammetry, are effectively used in analytical determination of very low metal concentrations. These techniques can be applied to wide variety of metals, e.g. in environmental analysis for qualitative and quantitative determination of heavy metals in natural waters [1]. High sensitivity and selectivity of stripping voltammetry are based on the fact that the analyte is accumulated before it is determined.

Anodic stripping voltammetry (ASV) with mercury as the working electrode can be used to determine all metals which are soluble in mercury with the formation of amalgams. The first step is reduction of the metal ions and formation of an amalgam, while in the second step (determination) re-oxidation occurs [2].

Our recent work was orientated towards membrane extraction of radionuclide $^{177}\text{Lu(III)}$ from aqueous solutions at very low concentrations [3]. In order to investigate the physicochemical parameters of transport of Lu(III) across supported liquid membrane, one needs a suitable analytical method which would enable us to determine low concentration of non-radioactive $^{176}\text{Lu(III)}$. ASV potentially offers the possibility to determine trace quantities of Lu(III).

To our best knowledge there is no published information related to voltammetric determination of lutetium yet. Thus, the aim of this study was to find a suitable supporting electrolyte for the determination of Lu(III) and to define its half wave potential using the most appropriate electrolyte.

Results and Discussion

A 797 VA Computrace analyser (Metrohm, Switzerland) was used for all voltammetric measurements. The analyser consists of a 797 VA Computrace Stand and is fully controlled with a 797 VA Computrace software ver. 1.2. The Metrohm Multimode Mercury electrode served as a working electrode, typically in a hanging mercury drop electrode (HMDE) mode, whereas a Pt-wire electrode was used as an auxiliary electrode and an Ag/AgCl ($3 \text{ mol}\cdot\text{dm}^{-3}$ KCl) electrode with ceramic diaphragm was used as a reference electrode. Dissolved oxygen was removed by nitrogen bubbling prior to

measurements. All measurements were carried out at laboratory temperature of 20 ± 2 °C.

The solution of LuCl_3 was prepared by dissolving Lu_2O_3 in hot hydrochloric acid and diluting it with deionised water to a final concentration of $5 \text{ mg}\cdot\text{dm}^{-3}$ Lu(III). Electrolytes used for the determination of Lu by ASV were: $3 \text{ mol}\cdot\text{dm}^{-3}$ potassium chloride, $1 \text{ mol}\cdot\text{dm}^{-3}$ potassium thiocyanate, $0.1 \text{ mol}\cdot\text{dm}^{-3}$ sodium oxalate, $0.1 \text{ mol}\cdot\text{dm}^{-3}$ ethylenediamine tetraacetic acid and $0.5 \text{ mol}\cdot\text{dm}^{-3}$ sodium tartrate. All experiments were performed in the voltammetry cell, containing 10 cm^3 of deionised water, 1 cm^3 of appropriate electrolyte and 0.1 cm^3 of $5 \text{ mg}\cdot\text{dm}^{-3}$ Lu(III). Blank solution was measured before each sample determination. Depending on the supporting electrolyte, the useable potential range was in the interval between 0 and -1.8 V . Method of standard addition was used to verify that the obtained peak originates from Lu(III).

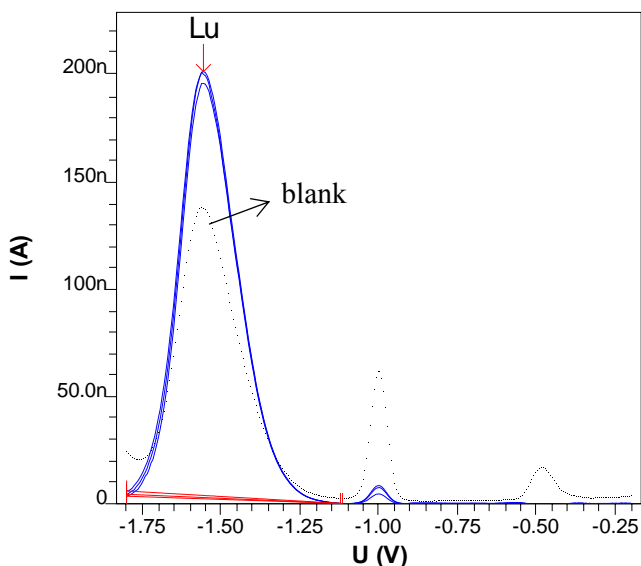


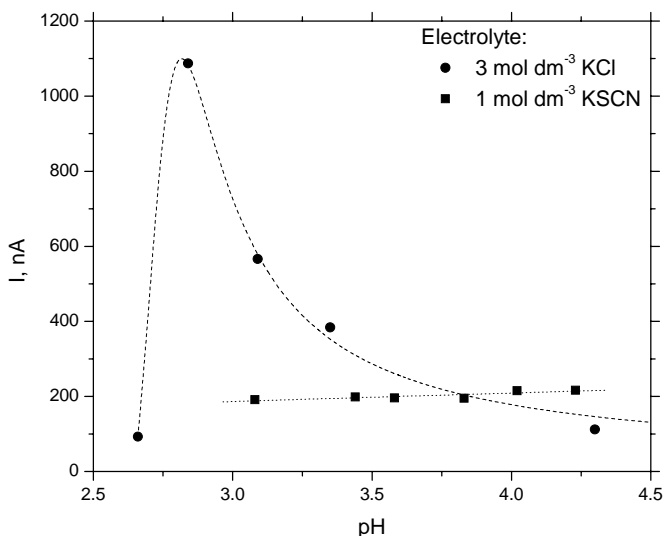
Fig. 1. Voltammogram of Lu(III) using $1 \text{ mol}\cdot\text{dm}^{-3}$ KSCN as supporting electrolyte

Fig. 1 shows a voltammogram of Lu(III) in $1 \text{ mol}\cdot\text{dm}^{-3}$ KSCN as electrolyte which demonstrates a well developed ASV peak with a half wave potential at $-1.55 \pm 0.05 \text{ V}$. The results of other supporting electrolytes mentioned above, are given in Table 1. The dependence of the current maximum on the electrolyte pH, was investigated for KCl and KSCN and given in Fig. 2. It can be seen that the influence of pH of electrolyte on the current maximum of lutetium is much stronger in the case of KCl than in the case of KSCN. Using KSCN, the current maximum of Lu(III) stays approximately constant in the pH interval 3.0 – 4.0.

Table 1. Half wave potentials of Lu^{3+} in various electrolyte solutions

Substance	Electrolyte solution				
	$3 \text{ mol}\cdot\text{dm}^{-3}$ KCl	$1 \text{ mol}\cdot\text{dm}^{-3}$ KSCN	$0.1 \text{ mol}\cdot\text{dm}^{-3}$ $\text{Na}_2\text{-oxalate}$	$0.1 \text{ mol}\cdot\text{dm}^{-3}$ $\text{Na}_2\text{-EDTA}$	$0.5 \text{ mol}\cdot\text{dm}^{-3}$ $\text{Na}_2\text{-tartrate}$
Lu^{3+}	-1.60 cw	-1.55 w	nr	nr	nr

w – very well defined peak; cw – catalytic hydrogen wave; nr – no peak

**Fig. 2.** The influence of electrolyte pH on the current maximum of Lu(III)

Conclusion

The half wave potential of Lu(III) was determined applying the ASV method. The results presented above illustrate that the determination of Lu(III) by ASV is best performed with $1 \text{ mol}\cdot\text{dm}^{-3}$ KSCN as supporting electrolyte. Also, $3 \text{ mol}\cdot\text{dm}^{-3}$ KCl can be applied as electrolyte, but this peak is coupled with catalytic hydrogen wave. The current maximum is influenced by the electrolyte pH and this influence is more pronounced in the case of KCl electrolyte. In the pH interval 3 - 4, which is of interest for our further investigations, the choice of $1 \text{ mol}\cdot\text{dm}^{-3}$ KSCN would be most suitable for the determination of Lu(III).

References

- [1] K. Siegel, Ü. Mauer, H. Keis, *Electrochimica Acta*, 1997, **42**, 2955-2960.
- [2] G. Henze, Monograph: Introduction to Polarography and Voltammetry, Metrohm, Switzerland, 2003.
- [3] K. Kumrić, T. Trtić-Petrović, E. Koumariou, S. Archimandritis, J.J. Čomor, Separation and Purification Technology, Article in press, 2006.

VOLTAMMETRIC AND HPLC MONITORING OF CEFOTAXIME AND ITS MAIN METABOLYTE DESACETYLCEFOTAXIME IN REAL URINE SAMPLE

B. Jocić¹, M. M. Aleksić², M. Zečević¹ and V. Kapetanović³

¹*Institute of Pharmaceutical Chemistry and Drug Analysis*, ²*Institute of Physical Chemistry*,

³*Institute of Analytical Chemistry, Faculty of Pharmacy, Vojvode Stepe 450, P.O.Box 146, Belgrade, (mzecevic@pharmacy.bg.ac.yu)*

Introduction

Cefotaxime (CFX) is third generation cephalosporin antibiotic used against most respiratory and urinary infections. In humans, CFX is metabolized by esterase to its microbiologically active metabolite desacetylcefotaxime (DCFX) and several non-active metabolites. The majority of the administered dose (50 – 60%) of CFX is excreted unchanged in the urine [1]. CFX possesses methoxyimino group, reducible at mercury electrode [2]. In acid buffer solutions four electron reduction of methoxyimino group gives one well formed voltammetric peak at about -0.5V, which is irreversible, diffusion controlled and strongly influenced by the adsorption. There are no literature data concerning DCFX reduction. Literature data are available concerning the HPLC separation of CFX and DCFX [3].

Experimental

The Voltammetric measurements were performed with an Amel 433-A computerized polarographic analyzer. Three-electrode system was employed: hanging mercury dropping electrode (HMDE), Ag/AgCl reference electrode and a Pt-auxiliary electrode.

A Hewlett-Packard HP 1100 chromatographic system was used. The method used a C₁₈ XTerra™ (150×3.9 mm, 5µm) column (Waters, USA) on temperature 25°C with detection at 262 nm. The mobile phase consisted of 0.007 M H₃PO₄ – acetonitrile (85:15) at flow rate of 1ml/min. Britton-Robinson (BR) buffer solution, pH 2.8, was used as a supporting electrolyte. CFX standard substance is produced by Sigma. DCFX was prepared by alkaline hydrolysis of CFX. Tolykar® (injections) was produced by Jugoremedija (Zrenjanin, SCG). Concentrated urine sample was treated with methanol as urine protein precipitating agent. After the vortex during ~30s, the precipitated protein was separated out by centrifugation for 25min at 3900rpm. The clear supernatant layer was filtered through 0.2 µm filters, diluted with redistilled water and BR buffer, and used in further procedure as protein-free urine.

Results and Discussion

The real urine sample was diluted with BR buffer. Adsorptive stripping differential pulse voltammograms were recorded with pulse amplitude of 100mV, pulse width of 20ms, scan speed 50 mVs^{-1} , accumulation potential of -100mV, accumulation time 30s, and presented in Fig. 1. There are two voltammetric peaks present at reduction potentials of -0.23V and -0.47V. The origin of these peaks was checked using standard addition method. After the CFX addition only peak at -0.47V increased proving that it was a consequence of the CFX reduction, as already supposed. On the other hand, after the DCFX addition peak at -0.23V increased significantly (92%), but at the same time peak at -0.47V increased about 14%. This was expected, since during the procedure of alkaline hydrolysis less than 20% of CFX remains unhydrolysed. Obtained results suggested that DCFX is also reducible at mercury electrode, but at more positive potentials about 250mV related to CFX, enabling the CFX and DCFX determination in the same real urine sample.

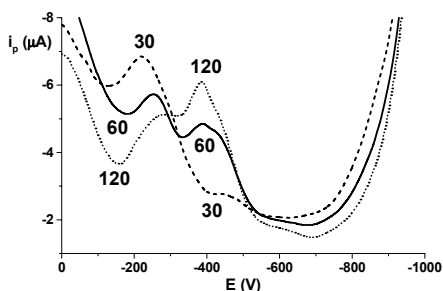


Fig. 1. Adsorptive stripping differential pulse voltammograms of real urine obtained at 30, 60 and 120 min after intramuscular administration of CFX ($v=50 \text{ mVs}^{-1}$, $E_{\text{acc}} = -100 \text{ mV}$, $t_{\text{acc}}=30 \text{ s}$).

These findings were confirmed by RP-HPLC method simultaneously performed. The peaks of CFX and DCFX are well separated as shown in Fig. 2. The origin of these peaks was proved after addition of CFX and DCFX. Besides, the components of the complex urine matrix did not influence the main CFX and DCFX peaks.

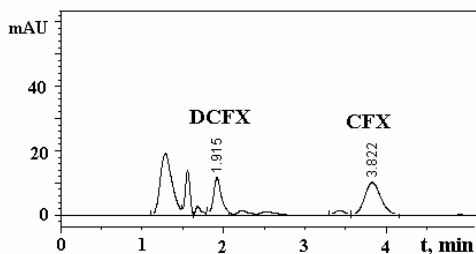


Fig. 2. Chromatogram of real urine sample obtained after 60 min of CFX administration.

The drug content in the real urine changes with the time of drug administration. With increasing time from 30 to 120 min concentration of CFX in the real urine sample increased, while the concentration of its metabolite DCFX decreased (Fig. 1). The biggest change is observed in the first hour. Identical results were obtained when HPLC was applied. Obtained values are presented in Table 1.

Table 1. Parameters of voltammograms and chromatograms of CFX and DCFX

Method	t (min)	SWAdSV		HPLC	
		E_p (V)	i_p (μ A)	t_R (min)	A (au)
CFX	30	-0.468	0.251	3.817	72.1
	60	-0.412	1.974	3.822	138.9
	120	-0.393	2.635	3.882	150.5
DCFX	30	-0.233	2.179	1.915	128.0
	60	-0.256	0.837	1.915	65.4
	120	-0.260	0.722	1.926	57.5

According to literature [1], the maximal concentration of CFX in plasma was achieved after T_{max} of 0.78 h. In this period, CFX is intensively metabolised, and DCFX is predominantly present in excreted urine sample. After that, the CFX concentration began increasing. Later on, it reached almost a constant value. At the same time, the DCFX began decreasing, reaching a constant value-approximately 3-4 times smaller compared to CFX. These findings are in good agreement with literature data concerning the CFX and DCFX distribution in serum.

Conclusion

The investigated drug CFX and its active metabolite DCFX can be simultaneously detected in urine after the drug administration using voltammetry and RP-HPLC methods. Therefore, both methods can be successfully used for monitoring the CEF and DCFX in real urine sample.

Acknowledgments

This work was supported by the Ministry of Science, Technology and Development of Serbia, Grant 142071.

References

- [1] K.B. Patel, D.P. Nicolau, C.H. Nightingale, R. Quintiliani, *Pharmacology*, 1995, **22**, 49-55.
- [2] V. Kapetanović, M. Aleksić, P. Zuman, *J. Electroanal. Chem.* 2001, **507**, 263-269.
- [3] T. Scanes, A.F. Hundt, K.J. Swart, H.K.L. Hundt, *Journal of Chromatography B*, 2001, **750**, 171-176.

ELECTROCHEMICAL BEHAVIOUR OF 5-SUBSTITUTED 2-ALKYLIDENE-4-OXO-THIAZOLIDINE DERIVATIVES

I. Cekić^{1,2}, D. M. Minić^{1,2}, V. Jovanović⁴ and R. Marković^{2,3}

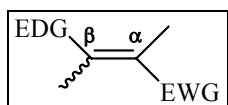
¹Faculty of Physical Chemistry, Studentski trg 12 (dminic@ffh.bg.ac.yu), Beograd, University of Belgrade, Serbia, ²Center for Chemistry ICTM, P.O.Box 473, Belgrade, ³Faculty of Chemistry, University of Belgrade, Studentski trg 16, Belgrade and ⁴ICTM, Department of Electrochemistry, P.O. Box 815, Belgrade

Abstract

Research on electrochemical behaviour of the variously 5-substituted 2-alkylidene-4-oxothiazolidines **1a-c** by cyclic voltammetry on Pt electrode in non-aqueous medium is currently the focus of our interest. Herein, we report the results regarding the influence of the substituents in the heterocyclic ring on processes of the electrochemical reduction and oxidation.

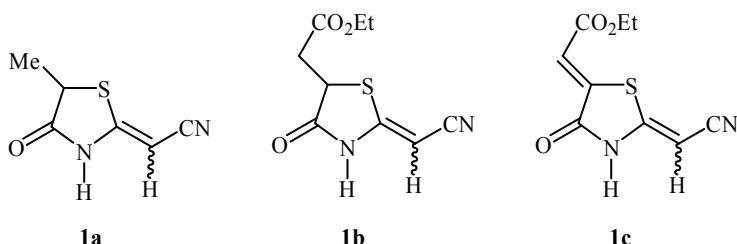
Introduction

Investigation of the physicochemical properties and chemical reactivity of *push-pull* alkenes of that type, carrying electron-donating group(s) (EDG) on C(β) and strongly resonatively electro-withdrawing group(s) (EWG) on C(α), as depicted below, attracts attention, due to a broad range of biological activity¹ and the fact that they are precursors for synthetic purposes²:



Compounds **1a-c** also represent an excellent model for investigation of the effects of weak noncovalent interactions on the structure-reactivity relationship in a solution and in the solid state, as well.³⁻⁵

5-Substituted 4-oxothiazolidines **1a**, **1b** and **1c** with one or two exocyclic double bonds attached to thiazolidine ring, exemplify typical *push-pull* compounds which have been synthesized according to procedures reported by us^{6,7}:



For the first time the cyclic voltammetry studies concerning the electrochemical characterization of 4-oxothiazolidines **1a-c** at room temperature will be presented.

Experimental

Cyclic voltammetry (CV) was performed on a CHI760b Electrochemistry workstation (CHI Instrument CO., USA) using one-compartment electrolytic cell (volumetric capacity 10 ml) with a three-electrode configuration. A platinum disc (2.0 mm diameter, CH Instruments, Inc.) and a platinum flag wire were served as the working and the counter electrode, respectively. A silver wire in 0.01M AgNO₃ solution of TBAHF₆ in acetonitrile (anhydrous) served as a non-aqueous reference electrode which was separated from the rest solution by a fine glass frit. Measurements were performed in pre-dried solution of 4mM 5-substituted 2-alkylidene-4-oxothiazolidine derivatives in 0.1 M TBAHF₆ in acetonitrile at a sweep rate of 100 mV/s in the potential range from -2 to 2 V.

Results

Based on the first scan cyclic voltammograms, shown in Figure 1, and potential values given in Table 1, all three compounds **1a-c** undergo irreversible processes of oxidation and reduction on the Pt-electrode.

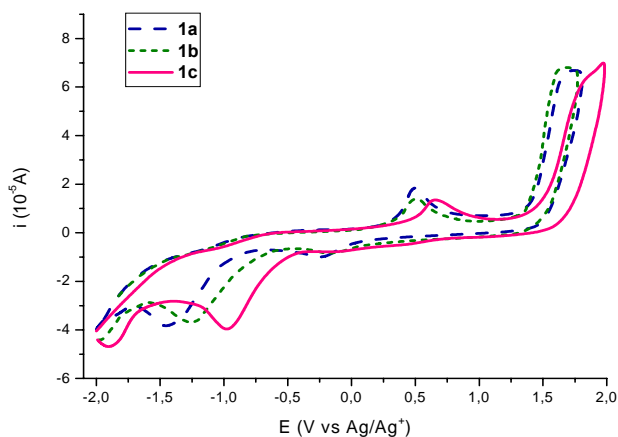


Fig. 1. Cyclic voltammograms of compounds **1a**, **1b** and **1c** in 0.1 M TBAHF₆ + CH₃CN, sweep rate 100mV/s

The order of the reduction potentials of 4-oxithiazolidines is as follows:



The rationale for this behaviour is most likely based upon increased electron-accepting ability of the etoxycarbonylmethylidene group at C-5 of **1c** versus that of the etoxycarbonylmethyl group in **1b**. In the case of precursor **1a**, containing the methyl group at C-5, different mode of reduction occurs, thus, making the precursor **1c** less reactive. On the other hand, the order of oxidation potentials follows the opposite direction.

In addition, we have investigated the possibility of employing this technique for a quantitative determination of heterocyclic derivatives by taking into account the relationship between the peak current and substrate concentration.

Table 1. The peak potentials of the compounds **1-c** versus Ag/Ag^+

Compound	CH_3CN ($V/S \text{ Ag}/\text{Ag}^+$)				
	Cathodic peaks			Anodic peaks	
	$E_{p,c1}$ (V)	$E_{p,c2}$ (V)	$E_{p,c3}$ (V)	$E_{p,a1}$ (V)	$E_{p,a2}$ (V)
1a	-1.36	-1.97	-0.24	0.49	1.69
1b	-1.17	-1.91	-0.14	0.49	1.65
1c	-1.01	-1.87	/	0.65	1.82

Conclusion

This study demonstrated the electrochemical activity of 4-oxothiazolidines **1a-c**. The effect of the substituent at the C-5 position on reduction and oxidation potentials was shown. The regions of the linear dependence of the peak current on concentration of the title compounds were determined.

References

- [1] R. G. Giles, N. J. Lewis, J. K. Quick, M.J. Sasse, M. W. J. Urquhart, *Tetrahedron*, 2000, **56**, 4531-4537.
- [2] R. Marković, M. Baranac, P. Steel, E. Kleinpeter, M. Stojanović, *Heterocycles*, 2005, **65**, 11.
- [3] H. Kessler, *Angew. Chem. Int. Ed. Engl.*, 1982, **21**, 512.
- [4] J.-C. Zhuo, *Magn. Reson. Chem.*, 1997, **35**, 311.
- [5] J.-M. Lehn, *Angew. Chem. Int. Ed. Engl.*, 1990, **29**, 1304.
- [6] R. Marković, M. Baranac, Z. Džambaski, *Heterocycles*, 2004, **63**, 851.
- [7] T. Kato, T. Ozaki, K. Tamura, Y. Suzuki, M. Akima, N. Ohi, *J. Med. Chem.*, 1999, **42**, 3134.

ENHANCEMENT OF THE ELECTROCATALYTIC ACTIVITY OF Ni ELECTRODE FOR HYDROGEN EVOLUTION BY ELECTRODEPOSITED V AND Co ON ITS SURFACE

N.I.Potkonjak¹, V.M. Nikolić¹, S.N. Blagojević¹, B.R. Simonović¹,
T.N. Potkonjak², M.P. Marčeta-Kaninski³ and D.Ž. Sužnjević¹

¹*Institute of General and Physical Chemistry, P.O. Box 551, Serbia*

²*University of Belgrade, Faculty of Physical Chemistry, P.O. Box 137, Serbia*

³*Vinca Institute of Nuclear Science, Laboratory of Physical Chemistry, P.O. Box 522, Serbia*

Abstract

Enhancement of the electrocatalytic effect of Ni electrode for hydrogen evolution reaction (HER) by co-electrodeposited V and Co at metallic Ni (Ni-V-Co) was studied by using quasi-potentiostatic polarization technique from 1 M KOH at 25 °C. The obtained exchange current density for HER with Ni-V-Co electrode, ($5.5 \times 10^{-4} \text{ A cm}^{-2}$), is about two orders of magnitude higher than for metallic Ni electrode. The results suggested the existence of the synergetic effect of V and Co deposit on the catalytic activity of Ni electrode for HER. By using X-ray fluorescence (XRF) analysis the presence of Co and V at metallic Ni support was proved.

Introduction

The increase of the Ni electrocatalytic effectiveness for HER is to be expected throughout co-deposition processes of appropriated Brewer intermetallic compounds. A series of prepared electrodes by co-deposition of V and Co were investigated. Throughout Tafel parameters G. Wu et al showed that Ni-Co and Ni-Co-LaNi₅ co-depositites have higher electroactivity for HER over the Ni electrode [1]. Optimization of the hydrogen evolution activity was found also on Ni-RuO₂ by A.C. Tavares and S. Trasatti [2]. Some novel trends in this field were presented by A. Damian and S. Omanovic [3] by improved intrinsic activity of Ni and electrodeposited Ni-Mo for HER in a three-dimensional polyaniline matrix. R.M. Abouatallah et al reported that addition of dissolved V₂O₅ in 8M KOH solution was found to produce the reactivation of Ni cathode by formation of vanadium-bearing deposit [4].

In this work, the electrocatalytic activity of Ni electrode was compared to the electrode obtained by electrodeposition of V and Co species on metallic Ni support (Ni-V-Co).

Experimental

The electrocatalytic activity of Ni and Ni-V-Co electrodes for the HER was studied by using quasi-potentiostatic polarization technique by applying of sweep rate 1 mV s^{-1} , corrosion measurement software (CorrWare[®]) with a Solartron 1286 electrochemical interface. Experiments were carried out in a two electrode compartment electrochemical cell containing 1M KOH as electrolyte at the temperature of $(25 \pm 0.1) \text{ }^\circ\text{C}$. The saturated calomel electrode (SCE) served as a reference one. Large-area Pt-mesh was used

as a counter electrode. Electrodeposition of V and Co on the metallic Ni support was provided from V_2O_5 and $[Co(en)_3]Cl_3$ dissolved in 1M KOH at -1.5 V vs. SCE during 500s.

The analysis of Ni electrode surfaces after electrodeposition was made by XRF spectrometer (ARL Optim'X 108) with a wavelength dispersive analysis system. The sample was excited with the Rh X-ray tube operated at 50 kV and 1 mA. The crystal analyzer was a plane LiF (200) and the emitted radiation was detected with a gas flow proportional counter. The 2θ angle of the spectrometer was scanned with steps of 0.1° , and the counting time was 1s in each step.

Results and Discussion

The Tafel plots for HER obtained by using Ni and Ni-V-Co electrodes are presented in Figure 1. From the obtained Tafel plot the Tafel slope b_c , and exchange current density j_o , was obtained. In case of Ni electrode obtained Tafel parameters are, $b_c = 0.117 \text{ V dec}^{-1}$, $j_o = 5.8 \times 10^{-6} \text{ A cm}^{-2}$. The same parameters for Ni-V-Co electrode are: $b_c = 0.133 \text{ V dec}^{-1}$, $j_o = 5.5 \times 10^{-4} \text{ A cm}^{-2}$.

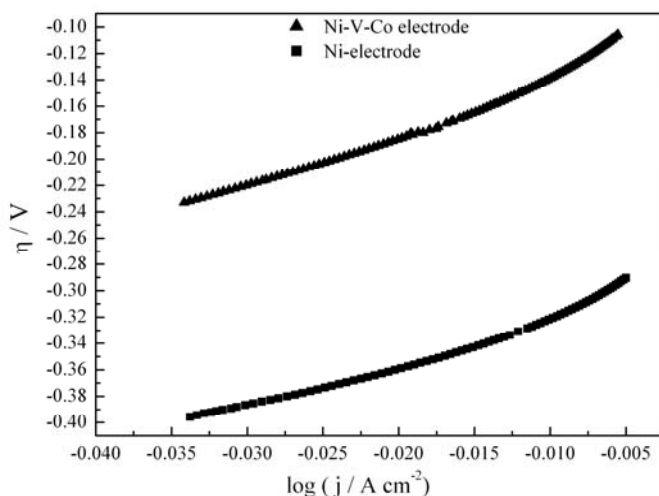


Fig. 1. The Tafel plots displays for HER on Ni and Ni-V-Co electrode in 1 M KOH at 25 °C .

The j_o value which characterized the charge transfer reaction occurring at the electrode surface during HER is generally accepted as an important parameter describing the electrocatalytic activity of the electrode. Based on the noticeable higher value of j_o obtained for Ni-V-Co electrode relative to the Ni one, suggests the existence of the synergetic effects of the hypo-hyper-d-electronic metals (V and Co) on improving electrocatalytic activity of conventional Ni electrode.

In order to prove the existence of the electrodeposited layer on the metallic Ni, XRF analysis was applied separately on the Ni and Ni-V-Co electrode. Figure 2. presents the XRF spectrum in the form of differences between these two electrodes. The

presence of the Ni spectral line suggested the partial coverage of the metallic Ni with electrodeposited V and Co, having also the corresponding lines.

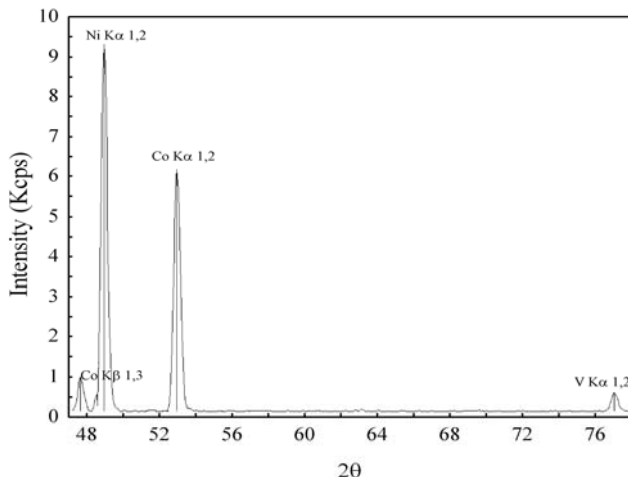


Fig. 2. XRF spectrum obtained from differences of spectral lines for Ni and Ni-V-Co electrode.

Conclusion

Based on the quasi-potentiostatic polarization technique applied on the investigated system, it was possible to determine the relevant Tafel parameters for hydrogen evolution reaction on the Ni, as well as on the Ni-V-Co electrode. The exchange current density determined for Ni-V-Co electrode is two order of magnitude higher compared to the Ni electrode. Existence of the electrodeposited layer containing V and Co was proved by means of XRF analysis.

References

- [1] G. Wu, N. Li, C.S. Dai, D. R. Zhou, *Mater. Chem. Phys.*, 2004, **83**, 307-314.
- [2] A.C. Tavares, S. Trassati, *Electrochim. Acta*, 2000, **45**, 4195-4202.
- [3] A. Damian, S. Omanovic, *J. Power Sources*, 2005, **158**, 464-476.
- [4] R.M. Abouatallah, D.W. Kirk, S.J. Thorpe, J.W. Graydon, *Electrochim. Acta*, 2001, **47**, 613-621.

Biophysical Chemistry
Photochemistry
Radiation Chemistry

(F)

CAN CHANGES OF ERYTHROCYTE MEMBRANE RHEOLOGY ACCOUNT FOR CARDIOTOXICITY OF CYTOSTATIC DRUGS? A cisplatin study.

S. Radaković¹, I. Spasojević² and G. Bačić^{1,2}

¹*Faculty of Physical Chemistry,* ²*Center for Multidisciplinary Studies, University of Belgrade*

Abstract

The objective of our study was to investigate effects of non-cardiotoxic, antineoplastic drug cisplatin on morphology, fluidity and protein composition of erythrocytes membrane and to compare those to the effects of cardiotoxic drug 5-Fluorouracil (5-FU) in order to investigate the cause of cardiotoxicity observed during chemotherapy. Cisplatin induced echinocytosis and increase of membrane fluidity, which were similar to the effects that have been observed for 5-FU, indicating that cardiotoxicity of citostatic drugs is not related to these changes. On the other hand, cisplatin did not induce any changes in the protein composition of erythrocytes membrane, while 5-FU has been reported to do so. Therefore, the cause of cardiotoxicity of citostatic drugs seems to be in intracellular changes which affect erythrocytes functionality, rather than in modified rheological properties of blood.

Introduction

Antineoplastic drugs show cardiotoxicity which is not fully understood and have various rationalizations, such as ischemia [1], which could be related to the changes induced on erythrocytes as main oxygen carriers. One possible explanation is based on the changes of erythrocytes morphology and membrane fluidity, which could lead to the increased blood viscosity and an inadequate oxygen supply of the heart. For example, highly cardiotoxic 5-FU [2] has been reported to induce echinocytosis, which may result in an increase of blood viscosity and consequent ischemia [3]. However, it has been observed that the viscosity of blood tend to decrease rather than increase during the 5-FU infusion [2]. Since the papers on the biophysical mechanisms of cardiotoxicity of antineoplastic drugs are scarce and the existing data could be interpreted in different ways, an additional thorough clinical study is needed to resolve this issue. Alternatively, a simple investigation of in vitro effects of non-cardiotoxic drugs on erythrocytes membrane could be used. Cisplatin is anticancer drug with no reported acute cardiotoxic effects when used alone in the chemotherapy. Therefore, we performed morphological, EPR spin-labeling, and SDS-PAGE studies of its effects on erythrocytes membrane and compared these results with the effects of 5-FU to access whether changes in rheological properties of blood are possible cause of myocardial injury during anticancer therapy.

Materials and Methods

Fresh blood was drawn from three healthy volunteers, using vacutainer tubes preloaded with K₃EDTA as an anticoagulant. Final concentration of cisplatin was 0.1 mg/ml. Samples were incubated for 30, 60, 120 and 180 min at 37 °C.

Changes in Erythrocyte Morphology. Following incubation erythrocytes were fixed according to the May-Grünwald Giemsa procedure. The degree of echinocytosis was

determined according to the criteria described earlier with echinocytes divided into four types: I - IV [4].

EPR measurements of erythrocytes membrane fluidity. Spin-labeling of erythrocyte membranes using doxyl stearate nitroxide spin-probes 7-DS and 12-DS, was performed as described earlier [4]. 7-DS was used to estimate fluidity near the membrane surface, while 12-DS was used to determine fluidity of inner layers of the membrane. EPR spectra were recorded using a Varian E104-A EPR spectrometer operating at X-band (~9.1 GHz) as described earlier [4]. The order parameter (S), calculated as shown in Fig. 1, was used as an indication of membrane fluidity.

SDS-PAGE. SDS-polyacrylamide gel electrophoresis of membrane proteins of untreated and erythrocytes treated with cisplatin was performed as described earlier [5].

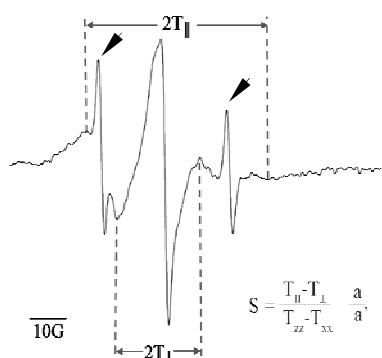


Fig. 1. Typical EPR spectrum of erythrocytes labeled with 12-DS. S : order parameter. $2T_{\parallel}$: outer hyperfine splitting. $2T_{\perp}$: inner hyperfine splitting. a : isotropic hyperfine coupling constant in crystal [$a = 1/3(T_{xx} + T_{yy} + T_{zz})$]. a' : isotropic hyperfine coupling constant in membrane [$a' = 1/3(T_{\parallel} + 2T_{\perp})$]. T_{xx} , T_{yy} , T_{zz} : hyperfine constants (for 12-DS, $T_{xx} = 6.26$ G, $T_{yy} = 5.81$ G, $T_{zz} = 33.46$ G). Two narrow lines (arrows) originate from the 12-DS in solution. For membrane labeled with 7-DS, S was calculated using constants: $T_{xx} = T_{yy} = 6.1$ G, $T_{zz} = 32.4$ G.

Results and Discussion

Cisplatin led to exposure-time-dependent transformation of erythrocytes into the echinocytic shape. Figure 2 shows similarity between the percentages of echinocytes induced by cisplatin and 5-FU. The concentration of cisplatin used here is close to the systemic concentration in the blood of patients, while the concentration of 5-FU is slightly higher than systemic, indicating that cisplatin should have higher *in vivo* potential for induction of echinocytosis in anticancer therapy than 5-FU. On the other hand, cisplatin predominantly induces formation of echinocytes type I (type II occurs only after 2h of exposure), while 5-FU led to the formation of echinocytes types II and III, which indicates different mechanisms of echinocytosis for these two cytostatics.

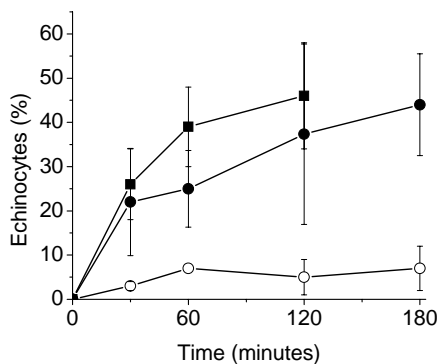


Fig. 2. Percentage of echinocytes (all four types) induced in the erythrocyte population. Samples were incubated with: 5-FU 6.5 mg/ml (■) [3], cisplatin 0.1 mg/ml (●); Control samples (○). Data for effects of 5-FU on erythrocytes morphology were re-plotted from [4].

Table 1 shows that cisplatin induces increase of the fluidity of the erythrocytes membrane near surface similar to the increase of fluidity induced by 5-FU. The fluidity of inner layers of the membrane are unchanged by cisplatin, indicating that cisplatin affects the membrane by accumulation in the surface layers which is the potential explanation for cisplatin induced echinocytosis [6].

Table 1. Effects of cisplatin and 5-FU on membrane fluidity described through order parameter (S). Data for effects of 5-FU on erythrocytes membrane fluidity were taken from [4].

Incubation period (h)		0.5	1	2	3
Samples		Order parameter (S) \pm S.D.			
7-DS	Control	0.691 \pm 0.008	0.692 \pm 0.007	0.691 \pm 0.001	0.690 \pm 0.010
	Cisplatin	0.649 \pm 0.016	0.658 \pm 0.016	0.660 \pm 0.005	0.659 \pm 0.004
	5-FU (10 mg/ml)	-	0.665 \pm 0.012	0.667 \pm 0.010	-
12-DS	Control	0.508 \pm 0.013	0.505 \pm 0.004	0.509 \pm 0.002	0.511 \pm 0.001
	Cisplatin	0.507 \pm 0.010	0.514 \pm 0.002	0.511 \pm 0.012	0.503 \pm 0.002

SDS-PAGE of the erythrocyte membrane proteins shows that, unlike 5-FU, cisplatin seems not to induce any changes in protein composition of erythrocytes membrane (data not shown). We reported earlier that 5-FU provoked increased level of membrane-bound hemoglobin and decreased intensity of Band 6 [5] which was related to the changes in the metabolism of phosphate compounds and oxygen which 5-FU induces in erythrocytes [7].

To conclude, effects of non-cardiotoxic antineoplastic drug cisplatin and cardiotoxic drug 5-FU on erythrocytes morphology and membrane fluidity are similar, therefore these changes are unlikely to be responsible for cardiotoxicity of citostatic drugs. On the other hand, cisplatin does not induce changes on protein composition of erythrocytes membrane, while 5-FU does. This indicates that cardiotoxicity of antineoplastic drugs is not related to the blood rheology, but is initiated by their effects on erythrocytes membrane proteins and/or by intracellular changes in the metabolism of phosphate compounds and oxygen, which affect erythrocytes functionality.

References

- [1] T.H. Edward *et al.*, *Circulation.*, 2004, **109**, 3122.
- [2] M. Cwikiel *et al.*, *Acta Oncol.*, 1995, **34**, 83.
- [3] G.M. Baerlocher *et al.*, *Br. J. Haematol.*, 1997, **99**, 426.
- [4] I. Spasojević *et al.*, *J. Chem. Inf. Model.*, 2005, **45**, 1680.
- [5] I. Spasojević *et al.*, *Proceedings of the 7th International Conference on Fundamental and Applied Aspects of Physical Chemistry, Belgrade, Serbia, (2004) 359.*
- [6] M.P. Sheetz., *J. Cell Biol.*, 1976, **70**, 247.
- [7] I. Spasojević *et al.*, *Ann. N.Y. Acad. Sci.*, 2005, **1048**, 311.

ADJUVANT ANTIPROLIFERATIVE AND CYTOTOXIC EFFECT OF ALOIN IN IRRADIATED HeLaS3 CELLS

A. Nićiforović, M. Adžić, B. Zarić, V. Vučić and M. B. Radojčić

*VINCA Institute of Nuclear Sciences
P.O. Box 522, Belgrade, Serbia*

Abstract

Naturally occurring phytoanthracycline, aloin, was used to radiosensitize HeLaS3 human cervix carcinoma cells. The results indicated that the cytotoxic adjuvant effect of aloin was synergistic with IR at all drug concentrations and comparable to the cytotoxicity of 5-10Gy IR alone. Radiosensitization of HeLaS3 cells was achieved by 60 μ M aloin which reduced IC₅₀ dose of IR from 3.4- to 2Gy. The cell damage by both agents compromised cell capacity to conduct programmed cell death by apoptosis, and led to the synergic cytotoxic cell death by necrosis.

Introduction

Ionizing radiation (IR) induces dose and time dependent inhibition of HeLaS3 human cervical carcinoma cell growth due to perturbation of cell-cycle and induction of apoptosis [1]. The cell proliferation was inhibited for 50% (IC₅₀) at 3.4Gy, while 50% cell cytotoxicity (EC₅₀) was not attainable within the dose range of 2-10Gy. These cellular effects correlated with increased activity of mitochondrial antioxidant enzyme Mn-superoxide dismutase (MnSOD), which was not coupled with the respective catalase (CAT) activity. The cytosolic CuZn-superoxide dismutase activity decreased [2]. Since IC₅₀ dose is rather high the aim of the presented study was to test the adjuvant phytoanthracycline, aloin, which possess less undesirable side-effects in comparison to other currently used drugs. Aloin is shown to cause perturbation of HeLaS3 cell-cycle, and increase percentage of cells in S phase and apoptosis [3]. Since aloin diminishes tumour metastatic potential induced by IR-triggered MnSOD overexpression [4], and since IR and aloin share, at least in part, a common pathways in the mechanism of their action, it is of interest to investigate their possible synergic activity in HeLaS3 cells.

Experimental Procedure

HeLaS3 cells were irradiated with 2-, 5- or 10Gy of gamma-rays from a ⁶⁰Co source at the dose rate of 20Gy/h. Different concentrations of aloin (20-100 μ M) were used to treat cells immediately after irradiation. The cell growth and viability were determined by the trypan blue exclusion assay. For cell cycle analysis, the cells were fixed in ice-cold 70% ethanol, treated with RNase-A, incubated with propidium iodide and analyzed by a FACS Calibur flow cytometer. Cell cycle distribution was determined using ModFIT software. Statistically significant differences were evaluated using one-way analysis of variance (ANOVA) and the Tukey *post-hoc* test. $p < 0.05$ was considered significant.

Results and Discussion

The adjuvant effect of aloin (20-100µM) was tested on HeLaS3 cells irradiated with standard clinical fraction dose of 2Gy and cell viability (% of viable cells, *Figure 1A*) and viability index (ratio of viable cells in treated vs. control sample, *Figure 1B*) were followed. The results clearly indicated that the cytotoxic adjuvant effect of aloin was synergistic with IR at all drug concentrations and comparable to the cytotoxicity of 5-10Gy IR alone. Moreover, 60µM aloin as adjuvant reduced IC₅₀ dose of IR from 3.4 to 2Gy.

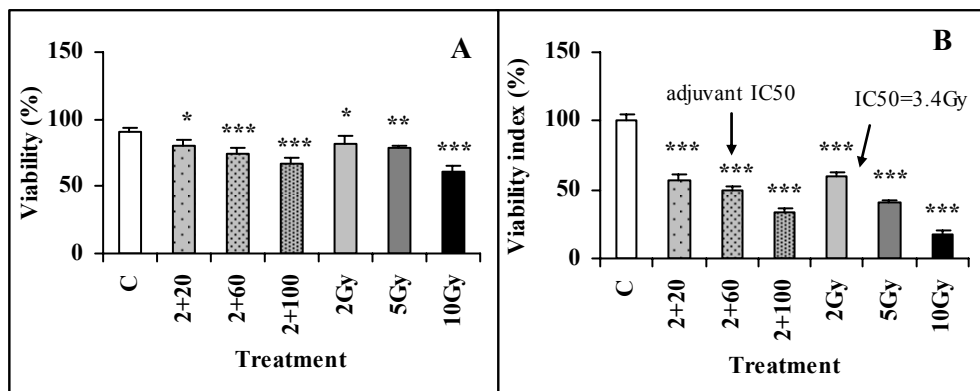


Fig. 1. Combined effect of IR (Gy)+aloin (µM) or IR alone on HeLaS3 cell viability (A) and viability index (B). Data are presented as mean ± SD (n=6)

Flow-cytometric analysis of PI stained HeLaS3 cells indicated perturbation of the cell cycle *i.e.* significant decrease of cells in G1 phase (*Figure 2*) which was followed by the increased arrest of cells in S phase and increased apoptotic cell death (subG0/G1 peak). The adjuvant effect of aloin was observed predominantly in the S phase of cell cycle, at all drug concentrations. Although, adjuvant effect of aloin on cell apoptosis was not observed, aloin was still effective cytotoxic agent leading to decreased viability of survived cells most probably by necrosis [2].

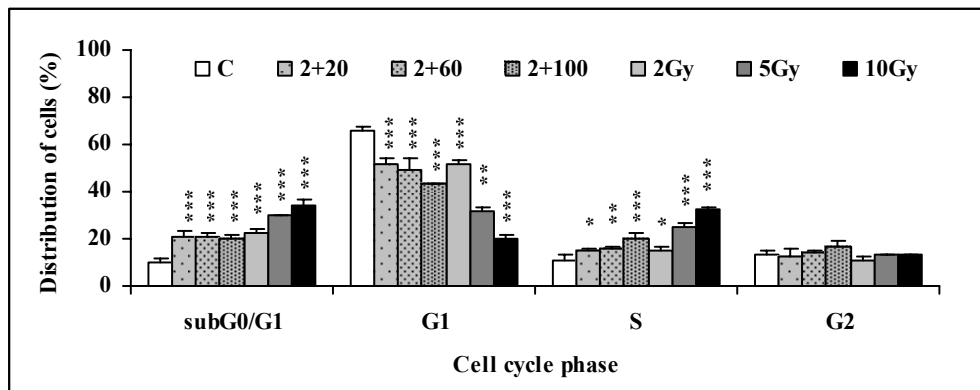


Fig. 2. Cell cycle distribution of HeLaS3 cell treated with IR (Gy)+aloin (µM) or IR alone. Data are presented as mean ± SD (n=3)

The synergic effect of aloin+IR on cell viability and in S-phase cell cycle arrest indicated that both agents may share a common regulatory pathway. Since, HeLaS₃ cells constitutively possess enhanced activity of MnSOD, and since both IR or IR+aloin caused its further elevation (which was not followed by the respective CAT activity) both agents caused H₂O₂ accumulation (data not shown). Increased concentration of this toxic ROS may lead to their synergism in cytotoxicity. High H₂O₂ concentration could also be the reason for down-regulation of CuZnSOD observed in either IR or IR+aloin treated cells (data not shown). Decreased CuZnSOD activity could contribute to decreased cell proliferation, emphasizing the importance of CuZnSOD in HeLaS₃ cell growth [5]. In addition to that, increased MnSOD and H₂O₂, *via* Cip1 (p21) and cyclins D3 inhibition, may lead to the S phase cell cycle arrest. Although, IR or aloin alone increased subG₀/G₁ peak, their synergic effect on cell apoptosis was not observed. This result indicates that the mechanism of apoptosis induction by IR and aloin are probably different. Due to that, simultaneous cell damage by both agents could compromise cell capacity to conduct programmed cell death by apoptosis, and instead may lead to the synergic cytotoxic cell death by necrosis. The synergism of IR+aloin induced cell cytotoxicity is reflected in reduction of IC₅₀ dose to 2Gy by 60μM aloin.

Conclusion

The adjuvant effect of aloin in irradiated HeLaS₃ cells is reflected in the reduction of IC₅₀ cytotoxicity dose from 3.4Gy to 2Gy in the presence of 60μM aloin. Its radiosensitizing effect is achieved through up-regulation of MnSOD activity leading to accumulation of toxic H₂O₂. This toxic ROS, either directly or through down-regulation of CuZnSOD activity, causes decrease in cell proliferation. Thus, through the altered redox balance, IR+aloin, compromises HeLaS₃ cell capacity to conduct programmed cell death by apoptosis, and instead lead to the synergic cytotoxic cell death by necrosis.

References

- [1] A. Nićiforović, B. Zarić, A. Dakić, N. Tišma, M. B. Radojčić, *Jugoslav.Med. Biochem.*, 2004, **23**, 1-8.
- [2] A. Nićiforović, M. Adžić, B. Zarić, V. Vučić, M. B. Radojčić, S.D.Spasić, submitted to *Redox.Report*-april 2006.
- [3] A. Nićiforović, M. Adžić, B. Zarić, M. B. Radojčić, S.D.Spasić, submitted to *Free Radical Res.*-april 2006.
- [4] E. Barrantes, M. Guinea, *Life Sci.*, 2003, **72**, 843-850.
- [5] T. T. Huang; M. Yasunami, E. J. Carlson, A. M. Gillespie, A. G. Reaume; E. K. Hoffman, P. H. Chan, R. W. Scott, C. J. Epstein, *Arch. Biochem. Biophys.* 1997, **344**, 424-432.

THE EFFECT OF HYDROGEN BONDING INTERACTIONS ON THE REACTIVITY OF A NOVEL DISULFIDE-SPECIFIC PEGYLATION REAGENT

M. Zloh¹, S. Balan², S. Shaunak³ and S. Brocchini²

¹Department of Pharmaceutical and Biological Chemistry and ²Department of Pharmaceutics, The School of Pharmacy, University of London, 29/39 Brunswick Square, London, UK
(mire.zloh@pharmacy.ac.uk)

³ Faculty of Medicine, Imperial College London, Hammersmith Hospital, Ducane Road, London W12 0NN, UK

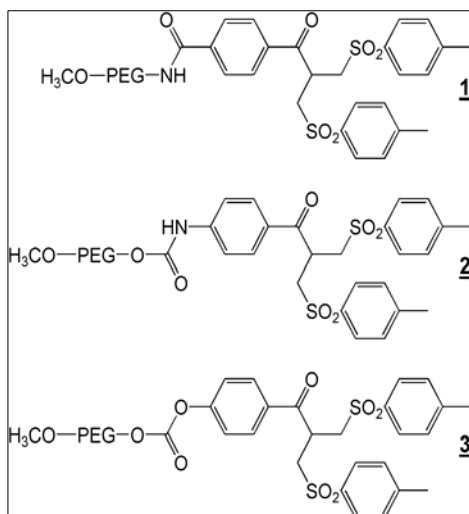
Abstract

PEGylation is an important technology to improve the pharmacokinetic properties of proteins and of peptides. Novel site-specific PEG *bis*-sulfone reagent was prepared and successfully conjugated to the disulfides of interferon α -2b with high efficiency. New PEG *bis*-sulfone reagents with different linkages between the PEG and the *bis*-sulfone moiety were prepared. Experimentally, they were found to display differences in their propensity for reaction. Molecular modelling of these reagents suggested that hydrogen bond mediated interactions led to conformational changes in the molecules and that these interactions accounted for the differences in the reactivity that was observed.

Introduction

The covalent conjugation of poly(ethylene glycol) (PEG) to a protein (PEGylation) is clinically proven to improve the properties of proteins as medicines. Our novel strategy to PEGylate proteins exploits the thiol selective chemistry of the two sulfur atoms that are derived from an accessible native disulfide bond [1]. It involves disulfide reduction to free the two cysteine sulfur atoms which then undergo reaction with the *bis*-thiol selective PEG reagent **1**. Site-specific PEGylation results via a three-carbon bridge insertion between the two cysteine sulfurs. The cross-functionalised bis-sulfone reagent **1** must first undergo facile elimination of one equivalent of cresol sulfonic acid to generate a double bond for reaction with thiolate. This results in elimination of the other cresol sulfonic acid to generate another double bond for the second thiolate addition.

Reagents **2** and **3** were prepared from less expensive PEG precursors than those used to prepare reagent **1**. Surprisingly, reagent **2** did not undergo protein conjugation because the first elimination of sulfonic acid did not occur. Here, we demon-



strate the use of molecular modeling to rationalize this unexpected difference in chemical reactivity even when the structural changes were well away from the functional end of the molecules.

Results and Discussion

The elimination reactions of the PEG *bis*-sulfones **1-3** were monitored by the formation of the corresponding alkenyl PEG mono-sulfone in phosphate buffer, pH 7.2 – 7.8 using RP-HPLC and $^1\text{H-NMR}$ [data not shown]. Elimination was rapid for the carbonate *bis*-sulfone **3**. In contrast, the urethane *bis*-sulfone **2** did not undergo elimination. It was first presumed that different inductive effects through the aromatic rings caused changes in the electron density and charges on the atoms involved in the elimination reaction.

All starting *bis*-sulfones with truncated PEG chains were subjected to Monte Carlo conformational search using Macromodel v9.1 [2] and the lowest energy structures were further optimized using DFT calculations (B3LYP/6-31**) utilizing Jaguar v6.5 [3]. Partial charges and the Highest Occupied (HOMO) and Lowest Unoccupied (LUMO) molecular orbitals of the *bis*-sulfones were similar (Figure 1). The HOMO-LUMO gap for all three reagents did not correlate to the different propensities for elimination of the *bis* sulfones. The induction effects caused by differences in PEG linkage structure (e.g. carbonate **3** vs urethane **2**) could not explain why the urethane **2** did not undergo elimination.

Although only 2 ethylene glycol repeat units were included in these calculations, it was noticeable that there was a difference in the 3D arrangement of the PEG chain (Figure 1). Subsequently, 22 more repeat units were added resulting in a 1 kDa PEG moiety. The full Monte Carlo Multiple Minimum (MMMC) conformational search was conducted for compounds **2** and **3** and their lowest energy structures are shown in Figure 2.

The carbonate bond and the negative oxygen atoms of **3** created an extended structure thereby exposing the *bis*-sulfone moiety to the solvent. The urethane moiety in **2** displayed a hydrogen bond donor site close to the aromatic ring which attracted a PEG oxygen. This conformationally constrained the PEG to localise close to the *bis*-sulfone rings through a network of favourable interactions. This crowding of PEG towards the sulfone moieties in **2** and consequent steric hindrance potentially caused the inability of the PEG *bis*-sulfone urethane **2** to undergo facile elimination as was observed for *bis*-sulfones **1** and **3**.

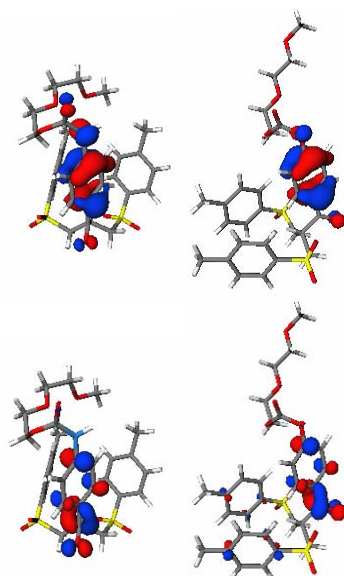


Fig. 1. HOMO (top) and LUMO (bottom) orbitals of **2** (left) and **3** (right).

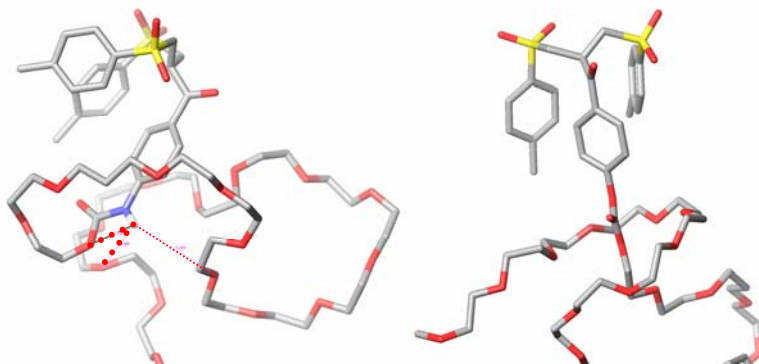


Fig. 2. Lowest energy structures of urethane **2** (left) and carbonate **3** (right) PEG *bis*-sulfone. Conformational search was carried out using MacroModel, MMFF force field and implicit representation of solvent using Generalized Born Surface Area (GBSA) method [4]. Non-polar H atoms omitted for clarity.

Since the hydrogen bonding of the urethane moiety with PEG could be the reason for the lack of elimination in an aqueous environment, molecular simulation of the urethane **2** immersed in the cluster of CHCl_3 molecules was performed to evaluate the effects of solvent. It was found that the hydrogen bonding interactions were not strong enough to bring the PEG close to the *bis*-sulfone moieties. This resulted in the *bis*-sulfone functional end of the molecule being more available for the elimination reaction. Further experiments using $^1\text{H-NMR}$ confirmed that urethane PEG *bis*-sulfone reagent **2** underwent elimination in CHCl_3 .

Conclusion

The propensity for elimination reaction and protein PEGylation was found to be dependent on the structure of the linkage between PEG and the *bis*-sulfone moiety. Theoretically, it was found that hydrogen bonding interactions in the urethane moiety of *bis*-sulfone **2** resulted in steric and conformational effects that could be the major determinants for the lower reactivity of this PEG *bis*-sulfone compared to *bis*-sulfones **1** and **3**.

References

- [1] S. Shaunak, A. Godwin, J.-W. Choi, S. Balan, E. Pedone, D. Vijayarangam, S. Heidelberg, I. Teo, M. Zloh & S. Brocchini, *Nature Chem. Biol.* 2006, doi:10.1038/nchembio786.
- [2] F. Mohamadi, N.G.C. Richards, W.C. Guida, R. Liskamp, M. Lipton, C. Caufield, G. Chang, T. Hendrickson, W.C. Still, *J. Comput. Chem.* 1990, **11**, 440-467.
- [3] Jaguar 5. 5. Schrodinger, L.L.C., Portland, OR, 1991–2005.
- [4] D. Qiu, P.S. Shenkin, F.P. Hollinger, W.C. Still, *J. Phys. Chem. A* 1997, **101**, 3005-3014.

MODELING THE TEMPERATURE DEPENDENCE OF CATALASE-LIKE ACTIVITY OF HORSE RADISH PEROXIDASE

A. Popović-Bijelić¹, G. Bijelić², Lj. Kolar-Anić¹ and V. Vukojević³

¹ Faculty of Physical Chemistry, Belgrade, ² Center for Multidisciplinary Studies, Belgrade, Serbia, ³ Department of Clinical Neuroscience, Karolinska Institute, Stockholm, Sweden

Abstract

Temperature dependence of the catalase-like activity of horseradish peroxidase was investigated experimentally in the temperature range 278-328 K. Extension of the model is proposed to account for the experimental observations and numeric simulations of the reaction kinetics at different temperatures were carried out.

Introduction

Catalase-like activity of horseradish peroxidase (HRP) is protective in plants and is typically being activated in response to environmental stress (pH, temperature, draught) or pathogen attack [1,2]. In addition, this reactive pathway is attracting considerable attention in food processing because of its impact on food quality [3] and in advanced technology for the building of bio-sensors [4]. Therefore, a renewed interest in studying and modeling [2-5] the reaction mechanism of this pathway has arisen.

Experimental

The reaction was initiated by adding $1.0 \cdot 10^{-6}$ mol dm⁻³ HRP to the reaction medium containing $5 \cdot 10^{-3}$ mol dm⁻³ H₂O₂ in $5 \cdot 10^{-2}$ mol dm⁻³ sodium phosphate buffer, pH = 6.0. The ratio of initial concentrations of hydrogen peroxide and HRP, $[\text{H}_2\text{O}_2]_0/[\text{HRP}]_0$, was set to 1000. The temperature was controlled within ± 0.01 °C. The course of the reaction was monitored spectrophotometrically and potentiometrically. The concentration of H₂O₂ was determined by measuring the absorbance at 240 nm, taking $\epsilon_{240\text{nm}} = 41.25 \cdot 10^3$ mol⁻¹ dm³ cm⁻¹ [2], the enzyme concentration was estimated using the Soret extinction coefficient, $\epsilon_{403\text{nm}} = 102 \cdot 10^3$ mol⁻¹ dm³ cm⁻¹ [6] and oxygen production was measured using an oxygen electrode.

Result and Discussion

Oxygen production curves (Figure 1) show distinct kinetic profiles, suggesting a change in the reaction mechanism due to the increase in temperature.

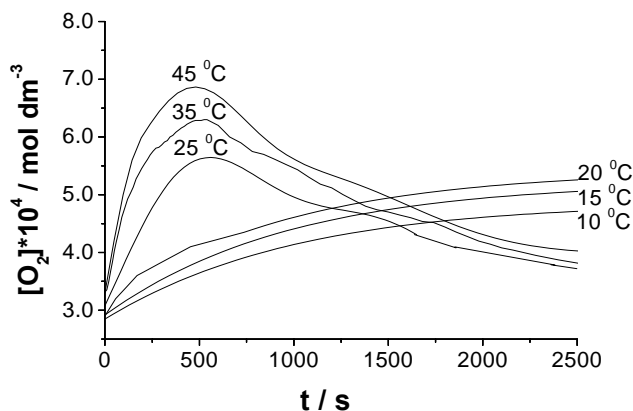


Fig. 1. Oxygen production at different temperatures. At temperatures lower than 298 K, a hyperbolic production profile typical for a product can be observed, whereas at higher temperatures the kinetic profile of oxygen production changes and resembles a profile of an intermediate.

Initial rates of oxygen formation (v_0) were determined from oxygen production measurements during the initial 25 s. They exhibit linear dependence on the initial concentration of the enzyme in the concentration range $7 \cdot 10^{-7} \leq [\text{HRP}]_0 \leq 5 \cdot 10^{-6} \text{ mol dm}^{-3}$ [5] and exponential dependence on temperature (Figure 2).

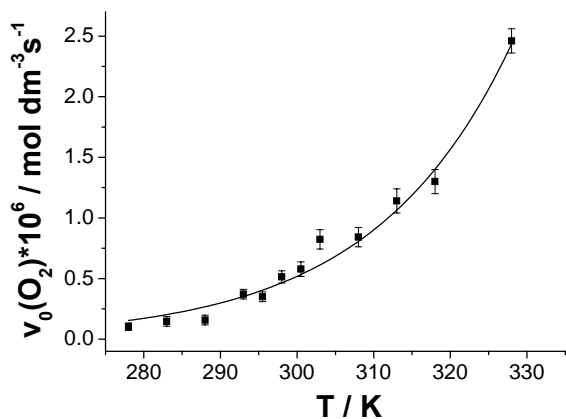
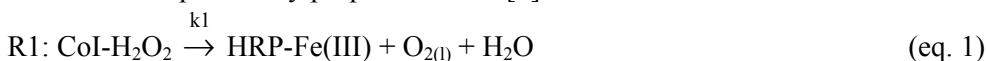


Fig. 2. Exponential increase of the initial rates of oxygen production at elevated temperatures.

To account for the consumption of oxygen, elementary steps proposed in [2] and [7] were added to previously proposed model [5]:



When the reaction is conducted in a solution, evaporation of oxygen from the reaction solution may become significant at higher temperatures. Therefore, evaporation of dissolved oxygen from the reaction mixture is introduced:



Thus, the rate of $\text{O}_{2(l)}$ formation in the enlarged model is:

$$v(\text{O}_{2(l)}) = k_1[\text{CoI-H}_2\text{O}_2] - k_2[\text{HRP-Fe(II)}][\text{O}_{2(l)}] + k_{-2}[\text{CoIII}] - k_3[\text{O}_{2(l)}] + k_{-3}[\text{O}_{2(g)}] \quad (\text{eq.4})$$

Results of numerical simulations of the reaction kinetics at different temperatures are given in Figure 3.

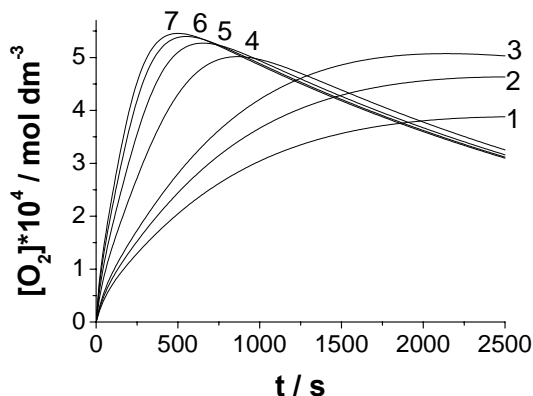


Fig. 3. Numeric simulations of temperature dependence of oxygen production by the enlarged model. Curve 3 is a simulation of actual oxygen production at 293 K. Curves 1, 2 and 4 – 7 were obtained by multiplying the relevant kinetic constants (k_1 , k_2 and k_{-2} from eq. 1 and 2) by factors 0.7, 0.85, 2, 4, 8 and 15, respectively.

Conclusion

It is shown that oxygen production through the catalase-like pathway increases exponentially with temperature in the range 278 – 328 K and shows different kinetic profiles below and above 298 K. Model simulations indicate that enhanced evaporation of molecular oxygen from the reaction solution is the main root through which oxygen is lost at elevated temperatures. However, in living plants or in technological processing, where the partial pressure of oxygen can be much higher, its catalytic degradation by HRP can be prominent. In plants this may be a secondary defense mechanism against oxidative stress.

Acknowledgment

This study was supported in part by The Ministry of Science and Environmental Protection, SCG; Project no.142025.

References

- [1] Penel, C., Gaspar, T.H., and Greppin, H. (eds) (1992) *Plant Peroxidases: 1980-1990*, University of Geneva, Geneva, Switzerland.
- [2] Hernandez-Ruiz, J., Arnao, M.B., Hiner, A.N.P., Garcia-Canovas, F., Acosta, M., *Biochem. J.*, 2001, **354**, 107-114.
- [3] Dicko, M. H., Gruppen, H., Traoré, A. S., Voragan, A. G. J., van Berkel, W. J. H., *Bio-technol. Mol. Biol. Rev.*, 2006, **1**, 21-38.
- [4] Dimcheva, N., Horozova, E., *Anal. Bioanal. Chem.*, 2005, **382**, 1374-1379.
- [5] Popović-Bijelić A., Bijelić, G., Kolar-Anić, Lj., Vukojević, V., *Ann.N.Y.Acad.Sci.*, 2005, **1048**, 457-460.
- [6] Dunford, H.B., (1999) *Heme Peroxidases*, J.Wiley and Sons Inc., New York.
- [7] Rodriguez-Lopez, J.N., Smith, A.T., Thorneley, R.N.F., *J. Biol. Chem.*, 1997, **272**, 389-395.

PARTITIONING OF QUINAPRIL ANION BETWEEN CETYLTRIMETHYLAMMONIUM BROMIDE MICELLES AND WATER

O. Čudina¹, S. Vladimirov¹, M. Čomor² and I. Janković²

¹*Institute of Pharmaceutical Chemistry and Drug Analysis, Faculty of Pharmacy, Vojvode Stepe 450,
P.O. Box 146, Belgrade, Serbia*

²*Laboratory for Radiation Chemistry and Physics, Vinča Institute of Nuclear Sciences, P.O. Box 522,
Belgrade, Serbia*

Abstract

The interaction of the anion of quinapril (QUIN), angiotensin converting enzyme (ACE) inhibitor, with cationic surfactant cetyltrimethylammonium bromide (CTAB) was studied as a model system for drug/membrane interactions. From the dependence of differential absorbance at $\lambda=272$ nm on CTAB concentration, by using mathematical model that treats the solubilization of QUIN anion as its binding to specific sites in the micelles (Langmuir adsorption isotherm), the binding constant K_b was obtained.

Introduction

Drug interactions with heterogeneous media (micelles, lipid bilayer vesicles, biomembranes) induce changes in some physicochemical properties of the drugs (solubility, spectroscopic and acid-base properties) [1]. By monitoring these changes it is possible to quantify the degree of drug/micelle interaction which is expressed as micelle/water partition coefficient, K_x , and/or binding constant, K_b . Their elucidation is important for the understanding of interactions with biomembranes and for the quantitative structure-activity relationship of drugs, as well as for the use of surfactants in HPLC or MEKC in drug quality control.

In this work, the effect of cationic micelles of cetyltrimethylammonium bromide, CTAB, on the spectroscopic properties of the anion of angiotensin converting enzyme (ACE) inhibitor quinapril (3-isoquinolinecarboxylic acid, 2-[2-[1-(ethoxycarbonyl)-3-phenylpropyl]amino]-1-oxopropyl]-1,2,3,4-tetrahydro-mono-hydrochloride, $C_{25}H_{30}N_2O_5ClH$), QUIN is described. The absorption spectrophotometry was used to quantify the micelle/water partition coefficient and QUIN anion/micelle binding constant, by applying pseudo-phase [2] and Langmuir adsorption isotherm [3] mathematical models respectively.

Experimental

Spectrophotometric measurements were recorded on a Perkin-Elmer Lambda 35, double-beam UV-vis spectrophotometer with 1.0 cm quartz cuvettes at 25°C. Instrumental conditions were: wavelength range 240 – 300 nm; slit width 1.0 nm; scan speed 60 nm min⁻¹. Stock solutions of 40 mM quinapril hydrochloride (Gödecke GmbH, Freiburg, Germany) were prepared by dissolving the compound in methanol.

Results and Discussion

Quinapril is a polyfunctional molecule with the pK_a values of 3.29 ± 0.40 and 5.38 ± 0.39 [4]. The absorption spectra of QUIN, both in aqueous and CTAB micellar solutions, were measured at $pH=1.7$ (QUIN cation) and $pH=8$ (QUIN anion). The effect of cationic micelles on the absorption spectrum of QUIN is observed only in basic solutions showing the importance of opposite charges in binding of quinapril ions to micelles. On adding CTAB the QUIN anion absorption maximum at 259.5 nm is shifted to 261 nm, with the formation of the shoulder at 264 nm and the pronounced new maximum at 272 nm (Figure 1). The bathochromic shift observed is the consequence of the QUIN anion being transferred from the highly polar phase (water) to a less polar site (micelle surface layer).

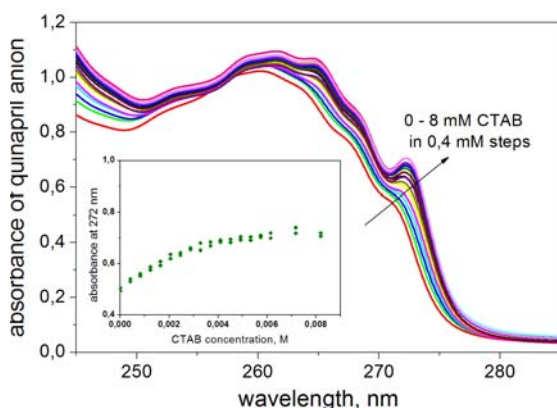


Fig. 1. Absorption spectra of 2mM QUIN containing increasing amounts of CTAB
Inset: A_{272} vs c_{CTAB}

The absorption spectra of 2 mM QUIN at $pH=8$ in the wavelength spectral range from 245 to 285 nm as a function of various concentrations of CTAB are depicted in Figure 1, with the inset showing the relation between A_{272} and c_{CTAB} . It is obvious that A_{272} asymptotically increases with increasing CTAB concentration, above its critical micelle concentration ($CMC=0.5$ mM determined by SLS), reaching the plateau (A_{272}^{∞}) when all added QUIN is solubilized in micelles. A_{272} can be used for the calculation of partition coefficient K_x , a thermodynamic parameter that represents the affinity of a given solubilize to the micellar phase relative to the aqueous one, according to the pseudo-phase model [2]:

$$\frac{1}{\Delta A_{272}} = \frac{1}{\Delta A_{272}^{\infty}} + \frac{n_w}{K_x \cdot \Delta A_{272}^{\infty} \cdot (c_{QUIN} + c_{CTAB} - CMC)}$$

where $\Delta A_{272} = A_{272} - A_{272}^w$, $\Delta A_{272}^{\infty} = A_{272}^{\infty} - A_{272}^w$, A_{272}^w being the absorbance of QUIN anions in water and $n_w = 55.5$ M the molarity of water

The partition coefficients K_x evaluated for series of micellar solutions containing increasing concentrations of CTAB ($c_{CTAB} = 0.5 - 8$ mM) and solubilizing different

concentrations of quinapril ($c_{\text{QUIN}} = 0.4 - 2 \text{ mM}$) were found to decrease with the increase of QUIN concentration. This indicates that solubilization is a competitive process that becomes progressively more difficult as the amount of drug incorporated into the micelles increases, the behavior being consistent with an adsorption-like phenomenon.

Hence, the solubilization of QUIN anion in CTAB micelles may be treated as an adsorption process by fitting the data to a Langmuir adsorption model [3]:

$$c_{\text{QUIN}} (1-f) = \frac{1}{K_b} + \frac{c_{\text{CTAB}} - \text{CMC}}{n} * \frac{(1-f)}{f}$$

where $f = \Delta A_{272} / \Delta A_{272}^{\infty}$ is the fraction of the associated QUIN anions, and n denotes the number of CTAB molecules forming the site for QUIN anion binding.

From the measurements of A_{272} in 2 mM QUIN containing increasing concentrations of CTAB (0.5 – 8 mM) at pH=8 following values of $K_b = (2.3 \pm 0.4) \times 10^3 \text{ M}^{-1}$ and $n = 0.94 \pm 0.09$ were obtained.

Conclusions

From the results obtained it was concluded that one CTAB molecule is forming the site for QUIN anion binding. QUIN anion is most probably situated in the micelle surface layer, with its aromatic part of the molecule immersed in the micelle and negatively charged carboxylate group at the same level as the positively charged quaternary ammonium groups of CTAB, both polar and electrostatic effects playing important role in its binding to CTAB micelles. The decrease of the partition coefficient with QUIN concentration is consistent with adsorption-like phenomenon.

References

- [1] S. Schreier, S. V. P. Malheiros, E. de Paula, *Biochim. Biophys. Acta*, 2000, **1508**, 210-234.
- [2] H. Kawamura, M. Manabe, Y. Miyamoto, Y. Fujita, S. Tokunaga, *J. Phys. Chem.*, 1989, **93**, 5536-5540.
- [3] L. Sepulveda, *J. Colloid Interf. Sci.*, 1974, **46**, 372-379.
- [4] S. Hillaert, W. Van den Bossche, *J. Chromatogr. A*, 2000, **895**, 33-42.

PROTOLYTIC EQUILIBRIA AND STABILITY OF QUERCETIN IN AQUEOUS SOLUTIONS

T. Momić, J.Savić and N. Miljević

*Vinča Institute of Nuclear Sciences, Department of Physical Chemistry, P.O. Box 522, Serbia
(momict@vin.bg.ac.yu),*

Abstract

The protonation constant of carbonyl group and dissociation constants of -OH groups of quercetin were determined from the changes in UV and IR spectra of aqueous solutions of various acidities. The distribution diagram of ionic species was calculated. Besides, the stability of quercetin was investigated as the function of pH and concentration. The analysis of kinetic curves indicated that a noncatalyzed conversion took place together with the autocatalyzed degradation of quercetin.

Introduction

Quercetin belongs to the group of flavonoids and is widely distributed in natural plants. It is a potent inhibitor of some enzymes (myeloperoxidase, reductase) and has the antioxidant properties due to free radical scavenging. Besides, it undergoes to rapid degradation in the biological systems [1,2]. The knowing of its ionic forms, stability and protolytic behavior in aqueous media is of a great importance for the potential biological and clinical use.

Experimental

UV and IR spectra were recorded in water solutions, immediately after preparation. The acidity of water was adjusted either by HCl or NaOH. The constant ionic strength was maintained (0.1 M) by NaCl. Stock solution of 1×10^{-2} M quercetin was prepared in ethanole. The measurements were carried out with a "sandwich" IR cell composed of two CaF_2 windows separated by a 200 μM polyethylene spacer. All kinetic measurements were performed at 18 °C.

Results and Discussion

Equilibrium studies of quercetin

The absorption spectra of 5×10^{-5} M quercetin (Fig.1) were recorded as the dependence of the acidity in the acidity range pH 2 - 10. The spectra showed two characteristic absorption maxima at about 260 nm and 380 nm. The pH increase induced the bathochromic shift of both maxima. The spectra changed due to the dissociation of -OH groups and protonation of carbonyl group. The protonation of carbonyl group was confirmed by comparison of IR spectra at pH 2 and pH 5 (Fig.1, inset). The characteristic band of quercetin ($>\text{C}=\text{O}$) at 1660 cm^{-1} can be noticed at pH 5, but disappears when the acidity of the solution increased to pH 2. To calculate

the protolytic constants from the spectrophotometric data a non-linear least squares regression analysis on Eq. 1 was performed in the appropriate pH ranges:

$$A = \frac{C_q [\epsilon_6 [H^+]^6 + \epsilon_5 \beta_5 [H^+]^5 + \epsilon_4 \beta_4 [H^+]^4 + \epsilon_3 \beta_3 [H^+]^3 + \epsilon_2 \beta_2 [H^+]^2 + \epsilon_1 \beta_1 [H^+] + \epsilon_0 \beta_0]}{[H^+]^6 + \beta_5 [H^+]^5 + \beta_4 [H^+]^4 + \beta_3 [H^+]^3 + \beta_2 [H^+]^2 + \beta_1 [H^+] + \beta_0} \quad (1)$$

where A=absorbance, C_q=analytical concentration of quercetin, ε_n=extinction coefficient, β_n=cumulative protonation constant. The equilibria and related protolytic constants are presented in Table 1.

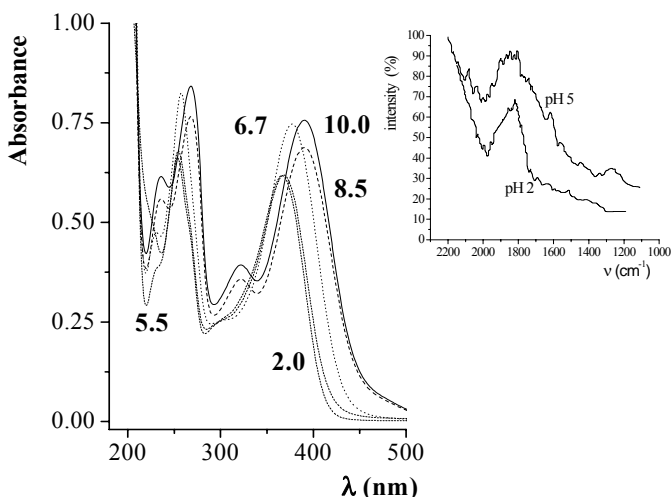


Fig. 1. Absorption spectra of 5×10^{-5} M quercetin at different acidities; Inset: IR spectra of quercetin at pH 2 and pH 5

The distribution species diagram was calculated using the experimentally found protolytic constants of quercetin and is shown on Fig.2. It is obvious from the distribution of ionic forms that at the pH 5 - 10 at least three ionic species were present in aqueous solutions.

Table 1. Protolytic constants of quercetin in aqueous media

equilibria	pK
$RH_5 + H^+ \leftrightarrow RH_6^+$	3.86 ± 0.21
$RH_4^- + H^+ \leftrightarrow RH_5$	5.50 ± 0.25
$RH_3^{2-} + H^+ \leftrightarrow RH_4^-$	7.15 ± 0.42
$RH_2^{3-} + H^+ \leftrightarrow RH_3^{2-}$	8.00 ± 0.46
$RH^4 + H^+ \leftrightarrow RH_2^{3-}$	9.57 ± 0.25
$R^{5-} + H^+ \leftrightarrow RH^4$	11.40 ± 0.24

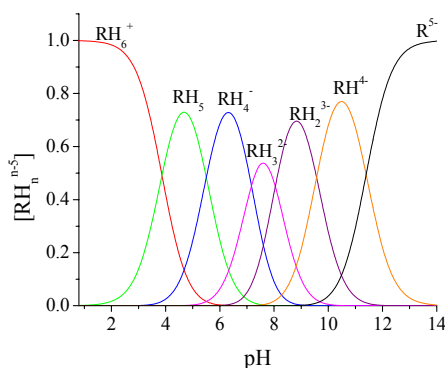


Fig. 2. Distribution of ionic forms of quercetin as a function of pH

Stability of quercetin in aqueous solutions

The stability of quercetin was investigated as the function of the medium acidity, by following the change of the absorption spectra as the function of time. The intensity of the both characteristic absorption maxima decreased, since the low intensity maximum at about 430 nm appeared, followed by the clear isobestic point at 410 nm (Fig.3, inset). The similar spectral changes were noticed in the whole acidity range. The S-shaped kinetic curves (Fig.3) were experimentally obtained, that indicated a non-catalyzed conversion together with the autocatalyzed reaction [4]. These data are in accordance with the earlier findings, which indicate that some flavonoids undergo to

the autoxidation by the air oxygen [3]. The experimental results obtained in this work showed that the rate of the autoxidation of quercetin increase with pH.

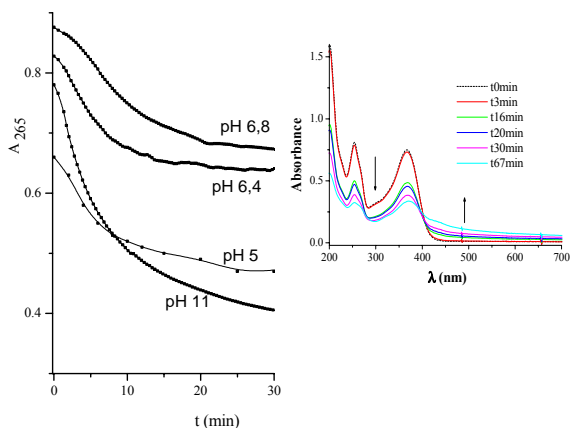


Fig. 3. Kinetic traces of 5×10^{-5} M quercetin at 265 nm;
Inset: Absorption spectra of quercetin at pH 6 as the
function of time

Conclusion

The present work shows that quercetin stability strongly depends on pH. It can be ascribed to the change of the ionic forms of the molecule, which leads to the formation of polyanions. These forms are highly effective in stabilizing radicals, thus allowing autoxidation to proceed under relatively mild alkaline conditions.

References

- [1] J. Pincemail, C. Deby, A. Thirion, M. de Bruyn-Dister and R. Goutier, *Experientia*, 1988, **44**, 450-453.
- [2] D.W. Boulton, U.K. Walle and T. Walle, *J. Pharm. Pharmacol.*, 1999, **51**, 353-359.
- [3] O. Dangles, G. Fargeix and C. Dufour, *J. Chem. Soc., Perkin Trans.* 1999, **2**, 1387-1395.
- [4] R. Schmid and V. N. Sapunov in: *Non-Formal Kinetics*, Vol. 14, H. F. Ebel (Ed.), Verlag Chemie GmbH, Weinheim, 1982.

INHIBITION OF MYELOPEROXIDASE BY QUERCETIN

T. Momić¹, Z. Vujčić² and V. Vasić¹

¹*Vinča Institute of Nuclear Sciences, Laboratory for Physical Chemistry, P.O. Box 522, Serbia, (momict@vin.bg.ac.yu),*

²*Faculty of Chemistry, University of Belgrade, P.O. Box 158, Serbia*

Abstract

Reaction mechanism of quercetin induced inhibition of myeloperoxidase isolated from human neutrophils was proposed by following peroxidase activity of the enzyme, using the *o*-dianisidine and H₂O₂ as substrates. The dependence of initial reaction rate vs. H₂O₂ concentration in the absence and presence of quercetin revealed the reaction mechanism that involved the enzyme inhibition by the excess of the substrate. The rate and equilibria constants for proposed reaction paths were determined

Introduction

The heme enzyme myeloperoxidase (MPO) is a major neutrophil protein and is also present in monocytes. Depending on substrate availability, this enzyme paths through halogenation and/or the peroxidase cycle [1]. Halogenating agents, especially hypochlorous acid, promote the oxidative killing of micro-organisms by neutrophils and the inflammatory tissue damage that the cells cause. Quercetin (3,5,7,3',4'-pentahydroxy flavon), one of the most prevalent member of flavonoids, exerts anticancer, antiviral, antioxidant and free-radical scavenging abilities [2]. In the present study the mechanism of quercetin induced inhibition of MPO was investigated.

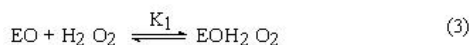
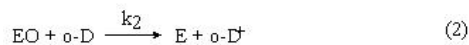
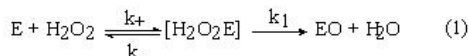
Experimental

MPO was purified from human neutrophils to a purity index (A_{430}/A_{280}) > 0.70 as described previously [3]. Enzyme activity was determined using the *o*-dianisidine (*o*-D) assay in 3 mL 50 mM phosphate buffer (pH 6.0) containing 110 ng MPO at 25°C. The reaction rate was followed in the initial reaction phase in the absence or presence of inhibitor and H₂O₂, while maintaining concentration of *o*-D constant.

Results and Discussion

MPO catalyses the oxidation of *o*-D by H₂O₂ [4]. Quercetin inhibits MPO activity with IC₅₀=(5.28 ± 0.36) μM, i.e. the inhibitor concentration that induced 50% of enzyme inhibition. The reaction mechanism between MPO and quercetin was investigated by measuring the initial reaction rate as the function of H₂O₂ in the concentration range from 2-700 μM. Two series of kinetic experiments were performed, using 0.53 mM and 1.5 mM *o*-D. The concentration of quercetin was varied from 2x10⁻⁶ to 8x10⁻⁶ M, since these concentrations significantly inhibited the enzyme activity. Fig. 1 shows the dependence of the initial rate of oxidation of *o*-D as

a function of H_2O_2 concentration in the absence (control) and the presence of 2×10^{-6} M quercetin in the reaction assay containing 1.5 mM *o*-D. The shape of the curves suggested the reaction mechanism that involved the substrate inhibition of the enzyme and is consistent with the reaction scheme presented below:



where E - free enzyme in fero state, H_2O_2E - the complex between H_2O_2 and enzyme, EO - feryl state of the native enzyme, EOH_2O_2 - the complex between H_2O_2 and compound I, Q - quercetin, EOQ - the complex between compound I and Q. k_1 and k_2 are rate constants for the formation of EO complex and oxidised form of *o*-D. K_1 is the equilibrium constant for the complex formation between the EO complex and H_2O_2 . K_i and K_i' are the equilibria constants for dissociation of quercetin complexes with enzyme. Under the experimental conditions with 1.5 mM *o*-D, the concentration of MPO fulfilled the relation $E \ll H_2O_2 + o-D$, and the concentration of $H_2O_2 \ll o-D$. The change of [*o*-D] during the course of the reaction underwent minimal changes. Using this into account and applying the steady-state assumption with respect to H_2O_2E and EO, the expression for the initial reaction rate of *o*-D⁺ generation as the function of H_2O_2 was obtained:

$$v_0 = \frac{k_1 k_2 K_M^{-1} [E]_0 [o-D]_0 [H_2O_2]}{\left(1 + \frac{[Q]}{K_i}\right) k_2 [o-D]_0 + K_M^{-1} k_1 \left(1 + \frac{[Q]}{K_i} + \frac{k_2}{k_1} [o-D]\right) [H_2O_2] + K_M^{-1} K_1 k_1 [H_2O_2]^2} \quad (6)$$

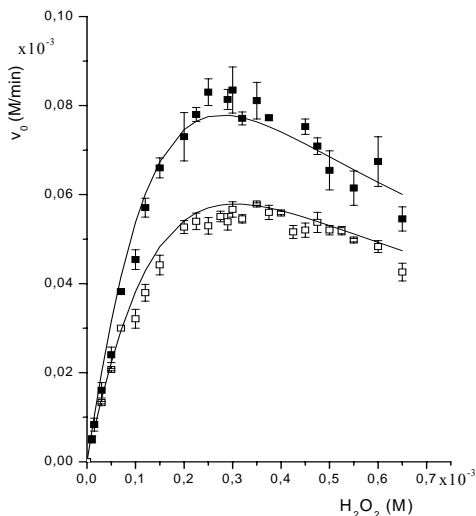


Fig. 1. Kinetics of H_2O_2 dependence of myeloperoxidase activity in the absence (solid symbols) and presence (open symbols) of $2 \mu M$ quercetin. *o*-D concentration was 1.5 mM. Symbols present the mean of at least three experiments \pm S.E., while the solid lines present the reaction rate calculated from eq.6, using parameters from Table 1

Table 1. Kinetic constants for the oxidation of *o*-dianisidine (0.53 mM and 1.5 mM) by MPO in the presence of quercetin.

	[<i>o</i> -D] (mM)	
	0.53	1.50
K_i (M)	$(2.85 \pm 0.22) \times 10^{-6}$	$(3.02 \pm 0.17) \times 10^{-6}$
k_2 (M ⁻¹ min ⁻¹)	$(3.05 \pm 0.15) \times 10^6$	$(2.59 \pm 0.18) \times 10^6$
K_1 (M)	$(5.20 \pm 0.26) \times 10^{-6}$	$(5.00 \pm 0.25) \times 10^{-6}$
K_M (M)	$(2.41 \pm 0.12) \times 10^{-3}$	$(2.63 \pm 0.14) \times 10^{-3}$
k_1 (min ⁻¹)	$(1.50 \pm 0.08) \times 10^4$	$(1.70 \pm 0.10) \times 10^4$
K_1 (M)	-	$(8.00 \pm 0.40) \times 10^3$

Eq.(6) enabled us to obtain the rate and equilibria constants for the reaction scheme presented above, by using its appropriate transformations. The treatment of the experimental data from Fig. 1 depended on whether the experimental points lied on the ascending or on the descending branch of v_o vs. $[H_2O_2]$ curves. Eq. (6) was rearranged to the Line- weaver - Burk form in the non-inhibiting H_2O_2 concentration range (below 0.25 mM):

$$\frac{1}{v_o} = \frac{1}{k_2[E]_0[o-D]_0} \left(\left(1 + \frac{[Q]}{K_i} + \frac{k_2[o-D]}{k_1} \right) + \frac{k_2[o-D]_0}{k_1 K_M^{-1}} \left(1 + \frac{[Q]}{K_i} \right) \frac{1}{[H_2O_2]} \right) \quad (7)$$

In this way the reaction scheme was reduced to the Michaelis-Menten type with K_M being dependent on the concentration of inhibitor and *o*-D. For the analysis of the experimental data in the range of inhibiting H_2O_2 concentrations (above 0.25 mM) the linearized form of eq. (6) was applied to the experimental results:

$$\frac{1}{v} = \frac{1 + \frac{k_2}{k_1}[o-D]}{k_2[E]_0[o-D]} \left(1 + \frac{[Q]}{K_i} + K_1[H_2O_2] \right) \quad (8)$$

The rate and equilibria constants consistent with the reaction scheme (eqs. (1) – (5)) were obtained from the graphical presentation of $1/v_o=f(1/H_2O_2)$ and $v_o=f(H_2O_2)$ and are given in Table 1. Besides, v_o was recalculated from eq. (6) using the obtained parameters and is presented in Fig.1 as solid line.

Conclusion

The results presented in Table 1 show good agreement of rate and equilibria constants obtained for two *o*-D concentrations. Calculated curves (Eq. (6)) fitted the experimental results in the range of experimental error and confirmed the proposed reaction mechanism.

References

- [1] S.J. Klebanoff, Proc. Assoc. Am. Phys., 1999, **111**, 383-389.
- [2] J.V. Formica and W. Regelson, Food Chem. Toxicol., 1995, **33**, 1061-1080.
- [3] R.L. Olsen, and C. Little, Biochem. J, 1983, **209**, 781-787.
- [4] P.P. Bradley, D.A. Priebe, R.D. Christensen and G. Rothstein, J. Invest. Dermatol., 1982, **78**, 206-209.

APPLICATIONS OF THE STATE-OF-THE-ART COMPUTATIONAL METHODS IN THE MODELING OF RRNA STRUCTURE

A. Rakić¹ and P.M. Mitrašinović²

¹Faculty of Physical Chemistry, University of Belgrade, Studentski Trg 12-16, Belgrade, Serbia
²Center for Multidisciplinary Studies, University of Belgrade, Kneza Visislava 1, Belgrade, Serbia
(pmitrasinovic@yahoo.ca).

Abstract

The conformational differences between hairpin triloops upon formation of the large ribonucleoligand complexes have been characterized using root-mean-square deviation (RMSD) and pseudotorsional (η , θ) approach at the nucleotide-by-nucleotide level. The answer to the question of how proximal to and how far from the actual ligand binding sites the structural changes occur is given. A simple measure for the determination of the strain of a triloop is introduced. The strategy used is suggested to bypass the difficulties of having sugar puckers and torsion angles unknown in the 2.5-3 Å resolution range.

Introduction

Knowledge of the molecular structures of biological macromolecules is a prerequisite for the understanding of their functions and interactions. Various recurrent motifs such as the U-turn, the E-loop, the GNRA tetraloop, the GNRA-like pentaloop, the A-minor motif, the kink-turn, the SRP motif, and the T-loop/lone pair triloop motif have been established as constitutive parts of large RNAs. The interaction motifs of hairpin loops have been recognized as possible targets for the binding of proteins [1]. Whereas triloops are common in a variety of naturally occurring RNAs and are unexplored by now, we herein investigate their local behavior upon ligand binding.

Methods

RMSDs were calculated using the Swiss-PdbViewer program [2]. Two pseudotorsions, η ($C4'_{i-1}-P_i-C4'_{i+1}$) and θ ($P_i-C4'_{i-1}-C4'_{i+1}$), around two virtual bonds, from P to $C4'$ and from $C4'$ to P, define conformation of a single nucleotide [3], [4]. The RNA-ligand contacts were determined by ENTANGLE [5]. The motifs were annotated by the MC-Annotate program [6] and represented by geometric nomenclature that is proposed in [7].

Results

The triloop nucleotides with the closing base pairs (BPs) in the complexes were compared with those in the original rRNA (1njp). In 1njn, 1nwy, and 1jzx: the average (*av*) RMSDs are 0.05, 0.85 and 5.36 Å, the *av* $\Delta(\eta, \theta)$ s are 1, 15 and 110 °,

the strains are 0.82, 0.66, and 0.73 Å (Table 1), the η - θ plots are linear (1njn), like an obtuse (1nwy) and acute angle (1jzx, Fig. 1), the closing c-g BPs are cis canonical Watson-Crick (WC) BPs (1njn and 1nwy) and a cis WC/WC edge-to-edge BP (1jzx), the c-G P...P distances are 4.66, 5.40 and 7.05 Å, the A-g P...P distances are 5.10, 4.80 and 6.30 Å (Fig. 3, bottom), respectively. We also note one conspicuous change ($\approx 90^\circ$) in strand direction between nucleotides 1185 and 1186 in both 1njn and 1nwy, while there are three consecutive turns ($\approx 90^\circ$), 1185-1186, 1186-1187 and 1187-1188, in 1jzx (Fig 3, top). The trends of values and distortions are expected to follow an increase in the loop free energy upon complex formation.

Table 1. Quantitative measures for the cGAAG motifs (1185-1189)^{a,b}

PDB ID	RMSD						$\Delta(\eta,\theta)$					
	<i>i</i>	<i>i+1</i>	<i>i+2</i>	<i>i+3</i>	<i>i+4</i>	<i>av</i>	<i>i</i>	<i>i+1</i>	<i>i+2</i>	<i>i+3</i>	<i>i+4</i>	<i>av</i>
1njp	-	-	-	-	-	-	-	-	-	-	-	-
1njn	0.03	0.03	0.11	0.03	0.03	0.05	0	1	2	1	0	1
1nwy	0.62	0.96	0.75	1.24	0.53	0.85	4	7	25	36	5	15
1jzx	4.58	9.30	4.69	3.91	4.35	5.36	40	138	250	93	32	110

^aThe 23S portion of the 50S ribosomal subunit 2 from *Deinococcus radiodurans* (PDB code: 1njp). The resolution of all four structures is 3.5 Å. RMSD (Å) with all atoms being superimposed. *i+1*, *i+2*, and *i+3* - triloop sequence, *i* and *i+4* - closing pair positions. $\Delta(\eta,\theta)$ ($^\circ$) is the difference in nucleotide morphologies based upon values of pseudotorision angles, η and θ , for two RNA worms of the same length [3]. For each nucleotide with sequence position *i* the difference is given by

$$\Delta(\eta,\theta)_i = \sqrt{(\eta_i^A - \eta_i^B)^2 + (\theta_i^A - \theta_i^B)^2}$$
 where *A* and *B* are two structures being compared. Nucleotides with $\Delta(\eta,\theta) < 25^\circ$ should be considered as being structurally similar to each other, while those with $\Delta(\eta,\theta) > 25^\circ$ should not (Fig. 2). For motif searches of the database, a search outcome should be considered as a match if $\Delta(\eta,\theta)_{av} < 25^\circ$ and $\Delta(\eta,\theta)$ for any single nucleotide within the match is less than 40° [4].

^bTriloop strain (Å) is defined by

$$\frac{1}{4} \cdot \sum_{k=i}^{i+3} |P_k P_{k+1} - 5.9|.$$

$P_k P_{k+1}$ is the phosphate...phosphate distance between two consecutive nucleotides, *k* and *k+1*. 5.9 Å stands for the phosphate...phosphate distance of C3'-endo conformation. The motif strain is 0.81, 0.82, 0.66, and 0.73 in 1njp, 1njn, 1nwy, and 1jzx, respectively [1].

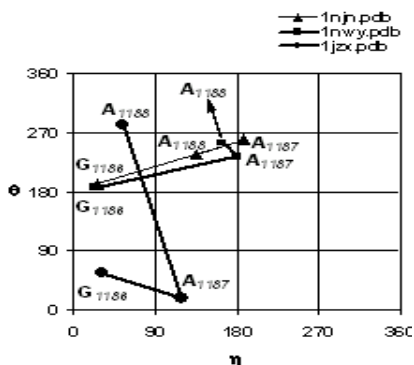


Fig. 1. η - θ plots.

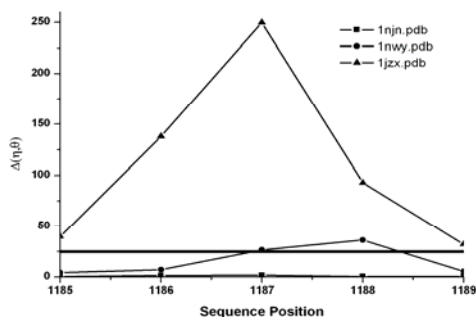


Fig. 2. $\Delta(\eta,\theta)$ vs. sequence position.

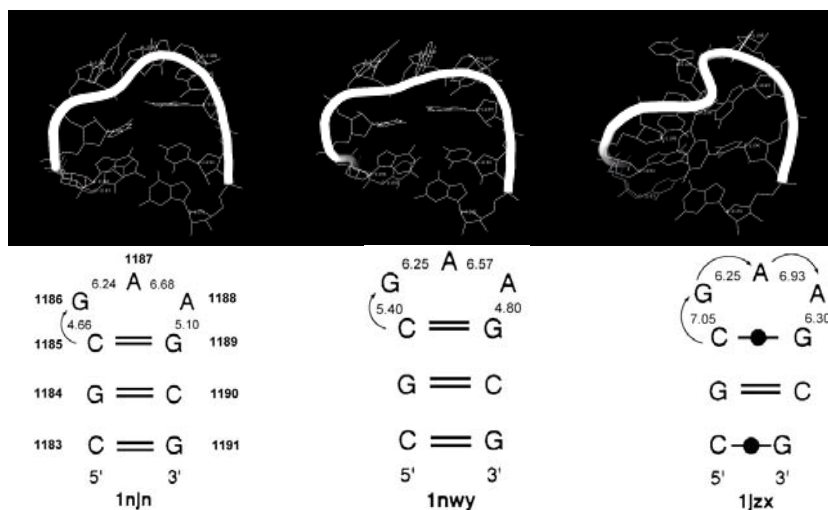


Figure 3. Strand orientations (top). 2D plots of the tertiary structures (bottom).

Conclusion

The ligands are found to be fairly far (in the range of 20 Å) away from the loops under study (Table 2), indicating the primary interactions of the loops with other parts of the ribosome. As the bound complexes represent ribosomal states at various stages of translation, the present study sheds more light on the conformational differences between the particular conformations involved in function of the ribosomal machinery.

Table 2. RNA residues in contact with the ligands

rRNA (subunit)	PDB ID	Contact Sites
23S (50S)	1njn	C2047, C2048, G2231, G2232, C2233, U2416, U2417, C2580, A2581
23S (50S)	1nwy	G57, A63, C64, U1325, C1348, G1351, A1353, A1354, C1614, C1615
23S (50S)	1jzx	G24, U25, C498, A502, G503, G504, A512, G514, U529, G761, A764, A1630, G1992, G1993, G1995

References

- [1] P. M. Mitrasinovic, *J. Struct. Biol.* 2006, **153**, 207-222.
- [2] N. Guex, M. C. Peitsch, *Electrophoresis*, 1997, **18**, 2714-2723.
- [3] C. M. Duarte, A. M. Pyle, *J. Mol. Biol.*, 1998, **284**, 1465-1478.
- [4] C. M. Duarte, L. M. Wadley, A. M. Pyle, *Nucleic Acids Res.*, 2003, **31**, 4755-4761.
- [5] J. Allers, Y. Shamoo, *J. Mol. Biol.*, 2001, **311**, 75-86.
- [6] P. Gendron, S. Lemieux, F. Major, *J. Mol. Biol.*, 2001, **308**, 919-936.
- [7] N. B. Leontis, E. Westhof, *RNA*, 2001, **7**, 499-512.

APPLICATION OF RESONANCE RAMAN SPECTRA OF CAROTENE FOR PROBING O₂ ACTION ON NERVE CELL

G.V. Maksimov¹, Č.N. Radenović², A.A. Churin¹ and V.V. Volkov¹

¹*Department of Biophysics, M.V.Lomonosov Moscow State University, Moscow Russia;*

²*The Maize Research Institute "Zemun Polje"; Serbia*

Abstract

The carotene content in nerve cell membrane is a crucial factor in the use of Raman spectroscopy for monitoring the membrane fluidity. The advantage of this method is the high sensitivity to any changes of nerve membrane fluidity and extra cellular O₂ changes.

Introduction

It is known, carotene have important not only photo biological roles. For our purposes carotene may be divided into two categories; those which do not readily photo isomerizes and those which do. The orange pigment β -carotene is the archetype of the former, while photo labile carotene, is exemplified by retinal, the chromophore responsible for the initial processes in vision. The strong resonance Raman spectra (RRS) of carotene have been used to good advantage for their detection in blood plasma and alga [1]. In another study, changes in the RRS of intrinsic carotene have been reported from a frog sciatic nerve during the propagation of an action potential [2]. Since RRS bands from carotene often occur in membrane preparations it is has been suggested that these features be used as probes of membrane conformations [3]. One system in which carotene are an important natural constituent is the membrane of photosynthetic bacteria. Koyama et al. have shown that the RRS of carotene in these membranes can be used as sensitive probes of membrane potential [4]. The latter causes small shifts in carotene absorption maxima. With judicious choice of the RRS excitation wavelength, small changes in λ_{max} can give rise to large variations in the intensity ratio of the RRS bands of the carotene. Thus, under these conditions, the intensity ratio of the RRS bands of the carotene becomes a sensitive monitor, not only for the cell membrane potential, but for the membrane fluidity too [7,8].

The purpose of this work was to examine the possible application of the Raman spectroscopy of carotene for the investigation of nerve membrane fluidity changes during extracellular O₂ changes.

Results

It is know that, following the depolarization of the cell membranes of frog sciatic nerve, the 1521 and 1156 cm⁻¹ RRS bands of carotene showed an increase in intensity RRS at excitation wavelengths 488, 496,5 and 514,5 nm respectively. None of the bands revealed any change with excitation at 441.6, 457.9, 472.7 and 476.5 nm [5]. These results can be explained, not only by an electro chromic shift of the excitation

profile of the RRS bands, but also in terms of changes of nerve membrane fluidity during O₂ consumption [6].

Using resonance Raman spectroscopy of carotene the changes of viscosity of excitable membranes was investigated [8]. The Raman resonance spectra of nerve carotene and alga *Nitella* cells have been excited by 514,5nm line of an argon ion laser. During cell excitation, the reduction of intensity and increase of the rations of intensity of major carotene bands with no noticeable shift in position of peaks was observed. The Arrenius plot of relative intensity rations of 1525 cm⁻¹ and 1160 cm⁻¹ bands of RSS versus reciprocal temperature shows a change of slope in the range 13-18 °C. This indicates a membrane phase transitions in which reorientation of carotene species takes place. The interpretation was supported by parallel calorimetric and EPR measurements. A decrease of viscosity with increasing temperatures is probably caused by conformational change of carotene polyene chains. We are suggesting that membrane viscosity during excitation nerve and alga cell is increasing and membrane-associated carotene act as viscosity sensitive sensor.

With the help of this methods we investigated changes of viscosity of nerve membranes at a variation of outside oxygen level. It has been established, that at variations of extra cellular oxygen on 60% (argon or oxygen changes) accompanied by decrease (increase) relative intensity rations of 1525 cm⁻¹ and 1160 cm⁻¹ bands of carotene RRS. The given result suggest an increase in viscosity of membranes of a nerve when an increase in the content of oxygen in the environment and decrease of oxygen deficit appear.

Discussion

It is known from theory and experiments that, in photosynthetic membranes, an increase in the strength of the electric field applied along the polyene chain causes a red shift in the carotene absorption spectrum. However, theory also predicts that, with a strong local field directed against the field generated by the membrane potential, the shift caused by the membrane potential changes is in the opposite direction. We believe that this phenomenon takes place in our case: as the ionic-gradient- induced electric field decrease, the excitation profile is shifted towards longer wavelengths, indicating that the field affecting the carotene molecules increase. Therefore we suggest that membrane fluidity also may be the case of nerve carotene conformation changes. It is suggested, that polar groups of membrane lipids or protein located close to the carotene molecule are responsible for this conformations. Possible, O₂ penetration in nerve during rhythmic excitation initiate changes of membrane fluidity and carotene conformation.

References

- [1] L.C. Hoskins and V. Alexander, *Anal.Chem.*,1977, **49**, 695.
- [2] B. Szalontai, Cs. Bagynka and L.Horvat, *Biochem. Biophys.Res.Commun.*,1977, **76**, 660.
- [3] S.P. Verma and D.F.H.Wallach, *Biochim.Biophys.Acta.*, 1975, **401**, 168-175.
- [4] Y.Koyama et al., *Biochim. Biophys. Acta.*, 1979, **548**, 153-167.

-
- [5] V.Z.Paschenko, A.O.Vershinin, A.A.Churin, J. Photochem. Photobiol.,1993, **18**, 127-130
- [6] G.V.Maksimov et al., Gen.Physiol.Biophys.,1990, **9**, 353-360
- [7] G.V.Maksimov et al., Biophysics, 1995, **40**, 127-130
- [8] G.V.Maksimov et.al., Biofizika (Russian)., 1996, **41**, 400-406

NON-CONVENTIONAL INTERACTIONS IN PROTEINS CONTAINING PORPHYRINE

S. Stojanović¹, V. B. Medaković¹ and G. Predović²

¹ Faculty of Chemistry, University of Belgrade, Studentski trg 16, P.O.Box.158, Belgrade, Serbia

² Faculty of Mathematics, University of Belgrade, Studentski trg 16, Belgrade, Serbia

Abstract

The significant number of XH/ π interactions with π -system of five-membered pyrrole rings and six-membered chelate rings from porphyrin was found in crystal structures of proteins. There is a larger number of the interactions with five-membered than with six-membered rings. Hydrogen-atom donors can be C-H and N-H groups. The number of CH/ π interactions is much larger than number of NH/ π interactions. The list of amino acids involved in CH/ π interactions contains more hydrophobic residues, which is probably due to the fact that these interactions are, on average, closer to the interior of the protein. Besides, amino acids involving in these interactions shows significant conservation score.

Introduction

A general concept of hydrogen bonding in proteins is emerging. This concept involves not only N-H and O-H donor groups, but also C-H, and not only N and O as acceptor groups, but also π -systems. Burley and Petsko [1] have termed these interactions 'weakly polar interactions' but they can also be classified as hydrogen bonds, although they are considerably weaker than 'classical' hydrogen bonds.

Further investigations by various research groups have established the role of non-conventional interactions in a variety of functions such as stabilizing factor in beta sheets, peptide beta-hairpins, helix termini, proline residues in protein structures, packing of transmembrane helices, collagen, DNA, ligand recognition, enzymatic action, protein-protein complexes and thermal stability of proteins [2]. Theoretical *ab initio* calculations have also been performed and have shown that the energy of these non-conventional interactions is less than the energy of a conventional hydrogen bond. However, since these interactions can occur more frequently than regular hydrogen bonds, they may well contribute to the protein's stability to the same extent as standard hydrogen bonds. Recently, Steiner and Koellner [3] have performed a comprehensive survey on the occurrence of such non-conventional hydrogen bonds involving π acceptors in proteins and analyzed recurrent structural patterns involving these interactions. The cases in which CH/ π interactions have been described in proteins include the formation of complexes of proteins with special ligands or cofactors such as the heme group [4].

By screening Cambridge Structural Database (CSD) it was shown that there are CH/ π interactions between C-H groups and the π -system of porphyrinato chelate rings. It was found 655 CH/ π interactions [5]. Here we used a non-redundant data base

of 2485 protein chains to examine systematically the occurrence and the role of XH/ π interactions in heme-protein structures.

Results and Discussion

For this study we used the Protein Data Bank (PDB) Select October 2004 list of non-redundant protein chains (25% threshold version, 2485 protein chains). The following criteria were employed to assemble the set: (1) no theoretical model structures and no NMR structures, were accepted, (2) only crystal structures with a resolution of 3.0 Å or better and a crystallographic R-factor of 25.0% or lower were accepted, (3) crystal structures containing porphyrine were accepted. Employing a program written in-house, all interatomic contacts of the five-membered and six-membered rings were sorted out that satisfy following criteria: (1) the distance d_{X-M} between the X (C or N) atom of the X-H-donor and the center of the π -system (M) was ≤ 4.5 Å, (2) the angle at the hydrogen atom \angle_{X-H-M} , defined as the angle between the X-H-bond and the center-of-mass of the π -system (M), was $\geq 110^\circ$ and (3) the angle between the X-M-line and the ring normal (an angle $\omega(X)$), was $\leq 35^\circ$. We used the Bayesian method for calculating rates of amino acid conservation scores.

Table 1. The number of different types of XH/ π interactions

	Five-membered porphyrine rings			Six-membered porphyrine rings	
	CH/ π	NH/ π	Porphyrine-H/ π	CH/ π	NH/ π
No. of C $^\alpha$ -H	7	-	-	2	-
No. of C _{ali} -H	93	-	16	31	-
No. of C _{aro} -H	23	-	-	12	-
No. of N-H	-	3	-	-	5

C $^\alpha$ is α -carbon atom, C_{ali} is carbon atom from aliphatic group; C_{aro} is carbon atom from aromatic group.

There are 142 interactions with five-membered and 50 with six-membered rings. The total number of CH/ π -interactions is 168 (Table 1). The number of CH/ π interactions is much larger than NH/ π interactions. The reason is one hand larger abundance of CH groups and an other hand large tendency of N-H groups to be involved in classical H-bonds. The number of the interactions with five-membered rings is larger than six-membered rings, since five-membered rings are easier accessible. There is the largest number of the interactions of aliphatic C-H-groups and five-membered rings. This is not surprising, since most C-H groups in proteins are belong to the C_{ali}-H. The C $^\alpha$ -H groups constitute the group with the least frequent involvement, probably because these hydrogen atoms are not as accessible as the side-chain hydrogen atoms, and also because the C $^\alpha$ -H groups are to a substantial extent involved in CH/O interactions. It is very interesting that CH groups at side chains of porphyrine can involve in CH/ π interactions with π -systems of another porphyrine in the protein. We found 16 of those interactions.

There are 7 C^{α} -H interactions with five-membered rings, six of them with Gly and one with Met. There are two interactions with six-membered rings, both of them with Cys. There are 93 interactions of C_{ali} -H with five-membered rings. The most frequently observed donor amino acid residues are Leu>Pro>Met>Cys>Ile>Val. The list contains more hydrophobic residues, which is probably due to the fact that these interactions are, on average, closer to the interior of the protein. There are 31 interactions with six-membered rings, and the frequently occurring amino acid residues constitute the top of the donor list (Met>Leu>Val>Lys>Pro). A total of 23 interactions (C_{aro} -H class) have been identified between aromatic C-H donor groups and five-membered rings, while 12 interactions were encountered in the class of interactions between aromatic C-H donor groups and six-membered rings of porphyrine. The most prominent donor amino acid residues with five-membered rings are Phe>His>Tyr>Trp (with six-membered rings: His>Phe>Trp). In total, 8 interactions between N-H groups and π -systems of porphyrine involve the Arg, Trp, Ile, Asn, Gln and Lys residues as the donor groups.

Analysis of the distances for C_{ali} and C_{aro} of CH/ π interactions shows for five-membered rings the peak of distribution for C_{ali} H/ π interactions is between 3.6 and 3.8 Å, while for C_{aro} H/ π interactions is between 3.8 and 4.0 Å. For six-membered rings the peak for C_{ali} H/ π interactions is between 3.8 and 4.0 Å and for C_{aro} H/ π interactions between 4.0 and 4.2 Å. These results indicate that C_{ali} makes interactions with shorter distances.

Bayesian method for calculating rates of amino acid conservation scores showed that amino acids involved in XH/ π interactions with porphyrin have significant conservation score.

Conclusion

The results show that large number of XH/ π interactions with porphyrin exists in crystal structures of proteins. The number of interactions and significant conservation score of amino acids that are involved in these interactions are strong argument for their importance.

References:

- [1] S. K. Burley, G. A. Petsko, *Adv. Protein Chem.*, 1998, **39**, 125-189.
- [2] B. S. Ibrahim, V. Patabhi, *Biochem. Biophys. Res. Commun.*, 2004, **325**, 1082-1089.
- [3] T. Steiner, G. Koellner, *J. Mol. Biol.*, 2001, **305**, 535-557.
- [4] M. Nishio, M. Hirota, Y. Umezawa, *The CH/ π interaction. Evidence, nature and consequences* Wiley-VCH, New York, 1988.
- [5] V. B. Medaković, M. K. Milčić, G. A. Bogdanović, S. D. Zarić, *J. of Inorg. Biochem.*, 2004, **98**, 1867-1873.

IDENTIFICATION OF β -GLUCOSIDASE AND PEROXIDASE FROM DOMESTIC BARLEY GRAIN

S. Gorjanović¹ and R. Gorjanović²

¹*Institute of General and Physical Chemistry, Studentski trg 12-16, P. O. Box 551, Belgrade, Serbia*

²*Faculty of Agriculture, University of Belgrade, P. O. Box 127, Belgrade, Serbia*

Abstract

Domestic barley (*Hordeum vulgare*) grain proteins were fractionated by ammonium sulphate precipitation and fraction of interest (40-80% saturation) subjected to three-step chromatography. After SDS-PAGE, proteins were electroblotted and N-terminally sequenced by Edman degradation. Using PubMed NCBI BLAST search proteins were identified as β -glucosidase isoforms and peroxidase.

Introduction

The endosperm of cereals is a storage organ in which starch and protein accumulate during grain development and are later degraded to provide energy and nitrogen during germination and seedling growth. Some of the proteins which accumulate in the developing endosperm may be involved in pathogen defense or in the later mobilization of storage components. In this work, we described identification of β -glucosidase isoforms and peroxidase. β -glucosidase is involved in barley seed development and germination catalysing hydrolysis of short-chain oligosaccharides [1]. Peroxidase belongs to pathogenesis-related proteins and can be utilized in plant in a variety of biosynthetic or degradable processes and in defense against pathogens or oxidative stress [2].

Experimental

Proteins were isolated using ammonium-sulfate precipitation (40-80% saturation) followed by anion-exchange chromatography on DEAE-Sephacel column equilibrated with 50 mM Tris-HCl buffer, pH 7.8, gel-permeation chromatography of unbound (basic) protein fraction on Sephadex G-75-50 column equilibrated with the same buffer and finally, cation exchange chromatography of fraction with Mw 35-60 kDa on CM-Sephacel CL-6B column equilibrated with 50 mM citrate-phosphate buffer, pH 5.8. Proteins were eluted from Sepharose column with the linear gradient of NaCl (0-0.2M). The isolated proteins were subjected on SDS-PAGE (4% stacking gel and 12% resolving gel) with reducing conditions, stained with Coomassie Brilliant Blue R-250 dye stain, electro transferred onto a PDVF membrane, excised and subjected to automated Edman protein sequencing of 10-12 N-terminal amino acids. BLAST was used for search of the PubMed protein data bank.

Results and Discussion

β -glucosidase and peroxidase were purified from fraction obtained by ammonium sulphate precipitation of barley grain extract by three-steps chromatography. The anion exchange chromatography of enriched ammonium-sulfate fraction resulted in the removal of acid proteins-basic proteins were concentrated in leading peak I (Fig. 1A). The gel-permeation chromatography of the basic proteins resulted in elution of four major peaks (Fig. 1B), first representing a protein mixture with MW=35-60kDa. The final cation-exchange step of first peak resulted in separation of the three peaks (Fig. 1C).

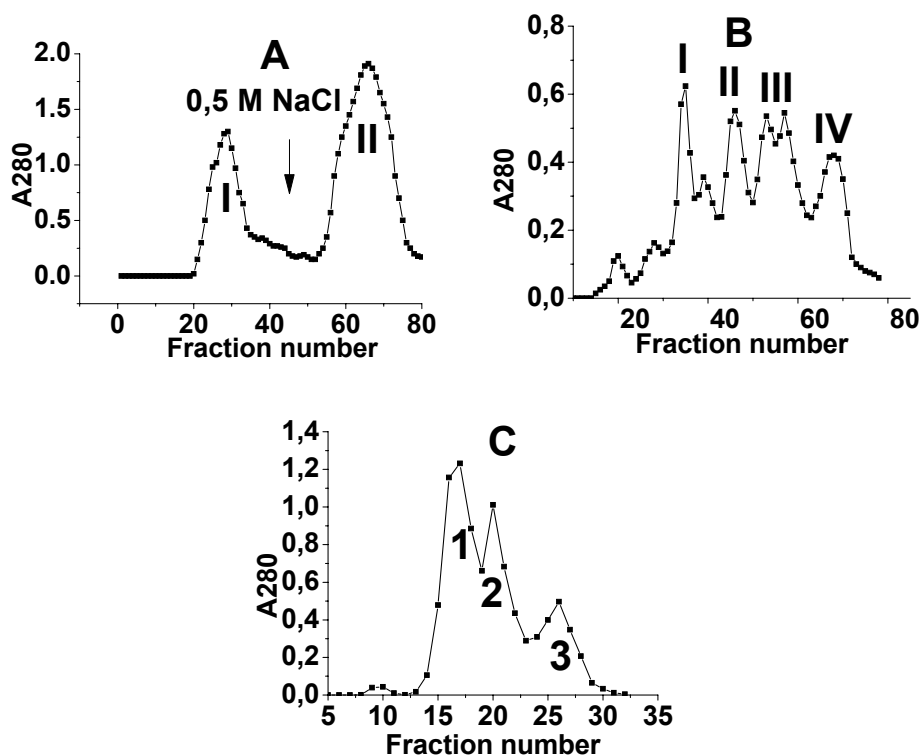


Fig. 1. (A) Isolation of the basic proteins from barley grain extract (fraction precipitated with 40-80% ammonium sulfate saturation), using anion-exchange chromatography on DEAE-Sephacel column (fraction I-basic proteins); (B) Gel-permeation chromatography of the basic protein fraction on a Sephadex G-75 column (Fraction I mixture of β -glucosidase and peroxidase); (C) Separation of β -glucosidase and peroxidase using cation-exchange chromatography on CM-Sepharose column.

The fractions obtained were analysed by SDS-PAGE and electroblotted onto PDVF membrane (Fig. 2). Molecular weights were approx. 35 and 60 kDa for peroxidase and glucosidase, respectively.

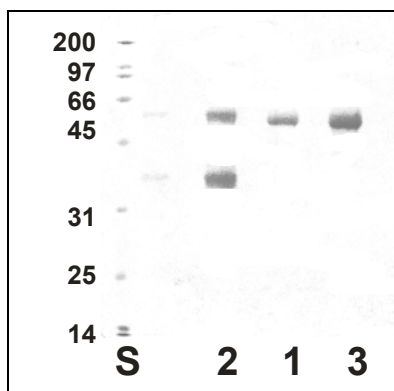


Fig. 2. Electroblot of SDS-PAGE of protein fraction 1, 2 and 3 onto PDVF membrane (S-molecular weight standards: aprotin (6.5 kDa), lysosyme (14.4 kDa), soybean trypsin inhibitor (21.5 kDa), carbonic anhydrase (31 kDa), ovalbumin (45 kDa), bovine serum albumin (66.2 kDa), phosphorylase b (97.4 kDa), β -galactosidase (116.25 kDa), myosine (200 kDa)).

Stained proteins were excised and subjected to automated Edman protein sequencing of 10-12 N-terminal amino acids. Search of the PubMed NCBI using BLAST identified sequenced proteins as β -glucosidase and peroxidase (Table 1.)

Table 1. Fragments of 10-12 N-terminal amino acid sequence of isolated proteins (query) aligned with β -glucosidase and peroxidase (1LIP, GI 1421524) (BLAST search). Unidentified amino acids are denoted by X.

Sample	Sequence	Identity
1	D-G-P-N-P-N-E-I-G	β -glucosidase
2 (upper band)	D-G-P-N-P-N-E-I-G	β -glucosidase
2 (lower band)	A-E-P-P-V-A-P-G-L-S-F-D	Peroxidase
3	X-X-P-N-P-N-P-E-I-G	β -glucosidase

Acknowledgements

This research was supported by the Ministry of Sciences and Environmental Protection of Republic of Serbia, grant No. 143020.

References

- [1] R. Leah, J. Kigel, I. Svendsen, J. Mundy, JBC, 1995, **270**, 15789-15797.
 [2] L. C. van Loon, E. A. van Strein, Physiol. Mol. Plant Pathol., 1999, **55**, 85-97.

TEMPERATURE AND Al^{3+} INFLUENCE ON ELECTROPHORETIC MOBILITY OF PORCINE PEPSIN

V. Pavelkić¹, K. Gopčević², D. Krstić² and M. Ilić³

¹ Vinca-Institute of Nuclear Science, Department of Physical Chemistry, P.O.Box 522, Belgrade

²School of Medicine, University of Belgrade, Višegradska 26, Belgrade,

³Institute of General and Physical Chemistry, Studentski trg 12-16, Belgrade, Serbia

Abstract

The influence of temperature and different concentrations of Al^{3+} on pepsin electrophoretic mobility was investigated. The increase of Al^{3+} concentrations causes the decrease the electrophoretic mobility of enzyme. Also the increase of temperature induced the same effect. The influence of both temperature and Al^{3+} ion concentrations is additive.

Introduction

Pepsin, an acidic protease, is the principal proteolytic enzyme of gastric juice. The primary and tertiary structures of pepsin are highly homologous to other aspartatic proteases. Porcine pepsin was the first aspartic protease to have its complete amino acid sequence determined [1]. The molecular weight is 35000 Da. The protein consists of 326 residues. The structure is bilobal, consisting of two predominantly β -sheet lobes related by a pseudo 2-folded axis [2, 3].

It is known that temperature and presence of Al^{3+} ion influence the three dimensional structure of proteins, as well as its net charge. Thus, the electrophoretic mobility of proteins is affected [4]. That influence depends on concentration of presenting ion and temperature range. The aim of this work was to examine the influence of Al^{3+} ion (in the concentration range from 1 – 10 mM) and temperature (from 25 – 70 °C), on electrophoretic moiety and enzyme activity of pepsin.

Experimental

Pepsin was purchased from Sigma Chemical Co. and used without further purification. Other chemicals were of reagent grade and were prepared prior to use. Water solutions of all samples (2 mg/mL of pepsin were dissolved in water) were titrated with HCl to pH 2, with addition of different concentrations of Al^{3+} ion (1, 5 and 10 mM; $\text{AlCl}_3 \times 6\text{H}_2\text{O}$ as a source of Al^{3+} ion was used). The samples were heated and thermostated for 10 minutes to obtain desired temperature (25, 37, 50 and 70 °C). Native electrophoresis of pepsin on polyacrylamide gel was carried out at 4°C according to the Laemmli procedure [5]. Electrophoresis was done at 4 °C during 90 min. Visualization was performed with Commassie Brilliant Blue G-250 dye. The gels are scanned and processed using Corel Draw.10.0 software package. Quantification of electrophoretic mobility of the molecule is carried out via R_f value, where it is defined by:

$$R_f = [\text{distance of protein migration}] / [\text{distance of tracing dye migration}]$$

Results and Discussion

The electrophoregrams of pepsin samples treated at different temperature values in absence or in the presence of Al^{3+} ion are presented in Figures 1 and 2. It could

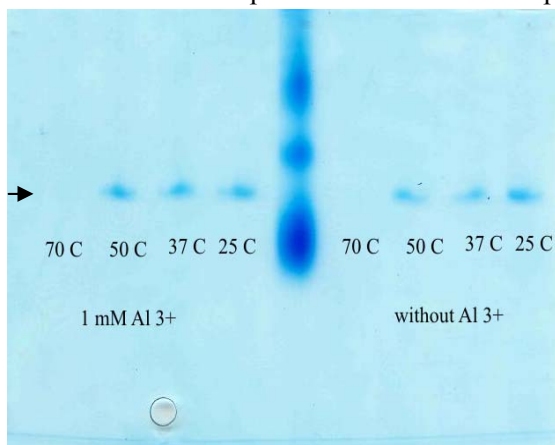


Fig. 1. Native PAGE electrophoregram of pepsin at 25 °C, 37 °C, 50 °C and 70 °C, without Al^{3+} and in a presence of 1 mM Al^{3+} at pH 2.

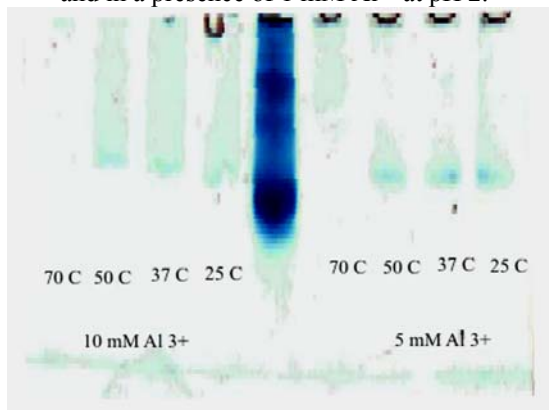


Fig. 2. Native PAGE electrophoregram of pepsin at 25 °C, 37 °C, 50 °C and 70 °C, in a presence of 5 mM and 10 mM Al^{3+} at pH 2.

be seen that in all cases increasing the temperature causes the decrease in electrophoretic moiety of pepsin. The decrease in electrophoretic moiety can be explained by thermally induced conformational changes in pepsin molecule. However, the pepsin bend is absent in samples treated at 70 °C, in the presence of all investigated Al^{3+} concentrations, as well as in the absence of Al^{3+} ion. This result is in agreement with previously reported data that temperatures of 70 °C and higher induce denaturation of an enzyme [6]. Moreover, the degree of pepsin electrophoretic mobility decrease depends on Al^{3+} concentration which the one has been exposed. For example, difference between R_s values obtained at 25 °C and 50 °C in absence of Al^{3+} ion is 0.02, while in the presence of 10 mM Al^{3+} it is 0.05 (Table 1). If we discuss the influence of Al^{3+} ion concentration on pepsin mobility at defined temperature it could be seen that increase in concentration of Al^{3+} decelerate the migration of pepsin samples on concentration dependent manner.(Table 1). For example, R_s values of pepsin at 37 °C in the absence of Al^{3+} is 0.47, while R_s values are 0.46, 0.44 and 0.42 in the presence 1 mM, 5 mM and 10 mM of Al^{3+} , respectively. The same trend was obtained for the other tested temperatures, except for 70 °C. The slow down in pepsin migration can be explained by conformational changes caused by Al^{3+} binding to enzyme. It is obviously that the highest investigated temperature and highest concentration of Al^{3+} result in the lowest electrophoretic mobility, and that influence is additive.

Table 1. R_f values of pepsin treated at different temperatures without and with various Al^{3+} ions concentrations

$C_{Al^{3+}}$ (mM)	R_s (25 °C)	R_s (37°C)	R_s (50°C)	R_s (70°C)
0	0.47	0.47	0.45	0
1	0.47	0.46	0.45	0
5	0.45	0.44	0.44	0
10	0.44	0.42	0.39	0

Conclusion

In the absence of Al^{3+} at all tested temperatures the electrophoretic mobility is the highest. Pepsin samples treated with different concentrations of Al^{3+} ions at pH 2 show the difference in electrophoretic mobility: increase in concentration caused decrease in R_s values. At the same time, increase in temperature cause the same effect – decrease in electrophoretic mobility.

References:

- [1] J. Tang, R. N. S. Wang, J. Cell Biochem, 1987, **33**, 53-63.
- [2] R. Sielecki, A. A. Fedorov, A. Boodhoo, N. S. Andreeva, M. N. G. James, J.Mol. Biol., 1990, **24**, 143-170.
- [3] J. B.Cooper, G. Khan, G. Taylor, I. J. Tickle, T. L. Blundell, J. Mol. Biol., 1990, **214**, 199-222.
- [4] A. Dorney et al., J. Inorg. Biochem., 2003, **97**, 118-123.
- [5] Laemmli, Nature, 1970, **227**, 680-685.
- [6] Privalov, P.L., Mateo, P.L., and Khechinashvili, N.N., J. Mol.Biol., 1981, **152**, 445-464.

ISOLATION AND IDENTIFICATION OF THAUMATIN LIKE PROTEINS FROM DOMESTIC BARLEY GRAIN

S. Gorjanović¹, M. V. Beljanski¹, M. Gavrović-Jankulović² and F. Bejosano³

¹*Institute of General and Physical Chemistry, Studentski trg 12-16, P. O. Box 551, Belgrade, Serbia*

²*Faculty of Chemistry, University of Belgrade, Studentski trg 12-16, P. O. Box 158, Belgrade, Serbia*

³*Cereal Quality Laboratory, Department of Soil and Crop Science, Texas A&M University, College Station, Texas 77843-2474*

Abstract

Two basic glycoproteins were isolated to homogeneity from common cultivar of barley grain (*Hordeum vulgare*). They have Mw about 22 kDa and 27 kDa in nonreducing and reducing conditions, respectively, and pI 9.3. Proteins were identified as members of thaumatin-like protein family by Western blot, while their amount in different domestic cultivars of barley grain was estimated using dot-blot immuno assay.

Introduction

Thaumatococcus-like proteins (TLP), named after their amino-acid sequence and structural similarity to the sweet tasting protein thaumatin from the fruits of the West African rain forest shrub *Thaumatococcus daniellii* Benth, belong to pathogenesis-related (PR) proteins (PR-5 family). From high-lysine mutant barley grain two isoforms, named S and R in accordance with nomenclature used for tobacco proteins, were isolated [1]. The purpose of this work was to estimate and compare level of TLPs in the grain of different domestic barley cultivars, and to isolate and characterize TLPs isoforms from barley cultivar with highest protein amount.

Experimental

Dot-blot analysis was performed as described by Bejosano [2]. R and S were isolated using ammonium-sulfate precipitation (40-80% saturation) followed by anion-exchange chromatography on DEAE-Sephacel column equilibrated with 50 mM Tris-HCl buffer, pH 7.8. Basic protein fraction was applied on column of Sephadex G-75-50 equilibrated with Tris-HCl buffer, pH 7.8. Fraction II was applied on column of CM-Sepharose CL-6B equilibrated with 50 mM citrate-phosphate buffer, pH 5.8. Proteins were eluted from Sepharose column with the linear gradient of NaCl (0-0.2M). The obtained protein fractions were subjected on SDS-PAGE (4% stacking gel and 12% resolving gel) with reducing conditions and then electrotransferred onto a nitrocellulose membrane. Immunodetection was performed according to the method of Harlow and Lane, using monoclonal antibody produced as described [3].

Results and Discussion

Presence and quantity of TLPs in different cultivars of domestic barley grain were tested immunochemically, using dot-blot method (Fig. 1). On the basis of result obtained, cultivar NS 294, with highest amount of TLP, was chosen for protein isolation.

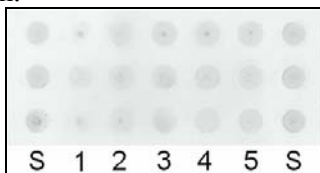


Figure 1. TLP presence in five domestic cultivars of barley grain, tested by dot-blot method (analysis performed in triplicate). S-standard; 1-NS 519; 2-NS 293; 3-NS 294; 4-NS 448; 5-NS 556;

The TLPs contained in the raw extract of barley grain were concentrated by fractional precipitation at 40-80% ammonium-sulfate saturation. The fraction enriched with TLP was depleted of acidic proteins by of anion-exchange chromatography (Fig. 2A). Basic (unbound) proteins concentrated in leading peak (fraction I) were separated by gel-permeation chromatography (Fig. 2B), four fractions were obtained. From fraction II, proteins S and R were isolated, using cation-exchange chromatography (Fig. 2C). Protein S appeared at 90 mM NaCl while R at 130 mM NaCl.

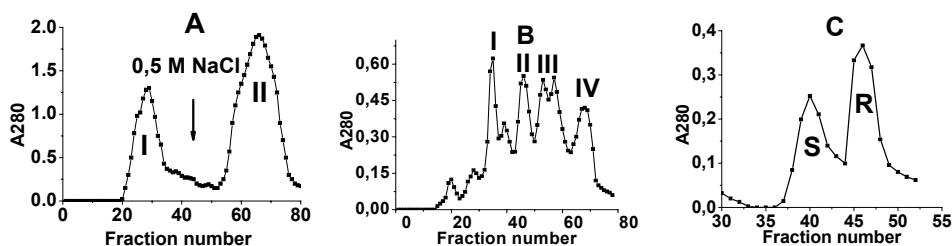


Fig. 2. (A) Isolation of the basic proteins from barley grain extract (fraction precipitated with 40-80% ammonium sulfate saturation), using anion-exchange chromatography on DEAE-Sephacel column (fraction I-basic proteins); (B) Gel-permeation chromatography of the basic protein fraction on a Sephadex G-75 column (fraction II-mixture TLPs, S and R); (C) Separation of S and R using cation-exchange chromatography on CM-Sephacrose column.

Homogeneity of the purified TLPs was checked using SDS-PAGE and IEF. Isolated proteins exhibited a single band upon SDS-PAGE (Fig. 3A) and IEF. Proteins have slightly different mobility at about 22 kDa in nonreducing and at about 27 kDa in reducing conditions. TLPs have anomalous migration in SDS-PAGE probably due to their high number of disulphide bridges; both isoforms showed presence of eight disulphide bridges, tested by Ellman method. Isoelectric point of 9.3 for both isoforms was estimated by IEF. Identity of isolated proteins was confirmed by immunoblotting assay (Fig. 3B).

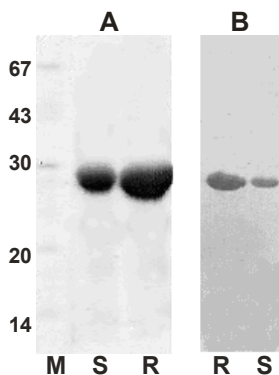


Fig. 3. The purity test and molecular weight determination of barley grain TLPs, S and R, performed on SDS-PAGE (**A**) (M-molecular weight standards: lactalbumin (14 kDa), trypsin inhibitor (20 kDa), carbonic anhydrase (30 kDa), ovalbumin (43 kDa) and human sera albumin (67 kDa)); (**B**) Immunodetection of TLPs by Western blot analysis.

Conclusion

Barley grain is rich source of TLPs which can be readily purified in large quantities using conventional methods for protein isolation. Isolated proteins resemble to the physico-chemical features of mutant barley TLPs isoforms R and S isolated by Hejgaard. They appeared at the similar position in the salt gradient cation-exchange chromatography; protein R being prevalent in the mixture, they are basic (pI above 9), sharing similar mobility in SDS-PAGE in non reducing conditions and have the same number of disulphide bridges. Finally, identity of isolated proteins has been confirmed by immunoblotting assay.

Acknowledgements

This research was supported by the Ministry of Sciences and Environmental Protection of Republic of Serbia, grant No. 143020.

References

- [1] J. Hejgaard, S. Jacobsen, I. Svendsen, *FEBS Lett.*, 1991, **291**, 127-131.
- [2] F. Bejosano, R. Waniska, W. L. Rooney, *J. Agric. Food Chem.*, 2003, **51**, 5911-5915.
- [3] M. Gavrović-Jankulović, T. Ćirković, O. Vučković, M. Atansković-Marković, A. Peterson, G. Gojgić, L. Burazer, R. Jankov, *J. Allergy Clin. Immunol.*, 2002, **110**, 805-810.

ZINC BINDING AND THERMOSTABILIZATION OF BOVINE SERUM ALBUMIN (BSA) STUDIED BY DSC

S. Ostojić, V. Dragutinović, M. Kićanović and B.R. Simonović

*Holding Institute of General and Physical Chemistry
Studentski trg 12/V P.O. Box 551, Belgrade, Serbia*

Abstract

Thermal denaturation process of BSA (0.050 mM) was studied under the low ionic strength conditions (deionised water) and with addition of various micromolar amounts of $\text{Zn}(\text{NO}_3)_2$. From DSC curves the thermodynamical parameters of protein denaturation were obtained: temperature of thermal transition maximum (T_m), calorimetric enthalpy (ΔH^{cal}), van't Hoff enthalpy (ΔH^{VH}). An increase of zinc concentration even in micro range (μM) brings a stabilization of the protein, expressed as a shift of the transition temperatures towards higher temperature values. Zinc binding center seems to be crucial for thermostabilization of the protein.

Introduction

Albumin is the major transport protein in blood for $\text{Zn}(\text{II})$. Zinc supports a healthy immune system and is needed for DNA synthesis [1-4], has structural and catalytical role for many proteins. It is a small hydrophilic, charged element, which can not cross biological membranes by passive diffusion [1-4]. Zinc transport is a temperature and pH-sensitive process [5]. Zinc binding to bovine serum albumin (BSA) have immediate consequences on protein stability, observed as altering the thermodynamic properties of the system and was studied by differential scanning calorimetry (DSC).

Experimental

BSA from Bioheringer Mannheim (Fraction V) was used without further purification. $\text{Zn}(\text{NO}_3)_2$ and chemicals were of p.a. grade and freshly prepared. All proteins were degassed before loaded into calorimeter. Calorimetric measurement were carried out on a MicroCal MC -2 sensitive differential scanning calorimeter (DSC) using a standard DA - 2 software package for data acquisition and Origin software for DSC data analysis (non two-state curve fitting model) for estimating thermodynamical parameters of protein unfolding: T_m temperature midpoint, ΔH^{cal} calorimetric enthalpy and ΔH^{VH} van't Hoff enthalpy (Fig. 1). All scans were performed in the temperature range from 283K to 383K, scan rate was 90 K/h.

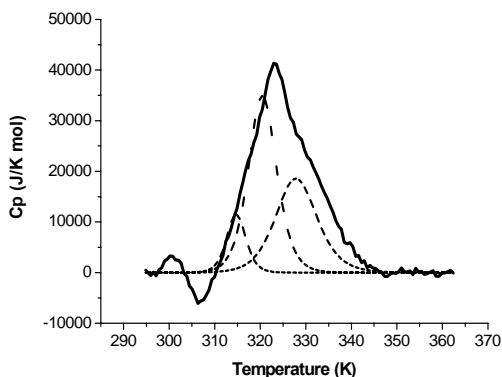


Fig. 1. DSC curve of BSA (0.05mM) thermal unfolding in the presence of 1.00 (μM) $\text{Zn}(\text{NO}_3)_2$. The solid line corresponds to experimental data; and dash lines correspond to the best fits.

Results and Discussion

Increasing zinc concentration brings a thermostabilization of the protein expressed as a shift of the transition temperatures towards higher temperature values (Tab.1).

Table 1. Thermodynamic parameters of BSA (0.050 mM) denaturation in deionised water and in presence of different micro molar Zn(II) concentrations (pH = 6.2) (values of T_m and ΔH^{cal} higher then values of T_m and ΔH^{cal} obtained for protein unfolding without presence of Zn(II) are highlighted).

Zn(NO ₃) ₂ (μM)	T_{m1} (K)	ΔH^{cal} (kJ/mol)	ΔH^{VH} (kJ/mol)	T_{m2} (K)	ΔH^{cal} (kJ/mol)	ΔH^{VH} (kJ/mol)	T_{m3} (K)	ΔH^{cal} (kJ/mol)	ΔH^{VH} (kJ/mol)
0	307.9	234.68	333.88	329.8	193.04	359.11	-	-	-
0.05	315.8	43.68	376.64	330.0	514.04	172.59	-	-	-
0.30	331.3	116.77	323.29	-	-	-	-	-	-
0.45	302.4	32.30	410.24	313.3	461.20	200.74	331.3	227.06	268.02
1.00	316.5	71.00	539.81	322.9	316.81	383.00	331.1	245.51	275.89
20.00	313.8	185.72	235.81	319.2	122.29	512.58	330.0	122.00	359.78

The average number of ligands bound per mole of native protein X_N , can be obtained from the heat capacity data by plotting inverse transition temperature ($1/RT_m$) versus logarithm of the total Zn(II) concentration ($\log \text{Zn}(\text{II})$), X_N can be determined from the slope of the plot (Fig. 2) [6]. Results obtained from DSC data for X_N , was 0.1 on transition temperature T_{m1} , 5.03 on transition temperature T_{m2} ($X_{\text{NII}}=5.03$) and 1.04 on transition temperature T_{m3} ($X_{\text{NIII}}=1.04$). It can be assumed that average degree of ligands bound per mole of native protein X_N , on the site I(T_{m1}) is lower then on sites II and III, meaning that site II were crucial for specific binding of Zn(II) to protein and protein thermostabilization, as found by Fujii et al. [8].

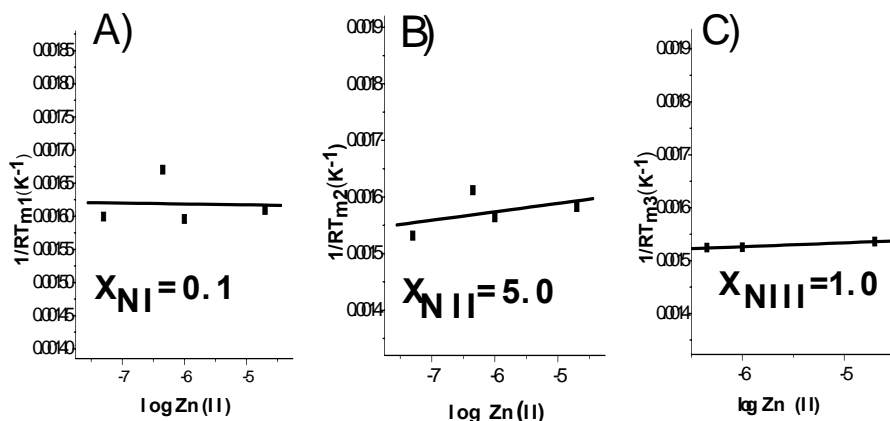


Fig. 2: Plot of inverse transition temperature ($1/RT_m$) versus logarithm of the total Zn(II) concentration ($\log \text{Zn(II)}$) of the BSA in the presence of different Zn(II) concentrations: (A) determination of the average degree of binding X_{NI} at the transition temperature (T_{m1}); (B) determination of the average degree of binding X_{NII} at the transition temperature (T_{m2}); (C) determination of the average degree of binding X_{NIII} at the transition temperature (T_{m3}). Solid lines are linear fit.

Conclusion

Obtained increase of calorimetric enthalpies ΔH^{cal} and temperature shifts towards higher values with increased zinc concentration are suggesting thermostabilization of bovine serum albumin (BSA). Results obtained from DSC data for the average number of ligands bound per mole of native protein X_N , for site II suggests that site II was crucial for specific binding of Zn(II) to protein and protein thermostabilisation.

References

- [1] A.S Prasad, Annu. Rev. Pharmac. Toxic., 1979, **20**, 393-398.
- [2] H.H Sanstead, Nutr. Rev., 1985, **43**, 129-138.
- [3] R.J. Cousins, Physiol. Rev., 1985, **65**, 238-247.
- [4] B.L. Valee, H.K. Falchuk, Physiol. Rev., 1993, **73**, 79-83
- [5] J.G. Reyes, Am. J. Physiol., 1996, **270**, C401-C404
- [6] J. Rosgen, H.J. Hinz, J. Mol. Biol., 2001, **306**, 80-86
- [7] M. Oobatake, T. Oui, Prog. Biophys. molec. Biol., 1993, **59**, 237-284
- [8] T. Fujii, Y. Hata, T. Wakagi, N. Tanaka, T. Oshima, Nat. Struct. Biol., 1996, 834- 339

ANTIBACTERIAL SCREENING OF NICKEL(II) AND ZINC(II) COMPLEXES WITH SOME 2-METHYLBENZIMIDAZOLES

S. O. Podunavac-Kuzmanović and D. M. Cvetković
Faculty of Technology, Bulevar Cara Lazara 1, Novi Sad, Serbia

Abstract

Nitrates of nickel(II) and zinc(II) react with 1-benzoyl-2-methylbenzimidazole or 1-(4-chlorobenzoyl)-2-methylbenzimidazole to give complexes of the type $M(L)_2(NO_3)_2$ ($M=Ni$ or Zn ; $L=(1\text{-benzoyl-2-methylbenzimidazole or } 1\text{-}(4\text{-chlorobenzoyl})\text{-2-methylbenzimidazole})$). The antibacterial activity of these complexes was tested against phytopathogenic strains of bacteria in order to obtain new potent formulations for plant protection. All the complexes were screened for their antibacterial activities against *Escherichia coli* and *Bacillus sp.* The effect of ligand and complex structure on the antimicrobial activity was discussed.

Introduction

Benzimidazole derivatives with substituents such as methyl and chloro in different positions have been found to possess inhibitory effect on the development of several yeasts and bacteria. Various benzimidazoles are effective inhibitors of the growth of lactobacilli, vaccinia virus, influenza virus and HIV-virus. Many different benzimidazoles have such activities as analgetics, anticarcinogens, sedatives, etc [1-6].

The coordination chemistry of benzimidazole and its derivatives has received considerable attention because of their biological significance and interesting spectral, magnetic and structural aspects. In view of previous observations [7-9], that presence of the metal ions considerably enhance the biological activity of organic molecules, we report the synthesis and study of nickel(II) and zinc(II) complexes with N-1-substituted-2-methylbenzimidazole derivatives. The antibacterial activity of these complexes against *Escherichia coli* and *Bacillus sp.* have also been investigated and are in complete agreement with their structures.

Materials and Methods

Complexes were synthesized according to a next procedure: a solution of 5mmol of metal salts in 20 cm³ EtOH was added into a solution of 10 mmol of the ligand in 20 cm³ EtOH. The resulting mixture was boiled under reflux on a water bath for about 2h and then cooled. The complexes which separated from the reactions were removed by filtration, washed with EtOH and dried *in vacuo* over CaCl₂. The yield of the complexes varied in the range of 45-50%.

Results and Discussion

The antibacterial activity of these complexes was tested against phytopathogenic strains of bacteria in order to obtain new potent formulations for plant protection. All the complexes were screened for their antibacterial activities against *Escherichia coli* and *Bacillus sp.* The relevant data are presented in Table 1.

As can be seen from Table 1, the majority of the investigated compounds displayed *in vitro* antimicrobial activity against very persistent microorganisms. Gram-positive bacteria *Bacillus species* was persistent only in the case of starting ligand 1-benzoyl-2-methylbenzimidazole. In the case of gram-negative isolate *Escherichia coli* all the ligands and their complexes exhibited antibacterial activity. However, zinc(II) ion coordinated with ligands increased the general antimicrobial activity of the benzimidazole derivatives, whilst nickel(II) complexes were low active.

Table 1. Antimicrobial activity of the benzimidazole derivatives and their complexes

Compound	<i>Bacillus sp.</i>	<i>Escherichia coli.</i>
L ¹	∅	+
NiCl ₂ (NO ₃) ₂ ·2H ₂ O	+	++
ZnCl ₂ (NO ₃) ₂	+++	+++
L ²	++	++
NiCl ₂ (NO ₃) ₂ ·H ₂ O	++	++
ZnCl ₂ (NO ₃) ₂	+++	+++

+ - low inhibitory activity; ++ - middle inhibitory activity;
+++ - high inhibitory activit; ∅- no activity

From the data, it is evident that both of the ligands have no same activity against *Escherichia coli* as well as in the case of the *Bacilus sp.* ligand L¹ is not active. Comparing the activities of the tested ligands, it was found that if the benzimidazole nucleus was substituted with a 4-chlorobenzyl group at the N1 atom, the antimicrobial activity was increased. Of the complexes, the most active compounds are those containing zinc(II). In view of the structural formula of the complexes that exhibited antimicrobial activity, it can be thought that some metal may play a significant role. This can be explained in terms of chelation theory, which states that a decrease in the polarizability of the metal can enhance the lipophilicity of the complexes. Also, this may be attributed to the high biological activity of free zinc(II) ions.

Conclusions

The ligands, 1-benzoyl-2-methylbenzimidazole (L¹) or 1-(4-chlorobenzoyl)-2-methylbenzimidazole (L²) react with nickel(II) and zinc(II) to give complexes of the type M(L)₂(NO₃)₂ (M=Ni or Zn). The majority of the investigated compounds

displayed *in vitro* antimicrobial activity against very persistent microorganisms: *Escherichia coli* and *Bacillus sp.* Comparing the activities of the tested ligands, it was found that if the benzimidazole nucleus was substituted with a 4-chlorobenzyl group at the N1 atom, the antimicrobial activity was increased. Of the complexes, the most active compounds are those containing zinc(II). In view of the structural formula of the complexes that exhibited antimicrobial activity, it can be thought that some metal may play a significant role.

Acknowledgment

These results are the part of the project "*Physico-chemical, structural and biological investigations of complex compounds*", supported by the Ministry of Science and Environment Protection of the Republic of Serbia.

References

- [1] P.T. M. Nguyen, J.D. Baldeck J. Olsson, R.E. Marquis, Oral Microbiol. Immunol., 2005, **20**, 93-99.
- [2] S. Ozden, H. Karatas, S. Yildiz, H.Goker, Arch. Pharm. Pharm. Med. Chem. 2004, **337** 556-562.
- [3] H. Goker, M. Alp, S. Yildiz, Molecules, 2005, **10**, 1377-1386.
- [4] A. Akbay, I. Oren, O. Temiz-Arpaci, E. Aki-Sener, I. Yalcin, Arzneim-Forch./Drug Res., 2003, **53**, 266-271.
- [5] L. Gata, F. Perna, N. Figura, C. Ricci, J. Holton, M. Miglioli, D. Vaira, J. Antimicrob. Chemother., 2003, **51**, 439-444.
- [6] H. Kucukbay, R. Durmaz, E. Orhan, S. Gunal, Il Farmaco, 2003, **58**, 431-437.
- [7] S.O. Podunavac-Kuzmanović, S.L. Markov, Lj.S. Vojinović, Acta Periodica Technologica, 2004, **35**, 247-254.
- [8] S.O. Podunavac-Kuzmanović, D.M. Cvetković, G.S.Ćetković, Acta Periodica Technologica, 2004, **35**, 231-237.
- [9] S.O. Podunavac-Kuzmanović, D.M. Cvetković, Lj.S. Vojinović, Acta Periodica Technologica, 2004, **35**, 239-246.

ANTIBACTERIAL INVESTIGATION OF COBALT(II) AND ZINC(II) COMPLEXES WITH N-1-SUBSTITUTED BENZIMIDAZOLES

S. O. Podunavac-Kuzmanović and D.M. Cvetković

Faculty of Technology, Bulevar Cara Lazara 1, Novi Sad, Serbia

Abstract

Cobalt(II) and zinc(II) nitrate react with N-1 substituted-2-aminobenzimidazoles to give complexes of the general formula $ML_2(NO_3)_2 \cdot nH_2O$ where $L^1=1$ -benzoyl-2-aminobenzimidazole and $L^2=1$ -(4-chlorobenzoyl)-2-aminobenzimidazole; $M=Co$ or Zn ; $n=0, 1$ or 2). Both the ligands and their complexes were evaluated for their *in vitro* antimicrobial activity against *Escherichia coli* and *Bacillus sp.* The results of antibacterial investigations indicate that both of the ligands are active against *Escherichia coli*. In the case of the *Bacillus sp.* ligand L^1 is less active. Of the complexes, the most active compounds are those containing cobalt(II). On comparing the biological activity of the ligand and its complexes, it was found that some complexes are more effective against the bacteria. Higher activity of the complexes as compared to free ligands could be understood in term of the chelation theory.

Introduction

Benzimidazole and its derivatives continue to be the most versatile class of compounds possessing different pharmacological activities. These groups of molecules are of wide interest because of their diverse biological activity and clinical applications. This ring system is present in numerous antiparasitic, antihelminthic and anti-inflammatory drugs. Also, these derivatives possess activities such as antibacterial, antifungal, antiallergic, antihistaminic, local analgesic, vasodilator, hypotensive and spasmolytic. A number of benzimidazole derivatives show anti-HIV activity and some of them have been used as anticarcinogenic agents [1-6]. They are also inhibitors of photosynthesis, and some exhibit appreciable herbicidal activity.

In our previous studies [7-9], we also observed that benzimidazole derivatives, as well as their complexes with transition metal ions, have shown considerable biological activity. Following our synthesis and antibacterial works on benzimidazole derivatives and their complexes, we now report the antibacterial activity of cobalt(II) and zinc(II) complexes with N-1-substituted 2-aminobenzimidazoles.

Materials and Methods

Complexes were synthesized according to a next procedure: a solution of 5 mmol of metal salts in 20 cm³ EtOH was added into a solution of 10 mmol of the ligand in 20 cm³ EtOH. The resulting mixture was boiled under reflux on a water bath for about 2h and then cooled. The complexes which separated from the reactions were removed by

filtration, washed with EtOH and dried *in vacuo* over CaCl_2 . The yield of the complexes varied in the range of 50-55%.

Results and Discussion

All the complexes were screened for their antimicrobial activities against *Bacillus sp.* and *Escherichia coli*. The relevant data are presented in Table 1. The basic antimicrobial activity of N-1 substituted-2-aminobenzimidazoles is produced by the presence of benzimidazole ring as a known pharmacophore.

Antimicrobial results shows that chlorine as substituent at the position 4 on benzene ring increased the general antimicrobial activity of the relevant benzimidazoles.

Table 1. Antimicrobial activity of the benzimidazole derivatives and their complexes

Compound	<i>Bacillus sp.</i>	<i>Escherichia coli.</i>
L^1	+	++
$\text{CoCl}_2(\text{NO}_3)_2 \cdot 2\text{H}_2\text{O}$	+++	+++
$\text{ZnCl}_2(\text{NO}_3)_2$	+	++
L^2	++	++
$\text{CoCl}_2(\text{NO}_3)_2 \cdot \text{H}_2\text{O}$	+++	+++
$\text{ZnCl}_2(\text{NO}_3)_2$	++	++

+ - low inhibitory activity; ++ - middle inhibitory activity;
+++ - high inhibitory activity

The proof of this is that the most active compound was 1-(4-chlorobenzoyl)-2-aminobenzimidazole (L^2), as well as its cobalt(II) complexes against both the bacteria (Table 1). In the case of the *Bacillus sp.* ligand L^1 is less active. On comparing the biological activity of the ligand and its complexes, it was found that cobalt(II) complexes are more effective against the bacteria. From the results, it can be concluded that zinc(II) does not increase the general antibacterial activity of the organic ligand.

The higher activity of the some complexes, as compared to the free ligand, can be understood in terms of the chelation theory. This theory explains that a decrease in the polarizability of the metal could enhance the lipophilicity of the complexes.

Conclusions

1-benzoyl-2-aminobenzimidazole and 1-(4-chlorobenzoyl)-2-aminobenzimidazole with cobalt(II) and zinc(II) formed complexes of the general formula $\text{ML}_2(\text{NO}_3)_2 \cdot n\text{H}_2\text{O}$ where L^1 =1-benzoyl-2-aminobenzimidazole and L^2 =1-(4-chlorobenzoyl)-2-aminobenzimidazole; $\text{M}=\text{Co}$ or Zn ; $n=0, 1$ or 2).

The results of antimicrobial investigations indicate that the most active compounds are cobalt(II) complexes. On comparing the biological activity of the ligands and their complexes, it was found that some complexes are more effective against the bacteria. From the results, it can be concluded that zinc(II) does not increase the general antibacterial activity of the organic ligand. Antimicrobial results show that chlorine as substituent at the position 4 on benzene ring increased the general antimicrobial activity of the relevant benzimidazoles.

Acknowledgment

These results are the part of the project "*Physico-chemical, structural and biological investigations of complex compounds*", supported by the Ministry of Science and Environment Protection of the Republic of Serbia.

References

- [1] H. Goker, M. Alp, S. Yildiz, *Molecules*, 2005, **10** 1377-1386.
- [2] P.T. M. Nguyen, J.D. Baldeck J. Olsson, R.E. Marquis, *Oral Microbiol. Immunol.*, 2005, **20** 93-99.
- [3] S. Ozden, H. Karatas, S. Yildiz, H.Goker, *Arch. Pharm. Pharm. Med. Chem.* 2004, **337** 556-562.
- [4] H. Kucukbay, R. Durmaz, E. Orhan, S. Gunal, *Il Farmaco*, 2003, **58**, 431-437.
- [5] A. Akbay, I. Oren, O. Temiz-Arpaci, E. Aki-Sener, I. Yalcin, *Arzneim-Forch./Drug Res.*, 2003, **53**, 266-271.
- [6] L. Gata, F. Perna, N. Figura, C. Ricci, J. Holton, M. Miglioli, D. Vaira, *J. Antimicrob. Chemother.*, 2003, **51**, 439-444.
- [7] S.O. Podunavac-Kuzmanović, S.L. Markov, Lj.S. Vojinović, *Acta Periodica Technologica*, 2004, **35**, 247-254.
- [8] S.O. Podunavac-Kuzmanović, D.M. Cvetković, G.S.Ćetković, *Acta Periodica Technologica*, 2004, **35**, 231-237.
- [9] S.O. Podunavac-Kuzmanović, D.M. Cvetković, Lj.S. Vojinović, *Acta Periodica Technologica*, 2004, **35**, 239-246.

ANTIMICROBIAL EVALUATION OF COPPER(II) COMPLEXES WITH SOME 2-AMINOBENZIMIDAZOLES

S. O. Podunavac-Kuzmanović and S.L. Markov

Faculty of Technology, Bulevar Cara Lazara 1, 21000 Novi Sad, Serbia

Abstract

Copper(II) nitrate reacts with 2-aminobenzimidazole derivatives to give complexes of the formula $\text{CuL}_2(\text{NO}_3)_2$, where L=2-aminobenzimidazole, 1-benzyl-2-aminobenzimidazole and 1-(4-methylbenzyl)-2-aminobenzimidazole. All the ligands and their copper(II) complexes were evaluated for their *in vitro* antimicrobial activity against *Pseudomonas aeruginosa*, *Bacillus* sp., *Staphylococcus aureus*, *Sarcina lutea* and *Saccharomyces cerevisiae*. The minimum inhibitory concentration (MIC) was determined for all ligands and their complexes. It was found that tested compounds were more active against gram-positive than gram-negative bacteria. None of the compounds were significantly effective against yeast *Saccharomyces cerevisiae*, except 1-(4-methylbenzyl)-2-aminobenzimidazole and its complex, which moderately inhibited the growth of yeast. The effect of ligand and complex structure on the antimicrobial activity was discussed.

Introduction

Benzimidazole and its derivatives are interesting heterocycles because of their presence in many various medicaments. It has been found that they possess antibacterial, antifungal, antihistaminic, cytostatic, local analgesic, hypotensive and antiinflammatory activity. It was confirmed to have a moderate *in vitro* anti-HIV activity [1-3]. In recent years, transition metal complexes have attracted particular interest because of their potential use in several homogeneously catalyzed processes, such as hydrogenation, hydroformylation and acetylation reactions. However, in the recent time, possible therapeutic properties of the metal complexes have been examined. It was found that the complexes of transition metals with benzimidazole derivatives showed a higher antimicrobial activity than the corresponding ligands.

Following our previous investigations[1-3], we evaluated the antimicrobial activity of this type of complexes in this study. We report *in vitro* antimicrobial activities of 2-aminobenzimidazoles and their copper(II) complexes against three gram-positive bacterial strains: *Bacillus* sp., *Staphylococcus aureus* and *Sarcina lutea*, one gram-negative isolate: *Pseudomonas aeruginosa* and yeast, *Saccharomyces cerevisiae*.

Results and Discussion

The antimicrobial activity of the 2-aminobenzimidazole derivatives and their copper(II) complexes was first tested by the agar disc-diffusion method against gram-positive and gram-negative bacteria and yeast. The results of these studies are summarized in Table 1.

Table 1. In vitro antimicrobial activity of ligands and their complexes at a concentration of 1000 µg/ml

Compound	<i>P.aeruginosa</i>	<i>Bacillus</i> sp.	<i>S. aureus</i>	<i>S. lutea</i>	<i>S. cerevisiae</i>
L ¹	+	∅	∅	∅	∅
Cu(L ¹) ₂ (NO ₃) ₂	∅	+++	+++	+++	∅
L ²	∅	++	++	++	∅
Cu(L ²) ₂ (NO ₃) ₂	+	+++	+++	+++	∅
L ³	++	++++	++++	++++	+
Cu(L ³) ₂ (NO ₃) ₂	++	+++	+++	+++	++

Very highly active +++++, Highly active +++, Moderately active ++, Slightly active +, Inactive ∅

From the data obtained in Table 1, it is clear that tested compounds were found to be more active against gram-positive bacteria than gram-negative *Pseudomonas aeruginosa*. It may be concluded that the antimicrobial activity of the compounds is related to cell wall structure of the bacteria.

None of the compounds were found significantly effective against yeast *Saccharomyces cerevisiae*, except Cu(L³)₂(NO₃)₂ which moderately inhibited the growth of yeast. 1-(4-methylbenzil)-2-aminobenzimidazole(L³) was found to be slightly active against *Saccharomyces cerevisiae*.

MIC of the tested compounds was performed by the agar dilution method. The results obtained indicated that the complex containing copper(II) was more active than starting ligand L¹ against *Bacillus* sp., *Staphylococcus aureus* and *Sarcina lutea* with a MIC value of 250µg/ml, but less active against *Pseudomonas aeruginosa*. On the other hand, the copper(II) complex was more active than starting ligand L² with a MIC value of 750µg/ml, as well as same active as ligand L³ with a MIC value of 500µg/ml against *Pseudomonas aeruginosa*. In the cases of other bacteria complex was more active than its ligand L², but less active than ligand L³. MIC value of Cu(L²)₂(NO₃)₂ was 250µg/ml, against *Bacillus* sp. and *Sarcina lutea*, as well as 60µg/ml against *Staphylococcus aureus*. The complex containing L³ were active against *Bacillus* sp., *Sarcina lutea* and *Staphylococcus aureus* with a MIC value of 250µg/ml, but its starting ligand is more toxic with a MIC value of 125µg/ml against the same bacteria.

Comparing the activities of the tested ligands and their complexes, it was found that if the benzimidazole nucleus was substituted with a 4-methylbenzyl group at the N1 atom, the antimicrobial activity was increased. Consideration of the structural formula of the compounds that exhibit antimicrobial activity, substituted ligands and copper moiety may play a role for the antimicrobial activity. The antimicrobial potencies of the investigated benzimidazole derivatives are similar to those of different benzimidazoles which were determined in the previous studies [4-6].

Conclusions

Copper(II) nitrate react with 2-aminobenzimidazole derivatives to give complexes of the formula $\text{CuL}_2(\text{NO}_3)_2$, where $\text{L}^1=2$ -aminobenzimidazole, $\text{L}^2=1$ -benzyl-2-aminobenzimidazole and $\text{L}^3=1$ -(4-methylbenzyl)-2-aminobenzimidazole. All the ligands and their copper(II) complexes were evaluated for their in vitro antimicrobial activity against *Pseudomonas aeruginosa*, *Bacillus* sp., *Staphylococcus aureus*, *Sarcina lutea* and *Saccharomyces cerevisiae*. It is found that tested compounds were more active against gram-positive than gram-negative bacteria. None of the compounds were found significantly effective against yeast *Saccharomyces cerevisiae*, except $\text{Cu}(\text{L}^3)_2(\text{NO}_3)_2$ which moderately inhibited the growth of yeast. 1-(4-methylbenzyl)-2-aminobenzimidazole was found to be slightly active against *Saccharomyces cerevisiae*. Comparing the activities of the tested ligands and their complexes, it was found that if the benzimidazole nucleus was substituted with a 4-methylbenzyl group at the N1 atom, the antimicrobial activity was increased. Consideration of the structural formula of the compounds that exhibit antimicrobial activity, substituted ligands and copper moiety may play a role for the antimicrobial activity.

Acknowledgment

These results are the part of the project "*Physico-chemical, structural and biological investigations of complex compounds*", supported by the Ministry of Science and Environment Protection of the Republic of Serbia.

References

- [1] H. Goker, M. Alp, S. Yildiz, *Molecules*, 2005, **10** 1377-1386.
- [2] P.T. M. Nguyen, J.D. Baldeck J. Olsson, R.E. Marquis, *Oral Microbiol. Immunol.*, 2005, **20** 93-99.
- [3] S. Ozden, H. Karatas, S. Yildiz, H.Goker, *Arch. Pharm. Pharm. Med. Chem.* 2004, **337** 556-562.
- [4] S.O. Podunavac-Kuzmanović, S.L. Markov, Lj.S. Vojinović, *Acta Periodica Technologica*, 2004, **35**, 247-254.
- [5] S.O. Podunavac-Kuzmanović, D.M. Cvetković, G.S.Četković, *Acta Periodica Technologica*, 2004, **35**, 231-237.
- [6] S.O. Podunavac-Kuzmanović, D.M. Cvetković, Lj.S. Vojinović, *Acta Periodica Technologica*, 2004, **35**, 239-246.

ANTIMICROBIAL ACTIVITY OF BARLEY GRAIN THAUMATIN LIKE PROTEINS

S. Gorjanović¹, M. V. Beljanski¹, R. Gorjanović² and G. Gojgić-Cvijanović³

¹*Institute of General and Physical Chemistry, Studentski trg 12-16, P. O. Box 551, Belgrade, Serbia*

²*Faculty of Agriculture, University of Belgrade, P. O. Box 127, Belgrade, Serbia*

³*Faculty of Chemistry, University of Belgrade, Studentski trg 12-16, P. O. Box 158, Belgrade, Serbia*

Abstract

Barley grain thaumatin-like proteins, assigned as S and R, inhibit growth of bacteria *Micrococcus lysodeikticus*, brewer's yeast *Saccharomyces cerevisiae*, fungi *Candida albicans* and the most important phytopathogenic *Fusarium sporotrichioides*. Protein S has more potent inhibitory activity. Antibacterial and antifungal activity of both isoforms was completely abolished by divalent (Ca^{2+} , Mn^{2+} , Mg^{2+}) and monovalent (K^{+}) ions, at concentrations approximating physiological and higher.

Introduction

Two basic proteins were isolated to homogeneity from common cultivar of barley grain (*Hordeum vulgare* L.). They have Mw about 22 kDa and 27 kDa in nonreducing and reducing conditions, respectively and pI 9.3. Proteins were identified as members of thaumatin-like protein (TLP) family by Western blot. They resemble to the physico-chemical features of mutant barley TLPs isoforms R and S [1]. Common barley TLP isoforms are glycosylated with different sugar content, 2.8% and 5% for R and S, respectively. Moreover, S possesses concavaline A (lectin that binds to manose and glucose) binding ability. The mixture of S and R isoforms inhibit brewers yeast growth, fermentation and respiration, as well as *C. albicans* growth [2]. Purpose of this work was to examine R and S individual influence on bacteria *Micrococcus* and fungi *Saccharomyces*, *Candida* and *Fusarium* growth. Also, we examined effect of some cations on R and S antimicrobial activity in order to elucidate if their mechanism of action is metal mediated like osmotins (member of TLP family) [3].

Experimental

Antifungal activity of barley grain TLP, R and S, was measured by microspectrophotometry. Synthetic growth medium with low ionic strength (SMF-) consisted of K_2HPO_4 2.5 mM, MgSO_4 50 μM , CaCl_2 50 μM , FeSO_4 5 μM , CoCl_2 0.1 μM , CuSO_4 0.1 μM , Na_2MoO_4 2 μM , H_3BO_3 0.5 μM , KJ 0.1 μM , ZnSO_4 0.5 μM , MnSO_4 0.1 μM , glucose (10 g/L), asparagine (1 mg/L), methionine (20 mg/L), myo-inositol (2 mg/L), biotin (0.2 mg/L), thiamine-HCl (1 mg/L) and pyridoxine-HCl (0.2 mg/L) was used. Cell number of *S. cerevisiae*, *C. albicans*, *F. sporotrichioides* and *M. lysodeikticus* was $10^5/\text{ml}$. After incubation for 24 h the absorbance at 595 nm was determined with an enzyme-linked immunosorbent assay reader. The activity was measured in same medium supplemented with several divalent cations added separately (SMF+), in differ-

ent concentration (1, 2.5, 5 and 10 mM of CaCl₂, MgCl₂, MnCl₂) or monovalent potassium cation (10, 50 and 100 mM KCl).

Results and Discussion

Both TLP isoforms display very strong antimicrobial activity (Fig. 1). Inhibition of phytopathogenic *Fusarium*, known to provoke cereal disease *Fusarium* head blight, is pointing to TLPs role in seed protection. This work is a first evidence of TLPs antibacterial activity.

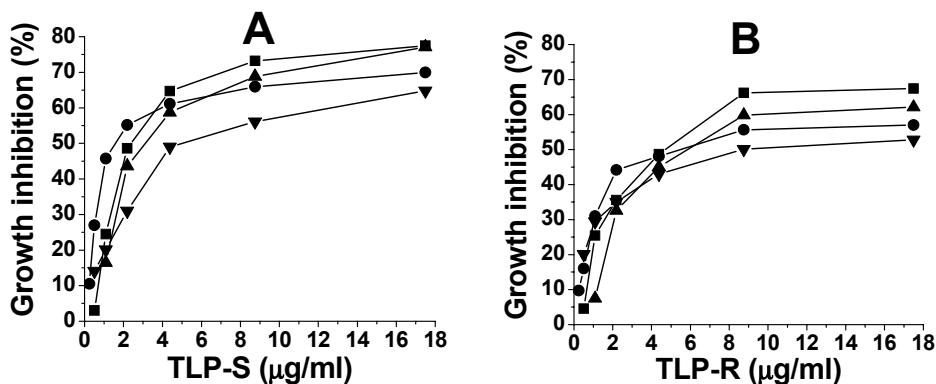


Fig. 1. *In vitro* antifungal activity of barley grain TLP-S (A) and TLP-R (B). Dose-response curve determined after 24 h incubation of *S. cerevisiae* (▲), *F. sporotrichoides* (■), *C. albicans* (●), and *M. lysodeikticus* (▼) in the synthetic low ionic strength medium.

As seen from Fig. 1, protein S possesses more potent inhibition effect on fungi, as well as bacteria, in comparison to R. In contrast to curves obtained for R, each tending to saturation at highest concentration, curves obtained for S in the case of *S. cerevisiae* and *M. lysodeikticus* are still growing. Antibacterial and antifungal activities of S and R are summarized in Table 1. The sensitivity of the antifungal and antibacterial activity of TLPs to the presence of cations in growth medium was tested measuring IC₅₀ in medium supplemented with several cations in different concentration. No antimicrobial activity could be observed in all mentioned cases regardless of protein and/or cation concentration (Table 1).

Table 1. Antifungal and antibacterial activity of TLP, S and R, in low (SMF-) and high (SMF+) syntetic medium; growth inhibition (GI) at final protein concentration and IC₅₀

	TLP-S			TLP-R		
	GI (%)	IC ₅₀ (µg/ml)		GI (%)	IC ₅₀ (µg/ml)	
		17.5 µg/ml	SMF- SMF+		17.5 µg/ml	SMF- SMF+
<i>C. albicans</i>	69.9	1.6	-	57.0	5.5	-
<i>F. sporotrichoides</i>	77.4	2.3	-	67.5	4.8	-
<i>S. cerevisiae</i>	77.1	3.1	-	62.1	6.0	-
<i>M. lysodeikticus</i>	64.8	4.9	-	52.7	9.0	-

Conclusion

Finding that protein S has a higher antifungal activity than R, supports hypothesis that sugar binding ability might facilitate protein interaction with cell wall. Higher antibacterial activity of S leads us to conclusion that carbohydrate binding is important in the case of bacteria also where a cell wall lipopolisaccharid is potential binding site. The antimicrobial activity of most PR proteins has been reported to be drastically reduced in the presence of physiological concentrations of inorganic cations. Presence of cations could disturb protein binding to cell wall components due to cation interaction with cell surface or with proteins themselves. Exception from the rule is osmotin whose activity is potentiated in the presence of cations. Although barley grain S and R, and osmotin are members of the same protein family, they seems to have different mechanism of action.

Acknowledgements

This research was supported by the Ministry of Sciences and Environmental Protection of Republic of Serbia, grant No. 143020.

References

- [1] J. Hejgaard, S. Jacobsen, I. Svendsen, *FEBS Lett.*, 1991, **291**, 127-131.
- [2] A. Cvetković, S. Gorjanović, J. Hranisavljević, D. Vučelić, *J. Serb. Chem. Soc.* 1997, **62**, 51-56.
- [3] R. Salzman, H. Koiwa, J. I. Ibeas, J. M. Pardo, P. M. Hasegawa, R. A. Bressan, *MPMI*, 2004, **17**, 780-788.

EFFECT OF EDTA ON THE INHIBITION OF RAT MYOMETRIAL ECTO-ATPASE ACTIVITY IN THE PRESENCE OF HEAVY METAL IONS I. MERCURY

M. Milošević, M. Demajo and A. Horvat

*Laboratory for Molecular Biology and Endocrinology, "Vinča" Institute of Nuclear Sciences,
P.O. Box 522, Belgrade, Serbia*

Abstract

The effects of increasing concentrations of HgCl_2 on rat uterine plasma membrane ecto-ATPase activity, in presence and absence of ethylenediamine tetra acetic acid (EDTA) were studied. The aim was to examine the ability of EDTA to prevent mercury induced inhibition of ecto-ATPase activity. Our results show that addition of 1 mmol/l EDTA to the reaction mixture potentiates Hg^{2+} induced inhibition of enzyme activity. We may concluded that formation of the HgEDTA complex increased capacity of Hg^{2+} to inhibit enzyme activity.

Introduction

Ecto-adenosine triphosphatase (ecto-ATPase) is an integral plasma membrane glycoprotein, with transmembrane domain at both the N- and C-terminus, and one large extracellular domain containing the active site. As a member of E-NTPDases (EC 3.6.1.5); a family of ectoenzymes, it hydrolyzes terminal phosphoanhydride bonds of extracellular nucleoside tri- and diphosphates in the presence of divalent cations (Ca^{2+} or Mg^{2+}). ATP and its products of hydrolysis are involved in signaling processes through interaction with extracellular receptors. These purinergic receptors control many physiological processes, including neurotransmission, blood clotting, pain perception and smooth muscle contraction. Also, the existence of purinoceptors in the rat female reproductive tract was confirmed [1]. High ecto-ATPase activity in myometrium tissue indicates its role in cell mechanisms of controlling extracellular concentrations of nucleotides.

Plenty of evidence indicates that Hg^{2+} is reproductive tissue toxicant [2]. The aim of this work was to investigate *in vitro* the ability of EDTA to prevent Hg^{2+} induced inhibition of ecto-ATPase activity.

Experimental

Experiments were performed on 3-months-old female Wistar albino rats obtained from the local colony. Myometrial plasma membranes (MPM) were isolated as described previously [3]. Incubation medium (200 μl) contained 50 mmol/l Tris-HCl (pH 7.4), 1 mmol/l MgCl_2 , 7 μg MPM protein and increasing concentration of HgCl_2 in absence or presence of 1 mmol/l EDTA. Incubation with HgCl_2 lasted 30 min at 37⁰ C and the enzyme reaction was started by the addition of 1 mol/l ATP and allowed to proceed for

additional 10 min. The enzyme reaction was stopped by the addition 22 μ l of ice cold 3mol/l perchloric acid. The inorganic phosphate (Pi) liberated from the hydrolysis of ATP was determined by the spectrophotometric method.

Results and Discussion

Mercury salt (HgCl_2) was added to the reaction mixture in concentration ranges from 1×10^{-7} to 0.1 mol/l. The effects of increasing concentrations of Hg^{2+} were measured in the absence and in the presence of 1mM EDTA. In both cases, ecto-ATPase activity was not affected in the presence of 1×10^{-4} mol/l of added HgCl_2 and lower. Almost total inhibition was achieved in the presence of 0.1 mol/l of HgCl_2 and the presence of EDTA potentiates the inhibitory effect of Hg^{2+} ions (Fig 1.). The half-maximum inhibitory activities (IC_{50}) determined by Hill analysis of experimental curves were 1.06×10^{-3} in the presence and 3.38×10^{-3} mol/l in the absence of EDTA.

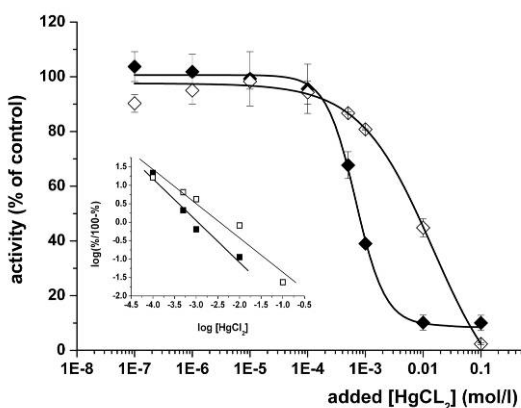


Fig. 1. Inhibition of ecto-ATPase activity by HgCl_2 in the absence (open symbol) and in the presence (solid symbols) of 1×10^{-3} mol/l EDTA. Inset: Hill plot of experimental data. The values given are the mean of at least three experiments \pm S.E.M.

The concentrations of ionic species were calculated, taking into account equilibrium reactions involving Mg^{2+} , ATP, EDTA and Hg^{2+} . The stability constants were found in the literature [4, 5] and calculated according to Sorer and Cornish-Bowden [6]. In absence of EDTA, since Hg^{2+} formed no complex with ATP, the experimental (added) and free concentrations of Hg^{2+} were the same. Metals have a number of toxic mechanisms including interaction with -SH, - NH_2 , -COOH, -OH groups in protein, the conformation changing or competition with free Mg^{2+} in substrate MgATP^{2-} complex. Hg^{2+} binds well to -SH groups and this being most expected mechanism of its toxicity. E-NTPDases contain 10 Cys residues in their extracellular domain but have no free sulphhidryl groups. These data may explain ecto-ATPase resistance to inhibition by Hg^{2+} ions and a relatively high IC_{50} value in the absence of EDTA.

Since EDTA binds Hg^{2+} with high affinity, almost all Hg^{2+} are trapped in the chelate. These results indicate that the HgEDTA complex (Fig.2.), not free Hg^{2+} ions (10^{-24} - 10^{-15} mol/l; data not shown), is responsible for inhibition. The toxicity of HgEDTA and HgEGTA was described previously [7]. Duhr at al. reported that complex HgEDTA , but not Hg^{2+} , induced inhibition of microtubule polymerization by inhibi-

tion of the brain β -tubulin activity by disrupting the interaction of the substrate, GTP (nucleotide triphosphate) with the enzyme-binding site. We propose similar mechanism in our experimental model. Binding of HgEDTA to or near to ATP (nucleotide triphosphate) hydrolysing site on the ecto-ATPase disable binding of substrate, ATP, and thereby inhibits the ecto-ATPase activity.

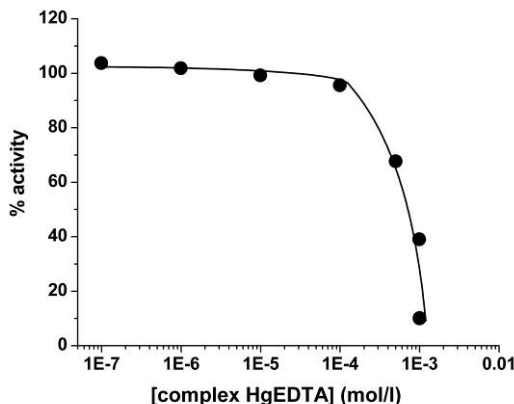


Figure 2. Inhibition of ecto-ATPase activity by HgEDTA complex in reaction mixture (calculated values). The values given are the mean of at least three experiments.

Conclusion

In the reaction medium containing Hg^{2+} , addition of the EDTA formed the HgEDTA complex which increases the capacity of Hg^{2+} to inhibit ecto-ATPase activity. According to our results and literature data, we may propose the possible mechanism of HgEDTA induced inhibition of ecto-ATPase activity: (i) HgEDTA prevents interaction of substrate MgATP^{2-} with active site of the enzyme and/or (ii) displaces bound MgATP^{2-} from the enzyme substrate binding site.

Acknowledgements

This study was supported by the Serbian Ministry of Sciences and Environmental Protection, Project No. 143044.

References

- [1] M Bardini, H.Y. Lee, G. Burnstock, 2000, *Cell Tissue Res.* **299**: 105–113
- [2] P. Kovačić, J. D. Jacintho, *Curr. Med. Chem.*, 2001, **8**, 863-892
- [3] M. Milošević, S. Petrović, M. Demajo, A. Horvat, *Ann.N.Y.Acad. Sci.*, 2005, **1048**, 445-448
- [4] L.G.Silen, A.E Martell, 1971, *Stability Constants of Metal-Ion Complexes*. The Chemical Society, London Special Publication No. 25
- [5] <http://www.cem.msu.edu/~cem333/EDTATable.html>
- [6] A.C.Sorer and A.Cornish-Bowden, 1976, *Biochem.J.* **159**, 1-5
- [7] E.F Duhr, J.C. Pendergrass, J.T. Slevin, B.E. Haley, 1993, *Toxicol. Appl. Pharmacol.*, **122**:2, 273-80

EFFECT OF EDTA ON THE INHIBITION OF RAT MYOMETRIAL ECTO-ATPASE ACTIVITY IN THE PRESENCE OF HEAVY METAL IONS II. CADMIUM

M.Milošević, A.Banjac, M.Demajo, A.Horvat

*Laboratory for Molecular Biology and Endocrinology, "Vinča" Institute of Nuclear Sciences,
P.O. Box 522, Belgrade, Serbia*

Abstract

The effects of ethylenediamine tetraacetic acid (EDTA) on the CdCl₂ cell toxicity was examined on rat myometrium. Activity of plasma membrane ecto-ATPase, as modulator of purinergic signaling in the presence of increasing concentrations of cadmium salt and in the presence or absence of EDTA were studied. The EDTA, chelating cadmium ions decrease inhibitory cadmium potency by increasing half-maximum inhibitory activities of this ion.

Introduction

Extracellular ATP and the products of its hydrolysis (ADP, AMP, adenosine) are involved in signaling processes. These compounds control many physiological processes through binding to purinergic receptors. Cell mechanism for modulation and termination of extracellular ATP mediated signaling is a set of ecto-enzymes responsible for degradation of ATP as well as its products. Ecto-ATPase (ATP diphosphohydrolase, EC 3.6.1.5) is one a member of these enzymes; it hydrolyzes adenosine tri- and diphosphates in the presence of divalent cations. Ecto-ATPase is an integral plasma membrane protein, with transmembrane domain at both the N- and C-terminus, and one large extracellular domain containing substrate (MgATP²⁻) binding site.

The reproductive organs are innervated by several groups of autonomic and sensory nerves. ATP is co-released from nerves with neurotransmitters, but is also released from non-nerve cells to act on P2 receptors in the myometrium [1]. High ecto-ATPase activity in myometrium tissue indicates its role in a signal termination mechanism for purinergic transmission.

The literature data classify cadmium as a reproductive tissue toxicant [2]. Effects of Cd²⁺ ions on rat synaptic and uterine plasma membrane ecto-ATPase activity was reported previously [3, 4]. The aim of this work was to investigate *in vitro* ability of EDTA to prevent cadmium induced inhibition of ecto-ATPase activity.

Experimental

Experiments were performed on 3-months-old female Wistar albino rats obtained from the local colony. Myometrial plasma membranes (MPM) were isolated as described previously [4]. Incubation medium (200μl) contained 50mol/l; Tris-HCl (pH 7.4), 1mmol/l MgCl₂, 1mmol/l ATP and 7μg MPM protein, in absence (control) and pres-

ence of increasing concentrations of CdCl_2 for 30 min at 37°C . The enzyme reaction was started by addition of ATP, allowed to proceed for additional 10 min and stopped by the addition $22\mu\text{l}$ of the ice cold 3mol/l perchloric acid. The inorganic phosphate (Pi) liberated from the hydrolysis of ATP was determined by the spectrophotometric method. All measurements were performed in triplicate.

Results and Discussion

Cadmium chloride was added to the reaction mixture in concentration ranges from 1×10^{-7} to 0.05 mol/l . The effects of increasing concentrations of Cd^{2+} were measured in the absence and in the presence of 1mmol/l EDTA. Ecto-ATPase activity was not changed up to $1 \times 10^{-5}\text{ mol/l}$ of added CdCl_2 . In the absence of EDTA, ecto-ATPase activity shows up to 90% inhibition, relative to the control sample in the presence of 0.05 mol/l of added CdCl_2 , but the same metal concentration in the presence of EDTA has an inhibition of about 80% (Fig 1.). The half-maximum inhibitory activities (IC_{50}) determined by Hill analysis of experimental curves (Fig.1 inset) were 1.17×10^{-3} and $5.22 \times 10^{-3}\text{ mol/l}$ in the absence or presence of EDTA, respectively.

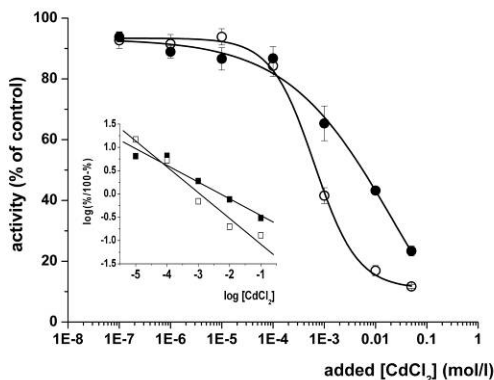


Figure 1. Inhibition of ecto-ATPase activity by CdCl_2 in the absence (open symbol) and in the presence (solid symbols) of $1 \times 10^{-3}\text{ mol/l}$ EDTA. The values given are the mean of at least three experiments $\pm\text{S.E.M}$

The concentrations of ionic species were calculated, taking into account equilibrium reactions involving Mg^{2+} , ATP, EDTA and Cd^{2+} (Tab.1). The stability constants were found in the literature [5, 6] and calculated according to Sorer and Cornish-Bowden [7].

Cadmium ions (Cd^{2+}) may have a number of toxic mechanisms including membrane lipid peroxidation, interaction with $-\text{SH}$, $-\text{NH}_2$, $-\text{COOH}$, $-\text{OH}$ groups and conformational changing enzyme protein, or compete with free Mg^{2+} in the MgATP^{2-} complex decreasing substrate concentration. Chelating metal ions, EDTA decreases free ion concentrations which may interact with the enzyme protein or with ATP. Effects of the complex CdEDTA on enzyme activity inhibition could not be excluded.

Table 1. The values of free Cd^{2+} calculated in the medium assay containing various CdCl_2 concentrations in the presence and absence of 1mmol/l EDTA.

CdCl_2 (mol/l)	free Cd^{2+} (mol/l)	
	Without EDTA	1mmol/l EDTA
1×10^{-7}	3.1×10^{-10}	4.1×10^{-19}
1×10^{-6}	3.1×10^{-9}	4.4×10^{-18}
1×10^{-5}	3.2×10^{-8}	7.3×10^{-17}
1×10^{-4}	4.5×10^{-7}	5.9×10^{-15}
1×10^{-3}	1.2×10^{-4}	2.5×10^{-10}
1×10^{-2}	9.0×10^{-3}	8.0×10^{-3}
5×10^{-2}	4.9×10^{-2}	4.8×10^{-2}

Conclusion

EDTA having high affinity for Cd^{2+} may prevent or decrease the toxic effects of this metal ion. According to the results presented in this work, 1 mmol/l EDTA increase by one order of magnitude CdCl_2 concentration for half-maximal inhibition (IC_{50}), by decreasing free Cd^{2+} concentrations capable to interact with enzyme protein or to produce the inactive complex CdATP^{2-} .

Acknowledgements

This study was supported by the Serbian Ministry of Sciences and Environmental Protection, Project No. 143044.

References:

- [1] M. Bardini, H.Y. Lee, G. Burnstock, Cell Tissue Res., 2000, **299**, 105–113.
- [2] P. Kovačić, J. D. Jacintho, Curr. Med. Chem., 2001, **8**, 863-892.
- [3] Vasić V., Jovanović D., Horvat A., Momić T., Nikezić G., Anal. Biochem., 2002, **300**, 113-120.
- [4] M. Milošević, S. Petrović, M. Demajo, A. Horvat, Ann.N.Y.Acad. Sci., 2005, **1048**, 445-448.
- [5] L.G.Silen, A.E Martell, 1971, Stability Constants of Metal-Ion Complexes. The chemical Society, London Special Publication No. 25.
- [6] <http://www.stanford.edu/~cpatton/maxc2cm.htm>.
- [7] A.C.Sorer and A.Cornish-Bowden, Biochem.J., 1976, **159**, 1-5.

INHIBITION OF ACHE BY MALATHION AND SOME STRUCTURALLY SIMILAR COMPOUNDS

D. Krstić¹, M. Bavcon-Kralj², P. Trebše², M. Čolović³,
K. Krinulović³ and V. Vasić³

¹*School of Medicine, University of Belgrade, Belgrade, Serbia*

²*Nova Gorica Polytechnic, Laboratory for Environmental Research, Vipavska 13, Nova Gorica, Slovenia*

³*Vinča Institute of Nuclear Sciences, Belgrade, Serbia*

Abstract

Inhibition of bovine serum acetylcholinesterase by *in vitro* exposure to malathion, malaoxon, isomalathion and diethyl maleate was investigated to elucidate the mechanism of the enzyme interaction with structurally similar organophosphorus compounds. IC₅₀ (half maximum inhibitory concentrations) were determined by Hill analysis of experimentally obtained inhibition curves. The values $(2.87 \pm 0.24) \times 10^{-6}$ M, $(2.65 \pm 0.61) \times 10^{-6}$ M, $(3.01 \pm 0.36) \times 10^{-4}$ M and $(5.69 \pm 0.7) \times 10^{-2}$ M were obtained for malaoxon, isomalathion, malathion and their hydrolysis product diethyl maleate, respectively. The relationship between the structure of the compounds and their potency to inhibit the enzyme activity was discussed.

Introduction

Organophosphorus compounds are commonly used as insecticides in agriculture [1]. When applied, they are usually completely removed by physico-chemical water treatment methods before getting into the potable water. The survey of pesticides trace amounts usually includes monitoring of parent compounds, but more polar, water-soluble transformation products (oxons) are usually not target analytes in monitoring surveys. The use of oxidation procedures or irradiation methods to remove the pollutants leads to different chemical transformations, e.g. hydrolysis, oxidation and isomerisation [2]. This work deals with the *in vitro* investigation of the mechanism of inhibition of bovine serum acetylcholinesterase (AChE, EC 3.1.1.7) by malathion and its three main degradation products found in irradiated solutions: malaoxon, isomalathion and diethyl maleate. The aim of our work was to investigate the toxic properties of malathion photochemical degradation products, which can be even more toxic than the parent compound.

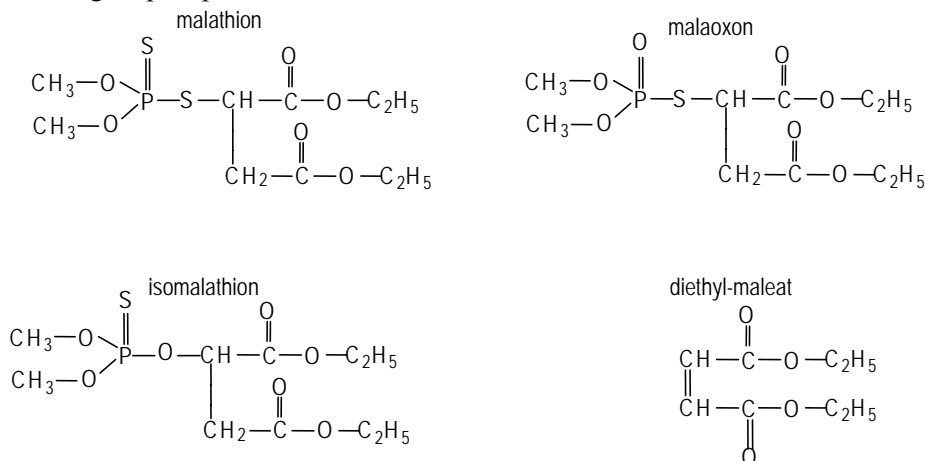
Experimental

All chemicals were of analytical grade. Standard solutions of malathion, malaoxon, isomalathion and diethylmaleate (0.1 M) were made in ethanol shortly before use. AChE, specific activity 0.28 UI/mg, from bovine serum was purchased from Sigma Chemicals Co. The AChE activity was measured by Ellman procedure [3]. The experiments were performed by single exposure of 200 µg enzyme to inhibitors in final volume 0.634 ml. All measurements were made in triplicate. The control tubes

contained the corresponding concentration of ethanole without organophosphate. Spectrophotometric measurements were performed on Perkin Elmer Lambda 35 UV VIS spectrophotometer.

Results and Discussion

The influence of organophosphates on AChE activity was investigated by *in vitro* exposure to the enzyme in the concentration range from 1×10^{-8} to 1×10^{-1} M. Besides, the inhibition potency of diethylmaleate was also investigated, since this compound is usually formed due to the chemical conversion or photochemical treatment of the selected organophosphates.



The results show, that malathion and its related compounds inhibit AChE in a concentration-dependent manner. The sigmoid shaped inhibition curves (Fig.1) were obtained in all cases. IC_{50} (half-maximum inhibitory concentration) and Hill coefficient n were determined using the Hill method (Fig.2), by linear regression analysis of $\log [\% \text{ activity}/(100 - \% \text{ activity})]$ vs. $\log C_{\text{inhibitor}}$ plots and are given in Table 1. Although the investigated organophosphates have similar structure (malaoxon and malathion are even isomers), it is obvious that the combination of the substituents at the central phosphorous atom is responsible for the inhibition power. This finding can be ascribed to the polarity of the chemical bond that binds phosphorous to sulfur (malathion, malaoxon) or oxygen (isomalathion) atom. However, the catalytic triad in AchE active site that performs the catalytic functions of the enzyme is composed of three amino acid residues: Ser 200, Glu 327 and His 440. It is generally considered that organophosphorus compounds inactivate the AChE by phosphorylation of serine (Ser 200) hydroxyl group in the active site of enzyme. It seems that the strong covalent character of malathion P-S complicates the nucleophilic attack to serine -OH group of protein. The consequence is the decrease of the fosforilation, i.e. relative high IC_{50} value. On contrary, P-S and P-O bonds in the case of isomalathion and malaoxon molecules are more electronegative, and facilitate the fosforilation. Moreover, oxygen atom in both cases increases the polarity of the central phosphorous atom, and favors the nucleophilic attack of serine -OH group from AChE. The consequence is the higher inhibi-

tory potency of these compounds. However, the inhibitory power of diethyl maleate is not significant.

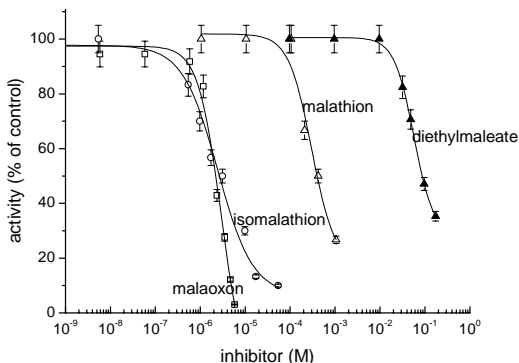


Fig. 1. Inhibition curves of AChE activity in the presence of malathion and its related compounds

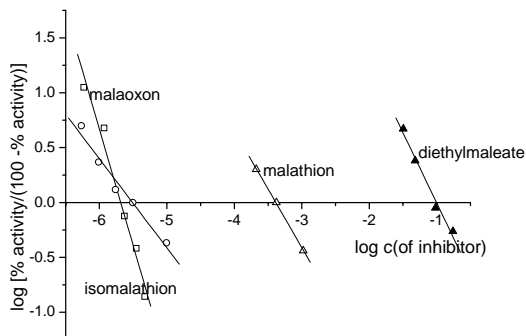


Fig. 2. Hill analysis of inhibition of AChE activity induced by malathion and its related compounds

Table 1. IC_{50} values of malathion and its related compounds obtained by fit of sigmoid inhibition curves and by Hill analysis

compound	IC_{50} , Hill [M]	n	IC_{50}
malaoxon	2.14×10^{-6}	2.12 ± 0.18	$(2.87 \pm 0.24) \times 10^{-6}$
isomalathion	3.18×10^{-6} M	0.81 ± 0.08	$(2.65 \pm 0.61) \times 10^{-6}$
malathion	4.32×10^{-4} M	1.06 ± 0.02	$(3.01 \pm 0.36) \times 10^{-4}$
diethyl maleate	0.10 M	1.28 ± 0.12	$(5.69 \pm 0.7) \times 10^{-2}$

Conclusion

The toxic effects of organophosphorus compounds and their transformation products (oxons, isomers) are primarily based on irreversible inhibition of acetylcholinesterase (AChE), enzyme which participates in the transfer of impulse in central synapses of the cholinergic nervous system through a chemical mediator, acetylcholine. The inhibition of AChE leads to acetylcholine accumulation and the exhibition of toxic effects, thus poisoning by these compounds is in fact poisoning by endogenous acetylcholine.

References

- [1] K. Musilek, K. Kuca, D. Jun, V. Donhal, M. Dolezal, Journal of Enzyme Inhibition and Medicinal Chemistry, 2005, **5**, 409-415.
- [2] M. Bavcon, P. Trebše, L. Zupančič-Kralj, Chemosphere, 2003, **50**(5), 595-601.
- [3] G.L. Ellman, K.D. Courtney, V. Andreas, Jr. R.M. Featherstone, Biochemical Pharmacology, 1961, **7**, 88-95.

PHOTODEGRADATION OF ISATIN-3-THIOSEMICARBAZONE

S. S. Konstantinović¹, D. Z. Marković¹ and B. C. Stojčeva-Radovanović²

¹*Faculty of Technology, Bulevar Oslobođenja 124, Leskovac*

²*Department of Chemistry, Faculty of Science, Višegradaska 33, Niš
(andjelkovic_s@yahoo.com)*

Abstract

The use of Schiff base for skin protection in cosmetics and pharmaceutical formulation is understandable since they are excellent UV-absorbers. Stability of isatin-3-thiosemicarbazone in DMF toward UV-A irradiation have been studied in this work. The proposed mechanism of photodegradation suggest hydrogen abstraction from solvent by Schiff base.

Introduction

The synthetic versatility of isatin has led to the extensive use of this compound in organic synthesis[1]. Since it's derivatives have a lot of potential biological and pharmacological applications. Thiosemicarbazone, as the representative, has attracted a considerable interest because of their reactivity and potential beneficial biological activities, such as antitumor, antibacterial, antiviral and antimalarial ones [2]. Many coordination compounds of transition metals with isatin derivatives show greater activity than the ligand alone. Though being very stable in the dark, these solid compounds become very unstable upon dissolution, especially when being irradiated by UV-light; this is not surprise because they are known as the excellent UV-absorbers [3]. Since UV-light is one of the major agents leading to melanoma skin cancer [4,5] Schiff bases have been used for some time in skin protection cosmetics and pharmaceutical formulations. Yet, the basic mechanisms related to their interactions with UV-light are still under investigations. For such a purpose stability of isatin-3-thiosemicarbazone toward UV-A irradiation has been studied in this work.

Experimental

Continuous irradiation of Schiff base in dimethylformamide (DMF) (10^{-6} mol·dm⁻³) was performed in Cylindrical photochemical reactor "Rayonnet", with 14 symmetrically placed lamps with emission maxima at 350 nm (UV-A), and total measured energy flux about 18 W·m⁻². The sample was irradiated in quartz cuvettes (1x1x4.5 cm) placed on rotating circular holder. Upon the irradiation the were taken immediately to Varian Cary-100 spectrophotometer: the UV-VIS spectra were recorded in the 300-600 nm range.

Results and Discussion

UV-VIS absorption spectra of isatin-3-thiosemicarbazone after continuous prolonged irradiation (0, 5, 15, 30, 45 i 60 min.) with UV-A light have been shown in Fig. 1. Both the absorption maxima ($\lambda_{\max}=348$ nm and $\lambda_{\max}=366$ nm) decrease, and a slight bathochromic shift have been detected, at the end of any particular UV-irradiating period. The log values of absorbance maxima plotted against irradiation time yielded a linear plot, suggesting the implying kinetics to be probably of pseudo-first order, depending on the isatin-3-thiosemicarbazone concentration only.

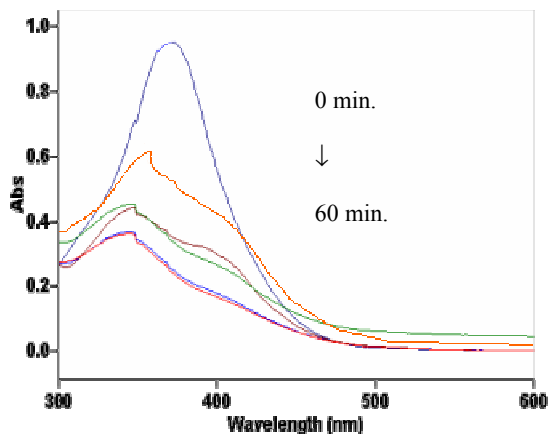


Fig. 1. The changes of absorption spectra of isatin-3-thiosemicarbazone after continuous prolonged irradiation (0, 5, 15, 30, 45 i 60 min.)

The mechanism leading to isatin-3-thiosemicarbazone concentration decrease certainly involves hydrogen abstraction from DMF by triplet state of isatin' C=O group, a well known reactive chromophore, playing an sensitizing role [7]; the other potential mechanisms (like electron-transfer mechanism) – but more related to use of UV-B or UV-C light – are probably minor or excluded in this case. The suggested UV-induced initiation step – emphasizing a crucial role of carbonyl chromophore - is shown in Fig.2. The consequent, radicals mediated events (the ketyl-radical and DMF-radical), can only be speculated, since the flash techniques were not available.

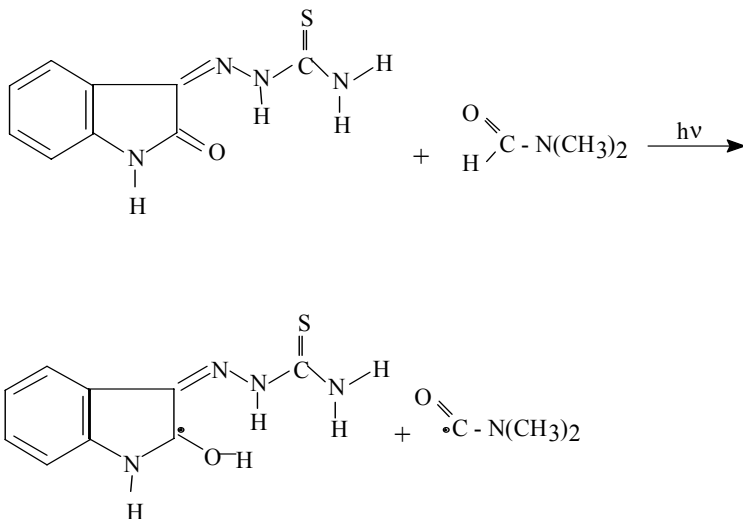


Fig. 2. Proposed mechanism of isatin-3-thiosemicarbazone photoreduction

Conclusion

The Schiff base isatin-thiosemicarbazone undergoes to UV-A induced change, probably based on hydrogen-abstraction from DMF solvent by triplet state of its carbonyl chromophore; the other potential mechanisms are probably minor or excluded. The concentration decrease follows pseudo-first order kinetics.

Reference

- [1] B. C. Radovanović, S. S. Konstantinović, *Chemical Industry*, 2003, **57**, 444.
- [2] N. M. Samus, T. A. Burdenko, V. V. Gylka and V. J. J. Tsapkov, *J. Chem. Pharma.* 1994, **12**, 40.
- [3] C. Soykan, J. Erol, *J. Polymer Science Part A.* 2003, **41**, 1942.
- [4] D. Z. Marković, T. Durand, L. K. Patterson, *Photochemi.Photobiol.*, 1990, **51**, 389.
- [5] D. Z. Marković, L. Patterson, *Photochemi.Photobiol.*, 1993, **58**, 329.
- [6] J. D. Coyle, *Introduction to Organic Photochemistry*, John Wiley & Sons, Great Britain, 1986.
- [7] J. C. Sciano, J. C. Sekyn, *Can, J., Chem* 1981, **59**, 2368.

UV-EFFECTS ON ANTIOXIDANT CAPACITIES OF β -CAROTENE AND LYCOPENE IN THE PRESENCE OF LECITHIN

D. Cvetković and D. Marković

University of Nish, Faculty of Technology, Leskovac, Serbia

Abstract

Antioxidant action of two carotenes (β -carotene and lycopene) on UV-induced lecithin' lipid peroxidation has been studied by TBA test, based on measurements of complex' absorbance formed between malondialdehyde (MDA – secondary product of lipid peroxidation), and thiobarbituric acid (TBA) at 532 nm. The antioxidant capacities of both carotenes are certainly affected by UV-action. High energy input of the involved UV-photons plays major governing role. The results suggest a minor contribution of both carotenes to prevention of the UV-induced lecithin peroxidation in the studied system, partly dependent of their structures.

Introduction

The depletion of the ozone shield leads to increase of biologically damaging UV-light at ambient levels (mainly UV-B light, 280-320 nm). UV-light can generally influence many crucial biologically important processes of global importance, such as DNA replication [1], photosynthesis [2], immune response [3], and it has been especially recognized as one of the major agents leading to skin cancer [4]. UV-light initiate these harmful processes triggering the very complex process of free radicals mediated lipid peroxidation (LP) by generating Reactive Oxygen Species (ROS) like hydroxy radicals (OH^\cdot) or peroxy radicals (ROO^\cdot). Lipid peroxidation is mostly controlled by antioxidants action. In recent years, carotenoids have received wide research interest as potential antioxidants. Antioxidant action of carotenoids is based on their conjugated chemical structures with multiple potential sites approachable for attack by ROS species [5]. UV-irradiation certainly affects carotenoids antioxidant function *in vivo* [2], though the involved mechanisms are not elucidated yet. Therefore, UV-irradiation effects on antioxidant capacities of two plants photosynthetic accessory pigments, β -carotene and lycopene *in vitro*, in the presence of lipoidal target (lecithin), have been studied in this paper. Lipid peroxidation has been induced by UV-light (UV-A, UV-B and UV-C). The extent of lipid peroxidation is monitored by thiobarbituric acid (TBA-MDA) test.

Experimental

β -carotene was extracted from spinach leaves (*Spinacia oleracea* L) by using petroleum ether/methanol mixture (1:2) for extraction. Methanol removes the water from the plant material and the petroleum ether takes up the pigments. Secondary extraction was performed using petroleum ether/diethyl ether mixture (1:1). The procedure was repeated three times [6]. The β -carotene fraction was isolated using a column chromatography with silica gel as the adsorbent and benzene as the eluent. Lycopene was extracted from tomato fruits by using acetone/petroleum ether (1:1) mixture for extraction. Petroleum ether layer was rinsed out by saturated solution of NaCl, 10% K_2CO_3 and water. The lycopene fraction was isolated using a column chromatography with alumina as the adsorbent and the mixture of petrol-ether/acetone (10:0.1) as the eluent. Presence of carotenoids in the separated fractions have been proved by

HPLC (Hewlet Packard, isocratic conditions: coulmn-ZorbaxEclipse XDB-C18, mobile phase (acetonitrile/methonol/etilacetate = 60:20:20), flow rate = 0,5 mlmin⁻¹. The antioxidant capacities of carotenes (% of inhibition of lipid peroxidation) was evaluated by TBA test, by using modified method from Choi *et al.* [7]. The test is based on a complex formed between malondialdehyde (MDA – which is a secondary product of lipid peroxidation) and TBA, producing an intensive pink colour. Lecithin (a mixture of phospholipids) was used as protection target in this work. Lecithin/carotenes mixtures were irradiated by UV-light, incubated 10 min with TBA at 37 °C, centrifuged, and the absorbance of supernatant TBA-MDA complex was measured at 532 nm. The initial concentrations were 7×10^{-6} moldm⁻³ for carotenes, and 2×10^{-3} moldm⁻³ for lecithin. Continuous irradiation was performed in cylindrical photochemical reactor “Rayonnet“, with 14 symmetrically placed lamps having emission maxima at: 254 nm (UV-C), 300 nm (UV-B) and 350 nm (UV-A). The total measured energy flux (hitting the samples) is about 25 W/m² for 254 nm, 21 W/m² for 300 nm and 18 W/m² for 350 nm. VIS spectra of the TBA-MDA complex were recorded on VARIAN Cary-100 Spectrophotometer, from 400 to 800 nm.

Results and Discussion

Decrease of inhibition of UV-induced lecithin peroxidation by the two carotenes (β -carotene and lycopene), as a result of increasing irradiation intervals, has been shown in **Fig. 1**. The kinetic log-plots obtained with UV-B and UV-A light (for β -carotene), and UV-C and UV-B light (for lycopene) have shown very similar shapes. The plots expressed a linear fitting, with an average R values of about 0.97. The absorbances measurements at 532 nm were done for *sample* and *control*. The *sample* contains mixtures of the pigments (β -carotene and lycopene) and lecithin. The *control* contains lecithin only.

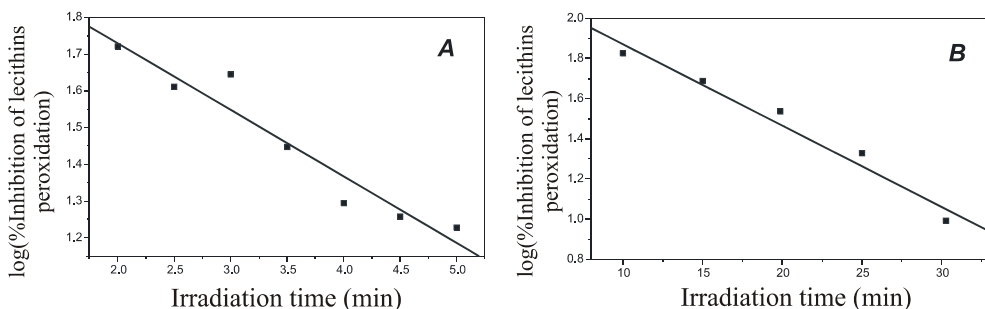


Fig. 1: Results of TBA-MDA test: decrease of inhibition of UV-induced lecithins peroxidation (A) in the presence of β -carotene during increasing UV-intervals at 254 nm (UV-C); (B) in the presence of lycopene during increasing UV- intervals at 350 nm (UV-A).

The slopes calculated from kinetic log-plots (**Fig. 1a-b**), represent the rates of inhibition decrease of UV-induced lecithin peroxidation (K_1), increase of *control* absorbance at 532 nm (K_2) and increase of *sample* absorbance at 532 nm (K_3). The rate constants are given in **Table 1**.

Such presentation provides the slopes (rates constants) comparison, reflecting changes in inhibition of lecithin peroxidation (by the two carotenes), and peroxidation kinetics for pure lecithin solution and lecithin/pigments mixtures, by UV-irradiation in all three ranges. It allows an insight to possible changes in protective function of the two carotenes toward UV-induced lecithin peroxidation.

Table 1. Kinetics of lipid peroxides production (K_2 , K_3) and inhibition (K_1) in a solution containing the mixture of two carotenes (7×10^{-7} moldm $^{-3}$) and lecithin (2×10^{-3} moldm $^{-3}$), during UV-irradiation with emission maxima in three different ranges: 254nm (UV-C), 300nm (UV-B) and 350nm (UV-A) – results of TBA-MDA test.

β -CAROTENE				LYCOPENE			
UV-irradiation wavelength (nm)	K_1 min $^{-1}$	K_2 min $^{-1}$	K_3 min $^{-1}$	UV-irradiation wavelength (nm)	K_1 min $^{-1}$	K_2 min $^{-1}$	K_3 min $^{-1}$
254	-0.180	0.193	0.113	254	/	/	/
300	-0.179	0.053	0.039	300	-0.150	0.042	0.058
350	-0.045	0.010	0.009	350	-0.041	0.009	0.018

$y_1 = K_1x + n$; y_1 - log (% of inhibition of lecithins peroxidation); x -irradiation time

$y_2 = K_2x + n$; y_2 - log (Control absorbance at 532nm); x - irradiation time

$y_3 = K_3x + n$; y_3 - log (Sample absorbance at 532nm); x - irradiation time

Conclusions

Inhibition of lecithin peroxidation in the presence of β -carotene is affected by UV-irradiation, based on results of TBA-MDA test (**Table 1**). β -carotene still do the inhibition – since K_2 rate constant (pure lecithin) is always bigger than K_3 (β -carotene + lecithin) – for all three UV-ranges. However, while the change of pigment' antioxidant (inhibition) capacity is most enhanced in UV-C & UV-B ranges (the K_1 values are the same), and negligible in UV-A range (compared to the former ones), this fact has been only partly confirmed through comparison of the K_3/K_2 ratios for all three UV-ranges: ranging from 1 for UV-A, via 0.74 for UV-B, to 0.59 for UV-C. Evidently, a different high energy input of the involved UV-photons plays a crucial role related to a change of β -carotene antioxidant action. A contraversial behaviour has been also seen with lycopene: (i) the $K_{1,UV-B}/K_{1,UV-A}$ ratio confirms a change in antioxidant capacity, while (ii) K_3/K_2 ratio ($>1!$) denies it.

Acknowledgements

Dragan Cvetković is a recipient of a fellowship granted by Ministry of Science and Environmental Protection, Republic of Serbia.

References

- [1] M. Ichihashi, M. Ueda, A. Budiyannto, T. Bitto, M. Oka, M. Fukunaga, K. Tsuru, T. Horikawa, *Toxicology*, 2003, **189**, 21-39.
- [2] A. Teramura, L. Ziska, *Photosynthesis and the Environment*, Kluwer, 1996.
- [3] T. Schwarz, *European Journal of Dermatology*, 1996, **6**, 3, 227-228.
- [4] A. Ouhtit, H. Ananthaswamy, *Journal of Biomedicine and Biotechnology* 1:1, 2001, 5-6.
- [5] G. W. Burton, K. U. Ingold, *Science*, 1984, **224**, 569-573.
- [6] W. A. Svec, *Chlorophylls*, CRC Press, Boca Raton, FL, 1991
- [7] Choi W. C., Kim C. S., Hwang S. S., Choi K. B., Ahn J. H., Lee Y. M., Park H. S., Kim K. S., *Plant Science*, 2002, **163**, 1161-1168.

UV-IRRADIATION INDUCED CHLOROPHYLLS BLEACHING IN PIGMENTS EXTRACTS

J. Zvezdanović and D. Marković

University of Nish, Faculty of Technology, Leskovac, Serbia

Abstract

Stability of chlorophylls toward UV-irradiation has been studied in extracts containing mixtures of photosynthetic pigments isolated from spinach leaves, in two different solvents: hexane and acetone. Chlorophylls undergo destruction (bleaching) obeying to first-order kinetics. The bleaching is governed by two major factors: UV-photons energy input and the solvents polarities.

Introduction

Beyond being the ultimate driving force of photosynthesis and its important regulatory factor, solar light is also a mayor source of stress to photosynthetic organisms. Depletion of stratospheric ozone has led to an increase of biologically damaging UV-light at ambient levels (mainly UV-B light, 280-320 nm). Though photosynthetic pigments such are chlorophylls and carotenoids absorb in VIS region, their composure is significantly altered when exposed to UV-light [1]. That may cause an impairment of photosynthetic function. Chlorophyll (Chl) is a major photosynthesis pigment. The chlorophylls perform light-harvesting function in antennas of photosynthetic apparatus, or act as exciton traps and electron-carriers in reaction centers (RC) [2]. Chlorophyll is a chlorin, porphyrin derivate, cyclic tetrapyrrol with isocyclic cyclopentanone ring, fused at the edge of the right-bottom pyrrole ring; the central Mg-atom plays a coordinating role. Stability of chlorophylls in extracts of photosynthetic pigments (obtained from spinach leaves) against UV-irradiation from three different ranges (UV-A, UV-B and UV-C) has been studied in this work.

Experimental

Photosynthetic pigments were extracted from spinach leaves (*Spinacia oleracea* L) by using Swec's method [3]. The pigments mixtures contain large amounts of various Chl-forms (with predominant contribution of Chlorophyll *a* - Chl*a*) as well as accessory pigments, carotenoids. The pigment extracts were evaporated and diluted (1:10) in hexane or acetone. Continuous irradiation in hexane and acetone was performed in cylindrical photochemical reactor "Rayonnet", with 14 symmetrically placed lamps having emission maxima at: 254 nm (UV-C), 300 nm (UV-B) and 350 nm (UV-A). The total measured energy flux (hitting the samples) is about 25 W/m² for 254 nm, 21 W/m² for 300 nm and 18 W/m² for 350 nm. VIS spectra of the pigment mixtures before and after UV-irradiation were recorded on VARIAN Cary-100 Spectrophotometer, from 300 to 800 nm. HPLC analysis, before and after irradiation, was done under isocratic conditions; coulumn: Zorbax Eclipse XDB-C18, mobile phase: acetonitrile/methanol/etilacetate, 60:20:20; flow rate: 0.5 mlmin⁻¹ [4]. The monitoring wavelength was 430 nm.

Results and Discussion

Chlorophylls have two major absorption regions in visible range: “red” (*Q*) band and “blue” (Soret or *B*) band [5]. The UV-induced changes were detected in the pigments mixtures with *Q*-bands (that belong to chlorophylls only, and not to carotenoids), at maximal absorption wavelengths (~ 680 nm): a series of hypochromic effects have been observed for irradiated chlorophylls, relative to irradiation time, t (min). Changes in the pigments mixtures absorption spectra after a continuous prolonged irradiation with UV-B light (300 nm), and a corresponding kinetic ln plot as a result of increasing irradiation intervals have been shown in **Fig.1 (A-B)**.

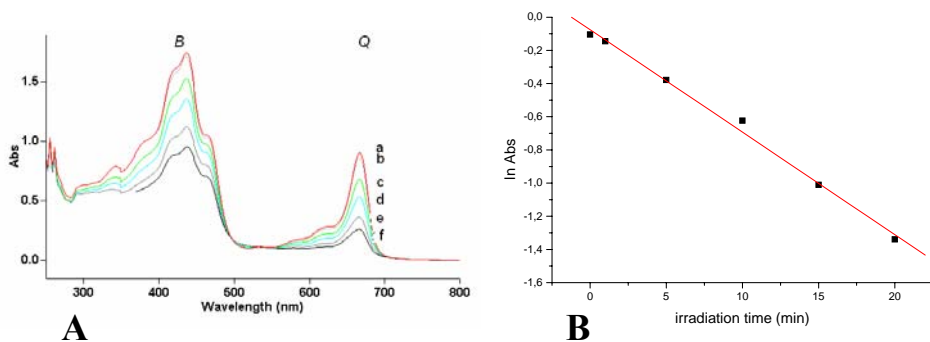


Fig.1: (A) Changes in the pigments mixtures absorption spectra following their exposure to UV-B radiation at 300 nm in hexane. The exposure time periods were: (a) 0 min; (b) 1 min; (c) 5 min; (d) 10 min; (e) 15 min; (f) 20 min. The approximate chlorophylls (*a+b*) concentration was $2,0 \times 10^{-5} \text{ moldm}^{-3}$; (B) The kinetic ln plot of the chlorophylls bleaching in hexane, during increasing UV-B irradiation. The absorbance (Abs) of chlorophyll was followed at A_{max} *Q*-band value (~ 680 nm).

The pigments absorption spectra have shown very similar answers during the same irradiation regimes with UV-A and UV-C light. Their kinetic ln plots are of very similar shapes with the presented one (**Fig.1B**). The plots express a linear fitting with average *R* values of about 0.99. The chlorophylls’ destruction (bleaching) kinetics seems to obey a first-order law [6] (**Fig.1B**). The calculated bleaching rate constants for all three UV-ranges and in two different solvents are shown in **Table 1**.

Tab.1: Kinetics of chlorophylls bleaching in hexane and acetone, during increasing UV-irradiation intervals in three different UV-ranges: 254 nm (UV-C), 300 nm (UV-B) and 350 nm (UV-A). Chlorophylls absorbances were followed at A_{max} *Q*-band value (680 nm).

UV-irradtn. (nm)	Chlorophylls bleaching in hexane	Chlorophylls bleaching in acetone
	$K \text{ (min}^{-1}\text{)}$	
254 (UV-C)	-0,40726	-0,28604
300 (UV-B)	-0,06176	-0,42701
350 (UV-A)	-0,00603	-0,13029

The HPLC chromatograms of the pigments mixtures exposed to UV-C radiation at 254 nm in acetone have been shown in **Fig.2 (A-B)**. The UV-induced changes were detected through decrease of the corresponding peaks' areas (the peaks with retention time ~11 min assigned to Chl**b**, and at ~18 min assigned to Chl**a**, were reduced). New peaks have not clearly observed (**Fig.2B**).

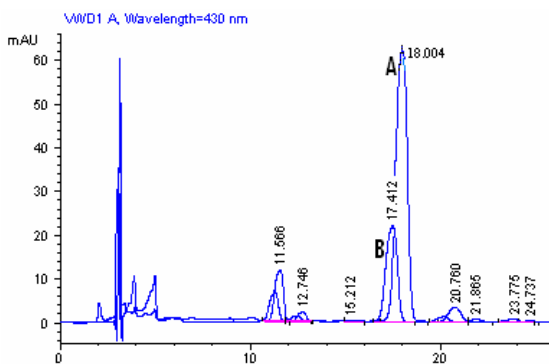


Fig.2: HPLC chromatograms of the pigments mixture; (A) non-irradiated; (B) after 5 min of irradiation with UV-C.

The results from **Table 1** show that chlorophylls bleaching in the pigments mixtures depend on UV-photons energy input and on the solvents polarities as well.

Knowing that chlorophylls are not UV-absorbers and still undergo to UV-induced bleaching put the emphasis on a role of radical species created by UV-action.

On the other hand the solvents polarities' influence highlight a role of chlorophylls molecules' organizations in the two solvents. Chlorophylls are efficient electron-donors and acceptors which enable them to build a "dimer" type of organization in non-polar hexane, whereas in highly polar acetone the neighbouring Chl molecules are connected *via* acetone's carbonyl chromophores "bridges" [7]. The different bleaching rate constant values from **Tab.1** confirm that UV-created radical species affect differently these two "different" chlorophylls (the other species presented in the pigments mixtures can not match Chls and acetone's donor-acceptor properties).

Conclusions

The chlorophylls undergo UV-induced destruction (bleaching) in the photosynthetic pigments mixtures, following first-order kinetics. The bleaching rates are highly dependent on the involved UV-photons energy input and the Chls molecular organizations in the two different solvents.

References

- [1] Teramura, L. Ziska, Photosynthesis and the Environment, Kluwer, 1996.
- [2] H. Scheer, CRC Handbook of organic photochemistry and photobiology, CRC Press, Boca Raton, FL, 2003.
- [3] W. A. Svec, Chlorophylls, CRC Press, Boca Raton, FL, 1991.
- [4] Y. Shioi, Chlorophylls, CRC Press, Boca Raton, FL, 1991.
- [5] J. Hoff, J. Amesz, Chlorophylls, CRC Press, Boca Raton, FL, 1991.
- [6] P. Cuny, J. C. Romano, B. Beker, J. F. Rontani, J. Exp. Mar. Biol. Ecol., 1999, **237**, 271-290.
- [7] J. J. Katz, L. L. Shipman, T. M. Cotton, T. R. Jason, The Porphyrins, Academic Press, 1978.

LOW DOSE GAMMA-IRRADIATION ALTERS THE EXPRESSION OF P53 PROTEIN IN THE RAT HIPPOCAMPUS

N. Veličković, A.D. Đorđević and N. Popović

*Laboratory for Molecular Biology and Endocrinology, "Vinča" Institute of Nuclear Sciences,
P.O. Box 522, Belgrade, Serbia*

Abstract

The tumor-suppressor p53 protein and glucocorticoid receptor (GR) respond to different types of stress. In an attempt to reveal the possibility that p53 protein is involved in the regulation of GR gene expression after low dose cranial irradiation (CI) with 2 Gy, we examined the expression of p53 mRNA and protein as well as expression of GR mRNA and protein in the hippocampus of 18-days-old rats. We found that p53 mRNA expression was unchanged after CI, while induction of p53 protein was rapid, leading to the accumulation of p53 protein in the cytoplasm. Irradiation leads to stimulated GR gene expression in a time-dependent manner, whereas the level of GR protein was unchanged after CI. Co-immunoprecipitation has not showed that wild type p53 protein physically interacts with the GR in the cytoplasm. Our data suggest that the low dose cranial irradiation leads to stabilization of the 53 protein, without interaction with GR protein in the cytoplasm.

Introduction

The tumor suppressor p53 gene encodes a nuclear phosphoprotein that functions as a key regulator of cell cycle arrest or apoptosis in response to various stresses, such as DNA damage, irradiation and hypoxia [1]. Glucocorticoid receptor (GR) is a member of the steroid receptor superfamily that mediates physiological processes controlled by glucocorticoids (GCs). The primary physiological function of GCs is to maintain homeostasis response to environmental changes [2]. Recently, evidence has been growing for cross-talk between the p53- and GR-mediated responses to stress. p53 physically interacts with and represses the activities of GR [3]. GCs prevent p53-induced apoptosis in human granulose cells [4]. Upon irradiation of cells with gamma-rays, the level of p53 protein is increased, presumably not followed with change in the mRNA level [5]. Our previous results showed the apparent induction of GR mRNA in the rat hippocampus after 10 Gy of gamma-irradiation. Because little is known about the functional interactions between signaling pathways mediated by GR and p53 under physiological conditions, we have investigated how p53 and GR regulate each other after low dose cranial irradiation (2 Gy) *in vivo* in rat hippocampus. The hippocampus was isolated at the following post-irradiation times: 1 h, 2 h, 4 h, 8 h, and 24 h. The level of GR and p53 mRNA was assessed by semi quantitative RT-PCR using as the internal standard mRNA for glyceraldehyde-6-phosphate dehydrogenase (GAPDH).

Results and Discussion

Low dose gamma radiation, routinely used in diagnostic protocols and clinical radiotherapy, have profound effects on the brain, leading to precursor cell dysfunction and debilitating cognitive decline. Although a plethora of molecular mechanisms are involved in acute effects of irradiation, one molecule is inevitable in decision between life and death: tumor-suppressor p53. Low dose irradiation rapidly stimulated p53 protein in a time-dependent manner (Figure 1), whereas the level of p53 mRNA expression showed no statistically significant changes (data not shown).

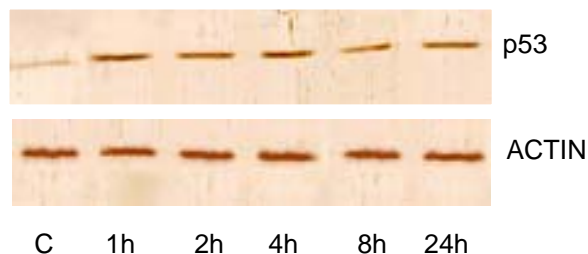


Fig. 1. Level of p53 protein expression in 18-days-old rats irradiated with dose of 2 Gy at different time points. The densitometric analysis of p53 protein were normalized to actin; C-immobilized control rats

involved in acute effects of irradiation, one molecule is inevitable in decision between life and death: tumor-suppressor p53. Low dose irradiation rapidly stimulated p53 protein in a time-dependent manner (Figure 1), whereas the level of p53 mRNA expression showed no statistically significant changes (data not shown).

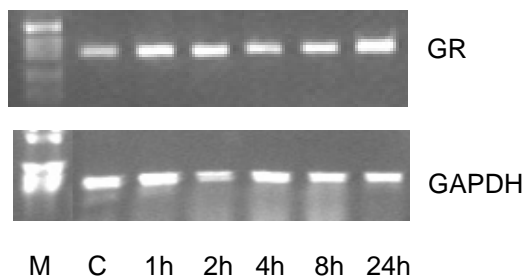


Fig. 2. Level of hippocampal GR mRNA expression in rats irradiated with 2 Gy at different time points. The densitometric analysis of GR mRNA were normalized to GAPDH M-DNA molecular weight marker C-immobilized control rats

Low dose CI (2 Gy) leads to induction of GR gene expression with peak expression observed after 2 h, remaining high up to at least 24 h (Figure 2). In contrast to GR mRNA, the dose of 2 Gy did not alter the level of GR protein as revealed by preliminary Western blot experiments (Figure 3).

On the other hand, in our previous experiments, irradiation with 10 Gy leads to cytoplasmatic sequestration of activated GR (after treatment with synthetic hormone dexamethasone).

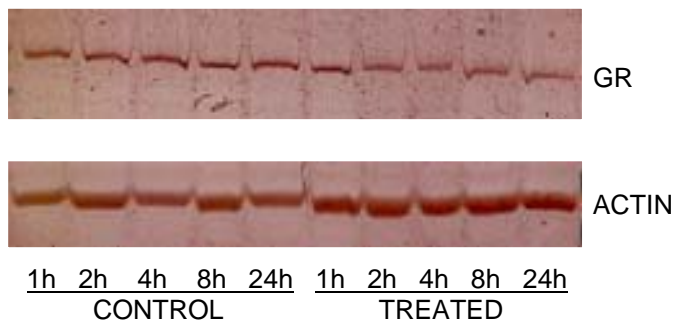


Fig. 3. Level of GR protein expression in 18-days-old rats irradiated with dose of 2 Gy at different time points. The densitometric analysis of GR protein were normalized to actin;
Control-immobilized control rats

According to other publications, GR forms a complex with p53 *in vivo* in neuroblastoma cells thus resulting in cytoplasmatic retention and inactivation of wild type p53 [3]. Our study has not showed that wild type p53 protein physically interacts with the GR in cytoplasm.

Conclusion

Our results showed that low dose gamma irradiation leads to rapid induction of p53 protein in the cytoplasm of rat hippocampal cells, without change in mRNA level. On the contrary, the GR mRNA was increased after irradiation with 2 Gy, while the level of GR protein was unchanged. Co-immunoprecipitation showed that the accumulation of p53 protein in the cytoplasm was not a result of physical interaction of GR and p53 protein. These data may contribute to unraveling the mechanism of antiapoptotic effects of GCs, since dexamethasone is frequently used as a co-treatment agent in cancer therapy.

Acknowledgement

This study was supported by the Serbian Ministry of Science and Environmental Protection, Project No. 143044.

References

- [1] L. J. Ko and C. Prives, *Genes Dev.*, 1996, **10** (9), 1054-1072.
- [2] C. Kellendonk, F. Tronche, H. M. Reichardt, G. Schutz, *J. Steroid Biochem. Mol. Biol.*, 1999, **69** (1-6), 253-259.
- [3] S. Sengupta, J.-L. Vonesch, B. Waltzinger, H. Zheng, B. Wasylyk, *EMBO J.*, 2000, **19** (22), 6051-6064
- [4] R. Sasson, K. Tajima, A. Amsterdam, *Endocrinology*, 2001, **142** (2), 802-811.
- [5] X. Lu, D. P. Lane, *Cell*, 1993, **75**, 765-778

REDOX-SENSITIVE TRANSCRIPTION FACTOR NFκB IN BRAIN OF STRESSED WISTAR RATS

M. Adžić, B. Zarić, A. Nićiforović and M. B. Radojčić

VINCA Institute of Nuclear Sciences, P.O. Box 522, Belgrade, Serbia

Abstract

Neuroendocrine stress (NES) causes stress-hormones increase and alters balance of intracellular reactive oxygen species (ROS) leading to vulnerability of brain neurons. Prolonged alterations of cell redox *milieux* may also lead to altered expression of redox sensitive transcription factors, such as NFκB, responsible for brain cell protection. In the presented study NFκB p65 (NFκB) levels were determined in hippocampus and brain cortex of Wistar male rats exposed to stress of different duration. The cytosolic NFκB level was unchanged in acute stress (A, 2h), but significantly down-regulated in either chronic (C, 21-day) or combined (C+A) stress. The depletion of NFκB from cell cytosol probably reflected its nuclear translocation and decoupling from the repressive action of glucocorticoid receptor. Through initially protective, NFκB overactivity may lead to accumulation of toxic H₂O₂ and compromise brain cell capacity to restore homeostasis.

Introduction

Neuroendocrine stress (NES) is followed by the marked increase in the concentration of stress hormones: catecholamines (CAM) and glucocorticoids (GCs). Such conditions are known to increase the basal production of reactive oxygen species (ROS) in stress-responsive brain structures, leading to increased vulnerability of brain neurons [1]. Neurotoxicity is brought about by the oxidative metabolic pathways of catecholamines (CAM) which generate highly reactive quinones, superoxide radical (O₂⁻) and H₂O₂, and by the GCs induced alterations in calcium metabolism [1]. Intracellular changes in ROS equilibrium are sensed by redox-sensitive transcription factors, such as nuclear factor κB (NF-κB) and glucocorticoid receptor (GR), which alter expression of antioxidant enzymes (AOE) and other stress responsive cellular enzymes. The extent of NES-triggered effects and the resulting neurotoxicity is related to the NES duration. Our previous results indicated that chronic social isolation is highly potent stressor which causes pulsed elevation of CAM and prolonged elevation of GCs concentration in Wistar male rat brain [2]. It is supposed that these conditions may alter redox *milieux* and alter expression of NFκB and GR in hippocampus and brain cortex [3] which is tested in this preliminary study.

Experimental

Adult Wistar rat males (2-3 months old, body mass 330-400g) were divided into four groups: Group I consisted of unstressed animals (control=Ctrl) kept four *per* cage; Group II was exposed to 4 °C for 2h as acute stressor (A); Group III was exposed to chronic isolation by individual housing for 21 day (C); Group IV was exposed to combined stress of chronic isolation plus acute cold (C+A). Hippocampus and cortex were homogenized in 20mM Na-phosphate buffer pH 7.0, 0.1mM EDTA-Na₂, 0.1mM EGTA-Na₂, 10% glycerol, 50mM NaCl, 1mM DTT, 1mM Na₂MoO₄, 1.5mM spermin, 1mM PMSF and 500μg/mL apro-

tinin. Cell nuclei and mitochondria were pelleted by centrifugation and supernatant was taken as cytosol. Cytosolic proteins were separated by sodium dodecylsulphate-polyacrylamide gel electrophoresis (SDS-PAGE), transferred to nitrocellulose and incubated with rabbit anti-NF κ B (NF κ B p65) or rabbit anti-actin antibody. A secondary goat anti-rabbit IgG-HRP conjugate was used for visualization of specific protein bands quantified by PC Imager. The data were presented as mean \pm S.D. (n=4). Analysis of variance (one-way ANOVA) and Tukey's post-hoc test were used to determine statistically significant differences ($P<0.05$).

Results and Discussion

Western blot (WB) quantification of redox-sensitive transcription factor NF κ B in hippocampus and brain cortex of Wistar male rats revealed significant down-regulation of its p65 subunit after either chronic social isolation (C) or combined stress (C+A) (Figure 1). The expression level of p65 was unchanged by the acute stress (A).

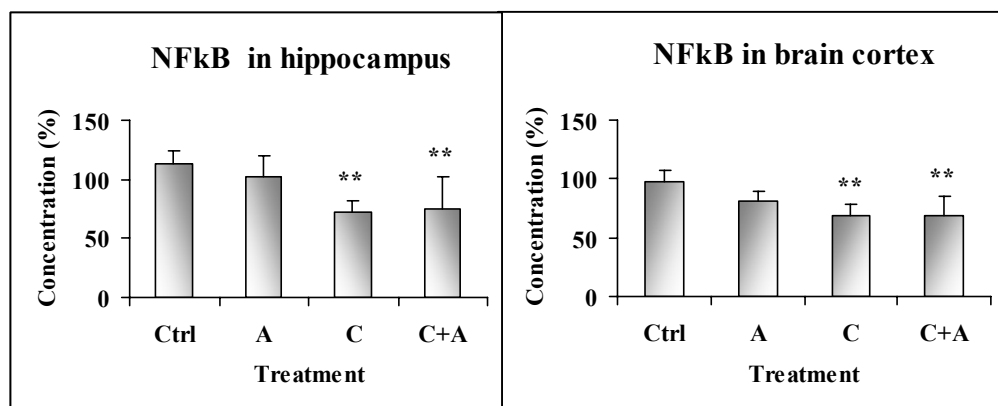


Fig. 1. NF κ B in control (Ctrl) acute (A), chronic (C) and combined (C+A) stress. Results are presented as mean \pm S.D (n=4)

Table 1. The expression level of NF κ B and GR proteins in brain cell cytosol
Results are presented as mean \pm S.D (n_{NF κ B}=4, and n_{GR}=6)

Structure	HIPPOCAMPUS				BRAIN CORTEX			
	Ctrl (%)	A (%)	C (%)	C+A (%)	Ctrl (%)	A (%)	C (%)	C+A (%)
NF κ B	100	102 \pm 17	72 \pm 9**	74 \pm 27**	100	81 \pm 8	69 \pm 9**	69 \pm 17**
GR ^[3]	100	60 \pm 7***	89 \pm 5**	71 \pm 3***	100	60 \pm 5***	83 \pm 7	70 \pm 7

As both *in vitro* and *in vivo* NF κ B p65 was found in association with GR, which led to their mutual transcriptional antagonism, the NES-triggered alterations in the expression of hippocampal and cortical NF κ B may be better understood if compared with the respective expression of GR determined in the previous study (Table 1) [3]. The unaltered level of NF κ B (p65) expression in the cytosol compartment after acute stress (A) is most probably

due to the GC-triggered nuclear translocation of GR and the repression of NFκB promoter. The cytosolic expression pattern of both NFκB and GR most probably reflects typical adaptive response to acute NES, resulting in successful restoration of cell homeostasis. Contrary to that the depletion of cytosolic NFκB after chronic isolation (C) may be linked to its translocation to the nucleus and activation of cellular defence mechanisms, particularly those related to oxidative stress response. One of the defence mechanisms involves CuZn-superoxide dismutase (CuZnSOD), the major cytosolic antioxidant enzyme whose expression is under NFκB control. CuZnSOD expression is shown to be up-regulated in chronic isolation [5]. Although CuZnSOD activity is primarily protective, if not coupled to the respective peroxidase activity, it may lead to accumulation of toxic H₂O₂. Moreover, H₂O₂ is a stimulator of NFκB activity, thus that it may trigger a positive feed-forward cycle with NFκB and enhance oxidative stress leading to neuronal cell death. In this way the price of cell accommodation to chronic stress may be paradoxal neurotoxicity. The incomplete nuclear translocation of cytosolic GR in chronic or combined NES (*Table 1*) may add to NFκB nuclear overactivity [3]. Taken together the results on NES exposed Wistar rats show that deregulation of the LHPA in chronic stress, affects also NFκB p65 expression level in cytosolic compartment. The lack of NFκB repression by GR might indicate that the brain cells will be continually experiencing NES-linked oxidative stress without resting, which, in a prolong period, may compromise their capacity to restore homeostasis and lead to cell energy exhaustion and cell death.

Conclusion

The cytosolic depletion of NFκB p65 found under chronic- and combined neuroendocrine stress (NES) conditions most probably reflects its nuclear translocation leading to transactivation of oxidative stress protective enzymes, such as CuZnSOD. However, due to deregulated GR and its cytosolic retention in chronic and combined stress, nuclear NFκB may be uncoupled from its GR repression at more levels. The overactivity of NFκB may lead to disproportional CuZnSOD enhancement and cell accumulation of toxic H₂O₂. In that way, *via* NFκB derepression, NES may be converted to oxidative stress, and instead of cell protection NFκB may compromise cell capacity to restore homeostasis.

References

- [1] J. Liu, A. Mori, *Neurochem.Res.*, 1999, **24**, 1479-1497.
- [2] S. Dronjak, Lj. Gavrilović, D. Filipović, M. B. Radojčić, *Physiol Behav.*, 2004, **81**, 409-415.
- [3] D. Filipović, S. Dronjak, Lj. Gavrilović, M. B. Radojčić, *Neuropsychobiology*, 2005, **51**, 107-114.
- [4] O. Perišić, M. B. Radojčić, D. T. Kanazir, *J.Biol.Chem.*, 1987, **262**, 11688-11591.
- [5] D. Filipović, M. B. Radojčić, *Ann.NY Acad.Sci.*, 2005, **1048**, 1-3.

LOW-DOSE IONIZING IRRADIATION AFFECTS NTPDase ACTIVITY IN NEURONAL CELLS OF YOUNG FEMALE RATS

I. Stanojević, A.D. Đorđević, A. Banjac and A. Horvat

*Laboratory for Molecular Biology and Endocrinology, "Vinča" Institute of Nuclear Sciences,
P.O.Box 522, Belgrade, Serbia*

Abstract

In the present study, time-dependent effects of low-dose ionizing irradiation on membrane-bound enzyme activity in neuronal cell endings of young female rat brains were studied. The ecto-adenosine triphospho diphosphohydrolases (NTPDases) hydrolyse the extracellular nucleotide di- and tri- phosphates (ADP and ATP) in the presence of divalent cations (Ca^{2+} and Mg^{2+}). The influence of whole-body irradiation on membrane enzymes ATP and ADP hydrolysing activity were monitored 1, 24 and 72 h after irradiation. Animals were divided into three groups: non-treated, under physiological conditions (C), immobilized and whole body irradiated with 50 cGy by γ -rays (R) and immobilized non-irradiated (I) animals. It was shown that the levels of ATP and ADP hydrolyses were not affected within 72h after immobilisation. Low-dose irradiation significantly decreased hydrolyses of extracellular ATP as early as 1h after irradiation. ADP hydrolyses within 72 h and ATP hydrolysis after 24 h were not altered.

Introduction

Low-dose ionizing irradiation (IR) effects cannot be explained only by direct damage to the DNA. The alternative target for low-dose effects (LDE) initiation in a cell are the plasma membranes which are highly sensitive to IR [1]. IR affects plasma membrane functions mediated through transmembrane proteins by altering their expression or changing the interaction(s) that normally take place between membrane lipids and proteins. Reactive oxygen species (ROS), generated following IR in the cell, act on polyunsaturated fatty acids of cellular membranes producing lipid peroxides which may alter functioning of plasma membrane proteins.

The ecto-enzymes are a family of transmembrane enzymes with a substrate-active site located in extra-cellular spaces. These enzymes hydrolyse nucleotide mono- di- and triphosphates. Adenosine triphosphate (ATP) functions as a fast excitatory neurotransmitter and neuromodulator in the central nervous system. The extracellular (synaptic) level of ATP is rapidly regulated by the conjugated action of synaptic plasma membrane (SPM)-bound, surface-located enzyme chain of ectonucleotidases. Ecto-ATPase (NTPDase2) are enzymes that hydrolyse preferentially ATP, whereas the ecto-ATPdiphosphohydrolase (NTPDase1) hydrolyses ATP equally well as ADP to AMP. The AMP formed is metabolized to adenosine by ecto-5'-nucleotidase [2]. As a result, an increased adenosine level, a main inhibitory neuromodulator, exerts neuroprotective function preserving the brain from excitotoxicity damage and has

various trophic roles during development. Inhibition of SPM ecto-ATPase activity would be expected to potentiate excitatory synaptic transmission by supporting synaptic efficacy of ATP and inhibiting the formation of adenosine.

Thus, the aim of this work is to study the LDE (50 cGy) of NTPDase activity through the rate of ATP and ADP hydrolysis, from the young rat brain SPM; 1h, 24h and 72h after whole body irradiation with gamma-rays.

Experimental Procedures

Female rats of the Wistar strain, 30 days old, were divided into three groups: the control group were under physiological conditions, the second was whole-body irradiated (50 cGy, 10.7cGy/min, ^{60}Co source). During irradiation, the animals were confined in plywood boxes. Because of the immobilisation stress as a positive control, the third group of animals were treated as the irradiated group but not subjected to irradiation (I). All groups were sacrificed 1h, 24h, and 72h after irradiation. Synaptic plasma membranes (SPM) were isolated from whole brains. Activities of NTPDase were determined under *in vitro* conditions: rate of ATP- and ADP-hydrolysis were measured by colorimetric determination of liberated inorganic phosphate in the presence of 40 μg SPM proteins, 1mmol/l ATP or ADP, 5 mmol/l MgCl_2 , 50 mmol/l Tris-HCl, pH 7.8, and incubations at 37 °C for 15 min. The specific enzyme activity was expressed as mean nmolPi/min/mg SPM protein \pm S.E.M. of the I animals in the respect to control animals or as a mean percentage \pm S.E.M. of irradiated animals in the respect to I, from 3 independent examinations performed in triplicate. The data were analyzed using Student's t-test and $p < 0.05$ values were considered significant.

Results and Discussion

To clarify if immobilization stress affects ATP and/or ADP hydrolyses, hydrolyzing activity of NTPDase from rats exposed to immobilising stress and non-treated (control) group were examined. Results show that hydrolysis of ATP and ADP were not affected by acute immobilisation (Fig.1).

Figure 2. presents the experimental result of time-dependent LDE (50 cGy) on the enzyme hydrolyzing activity. One hour after irradiation, ATP hydrolysis decreased by 20% ($p < 0,01$) when compared to I, but after 24 h as well as ADP hydrolyses within 72 h were not affected.

Analysis of the developmental profile of ATP hydrolyzing activity revealed that the activity reaches the maximum level at day 30. Thus, both NTPDase1 and 2 have a role in brain development at day 30 [3]. Several previous studies have reported that rat brain ecto-ATPase activity decreased under conditions that either promote or are associated with increased lipid peroxidation. The results demonstrate that low-pathologically relevance of 4-hydroxynonenal, the major product of membrane lipid peroxidation, selectively inhibits SPM NTPDase activity [4]. The low-dose (50 cGy) produces an inhibition of cell metabolism employed acutely.

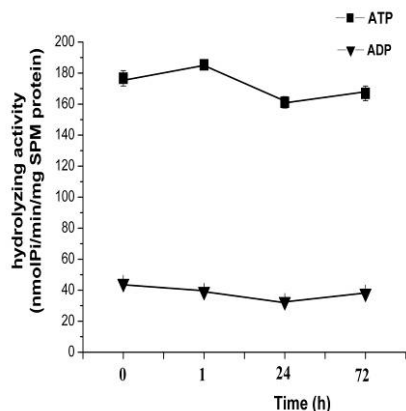


Fig. 1. Time-dependent effects of the immobilization on ATP and ADP hydrolysis activity of NTPDase. Enzyme specific activity of nucleotide hydrolyses presented as mean \pm S.E.M from three experiments done in triplicate.

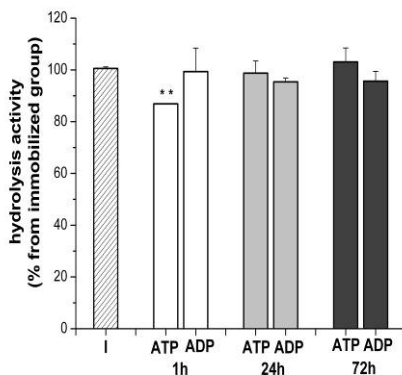


Fig. 2. Time-dependent LDE (50 cGy) on NTPDase activity represented in relative units, as percentage (%) of ATP and ADP hydrolysis in irradiated group compared with immobilized control I, (** $p < 0.01$). Results represent mean \pm S.E.M from three experiments done in triplicate.

Eidus [1] hypothesized that the inhibitory effect declines when the post-irradiation time period is sufficiently prolonged to enable the adaptive response to appear. Inhibition of ATP hydrolysing activity 1h after LD irradiation as shown in our study is in accordance with this hypothesis. Twentyfour hours is more than enough for the adaptive response to appear. On the other hand, only ATP hydrolysis is decreased but not ADP hydrolysis. This indicates that the enzyme structure of the NTPDase2 is more sensitive to LD of irradiation.

Conclusion

Whole body irradiation induces modulation of neuronal activity in young rat brain by decreasing extracellular ATP hydrolysis 1h after irradiation. After 24h, due to the adaptive response of neuronal cells, the effect is diminished.

Acknowledgements

This study was supported by the Serbian Ministry of Sciences and Environmental Protection, Project No. 143044.

References

- [1] L.Kh. Eidus, *Radiat. Environ. Biophys.*, 2000, **39**, 189-195.
- [2] H. Zimmermann, *Naunyn-Schmied. Arch. Pharmacol.*, 2000, **362**, 299-309.
- [3] A. Banjac, et al., *Physiol. Res.*, 2001, **50**, 411-418.
- [4] T.D. Foley, *Neurochem. Res.*, 1999, **24**, 1241-1248.

SUPEROXIDE DISMUTASES IN RADIORESISTANT PC-3 HUMAN PROSTATE CARCINOMA CELLS

J. Prokopović, M. Adžić, A. Nićiforović,
V. Vučić, B. Zarić and M. B. Radojčić

VINČA Institute of Nuclear Sciences, P.O. Box 522, Belgrade, Serbia

Abstract

The molecular mechanism of gamma-ionizing radiation (IR) resistance of human prostate cancer cells PC-3 is not known. Since low-LET-IR effects are primarily achieved through generation of reactive oxygen species (ROS), IR-induced expression of ROS-metabolizing antioxidant enzymes, Mn- and CuZn-superoxide dismutase (Mn- and CuZnSOD) and catalase (CAT), and their upstream regulator transcription factor NFκB was followed. Significant elevation of both SODs was found in cells irradiated with 10- and 20 Gy, while CAT and NFκB expression was unchanged. Since, such conditions lead to accumulation of H₂O₂, it is concluded that radioresistance of PC-3 cells may emerge from positive feed-forward vicious circle established between H₂O₂ activation of NFκB and elevated MnSOD activity.

Introduction

In the hormone refractory human prostate cancer cells metastatic to bone (PC-3) gamma-ionizing radiation (IR) exerts both antiproliferative and cytotoxic effects, with the former prevailing [1]. The IR dose which inhibits cell proliferation for 50 % (ID₅₀) is ≈ 11 Gy, which is rather high compared with other epithelial carcinomas, while 50 % cell cytotoxicity (EC₅₀) is not attainable within the dose range of 2-20 Gy (V. Vučić-Ph.D. thesis). At the IR dose of 20 Gy only 27 % of PC-3 cells died. The molecular mechanism of this remarkable IR-resistance of PC-3 cells is not known. It may be ascribed to the lack of functional p53 protein which under normal conditions regulates cellular response to IR. As most of low-LET IR effects are achieved indirectly, *i.e.* through radiolysis of water *via* reactive oxygen species (ROS), it was of interest to investigate regulatory pathways activated by ROS. One such pathway involves action of antioxidant defence enzymes (AOE) that are subject of this study: mitochondrial Mn-superoxide dismutase (MnSOD), cytosolic CuZn-superoxide dismutase (CuZnSOD), peroxisomal catalase (CAT) and their upstream regulator, transcription factor NFκB which might be responsible for the observed PC-3 cells' radioresistance [2].

Experimental

Cells were irradiated in the log phase of growth at 37 °C with 2, 10 or 20 Gy from ⁶⁰Co gamma-IR source, at the dose rate of 20 Gy/h. Cells were trypsinized, washed, and lysed by 1 % Triton X-100 in 10 mM TrisHCl buffer pH 7.4, containing 0.32 M sucrose and 5 mM MgCl₂. Total protein concentration (P in mg/mL) was determined by the method of Lowry. Cell lysates were denatured by sodium dodecyl-sulphate (SDS) containing La-

emlli buffer, boiled (100 °C, 3 min), separated by 10 % SDS-PAGE and transferred to nitrocellulose membranes. Membranes were blocked by 1 % BSA in 10 mM Tris buffer pH 7.4, containing 150 mM NaCl and 0.1 % Tween-20. For Western blot analysis (WB) membranes were separately incubated with commercial polyclonal antibodies raised in rabbit: (a) anti-MnSOD (Stressgen-SOD110), (b) anti-CuZnSOD (Stressgen-SOD100), (c) anti-catalase (Calbiochem-219010), (d) anti-NFκB (NFκB -p65, Santa Cruz-SC-372) or (e) anti-actin antibody (CSA-400). A secondary goat anti-rabbit IgG-HRP conjugate (Stressgen-SAB-300) was used for colorimetric antibody-antigen detection. The quantification of specific bands was performed by PC Imager and expressed in arbitrary units (AU/mgP) of n=4 independent measurements (mean±S.D.). Analysis of variance (one-way ANOVA) followed by Tukey's posthoc test was used to estimate statistically significant differences ($P<0.05$).

Results and Discussion

Quantification of antioxidant enzymes (AOE) in IR-treated PC-3 cells revealed significant induction of both MnSOD and CuZnSOD (*Figure 1*) by 10- and 20 Gy. The expression level of CAT was unchanged by IR-treatment, as well as the level of AOE upstream regulator NFκB (*Table 1*).

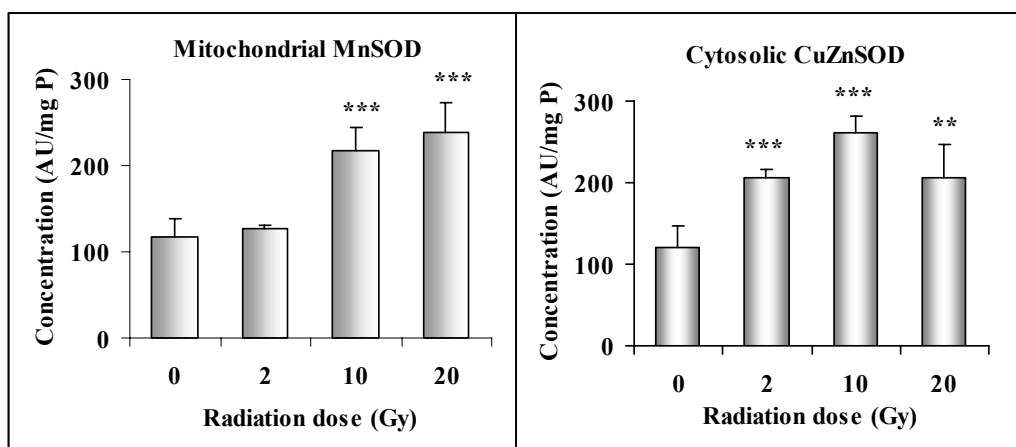


Fig. 1 Expression of antioxidant enzymes in irradiated PC-3 cell. Results are presented as mean± S.D. (n=4)

Table 1 Expression of NFκB and catalase in irradiated PC-3 cells Results are presented as mean± S.D. (n=4)

<i>Protein</i>	<i>IR Dose</i>	<i>0 Gy</i>	<i>2 Gy</i>	<i>10 Gy</i>	<i>20 Gy</i>
NFκB		110 ± 9	121 ± 16	124 ± 13	112 ± 9
CAT		92 ± 12	80 ± 26	103 ± 8	114 ± 11

Although the role of MnSOD in IR-response is highly dependent on the cell redox milieu in most cases its increased expression (*Figure 1*) enables protection against oxi-

dant injury which may be association with poor prognosis and resistance to radiation therapy [3]. This is specially the case in p53-deficient cells such as PC-3 which are constitutively adapted to prooxidative conditions and which respond to IR-treatment with further MnSOD induction. Scavenging of O_2^{\bullet} by MnSOD leads to an increase in H_2O_2 , due to the lack of concomitant increase in the peroxide-scavenging enzymes CAT (*Table 1*). The IR-adaptation of PC-3 cells most probably occurs through a feed-forward regulation of MnSOD upstream regulator NF κ B [4]. Although its expression is not enhanced by IR (*Table 1*) it may be activated by H_2O_2 through proteolytic cleavage of its inhibitory subunit I κ B. In addition to that, enhanced of H_2O_2 probably leads to formation of hydroxyl radical (OH $^{\bullet}$), which is thought to be more toxic oxygen molecule *in vivo*. Inhibition of IR-treated PC-3 cell growth may be primarily attributed to decreased cell division rather than increased cell death, which was also the case in another metastatic human prostate carcinoma cell line DU-145 [5]. IR-induced adaptive responses mediated *via* NF κ B activation involves genes such p21, Myc, 14-3-3 zeta, cyclin A, cyclin B1, and GADD153, regulating arrest of cell cycle progression, DNA repair, and apoptosis. All of them appear to be responsive to MnSOD expression. A pathway leading from NF κ B to MnSOD to effector's genes (with antiapoptotic functions) is therefore a possible contributor to IR-induced resistance. CuZnSOD is another AOE responsible for cell growth and survival, which was induced by 10- and 20 Gy IR (*Figure 1*). Its enhanced expression may lead to further accumulation of H_2O_2 and potentiaton of a feed-forward circle with NF κ B conferring PC-3 cell radioresistance.

Conclusion

High ionizing radiation resistance (IR) of human prostate cancer cells (PC-3) illustrated by $ID_{50} \approx 11$ Gy and $EC_{50} > 20$ Gy may be ascribed to the high constitutive and IR-induced expression of mitochondrial MnSOD and cytosolic CuZnSOD. In the absence of catalase expression enhancement of MnSOD and CuZnSOD may form positive feed-forward relation with the antiapoptotic NF κ B gene regulator, which leads to relatively successful PC-3 cell adaptation to prooxidative conditions induced by IR.

References

- [1] V. Vučić, M. Adžić, A. Nićiforović, N. Tišma, S. Ruždijić, M. B. Radojčić, *Jugoslav. Med. Biochem.*, 2004, **23**, 343-350.
- [2] R. Schmidt, P. Dent, S. Grant, R. B. Mikkelsen, K. Valerie, *Radiat. Res.*, 2000, **153**, 245-257.
- [3] T. Nakano, K. Oka, N. Taniguchi, *Cancer Res.*, 1996, **56**, 2771-2775.
- [4] M. Adžić, A. Nićiforović, V. Vučić, Z. Nešković-Konstantinović, S. Spasić, D. Jones, M. B. Radojčić, M. B. Spasić, *Redox. Report*, 2006, **11**, 39-44.
- [5] V. Vučić, E. Isenović, M. Adžić, S. Ruždijić, M. B. Radojčić, *Brazilian J. Med. Biol. Res.*, 2006, **39**, 227-236.

DIFFERENT INDUCTION OF DUAL CORTICOSTEROID RECEPTOR SYSTEM IN THE RAT HIPPOCAMPUS FOLLOWING GAMMA RADIATION

N. Veličković, A.D. Đorđević, N. Popović and M. Demajo

*Laboratory for Molecular Biology and Endocrinology, "Vinča" Institute of Nuclear Sciences,
P.O. Box 522, Belgrade, Serbia*

Abstract

Cranial radiotherapy (CRT) is an effective way to prevent CNS relapse in children with acute lymphoblastic leukemia (ALL). However, CRT also has serious side effects on normal tissues, including long-term neuroendocrine disturbances. In order to test this clinical protocol on animals, we examined the effects of CRT (10 Gy) on the level of mRNA for glucocorticoid receptor (GR) and mineralocorticoid receptor (MR) in the hippocampus of 8-days-old rats. Irradiation rapidly stimulated GR gene expression in a time-dependent manner, whereas the time-course of MR mRNA expression showed no statistically significant changes. At postnatal day 42, the level of GR mRNA was diminished while the level of MR mRNA remained unchanged compared to matched controls. Dexamethasone suppression test (DST) revealed the altered nucleocytoplasmic shuttling of activated GR after CRT in 42-days-old rats, as a long-term consequence of gamma irradiation.

Introduction

Ionizing radiation (IR) has proven to be a powerful tool in the treatment of childhood cancer. Children with acute lymphoblastic leukemia receive CNS therapy to improve long-term survival. Neurotoxic effects, such as cognitive impairment, have been associated with this therapy [1]. Glucocorticoids (GCs) are frequently used as cotreatment agent because they may have potent proapoptotic properties and reduce nausea, hyperemesis and acute toxicity of normal tissue [2]. However, little is known about the induction of dual corticosteroid receptor system in the hippocampus after radiation exposure. Glucocorticoid receptor (GR) activation induces apoptosis of the granule cells in the hippocampus. Unlike GR activation, neuroprotection is seen after mineralocorticoid receptor (MR) activation [3]. To this aim, we examined the level of mRNA for GR and MR in the hippocampus of 8-days-old rats after irradiation of 10 Gy (^{60}Co γ -source) by semi quantitative RT-PCR using as the internal standard mRNA for glyceraldehyde-6-phosphate dehydrogenase (GAPDH). The hippocampus was isolated at the following post-irradiation times: 1 h, 2 h, 4 h, 8 h, 24 h and at postnatal day 42 in order to estimate long-term effects of γ -irradiation. The level of GR protein was detected by Western blot after treatment with synthetic glucocorticoid hormone (dexamethasone) in order to estimate a hypothalamic-pituitary-adrenal (HPA) axis response to radiation.

Results and Discussion

Therapeutic brain irradiation can cause progressive decline in cognitive function, along with impaired verbal and visual-spatial memory abilities, attention, organization and motor output [1]. Many of these functions, especially cognitive function and memory processes, are associated with action of corticosteroids (CS) in hippocampus. Two types of CS receptors are found in the brain: glucocorticoid receptor (GR) and mineralocorticoid receptor (MR). MR occupation is essential for the maintenance of basal activity in hippocampal circuit. In contrast to MR, GR becomes occupied during stress, thus promoting stress response. Differential activation of this dual receptor system may account for the opposing action of CS on neuronal proliferation, survival or death in hippocampal neurons [3]. The results presented herein clearly show that a clinically relevant dose of ionizing radiation [1] differently affects gene expression of the two corticosteroid receptors in the rat hippocampus. The prominent increase of GR mRNA after CRT (Fig. 1A) probably results in the activation of the GR-mediated apoptotic signaling pathway [3] which will be confirmed (or rejected) by our future analysis of the ratio between proapoptotic (Bax) and antiapoptotic molecules (Bcl-2) after CRT.

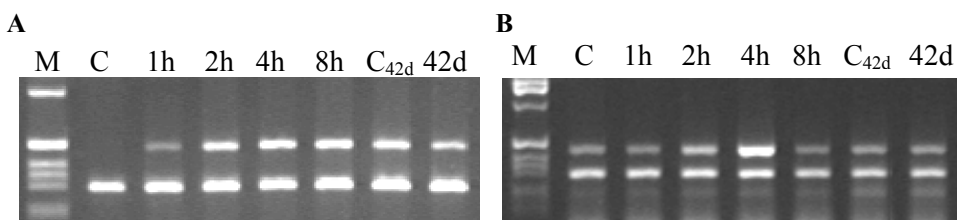


Fig. 1. Level of hippocampal GR mRNA (A) and MR mRNA (B) expression in rats irradiated with 10 Gy at different time points. The densitometric analysis of GR mRNA and MR mRNA were normalized to GAPDH (lower line).

M-DNA molecular weight marker

C-control (8-days-old rats)

C_{42d}- control (42-days-old rats)

42d-42-days-old rats, irradiated at the age of 8 days

Decrease of GR mRNA at postnatal day 42 (Fig. 1A, line C_{42d}, line 42d) points to a long-term attenuation of hypothalamic-pituitary-adrenal axis on the level of glucocorticoid negative feedback. Transient induction of MR mRNA, in contrast to induction of GR gene, revealed that the basal homeostasis response (mediated by MR) is not altered after CRT (Fig. 1B). This is confirmed by the unchanged level of MR mRNA in 42-days-old rats, irradiated at 8-days of age (Fig. 1B, line C_{42d}, line 42d).

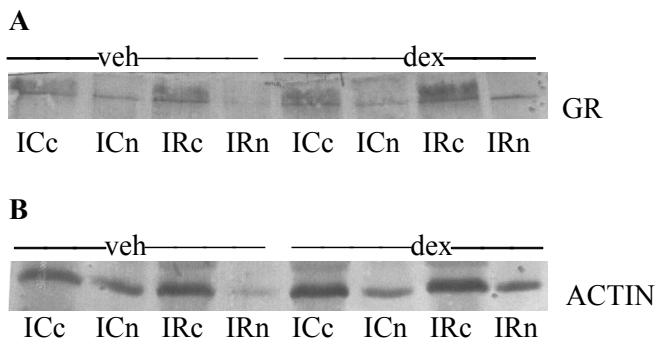


Fig. 2. Level of hippocampal GR (A) and actin (B) protein expression in 42-days-old rats irradiated with 10 Gy at age of 8 days. The densitometric analyses of GR protein were normalized to actin.

IC-immobilized control rats ; IR-irradiated rats
c-cytosolic proteins; n-nuclear extract proteins
veh-vehicle; dex-dexamethasone

These results were accompanied by altered nucleo-cytoplasmic shuttling of GR protein as revealed by Western blot (Fig. 2). The impaired translocation of activated GR (after treatment with dex) to nucleus in hippocampus of 42-days-old irradiated animals implicate to long-term attenuation of hypothalamic-pituitary-adrenal axis on the level of proteins.

Conclusion

According to these results, we may conclude that 10 Gy radiation treatment significantly affects the GR receptor system, both at the level of mRNA and protein, whereas the MR receptor system is not altered, thus probably leading to impairment of cognitive function and spatial learning. The attenuated HPA axis assessed late after brain irradiation may be involved in delayed brain response and could contribute to the observed clinical symptoms [1].

Acknowledgement

This study was supported by the Serbian Ministry of Science and Environmental Protection, Project No. 143044.

References:

- [1] P. J. Mullenix, W. J. Kernan, M. S. Tassinari, A. Schunior, D. P. Waber, A. Howes, N. J. Tarbell, *Pediatr. Res.*, 1994, **35** (2), 171-178.
- [2] I. Herr, E. Ucur, K. Herzer, S. Okouoyo, R. Ridder, P. H. Krammer, M. K. Doeberitz, K.-M. Debatin, *Cancer Res.*, 2003, **63** (12), 3112-3120.
- [3] O. F. X Almeida, G. L. Conde, C. Crochemore, B. A. Demenix, D. Fisher, A. H. S. Hassan, M. Meyer, F. Holsboer, T. M. Michaelidis, *FASEB J.*, 2000, **14**, 779-790.

EFFECTS OF SHORT TIME EXPOSURE OF HTB140 MELANOMA CELLS TO FOTEMUSTINE AND DACARBAZINE

J. Požega, L. Korićanac, I. Petrović and A. Ristić-Fira
Vinča Institute of Nuclear Sciences, P.O.Box 522, Belgrade, Serbia.

Abstract

Different experimental set-ups were designed to study cytotoxic and cytostatic effects on HTB140 melanoma cells after 1 h treatment with fotemustine (FM) or dacarbazine (DTIC). FM induced dose dependent cell inactivation, boosted by its toxicity, particularly for higher doses. DTIC treatment for 1 h was insufficient to provoke almost any effect on melanoma cells. Good correlation between viability and proliferation assays applied was detected for both drugs.

Introduction

Melanoma cells become resistant to a variety of chemotherapeutic drugs very soon after initial use. Inherent radio-resistance, as well as drug resistance, reprogram cell survival pathways and affect cell proliferation after each individual treatment [1, 2, 3]. Such behaviour of melanoma cells disables a long term application of most drugs with only a few cytotoxic compounds showing activity against this tumour. Fotemustine (FM), a member of the chloroethylnitrosourea (CENU) class of alkylating agents has been proven active against disseminated melanoma and primary brain tumours with clinical application being limited by its toxicity [4]. The addition of an aminophosphate to the nitrosourea radical provided higher permeability of FM through cell membranes and blood – brain barrier during the treatment. Spontaneous decomposition of nitrosoureas generates electrophilic species, responsible for DNA alkylation, thus producing therapeutic effects. Production of isocyanates cause toxic side effect of FM through carbamylation of proteins [5]. Another commonly used drug, approved and frequently used for melanoma treatment, is a monofunctional alkylating agent dacarbazine (DTIC) having relative responses in 15 to 20 % of cases, but with short duration [4, 6]. DTIC and its derivatives with higher membrane permeability somehow improved the response of melanoma brain metastasis.

Results and Discussion

Cytotoxic and cytostatic effects of alkylating agents FM (Ital farmaco S.p.A) or DTIC (Aventis Pharma S.p.A) were analysed on HTB140 human melanoma. Cells were exposed for 1 h to drug concentrations ranging from 0.05 to 2 mM.

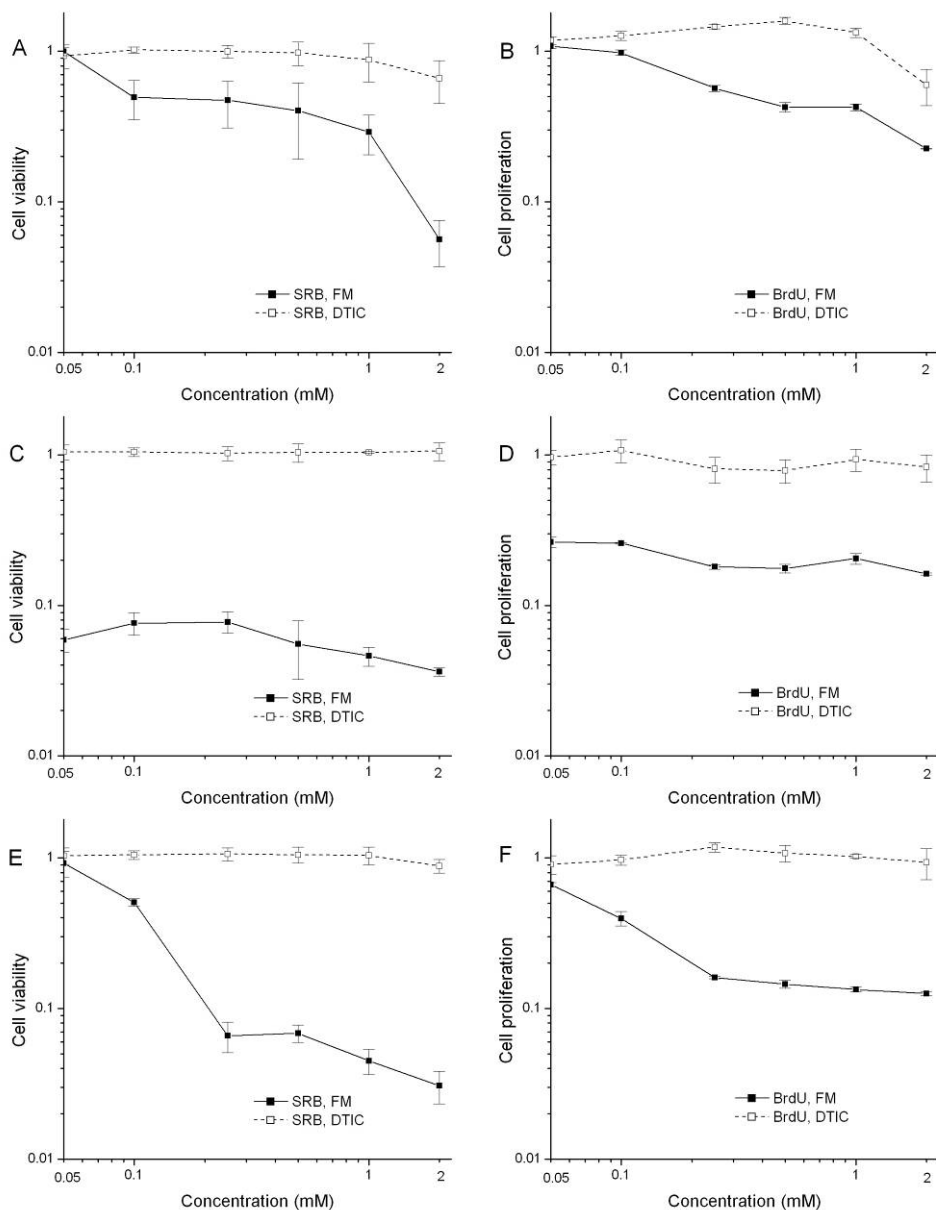


Fig. 1. Dose dependent cytotoxic (A, B) and cytostatic (C - F) effects of FM and DTIC 7 days after administration to HTB140 cells, estimated by SRB and BrdU.

Experimental conditions for evaluation of viability and cell proliferation capacity varied and were designed to follow short term drug effects *in vitro*.

In the first experimental set-up, when screening drug cytotoxicity, 24 h after plating cells were treated with FM or DTIC for 1 h when drug-containing medium was replaced with fresh medium (**Figure 1A, B**). When evaluating cytostatic effects of drugs, another two experimental set-ups were involved. After drug administration for 1 h, cells were either immediately replated (**Figure 1C, D**), or were incubated for 16 h in fresh medium and then replated (**Figure 1E, F**). In all experiments cells were incubated for 7 days, when cell viability and proliferation were assessed by SRB (MP Biomedicals, Inc) and BrdU (Roche Applied Science) assays respectively. The absorbance was measured using microplate reader (Victor, Wallac) at 450nm.

Obtained results implicated that in all three experimental set-ups, when HTB140 human melanoma cells were treated with DTIC, the drug administration for 1 h was not sufficient to provoke almost any effect on cell growth and proliferation (**Figure 1A-F**). Contrarily, the use of FM revealed major dose dependent cell growth inhibition under all three experimental conditions. Cytotoxicity of FM pointed out moderate dose dependent decrease of viability and proliferation capacity (**Figure 1A, B**). Replating of cells for evaluation of FM cytostatic power produced much stronger cell inactivation, except for the largest dose. Immediate replating (**Figure 1C, D**), compared to replating 16 h later (**Figure 1E, F**), does not allow cells to recover from the initial stress induced particularly by smaller FM doses, while higher doses made this replating time difference practically irrelevant.

It seems that FM treatment provoked certain viable cells to be more fragile and less adhesive to the support, thus lost during immediate replating procedure. However, incubating cells for 16 h enabled some of them to restore their growth ability so that they were not lost during tripsinization. Still, this is valid only for smaller drug doses. Estimated cell viabilities evaluated through total protein content (SRB) were supported by proliferative capacity (BrdU) of cells within each experimental set-up.

Conclusion

Large discrepancy in the level of cell elimination between DTIC and FM, when applied within a short time scale on HTB140 cells, was due not only to the different mechanisms triggered by each drug but also to the very high toxicity of FM.

Reference

- [1] I. Petrović et al., *Int. J. Radiat. Biol.*, 2006, **82**(4), 251-265.
- [2] M. S. Soengas and S. W. Lowe, *Oncogene*, 2003, **22**, 3138 – 3151.
- [3] I. Passagne et al., *J. Pharmacol. Exp. Ther.*, 2003, **307**(2), 816-823.
- [4] U. Jungnelius et al., *Eur. J. Cancer*, 1998, **34**(9), 1368-1374.
- [5] R. A. Kroes et al., *Proc. Natl. Acad. Sci.*, 1991, **88**, 4825-4829.
- [6] D. Grossman and D. C. Altieri, *Cancer Metast. Rev.*, 2001, **20**, 3-11.

EVALAUTION OF RADIOIODINATION OF SYNTHESISED **meta**-IODOBENZYLGUANIDINE CATALYZED BY *in situ* GENERATED Cu(I)

N.S. Nikolić, M.D. Mirković, S.D. Vranješ-Đurić and D.D. Đokić

*Vinča Institute of Nuclear Science, Laboratory for Radioisotopes,
P.O. Box 522, Belgrade, Serbia*

Abstract

Meta-iodobenzylguanidine (m-IBG) is a biogenic amine precursor, noradrenaline analogue, which is actively taken up by tumors. In tracer amounts, [$^{123/131}\text{I}$]-m-IBG is used as a radiopharmaceutical to target normal and malignant tissues of neuroadrenergic origin for **diagnostic scintigraphy**, and labeled with higher activities of ^{131}I , it is used for **therapy** of pheochromocytoma and neuroblastoma.

The increased clinical **therapeutic** use of **unlabeled m-IBG** at doses of up to 40 mg/m² emphasizes the need for **syntheses** and an established quality protocol for this substance that relies on verifiable analytical parameters.

Evaluation of **radioiodination** was necessary to obtain higher labeling yield (we achieved over 90% instead no more than 70%), because isotopic exchange labeling of m-IBG with ^{131}I catalyzed by Cu(I) is much more efficient than with conveniently used ammonium sulphate.

Introduction

Diagnostic scintigraphy with radioactive m- ^{131}I IBG after predosing with unlabelled m-IBG resulted in better biodistribution, with more intense m-IBG uptake in the tumor. In addition, more patients were eligible for the radioactive treatment after predosing [1]. Therapeutic options to effectively inhibit growth and spread of neuroendocrine gastrointestinal tumors are still limited. The administration of **unlabelled m-IBG** and interferon- γ (IFN γ) cause antineoplastic effects in neuroendocrine gastrointestinal (NE) tumor cells, so the combination of IFN γ with the NE tumor-targeted agent m-IBG leads to effective growth control at reduced doses of either drug [2,3].

The early radiolabelling method of m-IBG involved the solid phase exchange technique and ammonium sulphate has been widely used. There was, however, about 30% reduction in radiochemical yield (RC) [4]. Higher labeling yields based on the use of Cu(I) ions generated to act as catalyst, or Cu(II) ions for the exchange reaction were reported [5]. Nevertheless, a few problems were reportedly encountered in these methods [6]. While generating Cu(I) by reduction of CuSO₄ with SnSO₄, coloured solutions resulting from heating in the presence of ascorbic acid and sodium metabisulphite. In the present study, we report our experience in attempting to introduce modifications and the evaluation of the methods [6,7] and the product purification.

The m-iodobenzylamine hydrochloride (Aldrich), cyanamide (Sigma) and other chemicals of p.a. grade were obtained from Merck; Na ^{131}I solution obtained from Institute of Isotopes Co., Ltd. Budapest. Analysis of the products by RP-

HPLC/UV/ADC γ -detector was performed (Hewlett Packard HPLC system, Model HP 1050 Series). Separation is performed on an analytical column LiChroCART Supersphere 100 RP-18 (125mm x 4mm I.D.), particle size 4 μ m (Merck).

The m-IBG was produced by the reaction of m-IBA and cyanamide according to a slightly modified version of the method of Wieland et al. Product characterization by IR, $^1\text{H-NMR}$, elemental analyses and RP-HPLC/UV method was performed and it was found that the product was $\geq 99\%$ pure.

Detection (for m-IBG and m- ^{131}I IBG) was carried out at 225nm, the mobile phase (0.01M $\text{Na}_2\text{HPO}_4 \times 2\text{H}_2\text{O}:\text{CH}_3\text{CN}=80:20$ v/v) flow-rate was 1.0 ml/min and the column was maintained at 25 $^\circ\text{C}$, 5 μl samples were injected.

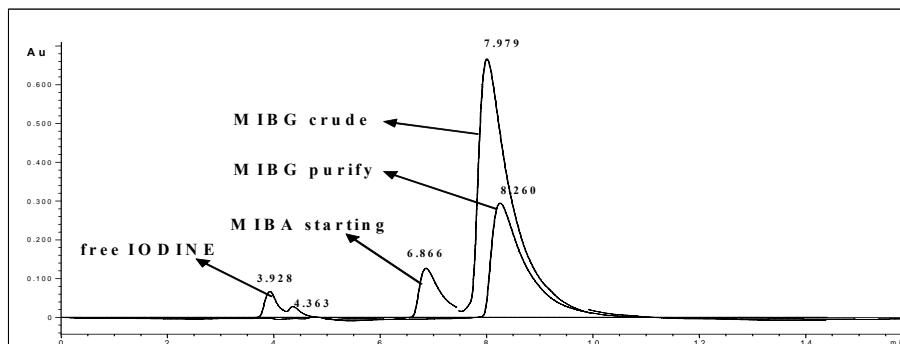


Fig. 1. The chromatogram of crude and purify m-IBG

Radioiodination involved nucleophilic exchange reaction (160 $^\circ\text{C}$, 45 min) catalyzed by Cu(I) generated *in situ* by addition of $\text{Na}_2\text{S}_2\text{O}_5$ to CuSO_4 . Purification of radiolabelled m-IBG by column chromatography (DEAE cellulose) is recommended.

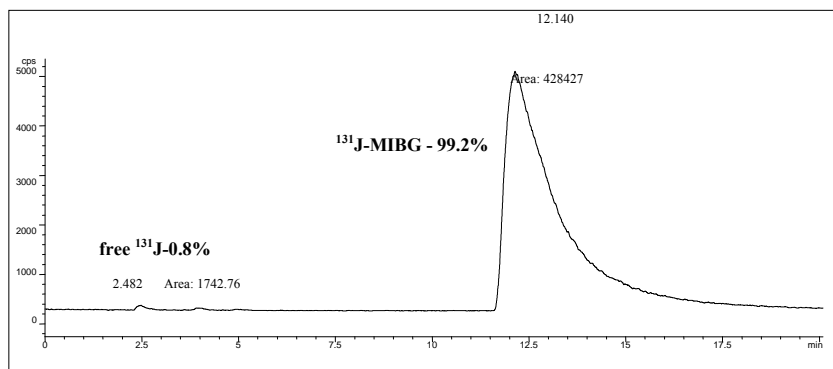


Fig. 2. The radiochromatogram of m- ^{131}I IBG prepared via Cu(I) method

In our experiments we compared RC yield of the three radioiodination exchange reactions with different catalysts. The RC yield for reaction catalyzed with Cu(I) was over 90%, while the RC purity of m- ^{131}I IBG was not less than 98%. The RC and stability of m-IBG- ^{131}I was confirmed by TLC and HPLC method.

Table 1. Prepurified product RC yield (%) of isotopic exchange labeling of m-IBG with ^{131}I and with different catalysts confirmed via TLC methods

Method	Radiochemical yield (%)		
	Reaction		
	1. Cu(I)	2. C(II)	3. $(\text{NH}_4)_2\text{SO}_4$
$\text{CH}_3\text{COOC}_2\text{H}_5:\text{C}_2\text{H}_5\text{OH}$ (1:1) silica gel	95.87	83.30	68.67
$\text{C}_4\text{H}_9\text{OH}:\text{NH}_4\text{OH}$ (3:1) Whatmann N ^o 1	96.22	83.92	69.94
	98.41	84.39	71.84
	97.67	85.37	72.85

Reaction 1: 1mg m-JBG+3.2 mg $\text{Na}_2\text{S}_2\text{O}_5$ + $\text{CuSO}_4 \cdot 5\text{H}_2\text{O}$ +140 μl $\text{CH}_3\text{COOH}_{glac}$

Reaction 2: 1mg m-JBG+ $\text{CuSO}_4 \cdot 5\text{H}_2\text{O}$ +140 μl $\text{CH}_3\text{COOH}_{glac}$

Reaction 3: 1mg m-JBG+2 mg $(\text{NH}_4)_2\text{SO}_4$ +140 μl $\text{CH}_3\text{COOH}_{glac}$

Conclusion

We obtained higher labeling yields of m-IBG with ^{131}I by using a different catalysts such as Cu(I) generated *in situ* or Cu(II) than convenient one $(\text{NH}_4)_2\text{SO}_4$, so the copper catalyzed radioisotopic exchange reaction can be conveniently employed for preparation of m- ^{131}I IBG suitable for clinical use.

Also, unlabeled m-IBG can be introduce as a therapeutic agent in therapy of pheochromocytoma and neuroblastoma, because now m-IBG could be commercially available in solution/lyophilized for routine clinical application.

References:

- [1] B.G. Taal , C. Hoefnagel, H. Boot et al., *Ann Oncol.*, 2000, **11**, 1437–1443.
- [2] M. Höpfner, A.P. Sutter, A. Huether, G. Ahnert-Hilger and H. Scherübl, *BMC Cancer*, 2004, **4**, 23.
- [3] J.M. Zuetenhorst, R A Valdes Olmos, M Muller, C.A. Hoefnagel and B.G. Taal, *Endocrine-Related Cancer*, 2004, **11**, 553-561.
- [4] T.J. Mangner, J. Wu., D.M. Wieland, *J. Org. Chem.*, 1982, **47**, 1484.
- [5] J.J.R. Mertens, , W. Vanryckeghem, M. Gysemans, et al. *Eur. J. Nucl. Med.*, 1987,**13**, 380.
- [6] M. Neves, A. Paulo, L. Patricio, *Appl. Radiat. Isot.*, 1992, **43**, 737.
- [7] G. Prabhakar, K. S. Mehra, N. Ramamoorthy, S. Chattopadhyay, R. Oommen, S. Narasimhan, N. A. Nair, S. Gunasekaran, *Appl. Radiat. Isot.*, 1999, **50**, 1011.

**^{99m}Tc -HEXAKIS-(2-METOXY-ISOBUTYL-ISONITRILE)
(^{99m}Tc -MIBI) A NEW MYOCARDIAL IMAGING AGENT:
SYNTHESIS OF MIBI, OPTIMISING CONDITIONS FOR
RADIOLABELLING WITH ^{99m}Tc AT HIGH RADIOCHEMICAL
PURITY AND *IN VIVO* BEHAVIOR**

D. Đokić¹, D. Janković¹, Lj. Stamenković¹, N. Nikolić¹,
M. D. Mirković¹ and I. Pirmettis²

¹Laboratory of Radioisotopes, Institute of Nuclear Sciences «Vinča»
POBox 522, Belgrade, Serbia

²Institute of Radioisotopes and Radiodiagnostic Products, NCSR "Demokritos"
POB 60228, 15310 Agia Paraskevi, Athens, Greece

Abstract

^{99m}Tc -MIBI is a promising radiopharmaceutical for myocardial perfusion imaging agent, but it has also shown good results in identifying several types of tumors, such as breast, lung and thyroid cancers. It is a lipophilic, cationic technetium (I) complex. In this paper a complete study on the synthesis of 2-methoxy-isobutyl-isonitrile (MIBI) as well as a formulation of a lyophilized kit for labeling with ^{99m}Tc is presented. Investigation on effective factors as well as finding out the optimum parameters to obtain the highest labelling efficiency and radiochemical purity of ^{99m}Tc -MIBI complex were performed. The radiochemical purity of the labelled preparation was high (>95%). Biodistribution study performed in health male Wistar rats showed satisfactory biokinetics results. ^{99m}Tc -MIBI was accumulated in sufficient amount into the heart tissue for myocardial perfusion imaging. MIBI in kit formulation was found to be stable and also safe for administration.

Introduction

[Hexakis-(2-methoxy-isobutyl) isonitriletechnetium (I)]⁺, developed as potential myocardial imaging agent, is a member of the class of lipophilic hexakisisonitriletechnetium (I) cationic complexes, [Tc(CNR)]⁺, where R is the alkyl group such as methyl, ethyl, n-propyl, tertiary butyl or methoxy isobutyl substituents [1]. It is a +1 complex, Tc in the center is symmetrically bounded to six monodentate CNR ligands resulting in stable cationic complexes. Isonitriles stabilize Tc(I) by their p-acceptor properties. These compounds don't undergo the *in vivo* reductive mechanisms in the human heart owing to the low oxidation state of technetium. An investigation into the mechanism of uptake has led to the belief that cations such as [Tc(MIBI)₆]⁺ accumulate *via* a diffusion mechanism and electrostatic binding due to a high mitochondrial membrane potential. The lipophilicity of the complex is known to be important for uptake into the heart. Tc(I) oxidation state is accessible directly from pertechnetate ($^{99m}\text{TcO}_4^-$) as the complex is obtained by the reaction of $^{99m}\text{TcO}_4^-$ and tetra-(2-methoxy-isobutyl-isonitril) copper tetrafluoroborate [Cu(MIBI)₄]BF₄ and in presence of SnCl₂ as reducing agent [2, 3].

Material and Methods

The synthesis of MIBI and chelate $[\text{Cu}(\text{MIBI})_4]\text{BF}_4$ was based on a method previously reported [4], with certain modifications. The compounds were characterized by elemental analysis, IR and $^1\text{H-NMR}$ spectroscopy. After optimization of reaction parameters, MIBI was prepared as a freeze dried kit. The labelling was performed by adding of 1-5 ml of $^{99\text{m}}\text{TcO}_4^-$ ($^{98}\text{Mo}/^{99\text{m}}\text{Tc}$ -generator, Vinča) and heating for fifteen minutes in boiling water bath. Analysis of the product included the radiochemical quality control, determination of pharmacokinetical parameters as well as biodistribution study. Radiochemical purity was assayed by Whatman 3MM paper chromatography and ITLC-SG in ethylacetate and two solvent system (acetone/saline) respectively. The standard trichloroacetic acid (TCA) precipitation method was used for determining the binding of $^{99\text{m}}\text{Tc-MIBI}$ to protein. All lipophilicity measurements were done by solvent extraction method with n-octanol. The biodistribution studies were carried out using health male Wistar rats (n=4-6). Animals were sacrificed at different times and samples of tissues or organs of interest were removed for assay of radioactivity.

Results and Discussion

The different concentrations and molar ratios of $[\text{Cu}(\text{MIBI})_4]\text{BF}_4$ and $\text{SnCl}_2 \times 2\text{H}_2\text{O}$ as well as the volume of $^{99\text{m}}\text{TcO}_4^-$ elute used for labeling, had a great influence on the labelling yield and stability of the preparation (Table 1 and 2). The optimum quantity of Sn(II) added into kit formulation was investigated by preparing MIBI kits containing various concentrations of Sn(II), while amounts of MIBI and others components were kept constant. The experimental results confirmed that concentration ratio: $[\text{Sn}]/[\text{MIBI}]=1/13.5$ and the presence of 0.025 mg/ml of $\text{SnCl}_2 \times 2\text{H}_2\text{O}$ in freeze-dried kit, gave satisfactory biological behavior in rats.

Table 1. The effect of Sn(II) concentration on radiochemical purity results of $^{99\text{m}}\text{Tc-MIBI}$ (Whatman 3MM, Ethyl Acetate), $V_{\text{TcO}_4^-}=3$ ml

Time after labelling	30 (min)		300 (min)	
	TcO_2^+ TcO_4^- Rf=0.0	Tc-MIBI Rf=0.6	TcO_2^+ TcO_4^- Rf=0.0	Tc-MIBI Rf=0.6
[Sn(II)] mg/ml				
0.25	4.5±0.2	95.5±0.2	5.1±0.5	94.9±0.5
0.025	2.2±0.2	98.0±0.9	2.4±0.4	97.6±0.8

Table 2. The effect of $^{99\text{m}}\text{TcO}_4^-$ volume on radiochemical purity results of $^{99\text{m}}\text{Tc-MIBI}$

$V_{\text{TcO}_4^-}$ (ml)	Labelling Yield (%)	
	TcO_2^+ TcO_4^-	Tc-MIBI
1	9.4±0.7	90.6±0.9
2	6.1±0.3	93.9±0.8
3	2.2±0.6	97.8±0.6
4	2.8±0.8	97.2±0.8
5	3.3±0.9	96.7±0.3

Reconstitution of the kit with 1-5 ml of $^{99\text{m}}\text{TcO}_4^-$ showed high radiochemical purity and stability. The freeze dried kit for $^{99\text{m}}\text{Tc-MIBI}$ is stable at least 5 h after labelling. The effect of heating on the radiochemical yield was tested. $^{99\text{m}}\text{Tc-MIBI}$ was pre-

pared with and without heating. Without heating much lower radiochemical purity results were obtained. The percentage of ^{99m}Tc -MIBI bound to protein was very high (94.8%). N-octanol-buffer distribution pH profiles showed that the distribution coefficient was around 0.5 and independent on pH. From values of radioactivity measured per organ of interest, the percentages of radioactivity related to administered dose were determined. *In vitro* studies showed the significant heart uptake and low blood and liver uptake (Table 3). The effect of Sn(II) concentration on *in vivo* behavior was remarkable.

Table 3. Effect of [Sn (II)] on biodistribution studies results of ^{99m}Tc -MIBI on Wistar rats, % Administered dose \pm SD per g (%/g), ($V_{^{99m}\text{TcO}_4^-}$ =5 ml)

Organ	[Sn(II)]= 0.025 mg/ml	[Sn(II)]= 0.25 mg/ml
Heart	3.12 \pm 0.38	3.77 \pm 0.21
Blood	0.02 \pm 0.01	0.03 \pm 0.01
Lungs	0.33 \pm 0.05	0.67 \pm 0.10
Liver	0.84 \pm 0.01	1.03 \pm 0.31
Spleen	0.46 \pm 0.12	0.32 \pm 0.12
Kidneys	2.17 \pm 0.30	1.75 \pm 0.20
Stomach	0.73 \pm 0.01	0.45 \pm 0.17
Intestine	2.20 \pm 0.12	1.12 \pm 0.18
Heart/Blood	198.89	132.59
Heart/Lungs	9.414	5.65
Heart/Liver	3.71	3.67

Conclusion

MIBI was prepared as freeze dried form. Reconstitution of the kit performed with 2-5 ml of $^{99m}\text{TcO}_4^-$ showed high radiochemical purity. A satisfactory biodistribution of ^{99m}Tc -MIBI behaviour in healthy test animals was obtained. Additional clinical studies could confirm the promising characteristic of ^{99m}Tc -MIBI.

References

- [1] L.I. Delmon-Moingeon; D. Piwnica-Worms, D.A. Van den Abbeele, *Cancer Research*, 1990, **50**(7), 2198-2202.
- [2] Technetium Tc 99m Sestamibi Injection, Official Monographs, USP XXV, 2002, USP-NF, 1601-1602.
- [3] M. Kosinski, C. Terwinghe, J.Cleynhens, In: *Technetium, Rhenium and Other Metals in Chemistry and Nuclear Medicine*, 6, M. Nicolini, U. Mazzi. ed. SG Editoriali: Italy, 2002, 551-553.
- [4] G. Subramanian, IAEA, TECDOC-532, 1989

THE LEVEL OF CuZn SUPEROXIDE DISMUTASE IN LIVER OF RATS EXPOSED TO ACUTE, CHRONIC OR COMBINED STRESS

D. Filipović

*VINČA Institute of Nuclear Sciences, Laboratory of Molecular Biology and Endocrinology 090,
P.O.Box 522, Belgrade, Serbia*

Abstract

The CuZn superoxide dismutase (CuZnSOD) protein expression in liver of Wistar male rats exposed to acute (immobilization or cold), chronic (isolation, crowding or daily swimming) or combined stressors was followed by Western immunoblotting. Relatively increase levels of CuZnSOD in acute stress conditions are required to remove high level of ROS in order to protect against ROS damage in liver. The moderate SOD up-regulation under chronic and combined stress may lead to inefficient ROS defense and increased oxidative damage of liver under the stress conditions. In that view, special care should be played to development of antioxidant therapeutics for antagonizing stress induced redox disbalances in cells.

Introduction

It is well known that intensive stress response results in creation of reactive oxygen species (ROS), e.g. hydrogen peroxide (H_2O_2), hydroxyl radical (OH \cdot) and superoxide anion radical ($O_2^{\cdot-}$) that can play an important role in tissue injury [1]. It has been suggested that chronic stress and high level of glucocorticoids (GCs), the adrenal steroids secreted during stress, affect diverse processes involve ROS and increase ROS by approximately 10% basally [2]. Also, GCs have been implicated as a regular factor for antioxidant enzymes in peripheral tissues that express corticosteroid receptor. In order to neutralize ROS, living cells possess three protective enzymes, superoxide dismutase (SOD), catalase (CAT) and glutathione peroxidase (GPX) to help the cells against a variety of oxidative stress. CuZnSOD (EC1.15.1.1) is the antioxidant enzyme that catalyses the dismutation of the highly reactive superoxide anion to O_2 and to the less reactive species H_2O_2 [3]. However the changes of endogenous defense enzymes in the liver of stressed rats remained obscure. Because liver is a prime target tissue for glucocorticoid action, in the present study, we were investigated the effect of 21 day isolation, crowding or daily swimming as chronic stressors, sole or in combination with 2h acute stress of immobilization or cold (4°C) on the level CuZnSOD protein expression in liver cytosol of Wistar male rats.

Experimental

Adult Wistar rat males, aged three months, weighing 330-400 g, were housed in groups of four individuals *per* cage and offered water and food *ad libitum*. For experimental purposes the animals were randomly divided into five groups. Group I con-

sisted of the unstressed animals (control); Group II contained animals exposed to acute stress by immobilization or cold; Group III was exposed to chronic isolation *i.e.* the rats were individually housed for 21 days; Group IV was exposed to chronic social crowding for 21 days, with eight animals *per* cage; Group V comprising four animals *per* cage was exposed to forced 15 min swimming for 21 day. Chronically stressed animals were subsequently exposed to immobilization or cold (4°C) for 2h. Unstressed controls or stressed animals were sacrificed 2 hrs following the end of the stress procedure. Separation of proteins in liver cytosol was examined by SDS-PAGE and quantification of level CuZnSOD by Western immunoblotting. The obtained data were analyzed by two-way ANOVA by Tukey post-hoc test. Statistical significance was accepted at $p < 0.05$.

Results and Discussion

Figure 1 (left panel) shows that both acute stressor, immobilization (IM) and cold (C), induced a significant up-regulation of CuZnSOD levels in the liver cytosol ($p < 0.05$), in relation to the unstressed controls. Interestingly enough, in spite of the differences in both type and intensity of acute stressors, a similar level of CuZnSOD changes was observed, as judged by the Tukey post-hoc test. The elevated CuZnSOD expression could indicate that the studied stress conditions, either directly or indirectly, act on the liver cell redox-equilibrium by shifting it towards prooxidant state. At least in part, the prooxidant state could result from 3-6 fold elevation of plasma corticosterone (CORT) under different stress conditions, as reported in our previous work [4]. Also, oxidative metabolic pathway of increase concentration of catecholamines may be the reason of elevated protein expression of CuZnSOD under acute stress conditions. Compared to acute stress effects, chronic stress conditions led to a moderate increase in the level of CuZnSOD (middle panels of Fig.1). The Tukey post-hoc test indicated that, within chronic stressors swimming (Sw) led to a significant increase ($p < 0.05$) of the level CuZnSOD, relative to the unstressed control. Evaluation of combined stress data indicated that only isolation followed by cold induced significant up-regulation of level CuZnSOD ($p < 0.05$; Fig.1, right panel). A moderate up-regulation the CuZnSOD level in chronic and combined stress may be inactivation of SOD by interaction with oxygen radical. Pigeolet et al., [5] reported the inactivation SOD by hydroxyl radical and hydrogen peroxide. The depression of SOD level may result in cellular injury by superoxide radical which could the propagate the chain reaction, producing one hydrogen peroxide and one GSSG for each turn in cycle [6]. As CuZnSOD expression is regulated by GR, moderate protein level of this enzyme may lead to inefficient ROS defense and more pronounced oxidative damage of liver.

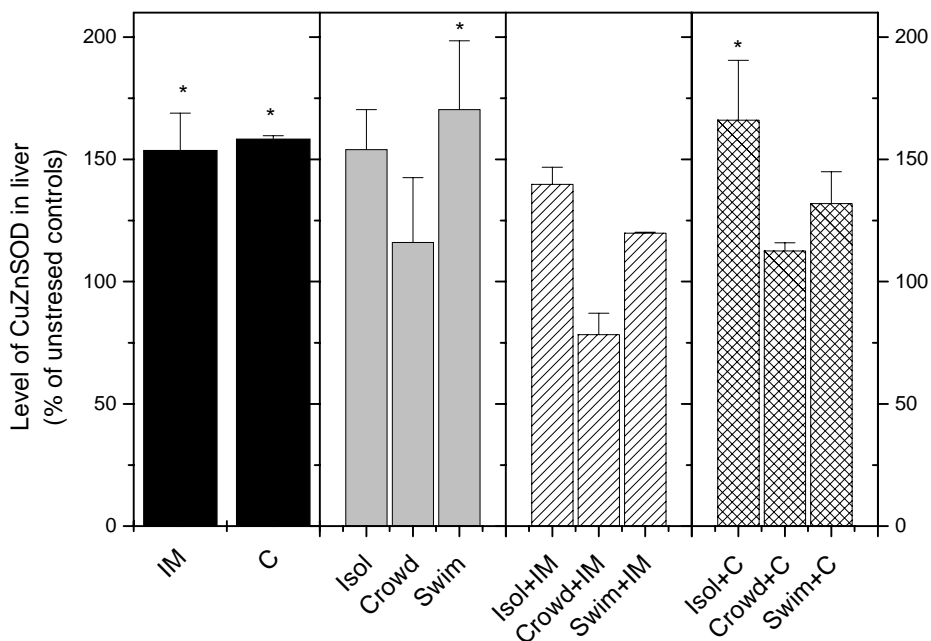


Fig. 1. Relative changes in the level of CuZnSOD in liver cytosol of animals exposed to acute stressors: immobilization (IM) or cold (C); chronic stressors: isolation (Isol), crowding (Crowd) or daily swimming (Swim), or combined stressors (mean±S.E.M, significant differences by Tukey post-hoc test is * $p < 0.05$).

Conclusions

Our study indicated that both acute and chronic stressors most probably generate intracellular imbalance between production and elimination of ROS, as judged by differential CuZnSOD protein induction. The presumed stress induced changes in redox equilibrium in liver may be prerequisite in generation and propagation of variety of pathological processes.

References

- [1] P. Kovacs, I. Juranek, T. Stankovicova, P. Svec, *Pharmazie.*, 1996, **51**, 51-53.
- [2] L. J. McIntosh, R. M. Sapolsky, *Exp Neurol.*, 1996, **141**, 201-206.
- [3] I. Fridovich, *Annu.Rev.Biochem.*, 1995, **64**, 97-112.
- [4] D. Filipović, Lj. Gavrilović, S. Dronjak, M. Radojčić, *Neuropsychobiology*, 2005 **51**(2), 107-114.
- [5] E. Pigeolet, P. Corbisier, A. Houbion, *Mech Ageing Dev.*, 1990, **51**, 283-297.
- [6] C. C. Winterbourn, *Free Radic Biol Med.*, 1993, **14**, 85-90.

DETECTION OF TNT-ANALOG TNP-TRIS IN IMMUNOASSAY WITH TWO RECOMBINANT scFv-ANTIBODIES

M. Simonović¹, B. R. Simonović¹, S. Zlatanovic-Milošević²,
E. Spillner³ and R. Bredehorst³

¹ Holding Institute of General and Physical Chemistry, Studentski trg 12, Belgrade, Serbia

² Faculty of Mathematics and Natural Sciences, University of Kragujevac, Radoja Domanovica 12, Kragujevac, Serbia

³ Institute of Biochemistry and Molecular Biology, University of Hamburg, Martin-Luther-King-Pl. 6, Hamburg, Germany

Abstract

Bivalent antibody construct were generated for performing competitive immunoassay for detection of TNT-analogs. For the first time the bivalent recombinant form of scFv antibodies was used. According to their high affinity (Kd-values in range 10^{-9} M) the quantity of as small as 25 fmol TNP-Tris was detected.

Introduction

The main aim of this work was to compare antibody constructs in order to analyze their affinity for TNT-derivatives, the impact of the molecule valence and dimension on the antibody binding in immunoassay. Starting from the two available TNT-specific scFv-fragments diverse immunoreagents were generated. These fragments had different origin: 11B3 was the mouse antibody and 3.5 was the selected human scFv form the synthetic Griffin library. The fragments were produced as bivalent antibodies (IgGΔC1 constructs). To analyze the binding properties of antibodies, the TNT analog TNP-Tris as well as the TNP-protein conjugates were used.

Material and Methods

Synthesis of different TNP-protein conjugates. The TNP-conjugates were synthesized according to the standard protocol (Wannlund *et al.*, 1983).

Synthesis of TNP-Tris. 18 mg TNBS·xH₂O was diluted in 1 ml 100 mM Tris-buffer pH 9.0. The TNP-Tris solution was further diluted with the same Tris-buffer in the ratio 1:1000 and the absorbance at 340 nm was measured (Coffee *et al.*, 1971). ELISA. ELISA was made according standard procedures (Ausubel *et al.*, 1991, 1996). For covering a strong diluted TNP-BSA conjugate (50 µg/ml) was used and as negative control served BSA. Then, the anti-TNT-antibody containing solution was incubated for 1 h at the room temperature (for competitive assay the antibody was incubated with a certain concentration of antigen (competitor, inhibitor) TNBS for 5-60 minutes before placing into ELISA-wells). Detection was made with anti-human-IgG-HRP conjugate and its substrate ABTS with subsequent measurements at 405 nm.

Affinity measurement in the solution using competitive ELISA. The method was based on antibody measurement, which bind on an immobilized antigen after preincubation with free antigen (Friguet *et al.*, 1985).

Results

To ensure the maximal signal intensity three TNP-BSA conjugates with a different TNP-density were tested. TNP-BSA-conjugates with a density of 3, 5 and 50 TNP per BSA were tested as covering antigen in ELISA. The conjugate with a density of 50 TNP pro BSA proved to give the best signal after binding of 11B3-IgGAC1 and subsequent detection.

To make a sensitive assay, a minimal antibody quantity had to be determined, which gave a measurable signal in ELISA (figure 1).

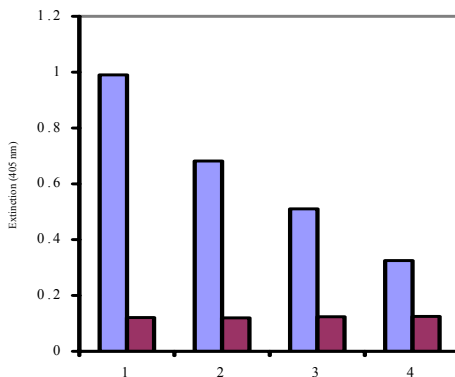


Fig. 1. Detection of minimal quantity of the antibody 11B3-IgGAC1.

The antibody dilutions 1800 ng/ml (1), 900 ng/ml (2), 450 ng/ml (3) and 225 ng/ml (4) were tested. Negative controls are dark grey.

The primary aim of assay was to establish the minimal quantity of competitor, which would still give the measurable signal inhibition in competitive assay after the preincubation with antibody. For this purpose the suitable dilution of TNP-Tris had to be made. From the figure 2 one can see, that the saturation region (completely lose of signal) started already from 200 fmol TNP-Tris. An important signal inhibition was detected at the quantity of 25 fmol TNP-Tris. This quantity meant the detection limit for the assay and so determined the sensitivity of assay.

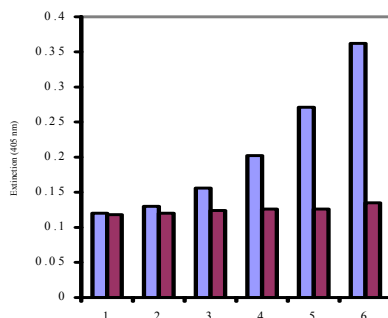


Fig. 2. Determination of detection limit for TNP-Tris in competitive ELISA.

The 11B3-IgGΔC1 antibody in the concentration of 225 ng/ml was preincubated with TNP-Tris for 5 minutes in the quantity of 2 pmol (1), 500 fmol (2), 200 fmol (3), 50 fmol (4) and 25 fmol (5). The antibody without TNP-Tris was positive control (6). Negative controls are dark grey.

The assay for the 3.5-IgGΔC1 antibody was performed under the conditions established for his analog 11B3-IgGΔC1. The quantity, which after 5 minutes preincubation gave the measurable signal inhibition in competitive assay, was 25 fmol TNP-Tris, just as for its analog 11B3-IgGΔC1.

From three calculated Kd-values for antibody 11B3-IgGΔC1 an average value of 1.88×10^{-9} M was calculated. In the same way the dissociation constant for 3.5-IgGΔC1 was determined and this Kd was 1.59×10^{-9} M.

Discussion

The main demands for biosensors are very similar for all application areas of biosensors and include high specificity, rapidness, sensitivity, low costs and the possibility to be transferred from one site to another. In this work the detection limit for TNT-analog TNP-Tris was 25 fmol or 87 pg/ml (87 ppt), what belonged to the most sensitive published assays regarding the detection range (Goldman 2003, Green 2002, Charles 2004). An important notice is the fact, that the bivalent antibodies in IgGΔC1 format were utilized, whereas in published assays the IgG-format was implemented.

Kd-values for both IgGΔC1 were in the area 10^{-9} M, which belongs to high affinity binding (the dissociation constants for high affinity antibodies are in the range from 10^{-8} to 10^{-10} M).

Literature

- [1] Charles P.T., Shriver-Lake L.C., Francesconi S.C., Churilla A.M., Rangasammy J.G., Patterson C.H. Jr., Deschamps J.R., Kusterbeck A.W.: Characterization and performance evaluation of in vivo and in vitro produced monoclonal anti-TNT antibodies for the detection of TNT. *J. Immunol. Methods*, 2004, **284**, 15-26.
- [2] Coffee C.J., Bradshaw R.A., Goldin B.R., Frieden C.: Identification of the sites of modification of bovine liver glutamate dehydrogenase reacted with trinitrobenzenesulfonate. *Biochemistry*, 1971, **10**, 3516-3526.
- [3] Friguet B., Chaffotte A.F., Djavadi-Ohanian L., Goldberg M.E.: Measurements of the true affinity constant in solution of antigen-antibody complexes by enzyme-linked immunosorbent assay. *J. Immunol. Methods*, 1985, **77**, 305-319.
- [4] Goldman E., Hayhurst A., Lingerfelt B., Iverson B., Georgiou G., Anderson G.: 2,4,6-trinitrotoluene detection using recombinant antibodies. *J. environ. monit.*, 2003, **5**, 380-383; Green T., Charles P., Anderson G.: Detection of 2,4,6-trinitrotoluene in seawater using a reversed-displacement immunosensor. *Analytical biochemistry*, 2002, **310**, 36-41.
- [5] Wanlund J., DeLuca M.: Bioluminescent immunoassays. *Methods in enzymology*, 1983, **92**, 426-432.

**Radiochemistry,
Nuclear Chemistry**

(G)

FACTORS AFFECTING LABELLING YIELD OF ^{111}In -DTPA-BSA

S. Vranješ¹, N. Nikolić¹, M. D. Mirković¹, D. Janković¹ and G. J. Bayer²

¹Laboratory for Radioisotopes, Vinča Institute, P.O.Box 522, Belgrade, Serbia

²European Organization for Nuclear Research, CERN, Geneva, Switzerland

Abstract

Radiolabelling of antibodies depends on a number of factors including the chemical characteristics of the nuclide and the techniques employed for its incorporation into protein. For preliminary research we used model system and investigate the influence of different factors affecting labelling. Obtained results were successfully used for further radiolabelling of antibodies with different trivalent metals.

Introduction

Development of the new radiopharmaceuticals for diagnostic and therapy purpose in nuclear medicine is still in the focus of the main research cancer centers. Antibodies labelled with alpha and beta emitters are radiopharmaceuticals with good characteristics for targeted cancer cell therapy with the minimum side effect on the surrounding healthy tissue. The purpose of this experiment was to optimize the conditions of labelling of polyclonal and monoclonal antibodies with ^{201}Tl (gamma emitter with favorable characteristics for radioimmunosintigraphy), ^{153}Sm (beta emitter for radioimmunotherapy of solid tumors) and ^{149}Tb (for radioimmunotherapy of hematological malignancies and diffuse types of cancer) and obtain *in vitro* and *in vivo* stable radioimmunoconjugates. However, as applicability of radionuclides (^{149}Tb and ^{153}Sm) used for the labelling of antibodies in these studies, has not been investigated enough and due to the low availability and high price of these radionuclides, it was not possible to use them for preliminary experiments where all conditions of labelling of antibodies with radionuclides should be settled. As a model for these trivalent radiometals, ^{111}In was used. ^{111}In is also trivalent radiometal, gamma emitter with good radiophysical characteristics for research and easily available. Bovine serum albumin (BSA) was used as a model for Rituximab antibodies for all chemical experiments.

In the preliminary experiment for chelating of BSA with bicyclic anhydride of DTPA (cDTPA) modified method of Hnatowitch was used [1]. This indirect method includes covalent coupling of bifunctional chelating agent to the BSA (antibody) which binds the radiometal. However as the stability of obtained complex ^{111}In -DTPA-BSA was low, it was necessary to optimize the conditions of formation of the complex.

Experimental

We studied a number of factors that are influencing the labeling procedure, in order to find one which lead to high yield of labeling:

- **Solvent solution for cDTPA:** Chelating of BSA with cDTPA needs specific conditions, because anhydride cDTPA hydrolyze very fast, therefore for low concentration of protein the yield of complex DTPA-protein is low. Two solvents for dissolving of cDTPA were investigated as well as addition of the solid cDTPA to the buffer (0.1 M sodium acetate buffer pH 5.6) with BSA;
- **Buffer volume for labelling:** Radiolabelling yield was determined for two (0.1 M sodium acetate) buffer volumes 0.95mL and 0.05 mL with pH 5.6;
- **Molar ratios BSA:cDTPA** from 1:1 to 1:100 were investigated;
- **Concentration of BSA:** Two different concentrations of the BSA, 1.4mg/mL and 4.6 mg/mL were used for the preparation of the conjugate, in order to see if BSA concentration affects labeling;
- **Temperature and incubation time** of chelating: The labeling was studied for the incubation time periods from 0-60 min for two temperatures, 4 °C and 24 °C. In all time points we used the same concentrations of BSA and cDTPA (C BSA=4.6mg/mL, BSA:cDTPA=1:100).

The labeling efficiency of prepared complex DTPA-BSA with ^{111}In was followed by chromatographic methods and gel filtration on PD-10 column.

Results and Discussion

The best labelling yield (89.8%) was obtained for the molar ratio BSA: cDTPA=1:100 with cDTPA added to the buffer solution in a solid form, therefore the hydrolysis of cDTPA was prevented.

Table 1. The effect of solvent and molar ratio BSA:cDTPA on the labelling yield of ^{111}In -DTPA-BSA (%)

Buffer volume (mL)	Solvent for cDTPA	Labelling yield ^{111}In DTPA-BSA (%)		
		Molar ratio BSA : cDTPA		
		1 : 1	1 : 10	1 : 100
	No solvent	/	87.7	89.8
0.95	Chloroform	72.3	78.1	81.2
	DMSO	43.3	55.6	61.7
0.05	Chloroform	53.5	57.1	62.4
	DMSO	27.5	39.7	42.5

For the low concentration of BSA (1.4mg/mL) conjugation process can't compete with the process of hydrolysis of cDTPA and radiolabelling yield is low (42.1%). In reaction with more molecules of BSA in reaction solution (4.6mg/mL), conjugation of DTPA is facilitated, therefore more binding places for radionuclide are available and

radiolabelling yield is higher (89.8%).

After 5 min. of incubation of BSA with cDTPA at room temperature labelling yield was 85%, while maximum was already obtained after 10 min. of chelating, and remained practically the same up to 24 h later.

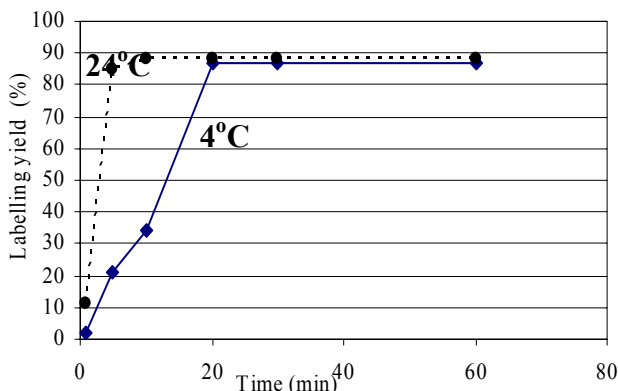


Fig. 1. The effect of incubation time and temperature on labelling yield of ^{111}In -DTPA-BSA (%)

Conclusion

These conditions (where the best results of radiolabelling yield were obtained) with minimal corrections were successfully used for labelling of different antibodies, including Rituximab antibodies, with ^{153}Sm , ^{149}Tb and later on with trivalent ^{201}Tl [2]. The cytotoxicity effect of obtained radiopharmaceuticals was determined by *in vitro* cell studies and *in vivo* on healthy mice [3, 4].

References

- [1] Hnatowich, D. J., et al., J. Nucl. Med., 1987, **28**, 1294-1301.
- [2] G.-J. Beyer, M. Miederer, S. Vranješ-Đurić, J. J. Čomor, G. Kuenzi, O. Hartley, R. Senekowitsch-Schmidtke, S. Soloviev, F. Buchegger, and the ISOLDE Collaboration, European Journal of Nuclear Medicine and Molecular Imaging, 2004, **1**, 547-554.
- [3] M. Fani, S. Vranješ, S. C. Archimandritis, S. Potamianos, S. Xanthopoulos, P. Bouziotis, A. D. Varvarigou, Applied radiation and isotopes, 2002, **57**, 665-674.
- [4] Miederer, M., Seidl, C., Beyer, G., Charlton, D.E., Vranješ-Đurić, S., Čomor, J., Huber, R., Nikula, T., Apostolidis, C., Schumacher, C., Becker, K., Senekowitsch-Schmidtke, R., Radiation Research, 2003, **159**(5), 612-620.

PROLIFERATION CAPACITY AND *p53* EXPRESSION OF HTB140 CELLS AFTER PROTON IRRADIATION

D. Todorović¹, I. Petrović¹, G. Cuttone² and A. Ristić-Fira¹

¹ Vinca Institute of Nuclear Sciences, P.O.Box 522, 11001 Belgrade, Serbia

² Istituto Nazionale di Fisica Nucleare, LNS, Catania, Italy

Abstract

Human HTB140 melanoma cells were used to investigate different responses to single irradiation with protons, regarding cell proliferation, induction of apoptosis and expression of *p53*. Exponentially growing cells were irradiated close to the Bragg peak maximum of the unmodulated 62 MeV proton beam. Doses applied ranged from 8 to 24 Gy at the dose rate of 15 Gy/min. Cell proliferation, measured 6 and 48 h post-irradiation, has shown highly significant dose and time dependent decrease. Protons induced apoptosis, 6 and 48 h after irradiation, decreasing with the increase of post-irradiation incubation time. The largest number of apoptotic cells was at 6 h after irradiation with 16 Gy protons. High level of *p53* expression was detected in all irradiated samples, as well as in controls and was independent of dose applied and post-irradiation incubation time.

Introduction

Proton irradiation performs higher relative biological effectiveness (RBE) and provokes better cell elimination even on radioresistant tumors, such as melanoma. This is due to their physical properties [1]. Previous results indicated that proton irradiation induced dose and time dependent inactivation of resistant human HTB140 melanoma cells [2] being more efficient than gamma rays [3]. In this study, we investigated the effects of irradiation within the Bragg peak of an unmodulated 62 MeV proton beam on HTB140 melanoma cell proliferation capacity, induction of apoptosis and expression of *p53* gene.

Results and Discussion

Exponentially growing HTB140 cells were irradiated with single doses, close to those applied in proton therapy, i.e. 8, 12 and 16 Gy as well as with 20 and 24 Gy, at the therapeutic dose rate of 15 Gy/min. Irradiations were carried out at the CATANA treatment facility at INFN, LNS-Catania, Italy. All assays were performed 6 and 48 h after irradiation. Cell proliferation was detected by 5-bromo-2'-deoxyuridine (BrdU) incorporation assay. Irradiation with 8 and 12 Gy protons at 6 h, induced statistically significant ($p < 0.05$) decrease of cell proliferation, compared to non-irradiated controls (Fig. 1). With increase of dose from 16 to 24 Gy cell proliferation decreased ($p < 0.001$) in comparison with non-irradiated controls. Forty eight hours after irradiation almost linear and highly significant ($p < 0.001$) decrease of cell proliferation was observed indicating that the reduced proliferation capacity of HTB140 cells after exposure to protons was dose and time dependent (Fig. 1). As compared to previously re-

ported results [2] considering cell growth inhibition, the effects of proton irradiation on cell proliferation were stronger than the effects on cell viability. Detected decrease of cell proliferation was depended on different signaling pathways involved in cell cycle regulation [4]. The induction of apoptosis was estimated by Annexin-V-FLUOS Kit (Roche, Germany). Apoptotic population was accessed using FACS analysis (Becton Dickinson, Heidelberg, Germany) and calculated using CellQuest computer program (Becton Dickinson, Heidelberg, Germany). Significant percentage of apoptotic cells was detected 6 h after irradiation (having values from $12.98\% \pm 0.55\%$ to $25.15\% \pm 1.30\%$) as well as after 48 h (ranging from $13.03\% \pm 0.24\%$ to $18.13\% \pm 1.00\%$). The highest number of apoptotic nuclei was at 6 h post-irradiation with 16 Gy protons ($25.15\% \pm 1.30\%$). With prolonged cell incubation up to 48 h within the same dose level, the number of apoptotic cells slightly decrease. These results clearly showed the ability of protons to eliminate resistant HTB140 human melanoma cells to a certain extent by inducing apoptosis. The level of proton induced apoptosis was in the range reported for resistant melanoma cell lines [5, 6].

To estimate changes of *p53* expression, total cellular RNA was isolated from irradiated HTB140 cells (1×10^6) using Qiagen RNeasy Total RNA Preparation Kit. For cDNA synthesis $1 \mu\text{g}$ of total RNA was reverse transcribed using First Strand cDNA Synthesis Kit (Fermentas). Amplification of samples in polymerase chain reaction (PCR) was performed using primers for *p53* and *GAPDH*. Primer sequences for *p53* were: sense 5'AGA TAG CGA TGG TCT GGC 3' and antisense 5'TTG GGC AGT GCT CGC TTA GT 3', and for *GAPDH* were: sense 5'CGG AGT CAA CGG ATT TGG TCG TAT 3' and antisense 5'AGC CTT CTC CAT GGT GGT GAA GAC 3'. In order to modify method for the detection and quantification *p53* proto-oncogene mRNA, together with *GAPDH* mRNA, various experimental conditions for RT-PCR were tested and optimized. PCR-amplified products were analyzed on 2.7% agarose gel and quantification was performed using GelDoc1000 (BioRad). The relative mRNA level of *p53* gene was normalized to the corresponding *GAPDH* mRNA level in individual samples and the respective mRNA changes were determined relative to the non-irradiated controls. The obtained results have shown that in HTB140 cells, 6 and 48 h after proton irradiation the level of *p53* expression was high and did not significantly change ($p < 0.05$). Prolonged incubation time did not provoke changes in *p53* expression (Fig. 2). It could be supposed that DNA damages induced by protons lead to an increase in *p53* protein synthesis as well as induced changes of their functional activity [7] or even lead to *p53*-independent apoptosis [8].

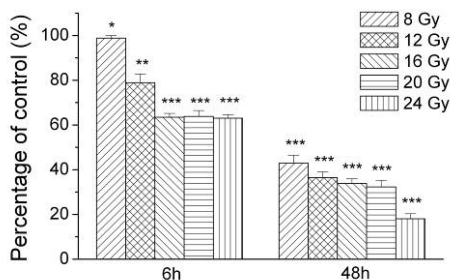


Fig. 1. Proliferation activity of HTB140 cells, 6 and 48 h after proton irradiation. Data presented are means±S.D. of three independent experiments performed in duplicates. * $p < 0.01$, ** $p < 0.001$

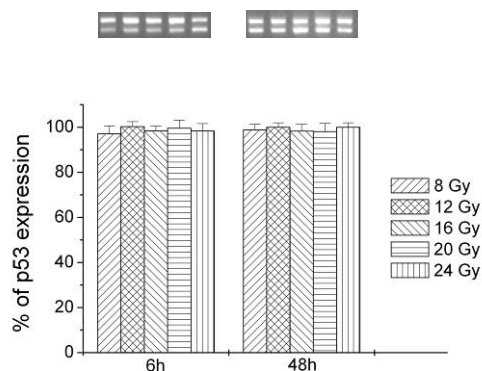


Fig. 2. Level of p53 mRNA expression after proton irradiation. Results are expressed as percent change relative to control levels set at 100%. Data presented are means±S.D. from a minimum three independent assays.

Conclusion

The decrease of HTB140 cell proliferation capacity up to 48 h after proton irradiation was dose and time dependent. The number of apoptotic nuclei at 6 and 48 h was significantly higher than in non-irradiated controls, showing a decrease with the increase of post-irradiation incubation time. The level of p53 expression remained high and did not change with dose and incubation time. Further studies are required to analyze changes that occurred in "up-" and "down-"regulation of signaling pathways involving p53 mediated response to DNA damage.

References

- [1] A. Ristic-Fira and I. Petrovic, Arch.Biol.Sci., Belgrade, 2000, **52**, 123-132.
- [2] I. Petrovic *et al.*, Phys.Chemistry, Proceedings, 2004, **2**, 426-428.
- [3] A. Ristic-Fira *et al.*, Oncology Reports, 2004, **12**, 1323-1328.
- [4] J.M. Karjalainen *et al.*, Br J Cancer, 1999, **79**, 895-902.
- [5] S. Ruzdijic *et al.*, Jugoslov. Med. Biochem., 2001, **20**(1), 9-18.
- [6] S. Kumala *et al.*, Cell. Mol. Biol. Letters, 2003, **8**, 655-665.
- [7] K. Satyamoorthy *et al.*, Cell Growth Differ., 2000, **11**, 467-474.
- [8] A. Takahashi *et al.*, Int. J. Radiat. Oncol. Biol. Phys., 2004, **60**(2), 591-597.

SENSITIVITY OF HTB140 CELL EXPOSED TO PROTONS AND ALKYLATING AGENTS

L. Korićanac¹, I. Petrović¹, G. Privitera², G. Cuttone³ and A. Ristić-Fira¹

¹*Vinca Institute of Nuclear Sciences, P.O.Box 522, Belgrade, Serbia*

²*Institute of Radiology and Radiation Oncology, University of Catania, Italy*

³*Istituto Nazionale di Fisica Nucleare, LNS, Catania, Italy*

Abstract

Malignant melanoma is a highly aggressive cancer with a poor prognosis due to resistance to radiotherapy and chemotherapy regimens. The mainstay of treatment remains DNA-alkylating agent dacarbazine (DTIC). Fotemustine (FM), chloroethylnitrosourea agent, also has demonstrated significant antitumoral effects in malignant melanoma. However, the resistance of melanoma cells limits their clinical application. In order to enhance the inhibition of melanoma cell growth, in this study, combined treatment of FM and DTIC with proton irradiation, was investigated. We analyzed the effects of combined treatment on HTB140 melanoma cell viability and proliferation. Significant inhibition of cell growth, especially cell proliferation, was obtained after treatment with protons and FM compare to single irradiation or drug treatment. Treatment with protons and DTIC has shown improved growth inhibition compare to appropriate single drug treatment, but not compare to irradiation as a single treatment.

Introduction

Malignant melanoma is an incurable cancer that frequently displays primary chemoresistance, and only a few cytotoxic drugs (including alkylating agents FM and DTIC) have shown activity against this tumor, albeit with low response rates of <25% for all agents [1, 2]. However, its clinical application is somewhat limited both by its toxicity and by the resistance of melanoma cells [3]. On the other hand, some forms of specially localized melanoma tumors, such as uveal melanoma, are curable to a certain extent by proton irradiation [4]. Proton irradiation offers several advantages over conventional therapy, including an optimal and uniform delivery of radiation to the entire tumor and minimal radiation damage to the surrounding normal tissue. These advantages are result of physical properties of proton beam, such as well defined range, small lateral scattering and especially, high energy deposition, just before the end of the range, marked as a Bragg peak. Whereas the Bragg peak is only a few millimeters wide, for proton therapy is used modified, *i.e.* spread-out Bragg peak (SOBP) [5].

Trying to realize more efficient elimination of melanoma cells, in this *in vitro* study, we investigated combined treatments of either DTIC or FM with proton irradiation.

Results and Discussion

For the analysis of the combined effects of alkylating drugs and protons, exponentially growing HTB140 human melanoma cells were treated with 100 and 250 μM of FM

(Ital farmaco S.p.A) or DTIC (Aventis Pharma S.p.A). Cells were irradiated with 12 and 16 Gy protons, 24 h after drug treatment. After irradiation, cells replated at 3×10^3 cells per well in 96-well plates. Cell viability and proliferation were assessed by SRB (MP Biomedicals, Inc) and BrdU (Roche Applied Science) assays respectively, 7 days after replating. The absorbance was measured using microplate reader (Victor, Wallac) at 450nm. Effects of combined treatment were compared with adequate single drug treatment and proton irradiation. Proton irradiation was performed within the spread-out Bragg peak (SOBP) of the 62 MeV proton beam, produced by the superconducting cyclotron at the CATANA (Centro di Adro Terapia e Applicazioni Nucleari Avanzati) facility at INFN, LNS – Catania. The corresponding relative dose was $99.42 \pm 0.58 \%$, while the mean energy of protons was 34.88 ± 2.15 MeV. Delivered single doses were 12 and 16 Gy, at dose rate of 15 Gy/min.

In our previous experiments we examined single effects of protons, FM and DTIC, as well as combined treatments of these drugs and protons on HTB140 human melanoma cell viability, 48h after irradiation. The combined treatment with either FM or DTIC and protons did not show significant changes of cell viability as compared to the effects of single agents. Therefore, in our present study, combined treatment of tested drugs and protons was investigated 7 days after irradiation (after at least six doubling times post-irradiation), thus enabling the proper condition for analysis of irradiation and drug treatment.

Obtained results implicated that irradiated HTB140 human melanoma cells, pre-treated with FM have shown slightly increased cell growth inhibition, as compared to single proton irradiation. Effects of combined treatment of FM and protons on cell viability were not improved, as compared to single FM treatment (**Figure 1A**). However, proliferation of these cells is significantly inhibited, comparing with single treatments (**Figure 1B**). Cells exposed to combined treatment with DTIC and protons, have shown moderate growth inhibition when comparing to irradiation. Stronger inhibition of cell growth was obtained when comparing the evaluated data with single DTIC treatment (**Figure 1C**). The effect of combined treatment with DTIC and protons on cell proliferation was better than corresponding effect of single DTIC application. However, cells exposed to combined treatment have shown weaker inhibition of proliferation than cells irradiated with protons (**Figure 1D**). This might be caused by activation of repair mechanism after DTIC treatment, because expression of the DNA repair protein O6-alkylguanine-DNA-alkyltransferase is inducible by DNA damaging agents, including DTIC and ionizing radiation [6].

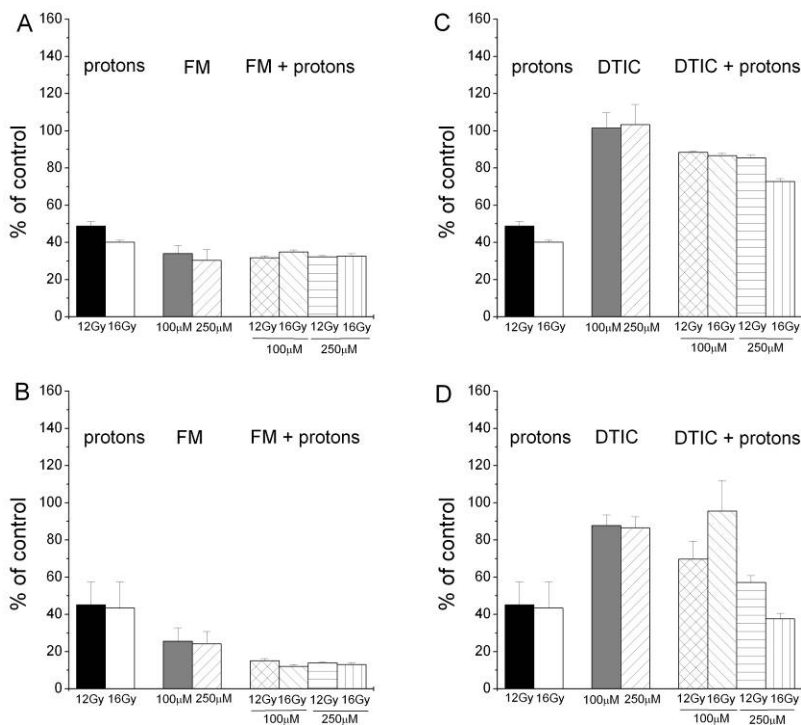


Fig. 1. Viability and cell proliferation of HTB140 cells estimated by SRB and BrdU assay respectively after single and combined treatments with FM and protons (panel A-SRB, panel B-BrdU) and DTIC and protons (panel C-SRB, panel D-BrdU). Applied irradiation doses were 12 and 16 Gy, while drug concentrations were 100 and 250 μM .

Conclusion

Obtained results have shown that FM and protons significantly affected HTB140 cell viability and proliferation, while combined treatment with DTIC and protons improved inhibition of cell viability and proliferation, compared to single DTIC treatment, not reaching inactivation level induced by proton irradiation.

References:

[1] R. M. Mackie et al., *Arch Dermatol.*, 2000, **136**, 71-73
 [2] K. A. DiVito et al., *Cancer Research*, 2004, **64**, 8773-8777
 [3] M. Christmann et al., *Int J Cancer.*, 2001, **92**(1), 123-9.
 [4] L. Kodjikian et al., *Am. J. Ophthalmol.*, 2004, **137**(6), 1002-1010.
 [5] A. Ristić-Fira and I. Petrović, *Arch. Biol. Sci.*, 2000, **52**(3), 123-132
 [6] J. A. Rafferty et al., *Oncogene*, 1996, **12**(3), 693-7

PATTERN RECOGNITION METHODS FOR CLASSIFICATION OF SOILS BASED ON THEIR RADIONUCLIDE CONTENT

S. Dragović¹ and A. Onjia²

¹ *Institute for the Application of Nuclear Energy – INEP, Banatska 31b, Belgrade, Serbia*

² *Vinča Institute of Nuclear Sciences, P.O. Box 522, Belgrade, Serbia*

Abstract

Multivariate data analysis methods were used to recognize and classify soils of unknown geographic origin. A total of 103 soil samples were differentiated into classes, according to regions in Serbia and Montenegro from which they were collected. Their radionuclide (²²⁶Ra, ²³⁸U, ²³⁵U, ⁴⁰K, ¹³⁴Cs, ¹³⁷Cs, ²³²Th and ⁷Be) activities detected by gamma-ray spectrometry were then used as the inputs in different pattern recognition methods. The prediction ability of linear discriminant analysis (LDA), *k*-nearest neighbours (KNN), soft independent modelling of class analogy (SIMCA) and artificial neural network (ANN) were 82.8%, 88.6%, 60.0% and 92.1%, respectively.

Introduction

There are only few studies on employing the chemometric approach to describe the correlation between locations and radioactive contamination, in which artificial neural networks was used [1,2]. This approach is used predominantly for identifying of radioactive isotopes [3], quantitative gamma-ray spectrometry analysis [4] and for optimization of gamma-ray spectrometric measurements [5,6].

In this work the feasibility of using pattern recognition techniques to predict soil origin based on its radionuclide content was examined. Four common pattern recognition techniques, LDA, KNN, SIMCA and ANN, were employed to classify soil samples based on their radionuclide contents determined by gamma-ray spectrometry. Since a predominant part of the radioactivity in soil is derived from the decay of the primordial radionuclides, ²³⁸U, ²³²Th and ⁴⁰K and the significant amounts of ¹³⁷Cs are also present in soil as a result of nuclear weapon tests and nuclear accidents, these radionuclides and their descendants are used for prediction. Soil samples (n=103) were collected from fifteen geographic regions of Serbia and Montenegro and their activities determined using an HPGe gamma-ray spectrometer ORTEC-AMETEK model GEM 25 (34% relative efficiency and 1.65 keV FWHM for ⁶⁰Co at 1.33 MeV, 8192 channels).

Details on employed pattern recognition methods can be found elsewhere [7]. It is only important to indicate the differences in their characteristics and in the way in which each of them define the classification rules. LDA is a parametric method which searches for optimal boundaries between classes while it assumes that all classes have the same multi-normal distribution and that they are linearly separable. KNN is a non-parametric method which is very simple from a mathematical point of view and free from statistical assumptions; however, it is very sensitive to gross inequalities in the number of objects in each class. ANN does not impose any condition on the data

structure. SIMCA is based on principal components for each category and critical distances with probabilistic signification; hence this implies that a spatial and probabilistic structure is present in the data.

Results and Discussion

Table 1 shows the activities (Bq/kg) of radionuclides in the analyzed soil samples. In general, radionuclide activities in these soils varied by a factor of up to 3-5 for ^{226}Ra , ^{238}U , ^{235}U , ^{40}K and ^{232}Th , 7 for ^7Be , 13 for ^{134}Cs , and 21 for ^{137}Cs . The distribution parameters (skewness and kurtosis) indicated normal (Gaussian) distribution.

Table 1. Descriptive statistics of radionuclide activities (Bq/kg) in soil samples

Variable	Mean	SD	Min.	Max.	Median	Skewness	Kurtosis
^{226}Ra	30.8	9.14	13.6	54.9	29.9	0.42	-0.45
^{238}U	29.7	9.42	14.6	53.4	30.2	0.44	-0.33
^{235}U	1.37	0.46	0.51	2.61	1.38	0.53	0.22
^{40}K	567	164	271	919	593	-0.17	-0.73
^{232}Th	40.7	13.5	18.3	83.4	39.7	1.20	2.18
^{134}Cs	0.09	0.07	0.02	0.26	0.05	0.91	-0.56
^{137}Cs	48.3	26.2	5.25	112	42.9	0.44	-0.39
^7Be	1.79	1.05	0.54	3.94	1.50	0.66	-0.91

The reliability of the classification models achieved was studied in terms of recognition ability (percentage of the members of the training set correctly classified) and prediction ability (percentage of the members of the test set correctly classified by using the rules developed in the training step).

Table 2 shows recognition and prediction abilities afforded with each multivariate technique. The recognition ability of these methods ranged from 86.4 to 100% and the prediction ability from 60.0 to 92.1%.

LDA produced a recognition rate of 95.1%; however, prediction ability was less satisfactory (82.8%). The highest rate of recognition achieved by KNN classifier was 86.4% and that of prediction was 88.6%. The number of neighbours (k) assayed were 1,3,5,7 and 9. The results obtained by SIMCA were very poor, giving only 60.0% of correct assignation for samples from test set containing autoscaled data. Meancentering of the data resulted in prediction ability of only 42.8%. In this application, ANN method overperforming the classification capabilities of other techniques. All soil samples presented to the network were correctly classified, i.e. the recognition ability was 100% and the prediction ability was 92.1%.

Table 2. Recognition and prediction ability of LDA, KNN, SIMCA, and ANN to classify soil samples

Method	Recognition ability (%)	Prediction ability (%)
LDA	95.1	82.8
KNN (K=1; inverse squared Euclidean distance)	86.4	88.6
SIMCA (normal range; $\alpha=0.05$)	86.4	60.0
ANN ($8 \times 7 \times 15$; $\eta=0.1$; $\mu=0.1$; sigmoidal transfer function)	100.0	92.1

Neural network are able to reproduce the training data in much more detail than other statistical techniques, which is particularly important if the specific problem under consideration requires a more detailed solution which the usual statistical approach based on means and variances may be unable to provide. The main advantage of neural network-based decision models lies in their adaptive behaviour.

In gamma-ray spectrometry ANNs have shown many advantages because of their full-parallel computing, simple implementation and nonlinearity. Automated pattern recognition systems such as neural networks are particularly useful in hazardous environments since an environment can be monitored without risk to human operators.

References

- [1] M. Kanevski, R. Arutyunyan, L. Bolshov, V. Demyanov, M. Maignan, *Geoinform.*, 1996, **7**, 5-11.
- [2] M. Kanevski, V. Demyanov, M. Maignan, Conference ICANN 1997, 1997, Lausanne.
- [3] P. Olmos, J.C. Diaz, J.M Perez, P. Gomez, V. Rodellar, P. Aguayo, A. Bru, G. Garcia Belmonte, J.L. de Pablos, *IEEE Trans. Nucl. Sci.*, 1991, **38**, 971-975.
- [4] V. Pilato, F. Tola, J.M. Martinez, M. Huver, *Nucl. Instr. Meth. A*, 1999, **422**, 423-427.
- [5] S. Dragović, A. Onjia, S. Stanković, I. Aničin, G. Bačić, *Nucl. Instr. Meth. Phys. Res. A*, 2005, **540**, 455-463.
- [6] S. Dragović, A. Onjia, *Appl. Radiat. Isot.* 2005, **63**, 363-366.
- [7] D. Massart, B. Vandeginste, S. Deming, Y. Michotte, L. Kaufman, *Chemometrics: A Textbook*, Elsevier, 1998, New York, USA.

PREPARATION OF CONCENTRATED RHENIUM SOLUTIONS

J. Vučina¹, D. Lukić¹, S. Milonjić² and M. Stoiljković³

¹Laboratory for Radioisotopes,

²Chemical Dynamics Laboratory,

³Department of Physical Chemistry,

Vinča Institute of Nuclear Sciences, 11001 Belgrade, P.O. Box 522, Serbia

Abstract

The conditions of the desorption of rhenium from the anion exchange resin Dowex 1×8 by nitric acid were determined. The solution (5×10^{-3} mol/dm³ Re in 0.15 mol/dm³ NaCl) was passed through the column containing 0.1 g of the resin. The total sorbed amount of rhenium was 200 mg/g of the resin. It was then eluted by nitric acid in the concentration range of 0.16-7.2 mol/dm³. The most favourable elution profile was found with 3.0 mol/dm³ HNO₃. Over 77% of the total rhenium was desorbed with 5 ml of this eluence. Over 95% of the sorbed rhenium was recovered by using 20 ml of nitric acid in the concentration range of 0.9-7.2 mol/dm³.

Introduction

Low concentrations of elements often restrict their intended use. Simple, rapid and effective methods are hence needed to achieve their favourable concentrations. There are reports in the literature describing several approaches to solve this problem. One of the most promising is based on ion exchange. The dilute solution of the desired element is passed through a column containing either inorganic or organic ion exchanger [1,2]. Then, it is recovered in much higher concentration by the elution with as small as possible volume of an appropriate eluent. The efficacy is determined by the elution profile, i.e. by the ratio of the desorbed element in the first fractions of the eluate and by the total volume of the eluent needed to desorb practically the whole quantity of the element from the resin.

Such concentration procedures find wide applications. They are used also in radiochemistry to achieve, for example, high radioactive concentration of a given radioisotope suitable for the preparation and use of radiopharmaceuticals [3,4].

The procedure under examination is based on the anion exchange resin Dowex 1×8 onto which rhenium, in the form of perrhenate anions, is sorbed. The paper presents the results of the determination of the conditions of its effective desorption by using nitric acid. The determinations of rhenium elution profiles and of the total elution volume in dependence on the concentration of the acid, are given.

The results of these experiments find application in the development of the procedures for the production of concentrated solutions of the radioisotope ¹⁸⁸Re whose physical, chemical and biological properties are suitable for the use in the therapeutic nuclear medicine [5,6].

Experimental

Potassium perrhenate (KReO_4 , p.a., Aldrich) and the resin Dowex 1×8 , 100-200 mesh (Aldrich) were commercially purchased p.a grade chemicals.

The experiments were performed in the glass column (5.5 mm I.D., 40 mm length) containing 0.1 g of Dowex 1×8 . The freshly prepared solution containing 5×10^{-3} mol/dm³ Re in 0.15 mol/dm³ NaCl was passed through the column. The total amount of sorbed rhenium was 200 mg/g of the resin. The flow rate was 3 ml/min.

The elution of rhenium was performed by nitric acid, concentrations 0.16, 0.9, 1.6, 3.0, 6.0 and 7.2 mol/dm³. The flow rate was 3 ml/min. The effluent solution was collected in 5 ml fractions.

The flow rate was kept constant by using Masterflex C/L pump (Cole Palmer Instrument Company).

The concentrations of rhenium in the solutions were determined by the direct current argon arc plasma atomic emission spectroscopy (DCP-AES) with aerosol supply [7].

The experiments were performed at room temperature.

Results and Discussion

In the experiments, the dependance of the efficiency of the elution of rhenium from the resin on the concentration of nitric acid was determined. Determined were the elution profile of Re, i.e., the ratio of the total sorbed rhenium found in the first 5 ml of the eluate and the total volume of the acid of the corresponding concentration, needed for the recovery of more than 95% of the sorbed rhenium. These results are given in Table I.

According to the data given in Table I it can be concluded that the elution profile depends on the concentration of HNO_3 . The most favourable result is obtained if rhenium is desorbed by 3.0 mol/dm³ HNO_3 . In this case the first fraction of the eluate (5 ml) contains 77.2% of the total Re.

It can also be seen that the total volume of the eluent needed to desorb practically all rhenium, depends on the concentration of HNO_3 , too. Except for the lowest (0.16 mol/dm³ HNO_3), for all higher concentrations of the acid used in the experiments (0.9 – 7.2 mol/dm³), more than 95% rhenium is desorbed by 20 ml of the eluent.

Table I. The dependance of the efficiency of the elution of rhenium from Dowex 1×8 on the concentrations of the eluent HNO₃

Sample	Volume (ml)	Eluted rhenium (%)					
		0.16 mol/dm ³	0.9 mol/dm ³	1.6 mol/dm ³	3.0 mol/dm ³	6.0 mol/dm ³	7.2 mol/dm ³
1	5	5.6	55.4	65.7	77.2	63.2	66.4
2	5	12.2	24.6	20.9	15.9	20.7	21.5
3	5	12.6	10.4	9.2	5.7	10.1	4.9
4	5	11.8	5.3	4.5	2.1	5.2	2.3
Σ	20	42.2	95.7	100.3	100.9	99.2	95.1

Column: 5.5 mm I.D., 40 mm length

Bed: 0.1 g Dowex 1×8, 100-200 mesh (Aldrich)

Total rhenium sorbed on the resin: 200 mg Re/g of the resin

Flow rate of the eluent HNO₃ solution: 3 ml/min

Conclusion

The results presented in this paper reveal that the perrhenate anions sorbed on Dowex 1×8, can be effectively desorbed by nitric acid. The elution profile and the total volume of the eluent needed to desorb practically all rhenium, depend on the concentration of the acid. The best results are obtained with 3.0 mol/dm³ HNO₃.

This confirms the applicability of the proposed concept of the concentration based on the sorption of rhenium from diluted solutions on anion exchangers and its subsequent elution by acid. However, before its introduction into routine practice, further investigations are needed.

Acknowledgement

This work has been financially supported by the Ministry of Science and Environmental Protection of the Republic of Serbia under Project No.142004B.

References

- [1] A. Mushtag, J.Radioanal.Nucl.Chem, 2004, **262**, 797-810.
- [2] R.M. Lambrecht, K. Tomiyoshi, T. Sekine, Radiochim.Acta, 1997, **77**, 103-123.
- [3] F. F. (Russ) Knapp, Jr, A.L. Beets, S. Guhlke, P.O. Zamora, H. Bender, H. Palmedo, H.-J. Biersack, Cancer Research, 1997, **17**, 1783-1796.
- [4] A. Mushtag, Appl.Radiat.Isotopes, 2003, **58**, 309-314.
- [5] J.L. Vučina, D. M. Lukić, M. M. Stoiljković, J.Serb.Chem.Soc., 2004, **69**,683-688.
- [6] J.L. Vučina, D.M. Lukić, S.K. Milonjić, M.M. Stoiljković, J.Radioanal.Nucl.Chem., 2006, **267**, 67-72.
- [7] F.M. Marinković, T.J. Vickers, Appl.Spectrosc., 1971, **25**, 319-322.

TRICARBONYLTECHNETIUM (I) LABELLED LIGANDS WITH NSO DONOR ATOM SET: *IN VITRO* AND *IN VIVO* EVALUATION

D. Janković¹, I. Pirmettis², Lj. Matović¹, D. Đokić¹ and S. Vranješ¹

¹Laboratory for Radioisotopes, INS "Vinča", POB 522, 11001, Belgrade, Serbia

²Institute of Radioisotopes and Radiodiagnostic Products, NCSR "Demokritos", POB 60228, 15310 Agia Paraskevi, Athens, Greece

Abstract

There is an increasing interest for the ^{99m}Tc labelling of biomolecules by using bifunctional chelating agents. To find new ligand, which can be linked to the small biomolecules and coordinated with technetium-99m tricarbonyl complexes, is a challenging task. The investigated NSC and NSC5 ligands allow the preparation ^{99m}Tc(I) stable complexes in high yield. The ^{99m}Tc complexes were characterized by comparing their HPLC profiles with those of the respective Re(I) compounds. Biodistribution and stability studies were carried out, including challenge with histidine. These complexes also proved to be stable *in vivo* and showed a very good biological behaviour. The radiochemical and biological features of the novel ^{99m}Tc complexes, as well as, the nature of the ligands, make them very promising candidates for labelling of tumour specific biomolecules.

Introduction

Technetium radiopharmaceuticals, as complexes of the ^{99m}Tc radionuclide, are of great importance in diagnostic nuclear medicine. However, the use of ^{99m}Tc for labelling small molecules, receptor ligands, has been rather limited. Over the last few years, the chemistry of a novel organometallic species, $M(\text{CO})_3^+$ ($M=\text{Tc}, \text{Re}$), has been intensively developed. The water soluble technetium tricarbonyl complex $[\text{}^{99m}\text{Tc}(\text{CO})_3(\text{H}_2\text{O})_3]^+$ was seen to be very versatile and effective precursor for labelling biomolecules [1]. The three coordinated molecules of water are labile and could be readily exchanged with various mono-, bi- and tridentate ligands. New chelating agents have been synthesized with the aim toward the design and development of site-specific radiopharmaceuticals [2], [3]. The aim of this study is to label ligands (2-benzimidazolylmethylthio) acetic acid (NSC) and N-1-Ethyl-(2-imidazolidinyl methylthio) acetic acid (NSC5) with ^{99m}Tc (I)-precursor. The stability of the formed complexes and its *in vitro* and *in vivo* properties were investigated too.

Materials and Methods

The samples of ligands (NSC, NSC5) were prepared by dissolving in water appropriate amount of substance for obtaining 10^{-3} mol dm⁻³ solutions. pH was adjusted to 5.0. ^{99m}Tc-carbonyl precursor was prepared according to manufacturer instruction (IsoLinkTM, Mallinckrodt Medical B.V., Netherlands). ^{99m}Tc-(I) ligands complex were

prepared by addition of 0.1 ml of ligand solutions to 0.4 ml of $[^{99m}\text{Tc}(\text{CO})_3(\text{H}_2\text{O})_3]^+$ precursor with appropriate pH values. The vials were heated for 30 min in boiling water bath. The labelling efficiency of ^{99m}Tc -carbonyl targeted ligands was determined using gradient HPLC equipped with UV and radioactive γ -detector on Nucleosil 100-5 C-18 column. The 0.1% solution of TFA (trifluoroacetic acid) in H_2O and 0.1% of TFA in acetonitrile were used as mobile phases.

TCA precipitation method for determining the percentage of $^{99m}\text{Tc}(\text{I})(\text{NSC5})$ bound to proteins (12% human albumin, incubation at 37°C for different time intervals) was very useful [4]. All lipophilicity measurements were done by solvent extraction method with n-octanol equilibrated with 0.15 M phosphate buffers (pH=6.0-7.5). Organ biodistribution studies were carried out on white health Wistar rats (four weeks old). The animals were sacrificed 5 and 120 minutes after application of 0.1 ml of $^{99m}\text{Tc}(\text{I})(\text{NSC5})$. The radioactivity per organ of interest was measured in a NaI (TI) detector.

Results

Table 1. Retention times and yields for ^{99m}Tc complexes

Ligand (L)	^{99m}Tc species	R_t (min)	Yield (%)
	$^{99m}\text{TcO}_4^-$	-	-
NSC	$[^{99m}\text{Tc}(\text{CO})_3(\text{H}_2\text{O})_3]^+$	-	-
	$^{99m}\text{Tc}(\text{CO})_3\text{-NSC}$	13.74	100.0
NSC5	$^{99m}\text{TcO}_4^-$	4.00	3.2
	$[^{99m}\text{Tc}(\text{CO})_3(\text{H}_2\text{O})_3]^+$	13.12	2.9
	$^{99m}\text{Tc}(\text{CO})_3\text{-NSC5}$	14.53	94.9

Table 2. UV chromatograms of Re(I) complexes

Re-complex	R_t (min)	Yield(%)
Re(I)-NSC	13.57	84.7
Re(I)-NSC5	14.39	95.1

The reactions produced a single product with yields greater than 90% (tab. 1, fig.1). The values of retention times varied for each complex. The identity of the ^{99m}Tc complexes was established by comparative HPLC studies using samples of the well characterized rhenium (I) complexes as reference (tab. 2, fig.2). At 1, 6 and 24 hours post labeling the radiochemical purity of the formulations remained high and practically unchanged. Also, the complexes are resistant against histidine challenge.

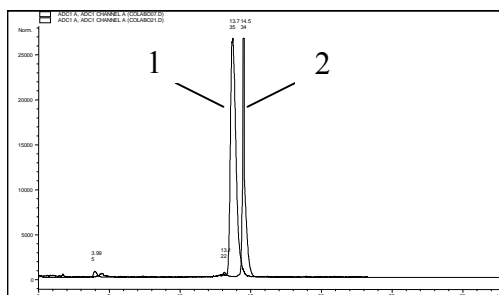


Fig.1. γ - chromatograms of $^{99m}\text{Tc}(\text{CO})_3\text{-NSC}$ (1) and $^{99m}\text{Tc}(\text{CO})_3\text{-NSC5}$ (2) complexes

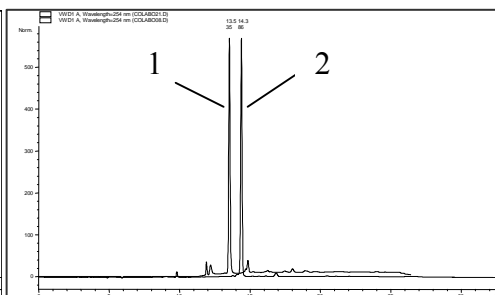


Fig.2. UV chromatograms of $\text{Re}(\text{I})\text{-NSC}$ (1) and $\text{Re}(\text{I})\text{-NSC5}$ (2) complexes

The percentage of $^{99m}\text{Tc}(\text{I})(\text{NSC5})$ protein binding was around 47%. The results of lipophilicity measurements of examined sample showed that most radioactivity remains in organic phase, thus the distribution coefficient is around 0,66. No change in extractability with pH was observed. Biodistribution studies showed minimal organ retention except liver (10.461%/g), intestine (3.012%/g) and kidneys (3.388%/g) of the injected dose at 1 hour p.i.

Discussion/Conclusion

The studied ligands, having a NSO donor atom set, were easily coordinated with ^{99m}Tc -tricarbonyl core in aqueous solution forming neutral complexes. Radiochemical purity and yield of labelling were very high. The complexes were very stable for at least 24 hours. HPLC analysis confirmed that these complexes were formed as singular chemical species. Moreover, the derivatization of the imidazolidine ring on the N-1 with an ethyl group did not reduce the labeling efficiency of the ligand as well as the stability of its $^{99m}\text{Tc}(\text{I})$ complex. This study showed that these ligands can be derivatized in order to modify the biological behavior by attaching the appropriate biomolecule on the N-1. The labelled NSC5 ligand has been shown to be very stable, and due to its relative lipophilicity has a very good biodistribution profile. With these points in mind this chelating agent provide a promising architecture for use in labelling tumor specific biomolecules.

References

- [1] R.Alberto, R.Schibli, A,Egli, P.A.Schubiger, *J.Am.Chem.Soc.*, 1998, **120**, 7987-7988.
- [2] R.Schibli, R.La Bella, R.Alberto, et al., *Bioconj.Chem.*, 2000, **11**, 345-351.
- [3] M.Santimaria, U.Mazzi, S.Gatto, et al., *J.Chem.Soc.Dalton Trans.*, 1997, **42**, 1765-1771.
- [4] W.C.Klingensmith, A.R.Fritzberger, V.M.Spitzer, *J.Nucl.Med.*, 1984, **25**, 42-48.

DOSIMETRY USING HS GafChromic FILMS

The influence of readout light on sensitivity of dosimetry

B. Šećerov¹, M. Daković², M. Sarić³, G. Bačić² and N. Borojević³

¹VINČA Institute of Nuclear Sciences, ²Faculty of Physical Chemistry, University of Belgrade, ³Institute of Oncology and Radiology of Serbia

Abstract

The goal of this study is to compare the sensitometric curves for HS model of Gaf-Chromic film using different dose read-out systems. Two commercial densitometers using fluorescent light source were tested and compared with results obtained using spectrophotometry. It was found that sublinear response of densitometers is due to the polychromaticity of emitted light and that response curve can be predicted by analysing absorption spectra of the film.

Introduction

Radiotherapeutic irradiation requires the exact knowledge not just about the dose but also its 3-dimensional or at least 2-dimensional distribution. The introduction of Gaf-Chromic radiochromic films (especially high sensitivity, HS films) has solved some of the problems associated with conventional 2D radiation detectors [1-3]. Blue coloration of films induced by irradiation is stable so radiochromic films do not require post-processing but a critical component in the GafChromic dose measurement process is the densitometer used for the film's optical density (OD) readout [3]. Here we examined how the nature of the analyzing light used by different densitometers affects the sensitivity curves obtained for HS films.

Experimental

Gafchromik HS dosimetric radiochromic film (ISP Technology, USA) were uniformly irradiated using either ⁶⁰Co γ -source or radiotherapeutic linear accelerator (PRIMUS, Siemens). The absorbance of irradiated films was measured in the wavelength range of 200 nm – 800 nm using a Perkin-Elmer Lambda 5 spectrophotometer or determined by scanners that use a fluorescent light source (FLC) with broad band emission spectra (250 – 75 nm): a desktop flat-bed Epson Perfection 1240U scanner operating in a transmission mode and VIDAR VXR-16. In addition, films were scanned using a red acetate filter overlay [4]. Data obtained from scanners were analyzed IMAGE J program.

Results and Discussion

Radiation induced absorption spectra of HS films are shown in Fig.1A. The absorption maxima at ~ 615 nm and ~ 675 nm are similar to those found for HS and other GafChromic films (e.g. MD-2) [1]. As expected, the highest sensitivity (defined as a fractional increase of A with the dose, i.e., the initial slope) can be achieved by using

the scanner operating at 675 nm (Fig. 1B). Departure from linearity (sublinear response) for doses above around 10 Gy is due to the high values of absorbance so the Lambert-Beer law is no longer valid, which is of no great concern since doses above 10 Gy are seldom used in radiotherapy. Unfortunately, only non-commercial densitometric scanners operate at this wavelength [3]. The sensitivity at 615 nm is lower and in addition no densitometers operate at this wavelength. Measurements at 633 nm would yield even lower sensitivity (but almost linear response over the investigated dose range), however this is the wavelength of He-Ne laser utilized by commercial scanners (e.g. LKB Pharmacia UltraScan XL).

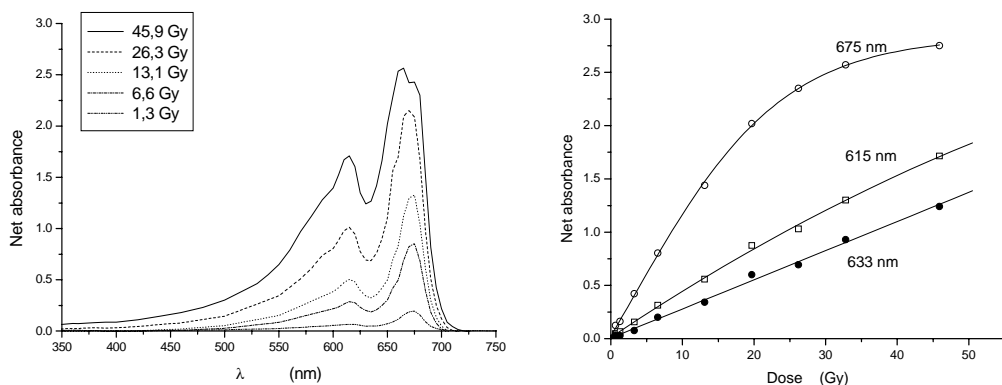


Fig. 1. (A) Gamma ray induced absorption spectra for HS GafChromic films irradiated to different doses. (B) The dose response curves measured at the indicated optical wavelengths.

Although measurements of the dose response using scanning monochromatic source at 633 nm occurs at a local minimum on the absorption spectra (Fig. 1) such measurements would be still more sensitive than using fluorescent light sources (Fig. 2A). Both scanners gave identical results and response was independent of the irradiation source.

Based on the common wisdom that the reduction of the bandwidth of the analysing light should result in increased sensitivity, an inexpensive red acetate filter has been proposed for that purpose [4]. The filter absorbs between 320 nm and 560 nm, i.e. below wavelengths of film spectral peaks. Sensitivity is significantly improved (Fig. 2A). Even further improvement can be achieved by using the RGB mode (Fig. 2A), but a Vidar scanner does not have such option. Unlike measurements using a single wavelength all response curves are sublinear and the low values of A indicate that a sublinear response should be due to the polychromaticity of emitted light [5].

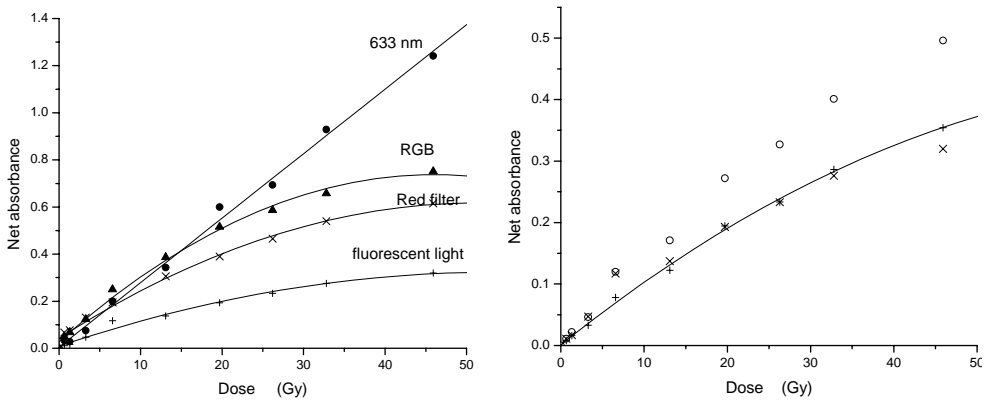


Fig.2. (A) The dose response curves for irradiated HS GafChromic films as measured with different setups of scanners using fluorescent light. Spectrophotometric data are given for comparison. (B) x – fluorescent light. Integrated absorbance from spectra (Fig. 1A): o - 500 nm range; + - 600 nm range.

Results shown in Fig. 2A are not particularly novel and similar conclusions can be extracted from literature [3, 4]. However, the effect of polychromaticity on the shape of the response curve have not been addressed so far. Using data in Fig. 1A we integrated the area under the spectrum for all absorbed doses and compared data with dose response obtained for 'white light' (Fig. 2B). Results clearly show that sublinear response is due to the polychromaticity. However, it should be noted that agreement with the measured response curve is achieved not for the proper range of emitted wavelengths, but for the slightly higher range. The reason for this is that a proper comparison can be obtained only when data obtained by integration are corrected with the spectral distribution of the source, which is not known in sufficient detail.

In conclusion, there are conflicting requirements for scanners (availability, price, sensitivity) for radiochromic film dosimetry. Spectrophotometry can not be used for 2D scanning, but results can be used to predict the dose response curve for any selected light source.

References

- [1] W.L. McLaughlin, et al., Radiat. Protect. Dosim. 1996, **66**, 263.
- [2] M.J. Butson, et al., Mater. Sci. Engin., 2003, **R41**, 61.
- [3] S. Devic, et al, Med.Phys. 2004, **31**, 2392.
- [4] B.Lj. Šećerov and B.B.Radak. Radiat. Phys. Chem. 1992, **40**, 191.
- [5] D.O. Odero, et al., Med. Phys. 2001, **28**, 1446.

Materials Science

(H)

HIGH PRESSURE BEHAVIOUR OF CARBON BY LASER-GENERATED SHOCKS

D.Batani¹, H.Stabile¹, M.Tomasini¹, G.Lucchini¹, F.Canova¹, M. Koenig²,
A. Benuzzi², H.Nishimura³, Y.Ochi³, J.Ullschmied⁴, J.Skala⁴, B.Kralikova⁴,
M.Pfeifer⁴, T.Mocek⁴, A.Präg⁴, T.Hall⁵, P.Milani⁶, E.Barborini⁶ and P.Piseri⁶

¹*Dipartimento di Fisica "G. Occhialini", Università di Milano Bicocca, Piazza. Della Scienza 3,
20126 Milano, Italy*

²*LULI, Ecole Polytechnique Palaiseau, France*

³*ILE, Osaka University, 2-6 Yamadaoka, Suita City, Osaka 565-0871, Japan*

⁴*PALS Research Centre, Za Slovankou 3, 18221 Prague 8, Czech Republic*

⁵*University of Essex, Wivenhoe Park, Colchester, CO4 3SQ, UK*

⁶*Università degli Studi di Milano, Via Celoria 16, 20133 Milano, Italy*

Abstract

We present experimental point for carbon equation of state (EOS) at Megabar pressures, obtained by laser-driven shock waves. Experiments were performed at the PALS and LULI laboratories using carbon samples with two different value of initial density, in order to explore a wider region of the phase diagram. Previously unreached pressures were obtained. Results are compared with previous experiments and with available theoretical models and seem to show high compressibility of carbon at Megabar pressures.

Introduction

The study of phase transitions of materials is an important part of physical chemistry and solid state physics. Such phase transitions may be induced by compressing materials to very high pressures. Megabar pressures can be obtained in the laboratory only by applying dynamical methods (shock waves). Among the various methods for creating shock waves, in recent years, it was shown that lasers are a useful tool for high-pressure physics, to compress materials at Megabar pressures and measure their Equation Of State (EOS) [1,2].

The goal of our experiment was to explore carbon EOS in the pressure range 1 - 15 Mbar. We got the first experimental points at pressures higher than 8 Mbar. Moreover, we substantially increased the number of EOS data for carbon at pressures > 1 Mbar (here we present 9 new EOS points against a total of about 20 points which, to our knowledge, were available in literature [3-7]).

Results and Discussions

The experiment is based on generating high quality shocks and using "two steps - two materials" targets (fig. 1). Relative EOS data of "unknown" materials (here C) are obtained by using a known reference (here Al). Al behavior at high pressure is well known, making it a typical reference material for shock experiments. The method is described in detail in refs. [2].

Some laser shots were done at LULI where 3 laser beams were focused at inten-

sities of $\approx 5 \times 10^{13} \text{ W/cm}^2$. To increase laser energy (and shock pressure), other shots were done with the PALS iodine laser [8], focused up to $2 \times 10^{14} \text{ W/cm}^2$. In both cases, large focal spots and Phase Zone Plates (PZP) [1] were used to get uniform illumination and avoid 2D effects in shock propagation.

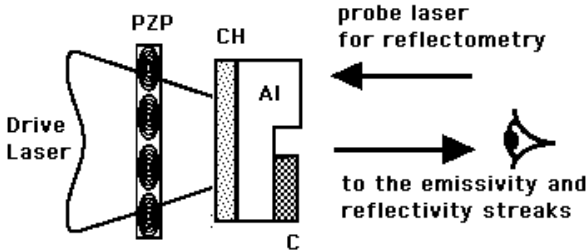


Fig. 1. Scheme of the experimental set-up. The CH layer may be present in order to reduce X-ray emission from laser irradiated side.

The main diagnostics was based on streak camera coupled to a photographic objective and a 12 bit CCD camera to measure the rear side time resolved imaging (to record target self-emissivity). This allows the measurements of the shock breakout times from the base and steps of the "two steps - two materials" target. Hence we measured the shock velocity in Al and C simultaneously on the same laser shot. Targets, and in particular the carbon layers, are an important part of the experiment. In our experiment, carbon layers with initial density $\rho_0 = 1.45 \pm 0.10 \text{ g/cm}^3$ and $\rho_0 = 1.6 \pm 0.10 \text{ g/cm}^3$ were used [9].

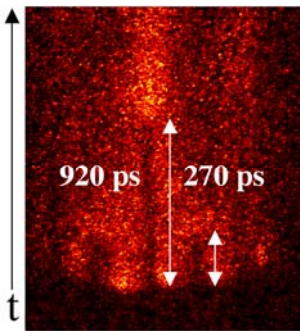


Fig. 2. Shock breakout streak image of the target rear side. Shot energy was 25.3 J. Arrows indicate the shock break-out from the Al step (right) and from the C step (left). The size of the image is $600 \mu\text{m} \times 1.7 \text{ ns}$.

Fig. 2 shows a typical obtained result. In total we obtained 5 good experimental points at LULI (2 for $\rho_0 = 1.45 \text{ g/cm}^3$ and 3 for $\rho_0 = 1.6 \text{ g/cm}^3$) and 4 good points at PALS (all for $\rho_0 = 1.6 \text{ g/cm}^3$). These are shown in Fig. 5 with all the other experimental results already available in the literature in the pressure range $P \geq 1.5 \text{ Mbar}$. Data, grouped according to their initial density ρ_0 , are compared to the shock polar curve derived from the Sesame tables.

All our data, for both initial densities, are below the shock polar curve derived from the Sesame tables. Let's notice that a deviation from Sesame is also observed for other points obtained at high shock pressure (for instance the point at $\approx 3 \text{ Mbar}$ for carbon with $\rho_0 = 1.85 \text{ g/cm}^3$ reported by Pavlovskii and Drakin [3]). Even more interestingly, the same behavior was observed by Nellis et al. [4] who, using underground nuclear

explosions as a compression tool, report two EOS points for graphite ($\rho_0 = 2.2 \text{ g/cm}^3$) at 4.76 and 7.61 Mbar.

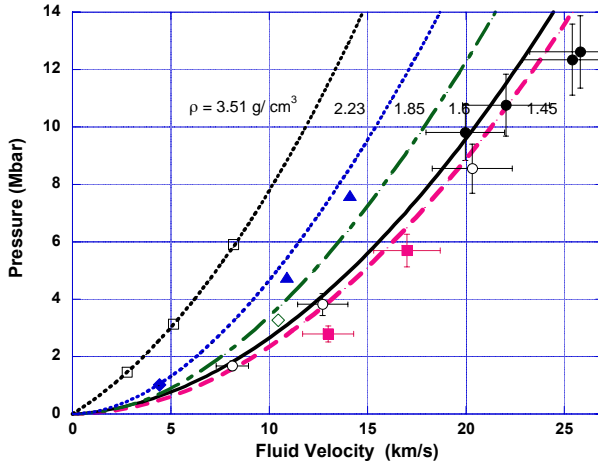


Fig. 3. Experimental EOS results from shock experiments. Only data with $P \geq 1.5$ Mbar and corresponding Hugoniot are shown. Our points [9]: full squares, 1.45 g/cm^3 LULI; empty circles, 1.6 g/cm^3 LULI; full circles, 1.6 g/cm^3 PALS. Previous points: empty diamond, 1.85 g/cm^3 Pavlovskii et al. [3]; triangles, 2.2 g/cm^3 Nellis [4]; full diamond, 2.23 g/cm^3 Pavlovskii et al. [3]; empty squares, 3.51 g/cm^3 (diamond) Pavlovskii [4].

Conclusions

The observed increased compressibility of carbon, suggests that at a given pressure along the Hugoniot, the density in the final state (liquid) is smaller than that for solid. Transitions to less dense phases also enhance thermal contributions, explaining the observed pressure discrepancy. This agrees with conclusions by Nellis et al. [4] and reinforces their observations.

References

- [1] M.Koenig, et al., Phys.Rev. E, 1994, **50**, R3314.
- [2] M.Koenig, et al., Phys. Rev. Lett., 1995, **74**, 2260; D.Batani, et al., Phys. Rev. B, 2000, **61**, 9287; D.Batani, et al., Phys. Rev. Lett., 2002, **88**, 235502.
- [3] M.N.Pavlovskii, V.P.Drakin, JETP Lett., 1966, **4**, 116.
- [4] W.J.Nellis, et al., J. Appl. Phys., 2001, **90**, 696.
- [5] M.N.Pavlovskii, Sov. Phys. Solid State, 1971, **13**, 741.
- [6] W.H.Gust, Phys. Rev. B, 1980, **22**, 4744.
- [7] *LASL Shock Hugoniot Data*, ed. by S.Marsch (Univ. California, Berkeley, 1980), pp. 28-51.
- [8] K.Jungwirth, et al., Phys. Plasmas, 2001, **8**, 2495.
- [9] D.Batani, H.Stabile. et al. Phys. Rev. Lett., 2004, **92**, 065503.

POLYMER BASED NANOCOMPOSITES

J. M. Nedeljković, M. Marinović-Cincović and J. Kuljanin-Jakovljević

Vinča, Institute of Nuclear Sciences, 11001 Beograd, P.O. Box 522, Serbia

Abstract

Dispersions consisting of spherical CdS and α -Fe₂O₃ particles in the nanometer and sub-micron size range, as well as β -FeOOH nanorods with three different aspect ratios were prepared using colloidal chemistry methods. After incorporation of filler particles into polystyrene and poly(methyl methacrylate) matrices influence of filler particles on the thermal stability and the glass transition temperature of polymer matrices was studied in details. Significant influence of content, size and shape of filler particles on thermal properties of polymer matrices was found.

Introduction

Nowadays, polymer composites are widely used in many fields of technology [1,2]. The properties of composites mostly depend on size and shape of filler particles, their concentration, as well as the type of interaction with polymer matrix. Also, polymer composites take advantage of desired properties of host polymers such as possibility to be designed in various shapes, long-term stability and reprocess ability.

Polystyrene (PS) and poly(methyl methacrylate) (PMMA) are important thermo-plastic materials with excellent transparency. However, their lower thermal stability restrains them from applications in higher temperature region. To improve the thermal properties of PS and PMMA, fillers such as oxides [3-5], metal chalcogenides [6-8], metals [9,10], organoclays [11] and graphite [12] were incorporated into PS and PMMA.

In this work, we present synthetic procedures for preparation of colloidal dispersions consisting of spherical CdS and α -Fe₂O₃ particles in the size range from a few nanometers up to a several hundreds of nanometers, as well as β -FeOOH nanorods (NRs) with three different aspect ratios. Also, we present synthetic methodology for incorporation of filler particles into polymer matrices. The prepared nanocomposites were characterized using structural and thermal techniques and influence of concentration, size and shape of fillers on the thermal properties of polymer matrices was discussed in details.

Experimental

Detailed information about preparation of colloidal dispersions consisting of spherical 5 nm CdS [13], 0.2-0.35 μ m CdS [7], 5-10 nm α -Fe₂O₃ [14], and 0.2-0.5 μ m α -Fe₂O₃ [3] particles can be found elsewhere. Dispersions consisting of β -FeOOH NRs with different aspect ratios (4, 80 and 130) were prepared by "forced hydrolysis", i.e., thermal hydrolysis of iron (III) chloride solution similar to the method described in literature [15]. Dispersions in organic solvents were obtained using phase transfer

from water after proper surface modification of above mentioned particles with amphiphilic molecules such as: sodium dodecyl sulfate, oleic acid, oleyamine, etc.

The polymer based nanocomposites were prepared by combining proper amount of organic dispersion with organic solution of PS (Edistir or Glaskar 143 E) or PMMA (Diakon CMG 314V). After evaporation of solvent, content of inorganic phase in PS or PMMA was determined by measuring atomic emission (ICP-AS Perkin-Elmer 6500 instrument) for Cd or Fe.

Microstructural characterization of synthesized particles was carried out on a transmission electron microscope (TEM) Philips EM-400 operated at 120 kV. Samples for microscopy analysis were deposited on C-coated Cu grids.

The differential scanning calorimetry (DSC) measurements of the pure PS and PMMA, as well as nanocomposites were performed on a Perkin-Elmer DSC-2 instrument in the temperature range from 50 to 130 °C, while the thermogravimetric analysis (Perkin-Elmer model TGS-2) was carried out under a nitrogen atmosphere in the temperature range from 30 to 550 °C.

Results and Discussion

The thermal stability of 5 nm CdS/PS and 5-10 nm α -Fe₂O₃/PS nanocomposites was compared with the thermal stability of the pure PS. The thermograms of the pure PS as well as CdS/PS and α -Fe₂O₃/PS nanocomposites with 4.8 and 3.6 mass% of inorganic phase, respectively, obtained under the atmosphere of nitrogen, are shown in Figure 1.

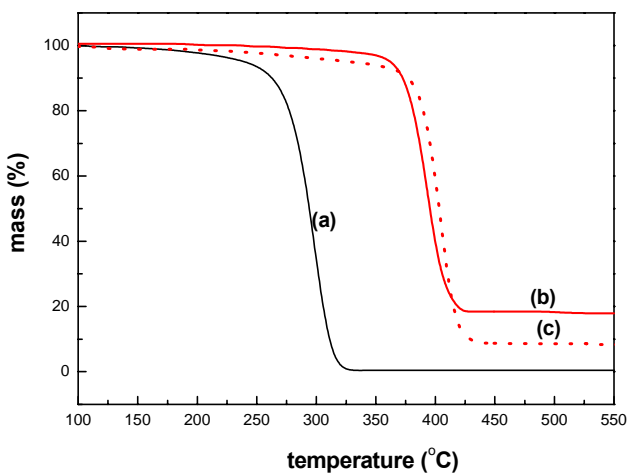


Fig. 1. The thermograms of the pure PS (a), as well as 5 nm CdS/PS (b) and 5-10 nm α -Fe₂O₃/PS (c) nanocomposites with 4.8 and 3.6 mass% of inorganic phase, respectively, obtained under the atmosphere of nitrogen.

The obtained results indicate that incorporation of nanoparticles (NPs) significantly alters the thermal properties of the PS matrix. The thermal decomposition of PS in the

presence of CdS and α -Fe₂O₃ NPs is shifted towards higher temperatures by about 100 °C. Incorporation of other nanofillers such as 5 nm Ni NPs [9], smaller than 10 nm Fe NPs [10], 10-12 nm HgS NPs [8], graphite [12] and clay [11] into the PS matrix induced significantly smaller improvement in its thermal stability. Based on comparison of the obtained results with the above-mentioned literature data we can conclude that the thermal stability of PS is significantly improved in the presence of CdS and α -Fe₂O₃ NPs.

In order to study influence of size of filler particles on the thermal stability of polymer matrix sub-micron spherical CdS (0.2-0.35 μ m) and α -Fe₂O₃ (0.2-0.5 μ m) particles were incorporated into PS. Thermograms of the pure PS and CdS/PS filled polymers with different contents of inorganic phase, obtained under the nitrogen atmosphere, are shown in Figure 2, while the 50% weight loss data concerning α -Fe₂O₃/PS composites are collected in Table 1. Improvement of the thermal stability of PS matrix can be noticed with the increase of the content of the inorganic phase, but this effect is less pronounced compared to improvement achieved using NPs.

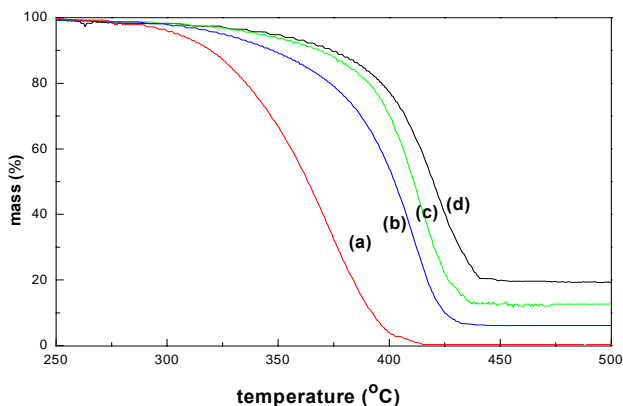


Fig. 2. The thermograms of the pure PS (a) and the 0.2-0.35 μ m CdS/PS composites with 6 (b), 12 (c) and 20(d) mass% of inorganic phase, obtained under the atmosphere of nitrogen.

For example, the thermal decomposition of the filled polymer with 17 mass% of 0.2-0.5 μ m α -Fe₂O₃ filler particles is shifted towards higher temperatures for about 70 °C, while 3.6 mass% of 5-10 nm α -Fe₂O₃ induced shift of about 100 °C.

Table 1. The 50 % weight loss temperature ($T_{50\%}$) of α -Fe₂O₃/PS composite

Content of inorganic phase (mass %)	0	5	10	17
$T_{50\%}$ (°C)	354.6	405.4	421.4	432.9

Although the origin of the enhanced stability as a result of adding CdS or α -Fe₂O₃ to PS is open to debate, we believe that the possible reason for it can be assigned to

reduced molecular mobility of the polymer chains. It is well-known that the changes in molecular weight during thermal degradation of PS are induced by scission of weak peroxide bonds formed by incorporation of oxygen during the polymerization, and due to intermolecular chain transfer reactions, which follow the initial step of the formation of primary free radicals [16]. The reduced molecular mobility induced by the presence of filler suppresses chain transfer reactions and consequently improves the polymer thermal stability. Of course, this effect is more pronounced with the decrease of the size of filler particles.

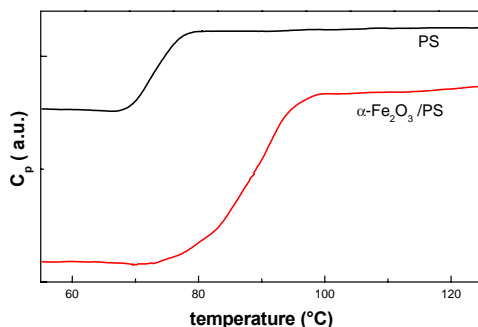


Fig. 3. The heat capacity curves of the pure PS and 5-10 nm α -Fe₂O₃/PS nanocomposite with 3.25 mass% of inorganic phase.

The heat capacity curves of the pure PS and α -Fe₂O₃/PS nanocomposite with 3.25 mass% of inorganic phase are shown in Figure 3. A shift in the slope of the heat capacity curves towards higher temperatures was observed after incorporation of α -Fe₂O₃ NPs into the PS matrix. This slope corresponds to the glass transition temperature of the polymer. It should be emphasized that the glass transition is not a true phase transition since the derivative of the heat capacity can be a continuous function of temperature. The different segmental motions lead to the glass transition spectrum. Therefore, the midpoint of the slope will be treated as the glass transition temperature, e.g., the glass transition temperature is taken to be at the maximum of the heat capacity derivative. Accordingly, a significant shift in the glass transition temperature of PS for 17 °C was observed after incorporation of α -Fe₂O₃ NPs. The observed effect can be explained as a consequence of decreased molecular mobility of the polymer chains due to adsorption of polymer segments onto the surface of nanofiller particles. It is obvious that the inter-particle distance of spherical fillers in composites with constant content of inorganic phase is proportional to the particle size. Consequently, there is much higher probability that the polymer segments will interact with nanofillers than with fillers in the sub-micron size range. For example, after incorporation of 0.2-0.5 μ m α -Fe₂O₃ particles in the PS matrix, the shift in the glass transition temperature was about 2.5 °C for the content of inorganic phase of 17 mass%.

In order to study influence of the shape of filler particles on the thermal properties of polymer matrix β -FeOOH NRs with three different aspect ratios were incorporated into the PMMA. Typical TEM images of the β -FeOOH NRs prepared on three differ-

ent ways are shown in Figure 4. The first dispersion (see Figure 4A) consists of 75-125 nm in length and 23-27 nm in diameter β -FeOOH NRs (aspect ratio of about 4). The second dispersion (see Figure 4B) consists of 250-350 nm in length and 3-5 nm in diameter β -FeOOH NRs (aspect ratio of about 80), while the third dispersion (see Figure 4C) consists of 550-1000 nm in length and 5-8 nm in diameter β -FeOOH NRs (aspect ratio of about 130). It is clear that it is more difficult to control length than the diameter of β -FeOOH NRs. Ability to control length of β -FeOOH NRs decreases with the increase of aspect ratio. Also, β -FeOOH NRs have tendency to array parallel to each other and to form bundle-like aggregates.

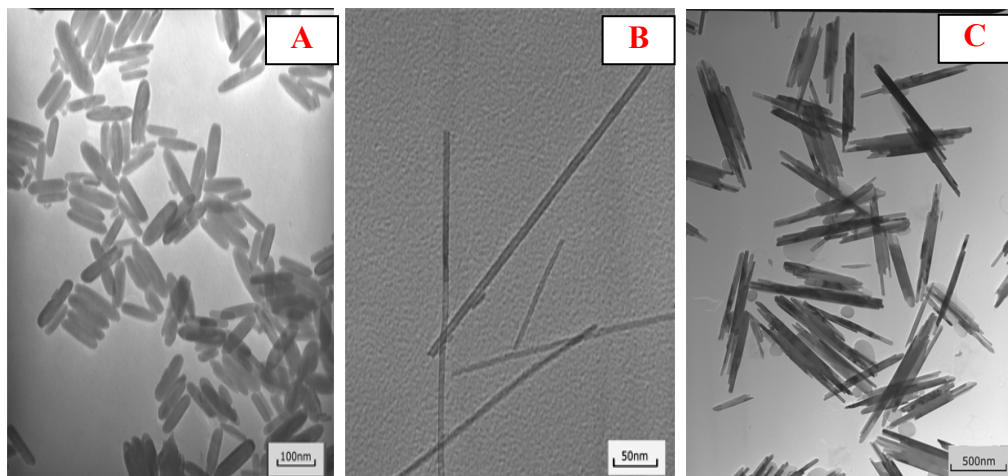


Fig. 4. Typical TEM images of β -FeOOH NRs with different aspect ratios: (A) 4, (B) 80 and (C) 130.

Data concerning the glass transition temperature of the pure PMMA and β -FeOOH/PMMA nanocomposites (aspect ratio 4, 80 and 130) with 1.5, 3.5 and 6.5 mass% of inorganic phase are collected in Table 2. Significant shift in the glass transition temperature of PMMA towards higher temperatures (20-30 °C) was observed after incorporation of β -FeOOH NRs. The increase of the glass transition temperature of more than 20 °C was observed when content of β -FeOOH NRs (all aspect ratios) was as low as 1.5 mass%.

Table 2. Glass transition temperature (°C) of β -FeOOH/PMMA nanocomposite

Content of inorganic phase (mass %)	Aspect ratio of β -FeOOH NRs		
	4	80	130
0	93.3	93.3	93.3
1.5	116.4	118.8	122.3
3.5	120.5	120.9	123.1
6.5	121.1	122.4	124.3

Further increase of the content of inorganic phase led to additional increase of the glass transition temperature. Also, for nanocomposites with the same content of inorganic phase increase of the glass transition temperature was observed with the increase of the aspect ratio of β -FeOOH NRs. Various nanofillers have sometimes completely opposite effects on the glass transition temperature of the PMMA. For example, the presence of 4 mass% of commercially available modified silica (AEROSIL[®] R805, R812 and R972) induced shift of the glass transition temperature for 18 °C towards higher temperature [17,18], while the presence of 6 mass% of poly(dimethylsiloxane) surfactant-modified clay increased the glass transition temperature of PMMA for 3 °C [19]. On the other hand, the presence of 0.5 mass% of 39 nm in diameter alumina particles decreased the glass transition temperature of PMMA for 25 °C [20]. Based on this, it seems that β -FeOOH NRs have pronounced effect on the glass transition temperature of the PMMA matrix. The observed effect can be again explained as a consequence of decreased molecular mobility of the PMMA chains due to adhesion of polymer segments onto the surface of β -FeOOH NRs.

Conclusion

Significant influence of filler particles (CdS, α -Fe₂O₃ and β -FeOOH) on the thermal stability and glass transition temperature of polymer matrices (PS and PMMA) was found. Basically, the thermal stability and glass transition temperature of polymer matrices is function of concentration, size and shape of filler particles. The increase of content of inorganic phase, the decrease of size of filler particles, i.e. increase of specific surface area and the increase of aspect ratio of rod-shaped filler particles induced improvement of thermal stability of polymer matrices and the increase of the glass transition temperature.

Acknowledgements

Authors are grateful to Dr Nataša Bibić, Maja Popović and Mirjana Novaković for performing TEM measurements. Financial support for this study was granted by the Ministry of Science and Environmental Protection of the Republic of Serbia (Project 142066).

References

- [1] D.Y. Godovsky, *Advan. Polym. Sci.*, 2000, **165**, 153.
- [2] W. Caseri, *Macromol. Rapid Commun.*, 2000, **21**, 705.
- [3] J. Kuljanin, M. Marinović-Cincović, S. Zec, M.I. Čomor, J.M. Nedeljković, *J. Mater. Sci. Lett.*, 2003, **22**, 235.
- [4] M. Marinović-Cincović, Z. Šaponjić, V. Djoković, S.K. Milonjić, J.M. Nedeljković, *Polym. Degrad. Stab.*, 2006, **91**, 313.
- [5] V. Djoković, J.M. Nedeljković, *Macromol. Rapid. Commun.*, 2000, **21**, 994.
- [6] D. Šajinović, Z.V. Šaponjić, N. Cvjetičanin, M. Marinović-Cincović, J.M. Nedeljković, *Chem. Phys. Lett.*, 2000, **329**, 168.
- [7] J. Kuljanin, M. Vučković, M.I. Čomor, N. Bibić, V. Djoković, J.M. Nedeljković. *Eur. Polym. J.*, 2002, **38**, 1659.

- [8] PS Nair, T Radhakrishnan, N Revaprasadu, CGCE van Sittert, V. Djoković, AS Luyt., *Mater. Lett.*, 2004, **58**, 361.
- [9] S. Wizel, S. Margel, A. Gedanken., *Polym. Int.*, 2000, **49**, 445.
- [10] R.V. Kumar, Yu Koltypin, O. Palchik, A. J. Gedanken., *Appl. Polym. Sci.*, 2002, **86**, 160.
- [11] MW Noh, DC Lee., *Polym. Bull.*, 1999, **42**, 619.
- [12] M. Xiao, L Sun, J Liu, Y Li, K Gong., *Polymer*, 2002, **43**, 2245.
- [13] J.M. Nedeljković, R.C. Patel, P. Kaufman, C. Joyce-Pruden, N. O' Leary, *J. Chem. Educ.*, 1993, **70**, 343.
- [14] M. Marinović-Cincović, S.K. Milonjić, G. Wang, M. Fedoroff, Z.V. Šaponjić, J.M. Nedeljković, *Mat. Sci. Forum* 2006, **518**, 63.
- [15] E. Matijević, P. J.Scheiner, *Colloid. Interface Sci.*, 1978, **63**, 509.
- [16] A.Marcilla, M. Beltrán, *Polym. Degrad. Stab.*, 1995, **50**, 117.
- [17] B. J. Ash, L. S. Schadler, R. W. Siegel, *Mater. Lett.*, 2002, **55**, 83.
- [18] Y-H Hu, C-Y Chen, C-C Wang , *Polym. Degrad. Stab.*, 2004, **84**, 545.
- [19] P. Jash, C. A.Wilkie, *Polym. Degrad. Stab.*, 2005, **88**, 401.
- [20] L. H. Lee, W. C. Chen, *Materials. Chem. Mater.*, 2001, **13**, 1137.

ADVANCED DENTAL RESTORATIVE COMPOSITES UTILIZING LOW POLYMERIZATION SHRINKAGE LIQUID CRYSTALLINE MONOMERS

S. T. Wellinghoff¹, D. P. Hanson¹, P. M. Thompson¹, S. M. Crumlett¹,
B. R. Furman², B. K. Norling² and H. R. Rawls²,

¹*Division of Chemistry and Chemical Engineering, Southwest Research Institute, 6220 Culebra Road, San Antonio, Texas, USA 78238,* ²*Restorative Dentistry, University of Texas Health Science Center, 7703 Floyd Curl, San Antonio, Texas, USA 78284*

Abstract

Mesogenic, platform molecules 1,4 [4'-hydroxybenzoyloxy] t-butyl (and methyl) phenylene, T(OH)₂ and M(OH)₂, respectively, are reacted in a low cost-single pot synthesis with a mixture of adipoyl (ACl₂) and sebacoyl chlorides (SCl₂) and terminated to bifunctional monomers with an excess of hydroxyethyl methacrylate. The thermotropic, nematic oligoester mixture (T_{N→N+1}=75 °C) which was designed to consist of more than 85 mole % species containing only one aromatic mesogen did not crystallize either as a neat liquid or in mixtures with inorganic fillers. The monomer mixtures were photo-polymerized to 80-90% conversion from the nematic state to tough, highly crosslinked, liquid crystalline glasses (E_{flex}^{25°C}= 1.8 GPa) with polymerization shrinkage of 2.73 V/V% at 23 °C, considerably less than the 4.4 V/V% expected for conversion of the double bonds to single bonds. Approximately 50% of the three point bend tests at 25 °C exhibited ductile, flexural shear yielding at 78 MPa which is unusual for such highly crosslinked systems. Especially low polymerization shrinkage and the high ductility of the polymer suggest the application of these monomers to advanced dental and other composites, optical adhesives, and resins for photolithographic processes such as stereolithography.

Introduction

The free radical polymerization shrinkage of certain sterically hindered nematic, diacrylate monomers is lower than that expected from reduction of Van der Waals volume and better polymer packing due to loss of molecular entropy [1]. Steric hindrance improves the packing density of nematic monomers but disrupts the packing of the crosslinked liquid crystalline polymers, thus compensating for some of the volumetric polymerization shrinkage that is expected from conversion of double to single bonds. In some cases multifunctional, nematic monomers can be polymerized to glasses containing finely distributed smectic domains that improve toughness by delocalizing failure and promoting shear yielding processes [2, 3]. Other advantages include the ability to orient liquid crystal monomers by electric or magnetic fields or with surface forces and then maintain orientation during polymerization to produce polymers with unique optical and electric properties [4,5]. Although these special characteristics of thermotropic liquid crystal monomers have been realized for some time, the high cost of monomer synthesis and the potential for premature monomer crystallization have limited their use in commercial applications.

Esthetics and the desired replacement of the mercury-based alloys presently in restorative use drives the market for tough, translucent, radio-opaque composites which match the rigidity of the surrounding dentin and tooth enamel. In addition, the non-toxic and non-mutagenic monomers must have low viscosity so that they can be mixed with a high volume percent of micron or even nano-sized inorganic fillers. High polymerization shrinkage and low toughness in commercial dimethacrylate resin-inorganic particulate composites leads to premature debonding of the restorative from the surface of the dentin or to cracking of the tooth or the composite.

Spiro ring terminated monomers that expand upon polymerization have been developed for free radical copolymerizations, but side reactions and mechanical property deterioration have limited the applicability of these systems [6]. We have thus concentrated on low-cost syntheses of photopolymerizable dimethacrylate monomer mixtures that do not crystallize on standing, especially in the presence of fillers.

Experimental

Synthesis

The details of the synthesis of the mixed monomer liquid crystal (MMLC) (Figure 1) appear in a recent patent application [7]. Quantitative characterization by HPLC and understanding of MMLC phase transitions were facilitated by synthesis and column purification of four $n=1$ standards, MS_2 , MA_2 , TS_2 , TA_2 where T and M represent $R_1-tC_4H_9$, CH_3 , respectively, and A and S represent $R_{2,2}-(CH_2)_4$ and $(CH_2)_8$, respectively. Fully aliphatic reaction products bis (oxyethyl methacrylate) adipate, A_2 , and the corresponding sebacate, S_2 , were also synthesized as standards as they can also appear as reaction products. Equal mole ratios of the mesogens, $T(OH)_2$ and $M(OH)_2$, were mixed with the methylene chloride solution of diacyl chlorides in a ratio, $ACl_2/(SCl_2 + ACl_2) = 0.4$, an excess of hydroxyethylmethacrylate, and tribenzylamine in the feed to produce the MMLC variant used in this study.

MMLC Component Characterization

HPLC was performed on a Waters Alliance HPLC System equipped with a 2487 Dual Wavelength UV detector. The column used was a Supelco Discovery C-18 operated with a mobile phase consisting of 20% 0.05M sodium phosphate, pH 2.75, 80% acetonitrile. 10 μ L of each sample were injected, eluted at a flow rate of 1.0 mL/min and detected by a UV at 254 nm. The monomer standards were employed in the quantitative determination of the column retention times and mole % of components within MMLC.

Proton NMR of MMLC and the component standards in deuterated chloroform solutions (Varian 400 MHz) was used in conjunction with HPLC to complete the MMLC component characterization.

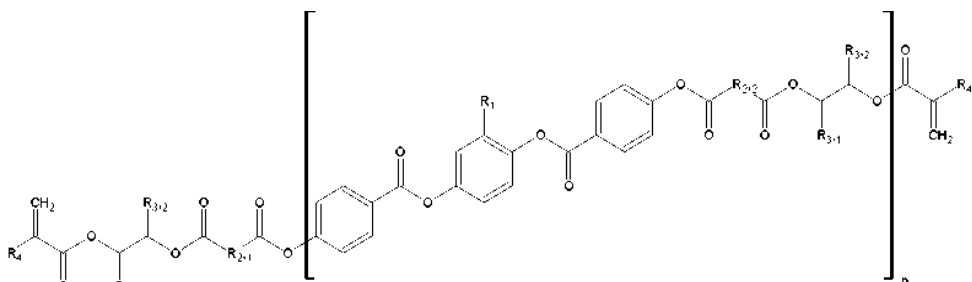


Figure 1. MMLC structure. R_4 -CH₃; $R_{3,2}$ $R_{3,1}$ -H; $R_{2,2}$ -(CH₂)₄ or (CH₂)₈; R_1 -tC₄H₉ or CH₃.

Phase Structure

Phase transitions were observed with a Nikon Optipot-POL microscope equipped with a heated stage and polarizers. Digital images were acquired by use of a Sony 3CCD color video camera, model #DXC-960MD. Samples were also analyzed on a TA Q1000 Differential Scanning Calorimeter to determine phase behavior.

Polymerization and Shrinkage Measurements

An initiator solution was prepared by co-dissolving 0.04 g methoxyphenol, 0.24 grams camphorquinone and 0.75 ml dimethyl aminomethacrylate and adding 12 microliter per 1 gram of monomer that was initially inhibited by 100 ppm t-butyl hydroquinone. Small beads of MMLC were photopolymerized by a Optilux dental curing lamp (Demetron Research Corporation) at 350 mW/cm² for 60 seconds on a Krytox coated, temperature controlled table in nitrogen atmosphere. The maximum temperature increase observed in each bead during photopolymerization was 20 °C, 10 °C due to heating by the photocuring lamp and the remaining originating from polymerization exotherm.

Density measurements were made on both MMLC (ρ_m) and MMLC polymerized at various temperatures (ρ_p) with a calibrated DC-1 (Techne) jacketed density gradient column held at 23 °C. The % volumetric polymerization shrinkage was determined using the following formula: $\Delta V/V$ (%) = $10^2(\rho_p - \rho_m)/\rho_p$.

Double Bond Conversion

Percent double bond conversion was measured on a Nicolet Magna-IR 560 spectrometer equipped with a Thunderdome, Attenuated Total Reflectance (ATR) cell by using the integral value of aromatic double bond stretch at 1605 cm⁻¹ as an internal thickness band and using it to calculate the decrease in the acrylate double bond stretch at 1640 cm⁻¹ as polymerization proceeded.

Mechanical Properties

A Rheometrics Fluids Spectrometer RFS2 with a cone and plate geometry was used in steady shear at rates from 0.1 to 2500 sec⁻¹ between 19 °C to 80 °C to determine the viscosity of the MMLC.

MMLC initiated as described above was photocured within square cross-section, thin-walled borosilicate glass tubing in a Proto-tech LED Curebox with a power flux of approximately 200 mW/cm² at an emission band of 460-470 nm. 2×2 mm square-section beams with a nominal length of 25 mm, removed from the encasing glass, were tested in three-point bending using a test span of 20 mm at a crosshead speed of 5 mm/minute.

Results and Discussion

Composition and Phase Morphology

The HPLC results for MMLC, after methanol extraction workup to remove most of the S₂, A₂, are shown in Table 1. Only six significant peaks were found. The MAS and TAS peaks were assigned by extrapolation.

The $n \geq 2$ species appeared in the HPLC as a large number of very small peaks because of the number of structural permutations permitted, thus precluding an accurate calculation of the mole % $n \geq 2$. Conveniently, proton NMR revealed a CH₂ resonance characteristic of an adipoyl group linking two mesogens in $n \geq 2$ and, together with the measured ratio of A/S in the product, enabled calculation of the percentage $n \geq 2$ in the mixture. Very little of the higher oligomers other than $n=2$ are present in the mixture since the mole ratio of hydroxyethylmethacrylate added was calculated to produce predominantly $n = 1$ species, and the diminished solubility of the oligomeric species in dichloromethane decreases their availability to the reaction.

The plot of the log η in the Newtonian region was not linear as a function of temperature and showed a transition to smaller activation energy as the temperature increased (Figure 2). This behavior is consistent with a transition from a one phase nematic state to a two phase nematic + isotropic morphology, which is typically observed for mixed monomer systems. The phase structure transitioned from a continuous nematic phase to a continuous isotropic phase as temperature was increased through the biphasic region until conversion to a one-phase isotropic state at 105 °C (Figure 2 insets).

Table 1. HPLC characterization of MMLC (RT = retention time)

	A ₂	S ₂	MA ₂	TA ₂	MAS	TAS	MS ₂	TS ₂	N _{≥2}
RT min	3.16	3.94	5.92	8.52	13.39	21.14	33.10	55.21	NMR
Mole %	1.2	0.8	8.4	6.5	22.8	17.9	17.3	12.3	12.8

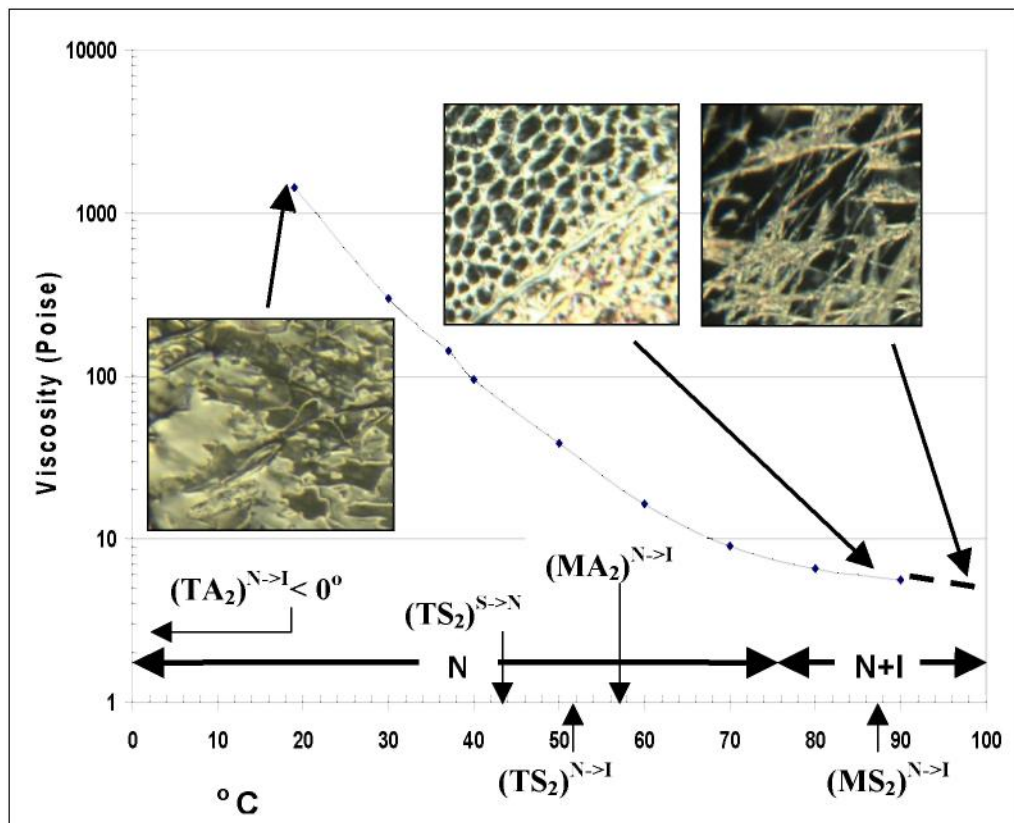


Figure 2. Viscosity (η) of MMLC at shear rate = 10/sec with inset optical micrographs of LC morphology (crossed polarizing filters) and mesomorphic transition temperatures of monomer components. $(TS_2)^{N \rightarrow I}$ is the nematic to isotropic transition temperature while $(TS_2)^{S \rightarrow N}$ is the smectic to nematic transition temperature.

Polymerization Shrinkage

The HPLC-NMR bifunctional component mole % and molecular weights and $\rho_m^{23^\circ C}$ can be used to calculate the number of double bonds/cc for MMLC assuming that all $n \geq 2 = 2$ with an average molecular weight of 1400. Assuming a volume decrease of 22.5 cc/mole [8] when double bonds are converted to single bonds, the calculated volumetric shrinkage is 5.47% using a calculated value of 1.23×10^{21} double bonds /cc.

FTIR measurement of the degree of double bond conversion using the change in the ratio of the alkene peak to the neighboring aromatic internal thickness band showed conversions of:

0.80 (± 0.04) at 21 °C and 0.87 (± 0.05) at 65 °C polymerization temperature.

Thus the calculated degree of shrinkage for 80% conversion is 4.37% as compared to the observed value of 2.73% for material polymerized at 23 °C for a differ-

ence of 1.64% (Table 2). For 87% conversion at 65 °C the expected value is 4.76% vs the extrapolated measured value of 3.65 % for a difference of 1.11%.

Table 2. Volumetric shrinkage calculated for polymerization at various polymerization temperatures, pT

pT	$\rho_p^{23^\circ\text{C}}$	$\Delta V/V(\%)$	
23	1.2232	2.73%	$\rho_m^{23^\circ\text{C}} = 1.1898 \text{ g/cc}$ (monomer density at 23 °C)
36	1.2200	3.14%	$\rho_p^{23^\circ\text{C}}$ = polymer density at 23 °C after polymerization at pT
54	1.2092	3.47%	
74	1.1972	3.83%	$\Delta V/V(\%) = 10^2(\rho_p^{23^\circ\text{C}} - \rho_m^{23^\circ\text{C}}) / \rho_p^{23^\circ\text{C}}$

In agreement with the literature describing other nematic monomers, the reduction in the polymerization shrinkage from that expected from the calculated value decreases as the polymerization temperature approaches the transition to the completely isotropic state. It should be noted that the MMLC polymerized to a liquid crystal morphology even at polymerization temperatures up to 74 °C.

Polymer Properties

The flexure strength, elastic modulus and fracture energy are all similar to that found in commercial, neat monomer systems. Interestingly, about half the samples did not fracture but underwent shear yielding. Considerable plastic deformation remained even after eight months of storage. In some cases, significant high-density crazing was observed prior to fracture. This behavior is somewhat unusual for a highly crosslinked glass and is probably related to the presence of LC-ordered microdomains in the test specimen. It may also be explained by bridging linear polymer chains originating from the dimeric species, which have sufficient chain length to bridge the more ordered microdomains and provide some measure of cohesion between the domains. Since the fracture energy was calculated only up to the point of brittle fracture, the ductile samples, not having fractured within the limits of testable deflection, are expected to have much larger fracture energy than that shown in Table 3 below. The investigation of the fracture process by the electron and optical microscopy of microtomed samples will reveal more of the mechanism of this interesting behavior.

Table 3. Mechanical properties (3 point bending) of polymerized MMLC at 25 °C using sample width = 2 mm, height = 2 mm and span = 20mm with no precrack.

	Flexural Strength (MPa)	Flexural Modulus (MPa)	FractureEnergy N-mm	% Conversion
Average	78	1800	42	90
Std. Dev.	18	68	13	5

Conclusions

The ester LC mix has a number of advantages which include: (1) facile high yield synthesis using low cost ingredients, (2) stability to crystallization, (3) a high $T_{n \rightarrow n+1} = 75$ °C which leads to a volumetric shrinkage of only 2.73% at 23 °C (a 35% improvement over the expected shrinkage) and 3.14% at body temperature, 36 °C (a 25% improvement), at better than 80% conversion, (4) flexure strength and elastic modulus comparable to existing, commercial dental resins, (6) ductile yielding for at least 50% of the test specimens, (7) a reasonably low viscosity of 100 P at 30 °C. The observation of a shear-yielding type of ductility in the polymerized blend is unusual for highly crosslinked systems.

In ongoing work, the polymer structure will be correlated with the deformation morphology and dynamic mechanical measurements in an attempt to understand the mechanism of shear yielding behavior and further optimize the system. Fracture toughness specimens will also be fabricated so that an accurate value of the fracture energy can be measured.

Some preliminary work indicates that the MMLC can be conveniently mixed with high volume fractions of barium glass fillers typical of dental restorative resins., Related formulations will be utilized in animal studies. MMLC has already been shown to have a lower cell toxicity than existing commercial monomer systems. The availability of low-shrinkage monomers that polymerize to tough matrices suitable for replacing current polymeric materials in dental restorative systems should solve the last remaining problems preventing such resins from being a universal replacement for amalgam in large posterior cavity preparations.

Acknowledgements

The authors would like to acknowledge the support of the US National Institutes of Health-National Institute of Dental and Craniofacial Research Program Project NIH-NIDCR PO1DE11688.

References

- [1] R.A.M Hikmet, B.H. Zwerver and D.J. Broer, *Polymer*, 1992, **31**(1), 89-95.
- [2] C. Ortiz, L.Belenky, C.K. Ober, and E.J. Kramer, *J. Mat. Sci.*, 2000, **35**, 2079-2086.
- [3] C. Ortiz, R. Kim, E. Rodighiero, C.K. Ober and E.J. Kramer, *Macromolecules*, 1998, **31**, 4074-4088.
- [4] F. Sahlen, M. Trollsas, A. Hult, and U.W. Gedde, *Chem. Mat*, 1996, **8**, 382-386.
- [5] J.W. Shultz and R.P. Chartoff, *Polymer*, 1998, **39**(2), 319-325.
- [6] E.L. Moon, J.Y. Lee, C.K. Kim and B.H. Cho, *J. Biomed. Mat. Res., Part B-Appl. Biomater*, 2005, **73B**(2), 338-346.
- [7] S.T. Wellinghoff and D.P. Hanson, WO 03/006570 A2.
- [8] R. Labella, K.W.M Davy, P. Lambrechts, B. Van Meerbeck and G. Vanherle, *Eur. J. Oral Sci.*, 1998, **106**, 816-824.

CLASSIFICATION OF FINELY DISPERSED SYSTEMS: PHYLOSOPHICAL BREAKPOINTS

A. M. Spasić

*Institute for Technology of Nuclear and Other Mineral Raw Materials
86 F. d'Esperey St. Belgrade, Serbia, Serbia*

Abstract

Over the last decade the biggest advances in physics, physical chemistry, and biochemistry have come from thinking smaller. This research presents a brief overview of the topic developing a new classification of finely dispersed systems based on entities. The considered scales are micro, nano and atto, using various theoretical approaches. Micro scales may cover more or less classical chemical engineering insight, while nano and atto scales focus on modern molecular and atomic engineering.

Classification Based On Scales

Macro and micro scale Classical chemical engineering has been intensively developed during a last century. Theoretical backgrounds of momentum, mass, energy balances and equilibrium states are commonly used as well as chemical thermodynamics and kinetics. Physical and mathematical formalisms are related to heat, mass, and momentum transfer phenomena as well as on homogeneous and heterogeneous catalysis. Entire object models, continuum models, and constrained continuum models are frequently used for the description of the events, and for equipment designing. Usual, principal, equipment are reactors, tanks and columns. Output is, generally, demonstrated as conventional products, precision products, chemistry (solutions), and biochemistry.

Nano scale Molecular engineering nowadays still suffers substantial development. Beside heat, mass, and momentum transfer phenomena, commonly used in classical chemical engineering, it is necessary to introduce electron transfer phenomenon. Description of the events is based on molecular mechanics, molecular orbits, and electro-dynamics. Principal tools and equipment are micro-reactors, membrane systems, micro analytical sensors, micro-electronic devices. Output is, generally, demonstrated as molecules, chemistry (solutions), and biochemistry.

Atto scale Atto-engineering already more than a whole century is in permanent and almost infinite development. Theoretical background is related to the surface physics and chemistry, quantum and wave mechanics, and quantum electrodynamics. Discreet models and constrained discreet models are convenient for description of related events. Tools and equipment are nano and atto dispersions and beams (demonstrations, ions, phonons, infons, photons, and electrons), ultra-thin films and membranes, fullerenes and bucky-tubules, Langmuir-Blodgett systems, molecular machines, nano-electronic devices, various beam generators. Output is, generally, demonstrated as finely dis-

persed particles in plasmas, fluosols-fogs, fluosols-smokes, foams, emulsions, suspensions, metals, vesicles, dispersoids.

Further Possible Classifications

Example given, related to the geometry: surface continuums, line continuums, and point discontinuums; Related to the forces of interaction: electrostatic, van der Waals, solvation, and steric; Related to the physical–chemical processes: diffusion, sorption, catalysis, membrane. Finally, here presented classification is based on *entities*, and may be considered as *the first philosophical breakpoint!*

Entities Since the events at the interfaces of finely dispersed systems have to be considered at the molecular, atomic, and/or entities level it is inevitable to introduce the electron transfer phenomenon beside the classical heat, mass, and momentum transfer phenomena commonly used in chemical engineering [1]. Therefore, an entity can be defined as the smallest indivisible element of matter that is related to the particular transfer phenomenon. Hence, the entity can be either differential element of mass/demon, or an ion, or a phonon as quantum of acoustic energy, or an infon as quantum of information, or a photon, or an electron [1].

A possible approach is proposed to the general formulation of the links between the basic characteristics, levels of approximation and levels of abstraction related to the existence of finely dispersed systems/**DS**. At first for the reason of simpler and easier physical and mathematical modeling, it is convenient to introduce the terms: homo-aggregate (phases in the same state of aggregation/**HOA**) and hetero-aggregate (phases in a more than one state of aggregation/**HEA**). Now the matrix presentation of all finely dispersed systems is given by

$$[(\mathbf{DS})^{ij} = (\mathbf{HOA})\delta^{ij} + (\mathbf{HEA})\tau^{ij}] \quad (1)$$

where i and j are integers (1, 2, 3) that refer to the particular finely dispersed system position, i.e. when $i = j$ than diagonal positions correspond to the homo-aggregate finely dispersed systems (plasmas, emulsions and dispersoids, respectively), and when $i \neq j$ than tangential positions correspond to the hetero-aggregate systems (fluosols/fogs, fluosols/smokes, foams, suspensions, metals, and vesicles, respectively). Furthermore, the interfaces may be deformable **D** and rigid **R**.

Now, related to the levels of abstraction and approximation it is possible to distinguish continuum models (the phases considered as a continuum i.e. without discontinuities inside entire phase, homogeneous, and isotropic) and discrete models (the phases considered according to the Born-Oppenheimer approximation: entities and nucleus/CTE motions are considered separately).

Hierarchy of entities Figure 1. a. shows a stereographic projection/mapping from Riemann sphere, i.e., Fig. 1. b. shows a “hierarchy” of entities, which have to be understood as a lim value of the ratio u_0/Z [withdrawn from magnetic Reynolds criteria ($Re_m = 4\pi l G u_0 / c^2$), where the conductivity G is expressed as a reciprocal of viscos-

ity/impedance Z ($G=1/Z$), l is the path length that an entity “override”, u_0 is the characteristic velocity, and c is the velocity of light].

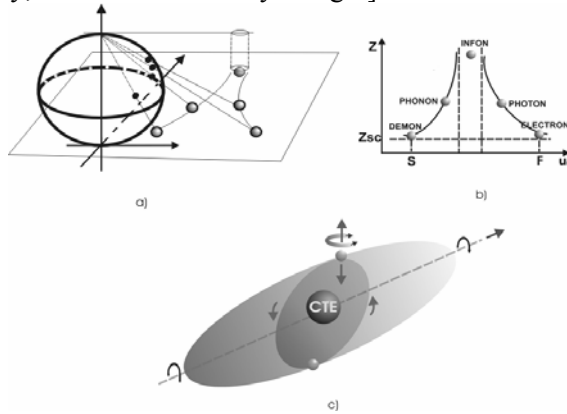


Fig. 1. a) & b) the first philosophical breakpoint, c) the second philosophical breakpoint.

In general S corresponds to the slow system/superfluid and F corresponds to the fast system/superconductor; now, it is possible to propose that all real dynamic systems are situated between these limits. Also, it seems sensible to think about the further structure of entities, *the second philosophical breakpoint* e.g., the basic entity can be understood as an energetic ellipsoid shown in Figure 1. c. (based on the model of electron following Maxwell-Dirac Isomorphism/MDI: electron is an entity at the same time quantum-mechanical/microscopic $N = -2$ and electrodynamics/macrosopic $N=3$). Now, spatio-temporal, five dimensional existence of an entity/e.g., electron may be presented by equation $[(x-a)^2 + (y-b)^2 + (z-d)^2 - (ct-e)^2 - ({}^kN_0\omega_N-f)^2 = 0]$, where kN_0 is the factor of spatio-temporal synergy (cm s), and ω_N is isotropic angle rotation (s^{-1}) [2].

Conclusion

This classification, including the first and the second philosophical breakpoints, permits further, deeper, studies of well characterized rigid and deformable interfaces in finely dispersed systems, and better understanding of e.g. spintronics and anyonics (fractional-quantum Hall effect-fluids, decoherence sensitivity, quantum computation, entities/quantum particles entanglement,).

References:

[1] A.M. Spasic, M. Mitrovic, D.N. Krstic in: Finely Dispersed Systems, 2005, **130**, A.M. Spasic, J.P. Hsu (Eds.), CRC Press, Taylor & Francis, Boca Raton-London-New York.
 [2] Dj. Koruga, Fullerenes and nanotubes review, 1997, **1**, 75-85.

THEORETICAL STUDY OF SOLIDIFIED SAMPLE INFLUENCED BY MELT SUPERHEAT

Z. S. Nikolic¹ and M. Yoshimura²

¹*Faculty of Electronic Engineering, Department of Microelectronics
University of Nis, 18000 Nis, PO Box 73, Serbia*

²*Materials and Structure Laboratory, Center for Materials Design
Tokyo Institute of Technology, Yokohama 226-8503, Japan*

Abstract

This paper presents the results of a theoretical study of solidification of sample on water-cooled substrate. Two-dimensional numerical method will be developed for simulation of heat transfer process during solidification and applied for thermal analysis of model problem, such as the influence of melt superheat on sample cooling rate.

Introduction

Heat transfer between a solidifying sample and a colder substrate is a very interesting phenomenon in many materials processes including rapid solidification. As the melt cools down and solidifies, the solidification front changes from an initial liquid-solid to a solid-solid contact, and the interfacial heat transfer rate changes too. Therefore, a good understanding of these sample-on-substrate-melting and solidifying phenomena is necessary to obtain a good control of the solidification process.

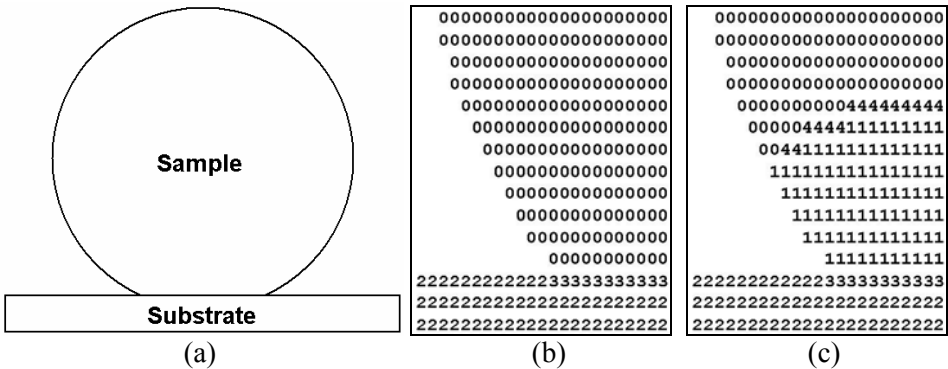


Fig. 1. Solidification model for molted sample (a) and the state matrix before (b) and during solidification (c).

We will define two-dimensional (2-D) heat transfer model of solid spherical sample on water-cooled solid substrate of a finite size (Fig. 1a). Since this radially symmetric heat-conduction problem will be solved numerically by assuming non-uniform temperature distribution inside the sample, and symmetric about the solidi-

fication axis. Thus the problem becomes 2-D. In that sense, 2-D space will be divided by square mesh, where each node (i,j) will be characterized by its temperature T_{ij} and states e_{ij} . The rules of transition liquid to solid phase, which determine the evolution of a given node during one time step, are defined according to the temperature and the states of the neighboring nodes. At the beginning of simulation each node in the sample has index "0" (the sample is initially liquid), the nodes which are located into substrate have indices "2", whereas the nodes near to the interface indices "3" (Fig. 1b). For the computation of time-dependent temperature $T_{ij}(t)$ in the sample and substrate, the governing heat conduction equations, assuming constant conductivity, are

$$\frac{\partial^2 T_\ell}{\partial x^2} + \frac{\partial^2 T_\ell}{\partial y^2} = \kappa_\ell \frac{\partial T_\ell}{\partial t} \quad (\kappa_\ell = \frac{\rho_\ell c_\ell}{\lambda_\ell})$$

where T is temperature, ρ is the density, c is the specific heat capacity, λ is the thermal conductivity, t is time, and the subscript $\ell = 1,2,3$ stands for the melt, solid and substrate, respectively. These equations will be solved by finite-difference technique [1] for specified initial and boundary conditions. At the beginning the sample will be assumed to be at uniform temperature T_0 , the substrate at uniform temperature $T_a = 308$ K, and the surrounding medium at temperature $T_a = 300$ K (air, ambient temperature). Both T_{sub} and T_a are well below the melting temperature of the sample (T_m). Since there is no heat source inside the sample, its surface temperature starts to decrease due to conduction, natural and forced convection and radiation. The boundary condition at the sample surface will be define by using the procedure described in details elsewhere [2]. Since the sample is much smaller than the water-cooled substrate, boundary condition for rectangular substrate will be the same at all boundary point except on the interface sample-substrate. Solidification begins on the sample surface across the contact interface with the substrate when the sample surface temperature reaches T_m . During this process interface starts to change from the initial liquid-solid contact to a solid-solid contact ($e_{ij} = 1$, Fig. 1c). After that the liquid-solid interface position ($e_{ij} = 4$, Fig. 1c), which follows the axisymmetric geometry, will be defined by a local equilibrium conditions [2].

Results and Discussion

Previous defined mathematical model we will apply for investigation how the melt superheat affects the interfacial heat transfer between solidified Ni sample of diameter 5 mm and Cu substrate and interface of diameter 2 mm. Materials properties for Ni ($T_m = 1726$ K) and Cu used in this calculation will be the same as in [3] and the interfacial heat transfer coefficient will be 10^4 W/m²K. Results for several initial melt temperatures ($T_m + 50$ K, $T_m + 150$ K and $T_m + 250$ K) are shown in Fig. 2. It is seen that all the bottom surface samples are cooled down to near T_m in less than 0.1 s. After that these surfaces continue to cool down with approximately the same rate. The superheat effects only the start (t_1) and the end (t_2) of solidification, i.e. the duration of solidification ($\Delta t = t_2 - t_1$). The top surface

samples are cooled down with the same rate after solidification, but reached T_m at different times due to the superheat (the convective heat transfer coefficient was $10^4 \text{ W/m}^2\text{K}$).

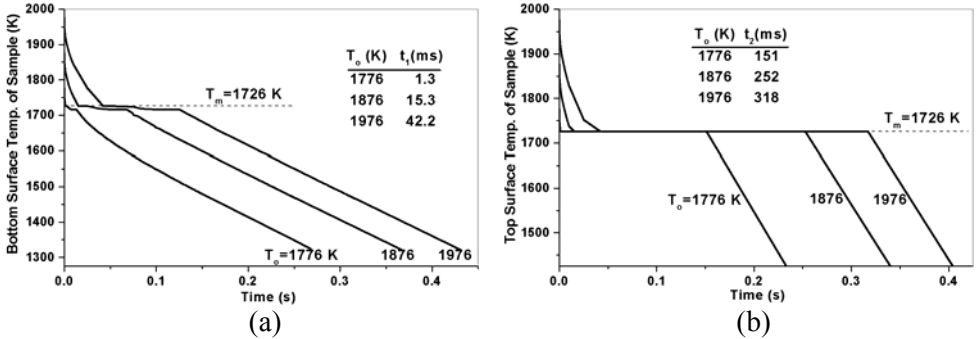


Fig. 2. Surface temperature at (a) the bottom and (b) the top of the sample as a function of time for several initial melt temperatures.

Conclusion

We have developed numerical method for simulation of heat transfer process during solidification of sample on water-cooled substrate, which takes into account phase change without undercooling. This method was applied for calculation of temperature history of solidifying sample. It was shown that start, end and duration of solidification has influenced by superheat, whereas the bottom and top surfaces of sample cooled down by almost same cooling rate. It should be noticed that using this method we are also able to obtain complete thermal analysis of stated model problem including investigation of the influence of substrate material on sample cooling rate.

Acknowledgements

The first author would like to thank the Japan Society for the Promotion of Science (Invitation Fellowship No. L-06544).

References

[1] J. Crank, *The Mathematics of Diffusion*, Oxford University Press, London, 1956.
 [2] Z.S. Nikolic, M. Yoshimura and S. Araki, *Mater. Sci. Forum*, 2005, **494**, 381-386.
 [3] G. -X. Wang and E. F. Matthys, *Int. J. Heat and Mass Transfer*, 2002, **45**, 4967-4981.

NUMERICAL PREDICTION OF HEAT TRANSFER BETWEEN SAMPLE AND SUBSTRATE DURING RAPID SOLIDIFICATION

Z. S. Nikolic¹ and M. Yoshimura²

¹*Faculty of Electronic Engineering, Department of Microelectronics
University of Nis, PO Box 73, Nis, Serbia*

²*Materials and Structure Laboratory, Center for Materials Design
Tokyo Institute of Technology, Yokohama 226-8503, Japan*

Abstract

The two-dimensional solidification model developed previously [1] will be modified for prediction of interface temperature history between solidified alumina sample and copper substrate during solidification with undercooling, for which the accurate prediction of the interface temperature during recolescence is very important.

Introduction

A common feature of many solidification processes is high cooling and solidification rates. For understanding and quantification of rapid solidification interfacial heat transfer phenomenon must be considered in details, because during solidification of molten sample on colder substrate very dynamic variations in the rate of interfacial heat transfer takes place.

In that sense, we will introduce two-dimensional (2-D) model problem: spherical sample on water-cooled solid substrate of a finite size (Fig. 1). If we assume

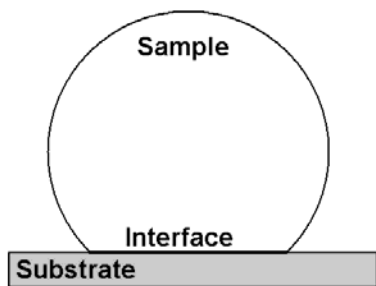


Fig. 1. Solidification model.

that the space of the model is divided by square mesh, then each node (x,y) will be characterized by its temperature $T(x,y)$ and the state liquid/solid/substrate. Solidification begins on the sample surface across the interface when the sample surface temperature reaches the interface undercooling

$$\Delta T = T_m - T(x,y),$$

where T_m is the equilibrium melting temperature. During recolescence (the effect of releasing the latent heat into the undercooled liquid)

the interface will reach a temperature below but close to T_m after that the interface liquid-solid will be treated as a zero thickness domain kept at T_m . During this process interface starts to change from the initial liquid-solid contact to a solid-solid contact. Due to solidification the evolution of nodes take place as it was described elsewhere [1].

The thermal contact between the sample and the substrate is quantified by an interfacial heat transfer coefficient h defined as

$$h = \frac{q(t)}{\langle T_{sam} \rangle - \langle T_{sub} \rangle},$$

where $q(t)$ is the heat flux through the interface from the sample to the substrate, and $\langle T_{sam} \rangle$ and $\langle T_{sub} \rangle$ are the average temperatures of the sample and substrate at the interface, respectively. If the coefficient h is known then the temperature at the interface can be computed by equations

$$-\lambda_\ell \left. \frac{\partial T_\ell(x,y)}{\partial y} \right|_{Interface} = h \cdot (\langle T_{sam} \rangle - \langle T_{sub} \rangle),$$

where the subscript $\ell = 1,2,3$ stands for the sample (liquid and/or solid) and substrate, respectively.

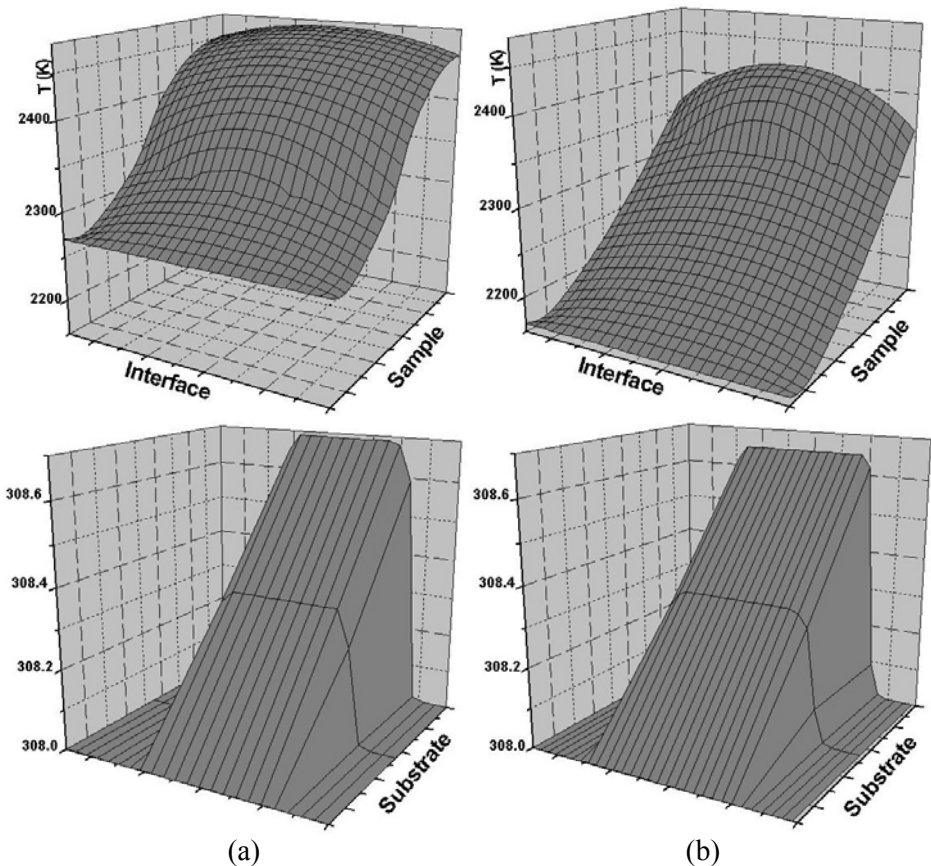


Fig. 2. Temperature profiles within the sample (from the sample interface up to its half height) and the substrate after (a) 5 s and (b) 8 s.

Results and Discussion

The previous equation we will incorporate in the solidification model [1] for prediction of interface temperature history between solidified alumina sample of diameter 4 mm and Cu substrate (the surface interface was 10^{-6} m²). For the interfacial heat transfer coefficient estimated value of $1.73 \cdot 10^3$ W/m²K [2] will be used (melt superheat was 175 K, the undercooling was 75 K, and simulated solidification started after 2.2 s and finished at 8.2 s). Materials properties for alumina and Cu used in calculation will be the same as in [2]. In paper [3] the same model system was analyzed from the point of time-dependent solid-liquid interface position and time-dependent solid and liquid fractions during its solidification.

As shown in Fig. 2, the temperature drop across the interface between the sample and the substrate is appreciable and decreases during solidification due to the heat transfer from the sample to the water-cooled substrate. Since the sample is much smaller than the substrate and the substrate will be permanently cooled by water during solidification (water cooling will take care of overall heating of the substrate over long periods of time), the temperature distribution changes much more in the sample than in the substrate. For the late stage of solidification temperature jump will be approached uniform value. It should be noticed that the jump is a function of the contact area (typically small) and the thermal contact resistance, but also of the interface surface roughness.

Conclusion

For the estimation of very dynamic variations in the rate of interfacial heat transfer during solidification of molten sample on colder substrate, 2-D solidification model developed previously [1] was modified for determination of interface temperature history between solidified alumina sample and copper substrate. The obtained temperature profiles shown the existence of the appreciable temperature drop across the interface, which is time dependent and decreases during solidification. This model can be used for investigation of the effect on heat transfer of the sample/substrate materials combination, the melt superheat, and the substrate surface roughness

Acknowledgements

The first author would like to thank the Japan Society for the Promotion of Science (Invitation Fellowship No. L-06544).

References:

- [1] Z.S. Nikolic and M. Yoshimura, Physical Chemistry, 2006.
- [2] Z.S. Nikolic, M. Yoshimura, S. Araki and T. Fujiwara, Science of Sintering, in Press.
- [3] Z.S. Nikolic, M. Yoshimura and S. Araki, Proc. Physical Chemistry 2004, Belgrade, 2004, 2, 568-570.

MODELING PORE GROWTH BY COALESCENCE FOR COMPUTER STUDY OF LIQUID PHASE SINTERING

Z. S. Nikolić

*Faculty of Electronic Engineering, Department of Microelectronics
University of Nis, PO Box 73, Nis, Serbia*

Abstract

Pore growth that two touching pores immediately coalesce to form a single pore will be modeled by complex, circular and ellipsoidal shape replacements. These models will be tested in order to conduct a study of diffusional effects on microstructural development during liquid phase sintering.

Introduction

In recent years, a range of computer models has been developed with the aim of simulating the detailed microstructural evolution during liquid phase sintering. Most of these studies ignored the effects of pores on grain growth and grain coarsening during liquid phase sintering by assuming zero porosity. However, Courtney [1] suggested pores could affect densification and structural development through migration and buoyancy. Unfortunately, understanding of pore behavior during liquid phase sintering is still limited.

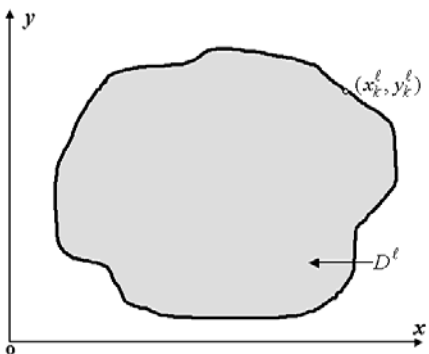


Fig. 1. 2-D domain definition.

Pore growth occurs by coalescence, where pores coalescence means that when two pores come into contact with each other, they immediately coalesce to form a single pore. Generally speaking coalescence phenomenon means that two or more domains (pores) join to form a new domain. Let two-dimensional (2-D) definition of l^{th} domain is closed boundary fully defined by n_l boundary points (Fig. 1), i.e.

$$D^l = \{ (x_k^l, y_k^l) \ (k = 1, 2, \dots, n_l) \} \quad (1)$$

If D^{p1} and D^{p2} are two pore domains of type (1) and if they touch each other they immediately coalesce to form a single pore domain D^p , which can be one of three possible shape types:

Type A - Complex pore shape domain defined by $D^p = D^{p1} \cup D^{p2}$.

Type B - Circular pore shape domain defined as

$$D^p = \{ (x_c^p, y_c^p), r^p \}, \ r^p = \sqrt{(D^{p1} \cup D^{p2})/\pi}$$

where (x_c^p, y_c^p) and r^p are the position of the center of new pore domain and its effective radius, respectively.

Type C - Ellipsoidal pore shape domain defined by $D^p \equiv \pi ab = D^{p1} \cup D^{p2}$, where a and b are the semimajor and the semiminor axes of new ellipsoidal pore domain, respectively. It should be noted that the mayor axis direction of new ellipsoidal pore domain will be determined by the line that connects two centers of touching pore domains D^{p1} and D^{p2} .

During pore coalescence domain overlapping will not be allowed. Thus, any of previously defined domain replacements will be possible if and only if the condition

$$D^p \cap D^\ell = \emptyset \quad (\ell = 1, 2, \dots; \ell \neq p)$$

is fulfilled.

Results and Discussion

For simulation of liquid phase sintering we will use previously defined simulation method [2] and an initial model shown in Fig. 2a (white colored regions are solid phase, black are pores, and gray is liquid phase). The pores will be treated as isolated and mobile, where the pore migration will be simulated by random walk [3]. New defined pore coalescence models will be tested in order to conduct a study of diffusional effects on microstructural development of W-Ni system. Physical properties used in calculation will be the same as in [3].

It is seen that due to solution-precipitation smaller solid-phase domains dissolve, diffuse through the liquid and precipitate on the larger ones. Therefore, larger ones grow at the expense of smaller ones. Densification results from the uniform center-to-center approach of neighboring domains and depends on the geometrical distribution of solid-phase and pore-phase domains. Before being filled pores can have great influence to create order or disorder in the domain structure around the pores. When the pore coalescence occurs, the solid-phase domain shape tends to accommodate itself. However the rearrangement only involves the repositioning of domains, leading to limited densification. From the point of densification it seems that type A (complex structure) gives a way to restricted packing density (Fig. 2b), whereas types B and C (Figs. 2c and 2d) are give possibilities to better packing through random walk.

Conclusion

Pore growth by coalescence can be treated as the nearly instantaneous formation of one large pore upon contact of two smaller pores. In that sense, three different types of pore replacement: complex, circular and ellipsoidal were defined and applied for study of diffusional effects on microstructural development of W-Ni system. It was shown that the complex shape replacement generates some restriction for good densification, whereas latter two types give the way to better packing density.

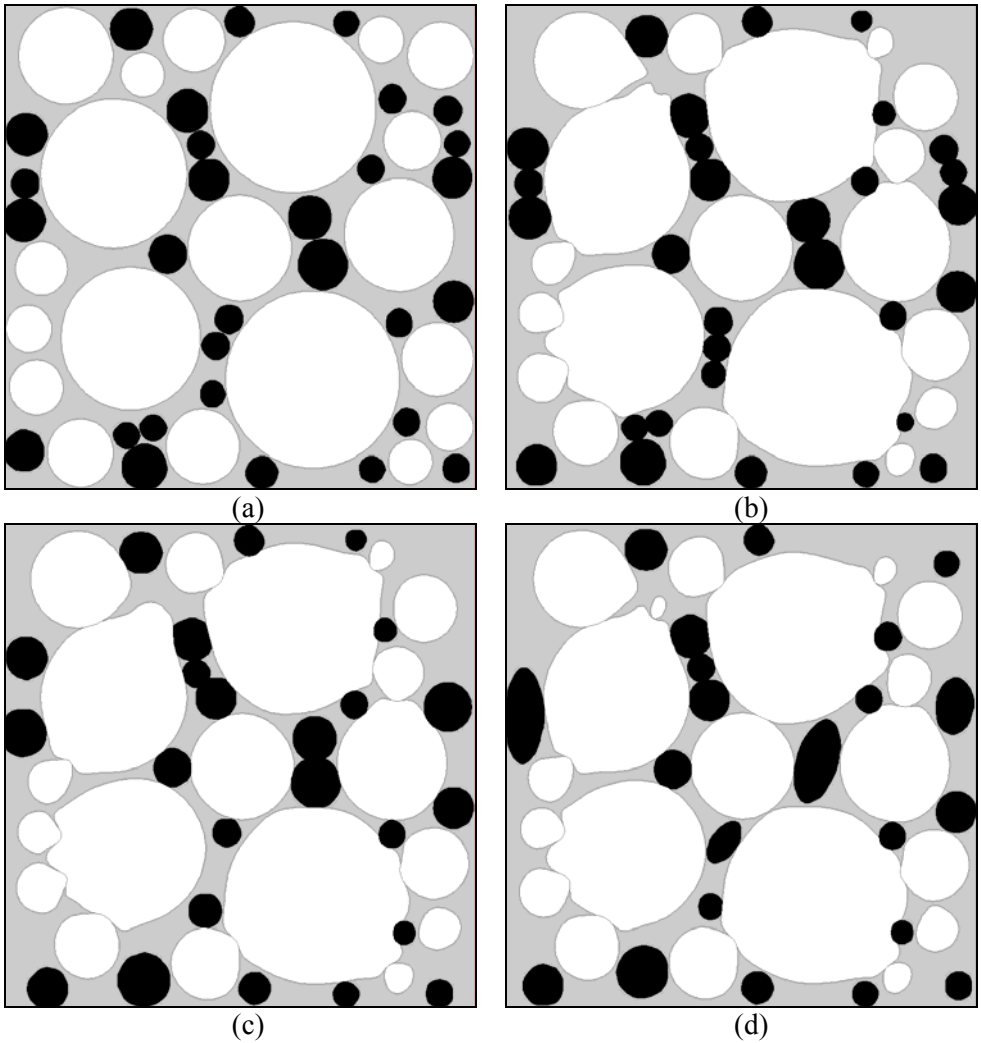


Fig.e 2. Computed microstructures. (a) Initial and after 20 min using pore coalescence model of type (b) A, (c) B, and (d) C.

Acknowledgements

The present work was performed under the project (No. 142011) supported financially by the Ministry of Science and Environmental Protection of the Republic of Serbia. The author would also like to thank the Japan Society for the Promotion of Science (Invitation Fellowship No. L-06544).

References:

- [1] T. H. Courtney, *Met. Trans. A*, 1984, **15A**, 1065-1074.
- [2] Z.S. Nikolic, *J. Mater. Sci.*, 1999, **34**, 783-794.
- [3] Z.S. Nikolic, *Science of Sintering*, 2006, **38**, 41-54.

PREPARATION OF COMPOSITE MATERIAL BCP/DLPLG WITH A DIFFERENT CONTENT OF CERAMIC AND POLYMER COMPONENT

M. Stevanović¹, N. Ignjatović¹, D. Miličević² and D. Uskoković¹

¹*Institute of Technical Sciences of the Serbian Academy of Sciences and Arts, Belgrade; Serbia*

²*The Vinča Institute of Nuclear Sciences, Laboratory for Radiochemistry and Physics, Serbia*

Abstract

Using a new approach of synthesis, homogenisation of DLPLG polymer powder and BCP gel, BCP/DLPLG composite material has been obtained with morphological and structural characteristics making it potentially very suitable for practical application in certain fields of the reconstructive medicine. The composite material has been synthesised with different ratios of ceramics and polymer BCP/DLPLG; 65/35w/w, 10/90 w/w, 5/95 w/w and 2/98w/w. The samples were characterized by Differential Scanning Calorimetry (DSC) and Scanning Electron Microscopy (SEM).

Introduction

Until now, various approaches were followed for obtaining composite material on ceramic basis and copolymer poly(DL-lactide-co-glycolide). Synthesis were performed either with solid component hydroxyapatite (HAp) being added into DLPLG solution of some solvent (dioxan, chloroform), or HAp powder was mixed with DLPLG powder [1], or DLPLG solution was infiltrated into melted apatite [2,3]. Until now synthesis where DLPLG powder was homogenized with BCP gel was not performed. This is why one of the aims of this investigation is obtaining the composite material with certain application characteristics using new BCP/DLPLG synthesis approach out of which successful implementation will greatly depend [4].

Experimental

Biphasic calcium phosphate was synthesised with precipitancy technique from calcium nitrate $\text{Ca}(\text{NO}_3)_2 \times 4\text{H}_2\text{O}$ and ammonium phosphate $(\text{NH}_4)_3\text{PO}_4$ in the alkali environment, which was then homogenized with polymer DLPLG powder in the appropriate ratio. Copolymer powder DLPLG was obtained with chemical method from the commercial granules, using chemical method with solvent/non-solvent systems, where the obtained solutions were afterwards centrifuged. DSC measurements were executed on Perkin-Elmer DSC-2 differential scanning calorimeter equipped with data processing system. The range of the temperature in which the measurements were performed was between 320K and 540K. The morphology of obtained particles of BCP/DLPLG were examined by scanning electron microscope (SEM) JEOL-JSM-646OLV with electron energy from 10 to 50 KeV.

Results and Discussion

On DSC diagrams of BCP/DLPLG we can see the peak of the glass transition because DLPLG copolymer is amorphous and BCP is thermally stable in the specified temperature range. With the increase of the copolymer participation in the composite, it is noticeable that peak of the glass transition is shifted toward lower temperatures, which is explained with the change of flexibility of the polymer chain [2]. The peak of the glass transition of the composite BCP/DLPLG 65/35w/w is on temperature 327.9K, BCP/DLPLG 10/90w/w is on 325.0K, BCP/DLPLG 5/95w/w is on temperature 323.6K while the peak for BCP/DLPLG 2/98w/w is on temperature 323.9K (fig. 1).

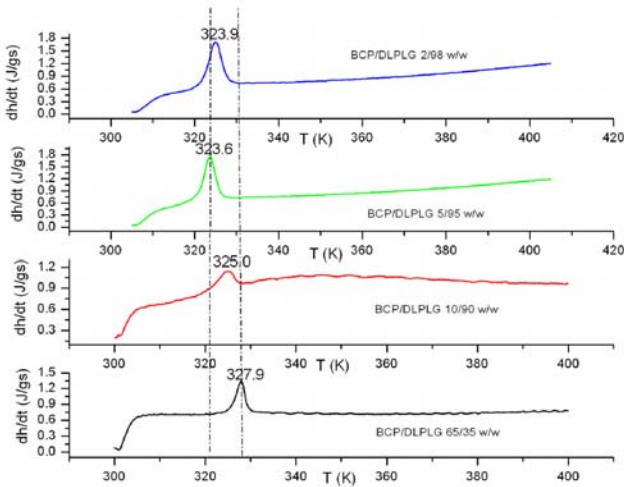


Fig. 1. DSC graph of BCP/DLPLG composite

From SEM pictures of BCP/DLPLG composite (Fig. 2) with the different ratios of ceramics and polymer, in cases with higher participation of polymer, it can be noted that particles are less agglomerated, more homogenised, spherical and with more regular shapes. It is obvious that non-homogenised distribution of BCP and DLPLG particles in the composite is more present with lesser participation of DLPLG.

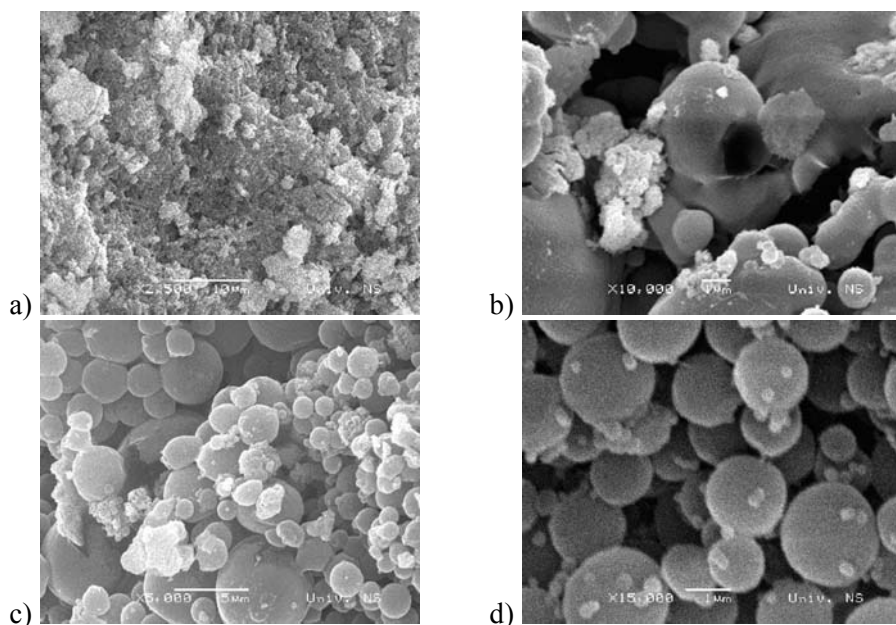


Fig. 2. SEM pictures of the composite a) BCP/DLPLG 65/35 w/w b) BCP/DLPLG 10/90 w/w c) BCP/DLPLG 5/95 w/w d) BCP/DLPLG 2/98 w/w

Conclusion

Homogenising of DLPLG polymer powder and BCP gel it is possible to obtain BCP/DLPLG composite material with morphological and structural characteristics which makes it potentially very suitable for use in certain fields of the reconstructive medicine. The composite material with the higher content of the polymer is less agglomerated; the particles are with more regular shapes and also better mutual distribution of the phases is achieved.

Acknowledgements

Authors would like to thank Miloš Bokorov for his help in SEM analysis. The Ministry of Science and Environmental Protection of Republic of Serbia supports this work through the project No. 142006.

References

- [1] K. G. Marra, L. E. Weiss, J. W. Calvert, P. N. Kumta; United States Patent 6,165,486
- [2] T. Watanabe, S. Ban, T. Ito, S. Tsuruta, T. Kawai, H. Nakamura, *Bioceramics*, 1999, **15**, 24-30.
- [3] C. C. Martinez-Sancho, R. Herrero-Vanrell, S. Negro, *Journal of Controlled Release*, 2004, **99**, 41-52.
- [4] M. Radić, N. Ignjatović, Z. Nedić, M. Mitrić, D. Miličević, D. Uskoković, *Materials Science Forum*, 2005, **494**, 537-542.

THE STUDY OF NANODISPERSED COMPOSITE MgH₂-Ti: EXPERIMENT AND THEORY

T. Brdarić¹, J. Grbović-Novaković¹, N. Novaković² and S. Mentus³

¹Laboratory of Material Sciences, Institute for Nuclear Sciences Vinča, Belgrade, Serbia

²Laboratory of Nuclear Physics, Institute for Nuclear Sciences Vinča, Belgrade, Serbia

³Faculty of Physical Chemistry, Belgrade, Serbia

Abstract

In order to obtain faster hydrogen sorption kinetics, MgH₂-Ti nanocomposites were prepared by high-energy ball milling, under Ar using 10:1 ball to powder ratio and 10% of catalyst. Microstructural and morphological characterization, performed by XRD and optical microscopy analysis, show a correlation with thermal stability and hydrogen desorption properties investigated by DTA. In order to obtain deeper insight into bonding mechanisms of Ti in MgH₂ fully relaxed structure, we have performed ab initio electronic structure calculations of MgH₂ + Ti system, using Full Potential Linearized Augmented Plane Wave method, as implemented in WIEN2K code.

Introduction

Among the metal hydrides, MgH₂ is considered as potential hydrogen storage material for vehicular application because of its high capacity and low cost. However, the slow reaction kinetics of the Mg-H system at low temperatures limits the practical application of MgH₂. Experiments show, however, that hydrogen binds too strongly in the Mg, having a binding energy of 0.39 eV/atom, and the hydride must therefore be heated to more than 247°C to release the hydrogen [1]. The dissociation of hydrogen molecules at the surface of Mg and the diffusion of hydrogen through the hydride are also so slow that loading and unloading of hydrogen takes excessively long time. Alloying or mixing magnesium with catalytic transition elements (TM), such as Ni, Co, Fe, and with intermetallic compounds [2,3] could significantly improve the hydriding and dehydriding kinetics of MgH₂. The task remains, however, to find Mg-TM alloy that remains stable during hydrogenation and dehydrogenation.

In the present work we have study the influence of 3d-transitional metal Ti on hydrogen desorption in the Mg-H system both from theoretical and experimental point of view.

Experimental Part

Magnesium hydride and Ti powders were used as starting material. Ball milling was performed in a Turbula Type T2C Mixer 20 hour under Ar atmosphere.

The microstructure of the powders was characterized by X-ray diffraction (XRD) with a Siemens KRISTALOFLEKX D-500, equipped with $\text{Cu-K}\alpha$ Ni filtrated radiation. Hydrogen desorption was investigated by DTA using a SDT 2090 (TA Instruments) under 99.999% pure Ar flow. Heating runs at a fixed heating rate of 15 K/min were carried out.

Preliminary MgH_2 electronic structure calculation was performed using XRD refined cell parameters. For MgH_2 -Ti compound atomic positions relaxation was performed without cell parameters optimization. The reason for that is the specific choice of supercell, without significant Ti states overlapping. Therefore, the reasonable assumption was that structure relaxation due to imposing of Ti atoms in the structure has negligible effect on overall cell size and c/a ratio.

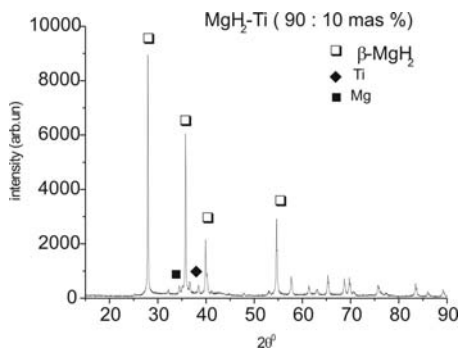


Fig. 1. XRD spectra for MgH_2 -Ti composites

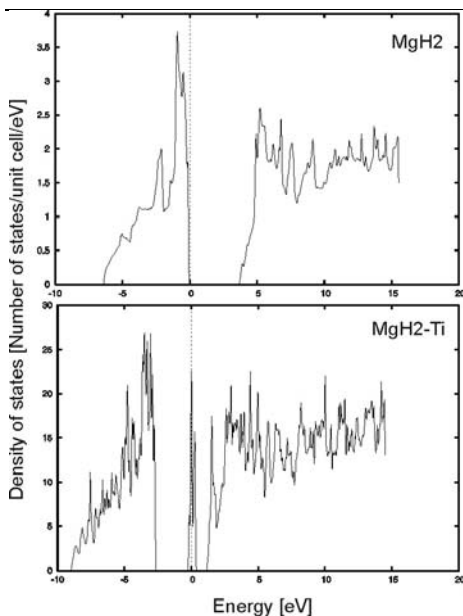


Fig. 2. a) Densities of states (DOS) of MgH_2 and b) MgH_2 -Ti compound

Results

In the Fig. 1 XRD spectra for MgH_2 -Ti composites are presented. The main effect is the diffraction peak broadening, related to the microstructural refinement imparted by ball milling. One can also see that in these experimental conditions there is no formation of binary alloys or intermetallic compounds between Mg and Ti. It is worth to notice that diffraction patterns of MgO are usually present after milling, which is not the case for this sample. The density of states (DOS) and the charge distribution were performed to address the intrinsic mechanism of the effect of titanium on the dehydrogenating properties of magnesium hydride. The total DOS-es of MgH_2 and MgH_2 -Ti systems were plotted in Fig. 2.

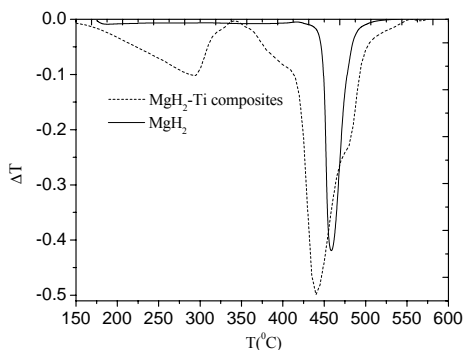


Fig.3 DTA traces of MgH_2 -Ti composite and pure MgH_2

favor of overall reduction of structure stability compared to that of pure MgH_2 . That is confirmed by low temperature DTA peak at 290°C . in Fig. 3.

Conclusion

The influence of Ti on the stability of MgH_2 was investigated by means of the electronic structure and the total energy calculation by using the FLAPW method and DTA analysis. DOS analysis has shown that the bonding between magnesium and hydrogen was weakened, although the interaction between titanium and hydrogen is stronger which is confirmed by preliminary DTA analysis

Acknowledgment

This work is supported by MSEP of Serbia under projects 142027, 141009 and 142047

Reference

- [1] A. Krozer, P. Hjort and B. Kasemo, *J. Alloys. Comp.*, 1996, **34**, 11.
- [2] A. Bassetti, E. Bonetti, L. Pasquini, A. Montone, J. Grbović, M. Vittori Antisari, *Eur. Phys. J. B*, 2005, **43**, 19-37.
- [3] Liang G, Huot J, Boily S, Van Neste A, Schulz R. *J Alloys Comp.*, 1999, **292**, 247-252.

TIMS AND MALDI TOF OF ENDOHEDRAL $^{99m}\text{Tc}@C_{60}$ METALLOFULLERENE

J. Đustebeč, J. Cvetičanin, V. Đorđević, S. Veličković,
M. Veljković and O. Nešković

*Vinča Institute of Nuclear Sciences, P.O. Box 522, 11000 Belgrade, Serbia
jasmina@vin.bg.ac.yu*

Abstract

Mass spectral studies (both TIMS – thermal ionization and MALDI TOF – matrix-assisted laser desorption time-of-flight mass spectrometry) of the endohedral metallofullerenes, $^{99m}\text{Tc}@C_{60}$ and $^{99m}\text{Tc}@C_{70}$, provided detailed structural and reactivity information about these unusual species. MS experiment revealed that both fullerenes and endohedral metallofullerenes fragment by multiple C2 loss. However, a difference in the terminal fragmentation products was observed for metallofullerene relative to C_{60} , suggesting that the encapsulation metal strongly impacts the fragmentation product. Singly charged cations of the metallofullerenes ($M@C_n^+$) were completely unreactive in the gas phase with oxygenated compounds such as ethylene oxide: however, the corresponding neutral species appear to react readily with oxygenated species. Collisional dissociation of the ionized endohedral fullerenes listed above revealed multiple C2 loss (either as sequential C2 loss or larger C_{2n} eliminations) to generate similar terminal fragmentation products, which might be predicted due to the similar ionic radii of the encapsulated metals. The observed ionization energies of endohedral molecules were, 5.1 ± 0.1 eV and 5.3 ± 0.1 eV, respectively.

Introduction

During the last few years, considerable progress has been made in the exploration of metallofullerene chemistry especially that endohedral [1-3]. As is well known, fullerenes have a unique type of inner empty space with their unusual cage-like structures. A wide variety of metal atoms may reside in this space and form endohedral metallofullerenes. These new series of materials with novel physical and chemical properties are very important for their potential application as new types of superconductors, organic ferromagnets, nonlinear optical materials, functional molecular devices, magnetic resonance imaging agents, biological tracing agents, etc., which will have great influence over electronics, optics, electromagnetics and medicine. Up to now, many metals including Group 3 metals (Sc, Y, La), Group 2 metals (Ca, Sr, Ba), alkali metals (Li, Na, K, Cs) and some tetravalent metals (U, Zr, Hf) have been successfully encapsulated into a fullerene cage to form mono-, di-, and trimetallofullerenes. Especially, the important progress has been marked by the successful isolation and purification of many metallofullerenes, which has led to further investigation of their molecular structures, physical and chemical properties as well as electronic states by a variety of experiment means, particularly that of spectroscopy. Subsequently, an active search for new of the selective synthesis of individual metallofullerenes was performed *in situ* in a mass spectrometer with the aim of exercising mass spectrometric

monitoring of gas phase reaction products. In favourable cases, small amounts of TIMS reaction products could be collected directly from the mass spectrometer on a cold plate for additional MALDI TOF characterization, even before macroscopic amounts were available.

Results

Tc@C₆₀, and TcC₇₀: Tc carbonyl was the first Tc reagent used successfully for the *in situ* thermal ionization incorporation ^{99m}Tc into C₆₀ and C₇₀ in a mass spectrometer. A series of experiments performed at 400-800 °C with various C₆₀ or C₇₀/Tc carbonyl ratios showed that endohedral fullerenes were the main products (Figures 1 and 2) without impurities. Observed ionization energies for Tc@C₆₀ and Tc@C₇₀ were 5.1 eV and 5.3 eV respectively. The following crucial information about behaviour of these species were: (a) they are thermally stable, since vacuum resublimation did not result in a change in composition of the mixture. Subsequent MALDI TOF mass spectral analysis of the powdered material collected from the cold parts of the ion source after completion of the reaction precisely reproduced the results obtained during the *in situ* experiments. Singly charged cations of the metallofullerenes (M@C_n⁺) were completely unreactive in the gas phase with oxygenated compounds such as ethylene oxide: however, the corresponding neutral species appear to react readily with oxygenated species. Collisional dissociation of the ionized endohedral fullerenes listed above revealed multiple C2 loss (either as sequential C2 loss or larger C2n eliminations) to generate similar terminal fragmentation products, which might be predicted due to the similar ionic radii of the encapsulated metals. Electron impact fragmentation of Tc@C₆₀ is showed in Figure 3.

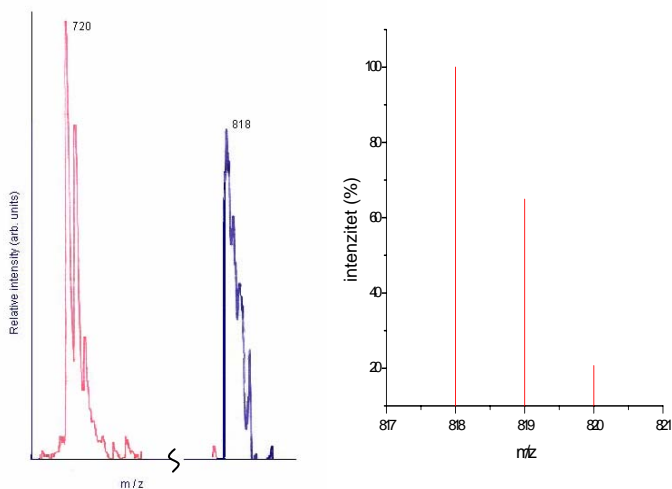


Fig. 1.

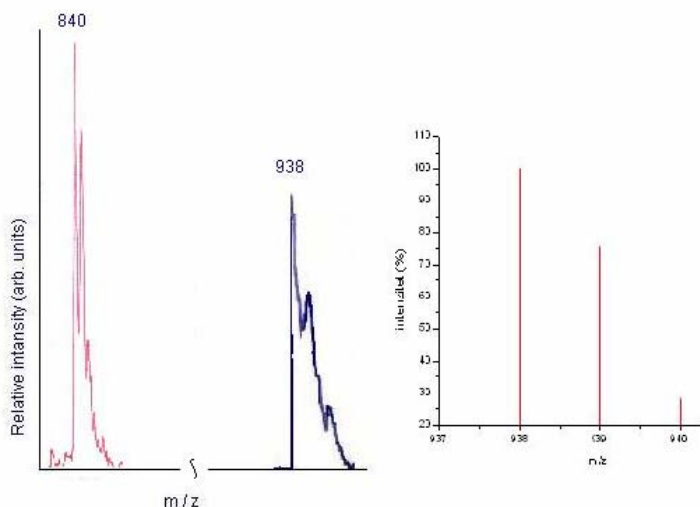


Fig. 2.

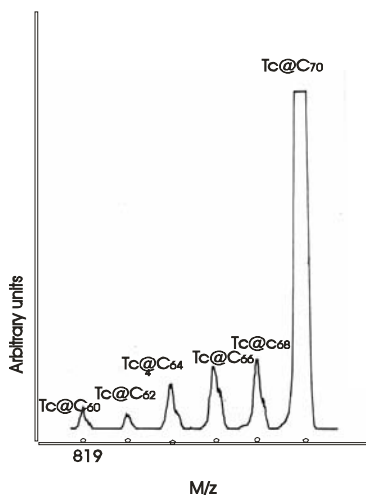


Fig. 3.

Fig. 1 and 2. Mass spectrum for an endohedral ^{99m}Tc C_{60} and C_{70} . experimental and theoretical spectrum.. In addition, one observes the isotopic composition of C_{60} and C_{70} .

Fig. 3. Electron impact fragmentation mass spectrum of $^{99m}\text{Tc}@C_{70}$.

Acknowledgments

This work was financially supported by the Ministry of Science and Environmental Protection, Republic of Serbia, under Project No. 142001..

References:

- [1] D.S. Bethune, R.D. Johnson, J.R. Salem, M.S. de Vries, S.C. Yannoni, *Nature*, 1993, **366**, 123-128.
- [2] S. Nagase, K. Kobayashi, T. Akasaka, *Bull. Shem. Soc. Jpn.*, 1996, **69**, 2131-2142.
- [3] S. Nagase, K. Kobayashi, T. Akasaka, *J. Mol. Struc. Theochem.*, 1997, **398-399**, 221-227.

AN SIMPLE TECHNIQUE FOR SYNTHESIS OF CARBON NANOTUBES BY UNDERWATER ARC PLASMA

N. Ćasić¹, M. Stoiljković², M. M. Kuzmanović¹,
M. Novaković³ and M. Popović³

¹ Faculty of Physical Chemistry, University of Belgrade, P.O. Box 137, Belgrade, Serbia

² Department of Physical Chemistry, The Vinča Institute, P.O. Box 522, Belgrade, Serbia

³ Department of Atomic Physics The Vinča Institute, P.O. Box 522, Belgrade, Serbia.

Abstract

Applicable, low cost technique for the production of carbon nanotubes by underwater (or solution) AC arc plasma discharge is described. The growth takes place in an AC arc in water solution between graphite electrodes.

Introduction

Since their discovery by S. Iijima[1], carbon nanotubes have attracted considerable attention because of their intriguing and remarkable physical properties. They can be thought of as a sheet of graphite (a hexagonal lattice of carbon) rolled into a cylinder. There are three conventional methods of synthesizing carbon nanotubes: a) arc discharge in an inert gas, b) laser vaporization and c) chemical vapor deposition (CVD). All three methods require sealed, water cooled vacuum chambers together with complex and time consuming gas handling equipment. From the stand-point of applications, the importance is still on high quality, high purity and low cost nanotubes growth by using a simple method.

The arc-discharge method has been easily adapted for operation in aqueous environment that avoid vacuum systems, inert atmosphere and very high temperature. Such an experimental set-up was used in this study to produce carbon nanotubes.

Experimental

Two graphite electrodes (spectrographic grade and 6 mm in diameter) were immersed into the glass vessel containing 2.4 dm³ of double distilled water or 5 % NaCl solution, Figure 1. Arc plasma was ignited and maintained at 30 V and AC current strength of 60 A, for a period of about 12 min. During the synthesis time, solution was continuously stirred. Solutions were cooled and kept to slag the carbon soot. The slag (the yields were 85 mg min⁻¹ and 77.6 mg min⁻¹ for pure water and NaCl solution, respectively) was sucked, washed and purified [2]. The purification was done by refluxing the slag with concentrated sulphuric and nitric acids (3:2) mixture, for 2 hours at 150 °C. After the slag has been washed with bidistilled water it was centrifuged for 20 minutes. The sample was prepared by suspending the soot in ethyl alcohol. The soot was investigated by TEM microscopy (Philips EM-400, 120 kV).

Results and Discussion

After the discharge finished, two types of products are observed in the vessel: in the case of pure water, floating material on the surface and hard carbon soot species

dispersed, but in the case of NaCl solution much less floating material was present. Also, arc burns more stable in solution of NaCl, in comparison to the pure water. Dimension of obtained soot species looks more uniform and without grains of graphite. The superior cooling ability of NaCl solution is useful for synthesizing carbon nanotubes and electrical conductivity supports arc discharge.

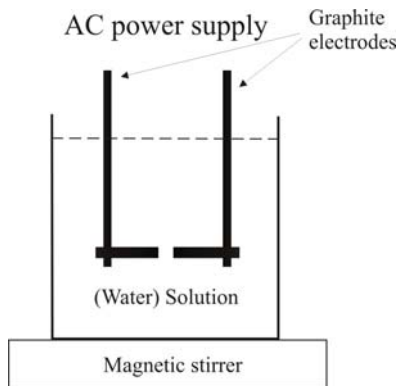


Fig. 1. A schematic drawing of the synthesis device.

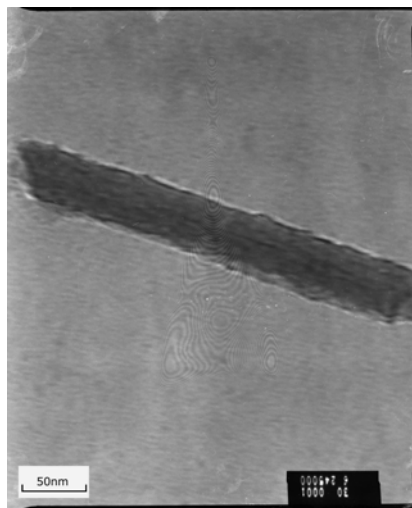


Fig. 2. TEM photograph of a single carbon nanotube produced by arc discharge in 5 % NaCl solution. Maximal magnifying of 310 000 is used.

An example of the single carbon nanotube produced in 5% NaCl solution is presented on Figure 2. This is well defined, 4.5 nm in diameter and 33.5 nm long carbon tube. It seems to be a single wall nanotube (SWNT).

Conclusion

The results have proofed that very simple arc discharge configuration in liquid environment can be used for synthesis of carbon nanotubes. The procedure allows a low cost continuous operation with minimal invention.

Acknowledgments

This work has been financially supported by Ministry of Science and Environmental Protection, Republic of Serbia, under Project No. 142065.

*This work has been a Bachelor degree thesis.

References

- [1] S. Iijima, *Nature* 1991, **354** (7), 56-58.
- [2] Yu Lin Hsin, Kuo Chu Hwang, Fu-Rong Chen, Ji-Jung Kai, *Adv. Mater.* 2001, **13** (1), 830-833.

INFLUENCE OF SILVER ADDITION ON TEXTURAL PROPERTIES OF NEW SYNTHETIC ACTIVATED CARBON

J. Krstić¹, O. Terzić², N. Vukelić³ and M. Mitrić⁴

¹*IChTM – Center for Catalysis and Chemical Engineering, Belgrade,
(jkrstic@nanosys.ihtm.bg.ac.yu)*

²*Faculty of Chemistry, University of Belgrade, Studentski trg 12-16,*

³*Faculty of Physical Chemistry, University of Belgrade, Studentski trg 12-16,*

⁴*The Vinča Institute of Nuclear Sciences, Belgrade, Serbia*

Abstract

Starting from macroporous styrene/divinylbenzene sulfonic acid ion exchange resin the two samples of synthetic activated carbons (SAC), with and without silver, were obtained through carbonization in controlled regime. Detailed sample preparation procedure is described. Characterizations of synthesized samples were conducted using XRD, SEM and N₂ physisorption at -196 °C measurements. The influence of applied silver on textural properties of CAS was discussed.

Introduction

The activity of research and development of materials with controlled porosity and shape has rapidly grown during the last ten years. As for synthetic carbons, the interest was driven by numerous potential application possibilities of these materials such as molecular sieves, adsorbents, catalyst supports, electrodes for electric double-layer capacitors, etc.

In the present work, detailed sample preparation procedure of new SAC is presented. Using controlled thermal decomposition in inert atmosphere [1] two SACs with and without of silver were synthesized. The influence of applied silver on textural properties of SAC was discussed.

Experimental

Sample preparation

Ion exchange resin Amberlite 200[®] (Rohm & Haas Company) in the Na⁺ form was washed with distilled water in a column, converted to the H⁺ form by passing through 2 mol/dm³ hydrochloric acid solution, and rinsed with distilled water in order to achieve neutral pH. This H⁺ form of resin was used as the starting material for preparation SAC samples.

First sample denoted as AH800 was obtained by controlled thermal decomposition of starting material. Heat treatment was performed in a horizontal metal tube ($\phi=3.40$ cm) with gas inlet, in a furnace modified for temperature programming. Approximately 20 g of starting material beads, dried at 105 °C for 16 hours, were placed between quartz wool plugs in a tube. AH800 was prepared applying the heat treatment procedure that includes a 1 h heat up to 200 °C and 1 h hold at 200 °C. Then, the temperature was raised by 100 °C increments during 0.5 h and held at the new temperature

for 0.5 h. The temperature rise cycles were repeated until the temperature of 800 °C was reached. After holding 1 h at 800 °C, the samples were allowed to cool down to room temperature during next 18 h. The entire heating and cooling procedure, was performed under the argon flow of 0.4 dm³/min. Immediately after cooling, the sample was placed in weighing bottle and stored in a vacuum desiccator containing anhydrous CaSO₄.

In order to prepare silver containing carbon designated as AAg800, the starting material was soaked in 1.0 mol/dm³ silver nitrate solution in dark for 12h. The washing with distilled water was conducted until no nitrate ions were detected in the eluate ("Brown Ring" Test). The final sample was obtained after drying at 105 °C in dark followed by same heating-cooling treatment procedure as for AH800.

Sample characterization

The phase analysis of the dried powder was carried out by X-ray diffraction (Philips Diffractometer, Philips PW 1710) using CuK α radiation.

The Scanning Electron Microscopy (SEM) was carried out on a Low Vacuum Scanning Electron Microscope (JEOL JSM-6460LV).

The texture characteristics of the precursors were estimated using N₂ adsorption-desorption at -196 °C (Sorptomatic 1990 Thermo Finnigan).

Results and Discussion

The obtained products are hard spheres with glassy shine, having average diameter 500 μ m. According to XRD patterns of AH800 (Fig. 1) the thermal decomposition of starting material leads in formation of glassy carbon like product.

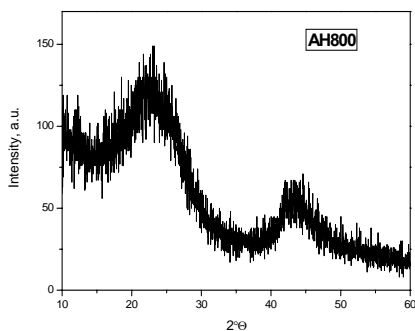


Fig. 1. XRD pattern of AH800

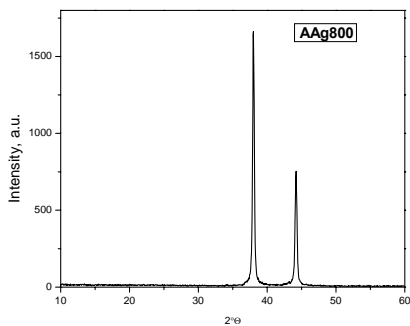


Fig. 2. XRD pattern of AAg800

Two broad, low intensity diffraction peaks at 23.5 and 43.5 of 2 θ corresponding to 002 plane (parallel graphene sheets) and 01 (two-dimensional reflectance of single graphene sheet) were observed [2].

XRD patterns of AAg800 sample are shown in Fig. 2. Diffractions corresponding to graphene sheets disappear and two intensive peaks originated from metal *fcc* silver phase (planes 111 and 200) exist.

Table 1. Textural data of CAS samples

Sample	S_{BET} m^2/g	V_{DR}^* cm^3/g	V_{mes}^{**} cm^3/g
AH800	446	0.220	0.251
AAG800	245	0.107	0.265

V_{DR}^* - Volume of Micropores by Dubinin-Radushkevich model

V_{mes}^{**} - Volume of Mesopores

thermal decomposition aggregation of silver is causing plugging of pores. This standpoint have stronghold in SEM pictures of synthesized materials (Fig 3, 4). External area of AH800 is porous, with obvious cavity on surface.

The data from N_2 sorption measurements (Table 1) show that addition of Ag^+ significantly changes the specific surface area (S_{BET}) of SAC. This change is dominantly originated from decrease in micropores region. However, some changes in mesopores region are also observed. Evidently, during

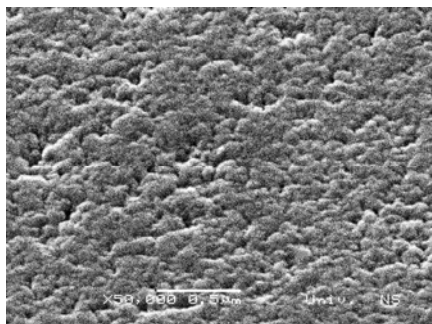


Fig. 3. SEM picture of AH800

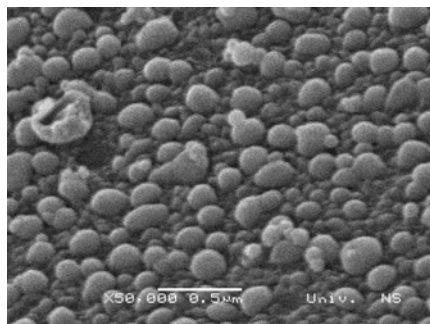


Fig. 4. SEM picture of AAG800

On the contrary AAG800 surface is overlaid by numerous spherical particles. These particles are made of metal silver that is created during thermal treatment. Although silver particle size distribution is not uniform, the most dominant class is around 100 nm.

Conclusions

Starting from H^+ form of resin Amberlite 200[®] using controlled thermal decomposition up to 800°C in inert atmosphere, glassy carbon spheres are formed. Embedding of Ag^+ ions in Amberlite 200[®] before thermal decomposition causes significant change in textural properties of produced SAC. Silver is accumulated on surface of carbon matrix in spherical forms of approx. 100 nm in diameter.

References

- [1] O. Terzić, J. Krstić, A. Popović, N. Dogović, Chem. Eng. Process, 2005, **11**, 1181-1187.
- [2] G. Jenkins and K. Kawamura, Nature, 1971, **231**, 175 – 176.

MONO- AND BIMETALLIC SPINELS. PART I: MECHANOCHEMICAL SYNTHESIS

E. Manova¹, D. Paneva¹, Z. Zheleva¹, B. Kunev¹, I. Mitov¹,
M. Stoyanova², and St. Christoskova²

¹*Institute of Catalysis, Bulgarian Academy of Sciences, 1113 Sofia, Bulgaria*

²*Department of Physical Chemistry, University of Plovdiv, 4000 Plovdiv, Bulgaria*

Abstract

A number of mono- and bimetallic spinels are prepared using mechanochemical synthesis method. The phase composition and structural properties of the obtained materials are investigated by X-ray diffraction and Moessbauer spectroscopy.

Introduction

The synthesis of spinel ferrites has been intensively studied, because of their large-scale application as magnetic materials, catalysts, etc. The role of the preparation conditions on the morphological and structural features of the ferrites have been discussed in [1]. The high-energy milling as a solid-state processing method has been subject of great interest in recent years [2]. A mechanochemical route for the preparation of ferrites has been reported in [3], but the synthesis was generally done using MeO and FeO as precursors. Mechanochemical synthesis of iron oxides and ferrites using different precursors (hydroxide carbonates and γ -FeOOH was described in our previous studies [4, 5].

The aim of this investigation was to mechanochemically synthesise and characterise iron and bimetallic (iron – cobalt and iron – nickel) oxide spinel samples.

Experimental

Mechanochemical synthesis (MCS) was made using a high-energy planetary ball mill “Fritsch-Pulverizate-5” with 100 cm³ steel reactors and grinding balls. The ball-to-powder mass charge ratio was 10:1. The Fe₃O₄ was obtained after 40 hours milling of γ -FeOOH in suspension of xylene medium [5]. The synthesis of iron-cobalt (Fe₂CoO₄ and FeCo₂O₄) and iron-nickel (Fe₂NiO₄ and FeNi₂O₄) oxides was performed in two steps: co-precipitation, and mechanical milling of the co-precipitation precursors. For the co-precipitation the procedure described in [4] was followed. The as-obtained precursors were milled for 3 hours.

The phase composition and structure of the samples was determined by X-ray diffraction (XRD) using TUR M62 diffractometer with Co K _{α} radiation. Data interpretation was carried out using JCPDS database. The transmission Moessbauer spectra (MS) were obtained at RT with a Wissel electromechanical Moessbauer spectrometer (Wissenschaftliche Elektronik GmbH, Germany) working at a constant acceleration mode (⁵⁷Co/Cr, 10 mCi, α -Fe standard). The experimentally obtained spectra were treated using the least squares method. The parameters of hyperfine interaction such as isomer shift (IS), quadrupole splitting (QS) and effective internal magnetic field (H_{eff})

as well as the line widths (FWHM) and the relative weight (G) of the partial components were determined.

Results and Discussion

The XRD pattern of the monometallic sample (Fig. 1a) shows monophase spinel composition of Fe_3O_4 , magnetite. The mean crystallite size was obtained from XR diffractogramme using the Sherer equation (PowderCell'2000) (Table 1).

The XRD patterns of the bimetallic ferrite precursors (not shown) are characteristic of layered double hydroxide carbonates [6]. After milling the cobalt-iron hydroxide carbonates for 3 hours the diffraction pattern of Fe_2CoO_4 (Fig. 1e) consists of broad peaks corresponding to spinel phase with cubic structure and lattice constant $a_0=8.38$ Å, while that of FeCo_2O_4 (Fig. 1d) contains lines of Co rich spinel oxide phase ($a_0=8.25$ Å). The diffractogramme of Fe_2NiO_4 (Fig. 1c) consists of broad peaks corresponding to Fe_2NiO_4 . In the case of FeNi_2O_4 sample only the peaks characteristic of the precursor are observed. Taking into account the width of the spectrum lines, the presence of a spinel phase Fe_2NiO_4 and NiO are not excluded. The unite cell parameter (a) and mean crystallite size (D) of synthesised spinels were also determined from the experimental XRD profiles (PowderCell'2000) (Table 1).

Table 1. Unit cell parameter (a) and crystallite size (D) of investigated samples

Sample	a, Å	D, Å
Fe_3O_4	8.38	160
FeCo_2O_4	8.25	70
Fe_2CoO_4	8.38	20
Fe_2NiO_4	8.31	20

The Moessbauer spectrum of monometallic sample (Fig. 2a) shows the two sextet components characteristic of magnetite. According to the method proposed by Topsoe [7], the non-stoichiometry (x) of the product has been determined from Moessbauer line areas belonging to the six and four coordinated iron cations. The obtained magnetite is a non-stoichiometric $\text{Fe}_{3-x}\text{O}_4$, $x=0.015$, i.e. $\text{Fe}_{2.985}\text{O}_4$ whose cationic vacancies are localized in octahedral sites of the magnetite lattice.

Fig. 2b-e shows the Moessbauer spectra of MCS bimetallic samples. They consist of doublet and/or sextet components. The doublets observed in all ferrites arise from Fe in ultradispersed ferrite particles (below 10 nm) exhibiting superparamagnetic behavior. This particle size effect is in good agreement with the XRD data. Only the Moessbauer spectrum of Fe_2CoO_4 consists of doublet (G=7%) and sextet part. It should be noted that acceptable data fitting of the Moessbauer spectra of this sample can be obtained only when the B-site pattern is assumed to be a superposition of more than one sextet. In our cases the hyperfine interaction of the B site could be fitted up to four overlapping six-line pattern, which agree with the observations of other authors for ferrite samples [3].

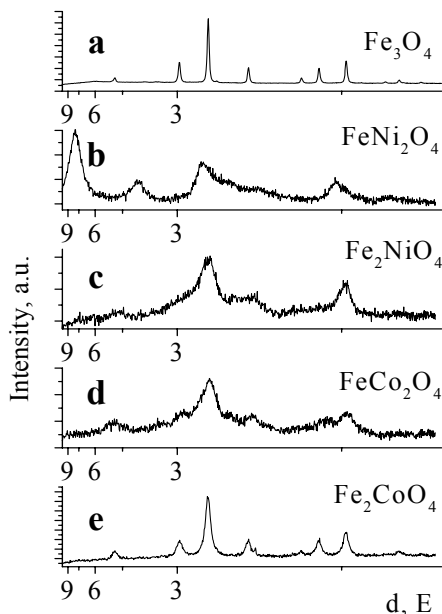


Fig. 1. Powder XRD patterns of MCS samples.

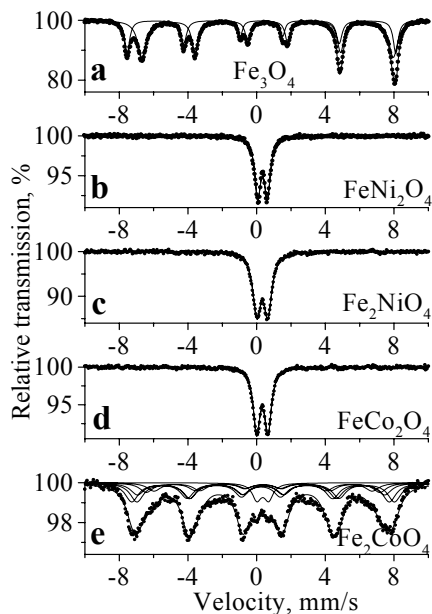


Fig. 2. Moessbauer spectra of MCS samples.

Conclusion

Mechanochemical synthesis is an appropriate method for obtaining new phase composition and high dispersity materials. Using this method nanodimensional cobalt ferrites and nickel ferrites are obtained. From these materials might be prepared highly active catalysts (see Part II).

Acknowledgments

The authors thank the National Science Fund of the Bulgarian Ministry of Education and Science for the financial support of Projects X-1504/05 and VUX-1105/05.

References

- [1] Y.J. Kim, D. Kim and C.S. Lee, *Physica B*, 2003, **337**, 42-51.
- [2] Proc. Int. Symp. Metastable, mechanically alloyed and nanocrystalline materials 2001, publ. in *Journal of Metastable and Nanocrystalline Materials*, v. **13**.
- [3] M.H. Mahmoud, H.H. Hamdeh, J.C. Ho, M.J. O'Shea and J.C. Walker, *J. Magn. Mater.*, 2000, **220**, 139-146.
- [4] E. Manova, B. Kunev, D. Paneva, I. Mitov, L. Petrov, C. Estournès, C. d'Orléans, J.L. Rehspringer and M. Kurmoo, *Chem. Mater.*, 2004, **16**, 5689-5696.
- [5] Z. Cherkezova, I. Mitov, B. Kunev, Proc. Sci. Techn. Conference "Tribology 2003", Ed. E. Assenova, Tribology centre, Published by TEMTO, ISBN 954-9566-22-6, 2003, **1**, 31-35.
- [6] F. Cavani, F. Trifirò and A. Vaccari, *Catalysis Today*, 1991, **11** (2), 173-301.
- [7] H. Topsoe, Ph. D.Thesis, Stanford University, 1972.

SYNTHESIS AND STRUCTURE OF $\text{LiMn}_{2-x}\text{Zn}_x\text{O}_4$ THROUGH ULTRASONIC SPRAY PYROLYSIS

D. Jugović¹, M. Mitrić², N. Cvjetičanin³, M. Miljković⁴, and D. Uskoković¹

¹*Institute of Technical Sciences of the Serbian Academy of Sciences and Arts,
Knez Mihailova 35/IV, Belgrade, Serbia*

²*The Vinča Institute of Nuclear Sciences, Laboratory for Theoretical and Condensed Matter Physics,
P.O. Box 522, Belgrade, Serbia*

³*Faculty of Physical Chemistry, University of Belgrade,
Studentski trg 12-16, P.O. Box 137, Belgrade, Serbia*

⁴*Faculty of Medicine, University of Niš, Serbia*

Abstract

Ultrasonic spray pyrolysis method was used for the synthesis of quaternary spinel oxide $\text{LiMn}_{2-x}\text{Zn}_x\text{O}_4$ ($x \approx 0.08$) powder, without additional annealing. Aqueous solutions of metal nitrates were atomized at a frequency of 1.7 MHz by the ultrasonic nebulizer. Aerosol was introduced in the horizontal electric furnace at the temperature of 1073 K. The crystal structure of the as-prepared powder was revealed by X-ray powder diffraction and identified as a single spinel phase with Fd3m space group. Particle morphology was determined by scanning electron microscopy (SEM).

Introduction

LiMn_2O_4 spinel is environmentally acceptable and low cost material which has attracted much attention as a promising cathode material for lithium-ion batteries [1, 2]. The major limitation of LiMn_2O_4 in battery applications is capacity fading upon electrochemical cycling. The largest improvements of the cycle life have been achieved by the substitution for some of the manganese by other metal cations (Li^+ , Ni^{2+} , Al^{3+} , Co^{2+} , Zn^{2+} , Cr^{3+}) [3]. This substitution increases the average oxidation state of the remaining manganese and produces more robust spinels with better capacity retention, but somewhat lower initial capacity.

In this paper we demonstrate the possibility to prepare quaternary spinel oxide $\text{LiMn}_{1.92}\text{Zn}_{0.08}\text{O}_4$ by using an ultrasonic spray pyrolysis method, without additional annealing. The structural and morphological properties of such synthesized material are presented.

Experimental

Starting solution was an aqueous solution of LiNO_3 (Laphoma), $\text{Mn}(\text{NO}_3)_2$ (Merck), and $\text{Zn}(\text{NO}_3)_2$ (Merck) p.a. chemicals, mixed in such a ratio to achieve the stoichiometry of $\text{LiMn}_{1.92}\text{Zn}_{0.08}\text{O}_4$. The total metal concentration was 0.98 mol/dm^3 . This solution was atomized at a frequency of 1.7 MHz by the ultrasonic nebulizer. The generated mist, with the average droplet diameter of approximately $2.5 \mu\text{m}$, was carried to the horizontal electric furnace by air, with a flow rate of $0.5 \text{ dm}^3/\text{min}$. The effective heating length of the reaction tube was 0.6 m with the

maximum temperature of 1073 K in the middle of the furnace. The residence time of droplets/particles inside the furnace and in the maximum temperature zone was 65 s and 6 s, respectively, assuming the air flow rate and droplet velocities to be equal. The heating rate of droplets/particles was 15 °C/s. The precipitated powder was collected from a quartz glass tube at the outlet of the reactor.

X-ray diffraction data were collected on a Philips PW 1050 diffractometer with Cu-K $\alpha_{1,2}$ radiation (Ni filter) at the room temperature. Measurements were done in 2 θ range of 10-100° with scanning step width of 0.02° and 10 s time per step. Crystal structure refinement was based on the Rietveld full profile method [4] using the Koalariet computing program. This program is appropriate for processing the data obtained from the samples with dominant microstructure parameters [5].

SEM was performed on a JEOL JSM-5300, with electron energy of 20 keV.

Results and Discussion

X-ray powder diffraction patterns were used for the structural analysis of the synthesized samples. The refinement results show that LiMn_{1.92}Zn_{0.08}O₄ powder is

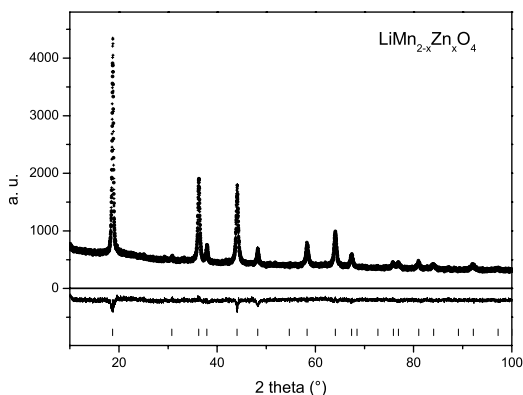


Fig. 1. The observed (\bullet), calculated ($-$), and difference (bottom) X-ray diffraction data of LiMn_{1.92}Zn_{0.08}O₄ taken at room temperature. Vertical markers below the diffraction pattern indicate positions of possible Bragg reflections.

well crystallized as single-phase spinel. The structure of LiMn_{1.92}Zn_{0.08}O₄ has been refined in the space group Fd3m (O_h⁷) in well-known spinel type with following crystallographic positions: Li⁺ ions in special crystallographic position 8a [0,0,0] with local symmetry $\bar{4}3m$, Mn³⁺ and Mn⁴⁺ ions in special crystallographic position 16d [5/8,5/8,5/8] with local symmetry 3m, and O²⁻ in special crystallographic position 32e [x,x,x] with local symmetry 3m. The observed and calculated X-ray diffraction profiles are given in Figure 1, while main results of the final Rietveld refinements are presented in Table 1. Throughout the

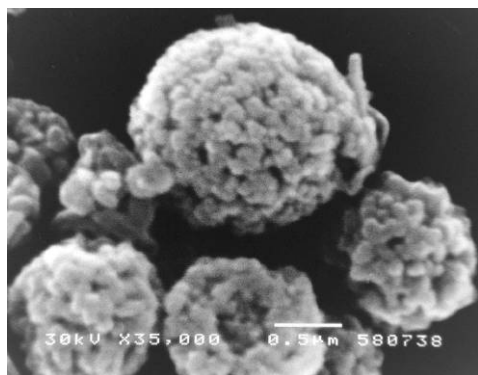
refinements the model with Zn in the tetrahedral (8a) site was applied. The inclusion of Zn on the tetrahedral site is in common with many spinel systems, resulting from the tendency of Zn to be four-coordinated and then to occupy this site. In addition, one of the peaks of the diffraction pattern, namely (220) at 2 θ = 30.708°, is allowed in the space group Fd-3m, but its appearance is sensitive to the presence of dopant ions on the Li⁺ (8a) tetrahedral site. It should be emphasized that lattice parameter of LiMn_{1.92}Zn_{0.08}O₄ (a=8.2324(3) Å) is appreciably reduced comparing to LiMn₂O₄ (a= 8.2410(1) Å) synthesized under the same conditions [6].

This is probably due to the increase in the average oxidation state of the manganese (average oxidation state 3.5) upon substitution of some Mn ions with Zn²⁺ ions, since the ionic radii of tetrahedral Li⁺ and Zn²⁺ are very similar, 0.73 and 0.74 Å, respectively.

Table 1. The final results of the structural refinement for LiMn_{1.92}Zn_{0.08}O₄

Lattice parameters [Å]	a = 8.2324(3)
Primitive cell volume [Å ³]	V = 139.48(4)
Mean crystallite size [Å]	660(20)
Microstrain [%]	0.51(1)
Strain [%]	0.13(1)
Free coordinates O ²⁻	u = 0.3849(4)
Li ⁺ crystall. position occ.	N _{Li} (8a) = 1-0.09(1)
R factors [%]	R _B = 4.5

Also, microstrain and strain parameters are reduced comparing to LiMn₂O₄. Strain parameter is in connection with Jahn-Teller distortion. Introduction of Zn to spinel structure impede Jahn-Teller distortion since it is dependent on the amount of Mn³⁺ ions. Reduced microstrain in comparison with LiMn₂O₄ means that more stable spinel structure was obtained.



Scanning electron microscopic image of the sample are shown in Figure 2. The particles are spherical in shape and non-agglomerated, showing porous microstructure. When metal nitrates melt at low temperature (in this case Zn(NO₃)₂·6H₂O, T_m=45°C), before the decomposition, molten salt retain solvent and porous particles appear.

Fig. 2. SEM image of LiMn_{1.92}Zn_{0.08}O₄

Conclusion

In summary, well-crystallized single-phased spinel LiMn_{1.92}Zn_{0.08}O₄ can be readily obtained by an ultrasonic spray pyrolysis. The structural refinement confirmed the presence of Zn²⁺ ion on the tetrahedral sites of the spinel. The synthesized powder had spherical particle morphology and non-agglomerated particles, with porous surface appearance.

References

- [1] D. Guyomard, J. M. Tarascon, *Solid State Ionics*, 1994, **69**, 222-237.
- [2] Y. Xia, M. Yoshio, *J. Power Sources*, 1995, **57**, 125-131.
- [3] Y. P. Wu, E. Rahm, R. Holze, *Electrochim. Acta*, 2002, **47**, 3491-3507.
- [4] H.M. Rietveld, *J. Appl. Cryst.*, 1969, **2**, 65-71.
- [5] R.W. Cheary, A. Coelho, *J. Appl. Cryst.*, 1992, **25**, 109-121.
- [6] D. Jugović, M. Mitrić, N. Cvjetičanin, M. Miljković, V. Jokanović, D. Uskoković, *Materials Science Forum* 453-454 (2004) 387-392.

ULTRASOUND MODIFICATIONS OF PHYSICAL PROPERTIES OF BaTiO₃ POWDERS

S. Marković¹, Lj. Kandić¹, M. Mitrić², G. Starčević³ and D. Uskoković¹

¹*Institute of Technical Science of the Serbian Academy of Sciences and Arts,
Knez Mihailova 35/IV, Belgrade, Serbia (smilja@ffh.bg.ac.yu)*

²*Institute of Nuclear Sciences "Vinča", Belgrade, Serbia*

³*NIS – Oil Refinery, Pančevo, Serbia*

Abstract

The starting BaTiO₃ powder was prepared by solid state reaction, and then modified by ultrasound into powders with different physical characteristics. The prepared barium titanate powders were characterized by X-ray powder diffraction (XRD), laser particle size analyzer, also, specific surface area and powders density were determined. The studies indicate that physical properties of BaTiO₃ powders were changed by sonochemical treatment. However, tetragonal crystal structure was maintained. It is shown that sonochemical method can be used for easy modification of barium titanate powder characteristics.

Introduction

Due to its ferroelectric and dielectric properties BaTiO₃ based materials have many applications in electronic devices such as multilayer ceramic capacitors, pyroelectric detectors, ferroelectric memories, sensors and positive temperature coefficient (PTC) thermistors [1].

The importance of the starting powders characteristics on the properties of the final ceramics is very well known from the literature [2]. The classical route to prepare barium titanate powder is the solid state reaction between BaCO₃ and TiO₂ at temperature interval 1000-1200 °C. This is a widely used method for large bath processing for barium titanate based powders. Powders prepared by solid state reaction are agglomerated and aren't highly reactive toward sintering. A narrow particle size distribution and a small average size may be achieved by powders milling before pressing and sintering. During milling impurities can be introduced into system. Instead milling, sonochemical treatment can be used for powders activation.

In this study, we prepare barium titanate powder by solid state reaction, and then modified them by sonochemical treatment into powders with different physical characteristics. We investigated powders crystal structure, density, particle size, crystallite size, particle size distribution and specific surface area.

Experimental

The BaTiO₃ (BT) starting powder was prepared by conventional solid state reaction. Mixture of BaCO₃ and TiO₂ was homogenized for 24 hours in ethanol, dried and calcined at 1100 °C for 2 h. After calcinations, starting barium titanate powder was modified by ultrasound treatment. The powder was dispersed in isopropanol and treated for

10, 60 and 180 minutes, with high-intensity ultrasound radiation using a direct-immersion titanium horn (Sonics VCX – 750, 20 kHz, 750 W). After the ultrasound process was stopped, the powders were filtered and dried.

The crystal structure of the barium titanate powders were investigated by XRD measurements, obtained on Philips PW-1050 automatic diffractometer using Cu K_{α} radiation. The diffraction measurements were done over scattering angle from 20 to 120 $^{\circ}2\theta$ with a step of 0.02 $^{\circ}$ and a counting time of 15s. The FullProf program was used for structural refinement. The average particle size and particle size distribution were determined in isopropanol using a laser particle size analyzer (Mastersizer 2000, Malvern Instruments Ltd, UK). The specific surface area (BET) and pore size of powders were measured by N_2 adsorption-desorption isotherms at -195.8 $^{\circ}C$ on a Micromeritics[®] analyzer, while powders density were measured by pycnometry in hexane.

Results and Discussion

After XRD measurements, we noticed that all powders were high crystalline, pure barium titanate with tetragonal symmetry. The crystallite size in the BT powders were calculated from the half-width of the XRD peaks of (002) and (200) planes, using by the Scherer's equation, and are shown in Table 1, as well as the tetragonality (c/a ratio). It can be noticed that these values are very similar, i.e. negligibly dependent on duration of ultrasound treatment. Fig. 1 shows Rietveld refinement of starting $BaTiO_3$ powder structure.

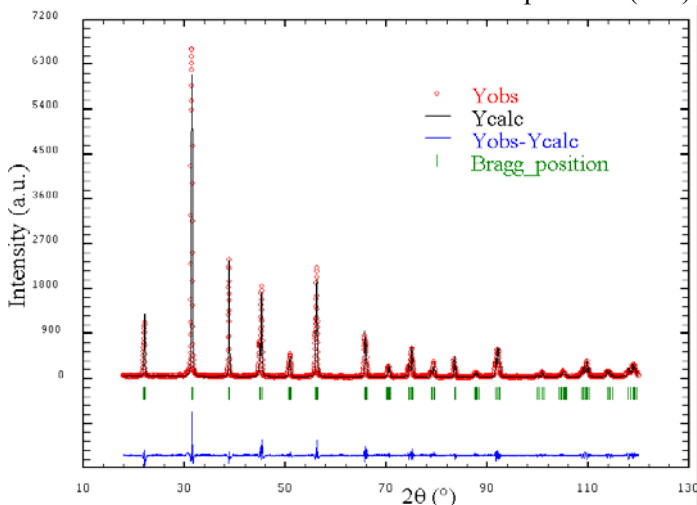


Fig. 1. Observed ($^{\circ} Y_{obs}$), calculated ($- Y_{calc}$) and residual (lower) XRD of starting $BaTiO_3$ powder.

Fig. 2 shows the particle size distribution of $BaTiO_3$ powders (distribution based on numbers). The particle size distribution of the starting barium titanate powder, prepared by solid state reaction, was very narrow, and average particle size was 1.399 μm . It is noticeable that during ultrasound treatment particles are de-agglomerated, and average particle sizes decreases, while, the width of the particle size distribution is broadened. Values of average particle size, specific surface area and powders density are shown in Table 1.

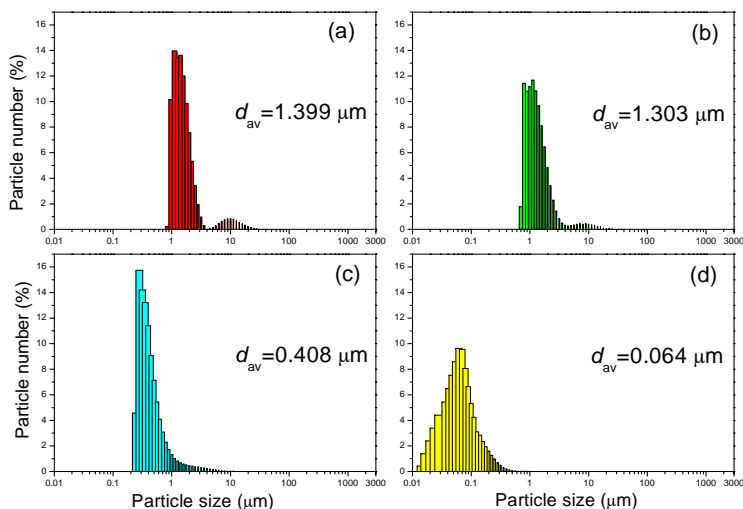


Fig. 2. Particle size distribution of BaTiO₃ powders (distribution based on number). Sonication time: (a) 0; (b) 10; (c) 60 and (d) 180 min.

Table 1. Characteristics of BaTiO₃ powders

Sonication time (min)	<i>c/a</i>	Crystalite size (Å)	Density (g/cm ³)	Average particle size (μm)	Specific surface area (m ² /g)
0	1.0077	(002) 318.6 (200) 695.7	5.58	1.399	1.01
10	1.0077	(002) 307.4 (200) 635.1	5.54	1.303	4.61
60	1.0077	(002) 327.4 (200) 645.3	5.63	0.408	4.79
180	1.0079	(002) 293.3 (200) 562.1	5.06	0.064	1.31

Results of our investigations indicated that using by ultrasound irradiation we could improve physical characteristic of BaTiO₃ powder previously prepared by solid state reaction, without changing of powder's crystal structure. After three hours of ultrasound treatment of tetragonal BaTiO₃ we obtained nanometer-sized, uniformly distributed particles, suitable for preparation of high density ceramics, and consequently, for ceramics with good dielectric properties.

Acknowledgments

The Ministry of Science and Environmental Protection of the Republic of Serbia provided financial support under grant no. 142006.

References

- [1] S. Gablenz, C. Damm, F.W. Müller, G. Israel, M. Rössel, A. Röder and H.-P. Abicht, Solid State Science, 2001, **3**, 291-299.
- [2] T. Tsurumi, T. Sekine, H. Kakemoto, T. Hoshina, S.-M. Nam, H. Yasuno, S. Wada, J. Amer. Ceram. Soc., 2006, **89** [4], 1337-1341.

CHANGES OF NANO PARTICLE SIZES IN THERMALLY TREATED PRECIPITATED SILICA

O. A. Kovačević¹, B. T. Kovačević¹, D. Arandelović¹, N. L. Lazić¹,
L. Pezo¹ and Ž. Lj. Tešić²

¹ *Holding Institute of General and Physical Chemistry,
Studentski trg 12/V P.O. Box 551 Belgrade, Serbia,*

² *Faculty of Chemistry, Belgrade, Studentski trg 12, Serbia*

Abstract

Thermally induced morphological changes of nanosized precipitated silica were studied directly by the SEM measurements. Nitrogen absorption measurements give valuable data about this type of material and enable calculation of an average size of the particles. During the thermal treatments below 950 °C, the nano structure of the precipitated silica as an amorphous material is preserved. A plot of the nano particle diameters, obtained by examination of SEM micrographs – D_{SEM} , versus the temperatures of the treatment is a curve with a minimum. The average particle diameters, obtained by calculation on the basis of the results of the adsorption measurements – D_{BET} , increase with the increase of the temperatures of the treatment. It is in accordance with the decreases of the specific surface areas and the external surfaces areas. The D_{BET} values lies in the field of the D_{SEM} values.

Introduction

Precipitated silica is a material of a great interest in the different branches of the industry, as it is the industry of drinks, or the rubber industry [1-4]. Material of this type is amorphous silica, with a short-range ordered structure [1,5,6], composed by the nano particles joint together in agglomerates, which structure, shape and magnitude are ordered by the process of the preparation [1,5-6]. This type of material has a great number of silanols, hydroxyls connected by Si atoms, with acidic character [1,5-7]. The changes of the number and type of the silanol groups and/or of the other precipitated silica characteristics are possible in some chemical and thermal treatments [5,6].

We study the morphological changes, especially changes of the nanoparticle diameters induced with the thermal treatment. For this purpose, we choose a silica sample with relatively large nano particle.

Experimental

The initial material is precipitated silica (88.02 % SiO₂, trade mark SIL from 1992. T.G. "Birač", Zvornik, BIH). Sample was treated in a furnace. The specific surface area (BET) was determined on the basis of the multi-point nitrogen surface areas measurements [ASTM D 4365 – 85, ISO/DIS 4652-2] using a Autosorb-6, Quantachrome and Data acquisition software PSORB2PC – an enhanced software for P_o Autosorb 6 Version 2.0. The average particle size was calculated as $D = 6000(\rho S)^{-1}$ [5,8], where D

is average diameter of the particle (nm), $\rho=2.2$ (gcm^{-3}) [5,8] and S is an external surface area (m^2g^{-1}). X-Ray diffraction (XRD) patterns were measured on a Philips PW-1710 Automated Powder Diffractometer System, using monochromatic CuK_α radiation, in the region of $3\text{--}65^\circ 2\theta$ and with steps $0.020^\circ 2\theta$ and sampling time 1.25 s/step. The particle size and habit were examined using a scanning electron microscope JEOL, JSM-6460.

Results and Discussion

Precipitated silica of the trademark SIL is an amorphous hygroscopic fluffy solid material. SEM micrographs of the SIL sample at an ambient temperature, S-0 sample, show a material with the nanosized particles, globular in the shape, with the size distribution in the region 62 ± 8 nm. Sample S-0 was thermally treated in the temperatures range $170\text{--}950^\circ\text{C}$, as

it is given in Table 1. The sizes of the prime nano particles were studied in a direct manner by the SEM micrographs of the samples, and in an indirect way by the nitrogen adsorption measurements. The diameters of the nano particles, obtained by the examination of the SEM micrographs, D_{SEM} values, are distributed within some range of D values. (Table 1). D_{BET} value, that is results of calculations on the basis of the adsorption measurements, represents an average particle diameter of the particles (Table 1). The average particle sizes D_{BET} lie inside the limits of the ranges of the D_{SEM} values, as it is seen on Fig. 1., where D values are plotted versus temperature of the thermal treatment. The plots of the D_{SEM} values (higher and lower limits of the ranges) versus the temperatures of the treatment are the curves with the minimums in the temperature interval $170\text{--}560^\circ\text{C}$. In the same time D_{BET} values increase continuously. That increase is in an agreement with the continuously decreasing values of the surface areas and the external surfaces areas, as it is given in table 1.

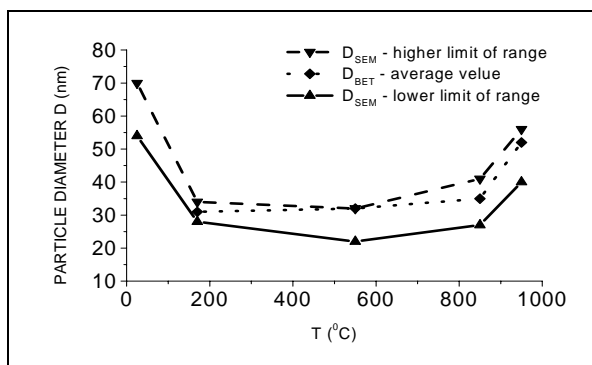


Fig. 1. The influence of the thermal treatment (T – temperature of treatment) on the particle size diameters (D values).

of the adsorption measurements, represents an average particle diameter of the particles (Table 1). The average particle sizes D_{BET} lie inside the limits of the ranges of the D_{SEM} values, as it is seen on Fig. 1., where D values are plotted versus temperature of the thermal treatment. The plots of the D_{SEM} values (higher and lower limits of the ranges) versus the temperatures of the treatment are the curves with the minimums in the temperature interval $170\text{--}560^\circ\text{C}$. In the same time D_{BET} values increase continuously. That increase is in an agreement with the continuously decreasing values of the surface areas and the external surfaces areas, as it is given in table 1.

Table 1. Sizes of thermally precipitated nano particles

Sample	Thermal treatment T(°C)	Surface area (m ² /g)	Micro pore surface area (m ² /g)	External surface area (m ² /g)	D _{SEM} (nm)	D _{BET} (nm)
S-0	25	-	-	-	62±8	-
S-1	170	105.3	16.6	88.7	31±3	31
S-2	550	92.8	8.4	84.4	27±5	32
S-3	850	78.0	0.2	77.8	34±7	35
S-4	950	56.1	3.4	52.7	48±8	52

Conclusion

Under thermal treatment in the range of the temperatures below 950 °C, the nano structure of the precipitated silica as an amorphous material is preserved. The nano particle diameters – D_{SEM}, are obtained by the examination of the SEM micrographs. The nitrogen absorption measurements give a valuable data about materials and enable calculation of the average size of the particles - D_{BET}. The D_{BET} values lies in the field of the D_{SEM} values.

Acknowledgment

The authors are grateful to Dr Miloš Bokorov for SEM analysis. The present investigations are partially supported by the Ministry of Science and Environmental Protection of the Republic Serbia under projects 1713 and TD007039.

References

- [1] M.P. Wagner, Rubber Chemistry and Technology, 1976, **49**, 703.
- [2] S. Wolff, Rubber Chem. Technol., 1996, **69**, 325.
- [3] N.L. Lazic, M. Sc. Thesis, University of Belgrade, Serbia and Montenegro, 2004.
- [4] M.B. Plavšić, Polymer Materials Science and Engineering, Naučna knjiga, Belgrade (1995), in Serbian.
- [5] R.K. Iler, Chemistry of Silica, A. Wiley-Interscience Publication, New York, 1979.
- [6] C.J. Brinker and G.W. Scherer, Sol-Gel Science, Academic Press, Inc. San Diego, 1990.
- [7] A.V. Kiselev, Trans. Faraday Soc. Disc., 1971, **52**, 14.
- [8] B.B. Bonstra, "Rubber Technology and Manufacture", 2.ed., C.M. Blow and C. Hapburn, Eds., Butterworth Sci., London, 1982, ch.,7.

SYNTHESIS OF FIBROUS SiC FROM NATURAL PRECURSOR

A. Devečerski¹, M. Logar², M. Pošarac¹, T. Brdarić¹, D. Božić¹ and B. Matović¹,

¹*Vinča Institute for Nuclear Sciences, Materials Science Lab. P.O. Box 522, Belgrade, Serbia*

²*Faculty of Mining and Geology, Studentski trg 12-16, Belgrade, Serbia*

Abstract

Fibrous magnesio-silicate (mountain leather asbestos) of Serbian origin was used as Si precursor for the synthesis of SiC by carbothermal-reduction process [1, 2]. As a reducing agent, sugar (saccharose) was used. Formation of SiC was confirmed by XRD analysis and optical microscopy images. Results showed that obtained SiC possess fibrous morphology. Due to the experimental procedure MgF_2 is also formed, which is known as an excellent additive for sintering of non-oxide ceramics.

Experimental

Mountain leather asbestos (MLA) sheets were cutted in 20mm x 10mm pieces, soaked into the sugar aqueous solution, dried and then heat treated at 1673K for 1 hour in continuous Ar flow (MLAC). Samples are then oxidized in air at 873K (MLAO), leached in diluted HF (1 part of HF + 3 parts of H_2O) for 5, 10 and 20 minutes, washed with H_2O and dried (MLAO5, MLAO10 and MLAO20).

Structural analysis was carried out by a Siemens D-500 powder diffractometer. $CuK\alpha$ radiation was used in conjunction with a $CuK\beta$ nickel filter.

Morphology was examined by the use of optical microscop »Zeiss«, AXIOVERT 25 (50-1000x magnif.), Germany.

Results and Discussion

XRD patterns of starting MLA and samples treated according to various steps of experimental procedure are presented in Fig. 1. In XRD pattern of MLAC sample (Fig. 1b), the reflections of original MLA disappeared and formation of SiC (JCPDS number 29-1129) is observed as well as the peaks of forsterite (Mg_2SiO_4 , JCPDS number 34-0189). Broad reflection about $2\theta = 26$ degree that belong to amorphous carbon, disappears after exposure to air at 873K (not showed). During leaching the samples in diluted HF, intensities of forsterite reflections decrease with prolonging leaching time (Fig. 1c-1e) whilst the forsterite reflections for MLAO20 sample are completely disappeared. FWHM of strongest SiC reflection ($2\theta \approx 35.5^\circ$) also increases with increasing HF leaching time, thus indicating that SiC grains are reduced in size, probably due to high stress exposition of SiC in presence of HF. Together with disappearance of forsterite reflections, new broad reflections arised in XRD patterns of HF leached samples ($2\theta \approx 27^\circ$, 40° and 43°), indicating formation of new amorphous phase. To clarify the nature of this phase, another MLAO sample is lefted overnight in HF solution (MLAO ∞ - Fig. 1f). After this tretment mentioned reflections become more pronounced and they can be attributed to MgF_2 (JCPDS file number 06-0290), which is obviously formed during reaction of forsterite with HF. The strongest SiC

reflection is also broaden and further decreasing in SiC crystallite size. This behaviour confirms that the SiC is unstable in presence of HF.

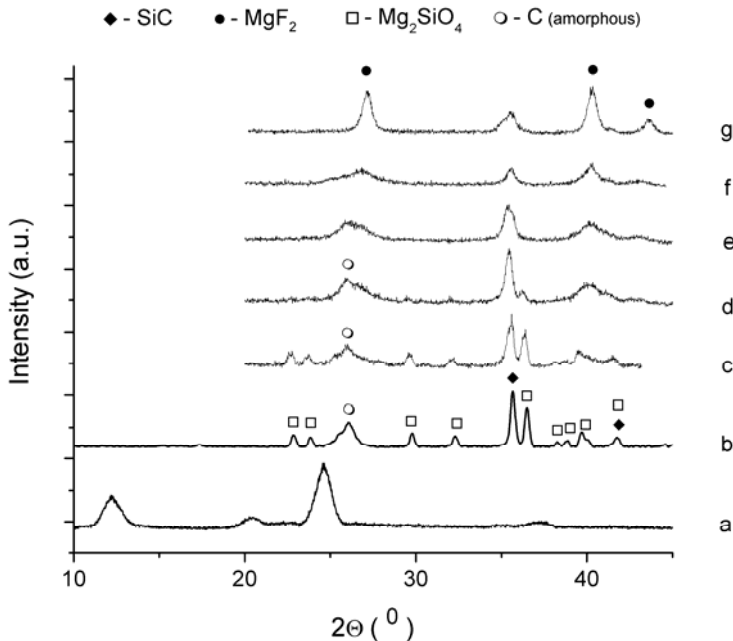


Fig. 1. XRD patterns: a) MLA; b) MLAC; c) MLAO5; d) MLAO10; e) MLAO20; f) MLAO ∞ ; g) MLAO ∞ exposed to air at 873K;

Relatively sharp peak at ≈ 26 degree in MLAO5, MLAO10 MLAO20 and MLAO ∞ XRD patterns, belong to carbon which is formed during SiC decomposition. This is proved by exposing MLAO ∞ again to air at 873K: peak at 26 degree disappeared (Fig. 1g), leaving only a peak centered at 27 degree which belongs to MgF₂. It should be also noticed that all MgF₂ reflections became sharper after this 873K treatment i.e. MgF₂ phase is now rather crystalline than amorphous. Presence of MgF₂ is quite appropriate, because it is known that fluorides of earth-alkali metals are very good additives for sintering of non-oxide ceramics [3].

Optical micrographs of samples are presented in Fig.2. MLAC sample retain its original shape after 1673K treatment ($\approx 20\text{mm} \times 10\text{mm}$ pieces). However, when MLAC samples are dipped into the HF solution, they divide into longish plate-like particles, ranging in size from several millimeters to less than one millimeter. Image of one such particle is given in Fig. 2a. Images of single SiC fibres fallen off from big particles are presented in Fig. 2b-2d.

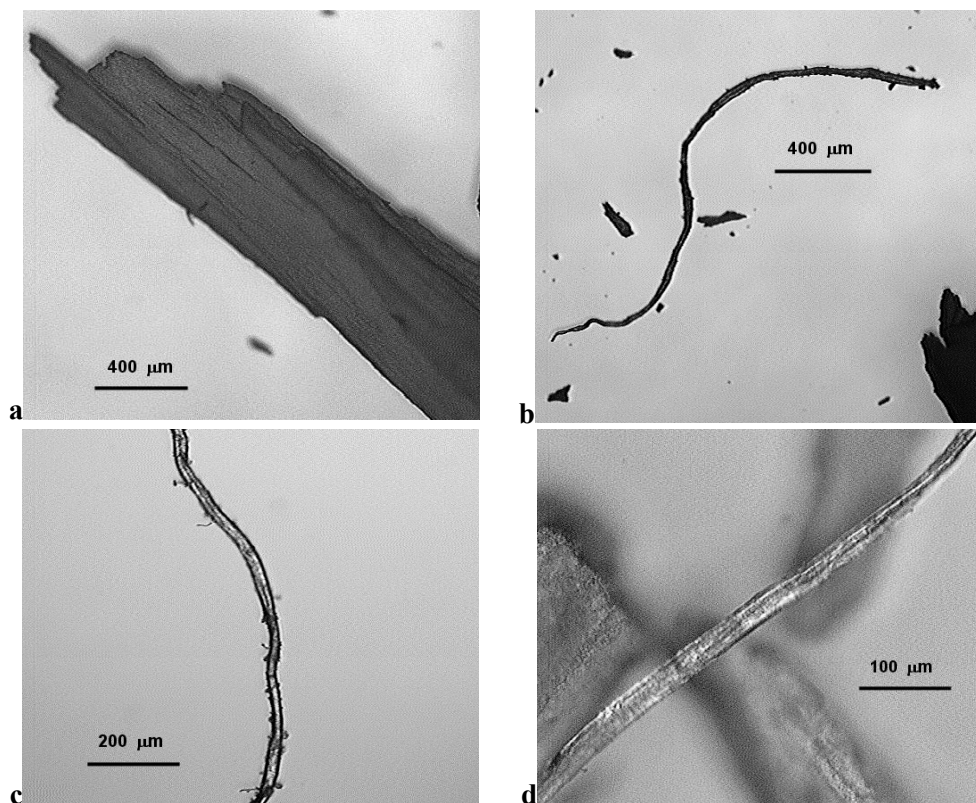


Fig. 2. Optical micrographs of samples, showing SiC fibrous morphology

Acknowledgment

This project was financially supported by the Ministry of Science and Environmental Protection of Serbia (project number: 142016).

References

- [1] C.Vix-Guterl, P.Ehrburger, *Carbon*, 1997, **35**, 1587-1592
- [2] C.Vix-Guterl, B.McEnaney, P.Ehrburger, *J.Eur.Ceram.Soc.*, 1999, **19**, 427-432
- [3] G.Petzow, M.Herrmann: *Structure and Bonding*, 2002, **102**, 47-166.

ANALYTE-TARGETED PATTERNING OF SUBWAVELENGTH APERTURE ARRAYS WITH EXTRAORDINARY OPTICAL TRANSMISSION FOR ENHANCED BIOSENSING

Z. Jakšić, D. Vasiljević-Radović and M. Sarajlić

*IHTM – Institute of Microelectronic Technologies and Single Crystals,
Njegoševa 12, Belgrade, Serbia. (jaksa@nanosys.ihm.bg.ac.yu)*

Abstract

We utilize the duality between the patterns of subwavelength nanoaperture arrays and the nanoscale surface patterns which localize biomolecules or living tissue through selectively promoted adhesion to obtain structures which enhance the sensitivity of optical biosensors and chemical sensors. The surface plasmon resonance (SPR) effect and extraordinary light transmission are used to detect the presence of an analyte. Owing to preferential surface adhesion in the areas of highest field intensities, the nanohole array-based structures allow for the detection of miniscule quantities of analytes with an improved sensitivity, while the very nature of the subwavelength aperture arrays ensures enhanced nonlinear optical effects. Similar or even identical structures can be used for adsorption-desorption based SPR chemical sensors for a range of different organic and inorganic analytes.

Introduction

Surface plasmon resonance (SPR)-based devices are probably the most important devices for highly selective all-optical sensors [1]. They respond to analyte layers adsorbed or otherwise attached to the surface. Due to evanescent nature of the SPR, they show extremely high sensitivities to refractive index changes (below 10^{-5}), respond to minute amounts of analytes (used to sense layers with a thickness well below 200 nm, often below a few tens of nm) and show a real time operation which makes them convenient for both in vitro and in vivo measurement. Sensor surface functionalization is very important, since it enables the fabrication of selective chemical sensors and biosensors.

Among SPR-based structures are nanoaperture arrays with extraordinary optical transmission, first described by Ebbesen et al. [2]). If an optically thick (opaque) film riddled with an array of nanoholes or with a single nanohole surrounded with surface undulations (Fig. 1) is illuminated by light at a wavelength much larger than the aperture radius, no radiation should be transmitted at all. However, owing to a SPR reaction a large portion of the radiation is transmitted if the screen is built of plasmon-supporting metal, a phenomenon denoted as extraordinary optical transmission (EOT).

The use of EOT nanoholes as sensors was described in [3]. It is in the nature of the SPR that fields are strongly confined at the surface, and especially in the holes.

Most often surfaces for biosensors must be functionalized in some way in order to enable better adhesion of analytes. One of the very important methods for this is surface nanopatterning [4], [5], which enables selective adherence of different biomolecules and tissues and is at the very foundations of biosensing.

In this paper we consider the possibility of use surfaces nanopatterning performed during fabrication of EOT subwavelength nanoholes as the adhesion promoter for select analytes. We utilize the fact that similar or even identical nanopatterns (including similar shapes, dimensions and materials) can be used for both. We perform a basic theoretical and experimental analysis of this concept. We designed nanoapertures intended for recognition of miniscule amounts of bioanalytes. We utilized scanning probe nanolithography to fabricate them and atomic force microscopy to characterize the obtained patterns.

Method Used

If the structure with nanoholes is dipped into a solution or a gaseous mixture containing an analyte, the dielectric permittivity near the nanoaperture is changed from ϵ_2 to ϵ_3 , which modifies the peak transmission and reflection. The new peaks can be determined if we consider the nanohole pattern to be either a diffractive grating (Fig. 1, top) with a lattice parameter a or a zonal diffractive optical element (Fig. 1, bottom). Using the well-known grating equation and replacing into it an incident angle equal to zero as the necessary condition for plasmon coupling, the transmission maximum peak wavelength $\lambda_{peak} = 2\pi / k_x$ is simply calculated as

$$\lambda_{peak} = \frac{a}{m} \sqrt{\frac{\epsilon_1(\lambda_{peak})\epsilon_2}{\epsilon_1(\lambda_{peak}) + \epsilon_2}} \quad (1)$$

The effective permittivity of the analyte for the case of evanescent modes exponentially decaying away from the surface as $[\exp(-z/l_d)]^2$ (l_d characteristic decay length) can be determined as

$$\epsilon_{eff} = \frac{1}{l_d} \int_0^{\infty} \epsilon(z) \exp(-z/l_d) dz \quad (2)$$

The properties of nanoaperture arrays can be determined *ab initio* starting from Maxwell equations or utilizing e.g. the analytical method presented in [6].

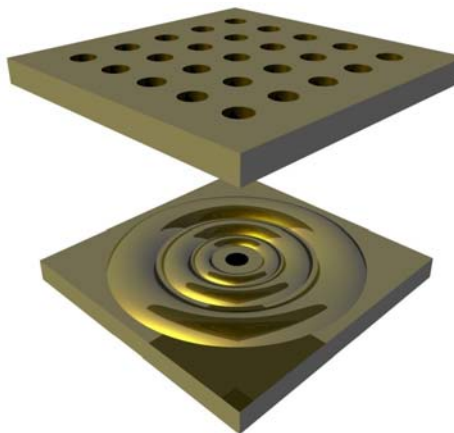


Fig. 1. Nanoapertures for EOT. Top: ordered array; bottom: a single aperture with annular surface corrugations.

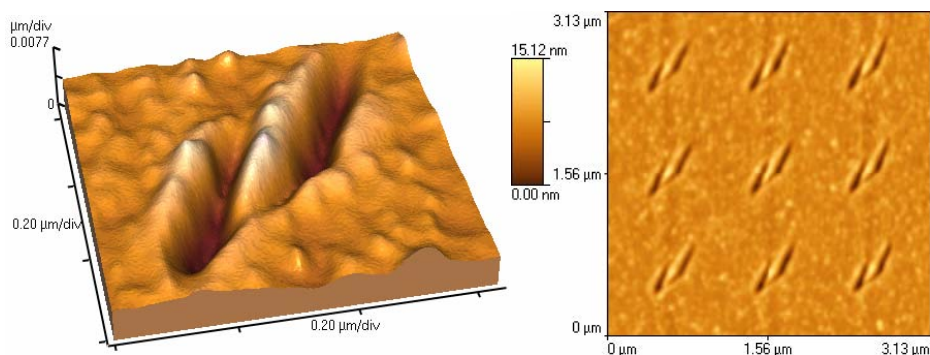


Fig. 1. Experimental nanoapertures in sputtered Ag. Left: An AFM magnified image of a single nanohole. Right: 2D scan of ordered V-shaped nanoholes

The substrate for our samples was double polished single crystalline Si spin-coated by positive photoresist 400 nm thick. A 20 nm thick silver layer was RF sputtered over unbaked photoresist. We utilized scanning probe nanolithography on our Veeco Autoprobe CP-Research atomic force microscope (AFM) – details can be found in [7]. The fabricated structures were characterized by AFM (Fig. 6). The design, dimension and material of the structures are fully compatible with those used for adhesion promotion [4] and are thus usable for sensor enhancement.

Conclusion

The paper presents a method to increase sensitivity of biosensors and chemical sensors by utilizing duality of EOT structure patterning and surface patterning utilized for analyte adhesion promotion. The analyte is located within a small volume near the nanohole (where illumination is confined), i.e. its dimensions are constrained along all three axes. This means that much smaller amounts of analyte are detectable in the case of EOT sensor than by the standard SPR devices. The method could enable fabrication of all-optical sensors with multiplexed readout.

References

- [1] J. Homola, S. S. Yee, G. Gauglitz, *Sensors and Actuators B*, 1999, **54**, 3-15.
- [2] T. W. Ebbesen, H. J. Lezec, H. F. Ghaemi, T. Thio, P. A. Wolff, *Nature*, 1998, **391**, 667-669.
- [3] A.G. Brolo, R. Gordon, B. Leathem, K. L. Kavanagh, *Langmuir*, 2004, **20**, 4813-4815.
- [4] Z. Ademovic, P. Kingshott in: *Surfaces and Interfaces for Biomaterials*, P. Vadgama (Ed.), Woodhead Publishing Limited, Cambridge, 2004.
- [5] J. W. Lussi, R. Michel, I. Reviakine, D. Falconnet, A. Goessl, G. Csucs, J. A. Hubbell, M. Textor, *Progress in Surface Science*, 2004, **76**, 55-69.
- [6] A. K. Sarychev, V. A. Podolskiy, A. M. Dykhne, V. M. Shalaev, *IEEE J. Quant. Electr.*, 2002, **38**, 956-963.
- [7] Z. Jakšić, D. Vasiljević-Radović, M. Maksimović, M. Sarajlić, A. Vujanić, Zoran Djurić, *Microelectronic Engineering*, 2006, **83**, 1786-1791.

Yb³⁺ DOPED DYPHILLOSILICATES PREPARED BY THERMALY INDUCED PHASE TRANSFORMATION OF ZEOLITES

B. Nedić¹, V. Dondur¹, A. Kremenović² and R. Dimitrijević²

¹*Faculty of Physical Chemistry, Studentski trg 12-16, Belgrade, Serbia (bojana@ffh.bg.ac.yu)*

²*Faculty of Mining and Geology, Djusina 7, Belgrade, Serbia*

Abstract

Aluminosilicate materials doped with rare earth ions are perspective materials for various applications. In this work, Ba- exchanged LTA zeolite samples has been synthesized and it has been doped with Yb³⁺. All synthesized materials have been annealed at 1000 °C. By the X-Ray Powder Diffraction (XRPD), it has been confirmed that the specimens have been composed of dyphillosilicates. Doped and non-doped samples have been characterized with Differential Scanning Calorimetry (DSC) and Infra-Red Spectroscopy (IR).

Introduction

Crystal phases, as well as glasses doped with rare earth ions are widely used materials. Rare earth glasses are used in lasers, sensors and radiation shield glasses [1]. This type of materials have been extensively investigated [2, 3]. BaMgAl₁₀O₁₇ doped with Eu²⁺ is mostly used in plasma display panels (PDPs) as a blue phosphor. This particular material is unstable, and efforts are made to find adequate substitution. It has been reported that new, promising materials for PDP could be dyphillosilicate and celsian doped with Eu²⁺ [4, 5]. The goal of this work is to characterize new system, Ba-dyphillosilicate phase doped with Yb³⁺.

Experimental

In this work, Ba-dyphillosilicate doped with Yb³⁺ has been synthesized. The initial substance was sodium form LTA zeolite structure type (Aldrich). Fully exchanged Ba-LTA has been prepared by aqueous ion-exchange procedure, as previously published [6]. The amount of residual Na⁺ ions has been checked by Varian Spectra AA55 Atomic Absorption Spectrophotometer (AAS). Ba-LTA has been doped by Yb³⁺, also by ion-exchange. Yb³⁺ have been obtained from Yb₂O₃, dissolving in HCl. The initial Ba-LTA as well as doped Ba-LTA sample have been thermally treated 4 hours at 1000 °C (from this point on, these samples would be denoted as BAS and BAS:Yb³⁺, respectively). XRPD patterns were collected on a Philips PW-1710 automated diffractometer using a Cu tube operated at 40 kV and 30 mA. The instrument was equipped with a diffracted beam curved graphite monochromator and Xe-filed proportional counter. A fixed 1° divergence and 0.1° receiving slits were used. Silicon powder was used as a standard for calibration of diffractometer. Diffraction data were collected in 5-120° 2θ region counting at every 0.02° for 14.30 seconds. Crystal structures of the samples have been refined by Rietveld method. The software package FullProf has been used [7]. Thermal properties of the synthesized samples have been

analyzed with Differential Scanning Calorimetry (DSC). The DSC has been performed on Setaram DSC 111 thermal analyzer (scanning rate 10 K/min) in He atmosphere. The IR measurements were made on a Perkin-Elmer 93 spectrophotometer using the KBr pellet technique, in the frequency interval 300-800 cm^{-1} .

Results and Discussion

The Rietveld refinement results on BAS:Yb^{3+} are presented in Figure 1. The sample has dyphillo-silicate form and BAS:Yb^{3+} crystal structure has been refined in the space group $P\bar{3}$ (No. 147). Also, BAS sample has dyphillo-silicate form. Values of unit cell parameters and unit cell volume for BAS and BAS:Yb^{3+} samples are shown in Table 1.

Table 1. Unit cell parameters and volume for BAS and BAS:Yb^{3+}

	BAS	BAS:Yb^{3+}
$a_0/\text{\AA}$	5.29645	5.29750(4)
$c_0/\text{\AA}$	7.7887	7.7849(1)
$V/\text{\AA}^3$	189.220	189.203(3)

It could be seen that these values are not significantly changed, what was expected because sample has been doped. Formula, calculated from the occupation factors, is: $\text{Ba}_{0.76}\text{Yb}_{0.11}\square_{0.13}\text{Al}_{2.1}\text{Si}_{1.95}\text{O}_8$ (\square denotes vacancies).

From the values of the agreement factors ($R_B=3.40\%$, $R_F=3.12\%$ and $\chi^2=1.50$), it could be concluded BAS:Yb^{3+} that the structure has been refined to the good agreement.

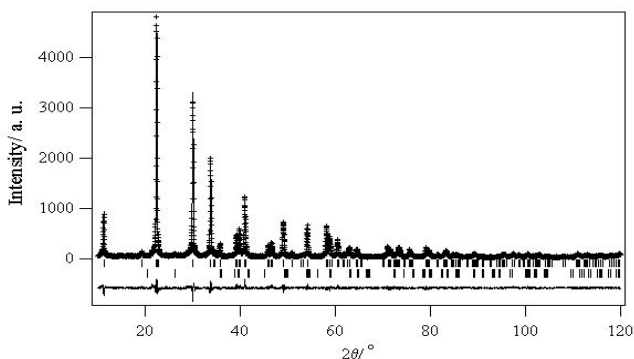


Fig. 1. Comparison of observed (marks) and calculated (line) intensities for BAS:Yb^{3+} . The difference pattern appears below. The vertical bars, at the bottom, indicate reflection position.

DSC results for BAS and BAS:Yb^{3+} are presented in the Fig. 2. BAS exhibits $\alpha \leftrightarrow \beta$ phase transformation at 339 $^{\circ}\text{C}$, which can be seen as a peak in DSC diagram, and the enthalpy of this transformation is 0.6506 J/g. BAS:Yb^{3+} does not show any peak in DSC. It could be concluded that Yb ions favorite formation of only one type of hexacelsian structure.

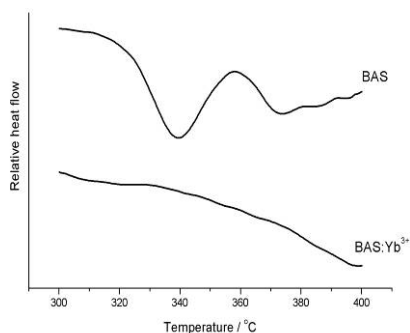


Fig. 2. DSC results for BAS and BAS:Yb³⁺ samples

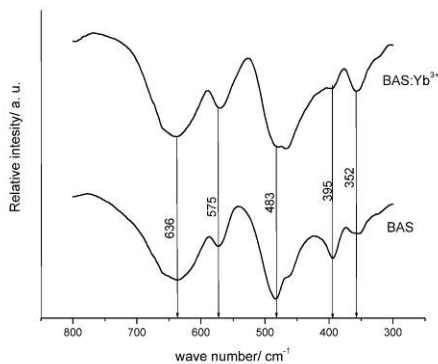


Fig. 3. IR absorption spectra for BAS and BAS:Yb³⁺ samples

IR absorption spectra for BAS and BAS:Yb³⁺ samples are presented in the Fig. 3. It could be observed that the all bands in BAS:Yb³⁺ spectra are slightly shifted comparing to those belonging to BAS. The bands on 483, 395 and 352 cm⁻¹, corresponding to internal and external ring vibrations, show different intensity in BAS:Yb³⁺ spectrum, than in BAS spectrum.

The results show differences in the BAS:Yb³⁺ and BAS structures, what is in agreement with previously published results [4, 5]

Acknowledgment

The authors would like to thank Ministry of Science and Environment Protection of Republic of Serbia for financial support within the framework of the project 142055.

References

- [1] J. Marchi, D. S. Morais, J. Shneider, J.C. Bressiani, A. H. A Bressiani, *J. Non-Cryst. Solids*, 2005, **351**, 863-868.
- [2] J. E. Shelby, J. T. Kohli, *J. Am. Ceram. Soc.*, 1990, **73** [1], 39-42.
- [3] N. J. Clayden, S. Esposito, A. Aronne, P. Pernice, *J. Non-Cryst. Solids*, 1999, **258**, 11-19.
- [4] W. B. Im, Y. Kim, D. Y. Jeon, *Chem. Mater.*, 2006, **18**, 1190-1195.
- [5] A. Kremenovic, Ph. Colomban, B. Piriou, D. Massiot, P. Florian, *J. Phys. Chem. Solids*, 2003, **64**, 2253-2268.
- [6] V. Dondur, R. Dimitrijević, A. Kremenović, Lj. Damjanović, M. Kićanović, H. M. Cheong, S. Macura, *Materials Science Forum*, 2005, **494**, 107-112.
- [7] Rodriguez-Carvajal J., FullProf.2k (Version 2.40-May 2003-LLB JRC) Computer program; www-llb.cea.fr/fullweb/fp2k/fp2k.htm.

PHASE EVOLUTION OF Si_3N_4 WITH Mg-EXCHANGED ZEOLITE ADDITIVE

M. Pošarac¹, S. Bošković¹, A. Devečerski¹, T. Husović² and B. Matović¹

¹INN Vinča, Material Science Lab. 11001 Belgrade

²TMF, Belgrade

Abstract

This paper deals with the chemical reactions and phase evolution during pressureless sintering of Si_3N_4 with Mg-exchanged zeolite as sintering additive. The XRD data show that the first MgO-rich liquid forms at as low as 1250 °C, which as a consequence results in a significant reduction of sintering temperature. At 1300 °C the β - Si_3N_4 phase had disappeared indicating its dissolution into the liquid phase. At 1500 °C the secondary phase had been completely converted into a glassy phase, however, no phase transformation from α - Si_3N_4 to β - Si_3N_4 had taken place. Thus the composition of this material consists of α - Si_3N_4 embedded in magnesium silicon oxynitride glassy phase.

Introduction

Since silicon nitride is a covalently bonded solid compound. The self-diffusivities of Si and N in pure Si_3N_4 are very low [1]. Therefore it cannot be sintered to full density without additives that form liquid phase upon firing [2]. Various types of sintering additives have been used which react with the adherent silica on the powder surface of Si_3N_4 and form a melt and thus promote liquid phase sintering [3]. The liquid acts as a medium for mass transport during densification. Thus, liquid-phase sintering is the only method applied for densification of Si_3N_4 ceramics. Magnesium aluminosilicate is known to melt at relatively low temperatures and is, in addition a low cost material. Moreover, $\text{MgO}\cdot\text{Al}_2\text{O}_3\cdot n\text{SiO}_2$ (Mg-Z) glasses can be crystallized easily [4] being a base for the development of good mechanical properties.

Mg-Z can be prepared from different sources, but the synthesis route starting from ion-exchanged zeolites offers several advantages [5]. This route represents a low-cost method that leads to formation of an amorphous phase with high chemical reactivity compared to crystalline phases. Ion-exchanged zeolites (Ba- and Li-zeolite) have been the only used additives for Si_3N_4 composite materials [6, 7], so far. No study has yet been performed by using Mg-exchanged zeolite as sintering additive for pressureless sintering of Si_3N_4 , although some good mechanical properties may be expected in the compositions containing Mg ions.

Experimental

The starting powders were commercial Si_3N_4 (UBE) and homemade Mg-exchanged zeolite (Mg-Z) powder. The Mg-exchanged zeolite was produced by ion exchange using water solution of MgCl_2 . The procedure was repeated several times to ensure

complete substitution of Mg for Na in synthetic LTA-zeolite. It was found that Mg-Z powder become XRD amorphous after heat treatment at 850 °C. Si_3N_4 powder with 10 wt% of amorphous Mg-Z powder was prepared by vibro milling in the presence of alcohol. Green pellets were obtained by applying cold uniaxial pressing under 100 MPa. Sintering was accomplished in a graphite-heated furnace under 0.1 MPa nitrogen atmospheres, in the temperature range from 900° to 1500 °C, with a heating rate of 100°C/min. The phase analysis of the quenched samples was performed by X-ray diffraction (XRD) using $\text{CuK}\alpha$ radiation.

Results and Discussion

The phase evolution of samples with 10 wt% of Mg-Z additive after heat treatments at temperatures between 900° and 1500 °C for 5 min is shown in Fig. 1. The main crystalline phase is α - Si_3N_4 for all stages of annealing. At 900 °C the initial Mg-Z sintering additive is present in an amorphous state due to collapse of Mg-zeolite structure at about 850 °C. At 1300 °C the β - Si_3N_4 has completely disappeared indicating its dissolution into the liquid phase. Also, the presence of a new phase (SiO_2) is associated with excess silica, which had crystallized from the liquid during cooling.

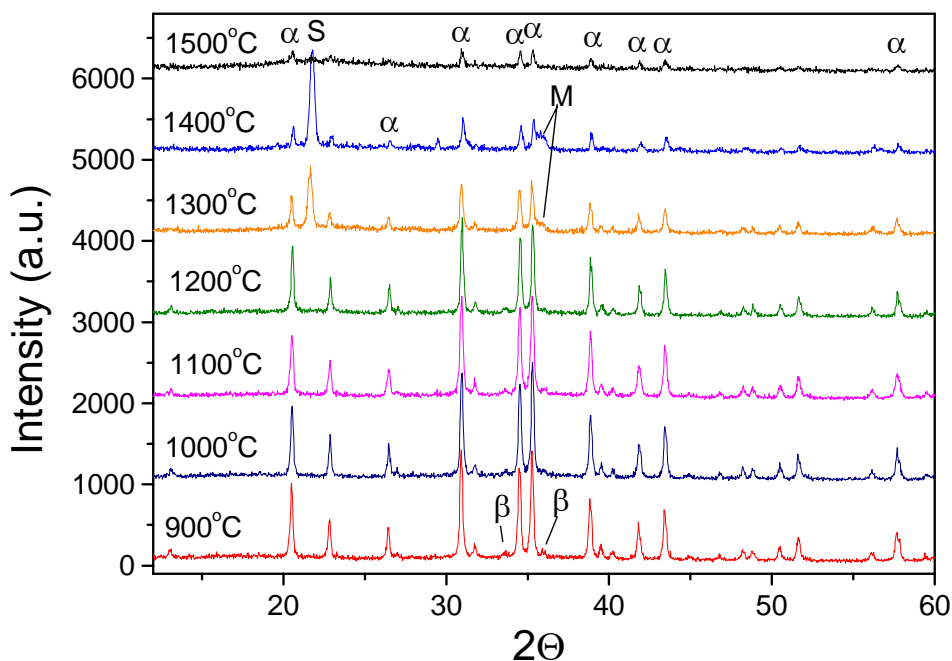


Fig. 1. Phase evolution during heating of mixture ($\text{Si}_3\text{N}_4/\text{Mg-Z}$) at different temperature for 5 min of soaking time.
(α - Si_3N_3 , β - Si_3N_3 , S- SiO_2 , M-Mg-Al-Si-N-O).

Thus, the appearance of the liquid in the sample starts between 1200° and 1300 °C. According to the phase diagram the lowest eutectic temperature in the system MgO-

$\text{Al}_2\text{O}_3\text{-SiO}_2$ is 1345 °C [8], however, the overall liquid forming temperature is lower than the nominal eutectic temperature because of the present nitrogen in the liquid phase. This confirms that Mg-Z acts as a very good flux and a solvent for Si_3N_4 which is also a prerequisite for a good sintering additive.

At 1300 °C, XRD pattern shows remarkable broadening and decrease of intensity of the diffraction lines especially in the region around 35–36° 2 θ which can be explained by the dissolution of $\alpha\text{-Si}_3\text{N}_3$ in the liquid phase based on Mg-Z composition. Thus, resulting liquid belongs to Mg-Al-Si-N-O system. The result also indicates that nucleation and crystallization of this liquid takes place in the temperature region at the onset of liquid formation. However, the secondary phase starts to re dissolve into the liquid as the temperature exceeds 1400 °C. Therefore, the total liquid content increases substantially and at 1500 °C, which upon cooling formed amorphous glassy phase. At this temperature the crystalline $\alpha\text{-Si}_3\text{N}_4$ phase, traces of silica as well as, oxynitride glassy phase are the only present phases.

Having in mind that $\alpha\text{-Si}_3\text{N}_4$ has a very high hardness as does magnesium silicon oxynitride glassy phase [2], the final ceramics might have promising mechanical properties. in spite of the low sintering temperature.

Conclusion

On the basis of the experimental results, it can be concluded that that Mg-exchanged zeolite acts as a very good solvent for Si_3N_4 resulting in silicon oxynitride glassy phase. Composition of material sintered at 1500 °C has potential for enhanced hardness.

Acknowledgement

We acknowledge the support of the project No. 142016 by the MSEP of Serbia.

Reference

- [1] F. Riley, *J. Am. Ceram. Soc.*, 2000, **83**, 245.
- [2] G. Petzow and M. Herrmann, in *Structure and Bonding*, Springer-Verlag, Berlin, 2002, **102**, 51.
- [3] G. Ziegler, J. Heinrich, G. Wötting, *J. Mater. Sci.*, 1987, **22**, 3041.
- [4] Z. Panek, *J. Mater. Sci.*, 1994, **29**, 5383.
- [5] V. Dondur, R. Dimitrijevic, *J. Solid State Chem.*, 1986, **63**, 46.
- [6] S. Boskovic, D. Kosanovic, V. Dondur, R. Dimitrijevic, *Ceram. Int.*, 2000, **26**, 33.
- [7] B. Matovic, G. Rixecker, F. Aldinger, *Proceedings 10th International Ceramics Congress, Firenca (2002)* 183.
- [8] M. Keith, J. Schairer, *J. Geol.*, 1952, **60**, 182.

SURFACE MODIFICATIONS OF TIN COATING BY PULSED TEA CO₂ LASER

M. S. Trtica and B. M. Gaković

*VINČA Institute of Nuclear Sciences, P.O. Box 522,
Belgrade, Serbia (etrtica@vin.bg.ac.yu)*

Abstract

Interactions of a TEA CO₂ laser, 100 ns pulse, with titanium nitride (TiN) coating deposited on AISI D2 steel, were studied. The energy absorbed from the laser beam is partially converted to thermal energy, which generates a series of effects such as melting, vaporization of the molten material, shock waves, etc. Morphological modifications of the titanium nitride surface can be summarized as follows: (i) ablation of the TiN coating in the central zone of the irradiated area with creation of grainy and cracked features, (ii) appearance of a hydrodynamic structure like resolidified droplets of the material in the periphery region. The process of sample irradiation was accompanied by the appearance of plasma. Color modifications of the sample, upon laser irradiation, indicate possible chemical changes like oxidation.

Introduction

Surface modification studies of titanium-based ceramic coatings, especially TiN deposited on steel substrates, by various types of energetic beams including laser beam are of great fundamental and technological interest. The last decade saw most of the studies of laser beam interaction with TiN. Beams of the Nd:YAG-[1], Ti:Sapphire-[2], excimer-XeCl-[3], and CO₂-[3,4] lasers have so far been used for this.

Interactions of pulsed TEA CO₂ [3,4] laser beams with TiN are not extensively reported in literature. TiN has extraordinary physical and chemical properties like a high melting point, thermodynamic stability, high hardness, etc. From these reasons it is attractive for industry, nuclear technology, bio-medicine, etc.

The present paper deals with effects of a pulsed infrared laser emitting at ~10.6 μm (TEA CO₂ laser) on TiN coatings deposited on high quality steel AISI D2. Special attention was paid to morphological surface modifications of TiN.

Experimental and Discussion

The TiN coatings, thickness of 10 μm, were deposited on AISI D2 steel substrate by CVD method. Sample irradiations were performed with the laser beam focused by a KBr lens of 6.0 cm focal length. The angle of incidence of the laser beam with respect to the surface plane was 90°. The irradiation was carried out in air atmosphere. The TEA CO₂ laser, during the experiment, was operated typically in the TEM₀₀ mode. Conventional (1 atm) CO₂/He gas mixtures were used for the laser operation. The FWHM of the laser pulse was about 100 nanoseconds. Various analytical techniques

were used for characterization of the samples: X-ray diffraction, optical microscopy, and scanning electron microscopy (SEM).

Laser induced TiN morphological changes showed dependence on the beam characteristics: primarily on the laser energy density (LED), peak power density, pulse duration, number of pulses. Morphological changes of the TiN after 500 laser pulses are presented in Figures 1 and 2. The LED of 25 J/cm^2 induces significant surface modifications and they can be presented as follows: (i) Partially ablation of the

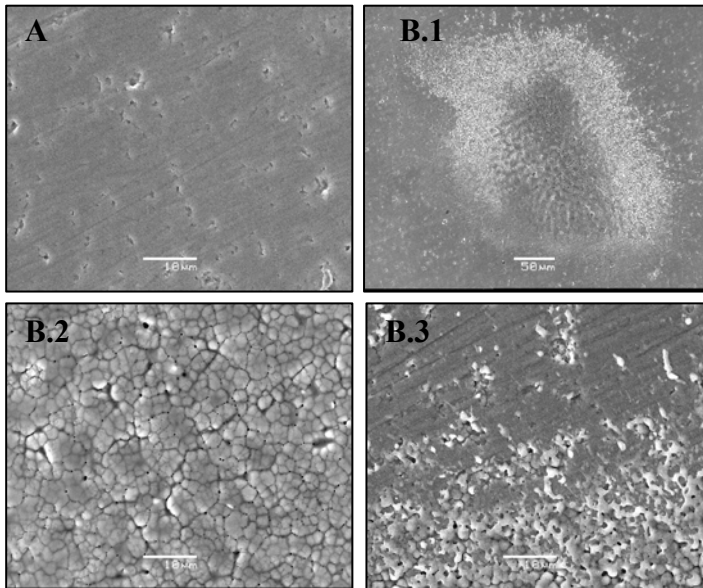


Fig. 1. TEA CO_2 laser-induced morphology changes of the TiN coating (SEM). (A)- The TiN coating prior to the laser action; (B)- TiN coating after 500 laser pulses. B.1, B.2 and B.3, entire spot, center and periphery of the damage area, respectively (LED, 25 J/cm^2).

coating in the central part. In this case the processes of rapid heating and cooling led to cracking (Fig.1, B2) as well as appearance of grainy structure (Fig.2, B) in the coating. Average size of grain was about 1.5 micron. (ii) roughly two zones in the periphery can be distinguished (Fig.1, B1 and B3). In these zones hydrodynamic effects resembling resolidified material are visible.

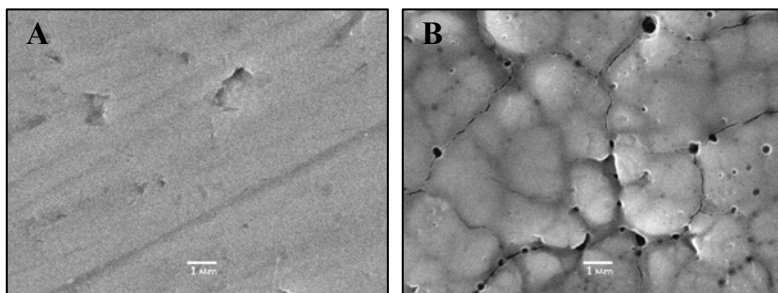


Fig. 2. TEA CO₂ laser-induced morphology changes of the TiN coating (SEM). (A)- The TiN coating prior to the laser action; (B)- The center after 500 laser pulses (LED, 25 J/cm²).

A form of spark-like plasma started to appear after about 20 cumulated laser pulses. Generally, the TEA CO₂ laser radiation interaction with TiN surface is complex. In a simple approximation the energy absorbed from the laser beam is converted to thermal energy, which causes melting, vaporization of the molten material, dissociation or ionization of the vaporized material and shock waves in the vapor and the solid.

Conclusion

A study of morphological changes of titanium nitride coating, deposited on AISI D2 steel, induced by a TEA CO₂ laser is presented. It is shown that laser energy density of 25 J/cm² was sufficient to induce structural changes in the target. The energy absorbed from the CO₂ laser beam is mainly converted to thermal energy, causing melting, vaporization, etc. The morphological modifications of the TiN coating can be considered as: (i) ablation of the coating in the central zone of the irradiated area with creation of grainy and cracked changes, (ii) appearance of a hydrodynamic feature like resolidified material in the surrounding peripheral zone. Upon laser irradiation the color modifications of the target indicate possible chemical changes, resembling oxidation.

Acknowledgement

This research was financially supported by the *Ministry of Science and Environmental Protection of the Republic of Serbia*, Contract No. 142065.

References

- [1] T.V. Kononenko, S.V. Garnov, S.M. Pimenov, V.I. Konov, V. Romano, B. Borsos, H.P. Weber, *Appl. Phys. A*, 2000, **71**, 627-631.
- [2] J. Bonse, H. Sturm, D. Schmidt, W. Kautek, *Appl. Phys. A*, 2000, **71**, 657-665.
- [3] M.S. Trtica, V.F. Tarasenko, B.M. Gakovic, A.V. Fedenev, Lj.T. Petkovska, B.B. Radak, E.I. Lipatov, M.A. Shulepov, *Appl. Surf. Science*, 2005, **252**, 474-482.
- [4] B.M. Gakovic, M.S. Trtica, T.M. Nenadovic, B.J. Obradovic, *Thin Solid Films*, 1999, **343-344**, 269-272.

SYNTHESIS OF CRYSTALLINE SILICON OXYNITRIDE COMPOSITES

A. Egelja, J. Dukić, S. Bošković, A. Radosavljević-Mihajlović and B. Matović

Vinča Institute of Nuclear Sciences, Material Science Lab., Belgrade, Serbia

Abstract

Silicon oxynitride / silicon nitride ($\text{Si}_2\text{N}_2\text{O}/\text{Si}_3\text{N}_4$) ceramics have been prepared from Si_3N_4 powder and amorphous silica (SiO_2) by hot pressing at different temperature. It was found that material sintered at lower temperature exhibit fine composite structure composed of equiaxed $\alpha\text{-Si}_3\text{N}_4$ grains and $\text{Si}_2\text{N}_2\text{O}$ crystals. At higher temperature the growing of $\text{Si}_2\text{N}_2\text{O}$ particles as well as phase transformation from $\alpha\text{-Si}_3\text{N}_4$ to $\beta\text{-Si}_3\text{N}_4$ phase take place.

Introduction

The ceramic silicon oxynitride ($\text{Si}_2\text{N}_2\text{O}$) has for the most part been considered as an inconvenient and undesirable by-product sometimes formed during the production of Si_3N_4 . However, in recent years the applications of $\text{Si}_2\text{N}_2\text{O}$ as a structural ceramic has begun to be considered owing to the excellent high temperature properties and chemical inertness of the material [1]. The refractory behavior of the $\text{Si}_2\text{N}_2\text{O}$ is explained by much better stability in oxidizing environments at high temperature than the Si_3N_4 material [2].

A convenient method for the formation of the $\text{Si}_2\text{N}_2\text{O}$ has yet to be established and it is for this reason that researchers have examined many alternative routes for its production. In this work $\text{Si}_2\text{N}_2\text{O}$ materials have been prepared by direct reaction between the two components:



It is well known that reaction (1) is very sluggish and sintering additives like Al_2O_3 and Y_2O_3 have to be added in order to enhance the reaction rate by forming a liquid phase [3]. As a silica source, usually is used crystalline quartz, however we have used amorphous silica powder.

The intention of this paper is to study the sintering reaction between Si_3N_4 and very reactive amorphous silica without using additive.

Experimental

Starting material for this investigation was a mixture of SiO_2 and Si_3N_4 (UBE) with the quantitative ratio 1:1. This mixture was treated in the vibratory mill for 2 h in the presence of liquid ethanol. The green bodies were heated by hot pressing in the graphite mould with the applied pressure of 25 MPa at $1400^\circ\text{C}/4$ h for the first sample and $1750^\circ\text{C}/1$ h for the second one. The reaction products were analyzed by XRD using diffractometer with $\text{CuK}\alpha$ as the target., while mechanical characterization included

Vickers hardness and toughness measurements. Density was determined by standard Archimedes method. Micrographs were obtained with a Philips scanning electron microscope (SEM).

Results and discussion

Fig. 1. shows the evolution of the crystalline phases formed as a function of the reaction temperature. At low temperature (1400 °C) there are two phases: $\text{Si}_2\text{N}_2\text{O}$ and $\alpha\text{-Si}_3\text{N}_4$ with 30 wt% and 70 wt% respectively. This indicates that $\text{Si}_2\text{N}_2\text{O}$ is obtained by direct reaction and without intermediate stages. At higher sintering temperature (1750 °C) the phase transformation from $\alpha\text{-Si}_3\text{N}_4$ to $\beta\text{-Si}_3\text{N}_4$ phase has already taken place. The amount of $\text{Si}_2\text{N}_2\text{O}$ slightly increases whilst the intensity of $\alpha\text{-Si}_3\text{N}_4$ is significantly reduced.

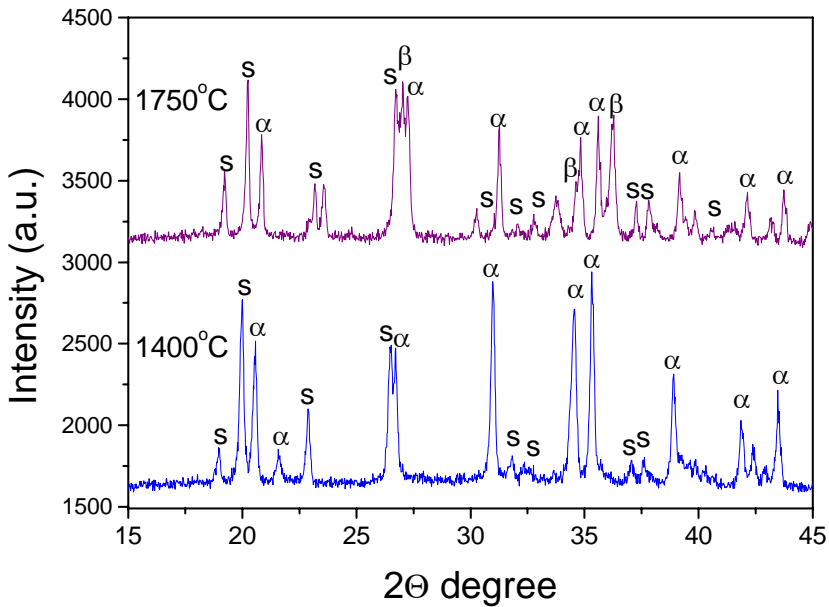


Fig. 1. XRD patterns of samples hot-pressed at 1400 °C and 1750 °C.
S- $\text{Si}_2\text{N}_2\text{O}$, $\alpha\text{-Si}_3\text{N}_4$, $\beta\text{-Si}_3\text{N}_4$.

The microstructure of ceramics sintered is shown in Fig. 2. Material sintered at 1400 °C exhibits fine and equiaxed $\alpha\text{-Si}_3\text{N}_4$ grains and very well formed crystals of silicon oxynitride having polyhedral form, which is combination of forms in trigonal system. With increasing sintering temperature the size of the silicon oxynitride particles increased. In the other side, morphology of the growing silicon nitride particles is changed significantly from equiaxed to elongated due to phase transformation from $\alpha\text{-Si}_3\text{N}_4$ to $\beta\text{-Si}_3\text{N}_4$ phase.

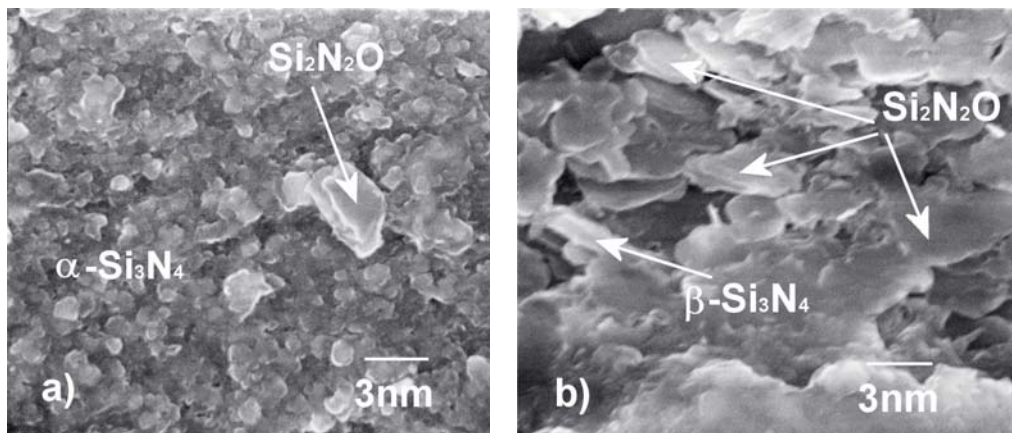


Fig. 2. SEM image of polished and chemical-etched cross section of hot-pressed Si₂N₂O composites produced from the mixture of Si₃N₄/SiO₂ at 1400 °C (a) and 1750 °C (b), respectively. The arrows show Si₂N₂O plate crystals, β-Si₃N₄ elongated grains and α-Si₃N₄ rounded grains.

Conclusion

On the basis of the experimental results, it can be concluded that at low temperature the reaction products are mixture of different oxides and Si₂N₂O with morphology that exhibit well-defined crystal geometry. Increasing temperature, the amount of Si₂N₂O slightly increases whilst the phase transformation from α-Si₃N₄ to β-Si₃N₄ phase takes place.

Acknowledgement

We acknowledge the support of the project No. 142016 by the MSEP of Serbia.

References

- [1] M. Washburn, *Ceram. Bul.*, 1967, **7**, 667-671.
- [2] D. Park, H. Choi, B. Han, H. Kim, D. Lim, *J. Mater. Res.*, 2002, **9**, 2275-2280.
- [3] H. Emoto, M. Mitomo, C. Wang, *J. Eur. Ceram. Soc.*, 1998, **18**, 527-533.

PHASE TRANSFORMATION OF $\text{Co}_{70}\text{Fe}_5\text{Si}_{10}\text{B}_{15}$ AMORPHOUS ALLOY INDUCED BY HEATING

D.M. Minić¹, A.M. Maričić² and R.Z. Dimitrijević³,

¹*Faculty of Physical Chemistry, University of Belgrade, dminic@ffh.bg.ac.yu*

²*Technical Faculty Čačak, University of Kragujevac*

³*Faculty of Mining and Geology, University of Belgrade*

Abstract

We present the results on complex structural changes of the $\text{Co}_{70}\text{Fe}_5\text{Si}_{10}\text{B}_{15}$ amorphous alloy during heating in the temperature range between 20-1000 °C.

Introduction

The amorphous metallic alloys represent a class of materials characterized by structure with absence of the long range order [1, 2]. The amorphous state of matter is, however, structurally and thermodynamically unstable and very susceptible to partial or complete crystallization during thermal treatment or nonisothermal compacting. The latter imposes the knowledge of alloys stability in a broad temperature range due to different crystallization processes [3], which appear during heating.

Experimental Procedure

The X-ray powder diffraction (XRD) patterns were recorded on a Philips PW-1710 automated diffractometer using a Cu tube operated at 40 kV and 30 mA. The instrument was equipped with a diffracted beam curved graphite monochromator and Xe-filled proportional counter.

Results and Discussion

The XRD pattern of initial non-heated amorphous $\text{Co}_{70}\text{Fe}_5\text{Si}_{10}\text{B}_{15}$ alloy is shown in Fig. 1a. The XRD powder patterns obtained after heating of initial alloy are shown in Fig. 1 (curves b-e).

It is obvious from this figure that initial sample undergoes through successive phase transformations during heating treatment. Between ambient temperature and 300 °C, initial alloy retains amorphous properties. Prolonged heating between 400 and 500 °C induces amorphous alloy recrystallization to, at least, two unidentified intermediary crystalline phases (1b and 1c). One of these two phases with characteristic peak at $2\Theta=44.20^\circ$, is more abundant. This peak represents the (111) interplanar distance of Co-rich FCC cubic crystal lattice. The phase is always present at 400 °C, Fig. 1b, which means that its crystallization from amorphous matrix started earlier between 300 and 400°. In other words, thermally induced elemental segregation in amorphous ribbon always starts in aforementioned temperature region.

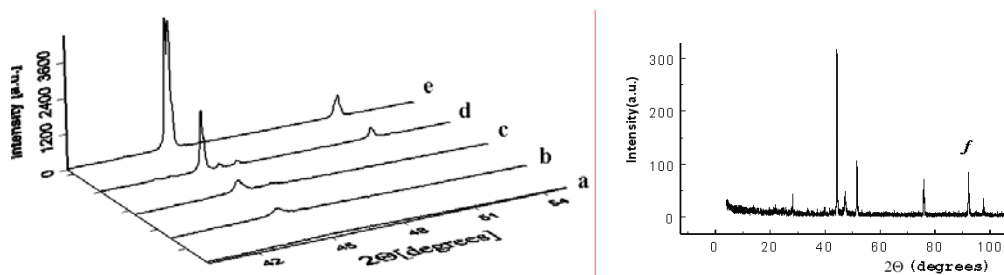


Fig. 1. Thermally induced phase evolution of the amorphous $\text{Co}_{70}\text{Fe}_5\text{Si}_{10}\text{B}_{15}$ alloy: a) initial alloy at ambient temperature; b) heated at 400 °C for 20 minutes; c) heated at 500 °C for 20 minutes; d) heated at 600 °C for 20 minutes; e) heated at 700 °C; f) heated at 1000 °C for 20 minutes.

Another growing intermediary phase is characterized by appearance of small peak at $2\theta=45.68^\circ$, Fig. 1c, which could not be indexed on FCC symmetry. The inspection of JCPDS[6] data base shows that discussed phase is the most similar to Co pattern (file card No. 5-0727) having hexagonal symmetry. It is important to notice that the samples heated at 400 and 500°C are still characterized by presence of considerable quantity of amorphous matter. However, we concluded from grain size measurements that temperature increase influenced directly growth of Co-rich cubic alloy. This is confirmed by crystallite size measurements at peak $2\theta=44.20^\circ$. Obtained values for $\langle D_{111} \rangle$ 125 Å; 165 Å and 610 Å for ribbons heated at 400, 500 and 600 °C, respectively; speak in favor of accelerated crystal growth between 400 to 600 °C temperature range, Fig.1 (curves b-d). The obtained data can be interpreted in terms of crystallochemical changes from nanostructured or strongly disordered to well ordered crystalline state, which have direct influence on physico-chemical characteristics of alloys. The complexity of heating process and dependence on different parameters clearly show our further considerations. Fig.1 (curve d) represents powder pattern of $\text{Co}_{70}\text{Fe}_5\text{Si}_{10}\text{B}_{15}$ alloy heated at 600 °C. Its basic characteristic is absence of amorphous substance. That means that recrystallization process i.e. reorganization of initially amorphous alloy into crystalline state is completely finished at 600 °C. In the phase composition of alloy obtained at this temperature, the so called Co-rich FCC phase is quantitatively dominant. The second unidentified crystalline phase, which started to grow between 400 and 500 °C, is present in traces, Fig.1 (curves c and d). The phase has the strongest peak at $2\theta=45.68^\circ$ and its optimal stability conditions correspond to temperature range between 600 and 650 °C. This conclusion is supported by phase instability at higher temperatures. Upon heating at 700 °C, the phase disappeared completely, whereas the FCC Co-rich phase stays stable, Fig.1e.

Phase analysis of XRD patterns obtained after thermal treatment of the sample between 700 and 1000 °C shown in Fig.1 (curves e and f) revealed an interesting order-disorder phenomena connected with dominant Co-rich FCC phase. This is manifested by splitting of all measured peaks in XRD pattern. This unexpected result indicates that FCC Co-rich phase undergoes additional order -disorder processes. Upon heating at 700 °C this is segregated into two FCC Co-rich phases characterized by different

cell dimensions like $a_I=3.5476(5)$ Å and $a_{II}=3.5384(6)$ Å. These results suggest following conclusions. If we compare unit cell dimensions mutually and compared to a FCC pure Co metal ($a=3.544$ Å, JCPDS card file No.15-0806 [6]), it is obvious that FCC Co-rich-I phase has greater (expanded), whereas FCC Co-rich-II phase has smaller (contracted) unit cell in relation to pure Co unit cell. These results undoubtedly speak in favor of Co metal isomorphous replacement by Fe, Si and B atoms and order-disorder phenomena in both segregated alloy phases.

Conclusion

The $\text{Co}_{70}\text{Fe}_5\text{Si}_{10}\text{B}_{15}$ amorphous alloy retains its amorphous structure up to near 400°C . Prolonged heating over 400°C initiates structural changes of the starting alloy. They are manifested by thermally induced atom interdiffusion accompanied by its elemental segregation and simultaneous crystallization. Grain size XRD measurements show that crystallization processes starts at near 400°C with nanosized crystallites. Their growth is temperature dependent. Recrystallization processes between 400 and 500°C are very complex and could not be completely resolved. However, in that temperature range a multiphase crystallization and phase transformation processes start simultaneously. They continue almost up to near 700°C , where two various FCC Co-rich phases are formed. Its XRD investigations showed that they are quantitatively dominant and stable at 1000°C . The results of unit cell dimension measurements, indirectly confirm its different chemical composition and final atomic segregation of initial amorphous alloy into a composite material.

References

- [1] J.D. Bernal, *Nature*, 1960, **185**, 68.
- [2] S. Takayma, *J. Mater. Sci.*, 1976, **11**, 164.
- [3] U. Köster and U. Herald, "Crystallization of metallic glasses", Springer, New York, 1981, p.225-259.
- [4] R.G. Garvey, *Powder Diffr.*, 1986, **1**, 114.
- [5] S. Krumm, *Materials Science Forum*, 1996, **228-231**, 183.
- [6] Joint Commity for Powder Diffraction Standards, file cards No. 15-0806 and 5-0727.

NUCLEATION BEHAVIOR OF POTASSIUM TITANIUM GERMANATE GLASS STUDIED BY DIFFERENTIAL THERMAL ANALYSIS

S. R. Grujić¹, N. S. Blagojević¹, M. B. Tošić²,
V. D. Živanović² and J. D. Nikolić²

¹*Faculty of Technology and Metallurgy, 4 Karnegijeva St., 11000 Belgrade, Serbia*

²*Institute for Technology of Nuclear and other Mineral Raw Materials,
86 Franchet d'Esperey St, Belgrade, Serbia*

Abstract

The nucleation behaviour of the potassium titanium germanate glass was studied by differential thermal analysis. The temperature of the maximum nucleation rate $T_n^{\max} = 585$ °C was determined from the plot of crystallization peak height, δT_p and inverse of crystallization peak temperature, T_p^{-1} as a function of the nucleation temperature, T_n .

Introduction

Crystallization in a glass starts with the formation of nuclei that are able to grow further. Knowing the temperature ranges of nucleation and crystal growth has scientific and technological importance. These data are important for understanding the stability of a glass where the crystallization must be avoided entirely as well as for other applications where crystallization is desired. For the investigation of nucleation by commonly used isothermal method, it is necessary to count the number of nuclei in the glass that is thermally treated at different temperatures for different time making this method time consuming and laborious. Methods using differential thermal analysis to investigate nucleation can be performed more easily, in less time, with smaller amounts of samples [1]. In this work the results of determination of the temperature of maximum nucleation rate in potassium titanium germanate glass by differential thermal analysis is presented.

Experimental

The glass with composition $K_2O \cdot TiO_2 \cdot 3GeO_2$ [2] was prepared by melting a homogeneous appropriate mixture of the starting materials (GeO_2 , K_2CO_3 , and TiO_2) at 1200 °C for 1 h in a Pt crucible. The melt was cast on a steel plate and cooled in air. Powder X-ray diffraction analysis (XRD) of the quenched melts confirmed it to be vitreous. The X-ray diffraction analysis was performed on a Philips PW- 1710 automated diffractometer using Cu tube operated at 40 kV and 35 mA. The powder glass samples granulation of 0.5-0.63 mm were nucleated at chosen temperatures in the range of 540-610 °C for $t=30$ min. DTA experiments were performed by using previously nucleated samples with heating rate $\nu=10$ °C/min and mass samples $m=100$ mg. DTA curves were recorded on a Netzsch STA 409 EP instrument. The experiments were performed in air, and Al_2O_3 was used as the reference material. To check that

DTA peak height is proportional to the total number of nuclei the experiments with different mass samples $m = 40-100$ mg were performed.

Results and Discussion

The total number of nuclei in a glass can be expressed as:

$$N_t = N_q + N_n + N_g \quad (1)$$

where: N_q - number of as quenched-in nuclei, N_n - number of nuclei formed at nucleation temperature, T_n and N_g - nuclei formed during DTA run. The determination of temperature of the maximum nucleation rate (T_n^{\max}) from DTA method, assumes that DTA peak height (δT_p) is proportional to the total number of nuclei present in the glass sample. The plot of δT_p vs. the mass sample, collected at a heating rate $\nu=10$ °C/min, justifies this assumption (Fig.1). This figure shows the linear dependence of δT_p with the mass sample.

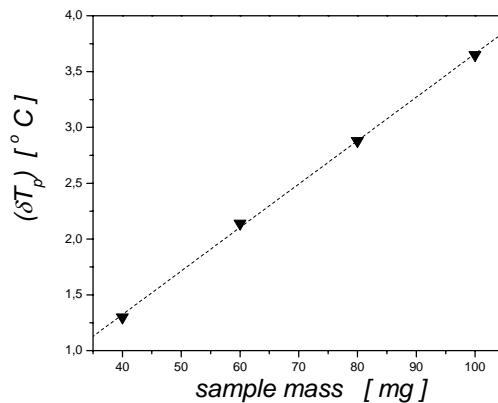


Fig. 1. DTA peak height as a function of the mass sample.

It has been shown theoretically [3, 4] that plot either δT_p and T_p^{-1} as a function T_n yields a curve that closely resembles the nucleation curve for a glass. Experimental values of the maximum height of the exothermic DTA crystallization peak, δT_p , as a function of the nucleation temperature, are shown in Fig. 2. In Eq.1, N_q can be considered as constant for glass samples of the same mass prepared from the same melt, while N_g should be negligibly small and the same because of the same heating rate for the DTA runs. Hence, any change in the height of the DTA peak should result from variation of N_n , which is proportional to the nucleation rate, I , at the nucleation temperature T_n . This means that maximum of the δT_p vs. T_n plot would correspond to the temperature for the maximum nucleation rate T_n^{\max} if there is no overlap of the temperature ranges of nucleation and crystal growth. The shape of the curve in the fig. 2 indicates that in investigated temperature range the I and U overlap in the considerable extent. During the nucleation stage on T_n the part of sample was crystallized so the number of nuclei available for crystallization during following DTA run is lowered. It

is obvious from the figure 2. that there is no available nuclei for crystallization during DTA run after nucleation stage on $T_n=610\text{ }^\circ\text{C}$ ($\delta T_p \rightarrow 0$). The figure 3 presents the dependence of the inverse the DTA peak temperature T_p^{-1} , on the nucleation temperature. It has been shown that the inverse of T_p is proportional to the concentration of nuclei present in the glass [3] and will increase as the number of nuclei increases, so the maximum from the T_p^{-1} vs. T_n plot corresponds to the temperature for the maximum nucleation rate T_n^{\max} . The functional dependence of T_p^{-1} on T_n is similar to that of I on T_n , irrespective of the presence or absence of any overlap between the I and U curves [5]. As may be seen from the Fig. 3 the temperature for the maximum nucleation rate is $T_n^{\max} = 585\text{ }^\circ\text{C}$.

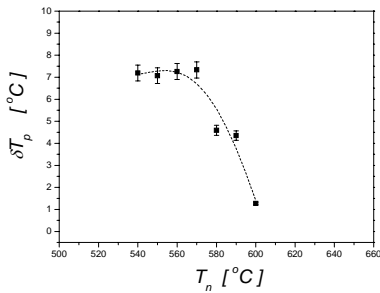


Fig. 2. The plot of the δT_p vs. T_n .

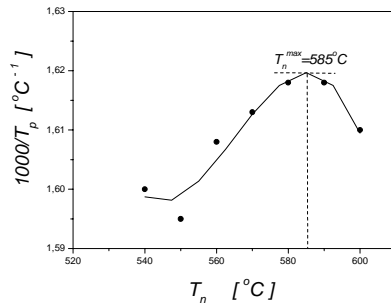


Fig. 3 The plot of the T_p^{-1} vs. T_n .

Conclusion

In this work the nucleation behaviour of $\text{K}_2\text{O}-\text{TiO}_2-3\text{GeO}_2$ glass was studied by DTA method. The linear relation between DTA peak height and mass sample was found and an overlapping of the temperature ranges of nucleation and crystal growth was detected. The maximum nucleation rate was determined as $T_n^{\max} = 585\text{ }^\circ\text{C}$.

References

- [1] C. Ray, D. Day, J. Am. Ceram. Soc., 1990, **73**, 439-442.
- [2] S. Grujić, N. Blagojević, M. Tošić, V. Živanović, B. Božović, J. Thermal. Anal. Cal. (2006) **83** (2) 463-466.
- [3] M. Weinberg, J. Am. Ceram. Soc., 1991, **74**, 1905-1909.
- [4] A. Marotta, A. Buri in: Advances Ceramics, Vol.4, J. H. Simmons, D. R. Uhlmann (Eds.), ACS, Columbus, 1982.
- [5] C. Ray, D. Day, J. Am. Ceram. Soc., 1997, **80**, 3100-3108.

THE EFFECT OF THE FREE ENERGY CHANGE ON CRYSTALLIZATION IN GERMANATE GLASS

M.B.Tošić¹, S.R.Grujić², N.S.Blagojević², V.D.Živanović¹ and J.D.Nikolić¹

¹*Institute for Technology of Nuclear and other Mineral Raw Materials,
86 Franchet d'Esperey St, Belgrade, Serbia*

²*Faculty of Technology and Metallurgy, 4 Karnegijeva St., Belgrade, Serbia*

Abstract

This paper presents the effect of free energy change on crystallization studied by the analyse of nucleation behaviour of germanate glass with 16 (wt%) TiO₂. It was shown that approximation where the heat capacities of liquid and crystalline phases are the same for this glass, is not enough reliable. To calculate ΔG , the determination of ΔC_p is necessary.

Introduction

In a number of studies of the volume crystal nucleation in silicate glasses, the classical nucleation theory was used [1]. According to this theory, the steady-state homogeneous nucleation rate (I) was described by an exponential dependence of two terms: the thermodynamic barrier (W^*) and the kinetic barrier (ΔG_D) for nucleation. The thermodynamic barrier is given [1,2] by $W^* = 16\pi V_m^2 \sigma^3 / \Delta G^2$, where V_m , σ and ΔG are the molar volume of the crystal phase, the crystal/liquid interfacial energy and the molar free energy difference between the liquid and crystal phase, respectively. Because of I on ΔG dependence, the accuracy of ΔG estimation is very important if ΔG is using in the analysis of nucleation phenomena in glasses. In the present work the influence of temperature dependence of ΔG estimated on the nucleation of potassium-germanate glass with 16 (wt%) TiO₂ was investigated.

Experimental

The starting materials used are reagent grade GeO₂, K₂CO₃, and TiO₂. The appropriate batch composition was melted at 1200 °C for 1 h in a Pt crucible. The melts were cast on a steel plate and cooled in air. Powder X-ray diffraction analysis (XRD) (Philips PW-1710), confirmed that the quenched melts were vitreous. The glass samples were transparent, without visible residual gas bubbles. The peak temperature of crystallization T_p and melting T_m as well as crystallization and melting enthalpy of the crystalline phase were determined by DSC run of glass powder (SDT Q600 V7.0 Build instrument). For studying the structure and phase compositions, the bulk glass samples were isothermally treated at selected temperatures for different times. Identification of the phase crystallized and its morphology was performed with the XRD and SEM measurements (Jeol JSM 840)

Results and Discussion

The temperature dependence of ΔG in the undercooled region can be obtained if the heat capacities of the liquid and crystalline phases of the glasses are known. However, the metastable nature of the undercooled phase makes it difficult to obtain the heat capacity data experimentally. For this reason, the estimation of the temperature dependence of ΔG is very important when ΔG is using in analysis of nucleation phenomena. Many attempts have been made to derive analytical expressions for ΔG in different materials. There is no expression for ΔG which is universally applicable and the choice of the approximation depends on the type of material. The difference in free energy between the liquid and crystalline phase for one component system can be approximated by [2,3] :

$$\Delta G = -\Delta H_m (T_m - T) / T_m + \Delta C_p [(T_m - T) - T \ln(T_m / T)] \tag{1}$$

where T_m is the melting temperature, ΔH_m the enthalpy of fusion and $\Delta C_p = C_p^l - C_p^c$ is the difference between the specific heats of undercooled liquid and the crystal. In the case for an ideal behaviour of these phases, $\Delta C_p = 0$ can be assumed which transforms Eqs.1 to :

$$\Delta G = -(\Delta H_m / T_m) (T_m - T) \tag{2}$$

For the silicate glasses as satisfactory approximation (upper bound), Eq (2) was often used. However, there is no enough reliable data for the germanate glasses. Therefore, for this analyse the data obtained from DSC run were used .

Table 1. Parameters used to calculate free energy difference ΔG , determined by DSC measurements

Run	T_p [K]	T_m [K]	ΔH_c [kJ/mol]	ΔH_m [kJ/mol]
DSC	921.16	1308.16	92.8	134.7

From the ratio $\Delta C_p \sim (\Delta H_m - \Delta H_c) / (T_m - T_p)$, ΔC_p was calculated, and the plot of ΔG as function of temperature in the range 500-700°C is shown in Fig.1. As may be seen from Fig.1, the values of ΔG according to Eq(1) ($\Delta C_p \neq 0$) and Eq(2) ($\Delta C_p = 0$) differ,

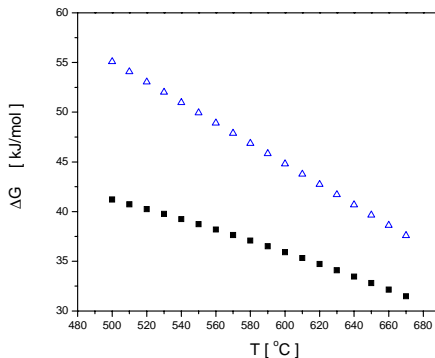


Fig. 1. | ΔG | calculated according to Eq(1) (■) and Eq(2) (Δ)

so that it has the significant affects on the nucleation rate. XRD pattern of the heated glass shows that the composition of crystalline $K_2O \cdot TiO_2 \cdot 3GeO_2$ phase formed is the same as glass. SEM investigation was displayed the presence of volume crystallization with the crystals growth in the form of spherulites that signifies the homogenous nucleation. The steady-state homogeneous nucleation rate is given [2]:

$$I = [A_c T / \eta] \exp(-W^* / kT) \quad (3)$$

where A_c is constant, T is temperature, η is the viscosity and k is the Boltzmann constant. Using η by [4] and ΔG from Eqs(1) and (2), I was calculated, Fig.2.

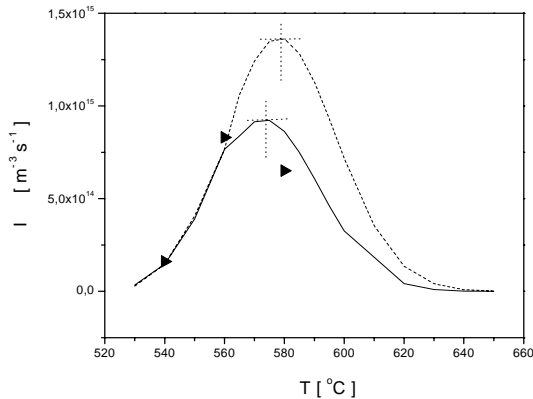


Fig. 2. Theoretical plots [ΔG according to Eq(1) (—) Eq(2) (---)] and experimental data (►) of nucleation rate

Fig. 2 also shows experimental results of the determination of the nucleation rate by the standard microscopic method at three temperatures. Fig.2 clearly shows the better agreement of the nucleation rate curve calculated by Eq(1) with the experimental results. This analyse shows that for this germanate glass the free energy change of crystallization estimated for $\Delta C_p=0$ is not appropriate approximation for the analyse of the nucleation behaviour.

Conclusion

The results presented show that the heat capacities of the liquid and crystalline phases of the germanate glass analysed significantly differ, so that the free energy change of crystallization estimated for $\Delta C_p=0$, is not enough reliable approximation in the analysis of nucleation phenomena. To calculate ΔG , $\Delta C_p \neq 0$ must be assumed.

References

- [1] V.M. Fokin, E.D. Zanotto, J. Non-Cryst. Solids, 2003, **321** 52-65
- [2] P.F. James, J. Non-Cryst. Solids, 1985, **73**, 517-540
- [3] K.N. Lad, K.G. Raval, J. Non-Cryst. Solids, 2004, **334&335**, 259-262
- [4] S. Grujić, N. Blagojević, M. Tošić, V. Živanović, Ceramics-Silikaty, 2005, **49**, 278-282

PLASMAELASTIC WAVES IN SEMI-INFINITE SEMICONDUCTOR

D. M. Todorović and T. Grozdić

*Center for Multidisciplinary Studies, University of Belgrade
Serbia*

Abstract

In this work the system of coupled plasma and elastic wave (plasmaelastic wave) equations in a semi – infinite semiconducting sample are analyzed. The solution of the coupled system of plasma and elastic equations are given.

Introduction

The photoacoustic (PA) and photothermal (PT) science and technology have extensively developed new methods in investigation of semiconductors and microelectronic structures during the last ten years [1, 2]. The PA and PT techniques were recently established as diagnostic methods with good sensitivity to the dynamics of photoexcited carriers [3].

Many authors analyzed the noncoupled system of plasma and elastic equations. The ED effect in semiconductors, i.e. partially coupled plasma and elastic waves, had been studied previously by Stearns and Kino [4] and Avanesyan, Gusev and Zheludov [5]. The thermoelastic and plasmaelastic effects in semiconductors theoretically analyzed in recently published papers by Todorović [6, 7].

Coupled Plasma and Elastic Fields

The coupled plasma, $n(\mathbf{r}, t)$, and elastic displacement, $\mathbf{u}(\mathbf{r}, t)$, transport equations in a vector form, for an elastic medium with isotropic and homogeneous electronic, thermal and elastic properties, are

$$\left(\frac{\partial}{\partial t} + t_o \frac{\partial^2}{\partial t^2} \right) n(\mathbf{r}, t) = D_E \nabla^2 n(\mathbf{r}, t) - \frac{n(\mathbf{r}, t) - n_o}{\tau} - \gamma_u \left(\frac{\partial}{\partial t} + t_o \frac{\partial^2}{\partial t^2} \right) \nabla \mathbf{u}(\mathbf{r}, t) + G(\mathbf{r}, t) \quad (1)$$

$$\rho \frac{\partial^2 \mathbf{u}(\mathbf{r}, t)}{\partial t^2} = \mu \nabla^2 \mathbf{u}(\mathbf{r}, t) + (\lambda + \mu) \nabla (\nabla \times \mathbf{u}(\mathbf{r}, t)) - \delta_n \nabla n(\mathbf{r}, t) \quad (2)$$

where D_E is the carrier diffusion coefficient, τ is the photogenerated carrier lifetime, n_o is the equilibrium carrier concentration, γ_u is the elastic coupling factor, μ , λ are the Lamé elastic constants, \mathbf{r} is the position-vector, t is the time, ρ is the density, $G(\mathbf{r}, t)$ is the carrier photogeneration 'source' term, δ_n is plasma coupling factor (the difference of deformation potential of conduction and valence band). The phenomena described by the system of equations (1)-(2) can be indicate as coupled dynamic generalized plasmaelastic problem. The first equation represents the hyperbolic plasma equation where it is assuming for the speed of carrier transport, c_E , that identical to the longitudinal wave velocity/pulse speed c_l . The plasma relaxation time $t_o = D_E / c_l^2$, where D_E

is the carrier diffusivity. The third term in the elastic equation (2) represents the ‘source’ term and describes the influence of the plasma waves on the elastic wave. We have defined the dimensionless quantities,

$$\delta^2 = \frac{c_2^2}{c_1^2}, \quad \gamma_u' = \frac{1}{n_o} \gamma_u = 1, \quad \gamma_N' = \frac{n_o}{c_1^2} \gamma_N,$$

$$\mathbf{r}' = \omega^* \mathbf{r} / c_1, \quad t' = \omega^* t, \quad (t_o' = 1), \quad \mathbf{u}' = \omega^* \mathbf{u} / c_1, \quad n' = n / n_o,$$

$$q' = c_1 q / \omega^*, \quad \sigma'_{ij} = \sigma_{ij} / \delta_n n_o, \quad G' = G / (\omega^* n_o). \quad \omega_E^* = \frac{c_1^2}{D_E},$$

where c_1, c_2 are, respectively, the longitudinal and shear wave velocities in the medium and γ_u, γ_N are the PE coupling factors, where q is the wave number, σ_{ij} the component of stress. Here ω_E^* is the characteristic frequency of the medium (a quantity characteristic of the plasmaelastic medium).

For temporally periodic and space uniform optical excitation of the surface of semi-infinite medium, it is possible take in consideration the one – dimension (1-D) hyperbolic case. Using $\mathbf{r}=(0,0,z)$, $\mathbf{u} = (0,0,w)$ and $w = \partial\phi/\partial z$, then the system of equations (1)–(2) becomes

$$\left(\frac{\partial^2}{\partial z^2} - \chi - \frac{1}{\tau} \right) N - \chi \frac{\partial^2 \phi}{\partial z^2} = -G \tag{2}$$

$$- \gamma_N N + \left(\frac{\partial^2}{\partial z^2} + \xi^2 \right) \phi = 0 \tag{3}$$

where $N(z,t) = n(z,t) - n_o$ is the photogenerated carrier density, $G(z,t) = G_o \exp(-\alpha z + i\zeta t)$ is the volume plasma source and α is a real parameter.

Plasmaelastic Waves

The solution of the system of equations (3) – (4) can be given as the sum of homogeneous part and particular integral

$$N(z) = N^o \exp(qz) + N^p \exp(-\alpha z), \tag{4}$$

$$\phi(z) = \Phi^o \exp(qz) + \Phi^p \exp(-\alpha z), \tag{5}$$

where N^o, Φ^o, N^p and Φ^p are dimensionless carrier density and potential wave amplitudes. Generally, in equations (5) and (6) the values q and ζ can be complex constants. If the value ζ is the real constant then we have *the wave of determined frequency*. On the other hand, if the value q is the real constant then we have *the wave of determined wavelength*. For our analysis of possible attention are the waves of determined frequencies.

Using the system of equations (3) – (4) with the solutions of (5) – (6) it can be obtain the characteristic equation for the homogeneous system:

$$q^4 + q^2 \left[\xi^2 - \chi(1 + \gamma_N) - \frac{1}{\tau} \right] - \xi^2 \left(\chi + \frac{1}{\tau} \right) = 0 \tag{6}$$

The roots of the characteristic equation are four complex numbers $q_m(\xi)$,

$$q_m(\xi) = \pm \left[\sigma_m(\xi) + i \frac{\xi}{v_m(\xi)} \right], \quad m = 1, 2; \quad (7)$$

and where $\sigma_m(\xi)$ and $v_m(\xi)$ are real functions.

In this moment it is not enough space to present further analyzing plasmaelastic waves and the secular equation. All that equation will be shown in presentation of paper.

Conclusion

The system of coupled plasma and elastic wave equations in a semi-infinite semiconductor was analyzed. The treatment considers a semiconductor elastic medium with isotropic and homogeneous elastic properties. The solution of the coupled system of plasma and elastic equations is a very complex problem. In most practical cases the partially coupled treatment is sufficient. A quantitative analysis of the coupling effects was given. The analysis showed, for the wave of determined frequency, that the plasmaelastic phenomena can be modeled with the superposition of the modified plasma and elastic waves. The modified plasma and elastic waves show the attenuation and disperse phenomena. Another characteristic in the coupled case, that the elastic wave is followed by plasma wave and vice versa.

Comparison this solution for coupled plasmaelastic problem with solution for uncoupled problem, it is possible to see that the modified elastic wave shows also the attenuation and disperse phenomena. The modified plasma waves show the attenuation and disperse phenomena, but for coupled case the attenuation factor and velocity are different functions of frequency. The plasma waves are much damped waves. Amplitude of these waves decrease with distance, while the phase velocity is the function of the frequency, i.e. the dispersion phenomena exists.

References

- [1] D.Almond, P.Patel, Photothermal Science and Techniques, Chapman&Hall, London, 1996.
- [2] A.Mandelis and K.H.Michaelian, Eds, Photoacoustic and Photothermal Science and Engineering, Special Section of Opt. Eng.,1997, **2**, 36.
- [3] Semiconductors and Electronic Materials, Eds. A.Mandelis and P.Hess, Series: Progress in Photothermal and Photoacoustic Science and Technology, Optical Engineering Press, New York, 2000.
- [4] R.G.Stearns, G.S.Kino, "Effect of electronic strain on photoacoustic generation in silicon,"Appl. Phys. Lett., 1985, **47**, 1048-1050.
- [5] S.M.Avanesyan, V.E.Gusev, N.I.Zheludov, "Generation of deformation waves in the processes of photoexcitation and recombination of nonequilibrium carriers in silicon", Appl. Phys. A, 1986, **40**, 163-166.
- [6] D.M.Todorović, Plasma, thermal and elastic waves in semiconductor, Rev.Sci.Instrum.,2003, **74**(1), 582-585.
- [7] D.M.Todorovic, Plasmaelastic and thermoelastic waves in semiconductors, J. Phys. IV France, 2005, **125**, 551-555.

INVESTIGATION OF MINERALOGICAL CHANGES IN BRICK CLAY ZORKA OF LOCALITY DONJE CRNILJEVO DEPENDING ON FIRING TEMPERATURE

S. Despotović¹, D. Babić² and M. Isaković³

¹Zorka EXA, 1 Hajduk Veljkova St, Sabac, Serbia, (slobodan@farmakom.co.yu);

²Faculty of Mining and Geology, University of Belgrad, 7 Djusina St, Belgrad, Serbia;

³Advanced Technological School, 8 Hajduk Veljkova St, Sabac, Serbia.

Abstract

The paper considers changes of mineralogical composition depending on firing temperature in brick Zorka Yellow Clay of locality Donje Crniljevo. Research of the influence of firing temperature on mineralogical composition this clay was performed on fraction samples with particle size up to 5 μ m of studied clay. The samples were then subjected to x-ray examination and to examinations by scanning electron microscopy. It was found that during firing brick Zorka Yellow Clay had the characteristic to develop mineralogical phases of Hematite, Melilite and Mullite. In this clay the decrease of porosity by increase of firing temperature was found as well as some presence of glassy phase which also was proportional to the increase of firing temperature.

Introduction

Yellow clay of locality Donje Crniljevo is the basic component for production of brick products in company Zorka Nemetali in Sabac. After preparation by decantation method, -5 μ m fraction of this clay's subjected to X-ray Diffraction Analysis (XRD) as well as to examinations by scanning electron microscopy (SEM) with the aim to establish mineral phase caused at various firing temperature.

Experimental Procedure

Samples of the tested clay in form of testing bodies prepared of -5 μ m fraction were subjected to thermal treatment at temperatures of 600 °C, 800 °C, 1000 °C and 1200 °C, in laboratory oven with the firing cycle of 24 hours and keeping 1 hour at maximum temperature. X-ray Diffraction Analysis (XRD) was performed on Phillips PW1710 diffractometer with filtered Cu radiation (40 kV, 30 mA) in the angular range of 4-60° (Figure 1). Study of fired samples by usage of Philips 2433 electronic scanning microscopy, SEM, was also performed (Figure 2).

Conclusion

Zorka yellow clay at firing temperature of 600 °C shows presence of distinct porosity with clay mineral dehydration process as well as formation of hematite as a new phase due to present iron hydroxide, while mica remains untransformed at this temperature. At temperature of 800 °C, rounding of grain borders takes place

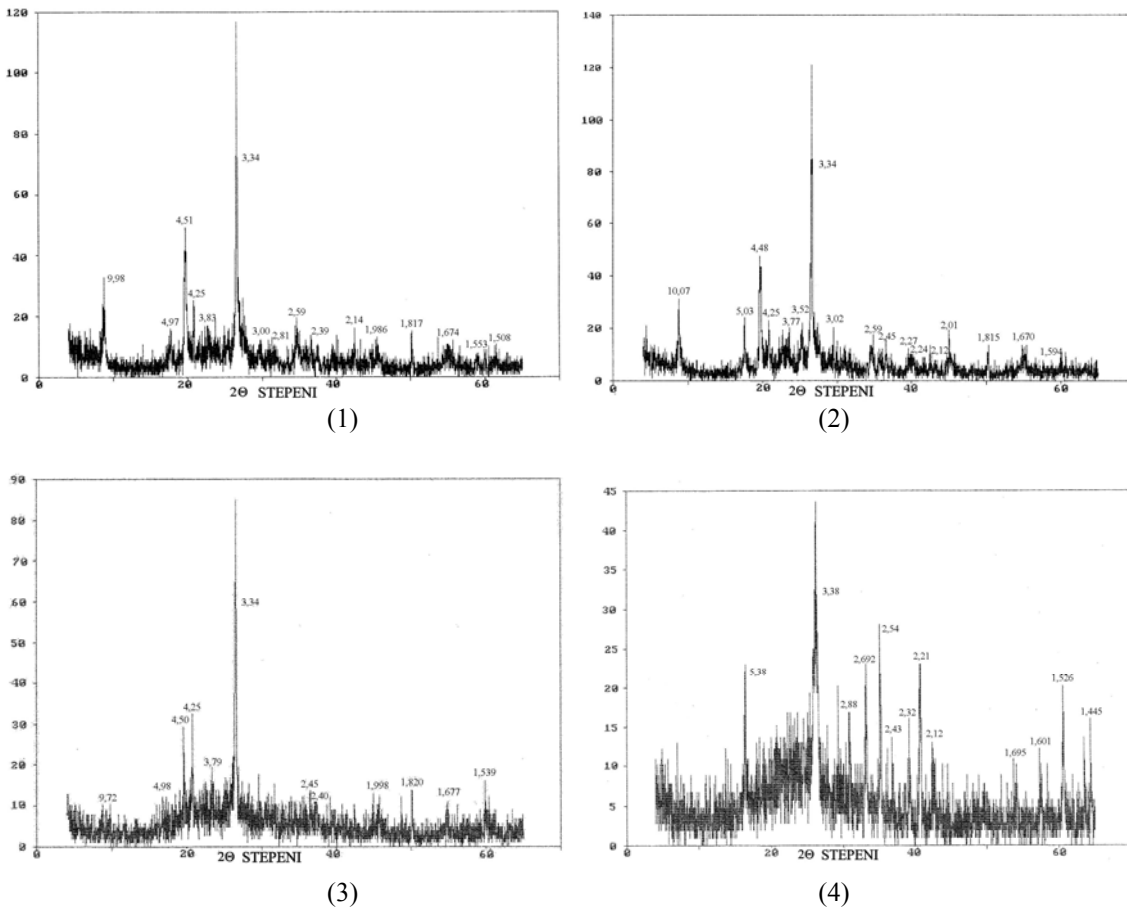


Fig. 1. XRD diagrams of -5 μ m fraction samples of Zorka yellow clay fired at 600 °C (1), 800 °C (2), 1000 °C (3) and 1200 °C (4).

and mica phase into the basic mass which is made of transformed amorphous clay minerals. At 1000 °C, appearance of melilite can be noticed, while reduction of mica quantity is noticeable due to hydration at this temperature. It can be also stated here that porosity with appearance of glassy phase is present here. At firing temperature of 1200 °C, presence of glassy phase which fills space within the present mullite and melilite aggregate is noticeable. Presence of hematite is also noticed here, as well as presence of relict remaining of feldspar. Porosity still exists, but at lower level compared to the one stated during the study of sample from the same raw material fired at previous temperature, which is consequence of considerably more distinct presence of glassy phase in this case.

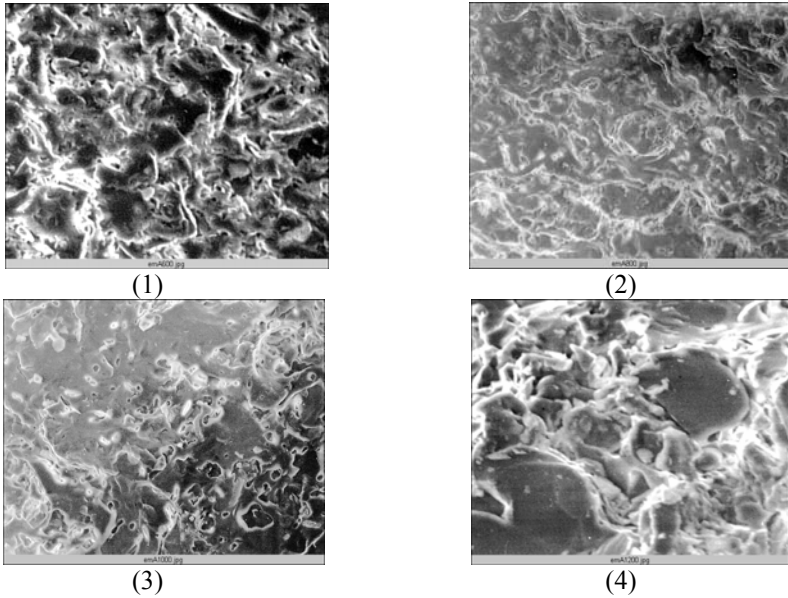


Fig. 2. SEM images -5µm fraction samples of Zorka yellow clay fired at 600 °C (1), 800 °C (2), 1000 °C (3) and 1200 °C (4). Magnification 2000x.

Table 1. Survey of mineral phase depending on firing temperature of - 5µm fraction sample of Zorka yellow clay (indicative).

Fraction -5µm	600 °C	800 °C	1000 °C	1200 °C	Mineral phases
Yellow clay Zorka Sabac					Hematite
					Melilite
					Mullite
					Porosity
					Glassy phase

The Table 1. gives illustration of mineral phases, depending on the firing temperature, of -5µm fraction sample of brick Zorka yellow clay of locality Donje Crniljevo.

References

[1] A. E. McHale, Phase diagrams and Ceramic processes, New York, 1997.
 [2] S. Despotović, PhD Thesis, University of Belgrad, 2000, 96-105.
 [3] W. E. Worral, Clays and Ceramic Raw Materials, APS Ltd, England, 1975.
 [4] S. Freyburg, Ziegelindustrie International, 1996, **12**, 875-877.
 [5] S. Caillere, S. Henin, M. Rautureau, Les argiles, Paris, 1989.
 [6] D.A.C. Manning, Introduction to Industrial Minerals, New York, 1995.

Solid State Physical Chemistry

(I)

KINETIC APPROACH TO THE ZEOLITE A CRYSTALLIZATION USING IN SITU ^{27}Al NMR SPECTROSCOPY

Z. Miladinović and J. Zakrzewska

Institute of General and Physical Chemistry, Studentski trg 12-16, Belgrade, Serbia

Abstract

Intensity curves obtained by in situ ^{27}Al NMR spectroscopy of zeolite A suspension has been used as a method for kinetic investigation of zeolite crystallization. Kinetic analysis was performed using modified Sharp and Hancock equation. Gel dissolving, phase boundary reaction and crystal growth processes were identified.

Introduction

The crystallization of zeolite consists of series of competing and consecutive processes with different rates and activation energies that determine the overall crystallization rate and the type of the crystallizing zeolite species. The growth process can be divided into several steps. The first step is the diffusion of the species from the solution phase to the surface. A second step is the reaction of these groups with reactive surface groups. This step is followed by the reaction of the attached species to a structural element of the final zeolite. [1]

Crystallization curves, obtained during zeolites synthesis, are usually obtained by diffraction quenching methods [2]. Recently, some spectroscopic methods [3,4] have been developed in order to overcome the problem of quenching experiments. This, so-called in situ approach, have a series of advantages comparing to the classical ex situ methods. First of all, it enables obtaining of satisfied number of experimental data, during synthesis, to perform kinetic investigation. Method of Sharp and Hancock [5] has been usually used in order to obtain kinetic parameters of crystallization process.

Here, the in situ ^{27}Al NMR spectroscopy as convenient method for kinetic investigation of zeolite crystallization is presented.

Experimental

^{27}Al NMR spectra were obtained from zeolite suspension, taken from reactor immediately after mixing and stirring aluminate and silicate components for about 2 min. The synthesis was continued in Bruker MSL 400 NMR spectrometer at 104.262 MHz, with 300s time intervals between spectra, 2 μs pulse width and 0.3s repetition time. The batch composition was Al_2O_3 : 2.5 SiO_2 : 3.68 Na_2O : 110 H_2O , and reaction temperature during synthesis was 82 °C.

Results

In situ ^{27}Al NMR spectroscopy was used to obtain experimental curves reflecting the changes of alumina presented in the solution and the solid/gel phase during synthesis.

Figure 1 shows changes of intensity of ^{27}Al NMR narrow line at 79 ppm from alumina in solution phase as well as changes of intensity and width at half-height of broad line at 59 ppm from alumina species incorporated in solid/gel phase.

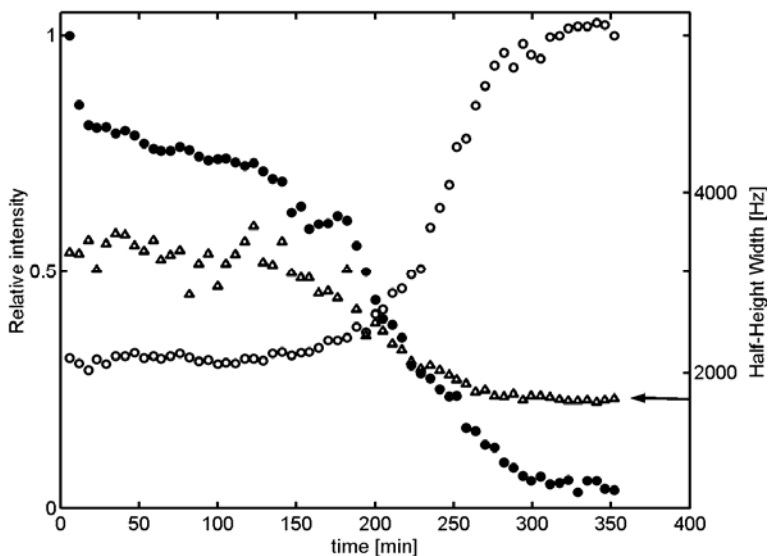


Fig. 1. Changes of relative intensity of ^{27}Al NMR line at 79 ppm (\bullet); changes of relative intensity (\circ) and width at half-height (Δ) of ^{27}Al NMR line at 59 ppm during reaction time of zeolite synthesis for batch composition with molar ratios Al_2O_3 : 2.5SiO_2 : $3.68\text{Na}_2\text{O}$: $110\text{H}_2\text{O}$

Clearly, from Fig. 1 presented curves mutually correspond in time domain. During crystallization intensity of the line at 79 ppm decreases, while the intensity of the broad line at 59 ppm increases and becomes narrower. This behavior can be explained by crystallization process in which the liquid phase alumina is incorporated into crystalline $\text{Al}(\text{OSi})_4$ [3]. Also, at the curve obtained for alumina species in the solution phase, some periods during crystallization can be identified, where the decreasing trend was paused for relatively short time. Such behavior, was already observed by Walton et al. [2].

Kinetic analysis was performed using modified Sharp and Hancock equation [5]:

$$\ln[-\ln(\beta)] = n \ln(t - t_0) + n \ln(k) \quad (1)$$

where n is Avrami-Erofe'ev coefficient, t_0 represents induction time, k is the rate constant, and β represents normalized values of intensity obtained from both curves shown in Fig. 1. Plots of $\ln(-\ln(\beta))$ and $\ln(-\ln(1-\beta))$ vs. $\ln(t-t_0)$ for narrow line at 79

ppm and broad line at 59 ppm respectively, are given in Fig. 2. Values of $n=1.54$ and $k=1.70 \cdot 10^{-4} \text{ s}^{-1}$, for curve reflecting the changes of Al in the solution phase, indicates that process of diffusion and phase boundary process dominated [5]. For curve representing changes in solid gel phase two distinctive lines fit the experimental data. At early stage of reaction, values of $n=1.09$ and $k=1.10 \cdot 10^{-4} \text{ s}^{-1}$, suggest that dominant mechanism is dissolving of aluminosilicate species from the gel phase and then, their diffusion into solution. Values of $n=3.33$ and $k=1.37 \cdot 10^{-4} \text{ s}^{-1}$, indicate that the Avrami-Erofe'ev nucleation growth model is dominant in later stage of synthesis.

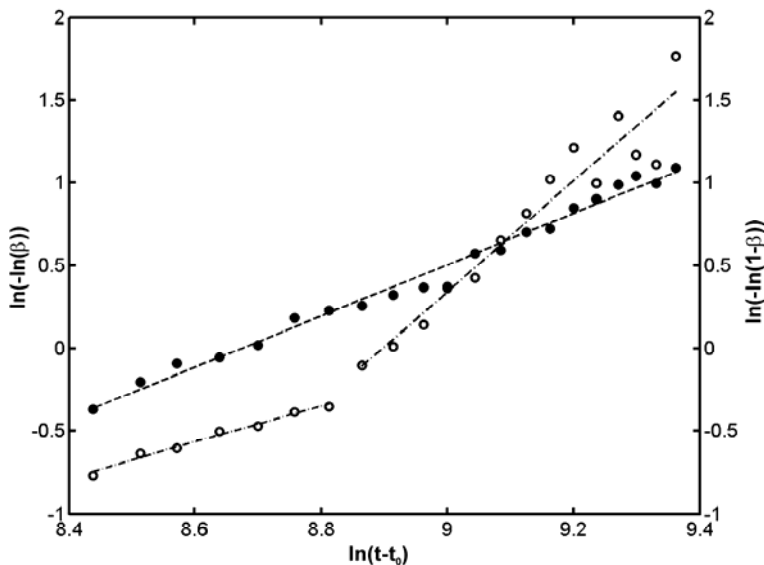


Fig. 2. Linear Sharp-Hancock plots obtained from crystallization curves which describing changes of intensity of ^{27}Al NMR line at 79 ppm (●) and broad line at 59 ppm (○) during of crystallization of zeolite A.

Conclusion

In situ ^{27}Al NMR spectroscopy could be applied for obtaining kinetic parameters during a synthesis. The use of Sharp and Hancock method enables identification of different kind of processes connected to zeolite crystallization in the liquid and solid/gel phase simultaneously, such as gel dissolving, phase boundary reaction and crystal growth.

References

- [1] H. Lechert, *Zeolites*, 1996, **17**, 473-482.
- [2] R. I. Walton, F. Millange, D. O'Hare, A. T. Davies, G. Sankar and R.A. Catlow, *J. Phys. Chem. B*, 2001, **105**, 83-90.
- [3] J. M. Shi, M. W. Anderson and S. W. Carr, *Chem. Mater.*, 1996, **8**, 369-375.
- [4] R. J. Francis, D. O'Hare, *J. Chem. Soc., Dalton Trans.*, 1998, **19**, 3133-3148.
- [5] J. D. Sharp, J. H. Hancock, *J. Am. Ceram. Soc.*, 1972, **55**, 74-77.

SURFACE CHARACTERIZATION OF Ni-BASED CATALYSTS FOR DRY REFORMING

S. Damyanova¹, K. Arishtirova¹, B. Pawelec², J.L.G. Fierro² and L. Petrov¹

¹*Institute of Catalysis, Bulgarian Academy of Sciences, 1113 Sofia, Bulgaria*

²*Instituto de Catalis y Petroleoquimica, CSIC, Cantoblanco, 28049 Madrid, Spain*

Fax: 359 2 9712967, soniad@ic.bas.bg

Abstract

PtNi catalysts supported on ZSM-5 with different amount of Ni (1-12 wt%) were prepared. The effect of the ratio Ni/noble metal on the surface properties of nickel-based catalysts was studied. The samples were characterized by N₂ adsorption-desorption isotherms, Diffuse reflectance spectroscopy, X-ray diffraction, Fourier transformed infrared spectroscopy of adsorbed CO and X-ray photoelectron spectroscopy. It was shown that addition of Pt into Ni catalyst leads to formation of nano-sized Ni-based catalysts. The dispersion and reducibility of nickel oxide species increased in the presence of Pt.

Introduction

The conventional catalysts used in the industrial processes for catalytic reforming of methane with carbon dioxide reaction (dry reforming) for hydrogen production are alumina-supported Ni catalysts due to their low price and high conversion. However, the nickel catalysts are deactivated quickly caused by the formation of coke on the surface of the active phase. Compared with the non-noble metal catalysts the noble metal catalysts exhibit excellent activities and selectivity, and higher stability, due to lower sensitivity to carbon deposition [1,2]. However, the major drawback of the noble metal catalysts is their high cost and limited availability, which restrict their potential use in the industrial processes. The subject of this work is to develop new effective Ni-containing catalysts supported on a suitable support and modified with a small amount of Pt that can result in a non-expensive bimetallic supported system assuring the both, high activity of catalyst for hydrogen production and low carbon deposition. The effect of the ratio Ni/noble metal on the surface properties of the nickel-based catalysts was investigated.

Experimental

Zeolite-supported Ni-containing catalysts modified with Pt (0.5 wt%) were prepared by sequential impregnation technique using aqueous precursor solutions of Ni(NO₃)₂·6H₂O and H₂PtCl₆·6H₂O in ethanol. The samples were dried at 384 K for 12 h and calcined at 823 K for 4 h. The amount of Ni was in the range of 1-12 wt%. The samples were characterized by N₂ adsorption-desorption isotherms, Diffuse reflectance spectroscopy (DRS), X-ray diffraction (XRD), Fourier transformed infrared spectroscopy (FTIR) of adsorbed CO and X-ray photoelectron spectroscopy (XPS).

Results and Discussion

The textural properties of zeolite-supported bimetallic PtNi samples (Table 1) showed that the S_{BET} surface area and pore volume decrease with increasing the Ni content, which is caused by the plugging of the pores with nickel oxide particles. There was no influence of the presence of Pt on the textural properties of the samples.

The DR spectra of all Ni-containing samples display a major band at 268 nm which is due to Ni^{2+} -O charge transfer transitions. The intensity of the band increased with increasing the Ni content in the samples.

Table 1. S_{BET} , NiO size (D_{XRD}) and XPS atomic ratios for zeolite-supported PtNi samples

Samples	S_{BET}	D_{XRD} , NiO	XPS	
	m^2/g	nm	Ni/Si	Pt/Si
ZSM-5	401	-	-	-
Pt1Ni	389	-	44	3.4
Pt3Ni	374	-	122	6.1
Pt6Ni	365	8.7	159	7.2
Pt12Ni	335	11.1	522	11
0.3Pt6Ni	367	9.7	170	5.2
Pt6Ni-co ¹	367	10.3	129	6.9
6Ni	341	11.1	316	-
Pt	399	-	-	21

¹ prepared by co-impregnation technique

XRD spectra of bimetallic zeolite-supported PtNi samples with Ni loading ≤ 3 wt% did not show any diffraction peak of NiO phase meaning that NiO is in amorphous state. Diffraction peaks of NiO at $2\theta=43.8^\circ$ were detected in the spectra of the samples with higher Ni content of 6 and 12 wt% Ni. No diffraction peaks due to formation of platinum oxide species were observed for all calcined samples, that means well dispersed Pt on the surface of PtNi catalysts. The presence of Pt in PtNi samples provokes the decrease of the NiO size; the Ni-containing sample without Pt (6Ni, Table 1) revealed relatively bigger crystallites of NiO (10.3 nm) compared to Pt6Ni sample (8.7 nm).

DRIFT spectra of adsorbed CO on reduced monometallic Pt and Ni samples, as well as on bimetallic PtNi catalysts with 6 and 12 wt% Ni, demonstrated the effect of the Ni content on the kind of the surface species. The linear-bonded CO species on reduced Ni^0 was revealed at 2047 cm^{-1} . The bands at 1951 and 1872 cm^{-1} , associated with bridge-bonded CO species, appeared in the spectrum of PtNi sample with the highest Ni content (12 wt%). A high-frequency band shift from 2092 to 2085 cm^{-1} was observed, which intensity decreased after introduction of Pt into Ni sample with 6 wt%. This frequency band shift was related to the change of electronic state of metal

atoms that can be attributed to a subsequent reduction of partially oxidized $\text{Ni}^{\sigma+}$ atoms in the presence of Pt (fully reduced Ni^0). The bridge-bonded CO species at 1951 and 1872 cm^{-1} practically disappeared in the spectrum of Pt6Ni. Most probably, a “dilution” effect of Pt atoms at this ratio of Pt/Ni was responsible for more uniform distribution of Ni species on the catalyst surface.

The $\text{Ni}2p_{3/2}$ spectral region for all reduced zeolite-supported PtNi samples showed a major peak at ca. 852.7-853.0 eV, which is characteristic of Ni^0 and a small one at ca. 855.7-856.0 eV, which was related to the non-reduced Ni^{2+} ions interacting with zeolite lattice oxygen. It means that the nickel oxide particles were not completely reduced. However, the reducibility of nickel increased in the presence of Pt (spill-over effect). The XPS atomic ratio of Ni/Si for reduced zeolite-supported PtNi samples increased with increasing the Ni content (Table 1). This phenomenon was expected for Ni but for Pt an increase of XPS Pt/Si ratio at the same Pt loading was surprising. The increase of Pt/Si surface ratio suggested a location of Pt on the nickel particles because the photoelectron spectroscopy is a technique sensitive to the outer layers of solid.

Conclusions

The presence of a small amount of noble metal (Pt) in zeolite-supported Ni catalysts leads to: (i) formation of nano-sized NiO particles; (ii) better dispersion of NiO particles due to a “dilution effect” of Pt and (iii) easy reduction of nickel oxide species to Ni^0 .

Acknowledgements

The financial support of the project between the National Council of Scientific Research (CSIC), Spain and Bulgarian Academy of Sciences is gratefully acknowledged. The authors acknowledge financial support by project No X-1515/05 from National Science Fund at the Bulgarian Ministry of Education and Science.

References

- [1] S. Damyanova, J.M.C. Bueno, Appl. Catal. A: Gen. 2003, **253**, 135-150.
- [2] B.A. Riguetto, S. Damyanova, G. Gouliev, L.Petrov, J.M.C.Bueno, C.M.P. Marques, J. Phys. Chem. B 2004, **108**, 5349-5358.

STRUCTURAL TRANSFORMATION OF MIXED WV AND MoV HETEROPOLY COMPOUNDS UPON HEATING

A. Predoeva¹, E. Gaigneaux², S. Damyanova¹ and L. Petrov¹

¹*Institute of Catalysis, Bulgarian Academy of Sciences, 1113 Sofia, Bulgaria*

²*Universite Catholique de Louvain, Unite de Catalyse et Chimie de Materiaux Divises, Place Croix de Sud, 2/17, 1348 Louvain-la-Neuve, Belgium*

Abstract

The transformation of mixed MoV and WV heteropoly compounds (HPCs) with Keggin structure anions into the corresponding oxides in dependence of temperature treatment was depended on the type of peripheral atoms (Mo or W) and the number of vanadium. The samples were characterized by X-ray diffraction (XRD), infrared (IR) and Raman spectroscopy.

Introduction

Heteropoly compounds based on 12-molybdo- and 12-tungstophosphoric acids they are widely used as catalyst precursors for hydrogenation or oxidation processes, due to the unique properties (acid-base and redox). The knowledge of their structural transformation throughout their activation and working catalytic process is very important for obtaining active and stable catalysts. The subject of the present work is to investigate the change of structure and thermal stability of mixed MoV and WV heteropoly compounds as a function of temperature treatment in the range of 50-650 °C, and a number of V atoms substituted Mo or W atoms in the heteropoly anions.

Experimental

The samples, synthesized as described by Tsigdinos [1], are noted as follow: HPMo₁₂, HPMo₁₁V₁, HPMo₉V₃, HPW₁₂, HPW₁₁V₁ and HPW₉V₃. The amount of Mo or W was about 12 wt%. The samples were characterized by XRD, IR and Raman spectroscopy.

Results And Discussion

XRD. The XRD patterns of bulk HPMo₁₂ calcined up to 450 °C (not shown) are typical for heteropoly acid with Keggin structure. The presence of the lines of α -MoO₃ ($2\theta=23.4, 25.73$ and 27.4°) in the XRD spectra of the sample after calcination at 550 °C suggests a destruction of the Keggin structure. However, for V substituted HPMo₁₁V₁ and HPMo₉V₃ samples the peaks characteristic for α -MoO₃ are clearly visible after temperature treatment at 650 °C. In contrast to HPMo₁₂, the crystallinity of HPW₁₂ maintain at 450 °C. The peaks are considerable broad and their intensity decrease upon heating at 550 °C, indicating a reduction of the crystallinity of the acid. At 650 °C peaks at $2\theta = 23.32, 23.75, 28.84, 33.55$ and 41.44° of tungsten oxide appeared in the spectra of HPW₁₂ and HPW₁₁V₁ samples meaning

the destruction of the heteropoly anion. However, in the spectra of HPW_9V_3 sample at 650°C , peaks are detected corresponding to various phases of tungsten oxide.

IR. The IR spectra of HPCs at different temperatures of calcination are shown in Figure 1. Strong absorption bands at ca. 1065 , 963 , 870 and 787 cm^{-1} related to the vibrations of P-O bond, Mo=O bond, and Mo-O-Mo bond of different locations, respectively, characterize the heteropoly anions with Keggin structure of HPMo_{12} , $\text{HPMo}_{11}\text{V}_1$ and HPMo_9V_3 . For HPMo_{12} this structure is preserved up to 450°C (Fig. 1A, a). Strong disorder of the heteropoly anion and its transformation to molybdenum oxides are observed after increasing the temperature up to 550°C , confirmed by the presence of bands of MoO_3 at 990 , 816 , 872 cm^{-1} (Fig. 1A, b).

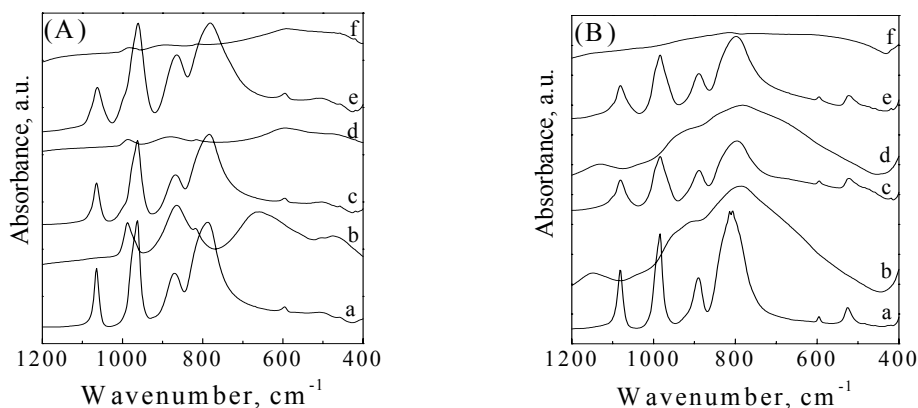


Fig. 1. IR spectra of mixed MoV and WV HPCs at different temperature treatment: HPMo_{12} at 450 and 550°C (A(a,b)); $\text{HPMo}_{11}\text{V}_1$ at 550 and 650°C (A(c, d)); HPMo_9V_3 at 350 and 650°C (A(e, f)); HPW_{12} at 450 and 650°C (B(a,b)); $\text{HPW}_{11}\text{V}_1$ at 550 and 650°C (B(c,d)); and HPW_9V_3 at 550 and 650°C (B(e,f)).

The introduction of one V atom into the heteropoly anion of HPMo_{12} leads to increasing the thermal stability. The typical Keggin pattern is preserved up to 550°C in the IR spectra of $\text{HPMo}_{11}\text{V}_1$ (Fig. 1A, c). However, HPMo_9V_3 sample shows good crystallinity up to 350°C (Fig. 1A, e). Increasing the temperature to 550°C the bands broadened and their intensity decreased. At the highest temperature (650°C) the main characteristic features of bulk HPA are not observed in the IR spectra of mixed MoV compounds, which is evidence of the loss of the Keggin structure (Fig. 1A, d, f). For HPW_{12} the bands at ca. 1081 , 984 , 888 and 804 cm^{-1} characteristic for the typical anti-symmetrical stretching vibrations of P-O, W=O and W-O-W bonds, respectively, did not change upon heating to 450°C indicating the stability of the bulk at that temperature (Fig. 1B, a). The broad bands at 1149 and 786 cm^{-1} in the IR spectrum of HPW_{12} at 650°C are the indication for a disorder of the Keggin structure and formation of tungsten oxide (Fig. 1B, b). IR spectra of $\text{HPW}_{11}\text{V}_1$ and HPW_9V_3 samples show a slight decrease in the characteristic features of Keggin structure. The typical Keggin pattern is preserved up to 550°C in the spectra of these samples (Figure 1B, c, e). A strong disorder of the Keggin heteropoly anions is observed at 650°C (Fig. 1B, line d,

f). Broad bands at 1135, 941 and 786 cm^{-1} assigned to formation of WO_3 are detected for $\text{HPW}_{11}\text{V}_1$ (Fig. 1B, d).

Raman. In the Raman spectra (not shown) of HPMo_{12} calcined up to 450 °C the main bands characteristic for heteropoly anion with Keggin structure are observed at 1010 cm^{-1} with a shoulder at 996 cm^{-1} , 967, 908, 610 and 250 cm^{-1} , which can be, respectively, assigned to stretching modes $\nu_s(\text{Mo-O}_t)$, $\nu_{as}(\text{Mo-O}_t)$, $\nu_s(\text{Mo-O}_b\text{-Mo})$, $\nu_s(\text{Mo-O}_c\text{-Mo})$ and $\nu_s(\text{Mo-O}_a)$. Bands at 993, 820 and 660 cm^{-1} assigned to MoO_3 present in the spectra of the HPMo_{12} after treatment at 550 °C. For $\text{HPMo}_{11}\text{V}_1$ sample, the main characteristic bands keep their position at: 1009 cm^{-1} with shoulder at 995 cm^{-1} and at 246 cm^{-1} . A splitting of the bands assigned to $\nu_s(\text{Mo-Ob-Mo})$ and $\nu_s(\text{Mo-Oc-Mo})$ is observed up to 250 °C. A very weak band at 1033 cm^{-1} is observed in the region typical for vanadyl species after treatment of $\text{HPMo}_{11}\text{V}_1$ at 450 °C. Nevertheless, the Keggin structure is preserved up to 550 °C. A disorder of the structure is observed at 650 °C revealed by the bands of MoO_3 . The main characteristic bands for Keggin structure stretching modes (1008 cm^{-1} with shoulders at 993 and 986 cm^{-1} , and 240 cm^{-1}) are detected in Raman spectra of HPW_{12} sample upon heating to 450 °C. The band assigned to vibration of $\nu_s(\text{Mo-O}_t)$ bond shifts to 1026 cm^{-1} and other bands disappear after increasing the temperature up to 550 °C. The destruction of Keggin heteropoly anion is observed after treatment of the sample at 650 °C. Introduction of V atoms did not change the Keggin structure of mixed WV compounds. The clear bands at ca. 1009, 989 and 240 cm^{-1} preserved in spectra of $\text{HPW}_{11}\text{V}_1$ and HPW_9V_3 samples up to 250 °C. After this temperature the band at 1009 cm^{-1} is shifted to higher wavenumbers and some broadening of all bands is observed. Independently of these facts, the Keggin structure is maintained up to 550 °C. At the highest temperature of treatment only bands belong to tungsten oxide at 805, 714, 329 and 272 cm^{-1} are detected in Raman spectra of $\text{HPW}_{11}\text{V}_1$ and HPW_9V_3 samples.

Conclusion

The results show that the Keggin anion decomposition occurs at higher temperature when vanadium atoms are introduced into the heteropoly anion. In other hand, the W-containing samples are destroyed at higher temperatures of treatment compared to those for Mo-containing HPCs.

Acknowledgements

The research has been partly supported by the National Science Fund of the Bulgarian Ministry of Education and Science under project MY-X-1505.

References

- [1] B. Tsigdinos, C. Hallada, *Inorg. Chem.*, 1968, 7, 437-441.

CVM STUDY OF CHARGE TRANSFER IN $\text{YBa}_2\text{Cu}_3\text{O}_{6+x}$ MATERIAL

M. Milić, V. M. Matić and N.Đ. Lazarov

*Laboratory for Theoretical Physics, Institute of Nuclear Sciences VINCA,
P.O.Box 522, Belgrade, Serbia*

Abstract

The number of positive holes transferred from the CuO_x basal planes to the superconducting CuO_2 planes of $\text{YBa}_2\text{Cu}_3\text{O}_{6+x}$ material was calculated as a function of oxygen content x , by the use of numerical cluster variation method (CVM). The calculations were performed for the set of three different temperatures and for the different values of the parameter ξ_l which represents the ratio of the number m of divalent oxygen ions in the chain fragment and the total number l of oxygen ions in the chain fragment. The obtained hole count versus x dependence showed no plateau behavior for low temperatures ($t=0.25$ and $t=0.35$) while for $t=0.45$ indication of plateau behavior is present.

Introduction

The high T_c superconductor $\text{YBa}_2\text{Cu}_3\text{O}_{6+x}$ is well known for its characteristic two plateaus in T_c (critical temperature of superconducting transition) versus x dependence [1]. While the origin of lower 60K plateau is still unclear, the existence of the plateau at 93K is associated with an optimal doping of the superconducting CuO_2 planes [2]. Though, it is believed that the plateau at 60K is related to the degree of oxygen ordering in CuO_x planes [3], which act as a reservoir of holes from where they are transferred to the CuO_2 planes. The dependence of number of holes transferred from CuO_x planes on x is expected to exhibit behavior similar to that of $T_c(x)$. Doping of CuO_2 planes with holes through the increase of the oxygen content is related to the valence change of Cu(1) ions (Cu ions in the basal planes). In the parent $\text{YBa}_2\text{Cu}_3\text{O}_6$ compound all the Cu ions in the basal planes are monovalent being surrounded by only two apical oxygen atoms. With increase of oxygen content the chain fragments (sequences of Cu and oxygen ions aligned along b crystallographic axes) are formed, and can be characterized by its length l and by its charge. The general form of the chain fragment of length l can be written as $\text{Cu}_{l+1}^{+2}\text{O}_m^{-2}\text{O}_{l-m}^-$. Since the neutral chain fragment includes only one divalent oxygen ion it follows that the chain having m divalent oxygen ions must have transferred $m-l$ holes [4]. The optimal value of the parameter $\xi_l = m/l$, governing for the charge transfer is estimated to be $\xi_{l(\text{opt})} \approx 0.7$ for long chains ($l \gg 1$). It is not expected that this value differs much for the short chains. Thus the optimal chain configurations have been established to be $\text{Cu}_3^{2+}\text{O}^{2-}\text{O}^-$ for $l=2$, $\text{Cu}_4^{2+}\text{O}_2^{2-}\text{O}^-$ for $l=3$, and $\text{Cu}_5^{2+}\text{O}^{2-}\text{O}^-$ for $l=4$. For the longer chains this rule can be generalized as: $m = \text{nint}(l(m/l)_{\text{opt}})$ (nint is the nearest integer). Applying this rule to estimate the number of holes transferred from the chains of different lengths the total amount of holes transferred from the CuO_x planes can be calculated.

Results and Discussion

The number of holes n_h transferred from the basal planes to the CuO_2 planes is given by the following formula [5]:

$$n_h = \sum_{l=1}^{\infty} [l \text{int}(\xi_l l) - 1] p(l) , \quad (1)$$

where $p(l)$ is the probability of finding a chain of length l in the system, and it is determined by the expression [6]:

$$p(l) = \frac{(l_{av} - 1)^{l-1}}{l_{av}^l} , \quad (2)$$

where l_{av} is the average chain length.

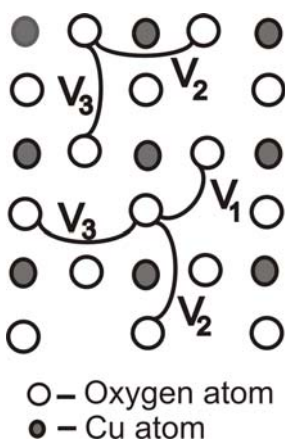


Fig. 1. Basal plane lattice with ASYNNNI model interactions

In order to calculate the hole count n_h we have employed the numerical cluster variation method and the well known ASYNNNI model which describes the thermodynamics of oxygen ordering in terms of two dimensional Ising model with asymmetric interactions of next nearest neighbors (Fig. 1). For the values of model interactions we used those obtained, from the first principles calculations, by Sterne and Wille [7]. The hole count was calculated for different values of ξ_l ranging from 0.1 to 1.0. The calculated values of hole count are shown at figure 2. as a function of oxygen content x and for three different temperatures $0t = k_B T / V_1$. It can be seen that for $t=0.25$ and for $t=0.35$ no indications of possible plateau existence in the range of stability of OrthoII phase is present, but only a kink occurs for the value of x for which the onset of the plateau could be expected. For $t=0.45$ the $n_h(x)$ function exhibits a close to plateau behavior for some values of parameter ξ_l .

Conclusion

The number of holes transferred from the CuO_x planes was calculated as a function of oxygen content x for different temperatures and for different values of parameter ξ_l . The choice of parameter ξ_l has no much influence on the shape of the n_h versus x curve except that its higher values bring in holes to the CuO_2 planes for lower values of x . At low temperatures no plateau is present in the hole count which is due the fact that at low temperatures long oxygen chains dominate at $x=0.5$ and that additional oxygen atoms tend to form chains thus producing holes, which is not the case at higher temperatures when additional oxygen can exist as isolated, creating no holes and producing a plateau in n_h versus x dependence.

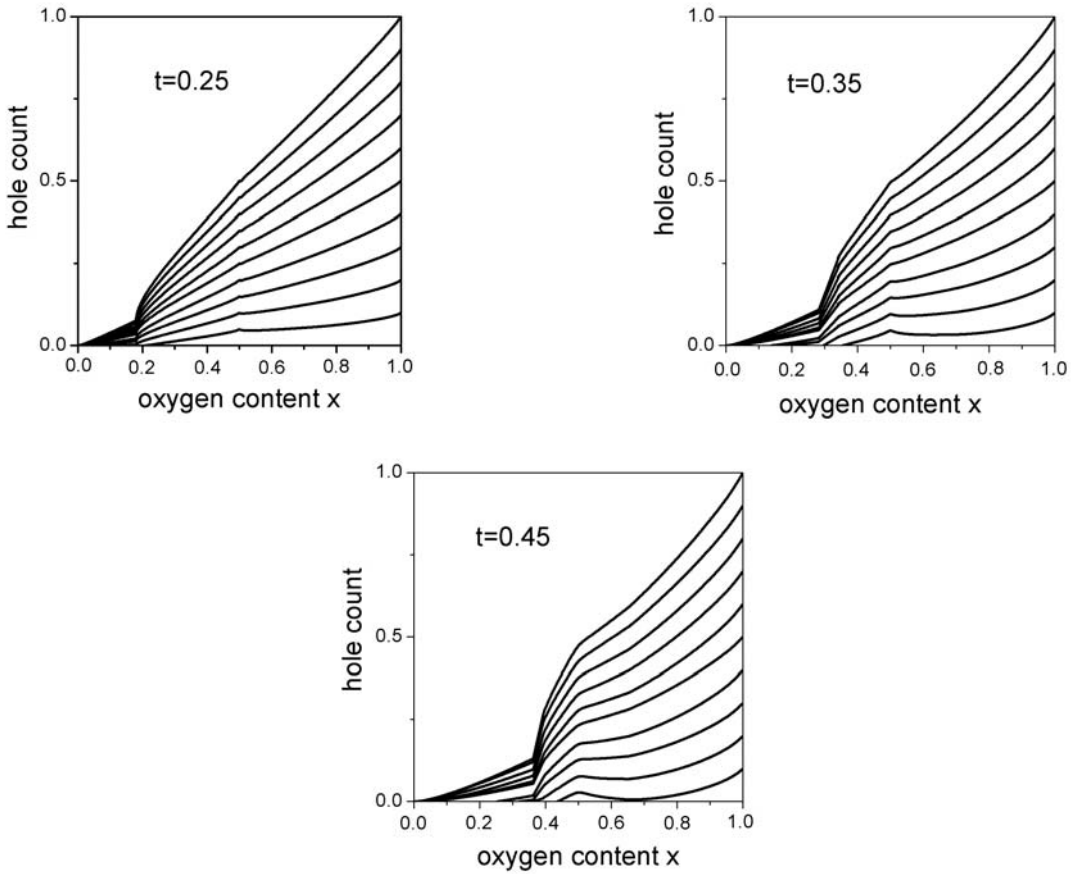


Fig. 2. Hole count as a function of oxygen content x for three different temperatures. For each temperature $n_h(x)$ is shown for ten different values of parameter ξ_i from 0.1 (lowest curve) to 1.0 (highest curve), with step of 0.1.

References

- [1] R. J. Cava, B. Batlogg, C. H. Chen, E. A. Rietman, S. M. Zahurak, and D. Werder, *Phys. Rev. B*, 1987, **36**, 5719.
- [2] J. L. Tallon, C. Bernard, H. Shaked, R. L. Hitterman, J. D. Jorgensen, *Phys. Rev. B*, 1995, **51**, 12911.
- [3] F. Yakhou, J.-y. Henry, P. Burllet, V. P. Plakhty, M. Vlasov, S. Moskhin, *Physica C*, 2000, 333, 146.
- [4] P. Gawiec, D. R. Grempel, G. Uimin, and J. Zittartz, *Phys. Rev. B*, 1996, **53**, 5880.
- [5] W. Selke and G. Uimin, *Physica C*, 1993, **214**, 37.
- [6] V. M. Matic, N. Dj. Lazarov and M. Milic, *Physica C*, 2005, **421**, 49.
- [7] P. A. Sterne and L. T. Wille, *Physica C*, 1989, **162**, 223.

RE-ENTRANT SPIN GLASS TRANSITION IN $\text{LiCr}_{0.175}\text{Mn}_{1.825}\text{O}_4$ SPINEL

V. Kusigerski¹, N. Cvjetičanin², D. Marković¹, V. Spasojević¹ and J. Blanuša¹

¹The "Vinča" Institute, Condensed Matter Physics Laboratory,
P.O. Box 522, Belgrade, Serbia

²Faculty of Physical Chemistry, University of Belgrade, Studentski Trg 12-16,
P.O. Box 137, Belgrade, Serbia

Abstract

Magnetic properties of Cr^{3+} substituted LiMn_2O_4 spinel have been investigated by measuring both temperature and field dependence of DC magnetization, as well as temperature dependence of AC susceptibility. Obtained results point to the re-entrant spin glass behavior in the low temperature region where system undergoes long range antiferromagnetic transition at $T_N=42$ K followed by the spin glass transition at $T_F=22$ K. High temperature behavior is of the Curie-Weiss type with effective magnetic moment corresponding to the sample's chemical composition.

Introduction

During the last decade LiMn_2O_4 spinel compound and its metal cation substitutes $\text{LiM}_x\text{Mn}_{2-x}\text{O}_4$ ($M=\text{Al}^{3+}$, Zn^{2+} , Ti^{4+} , Cr^{3+} , Co^{2+} , Ni^{2+}) have been attracting extensive attention from both application-oriented and fundamental reasons. The primary interest had been provoked by LiMn_2O_4 as the promising cathode material for rechargeable lithium-ion batteries [1], while its metal substitutes were investigated in order to reduce capacity fading upon electrochemical cycling [2].

From the magnetic viewpoint LiMn_2O_4 is an intriguing system due to a several key intrinsic properties: (i) magnetic Mn^{3+} and Mn^{4+} ions are placed at the corners of a network of corner-sharing tetrahedras ("pyrochlore network") that leads to a spin frustration in case of antiferromagnetic (AF) interactions [3]; (ii) Mn^{3+} ions in a high-spin state ($t_{2g}^3 e_g^1$) are well known example of Jahn-Teller (JT) ions that can produce the distortion of $\text{Mn}^{3+}\text{O}_6^{2-}$ octahedras [4]; (iii) superexchange 90° Mn-O-Mn interactions can be ferromagnetic (FM) for pair of Mn^{4+} ions or AF for both $\text{Mn}^{3+}/\text{Mn}^{3+}$ and $\text{Mn}^{3+}/\text{Mn}^{4+}$ combinations [3]. These properties lead to a complex magnetic behavior at low temperatures [5,6]. In addition, the substitution of manganese ions by some other 3d cation (Cr^{3+} , Ti^{4+}) [7] offers the possibility to study effects of bond and/or site disorder on the geometrically frustrated magnetic system. In this work we focus our attention on the magnetic properties of Cr^{3+} substituted spinel compound $\text{LiCr}_{0.175}\text{Mn}_{1.825}\text{O}_4$.

Results and Discussion

The powder $\text{LiCr}_{0.175}\text{Mn}_{1.825}\text{O}_4$ sample was prepared by a rapid glycine-nitrate method (GNM), described elsewhere [8]. The XRPD experiments were performed on the Philips 1050 diffractometer by using $\text{CuK}\alpha_{1,2}$ radiation. All reflections of the

obtained XRPD pattern correspond to pure spinel phase. For the crystal structure refinement $15 \leq 2\theta \leq 115^\circ$ range was used with the 0.02° step and 10 seconds exposition. Refinement was done using the FullProf computing program based on the Rietveld full profile method. The structure has been refined in the space group $Fd3m$ (O_h^7) in well-known spinel type. The refinement results show that all Cr^{3+} ions substitute Mn^{3+} ions only, while no migration of lithium ions in the octahedral cation sites was obtained within the refinement accuracy.

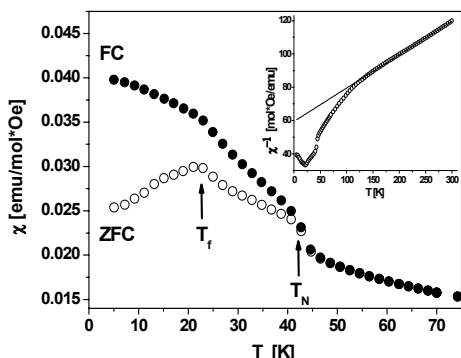


Fig. 1. Molar magnetic susceptibility χ in ZFC and FC regimes. *Inset:* Experimental (dots) and fitted (line) ZFC χ^{-1} values.

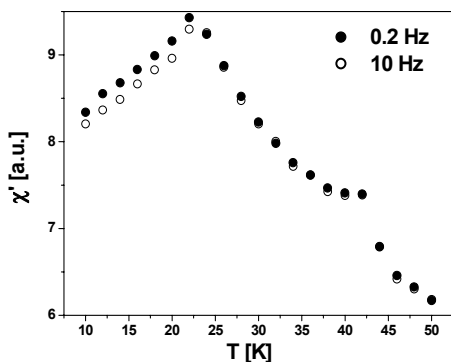


Fig. 2. Real part χ' of the AC susceptibility.

ability is a signature of the re-entrant spin glass behavior which means that spin-glass (SG) phase develops from the magnetically ordered state with the decrease in temperature [9]. Further information on the nature of the ordered phase can be gained from the isothermal $M(H)$ measurements, Fig. 3. The magnetization dependence versus field recorded at 40 K (i.e. below the phase transition at 42 K) is linear up to ± 5 T field which is a signature of a long-range AF order. Consequently, the temperature of 42 K is a Néel temperature of the sample under consid-

DC magnetic measurements were done in the applied field of 100 \AA in both zero-field-cooled (ZFC) and field-cooled (FC) regimes in the 4-300 K range. Obtained molar magnetic susceptibilities corrected for underlying ionic diamagnetism are reported in Fig. 1. Bifurcation between ZFC and FC curves is obvious for temperatures below 45 K. In the ZFC branch below this temperature two singularities can be observed: the first one at about 42 K and the second one at 22 K. In order to clarify the origin of these singularities we have conducted AC susceptibility measurements in the low temperature region. The AC susceptibility was measured in the zero applied DC field and with the AC driven field of $H_{ac} = 4$ \AA . The obtained real part χ' for field frequencies of 0.2 Hz and 10 Hz are depicted in Fig. 2. One can see that frequency dependence of χ' can be observed only below the singularity at 22 K, while signals for both frequencies coincide above this temperature. Consequently, χ' singularity at 42 K is frequency insensitive i.e. this points to the presence of the magnetically ordered phase below this temperature. Such a dependence of the in-phase AC suscepti-

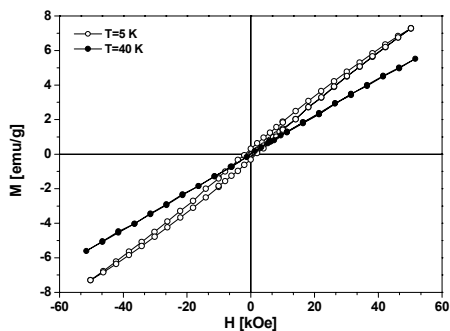


Fig. 3. $M(H)$ dependence recorded at 5 K and 40 K in the field range of ± 5 T.

From the fit to a Curie-Weiss law in the high temperature region (200-300 K), shown in the inset of Fig. 1, the effective magnetic moment of $\mu_{\text{eff}}=4.40 \mu_{\text{B}}$ was found. This value is in good agreement with the calculated moment of $\mu_{\text{eff}}^{\text{calc}}=4.32 \mu_{\text{B}}$ obtained under the assumption that Cr^{3+} ions replace Mn^{3+} ions only. In addition, this confirms the findings of the crystal structure refinement.

Conclusion

In pure LiMn_2O_4 the charge ordering of manganese ions is accompanied by the collective JT effect which leads to the removal of the spin frustration on the pyrochlore network. This results in the emergence of the long range AF ordering below $T_{\text{N}}\approx 65$ K [10]. The partial substitution of the Mn^{3+} (JT ion) by the Cr^{3+} (non-JT ion) causes the emergence of the partial system frustration that leads to the re-entrant SG behavior - the Néel temperature is lowered to 42 K and the formation of the SG phase occurs below $T_{\text{f}}=22$ K.

References

- [1] Y. Shin, A. Manthiram, *Electrochem. Solid-State Lett.*, 2002, **5(3)**, A55-58.
- [2] Y. P. Wu, E. Rahm, R. Holze, *Electrochim. Acta*, 2002, **47**, 3491-3507.
- [3] J.E. Greedan, *J. Mater. Chem.*, 2001, **11**, 37-53.
- [4] R. Englman, B. Halperin, *Phys. Rev. B*, 1970, **2**, 75-94.
- [5] Young-II Jang, F.C. Chou, Y.-M. Chiang, *Appl. Phys. Lett.*, 1999, **74**, 2504-2506.
- [6] A.S. Willis, N.P. Raju, J.S. Greedan, *Chem. Mater.*, 1999, **11**, 1510-1518.
- [7] M.A. Arillo, G. Cuello, M.L. López, P. Martin, C. Pico, M.L. Veiga, *Sol. Stat. Sci.*, 2005, **7**, 25-32.
- [8] I. Stojković, A. Hosseinmardi, D. Jugović, M. Mitrić, N. Cvjetičanin, *Solid State Ionics*, 2006, **177**, 847-850.
- [9] J.A. Mydosh, *Spin Glasses*, Taylor and Francis, London, 1993.
- [10] I. Tomeno, Y. Kasuya, Y. Tsunoda, *Phys. Rev. B*, 2001, **64**, 094422:1-8.

Macromolecular Physical Chemistry

(J)

SYNTHESIS OF CONDUCTIVE POLYANILINE NANOPARTICLES BY OXIDATION OF ANILINE WITH CERIUM(IV) SULFATE

G. Ćirić-Marjanović¹, Z. Jovanović¹, B. Marjanović² and I. Juranić³

¹*Faculty of Physical Chemistry, University of Belgrade, Studentski trg 12-16, POB 137, Belgrade, Serbia. (gordana@ffh.bg.ac.yu)*

²*Centrohem, Karadjordjeva 129, 22300 Stara Pazova, Serbia.*

³*Faculty of Chemistry, University of Belgrade, Studentski trg 12-16, POB 158, Belgrade, Serbia.*

Abstract

The conductivity and morphology of nanostructured polyaniline, synthesized by the chemical oxidative polymerization of aniline with cerium(IV) sulfate in aqueous solution without added acid, were studied as a function of oxidant/monomer initial mole ratio, reaction time and temperature. Polyaniline nanoparticles, exhibited mainly ordinary spherical shape with particle size of about 30–220 nm, were prepared by using Ce(IV)/aniline initial mole ratios in the range 2.0–2.5. Optimum reaction conditions for the synthesis of the most conductive nanostructured polyaniline with uniform particle size (30–80 nm) were found to be Ce(IV)/aniline initial mole ratio ~2.3, low initial reaction temperature ~2 °C, and relatively short reaction time (3 h). The early stages of aniline oxidation in water with one-electron oxidant Ce(IV) were theoretically studied by the AM1 semi-empirical quantum chemical method.

Introduction

Nanostructured conducting polyaniline (PANI) has attracted recently increasing attention from a wide area of scientific interests. PANI nanoparticles have the following advantages: firstly, the decrease in particle size can promote more effective doping, strengthen inter- or intrachain interactions and enhance the degree of crystallinity; secondly, PANI nanoparticles have some special electrical, optical and opto-electrical properties due to their smaller size; thirdly, with the decrease of PANI particle size, PANI dispersion medium become more stable and uniform, and helpful for producing uniform, transparent, conducting polymer thin film, thus overcoming the problem of processability [1–3]. Various supramolecular structures of the PANI were obtained, depending on the conditions of the reaction [4, 5]. In the case of aniline oxidation with ammonium peroxydisulfate (APS) in aqueous solutions it was found that the morphology of PANI depends on the acidity conditions during the reaction [4]. In solutions of sulfuric acid, granular PANI was produced; in solutions of acetic acid, PANI nanotubes were obtained. The evolution of polyaniline morphology during the course of aniline oxidation with APS in aqueous solutions, in the absence of any added acid, was also analyzed [5]. Although the conductivity of PANI thus prepared is rather low [5], $\sim 10^{-2}$ S cm⁻¹, the observed nanotubular morphology of the products makes such a system of substantial

interest. The knowledge and understanding of the factors that control the nanostructured morphology of PANI present a challenge.

In this paper, we analyze the influence of oxidant/monomer initial mole ratio, reaction time and temperature on the conductivity and morphology of nanostructured PANI, prepared by oxidation of aniline with cerium(IV) sulfate in aqueous solution without added acid.

Results and Discussion

Oxidation of aniline with cerium(IV) sulfate in water yields mixture of PANI hydrogensulfate (polaronic form) and PANI sulfate (bipolaronic form). Sulfuric acid and cerium(III) sulfate are byproducts, Fig. 1.

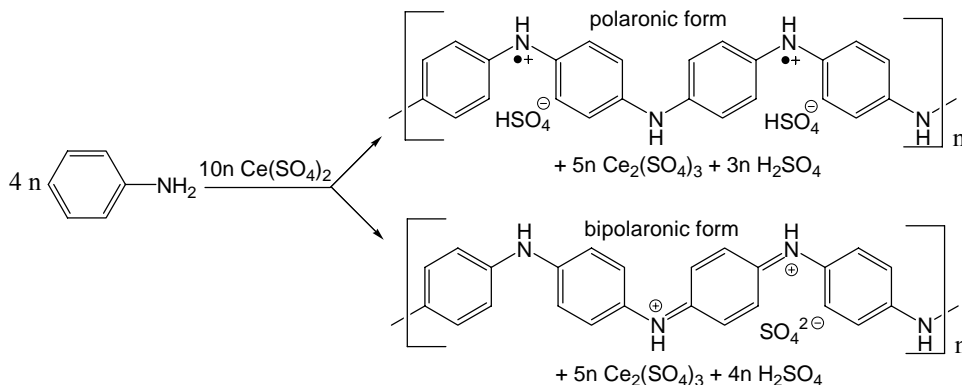


Fig. 1. Oxidation of aniline with cerium(IV) sulfate in water.

The conductivity of PANI thus prepared is $\sim 10^{-3}$ S cm^{-1} . Conductivity of PANI doped by HCl, prepared by using different Ce^{4+} /aniline mole ratios (reaction time 24 h, room temperature), is $\sim 10^{-2}$ S cm^{-1} , Table 1.

Table 1. Conductivity of PANI HCl.

Mole ratio Ce^{4+} / aniline	Conductivity (S cm^{-1})
2.0	0.028
2.1	0.022
2.2	0.031
2.3	0.036
2.4	0.026
2.5	0.023

It was found that the optimum mole ratio Ce^{4+} /aniline, producing the most conductive PANI, is 2.3. It is important to note that this mole ratio oxidant/monomer is slightly lower than theoretically expected (2.5). This can be explained by participation of dissolved oxygen in oxidation process. Decrease of the initial reaction temperature (room temperature to 2 °C), as well as decrease of reaction time (24 h to 3 h) induced increase of PANI conductivity.

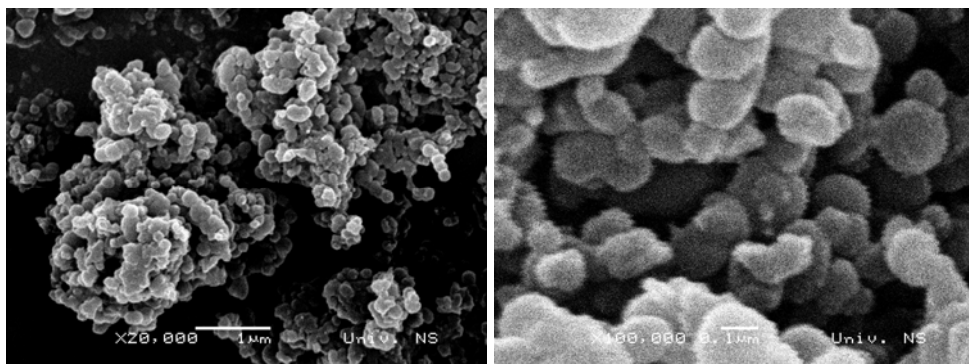


Fig. 2. SEM images of PANI doped with HCl ($[\text{Ce}^{4+}]/[\text{aniline}]=2.3$; RT; $t_{\text{polym.}}=3\text{h}$)

Scanning electron microscopy investigation of the morphology of undoped and doped PANI revealed formation of PANI nanoparticles, prevalently nanospheres with particle size 30–220 nm, in the whole range of studied experimental conditions, Fig. 2. The preparation of the smallest nanoparticles with the narrowest particle size distribution (30–80 nm) was achieved by using Ce(IV)/aniline initial mole ratio ~ 2.3 , initial reaction temperature 2 °C, and reaction time 3 h.

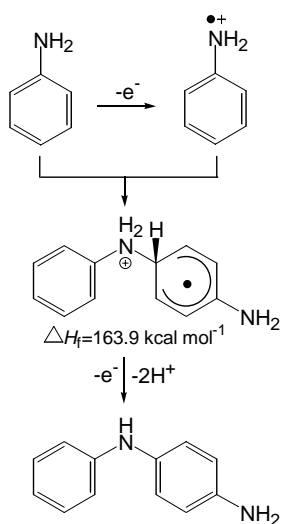


Fig. 3. Aniline dimerization mechanism

Semi-empirical quantum chemical AM1 computations of the heat of formation and spin density of solvated reactive species and intermediates show prevalence of N–C4 aniline dimer units (Fig. 3).

Conclusion

The use of cerium(IV) sulfate in the chemical oxidative polymerization of aniline in aqueous solution without added acid leads to the formation of PANI nanospheres. The conductivity and particle size of nanostructured PANI depend considerably on the initial Ce(IV)/aniline mole ratio, reaction temperature and time.

References

- [1] H. Xia, Q. Wang, *J. Nanopart. Res.*, 2001, **3**, 401.
- [2] L. Rongguan, S. Zhang, Q. Shi, J. Kan, *Synth. Met.*, 2005, **150**, 115.
- [3] D. Cheng, S-C. Ng, H.S.O. Chan, *Thin Solid Films*, 2005, **477**, 19.
- [4] E. N. Konyushenko, J. Stejskal, I. Šeděnková, M. Trchová, I. Sapurina, M. Cieslar, J. Prokeš, *Polym. Int.*, 2006, **55**, 31.
- [5] M. Trchová, I. Šeděnková, E. N. Konyushenko, J. Stejskal, P. Holler, G. Ćirić-Marjanović, *J. Phys. Chem. B*, 2006, **110**, 9461.

CHEMICAL OXIDATIVE POLYMERIZATION OF DI-ANILINIUM 5-SULFOSALICYLATE

G. Ćirić-Marjanović¹, A. Janošević¹, B. Marjanović², M. Trchová³,
J. Stejskal³ and P. Holler³

¹Faculty of Physical Chemistry, University of Belgrade,
Studentski Trg 12-16, POB 137, Belgrade, Serbia. (gordana@ffh.bg.ac.yu)

²Centrohem, Karadjordjeva 129, 22300 Stara Pazova, Serbia.

³Institute of Macromolecular Chemistry, Academy of Sciences of the Czech Republic,
Heyrovsky Sq. 2, 162 06 Prague 6, Czech Republic.

Abstract

The di-anilinium 5-sulfosalicylate was prepared *in situ* and polymerized in aqueous solution using ammonium peroxydisulfate as an oxidant. The precipitated polyaniline 5-sulfosalicylate (PANISSA) was soluble in polar aprotic solvents and showed conductivity of $\sim 0.1 \text{ S cm}^{-1}$. The weight-average molecular weight and polydispersity index were determined by gel-permeation chromatography to amount 53000 and 9.0, respectively. The molecular structure of polyaniline 5-sulfosalicylate was studied by FTIR and Raman spectroscopies, and its morphology was investigated by scanning electron microscopy. FTIR spectroscopy study, combined with MNDO-PM3 and AM1 semi-empirical quantum chemical study of the polymerization mechanism, indicate covalent as well as ionic bonding of sulfosalicylate to polyaniline chains.

Introduction

Polyaniline (PANI) is a conducting polymer that has been extensively studied due to its simple preparation, good thermal and environmental stability, structure versatility, and wide applicability. Chemical oxidative polymerization of commercially available aniline salts such as hydrochloride and sulfate gives polyaniline salts with poor solubility in common solvents. These unprocessable PANI salts commonly must be transformed by dedoping-redoping procedure to more processable PANI doped by functionalized acids. Many attempts to synthesize processable PANI salts *via* direct oxidation of various aniline salts with ammonium peroxydisulfate (APS), most often used oxidant in industrial production of PANI, have failed because hydrogensulfate, formed as a by-product during polymerization, was incorporated into the PANI structure instead of functionalized dopant anion [1]. It was shown that the solubility, crystallinity, thermal stability, electrochemical stability at higher potentials, and anticorrosive properties of PANI have been improved using 5-sulfosalicylic acid (SSA) as a dopant [2–4]. In these reports, PANI sulfosalicylate has been prepared *via* direct oxidation of *in-situ* prepared anilinium sulfosalicylate in large excess of SSA, or by redoping treatment of PANI base with SSA. In continuation of our recent work on efficient, cheap aniline salt precursor for direct synthesis of processable, soluble conducting PANI

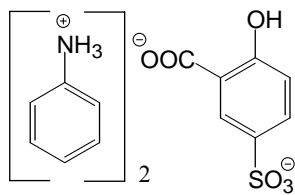


Fig. 1. di-Anilinium 5-sulfosalicylate.

salt [5], in the present paper, we prepared *in situ* di-anilinium 5-sulfosalicylate (di-ANISSA), Fig. 1, and performed its polymerization with APS in aqueous solution. Novel polymeric material is characterized by gel-permeation chromatography (GPC), FTIR and Raman spectroscopies, scanning electron microscopy and conductivity measurements. The early stages of the polymerization mechanism were theoretically studied by MNDO-PM3 and AM1 methods.

Results and Discussion

The di-ANISSA was prepared *in-situ* by the slow addition of 40 mmol of the aniline to continuously stirred aqueous solution (100 ml) of the 20 mmol SSA. Reaction solution was heated to boiling and then cooled to room temperature. The aqueous solution of 50 mmol APS (100 ml) was slowly added to the stirred solution of the di-ANISSA at room temperature. Reaction solution was stirred 24 h. The PANISSA precipitate was separated by filtration, washed with water (procedure I) or 1 mol dm⁻³ SSA (procedure II) and acetone, and then dried *in vacuo* at 70 °C.

Obtained green PANISSA precipitates have conductivities ~0.01 S cm⁻¹ (procedure I) and ~0.1 S cm⁻¹ (procedure II). The conductivity of the PANISSA prepared by procedure II is very similar to that of the PANISSA prepared by Trivedi *et al.* by using large molar excess of the SSA [2].

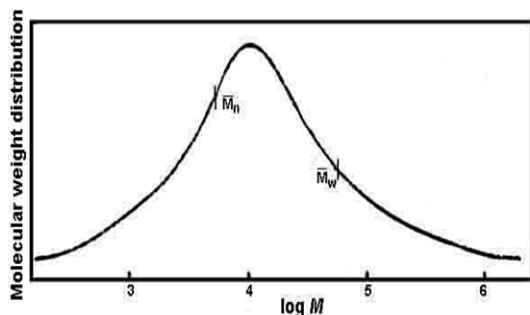


Fig. 2. Molecular weight distribution as obtained by GPC for the PANISSA sample.

One large peak appeared in the gel permeation chromatogram of the PANISSA, Fig. 2. The weight-average molecular weight $M_w = 53000$; the number average molecular weight $M_n = 5900$; polydispersity index $PDI = 9.0$. In comparison to PANISSA obtained by chemical oxidative polymerization of the anilinium 5-sulfosalicylate, showing bimodal molecular weight distribution (MWD) [6],

the PANISSA obtained by oxidation of di-ANISSA exhibits unimodal MWD with considerably higher values of M_w and M_n .

As-synthesized PANISSA in its doped, protonated emeraldine salt form shows good solubility in N-methyl-2-pyrrolidone, dimethylsulfoxide and N,N-dimethyl-formamide.

Both FTIR spectra of doped and dedoped PANISSA (Table 1) exhibit benzenoid (~1500 cm⁻¹) to quinonoid (~1600 cm⁻¹) band intensity ratio characteristic of the PANI emeraldine form. The strong band at 810 and 830 cm⁻¹ for doped and dedoped

Table 1. Main FTIR bands of PANISSA (B-benzenoid ring, Q-quinonoid ring; ν –stretching, δ –in plane bending, γ –out-of- plane bending vibration).

Wavenumber / cm^{-1}		Assignment
PANISSA doped	PANISSA dedoped	
3464	3460	$\nu(\text{N-H}) + \nu(\text{O-H})$
1673	1673	$\nu(\text{C=O})$ in COOH
1578	1589	$\nu(\text{C=C})$ of quinonoid ring
1480	1496	$\nu(\text{C=C})$ of benzenoid ring
1305	1301	$\nu(\text{C-N})$ second. arom. amine
1241	1237	$\nu(\text{C-N}) + \delta(\text{C-H}) + \nu(\text{C-O})$
1143	1145	$\text{Q}=\text{N}^+\text{H}-\text{B} / \text{B}-\text{NH}-\text{B}$
1028	1026	sym. $\nu(\text{SO}_3^-) + \text{arom. } \delta(\text{C-H})$
882	955	$\gamma(\text{C-H})$ (1,2,4-trisubstit. ring)
800	826	$\gamma(\text{C-H})$ (1,4-disubstit. ring)

PANISSA, respectively, is assigned to the C–H out-of-plane deformation vibration of the 1,4-disubstituted benzene ring. The absorption band due to the symmetric $-\text{SO}_3^-$ stretching vibration at $\sim 1030 \text{ cm}^{-1}$ is very strong in the monomer spectrum, and is also present with decreased intensity in the spectrum of the doped PANISSA. This band did not vanish in the spectrum

of dedoped sample. This may be explained by the covalent bonding between sulfosalicylate and PANI.

MNDO-PM3 and AM1 semi-empirical quantum chemical calculations show that sulfosalicylate dianion is more oxidizable (ionization energy $E_i=9.7 \text{ eV}$) than anilinium cation ($E_i=10.2 \text{ eV}$), indicating that polymerization is initiated by the generation of sulfosalicylate radicals which can be covalently incorporated into the PANI macromolecular structure, Fig. 3. Coupling

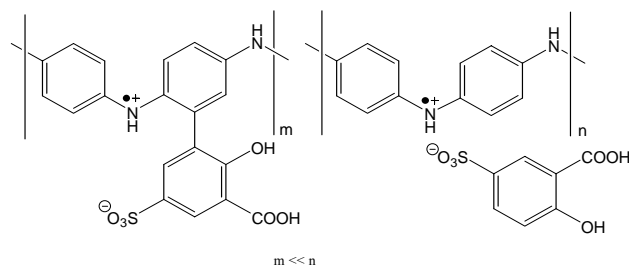


Fig. 3. Macromolecular structure of PANISSA are proposed as dominating, based on the spin and charge density distribution of reactive species.

Conclusion

The oxidation of the di-anilinium 5-sulfosalicylate with ammonium peroxydisulfate, in aqueous solution, leads to the formation of the conductive, processable polyaniline sulfosalicylate, soluble in aprotic polar solvents.

References

- [1] J. Stejskal; D. Hlavatá; P. Holler; M. Trchová; J. Prokeš; I. Sapurina, *Polym. Int.*, 2004, **53**, 294.
- [2] D. C. Trivedi, S. K. Dhawan, *Synth. Met.*, 1993, **58**, 309.
- [3] A. Raghunathan, G. Rangarajan, D. C. Trivedi, *Synth. Met.*, 1996, **81**, 39.
- [4] G. Ćirić-Marjanović, B. Marjanović, M. Popović, V. Panić, V. Mišković-Stanković, *Russ. J. Electrochem.* 2006, *in press*.
- [5] B. Marjanović, G. Ćirić-Marjanović, I. Juranić, P. Holler, The 7th YUMRS Conference YUCOMAT 2005, Herceg Novi, SCG, The Book of Abstracts, p. 75.

STUDY OF COPPER ADSORPTION ON AMINOFUNCTIONALIZED MACROPOROUS POLY(GMA-co-EGDMA)

A. Nastasović¹, Z. Sandić², Lj. Malović³,
D. Jakovljević¹ and J. Marković⁴

¹*ICTM -Center for Chemistry, Studentski trg 12-16, Belgrade, Serbia.
(anastaso@chem.bg.ac.yu)*

²*Faculty of Science, Mladena Stojanovića 2, Banja Luka, BIH.*

³*Faculty of Forestry, Kneza Višeslava 1, Belgrade, Serbia.*

⁴*Vinča Institute of Nuclear Sciences, P.O. Box 522, Belgrade, Serbia.*

Abstract

Macroporous crosslinked copolymer of glycidyl methacrylate and ethylene glycoldimethacrylate (PGME) was synthesized by suspension copolymerisation and modified by ring-opening reaction of epoxy groups with ethylene diamine, diethylene triamine and triethylene tetramine. The uptake of copper ions by amino-functionalized macroporous PGME from aqueous solutions was investigated in batch experiments. The equilibrium data fitted well with the Langmuir model.

Introduction

Metal adsorption through precipitation and ion exchange/chelation is a common approach for reducing the toxicity of the wastewater streams of hydro-metallurgical and other industries [1]. Chelating copolymers that consist of crosslinked copolymer (solid support) and ligand with O, N, S and P atoms that coordinate different metal ions, are often used for that purposes. Amino-functionalized macroporous glycidyl methacrylate copolymers, obtained by reaction of epoxy groups of the copolymer with amines possess high capacity and good selectivity for heavy metal ions, combined with chemical and mechanical stability [2,3]. In this study, macroporous crosslinked copolymer of glycidyl methacrylate and ethylene glycoldimethacrylate (PGME) was modified with ethylene diamine (PGME-en), diethylene triamine (PGME-deta) and triethylene tetramine (PGME-teta). Amino-functionalized samples were used for copper sorption. The experimental data were analysed by the Langmuir model of adsorption.

Experimental

Macroporous PGME (surface area $36 \text{ m}^2 \text{ g}^{-1}$, pore diameter 87 nm, particle size 150-500 μm) was prepared by suspension copolymerisation [6]. PGME-en was obtained by heating the mixture of 4.0 g of PGME, 10.0 g of ethylene diamine and 100 ml of toluene at 80 °C for 6 h. PGME-deta was obtained by heating the mixture of 3.6 g of PGME, 15.7 g of diethylene triamine and 100 ml of toluene at 80 °C for 6 h. PGME-teta was obtained by heating the mixture of 5.0 g of PGME, 7.75 g of triethylene tetramine and 30 ml of toluene. After the reaction, samples were filtered, washed with

ethanol and dried. Sorption of Cu(II) ions was studied by contacting 0.1 g of copolymer with 50 ml of metal salt solution. After 3 h, samples were filtered and the Cu(II) concentration in filtrate was determined by atomic absorption spectrometry (AAS, SpectrAA Varian Instruments). The sorption capacity was calculated from expression:

$$Q = \frac{(C_0 - C) \times V}{m} \quad (1)$$

where C_0 and C are the concentrations of the metal ions in the initial solution and in the aqueous phase after treatment for certain period of time, respectively, V is the volume of the aqueous phase and m is the amount of the copolymer beads used for the experiment.

Results and Discussion

The adsorption isotherms of Cu(II) on amino-functionalized samples are shown in Fig. 1. The maximum uptake for PGME-en, PGME-deta and PGME-teta are 1.38, 2.20 and 2.62 mmol g^{-1} . Obviously, the Cu(II) uptake increases with the increase of equilibrium concentration until reaching the saturation value, after which the concentration no longer affects the uptake capacity. The affinity of the adsorbent towards the metal ions may be verified by plotting the adsorption data according to Langmuir adsorption model [5]:

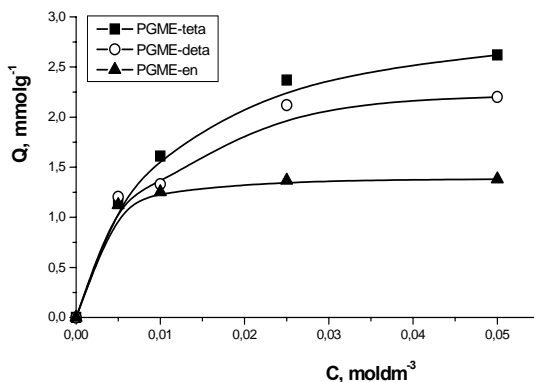


Fig. 1. Adsorption isotherms of Cu(II) on PGME-en, PGME-deta and PGME-teta at pH 4 and 25 °C.

$$\frac{C_e}{q_e} = \frac{C_e}{q_s} \frac{1}{Kq_s} \quad (2)$$

where C_e is the equilibrium concentration of metal ions in solution, q_e the adsorbed value of metal ions at equilibrium concentration, q_s the saturated adsorbing capacity and K is the binding constant, related to the energy of adsorption. Plots C_e/q_e vs. C_e gave a straight line, indicating that the adsorption corresponds to Langmuir isotherm. The values of q_s and K for adsorption of Cu(II) on PGME-en, PGME-deta and PGME-teta were obtained from the slopes and intercepts of the lines in Fig. 2 and reported in Table 1. The value of correlation coefficient (r^2) and experimental value of saturation capacity, $q_{e, \text{exp}}$, indicate that the Langmuir isotherm

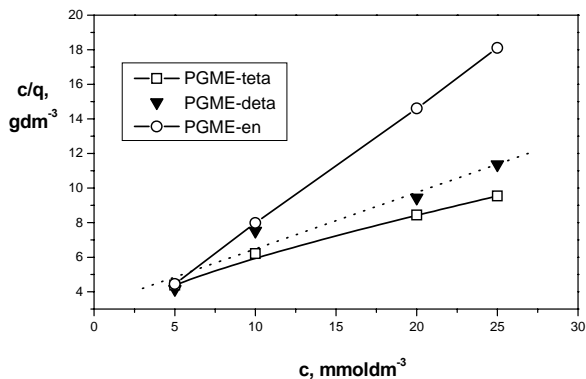


Fig. 2. Langmuir isotherms for Cu(II) adsorption on PGME-en, PGME-deta and PGME-teta.

has been best fitted for Cu(II) sorption on PGME-en. The lowest value of correlation coefficient (0.970) indicate deviation from Langmuir model in the case of Cu(II) uptake on PGME-deta.

Table 1. Parameters of Langmuir adsorption isotherm for the Cu(II) adsorption on amino-functionalized samples at 25 °C.

Sample	$q_{e,exp}$, mmolg ⁻¹	q_s , mmolg ⁻¹	K dm ³ mmol ⁻¹	r^2
PGME-en	1.38	1.47	0.62	0.999
PGME-deta	2.20	3.06	0.10	0.970
PGME-teta	2.62	3.98	0.07	0.994

Conclusion

The obtained results show that the equilibrium distribution of Cu(II) between the sorbent and solution phases can be described using the Langmuir model of monomolecular layer adsorption. The best fit for the Cu(II) adsorption data was observed for PGME sample modified with ethylene diamine.

Acknowledgement

This work was supported by the Serbian Ministry of Science and Environmental Protection.

References

- [1] S. D. Smith, S. D. Alexandratos, *Solvent Extr. Ion Exch.*, 2000, **18**, 779-807.
- [2] F. Švec, H. Hrudkova, D. Horak, J. Kalal, *Angew. Makromol. Chem.*, 1977, **63**, 23-36.
- [3] A. Nastasović, S. Jovanović, D. Đorđević, A. Onjia, D. Jakovljević, T. Novaković, *React. Funct. Polym.*, 2004, **58**, 139-147.
- [4] S. Jovanović, A. Nastasović, N. Jovanović, K. Jeremić, *Mater. Sci. Forum*, 1996, **214**, 155-162.
- [5] A. Atia, A. M. Donia, K. Elwakeel, *Sep. Purif. Technol.*, 2005, **43**, 43-48.
- [6] P. K. Malik, *J. Hazard Mater.*, 2004, **B113**, 81-88.

KINETICS OF HEAVY METAL SORPTION ON MACROPOROUS VINYLPIRIDINE BASED COPOLYMER

A. Nastasović¹, S. Kljajević¹, D. Jakovljević¹,
Z. Vuković² and J. Marković³,

¹ICTM -Center for Chemistry, Studentski trg 12-16, Belgrade, Serbia.
(anastaso@chem.bg.ac.yu)

²ICTM -Center for Catalysis, Njegoševa 12, Belgrade, Serbia.

³Vinča Institute of Nuclear Sciences, P.O. Box 522, Belgrade, Serbia.

Abstract

Sorption of copper, nickel and cobalt on macroporous crosslinked copolymer of 4-vinylpyridine and ethylene glycol dimethacrylate, PVPE, was studied. The kinetics models (pseudo-first and pseudo-second order equations) were applied to the data obtained from batch sorption experiments at room temperature. The sorption of heavy metals was found to proceed according to pseudo-second order kinetics.

Introduction

Wide ranges of processes are available for the removal of heavy metals from wastewaters, like coagulation, filtration, ion exchange, liquid-liquid extraction, etc. [1]. The usage of chelating polymers is one of the most effective techniques for the removal of heavy metals from wastewaters. Macroporous crosslinked copolymers based on vinylpyridine obtained by suspension copolymerization in the shape of regular beads of required size, have been used for heavy metal removal [2-4]. In this paper, sorption rates for Cu(II), Ni(II) and Co(II) ions of macroporous crosslinked copolymer of 4-vinylpyridine and ethylene glycol dimethacrylate, PVPE, were determined in batch experiments. The experimental data was analysed with pseudo-first and pseudo-second order kinetic models to determine the best-fit equation for heavy metals sorption by PVPE.

Experimental

Macroporous PVPE (surface area 8.8 m²g⁻¹, pore diameter 2400 nm, particle size 150-500 μm) was prepared by suspension copolymerisation [5]. For determination of metal sorption rate, 0.5 g of copolymer was contacted with 50 ml of 0.05 M metal salt solution. At appropriate times, 1 ml of aliquots were removed and diluted to 100 ml. The concentration of Cu(II), Ni(II) and Co(II) ions was determined by atomic absorption spectrometry (AAS, SpectrAA Varian Instruments). The experimental data were first treated with pseudo-first order equation [6]:

$$\log(q_e - q_t) = \log q_e - \frac{(k_1 t)}{2.303} \quad (1)$$

where k_1 is the rate constant (min^{-1}), q_e , q_t are the amounts of sorbed metal ions at equilibrium and at time t (mmol g^{-1}), respectively. Kinetic data were further treated with linear form of the pseudo-second-order kinetic model [6]:

$$\frac{t}{q_t} = \frac{1}{k_2 q_e^2} + \frac{1}{q_e} t \tag{2}$$

where k_2 ($\text{g}^{-1} \text{mmol}^{-1} \text{min}^{-1}$) is the rate constant of pseudo-second order sorption.

Results and Discussion

One of the most important properties of the chelating polymers is the rate of establishing the equilibrium metal sorption. Thus, sorption rate for Cu(II), Ni(II) and Co(II) ions on PVPE was determined (Fig. 1). The sorption of heavy metal ions on macroporous PVPE was found to be relatively rapid. Namely, after 30 minutes, PVPE sorbed approximately 90 % of metal ions from aqueous solutions. The sorption half

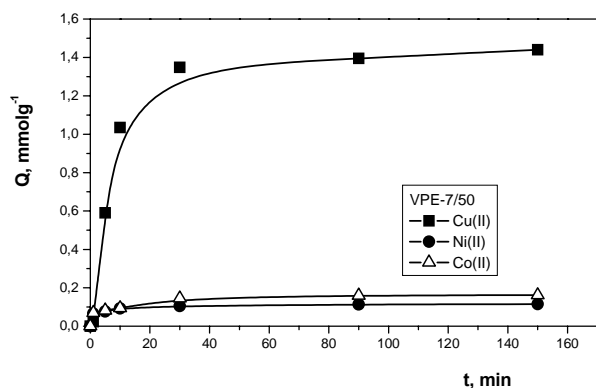


Fig.1. Sorption of Cu(II), Ni(II) and Co(II) ions by PVPE at pH = 4 and 25 °C.

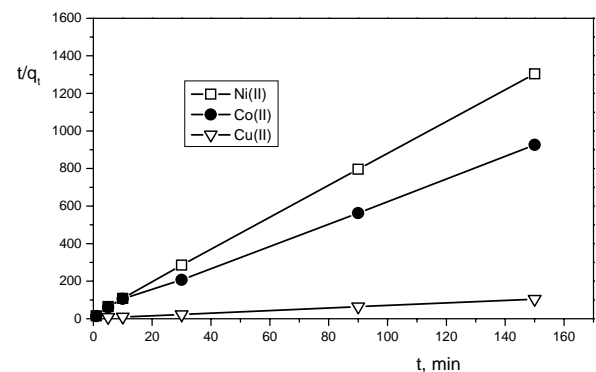


Fig. 2. Pseudo-second order kinetics of Cu(II), Ni(II) and Co(II) ions sorption by PVPE

time, $t_{1/2}$, defined as the time required to reach 50% of the total sorption capacity, was 4 min for Ni(II) and around 7 min for Cu(II) and Co(II) ions. The $t_{1/2}$ values obtained for PVPE are comparable with literature data. Sugii et al. found the $t_{1/2}$ values for Cu(II) and Ni(II) sorption on poly(4-VP-co-DVB) to be 3 and 5 min, respectively [2,3]. The maximum Cu(II) capacity of PVPE was 12 and 9 times higher than maximum capacities for Ni(II) and Co(II) ions, respectively. Rate constants and q_e values calculated from intercepts and slopes of Eq. 1 and 2, as well as experimental values of equilibrium sorption capacity, $q_{e, \text{exp}}$ are given in Table 1. As seen, q_e values estimated from the pseudo-first-order model do not agree with experimental ones. However, the linear plots of t/q_e versus t show a good agreement of experimental data with the pseudo-second-

order kinetic model for both samples (Fig. 2). The correlation coefficients for all samples are higher than 0.99, and the calculated q_e values agree very well with the experimental data. This implies that sorption proceeds according to pseudo-second-order kinetic depending upon both metal concentration and the properties of amino-functionalized macroporous copolymer.

Table 1. Kinetic data for Cu(II), Ni(II) and Co(II) sorption on PVPE.

Metal ion	$q_{e,exp}$, mmolg ⁻¹	Pseudo-first order kinetics			Pseudo-second order kinetics		
		k_1 , min ⁻¹	q_e , mmolg ⁻¹	R	k_2 , gmmol ⁻¹ min ⁻¹	q_e , mmolg ⁻¹	R
Cu(II)	1.44	0.016	3.81	0.732	0.13	1.49	0.999
Ni(II)	0.11	0.002	1.38	0.622	3.75	0.12	0.999
Co(II)	0.16	0.061	1.26	0.770	1.29	0.17	0.999

Conclusion

Macroporous crosslinked copolymer of 4-vinylpyridine and ethylene glycol dimethacrylate (PVPE) was used for sorption of Cu(II), Ni(II) and Co(II) ions. The sorption of heavy metal ions was found to be relatively rapid. Namely, after 30 minutes PVPE sorbed approximately 90 % of metal ions from aqueous solutions. The sorption half time was 4 min for Ni(II) and around 7 min for Cu(II) and Co(II) ions. The uptake of Cu(II), Ni(II) and Co(II) on PVPE follows the pseudo-second-order kinetic.

Acknowledgement

This work was supported by the Serbian Ministry of Science and Environmental Protection.

References

- [1] S. D. Smith, S. D. Alexandratos, *Solvent Extr. Ion Exch.*, 2000, **18**, 779-807.
- [2] A. Sugii, N. Ogawa, Y. Iinuma, H. Yamamura, *Talanta*, 1981, **28**, 551-556.
- [3] A. Sugii, N. Ogawa, K. Harada, K. Nishimura, *Analytical Sciences*, 1988, **4**, 399-402.
- [4] V. Neagu, I. Untea, E. Tudorache, C. Luca, *React. Funct. Polym.*, 2003, **57**, 119-124.
- [5] S. Jovanović, A. Nastasović, N. Jovanović, T. Novaković, *Hem.Ind.*, 2001, **55**, 493-499.
- [6] A. Atia, A. M. Donia, K. Z. ElWakeel, *Sep. Purif. Technol.*, 2005, **43**, 43-48.

HEALTHCARE AND HYGIENE PRODUCTS MADE OF NONWOVEN TEXTILE MATERIALS

S. Lukić¹, A. Milutinović-Nikolić², K. Asanović¹ and G. Popović³

¹*Faculty of Technology and Metallurgy, Belgrade, Serbia*

²*Institute of Chemistry, Technology and Metallurgy,
Department of Catalysis and Chemical Engineering, Belgrade, Serbia*

³*CIS Institute, Belgrade, Serbia*

Abstract

The paper provides some examples of engineering nonwoven textile materials in order to fulfill desired attributes for modern disposable articles in healthcare and hygiene. The physical and mechanical characterization of constituents that will be used for synthesis of composites based on spunbond thermobonded nonwoven polypropylene textile materials was performed. The investigated nonwovens are thin, soft and have satisfactory tensile force and elongation enabling their embedding into desired composites. The main difference between samples is in their air permeability.

Introduction

Healthcare and hygiene products are an important sector in the field of medicine and surgery. The range of products available is vast but typically they are used either in the operating theater or on the hospital ward for the hygiene, care, and safety of staff and patients. Beside already well known products like uniforms, surgical cloths, covers, bedding and wipes contemporary products include incontinence diaper and sheets. Incontinence products are composite articles consisting of an inner covering layer, an absorbent layer and outer layer. These three layers are facing, soaker and barrier. They are combined together to achieve the optimal characteristics of moisture wicking of incontinence products [1, 2].

There are various methods to obtain nonwovens; among them the spunbonded process is preferred for incontinence products because of its low cost which allows one time use. Spunbond product are obtained directly from polymer in a form of long continuous fibers that are bonded into nonwoven either by heat (thermobonded) or by adhesive [3]. In this paper the physical and mechanical properties of three different nonwoven textile materials were investigated in order to use them as raw materials for composite material. These composites are designed to be used either for breathable nonwoven backsheet that allows air to circulate for healthier skin while protecting the mattress from excessive soilage or for total protection against leaking.

Experimental

The investigated constituents were: spunbond thermobonded nonwoven polypropylene, super soft -hydrophilic (NW1), spunbond thermobonded nonwoven polypropylene-hydrophobic (NW2) and double layered nonwoven material (NW2 thermally bonded with polyethylene film) –NW3. The difference in hydro-affinity of nonwovens (NW1-

hydrophilic and NW2 and NW3-hydrophobic) is obtained by surfactant treatment used in the production process. The NW1 is going to be inner layer of composite, while NW2 and NW3 are going to be future outer layers of two different types of composites designed for incontinence sheets. The role of polyethylene film is to stop the liquid from leaking and therefore NW3 should not be used for breathable products.

The properties of nonwoven constituents were evaluated as per the standard methods [4-7]. The standard investigations include: thickness [4], basis weight [5], tensile force and elongation [6] as well as the air permeability [7]. The tensile force and elongation were measured in both production direction (\uparrow) and perpendicular to this direction (\rightarrow). Air permeability is defined as "the rate of air flow through a material under different pressure between two fabric surfaces" [8]. It was calculated from the rate of air flow passing perpendicularly through the known area of fabric to obtain a prescribed pressure difference. All standard methods are performed on set of experiments and therefore the measuring results are given as average values, their standard deviations and the coefficients of variations.

Results and Discussion

The results of investigation are summarized in Tables 1 and 2.

Table 1. Physical properties of investigated samples

Sample		NW1	NW2	NW3
Thickness	Average value, mm	0.127	0.112	0.113
	Standard deviation, mm	0.014	0.013	0.013
	Coefficient of variation, %	11.2	11.6	11.7
Basis weight	Average value, $\text{g}\cdot\text{m}^{-2}$	17.2	15.3	23.4
	Standard deviation $\text{g}\cdot\text{m}^{-2}$	0.8	0.6	0.9
	Coefficient of variation, %	4.6	3.8	3.7
Air permeability	Average value, $\text{m}^3\cdot\text{min}^{-1}\cdot\text{m}^{-2}$	15.04	6.35	0
	Standard deviation, $\text{m}^3\cdot\text{min}^{-1}\cdot\text{m}^{-2}$	1.25	0.48	-
	Coefficient of variation, %	8.3	7.6	-

For investigated nonwovens is essential to be thin and soft, particularly for NW1 that should be in contact with skin. All these samples have these qualities. The investigated nonwovens have similar values for thickness and basis weight. The main difference between samples is in their air permeability. NW1 is going to be inner layer of composite to be synthesized and therefore should have high air permeability. The investigated NW1 fulfills this criterion since it has approximately same value of air permeability as the surgical masks [8]. The NW2 has medium air permeability, while NW3 presents obstacle for air flow.

Table 2. Mechanical properties of investigated samples

Sample		NW1	NW2	NW3
Tensile force (\uparrow)*	Average value, N/5cm	46.1	33.2	35.3
	Standard deviation, N/5cm	3.1	1.6	3.8
	Coefficient of variation, %	6.5	4.7	10.7

Elongation (\uparrow)*	Average value, %	36	50	47
	Standard deviation, %	3.1	2.6	3.6
	Coefficient of variation, %	8.6	5.1	7.5
Tensile force (\rightarrow)*	Average value, N/5cm	4.5	14.2	26.5
	Standard deviation, N/5cm	0.5	2.5	2.9
	Coefficient of variation, %	11.9	17.3	11.1
Elongation (\rightarrow)*	Average value, %	78	70	76
	Standard deviation, %	7.7	5.8	8.1
	Coefficient of variation, %	9.8	8.2	10.6

* : (\uparrow) -in production direction and (\rightarrow)- perpendicular to production direction

All investigated nonwovens have satisfactory tensile force and elongation enabling their embedding into desired composites.

Conclusion

The physical and mechanical characterization of constituents that will be used for synthesis of composites based on nonwoven textile materials was performed. The investigated spunbond thermobonded nonwoven polypropylene materials are thin, soft and strong. The hydrophilic nonwoven NW1 has high air permeability and might be used as inner layer of composite that is in direct contact with human skin. According to air permeability data the hydrophobic nonwoven NW2 might be used as outer layer of breathable incontinence product and NW3 for outer layer of composites that prevent leaking. The investigations are still in progress.

Acknowledgements

This work was supported by the Ministry of Science & Environmental Protection of Republic of Serbia (Project TR 6713).

References

- [1] A.J.Rigby, S.C.Anand, Medical textiles, in Handbook of Technical Textiles, Woodhead Publishing Limited, Cambridge, 2000, 407-424.
- [2] R.Czajka, Fibres & Textiles in Eastern Europe, 2005, **13**(1), 13-15.
- [3] J. Lunenschloss, W. Albrecht, Vliesstoffe, Stuttgart, Georg Thieme Verlag, 1982.
- [4] Yugoslav Standard: JUS.FS2.021, 1986.
- [5] Yugoslav Standard: JUS.FS2.016, 1986.
- [6] Yugoslav Standard: JUS.FS2.017, 1982.
- [7] US Standard: ASTM, D-737-75, 1995.
- [8] H. Epps, K. K. Leonas, Int. Nonwovens J. 2002, **9**(2), 55-62.

CURE CHARACTERISTICS OF RECYCLED RUBBER POWDER FILLED STYRENE BUTADIENE /CHLOROSULPHONATED POLYETHYLENE RUBBER BLENDS

G. Marković¹, M. Marinovic-Cincović² and B. Radovanović³,

¹*Tigar, Pirot, gmarkov@tigar.com*

²*VINČA Institute of Nuclear Science, Belgrade,*

³*Faculty of Science, Niš, Serbia*

Abstract

The effect of recycled rubber powder (RRP) on cure characteristics of styrene butadiene and chlorosulphonated polyethylene rubber blends (SBR/CSM) was investigated in the concentration range of 0 to 20 phr. Results indicate that the minimum torque and Mooney viscosity of the SBR/CSM rubber blends increase with increasing RRP loading whereas the scorch time and cure time exhibit a decreasing trend. Increasing RRP loading also gives SBR/CSM rubber compounds reduces the elongation at break but the tensile stress, M 200 (stress at 200% elongation) increases slightly.

Introduction

Scrap rubbers are made up of rubber that does not meet processing and product specifications, leftover rubber from manufacturing activities and also old and defective rubber products. The scrap rubbers are waste and usually discharged. To reduce this pollution there is a need to recycle scrap rubber [1]. Reclamation of scrap (vulcanized) rubber can be done by mechanical [2-3] and chemical processes [3-4]. Crane and Kay [6] have shown that scrap rubber vulcanisates could be depolymerized to a product known as “depolymerized scrap rubber”, which should be useful as a rubber compounding ingredient and as a fuel-oil extender. Styrene butadiene rubber has been studied and reported on extensively because of its superior performance in tire applications. Hypalon is a Chlorosulfonated polyethylene manufactured by DuPont, resistant to interactions with alcohol's and strong acids and bases. The purpose of this study is to investigate the cure characteristics of recycled rubber powder (RRP) filled styrene butadiene/chlorosulphonated polyethylene (SBR/CSM) rubber blends.

Results and Discussion

Table 1. shows that increasing the recycled rubber powder loading in styrene butadiene and chlorosulphonated polyethylene rubber blends reduces the scorch time. This is because of the presence of cross-linked precursors and unreacted curative in the rubber powder [1-2]. The existence of unreacted accelerator in rubber powder waste has been reported by Mathew et al. [5]. The other reason is diffusion of sulfur from the rubber matrix phase to the rubber powder phase, which lowers the concentration of sulfur in the rubber matrix [2-3]. Increasing the recycled rubber powder loading in SBR/CSM rubber blends also reduces the cure time t_{90} , as shown in Table 1. Similar trends were

also observed by Baharin et al. [1], Ishiaku et al. [6] using different types and sizes of rubber powder particles.

The minimum torque, a measure of the stock viscosity, shows a slight increase with increasing rubber powder loading. This indicates that the processability of the compounds becomes a little more difficult. A similar observation can be seen in Fig. 1 for the Mooney viscosity of RRP filled SBR/CSM rubber blends at 140 °C.

Table 1. Curing characteristics of recycled rubber powder filled 1 styrene butadiene rubber/ chlorosulphonated polyethylene rubber blends

Curing characteristics	Rubber powder loading (phr)				
	0	5	10	15	20
Scorch time (min)	8	11	12	13.5	13.8
Cure time (min)	22	25	28	29	30
Cure rate index (CRI)	0.07	0.07	0.06	0.06	0.06

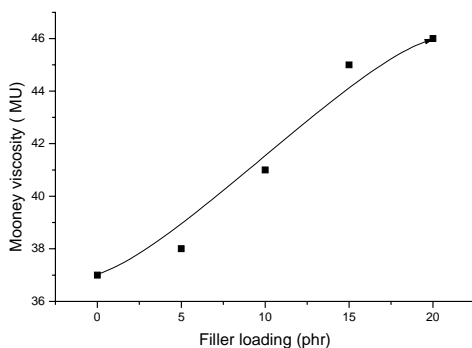


Fig. 1. Mooney viscosity of RRP-filled styrene butadiene rubber/ chlorosulphonated polyethylene rubber blends

Tensile properties

The tensile strength gradually increased to a maximum at 10 phr of rubber powder as shown in Tab. 2. As the rubber powder concentration increases, agglomeration and hence particle–particle interaction of the rubber powder also increases. The elongation at break of SBR/CSM rubber blends decreases with increasing recycled rubber powder loading. However, the decrease is small, particularly after 10 phr of recycled rubber powder loading. A similar observation was reported by Baharin et al. [1]. It can be seen that M 200 increase slightly with increasing recycled rubber powder.

Table 2. Mechanical characteristics of recycled rubber powder filled styrene butadiene rubber/ chlorosulphonated polyethylene rubber blends

Mechanical characteristics	Rubber powder loading (phr)				
	0	5	10	15	20
Tensile strength (MPa)	8	10	13..5	9	7.5
Elongation at break (%)	137	135	134	132	130
Modulus M 200 (%)	62	72	81	94	115

Conclusion

Cure characteristics such as scorch time and cure time of the styrene butadiene rubber/ chlorosulphonated polyethylene rubber blends increase with increasing recycled rubber powder loading but show slight decreases in CRI values. Tensile properties such as tensile modulus slightly increase with increasing recycled rubber powder loading whereas the elongation break shows a decreasing trend.

References

- [1] A. Baharin, M. Nasir, A.R. Rohaidah, Rubber powder from overcure, latex and its usage, International Rubber Conference, Kuala Lumpur, Malaysia, 6-9 October 1997, p. 277.
- [2] R.P. Burford, M. Pittolo, Rubber Chem. Technol., 1982, **55**, 1233.
- [3] V.M. Makarov, V.F. Drozdoski, Reprocessing of Tyres and Rubber Wastes Recycling from Rubber Product Industry, Ellis Horwood, New York, 1991 p. 28.
- [4] C. Roy, A. Rastegar, S. Kaliaguine, H. Darmstadt, Plast. Rubber Comp. Process Appl., 1995, **23**, 21.
- [5] G. Mathew, R. Singh, P. Lakshminarayanan, S. Thomas, J. Appl. Polym. Sci., 1996, **61**, 2035.
- [6] U.S. Ishiaku, C.H. Chong, H. Ismail, Polym. Testing, 2000, **19**, 507.
- [7] G. Crane, E.L. Kay, Rubber Chem. Technol., 1975, **48**, 50

DIFFUSION AT MOLECULAR LEVEL PROBED BY Ru(BPY)₃²⁺ LUMINESCENCE QUENCHING

David M. Sovic and Bratoljub H. Milosavljevic

*Marshall University, Department of Chemistry,
One John Marshall Drive, Huntington, WV 25755, USA
bmilosav@cas.usf.edu*

Abstract

The kinematic viscosities of water, 5% (molar) glycerol-water, and 5% (w/w) poly(vinyl alcohol), PVA, in water were measured at 19 °C using an Ostwald viscometer. In the same media, the rate constants of the tris-(2,2'-bipyridine) ruthenium (II), Ru(bpy)₃²⁺, excited state quenching by oxygen and methyl viologen, MV²⁺, were measured using a pulse laser photolysis technique. The data obtained did not correlate as predicted by Stokes-Einstein equation, which was attributed to the difference between the macro- and microviscosity of solutions comprising components of different molecular masses.

Introduction

Smoluchowski showed that the rate constant for a diffusion-controlled reaction $A + B \rightarrow P$ of spherical solute molecules of radius R and diffusivity D , undergoing Brownian motion in a viscous liquid is given by [1],

$$k = 4\pi(D_A + D_B)(R_A + R_B)$$

Calef and Deutch have reviewed the derivation of Smoluchowski's equation and showed that by replacing the D by the viscosity of the solvent, η_s , according to the Stokes-Einstein equation, the above equation may be written as [2],

$$k = \frac{2RT}{3\eta_s} \left[\frac{(R_A + R_B)^2}{R_A R_B} \right].$$

According to the above equation the rate constant for a diffusion-controlled reaction is inversely proportional to the solvent viscosity, *i.e.*, $k \propto 1/\eta_s$. Therefore, changes in the rate constant vs. solvent viscosity can comment on the diffusion at the molecular level, or the microviscosity; the phenomena found to be very important in polymer technology [5], molecular biology [6], etc. Use of *Ru(bpy)₃²⁺, the life time of which is on the order of one μ sec, allows probing translation diffusion which is more closely related to the laminar flow (mean free path for the quenching by O₂ in H₂O, $x = (2Dt)^{1/2} = \sim 10 \mu\text{m}$) than other physical parameters measured for the same purpose.

Results and Discussion

Figure 1 shows the luminescence decays of the excited Ru(bpy)₃²⁺ in an aqueous solution containing various concentrations of oxygen. Insert shows the linear relation be-

tween the pseudo-first order quenching rate constant and oxygen concentration. From the slope, the rate constant for the diffusion controlled reaction $*\text{Ru}(\text{bpy})_3^{2+} + \text{O}_2 \rightarrow \text{Ru}(\text{bpy})_3^{2+} + {}^{15}\text{O}_2$ was found to be $3.2 \times 10^9 \text{ mol}^{-1} \text{ dm}^3 \text{ s}^{-1}$. Using the same experimental procedure, the rate constants of $*\text{Ru}(\text{bpy})_3^{2+}$ quenching by O_2 and MV^{2+} were measured in 5% (molar) glycerol-water and 5% (w/w) PVA. The data obtained are listed in Tables I and II.

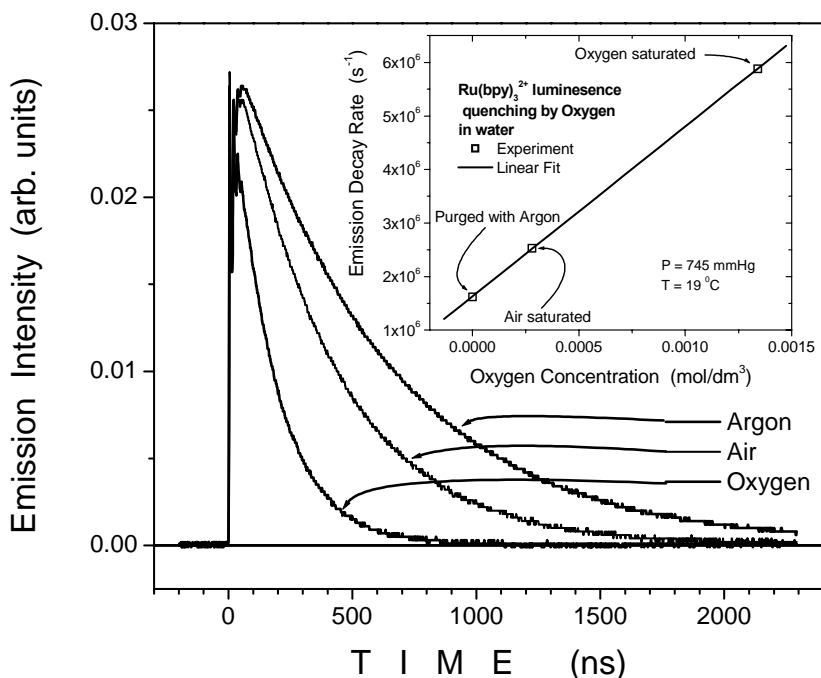


Fig. 1. Pulse laser photolysis measurements of Ru(II) luminescence decays in an aqueous solution containing various oxygen concentrations. Insert shows the linear plot of the pseudo-first order rate constants versus oxygen concentrations at 19 °C.

Table I. Ru(bpy)₃²⁺ excited state quenching by oxygen at 19 °C

Medium	Viscosity measured [mPa]	Rate constant measured [mol ⁻¹ dm ³ s ⁻¹]	Rate constant predicted [mol ⁻¹ dm ³ s ⁻¹]	Difference [%]
Water	1.03	3.17×10^9	÷	÷
5% (m) Water-Glycerol	1.83	2.86×10^9 ^a	1.78×10^9	+60
5% (w/w) PVA	50.0	4.20×10^9	6.34×10^7	+6500

^a The oxygen concentration was taken from Ref [3]

Table II. Ru(bpy)₃²⁺ excited state quenching by methyl viologen at 19 °C

Medium	Viscosity measured [mPa]	Rate constant measured [mol ⁻¹ dm ³ s ⁻¹]	Rate constant predicted [mol ⁻¹ dm ³ s ⁻¹]	Difference [%]
Water	1.03	3.30 × 10 ⁸	÷	÷
5% (w/w) PVA	50.0	3.58 × 10 ⁸	6.80 × 10 ⁶	+4580

One can notice that the presence of 5% (w/w) PVA in H₂O increases the kinematic viscosity about 50 times while the rate constants for diffusion controlled reactions essentially remain the same as in pure water. This means the diffusion of “very small” molecules such as O₂ (r = ~ 0.1 nm) through polymeric solutions is not affected by the presence of “large” PVA molecules. It has been shown earlier that the diffusion coefficients of the latex particles (r = 100 nm) measured in glycerol/water solutions obey Stokes-Einstein behavior over a range of solvent viscosity and temperature. However, our measurement performed in 5% (molar) glycerol-water shows that oxygen diffuses faster than predicted. The same type of interaction between water and glycerol and water and PVA (hydrogen bonding) indicates that the size effect may be more important than the type of interaction between the solvent components. The quenching by MV²⁺ in PVA solution is also much faster than expected but somewhat less than in the case of O₂; the larger MV²⁺ radius (r = ~ 1 nm) could be the reason for the difference measured.

Conclusion

The discrepancy between the measured rate constants for diffusion controlled Ru(bpy)₃²⁺ luminescence quenching and the values predicted by Stokes-Einstein equation based on the measured kinematic viscosities was attributed to the difference between the micro- and macroviscosity of solutions comprising components of different molecular masses.

References

- [1] M. V. Smoluchowski, *Physik* **17** (1916) 557, 585; *Physik. Chem.* 1917, **92** 192.
- [2] D. F. Calef and J. M. Deutch, *Ann. Rev. Phys. Chem.* 1983, **34** 493.
- [3] I. Kutsche, G. Gildehaus, D. Schuller, and A. Schumpe, *J Chem. Eng. Data* 1984, **29** 286-287.
- [4] D. E. Dunstan and J. Stokes, *Macromolecules* 2000, **33**, 193-198.
- [5] B. Strehmel, V. Strehmel and M. Younes, *J. Polym. Sci. Part B Polym. Phys.*, **37** (1999) 1367-1386
- [6] P. H. Kao, J. R. Abney and A. S. Verkman, *J. Cell Biol.*, **120** (1993) 175-184

Environmental Protection

(K)

INSTRUMENTAL ASPECTS OF THE ENVIRONMENTAL PROTECTION

A. Stamatović

Faculty of Physics, Beograd, POB 368, Serbia

Abstract

A short review of the environmental analytical instrumentation methods and techniques has been given and the importance of the rapid development of the adequate instrumentation in dealing with the environmental issues has been emphasized. It has been pointed that instrumental aspects, as opposed to legislative and social aspects, of the environmental protection might be the only one with a corresponding response to the environmental protection needs and demands in the past and present time. Several common environmental issues have been mentioned as to underline the role of proper instrumental methods and techniques in understanding the processes and making the decisions how to handle them.

Introduction

The environmental protection has many aspects, but they could be grouped in the following tree: legislative, social and instrumental. The instrumental aspect comprises the possession of the adequate analytical instrumentation for monitoring of the Environment, detection of the changes in it, the quantitative measurements of the changes, analysis of the results of the measurements and modeling for the purpose of testing the possibility of the proper prediction of future changes.

The development of the analytical instrumentation is a good example of an excellent cooperation between different Sciences and Technologies. This cooperation has enabled very rapid development of the adequate and easy to use instrumentation. Provided with adequate and easy to use analytical instrumentation the Environmental Science has experienced an evidently large development and also has made a very positive influence on the development of the awareness of the majority of the world population and governmental authorities in charge for the environmental issues. A complete review of the environmental instrumentation is impossible to present on a given limited space. The emphasis will be given to the air pollution instrumentation and its influence on the Environmental Science. Within this, certainly not limited field, the special accent will be given to the mass spectrometry based instrumentation because it has the possibility of real time measurements of several compounds simultaneously, which is important for the study and the understanding of the dynamics of the processes involved.

Common environmental issues

In the past fifty years several rather common environmental issues have attracted considerable attention of the environmental scientists as well as the large part of the world population aware of the danger of environmental damage. Although the time of sur-

face tests of nuclear weapons belongs to the past, some of their consequences are still present. Twenty years after the Chernobyl accident, the large part of the Ukrainian population is suffering from the disastrous consequences. The formation processes of the intensive and annoying photo smog on the specific locations have been mainly understood owing to the adequate instrumentation available, but their prevention is far from being successful. Stratospheric ozone depletion is certainly the environmental issue number one and it continues to attract a lot of scientific interest. In order to understand the processes of the ozone destruction very intensive measurements have been done in situ and in the laboratory, using the available instrumentation and the new instrumentation developed for this purpose. The tropospheric chemistry of polluted air is an open field for intensive research. The steadily increasing amount of the green house active gases (CO_2 and others) in the atmosphere is having as a consequence the global warming, which seems to be obvious. Several models have been used in order to predict the sea level rise as a consequence of the global warming. It seems however that much less attention has been given to the increase of the water vapor content in the atmosphere that might be the cause of climate change in many regions. Considerable attention has also been given to the following aspects of the environmental pollution: waste water treatment; oil spills - tanker accidents; radioactive waste; depleted uranium ammunition pollution (showing that up to now there was a large underestimate of the total negative effects) and the particulate pollution and its effects on the human health. The transport related impact on environment is evident through the air pollution, the noise, the soil and the water pollution, the change of the landscape, fauna and flora. This issue is the subject of numerous efforts and research projects aimed to decrease the effect of various forms of transportation on the environment. Quite a number of conferences are dealing with this subject, taking place all over the world. "The challenges of air pollution in the transport sector (from the French case)" by Robert Joumard 2006. [1] presents a clear analysis of the road transport air pollution based on the data from France, which should be representative for Western Europe. The need for a systemic approach to the issue of Environment and transport has been emphasized and the suggestion for the further research with the sustainable development in sight has been given. Oil spills do have often a size of a catastrophe on a local scale and considerable contribution to the water pollution on a regional scale. Continental surface water (lakes and rivers) are seriously jeopardized by waste water of communal and industrial origin, so that any additional pollution coming from the water surface transport caused by leakage of barge tanks or simply by vessels maintenance makes the situation even worse. The air transport aspect of the influence on the environment could be divided on the pollution by supersonic/stratospheric flights, influencing mostly the stratosphere, and subsonic flights influencing troposphere. The noise nuisance in the vicinity of airports and the air pollution, as well as the water and the soil pollution on the airports, common for both supersonic and subsonic transports, is not to be forgotten. In the past decade, the project with an acronym **SUCCESS** (**S**UBsonic aircraft **C**ontrail and **C**loud **E**ffects **S**pecial **S**tudy) has been performed and a lot of very interesting data have been collected, most of them already published [2]. The goal of the project was to give answer to the major

questions on the atmospheric effects of aviation and microphysics of contrails and cirrus clouds. Observations have been made from ground level stations, special flights and from the Space. Before and after intensive measurements, a lot of computational and modeling effort has been invested, aiming to the better understanding of the processes involved in contrails formation and transformation. It has been found that the contrails in some area could contribute as much as 20% to the cirrus cloudiness. This type of clouds influences a lot the radiation budget of the Earth. One of the interesting findings is that the agreement between theory and experimental results for contrail formation by given temperature, humidity and pressure could be achieved only if it is assumed that the ions take part in the condensation process [3]. Experimental study of the jet engine exhaust has given evidence for the presence of considerable density of the ions in the exhaust plume [4]. Recently, the measurements of ions in the plume of the contrails from the commercial jet plane under cruise condition have been done [5], but unfortunately with a limited mass range, leaving several questions open, like aging of primary ions from jet engine and influence of the ions in surrounding atmosphere on the contrail development and transformation to the cirrus clouds.

The indoor pollution, caused by furniture and the construction materials, working tools and accessories, human indoors activity and the penetration of open-air pollution has received less attention than it should be. The effects of the indoor air quality on the human performance and the productivity have been studied by Wyon 2004. [6].

Analytical methods and techniques

In the past the analytical instrumentation has been based mostly on the wet chemical methods and the optical spectroscopy. The analytical methods, techniques and instruments were developed usually for single pollutant measurements. The real time measurements, enabling the study of dynamics of processes, have been seldom possible with this type of instruments. The fast development of the micro electronics and well financed military and space projects have enabled the use of the new technologies in the analytical instrumentation development and even deploying part of it on the space platforms, opening a new era of remote sensing. The wet chemical methods as well as the optical spectroscopy have been enhanced using the results of above-mentioned development. For example, both emissive and atomic absorption spectroscopies have taken advantage of electrode less Inductively Coupled Plasma (ICP) torches. Remote sensing using the radiation coming from the volume that should be analyzed could be divided to the passive remote sensing using the natural existing radiation and the active remote sensing in which case the beam of intensive radiation is send in the volume to be analyzed and the spectral information of back scattered radiation is collected. The availability of the powerful coherent light sources has enabled the realization of several laser-based remote-sensing methods like Light Detection and ranging (LIDAR); Laser Induced Fluorescence (LIF); Differential Absorption LIDAR (DIAL) and Differential Optical Absorption Spectroscopy (DOAS). For a comprehensive review see Panne 1998. [7].

The fact that the passive remote sensing methods, that are using natural radiation sources, are in principle less demanding on the capacity of the energy supplies, has

enabled deploying them on the space platforms and so have opened a new era of remote sensing starting with Nimbus 1 satellite as early as 1964. The satellite applications for probing the chemistry of the troposphere and European contribution to the subject have been reviewed by Borell et al 2003. [8].

Gas Chromatography

The standard technique for measuring, beside other compounds, Volatile Organic Compounds (VOC) in the air is the Gas Chromatography (GC), which uses the temporal separation of different VOCs that are moving through an analytical column. GCs have been used and improved over the last decades to an extent that the complex mixtures can be quantitatively analyzed down to one part per trillion (pptv). To achieve such low detection limits air samples to be analyzed have to be collected and focused on the GC column. This process takes up to 30 minutes. The variation on the theme GC, so called multidimensional gas chromatography (MDGC) is almost twenty years in continuous development. The environmental application of the MDGC in connection with a mass spectrometer has been described in details by Striebich et al. [9].

Mass Spectrometry

Mass Spectrometry (MS) has become widely available owing to the introduction of the relatively inexpensive, compact in size and low weight linear quadrupole mass spectrometers (QUAD MS) and even smaller quadrupole ion traps (QUAD Trap). Serious deficiency of this type of MS - relatively low mass range for the single charged ions (several thousands of Daltons) has been compensated by Electro Spray Ionization (ESI) that gives readily tenfold and higher charged ions. This has made QUAD MS applicable in analysis of the high mass organic compounds and the biological samples. Small size of the QUAD MS and QUAD Traps has made them ideal mass selective and relatively fast detectors for Gas Chromatographs. The reduction in size of both GC and MS has made possible realization of this powerful combination in portable form [10], ready for the field applications. The Compound-Specific Isotope Analysis (CSIA) that uses isotope ratio monitoring gas chromatography-mass spectrometry (GC-IRM MS) is another example of the fruitful application of GC-MS [11]. The power of the quadrupole ion-trap gas chromatography-mass spectrometry in environmental applications is clearly presented in the review by Plomley et al. 2000. [12]. Above-mentioned ICP torches are used in connection with MS too, giving an ion source specially suited for the analysis of the traces of heavy metals, because the ICP source has no metal parts that could contaminate the sample. Beside this salient feature ICP is characterized with a very good sensitivity [13].

The Proton-Transfer-Reaction Mass Spectrometry

The Proton-Transfer-Reaction Mass Spectrometry (PTR MS) combines a fast time response with a low detection limit. The PTR MS technology has been developed by Lindinger et al. 1998. [14] and has become a leading technique in the on-line VOC analysis. This kind of instruments is commercially produced by Ionicon Analytics,

Austria. The current detection limits from 10-100 pptV (3σ , 1 sec signal integration) and response time of 150 ms, make it one of the fastest, very sensitive, currently available VOC sensor. The implementation of sophisticated mass spectrometric equipment (ion traps, time of flight) has led to a gain in duty cycle and in analyte specificity (MS/MS capability). In the latest version the instrument's performance for formaldehyde detection has been also significantly improved [15]. In principle PTR is a Chemical Ionization (CI), using H_3O^+ as a reactant ion. All compounds that have the proton affinity greater than water overtake the proton from the reactant ion and form an ion of the mass $M+1$ in the spectrum. Theoretical values for the proton transfer reaction rate constants between hydronium ion (H_3O^+) and VOC have been published by Zhao and Zhang [16]. As opposed to classical CI, H_3O^+ ions are produced in a separate reactant ion source. The reaction of proton transfer takes place in the drift tube under controllable conditions that define the mean energy of collision. If the sum of this energy and the difference in the proton affinity of the water and the analyzed compound is not greater than the dissociation energy of the compound no fragmentation takes place. PTR is one of the several so-called soft ionization techniques. This fact makes the interpretation of the spectra considerable easier. Warneke et al. 2003. [17] have coupled GC column to the PTR MS so they were able to follow the contributions of the different VOC to an individual mass to charge ratio monitored by PTR MS. Collision induced dissociation (CID) and ion - molecule reactions in an ion trap mass spectrometer can be used to distinguish between isomers produced in the drift tube/reactor of the PTR MS. The simplest way to achieve that is to use the QUAD Trap instead of the quadrupole. The more straightforward solution would be tandem MS-CID-MS, so called triple MS configuration.

Negative ion mass spectrometry

Starting with the development of the electron capture detector for GC, negative ions have been used for the environmental analytical applications. In the past decade, Negative Ion Mass Spectrometry (NIMS), or more closely described as Chemical Ionization (CI) and Electron Capture Negative Ion Mass Spectrometry (ECNIMS), have been established as a specific, very sensitive analytical methods for the trace level Environmental Applications [18]. They are not conceived as a concurrent methods to the well established positive ion MS, or to the novel, very specific and sensitive PTR MS, but rather as a complementary, or alternative methods with some advantages and disadvantages compared to the methods just mentioned above. Our knowledge of Low Energy Electron Molecule Interaction, LEEMI [19,20] has increased considerably over last half of the century. As a consequence of that fact, the applications of the recognized advantages of ECNIMS has evolved to several different methods/techniques (Free Electron Beam, Retarded Electron Beam, Bound Electron Transfer Ionization), that are already in the applications [18] and partly in commercial production [21]. Future development of these methods are expected in the form of new ion source geometries that are going to enhance even more the sensitivity, but preserve reproducibility and linearity of response.

Atmospheric Pressure Ionization MS (API MS)

One of the major drawbacks of MS is the necessity of the good vacuum for undisturbed motion of ions from the ion source through the analyzer to the ion detector. Differential pumping of the ion source was the first step in the direction of API MS. The main idea was to ionize the sample before decreasing the pressure for seven or more orders of magnitude and then to focus the ions on the orifice of the first stage of the differential pumping. Several ionization methods have been used, like corona discharge, radioactive source, UV and Penning ionization [22,23].

Ion Mobility Spectrometry

Although lacking the selectivity of Mass Spectrometry Ion Mobility Spectrometry (IMS) has been making considerable progress in last two decades, expressed in appreciable miniaturization of the instruments and increasing the sensitivity of the method. Hand held instruments are routinely in use for drug and explosive detection [24].

Data management

The extremely fast development of the microelectronics and microcomputers has made easy the data logging of the ample data set from the environmental measurements. The pollution of the atmosphere, hydrosphere and soil is strongly correlated with the meteorological and hydrological data. Integration of these data sets in the course of the analysis of the pollution data is inevitable. The interpretation of the environmental data is far from being simple, on the contrary, it is often tedious enough and time consuming task. Fortunately, the tremendous increase of the computing power easily available, and the level of the available software, enables the use of the artificial intelligence methods in some complicated cases. For the same reason the application of rather complicated and computer time consuming statistical methods of the data analysis and interpretation are nowadays possible.

Numerical modeling

Predicting the spread of pollution and back tracing the transport of pollutant during the past episodes in order to locate the source is nowadays-manageable task. Numerical modeling of environmental data could be based on the modeling approach based on one of several methods developed for different cases and taking the meteorological data in the account. From the other side some of the meteo models could include the transport of pollutant by air masses and thus enable tracing back the source.

Future prospects

The outlook for the further development of the environmental instrumentation is very bright owing to the on march of micromachining methods, microelectronics and nanotechnology. The micro engineering and machining are going to enable the further minimization of the instrument size. The nanotechnologies are making available the new membranes, filters, large reactant surface etc. The electrochemical chip sensors

(ech-chip sensors) are also very promising basis for development of the instruments with a whole palette of miniature specific sensors that are going to be in continuous application and widely available owing to the low price. The time when the hand held instruments for the complex and complete analytical measurements in the Environment will be available seems to be coming soon.

Conclusion

The ever better instrumentation will continue to contribute to the further progress of the Environmental Protection and the consciousness of the global population and the corresponding authorities for the Environmental issues. The process of development of different specific sensors, instruments and measurement methods and techniques shall not stop to be an attractive field of the scientific and technical activities. But it is still questionable whether the legislative and social aspects of the Environmental Protection are going to develop with adequate speed in order to make it effective.

References

- [1] Robert Joumard, EURASAP Newsletter, 2006. **58**, 2-23.
- [2] O.B. Toon and R. Miake-Lye, *Geophys.Res.Lett.*, 1998. **25**, 1109-1112 and all the papers in the same issue.
- [3] F. Yu, R.P. Turco, B. Kaercher, F.P. Schroeder, *Geophys.Res.Lett.*, 1998. **25**, 3839-3842.
- [4] Arnold, F., Stilp, T., Busen, R. and Schumann, U., *Atmos. Env.*, 1998. **32**, 3073-3077.
- [5] F. Arnold, K.H. Wohlfrom, M.W. Klemm, J. Schneider, and K. Gollinger, *Geophys.Res.Lett.*, 1998, **25**, 2137-2140.
- [6] D.P. Wyon, *Indoor Air*, 2004. **14**, Supplement, 7, 92-101.
- [7] U. Panne, *Trends in Anal. Chem.*, 1998. **17**, 491-500
- [8] P. Borell, J.P. Burrows, A. Richter, U. Platt, T. Wagner, *Atmos. Env.*, 2003. **37**, 2567-2570
- [9] R.C. Striebich, W.A. Rubey, J.R. Klosterman, *Waste Management*, 2002. **22**, 413-420
- [10] B.A. Eckenrode, *J. Am. Soc. Mass Spectrom.*, 2001, **12**, 683-693
- [11] A. Kronimus, J. Schwarzbauer, L. Diskowitzky, R. Littke, *Environ. Chem. Lett.*, 2006, **4**, 23-28
- [12] Jeffrey B. Plomley, Mila Lausevic and Raymond E. March, *Mass Spectrometry Reviews*, 2000, **19**, 305-365
- [13] J.A. McLean, J.S. Becker, S.F. Boulyga, H.J. Dietze, A. Montaser, *Int. J. Mass Spectrom.*, 2001, **208**, 193
- [14] Lindinger W, Hansel A, Jordan A, *Int. J. Mass Spectrom. Ion Proc.*, 1998, **173**, 191-241.
- [15] Wisthaler A, Hansel A, Maerk TD, 15th Symposium on Atomic and Surface Physics and Related Topics, Obergurgl-Austria-February 4-9, 2006. Contributions, Eds: V. Grill, T.D. Maerk, p.27.
- [16] J. Zhao, R. Zhang, *Atmos. Env.*, 2004, **38**, 2177-2185.
- [17] C. Warneke, J.A. de Gouw, P.D. Goldan, W.C. Kuster, R. Fall, *Environ. Sci. Tech.*, 2003, **37**, 2494-2501
- [18] J. A. Laramée, P. Mazurkiewicz, V. Berkout, and M. L. Deinzer, *Mass Spectrometry Reviews*, 1996, **15**, 15-42
- [19] Eugen Illenberger, *Chem. Rev*, 1992, **92**, 1589-1609

-
- [20] Int. J. Mass Spectrom., 2001, **205**, Nos. 1-3, Special issue: Low Energy Electron- Molecule Interactions
- [21] JEOL data announcement; www.jeol.com/ms/docs/HFIPA_TEEM.pdf
- [22] C. Jost, D. Sprung, T. Kenntner, T. Reiner, Int. J. Mass Spectrom., 2003, **223-224**, 771-782
- [23] R.B. Cody, J.A. Laramee, J.M. Nilles, and H. Dupont Durst, JEOL News, 2005, **40**, 8-12.
- [24] F. Li, Z. Xie, H. Schmidt, S. Sielemann, J.I. Baumbach, Spectrochimica Acta Part B, 2002, **57**, 1563-1574.

ENVIRONMENTAL ISOTOPE INVESTIGATION OF THE RIVER CATCHMENTS

N. Miljević

Vinča Institute of Nuclear Sciences, POB 522, Belgrade, Serbia

Introduction

The term environmental isotopes refers to isotopes, both stable and radioactive, that are present in the natural environment, either as a result of natural processes or introduced by anthropogenic activities. The original studies on isotopes in water were concerned with seawater and precipitation. During the transition of water from one phase to another (evaporation and condensation), the concentration ratio of the isotopes of an element (hydrogen and oxygen relevant in the hydrological cycle) changes, undergoes so-called isotope fractionation. Observing differences in especially the stable isotope composition are far from randomly distributed, they inform us about certain geochemical or hydrological process that took place relying on specific input pattern. Radioactive decay offers the possibility to determine an age, the time elapsed since the infiltration of the water. Isotope methods were introduced into catchment hydrology research in the 1960s as complementary tools to conventional hydrological methods for addressing questions of where water goes when it rains, what pathways it takes to the stream and how long water resides in the catchment [1]. The variety of isotopes used for this intention in isotope hydrology is presented in Fig. 1. Atmospheric thermonuclear weapon tests substantially increased the ^3H (tritium) content in the rapidly circulated parts of the hydrological cycle, with the peak around 1963 facilitating its use for the first systematic estimation of water age in catchments [2]. Stable isotopes of ^2H (deuterium) and/or ^{18}O (oxygen-18) have been common tools for assessing relative contributions of flow derived from uniquely labeled geographical sources or distributed components such as direct precipitation runoff, shallow and deep groundwater, surface waters including lakes and wetlands and water dating up to about five years of age, which typically occur in shallow aquifers connected to streams [3]. While nuclear explosion spike ^3H signal in natural systems decreases, the resolution of tritium method has declined and new tools needed for age determination. "New" methods using noble gases such as ^3He [4], $^3\text{H}/^3\text{He}$ [5], ^{85}Kr [6] and ^{222}Rn [7], solutes such as ^{35}S [8] and the anthropogenic compounds, chlorofluorocarbons (CFCs) [9] and SF_6 [10] have been developed for water dating methods from a few days up to decades. Solute isotopes such as ^{87}Sr [11], ^{13}C , ^{34}S and ^{15}N [12] have provided important information on bio (geo) chemical processes in the hydrological environment.

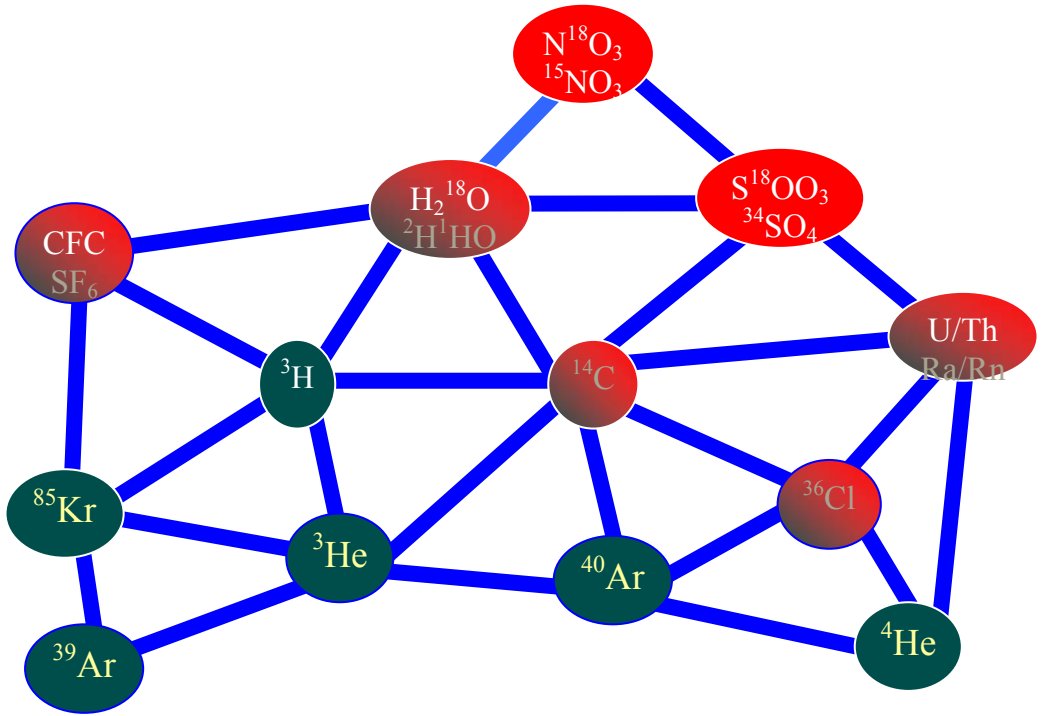


Fig. 1. Network of Isotope Hydrology

Analytical Techniques

Nuclear science has developed an array of methodologies and analytical techniques which use various isotopes of water to characterize water masses and trace their history and movement through the hydrological cycle. The observed variations of stable isotope composition within the water cycle are relatively small in absolute terms but can be measured with an adequate precision and accuracy by isotope ratio mass spectrometry (IRMS). The heavy isotope content of the sample is defined as the relative deviation from the adopted international reference standards and usually expressed in delta notation (δ) in permill (‰) [13]

$$\delta \text{ (isotope deviation)} = \frac{R_{\text{sample}} - R_{\text{standard}}}{R_{\text{standard}}} \times 1000$$

where R is the isotope ratio of the heavy isotope to the more abundant light isotope ($^2\text{H}/^1\text{H}$, $^{13}\text{C}/^{12}\text{C}$, $^{18}\text{O}/^{16}\text{O}$). The most common chemical preparation treatments of the samples for deuterium measurements is the reduction of water to hydrogen with uranium [14], zinc [15], chromium [16] or equilibration of the sample with hydrogen gas using a platinum catalyst [17]. The ^{18}O abundance in water samples is usually measured using a modified $\text{CO}_2/\text{H}_2\text{O}$ equilibration technique [3]. The

standard deviations of repeatability for ^2H and ^{18}O determinations are 1 and 0.1%, respectively.

The radioactive sample is measured as an internal source, i.e. it is mixed with the counting medium, responsible for the operation of the instrument. Tritium content in water samples can be directly determined after electrolytic enrichment and mixing with a scintillating liquid (cocktail of various constituents) using liquid scintillation spectrometer (LSS) [18].

River Waters

River discharge consists mainly of two principal components, surface run-off of precipitation and groundwater seepage. Isotope signals in river discharge can potentially contribute to better understanding of the continental portion of the hydrological cycle including information such as water origin, mixing history, water balance, water residence times, surface-groundwater exchange and renewal rates, and evaporation-transpiration partitioning. Naturally occurring radioactive (Table 1) and stable (Table 2) isotopes of the elements of the water molecules and the components dissolved in water have increasingly been used to study the dynamics of surface water systems, their interaction with groundwater and vulnerability to pollution in river basins and catchment areas.

Table 1. Natural abundance, typical specific activities of radioactive isotopes used in river studies

Nuc.	Nature abundance	Standards/ Absolute value	Half-life [years]	Spec. act. [Bq/l]	Application
^3H	$< 10^{-17}$	NBS-SRM 4361 $^3\text{H}/^1\text{H}=6600$ TU	12.33	1.55×10^{-4}	Water balance and dynamics in river catchments, surface-groundwater interaction
^{14}C	$< 10^{-12}$	Oxalic acid 13.56 dpm/gC	5730	1.11×10^{-2}	Riverine carbon cycle, sediments dating, dating of flood events
^{238}U	0.9927		4.5×10^9	4×10^{-3}	Weathering, erosion and sedimentation

In addition, ^{232}Th and ^{230}Th are used in river studies [19], mostly combined with other uranium and thorium decay-series radionuclides such as isotopes of ^{226}Ra and ^{222}Rn .

Table 2. Natural abundance of stable isotope used in river studies

Isotope	Relevant isotope ratio	Average natural abundance	Standards/ Absolute value	Application
^2H	$^2\text{H}/^1\text{H}$	1.55×10^{-4}	V-SMOW 0.00015575	Water balance and dynamics in river catchments
^{13}C	$^{13}\text{C}/^{12}\text{C}$	1.11×10^{-2}	VPDB 0.0112372	Riverine carbon cycle, pollution
^{15}N	$^{15}\text{N}/^{14}\text{N}$	3.66×10^{-3}	atmospheric air V-SMOW 0.0020052	Pollution, biological processes
^{18}O	$^{18}\text{O}/^{16}\text{O}$	2.04×10^{-3}	VPDB for carbonate 0.0020672	Surface-groundwater interaction
^{34}S	$^{34}\text{S}/^{32}\text{S}$	4.22×10^{-2}	VCDT 0.0441626	Pollution, salt depositional processes
^{87}Sr	$^{87}\text{Sr}/^{86}\text{Sr}$	0.709939	NBS 987 0.710245	Influence of tributaries on chemistry and pollution

V-SMOW - Vienna Standard Mean Ocean Water (water)

VPDB – Vienna Pee Dee Belammite (calcite)

VCDT - Vienna Canyon Diablo Troilite (FeS)

The stream $\delta^{18}\text{O}$ composition generally reflected the temporal pattern of the precipitation $\delta^{18}\text{O}$ composition with the signals significantly damped at all sites within the catchment. A two-year observation of the marked seasonal variation of ^{18}O content in monthly composite precipitation at the station Smederevska Palanka with high values in summer and more depleted ones during winter and strongly reduced amplitude in bimonthly grab river samples at locations Ljubicevski most and Varvarin are illustrated in Fig. 2. $\delta^{18}\text{O}$ of the Velika Morava river isotopic signal is controlled by the low $\delta^{18}\text{O}$ values of the input winter precipitation signal in the drainage area with a few month time lags.

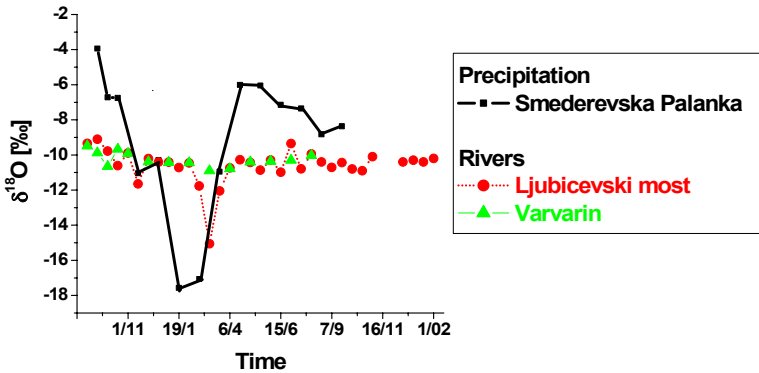


Fig. 2. Temporal variation of oxygen-18 composition in precipitation and river water in the Velika Morava catchment for the period September 2004 – February 2006

Mean Residence Time

The water “residence time” means the period of time that water molecules spend in the basin since the water molecule entered the catchment as recharge to when it exits at some discharge point (i.e., catchment outlet, monitoring well, and soil water sampler). During that time, water in the catchment is a mixture of the past recharges with different residence times, and the more appropriate term is the “mean residence time” (MRT) having not only important implications for flow pathways and storage, as well as for water quality, since many biogeochemical reactions are time-dependent.

The tracer composition of precipitation that falls uniformly on a catchment will be delayed by some timescale(s) before reaching the stream. More explicitly, the stream outflow composition at any time $\delta_{out}(t)$ consists of tracer, $\delta_{in}(t - \tau)$ past inputs lagged according to their residence time distribution $g(\tau)$ [20] it can be mathematically expressed by the convolution integral,

$$\delta_{out}(t) = \int_0^{\infty} g(\tau) \delta_{in}(t - \tau) d\tau$$

where τ are the lag times between input and output tracer composition. A range of models are available for assessing catchment residence times using tracer data [21, 22]. Seasonal trends in $\delta^{18}\text{O}$ in precipitation and stream water were modeled using periodic regression analysis [23] to fit seasonal sine wave curves to annual $\delta^{18}\text{O}$ variations in precipitation (Fig. 3a) and stream water (Fig. 3b) defined as

$$\delta^{18}\text{O} = X + A[\cos(ct - \theta)]$$

where X is the weighted mean annual measured $\delta^{18}\text{O}$ (‰), A is the estimated $\delta^{18}\text{O}$ annual amplitude (‰), c is the radial frequency of annual fluctuations

($0.017214 \text{ rad d}^{-1}$), t is the time in days after the start of the sampling period, and θ is the phase lag or time of the annual peak $\delta^{18}\text{O}$ in radians [24].

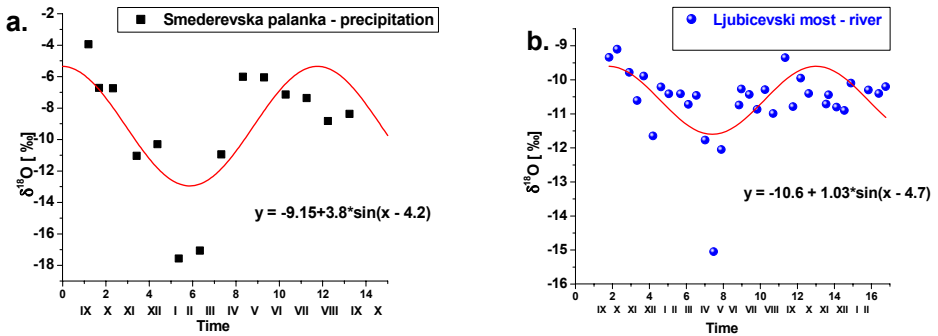


Figure 3. Fitted annual regression models to $\delta^{18}\text{O}$ for precipitation (a) and stream water (b) in the Velika Morava catchment

Sine wave models fitted to precipitation and stream water $\delta^{18}\text{O}$ variations were used to calculate MRT (T in month) expressed mathematically as

$$T = \frac{6}{\pi} \sqrt{\left(\frac{A_p}{A_r}\right)^2 - 1}$$

where A_p is the amplitude of precipitation $\delta^{18}\text{O}$ (‰), and A_r is the amplitude of the river water $\delta^{18}\text{O}$ (‰). The preliminary estimated values within the Velika Morava catchment were in the range from short (3.5 months for Ljubicevski most) to longer MRTs (12 months for the Ibar) with 95% confidence limits.

River Water - Groundwater Interaction

Based on tritium content in precipitation, the Sava river and groundwater in the area of Makiš alluvial aquifer ($\sim 25 \text{ km}^2$) the infiltration rate and MRT of shallow groundwater body that serves for drinking water supply of Belgrade were determined [25]. The significant vertical age structure was found in the early pumping history of production wells (Fig. 4a). The "old" groundwater component (mean yearly tritium content of 17 TU) was identified in the upper water bearing layer, average thickness of about 10 m with a small infiltration. The lower layer, thickness between 10-15 m with

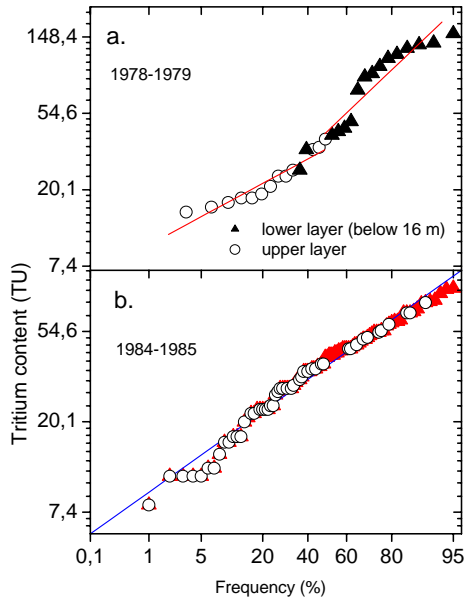


Fig.4. Frequency distribution of tritium content in water bearing layers during the production wells exploitation

means yearly value of tritium content of 51 TU was characterized by fast turnover exist. The origin of these groundwaters was dominated (~ 80%) by the Sava river water infiltration through the pumped wells. During exploitation the natural dynamics of groundwater flow had been changed with a preferential flow of young water into upper deposits (Fig. 4b). An efficient groundwater pathway could cause a non-acceptable contamination of the main aquifer. These findings were used in setting optimum strategies for a sustainable management of groundwater resource in this basin.

Conclusion

Isotopic abundance of light elements (hydrogen, carbon, nitrogen, oxygen, sulfur) as well as noble gases (helium, argon) is widely applied for identification of hydrological sources, flow paths under different flow conditions and estimation of mean catchment residence times. A more intensive merging of isotopic survey data in rivers is important to validate more accurate hydrological models related to water resources assessment (use of groundwater resources in the catchments), environmental studies and management.

References

- [1] J.J. McDonnell, *Hydrol. Processes*, 2003, **17**, 175–181.
- [2] E. Erikson, *Tellus*, 1963, **15**, 305-308.
- [3] S. Epton, T. Mayeda, *Geochim. Cosmochim. Acta*, 1953, **4**, 213-224.

- [4] T. Torgersen, W.B. Clarke, W.I. Jenkins, *Isotope Hydrology*, 1979, Vol. 2, IAEA, Vienna, 917-930.
- [5] D.K. Solomon, S.L. Schiff, R. J. Poreda, W.B. Clarke, *Water Resour. Res.*, 1993, **29**, 2951-2962.
- [6] K. Rozanski, T. Florkowski, *Isotope Hydrology*, 1979, Vol. 1, IAEA, Vienna, 73-91.
- [7] A.S. Rogers, *U.S. Geological Survey Bulletin*, 1958, 1052-E, 187-212.
- [8] D. Lal, B. Peters, 1966, *Handbuch der Physik* (K. Sitte ed.) Springer-Verlag, Berlin, 551-612.
- [9] G.M. Thompson, L.M. Hayes, S.N. Davis, *Geophysical Research Lett.*, 1974, **1**, 177-180.
- [10] M. Maiss, I Levin, *Environ. Sci. Technol.*, 1994, **104**, 541-549.
- [11] A.M. Stueber, P. Pushkar, E.A. Hetherington, *Appl. Geochem.* 1987, **2**, 477-494.
- [12] D.H. Kohl, G.B. Shearer, B. Commoner, *Science*, 1971, **174**, 1331-1334.
- [13] IAEA, 1981, *Stable Isotope Hydrology: Deuterium and Oxygen-18 in the Water Cycle*, Technical Reports Series no 210, Vienna, Austria
- [14] J. Bigelaisen, M. Perlman, H.C. Prosser, *Anal. Chem.*, 1952, **24**, 1356-1357.
- [15] M. Coleman, T.J. Shepherd, J.J. Durham, J.E. Rouse, G.R. Moore, *Anal. Chem.*, 1982, **54**, 993-995.
- [16] M. Gehre, R. Hoefling, P. Kowski, G. Strauch, *Anal. Chem.*, 1996, **68**, 4414-4417.
- [17] O. Breas, C. Guillou, F. Reniero, E. Sada, G. Tanet, *Rapid Commun. in Mass Spectrom.*, 1996, **10**, 246-249.
- [18] LSC 1992, *International Conference on Advance in Liquid Scintillation Spectrometry* (J.E. Noakes, F. Schonhofer, H.A. Polach, eds), *Radiocarbon*, University of Arizona, Tucson, 1993.
- [19] A. Van der Wijk, W.G. Mook, M. Ivanovich, *Sci. Total Environ.*, 1988, **70**, 19-40.
- [20] P. Maloszewski, A. Zuber, *J. Hydrol.*, 1996, **179**, 1-21.
- [21] P. Maloszewski, A. Zuber, *J. Hydrol.*, 1982, **57**, 207-231.
- [22] J.V. Turner, C.J. Barnes, *Isotope Tracers in Catchment Hydrology*, edited by: Kendall, C. and McDonnell, J. J., Elsevier, Amsterdam, 723-760, 1998.
- [23] C.L. Bliss, *Statistics in Biology*, Vol. 2, McGraw Hill, New York, 639 pp, 1970.
- [24] P. Rodgers, C. Soulsby, S. Waldron, D. Tetzlaff, *Hydrol. Earth System Sci.*, 2005, **9**, 139-155.
- [25] N. Miljevic, D. Golobocanin, V. Sipka, 1997, *Proceedings International Symposium on Engineering Geology and the Environment*, Athens, Greece, 23-27 June 1997, A.A. Balkema, Rotterdam, 1381-1386.

CHEMICAL THREATS

P. Manojlović

*Permanent Representation of the Republic of Serbia to the OPCW,
The Hague, The Netherlands*

Abstract

Despite the significant results that have been achieved at the international level to ban development, production and deployment of CW the threat is not eliminated. Today we are facing three possible scenarios of chemical threats: terrorism, attack on chemical industry objects, and chemical accident. The terrorist attacks against the USA on 11 September 2001 have changed global priorities. The threat of the use of weapons of mass destruction by terrorists is real and continuing. Use of chemical weapons by terrorists could have devastating consequences, resulting in thousands of casualties. That terrorists will not be deterred from using chemical weapons was clearly demonstrated by their use of sarin in the Tokyo subway in 1995. Struggle against terrorism suppose to be the most important and relevant goal of international community. The basic principles for terrorism elimination are: prevention, causes removal, and deterring.

Introduction

The development of the new technologies and the miniaturization of the weapons for the mass destruction have greatly drawn the attention of the terrorists. The terrorist attack with the nerve gas SARIN, in Tokyo in 1995, organized by the religious sect "AUM SHINRIKYO", was a warning to the world that the terrorism has moved the limits that had been previously set, which the international anti-terrorist experts have feared for decades. Tokyo has avoided the worst, because SARIN which was used in the attack (the middle dose that causes death is 0,063 mg/kg) was either produced by non-experts, or it was over dissolved. Nevertheless, the precedent has been made. The nerve gas has been used in the terrorist attack. It could happen again, and the fact that the terrorists nowadays do not refrain from the actions that result in a great number of innocent casualties (the New York's World Trade Center attack on 11th September in 2001.) is what makes the future attacks quite probable.

1.Terrorism: The modern international terrorism is in constant growth, despite the very organized struggle of the international community and the measures they take for its suppression. **The basic characteristics of terrorism today are:** the biggest threat to the international security; constantly improving at the higher technological level with increased efficiency; the victims are not only individuals, but entire states and regions; all available weapons and devices are used including the weapons of mass destruction; in addition, terrorism has in this moment and it will certainly have consequences on the global security in the future; terrorist are no longer ideologically motivated. The driving forces behind modern terrorism are predominantly ethnic or religions extremism. (fanatics willing to commit suicide actions); the basic goal of terror-

ists is to create massive causalities and psychological destruction among civil population as well. **Modern and future terrorist mainstays are:** extreme religious groups; members of charismatic or cult groups and religious sect (Example ‘‘Aum Shinrikyo’’); some terrorist groups inside the state unsatisfied with their social position and poverty; organized criminal groups and mafia could apply some terrorist methods aimed at deterring the Gov in order to keep their illegal position.

The toxic chemical that could be used in a terrorist attacks - The development of chemical industry and technology made possible the discovery of several millions of newly synthesized chemical compounds. The variety of new products in this field represents a convenient source of supply for the terrorists as well. INTERNET could be used as a source of information needed by terrorists to learn more about features, methods of their chemical synthesis, delivery and application. **Which TC could be used in a terrorist attack??** The most important TC features relevant for possible application are: **phase state** and **toxically** characteristics. The most important TC characteristic relevant in case of a massive contamination is **volatility** which can be described by **Cicp** (Coefficient of inhale contamination possibility) parameter.

$$Cicp = \frac{C_{\max}^{20}}{LC_{50}}$$

C^{20} – is the maximum concentration of the gas (vapor) at 20°C, mgm^{-3} max

LC_{50} – is the medium deadly concentration of the gas (vapor) in the air when applied to mice (the time of effect 1 to 4 h), mgm^{-3}

Some **Cicp** values for TC with massive application in industry (arsine, phosgene, HCN, ammonia, FH, ethylene oxide...) are 10-200 times bigger than TC on the Schedule 1 in the CW Convention! **Example:** VX which represent one of the most toxic TC (the lowest LC_{50}) according to the **Cicp** parameter is in the middle level. Phosgene, chlorine... which toxicity is $2,5 \times 10^2 - 1,8 \times 10^3$ lower than VX, potentially are able to create more dangerous situation for natural environment

then the same quantity of spilled VX. (This conclusion concerns the accidents, which are to be differentiated from the war application of the chemical warfare agents.). According the **Cicp** parameter sequence of TC is as follows: methyl isocyanides > phosgene > chlorine > sarin > ammonia > S-mustard > VX > lewisite > ...

Such gradation of level of danger is explained by the fact that the degree of the poisoning by inhalation is determined by the ratio between the evaporation and the toxic effects of a given substance. However, **Cicp** parameter doesn't allow for inherent individual reactions of humans on the appearance of threats using the senses, especially sense for odor. That is a reason odorless TC are more dangerous (sarin, soman...). All this features and conditions were known by ‘‘Aum Shinrikyo’’ sect !!!

What kind of TC are moist likely to be used? SARIN, N-mustard, VX, Be salts, Hard metals salts (Hg, Zn, Cd, Cr, Cu...), toxins (T-2, aphla toxin...) as well as resistant BA (anthrax...). On **Figure 1.** is presented the wide range of groups of TC that could be used in the terrorists attacks.

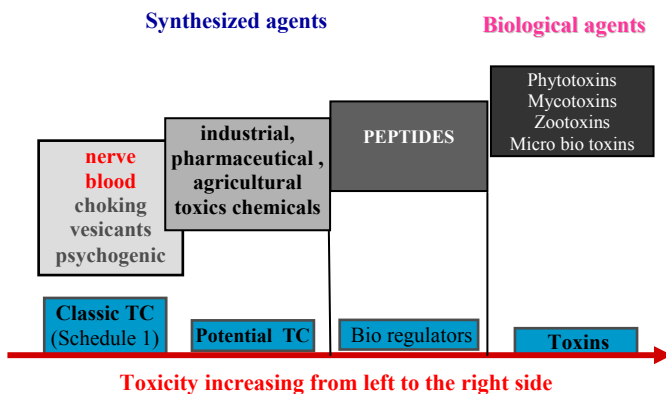


Fig. 1. Wide range of groups of TC that could be used in terrorist attacks

On the Table 1. is presented the comparative analysis of toxicity of potential TC. Those are highly TC warfare agents, TC that have psychochemical effect, the industrial TC-insecticides, pesticides etc., the TC of the biological origin-toxins.

Table 1. Comparative analysis of toxicity of potential TC

TC Type	TC Name	Source/Origin	Dosage (µg/kg)
Toxins	Botulinum toxin A	Bacteria	0.00003
	Tetanus toxin	Bacteria	0.01
	Ricine	Plant	0.02
	Diphtheria toxin	Bacteria	0.2
	Coco toxin	Frog	2.7
	Buffo toxin	Frog	390.0
	Curare	Plant	400.0
	Strychnine	Plant	3000.0
TC (War Agents)	VX	Synthetic	7.5
	SOMAN	Synthetic	50.0
	SARIN	Synthetic	63.0
	TABUN	Synthetic	150.0
Incapacitate TC	LSD-25	Synthetic	0.002 mg/kg
	ALD-52	Synthetic	0.002 mg/kg
	BZ	Synthetic	0.0024 mg/kg
	DMHP	Synthetic	0.06 mg/kg
	STR	Synthetic	0.07 mg/kg

TC in the solid and liquid form with low values of vapor tension (it is not possible create dangerous concentration in vapor form) could be used for food and water contamination. Prerequisites that TC have to satisfy in order to be used in terrorist actions: good solubility in the water or food; high toxicity; high degree of hydro stability or small propensity for chemical interaction with food components.

Advantages and disadvantages of application of TC in terrorist attacks (terrorist 's viewpoint) – Advantages: frightening nature and great number of casualties; difficult TC detection, protection and decontamination; low price of

TC and availability. Disadvantages: possibility of retaliation of attacked countries and international community; public condemn, condemn of their supporters and losing the support; security of terrorist during application. **Principles and delivery methods – Main principles of TC application are**: Sudden and hidden action; providing immediate high TC concentrations in vapor form; causing large number of casualties; causing shocking psychological effects (fear, panic, feels of weakness and disorientation est. similar). TC delivery forms are: different thermo vaporizers; sorbents with great active surfaces (clay, sponges and other porous material); containers (plastic or glass) with precursors which can be activated in the moment of attack (binary principle-example attack in Tokyo); systems with artificial ventilation; different explosive devices.

Targets of terrorist actions - Maximal effects could be attained by attacks: on the small areas with large number of population; inside the objects where dispersion of TC concentration is low. The possible targets are: human, as individual or group; modern systems for water distribution and supply; ventilation systems (big building, business centers, subways..); public transport (buses, trains, underway..) places with massive people gathering (stadiums, cinemas, department stores, markets..); food poisoning (companies, storages..). That's why the choice of the Tokyo subway is considered to be the result of the thorough analysis. The similar case was the application of the tear gas at the Hazel stadium in Brussels (in 1986.), which, besides achieving the maximum effects, produced some additional casualties as a side effect (the maneuvering space was too small, which led to panic and the additional blockade).

Defense against Terrorism - The basic principles for terrorism elimination are: **prevention, causes removal, and deterring**. Terrorism is the most serious global security challenge at the moment. Without serious efforts being made in the field of "cause removal" there will not be solutions for this problem. Deterring (police and military repressive measure) without removal of causes of terrorism could not solve or decrease this treat to world peace. The most significant results in the against terrorism, especially in the struggle to prevent any use of TC in terrorist actions, in the past few years, have been achieved at the international level (treaties & conventions). Chemical Weapons Convention (CWC) signed by now 178 countries is important precondition for TC control and prevention. Since 2000 Serbia has performed all the most important obligations. The most important thing was destruction of former facilities for chemical weapons productions. In that way Serbia gave its own contribution to the process of chemical terrorism elimination. Regardless of the obvious progress made of the international level on CW ban, CW will probably stay the means of achieving military and terrorist goals and the likely hood of their use will still be high. **The following Iranian proverb contains the core of the problem and gives the best answer for strragling against terrorism-cooperation and joint efforts of international community**: *Once one knight met on the road a sparrow laying down with the legs toward sky. Amazed knight ask the sparrow what he is doing on the road in this strange position? Sparrow replied him that sky should fall dawn on the ground! Astonished knight with smile on the face asked him: "Do you think that you are able to save the world with your small legs?". "I am going to give my contribution!", replied the brave sparrow.*

2. Attacks on the chemical industry objects: Another possible scenario of chemical threat is attack on the chemical industry objects. Targeting industrial TC storage facilities in war conflicts is typical example of abuse of military power and lack of necessary conventions which would ban such actions. (Examples: former FRY, IRAQ..). Consequences on the population and natural environment caused by this type of actions are very long and they can create disaster.

3. Chemical accidents: The third scenario of chemical threat is chemical accidents. Chemical accidents—sudden and uncontrolled release of huge quantities of TC in the atmosphere, water and ground with adverse effect on living organisms and environment.

Chemical installations accidents— same effects as CW:

- Average lethal dose for Ammonia 19 gmin/m^3 (19 grams a minute per cubic meter)
- Average lethal dose for SARIN $0,1 \text{ gmin/m}^3$ (0,1 grams a minute per cubic meter)

Technical malfunctions are the most common cause of chemical accidents in chemical industry facilities but terrorist attacks could also cause such accidents. Consequences could be huge (example MIC-Bhopal, 3000 death, 200000 contaminated, 20000 blinded). Taking into consideration profile of contemporary terrorist this threat seems real.

- Bhopal (MICN) – 3000 death, 200.000 contaminated (20.000 blinded);
- Sevezo (TCDD) – destroyed vegetation 230 ha, 12.000 animals killed, 50.000 persons evacuated. Compensation requests amounted to USD 80 million;
- Cameron– 1.200 death, all animals around killed;
- Mexico City (gas explosion inside the tanks) – 452 death, more than 4.000 injured, 30.000 houses destroyed, 250.000 persons evacuated!

Above mentioned examples of massive disasters imposed requests for establishment of institutional framework and introduction of practical actions intended to prevent and relief the consequences of these events.

Conclusion

- There is a real possibility of use of TC in terrorist actions!
- The biggest applicability would have TC with possibility for application with high toxicity, volatility, simplicity in handling and with low detectability (sarin, toxins...)!
- Necessary TC are available in the market and using the Internet as a source of information it is not hard to synthesize TC!
- Targets of possible action would be places with massive people gathering!
- Struggle against terrorism is very hard and entails engagement of international community, primarily in the prevention and disaster relief!

- CWC has a great role in decreasing the global chemical terrorism threat level and OPCW and member states have to give their full contribution to that endeavor!
- Terrorist attacks on industrial facilities containing TC represent a real threat catastrophic on the humans and natural environment. The consequences are almost the same as with CW application!
- Targeting industrial TC storage facilities in war conflicts is example of abuse of military power and lack of necessary conventions which would ban such actions!

References

- [1] Franke S., Lehrbuch der Militarchemie-band, Deutscher Militaverlag, Berlin, 1967.
- [2] R. Jovic, N(R)CB accidents, diversion and terrorism, RO za unapredjenje organizacije rada i usavrsavanje kadrova, Belgrade, 1989.
- [3] P.Manojlovic, Terrorism – way of using force in international relations, Research thesis in School of National Defence, Belgrade, 1997.
- [4] B.M.Petkovic, Terrorism – continuing war, Vojno delo 2/97, Belgrade, 1989.
- [5] B.M.Petkovic, Geopolitical Parallels at the beginning of 21st Century, NIGP „Kalekom“ Belgrade, 1997.
- [6] Convention on the Prohibition of the Development, Production, Stockpiling and Use of Chemical Weapons and on Their Destruction (CWC), 1993.
- [7] Prophet of poison - TIME, 03.04.1995.
- [8] INTERNET; "Terrorist Use of Chemical Weapons", 1997.

ACCUMULATION OF TRACE ELEMENTS IN TREE LEAVES IN RELATION TO ATMOSPHERIC CONCENTRATIONS

M. Tomašević¹, Z. Vukmirović¹, S. Rajšić¹, M. Tasić¹ and B. Stevanović²

¹*Environmental Physics Laboratory, Institute of Physics, University of Belgrade,
Zemun, Pregrevica 118, Serbia, milica@phy.bg.ac.yu*

²*Faculty of Biological Sciences, Institute of Botany and Botanic Garden, University of Belgrade,
Takovska 43, Belgrade*

Abstract

Leaves of deciduous tree species horse chestnut (*Aesculus hippocastanum* L.) and Turkish hazel (*Corylus colurna* L.) were used as accumulative biomonitors of trace metal pollution in the urban area of Belgrade. Two successive experimental years with remarkably different atmospheric trace metal concentrations were analyzed. Trace metal concentrations (Pb, Cu, Zn, Cd) were analysed on a single leaf level. An increase of trace metal concentrations in leaves of *A. hippocastanum* reflected a higher trace metal atmospheric pollution. The contents of Pb and Zn in soil for the same period also followed this trend. As accumulation of trace metals was more pronounced in *A. hippocastanum* than in *C. colurna*, the former may be suggested as a suitable biomonitor.

Introduction

Higher plants are not as suitable biomonitors as lichens and mosses [1]. However, in industrial and in urban environment, in highly polluted areas, where lichens and mosses are often absent, higher plants can act as appropriate indicators and biomonitors. Using plant leaves primarily as accumulative biomonitors of trace metal pollution has attained great ecological importance. The aim of this study was to estimate a validity of the use of some broad-leaved deciduous tree species as biomonitors in relation to variations of the level of urban trace metal pollution.

Experimental

Leaves were sampled from two deciduous tree species: horse chestnut (*Aesculus hippocastanum* L.) and Turkish hazel (*Corylus colurna* L.) in the Belgrade Botanic Garden, which is located in a heavy traffic urban area. Both species are commonly planted in urban parks, gardens, and/or along the streets. Samples for metal accumulation analyses were taken at the beginning (May - June) and at the end (September - October) of the seasonal vegetation cycles (in 1996 and 1997). Topsoil sampling was conducted at the same time of the seasons, in June of both investigated years. Leaves were washed off in double distilled water, dried at 105 °C to constant weight; ashing carried out gradually for 6 hours at 450 – 500 °C, at the rate of 50 °C per hour. The ash was dissolved in 0.1M HNO₃ prior to analyses. Results related to the concentrations in this water-soluble fraction were published previously [2]. An electrochemical method, the differential pulse anodic stripping voltammetry with a hanging mercury

drop electrode (DPASV) was used for determination of trace metals contents (Pb, Cd, Cu and Zn) on the single leaf level. After wet acid digestion, trace and other elements of the topsoil (0 - 15 cm) samples were analyzed by the method of atomic absorption (Perkin-Elmer 373).

Results and Discussion

The results of determined trace metal concentrations on single leaf level, for both investigated species, are presented in Table 1. Concentrations of Cd were below the detection limit in most of the samples. Generally, the concentrations of analyzed trace metals, Pb, Cu and Zn, in leaves of both species showed an increasing tendency during the vegetation seasons in both years. The results of t-statistics confirmed a considerably higher concentration of trace metals in *A. hippocastanum* than in *C. colurna* leaves in the end of the second experimental year (1997), (Table 1a, b).

Table 1. Trace metal concentrations in $\mu\text{g g}^{-1}$ in *Aesculus hippocastanum* (a) and in *Corylis colurna* (b) leaves in the beginning and in the end of the vegetation periods of the years 1996. and 1997

(a)						
month	Zinc		Copper		Lead	
	X_a	S_a	X_a	S_a	X_a	S_a
May '96	18.36	16.6	4.67	2.2	8.05	6.6
June '96	19.01	6.9	4.78	2.0	9.98	6.7
September '96	21.36	10.1	5.25	0.8	15.14	3.4
May '97	6.99	2.1	5.10	2.2	5.01	2.3
September '97	32.18	14.3	13.25	2.6	35.35	11.7

(b)						
month	Zinc		Copper		Lead	
	X_a	S_a	X_a	S_a	X_a	S_a
May '96	18.08	9.4	3.63	1.6	6.77	2.6
June '96	21.03	9.3	5.99	4.3	12.74	9.3
September '96	21.97	7.8	6.93	2.8	16.48	6.8
May '97	12.78	4.5	7.45	4.6	10.54	1.1
Sept '97	20.81	5.2	9.0	2.3	18.32	4.5

X_a -arithmetic mean; S_a -standard deviation

The increased atmospheric trace metal concentrations in the Belgrade downtown area affected their contents in leaves of investigated deciduous trees as well as in soil. A period chosen for this study refers to two successive experimental years with different traffic and industrial emissions due to the conditions of the UN economic sanctions imposed on this country. During the first experimental year, considerably lower pollutant emissions were evident as compared to the following year

(1997), when the economic sanctions were partly lifted and traffic markedly increased. According to the Annual Report on the Air Quality in Belgrade, published by the Institute of Public Health of Belgrade [3], concentrations of air pollutants, including trace metals, were much higher in the Belgrade urban area in that year than in the previous year. Thus, in 1997, in relation to the same period of the previous vegetation season, the mean Pb concentrations were more than doubled in the total atmospheric deposition and almost doubled in the total suspended particulate matter (TSP). The Pb concentrations in the total atmospheric deposition were 30.5 and 82.1 $\mu\text{g m}^{-2} \text{ day}^{-1}$ and Pb in TSP were 33.7 and 58.9 ng m^{-3} in September of the two experimental years, respectively.

Conclusion

Leaves of deciduous tree species (*Aesculus hippocastanum* L. and *Corylus colurna* L.) were used as accumulative biomonitors of trace metal pollution in the urban area of Belgrade. Two successive experimental years with remarkably different atmospheric trace metal concentrations were analyzed. Trace metal concentrations (Pb, Cu, Zn, Cd) in leaves, measured at single leaf level, in both species, increased during the investigated vegetation seasons. Our results establish a correspondence of an increase of atmospheric trace metal concentrations, in the second experimental year, to their contents in leaves and soil. It may be suggested that lead in leaves originates from the atmospheric deposition and was mostly emitted from the traffic. The plant water status may have also contributed to the amount of trace metal accumulation in leaves of the investigated species. The response of *A. hippocastanum* to the change of concentrations of trace metals in the atmosphere corroborates our choice of this plant species for a suitable biomonitor of air pollution in urban areas.

References

- [1] R. Bargagli, In: Trace Elements in Terrestrial Plants Springer-Verlag Berlin, Heidelberg, N. Y., 1998.
- [2] M. Tomašević, Z. Vukmirović, S. Rajšić, M. Tasić and B. Stevanović, Chemosphere, 2005, **61**, 753-760.
- [3] Annual Report on the Air Quality in Belgrade, Institute of Public Health of Belgrade, 1997.

HEAVY METAL CONTENT OF PM₁₀ AND PM_{2.5} WITHIN URBAN AREA OF BELGRADE

S. Rajšić¹, Z. Mijić¹, M. Tasić¹, D.Đorđević², M.Radenković³ and J. Joksić³

¹*Institute of Physics, Pregrevica 118, Belgrade (rajsic@phy.bg.ac.yu),*

²*ICTM-Centre of Chemistry, Njegoševa 12, Belgrade, Serbia*

³*Institute for nuclear sciences-Vinča, PO.Box 522, Belgrade, Serbia, Serbia*

Abstract

An assessment of air quality of Belgrade was performed by determining the trace element content in airborne PM₁₀ and PM_{2.5} in two years period. Samples were collected at two locations in a heavy polluted area. The concentrations of Al, Cr, Cu, Fe, Mn, Ni, Pb, V and Zn were determined with AAS. Results indicated that the ambient concentration of Zn in the PM₁₀ and PM_{2.5} was the highest (1389.18 and 1998.00 ng m⁻³ respectively). Also, the highest enrichment factor (EF) value was obtained for Zn, following with high EF for Cd and Pb in PM₁₀, reflecting the importance of anthropogenic inputs. The limit values of toxic trace elements from WHO and EC Air quality guidelines were not exceeded except for Ni.

Introduction

Besides natural emissions, heavy metals are released to the atmosphere by the human activities such as combustion of fossil fuels and high temperature industrial activities. Trace metals are found in almost all aerosol size fractions what may have a great effect on the toxicity of metals when inhaled because the degree of respiratory penetration is particle size dependent [1].

Sampling of particulate matter with aerodynamic diameter $D < 10 \mu\text{m}$, PM₁₀ and $D < 2.5 \mu\text{m}$, PM_{2.5} was conducted at two sites in the very urban area of Belgrade during the June 2003 - July 2005. Suspended particles were collected on Pure Teflon and Teflon-coated Quartz, Whatman, (47 mm diameter) filters, using the air sampler Mini-Vol Airmetrics Co., Inc., (5 l min⁻¹ flow rate). The duration of each sampling period was 24 hours. Particle mass was gravimetrically determined and filter samples were digested in 0.1N HNO₃ on ultrasonic bath and metals were analyzed with AAS.

Extraction with dilute acid has been used for the evaluation of elements which can become labile depending on the acidity of the environment. This procedure gives the valid information on the extractability of elements, because the soluble components in aerosol are normally dissolved by the contact with water or acidic solution without us in the actual environment [2].

During the sampling, conventional meteorological parameters were regularly recorded at the Meteorological Station of the Hydro-Meteorological Institute of Republic of Serbia, located inside central urban area.

Results and Discussion

The total mean concentrations of individual metals detected are shown in Table 1.

Table 1. Statistical parameters of heavy metal concentrations in PM10 (ng m⁻³)

	Pb	Cu	Zn	Mn	Fe	Cd	Ni	V	Al	Cr
N	210	210	210	210	210	210	210	210	210	167
mean	46.5	71.3	1389.2	20.8	1462.9	1.4	17.7	36.6	873.8	10.2
st.dev	128.5	118.7	2313.4	15.9	1911.9	2.2	17.7	48.8	914.1	11.4
max	1525.0	947.5	17239.6	72.7	20283.0	17.7	107.7	282.4	6104.2	58.0
min	0.5	0.2	2.1	0.2	0.5	d.l.	0.4	0.6	2.1	0.1
median	19.1	42.4	400.2	14.6	746.7	0.5	12.0	10.8	598.5	7.5
98 perc.	322.4	556.6	7018.3	62.4	5749.1	7.9	71.6	166.2	4126.9	46.3

The results indicated that the Fe content was the highest in the suspended particles with diameter less than 10 µm. Concentrations of Zn were, also, very high.

The highest mean concentration in PM2.5 was for Zn (1998 ng m⁻³). Zn is reliable tracer of unleaded fuel and diesel oil motor vehicle emissions. Besides, Zn could be released from tires friction. Cu showed relatively high mean value of 71.3 in PM10.

Table 2. Statistical parameters of heavy metal concentrations in PM2.5 (ng m⁻³)

	Pb	Cu	Zn	Mn	Fe	Cd	Ni	V	Al	Cr
N	64	64	64	64	64	64	64	64	64	64
mean	21.0	20.8	1998.0	15.2	1081.2	0.9	28.4	59.8	1180.3	6.2
st.dev	27.0	19.2	1846.4	13.7	1360.3	1.2	43.1	56.3	1657.4	3.8
max	193.9	99.6	6642.4	50.7	5996.5	4.8	315.0	248.5	7875.0	26.0
min	0.5	0.2	115.2	2.1	49.7	d.l.	0.4	5.2	159.1	1.6
median	13.5	17.4	1153.3	10.1	488.4	0.4	17.3	50.2	500.7	5.9
98 perc.	66.8	80.6	6101.7	47.9	5380.6	4.1	107.9	208.7	7307.3	13.2

This trace element is associated with industrial activities, but in urban areas road traffic (diesel engines and wearing of break vehicles) could be mainly source [3]. Vanadium is related to oil combustion almost 100%. The obtained mean value was 60.0 ng m⁻³ in PM2.5. Ni is mainly associated with fossil fuel use, and emissions from industrial sources. Mean Ni concentration of 28.4 ng m⁻³ in PM2.5 fraction was above the critical value. Mean concentrations of Pb, Cd, V, and Mn did not exceed the current air quality guideline values during three-years sampling period.

The Directive EU Air Quality setting a Pb annual limit value of 500 ng m⁻³. The mean annual concentration proposed for As is 6 ng m⁻³, 20 ng m⁻³ for Ni and 5 ng m⁻³ for Cd, all measured in the PM10 particulate fraction [4]. WHO Air Quality Guidelines includes an annual tolerance concentration of 150 ng m⁻³ for Mn, and for V the proposed 24-h concentration is 1 µg m⁻³ [5].

The results of enrichment factor (EF) can provide useful evidence for the sources identification of the elements in aerosols. The EF closed to unity suggests that the element is dominantly from crustal materials. EF of Zn was the highest (678 for PM10 and 1320 for PM2.5); EF of Cd (237 for PM10 and 196 for PM2.5) and EF of Pb with the value 122 for PM10 and 75 for PM2.5; intermediately enriched (EF between 10 and 100) were Cu, V and Ni.

Conclusion

The first results of heavy metals measurements in PM10 and PM2.5 in the urban area of Belgrade showed that concentrations for most metals remained below assessment thresholds and legislated limit value, except for Ni in PM2.5 fraction. A very high Zn contents were found for course and fine particles. It should be noted, that obtained concentration levels were, probably, lower than total metal contents in particles because a mild acid digestion was applied. The main sources of heavy metals in PM10 and PM2.5, suspended in Belgrade ground-level atmosphere, were traffic emission, road dust resuspension and emission from stationary combustion of fossil fuels (mostly for heating).

References

- [1] Espinosa, Rodriguez, De la Rosa, Sanchez, Atmospheric Environment, 2002, **36**, 773-780.
- [2] T.Kyotan , M.Iwatsuki, Atmospheric Environment, 2002, **36**, 639-649.
- [3] J.M.Pacyna, E.G.Pacyna, Environment Review, 2001, **9**, 269-298.
- [4] EC, European Commission, 2003.
- [5] WHO, Air quality Guidelines, 2000.

ASSESSMENT OF TRACE ELEMENT ATMOSPHERIC DEPOSITION IN BELGRADE AND SOURCE APPORIONMENT USING MOSS AND INAA

M. Aničić, M.V. Frontasyeva², M. Tomašević¹ and A. Popović³

¹*Institute of Physics, Belgrade, Serbia, manicic@phy.bg.yu*

²*Joint Institute for Nuclear Research, 141980 Dubna, Russia*

³*The Faculty of Chemistry, University of Belgrade, Belgrade*

Abstract

The level of atmospheric deposition of heavy metals and other elements in Belgrade urban area was evaluated using the moss biomonitoring technique. The concentrations of 36 elements (Na, Mg, Al, Cl, K, Ca, Sc, Ti, V, Cr, Mn, Fe, Co, Ni, Zn, As, Se, Br, Rb, Sr, Mo, Sb, I, Cs, Ba, La, Ce, Sm, Tb, Dy, Hf, Ta, W, Hg, Th, U) were determined by INAA. The accumulation abilities of two moss genera, *Brachythecium sp.* and *Eurhynchium sp.*, were examined and these could be combined for biomonitoring purposes. High enrichment factors for As, Zn, Mo, Br, Sb, Se, Hg and Cl, calculated to continental crust composition and local topsoil content, gave an evidence for anthropogenic impact, mainly due to intensive vehicular traffic and fossil fuel combustion.

Introduction

Ectohydric moss, which takes up water and elements through their entire surface, are regularly used as biomonitors for deposited airborne pollutants [1], [2], [3]. The present research is focused on the implementation of two moss genera: *Brachythecium sp.* (*B. rutabulum* & *B. salebrosum*) and *Eurhynchium sp.* (*E. hians* & *E. striatum*) for assessment of atmospheric deposition of heavy metals and other elements. The main objectives of this study were to evaluate the accumulation abilities of the studied moss species as biomonitors and sources identification.

Experimental

The study was carried out in urban area of Belgrade, at two sampling sites, Kalemegdan Park and Zemun, autumn of 2004. Collection of moss and local topsoil samples was performed according to a recent study [3].

Table 1. Flux parameters of irradiation positions [4]

Irradiation position	$\Phi_{th} \cdot 10^{12} [n \text{ cm}^{-2} \text{ s}^{-1}]$ E=0±0.55 eV	$\Phi_{th} \cdot 10^{12} [n \text{ cm}^{-2} \text{ s}^{-1}]$ E=0.55±10 ⁵ eV	$\Phi_{th} \cdot 10^{12} [n \text{ cm}^{-2} \text{ s}^{-1}]$ E=10 ⁵ ±25 10 ⁶ eV	T [°C]
Ch1	0.023	3.3	4.2	70
Ch2	1.23	2.9	4.1	60

Heavy metals and other element concentrations in the moss samples were analyzed by the method of instrumental neutron activation analysis (INAA) at the Frank Laboratory of Neutron Physics, Joint Institute for Nuclear Research, Dubna, Russia. The irra-

diation facilities of the used fast pulsed reactors IBR-2 are described in Table 1 [4]. To provide quality control, content of elements was determined using certified standard reference materials: lichen, cabbage and lake sediment from IAEA as well as pine needles and coal fly ash from NIST.

Results and Discussion

The obtained concentration of elements in moss tissue of investigated moss genera, *Brachythecium sp.* and *Eurhynchium sp.*, are quite comparable (Figure 1). For a majority of the 36 determined elements, the difference between moss contents in the two genera was within the range of specific experimental error.

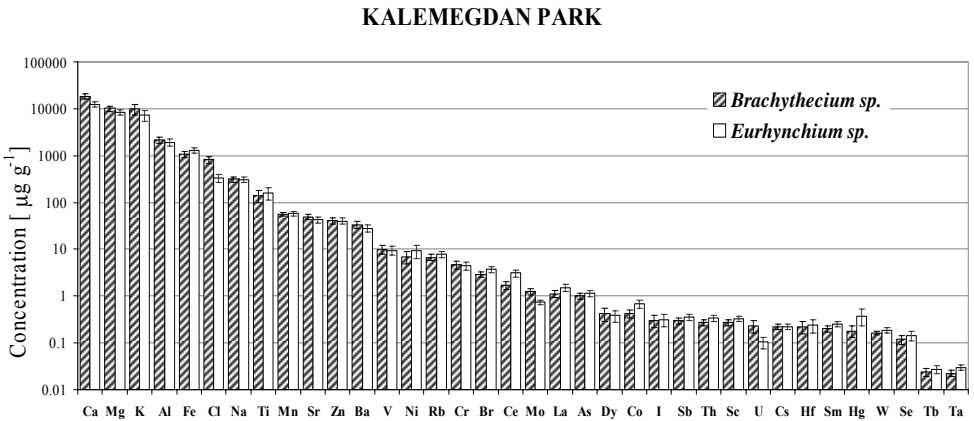


Fig. 1. Comparison of accumulation abilities of the studied moss genera

The enrichment factor (EF) of each element has been calculated to assess the contribution of anthropogenic in relation to crustal sources. The EF of an element (E) in moss relative to crustal reference element (R) is defined as:

$$EF = [E/R]_{\text{moss}} / [E/R]_{\text{Crust}}$$

If EF approaches unity, crustal material is likely the predominant source for an element; if EF is > 10, the element has a significant fraction contributed by non-crustal sources. Figure 2 presents the EFs of elements in analyzed moss samples calculated to the earth’s crustal mean abundances of the elements [5], (Figure 2a) and also according to element concentrations in topsoil samples at the studied sites (Figure 2b). Al was used as a reference element. High EFs for K, Mg, Ca, As, I, Zn, Mo, Br, Sb, Se, Hg and Cl (from 14 to 238) were calculated according to the crustal values. However, the EFs for the same elements, determined according to the local topsoil element content, were significantly lower (from 2 to 77). It suggests a significant contamination of local topsoil from atmospheric deposition.

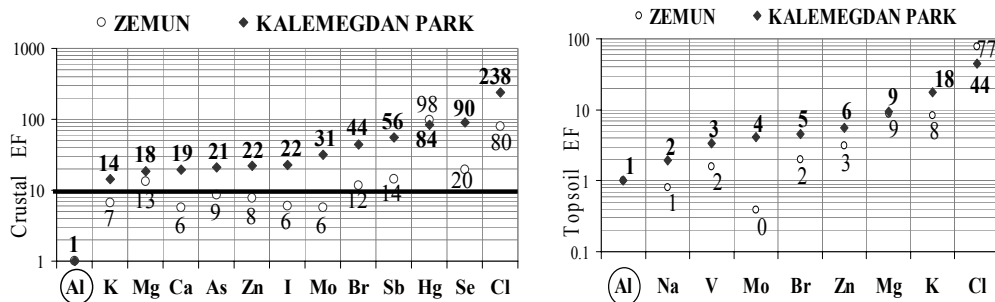


Fig. 2. Enrichment factors (EF) of elements in moss, sampled at Zemun and Kalemegdan Park, calculated to: (a) crustal element composition (b) concentration of elements in local topsoil determined in this study

Elements such as Br, Sb, As, Mo and Zn are considered as indicators of emission from fossil fuel combustion processes, including vehicle exhausts [6], [7]; Cl, Hg and Se are tracers for coal combustion [8]; leaded gasoline and diesel fuel (still widely used in Belgrade) contain a large amount of Br and Mo [6]; tire and brake lining wear might be a significant source of Sb [7]; re-suspension of soil and road dust (K, Ca) and leaching from living or dead plant tissue (Mg, Zn), [2]. The fuel used in the complex of coal-fired power plants (20 km SE from Belgrade), as well as for local domestic heating in Belgrade, is mainly lignite-brown coal or crude oil. These fuels are significant sources of the enriched elements at both studied sites, including traffic emission [9].

Conclusion

The following conclusions can be drawn from this study:

1. The studied moss species, *Brachythecium sp.* and *Eurhynchium sp.*, could be combined for biomonitoring purposes;
2. K, Mg, Ca, As, I, Zn, Mo, Br, Sb, Se, Hg and Cl in moss were enriched from some anthropogenic sources (fossil fuel combustion, traffic, dust re-suspension);
3. Local topsoil is significantly contaminated from atmospheric deposition and thus unsuitable for calculations of enrichment factors.

References

- [1] Å. Rühling, G. Tyler, *J Appl Ecol*, 1971, **8**, 497-507.
- [2] E. Steinnes, J. P. Rambaek, J. E. Hansenn, *Chemosphere*, 1992, **35**, 735-752.
- [3] UNECE ICP Vegetation, University of Wales Bangor, 2003, United Kingdom [4] M. V. Frontasyeva, S. S. Pavlov, *JINR Preprint*, E14-2000-177, Dubna.
- [5] B. Mason, In: *Principles of Geochemistry*, Wiley, New York, 1966.
- [6] J. M. Pacyna, E. G. Pacyna, *Environmental Review*, 2001, **9**, 269-298.
- [7] A. Arditoglou, C. Samara, *Chemosphere*, 2005, **59**, 669-678.
- [8] G. J. Watson, C. J. Chow, J. E. Houck, *Chemosphere*, 2001, **43**, 1141-1151.
- [9] S. Rajšić, M. Tasić et al., *Environ Sci Pollut R*, 2004, **11** (3), 158-164.

CHARACTERISTICS OF WINTERTIME POLYCYCLIC AROMATIC HYDROCARBON ASSEMBLAGE IN THE SUBURBAN ADRIATIC ATMOSPHERE

V. Ž. Jovanović¹, P. A. Pfendt^{2,1} and A. J. Jovanović³

¹*Institute of Chemistry, Technology and Metallurgy, Njegoševa 12, Belgrade, jovanovicvlada@yahoo.com*

²*Faculty of Chemistry, University of Belgrade, Belgrade,*

³*Institute of Public Health, Belgrade, Serbia*

Abstract

The results of analysis of polycyclic aromatic hydrocarbons (PAHs) in the aerosol samples, collected from the atmosphere of Herceg Novi during winter months of 1998 and 1999, are presented. Analysis was carried out by GC-MS method. The content and nature of identified PAHs suggested generally their similar origin during analyzed periods. Diagnostic ratios were used to indicate the main PAH sources, while the principal component analysis (PCA) was applied to test the influence of meteorological parameters on the PAH abundance.

Introduction

Scientific interest in the study of PAHs become widespread in Europe after the adopting of the 4th *European Daughter Directive on air quality* [1], but the available data, especially for Mediterranean area, are still scarce. To our knowledge, there are no detailed air pollution studies related to these compounds in the Adriatic aerosol.

Results reported in this work represent a part of our integrated study on the chemical characterization of Mediterranean aerosol in the Adriatic region. We deemed interesting to investigate the characteristics of air pollution with respect to PAHs, that is to investigate the intensity and origin of emissions from dominant sources in the Herceg Novi environment (Adriatic coast of Montenegro) during the winter periods of two successive years.

Since in a suburban environment, such as the area investigated, the pollution features affected by the local sources may be greatly modified by the meteorological conditions thus changing the abundance of specific PAHs in aerosols, the effects of meteorological parameters on the abundance of particle-bound PAHs have been also investigated.

Experimental

A total of 30 aerosol samples have been collected and analysed for the purpose of the investigation. Fifteen samples were taken during winter months of 1998 and the other fifteen during the same period of 1999. The sampling site, located in the eastern suburb of Herceg Novi, is included in the network of stations of the international program of the World Meteorological Organization for monitoring and investigating air pollution in the Mediterranean (MED POL).

Sampling of total suspended particles (TSP) was carried out with a high volume sampler equipped with glass-fibre filters. Operation time was 24 h and the sampling frequency was 1-in-6 day. Meteorological parameters: temperature (T), relative humidity (RH), wind direction (WD) and wind velocity (WV) were measured at the sampling site during collection. Content of TSP was quantified gravimetrically. Total solvent organic extracts (TSOE) from the filter material have been recovered by ultrasonic agitation. The extracts were quantified gravimetrically and analysed using standard GH-MS system. Some PAHs that were difficult to separate by gas chromatography and were of identical quality, were presented as total amount of the isomers, and one of the isomers was used as a standard because of their identical responses to the flame ionisation detector [2].

Results and Discussion

As seen in Fig. 1, relative concentration distribution of the identified PAHs in analysed aerosol samples from two years are almost the same, indicating the similar type of PAH sources for both analysed periods.

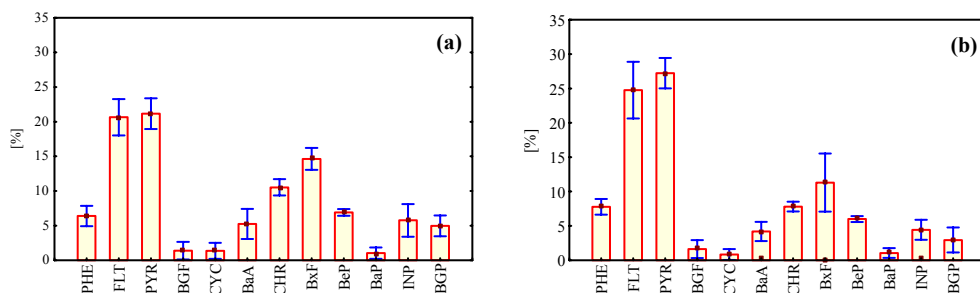


Fig. 1. Composition of PAH assemblages for winter samples of 1998 (a) and 1999 (b):

PHE - phenanthrene+anthracene (determined cumulatively as unresolved by GS analysis);
 FLT - fluoranthene; PYR - pyrene; BGF - benzo[ghi]fluoranthene;
 CYC - cyclopenta[cd]pyrene; BaA - benz[a]anthracene; CHR - chrysene+triphenylene;
 BxF-benzo(j+b+k)fluoranthene; BeP - benzo(e)pyrene; BaP - benzo(a)pyrene;
 INP - indeno[1,2,3-cd]pyrene; BGP - benzo[ghi]perylene.

Comparison of derived diagnostic ratios of the characteristic PAHs [$FLT/(FLT+PYR) = 0.48$, $INP/(INP+BGP) = 0.56$, $BeP/(BeP+BaP) = 0.78$, $[BeP/(BeP+BaP) = 0.78$, $BaA/(BaA+CHR) = 0.37]$ with those known from the literature [3, 4, 5], suggested the wood and fossil fuel burning, resuspension and emissions from petrol and diesel engines as main sources of PAHs during analysed periods.

The PCA with Varimax rotation has been applied to 12 identified PAHs, TSP, TSOE and four meteorological parameters mentioned above with the aim to find the groups of PAHs with similar behavior and to investigate possible effects of meteorological parameters on the PAH abundance.

Using Kaiser criterion [6], four principal components (PCs) have been selected for set data from 1998 and three PCs for those from 1999. Analysis showed that first PC accounts 61% of the variance in set data of 1998 and 54 % of variance in set data of 1999, and in both cases includes all identified PAHs with a high loadings (> 0.7) indicating the influence of prevalent similar sources and/or poor selectivity of factors that control PAH binding to particles. The first PCs are also positively correlated with RH (loading 0.79) and moderately negatively (loading -0.56) with WV. The other PCs explain from about 7% to 20% of the variance in data for samples from both years. Some of these components are also positive correlated with RH and negative with WV. It is known that an increase of humidity causes a decrease of adsorption capacity, consequently, these results point out the other mechanisms of scavenging by particles, which are inherently nonselective processes. Moderate negative correlation with WV indicates small decrease of PAH concentration caused by wind. The other explanation could be, that under weak (slow) wind conditions, the influence of local emissions increases in regard to transport from distance, therefrom, it could be concluded that PAHs arise from local sources.

Conclusion

The following conclusions can be drawn from this study: 1.- there are no significant differences of PAH composition in analyzed aerosol samples collected during winter months of 1998 and 1999; 2. diagnostic ratios of characteristic PAHs suggest three main PAH sources: combustion of fossil fuels, emissions from petrol and diesel motors and resuspension; 3. the correlation of PAHs with meteorological parameters RH and WV can be explained as a consequence of influence of RH on adsorption of organic vapors on the surface of atmospheric particles, and the impact of WV on decreasing concentration due to dilution.

Acknowledgement

This work was supported by the Ministry of Science and Environmental Protection of the Republic of Serbia.

References

- [1] Directive 2004/107/EC of the European Parliament and of the Council.
- [2] H.Yamasaki, K.Kuwata, H.Miyamoto, *Environ. Sci. Technol.*, 1982, **16**, 190-196.
- [3] E. Manoli, A. Kouras, C. Samara. *Chemosphere*, 2004, **56**, 867-878.
- [4] W.F Rogge.,L.M.Hildermann, M.A.Mazurek and G.R. Cas, *Environ. Sci. Techno*, 1993, **27**, 636-651.
- [5] I.G Kavouras et al., *Atm. Environm*, 1999, **33**, 4977-4986.
- [6] N.J Gotelli and A.M Ellison, *A Primer of Ecological Statistics*, p. 416. 2004, Sunderland, Massachusetts U.S.A
- [7] J.F Pankow, J.M.E Storey and H. Yamasaki. *Environ. Sci. Technol.*, 1993, **27**, 2220-2226.

PRECIPITATION CHEMISTRY IN THE VELIKA MORAVA CATCHMENT

D. Golobočanin, A. Žujić and N. Miljević

Vinča Institute of Nuclear Sciences, POB 522, 11001 Belgrade, Serbia

Abstract

Bulk precipitation chemistry on a daily basis was studied for seven years (1998-2004) at three meteorological stations (Smederevska Palanka, Kraljevo, Niš) in the Velika Morava catchment. Samples were analyzed for the anions Cl^- , NO_3^- and SO_4^{2-} , and for the cations Na^+ , NH_4^+ , K^+ , Mg^{2+} and Ca^{2+} in addition to pH and conductivity measurements. The most abundant ion was SO_4^{2-} , followed in descending order by $\text{Ca}^{2+} > \text{NH}_4^+ > \text{Mg}^{2+} > \text{Cl}^- > \text{Na}^+ > \text{NO}_3^- > \text{K}^+$. A significant wet deposition of sulfate of $58\text{-}134 \text{ mmol}\cdot\text{m}^{-2}\cdot\text{yr}^{-1}$ was calculated caused by heating emission during combustion of low-quality sulfur-rich lignite.

Introduction

Precipitation is an efficient pathway for removing the gases and particles from the atmosphere playing a significant role in controlling their concentration. Determination of chemical composition of rainwater provides an understanding of the source types that contribute to precipitation chemistry, and enhances the understanding of the local and regional dispersion of pollutants and their potential impacts on ecosystems through deposition processes [1]. Sulfur dioxide (SO_2) is considered the main atmospheric pollutant of anthropogenic origin. The main pathway of the sulfate removal from the atmosphere is rain scavenging. The aim of this paper was to evaluate the natural composition of precipitation and to identify possible sources that contribute to precipitation chemistry of the Velika Morava catchment.

Results and Discussion

The precipitation collection and its analyses were conducted by the Republic Hydro-meteorological Service of Serbia following the recommendation of the WHO [2]. The amount of precipitation varied considerably from year to year in the different regions with a minimum of 297 mm (in 2000) and a maximum of 822 mm (in 2004) which corresponded to 47% and 123% respectively to the values of the 30 years averages (1961-1990). The pH values of collected precipitation covered a wide range from acidic (minimum of 3.3) to alkaline (maximum of 9.5). Approximately 50% of the rain events had pH between 6.0 and 7.0, indicating highly alkaline nature of rainwater at the catchment area with mean values of 6.1 (Smederevska Palanka and Kraljevo) and 6.3 (Niš) due to extensive neutralization of acidity. The neutralizing agents are primarily ammonia, soil dust and fly ash components (predominantly, CaCO_3 , MgCO_3 , oxides, silicates). The quality control for the entire database was checked for each rain sample by calculating the cation and anion balance (ID, ion difference in %)

$$\text{Ion Difference (\%)} = 100 \cdot (\text{CE} - \text{AE}) / (\text{CE} + \text{AE})$$

where AE is the sum of anion equivalents (μeL^{-1}) and CE is the sum of cation equivalents (μeL^{-1}). Linear regression of cation sum on anion sum for the sets of samples considered in this study gave r^2 values of 0.90-0.95 indicating that the quality of the data was good. The mean monthly concentrations for each analyzed species have been calculated as volume-weighted mean (VWM) by taking into account the event rainfall.

The annual level of SO_4 (155-394 $\mu\text{eq.L}^{-1}$) was high and comparable with concentration for sites to the time before the unification of Germany and the reorganization in the other countries of Eastern Europe [3]. Regarding the same period the annual mean concentrations of SO_2 registered at those sites were in the range of 14-54 $\mu\text{g.m}^{-3}$ with maximum in winter months (November-February, exceeding permissible limits of 150 $\mu\text{g.m}^{-3}$ for averaging 24 hour period) and a slightly decline since 2001 due to combustion of low-quality lignite with high sulfur and/or salt and ash content. The emissions of SO_2 were estimated to 396 kt in Serbia in 2003 [4]. The second abundant element was Ca (98- 449 $\mu\text{eq.L}^{-1}$) indicating its anthropogenic origin emitted by human activities such as traffic, cement factory work and fly ash through short and intermediate range transport phenomena. The latter from sulphur-rich lignite burned contains 12–28% CaO on average which quantity was estimated at around $6,6 \times 10^6 \text{ t.y}^{-1}$ [4]. The good correlation ($r^2=0.90$) of calcium in precipitation with chloride is a hint at lignite burning as well as the dilution effect of the precipitation amount on their concentrations. The nitrate concentration in rain exhibited interannual changes (between 5 and 85 $\mu\text{eq.L}^{-1}$) with decreasing trend probably due to restructuring of industry, a reduction of stock farming and a reduction in the numbers of animals. On the other hand, ammonium concentration (6-92 $\mu\text{eq.L}^{-1}$) showed increasing trend mostly due to the volatilization of NH_3 from soils having pH values greater than 6.0. The annual wet deposition was calculated as the product of ion concentration ($\mu\text{eq.L}^{-1}$) and amount of precipitation (mm) over the sampling time (Fig. 1).

Conclusion

In general, VWM concentrations were not statistically distinct among sampling sites. The heating emission situation in Serbia was characterized by combustion of low-quality lignite with high sulfur generating significant SO_4^{2-} fluxes from 58 to 134 $\text{mmol.m}^{-2}.\text{yr}^{-1}$ during high precipitation levels.

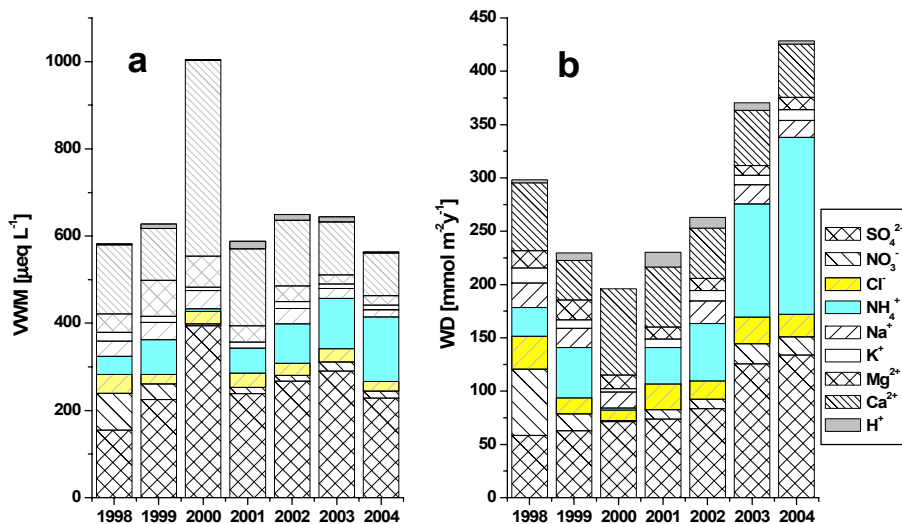


Fig. 2. (a) Annual average volume weighted mean concentration in precipitation for seven years (1998-2004) and (b) Annual wet deposition in the Velika Morava catchment

References

- [1] P. C. Mouli, S. V. Mohan, S. J. Reddy, *Atmos. Environ.*, 2005, **39**, 999-1008.
- [2] Manual for the GAW Precipitation Chemistry Programme, Guidelines, Data Quality Objectives and Standard Operating Procedures, GAW precipitation chemistry science advisory group, WMO TD no. 1251, World Meteorological Organization Global Atmosphere Watch, no. 160, (Ed. M.A. Allan), WMO, Geneva, November 2004.
- [3] W. Marquardt, E. Brüggemann, R. Auel, H. Herrmann, D. Moller, *Tellus* 2001, **53B**, 529-545.
- [4] Republic Hydrometeorological Service of Serbia, *Meteorological Yearbook 3, Air Quality*, 2004, Belgrade.
- [5] G. Stefanović, Lj. Čojbašić, Ž. Sekulić, S. Heckmann, *Facta Universitatis*, 2004, **2**, 141-151.

A SPECTROMETRIC METHOD FOR BROMATE ANALYSIS IN DRINKING WATER

A. Moise, E. Mihaila and I. Ciurcanu

*National Research and Development Institute for Industrial Ecology-ECOIND,
90-92 Panduri St., 050663 Bucharest – 5, Romania*

Abstract

A spectrometric method for bromate determination was optimized for water samples analysis.

The main purpose of the study was to investigate the most important analytical parameters, like the optimal reagent concentration for a stable reaction product, time needed for maximum color development, stability in time of the colored compound, optimal wavelength for absorbance measurement, linear concentration range, in order to obtain maximum sensibility and reproducibility for bromate determination in drinking water samples.

For the proposed, optimized, method, the basic quality performance parameters (linearity range, regression coefficients, S_y , S_{x_0} , CV) have been fully evaluated.

The recovery rates of the bromate from some matrixes like surface water have been found in the range of 96 –107.5 %.

The performance parameters of the proposed optimized method make it suitable for the application in bromate analysis in surface water.

Introduction

Bromate in the drinking water is a by-product from water ozonization, resulting from ozone oxidation of bromide [1].

The total bromine concentration in raw water, which is purified for producing the drinking water, is the range from a few micrograms to some milligrams per liter. The main bromide sources from the ground water are linked with the geological characteristics of a particular site, anthropogenic pollution sources, potassium and coal mining [2].

The usual bromate concentration in drinking water is in the range of 3–8 $\mu\text{g/l}$, though in some infrequent instances levels of 0.05 $\mu\text{g/l}$ [3] or more than 30 $\mu\text{g/l}$ [4] could be encountered. The bromate level in drinking water depends upon a lot of different variables [4] the most important being bromide concentration in the raw water and ozone concentration during the treatment. For a starting bromine concentration of 35 - 50 $\mu\text{g/l}$ and using 1mg/l ozone, the final bromate concentration could be about 25 $\mu\text{g/l}$ or even grater than that. This proves that an increased ozone concentration is linked with high bromate concentration [5].

Since 1990 there are some reports that bromate have a cancerigen effect [5] and EPA (Environmental Protection Agency -USA) considered necessary to include it in the list of dangerous substances. The maximum accepted limit for bromate, originally established at 25 $\mu\text{g/l}$, was reduced subsequently to 10 $\mu\text{g/l}$, in view of the cancerigen

effect of this compound. The same value was proposed by the Drinking Water Commission of European Union [6].

The aim of this study was the optimization of the method for bromate analysis and the evaluation its suitability for bromate determination in drinking water.

Results and Discussion

All the analytical parameters have been evaluated in order to obtain the best performances of the analytical system for bromate determination: the optimal reagent concentration for a stable reaction product, time needed for maximum color development, stability in time of the colored compound, optimal wavelength for absorbance measurement, linear concentration range. The following calibrating procedure has been used: a) volumes of 0, 1, 2.5, 5, 7.5 and 10 ml from the standard stock solution ($1 \text{ mg.L}^{-1} \text{ BrO}_3^-$) are diluted to 20 ml with deionized water ;b) add to the above solutions 1 ml KI (0.1%), 1 ml of HClO_4 (35 %) and 2 ml of 3,3'-dimetilnaftidine (0.5%); c) the samples are left for 15 min. for color development and the absorbance is measured at 546 nm (50 mm path length). Using linear regression, the calibration curve was plotted, and the most relevant performance features of the method have been evaluated (regression quotients a and b, linearity range, S_y , S_{x_0} , CV_{x_0}) [7].

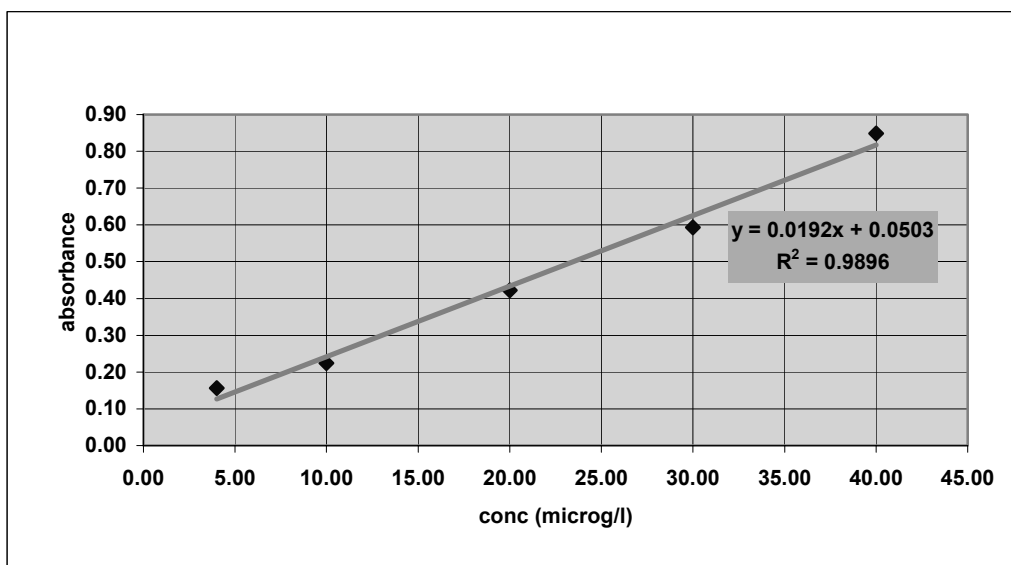


Fig. 1. Bromate calibration curve

Aliquots (20 ml) from the unknown water samples are processed in the same way as calibrating solutions. The method was validated "in house" for bromate determination in drinking water. In Table 1 we present the optimal parameters found during the study.

Table 1. Performance parameters of the bromate determination method which has been validated "in house"

Nr. crt.	Parameter	Atomic molecular spectrometry bromate determination
1	Exactitude	98,59%
2	Fidelity	CV% = 1,72%
3	Repeatability	r = 0,95 $\mu\text{g/l}$
4	Reproducibility	$R_L = 1,81 \mu\text{g/l}$
5	Sensibility	b = 0,022
6	Detection limit	LoD = 0,3286 $\mu\text{g/l}$
7	Quantitation limit	LoQ = 0,5475 $\mu\text{g/l}$
8	Concentration range	4 $\mu\text{g/l}$ – 40 $\mu\text{g/l}$
9	Average recovery rate	Recovery = 99,25 %

Conclusions

The most relevant analytical parameters and equipment settings have been evaluated and optimized for the analysis of bromate by atomic molecular method: the optimal reagent concentration for a stable reaction product, time needed for maximum color development, stability in time of the colored compound, optimal wavelength for measurement, linear concentration range.

The method for bromate analysis has been validated "in house" by evaluating the relevant method's parameters: exactitude, fidelity, repeatability, reproducibility, sensibility, detection limit, quantitation limit, concentration range, recovery rate [7].

The proposed method can be used for quantitative determination of bromate in drinking waters.

References

- [1] Krasner, S.W., Glaze, W.H., Weinberg, H.S., Daniel, D.A. and Najm. I.M. – Formation and control of bromate during ozonation of waters containing bromide, J. Am. Water Works Assoc., 1993, January, 71-83.
- [2] Colombini, S., Polesello, S., Valsecchi S., Cavalli S., J. Chromatogr. A, 1999, **847**(1-2), 279- 284.
- [3] Voltera, L; - Acqua & Aria, 1997, Gennaio, 81.
- [4] Mills, A; Belghazi, A. and Rodman, D. – Waters Res., 1996, **9**, 973.
- [5] Von Gunten, U., Bruchet, A., and Costentin, E., J.AWWA, 1996, June, 53.
- [6] Commission of the European Communities, Proposal for a Council Directive Concerning the Quality of Water Intended for Human Consumptions, CEC, Brussels, 1994.
- [7] W. Funk, V. Dammann, G. Donnevert, Quality Assurance in Analytical Chemistry, VCH, Weinheim, New York, Basel, Cambridge, Tokyo, 1995.

THE EFFECT OF SIMULATED ACID RAIN ON METAL DESORPTION FROM *CETRARIA ISLANDICA*

A. Čučulović¹, M. S. Pavlović², D. Veselinović³ and Š. S. Miljanić³

¹INEP - Instit. for the Application of Nuclear Energy, Banatska 31B, Zemun, anas@inep.co.yu

²Laboratory of Physical Chemistry, The Vinča Institute, P.O. Box 522, Belgrade

³Faculty of Physical Chemistry, University of Belgrade, P.O. Box 137, Belgrade, Serbia

Abstract

In this paper the possibility of extracting metals: K, Al, Ca, Mg, Fe, Cu, Ba, Zn, Mn and Sr, from *Cetraria islandica* lichen with solutions simulating acid rain (H₂SO₄-HNO₃-(NH₄)₂SO₄), pH 2.00 (1) and 3.28 (2) has been investigated. The results obtained suggest that the investigated elements can be classified into ones where the highest percentage was extracted with the first extraction (K, Al, Mg, Ba, Zn and Mn) and others where the extraction percentage is relatively uniform (Ca and Fe). This indicated different bonding methods in lichen that is in accordance with literature data where two cation bonding methods in lichen were shown.

Introduction

Lichen is sensitive to pollutants in the air such as: ozone, SO₂ and ammonia. Acid rain, formed from SO₂ and NO₂ building H₂SO₄ and HNO₃ during atmospheric transfer and transformation, can cause extinction of lichen¹. The purpose of this paper is to investigate extraction of K, Al, Ca, Mg, Fe, Cu, Ba, Zn, Mn and Sr from *Cetraria islandica* lichen with acid solutions corresponding through acid rain and thus possible transfer of these elements into the environment.

Materials and Methods

C. islandica lichen (from the Sinjajevina Mountain, Montenegro, collected in 1994) was cleaned from impurities and mechanically chopped. After drying in air until a constant mass was reached, 0.500 grams was measured out for experiments. The K, Al, Ca, Mg, Fe, Cu, Ba, Zn, Mn and Sr content was measured in untreated samples before extraction and in solutions after each of the five consecutive extractions for the same sample. In order to determine the element content in lichen before extraction the sample was treated with liquid nitrogen, chopped up and completely homogenized and then it was dissolved in Teflon cups in a mixture of concentrated HNO₃/HClO₄/HF (10:1:1) acid². Cooled solutions were filtrated and diluted with distilled water until the volume of 100 mL was attained. The K content was measured with a stabilized d.c. arc. All other elements were measured using a Spectro-Flame ICP spectrometer. The extraction solution was made of concentrated H₂SO₄ and HNO₃, by separately adding them to distilled water until the desired pH of 2.00 (1) or 3.28 (2) was reached. Then 100 cm³ of each acid solution was mixed, 1 g of (NH₄)₂SO₄ per 100 cm³ of the mixture was added and the pH was adjusted with concentrated sulfuric acid. Extractions were performed at room temperature (ca 22⁰C) for 24 hours with occasional mixing. All

extractions were repeated twice. The lichen samples were dried at room temperature after each extraction until a constant mass was reached and then they were extracted again using corresponding solutions.

Results and Discussion

The K, Al, Ca, Mg, Fe, Ba, Zn, Mn, Cu and Sr content in lichen before extraction and the extracted percentage of these elements in extracted solutions after each extraction with solutions (1) and (2) is shown in Table 1. Most probably, H^+ participated in the cation-exchange process, thus leading to even higher H^+ ion exchange with cations accumulated in the lichen. All extractions performed with solution (1) were more efficient than extractions performed with solution (2).

Table 1. K, Al, Ca, Mg, Fe, Ba, Zn, Mn, Cu and Sr content in untreated lichen and their extraction percentage with solutions (1) and (2) after every extraction

Elements	K	Al	Ca	Mg	Fe	Ba	Zn	Mn	Cu	Sr	
Starting content ($\mu\text{g/g}$)	1475	450	6880	260	265	13	30	10	6	10	
Ex-trac-tion	Solu-tion	Percentage of extracted elements in solutions in relation to the starting content (%)									
I	(1)	60	6,8	19	43	8,5	4,6	40	48	*	16
	(2)	52	4,8	7,7	35	1,6	1,5	13	24	*	8,0
II	(1)	2,1	1,2	12	2,2	2,9	*	*	*	*	2,0
	(2)	2,3	1,5	4,4	3,0	1,2	*	*	*	*	*
III	(1)	0,3	0,7	15	1,7	2,3	*	*	*	*	2,0
	(2)	0,1	0,6	5,0	1,4	1,2	*	*	*	*	*
IV	(1)	0,08	0,6	16	1,5	1,7	*	*	*	*	2,0
	(2)	0,07	0,5	5,6	1,8	1,4	*	*	*	*	*
V	(1)	0,19	0,8	24	3,1	2,1	*	13	*	67	6,0
	(2)	0,08	0,6	8,5	2,5	2,1	*	*	*	*	*
Percentage of total extracted elements from lichen (%)											
(1)	63	10	94	52	18	5	40	48	67*	288	
(2)	55	8	31	44	8	2	13	24			

* Concentration of elements in these extracts is below the detection limit

Analysis of the results obtained enables the conclusion that K, Mg and Mn desorbed the most in solutions obtained after the first extraction. Earlier research has shown that passive pollutant adoption is dominant over active and hyper accumulation of metals is the consequence of a reactive mechanism with organic acids formed by the lichen and the sensitivity to metals becomes higher due to the formation of different complex

compounds^{3,4}. Some cations are actively and passively adopted that is reflected in where they are found. Passive ion adoption by ionic exchange or complexation results in ion distribution outside the cell. It was established that passive cation adoption by lichen represents a universal cation-exchange process modified by the formation of metal complexes where oxygen or oxygen-nitrogen donors represent the adsorption points⁵. Analysis of our results enables the conclusion that they are in accordance with the two described cation bonding methods in lichen⁵. The elements in Table 1 can be grouped into ones where the highest percentage was extracted by the first extraction (K, Al, Mg, Ba, Zn and Mn) and ones where the extraction percentage is relatively uniform (Ca and Fe). This clearly indicates that two types of sorption (bonding) can be clearly differentiated for the first group of elements as described in literature. Compared to that, Ca⁺⁺ is extracted evenly and two types of sorption cannot be clearly differentiated. Copper starts to be extracted significantly during the fourth extraction and we assumed that it is most probably dominantly bonded deep inside the cell. Special behaviour is also noted for Sr where the amount of extracted element varies from extraction to extraction.

Conclusion

Extraction of K, Al, Ca, Mg, Fe, Cu, Ba, Zn, Mn and Sr elements from *C. islandica* lichen with solutions corresponding to acid rain (H₂SO₄-HNO₃-(NH₄)₂SO₄), pH 2,00 (1) and 3,28 (2) can lead to transfer of these elements into the environment. All sorption performed with solution (1) were more efficient than desorption performed with solution (2).

Acknowledgement

This work was supported by the Ministry for Science and Environmental Protection of the Republic of Serbia (Project No. ON 142039 and ON 142065)

References

- [1] J. E. Sloof, Environmental Lichenology: biomonitoring Trace-Element Air pollution, doctoral thesis, Tehnical Univ., Delft, The Netherlands, 1993.
- [2] M. Kuzmanović, M.S. Pavlović, M. Marinković, Spectrosc. Lett., 1996, **29**(2), 205-215.
- [3] R.P. Beckett, The Lichenologist, 1996, **28**(3), 257.
- [4] M. Hyvärinen et al., Environ. Exp. Botany, 2000, **43**, 211-218.
- [5] A. Čučulović et al., 44. Savetovanje SHD, 2006, 193-196, Beograd.

THE CORRELATION BETWEEN THE AMOUNTS OF CADMIUM IN WATER AND IN SOIL

D. Veselinović², D.A. Marković², A. Savin¹, S. Filip³ and D. Bengin¹

¹"Eko-Lab", Idustrijska zona bb, P. Skela, Belgrade, Serbia

²Faculty of Physical Chemistry, University of Belgrade,
12-16 Studentski Trg P.O. Box 137, Belgrade, Serbia

³"Mihajlo Pupin" Technic faculty, Dj. Djakovica bb, 23000 Zrenjanin

Abstract

It has been investigated the correlation of the cadmium amount in the wastewater and total and plant-available Cd in the soil, as well as Cd amount in the leaf and stalks of the pepper. The plant-available amount of Cd in the soil has been determined by different extraction solutions. The sampling took place on the parcel of the Prokuplje. Total and plant-available Cd amount in the soil has been determined after soil covering with different industrial wastewater. It has been concluded that the total and plant-available Cd in the soil is higher after soil treatment with waste water.

Introduction

The sampling took place on the parcel of the Prokuplje. The sampling was carried out by a sound (depth 0-30 cm). The wastewater took place with different source in place neighborhood of the Prokuplje.

The total amount of Cd in the industrial wastewater determined after sample digestion with HNO₃ acid (1:4).[1] The plant-available amount of Cd in the soil was determined by AAS after extraction procedures performed using: **1)** 0.5 M Na₂EDTA, pH=5.2[2]; **2)** 1 M KCl, pH=7[2]; **3)** 0.1 M KCl, 0.05 M Na₂EDTA, pH=6.2[3]; **4)** 2 % CH₃COOH, pH=2.5[2]; and **5)** 1 M CH₃COONH₄, pH=4.8[2]. The determination of the total Cd amounts in the soil: A corresponding amount of air-dried sample was measured and wet-ashed with HNO₃ and HClO₄ (conc.)[2]. The plant material was destructed with HNO₃ and HClO₄[4]. The Cd concentrations in solutions was determined by atomic absorption spectrophotometry. Each samples has been analysed 3 times.

Results and Discussion

The obtained mean Cd amounts are given in the Table I.

The complexes of Cd with components in extraction solutions and corresponding stability constants are given in the Table II.

Table I The Cd amounts in the soil (total and plant-available), wastewater and in the peper plant parts

Wastewater (Cd amount, mg/L)	0.0013	0.0016	0.0022	0.0035	0.0019	0.0019	
	Cd amount in samples, mg/kg						
Soil, Total amount	0.61	0.81	0.84	0.71	0.77	0.87	0.84
Soil, Plant-available amount Extragens							
2% CH ₃ COOH, pH=2,5	0.031	0.031	0.038	0.044	0.056	0.038	0.037
1M CH ₃ COONH ₄ , pH=4,8	0.075	0.225	0.231	0.219	0.200	0.188	0.194
1M KCl, pH=7	0.212	0.218	0.229	0.224	0.229	0.224	0.229
0,5 M Na ₂ EDTA, pH=5,2	0.093	0.170	0.141	0.129	0.141	0.147	0.129
mixture 0,1M KCl and 0,05 M Na ₂ EDTA, pH=6,2	0.112	0.219	0.225	0.219	0.200	0.225	0.225
stalks	0.51						
leaf	0.68						

Table II The complexes of Cd and corresponding stability constants:[5,6]

ligand	stability constants			temperature (°C)	ion strength (μ)
	middle value	minimal value	maximum value		
chlorid	$\beta_2=2.28$	1.60	2.74	0 – 45	0 – 0.3
acetate	$\beta_2=2.38$	2.19	2.70	25 – 30	0 – 0.3
EDTA ²⁻	$\beta_1=16.2$	15.0	16.6	20 – 25	0.1 – 0.2

The linear dependence of Cd amounts in soil from the Cd amounts in wastewater is obtained.

The low value of the plant-available amount of Cd is obtained using CH_3COOH . When using $\text{CH}_3\text{COONH}_4$ extragens the obtained plant-available amount of Cd is higher. On the basis of the obtained data it can be concluded that in both cases are formed acetate complexes as well as and complexes with amonia the obtaind plant-available amount of Cd is depend on pH-value extraction solutions.

The extraction by 1 M KCl and mixture 0,1M KCl and 0,05 M Na_2EDTA also give similar plant-available amount of Cd values. Also, in both cases it can be concluded that chloride complexes of Cd are formed. The values were obtained by using the pure KCl solution, although makes the complexes with lower stability constant than the complexes with EDTA. In both cases it can be concluded that chlorine complexes of Cd are formed.

The values of the plant-available Cd amount, when using extragens 0.5 M Na_2EDTA , pH=5.2 is not in function of stability constants (β)[5,6].

Conclusion

On the basis of the obtained data it is concluded that the existence of the linear dependence of amount Cd in the water and total amounts Cd in the soil. Plant-available amount Cd in the soil depedence of the stability constant and increase total amount Cd in the soil is not influence on the obtain plant-available amount Cd in the soil.

It has been concluded that the amount plant parts of peper (leaf and stalks) is relative high.

The cadmium amounts in leaf is higher than in the stalks.

References

- [1] Standard Methods For the Examination of Water and Wastewater, 15th Edition, 1980, APHA-AWWA-WPCF.
- [2] P.R. HESSE, "A Textbook of Soil Chemical Analysis", John Murray Ltd, 1971, p: 371-377, 388.
- [3] D.Veselinovic, A.Savin, M.Gojkov, S. Filip, M.Milovac, 2nd International Conference of the Chemical Societies of the South-Eastern European Countries on Chemical Sciences for Sustainable Development, Book of Abstract, Vol. I, 2000.
- [4] John C. Van Loon, Analytical Absorption Spectroscopy, Accademic Press, p-161.
- [5] Lange's, Handbook of Chemistry, Mc. Grav. Hill, New York, 1973.
- [6] J. Serb. Chem. Soc., 2004, **69** (12), 1145-1151, JSCS-3240.

URANIUM(VI) ADSORPTION ON ACID MODIFIED CLINOPTILOLITE / HEULANDITE RICH TUFF

S. Matijašević, A. Daković, M. Stojanović and D. Ileš

¹*Institute for Technology of Nuclear and Other Mineral Raw Materials,
Franchet d Esperey 86, Belgrade, Serbia*

Introduction

Uranium is a toxic heavy metal arising from the nuclear industry as well as from anthropogenic activities. It has a long half life and is observed to have a coordination chemistry consisting of multiple stable oxidation states and stable solid and aqueous forms within the ecosphere. Under standard environmental conditions, uranium typically occurs in the hexavalent form as the mobile, aqueous uranyl (UO_2)²⁺ ion. This ion has been shown to be strongly adsorbed onto clay minerals and metal oxides under appropriate chemical conditions. The extent that uranium (VI) is removed from aqueous solutions is a function of the aqueous solution properties such as pH, uranium (VI) concentration, complexing ligands, and the sorptive phase characteristics. Adsorption of uranium (VI) onto various solids is important from purification, environmental and radioactive waste disposal points of view [1, 2].

In this paper the investigation results of adsorption of uranium (VI) on natural and acid modified zeolitic mineral clinoptilolite/heulandite are presented.

Experimental

Starting material used in these experiments was natural zeolitic tuff from Beočin deposit (Fruška Gora, Serbia and Montenegro). Based on qualitative mineralogical analysis, the content of clinoptilolite/heulandite was over 80%, while the accessory minerals were quartz, feldspar, mica, calcite and clay minerals. The cation exchange capacity (CEC) of the zeolitic tuff was 168 meq/100g and the external cation exchange capacity (ECEC) was 10.5 meq/100g. The CEC of clinoptilite rich tuff was measured with 1M NH_4Cl while its ECEC was determined using the method of Ming and Dixon [3].

The hydrochloric acid (1M) was used for the preparation of the acid modified zeolite. The constant quantity of zeolitic tuff (100g) was treated with 1000 ml of acid solution for 60 minutes at 50°C. After mixing, the suspension was filtrated and the concentrations of exchanged Ca^{2+} , Mg^{2+} , Na^+ and K^+ were measured in the supernatant using atomic absorption spectrophotometry (AAS). The acid modified zeolite was rinsed with distilled water until Cl-ions were no longer detected and then dried at 60°C. This product was denoted as H-clino.

Uranium (VI) solutions for adsorption experiments were prepared using uranyl nitrate hexahydrate ($\text{UO}_2(\text{NO}_3)_2 \cdot 6\text{H}_2\text{O}$) (Sigma-Aldrich Co). The preliminary batch studies were carried out by shaking known amounts of each adsorbent and uranium (VI) solution, at room temperature for at least 24 h, at pH 6. In order to investigate influence of the amount of H-clino in suspension on uranium (VI) adsorption, at pH 6, the

experiments were performed as follows: the volume of solution (50 ml) and the concentration of uranium (VI) (50 mg/l) were kept constant while the amount of adsorbent varied from 0.025 to 1 g. The suspensions were shaken for 2 h, at room temperature. After the reaction time, the solids were separated by centrifugation and in supernatants, the remained uranium (VI) concentration was determined.

In order to investigate uranium (VI) adsorption isotherms on H-clino, to each tube 0.125 g of adsorbent and 50 ml of uranium(VI) solution were added at concentration of 10, 20, 25, 30, 40, 50 mg/l. The adsorption of uranium (VI) ion on H-clino was studied at different pH values, with each sample being done in duplicate. Samples were shaken for 2 h, centrifuged at 10000 rpm for 10 min and uranium (VI) concentration were measured in supernatants. Initial uranium (VI) concentrations, as well as equilibrium uranium (VI) concentration in solutions were determined using fluorometric method based on the fluorescence of U in fused mixture of NaF, Na₂CO₃ and K₂CO₃ [4].

Results and Discussion

In order to determine the equilibrium time for uranium(VI) adsorption on H-clino, the kinetics of adsorption was investigated. It was found that adsorption begins very fast and that the most of uranium (VI) ion is adsorbed in less than 2 hours (>95%). Practically there were no changes in adsorption within next 48 h. Based on these results subsequent adsorption experiments were conducted with a 2 hours reaction time.

Preliminary uranium (VI) ion adsorption experiments on natural unmodified zeolitic mineral at mass ratio adsorbent : uranium (VI) ion 1000: 1, at pH 6, showed that uranium (VI) adsorption index was 34,8% (0.34 mg uranium (VI)/g adsorbent), while uranium(VI) adsorption on H-clino, at pH 6, was 95,3% (0,92 mg uranium (VI)/g adsorbent). At mass ratio adsorbent : uranium (VI) ion 400 : 1, adsorption index was 93,1% (2,25 mg/g) and at mass ratio adsorbent : uranium (VI) ion 200:1 index was 63% (3,04 mg/g) on H-clino. From these results, it can be seen, that decreasing the amount of H-clino in suspension, decrease the adsorption of uranium (VI).

The isotherms of uranium (VI) adsorption on H-clino, at different pH values, are given on Figure 1. The isotherms were obtained by plotting the equilibrium concentration of uranium (VI) in solution against the amount of uranium (VI) adsorbed per unit of weight of H-clino.

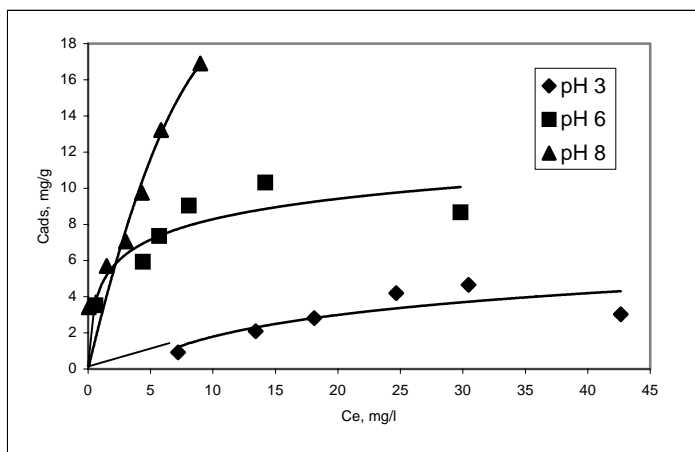


Fig. 1. Adsorption isotherms of uranium(VI) on H-clino, at different pHs

As can be seen from Fig. 1, uranium (VI) adsorption on H-clino, according to IUPAC classification, is well described by the Langmuir type of isotherm, only at pH 6 (Type I). The adsorption maximum calculated from Langmuir linear plot give estimates of the H-clino adsorption capacity for uranium(VI) ion, and the calculated maximum are 9.22 mg/g at pH 6. However, the highest adsorption of uranium (VI) on H-clino was achieved at pH 8. In acidic solution (pH = 3), acid modified zeolite was less effective for the removal of uranium (VI) from aqueous solutions.

Conclusions

Results demonstrated that presence of H-ions in zeolite improve adsorption of uranium(VI) ion and that adsorption increase in following order pH 8 > pH 6 > pH 3. The results of this study indicate that acid modified natural clinoptilolite/ heulandite rich zeolitic tuff may be used for the uranium (VI) removal from aqueous solutions.

References

- [1] E. R Sylwester, E. A. Hudson, P. G. Allen, *Geochim. Cosmochim. Acta*, 2000, **64** (14), 2431.
- [2] A. Krestou, A Xenidis, D. Pnias, *Minerals Engineering*, 2003, **16**, 1363.
- [3] D Ming, J. Dixon, *Clay. Clay Miner.*, 1988, **36**, 244.
- [4] H Lewandowski, The fluorimetric determination of traces of irradiated uranium in sodium. Report CNEN-CSN-Casaccia, RT/OPEC/71/7.

REMOVAL OF PESTICIDES FROM AQUEOUS SOLUTION BY FUNCTIONALIZED ZEOLITES

V. Jovanović¹, G. Jordanov¹, V. Dondur¹, Lj. Damjanović¹ and V. Rakić²

¹*Faculty of Physical Chemistry, Studentski trg 12-16, Belgrade;*

²*Faculty of Agriculture, Nemanjina 6, Belgrade-Zemun; Serbia*

Abstract

Functionalized zeolites are recognized as improved materials for environmental application due to their excellent instantaneous pollutants adsorption. In this work we have studied the effective behavior of clinoptilolite and FAU type of zeolites functionalized by cationic surfactant (distearyl-dimethyl-ammonium chloride) for the removal of organophosphorus insecticides (malathion and fenitrothion), pyrethroid ester insecticides (deltamethrin) and herbicides (glyphosate) from water solutions. The adsorption efficiency of pesticides depends on the zeolite type and hydrophobicity of these molecules. Obtained results have shown that functionalized zeolites can be used for removal of pesticides from the environment. It is shown that mixture of pesticides with different properties, hydrophobic as well as hydrophilic, can be adsorbed on one adsorbent.

Introduction

A number of different methods for the removal of pesticides from waste water have been used including membrane technology, solid phase extraction, ozone and chemical oxidation, photocatalysis and adsorption on different solid substrates. Among these methods, adsorption process has a great significance since pollutants can be instantaneously removed from the environment. Also, after adsorption pollutants are localized and accumulated onto the adsorbent which makes easier their further treatment. The extent of pesticide contamination of the water environment has recently raised much concern because of the entry of these compounds into the food chain. Most agricultural pesticides are hydrophobic organic compounds, while some of them are hydrophilic or even the ionic compounds. The wide range of pesticides used, makes design of the one adsorbent which will be efficient in removal of diverse pesticides extremely difficult. Functionalization of zeolites with cationic surfactants modifies the surface of these materials, changing the hydrophilic surface to hydrophobic [1-3]. The aim of this work was to investigate the effectiveness of surfactant-modified clinoptilolite and FAU type of zeolites in the removal of the pesticides from aqueous solution.

Experimental

Clinoptilolite (CLI) from Zlatokop, Serbia and a FAU zeolite (NaY, Si/Al= 2.5) purchased from Union Carbide were used. The Ca form of Y zeolite was prepared by standard ion exchange procedure using Ca(NO₃)₂. The long-chain quaternary ammonium compound distearyl-dimethylammonium (DSDMA) chloride purchased from Clariant was used. The critical micellar concentration of surfactants in water solutions

were determined by conductivity measurements. The adsorption of selected pesticides on surfactant-modified zeolites was investigated using a batch equilibrated method. The pesticides used in this study were technical grade. The adsorbed pesticides were washed off the zeolites with methanol and gas chromatography was performed on those solutions.

An Agilent 6890N gas chromatograph, equipped with split/splitless-injector, Agilent 7683 autosampler and DB-5MS column (30 m length, 250 μm I.D., 0.25 μm d_f bonded phase of 5% diphenyl-/95% dimethylpolysiloxane on fused silica), was used with an Agilent 5973 inert mass-selective detector. Ionization mode was positive electron impact (EI), 70 eV at 230 $^{\circ}\text{C}$. The injection port temperature was set to 250 $^{\circ}\text{C}$, the transfer line temperature to 280 $^{\circ}\text{C}$ and the quadrupole temperature to 150 $^{\circ}\text{C}$. Carrier gas flow was 1.5 ml/min helium (constant flow mode). The oven temperature programme was ramped from 45 $^{\circ}\text{C}$ (1.5 min holdup time) to 300 $^{\circ}\text{C}$ (6 $^{\circ}\text{C}/\text{min}$) and the total run time was 44 min. The injection volume was 1 μl .

Results and Discussion

The adsorption of mixture of four pesticides (dimethoate, malathion, fenitrothion and deltamethrin) whose characteristics vary from hydrophilic to hydrophobic, was performed on unmodified zeolites CLI and CaY, as well as on surfactant-modified CLI and CaY. The zeolites covered with maximum amount of cationic surfactant were used. The maximum adsorption capacity of DSDMA on CLI and CaY was 158 $\mu\text{mol}/\text{g}$ and 77 $\mu\text{mol}/\text{g}$, respectively. Zeolites which were not modified with cationic surfactants also showed adsorption of pesticides, but the amounts of adsorbed pesticides were lower than the values obtained for both surfactant-modified zeolites. The highest adsorption indexes for pesticides were achieved on surfactant-modified CLI. The quantitative experimental results are summarized in Table 1.

Table 1. Adsorption index of pesticides on unmodified and surfactant-modified CLI and CaY

Pesticides	I_s (%)			
	CLI	CaY	CLI/DSDMA	CaY/DSDMA
Dimethoate	56	48	84	78
Malathion	61	52	86	72
Fenitrothion	71	61	94	85
Deltamethrin	82	68	99	95

Water solubility of used pesticides and retention times are shown in Table 2.

Table 2. The water solubility and retention times for investigated pesticides

Pesticide	Water solubility, g/l	Retention time, min
dimethoate	25	24.00
malathion	0.14	28.17
fenitrothion	0.02	27.78
deltamethrin	$0.002 \cdot 10^{-3}$	42.48

Small molecules, such as fenitrothion and dimethoate, can enter the internal pores and channels of used zeolites and undergo dual-mode adsorption.

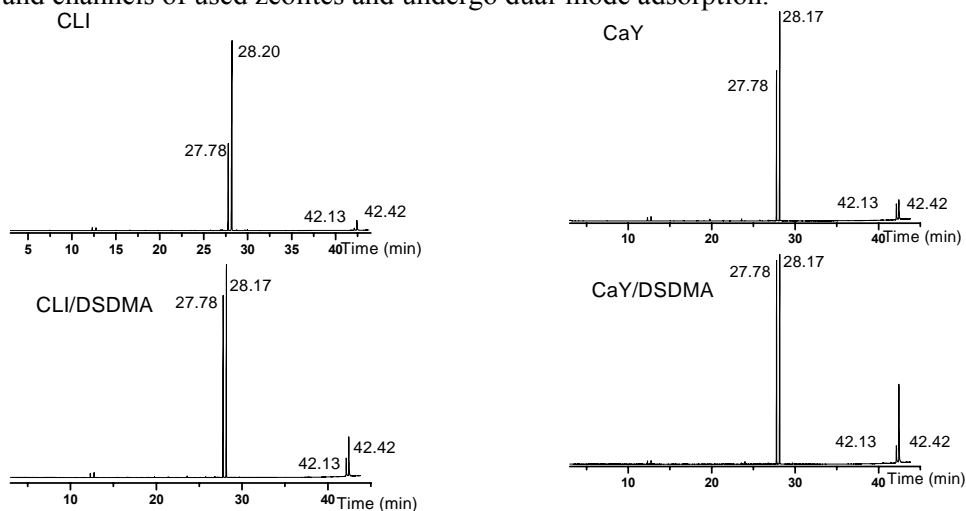


Fig. 1. The gas chromatographs of adsorbed pesticides on unmodified and surfactant-modified CLI and CaY

Dimethoate, the smallest and the most hydrophilic molecule compared to other used pesticides, is strongly bonded to zeolites and is not detected by gas chromatography.

The surface functionalization of zeolites can be a useful method for preparation of efficient adsorbent for pesticide elimination from aqueous solution.

Acknowledgment

The authors would like to thank Ministry of Science and Environment Protection of Republic of Serbia for financial support within the framework of the project 142055.

References

- [1] R.S. Bowman, *Microporous and Mesoporous Mat.*, 2003, **61**, 43-56.
- [2] A. Daković, M. Tomašević-Čanović, V. Dondur, G.E. Rottinghaus, V. Medaković, S. Zarić, *Colloids Surface. B: Biointerfaces*, 2005, **46**(1), 20-25.
- [3] V. Jovanović, V.T. Dondur, Lj. Damjanović, J. Zakrzewska, M. Tomašević-Čanović, *Materials Science Forum*, 2006, **518**, 223-228.

ESTIMATION OF EXTERNAL GAMMA EXPOSURE FROM SURFACE SOILS IN SERBIA

Lj. Janković¹, S. Dragović² and G. Bačić³

¹*Military Medical Academy, Crnotravska 17, 11000 Belgrade*

²*Institute for the Application of Nuclear Energy - INEP, Banatska 31b, Belgrade*

³*Faculty of Physical Chemistry, University of Belgrade, Studentski trg 12-16, Belgrade, Serbia*

Abstract

The annual effective doses and external hazard indexes due to terrestrial naturally occurring radionuclides (²²⁶Ra, ²³²Th and ⁴⁰K) were calculated based on their activities in soil samples as determined by gamma-ray spectrometry. The total absorbed gamma dose rate due to these radionuclides varied from 16.9 to 108 nGy h⁻¹ with a mean of 61.2 nGy h⁻¹. Assuming a 20% occupancy factor, the corresponding annual effective dose varies from 2.07×10^{-5} to 13.1×10^{-5} Sv with the mean value of 7.5×10^{-5} Sv, i.e. in the range of world wide average values. According to the values of external hazard index obtained in this study (mean $H_{ex} = 0.35$), the radiation hazard was found to be insignificant for the population living in investigated areas.

Introduction

Knowledge of the distribution pattern of both anthropogenic and natural radionuclides is an essential pre-requisite for evaluation and control of public exposure and is a reference study to document changes in environmental radioactivity in soil due to human activities. It is also needed for implementation of precautionary measures whenever the dose is found to be above the recommended limits. The growing worldwide interest in natural radiation exposure has lead to extensive surveys in many countries [1]. In Serbia and Montenegro, there has been only one study which encompasses soils only in one province [2], so we conducted our study in other parts of Serbia by measuring the specific activities of primordial radionuclides ²²⁶Ra, ²³²Th and ⁴⁰K in surface soil samples, and use them to calculate external radiation exposure.

Materials and Methods

Surface soil samples (n=160) were taken from twenty five regions in Serbia during 2003-2006. The specific activities of radionuclides ²²⁶Ra (i.e. activity of ²³⁸U family), ²³²Th and ⁴⁰K were measured on a HP Ge gamma ray spectrometer (see [3] for details). From these results the outdoor annual effective doses and external hazard indexes (H_x) were calculated according to the internationally accepted activity-to-dose rate conversion equations [1, 4].

Results and Discussion

Results are presented in Table 1. Uncertainties of measurements at a given location are less than 5%, but the relatively large range of values is the consequence of the variety

of lithological components (magmatic, sedimentary, and/or metamorphic rock complexes). Consequently, the outdoor annual effective dose ranges from 2.07×10^{-5} to 13.1×10^{-5} Sv, with the mean value of 7.5×10^{-5} Sv.

Table 1. The annual effective doses and external hazard indexes due to exposure to gamma irradiation from ^{226}Ra , ^{232}Th and ^{40}K at different locations in Serbia.

Region	Total dose rate (nGy h ⁻¹)	Annual effective dose (10 ⁻⁵ Sv)	H _{ex}
Arandelovac	77.8	9.53	0.45
Beograd	69.7	8.55	0.40
Čačak	97.1	11.9	0.56
Indija	27.8	3.41	0.15
Kosjerić	54.1	6.64	0.30
Kragujevac	70.8	8.68	0.40
Kraljevo	64.4	7.90	0.37
Kruševac	79.5	9.75	0.45
Loznica	57.4	7.03	0.33
Markovac	62.9	7.71	0.35
Mladenovac	60.6	7.43	0.35
Novi Sad	33.4	4.09	0.19
Pančevo	29.9	3.67	0.17
Paraćin	81.4	9.98	0.46
Ralja	53.3	6.54	0.30
Slankamen	65.1	7.98	0.37
Sombor	44.3	5.43	0.25
Surdulica	73.2	8.98	0.42
Šabac	39.3	4.82	0.23
Topola	76.4	9.36	0.43
Užice	16.9	2.07	0.10
Valjevo	108	13.1	0.63
Vranje	95.7	11.7	0.55
Vrčin	26.0	3.19	0.14
Vršac	66.2	8.11	0.37

The world wide average of the outdoor annual effective dose obtained using similar measurements of activity of terrestrial naturally occurring radionuclides is approximately 7.5×10^{-5} Sv [1]. Our result for the average annual effective dose is within the range of world wide average values.

The values calculated for external hazard indexes H_x for the soil samples investigated in this work range from 0.10 to 0.63 (Table 1). These values fall within the range of values reported for neighboring countries as well as for countries worldwide [1]. None of the H_{ex}, regardless of the location and soil composition, exceeds the

safety limits, pointing out to the insignificant radiation hazard arising from terrestrial naturally occurring radionuclides.

Conclusions

The environmental dose assessments for the population of Serbia were calculated using dose rate conversion factors for external exposure from the terrestrial photon emitters in soil. The calculated annual effective doses due to terrestrial radiation were in range of the world wide average value. The results of this study are useful as a data baseline for preparing a radiological map of the studied area, but before more definite conclusions of hazards of population exposure to natural radionuclides are drawn, a more systematic survey of the area is needed. Data obtained in this study can be exploited to enrich the world's data bank, which is greatly needed for evaluating world-wide average values of radiometric and dosimetric quantities.

References

- [1] UNSCEAR. Sources and effects of ionizing radiation. Report to General Assembly, with Scientific Annexes, 2000, United Nations, New York.
- [2] I.S. Bikit, et al., J. Environm. Radioact. 2004, **35**, 147-154.
- [3] S. Dragović, et al., Radiat. Meas., 2006, in press.
- [2] J. Beretka, P.J. Mathew, Health Phys., 1995, **48**, 87-95.

CHEMICAL AND RADIOCHEMICAL FRACTIONATION OF DEPLETED URANIUM IN CONTAMINATED SOILS

M. Radenković¹, A. Kandić¹, I. Vukanac¹, J. Joksić¹, and D. Đorđević²

¹*Institute of Nuclear Sciences "Vinča", P.O. Box 522, Belgrade*

²*ICTM-Centre of Chemistry, Njegoševa 12, Belgrade, Serbia*

Abstract

The results of the chemical and radiochemical characterization of depleted uranium present in the soils since it was used in Balkan intervention, 1999, are presented. The contamination levels and uranium fractionation in the soil substrates was examined using radiation spectrometry methods and by application of the five-step sequential extraction procedure. Alpha-spectrometric uranium isotopic analysis enabled to find out the recently appeared uranium in the environment mobility and/or fixation into stable forms in the soil, distinguishing depleted from naturally occurring uranium on the basis of $^{234}\text{U}/^{238}\text{U}$ and $^{235}\text{U}/^{238}\text{U}$ activities ratios.

Introduction

To assess the environmental impact of depleted uranium ammunition used during 1999 in Balkans, a comprehensive study was done on depleted uranium physical/chemical behavior and its status in contaminated soils a few years after the appearance. Here will be presented results related to the soil samples collected in 2002 at contaminated locations. After the gamma spectrometric based investigation on depleted uranium levels in soil, some samples are subjected to a modified five-step Tessier's sequential extraction procedure [1] and further radiochemical treatment and isotopic analysis to determine depleted uranium distribution in obtained extracts. As a result, depleted uranium fractionation with clear indication on the type of physical/chemical bonds and potential associations with substrates in soils is revealed.

Experimental

The soil samples were collected in Serbia and Montenegro and Bosnia and Herzegovina. Gamma spectrometry measurements were done using HP Ge detector (23% efficiency) in Marinelly geometry without radioactive equilibrium reached because of the interruption after a fourth ^{238}U -series member.

Twelve selected soil samples taken at three locations were subjected to a set of successive solid/liquid extractions, with highly selective extractive reagents simulating mild to severe environmental conditions. The reagent used in the first phase was 1M $\text{CH}_3\text{COONH}_4$ (pH 7); the residue was treated with 0.6M HCl and 0.1M NH_2OH in 0.01M HCl (pH 4). In the third phase the extractant was 0.2M $(\text{COOH})_2/0.2\text{M}$ $\text{NH}_4\text{H}(\text{COO})_2$ mixture (pH 3); in the fourth: 30% H_2O_2 in 0.01M HNO_3 at 85 C (pH 2), and 6M HCl at 85 C in the fifth phase. Extractions were per-

formed in mechanical rotational shaker at 20 C and the solid/liquid ratio was 1:45. Replicates were not done.

After the ion-exchange based radiochemical separation procedure [2], a thin-layer alpha-sources were electrodeposited from 60 obtained extracts, according Talvitie's procedure [3] and counted about 3×10^5 s, in the vacuum chamber (20 mbar) using PIPS alpha detector with 15.3% efficiency. Extracts were spiked with 0.1 Bq ^{232}U standard tracer solution for yield recovery.

Results and Discussion

The specific activities of ^{238}U in topsoil samples taken at the projectile entrance spot and path through the soil were of 10^4 Bq/kg magnitude order, and in the nearest soil layer it was 10^5 Bq/kg. The contamination decreases with the distance and at 150 mm to the source (penetrator) it falls to 1% of the initial value. The naturally occurring uranium concentration is within 20-60 Bq/kg in investigated soils. Radiochemical characterization of the projectile confirmed presence of the ^{237}Np (Fig.1.), $^{239,240}\text{Pu}$ and ^{236}U traces indicating irradiated fuel origin of depleted uranium material [4] but there are no these isotopes in investigated soil samples.

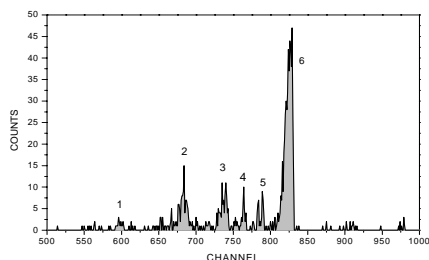


Fig. 1. The alpha spectrum of ^{237}Np (2) and ^{239}Pu (3), ^{238}Pu (5) with traces of ^{238}U (1) in projectile sample spiked with and ^{236}Pu (6) and ^{232}U (4)

Non-selectively bonded uranium (both poorly soluble U (IV) and soluble U (VI) forms) within various substrates in soil is extracted in the first phase of the five-step Tessier's procedure. In the second step, dissolution of carbonates and manganese hydroxides is provoked where the soluble uranyl-ion (VI) may be expected. The presence of uranium in a high excess in these two phases of extraction is anthropogenic influenced and related to contamination. Low clay and humus content in the most of the samples indicated hydrous (crystalline) oxides of the iron and manganese as prevailing substrates for uranium extracted in the third phase. In the fourth step treatment the oxidative degradation of the organic matter and therefore mobilization of organic bonded (humic and fulvic acids) uranium is done. Consequently, only in the surface soil samples uranium shares are significant in the fourth phase extracts. The crystalline iron oxides and partly the silicate matrix are attacked in the fifth phase where acid soluble uranium associations are extracted. A strong dependence of the fractionation on the contamination levels was evident (Fig.2.), resulting with weakly bonded exchangeable uranium in high contaminated soils, no matter the soil geochemical structure.

Assuming the reduction of ^{235}U content to 0.2% in depleted uranium, and ^{234}U isotope leaching precede, the ratios $^{235}\text{U}/^{238}\text{U}$ and $^{234}\text{U}/^{238}\text{U}$ determined in the extracts obtained by alpha spectrometric analysis, between 0.1-0.5 and 0.5-1, respec-

tively, may be attributed to the mixture of depleted and naturally occurring uranium in varying proportions.

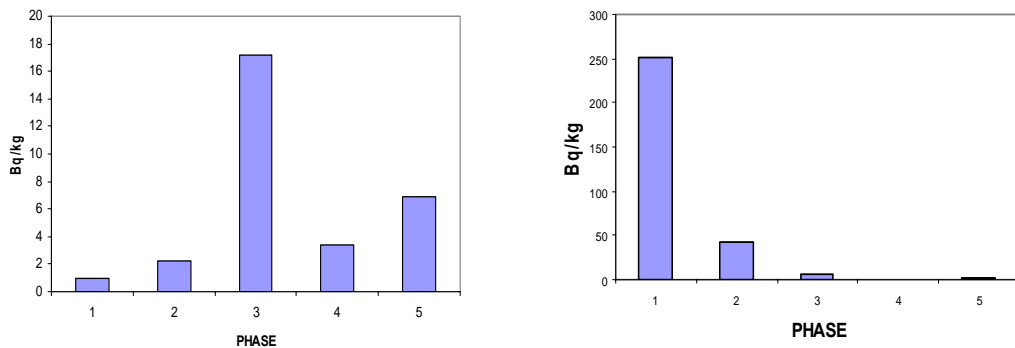


Fig. 2. Uranium distribution in five phases of sequential extraction for low and high contaminated soil samples, respectively, both taken at 50 cm depth

Depleted uranium covered the naturally occurring uranium in highly contaminated samples and naturally ratios were found as dominant in deep-layer soils and uncontaminated samples. Assuming the sequential extraction procedure selective enough, these proportions are the result of depleted uranium capability to be incorporated into exchangeable or structural physical/chemical associations and forms in soil in the time of exposition in certain meteorological conditions and geochemical environment.

Conclusion

The contamination levels at the weapon impact-zone are still significant in the vicinity of projectiles penetrators. Depleted uranium distribution in the sequential extraction phases indicated carbonates and the iron and manganese oxides in soil as the most probable substrates for depleted uranium originated from the weapons, in the three years time elapsed. There is a strong dependence of depleted uranium fractionation on the contamination levels.

References

- [1] A. Tessier, P.G.C. Campbell, M.Bisson, *Analytical Chemistry*, 1979, **54**, 844-851
- [2] M.Radenković, D.Vuković, V.Šipka, D.Todorović, *Journal of Radioanalytical and Nuclear Chemistry*, 1996, **208**/2, 467-475
- [3] N. A. Talvitie, *Analytical Chemistry*, 1972, **44**, 280-283.
- [4] V.Šipka, M.Radenković, D.Paligorić, J.Djurić, *Proc.of XXI Conference of JDZZ, Kladovo*, 2001, 69-72

VISIBLE-LIGHT PHOTOCATALYTIC DEGRADATION OF HERBICIDE MECOPROP IN N-DOPED TiO₂ SUSPENSIONS

D. V. Šojić¹, N. D. Abazović², V. B. Anderluh¹,
B. F. Abramović¹ and M. I. Čomor²

¹*Department of Chemistry, Faculty of Sciences, University of Novi Sad,
Trg D. Obradovića 3, Novi Sad, Serbia (abramovic@ih.ns.ac.yu)*

²*Vinča, Institute of Nuclear Sciences, Beograd, PO Box 522, Serbia (mirjanac@vin.bg.ac.yu)*

Abstract

In this study, the nitrogen-doped TiO₂ crystalline nanopowder was synthesized by calcination of the hydrolysis product of titanium tetraisopropoxide in ammonia. Obtained nanopowder was characterized by XRD and UV-Vis reflection techniques. The kinetics of visible-light (400-800 nm) photocatalytic degradation of herbicide mecoprop in N-doped TiO₂ nanopowder aqueous suspensions was investigated and compared to results obtained for undoped TiO₂.

Introduction

Among the different approaches to pesticide elimination from wastewaters, heterogeneous photocatalysis using semiconductor particles under band gap irradiation has been frequently investigated [1]. Titanium dioxide is the most effective photocatalyst for mineralization of the chemicals in air and water [2]. From the point of view of solar to chemical energy conversion, however, the band-gap energy of TiO₂ is too large for its spectral response to visible, *i.e.* solar light. For utilizing the solar energy efficiently, development of new materials with visible-light-driven photocatalysis is a vital step. Some approaches for shifting of the absorption edge to lower energy, based on TiO₂ modification have been reported [3]. Among these, the simplest and the most feasible approach seems to be nitrogen-doping *i.e.* doping nitrogen atoms into substitutional sites in the crystal structure of TiO₂ (gaining TiO_{2-x}N_x). This paper describes the synthesis, and characterization of N-doped TiO₂ nanopowder. Special attention was paid to visible-light photocatalytic activity of N-doped TiO₂ in comparison to commercial undoped TiO₂ (Degussa P25), in reaction of photocatalytic degradation of herbicide RS-2-(4-chloro-*o*-tolylxy)propionic acid (mecoprop) as a model compound.

Experimental

All chemicals used in the experiments were of the highest possible purity. TiO₂ Degussa P25 was used as an undoped photocatalyst. The X-ray diffraction was carried out on a Philips PW 1710 instrument. The UV/Vis reflection spectra of the catalysts were measured using a spectrophotometer Lambda 35 referenced to BaSO₄. Kinetics of the degradation was monitored at 229 nm by a Secomam anthelie Advanced 2 spectrophotometer. Conditions of the photocatalytic experiments were previously described [4]. Irradiation in the visible range (400-800 nm) was performed using a 50 W

halogen lamp (Philips). The Vis wavelengths were controlled with a 400 nm cut-off filter.

Nitrogen-doped TiO₂ crystalline nanopowder was synthesized by calcination of the hydrolysis product of titanium tetraisopropoxide in ammonia. Titanium tetraisopropoxide and ammonia were mixed in 1:1 ratio at 0°C with vigorous stirring. White precipitate was formed immediately. After washing with water the precipitate was dried at room temperature and calcinated in air.

Results and Discussion

The XRD measurements of the obtained powder revealed that N-doped TiO₂ was in the anatase crystalline phase. From the obtained diffractogram, we calculated the average crystalline size of 12 nm, using the Scherrer formula.

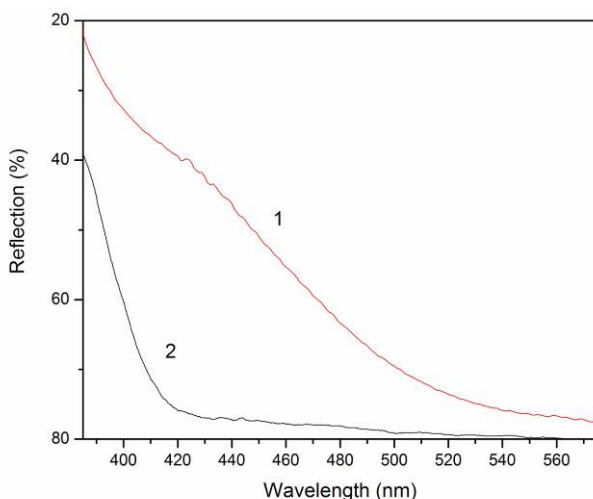


Fig. 1. Reflection spectra of: (1) N-doped TiO₂ nanopowder; (2) TiO₂.

UV/Vis reflection spectra are shown in Fig. 1. It can be seen that nitrogen doping causes the shift of the absorption edge of TiO₂ to lower energy (curve 1) in comparison to undoped TiO₂ (curve 2) from 410 nm to 530 nm.

In order to explore the visible-light photocatalytic activity of TiO₂ and N-doped TiO₂, the degradation of mecoprop in TiO₂ suspensions by visible-light was investigated. Kinetic curves for direct photolysis of mecoprop (curve 1), as well as for photocatalytic degradation in TiO₂ (curve 2) and N-doped TiO₂ (curve 3) suspensions are presented in Fig. 2. Kinetic curves presented in Fig. 2 were obtained by spectrophotometric monitoring of mecoprop degradation. N-doped TiO₂ showed higher visible-light photocatalytic activity ($v = 1.36 \times 10^{-6} \text{ mol dm}^{-3} \text{ min}^{-1}$) in comparison to undoped TiO₂ ($v = 0.85 \times 10^{-6} \text{ mol dm}^{-3} \text{ min}^{-1}$).

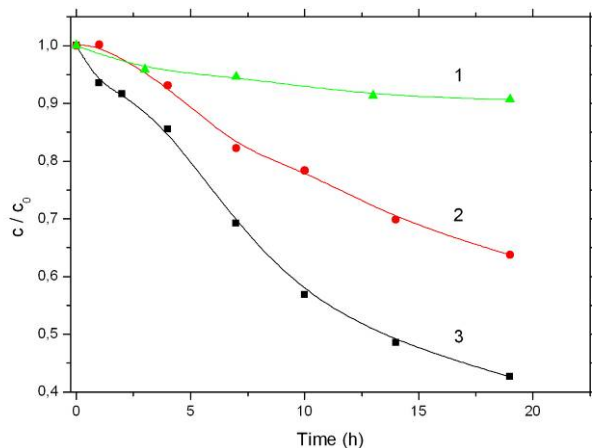


Fig. 2. Kinetics of degradation of mecoprop ($2.7 \times 10^{-3} \text{ mol dm}^{-3}$) by using halogen lamp: (1) direct photolysis; (2) TiO_2 (2 mg cm^{-3}); (3) N-doped TiO_2 (2 mg cm^{-3}).

It is considered that nitrogen atoms in doped TiO_2 crystalline nanopowder were responsible for the significant enhancement of its photoactivity under visible light irradiation. However, the obtained visible-light photoactivity of undoped TiO_2 was unexpected. This finding can be explained by the polycrystallinity of TiO_2 Degussa P25: 75% anatase crystalline phase ($E_g = 3,2 \text{ eV}$, $\lambda_{\text{edge}} = 385 \text{ nm}$) and 25% rutile crystalline phase ($E_g = 3,0 \text{ eV}$, $\lambda_{\text{edge}} = 410 \text{ nm}$), which enables TiO_2 to absorb a small fraction of visible light (400-800 nm) and subsequently photocatalyse degradation of mecoprop.

Conclusion

The proposed synthetic method resulted in formation of N-doped TiO_2 powder in anatase crystalline phase with particle size $\sim 12 \text{ nm}$. Nitrogen-doping of TiO_2 shifts its absorption edge to lower energy (longer wavelengths $\sim 530 \text{ nm}$) in comparison to undoped TiO_2 . As a result, visible-light photocatalytic activity of N-doped TiO_2 towards degradation of herbicide mecoprop, was 1.5 times higher than that of undoped TiO_2 (Degussa P25).

References

- [1] Photocatalysis, M. Kaneko, I. Okura (Eds.), Springer-Verlag, Berlin, 2002, pp. 109-182.
- [2] M.R. Hoffmann, S.T. Martin, W. Chio, D.W. Bahnemann, Chem. Rev., 1995, **95**, 69-96.
- [3] J.L. Gole, J.D. Stout, C. Burda, Y.B. Lou, X.B. Chen, J. Phys. Chem. B, 2004, **108**, 1230-1240, and references therein.
- [4] A.S. Topalov, D.V. Šojić, D.A. Molnar-Gabor, B.F. Abramović, M.I. Čomor, Appl. Catat. B: Environ., 2004, **54**, 125-133.

DETERMINATION OF FENICOLS IN MILK BY LC-MS/MS

V. Batas, S. Janković, S. Stefanović, R. Petronijević, T. Radičević and A. Spirić

*Institute of Meat Hygiene and Technology,
Kačanskog 13, 11000 Belgrade, Serbia, meatinst@beotel.yu*

Abstract

Fenicols are very effective antibacterials. Some compounds, like thiamphenicol (TAP) and florfenicol (FF), are widely used in animal breeding. Chloramphenicol (CAP) is not approved for use in animal production, but its misuse or approved use in some non European countries can result in the entering of its residues into the food chain. Thiamphenicol and florfenicol are approved for use in EU. MRLs for their residues in tissues of food producing animals and primary animal products have been set.

For the purpose of determination of fenicol residues we introduced simple, rapid and sensitive LC-MS/MS method. Following validation, based on criteria set in Commission Decision 2002/657/EC, we applied this method for multiresidual determination of CAP, TAP and FF in row cow's milk. The LC-MS/MS analyses were performed on a HPLC system and Micromass Quattro Micro mass spectrometer, in negative electrospray ionization mode. Chromatography was performed isocratically on C₁₈ X Terra column.

Introduction

Fenicols (chloramphenicol, florfenicol and thiamphenicol) are broad spectrum antibiotics commonly used in veterinary practice. Chloramphenicol (CAP) is effective against Gram-positive and Gram-negative microorganisms, chlamydiae and mycoplasmas. Its broad spectrum and low cost results in widespread usage of the drug in treatment of food producing animal diseases. However, in 1994 the use of CAP was banned by the European Union (EU), due to the potential health risk (bone marrow depression and fatal aplastic anemia) and consequently zero tolerance for CAP was established [1],[2].

Thiamphenicol (TAP) and Florfenicol (FF) are approved drugs with established MRLs [3].

According to Commission Decision 2002/657/EC [4] there is a demand for confirmatory determination of CAP at trace levels, therefore mass spectrometry is the required technique for its confirmation. For TAP and FF the proposed confirmatory technique is liquid chromatography with UV-diode array detection.

There are several recently published LC-MS/MS methods for determination of CAP residues in various matrices, but none is multiresidual [5],[6].

This paper presents a multiresidual liquid chromatography - tandem mass spectrometry (LC-MS/MS) method for multiresidual detection and confirmation of CAP, TAP and FF in raw milk.

Experimental

The LC-MS/MS equipment consists of Allience separation module 2695 and mass spectrometric detector, Quattro Micro (Micromass). The separation was performed on a X-Terra MS C-18 3.5 μm column, 100x2.1 mm I.D.(Waters) and X-Terra MS C-18 3.5 μm , 20mm(L)x2.0mm (I.D.) guard column. The column oven temperature was set at 40 °C. The mobile phase consisted of methanol and 0.01 M formic acid (60:40 v/v). The analysis was carried out in isocratic mode. Flow was set at 0.3ml min⁻¹. The mass spectrometer operated in negative ion mode with an electro - spray ionization (ESI) source. The following source parameters were employed: capillary voltage 3.2kV, cone voltage 35V, source temperature 115 °C, desolvation temperature 350 °C, desolvation flow 750 l h⁻¹ and cone flow 60 l h⁻¹. The data were acquired in MRM (multiple reaction monitoring) mode with ion transitions 321→152; 321→257; 321→194 for CAP, 354→185 for TAP and 356→119 for FF. The dwell time was 200ms. The collision energies for CAP, TAP and FF were 12eV, 20eV and 35eV, respectively.

After extraction and purification the dry residue was dissolved into 1mL of mobile phase, vortexed and centrifuged at 3500 rpm for 10 minutes. 50 μl was injected into LC-MS/MS system.

Results and Discussion

This study included extraction of CAP, TAP and FF from milk, it's determination and confirmation.

Table 1. shows recovery values for fenicol, which has been calculated as a slope ratio of spiked calibration curve and standard calibration curve, expressed as percentage value.

Table 1. Recovery values for fenicol in milk

		R _{CAP} (%)	R _{TAP} (%)	R _{FF} (%)
1st DAY	series 1	83.1	60.0	75.0
	series 2	87.9	55.5	71.0
	series 3	81.0	65.4	68.8
2nd DAY	series 1	89.7	57.1	62.3
	series 2	91.6	59.6	65.4
	series 3	87.5	52.0	70.9
3rd DAY	series 1	96.0	63.0	67.6
	series 2	93.9	65.4	79.9
	series 3	88.4	56.4	77.0

Table 2. Statistical parameters for recovery values for fenicol in milk

Analyte	Mean R (%)	SD	C.V. (%)
CAP	88.8	4.7	5.3
TAP	59.4	4.6	7.8
FF	70.8	5.6	7.8

The quantitation of CAP, TAP and FF was performed using calibration curve of fortified samples.

Reproducibility was calculated and expressed as coefficient of variation (C.V.) of recovery. Standard deviation (Sd) of recovery repeatability was also calculated (Table 2).

Chromatograms presented in Figure 1 and Figure 2 show, by comparison of blank milk and spiked milk at 0.3ng g⁻¹ level, specificity and sensitivity of the presented method. The value of 0.3ng g⁻¹ represents the lowest quantities of drugs which may be quantified.

The presented chromatograms indicate that appropriate clean-up procedure was used, showing no interferences in CAP, TAP and FF retention times.

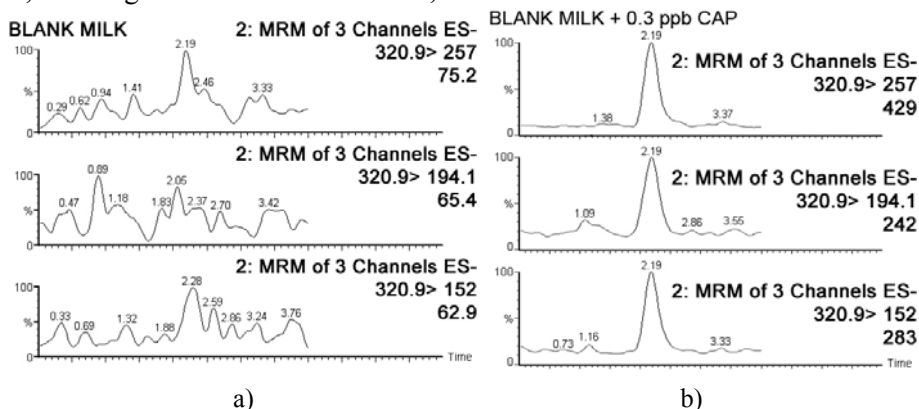


Fig. 1. – Chromatograms of: a) blank milk; b) spiked milk with 0.3 ng g⁻¹ CAP.

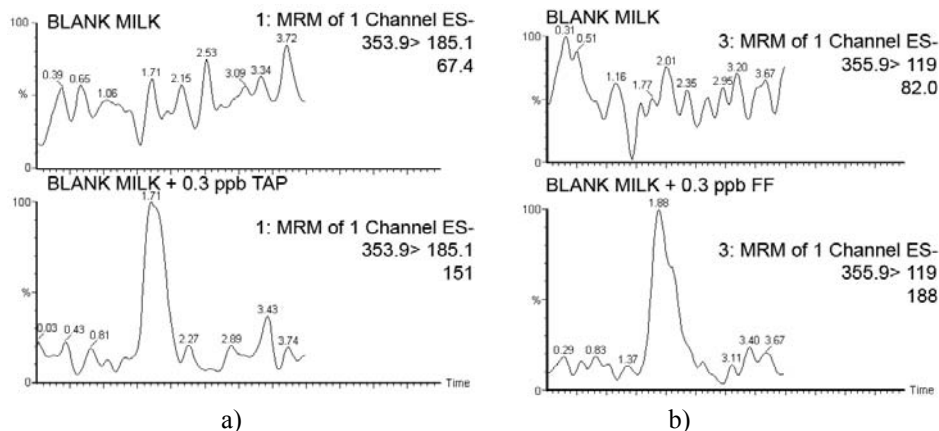


Fig. 2. a) Chromatograms of blank milk and spiked milk with 0.3 ng g⁻¹ TAP; b) Chromatograms of blank milk and spiked milk with 0.3 ng g⁻¹ FF.

Conclusion

The presented method allows detection, quantitation and confirmation of CAP, TAP and FF in raw milk with high sensitivity and specificity.

The advantage of the presented method is the possibility of multiresidual determination and confirmation of fenicol (CAP, TAP and FF) at trace levels.

References

- [1] A. Yunis, *Am. J. Med.*, 1989, **87** (3), 44N-48N.
- [2] C. Ruef, J. Blaser, *Meyler's Side Effects of Drugs*, 14th ed., Elsevier, Amsterdam, 2000.
- [3] S. Teixeira and L. Gormely, presented at the Euroresidue V conference, Noordwijkerhout, 10th-12th May, 2004.
- [4] Commission Decision 2002/657/EC, *Off. J. Eur. Commun.*, L221 (2002).
- [5] L. Santos, J. Barbosa, M. C. Castilho, F. Ramos and others, *Analytica Chimica Acta*, 2005, **529**, 249-256.
- [6] A. Gantverg, I. Shishani and M. Hoffman, *Analytica Chimica Acta*, 2003, **483**, 125-135.

IMPACT OF THE PROCESS OF POLYMERIZATION OF POLYOL AND TOLUEN DIISOCYANATE ON THE ENVIRONMENT

S. S. Milovanović¹, M. A. Lješević² and B. M. Babić¹

¹*Institute of Nuclear Sciences Vinca, P.O. Box 522, Beograd, Serbia*

²*Faculty of Geography, University of Belgrade, Studentski Trg 4/III, Belgrade, Serbia*

Abstract

The aim of this study was to investigate the impact of the process of polymerization of polyol and tolyendiisocyanate on the environment. Toluene diisocyanates are important industrial intermediates used in conjunction with polyether and polyester polyols as coreactants polyurethane foams, paints, varnishes, elastomers and coatings. This presentation summarizes existing information on the release and behavior of the process of polymerization of polyol and toluen diisocyanate on the environment. A major reaction of TDI in the environment is formation of solid inert polyureas from reaction with water. In use, TDI is reacted with polyols to form many different polyurethane products. Polyurethanes have been show to be stable in the environment and in disposal have no adverse impact on municipal waste handling processes, landfills or incineration.

Introduction

The industry “Vapex” in Čačak is the manufacturer of polyurethane foam. TDI-based polyurethane foams are widely used in the automotive and furniture industries and packaging and insulation. TDI and products containing unreacted TDI are potentially hazardous materials. Toluene diisocyanates released into the environment, will tend to partition into water and undergo rapid hydrolysis (half-life of 0,5 seconds-3 days in water, depending on pH and water turbidity) leading predominantly to the formation of relatively inert polymetic ureas.

Experiment

Toluene diisocyanate (TDI) are synthetic organic chemicals with a molecular formula of $C_9H_6N_2O_2$; a relative molecular mass of 174,17; and the following chemical structure ($R=N=C=O$). Toluene diisocyanates are produced as 2 isomers (2,4-toluene diisocyanate (2,4-TDI) and 2,6-toluenediisocyanate(2,6-TDI). Toluene diisocyanates are colourless liquids or crystals, turning pale yellow on standing, and having a characteristic sharp pungent, sweet, fruity odour. **Toluene diisocyanates also react with (-NH)-containing compounds to form ureides or ureas.** The reaction of polymerization pathway is important in terms of the health hazard potential associated with toluene diisocyanates, as well as commercially, and occur at room temperature.

Toluene diisocyanates are reactive intermediates that are used in combination with polyether and polyester polyols to produce polyurethane products [1,2]. The production of flexible polyurethane foam represents the primary use of toluene diisocyanates (~90% of the total supply). The 80:20 mixture is used in their production at an average of

30 % by weight. Reactions with some of these products may be violent, generating heat, which can result in an increased evolution of TDI vapor and the formation of CO₂. Polyurethane coatings represent the second largest market for toluene diisocyanates [3,4]. Toluene diisocyanates are also used in the production of polyurethane elastomeric casting systems, adhesives, sealants and other limited uses.

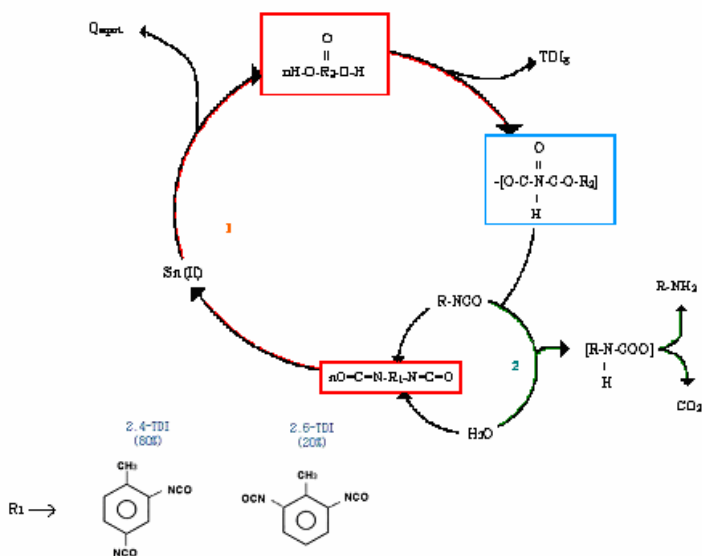


Fig. 1. Process polymerization polyol and toluene diisocyanate

Result and Discussion

Toluene diisocyanates would also be expected to undergo photolysis and hydroxy radical oxidation. In the gaseous phase, TDI vapour and water vapour do not react to form diaminotoluenes. A rate of loss is about 20% of TDI-vapour per hour could be explained by surface adsorption. This rate of loss was much higher and more rapid when comparable concentrations of an aliphatic amine were simultaneously present in the chamber. In the industrial “Vapex”, toluene diisocyanates are hydrolysed by water to give the corresponding polymeric ureas and carbon dioxide. Absorption of toluene diisocyanates through the respiratory tract is suggested by:

- Their high acute toxicity for animals via inhalation
- Reports on systemic effects and antibody formation in individuals exposed to toluene diisocyanates primarily via inhalation

Toluene diisocyanates are very toxic for animals. TDIs, ingested orally or in contact with the skin, are relatively less toxic in terms of lethal dose. Liver, kidney and skin damage occur via these routes. Toluene diisocyanates are irritants for the mucous membranes of the respiratory tract, eyes and skin and are sensitizers of the respiratory tract and skin. Dermal application of toluene diisocyanates in one animal model resulted in sensitization, and subsequent bronchial challenge produced a hypersensitive response.

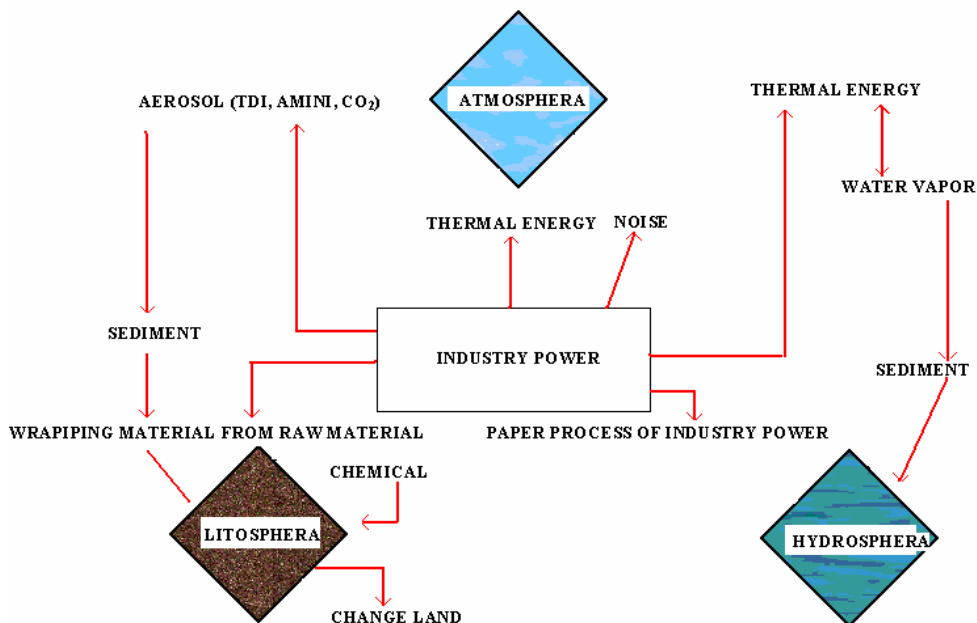


Fig. 2. Impact on industry "Vapex" Cacak

Conclusion

To come to a conclusion, exposure to toluene diisocyanates can lead to adverse effects on the respiratory tract, skin, eyes and gastrointestinal tract. The risk of respiratory toxicity from repeated exposure can be summarized as follows:

- Chronic loss of ventilatory capacity, as measured by forced expiratory volume and forced vital capacity
- Immediate and/or delayed asthmatic responses.

Toluene diisocyanates may react with naturally occurring proteins or polysaccharides and form immuno hapten complexes.

Acknowledgment

This work is supported by Ministry of Science and Environment Protection of Serbia.

References

- [1] M.L.Pinto, J. Pires, A.P. Carvaloh, J.Appl. Poly. Sci., 2004, **92**(3) 2045-2053.
- [2] R.Tessa, M.D. Serio, A. Schafani, J. Appl. Poly. Sci., 2004, **82**(3) 1875-1886.
- [3] M.Ravey, Eli M.Pearce, J. Appl. Poly. Sci., 1998, **63**(1) 47-74.
- [4] Christaia Fischer, Hazardous waste generation in selected European countries, EPA of Denmark and City of Copenhagen, Topic report No 14/1999, Copenhagen, 1999.

SPATIAL DISTRIBUTION OF BELGRADE AIR POLLUTION

A.M. Žujić, Z.J. Gršić, and B.B. Radak

Vinča Institute of Nuclear Sciences, POB 522, 11001 Belgrade, Serbia.

Abstract

Belgrade air pollution has been monitored by two monitoring networks for more than a decade now, but no overall characterization of the pollution based on those results has been published so far. We give here seasonal spatial distributions of SO_2 , NO_2 , and BS (black smoke) over the city area, and discuss the characteristics in terms of likely sources and their seasonal contributions.

Introduction

Air pollution in a developing urban area usually initially increases, passes through a maximum and then decreases, when pollution abatement becomes effective [1]. Cities in the industrialized western world are in some respects at the last stage of this development. In transition economies many cities are in the stabilization stage. In developing countries the pollution levels are still rising.

Belgrade is a hilly city with an average elevation of 116.75 m, and lies at the southern rim of the large Pannonian Plane.

There are 20 air pollution monitoring stations in the Belgrade city area, belonging to the network of the Institute of Public Health, IPH, (17 stations) or the Hydrometeorology Service of the Republic of Serbia, HSRS, (3 stations) [2]. They monitor various pollutants, but SO_2 , NO_2 , and BS (black smoke) are common to all. All 3 of the HSRS stations are equipped for automatic monitoring (except for BS), and only 3 out of 17 stations belonging to IPH are such.

Results and Discussion

After a critical analysis [3] the results of all 6 automatic monitoring stations of the two existing networks were selected to form the main input of a surfer-type software that plots spatial distributions of the concentrations. The results of only a few other "manual" stations were deemed reliable and included in the input. The plots of SO_2 , NO_2 , and BS concentrations are plotted in Figures 1, 2, and 3, respectively.

The plots of SO_2 (Fig. 1) indicate that the maximum in winter months is concentrated around the area with several poorly filtered large heating systems near the centre of the city. In summer, the maximum is shifted more to the industrial area near the Danube riverbank. This is a strong indication of extensive use of classical fossil fuels (coal and oil) for heating.

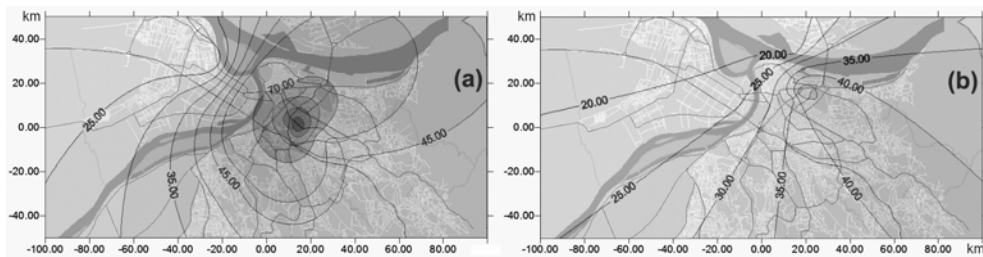


Fig. 1. Spatial distribution of SO_2 in (a) winter and (b) summer.

The plots of NO_2 (Fig. 2) feature open iso-concentration curves in some parts, which may be an artefact due to lack of data in those parts, but the winter superposition (Fig. 2a) indicates the contribution of the district heating plants located more prevalently in the western parts of the city. This contribution is absent in summer (Fig. 2b), and the summer plot basically reflects the traffic density distribution. However, overall NO_2 concentrations are moderate, indicating a moderate traffic load.

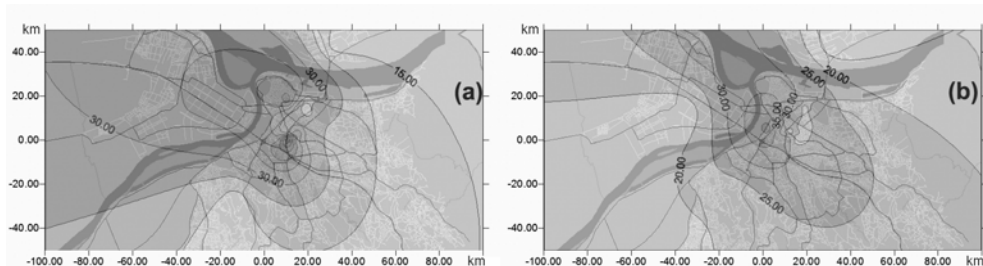


Fig. 2. Spatial distribution of NO_2 in (a) winter and (b) summer.

Both the winter and the summer plots of BS (Fig. 3) show a clear "island" of "clean" air around the monitoring station Košutnjak, which is expected, as it is an elevated urban background point. Generally, high BS concentrations seem to be confined to lower parts of the city, where particulate matter naturally accumulates. That indicates natural and traffic sources of this pollution. High summer BS concentrations to the north from the main city area also indicate a strong natural source of this parameter - natural dust, which is quite present in the north, towards the Pannonian Plain. In winter, there is an "island" of high BS pollution around the city centre, where most of the individual and poorly filtered heating sources are situated (Fig. 12a). In that period, district heating plants in the western parts of the area apparently add the seasonal contribution as well [4].

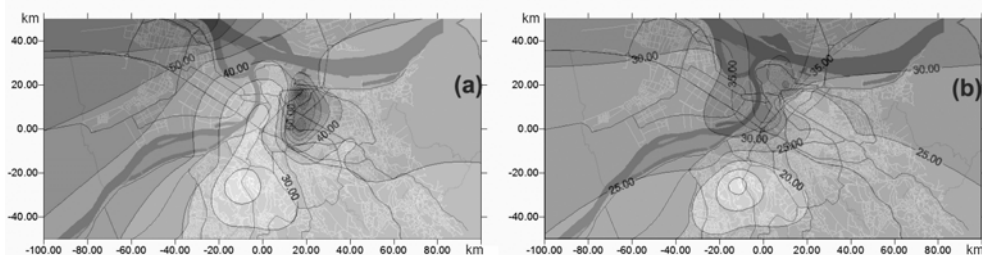


Fig. 3. Spatial distribution of black smoke in (a) winter and (b) summer.

Conclusion

The most significant characteristics of air-pollution in Belgrade are: high SO_2 and elevated BS pollution in the cold season mainly caused by domestic heating, NO_2 pollution that follows the temporal and spatial variations of traffic emissions and indications of significant natural contributions to BS.

In most respects, air pollution in Belgrade has characteristics of most East-European cities in the past decade, of countries in transition in which economic conditions have a strong effect on the atmospheric environment (the quality of the car fleet and types of environmental protection related installations at the stationary sources, as well as the type of home heating) [5].

References

- [1] Fenger J. 'Urban air quality', *Atmospheric Environment*, 1999, **33**, 4877-4900.
- [2] Matic-Besarabic S., Kostoski S. 'Air pollution in the republic of Serbia 2000', Report, *Republic of Serbia - Ministry of Health and Environmental Protection*, Belgrade, 2001.
- [3] A.M. Žujić, B.B. Radak, D.A. Marković, unpublished results.
- [4] S. Matic-Besarabic, M. Gojkovic, V. Dudic, Pantelic G. in: Quality of the Environment of the city of Belgrade (srb), Chapter 4, Grubacevic M. et al. (eds.). Regional Environmental Center, Belgrade, 2006.
- [5] L. Bozo, H. Eerens, S. Larssen, M. M. Millan, N. Moussiopoulus, S. Papalexioiu, Z. Samaras in: Urban air pollution: European aspects, Chapter 25, Fenger J. et al.(eds.), Kluwer Academic Publishers, Dordrecht, 1988.

Phase Boundaries

(L)

ADSORPTION-DESORPTION NOISE IN SURFACE PLASMON RESONANCE SENSORS

Z. Jakšić, Z. Đurić, O. Jakšić, I. Jokić and M. Frantlović

*IHTM – Institute of Microelectronic Technologies and Single Crystals,
Njegoševa 12, Belgrade, Serbia. (jaksa@nanosys.ihm.bg.ac.yu)*

Abstract

The paper analyzes adsorption-desorption (a-d) fluctuations in structures based on metallodielectric nanocomposites and/or thin metal films which utilize the surface plasmon resonance effect for chemical sensing or biosensing. The influence of a-d noise to the ultimate performance of these structures is considered. As a special case, plasmonic structures for the detection of a single gas or a mixture of gases are investigated. It has been established that a-d noise is a very important limiting factor in process kinetics monitoring. Spectral analysis of refractive index fluctuations can be used to distinguish between different analytes. The present analysis may be usable in environmental sensing and biosensing.

Introduction

Adsorption-desorption (a-d) processes of inorganic and organic analytes in plasmonic structures are the basis of one of the most important and extremely sensitive class of optical sensors [1]. These sensors are based on surface plasmon resonance (SPR), where the electromagnetic field is localized on the metal-dielectric interface, exactly in the position where the analyte layer is adsorbed. Thus sensitivities in excess of 0.004 nm or 0.5 ng/cm² (0.003 monolayers) are readily achievable [2]. Due to the speed of plasmon processes, such sensors are convenient for real-time monitoring of process kinetics.

The main mechanism to limit the ultimate performance of such sensors, including both their sensitivity and speed of response, is connected with the a-d process, the same ones which enable the very function of the nanoplasmonic sensors. Random fluctuations of the number of adsorbed particles on the plasmonic surface (a-d noise) determine the usability of the sensor for a given set of conditions (temperature, pressure, analyte composition and concentration, etc.) The role of a-d noise is especially important in coupled resonator structures where it will easily disturb the resonance conditions and thus the very operation of the sensor [3]. In spite of that, analyses of the a-d fluctuations influence to the performance of SPR sensors and their kinetics are relatively seldom met.

In this paper we utilize the recent approaches to SPR a-d noise based on a parallel between this mechanism and the charge carrier generation-recombination in semiconductor structures, as proposed in [4]. We analyze the case of gas adsorption on plasmonic surfaces for the case of pure gases.

Theory and Results

A-d process on a nanoplasmonic structure is schematically shown in Fig. 1. Adsorbate may partially or fully cover active plasmonic (typically metal) surface which itself may be patterned to coincide with a part or the whole area of the sensor. Adsorption and desorption compete in a manner similar to that of g-r processes in semiconductors [4].

For a physisorbed monolayer (Langmuir's isotherm is valid) the fluctuation of the adsorbed particles number ΔN is

$$\frac{d\Delta N}{dt} = -C_2 \left(\frac{\alpha_s C_1 p}{N_m C_2} + 1 \right) \Delta N = -\frac{\Delta N}{\tau} \quad (1)$$

where τ is mean time between adsorption and desorption, calculated as $\langle \tau \rangle = \tau_0 \exp(E_d/RT)$ where E_d is the desorption energy, N_m is the maximum adsorbable number of particles per unit area, C_1 and C_2 are adsorption parameters [4], α_s is the sticking coefficient and p is gas pressure.

By utilizing the Wiener-Khinchine theorem (spectral power density equals Fourier transform of the autocorrelation function) a solution is obtained in the Lorentz form

$$\overline{\Delta N^2(f)} = 4 \frac{C_2 N_m b p A}{C_2^2 (b p + 1)^3 + 4 \pi f^2 \tau^2} \quad (2)$$

where A is the sensor active (adsorbing) area, f is frequency and b is a parameter given as $b = \alpha_s C_1 \tau / N_{max}$. For the case of several gases (1) is written for each gas and its partial pressure. These differential equations are inter-dependent and form a system which is solved simultaneously [6].

For a Langmuir monolayer the adsorbed thickness must always be equal to the adsorbed particle diameter and the effective index of the adlayer is found by averaging over the sample surface. If the refractive index of a bulk analyte is n_A and that of the surrounding medium n_e , the spectral density of mean square refractive index fluctuations is

$$\overline{(\Delta n(f))^2} = \left(\frac{n_e - n_A}{N_m A} \right)^2 \overline{\Delta N^2(f)} = 4 \left(\frac{n_e - n_A}{N_m A} \right)^2 \frac{C_2 N_m b p A}{C_2^2 (b p + 1)^3 + 4 \pi f^2 \tau^2} \quad (3)$$

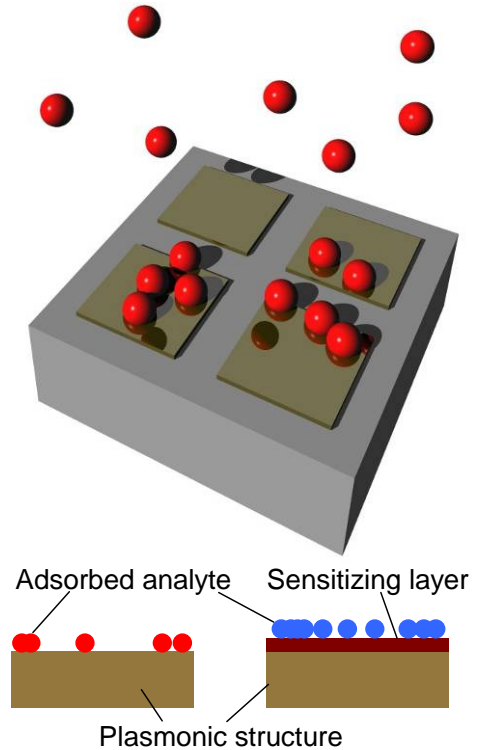


Fig. 1. Adsorption to nanopatterned surface of a SPR sensor. Bottom: the case of analyte directly adsorbed to metal (left) and the case with a functionalizing layer (right)

The effective index of the adlayer as "seen" by a plasmon (i.e. a wave exponentially decaying away from the surface with a decay length l_d) is found by integrating from 0 to the adlayer particle diameter the sum of the index value averaged over the sample area and its mean fluctuation caused by the a-d noise multiplied by a weight factor $\exp(-z/l_d)$.

We performed our calculations for nitrogen and hydrogen adlayers. For the refractive index of nitrogen we used 1.197 and 1.12 for hydrogen [5], i.e. the values valid for close packing of N, H atoms (as defined by the atoms' radii) instead of the values for free gas (1.000298 N₂, 1.000132 H₂). Fig. 2 shows the refractive index fluctuations in dependence on frequency with pressure as parameter. The knee of the spectral density curve is inversely proportional to the a-d time constant.

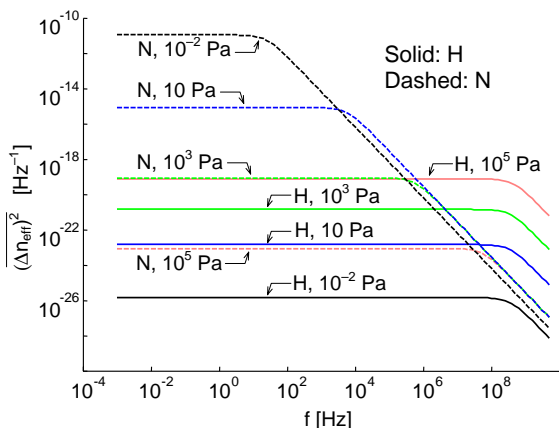


Fig. 2. Spectral power density of refractive index fluctuations due to a-d noise for adsorbed H and N under different gas pressures

Conclusion

We analyzed the influence of adsorption-desorption fluctuations to the changes of effective refractive index in SPR sensors. Single gaseous analytes were analyzed. The approach is also usable for gas mixtures and liquid analytes, which will be the topic of our future investigations. The case of an analyte monolayer was considered, and one of the possible

directions for generalization is the analysis of the response of sensor surfaces functionalized by a sensitizing layer, by surface nanopatterning or both. One of the obvious results is that a-d noise is the crucial limiting factor in process kinetics monitoring, but also that spectral analysis of a-d fluctuations may be used to distinguish between different analytes.

References

- [1] J. Homola, S. S. Yee, G. Gauglitz, *Sensors & Actuators B*, 1999, **54**, 3-15.
- [2] L. S. Jung, C. T. Campbell, T. M. Chinowsky, M. N. Mar, S. S. Yee, *Langmuir*, 1998, **14**, 5636-5648.
- [3] S. Feng, J. M. Elson, P. L. Overfelt, *Phys. Rev. B*, 2005, **72**, 085117.
- [4] Z. Djurić, O. Jakšić, D. Randelović, *Sensors & Actuators A*, 2002, **96**, 244-251.
- [5] <http://www.webelements.com/>
- [6] Z. Djurić, I. Jokić, M. Frantlović, O. Jakšić, D. Vasiljević-Radović, *Proc. 24th Int. Conf. MIEL 2004*, 1, Niš, May 16-19, 2004, 197-199.

OXYGEN CHEMISORPTION ON GOLD NANOCUSTER: QUANTUM-CHEMICAL STUDY

D. A. Pichugina^{1,2}, A. F. Shestakov² and N. E. Kuz'menko¹

¹Laboratory of Molecular Spectroscopy, Department of Chemistry, M.V. Lomonosov MSU, 1 Leninskie gory, 119992 Moscow, Russia, (daria@phys.chem.msu.ru, nek@educ.chem.msu.ru)

²Institute of Problems of Chemical Physics RAS, 1 prosp. Akad. Semenova, 142432 Chernogolovka, Moscow Region, Russia (as@icp.ac.ru)

Abstract

The interaction of O and O₂ with Au₂₀ gold cluster is investigated through the use of density functional theory with PBE functional and gold relativistic pseudopotential. Oxygen atom may be bonded with one apex Au atom (33.7 kcal/mol), one facet Au atom (15.6 kcal/mol) or with two atoms in edge with apex gold (46.6 kcal/mol) and without apex gold (62.7 kcal/mol). For O₂ chemisorption it was found that dissociative adsorption is more favorable (two Au-O-Au bonds, 34.9 kcal/mol) than molecular adsorption (Au-O-O bond, 19.3 kcal/mol). The reactions of Au₂₀O complexes with methane are exothermic and have rather low energy barriers.

Introduction

Oxygen molecules are not adsorbed on flat gold surfaces at room temperature, but recent experimental results have demonstrated oxygen adsorption on small anion gold nanoparticles [1]. Nanosized gold clusters have attracted attention in the past decade due to their unique catalytic activity. The origin of this activity is still not understood rather well. Moreover the question arises whether adsorbed oxygen molecules can influence on gold catalytic activity. So, the comparison of the reactivity of oxidized neutral Au₂₀ cluster with respect to methane are very important.

Results and Discussion

Here we report density functional calculations of dissociative and molecular oxygen adsorption on Au₂₀ cluster [2] and quantum-chemical simulation of the interaction of Au₂₀O₂ complex with methane. All calculations were carried out by density functional theory with the use of the nonempirical local PBE (Perdew—Burke—Ernzerhof) functional, which we have used earlier in the study of gold complexes [3]. Calculations were performed with the use of the PRIRODA program [4].

The basis set with the SBK pseudopotential was used [5]. In this pseudopotential, the outer electron shells are described by the following basis sets: H [311/1], C [311/311/11], O [311/311/11] and Au [51111/51111/51111]. The types of stationary points on potential energy surfaces were determined from analysis of Hessians; the second derivatives were calculated analytically. The character of transition states of the reactions between methane and Au₂₀O complexes was confirmed by calculations of the intrinsic reaction coordinate. The zero-point energy was calculated in the harmonic approximation.

The calculation of the Au_{20} cluster optimized structure reveals that the most stable structure is complicated pyramid composed from Au_4 tetrahedrons (fig. 1). All obtained bond distances, angles and frequencies agree well with the experimental data [2].

We find that chemisorption energy of atomic and molecular oxygen on Au_{20} cluster has typical value of 2.7-34.9 kcal/mol. From all possible structures of the oxygen atom coordination on Au_{20} nanocluster only four of them are realized: monodentate coordination on the apex, $\text{Au}_1\text{-O}$ (with bond energy of 33.7 kcal/mol) and on the facet, $\text{Au}_4\text{-O}$ (15.6 kcal/mol), and two kinds of bidentate coordination on the edge on the ending, $\text{Au}_1\text{-O-Au}_2$ (with bond energy of 46.6 kcal/mol) and in the center of edge, $\text{Au}_2\text{-O-Au}_3$ (with bond energy of 62.7 kcal/mol) (Table 1).

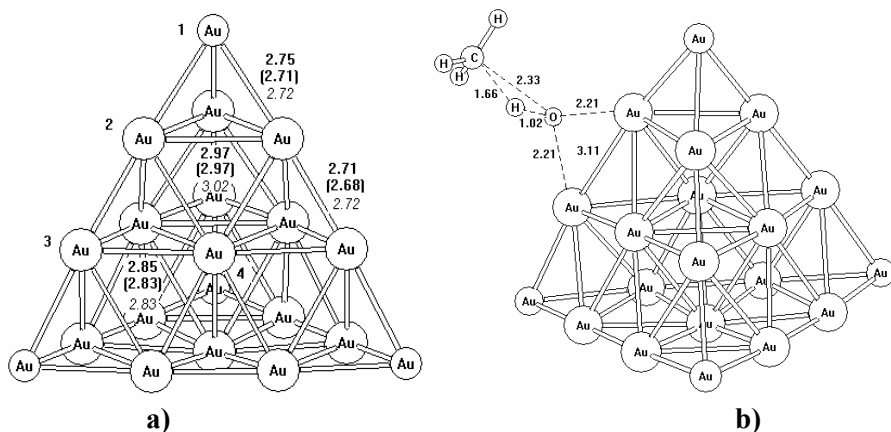


Fig. 1. a) lowest-energy configuration of Au_{20} cluster and the calculated bond lengths (E). Experimental data are given in square brackets, the calculation data [2] are given in italic. Coordination of atomic oxygen is possible on gold atoms with numbers 1-4. **b)** Structure of the transition states of reaction of Au_{20}O complex (№4 in Table 1) and methane and the calculated bond lengths (E).

Table 1. Calculated Energies for Adsorption (ΔE) of Oxygen Atom to Au_{20} Clusters

№	Bond	ΔE , kcal/mol
1	$\text{Au}_4\text{-O}$	15.6
2	$\text{Au}_1\text{-O}$	33.7
3	$\text{Au}_1\text{-O-Au}_2$	46.6
4	$\text{Au}_2\text{-O-Au}_3$	62.7

We consider both molecular chemisorption, where the O-O molecular bond is preserved, and dissociative chemisorption, where the two O atoms do not form a direct bond. We search a large number of structures to determine the low-energy configuration. In the most stable configurations for dissociative chemisorption, the two oxygen atoms acts as Au-O-Au bridges ($\text{Au}_2\text{-O-Au}_3$ and $\text{Au}_6\text{-O-Au}_7$, 34.9 kcal/mol).

Catalytic functionalization of methane is one of the most important problems of modern chemistry. Gold clusters are catalysts of some hydrocarbon oxidation [6], but it is unknown if they can catalyze methane oxidation process. Our calculation reveals that Au₂₀ cluster does not react with CH₄ to form the active intermediate. On the other hand the reactions between methane and Au₂₀O (Au₁-O or Au₂-O-Au₃) complexes to form methanol and Au₂₀ cluster are accompanied by a decrease in the free energy by 64.0 kcal/mol (TS=2 kcal/mol) or 30.9 kcal/mol (TS=22.8 kcal/mol, fig. 1b) for Au₁-O or Au₂-O-Au₃ complexes.

Conclusion

We show that O and O₂ can be involved in the chemisorptions on Au₂₀ cluster. This process increases the catalytic reactivity of cluster, in particular, with respect to methane.

The information provided by this study could provide the impetus for further experimental studies on structure of gold nanoparticles, the interaction of oxygen with gold clusters and their catalytic reactivity.

Acknowledgments

This study was financially supported by the Technical Program and Young Scientists, Grants MK-1615.2005.3 and the Russian Foundation for Basic Research (Project № 06-03-33131-a).

References

- [1] B.E. Salisbury, W.T. Wallace, R.L. Whetten. *Chem. Phys.*, 2000, **262**, 131-141.
- [2] J. Li, X. Li, H.-J. Zhai, L.-S. Wang. *Science.*, 2003, **299**, 864-867.
- [3] D.A. Pichugina, A.F. Shestakov, N.E. Kuz'menko. *Rus. Chem. Bull., Int. Ed.*, 2006, **55** (2), 191-201.
- [4] D. N. Laikov. *Chem. Phys. Lett.*, 1997, **281**, 151-168.
- [5] H. Basch, P. G. Jasien. *Can. J. Chem.*, 1992, **70**, 612-630.
- [6] G.J. Hutchings. *Gold Bulletin*, 2004, **37** (1), 3-11.

NON-ISOTHERMAL THERMOGRAVIMETRIC ANALYSIS OF THE PARTIAL REDUCTION OF NICKEL OXIDE BY HYDROGEN

B. Janković and B. Adnađević

*Faculty of Physical Chemistry, University of Belgrade, Studentski trg 12-16,
P.O. Box 137, Belgrade, Serbia*

Abstract

The kinetics of the partial reduction of nickel oxide by hydrogen was investigated by non-isothermal thermogravimetric analysis. It was established that the conversion curves of non-isothermal reduction can be completely described by Weibull distribution of reaction times. The linear and exponential dependences of Weibull distribution parameters from the heating rate were established. New procedures for determination of kinetics parameters of non-isothermal partial reduction of NiO by hydrogen, based on Weibull distribution function were developed. The obtained values of kinetics parameters are in good agreement mutually, and they are in good agreement with literature data.

Introduction

Among the transition-metal oxides, the reduction of NiO by hydrogen has been the object of the most extensive fundamental studies [1,2], becoming an important reference system in this topic. Nakajima et al. [3] were used Kissinger method for calculation of activation energy of the non-isothermal partial reduction of nickel oxide by hydrogen. The values of activation energies of 65-99 kJmol⁻¹ were obtained from thermogravimetric experiments with small-grain powders in loosely packed samples or in the thin slabs [3]. Also, in these non-isothermal experiments, the influence of heating rate on thermogravimetric curves was observed [3]. The procedure for describing of thermogravimetric curves of the investigated process using Weibull distribution function is presented in this paper. It was established the connection between the parameters of Weibull distribution and the heating rate of the considered system. New approach for determination of kinetics parameters, based on Weibull distribution function was also presented.

Experimental

Sample. The nickel oxide samples (in powder form) was obtained by sol-gell procedure [2]. **TG analysis.** The TG experiments for the title compound were performed using a TA Instruments-SDT simultaneous TGA-DSC thermogravimetric analyzer model 2960. The heating rates used were 2.5, 5, 10 and 20 °Cmin⁻¹ from the ambient to 500 °C, and the sample mass was 25 - 30 ± 1 mg. The pure hydrogen was used as an experimental atmosphere, with a gas flow rate of 10 mL min⁻¹. The extent of conversion is expressed as $\alpha = (m_0 - m) / (m_0 - m_f)$, where m_0 , m , m_f refer to the initial, actual and final mass of the sample. The kinetics parameters (the activation energy (E) and the pre-exponential factor ($\ln A$)) of the investigated reduction process were obtained by applying Kissinger [4] and stationary point methods [5].

Results and Discussion

The thermogravimetric curves of the partial reduction of nickel oxide by hydrogen, obtained at different heating rates (2.5, 5, 10 and 20 °Cmin⁻¹) are presented in Fig.1. Table 1 shows the influence of v_h on the initial and the final reduction temperature.

$v_h / ^\circ\text{Cmin}^{-1}$	T_0 / K	T_f / K
2.5	260	395
5	275	455
10	285	470
20	295	485

Table 1 The influence of heating rate (v_h) on the values of initial (T_0) and final (T_f) reduction temperature (Fig. 1)

Table 1 shows that the increase of the heating rate leads to increasing values of T_0 , T_p and T_f . Under the considered con-

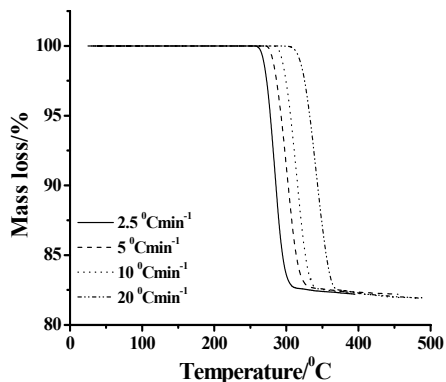


Fig. 1 Non-isothermal TG curves for the partial reduction of NiO by hydrogen

ditions, the shape of the thermogravimetric curves and the values of kinetic parameters (E and A) is, obviously, a function of the applied heating rates. Having positive experience with probability functions [6] we decided to apply the Weibull distribution function, in order to describe the conversion (α - T) curves of the non-isothermal partial reduction process of NiO by hydrogen.

Accordingly, the extent of conversion (α) of the studied reduction process as a function of reaction time (t) of a given TG curve at the selected heating rate can be described by following equation:

$$\alpha(t) \equiv F(t) = 1 - \exp\left[-\left(\frac{t}{\eta}\right)^\beta\right] \quad (1)$$

where $F(t)$ is the cumulative Weibull distribution, t is the reaction time (where is $t = (T - T_0)/v_h$), β is the shape parameter and η is the scale parameter [6]. In order to obtain the parameters β and η , Eq. (1) can be linearized by a double logarithmic. The values of η and β can be calculated from the intercept and slope of a $\ln[-\ln(1 - F(t))]$ versus $\ln t$. The obtained values are shown in Table 2.

$v_h / ^\circ\text{Cmin}^{-1}$	α	$1/\eta / \text{min}^{-1}$	β	η / min	r
2,5	0.08-0.96	0.09066	2.52	11.03	0.9995
5	0.11-0.96	0.15761	2.65	6.34	0.9997
10	0.06-0.96	0.29546	2.82	3.38	0.9992
20	0.06-0.96	0.39405	3.20	2.54	0.9998

Table 2 The linear domains of dependence $\ln[-\ln(1 - F(t))]$ vs. $\ln t$ and the values of parameters $1/\eta$, β and η of the Weibull distribution function, obtained for the partial reduction of nickel oxide by hydrogen

The obtained values of parameters β and η are functions of the heating rate v_h . The values of shape parameter increasing, until the values of scale parameter (η) decreasing, with increased the heating rate. The empirical dependences of β and η parameters on v_h can be described by the relations:

$$\beta = a_0 + bv_h \quad (2)$$

$$\eta = \eta_0 + \eta_a \exp(-v_h / \varphi) \quad (3)$$

where $a_0 = 2.44$, $b = 0.04 \text{ min}^\circ\text{C}^{-1}$, $\eta_0 = 2.54 \text{ min}$, $\eta_a = 18.76 \text{ min}$, and $\varphi = 3.15 \text{ }^\circ\text{Cmin}^{-1}$.

By means of the obtained values for β and η (Table 2) and Eq. (1), the corresponding α - T curves were calculated (Fig. 2). Experimental α - T curves (lines) and α - T curves (symbols) calculated using the Weibull parameters corresponding to each heating rate (Table 2) are compared in Fig. 2. A very good agreement can be seen between the calculated theoretical curves based on Weibull distribution and those experimentally determined. Furthermore, by the differentiation of equation (1) respect to time (dF/dt), the Weibull density distribution function of reaction times $f(t)$ was obtained. The activation energy (E) and pre - exponential factor (A) can be calculated from the slope and intercept of the straight line $\ln[f(t)]$ versus $(1/T)$ ($f(t)$ is proportional to velocity of reduction process at the selected heating rate, v_h). Besides, from linear dependence $\ln[(1 - g(\alpha)/T^2)] = f(1/T)$ where $g(\alpha) = \exp[-(t/\eta)^\beta]$, the kinetics parameters $\ln A$

and E can be calculated from the intercept and slope, respectively. The functional relationship $\ln[(1-g(\alpha)/T^2)] = f(1/T)$ represents the modified method of Coats and Redfern [7].

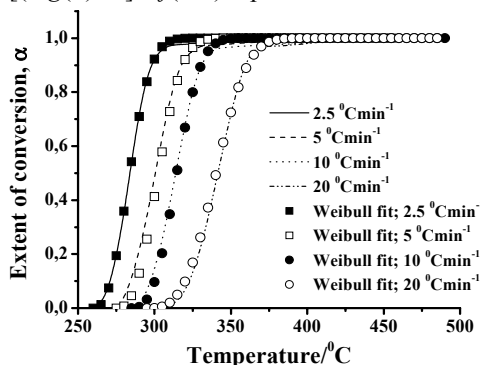


Fig. 2 Experimental (lines) and calculated (symbols) α - T curves for the partial reduction of NiO by hydrogen at different heating rates: 2.5 (■), 5 (□), 10 (●) and 20 (○) $^{\circ}\text{Cmin}^{-1}$

Table 3 shows the values of kinetics parameters ($\ln A$, E) for investigated reduction process, obtained by Kissinger [4], stationary point [5], and by two methods based on Weibull distribution whose are described above.

Table 3 The values of kinetics parameters ($\ln A$, E) for the non-isothermal partial reduction of nickel oxide by hydrogen, calculated by different kinetic methods

Method	v_h / $^{\circ}\text{Cmin}^{-1}$	$\ln A$ / min^{-1}	E / kJmol^{-1}
Kissinger	2.5 - 20	18.93	98.4
Stationary point (experimental data)	2.5 - 20	17.85	96.8
Stationary point (density distribution function)	2.5 - 20	18.32	97.5
Modified Coats - Redfern	2.5	16.78	95.8
	5	18.62	97.9
	10	18.85	98.4
	20	19.44	99.6

The obtained kinetics parameters ($\ln A$ and E) (Table 3) of the investigated reduction process are in good agreement mutually, and also they are in good agreement with kinetics data reported in reference [3].

Conclusion

The thermogravimetric analysis of the partial reduction of nickel oxide by hydrogen, performed under non-isothermal conditions at four different heating rates was performed. The conversion curves of the partial reduction of NiO by hydrogen were successfully described by Weibull distribution function in wide range of α value. The parameters of Weibull distribution were changed with increasing of heating rate. The obtained kinetics parameters are in good agreement mutually, and they are in very good agreement with results of kinetics parameters, reported in literature [2,3].

References

[1] B. Delmon, In *Handbook of Heterogeneous Catalysis*; G. Ertl, H. Knözinger and J. Weitkamp, Eds.; Wiley-VCH: New York, 1997, p. 264.
 [2] R. P. Furstenau, G. McDougall, M. A. Langell, *Surf. Sci.*, 1985, **150**, 55.
 [3] M. Nakajima, S. Shimizu, K. Onuki, Y. Ikezoe, S. Sato, *Chem. Soc. Jpn.*, 1989, **4**, 681.
 [4] H. E. Kissinger, *Anal. Chem.*, 1957, **29**, 1702.
 [5] I. Klarić, U. Roje, T. Kovačić, *J. Therm. Anal. Cal.*, 1995, **45**, 1373.
 [6] Lj. Kolar-Anić, S. Veljković, S. Kapor, B. Dubljević, *J. Chem. Phys.*, 1975, **63**, 663.
 [7] A. W. Coats, J. P. Redfern, *Nature*, 1964, **201**, 68.

THE ADSORPTION PROPERTIES OF Mn-EXCHANGED ZSM-5 ZEOLITES

V. Rac¹, R.Hercigonja², V. Rakić¹ and A.Auroux³

¹*Faculty of Agriculture, Nemanjina 6, Belgrade-Zemun,*

²*Faculty of Physical Chemistry, Studentski trg 12-16, Belgrade, Serbia*

³*Institut de Recherches sur la Catalyse CNRS, 2 Av. A Einstein, 69626 Villeurbanne; France*

Abstract

The adsorptions of N₂O and CO on Mn²⁺-exchanged ZSM-5 zeolites have been investigated by microcalorimetry and FTIR techniques. The adsorptions of both gases have been found on MnZSM-5 zeolite; these adsorptions being influenced by the presence of Cu²⁺ or Fe²⁺ ions.

Introduction

Zeolite lattices with their net negative charge can serve as a counter-anion for complexes of metal cations and among the others; transition metals are very often used charge-balancing cations. Transition metal ion-exchanged zeolites are able to catalyze reduction, oxidation, and carbonylation reactions, and hence these catalytic reactions have been extensively tested on Co²⁺, Fe³⁺, Cu²⁺ and Cu⁺ exchanged zeolites[1]. Nowadays; there is growing interest for manganese incorporation in zeolitic lattices, mainly because of the role of this metal in numerous metallo-enzymes[2]. Besides, Mn²⁺ has shown to be a very active catalyst for SO₂ oxidation in aqueous phase[3]. In this work, we investigated the adsorption properties of Mn²⁺-exchanged ZSM-5. The adsorption of two important atmospheric pollutants: N₂O and CO has been tested.

Experimental

The ion-exchange of parent home synthesized ZSM-5 zeolite was performed at room temperature, using 0.01M solution of Mn(II)-acetate. In this work, bi-metallic samples containing both Mn²⁺ and Cu²⁺ or Fe²⁺ ions were investigated; consecutive ion exchange with corresponding di-valent salts was applied in order to obtain the bimetallic samples. The crystallinity of all samples was checked by XRD methods, performed on a Bruker (Siemens) D5005 diffractometer at room temperature using Cu K α (radiation, 0.154 nm) from 38 to 808 2 θ in a 0.028 steps with 1 s. The structure of ZSM-5 zeolite remains unaffected by ion-exchange procedure. Surface areas were determined by the BET method from the adsorption of nitrogen at 77 K after pre-treatment for 4.0 h at 673 K under vacuum. The cations contents were determined by AES-ICP in a Spectroflame-ICP instrument, the results are presented in Table 1, as well as BET surface areas.

The adsorption of N₂O and CO was investigated by microcalorimetry and FTIR spectroscopy. The heats of adsorption were measured after the pretreatment at 673K in vacuum, overnight, in a heat-flow calorimeter of the Tian-Calvet type (Setaram C80), linked to a glass volumetric line. Both thermal effects and volumetric isotherms were

detected. The details about microcalorimetric experiments are presented in reference [4].

Table 1. Chemical composition and BET surface areas

Sample	Mn content, %	Fe content, %	Cu content, %	BET specific surface area (m ² /g)
MnZSM-5	0.55			337
Fe,MnZSM-5	0.42	0.2		325
CuMnZSM-5	0.45		0.9	340

FTIR spectra were recorded using FTIR Bruker spectrometer equipped with OPUS 22 software. A self-supported pallet was placed in an IR cell with CaF₂ windows; the activation was done in situ in the oxygen flow from 298 K up to 673 K, and the sample was held at 673K for 4 h. Subsequently, the sample was evacuated in vacuum (10⁻³ Pa) during 2 h. The adsorption of N₂O and CO was done after cooling up to room temperature and the collections of 100 scans spectra at 2 cm⁻¹ resolution were recorded. Either N₂O or CO was adsorbed on the surface, then, the cell was evacuated, and the adsorption of other gas was performed.

Results and Discussion

Figures 1 and 2 show adsorption isotherms and differential heats of N₂O and CO on FeZSM-5, Fe,MnZSM-5 and Cu,MnZSM-5. It is evident that both N₂O and CO were adsorbed on all investigated samples. However, it has to be noticed that adsorption capabilities of these zeolites are not the same: it seems that the adsorption possibility (the adsorbed amounts and the heats of interaction) of MnZSM-5 for CO are increased with the addition of Cu²⁺, while it is decreased with the addition of Fe²⁺ ions. In case of N₂O, the adsorption is similar on MnZSM-5 and Cu,MnZSM-5, while the addition of Fe²⁺ decreased importantly the heats of interaction and the adsorbed amount.

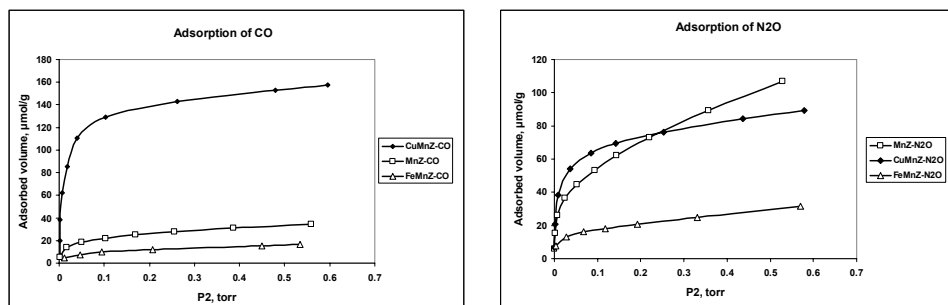


Fig. 1. Adsorption isotherms of N₂O and CO on Mn(II)-exchanged ZSM-5 samples

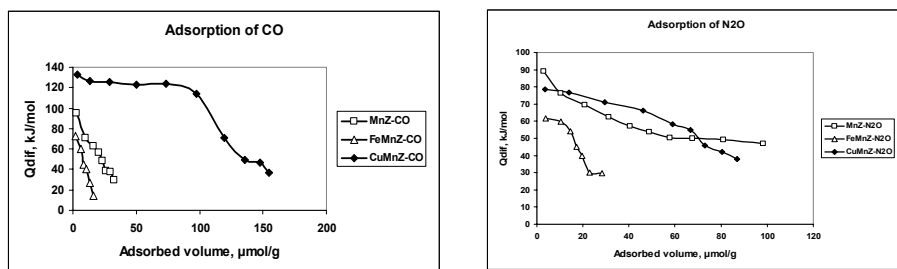


Fig. 2. Differential heats of N_2O and CO on Mn(II)-exchanged ZSM-5 samples

In this work, the competitive adsorption between N_2O previously adsorbed on MnZSM-5, and CO incoming from the gas phase, has been tested by FTIR.

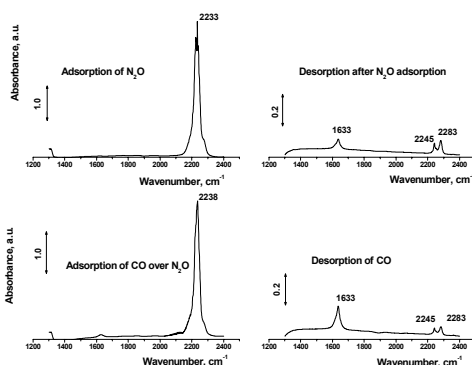


Fig. 3. FTIR spectra collected after N_2O and CO were admitted to MnZSM-5 zeolite

In that way, it was noticed that the bands in $2200\text{--}2300\text{ cm}^{-1}$ spectral region, typical for adsorption of N_2O , were stable after 30 minutes of evacuation indicating the existence of some chemisorbed N_2O . In addition, it was noticed that CO can not expel this strongly adsorbed N_2O from the surface, contrary to ZSM-5 zeolite containing Cu^{2+} , Fe^{2+} or Co^{2+} , investigated previously.

Acknowledgment

The authors would like to thank Ministry of Science and Environment Protection of Republic of Serbia for financial support (project 142055).

References

- [1] A. Corma, Chem. Rev., 2003, **G103**, 4307-4365.
- [2] P.-P. Knops-Gerrits, D. E. De Vos, P. A. Jacobs, J. Mol. Cat. A: Chemical, 1997, **117**, 57-70.
- [3] J. Garcia-Martinez, D. Cazorla-Amorós, A. Linares-Solano, Applied Catalysis B: Environmental, 2004, **47**, 203-207.
- [4] V. Rakić, V. Rac, V. Dondur, A. Auroux, Cat. Today, 2005, **110**, 272-280.

THE DETERMINATION OF THE GELATIN ADSORPTION DEGREE ON THE COPPER AND BRASS

D. Todorović¹, Z. Dražić-Janković², Lj.M. Ignjatović² and D.A. Marković²

¹ High School of Technics and Technology, Kosančićeva 22, Kruševac

² Faculty of Physical Chemistry, University of Belgrade, Studentski trg 12-16, Beograd

Abstract

Efficiency of gelatin as inhibitor directly depends on the way of forming and the structure of adsorbed layer which was used to follow the adsorption process by measuring level of the corrosion. In this experiment, the temperature of copper and brass plates had changed (20-80 °C), before they immersed in inhibitor solution and then the specimens were exposing to the corrosion effect on same conditions (electrolyte and treatment time). By tracking corrosion parameters and comparison to the presumed gelatin adsorption degree we determined dependence between corrosion and adsorption which was then used to determine the activation energy of the gelatin adsorption on copper and brass surface.

Introduction

Inhibition means protection from corrosive process on the boundary of phases by use of materials which can be adsorbed on the metal surface and lower the corrosive action. Substances which are used for protection are called the adsorptive inhibitors of corrosion. In order to have the good inhibitory characteristics a compound must possess atoms with one or more free electron pairs [1].

Molecules bound by Van der Waals forces vibrate and may leave the surface because of small bond dissociation energy, so the desorption process can be described by the Arrhenius type equation, where the desorption degree k_{des} is [2]:

$$k_{des} = A \exp(-U_{ad}/RT)$$

A - the vibration frequency of the adsorbed molecule (s^{-1})

U_{ad} - the molar activation energy of the adsorption (J/mol)

R - universal gas constant (J/molK)

T - absolute temperature (K)

Experimental

Experiment is performed with 24 samples of copper and brass (Cu63Zn37) plates (50×50×0.5 mm). The 2 % gelatin solution in water was used as inhibitor, and as electrolyte 10 % and 20 % solutions of citric acid. Copper and brass plates were thoroughly cleaned with fine polishing paper before treatment. The plates were tempered on 20 °C, 30 °C, 40 °C, 60 °C, 70 °C and 80 °C, and then gradually inhibited by immersing into the 2 % solution of gelatin for 15 min at 35 °C.

The plates are then dried in a stream of warm air at 30-40 °C and put into the plastic bags before treating in the electrolyte. Each of the samples was marked and weighed. Each of the plates was being held in 10 % and 20 % citric acid for 48 hours. After that time the plates were removed from the electrolyte and dried. The corrosive layer was then removed mechanically (by a fine polishing paper) and chemically (by treating the plates in 5 % sulphuric acid at room temperature for 30 min).

Results and Discussion

The results of the corrosion measurements, considering the mass loss (Δm (g)), corrosion degree (I (%)) and the corrosion rate (A ($\text{g}/\text{m}^2\text{day}$)), are given in Tables 1. and 2.

Table 1. The results of corrosion measurements for copper plates with 2 % gelatin in 10 % citric acid

Specimen	T, °C	Δm , g	I, %	A, $\text{g}/\text{m}^2\text{day}$	D, %
1	20	0,0064	0,077	2,130	100,0
2	30	0,0110	0,144	3,670	58,18
3	40	0,0152	0,197	5,067	42,20
4	60	0,0288	0,414	9,600	22,22
5	70	0,0358	0,514	11,97	17,82
6	80	0,0391	0,760	13,03	16,37

Table 2. The results of corrosion measurements for brass (Cu63Zn37) plates with 2 % gelatin in 20 % citric acid

Specimen	T, °C	Δm , g	I, %	A, $\text{g}/\text{m}^2\text{day}$	D, %
1	20	0,0330	1,904	11,00	100,0
2	30	0,0582	3,180	19,40	56,70
3	40	0,0848	4,760	28,27	38,91
4	50	0,1229	6,600	40,90	26,85
5	60	0,1533	7,973	51,10	21,53
6	70	0,1560	9,380	61,87	17,78

The results obviously show that the loss of mass and the rate of the corrosion increase as the temperature of metal plates rises. Examination showed the direct dependence between the area that is covered by adsorption layer and its stability and the resistance of the metal surface to the corrosion, that is, the stability of corrosion layer was decreasing as the temperature was rising. At 70 °C and 80 °C the rate of the corrosion was greater in regard to uninhibited plates, because the adsorptive layer was destroyed in such a scope, so that conditions for forming local cathode and anode areas on the metal surface were created, which accelerated the corrosion.

Being the measurements of desorption rate were not possible, we introduced the relative adsorption degree, D, as:

$$D = A \exp(U_{ad}/RT)$$

with the same meaning of the constants and parameters as in previous formula.

We assumed that at 20 °C the adsorption of gelatin on metal surfaces is 100%. As the degree of adsorption is reciprocal to the loss of mass during the corrosion, it was calculated for the rest of the temperatures and the obtained values are given in the last columns of Tables 1 and 2.

The obtained $\ln D - 1/T$ dependences are linear. For the adsorption of gelatin on copper the derived equation is:

$$D = 0.001994 \exp (- 26.14/RT)$$

and for adsorption of the gelatin on CuZn37:

$$D = 0.00638 \exp (- 23.16/RT)$$

Conclusion

The acquired results lead us to the following conclusions:

1. With the increase of the plates temperature, the corrosion process rises, as the consequence of increasing desorption of the inhibitor.
2. At overheating temperatures of 70-80 °C the remains of the inhibitor were not only ineffective but also increased the corrosion in regard to the uninhibited specimens.
3. On the basis of the calculated values for the activation energy of gelatin adsorption on copper ($U_{ad} = 26.14$ J/mol), and on brass ($U_{ad} = 23.16$ J/mol) surface we can conclude that specified inhibitor is adsorbed on the metal surface mainly by physical adsorption.

References

- [1] L.I. Antropov, E.M. Makušin: Inhibitori korozii metalov, Tehnika, Kiev, 1981.
- [2] G. Woodbury: Physical Chemistry, Brooks/Cole Publishing Company, New York, 1996.

Complex Compounds

(M)

STUDY ON INTERACTIONS OF COORDINATED WATER WITH PHENYL GROUP IN CRYSTAL STRUCTURES OF METAL COMPLEXES

G. V. Janjić, M. K. Milčić, S. D. Zarić

*Department of Chemistry, University of Belgrade, Studentski trg 16,
P.O. Box 158, Belgrade, Serbia, szaric@chem.bg.ac.yu*

Abstract

Water molecule, coordinated to a metal in transition metal complexes, and phenyl ring can involve in two types of interactions; $\text{OH}\cdots\pi$ and $\text{CH}\cdots\text{O}$. In $\text{OH}\cdots\pi$ interactions water molecule is hydrogen atom donor, while π -system of phenyl ring is hydrogen atom acceptor. In $\text{CH}\cdots\text{O}$ interactions aqua ligand is hydrogen atom acceptor, and phenyl group hydrogen atom donor; the interactions occurs between CH group from phenyl and oxygen from water. In the crystal structures of transition metal complexes these interactions were found by screening Cambridge Structural Database (CSD). We found 84 interactions where water molecule is hydrogen atom donor, and 3239 interactions where water molecule is hydrogen atom acceptor. Much larger number of interactions with water molecule as hydrogen atom acceptor show clear preference for $\text{CH}\cdots\text{O}$ interactions between aqua ligand and phenyl group.

Introduction

The $\text{XH}\cdots\pi$ and $\text{CH}\cdots\text{O}$ interactions are considered to be weak but important non-covalent bonding forces in a wide range of molecular systems. The investigations of these interactions in proteins and peptides show that these interactions contribute as much to stability as more conventional interactions [1], and in some cases may also be directly involved in the mechanism of enzymatic reactions [2].

Specific type of $\text{XH}\cdots\pi$ interactions are interactions of water molecule, coordinated to the metal, and aromatic ring. These interactions are some of metal-ligand aromatic cation- π (MLAC π) interactions [2-4]. In our previous study it was shown that coordinated water molecule, as a hydrogen atom donor, and phenyl group, as a hydrogen atom acceptor, can make some of the shortest $\text{XH}\cdots\pi$ interactions [4]. However, coordinated water molecule (aqua ligand) and phenyl group can interact in another way. Namely, aqua ligand can be hydrogen atom acceptor, and phenyl group hydrogen atom donor, making $\text{CH}\cdots\text{O}$ interaction between CH group from phenyl and oxygen from water.

Here, in order to study interactions between coordinated water molecule and phenyl group in crystal structures of metal complexes we searched Cambridge Structural Database (CSD) and obtained crystal structures with $\text{OH}\cdots\pi$ and $\text{CH}\cdots\text{O}$ interactions between aqua ligand and phenyl group. The data enabled to find out if aqua ligand and phenyl group prefer to make $\text{OH}\cdots\pi$ or $\text{CH}\cdots\text{O}$ interactions.

Results and Discussion

Crystal structures of aqua complexes and phenyl group were obtained from Cambridge Structural Database (CSD). The structures of these complexes were screened for interactions between aqua ligands and phenyl groups, with the geometric criteria used in previous studies.

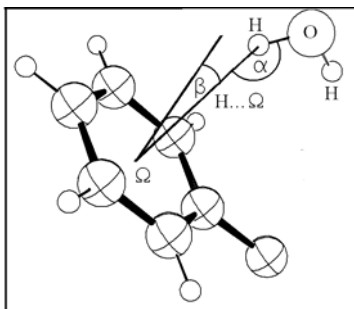


Fig. 1. Geometrical parameters describing the $\text{OH}\cdots\pi$ interaction.

We searched for structures in which the distance between a hydrogen atom of water molecule and the center of a phenyl ring was less than 3.1 Å (Figure 1), and structures in which the distances between hydrogen atom of phenyl group and oxygen atom of water molecule was less than 3.5 Å (Figure 2). By searching CSD we found 84 interactions, where water molecule is hydrogen atom donor and phenyl ring is acceptor ($\text{OH}\cdots\pi$ interactions), and 3239 interactions where phenyl group is hydrogen atom donor and water molecule is acceptor ($\text{CH}\cdots\text{O}$ interactions). Much larger number of interactions where phenyl ring is hydrogen atom donor show clear preference for $\text{CH}\cdots\text{O}$ interactions between aqua ligand and phenyl group. This preference can be caused by the larger interacting energy or by steric reasons. The data about interacting energies are not known, however, from the geometries of $\text{OH}\cdots\pi$ and $\text{CH}\cdots\text{O}$ interactions it is obvious that $\text{CH}\cdots\text{O}$ interactions are favored by steric reasons.

The data about $\text{OH}\cdots\pi$ intermolecular interactions show that these interactions occur between aqua ligand in cationic complex and phenyl ring that is part of an anion, or between two equivalent molecules that contain both aqua ligand and phenyl group. In the last case most of the complexes are neutral. Complexes with intramolecular $\text{OH}\cdots\pi$ interactions are also mainly neutral.

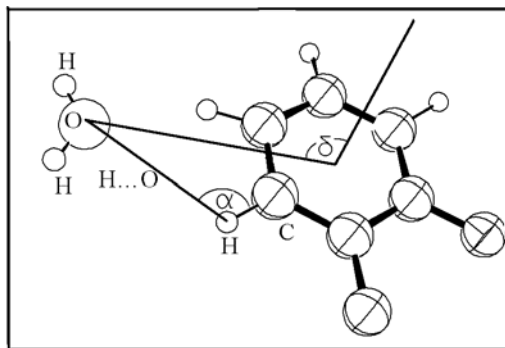


Fig. 2. Geometrical parameters describing the CH...O interaction.

Based on the number of phenyl groups interacting with same aqua ligand from metal complex, there are two types of OH... π and CH...O interactions. In the first type, one phenyl group interacts with one aqua ligand, in the second type one water molecule interacts with two phenyl groups

Conclusion

The results show that water molecules, coordinated to a metal ion, can be involved in OH... π and CH...O interactions with phenyl group. The crystal structures with these interactions were found by screening Cambridge Structural Database (CSD). We found 84 OH... π interactions and 3239 CH...O interactions. Much larger number of interactions with water molecule as hydrogen atom acceptor show clear preference for CH...O interactions between aqua ligand and phenyl group.

References

- [1] J. P. Gallivan, D. A. Dougherty, Proc. Natl. Acad. Sci, USA, 2000, **96**, 9459-9464.
- [2] S. D. Zarić, D. Popović, E. W. Knapp, Chem. Eur. J., 2000, **6**, 3935-3942.
- [3] M. Milčić, S. D. Zarić, Eur. J. Inorg. Chem, 2001, 2143-2150.
- [4] M. Milčić, Z. D. Tomić, S. D. Zarić, Inorg. Chim. Acta, 2004, **357**, 4327-4329.

STACKING INTERACTIONS BETWEEN CHELATE AND PHENYL RINGS IN SQUARE-PLANAR COMPLEXES OF Cu, Ni, Pt AND Pd

D. N. Sredojević², Z. D. Tomić¹ and S. D. Zarić²

¹*'Vinča' Institute of Nuclear Sciences, Laboratory of Theoretical Physics and Condensed Matter Physics, Belgrade, P. O. Box 522, Serbia,*

²*Department of Chemistry, University of Belgrade, Studentski trg 16, Belgrade, Serbia, szaric@chem.bg.ac.yu*

Abstract

Previous analysis of geometrical parameters in the crystal structure of square-planar complexes, with and without chelate rings, of all transition metals from Cambridge Structural Database shows that there are stacking interactions between the phenyl ring and the chelate ring with delocalized π -bonds. To investigate whether the type of metal atom influence this interaction we compare stacking parameters for the complexes with and without chelate rings in the complexes containing Cu(II), Ni(II), Pd(II) and Pt(II) metals. While the overall picture is similar for all four cases, complexes of Pd and Pt without chelate ring show tendency to form shorter contacts towards aromatic carbon. It was found that this behaviour is associated with the presence of cyano or isocyano derivatives as ligands.

Introduction

The noncovalent interactions of π -systems have been studied intensively in recent years. The importance of these interactions have been shown in different molecular systems from supramolecular structures to biomolecules. Recently, a few studies of noncovalent interactions with chelate ring as a π -system were published [1-4]. Chelate ring can be involved in CH/ π interactions with organic moieties [1-2] and in stacking interactions with phenyl rings [3-4].

Our previous results [4] show that there are stacking interactions between chelate and phenyl rings in square-planar transition metal complexes, indicating that chelate rings can behave similar to organic aromatic rings. Here we present results about stacking interactions of chelate and phenyl rings in square-planar complexes of Cu, Ni, Pd, and Pt.

Results And Discussion

By searching Cambridge Structural Database (CSD) many complexes with planar chelate ring with delocalized π -bonds and phenyl group were found. There are only four of metals (Cu, Ni, Pd, Pt) that have enough large number of structures that makes possible to analyze structures of these metals. All these metals have large tendency to make square-planar complexes.

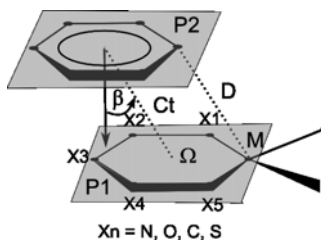


Fig. 1. Geometrical parameters describing interaction of square-planar complex with phenyl ring.

Crystal structures of complexes with and without chelate ring were separately analyzed for any of these four metals. As was shown for Cu [3] and all metals together [4], complexes of Ni, Pt and Pd (Figure 2) with chelate rings also show tendency for shorter metal-carbon distances, below the sum of van der Waals radii ($\Delta > 0$).

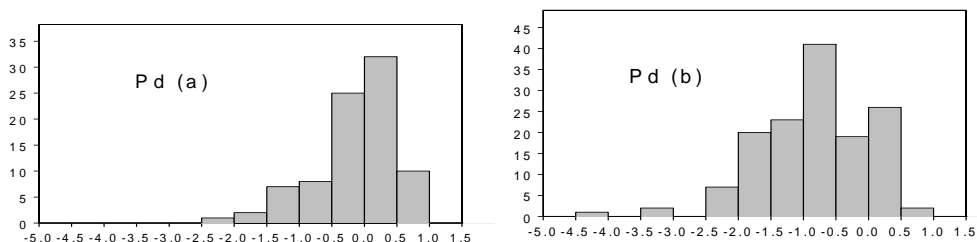


Fig. 2. Histograms showing the distribution of parameter Δ (Å) in crystal structure with (a) and without (b) chelate ring for Pd complexes. The parameter Δ is difference of sum of the van der Waals radii and the distance between the metal and the closest phenyl carbon (D) (Figure 1) ($\Delta = \Sigma vdW - D$).

Distributions of the angle θ in structures of Pd with and without chelate ring are shown in Figure 3. In the structures with chelate ring, phenyl ring has large tendency to be oriented approximately parallel to the mean coordination plane (Figure 3a). Other metals (Cu, Ni, and Pt) show similar tendency.

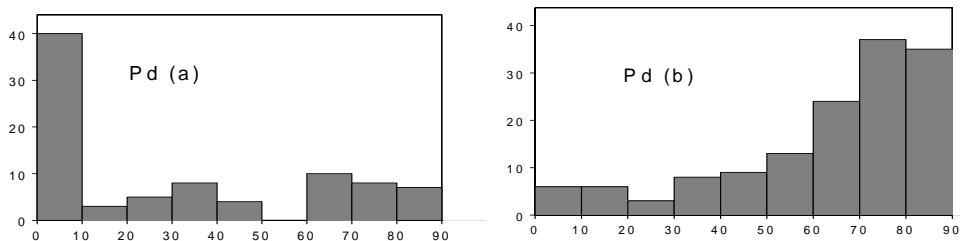


Fig. 3. Histograms showing the distribution of the dihedral angle θ ($^{\circ}$) between the mean plane of the phenyl ring (P2) and the mean plane of the metal with coordinated atoms (P1) with (a) and without (b) chelate ring for Pd.

However, there are some differences for structures without chelate rings among metals. While in Ni and Cu complexes there is very small number of structures with $\theta < 20^{\circ}$ in cases of Pt and Pd there is larger number of structures with $\theta < 20^{\circ}$. We screened these complexes and found that in most cases when the dihedral angle is small ($\theta < 20^{\circ}$) there are short metal-carbon distances ($\Delta > 0.0 \text{ \AA}$). Further analyses show that in many cases these complexes possess common constitution of coordination sphere with coordinated cyano or isocyano phenyl derivatives.

Conclusion

Interactions of phenyl and chelate rings in crystal structures of square-planar complexes of every of four metals (Cu, Ni, Pd and Pt) show very similar behaviour. In complexes with chelate ring there are shorter metal-carbon distances and parallel orientation of phenyl ring with respect of chelate ring indicating that there are stacking interactions. However, there are some differences among metals for structures without chelate rings.

References

- [1] G. A. Bogdanović, A. S. Biré, S. D. Zarić, *Eur. J. Inorg. Chem.*, 2002, 1599-1602.
- [2] A. Castineiras, A. G. Sicilia-Zafra, J. M. Gonzáles-Pérez, D. Choquesillo-Lazarte, J. Nicolás-Gutiérrez, *Inorg. Chem.*, 2002, **41**, 6956-6958.
- [3] Z. D. Tomić, S. B. Novaković, S. D. Zarić, *Eur. J. Inorg. Chem.*, 2004, 2215-2218.
- [4] Z. D. Tomić, D. N. Sredojević, S. D. Zarić, *Crystal Growth & Design.*, 2006, **6**(1), 29-31.

MECHANISM OF COMPLEX FORMATION BETWEEN $[\text{AuCl}_4]^-$ AND L-METHIONINE

A. Vujačić¹, V. Vasić¹, J. Savić¹ and S. Sovilj²

¹*Vinča Institute of Nuclear Sciences, P.O.Box 522, Belgrade, Serbia*

²*Faculty of Chemistry, University of Belgrade, P.O.Box 158, Belgrade*
(e-mail: anavu@vin.bg.ac.yu)

Abstract

The kinetics of the reaction between tetrachloroaurate(III) ion and L-methionine has been studied spectrophotometrically by using stopped-flow technique in 0.1 M HClO_4 as the function of temperature. The fast reaction was ascribed to the formation of short living square-planar $[\text{AuCl}_2\text{Met}]^+$ complex ion, that was reduced in the slower reaction step. The activation parameters (ΔH^\ddagger and ΔS^\ddagger) for complex formation were determined. The entropy of activation was compatible with an associative reaction mechanism.

Introduction

L-methionine (L-Met) belongs to the naturally occurring amino acids containing thiol group. It forms chelates with many metal ions mostly by coordinative binding to amino- and carboxyl groups of α -amino acid residue [1]. This work deals with the investigation of the equilibrium and kinetics of complex formation between $[\text{AuCl}_4]^-$ and L-Met. Since Au(III) is isoelectronic to Pt(II), this reaction is an excellent model system for the elucidation of the reaction mechanism between biomolecules and Pt(II) complexes that exert anticancer activity.

Experimental

1×10^{-2} M stock solutions of $\text{HAuCl}_4 \cdot 3\text{H}_2\text{O}$ and L-methionine were prepared in 0.1 M HClO_4 shortly before use (all used chemicals were p.a. quality). The absorption spectra were recorded using Perkin Elmer Lambda 35 spectrophotometer. Kinetic measurements were performed using HI-TECH stopped-flow equipment in the temperature range from 282 to 303 K.

Results and Discussion

The absorption spectra of solutions containing 1×10^{-5} M $[\text{AuCl}_4]^-$ and 5×10^{-5} M L-Met were followed in 0.1 M HClO_4 as the dependence of time. The spectral changes indicated two processes, according to the relations:

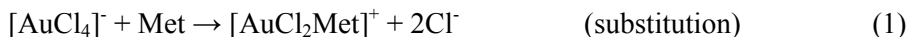


Fig.1 represents the changes of the absorption spectra in the fast reaction step, which were followed by two well defined isobestic points. These spectral changes were ascribed to the substitution reaction due to the formation of $[\text{AuCl}_2\text{Met}]^+$

complex ion according Eq.1, with the shoulder around 280 nm. The second process (Eq. 2), followed by the disappearing of the absorption spectra, was considered to be the reduction of $[\text{AuCl}_2\text{Met}]^+$ complex ion. The change of the absorbance vs. time at 280 nm is presented in Fig.1 (inset).

The stoichiometry of the reaction (1) was confirmed by the molar ratio and Jobb's methods [2], using the absorbance at the maximum of the kinetic curves as the measure of concentration of complex ion.

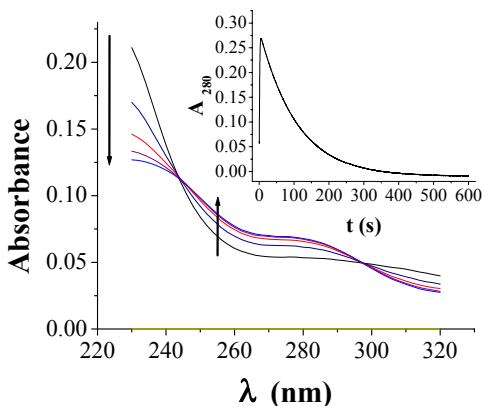


Fig. 1. Time dependence of absorption spectra of solution containing 1×10^{-5} M $[\text{AuCl}_4]^-$ and 5×10^{-5} M L-Met at pH 1. Inset: kinetic curve at 280 nm

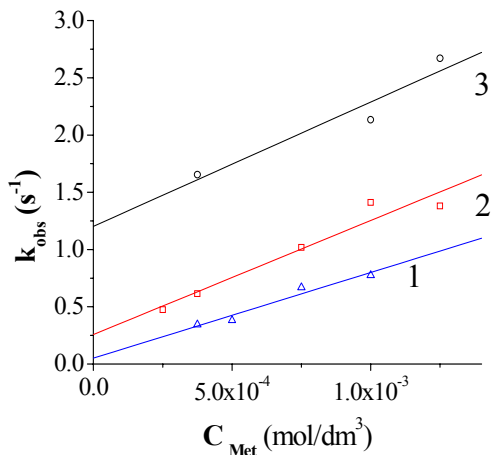


Fig. 2. Experimental rate constants (k_{obs}) as a function of L-Met concentration at pH 1 and 282 K (1); 294 K (2); 303 K (3).

The kinetic of the reaction between $[\text{AuCl}_4]^-$ and L-Met was investigated at pH 1 under the pseudo first order conditions as the function of temperature, keeping the concentration of Au(III) complex ion constant (5×10^{-5} M) and varying [L-Met] from 2×10^{-5} M to 1×10^{-3} M. The kinetic curves in the fast reaction step were fitted to the function $(A_f - A)/(A - A_o) = \exp(-k_{\text{obs}}t)$ (A_o and A_f were the initial and final (on the plateau of A vs. t curve) absorbancies, respectively). The typical dependence of k_{obs} vs. [L-Met] for the substitution reactions of square planar complexes was obtained in the fast reaction step:

$$k_{\text{obs}} = k_I + k_{II} [\text{L}_f] \quad (3)$$

where k_{obs} represents the observed pseudo first order rate constant, k_I is the solvent dependent rate constant and k_{II} is the second order rate constant which is characteristic for direct nucleophile attack. The linear plots of k_{obs} vs. [L-Met] were obtained in all cases and are presented on Fig.2. k_I and k_{II} were determined from the intercept and the slope of the plots, and are given in Table 1. The dependence of k_{II} on temperature allowed the calculations of the activation parameters of complex formation (Eq. 4).

$$k_{II} = kT/h \exp(\Delta S^\ddagger/R) \exp(-\Delta H^\ddagger/RT) \quad (4)$$

The values of enthalpy ($\Delta H^\ddagger = 9.9$ kJ/mol) and entropy ($\Delta S^\ddagger = -154.3$ J/mol K) were obtained using Eyring's equation.

Table 1. Values of rate constants k_I and k_{II} obtained from linear plots k_{obs} vs. L-Met concentration

T(K)	$10^2 \times k_{II}(\text{M}^{-1}\text{s}^{-1})$	$k_I(\text{s}^{-1})$
282	7.48	0.051 ± 0.001
294	9.17	0.257 ± 0.001
303	10.86	1.202 ± 0.001

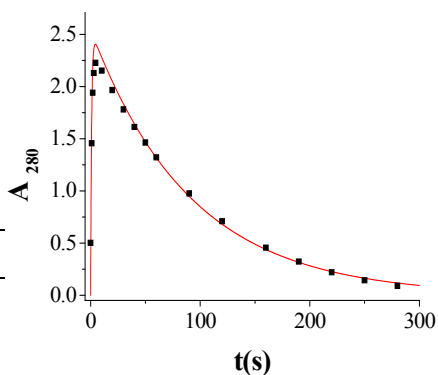


Fig. 3. Dependence of absorbance at 280 nm on time; solid curve calculated according Eq.(5); points - experimental results

The experimental kinetic curves at 280 nm (Fig.1, inset) are typical for two consecutive reactions [3]. The dependence of absorbance on time can be presented as:

$$A = \frac{k_1}{k_2 - k_1} A_\infty (e^{-k_1 t} - e^{-k_2 t}) \quad (5)$$

where k_1 and k_2 are pseudo first order rate constants for reactions (1) and (2), respectively, and $[A]_\infty$ is the absorbance on the plateau of A vs. t curve. Using Eq. 5, the rate constants $k_1=1.06$ s $^{-1}$ and $k_2=0.01$ s $^{-1}$ for the solution containing $[\text{AuCl}_4]^- = 2.5 \times 10^{-5}$ M and $[\text{Met}] = 10^{-4}$ M were obtained. Using these values the dependence of absorbance at 280 nm (A_{280}) vs. t was recalculated and presented on Fig. 3 as solid line, since the points represent the experimental results. As can be seen, the calculated results are in good agreement with the experimental data. These finding supports the proposed reaction model.

Conclusion

The reaction between $[\text{AuCl}_4]^-$ and L-methionine involves ligand substitution followed by the reduction of the formed complex ion. The large negative value of the entropy indicated an associative mode of activation (I_a or A mechanism) in the first reaction step. This finding indicates that bond-making with the entering ligand is important in the activation processes and that the leaving group is still tightly bound to the metal center in the transition state. The effect of ligand on the reduction step is under the investigation.

References

- [1] E. Raux, H. K. Leech, R. Beck..., *Biochem. J.*, 2003, **370**, 505-516.
- [2] J. Luthern, A. Peredes, *Journal of Materials Science Letters*, 2000, **19**, 185-188.
- [3] R. Schmidt, V. N. Sapunov, *Non-formal kinetics*, Verlag Chemie, Basel, 1982.

CORRELATION BETWEEN STRUCTURAL PROPERTIES AND INHIBITION EFFICIENCY OF SOME COBALT(III) COMPLEXES USING MOLECULAR MODELING CALCULATIONS

V.M. Jovanović¹, K. Babić-Samardžija^{2*} and S.P. Sovilj³

¹ICTM, Department of Electrochemistry, Njegoševa 12, P.O. Box 815, Belgrade, Serbia

²Rice University, Chemistry Department MS60, 6100 Main St., Houston, TX 77005, USA

*Present address: Baker Petrolite, 12645 West Airport Blvd., Sugar Land, TX 77478, USA

³Faculty of Chemistry, University of Belgrade, P.O. Box 158, Belgrade, Serbia

Abstract

A series of Co(III) mixed-ligand complexes of the general formula $[\text{Co}(\text{Rdtc})\text{cyclam}](\text{ClO}_4)_2$ were electrochemically investigated in 0.1 M HClO_4 at Fe electrode. Anodic polarization of an Fe electrode in the presence of the complexes exhibits in perchloric acid their influence not only on the dissolution of iron but also on the hydrogen evolution reactions. The inhibiting effect for iron corrosion is related closely to the electronic properties of the heterocyclic dithiocarbamates.

Introduction

Molecular orbital theory is useful in explaining chemical reactivity. It can be used as one of the approaches to study metal-inhibitor interaction and to predict the adsorption centres of the inhibitor molecule responsible for the interaction with metal surface [1-3]. The energy gap between the E_{HOMO} (highest occupied) and E_{LUMO} (lowest unoccupied) molecular orbitals could be used to show important interaction between two molecules and it can be related to energy difference i.e., to the molecules that can be more easily excited and/or more readily undergo a charge transfer interaction with the metal surface [2,3]. We have shown earlier [4] that reaction on an Fe electrode in deoxygenated 0.1M HClO_4 solution was inhibited in the presence of the $[\text{Co}(\text{cyclam})\text{Pzdtc}](\text{ClO}_4)_2$ complex in some extent better than by amine piperazine.

The aim of this work is to examine the behavior of a series of the $[\text{Co}(\text{cyclam})\text{Rdtc}](\text{ClO}_4)_2$ complexes in HClO_4 acid. Using Fe electrode, effect of these compounds was followed throughout their influence on hydrogen evolution and metal dissolution reactions. Structural properties of the complex species and their inhibition efficiency were correlated using molecular modeling calculations.

Experimental

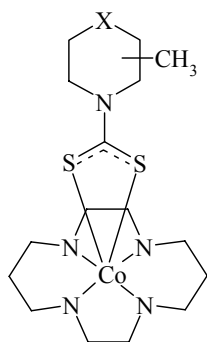
Eight heterocyclic cobalt(III) complexes of the general formula $[\text{Co}(\text{cyclam})\text{Rdtc}](\text{ClO}_4)_2$, [$\text{Rdtc}^- = \text{morpholine- (Morphdtc)}$, thiomorpholine- (Timdtc), piperazine- (Pzdtc), N-methylpiperazine- (Mepzdtc), piperidine- (Pipdtc), 2-, 3- and 4-methylpiperidine- (2-, 3- or 4-Mepipdtc) dithiocarbamates, respectively] as well as corresponding heterocyclic amines were examined as possible iron corrosion inhibitors at 10^{-4} M in 0.1M HClO_4 solution. Iron rod was mechanically buffed with

emery paper. The Fe electrode was polarized between -0.65V to -0.2V vs SCE with the sweep rate of 5mV/s . The solutions were prepared from analytical grade reagents using $18\text{M}\Omega$ H_2O and were maintained oxygen-free by purging with nitrogen. The electrode was immersed for one hour before starting measurements. All of the experiments were performed at room temperature in three-electrode compartment electrochemical cell. The counter electrode was a Pt wire and the reference electrode was a double junction SCE.

For molecular modeling, a quantum mechanical program Hyperchem 7 was used. Molecular orbital calculations are based on the semi-empirical Self-Consistent Field (SCF) method. A full optimization of all geometrical variables without any symmetry constraint was performed using the ZINDO/1 method.

Results and Discussion

The inhibiting effect of cobalt(III) complexes of general formula $[\text{Co}(\text{cyclam})\text{Rdtc}](\text{ClO}_4)_2$ (Fig. 1) and corresponding free amino-ligands were studied at iron electrode in perchloric acid.



<i>Morphdtc</i>	X=O
<i>Timdtc</i>	X=S
<i>Pzdtc</i>	X=NH
<i>Mepzdtc</i>	X=N-CH ₃
<i>Pipdtc</i>	X=CH ₂
<i>2-Mepipdtc</i>	X=CH ₂ <i>o</i> -CH ₃
<i>3-Mepipdtc</i>	X=CH ₂ <i>m</i> -CH ₃
<i>4-Mepipdtc</i>	X=CH ₂ <i>p</i> -CH ₃

Fig. 1. The structure of $[\text{Co}(\text{cyclam})\text{Rdtc}](\text{ClO}_4)_2$ Complexes

The results show that cobalt complexes have stronger effect on hydrogen evolution reaction than on oxidation of iron. It seems that inhibition of iron dissolution is better in the presence of the complexes with piperidine and derivatives than in the presence of the complexes with a heteroatom O, S or N in the ring. The corresponding uncoordinated N-heterocyclic amines exhibit the opposite effects. Moreover, the weaker inhibiting effect of the free amine gives stronger effect for the corresponding complex. It was found that the stronger metal-ligand bond in the complex leads to the higher electron density and thus higher inhibition, as correlated previously using the spectroscopic IR and NMR data of the complexes [5,6].

Molecular modeling calculations, using some key quantum chemical parameters such as the energies of molecular orbitals E_{HOMO} (highest occupied) and E_{LUMO} (lowest unoccupied), were used to correlate structural properties of the complex species and inhibition efficiency [2,3]. According to ZINDO/1 semi-empirical SCF-MO method and crystal data known, the complex molecules are in distorted octahedron geometry with typical conformational flexibility of a large cyclic ring with a minimum steric

constrains and with significant delocalization along the $>\text{NCS}_2$ group of Rdtc ligand. Fig. 2 shows ZINDO/1 optimized structure for *cis*-[Co(cyclam)morphdtc](ClO₄)₂ (a) and *cis*-[Co(cyclam)2-mepipdtc](ClO₄)₂ (b) complexes.

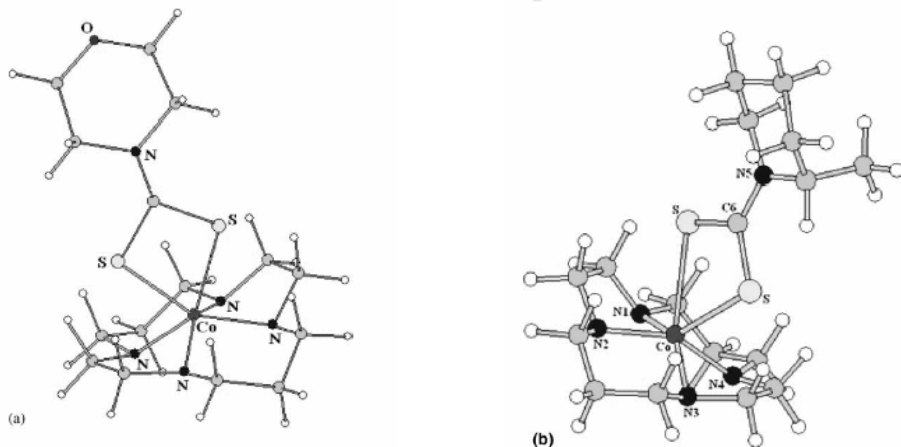


Fig. 2. ZINDO/1 optimized structures for the complexes:

- a) *cis*-[Co(cyclam)morphdtc](ClO₄)₂
- b) *cis*-[Co(cyclam)2-mepipdtc](ClO₄)₂

The analysis show that the small differences in inhibiting behavior of the complexes are a consequence of electronic and structural effects along with conjugation of double bonds through the $>\text{NCS}_2$ group of Rdtc ligand. We could hypothesize that cobalt complexes interact and/or adsorb on the metal surface through the coordinate-type link formed due to electron transfer. Therefore, greater adsorption and inhibition efficiency should be expected for those compounds with greater electron density at the adsorption center.

References

- [1] P.Mutombo, N.Hackerman, *Anti-Corrosion Methods and Materials* 1998, **45**, 413-417.
- [2] K.Babić-Samardžija, K.F.Khaled, N.Hackerman, *Appl.Surface Science*, 2005, **240**, 327-340.
- [3] K.F.Khaled, K.Babić-Samardžija, N.Hackerman, *Corrosion Science*, 2006, in press.
- [4] V.M.Jovanović, K.Babić-Samardžija, S.P.Sovilj, *Electroanal.*,2001 **13**, 1129-1135.
- [5] S.P.Sovilj, G.Vučković, K.Babić-Samardžija, N.Matsumoto, V.M.Jovanović. *J.Mrozinski, Synth.React.Inorg.Met.-org.Chem.*, 1999, **29**, 785-803.
- [6] S.P.Sovilj, G.Vučković, K.Babić, S.Macura, N.Juranić, *J.Coord.Chem.*, 1997, **41**, 19-25.

STUDY OF C-H... π INTERACTIONS WITH PYRROLE AND CHELATE RINGS IN METAL-PORPHYRIN COMPLEXES

V. B. Medaković¹, M. K. Milčić¹ and G. A. Bogdanović²

¹*Department of Chemistry, University of Belgrade, Studentski trg 16, Belgrade, Serbia*

²*Laboratory of Theoretical Physics and Condensed Matter Physics, Vinča Institute of Nuclear Sciences, Belgrade, P.O. Box 522, Serbia*

Abstract

The Cambridge Structural Database (CSD) was screened in order to find and investigate specific C-H... π interactions between C-H groups and two types of rings with delocalized π -bonds that exist in porphyrin: pyrrole and six-membered chelate. Statistical analysis of geometrical parameters for interactions in both types of rings was done. In order to determine preferred positions in porphyrinato ring for C-H... π interactions fifteen different points distributed over porphyrin ring have been chosen and each of them have been analyzed. Calculations of these interactions by density functional theory (DFT) have been done on three different model systems.

Introduction

Porphyrin molecule and derivatives of porphyrine possess four pyrrole rings with delocalized π -systems. When porphyrin is coordinated as a tetradentate ligand to a metal, additional four six-membered chelated rings with delocalized π -bonds are formed. In our previous study [1], we have shown that the chelate ring π -systems of the coordinated porphyrin can be involved in C-H... π interactions. The Cambridge Structural Database (CSD) was screened in order to find specific C-H... π interactions between C-H groups and the π -system of porphyrinato chelate rings in metal complexes. It was found 655 interactions (411 are intermolecular and 244 are intramolecular). Calculations of these interactions by density functional theory (DFT) show energy of the interactions of about 1.5 kcal/mol, and that the strongest interaction occurs when the distance between hydrogen atom and the center of the chelate ring is 2.6 Å. This result is in a good agreement with the distances for intermolecular interactions found in the crystal structures.

The fact that porphyrin possess two different types of rings with delocalized π -bonds, pyrrole and six-membered chelate, prompted us to study and compare C-H... π interactions for both of them. In order to determine preferred positions in porphyrinato ring for C-H... π interactions we have chosen fifteen different points distributed over porphyrin ring and have analyzed each of them. These fifteen positions include the centroids of five and sixmembered rings, points around the centroids and on the edge of the ring, nitrogen and carbon atoms.

Results and Discussion

The structures of metal complexes with coordinated derivatives of porphyrin were screened using geometric criteria described briefly below. We searched CSD for structures where the distances between an hydrogen atom and the points of the rings (Ω) were shorter than 3.1 Å, and presenting a C–H... Ω axis makes narrow cone perpendicular to the ring ($\alpha > 110^\circ$, $\beta < 6^\circ$). The calculations were done using density functional theory (DFT), specifically the PW91, exchange and correlation functional. These calculations were carried out using the Gaussian 98 program. The LANL2DZ basis set was chosen for the nickel atom and 6-31G** basis sets were chosen for the carbon, nitrogen and hydrogen atoms. The bonding energies were calculated as the difference between the energy of the [Ni(por)]–C₂H₂ system (Figure 1) and the sum of the energies of the [Ni(por)] complex and acetylene. Single point calculations have been done for different H... Ω distances from 2.2 to 3.0 Å. In order to determine the contribution of electrostatic energy to total energy, the distributed multipole analysis has been used.

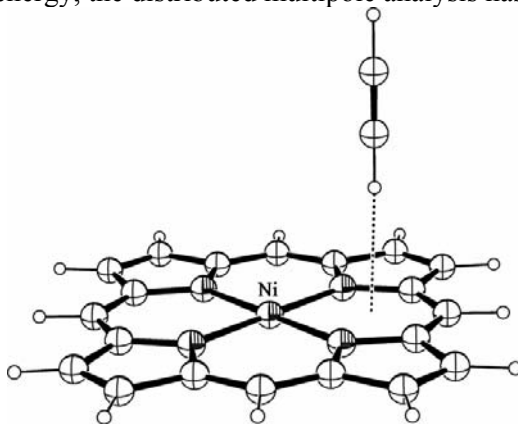


Fig. 1. [Ni(por)]–C₂H₂ - model system for calculations

In searching crystal structures of transition metal complexes from the CSD for specific intermolecular CH/ π interactions, interactions between C–H groups and the π -system of porphyrinato pyrrole and six-membered chelate rings in metal complexes, we found 1746 such interactions. Among them, 1184 are found with five-membered ring and 562 with six-membered ring. Histogram with number of CH/ π interactions for every investigated position is shown in Figure 2. The largest number of CH/ π interactions have been found for positions O5 and D4, both from the five-membered ring.

However, at the short distances, total number of CH/ π interactions is larger for the six-membered ring indicating that the interaction is stronger for six-membered ring. For example, the largest number of interaction for the position O6 (the center of the six-membered ring) is found at the distances between 2.6 and 2.7 Å.

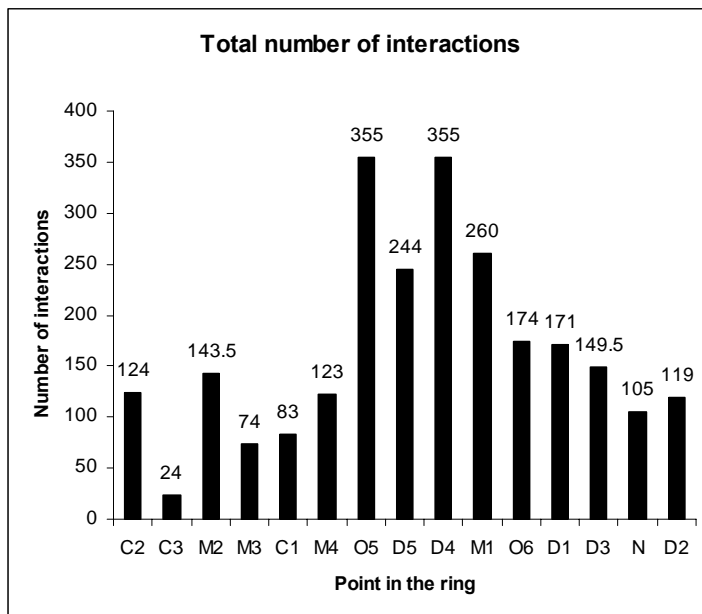


Fig. 2. Histogram showing the total number of CH/ π interactions for all investigated positions in porphyrinato ring.

The results of DFT calculations show that there is attractive interaction in the investigated range. The differences in interaction energies for different positions are small, and at the minima energies are between -2.83 and -2.05 kcal/mol.

Conclusion

The crystal structures of transition metal complexes from Cambridge Structural Database (CSD) were screened in order to find CH/ π interactions with pyrrole and chelate rings from porphyrine. Statistical analysis show that there is difference in distribution of the geometrical parameters, depending on the presence of the substituents on porphyrinato ring and different positions. In order to investigate the influence of different positions and of side groups of porphyrinato ring, DFT calculations have been done on three different model systems. The results show that the differences in interaction energies for different positions are small, and at the minima interacting energies are between -2.83 and -2.05 kcal/mol.

References

- [1] V. B. Medaković, M. K. Milčić, G. A. Bogdanović, S. D. Zarić, *Journal of Inorganic Biochemistry*, 2004, **98**, 1867–1873.

THE NATURE OF CH/ π INTERACTIONS IN TRANSITION METAL COMPLEXES

M. K. Milčić, V. B. Medaković and S. D. Zarić

Department of Chemistry, University of Belgrade, Studentski trg 16, Belgrade, Serbia

Abstract

The CH groups of acetylacetonato ligand in transition metal complexes can be involved in CH/ π interactions with phenyl rings. Interaction energy calculated with the MP2 method at the complete basis set limit (MP2/CBS) is 3.91 kcal/mol. This interaction is 2.17 kcal/mol stronger than interaction between benzene and methane molecule. Energy decomposition has shown that the nature of this CH/ π interaction is mainly dispersion.

Introduction

Noncovalent interaction of π -systems have been extensively studied in recent years, and their importance has been shown in different molecular systems from molecular biology to crystal engineering. Noncovalent interactions involving metal cations have gained particular attention with the recognition that simple metal cations can bind to the aromatic system, and the explanation of this in terms of cation- π interaction.

Cation- π interactions between ligands coordinated to a metal cation and aromatic groups, so-called metal ligand aromatic cation- π (MLAC π) interactions, have been found in crystal structures of metalloproteins from the Protein Data Bank, and in crystal structures of transition metal complexes from Cambridge Structural Database (CSD). These can be considered also as a type of XH/ π hydrogen bonds (X = N, O, C) [1,2].

Acetylacetonato ligand is monoanion and by coordinating to metal atom makes planar chelate ring, with delocalized bonds. Because of delocalization, negative charge is transferred from coordinated ligand to the metal cation, giving hydrogen atoms of acetylacetonato ligand partially positive. Hence, transition metal complexes with acetylacetonato ligand can be involved in CH/ π interactions with aromatic moieties [3]. In this work we present results on the nature of the CH/ π interactions of CH group of the coordinated acetylacetonato ligand and benzene molecule.

Results and Discussion

Model system for the calculations is shown on Figure 1a. In order to understand the nature of CH/ π interactions between transition metal complex and benzene molecule we analyzed the contributions of separate energy terms to the total interaction energy.

Interaction energy obtained by Hartree-Fock (HF) method (E_{HF}) can be approximated as the sum of the exchange-repulsion (E_{rep}) and electrostatic (E_{es}) energies. The exchange-repulsion interactions is the short-range interactions ($E \sim e^{-\alpha R}$) and also includes other terms such as induction energy. E_{rep} is calculated as the difference between HF and electrostatic energy. The electrostatic interaction is long-range interaction ($E \sim R^{-n}$) and it was calculated as an interaction between distributed multipoles obtained from the MP2 wave functions of isolated molecules. E_{HF} , E_{es} , E_{rep} , and E_{tot} for different benzene-transition metal complex distances are shown at the Figure 1b.

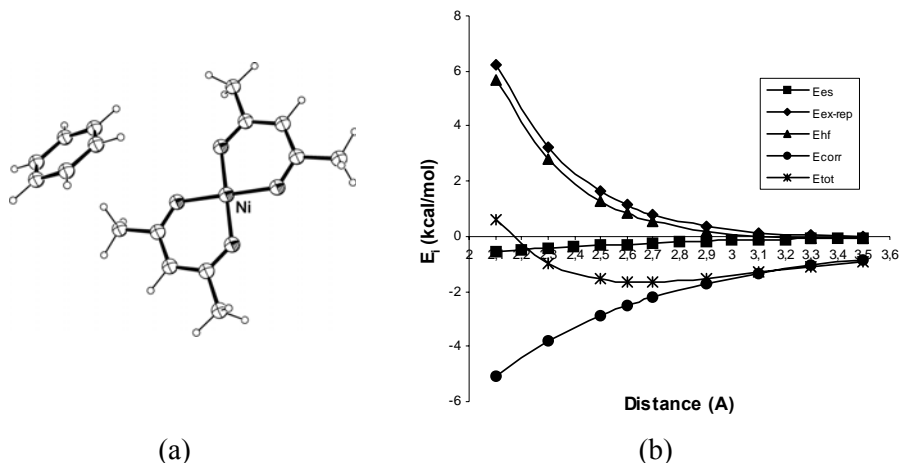


Fig. 1. (a) Model system for the calculation; (b) Different components of the interaction energy.

Data in Figure 1b show that HF interaction energies are positive (repulsive) for closer molecule separations and becomes slightly negative (-0.04 kcal/mol) at distances above 3.3 Å. This is because short-range exchange-repulsion term is dominant at shorter distances. At the longer distances E_{rep} is negligible and long range attractive electrostatic term predominates giving negative E_{HF} . The difference between the *post-HF* and the HF interaction energies is termed correlation energy (E_{corr}) and this is the upper bound of attractive long-range dispersion interaction energy. E_{corr} calculated as the difference between MP2 and HF interaction energies are shown at the Figure 1b. Exchange-repulsion term is dominant term at the shorter intramolecular separations, but it deteriorates toward zero with increasing intramolecular separation. At the distances larger than 2.3 Å long-range dispersion interactions becomes dominant interactions giving negative MP2 binding energy. Interaction energy at the optimum distance of 2.6 Å is a compromise between repulsive E_{rep} and attractive E_{corr} energy terms. The role of electrostatic interactions is negligible. From all this it is obvious that CH/ π interactions between transition metal complex and benzene are dispersion interaction in nature.

The calculated interacting energy at the MP2/CBS limit is significantly larger than the interacting energy obtained for benzene-methane system by Tsuzuki et al [4]. In order to understand the origin of this discrepancy, we compare the contributions of separate energy terms to the total MP2/CBS interaction energy for two systems.

Data about decomposition of the MP2/CBS interaction energy are shown in the table. Difference between total interaction energy of the two systems is 2.17 kcal/mol. Electrostatic and exchange-repulsion term are almost the same in the both systems indicating that the most of the difference is coming from the dispersion energy term.

Table 1. Interaction energy at the basis set limit.

System	E_{total}	E_{es}	E_{rep}	E_{corr}
Ni(acac) ₂ -C ₆ H ₆	-3.91	-0.29	1.18	-4.80
CH ₄ -C ₆ H ₆ ^a	-1.74	-0.25	1.10	-2.59

^adata taken from ref [4]

The reason for much larger dispersion energy in Ni(acac)₂-C₆H₆ system is probably due to the partial stacking interaction between benzene molecule and part of the acetylacetonato ligand. For instance, distance between benzene carbon atom and oxygen atom from the acetylacetonato ligand is 3.99 Å which is close enough for substantial dispersion interaction between two rings.

References

- [1] M. Milčić, S. D. Zarić, *Eur. J. Inorg. Chem.*, **2001**, 2143-2150.
- [2] S. D. Zarić, D. Popović, E. W. Knapp, *Chemistry Eur. J.*, **2000**, **6**, 3935-3942.
- [3] M. K. Milčić, V. B. Medaković, D. K. Sredojević, N. Juranić, S. D. Zarić, *Inorg. Chem.*, in press.
- [4] S. Tsuzuki, K. Honda, T. Uchamaru, M. Mikami, K. Tanabe, *J. Am. Chem. Soc.* **2000**, **122**, 3746-3753.

INVESTIGATION OF ALUMINIUM COMPLEXES OF FLAVONOLS

L. Molnár-Hamvas¹, E. Börcsök¹, R. Csonka-Rákosa¹,
J. Molnár² and K. Németh¹

¹ University of West Hungary, Institute for Chemistry,
H-9400 Sopron, Bajcsy-Zs. u. 4., Hungary, (lhamvas@emk.nyme.hu)

²Dániel Berzsenyi Lutheran Lyceum, H-9400 Sopron, Széchenyi tér 11, Hungary,

Abstract

Quercetin and rutin are essential molecules with antioxidant activity, as well as they are excellent chelating agents, and their complexes also play significant role in the human health.

The coordination of Al(III) ion to quercetin or rutin were studied by UV/Vis spectrophotometry in ethanol-water solvent mixture (50/50 v/v) containing KCl standard electrolyte or KAc and HAc buffer solution. Our investigations were limited to neutral and acidic pH range, because earlier studies demonstrated that quercetin might undergo an irreversible structural change even in weak basic solutions. At high metal ion and flavonol ratio mainly binuclear complexes of the polyphenols have been appeared in buffered medium (pH 5.2). It was pointed out that the aluminium ions have not coordinated to the two different sides of the ligands. The apparent stability constants of Al₂Q and Al₂Ru complex formation also have been determined by computational iteration method in buffered medium.

Introduction

Quercetin (Fig. 1.a), the most common polyhydroxyflavone, is widely distributed in the plant kingdom. On the other hand rutin (Fig. 1.b), quercetin 3-O-rhamnosylglucoside, is individual in several plants, e.g. large quantity can be found in the flowers of *Sophora Japonica*. Lots of biological functions of these polyphenolic compounds have been reported [1] and their role are closely connected with antioxidative activity and chelating properties.

Flavonols are useful ligands for spectrophotometric analysis of aluminium [2, 3], and Al(III) is sensitive and selective reagents for determination of flavonols in complex form by HPLC or TLC [4, 5].

Quercetin (Q) and rutin (Ru) show strong electron-donor properties in ethanol-water solution [6] and have some possible chelating sites in consequence of the number and the position of OH-substituents in the molecules [7].

AlQ and AlRu complexes were found by [8] and the stability constants were calculated in acetate buffered methanol (pH = 5.0).

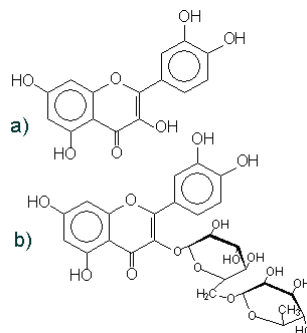
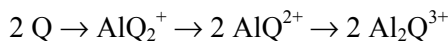


Fig. 1. Chemical formula of quercetin (a), rutin (b)

Spectrophotometric measurements, different ratio of metal ion and quercetin were used by [9], and presence of AlQ, Al₂Q and Al₂Q₃ particles were presumed. Chelating of one Al(III) at 4-oxo and 3-OH groups was supposed [8, 9], and the second at 3'-OH and 4'-OH groups of quercetin [9].

Three stages of complex forming were distinguished in neutral conditions by [10]. Following processes were hypothesized at increasing Al(III) concentration:



The different composition of particles was based on the molar ratio method of complexation.

Results

Strong complex forming of Al(III) and quercetin or rutin was detected in ethanol-water (50/50 v/v) solvent mixture additional presence of standard electrolyte or buffer solution. The solutions turned strong yellow after a few minutes, but the equilibrium of chelation required longer time. Pronounced bathochromic shifts and the isobestic point of the spectral bands of the flavonols were observed.

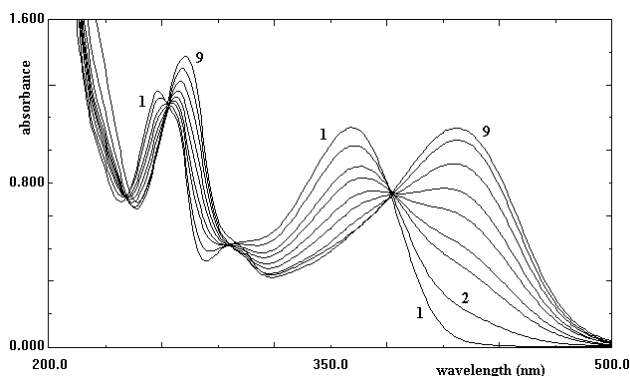


Fig. 2. Al(III)-rutin complex forming at constant rutin ($5.72 \cdot 10^{-5}$ M) and variable AlCl₃ ($2 \cdot 10^{-5}$ - $2.4 \cdot 10^{-2}$ M) concentration in KAc:HAc buffered ethanol-water solvent mixture (pH = 5.44)

The absorption spectra of Al(III)-quercetin and Al(III)-rutin system (Fig. 2.) were recorded at different Al(III) concentrations in the range of 200 to 500 nm wavelength by a Shimadzu UV-3101PC type UV-VIS-NIR Scanning Spectrophotometer, and the spectra were evaluated by version 2.2 of UV-2101/3101PC Personal Spectroscopy Software.

Complex forming of Al₂Q and Al₂Ru particles

were demonstrated in buffered medium by molar ratio method (Fig. 3.).

The apparent stability constants of aluminium-quercetin and aluminium-rutin complex formation have been determined by computational iteration method with using the measured absorbance at several wavelengths. The coordination of dimeric Al(III) form was presumed for the calculation. The equilibrium constants were calculated by the help of SCIENTIST for Windows computer program.

Table 1. Stability constants for aluminium complexes of quercetin and rutin

composition	log K
Al ₂ Q	3.96±0.05
Al ₂ Ru	3.61±0.04

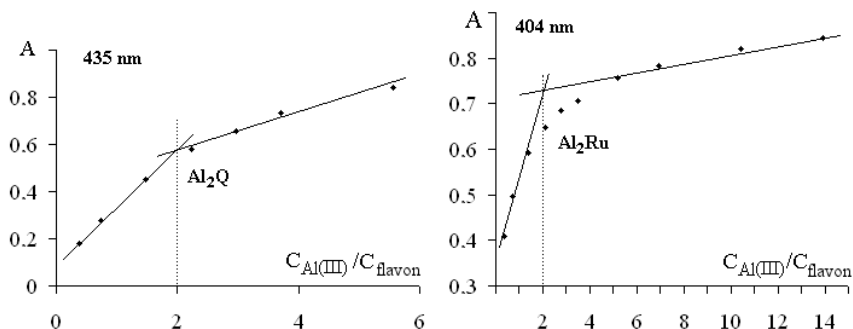


Fig. 3. Molar ratio method for complex forming of Al₂Q and Al₂Ru in buffered medium at high Al(III) concentration

Conclusion

It was established that mainly binuclear complexes of the flavonols have been formed in the aluminium-quercetin and aluminium-rutin coordination, if the metal ion and flavonol ratio is high. It was pointed out that dimeric form of aluminium hydroxyl particle has been connected to quercetin or rutin. The apparent stability constants of complexes have been determined by computational iteration method. In accordance with our previous supposition the spectrophotometric and calculation results have been proved the complex forming of Al₂Q or Al₂Ru in one step, and the aluminium ions have not been coordinated to the two different positions of OH-groups of the ligands.

References

- [1] B. H. Havsteen: *Pharmacology & Therapeutics*, 2002, **96**, 67-202.
- [2] N. V. Chernaya, V. G. Matyashov: *J. Anal. Chem. USSR*, 1975, **30**(4), 586-589.
- [3] E.A. Saad, *et. al*: *Microchim. Acta*, 2002, **140**(1-2), 87-91.
- [4] P.C.H. Hollman, *et. al*: *Analytical Chemistry*, 1996, **68**(19), 3511-3515.
- [5] S. Garcia, *et. al*: *Chromatographia*, 1993, **35**(7/8), 430-434.
- [6] L. Molnár-Hamvas, *et. al*: Acid-base properties of flavonoids in ethanol-water solvent mixture, *Proceeding of 39th International Conference on Solution Chemistry, Portorož (Slovenia), 21-25 Aug 2005*, 190.
- [7] L. Molnár-Hamvas, *et. al*: Interaction of metal ions and flavonol components of wood extractives, *Proceedings of 7th European Workshop on Lignocellulosics and Pulp, Turku (Finland) 26-29 Aug 2002*, 249-252.
- [8] B. Alluis, O. Dangles: *Helvetica Chim. Acta*, 2001, **84**, 1133-1156.
- [9] A.C. Gutierrez, M.H. Gehlen: *Spectrochimica Acta Part A*, 2002, **58**, 83-89.
- [10] J-P. Cornard, J-C. Merlin: *J. Inorg. Biochemistry*, 2002, **92**, 19-27.

SYNTHESIS, CHARACTERIZATION AND BIOLOGICAL ACTIVITY EVALUATION OF Zn(II), Pd(II) AND Pt(II) COMPLEXES WITH HETEROCYCLIC HYDRAZONE LIGANDS

N.R. Filipović¹, M.B. Rajković¹, T.R. Todorović², D.M. Sladić²,
I.T. Novaković³ and K.K. Anđelković²

¹Faculty of Agriculture, University of Belgrade, Nemanjina 6, Zemun;

²Faculty of Chemistry, University of Belgrade, P.O. Box 158, Belgrade;

³Institute of Chemistry, Technology and Metallurgy, Njegoševa 12, Belgrade, Serbia

Abstract

Two Pt(II) complexes with ligands derived *in situ* from ethyl hydrazinoacetate (etha) and either 2-acetylpyridine (ap) or 2-quinolinecarboxaldehyde (qa), were prepared and structurally characterized. Biological activity of novel Pt(II) complexes, as well as of previously synthesized Zn(II) and Pd(II) complexes with condensation derivatives of etha and ap, was tested by the brine shrimp test. All the compounds showed a moderate activity, the Pt(II) complexes being generally more active than Zn(II) and Pd(II) complexes. The results justify further study of biological effects of the complexes.

Introduction

Recently, we have reported the synthesis and characterization of symmetrical condensation derivatives of ap and either oxalic acid dihydrazide, *N',N''*-bis[(1*E*)-1-(2-pyridyl)ethylidene]ethanedihydrazide (H₂L1), or malonic acid dihydrazide *N',N''*-bis[(1*E*)-1-(2-pyridyl)ethylidene]propanedihydrazide (H₂L2) [1]. Cytotoxic activity of H₂L1 and H₂L2, as well as their complexes with Zn(II), [Zn(HL1)]ClO₄ (**1**), and [Zn(H₂L2)](ClO₄)₂ (**2**), against HeLa human cervical cancer and B16 murine melanoma cell lines was evaluated [2]. Both ligands and Zn(II) complexes showed IC₅₀ values in the low micromolar range. As the continuation of our research and as a part of further cytotoxic activity evaluation, Zn(II) and Pd(II) complexes, [Zn(apha)Cl] (**3**) and [Pd(aphaoet)Cl₂] (**4**), with asymmetrical condensation derivatives of ap and etha, (*E*)-2-[*N'*-(1-pyridin-2-yl-ethylidene)hydrazino]acetate (apha) and (*E*)-2-[*N'*-(1-pyridin-2-yl-ethylidene)hydrazino]acetic acid ethyl ester (aphaoet) have been synthesized [3].

In the present study, synthesis and characterization of two Pt(II) complexes, with aphaoet ligand and with a novel ligand, condensation derivative of qa and etha is reported. In addition, results of the biological activity evaluation for previously synthesized complexes **3** and **4**, as well as new Pt(II) complexes are reported.

Experimental

Measurements

IR spectra were recorded on Perkin-Elmer FT-IR 1725X spectrophotometer by the KBr technique. NMR spectra were obtained in DMSO-*d*₆ using Varian-Gemini 2000 spectrometer (¹H at 200 MHz, ¹³C at 50.3 MHz). Chemical shifts (δ) are given in ppm

using tetramethylsilane as internal standard. Elemental analysis (C, H, N) was performed by the standard micromethod at the Center for Instrumental Analysis of the Faculty of Chemistry, University of Belgrade, using the ELEMENTARVario ELIII C.H.N.S=O analyser. Biological activity of all complexes was tested by the brine shrimp test (toxicity to *Artemia salina*).

The complexes **3** and **4** were prepared according to the previously described methods [3].

Preparation of [Pt(aphaoet)Cl₂] (**5**)

To a solution of potassium tetrachloroplatinate(II) (0.16 g, 0.39 mmol) in water (1.5 cm³), a solution of etha-HCl (0.06 g, 0.39 mmol) and ap (0.05 g, 0.39 mmol) in ethanol (10 cm³) was added. The reaction mixture was heated with stirring at 65°C for 30 min, and a brown, microcrystalline product was obtained. The precipitate was filtered off and washed with water and ethanol (yield 72%). Anal. Calcd for C₁₁H₁₅Cl₂N₃O₂Pt (%): C, 27.1; H, 3.1; N, 8.6. Found: C, 27.4; H, 2.8; N, 8.4.

Preparation of [Pt(qahaoet)Cl₂] (**6**)

To a solution of potassium tetrachloroplatinate(II) (0.08 g, 0.19 mmol) in water (1.0 cm³), a solution of etha-HCl (0.03 g, 0.19 mmol) and qa (0.03 g, 0.19 mmol) in ethanol (10 cm³) was added. The reaction mixture was heated with stirring at 65°C for 20 min, and an orange, microcrystalline product was obtained. The precipitate was filtered off and washed with water and ethanol (yield 66%). Anal. Calcd for C₁₄H₁₇Cl₂N₃O₂Pt (%): C, 32.0; H, 3.3; N, 8.0. Found: C, 32.4; H, 3.1; N, 7.8.

Results and Discussion

Starting from 2-acetylpyridine or 2-quinolinecarboxaldehyde, K₂[PtCl₄] and ethyl hydrazinoacetate hydrochloride (molar ratio of 1:1:1) from ethanol/water solution under heating with stirring, the neutral square-planar Pt(II) complexes, [Pt(aphaoet)Cl₂] (**5**) and [Pt(qahaoet)Cl₂] (**6**), were obtained, respectively. In the complexes **5** and **6**, hydrazone ligand was coordinated in neutral form as a bidentate, analogously to the Pd(II) complex **4**. The third and fourth coordination sites, in both new complexes, were occupied by Cl⁻ ions (Fig. 1).

The positions of characteristic IR bands of complexes **5** and **6** are presented in the Table 1.

Table 1. Selected IR bands (cm⁻¹) of the complexes **5** and **6**

Complex	$\nu_{\text{N-H}}$	$\nu_{\text{C=O}}$	$\nu_{\text{C-O}}$	$\nu_{\text{C=N}}$	$\nu_{\text{N-N}}$
5	3600–3200	1735 s	1218 s	1609 m	1024 m
6		1737 s	1217 s	1579 m	1019 m

s – strong; m – medium

The common feature of ¹H NMR spectra for both complexes is the doublet of the methylene group attached to NH, centered at 4.19 (**5**) and 4.33 ppm (**6**). In the ¹H NMR spectrum complex **6**, the triplet at 1.24 and the quartet at 4.21 ppm of the ethoxy group are also present. Similar signals are present in the spectrum of complex **5**.

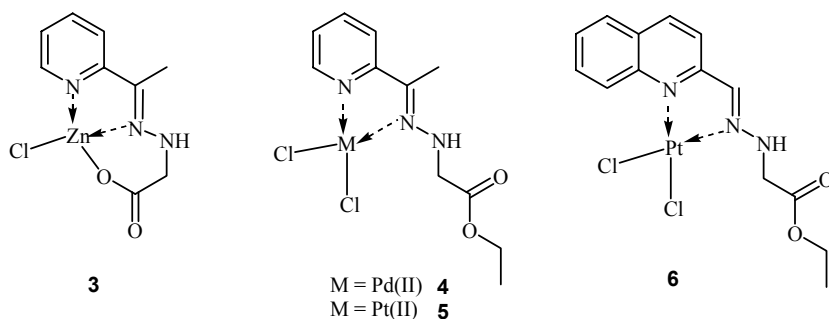


Fig. 1.

Biological activity of complexes **3** – **6** was tested by the brine shrimp test -toxicity to *Artemia salina* (Table 2).

Table 2. Toxic effect (expressed as LC₅₀ values in mM) of the complexes on *Artemia salina*

Complex	3	4	5	6
LC ₅₀ (mM)	2.56	0.80	0.49	0.54

All the compounds showed moderate activity, the Pt(II) complexes being generally more active than Zn(II) and Pd(II) complexes.

Conclusion

Two novel square-planar Pt(II) complexes with polydentate hydrazone type ligands were synthesized and characterized. Biological activity evaluation - toxicity to *Artemia salina* for new Pt(II) and for previously obtained Zn(II) and Pd(II) complexes, was performed. The Pt(II) complexes were more active than Zn(II) and Pd(II) complexes. The results justify further study of biological effects of the complexes.

Acknowledgements

This work was financially supported by the Ministry of Science and Environmental Protection of Serbia (Project № 142062).

References

- [1] K. Anđelković, D. Sladić, A. Bacchi, G. Pelizzi, N. Filipović and M. Rajković, *Transition Met. Chem.*, 2005, **30**, 243-250.
- [2] M. Lazić, S. Radulović, T. Todorović, D. Sladić, Ž. Tešić and K. Anđelković, *Mater. Sci. Forum*, 2006, **495**, 513-518.
- [3] N.R. Filipović, A. Bacchi, G. Pelizzi, R. Marković, D. Mitić and K.K. Anđelković, *J. Coord. Chem.*, 2005, **58**, 1541-1550.

SYNTHESIS AND STUDY OF THE COMPLEX [CO₂(CL)₂TPMC](BF₄)₂

G. Vučković¹, S. B. Tanasković², M. Antonijević-Nikolić³ and D. D. Radanović⁴

¹Faculty of Chemistry, University of Belgrade, Studentski trg 16, Belgrade, Serbia
(gordanav@chem.bg.ac.yu)

²Faculty of Pharmacy, University of Belgrade, Vojvode Stepe 450, Belgrade, Serbia
(sladjana@pharmacy.bg.ac.yu)

³High School of Technology, 15000 Šabac, Serbia

⁴Institute of Chemistry, Technology and Metallurgy, University of Belgrade,
Njegoševa 12, Belgrade, Serbia

Abstract

A new complex, [Co₂(Cl)₂tpmc](BF₄)₂ (tpmc = *N,N',N'',N'''*-tetrakis(2-pyridylmethyl)-1,4,8,11-tetraazacyclotetradecane), was isolated and studied by: UV/VIS spectra, IR, EPR (X-band), molar conductivity, magnetic measurements (SQUID) and X-ray diffraction analysis at low temperature. This is the first Co(II)tpmc complex for which crystal structure confirmed *chair* conformation of macrocycle.

Introduction

Dimeric Co(II) complexes with tpmc (fully *N*-substituted cyclam with 4 pendant 2-pyridylmethyl groups) [1] and various monodentate or chelate ligands were intensively studied [2] but up to now the X-ray analysis was performed for only one of them. It was μ -oxalato complex having tpmc in *boat* conformation [2b]. Although the majority of these compounds were air stable and for many of them *chair* conformation was proposed, it was difficult to isolate the suitable single crystals due to their decomposition or competition of solvent molecules and reactants for coordination sites, side reactions *etc.* Continuing these investigations, here we report the preparation of [Co₂(Cl)₂tpmc](BF₄)₂ and some of its physical and chemical properties including crystal structure [3].

Results and Discussion

The ligand tpmc was prepared according to the previously described procedure [1]. Reagent mixture (CoCl₂ · 6H₂O and tpmc in molar ratio 2:1 in CH₃CN-water) was heating at 80°C (reflux) and adding excess of NaBF₄.

[Co₂(Cl)₂tpmc](BF₄)₂ was synthesized in good yield (42.5%). The pure purple compound is well soluble in DMSO and CH₃CN, partially in CH₃OH, C₂H₅OH and cold CH₃CN, but insoluble in cold distilled water. The complex was stable up to 260°C. *Anal. Calc.* for Co₂C₃₄H₄₄N₈Cl₂B₂F₈ (FW = 927.15): C, 44.05; H, 4.78; N, 12.09. Found: C, 44.16; H, 4.75; N, 12.10. The single crystal suitable for X-ray analysis was chosen mechanically. Molar electrical conductivity in CH₃CN of 265

$\text{Scm}^2\text{mol}^{-1}$ is in agreement with a 1:2 electrolyte type (literature range is 220-300 $\text{Scm}^2\text{mol}^{-1}$) [4].

UV/VIS spectrum of $[\text{Co}_2(\text{Cl})_2\text{tpmc}](\text{BF}_4)_2$ in CH_3CN is typical for a high-spin Co(II) complex exhibiting maxima at 479 nm ($\epsilon=104 \text{ dm}^3\text{mol}^{-1}\text{cm}^{-1}$), 549 nm ($\epsilon=134 \text{ dm}^3\text{mol}^{-1}\text{cm}^{-1}$) and 589 nm ($\epsilon=156 \text{ dm}^3\text{mol}^{-1}\text{cm}^{-1}$). The absorption maximum for CT transitions is at ~ 212 -215 nm ($\epsilon=6000$ -8700 $\text{dm}^3\text{mol}^{-1}\text{cm}^{-1}$) [4b]. In reflectance spectrum there is the maximum at 546 nm and shoulders at 508 nm and 573 nm.

The IR spectrum of the complex displays characteristic bands (cm^{-1}): $\nu(\text{C-H})$ at 2948 (medium), $\nu(\text{BF}_4^-)$ at 1068 (strong, sharp); skeletal pyridine vibration from tpmc at 1610 (strong) suggesting coordination of tpmc and the presence of BF_4^- as counter ion [4c]. The structure was solved by direct methods [5] Crystal data: monoclinic, space group $P2_1/c$, $a = 8.843(2)$, $b = 20.985(4)$, $c = 11.030(2)$ Å, $\beta = 109.43(3)^\circ$, $V = 1930.3(7)$ Å³, $Z = 2$, $D_c = 1.595 \text{ g cm}^{-3}$, $\lambda(\text{MoK}\alpha) = 0.71073$ Å, $T = 130\text{K}$, $\mu = 1.075 \text{ mm}^{-1}$, $F(000) = 948$. The ORTEP drawing of the $[\text{Co}_2(\text{Cl})_2\text{tpmc}]^{2+}$ is depicted in Figure 1. The geometry around each Co(II) is distorted trigonal bipyramide formed by two cyclam N atoms and two N from pyridyl groups (*exo* coordination). The fifth coordination site is occupied by Cl⁻ and tpmc adopted *chair* conformation. Magnetization measurements in the temperature range of 1.9 – 300 K were carried out on powdered samples, and EPR spectra (X-band) in the temperature range 4.2 - 300 K. Co(II) magnetic centers in the described complex are sufficiently separated from each other (5.710 Å) and both bridging systems (Co-N-C-C-C-N-Co) are ineffective for the magnetic exchange interaction. The value of the $\chi_m T$ at 300 K is $2.65 \text{ cm}^3\text{Kmol}^{-1}$ (μ_{eff} per Co^{II} center equals 4.61 B.M.) which is larger than that expected for the spin-only value of high-spin cobalt(II), $\chi_m T = 1.87 \text{ cm}^3\text{Kmol}^{-1}$ $S=3/2$ ($\mu_{\text{eff}}=3.87$ B.M.). It indicates that an important orbital contribution is involved. The $\chi_m T$ values continuously decrease with lowering temperature, to the value $1.19 \text{ cm}^3\text{Kmol}^{-1}$ at 1.8 K. The χ_m curve starts from $0.00873 \text{ cm}^3\text{mol}^{-1}$ at 300 K and increases in a uniform way to $0.663 \text{ cm}^3\text{mol}^{-1}$ at 1.8 K. The values of Curie (C) and Weiss (θ) constants, for the higher temperature range 50-300 K are equal to $2.695 \text{ cm}^3\text{Kmol}^{-1}$ and -8.8 K, respectively. The absence of a maximum in χ_m curve indicates that possible antiferromagnetic coupling is very weak. As a consequence of the fast spin-lattice relaxation time of Co(II) magnetic centre, EPR signals were observed only at the lowest temperatures. In the spectrum of the complex at 4.2 K an asymmetric signals characteristic for a highly anisotropic g factor, appeared. Spectroscopic splitting factors are equal: $g_1=5.04$, $g_2=3.52$ and $g_3=2.01$, which are assigned to $\Delta m = \pm 1/2$ transition of the $S=3/2$ system. As the temperature of sample is increased, spectrum become broader, and disappeared at around 30K.

Conclusion

New $[\text{Co}_2(\text{Cl})_2\text{tpmc}](\text{BF}_4)_2$ complex was prepared, and studied by spectroscopic, magnetic measurements and its crystal structure solved by X-ray diffraction analysis. This is the first Co(II) complex for which is confirmed a *chair* conformation of tpmc ligand.

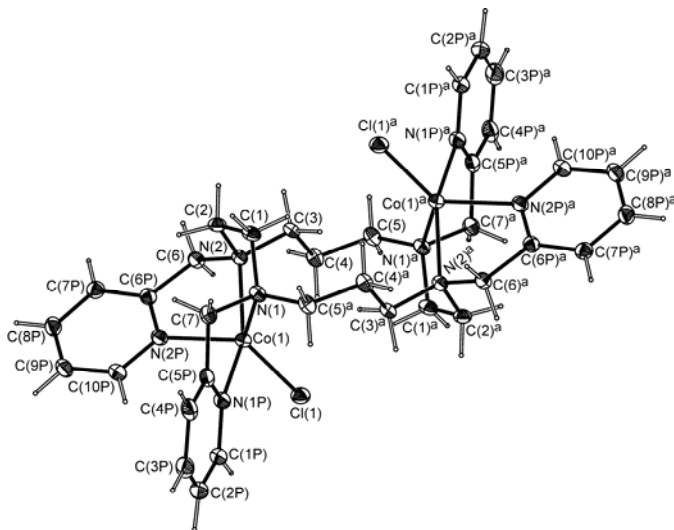


Fig. 1. The ORTEP drawing of the $[\text{Co}_2(\text{Cl})_2\text{tpmc}]^{2+}$

References

- [1] S-G. Kang, S-J. Kim, Bull. Korean. Chem. Soc., 2003, **24**, 269;
- [2] a) H. Harada, M. Kodera, G. Vučković, N. Matsumoto, S. Kida, Inorg. Chem., 1991, **30**, 1190; b) S.P. Sovilj, G. Vučković, K.B. Babić-Samardžija, N. Matsumoto, V.J. Jovanović, J. Mroziński, Synth. React. Inorg. Met.-Org. Chem., 1999, **29**, 785 c) G. Vučković, M.T. Šumar, I.D. Brčeski, V.M. Leovac, D.S. Mitić, J. Serb. Chem. Soc., 1999, **64** (3), 191; d) G. Vučković, V. Stanić, S.P. Sovilj, M. Antonijević-Nikolić, J. Mroziński, J. Serb. Chem. Soc., 2005, **70** (8-9), 1121.
- [3] G. Vučković, S.B.Tanasković, U.Rychlewska, D.D.Radanović, J.Mrozinski, M.Korabik, J.Mol.Struc., 2006, accepted for on-line publication
- [4] a) W. J. Geary, Coord. Chem. Rev., 1980, **33**, 227; b) B. P. Lever, Inorganic Electronic Spectroscopy, 2nd ed., Elsevier, Amsterdam, 1984, pp.554-573; 481-505; c) K. Nakamoto, Infrared and Raman Spectra of Inorganic and Coordination Compounds, Part B, 5th ed. Willey and Sons, New York.
- [5] a) G.M. Sheldrick, Acta Crystallogr. Sect. A, 1990, **46**, 467. b) G.M. Sheldrick SHELXL-97, Program for the refinement of crystal structures, University of Göttingen, Germany, 1997.

COMPLEX COMPOUNDS OF Pd(II) AND *O,O'*-DIISOPROPYL-(*S,S*)-ETHYLENEDIAMINE-*N,N'*- -DI-2-PROPANOATO LIGAND

B. B. Krajčinović¹, G. N. Kaluđerović^{1,2}, D. Steinborn², Ch. Wagner²,
K. Merzweiler², S. R. Trifunović³, Z. M. Miodragović⁴ and T. J. Sabo⁴

¹Department of Chemistry, Institute of Chemistry, Technology and Metallurgy,
Studentski trg 14, Belgrade, Serbia

²Institut für Anorganische Chemie, Martin-Luther-Universität Halle-Wittenberg,
Kurt-Mothes-Straße 2, D-06120 Halle, Germany;

³Department of Chemistry, Faculty of Science, University of Kragujevac, 34000 Kragujevac, Serbia

⁴Faculty of Chemistry, University of Belgrade, P.O. Box 158, Belgrade, Serbia

Abstract

Two novel palladium complexes were synthesized in a reaction of $K_2[PdCl_4]$ with *O,O'*-diisopropyl-(*S,S*)-ethylenediamine-*N,N'*-di-2-propanoate. Complex **1**, $[PdCl_2\{dip(S,S)eddp\}]$, dichloro(*O,O'*-diisopropyl-(*S,S*)-ethylenediamine-*N,N'*-di-2-propanoate)palladium(II), was characterized by elemental analysis, IR, ¹H and ¹³C NMR spectroscopy. The structure of complex **2**, $[PdCl\{ip(S,S)eddp\}]$, chloro(*O*-isopropyl-(*S,S*)-ethylenediamine-*N,N'*-di-2-propanoate)palladium(II), was determined by the X-ray diffraction analysis.

Introduction

In our previous work it was found that the cytotoxic action of Pt(IV) complexes with *N,N* bidentate ethylenediamine-*N,N'*-di-3-propanoate esters is fairly comparable to that of cisplatin [1,2].

It was interesting to try to synthesize similar compounds with palladium and two novel palladium complexes were synthesized in a reaction of *O,O'*-diisopropyl-(*S,S*)-ethylenediamine-*N,N'*-di-2-propanoate, $[dip(S,S)eddpH_2]Cl_2$, with $K_2[PdCl_4]$. These complexes may also have cytotoxic activity so the goal of our future research will be to investigate that.

Experimental

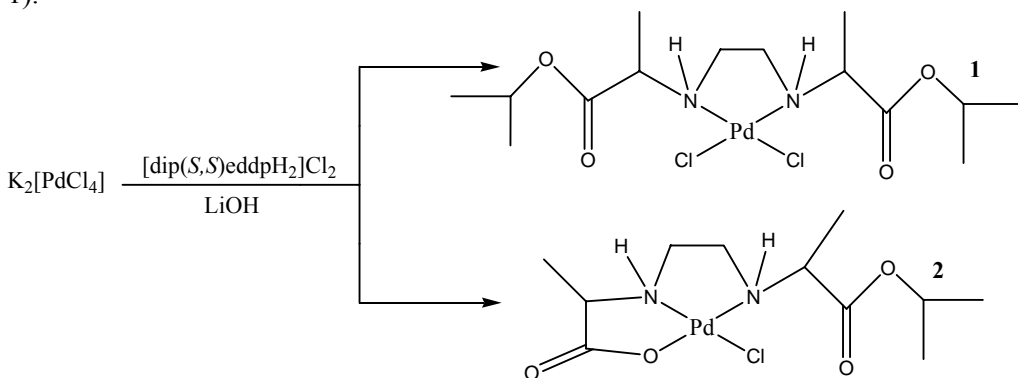
$K_2[PdCl_4]$ (0.158 g, 0.512 mmol) was dissolved in 20 ml of water on a water bath on 40 °C, and $[dip(S,S)eddpH_2]Cl_2$ (0.185 g, 0.512 mmol) was added in the solution. During two hours of stirring 10 ml of 0.1M LiOH (0.040 g, 1.024 mmol) was added in small portions to the reaction solution. Cooling to the room temperature yellow precipitate was obtained (scheme 1, complex **1**). Yield: 56 %. Anal. calcd. for **1**: %C=36.11, %H=6.06, %N=6.02; found: %C=35.79, %H=6.33, %N=5.77.

Crystals of complex **2** suitable for X-ray diffraction measurements were obtained from mother liquor of complex **1**. Intensity data were collected on a STOE IPDS diffractometer at 220 K using graphite monochromatized Mo $K\alpha$, radiation ($\lambda = 0.71073$ Å). Crystallographic data: $C_{11}H_{21}ClN_2O_4Pd$, monoclinic system, space group $P2_1$, $a =$

5.877(1) Å, $b = 9.672(2)$ Å, $c = 14.424(3)$ Å, $\alpha = \gamma = 90^\circ$, $\beta = 100.78(2)^\circ$ $V = 805.5(3)$ Å³, $Z = 2$, $D_c = 1.584$ Mg/m³, $\mu(\text{MoK}\alpha) = 1.328$ mm⁻¹, $F(000) = 386$. Data collection: $2.55 < \theta < 25.80^\circ$, no. of parameters: 194 $R = 0.035$, $wR2 = 0.085$ for 1543 reflections with $I > 2\sigma(I)$; Flack parameter = 0.06(4).

Results and Discussion

The addition of an aqueous solution containing the $[\text{dip}(S,S)\text{eddpH}_2]\text{Cl}_2$ to a solution of $\text{K}_2[\text{PdCl}_4]$ after cooling produced yellow precipitate (Scheme 1, complex **1**). The mother liquor of complex **1** was left for several days on room temperature and crystal suitable for X-ray crystallography were obtained (Scheme 1, complex **2**; Fig 1).



Scheme 1. Reaction of $\text{K}_2[\text{PdCl}_4]$ with $[\text{dip}(S,S)\text{eddpH}_2]\text{Cl}_2$.

Complex **1** was characterized by elemental analysis, IR, ^1H and ^{13}C NMR spectroscopy. IR spectrum of the ligand shows specific absorption bands: $\nu(\text{C}=\text{O})$ at 1734 cm^{-1} (strong), (typical absorption for aliphatic esters); $\nu(\text{C}-\text{O})$ at 1239 cm^{-1} (strong) and $\nu(\text{CH}_3)$ at 2982 cm^{-1} (medium); however, the IR spectrum of complex **1** shows the absence of absorption bands for secondary ammonium salts, and the band for $\text{C}=\text{O}$ group is at the exactly same position as in the spectrum of the free ligand, indicating that coordination occurred *via* nitrogen atoms of the secondary amino group. This is also confirmed by the existence of an absorption band $\nu(\text{N}-\text{H})$ at 3153 cm^{-1} . Absorption band assigned to $\nu(\text{CH}_3)$ is almost at the same position 2983 cm^{-1} , indicating that the ester groups did not hydrolyze [3]. In the ^1H NMR spectrum of complex **1** resonance of the methyl H-atoms from the iso-propyl ester groups at 1.61 and 1.69 ppm as doublets was found (free ligand 1.61 ppm, doublet). Also, the resonances arising from the ester C-atoms were found at 170.9 and 169.4 ppm (free ligand 172.2 ppm).

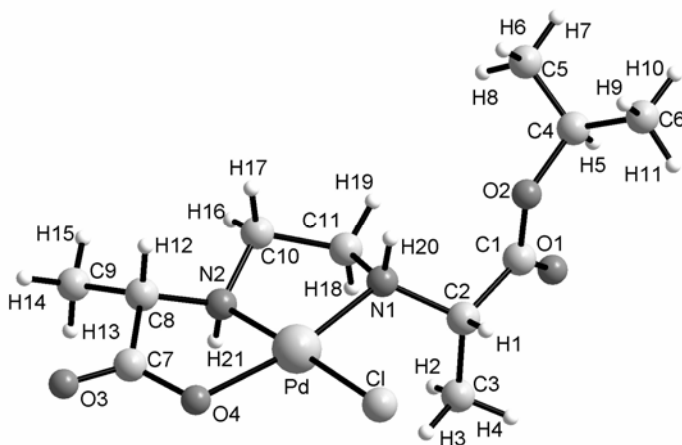


Fig. 1. Structure of $[\text{PdCl}\{\text{ip}(\text{S},\text{S})\text{eddp}\}]$, complex **2**.

A square-planar geometry of Pd(II) ion in complex **2** was found, with two nitrogen, one oxygen and one chlorine atom in the coordination sphere. X-ray data of complex **2** have shown that one of the ester groups hydrolyzed, and that the free carboxylate group took place in coordination with the Pd(II) ion. The bond distances Pd–N, Pd–O and Pd–Cl are in agreement with the similar complexes described in literature data [4].

Conclusion

Reaction of $\text{K}_2[\text{PdCl}_4]$ and $[\text{dip}(\text{S},\text{S})\text{eddpH}_2]\text{Cl}_2$ in aqueous solution afforded $[\text{PdCl}_2\{\text{dip}(\text{S},\text{S})\text{eddp}\}]$ and $[\text{PdCl}\{\text{ip}(\text{S},\text{S})\text{eddp}\}]$ complexes. The presence of the esters methyl groups for complex $[\text{PdCl}_2\{\text{dip}(\text{S},\text{S})\text{eddp}\}]$ was confirmed by infrared, ^1H and ^{13}C NMR spectroscopy. In $[\text{PdCl}\{\text{ip}(\text{S},\text{S})\text{eddp}\}]$ complex hydrolysis of one ester group from $[\text{dip}(\text{S},\text{S})\text{eddpH}_2]\text{Cl}_2$ ligand was confirmed by X-ray crystallography.

References

- [1] G. N. Kaluđerović, D. Miljković, M. Momčilović, V. M. Djinović, M. Mostarica-Stojković, T. J. Sabo, V. Trajković, *Int. J. Cancer*, 2005, **116**, 479–486.
- [2] S. Mijatovic, D. Maksimović-Ivanić, J. Radovica, D. Miljković, G. N. Kaluđerović, T. J. Sabo, V. Trajković, *Cell. Mol. Life Sci.*, 2005, **62**, 001–008.
- [3] T. J. Sabo, G. N. Kaluđerović, S. R. Grgurić-Šipka, F. W. Heinemann, S. R. Trifunović, *Inorg. Chem. Comm.*, 2004, **7**, 241–244.
- [4] G. N. Kaluđerović, F. W. Heinemann, N. Ž. Knežević, S. R. Trifunović, T. J. Sabo, *J. Chem. Crystall.*, 2004, **34**, 185–189.

STUDY OF COPPER(II)-DEXTRAN COMPLEXES STABILITY BY CONDUCTOMETRY METHOD

G.S. Nikolić¹, Ž. Mitić², M. Cakić¹ and Lj. Ilić³

¹*Faculty of Technology, Bulevar Oslobođenja 124, 16000 Leskovac, Serbia
(goranchem_yu@yahoo.com)*

²*Faculty of Medicine, Bulevar dr Žorana Djindjića 81, 18000 Niš, Serbia*

³*Pharmaceutical and Chemical Industry "Zdravlje", 16000 Leskovac, Serbia*

Abstract

Water solutions stability of Cu(II) complexes with reduced low-molar dextran (RLMD) were investigated by conductometry methods. Formation of three different types of complexes with deprotonized dextran monomer units (Glc⁻) is suggested: Cu(Glc)₂(H₂O)₂ at pH 7-8, Cu(Glc)₂(H₂O)(OH)⁻ at pH 8-10 and Cu(Glc)₂(OH)₂²⁻ at pH 10-12. The results of conductivity investigations showed that the complex synthesized in weak alkaline solution (pH 7-8) has the greatest stability. The decomposition and conversion of Cu(II)-dextran complex to a new Cu(OH)₄²⁻ complexes at pH ≥ 12 is confirmed by conductometric data.

Introduction

Biometal complexes of a polysaccharide dextran are the subject of the intensive research mainly because of its possible application in veterinary and human medicine [1]. Copper(II) complexes are of a special interest since they could be used for the treatment of hypocupremia and anemia. In this paper we present the results of correlations between the structure and the stability study of copper(II) complexes with RLMD by conductometry methods.

Experimental

Low-molar dextran (LMD, M_w = 5000 g mol⁻¹) was obtained from the pharmaceutical company "Zdravlje" (Leskovac, Serbia). The reduction of dextran was performed with NaBH₄, with subsequent purification on ion-exchange columns (Amberlite IR-120 and Amberlite IRA-410 resins). The reduced group content in the final product was measured by the Somogyi method and found to be below 0.1%. The synthesis of the complexes was performed at the pH values ranging from 7 to 12 by boiling the reactant solution containing reduced low-molar dextran and CuCl₂ [2]. The green solution of the complex was filtrated and the complex precipitated by the addition of 96% ethanol. Unbounded Cu(II) ions were removed by dialysis. Conductivity meter HANNA HI 8020 (HANNA Instruments) was employed for the conductivity measurements. Conductivity meter was calibrated with the HI 7031 standard solution. Conductivity of water solutions (200 mg complex in 20 cm³ of redistilled water) was monitored 50 days and measured three times a day at room temperature with a constant stirring on magnetic stirrer.

Results and Discussion

With the complexes Cu(II)-RLMD that are synthesized in the neutral and weak alkaline solution (pH 7.5 i pH 8) very low conductivity values are noticed (105 and $215 \mu\text{Scm}^{-1}$, respectively, Fig. 1), comparing with the conductivity of the Cu(II) ions water solution of the same concentration ($2580 \mu\text{Scm}^{-1}$). The conductivity growth during the first 20 days is approximately $20 \mu\text{Scm}^{-1}$, and then the conductivity value of the solution remains constant. With the complex Cu(II)-RLMD that is synthesized in the alkaline solution (pH 10) conductivity values are considerably higher ($640 \mu\text{Scm}^{-1}$), which indicates the more unstable complex. The conductivity growth during the first 20 days is a little bit increased than in the previous case ($30 \mu\text{Scm}^{-1}$), and then the conductivity value of the solution rapidly decreases below the initial value (Fig. 1). The fact indicate precipitation of the insoluble $\text{Cu}(\text{OH})_2$. And afterwards it keeps the constant value, similar to the previous case. With the complex Cu(II)-RLMD that is synthesized at pH 12, conductivity value is 10 times higher comparing to the conductivity of the complex obtained at pH 7.5. The conductivity rapidly increases in the same period of time of 20 days, with the considerably higher growth of $60 \mu\text{Scm}^{-1}$, and then rapidly decreases to its initial value (Fig. 1).

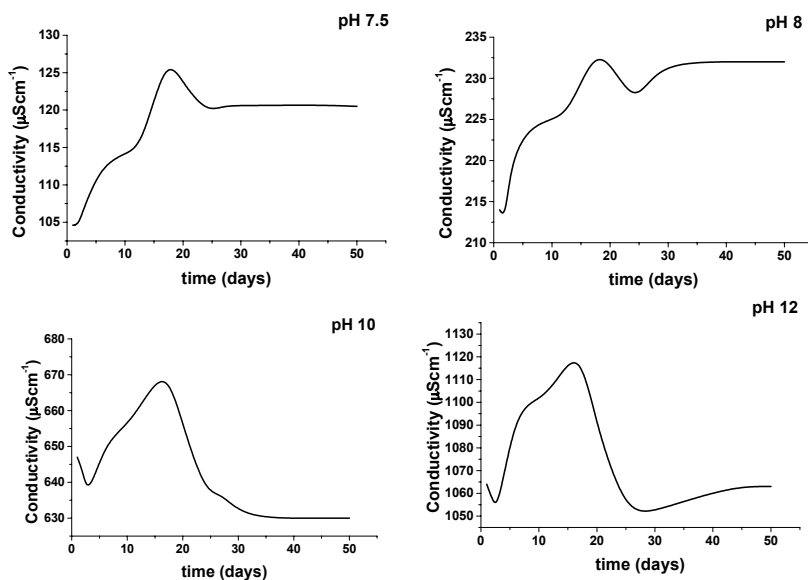


Fig. 1. Water solution conductivity of Cu(II) complexes with RLMD in function of time, at different pH synthesis values.

On the basis of the obtained results by spectrophotometric investigation of this complexes [3] three different types of Cu(II) complexes structure with dextran monomer unit are suggested depending on pH synthesis (Fig. 2).

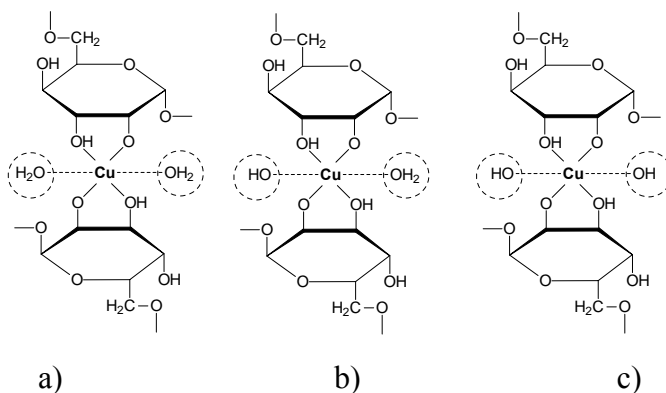


Fig. 2. Structure models of Cu(II) complexes with RLMD:
 a) type I, pH 7-8 b) type II, pH 8-10 c) type III, pH 10-12

Having in mind the small conductivity of the complexes got in the range pH 7-8 (Fig. 1), as well as the fact that the structure having two coordinated water molecules (type I, Fig. 2a), it can be concluded that the conductivity growth originates from free Cu(II) ions. Considerably higher conductivity values of the complexes obtained in the alkaline solution (pH 10), indicate a less stable Cu(II) complex. Considering the fact that one OH⁻ ion displaces a water molecule in the structure of this complex (type II, Fig. 2b), it is clear that the higher conductivity and the higher growth probably partly originated from free Cu(II) ions and partly from a negatively charged complex molecule due to the presence of the OH⁻ ion. The fact is also confirmed by means of spectroscopic techniques (ESR, LNT FTIR, UV-VIS) [4]. With the Cu(II)-RLMD complex that is synthesized at pH 12, two OH⁻ ions are involved (type III, Fig. 2c), and so the conductivity value is twice higher in relation to the complex obtained at pH 10. During the first 20 days the conductivity reaches the maximum value of 1120 μScm^{-1} , and then rapidly decreases due to precipitation of the insoluble Cu(OH)₂. The further slightly increase of conductivity values indicates decomposition and conversion of Cu(II)-dextran complex to a new Cu(OH)₄²⁻ ions.

Conclusion

According to the results obtained by the conductivity investigation it can be concluded that the complex synthesized in weak alkaline solution (pH 7-8) shows the greatest stability.

References

- [1] B. Gyuresik, L. Nagy, *Coord. Chem. Rev.*, 2000, **203**, 81-149.
- [2] G. Nikolić, M. Cakić, Ž. Mitić, R. Nikolić, *Chemical Industry*, 2005, **59**, 9-14.
- [3] Ž. Mitić, M. Cakić, Lj. Ilić, G. Nikolić, *Svet polimera*, 2004, **7**, 225-229.
- [4] G.M. Nikolić, Lj. Ilić, M. Cakić, G.S. Nikolić, R.S. Nikolić, Ž. Mitić, 7th ICFAAPC, Belgrade, Serbia, Conference Proceedings, 2004, **Vol II**, 775-777.

COPPER(II) COMPLEXES OF REDUCED LOW-MOLAR DEXTRAN: A DECONVOLUTED LNT-FTIR STUDY

G.S. Nikolić¹, M. Cakić¹, Ž. Mitić² and Lj. Ilić³

¹*Faculty of Technology, Bulevar Oslobođenja 124,
16000 Leskovac, Serbia (goranchem_yu@yahoo.com)*

²*Faculty of Medicine, Department of Pharmacy, Bulavar dr Zorana Djindjića 81,
18000 Niš, Serbia (zak_chem2001@yahoo.com)*

³*Pharmaceutical and Chemical Industry "Zdravlje", Vlajkova 199,
16000 Leskovac, Serbia*

Abstract

Origin synthesized Cu(II) complexes with reduced low-molar dextran (RLMD, Mw 5000 g mol⁻¹) were investigated by LNT-FTIR methods. Deconvoluted RT- and LNT-FTIR spectra of dextran and its complexes with copper(II) were analyzed in order to find the most specific spectral peculiarities. The changes in intensity and width of the IR bands in region 1450-1050 cm⁻¹ were related to changes in conformation and short-range interactions of the dextran. The results of the FTIR spectroscopy study allowed one to suggest a predominant crystalline form of copper(II)-dextran complexes.

Introduction

The numerous investigations have indicated that the dextran has the extraordinary power of forming the water-soluble complexes with various biometals [1]. It has been established that the degree of copper binding within the complex depends primarily on the pH of the solution, as well as on the participation both of the OH groups and the H₂O molecules in the coordination sphere of copper. The emergence of modern structural chemical methods such as Fourier-transform infrared spectroscopy (FTIR) made it possible to assign the binding OH or other groups, and also to characterize the metal ion coordination of carbohydrates, monitoring the ligand conformation or/and configuration changes forced by the complexation processes.

Experimental

The synthesis of the complexes was performed at the pH values ranging from 7 to 12 by boiling the reactant solution containing RLMD and CuCl₂. For IR sample preparation was used KBr pastille method. The dryness of the pastille was controlled by the band at ca. 1640 cm⁻¹, which is associated with the deformation vibrations of the OH bond from water molecules. The IR spectra as average of 40 scans were recorded at room (298 K) and liquid-nitrogen (77 K) temperature on FTIR spectrometer BOMEM MB-100 (Hartman-Braun) equipped with standard DTGS/KBr detector, in the range 4000-400 cm⁻¹ with resolution of 2 cm⁻¹, by Win-Bomem Easy software. A variable temperature cell Specac P/N 21525 was used for the LNT measurements. In the region all spectra were baseline corrected and area normalized. A Fourier self-deconvolution based on the Griffiths/Pariente method was applied to enhance resolution in the spec-

tral region of $4000 - 400 \text{ cm}^{-1}$. A gamma factor of 12, corresponding to a peak width of 24 cm^{-1} , was used. Deconvoluted spectra were smoothed by the 30-point Savitzky-Golay filter method.

Results and Discussion

IR spectrum of the dextran consist characteristic bands: $\nu(\text{OH}) 3400 \text{ cm}^{-1}$, $\nu(\text{CH}) 2930 \text{ cm}^{-1}$, $\delta(\text{HOH}) 1640 \text{ cm}^{-1}$, $\delta(\text{CH}) 1450$ and 1345 cm^{-1} , $\delta(\text{OH}) 1420 \text{ cm}^{-1}$, complex band $\nu(\text{CO})$ and $\nu(\text{CC}) 1200-1000 \text{ cm}^{-1}$, $\gamma(\text{CH}) 1000-700 \text{ cm}^{-1}$. Dextran and its complexes with Cu(II) have one crystallographic type of water molecule (1640 cm^{-1}). Water protons take part in the formation of relatively weak hydrogen bonds [2]. Spectroscopic IR study in particular region of OH (3400 and 1420 cm^{-1}) and CH (2900 , 1460 and 1350 cm^{-1}) vibrations indicates different binding between central metal ion and ligand, depend of pH and metal contents. The main bands found in the deconvoluted spectra of dextran and complex at ca. 1154 , 1108 , 1077 , 1042 and 1015 cm^{-1} are due to coupled valent vibrations of the C-O and C-C bonds and deformational vibrations of the CCH, COH and HCO bonds. The band at about 1150 cm^{-1} has been assigned to valent vibrations of the C-O-C bond and glycosidic bridge. The broad peak at 1108 cm^{-1} should be most likely ascribed to the vibration of the C-O bond at the C4 position of glucose units. Complex vibrations involving the stretching of the C6-O6 bond with participation of the deformational vibrations of the C4-C5 bond result in an appearance of the band at 1077 cm^{-1} . The band at 1077 cm^{-1} in the spectra of dextran is less pronounced than in the spectra of complex. The band at about 1042 and 1015 cm^{-1} found for saccharide in the spectra of dextran and complex were shown to relate to the crystalline and amorphous phases, respectively [3]. The changes in intensity of these bands are strongly associated with the alterations in the macromolecular order. These bands in the spectra of dextran and complex may be responsible for the more and less ordered structures, respectively.

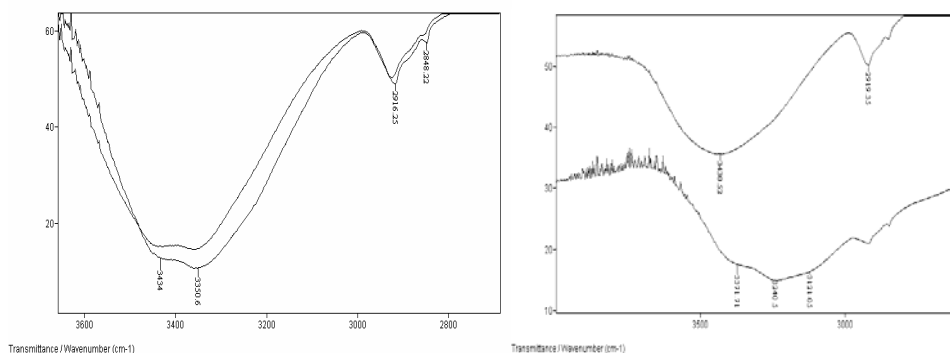


Fig. 1. RT and LNT FTIR deconvoluted spectra of: Cu(II)-RLMD at pH 7.5 (A); Cu(II)-RLMD complex at pH 12 (B);

The infrared spectra of Cu(II)-dextran complexes synthesized at different pH (S2-complex at pH 7-8, and S4-complex at pH 10-12) recorded at RT (298 K) and LNT (77 K) are presented on Fig. 1. The correlation between OH stretch frequency and H-

bond strength ($3600\text{--}3100\text{ cm}^{-1}$) predicts a red-shift of the bonded OH stretching band on cooling (from 3425 to 3371 cm^{-1}). It is expected that non-interacting OH group (3430 cm^{-1}) to be much less sensitive to cooling and consequently will show smaller red-shifts. The red-shift of the band is an indication for the involvement of the appropriate OH proton in a weak H-bond. In the LNT-IR spectra of complex S2 two bands (3440 and 3356 cm^{-1}) are found in the region of $\nu(\text{OH})$ vibrations. In this region, there are three bands (3371 , 3238 and 3127 cm^{-1}) in LNT spectra of complex S4. The different of the number, frequencies, intensity and shape of these bands implies that in the complexes S4 there are displacement of H_2O molecules by the OH groups in the first coordination sphere of copper. As follows from the LNT-IR spectra of the complex S2, all other bands in the $\gamma(\text{OH})$ bending region from libration of water molecule (823 , 720 , 708 and 570 cm^{-1}) show blue-shifts on cooling. The vibrations of OH group in this region of complex S4 were much less sensitive to cooling. The observation allowed one to suggest that the most probable water molecules are coordinated around copper(II) in the complex S2. These results agree with a structural studies of the investigated complexes have been based on UV-Vis and ESR spectrophotometry [4].

Conclusion

On forming the copper(II)-dextran complexes there have been included the OH groups on C2 and C3 by atoms of the dextran-monomer unit (the glucose) and that there are no effects leading to the changes in conformation of the macromolecules. Dextran complexes are formed by the displacement of H_2O molecules from the first coordination sphere of copper by the OH groups. From LNT-IR it follows that non-donating OH group is insensitive to temperature variation whereas a bonded OH shows a significant red-shift upon cooling.

Acknowledgement

This study was supported by the Ministry of Science and Environmental protection of the Republic of Serbia, for the scientific research under the Project TR 6708.

References

- [1] V.N. Tolmachev, Z.A. Lugovaya, Vysokomol. Soedin., 1976, **18**(B) 548.
- [2] M. Cakić, G. Nikolić, Lj. Ilić, Bull. Chem. Technol. Macedonia, 2002, **21**(2), 135-146.
- [3] G. Nikolić, M. Cakić, D. Cvetković, Lj. Ilić, P. Premović, Spectrosc. Lett., 1996, **29**(7), 1437-1448.
- [4] G. Nikolić, M. Cakić, Ž. Mitić, R. Nikolić, Lj. Ilić, Chemical Industry, 2005, **59**, 9-14.

General Physical Chemistry

(N)

GEOCHEMISTRY OF “IMPACT LAYER” OF THE CRETACEOUS-TERTIARY BOUNDARY (KT) FISH CLAY AT HØJERUP (STEVNS KLINT, DENMARK)

P. I. Premović

*Laboratory for Geochemistry, Cosmochemistry & Astrochemistry, University of Niš,
P.O. Box 224, 18000 Niš, Serbia. (asteroid.pavle@yahoo.com)*

Abstract

Fish Clay at Højerup consists of a thin red clay layer overlain by a thick of black marl. The red (“impact”) layer is made up mainly from the distinctive cheto Mg-smectite; it also has distinct characteristics, such as the extreme thinness (maximum *ca.* 0.3-0.5 cm), a high content of the pyritized microspherules, shocked quartz grains, and non-altered/altered impact-derived glass shards and meteoritic fragments. It is considered by many researchers of KT that the red layer of Fish Clay at Højerup represents the original impact-ejecta fallout created by the KT asteroidal impact at Chicxulub (Yucatan Peninsula, Mexico). I discuss its unique geochemical characteristics which may be important in understanding of the geochemical and depositional processes that occurred during the sedimentation of Fish Clay at Højerup.

Introduction

Fish Clay at Højerup is a classic KT boundary. We can differentiate four distinctive layers (II, III, IV and V) within this boundary. II is underlain by the Maastrichtian chalk (I), and V is overlain by the Danian cerithium limestone (VI). III can be subdivided into the red layer IIIA (*ca.* 0.3-0.5 cm thick) which is overlain by the black marl IIIB (*ca.* 2 cm thick), Fig. 1. IIIA/B is here considered to constitute the main part of the KT boundary section at Højerup. There is, however, no sharp boundary between IIIA and IIIB and it makes difficult to distinguish the top of IIIA and the base of IIIB.

The mineralogy of IIIA is comparatively simple and the characteristic cheto Mg-smectite being the principal components. The origin of IIIA is still controversial. Kyte *et al.* [1] consider that only IIIA (referred usually as the “impact layer”) is a sole representative of the original impact-ejecta fallout generated by the KT asteroidal impact at Chicxulub. Recently, Bauluz *et al.* [2] provided some experimental evidence (scanning electron microscopy and transmission electron microscopy/analytical electron microscopy) which support this conclusion. In stark contrast, Schmitz [3] concluded that IIIA is made up of locally derived clays. This author, also, argued that a very small part, if any, of smectite of IIIA/B was derived from the impact fallout (asteroidal/target rocks). In this report, we review the geochemical data for IIIA, including those related to Cu²⁺-porphyrins, low biogenic calcite content and the concentrations/distributions of Ni, Co, Zn, Cu and Ir.

Interpretation and Discussion

Cu²⁺-porphyrins and IIIA. Geochemical analyses show that the carbonate-free fraction of IIIB contains a relatively high content (up to 6 %) of kerogen (Schmitz [3], [4]; Premović *et al.* [5]). Premović *et al.* [5] reported that this kerogen contains anomalously high level (up to 1000 ppm) of Cu and it is predominantly (>90 %) in the Cu²⁺-porphyrin form. They concluded that humic substances (enriched with Cu²⁺-porphyrins) were, probably, transported by the (impact-

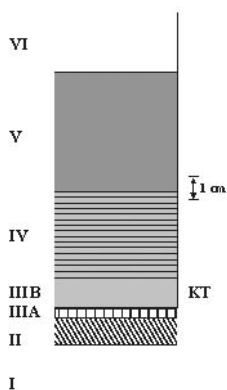


Fig. 1. Schematic illustration of the internal layering in a stratigraphic section of Fish Clay

derived acid?) surface waters from the nearby (oxic) soil to the shallow seawater at Stevns Klint. Humics later underwent alteration by the low temperature diagenetic process to form IIIB kerogen. During this process Eh fell down, creating strong anoxic conditions. The fact that IIIA contains no kerogen indicates that the deposition of IIIA (and the associated spherules) occurred under oxic conditions and it was preceded by the accumulation of humics (enriched with Cu^{2+} -porphyrins) in IIIB. Thus, it is likely that the deposition of IIIA and IIIB were two separate sedimentary events at Højerup. In addition, small interbiohermal troughs at Højerup provided a suitable platform for the accumulation of IIIA. Since these troughs were formed by a series of mounds in the latest Maastrichtian chalks (Hart *et al.* [6]) it appears that the deposition of IIIA smectite probably took place between the earliest Danian and latest Maastrichtian, i.e.

at the KT boundary.

Biogenic calcite of IIIA. Premović *et al.* [5] consider that IIIA/B represent the first decades or centuries following the KT impact event. Thus, IIIA was probably deposited relatively quickly on the seafloor. The problem is, however, that during the formation of IIIA may have been extremely condensed, attributed to the biogenic calcite dissolution, and a significant time may have elapsed between the formation of IIIA and IIIB (Schmitz *et al.* [7]). The low amount of biogenic calcite in IIIA could be, also, due to a low input of biologically-derived calcite shells because of low biological productivity in the photosynthetic zone of the surface seawater. This could be induced by the impact-related environmental disturbances. In addition, if IIIA was deposited too quickly, there would have been no sufficient time for biogenic calcite to accumulate within IIIA.

Ni, Co, Zn, Cu and Ir of IIIA spherules. Schmitz [4] and Graup *et al.* [8] reported that IIIA contains the spherules vary in size from 0.125 m to 0.800 m in diameter and are similar in appearance in the KT successions worldwide. Schmitz [4] found that these spherules make up about 10 wt % of IIIA and they are its original constituents. IIIA spherules are either wholly pyritic or partly to fully weathered to goethite (Schmitz [3], [4]; Graup *et al.* [8]). These spherules are highly enriched with Ni (5000 ppm), Co (460 ppm), Zn (3400 ppm) and Cu (690 ppm) (Schmitz [4]) and Ir (up to 17 ppb) (Jéhanno *et al.* [9]).

As the spherules cannot be remobilized by any postdepositional process, their stratigraphic distribution, as expected, is very narrow within Fish Clay (Schmitz [3], [4]; Graup *et al.* [8]; Jéhanno *et al.* [9]), inferring that their accumulation occurred during a very brief time interval. If this is a case, the deposition of IIIA had to be a single/very brief sedimentary event, geologically speaking instantaneous, that excludes any long duration mechanism. In addition, the profound distribution narrowness of the spherules in IIIA indicates that physical processes such as reworking or bioturbation did not mix the bulk material of IIIA with that of IIIB.

Graup *et al.* [8] performed a stratification of IIIA on the mm scale. They recognized four sublayers of IIIA: the basal 1 mm (A_1) rich in small spherules of about 100 μm in diameter covered by clay enriched with the larger spherules (A_2/A_3) overlain by the clayey sublayer (A_4). The goethite spherules of IIIA₁ are highly enriched with Ni (≤ 1300 ppm) and Ir (up to ca.

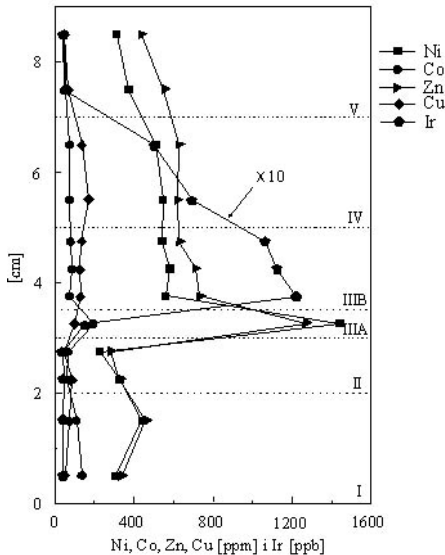


Fig. 2. The distribution of Ni, Co, Zn, Cu and Ir of the smectite concentrate of II, IIIA, IIIB, IV and V layers

with its smectite.

Schmitz [3] also reported the analytical data for cosmogenic Ir (on a carbonate-free basis) within Fish Clay. Based on these results, the concentration profile of this metal across this boundary clay is also presented in Fig. 2. The Ir values reach a profound peak concentration of 140 ppb in the base of IIIB. Upward from this level, Ir concentrations decrease gradually, indicating a single external input of this metal to Fish Clay. (Note that Ir concentrations in the smectite concentrate of IIIB are by a factor of 7-8 higher than in that fraction of IIIA). Finally, simple geochemical calculations show that IIIA only contains <10 % of total Ir, Ni, Co, Zn and Cu of Fish Clay.

References

- [1] F.T. Kyte, J. Smit, J.T. Wasson, *Earth Planet. Sci. Lett.*, 1985, **73**, 183-195.
- [2] B. Bauluz, D.R. Peacor, W.C. Elliott, *Earth Planet. Sci. Lett.*, 2000, **182**, 127-136.
- [3] B. Schmitz, *Geology*, 1988, **16**, 1068-1072.
- [4] B. Schmitz, *Geochim. Cosmochim. Acta*, 1985, **49**, 2361-2370.
- [5] P.I. Premović, N.D. Nikolić, I.R. Tonsa, M.S. Pavlović, M.P. Premović, D.T. Dulanović, *Earth Planet. Sci. Lett.*, 2000, **177**, 105-118.
- [6] M.B. Hart, S.E. Fiest, G.D. Price, M.J. Leng, *J. Geol. Soc.*, 2004, **161**, 885-892.
- [7] B. Schmitz, G. Keller, O. Stenvall, *Palaeogeog. Palaeoclim. Palaeoecol.*, 1992, **96**, 233-260.
- [8] G. Graup, H. Palme, B. Spettle, *Lun. Planet. Sci.*, 1992, **23**, 445-446.
- [9] C. Jéhanno, D. Boclet, P. Bonté, J. Devineau, R. Rocchia, *Mem. Soc. Geol. France*, 1987, **150**, 81-94.

20 ppb). We speculate that A₁ sublayer solely represents the true “impact layer”, in the sense of Kyte *et al.* [1], i. e. the impact fallout deposited directly on the seafloor after settling through seawater column. If this is correct then the sublayers IIIA₂₋₄ could represent a sedimentary continuum between IIIA₁ and IIIB.

Ni, Co, Zn, Cu and Ir across Fish Clay. Schmitz [3] reported ICP-OES data for trace metals in the carbonate-free fractions (mainly the smectite concentrates) in more-closely spaced samples across Fish Clay. The Ni, Co, Zn and Cu data are shown as concentration profiles vs. stratigraphic height in Fig. 2. This figure shows that the Ni, Co, Zn and Cu values reach a profound peak concentration of about 1440 ppm, 195 ppm, 1270 ppm and 100 ppm, respectively. A simple calculation indicates that less than one third of the total content of these metals of IIIA can be attributed to the spherules. The metal remaining is probably associated

THE FORMATION OF $\text{ZnCl}^+(\text{aq})$ ION-PAIRS IN SOLUTIONS OF $\text{ZnCl}_2(\text{aq})$ AT $T = 298.15 \text{ K}$

R. Ninković¹, J. A. Rard², J. Miladinović^{1*}, M. Todorović¹ and S. Grujić¹

¹*Department of Inorganic Chemical Technology, Faculty of Technology and Metallurgy, University of Belgrade, Karnegijeva 4, Belgrade, Serbia; *duma@tmf.bg.ac.yu*

²*Energy and Environment Directorate, Lawrence Livermore National Laboratory, University of California, Livermore, California 94550, USA; rard1@llnl.gov*

Abstract

In the treatment of activity data for $\text{ZnCl}_2(\text{aq})$ solutions at $T = 298.15 \text{ K}$, the presence of $\text{ZnCl}^+(\text{aq})$ ion-pairs was taken into account. Literature data at low and moderate concentrations up to $2.4 \text{ mol}\cdot\text{kg}^{-1}$ were used to obtain the equilibrium molalities of $\text{ZnCl}^+(\text{aq})$, $\text{Zn}^{2+}(\text{aq})$ and $\text{Cl}^-(\text{aq})$ by the method of successive approximations. The ionic activity coefficients were approximated by an extended ion-interaction (Pitzer) model.

Introduction

The system $\text{ZnCl}_2(\text{aq})$ exhibits really peculiar behavior at $T = 298.15 \text{ K}$. It acts as a solution of strong electrolyte up to about $0.10 \text{ mol}\cdot\text{kg}^{-1}$ but then rapidly becomes complexed as the concentration of the solution increases further. Evidence exists for different zinc-chloride complexes ZnCl_x^{2-x} at moderate and high molalities [1], where $x = 1, 2, 3, 4$.

As pointed out by Rard and Miller[2] the osmotic coefficients of $\text{ZnCl}_2(\text{aq})$ at $T = 298.15 \text{ K}$ initially decrease and then, due to complexing, have a plateau-like region in the molality range from 0.1 to $0.4 \text{ mol}\cdot\text{kg}^{-1}$, followed by further gradual decrease to a minimum at $1.6 \text{ mol}\cdot\text{kg}^{-1}$, that is uniquely characteristic of $\text{ZnCl}_2(\text{aq})$.

Values of the Emf have been reported as a function of molality from several different cells containing $\text{ZnCl}_2(\text{aq})$ with most studies at $T = 298.15 \text{ K}$. Among them, Lutfullah *et al.*[3] reported very precise Emfs over a molality range from 4.3×10^{-4} to $0.8766 \text{ mol}\cdot\text{kg}^{-1}$, and this study probably provides the most accurate set of Emfs (and thus activity coefficients) for a cell containing $\text{ZnCl}_2(\text{aq})$. According to these authors, in the dilute molality region below $0.008 \text{ mol}\cdot\text{kg}^{-1}$ ZnCl_2 behaves as a completely dissociated electrolyte. At higher concentrations from 0.01 to $0.88 \text{ mol}\cdot\text{kg}^{-1}$ ZnCl^+ complex formation becomes increasingly significant. The analysis of Lutfullah *et al.* required the iterative calculations of the equilibrium molalities of $\text{ZnCl}^+(\text{aq})$, $\text{Zn}^{2+}(\text{aq})$ and $\text{Cl}^-(\text{aq})$ based on this assumed speciation (satisfying mass balance and electroneutrality conditions) that were obtained by the method of successive approximations. The activity coefficients, needed for this calculation, were approximated by an extended Debye-Hückel equation including an additional term, linear in the ionic strength, containing an appropriate empirical coefficient. This coefficient, together with standard potential of the cell and the association constant for formation of $\text{ZnCl}^+(\text{aq})$, were least-squares variables.

Following the same basic procedure, but using recently published activity data on $\text{ZnCl}_2(\text{aq})$ at $T = 298.15 \text{ K}$, and some newer model equations for the activity coefficients, would generally lead to improvement of fitting of the data in the more concentrated region. In principle, it is possible to include all four stability constants for complex formation in this treatment. Even though significant concentrations of higher order zinc chloride complexes may also be presented in this solution, it was possible to represent the activity data accurately by explicitly including only the predominant complex $\text{ZnCl}^+(\text{aq})$.

Results and Discussion

Clegg *et al.*[4] generalized the extended ion interaction model of Pitzer for binary solutions including those with self-association equilibria. This model was used in the treatment of $\text{ZnCl}_2(\text{aq})$ data originating from paper of Miladinović *et al.*[5], for the osmotic coefficient up to molality $2.4 \text{ mol}\cdot\text{kg}^{-1}$ and of Robinson and Stokes[6] and Lutfullah *et al.*[3] for the ZnCl_2 activity coefficient, while assuming the presence of $\text{ZnCl}^+(\text{aq})$ ion-pairs.

Ionic species present in the solutions must satisfy mass balance and electroneutrality conditions (assuming that the concentration of free hydrogen and hydroxide ions are negligible):

$$m = m(\text{Zn}^{2+}) \{1 + K_1 m(\text{Cl}^-) [\gamma(\text{Zn}^{2+}) \gamma(\text{Cl}^-) / \gamma(\text{ZnCl}^+)]\}, \quad (1)$$

$$2m = m(\text{Cl}^-) \{1 + K_1 m(\text{Zn}^{2+}) [\gamma(\text{Zn}^{2+}) \gamma(\text{Cl}^-) / \gamma(\text{ZnCl}^+)]\}, \quad (2)$$

where m is the stoichiometric molality of the $\text{ZnCl}_2(\text{aq})$ solution and K_1 is the corresponding thermodynamic association constant for formation of $\text{ZnCl}^+(\text{aq})$ defined by:

$$K_1 = m(\text{ZnCl}^+) \gamma(\text{ZnCl}^+) / [m(\text{Zn}^{2+}) \gamma(\text{Zn}^{2+}) m(\text{Cl}^-) \gamma(\text{Cl}^-)]. \quad (3)$$

For the ionic activity coefficients, $\gamma(\text{Zn}^{2+})$, $\gamma(\text{Cl}^-)$ and $\gamma(\text{ZnCl}^+)$, the extended ion-interaction (Pitzer) model was used, where ion-interaction parameters for $(\text{Zn}^{2+}, \text{Cl}^-)$ and $(\text{ZnCl}^+, \text{Cl}^-)$ interactions occur. The ionic strength of the solution is based on the equilibrium speciation:

$$I_e = \frac{1}{2} \{ m(\text{ZnCl}^+) + 4 m(\text{Zn}^{2+}) + m(\text{Cl}^-) \} = 2m(\text{Zn}^{2+}) + m. \quad (4)$$

The procedure for determining $m(\text{ZnCl}^+)$ and free zinc and chloride ions, required some initial assumptions about the model parameter values[5] of the ion-interaction model, and the value for the thermodynamic association constant $K_1 = 4.5$ that was chosen as the best available estimate[3]. A first approximation to $m(\text{Zn}^{2+})$ was obtained from Eqs. (1) and (2). This initial estimate may be used to evaluate the ionic strength from Eq. (4) and in turn the ionic activity coefficients $\gamma(\text{Zn}^{2+})$, $\gamma(\text{Cl}^-)$, $\gamma(\text{ZnCl}^+)$ again, which then allows a better value of $m(\text{Zn}^{2+})$ to be evaluated. These cyclic calculations were iterated until the value of $m(\text{Zn}^{2+})$ was constant to within 0.01 %. Then the parameters of the ion-interaction model were optimized to give the minimum deviations between the calculated and measured values of the activity coefficients.

Figure 1 illustrates the agreement between equilibrium molalities of $\text{ZnCl}^+(\text{aq})$, $\text{Zn}^{2+}(\text{aq})$ and $\text{Cl}^-(\text{aq})$ reported in paper of Lutfullah *et al.* and the results obtained in this work.

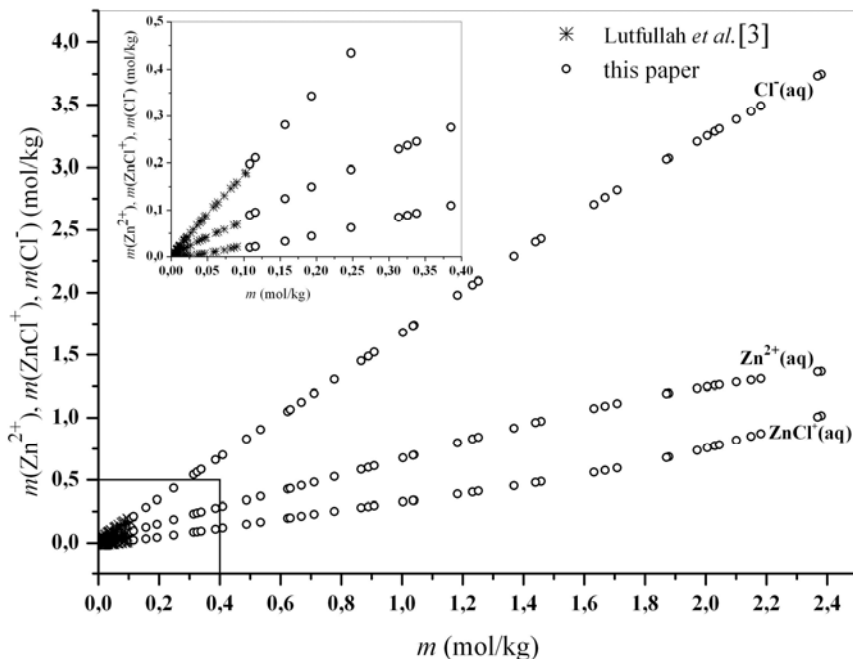


Fig. 1. The equilibrium molalities of ionic species: Zn^{2+} , ZnCl^+ and Cl^- present in the solution $\text{ZnCl}_2(\text{aq})$ vs. molality of solution: * data obtained in paper of Lutfullah *et al.* [3], \circ data obtained in this paper.

Conclusion

In the treatment of activity data of solution $\text{ZnCl}_2(\text{aq})$ at $T = 298.15$ K, it is preferable to include explicitly the presence of equilibrium amounts of complexes in order to obtain accurate fitting of experimental data by a quantitative ion–interaction model.

References

- [1] D. G. Miller, J. A. Rard, *J. Mol. Liq.*, 1992, **52**, 145-179.
- [2] J. A. Rard, D. G. Miller, *J. Chem. Thermodyn.*, 1989, **21**, 463-482.
- [3] Lutfullah, H. S. Dunsmore, R. Paterson, *J. Chem. Soc. Faraday Trans. I*, 1976, **72**, 495-503.
- [4] S. L. Clegg, J. A. Rard, K. S. Pitzer, *J. Chem. Soc. Faraday Trans.*, 1994, **90**, 1875-1894.
- [5] J. Miladinović, R. Ninković, M. Todorović, V. Jovanović, *J. Chem. Thermodyn.*, 2003, **35**, 1073-1082.
- [6] R. A. Robinson, R. H. Stokes, *Trans. Faraday Soc.*, 1940, **36**, 740-748.

MICROWAVE ASSISTED ELECTROLYSIS OF ALKALINE WATER SOLUTION

D. Stanisavljev¹, T. Grozdić², M. Marčeta-Kaninski³, A. Đorđević⁴ and D. Stojić³

¹*Faculty of Physical Chemistry, University of Belgrade, Studentski trg 12-16, P.O. Box 35-54, Belgrade, Serbia (dragisa@ffh.bg.ac.yu)*

²*Center for Multidisciplinary Studies, University of Belgrade, Kneza Višeslava 1, Belgrade, Serbia*

³*Vinča Institute of Nuclear Sciences, Department of Physical Chemistry, P.O. 522, Serbia*

⁴*School of Electrical Engineering, University of Belgrade, King Alexander's Boulevard 73, P.O. Box 35-54, Belgrade, Serbia*

Abstract

The effect of microwaves (MW) on the electrolytic process of 6M KOH water solution is investigated in the temperature range from 291 K to 337 K. At lower temperatures, microwaves facilitate electrolytic process, whereas the effect is reversed at higher temperatures.

Introduction

Although the fact that microwaves are widely exploited in chemical synthesis due to the efficient heating, [1] investigations of various processes, such as electrolysis of water solutions during irradiation are much difficult. The reason is that metal parts, which are present in the MW field, act as antennas emitting dangerous radiation to the environment and transmitting high voltages to the measuring apparatus. However, careful construction enables electrochemical measurements in presence of microwaves [2,3]. There is no general explanation of the MW field effects and these investigations could be of high scientific importance. We performed initial investigations of the water electrolysis influenced by microwaves.

Electrolytic water splitting has gained importance in recent years because of hydrogen production without adverse environmental impact. Hydrogen's energetic potential lies in its ability to serve as an energy source and medium, convenient for efficient energy storage, transport and manipulation.

The alkaline electrolysis from concentrated KOH aqueous solutions using nickel electrodes is a conventional process, which has been in commercial use for more than 80 years [4,5]. Mostly 20-30 wt. % KOH solutions are used because of their optimum conductivity. Regarding economical requirements, alkaline water electrolysis has not had a significant commercial impact because it has not been cost-effective, due to high electricity consumption (4.5 to 5 kWh/m³ H₂ in most industrial electrolyzers). However, it is technologically very simple and delivers very clean gases [6,7].

In the light of these efforts, the main idea of this work was to observe the influence of the microwave field on the energy consumption in the alkaline water electrolyser.

Experimental

All experiments were performed in a glass-made cell of defined geometry specially designed to match our goal. It was constructed to fit a MW cavity. The special metal

shield was used for protecting leading wires of the electrodes from the MW field. The cell was externally thermostated at a desired temperature with accuracy of 0.5 K, with a water ultrathermostat. The cell was made to be one compartment and evolved gases (hydrogen and oxygen) were collected in the same measuring volume, in order to increase the rate and accuracy of recording.

Evolved gases under their own pressure continuously filled the U-tube water manometer, which was previously filled with water. Time of evolution of a certain volume of hydrogen + oxygen (2:1) is used to calculate the corresponding energy consumption at a given temperature and current density.

The nickel electrodes were utilized. They were rectangularly shaped, and the anode surface was approximately two times bigger than the cathode. Electrolyte was 30 wt. % KOH (standard electrolyte).

Results and Discussion

The energy requirement for the electrolytic process was calculated using the relation $Q = I \times U \times t$, where I (A) and U (V) are the overall current and voltage through the cell, and t (s) is the time of evolution of a one mole of hydrogen.

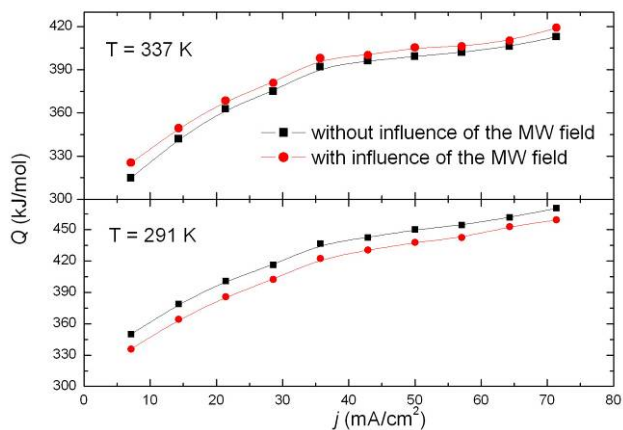


Figure 1. Energy consumption per one mol of hydrogen evolved as a function of current density at $T = 337$ K and $T = 291$ K.

All experiments were performed in the current range from 10 mA to 100 mA, which corresponds to the current density range from 7.1 to 71.4 mA cm⁻². The applied temperatures were from 291 K to 337 K (from 18 °C to 64 °C) and absorbed power of MW 2.5 W.

The general effects of microwaves are illustrated at Figure 1 for the lowest investigated temperature $T = 18$ °C and the highest temperature of $T = 64$ °C. In the temperature range from 18 °C to 33 °C, the energy consumption of the electrolytic process is lowered under the influence of the MW field, while above 33 °C, the energy requirements under this influence are higher.

Conclusion

The effect of microwaves on the electrolytic process of KOH water solution is confirmed. It is investigated in the temperature range from 291 K to 337 K. At lower temperatures microwaves facilitate the process, but the effect is reversed at higher temperatures Figure 1. This peculiar temperature dependence is an indication that the MW effects cannot be explained by the simple overheating of the solution. Further investigations are necessary to explain mechanism of microwave effects and determine optimal design of experimental setup.

Acknowledgement

The present investigations are supported by the Ministry of Science and Environmental Protection under projects 142025 and 142067.

References

- [1] C. Oliver Kappe, A. Stadler, *Microwaves in Organic and Medicinal Chemistry*, Wiley-VCH Verlag GmbH and Co.KgaA, Weinheim, 2005.
- [2] F. Marken, U. Kumar Sur, A. B. Coles, G. R. Compton, *Electrochimica Acta*, 2006, **51**, 2195.
- [3] R. D. Stanisavljev, R. A. Djordjević, D. V. Likar-Smiljanić, *ChemPhysChem*, 2004, **5**, 140.
- [4] D. E. Hall, *J. Appl. Electrochem.* 1984, **14**, 107.
- [5] E. Potvin, H. Menard, L. Brossard and J. M. Lalancette, *Int. J. Hydrogen Energy* 1990, **15**, 843.
- [6] A.J. Appleby, G.J. Richter, J.R. Selman, A. Winsel, Conversion of hydrogen in fuel cells, in *Electrochemical Hydrogen Technologies*, (Ed. Hartmut Wendt), Elsevier, Amsterdam, 1990.
- [7] *Hydrogen as an Energy Carrier*, (Eds. C-J. Winter, J. Nitsch), Springer-Verlag, Berlin, 1988.

EXPERIMENTAL DETERMINATION OF ADSORPTION ENERGIES, LOCAL MONOLAYER CAPACITIES AND LOCAL ADSORPTION ISOTHERMS FOR ORGANIC ACID-COPPER SYSTEMS

A.V. Dremetsika¹, P.A. Siskos¹ and N.A. Katsanos²

¹*Environmental Analysis Group, Laboratory of Analytical Chemistry, Department of Chemistry, University of Athens, Panepistimioupoli, 15771 Zografos, Athens, Greece. (siskos@chem.uoa.gr)*

²*Physical Chemistry Laboratory, University of Patras, 26504 Patras, Greece.*

Abstract

The reversed-flow gas chromatography (RF-GC) method was used to determine local adsorption energies, monolayer capacities and adsorption isotherms as a function of experimental time, when acetic and formic acid vapors are adsorbed on heterogeneous surfaces of copper. The results lead to a characterization of the metal surface, and also to the mechanism of the damage that metallic artifacts suffer when they are exposed to organic acids' atmosphere.

Introduction and Theory

Reversed Flow - Gas Chromatography (RF-GC) [1] has been applied to measure the time separation of adsorption energies, local monolayer capacities and local adsorption isotherms, when acetic and formic acid vapors are adsorbed on the heterogeneous surfaces of copper.

The mathematical model used to calculate the physicochemical parameters mentioned above is based on well known equations [2]. The method depends on the time function of the chromatographic peaks obtained by short flow-reversals of the carrier gas, as Eq (1) shows:

$$H^{1/M} = \sum_{i=1}^4 A_i \exp(B_i t) \quad (1)$$

where H is the peak height, M the response factor of the detector, A_i the pre-exponential factors and B_i the exponential coefficients of time t .

The necessary relations for the calculation of adsorption energy ε , local monolayer capacity c_{\max}^* , and local adsorption isotherm θ , have been obtained from Eq.(1) and the Jovanovic isotherm model [3]:

$$\theta(p, T, \varepsilon) = 1 - \exp(-Kp) \quad (2)$$

where K is Langmuir constant, and p the pressure of the acid vapor. The final relations for the calculations of the three parameters are:

$$\varepsilon = RT[\ln(KRT) - \ln(RT) - \ln K^0] \quad (3)$$

$$c_{\max}^* = c_s^* + \frac{1}{KRT} \frac{\partial c_s^*}{\partial c_y} \quad (4)$$

$$\theta = 1 - \frac{1}{c_{\max}^*} \frac{1}{KRT} \frac{\partial c_s^*}{\partial c_y} \quad (5)$$

where K^0 is given by the statistical mechanics [4], c_s^* is the equilibrium adsorbed concentration and c_y the gaseous concentration of the acid into the solid bed at time t .

Experimental

The experimental arrangement has been described in the past [1-2,5]. A simply modified gas chromatograph with FID detector was used and nitrogen with a flow rate of $30 \text{ cm}^3 \text{ min}^{-1}$ was employed as a carrier gas. Section L_1 was empty, of 58 cm long, while section L_2 contained the solid bed and had a length of 8.0-8.6 cm.

The procedure consists in repeatedly reversing for 5 s the direction of the carrier gas flow by means of a four-port gas sampling valve. Following each flow reversal, an extra narrow "sample peak" appears in the recorder. Measurements were performed at various temperatures in the range 353 - 423 K.

Results and Discussion

Figures 1 and 2 show the time dependence of adsorption energy, local adsorption isotherm, and local monolayer capacity for the systems acetic acid-Cu and formic acid-Cu respectively at 353 K. Similar plots can be obtained for the other three temperatures at which experiments were also performed.

From the diagrams it is clearly seen that the maxima in the plots of the adsorption energy correspond to the maximum values of the local adsorption isotherm, and to the minimum values of the local monolayer capacity while the opposite seems to happen for the minimum values of the adsorption energy.

In the case of acetic acid, the maximum of adsorption energy values appears earlier as temperature increases, while at higher temperatures a second maximum is observed. In the case of formic acid, two maxima appear at all temperatures. In both cases, it seems to be a leveling off after some period of time, again as earlier as temperature increases.

Conclusions

Generally, it is observed that both acetic and formic acids have shown about the same behavior concerning the adsorption phenomenon onto the heterogeneous surface of copper. The results can be used for a physicochemical characterization of the metal surfaces, and for finding the mechanism of the possible corrosion that occur, when metallic objects are exposed to such an atmosphere.

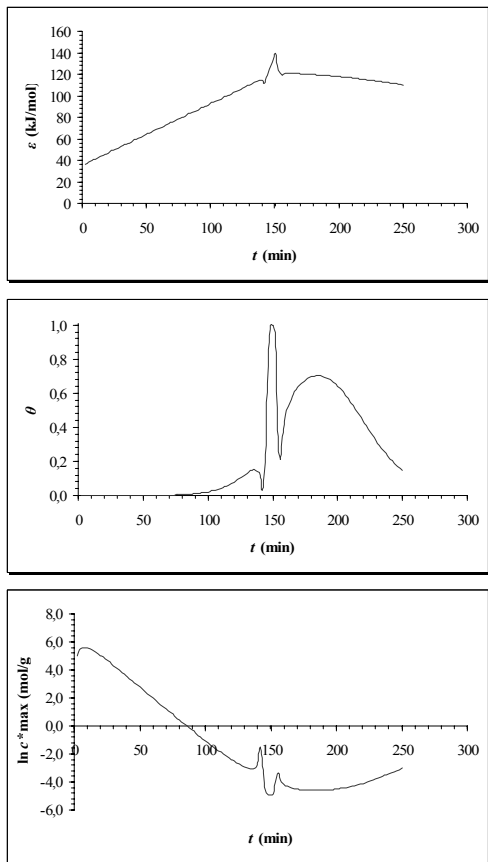


Fig. 1. Time-resolved analysis of the adsorption energy ϵ , the local adsorption isotherm θ , and the local monolayer capacity c^*_{\max} for the system acetic acid-Cu

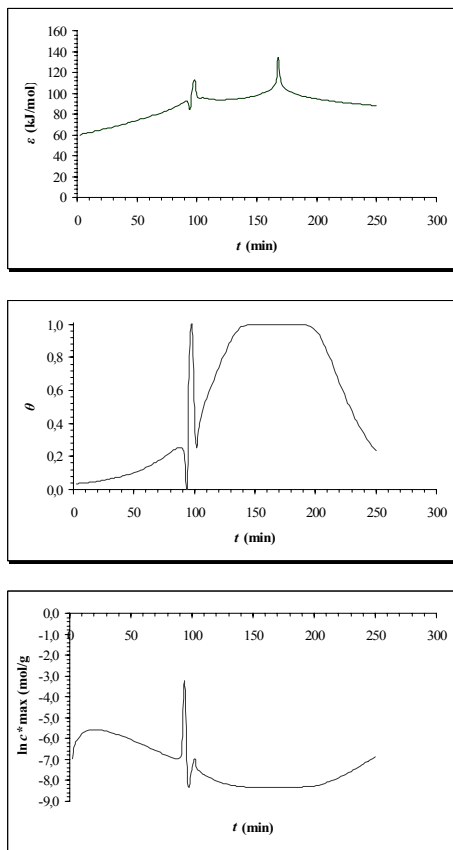


Fig. 2. Time-resolved analysis of the adsorption energy ϵ , the local adsorption isotherm θ , and the local monolayer capacity c^*_{\max} for the system formic acid-Cu

References:

[1] N.A. Katsanos, J.Chromatogr.A, 2002, **969**, 3-8.
 [2] N.A Katsanos. G. Karaiskakis, Time resolved inverse gas chromatography and its applications, HNB Publishing, New York, 2004.
 [3] Jovanovic D.S., Colloid.Polym.Sci., 1969, **235**, 1203-1214.
 [4] R.H. Fowler, Statistical Mechanics, Cambridge University Press, Cambridge, 1936.
 [5] N.A. Katsanos, F. Roubani-Kalantzopoulou, Adv.Chromatogr., 2000, **40**, 231.

STUDY ON PROTOLYTIC EQUILIBRIA OF LORATADINE AND DESLORATADINE

G. Popović and M. Čakar

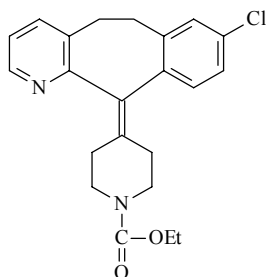
*Faculty of Pharmacy, University of Belgrade, P.O. Box 146,
Vojvode Stepe 450, Belgrade, Serbia*

Abstract

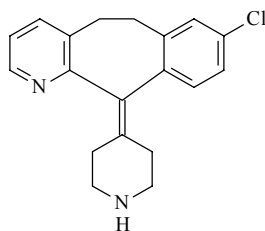
Protolytic equilibria in homogeneous and heterogeneous aqueous systems of loratadine (monoprotic base) and desloratadine (diprotic base), two sparingly soluble antihistamine drugs, were studied. Acidity constants and equilibrium constants in heterogeneous systems were determined. The obtained values of the constants served to calculate the solubility and the distribution of the equilibrium forms of drugs as a function of pH.

Introduction

Loratadine and desloratadine are a long-acting antihistamine. Unlike most other antihistamines, this drug does not enter the brain from the blood and, therefore, does not cause drowsiness.



Loratadine



Desloratadine

Chemically, loratadine and desloratadine are monoprotic and diprotic base, respectively, which molecular forms are slightly hydrosoluble. The studies of protolytic equilibria and solubility of pharmacologically active substances are of special importance in biochemical pharmacology, because absorption of drugs in gastrointestinal tract and transport through the cell membranes are affected by the properties of the chemical species involved. Knowledge of distribution of species as a function of pH are important for choice of optimal conditions for drug analysis. However, there are no data in the available literature on protolytic equilibria in homogeneous and heterogeneous water system of loratadine and desloratadine and the aim of this work was devoted to these studies.

Results and Discussion

In the pH range 0-14 loratadine posses one (pyridine nitrogen) and desloratadine two (pyridine nitrogen and piperazine nitrogen) basic centers. Stoichiometric acidity constants (K_a^c) were determined according to the classical spectrophotometric method [1] under the following conditions:

- Loratadine: 300 nm, pH range 2-8, $c = 2 \times 10^{-5}$ M
- Desloratadine: 300 nm, pH 2-7 (pK_{a1}^c); 240 nm, pH 7-12 (pK_{a2}^c); $c = 1 \times 10^{-4}$ M.

The values of the determined acidity constants are listed in Table 1.

Since loratadine and desloratadine in molecular form are slightly hydrosoluble, in heterogeneous system between the solid base (B_s) and saturated water solution the following equilibria get established:



(Loratadine: equilibrium (1) and (2); desloratadine: equilibrium (1)-(3))

Equilibrium constant K_{s0}^c (intrinsic solubility) was estimated spectrophotometrically applying a solubility method [2]. The determination was performed within pH ranges where molecular form B is dominant in saturated solution, $pH > 7.5$ (loratadine) and $pH > 11.5$ (desloratadine):

$$S = [B] = K_{s0}^c \quad (4)$$

Constants K_{s1}^c and K_{s2}^c were calculated according to the determined constants K_{s0}^c and acidity constants. Namely, from equation (1)-(3) using term for acidity constants it follows that:

$$\text{Loratadine} \quad K_{s1}^c = \frac{K_{s0}^c}{K_{a1}^c} \quad (5)$$

$$\text{Desloratadine} \quad K_{s1}^c = \frac{K_{s0}^c}{K_{a2}^c} \quad (6) \quad K_{s2}^c = \frac{K_{s0}^c}{K_{a1}^c K_{a2}^c} \quad (7)$$

The stoichiometric equilibrium constants determined in homogeneous and heterogeneous system of loratadine and desloratadine are summarized in Table 1. On the basis of the determined equilibrium constants, the molar fraction (X) of the equilibrium particles and solubility (S) of the investigated drugs were calculated by following equations:

Desloratadine

$$X_{\text{BH}_2^{2+}} = \frac{[\text{H}_3\text{O}^+]^2}{[\text{H}_3\text{O}^+]^2 + K_{a1}^c[\text{H}_3\text{O}^+] + K_{a1}^c K_{a2}^c} \quad (8)$$

$$X_{\text{BH}^+} = \frac{K_{a1}^c[\text{H}_3\text{O}^+]}{[\text{H}_3\text{O}^+]^2 + K_{a1}^c[\text{H}_3\text{O}^+] + K_{a1}^c K_{a2}^c} \quad (9)$$

$$X_{\text{B}} = \frac{K_{a1}^c K_{a2}^c}{[\text{H}_3\text{O}^+]^2 + K_{a1}^c[\text{H}_3\text{O}^+] + K_{a1}^c K_{a2}^c} \quad (10)$$

$$S = [\text{B}] + [\text{BH}^+] + [\text{BH}_2^{2+}] = K_{s0}^c + K_{s1}^c[\text{H}_3\text{O}^+] + K_{s2}^c[\text{H}_3\text{O}^+]^2 \quad (11)$$

Loratadine

$$X_{\text{BH}^+} = \frac{[\text{H}_3\text{O}^+]}{[\text{H}_3\text{O}^+] + K_{a1}^c} \quad (12)$$

$$X_{\text{B}} = \frac{K_{a1}^c}{[\text{H}_3\text{O}^+] + K_{a1}^c} \quad (13)$$

$$S = [\text{B}] + [\text{BH}^+] = K_{s0}^c + K_{s1}^c[\text{H}_3\text{O}^+] \quad (14)$$

Table 1. The stoichiometric equilibrium constants in homogeneous and heterogeneous systems of loratadine and desloratadine. $t=25$ °C; $I=0.1$ M (NaCl).

Constant	Loratadine	Desloratadine
$\text{p}K_{a1}^c$ (pyridine nitrogen)	5.28 ± 0.01	4.56 ± 0.01
$\text{p}K_{a2}^c$ (piperazine nitrogen)	-	9.25 ± 0.05
$\text{p}K_{s0}^c$	4.66 ± 0.03	3.42 ± 0.01
$\text{p}K_{s1}^c$	-0.62 ± 0.03	-1.14 ± 0.01
$\text{p}K_{s2}^c$	-	-10.4 ± 0.05

Acknowledgements

This work was supported by the Ministry for Science and Environmental Protection of Republic of Serbia, Grant # 142071B.

References

- [1] A. Albert, E.P. Serjeant, The Determination of Ionization Constants, Chapman and Hall, 1971.
- [2] L. Pfenndt, D. Sladić, T. Janjić, G. Popović, *Analyst*, 1990, **115**, 383-387.

STATISTICAL OPTIMIZATION APPLIED TO SIMULTANEOUS DETERMINATION OF MAPROTILINE, DESIPRAMINE AND MOCLOBEMIDE BY RP-HPLC

Z. Vujić, V. Kuntić, B. Ivković and K. Ilić

Faculty of Pharmacy, Vojvode Stepe 450, Belgrade, Serbia

Abstract

A method for separation of three antidepressants, maprotiline, desipramine and moclobemide by RP-HPLC was developed and validated. To find optimal conditions and estimate the impact of individual parameters on the separation a complete set, 2^3 , of interdependent relationships between the mobile phase composition, temperature and the volume flow rate, was examined. Full separation of the investigated components from a laboratory mixture was achieved on a Supelcosil LC-18 (120mm×4.6mm, 5 μ m) column, using two solvent systems, 3 % ammonium in water/ethanol and acetonitrile, and alternating isocratic-gradient-isocratic elution modes.

Introduction

To alleviate the symptoms of depression, two major groups of biologically active compounds are typically being used, monoamine oxidase inhibitors or tricyclic antidepressants [1], exemplified in this work by maprotiline, desipramine and moclobemide. Due to the wide prevalence of symptoms and the nature of the disease, antidepressant drugs are commonly abused and cause severe, often fatal intoxication. Up to now, different methods were proposed, including capillary gas chromatography, thin-layer chromatography, spectrofluorimetric and isotachophoretic methods [2-3]. The aim of the present study is to develop and validate a RP-HPLC method for simultaneous determination of maprotiline, desipramine and moclobemide, which are three most-frequently prescribed antidepressants in our market. Considering the high rate of abuse of the above mentioned antidepressants and the notion that they are occasionally used at the same time, methods for their simultaneous determination may be relevant for therapeutic drug monitoring in clinical or forensic toxicology. The proposed method is fully validated for a ternary laboratory mixture.

Experimental

Maprotiline (N-methyl-9,10-ethanoanthracene-9(10H)-propanamine) as reference standard was obtained from Zdravlje (Leskovac). Desipramine (10, 11-dihydro-N-methyl-5H-dibenz [b, f] azepine-5-propamine) and Moclobemide (4-chloro-N-[2-(4-morpholinyl) ethyl] benzamide) were purchased from Sigma (Aldrich). Solvents for preparing the mobile phase, absolute ethanol and acetonitril (Merck, Darmstadt), and 32 % ammonia solution (Zorka Pharm, Šabac) were of HPLC grade.

RP-HPLC was performed using the Hewlett Packard HPLC station (HP 1100), Rheodyne model injector with a sample loop of 20 μ L and a Supelcosil LC-18 (120

mm \times 4.6 mm, 5 μ m) column. Mobile phase I was prepared by mixing a 3 % aqueous solution of ammonia with ethanol in the proportion 6:94, v/v. Mobile phase II was acetonitrile (ACN). Fractions were detected by monitoring the absorbance at $\lambda = 272$ nm.

HPLC data were analyzed using the ChemStation software package. Application of the factorial design, analysis of the measured response variables and multivariate regression were performed using the statistical graphic software system "Sgwin". By applying the PACO software the octanol/water partition coefficient, $\log P$, was calculated for each of the substances examined.

Results and Discussion

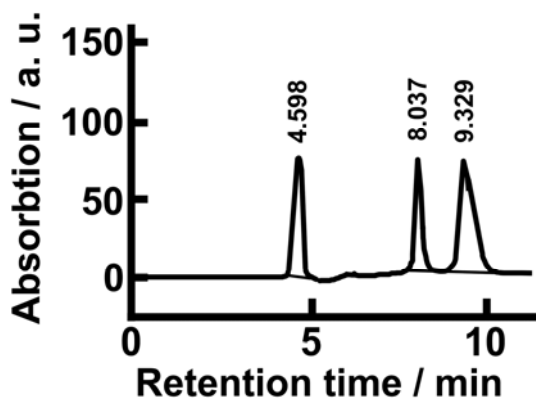
To find optimal conditions for separation of these antidepressants, complete factor design, 2^3 , with one central point was conducted. Combined effects of three variables: composition of the mobile phase, *i.e.* the concentration of ammonium ions in the mobile phase; temperature and the volume flow rate, were investigated. Choosing selectivity of maprotiline over desipramine ($\alpha_{\text{map/des}}$) as the systems response factor, a design matrix with eight different treatment combinations with low or high levels of the factors and with one central point was constructed.

From the factors' effects estimation, $\alpha_{\text{map/des}}$ was found to be less sensitive to the variation of the flow rate and temperature, than to the composition of the mobile phase. By applying the ANOVA package for statistical analysis, statistical significance of each effect was tested by comparing the mean squares against estimates of the experimental errors. Two factors showed significant values, the concentration of ammonium ions in the mobile phase and the flow rate (both with $p < 0.05$). The multiple correlation coefficient, R^2 , indicates that the fitted model accounts for 95.94 % of the variability of the response and values signifying the lack-of-fit (large F -value and $p > 0.05$), suggesting that the selected model represents adequately the observed data.

Combined effect of the mobile phase composition and the flow rate on the factor of selectivity of maprotiline over desipramine can be described by a linear relation: $\alpha_{\text{map/des}} = 1.1 - 0.3925 \cdot A - 0.345 \cdot C$, indicating that the concentration of ammonium ions in the mobile phase, particularly when it is low, affects the separation considerably more than the volume flow rate.

Good separation of maprotiline and desipramine can be achieved at low flow rates. However, under these conditions moclobemide is strongly retained at the column, with a retention time longer than 20 min and with obvious peak "tailing". This problem can be overcome by reducing the flow rate of the mobile phase after elution of moclobemide while keeping the concentration of ammonium ions at 3 % and using a gradient elution mode with linearly increasing concentrations of ACN, in the way given in table:

Time (min)	Mobile phase	Elution modes	Flow rate (mL min ⁻¹)
0.0 - 4.0	I	Isocratic	0.7
4.1 - 12.0	II	Linear gradient up to 20 % ACN	0.3
12.1 - 20.0	I	Isocratic	0.7



The obtained chromatogram is presented in Fig., with retention times for moclobemide, desipramine and maprotiline 4.6, 8.0 and 9.3 min, respectively.

Retention chromatographic parameters: factor of capacity, k' ($k'_{\text{map}} = 8.12$, $k'_{\text{des}} = 12.75$, $k'_{\text{moc}} = 7.30$); factor of selectivity, α ($\alpha_{\text{des/moc}} = 1.75$, $\alpha_{\text{map/des}} = 1.13$); and the factor of resolution, R ($R_{\text{des/moc}} = 7.42$, $R_{\text{map/des}} = 2.36$); as well as

the octanol/water partition coefficients, $\log P$, $\log P_{\text{map}} = -4.13$, $\log P_{\text{des}} = -4.37$, $\log P_{\text{moc}} = 1.25$, were calculated.

The method was validated. Low values of relative standard deviation for repeatability, $\text{RSD} < 2.5\%$, and high recovery, indicate very good precision of the proposed method.

Conclusion

HPLC provides a convenient and efficient method for simultaneous determination of antidepressants maprotiline, desipramine and moclobemide. The developed method does not require usage of phosphate or other buffers. The results obtained in this study corroborate that the proposed HPLC method is sufficiently precise, rapid and sensitive to be used for routine quantitative analyses of the investigated compounds in a mixture.

References

- [1] W. Foye, T. Lemke, D. Williams, In: Principles of Medicinal Chemistry, Williams & Wilkins (1995).
- [2] N. Rifai et al, Ther. Drug. Monit., 1998, **10**(2), 194.
- [3] M. Cakrt, T. Buzinkaiova, J. Polonsky, V. Korinkova, Electrophoresis, 2000, **21**, 2834.

GALLIUM EXTRACTION FROM DECOMPOSED BAYER'S ALKALINE SOLUTIONS

D.Tošković¹, M.B.Rajković², D.Stanojević,¹ and Lj.Vasiljević¹

¹*Faculty of Technology, Zvornik, University of East Sarajevo, Bosnia&Herzegovina*

²*Faculty of Agriculture, Zemun, University of Belgrade, Serbia*

Abstract

This paper shows the results of liquid-liquid gallium extraction, by extractor solution (substituted 8-hydroxyquinoline in kerosene, which contains higher aliphatic alcohols) from the solution of decomposed Bayer alkali, all based on the experimental results in laboratory (glass) charge in 120 min. duration, under 15% extractor concentration. Re-extraction of Ga by H₂SO₄ showed the best results with sulphuric acid of 1.5 mol/dm³ concentration at 1:10 quantity ratio of organic and water phase.

Introduction

Specific attributes of gallium and its compounds of A₃B₅ type are widely used in different fields of technique, especially in electronics, radiation and atomic techniques, rocket construction etc. The main raw material sources for gallium production are bauxite and sphalerite where its content is 0.001-0.05%. It is possible to separate certain amount of metal gallium by introducing new productively intensive methods of extraction, concentration and electrolysis. Extraction and sorbing methods are distinguished by high productivity and selectivity, which is especially important because gallium is extracted from large quantities of complex configuration solutions, with small amount of gallium. Such a solution is also the one of decomposed Bayer's alkaline solution, having average content of 150-300 mg/dm³ Ga, 160 mg/dm³ Na₂O and 90 mg/dm³ Al₂O₃.

All the results of liquid-liquid gallium extraction from previously mentioned solution are based on experimental results obtained under laboratory conditions. The method provides continual counter-current gallium extraction by extractor solution (substituted 8-hydroxyquinoline (Kelex 100 or LIX 26) in kerosene with the addition of 10% n-decanol).

Material and Methods

Extraction and concentration of gallium, which is present in decomposed Bayer's alkaline solutions (basic solution) having average content of 90 g/dm³ Al₂O₃, 160 g/dm³ Na₂O and 250 mg/dm³ Ga₂O₃ consists of the following phases [1,2]:

I PHASE: Extraction – re-extraction (I)

Extraction (I) of gallium from basic solution with 8% extractor solution. **Re-extraction (I)** of gallium by H₂SO₄. In re-extract (I), besides gallium, certain amount of aluminium also transfers.

II PHASE: Transferring Ga and Al sulphates into chlorides with addition of solid NaCl.

III PHASE: Extraction (II) of gallium(III)-chlorides by butyl-acetate. $AlCl_3$ remains in water phase. Partial distillation of butyl-acetate and re-extraction (II) by HCl. Re-extract (II) is sent to electrolysis.

If it is proved that electrolysis from alkali solution is more efficient, phases II and III are omitted and re-extract I, $Ga(OH)_3$ is precipitated by solid NaOH. The former is separated and, for purpose of electrolysis, is soluted in order to obtain adequate Ga concentration in the form of gallates.

Results and Discussion

Gallium is separated from the basic solution in laboratory (glass) charge type extractor by 8% extractor solution. The following analysis was done at 1:1 organic and water phase ratio.

Extraction

a) Temperature dependence of extraction speed

According to the temperature of basic solution and in the process of production alumina, the efficiency of gallium extraction of gallium at 50°C and 70°C with 8% extractor solution, was analysed. Received results are shown in Table 1. while the extraction efficiency was determined by the following equation (1):

$$(1): \frac{C_p - C_E}{C_p} \cdot 100\%$$

where C_p – is concentration of Ga in basic solution (mg/dm^3), and C_E – concentration of Ga in water layer after extraction (mg/dm^3).

Table 1. The efficiency of Ga extraction by 8% extractor solution

Time of extraction (in min)	Efficiency of extraction (in %) at different temperatures	
	50°C	70°C
30	75%	64%
60	90%	91%
90	97%	92%
120	99%	100%

b) The influence of extraction concentration

The efficiency of gallium extraction, depending on extractor concentration was analysed at 50°C and in 2-hour-extraction time. Received results are shown in Table 2. while extraction efficiency was determined by the following equation (1).

Table 2. The efficiency of Ga extraction by 8% extractor solution

% extractors	Efficiency of extraction Ga (in %)
1%	17
5%	86
10%	963
15%	100

Re-extraction

a) The influence of sulphur acid concentration

Ga re-extraction was done by different H_2SO_4 concentrations. It was done at room temperature. The separation of layers is developing slowly and in order to increase the process, the solution was heated on approximately 50°C . Received results are show in Table 3, where C_P – is concentration of Ga in an original solution (mg/dm^3) and C_R – is concentration of Ga in water layer after re-extraction (mg/dm^3). Ga re-extraction is over 100% because is was done by previously used Kelex where Ga remained from previous experiments.

b) The analysis of the possibilities of gallium concentration by varying quantity ratio of water and organic phase in re-extraction

Organic layer after extraction, where quantity ratio of organic and water phase was $V_o:V_{aq} = 1:1$, was used for re-extraction, varying $V_o:V_{aq}$ and H_2SO_4 concentration ratio. Received results are shown in Table 4, where C_P – is Ga concentration in original solution (mg/dm^3) and C_R - Ga concentration in water layer after re-extraction.

Table 3. Re-extraction of Ga by H_2SO_4 acid of different concentrations

0.5 mol/dm ³ H ₂ SO ₄		1.5 mol/dm ³ H ₂ SO ₄		3 mol/dm ³ H ₂ SO ₄	
C _R	C _R /C _P ·100%	C _R	C _R /C _P ·100%	C _R	C _R /C _P ·100%
0.0	0%	225	115%	210	107%

Table 4. Re-extraction of gallium by varying $V_o : V_{aq}$ ratio

1.5 mol/dm ³ H ₂ SO ₄ $V_o : V_{aq} = 1 : 5$		3 mol/dm ³ H ₂ SO ₄ $V_o : V_{aq} = 1 : 5$		6 mol/dm ³ H ₂ SO ₄ $V_o : V_{aq} = 1 : 10$	
C _R	C _R /C _P ·100%	C _R	C _R /C _P ·100%	C _R	C _R /C _P ·100%
0.0	0%	993	4.3%	3.563	15%

Conclusion

This paper presents the results of liquid-liquid gallium extraction by solution of substituted 8-hydroxyquinoline in kerosene that contains n-decanol from Bayer's alkaline solutions in laboratory extractor of charged type. Received results showed that the highest efficiency of extraction is at 70°C in 120 min duration with 15% extractors concentration. Ga re-extraction by H_2SO_4 showed the best results by $1.5 \text{ mol}/\text{dm}^3$ H_2SO_4 concentration, at 1:10 organic and water phase quantity ratio.

References

- [1] D.A.Kramer, Gallium and Gallium Arsenide: Supply and Technology, and Uses, USBM IC 9208, 1988.
- [2] D.D.Harbut, J.W.Morrison and C.F.Davidson, Light Metals 1989, ed. P.G.Campbell (Warrendale, PA; TMS, 1988), 983-989.

Ni AND Co IN THE SMECTITE FRACTION OF THE CRETACEOUS-TERTIARY (KT) BOUNDARY FISH CLAY NEAR RØDVIK (STEVNS KLINT, DENMARK)

M. M. Krsmanović, B. Z. Veličković,
N. N. Mišković and P. I. Premović

*Laboratory of Geochemistry, Cosmochemistry and Astrochemistry, University of Niš, P.O.Box 224,
18000 Niš, Serbia. (asteroid.pavle@yahoo.com)*

Abstract

Fish Clay of Stevns Klint near Rødvig is made up mainly from biogenic calcite and cheto-smectite. The smectite fraction of this marl shows enhanced concentrations of Ni (465 ppm) and Co (50 ppm). Our conclusion is that this enrichment represents the sudden/rapid input of high Ni and Co into the late Cretaceous seawater at Stevns Klint. The source of these metals was probably the impact-ejecta fallout on nearby soil.

Introduction

Lithological units of Fish Clay appear to be remarkably persistent over the length (ca. 12 km) from Bøgeskov (in the north) to Rødvig (in the south). Similar boundary units can be also distinguished in other parts of the world (Schmitz [1]). An anomalously high Ir concentration in the Fish Clay at Højerup has been reported by Alvarez *et al.* [2]. The authors proposed that this enhanced Ir was produced by a late Cretaceous asteroid impact. According to the current pedagogy the impactor was a carbonaceous chondrite. Apart from Ir, this boundary is also enriched with the other trace metals such as Ni and Co.

In the previous studies, attention was focused on Ni and Co in Fish Clay at Højerup, but no attention was paid to geochemistry of these metals in the other nearby boundary sites, such as that close to Rødvig (the southernmost part of Stevns Klint, about 4 km from Højerup). Fish Clay near Rødvig (hereafter FCR) is thin gray marl containing mainly biogenic calcite/smectite. We analyzed Ni and Co in the smectite fraction of a sample from this site.

Experimental

We analyzed Ni and Co in the whole sample of FCR and in its smectite fraction employing Inductively Coupled Plasma-Optical Emission Spectroscopy (ICP-OES). A Spectroflame ICP-OES instrument was employed and Ar was used as the plasma gas. Total uncertainties (including accuracy error) of the analyses for these metals range from 5 % to 20 %.

Results and Discussion

The smectite fraction of FCR shows enhanced concentrations of Ni (465 ppm) and Co (50 ppm), Table 1. The incorporation of Ni and Co into FCR smectite probably oc-

Table 1. Geochemical concentrations [ppm] of Ni and Co in FCR close to Rødvig

Metal	Whole rock	Smectite fraction*
Ni	254	465
Co	18	50

* The percentage of the smectite fraction: 55 %.

curred in an ordinary (oxygenated) seawater (with common pH about 8). In this case, Ni^{2+} and Co^{2+} ions would be almost solely present in the seawater. Smectites possess a large specific surface area ($6\text{-}8 \times 10^5 \text{ m}^2 \text{ kg}^{-1}$) and a relatively high structural charge

(up to 1200 meq kg^{-1}) imparting them with important sorptive properties. It is quite, therefore, possible that metal ions like Ni^{2+} and Co^{2+} reside in the exchangeable Mg^{2+} interlayer sites of FCR smectite. These positions are excellent coordinating sites which would be very rapidly filled by these metal ions after early diagenesis under oxic conditions. Indeed, Rybicka *et al.* [3] investigated the adsorption/desorption behavior of Ni on cheto-smectite (Arizona, USA). According to these authors, the adsorbed amount of Ni was relatively high about 40-50 %. The ability of cheto-smectite to these two metals in a few days (Rybicka *et al.* [3]) suggests the feasibility of their continued accumulation into FCR smectite from the pore seawater enriched with Ni for tens or even hundreds thousands of years after its formation. Therefore, this smectite was open to exchange (after early diagenesis) with the oxygenated seawater that was already enriched with Ni. This must also be true for Co which shows a similar geochemical behavior as Ni in sedimentary environments. The relative thinness of FCR would, undoubtedly, tend to facilitate a high exchange of Ni and Co within the boundary column with the pore seawater.

The distribution patterns of Ni and Co in most marine KT boundaries throughout the world are very similar and these metals are well correlated with cosmogenic Ir and with one another (e. g. Gilmour and Anders [5]). As Ir is a highly compatible metal the only sources for it in these boundaries are either the deep mantle or asteroidal infall. The fact that only large scale volcanic activity at the KT time, Deccan Traps, shows low amounts (<35 ppt) of Ir in its predominant tholeiitic basalts (99 %) indicates an asteroidal source (Shukla *et al.* [6]). It also appears that in the worldwide boundaries Ni and Co have their maxima at about the same stratigraphical level (e. g. Strong *et al.* [7], Schmitz [1]) and that the boundary clays are the dominant carrier phase of these metals. These facts strongly indicate Ni and Co of these boundaries (including FCR) have a common origin and argue against a local source for these metals, e. g. chemical weathering of the terrestrial rocks on land.

Conclusions

Simple geochemical calculations suggest that the primary (airborne) impact fallout directly settled down into the seawater at Stevns Klint could partly source these two metals in FCR smectite. Another, but more abundant, source for Ni and Co in this water could be the impact fallout on nearby soil. Indeed, Davenport *et al.* [8] estimated

that the top of soil after the Alvarez *et al.* [2] impact would be covered with the fallout, having Ni that is one or two order of magnitude greater than the contemporary average level of Ni (16 ppm) in soil. According to these authors, the impact infall would have Ni and Co concentrations of between 133-1330 ppm and 7-70 ppm, respectively. We suggest, therefore, that Ni and Co in FCR smectite were probably sourced by the impact fallout on nearcoastal soil. The fallout was leached from these metals by the (impact-derived acid?) surface waters. Finally, most of Ni and Co in FCR smectite was probably sourced by the chondritic component of the fallout.

References

- [1] B. Schmitz, *Geology*, 1988, **16**, 1068-1072.
- [2] L.W. Alvarez, W. Alvarez, F. Asaro, H.V. Michel, *Science*, 1980, **208**, 1095-1108.
- [3] E.H. Rybicka, W. Calmano, A. Breeger, *Appl. Clay Sci.*, 1995, **9**, 369-381.
- [4] D.E. Erikson, M. Dickson, *Geology*, 1987, **15**, 1014-1017.
- [5] I. Gilmour, E. Anders, *Geochim. Cosmochim. Acta*, 1989, **53**, 503-511.
- [6] P.N. Shukla, N. Bhandari, A. Das, A.D. Shukla, J. S. Ray, *Proc. Indian Acad. Sci.*, 2001a, **110**, 103-110.
- [7] C.P. Strong, R.R. Brooks, S.M. Wilson, R.D. Reeves, C.J. Orth, X.-Y. Mao, R.L. Quintana, E. Anders, *Geochim. Cosmochim. Acta.*, 1987, **51**, 2769-2777.
- [8] S.A. Davenport, T.J. Wdowiak, D.D. Jones, P. Wdowiak, *Geol. Soc. Am. Spec. Pap.*, 1990, **247**, 71-76.

THE CRETACEOUS-TERTIARY BOUNDARY FISH CLAY AT HØJERUP (STEVNS KLINT, DENMARK): Ni IN THE BIOGENIC CALCITE-RICH FRACTION

N. D. Nikolić¹, B. Ž. Todorović² and P. I. Premović¹

¹Laboratory for Geochemistry, Cosmochemistry and Astrochemistry, Department of Chemistry, University of Niš, P.O. Box 91, 18000 Niš, Serbia. (asteroid.pavle@yahoo.com)

²Laboratory for General Chemistry, Faculty of Tehnology, University of Niš, P.O. Box 79, 16000 Leskovac, Serbia.

Abstract

Geochemical study of Ni in the biogenic calcite-rich fraction of the Cretaceous-Tertiary boundary Fish Clay at Højerup has been undertaken. The Biogenic calcite-rich fraction shows enhanced concentration of Ni (245ppm). Our conclusion is that this enrichment represents the sudden and rapid input of high Ni into the late Cretaceous seawater at Stevns Klint.

Introduction

An anomalously high Ir concentration in the Cretaceous-Tertiary boundary Fish Clay at Højerup has been reported by Alvarez *et al.* [1]. The authors proposed that this enhanced Ir concentration was produced by a late Cretaceous asteroid impact. Apart from Ir, this boundary is also enriched in the other trace metals such as Ni. Fish Clay at Højerup belongs to one of the classic KT boundaries at Stevns Klint. We can differentiate five distinctive layers (i. e. II, IIIA, IIIB, IV and V) within this boundary. IIIB is here considered to constitute the main part of the KT boundary section at Højerup. Ni was chosen primarily because of its distinctive (but relatively simple) geochemical activity and property.

Experimental

The bulk sample of Fish Clay from an outcrop 200m south of Højerup Church was collected by Dr Helle Schummel. In this report, Ni in the biogenic calcite-rich fractions of II, IIIB, IV and V were determined by Inductively Coupled Plasma-Optical Emission Spectrometry (ICP-OES). A Spectroflame ICP-OES instrument was employed and Ar was used as the plasma gas. Total uncertainties (including accuracy error) of the analyses for these metals range from 5% to 20%.

Results and Discussion

The distribution of Ni across Fish Clay shows that the biogenic calcite-rich fraction of II contains less than 20 ppm of Ni and this metal is the highest in IIIB, diminishing upward (IV) and ultimately disappears (V), Figure 1. A more than 10-fold increase of Ni in IIIB fraction is consistent with a single/rapid introduction of (probable cosmogenic) Ni into the seawater at Stevns Klint. The background value of Ni in V frac-

tion suggest that after deposition of IIIB this influx of Ni into the seawater probably ceased to exist at all.

Ni associated with the biogenic calcite-rich fraction of IIIB may mainly reside in this mineral. If this is a case then Ni in this IIIB fraction represents biological Ni i.e.

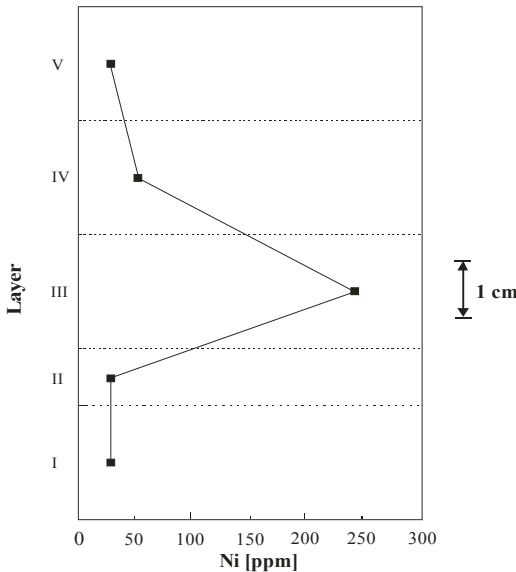


Figure 1. Distribution of Ni [ppm] within the carbonate fractions of the layers I, II, III, IV and V

the direct (biochemical) incorporation of their 2+ ions into the shells of calcareous microbiota. This process could take place during their metabolic uptake of the surface Ni associated with the biogenic calcite-rich fraction of IIIB may mainly reside in this mineral. If this is a case then Ni in this IIIB fraction represents biological Ni i.e. the direct (biochemical) incorporation of their 2+ ions into the shells of calcareous microbiota. This process could take place during their metabolic uptake of the surface seawater already enriched with these ions. IIIB contains relatively abundant calcareous benthic foraminifera, dinoflagellates and also a low number of planktic foraminifera and nannofossils.

Thus, if Ni is incorporated into the biogenic calcite of IIIB than the calcitic shells of these microfossils are probably their hosts.

The ICP-OES analysis shows that the carbonate fraction (mainly biogenic calcite) of the Fish Clay near Rødvig (4km far from Højerup), contrary to expectations, contains no enhanced concentration of Ni (<10 ppm, Table 1) compared to background. If the biochemical uptake of calcareous microbiota led to the formation of the calcite shells enriched with Ni at Højerup than it rather would be strange that the corresponding material at nearby Rødvig shows no evidence at all of this activity.

An alternative possibility is that Ni actually occurs in another phase. Apparently the use of 1.0 M sodium acetate is an established method for the dissolution of sedimentary carbonates. However, the effect of this reagent is not limited to carbonate dissolution. Considerable amounts of specifically sorbed Ni may be solubilized by this

Table 1. Geochemical concentration of Ni [ppm] in the carbonate fractions of the layers I, II, III, IV and V

Layers				
I	II	IIIB	IV	V
25	25	245	50	25

buffer at pH 5.0 [2]. A previous geochemical study, however, suggests that contamination of this source represents a serious problem only if the trace metal concentrations in the acetate buffer leachate are less than 10 ppm [3].

Whether biogenic Ni or sorbed Ni best explains their association with the carbonate fraction of IIIB it does represent the sudden influx of this metal into the seawater at Stevns Klint. Evidently, the injection of high Ni into this water would be particularly vulnerable to marine (calcareous) microbiota [4,5,6]. Considering the long scale of Ni (90,000 y) residence time, we hypothesize that toxicosis of this metal can be far more substantial than the other environmental effects (including acid rainfall, inhibition of photosynthesis, drop of temperature and greenhouse effects) induced by the late Cretaceous asteroid impact.

Conclusion

Our geochemical study suggests that biogenic Ni or sorbed Ni in the IIIB biogenic calcite-rich fraction does represent sudden influx of this metal into seawater at Stevns Klint. We suggest that Ni in this fraction was probably sourced by impact fallout on land (soil).

References

- [1] L.W. Alvarez, W. Alvarez, F. Asaro, H. V. Michel *Science*, 1980, **208**, 1095-1108.
- [2] M.G. Hickey, A. Kitrick, *J. Environ. Qual.*, 1984, **13**, 372-376.
- [3] E.A. Boyle, S.S. Husted, S.P. Jones, *J. Geophys. Res.*, 1981, **86**, 8048-8066.
- [4] R.G. Prinn, B. Fegley, *Earth Planet. Sci. Lett.*, 1987, **83**, 1.
- [5] D.E. Erikson, M. Dickson, *Geology*, 1987, **15**, 1014.
- [6] S.A. Davenport, T.J. Wdowiak, D.D. Jones, P. Wdowiak, *Geological Society of America Special Paper* 1990, **247**, 71-76.

THE INFLUENCE OF *ORTHO*-EFFECT ON THE EXTRACTION OF CRESOLS AND DIHYDROXYBENZENES BY ETHERS

G.M. Nikolić¹, R.S. Nikolić² and J.M. Perović²

¹ Department of Chemistry, Faculty of Medicine,

Bulevar dr Zorana Đinđića 81, 18000 Niš, Serbia, goranhem@yahoo.com

² Department of Chemistry, Faculty of Sciences, Višegradska 33, 18000 Niš, Serbia

Abstract

Extraction of *ortho*- and *para*-methylphenols (cresols) and dihydroxybenzenes (catechol and hydroquinone) was performed with diethyl and diisopropyl ether from water and aqueous solutions of NH₄Cl, (NH₄)₂SO₄, NaCl, Na₂SO₄, KCl, K₂SO₄, MgCl₂, and MgSO₄. In both cases the D values for *ortho*- isomers were higher in comparison to the D values obtained for *para*- isomers. Significantly higher ratio of D(*ortho*)/D(*para*) for dihydroxybenzenes in comparison to cresols is probably the consequence of intramolecular hydrogen bond formation in catechol. It is also worth mentioning that much higher polarity of –OH group in comparison to methyl group largely decreased D values for the extraction of dihydroxybenzenes in comparison to cresols.

Introduction

The position of substituents on the benzene ring in disubstituted aromatic compounds has a great influence on the various physicochemical properties of these compounds. Among others there is a significant influence on the partitioning of these compounds in the water-immiscible organic solvent systems [1].

The knowledge of factors governing the distribution of organic compounds between water and immiscible organic solvents is very important [2]. Beside helping better understanding of liquid-liquid extraction processes, such knowledge may be useful for clarifying mechanisms of action of organic compounds in biological systems [3].

In this work we investigated the relationships of distribution ratios for *ortho*- and *para*- methylphenols (cresols) and dihydroxybenzenes obtained by the extraction with diethyl ether and diisopropyl ether from water and aqueous solutions of different inorganic salts.

Experimental

All the chemicals used in this work were of analytical grade purity and have been used without further purification. Stock solutions (1 g dm⁻³) of phenolic compounds were prepared by dissolving exactly weighted amount of substance in distilled water and pH of the solution was adjusted to 2 by the addition of HCl. The stock solution of each phenolic compound (2 cm³) was diluted to 20 cm³ with water or saturated aqueous salt solution and then extracted with diethyl or diisopropyl ether. The absorbance of aque-

ous phase was measured at λ_{\max} for each phenolic compound and the D value was calculated according to the equation [4]:

$$D = \frac{A_0 - A}{A} \frac{V_{aq}}{V_{org}}$$

where A_0 and A are the absorbances of the aqueous phase before and after extraction, and V_{aq} and V_{org} are the volumes of aqueous and organic phase, respectively.

SPECORD UV/VIS spectrophotometer (Carl Zeiss, Jena) was employed for absorbance measurements.

Results and Discussion

Extraction of *ortho*- and *para*-cresol was performed with diethyl and diisopropyl ether from water and aqueous solutions of NH_4Cl , $(\text{NH}_4)_2\text{SO}_4$, NaCl , Na_2SO_4 , KCl , K_2SO_4 , MgCl_2 , and MgSO_4 . The relationship between D values obtained for *ortho*- and *para*-cresol is shown on the Figure 1.

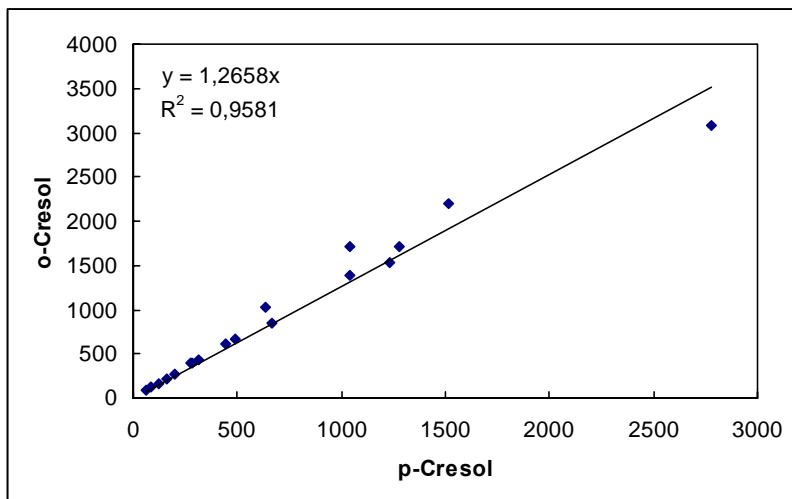


Fig. 1. Relationship between D values obtained for *ortho*- and *para*-cresol.

Extraction of catechol (*ortho*-dihydroxybenzene) and hydroquinone (*para*-dihydroxybenzene) was performed with diethyl and diisopropyl ether from water and aqueous solutions of NH_4Cl , $(\text{NH}_4)_2\text{SO}_4$, NaCl , Na_2SO_4 , KCl , K_2SO_4 , MgCl_2 , and MgSO_4 . The relationship between D values obtained for catechol and hydroquinone is shown on the Figure 2.

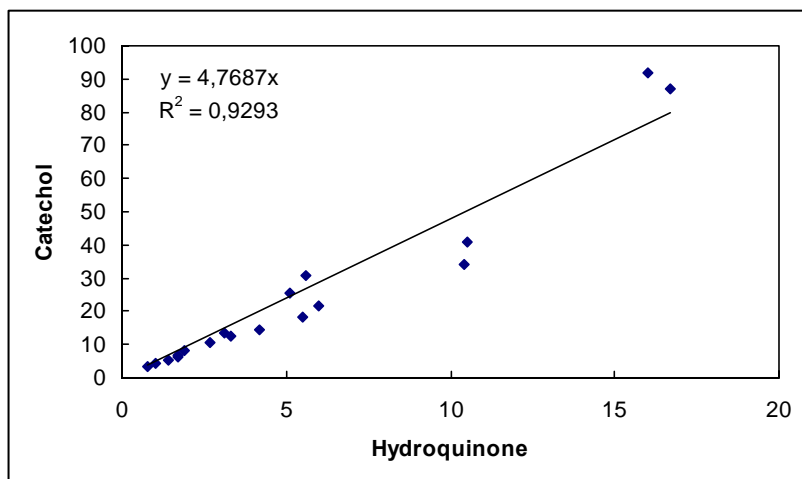


Fig. 2. Relationship between D values obtained for catechol and hydroquinone.

Both in the case of cresols and dihydroxybenzenes the D values were higher for the extraction of *ortho*- isomers which is in accordance with literature data for similar systems [1,5,6]. However, the ratio $D(\textit{ortho})/D(\textit{para})$ was about 1.27 for cresols while it was about 4.77 for dihydroxybenzenes. This large difference is probably the consequence of intramolecular hydrogen bond formation in catechol. It is also worth mentioning that much higher polarity of $-\text{OH}$ group in comparison to methyl group largely decreased D values for the extraction of dihydroxybenzenes in comparison to cresols.

References

- [1] Ya.I. Korenman, Zh. Obsch. Khim., 1977, **47**, 742-745.
- [2] Ya.I. Korenman, J. Anal. Chem., 2002, **57**, 900-906.
- [3] N. El Tayar, R-S. Tsai, B. Testa, P-A. Carrupt, A. Leo, J. Pharm. Sci., 1991, **80**, 590-598.
- [4] I. Kojima, S.S. Davies, Int. J. Pharm., 1984, **20**, 247-251.
- [5] Ya.I. Korenman, T.N. Ermolaeva, Zh. Prikl. Khim., 1989, **62**, 114-117.
- [6] Ya.I. Korenman, T.N. Ermolaeva, E.V. Bobrinskaya, L.A. Kharitonova, Zh. Prikl. Khim., 1994, **67**, 1569-1571.

THE CONCEPT OF THE PILOT-PLANT IN THE AIM TO THE WET-PROCESS DERIVED H_3PO_4 FOR COMMERCIAL PRODUCTION OF PHOSPHATE SALTS

M.B. Rajković¹, Č. Lacnjevac¹, D. Tošković² and D. Stanojević²

¹Faculty of Agriculture, Zemun, University of Belgrade, Serbia

²Faculty of Technology, Zvornik, University of East Sarajevo, Bosna&Herzegovina

Abstract

This paper presents the concept of the pilot-plant and its possibilities to be an annex on the existing technological process of the production of phosphoric acid and sodium-tripolyphosphate, as raw material for production of detergents. In this study the blow-out fluorine method using air, steam or steam-air mixtures, either in the presence of active compounds containing silicon, or without these substances was employed for purification of phosphoric acid, either in the laboratory practice or pilot-plant scale.

Introduction

The analysis of phosphoric acid, previously prepared in the installations for sodium-tripolyphosphate (TPP) in the IHP Prahovo have clearly confirmed the efficiency of fluor removal from the concentrated phosphoric acid (50% P_2O_5) by the method of exhausting using *bentonite* ($\text{Al}_2\text{O}_3 \cdot \text{Fe}_2\text{O}_3 \cdot 3\text{MgO} \cdot 4\text{SiO}_2 \cdot 4\text{H}_2\text{O}$) [1]. The purpose of the research in this paper has been to confirm the results of laboratory tests of the outlined apparatus and technological process on the semi-industrial level. For that reason this paper presents the pilot project, pilot plant of the semi-industrial installations and the possibility of building the installations into the already existing technological process has been discussed.

Experimental

Technological scheme of the semi-industrial installations is shown in Fig. 1. [2]

From Fig. 1 it is seen that the defluorination process is divided into four sections: In **Section A**, the preparation of suspension is carried out. Concentrated 50% P_2O_5 acid from the tank-decanter is brought into the suspension preparation container which is kept at the temperature of 70-80 °C by means of a warming body. A controlled dosing of bentonite through snailish doser is carried out simultaneously with the acid. The prepared suspension is brought into the suspension doser by means of the pump. **Section B** serves for removing fluor inside the defluorinator and that is the most important part of the process. **Section C** is planned for purification of waste fluorine gases, during which H_2SiF_6 is formed (concentration of the silicofluorohydrogen acid is 8-10%), and which is collected in the receiving tank. **Section D** presents a final degree of phosphoric acid purification, that is, the degree of obtaining the defluorinated and purified phosphoric acid-*green acid*. Upon the completed defluorination process, the suspension is transported to the filtration appliance from which, as a filtrate, the acid free from

bentonite and purified to the highest degree, is obtained. The process is planned to function both continually and discontinually depending on the installed consumer.

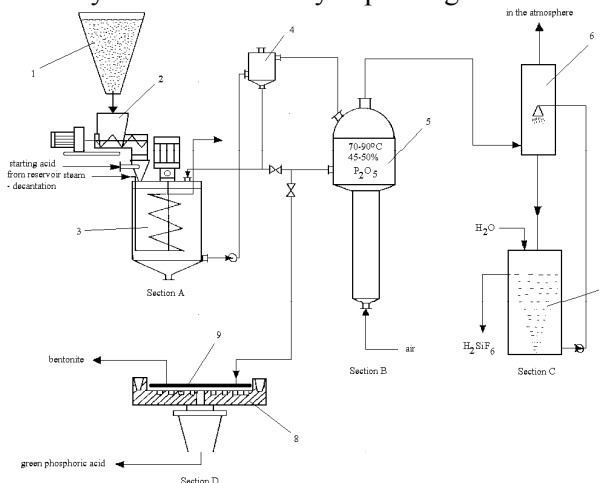


Fig. 1. Scheme of the semi-industrial installations for H_3PO_4 defluorination: 1-bunker for bentonite; 2-snailish doser; 3-suspension forming container; 4-suspension dosing container; 5-defluorinator; 6-absorber; 7-tank; 8-filtration appliance; 9-filter fabric.

The presented scheme of the semi-industrial installations is outlined for the purpose of formulating the optional procedure for obtaining the purified and deluorinated acid, which as an independent unit, can become applicable within the existing utility in the installations for the phosphoric acid production.

The installations for purification-defluorination of the phosphoric acid can be connected to: tank-decanter 50% P_2O_5 phosphoric acid (case A) or directly to a drainpipe (case B). It is most optimal to connect it with the tank-decanter for the concentrated acid.

Results and Discussion

Phosphoric acid used for our experiments was previously defluorinated in an industrial scale to meet the standard quality requirements, but these are not appropriate for use in food industry ($< 0.1\%$). The efficiency of defluorination by using the blowout method was evaluated in comparison with conventional methods. We used 12 kg of bentonite per 1 t phosphoric acid. The effects of different methods used for phosphoric acid defluorination are presented in Table 1.

Table 1. Results of different methods for phosphoric acid defluorination in the presence of different substances containing silicon

Method	F (%)	%F to P_2O_5 ratio	Defluorination effect
Initial acid	0.350	0.874	-
Evaporation method	0.220	0.442	37.10
Blowout method	0.100	0.178	71.40
Blowout method with bentonite	0.057	0.105	83.70

Figure 2 illustrates the dependence of time on the blowout efficiency. The graph was constructed on the basis of all available measurements.

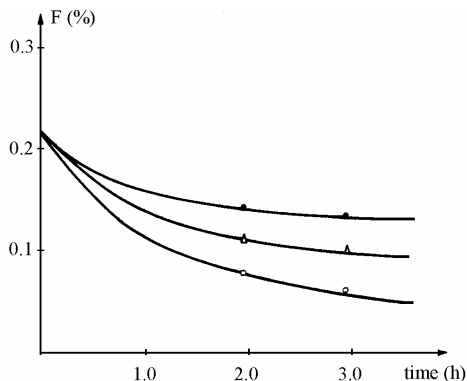


Fig. 2. The effect of blowout time on fluorine content in phosphoric acid at 70°C: Δ - in the absence of additives; ○ - in the presence of bentonite; ● - in the presence of white soot.

The curve representing the effect of bentonite has a maximum slope and only in this case a fluorine content in the product was less than 0.10%.

Conclusion

The exhaustion method has shown a series of advantages in relation to conventional procedures of phosphoric acid defluorination. The conception of semi-industrial installations enables not only the discontinual but also the continual process of phosphoric acid defluorination, for obtaining the product which can be used in food industry. The reduction of fluorine content to below 0.10% can be achieved by adding only 12 kg of bentonite per 1 ton of acid. The acid temperature in the working zone of apparatus should be kept at 70-80 °C. The processing time should not be shorter than 3 hours for an efficient process to be obtained.

Acknowledgements

The work was supported by the Ministry of Science and Environmental Protection of the Republic of Serbia (Grant ON 142039).

References

- [1] M.B.Rajković, G.Vladislavljević, The 12th International Congress of Chemical and Process Engineering, CHISA'96, Praha, Czech Republic, 25-30 August 1996, General topics, P1.102 [137].
- [2] M.B.Rajković, D.Tošković, I.Čirić, G.Vladislavljević, Glasnik hemičara i tehnologa Republike Srpske, 2002, **43**, 93.

Education

(0)

CONTRIBUTION TO THE BIOGRAPHY OF THE FIRST NOBEL PRIZE WINNER AND PHYSICAL CHEMIST Jacobus Henricus Van't Hoff

T. Halaši

Departman za hemiju, PMF, 21000 Novi Sad, Trg Dositeja Obradovića 3, halasi@ih.ns.ac.yu

Abstract

Jacobus Henricus van't Hoff (30. August 1852, Rotterdam-1. March 1911, Steglitz/Berlin) was the first Nobel Prize Winner from chemistry for 1901. He was the founder of three theories: of Stereochemistry, the Chemical Dynamics and of the Law of the Osmotic pressure. Van't Hoff with Svante August Arrhenius (19. February 1859, Gut Vik/Uppsala - 2. October 1927, Stockholm) and Wilhelm Ostwald (21. August, Riga - April 1932, Grossbothen/Leipzig) founded the contemporary Physical chemistry. They are known in the History of Physical chemistry among of the first Nobel Prize Winners: van't Hoff 1901, Arrhenius 1903, Ostwald 1909. and also as a good friends and coworkers related to interesting correspondence.

Introduction

The biographers pointed out that van't Hoff and Ostwald in „Realschule” weren't good in success. Later, van't Hoff builded up an excellent carrier harmonizing the laboratory technique, skills and the theory. Van't Hoff, Arrhenius and Ostwald published many scientific and philosophical essays [1-3], papers from History of science and Physical chemistry. In this paper were used original and relevant literature which help to present van't Hoff, as an excellent scientist and interesting person.

The origin of the van't Hoff family

In this paper is shown a specific view to the van't Hoff biography [4]. There were searched an archives material about the origin of the van't Hoff family name which appears by 1. October 1689. when was born Leendert Adriaensz, de jongste van't hof. „Hof” on dutch language means „garden”. They lived on the Maas river side, on their land which was like terrace. Their family name was written as Hof, Van t Hoff, Vant Hof, Vant Hoff, van't hof, van't Hof, van't Hoff. Leendert was a landowner, who married with Pietertje Pieters Verduyn from Barendrecht. They had two daughters and two sons. In the Protocol of Deichrat Place 29. June, 1733 was registred a family Van't Hof. After the dead of Leendert, the younger son continued with family tradition and Pieter became the village mayor (1779-1796). He died in May 1801. His son Jacob was born 2. August, 1773. and became village mayor in Kleine Lind. He was a respectable person. In college he got his special glass with painted words „vrijheid, gelijrheid, broederschap”. It shows his progressive thinking also. He married on 23. October 1797. Maria Margaretha de Reus from Hedel, from province Nordbrabant. They had seven children already in alive. Jacob died in Typhus 12/13. April, 1827. and the family sold the „Het Hof”. The oldest son became the lord mayor of Grote

Lind and the property was moved to Meerdervoort. The third brother Jacob Marius (4. April, 1809-16. March, 1847) was secretary of the Military Court in Dordrecht. Jacobus Henricus (14. June 1817) was a sailor physician and lived on South Holland Island Over-Flakkee in Sommelsdijk. He married (23. March, 1848) Alida Jacoba Kolff (born 16. December, 1820. in Middelharniss). She was the daughter of wine dealer. The family moved to Rotterdam. They had seven children, two daughters and five sons. Among the sons was Jacobus Henricus jr. the scientist, who was born 30 th August 1852. He was named Henry and he later signed himself Henri van 't Hoff.

The short biography of. J.H. van't Hoff

Henry and his brother Jacob be at school in Rotterdam. They attended elementary school *Herrn Delfos*. On that time Henry was an excellent pupil, good from mathematic and biology. After elementary school he attended secondary school „*Hoogere Burgersschool*” where existed the *Thorbeck* reform system. There, Henry learned first time chemistry, lectured by Dr. Hubrecht. Henry graduated after the fourth class in September 1867. In fifth class he was excellent from Mathematics and Mechanics, very good from Physical Science, including Chemistry, enough from Languages, Literature and Drawing. Later he proved himself as poet, using Byron's style.

Henry studied Polytechnical high school in Delft, preparing himself for technology. Organic and Inorganic Chemistry learned from A.C. Gudemans. He was enthusiastic about laboratory work, but often neglected other subjects. Henry graduated Technology 8 th July 1871.

He started with study in Leiden. In meantime he read August Comte (1798-1837), William Whewell (1794-1866), Robert Burns (1759-1896) and Heinrich Heine (1794-1866). In Leiden he studied Mathematic in the class of professors van Geer and Biereus de Haan. Henry took his Kandidat examen only with grade „Good”, 21. June 1872. He doesn't liked Leiden city and that for the doctoral study continued in Bonn. He said: Leiden is prose but Bonn is poetry. In Bonn Henry learned about valence and polyatomic radicals. The University in Bonn had a good equipped laboratories. The working hours were from 9 am to 6 pm. The leading professor in Bonn was August Kekulé von Stradonitz (7.9.1829, Darmstadt-13.7.1896. Bonn), who solved the Benzene structure. On that time one of the assistants was Otto Wallach (27.3.1847, Königsberg-26.2.1936, Göttingen), a later Nobel prize winner in 1910.



Jacobus Henricus van't Hoff, as student in Bonn.

Henry left Bonn 1873. and started to work in Paris on *École de médecine* with Adolph Wurtz (1817-1884), till 1874. After that he returned to Holland where he obtained his doctor's degree, 22 th December 1874. in Utrecht The thesis title was: *Beitrag zur Kenntnis der Cyanessigsäure und Malonsäure*. He was promoted to: *Matheseos-Magister et philosophiae naturalis Doctor*. Van't Hoff started with carrier as lecturer at *Veterinary College* at Utrecht 1876. In 1878. he was appointed as Professor of Chemistry, Mineralogy and Geology at the University of Amsterdam. In 1896. appointed as Honorary Professor in Berlin University, there became member of the Royal Prussian Academy of Sciences. At this post he worked till the end of his life.

Jacobus Henricus van't Hoff in 1901. received the *First Nobel Chemistry Prize* for his pioneering work on *Chemical dynamics and Osmotic pressure in solutions* [5].

Literature

- [1] J. H. v't Hoff, *Etudes de dynamique chimique*, Amsterdam, Frederik Müller co, 1884.
- [2] W. Ostwald, *Grosse Männer von Wilhelm Ostwald*, Akadem. Verlagsgesellschaft m. b. H, Leipzig, 1909.
- [3] S. Arrhenius, *Bemerkungen über einige gegen die Hypothese der elektrolytischen Dissociation erhobenen Einwände*, Ber., 1891, Bd. 24, S. 2255-2264.
- [4] E. Cohen, *Jacobus Henricus van't Hoff, Sein leben und Wirken*, 1912, Akademische Verlagsgesellschaft m.b.H., Leipzig.
- [5] V. Junk, *Die Nobelpristräger, 30 Jahre Nobelstiftung*, 1930, Verlag Michael Winkler, Wien/Leipzig, s. 93-94.

Author Index

N.D. Abazović,	657	E. Böresök,	707
B.F. Abramović,	657	N. Borojević,	463
A. Abu Rabi,	317	S. Bošković,	534, 540
B. Adnađević,	186, 189, 677	D. Božić,	525
M. Adžić,	344, 416, 422	T.P. Brdarić,	102
M.M. Aleksić,	329	T. Brdarić,	501, 525
V.B. Anderluh,	657	R. Bredehorst	440
K.K. Anđelković,	710	S. Brocchini	347
M. Aničić,	627	M. Cakić,	719, 722
S. Anić,	252, 258	F. Canova,	469
A. Antić-Jovanović	93, 96	P. Carranceja,	183
M. Antonijević-Nikolić,	713	I. Cekić,	49, 332
D. Arandelović,	174, 522	R. Cervellati,	255
K. Arishtirova,	564	Z. Cherkezova-Zheleva,	171
Z. Arsenijević,	204	A.G. Chmielewski	38
K. Asanović,	591	St. Christoskova,	198, 513
A. Auroux	123, 680	A.A. Churin,	365
B.M. Babić	663	I. Ciurcanu	636
D. Babić,	555	R.G. Compton	314
K. Babić-Samardžija,	698	S.M. Crumlett,	479
G. Bačić	341, 463, 651	R. Csonka-Rákosa,	707
D. Bajuk-Bogdanović,	111	G. Cuttone,	448, 451
D. Bakeš,	246	J. Cvetičanin	117
S. Balan,	347	J. Cvetičanin,	504
P. Banković	162, 168, 180	D.M. Cvetković	383, 386
C.E. Banks,	314	D. Cvetković,	407
A. Banjac,	398, 419	I. Cvijović,	58
J.M. Baranac,	99, 102	N. Cvjetičanin,	516, 573
E. Barbarini,	469	M. Čakar	739
J. Barek,	285	J. Čejková,	273
D. Batani,	469	M. Čolović,	401
V. Batas,	660	J.J. Čomor	326
M. Bavcon-Kralj,	401	M.I. Čomor	353, 657
G.J. Bayer	445	A. Čučulović,	639
N. Begović	150	O. Čudina,	353
F. Bejosano	377	Ž. Čupić	162, 252, 264
M.V. Beljanski,	276, 377, 392	N. Časić,	507
D. Bengin	642	G. Ćirić-Marjanović,	579, 582
A. Benuzzi,	469	A. Daković,	645
G. Bijelić,	350	M. Daković,	463
N.S. Blagojević,	546, 549	Lj. Damjanović,	174, 648
S.M. Blagojević,	252, 258	S. Damyanova,	564, 567
S.N. Blagojević,	252, 261, 335	M.L. Dašić	99
C. Blanco,	183	F.C. De Schryver,	108
J. Blanuša	573	D. Debeljković,	213
G.A. Bogdanović,	701	M. Demajo	395, 398, 425
V. Bojović,	93, 96	S. Despotović,	555
H. Bönnemann,	304	A. Devečerski,	525, 534

J.M. Dimitrić-Marković,	99, 102	T. Halaši	763
R.Z. Dimitrijević,	531, 543	T. Hall,	469
V. Dondur,	174, 531, 648	D.P. Hanson,	479
S. Dragović,	454, 651	R. Hercigonja,	680
V. Dragutinović,	380	K. Hermansson	67
Z. Dražić-Janković,	323, 683	Ch. Hilgardt,	273
A.V. Dremetsika,	736	J. Hofkens	108
V. Drobñjak,	162	I. Holclajtner-Antunović,	111
J. Dukić,	540	P. Holler	582
D. Đikanović,	105	A. Horvat	395, 398, 419
D.D. Đokić	431, 434, 460	T. Husović,	534
A.D. Đorđević,	413, 419, 425	Lj.M. Ignjatović,	323, 683
A. Đorđević,	733	N. Ignjatović,	498
D. Đorđević,	174, 624, 654	D. Iles	645
V. Đorđević,	117, 504	D. Ilić,	311
Z. Đurić,	671	K. Ilić	742
J. Đustebeek,	117, 504	Lj. Ilić	719, 722
R. Edreva-Kardjjeva,	165, 207, 210	M. Ilić	374
A. Egelja,	540	M. Isaković	555
M. Endo	3	B. Ivković,	742
J.L.G. Fierro,	564	L. Izrael-Živković,	192
S. Filip,	642	D. Jakovljević,	585, 588
D. Filipović	437	M.M. Jakšić,	304
N.R. Filipović,	710	O. Jakšić,	671
M. Frantlović	671	Z. Jakšić,	528, 671
M.V. Frontasyeva,	627	I. Janković	353
B.R. Furman,	479	B. Janković,	677
S.D. Furrow	255	D. Janković,	434, 445, 460
M. Gabrovska,	165, 207, 210	Lj. Janković,	651
E. Gaigneaux,	567	S. Janković,	660
B.M. Gaković,	537	A. Janošević,	582
N. Gavrilov,	210	G.V. Janjić,	689
M. Gavrović-Jankulović,	377	S. Jelić,	264, 267
G. Gojgić-Cvijanović	392	M. Jeremić,	105
D. Golobočanin,	633	B. Jocić,	329
L. Gomidželović,	52	I. Jokić,	671
F. González	183	J. Joksić	624, 654
K. Gopčević,	374	G. Jordanov,	648
R. Gorjanović	371, 392	A.J. Jovanović	630
S. Gorjanović,	371, 377, 392	D. Jovanović	165, 207, 210
Ž. Grbavčić	204	J. Jovanović,	186, 189
B. Grbić,	204	Lj.S. Jovanović,	290
J. Grbović-Novaković,	501	M. Jovanović,	213
B.N. Grgur,	296	V. Jovanović,	332, 648
T. Grozdić	552, 733	V.M. Jovanović,	698
Z.J. Gršić,	666	V.Ž. Jovanović,	630
S. Grujić	730	Z. Jovanović,	579
S.R. Grujić,	546, 549	D. Jugović,	516
C. Guimon,	123	I. Juranić	579

G. Kadinov	171	M. Logar,	525
A.J. Kalauzi,	105	D. Lončarević,	162, 207
G.N. Kaluđerović,	716	G. Lucchini,	469
A. Kandić,	654	D. Lukić,	457
Lj. Kandić,	519	S. Lukić,	591
V. Kapetanović	329	V.V. Lunin,	144
I. Karadžić ,	192	M.A. Lješević,	663
N.A. Katsanos	736	G.V. Maksimov,	276, 365
A.L. Kawczyński	15, 270	N. Maksimova,	276
J. Keranen,	123	Lj. Malović,	585
M. Kićanović,	61, 380	D. Manasijević,	55
J. Kiurski,	159	P. Manojlović	615
S. Kljajević,	588	E. Manova,	198, 513
M. Koenig,	469	M.P. Marčeta-Kaninski,	733, 335
Lj. Kolar-Anić	252, 264, 350	A.M. Maričić,	543
M.K. Koleva,	230	M. Marinković	81
S.S. Konstantinović,	404	R. Marinković-Nedučin	159
L. Korićanac,	428, 451	M. Marinović-Cincović,	472, 594
A. Kostić,	189	B. Marjanović,	579, 582
B. Kovačević,	213	S.L. Markov	389
B.T. Kovačević,	522	D. Marković,	407, 410, 573
O.A. Kovačević,	522	D.A. Marković,	323, 642, 683
B.B. Krajčinović,	716	D.M. Marković,	84, 90
B. Kralikova,	469	D.Z. Marković,	404
A. Kremenović,	531	G. Marković,	594
K. Krinulović,	401	J. Marković,	585, 588
M.M. Krsmanović,	748	R. Marković,	49, 332
D. Krstić,	374, 401	S. Marković,	147, 150, 519
I. Krstić,	320	Z. Marković,	61, 147, 150
J. Krstić,	171, 210, 510	V.M. Matić,	570
V. Krstić,	183	S. Matijašević,	645
A.A. Kubasov,	132	B. Matović	534, 540, 525
J. Kuljanin-Jakovljević	472	Lj. Matović,	460
K.R. Kumrić,	326	V.A. Matyshak,	144
B. Kunev,	198, 513	R. Meckenstock	75
V. Kuntić,	742	V.B. Medaković,	368, 701, 704
V. Kusigerski,	573	S.M. Melnikov,	108
N.E. Kuz'menko	674	S. Mentus,	317, 320, 501
M. Kuzmanović,	93	K. Merzweiler,	716
M.M. Kuzmanović,	81, 507	E. Mihaila	87, 636
T.G. Kuznetsova,	144	Z. Mijić,	624
Č. Lacnjevac,	757	J. Miladinović,	730
C. Lapierre,	105	Z. Miladinović,	561
N.Đ. Lazarov	570	P. Milani,	469
P. Lazić	201	M.K. Milčić,	689, 701, 704
N.L. Lazić,	522	D. Milenković,	147
R.M. Leblanc	11	D. Miličević,	498
M. Leda,	270	M. Milić,	570
B. Legawiec	270	M. Milojević,	174

S. Milonjić,	457	H. Nishimura,	469
M. Milošević,	395, 398	B.K. Norling,	479
G.A. Milovanović,	195	I.T. Novaković,	710
S.S. Milovanović,	663	M. Novaković,	507
A. Milutinović-Nikolić,	180, 591	N. Novaković,	501
Š.S. Miljanić	639	T. Novaković,	156
N. Miljević	356, 607, 633	I. Novović,	84, 90
M. Miljković,	516	D. Obadović,	159
D. Minić,	55	Y. Ochi,	469
D.M. Minić,	49, 332, 543	A. Onjia	454
U. Mioč,	111	S. Ostojić,	61, 380
Z.M. Miodragović,	716	N.M. Ostrovskii	138
M.D. Mirković,	431, 434, 445	D. Paneva,	198, 513
N.N. Mišković,	748	G. Papakonstantinou,	304
S.S. Mitić	114, 177	I. Parezanović	58
Ž. Mitić,	719, 722	F.T. Pastor,	195
I. Mitov,	171, 198, 513	V. Pavelkić,	374
P.M. Mitrašinić,	279, 362	M. Pavlović,	61
M. Mitrić,	510, 516, 519	M.S. Pavlović,	81, 639
T. Mocek,	469	B. Pawelec,	564
A. Moise,	87, 636	N. Pejić,	252, 258
Z. Mojović,	180, 320	Lj. Pejov,	67
J. Molnár,	707	J.M. Perović,	754
L. Molnár-Hamvas,	707	C. Pesquera,	183
T. Momić,	356, 359	O. Pešek,	238, 249
L. Morozova-Roche	23	R. Petronijević,	660
G. Munteanu,	153	L.A. Petrov,	230, 564, 567
K.S. Nagabhushana,	304	I. Petrović,	428, 448, 451
A. Nastasović,	585, 588	S. Petrović,	156
J.M. Nedeljković,	472	L. Pezo,	213, 522
B. Nedić,	531	M. Pfeifer,	469
Z. Nedić,	49	P.A. Pfenđt,	630
K. Németh,	707	D.A. Pichugina,	674
S.G. Neophytides,	304	I. Pirmettis,	434, 460
O. Nešković	117, 504	P. Piseri,	469
A. Nićiforović,	344, 416, 422	S.O. Podunavac-Kuzmanović,	383, 386, 389
G.M. Nikolić,	754	A. Popović,	189, 627
G.S. Nikolić,	719, 722	G. Popović,	591, 739
J.D. Nikolić,	546, 549	M. Popović	507
N. Nikolić,	434, 445	N. Popović,	413, 425
N.D. Nikolić,	751	A. Popović-Bijelić,	350
N.S. Nikolić,	431	M. Pošarac,	525, 534
R.S. Nikolić,	754	N.I. Potkonjak,	261, 335
V. Nikolić,	90	T.N. Potkonjak,	261, 335
V.M. Nikolić,	335	J. Požega,	428
Z.S. Nikolić,	489, 492, 495	A. Präg,	469
S. Nikolić-Mandić	174	A. Predoeva,	567
D. Nikolova,	165, 210	G. Predović,	368
R. Ninković,	730	P.I. Premović,	727, 748, 751

G. Privitera,	451	I. Spasojević,	341
J. Prokopović,	422	V. Spasojević,	573
V. Rac,	680	M. Spiegel,	58
B.B. Radak,	666	E. Spillner,	440
S. Radaković,	341	A. Spirić	660
D.D. Radanović	713	D.N. Sredojević,	692
M. Radenković,	624, 654	H. Stabile,	469
Č.N. Radenović,	276, 365	A. Stamatović	599
T. Radičević,	660	Lj. Stamenković,	434
N. Radić,	204	N. Stanić	153
M.B. Radojčić,	344, 416, 422	D. Stanisavljev,	733
A. Radosavljević-Mihajlović,	540	M. Stanković,	165
K. Radotić,	105	M. Stanković,	168, 213
B. Radovanović,	594	D. Stanojević,	745, 757
M.B. Rajković,	710, 745, 757	I. Stanojević,	419
S. Rajšić,	621, 624	S. Stanojlović,	213
A. Rakić,	362	G. Starčević,	519
V. Rakić,	174, 648, 680	S. Stefanović,	660
D. Ranković,	204	D. Steinborn,	716
J.A. Rard,	730	J. Stejskal,	582
H.R. Rawls,	479	N.F. Stepanov,	132
A. Ristić-Fira	428, 448, 451	B. Stevanović	621
A. Rosić	180, 320	M. Stevanović,	498
J.R.H. Ross	144	M. Stoilković,	81, 457, 507
A.Ya. Rozovskii,	144	M. Stojanović,	645
Lj. Rožić,	156	S. Stojanović,	368
T.J. Sabo	716	B.C. Stojčeva-Radovanović	404
V.A. Sadykov,	144	D. Stojić	733
Z. Sandić,	585	M. Stoyanova,	198, 513
M. Sarajlić	528	S.M. Sunarić,	114, 177
M. Sarić,	463	D.Ž. Sužnjević	335
J. Savić,	356, 695	B. Šećerov,	463
A. Savin,	642	H. Ševčíková	273
J.J. Savović,	81	B. Šljukić,	314
G. Schmitz,	219	D.V. Šojić,	657
I. Schreiber	246, 249, 238	P. Špás,	238
L. Schreiberová,	238, 246, 249	S.B. Tanasković,	713
S. Shaunak,	347	M. Tasić,	621, 624
A.F. Shestakov,	674	O. Terzić,	510
M. Shopska,	171	Ž.Lj. Tešić	522
B.R. Simonović	380, 335, 440	P.M. Thompson,	479
M. Simonović,	440	Ya.V. Tikhii	132
M. Sindić	186	B.Ž. Todorović,	751
P.A. Siskos,	736	D. Todorović,	323, 448, 683
J. Skala,	469	D.M. Todorović,	552
D.M. Sladić,	710	M. Todorović,	111, 195, 730
G. Smulevich,	31	T.R. Todorović,	710
S.P. Sovilj	695, 698	M. Tomasini,	469
A.M. Spasić	486	M. Tomašević,	621, 627

Z.D. Tomić,	692	J. Vučina,	457
M.B. Tošić,	546, 549	D. Vučinić,	201
D. Tošković,	757, 745	G. Vučković,	713
M. Trchová,	582	A. Vujačić,	695
P. Trebše,	401	Z. Vujčić,	359
S.R. Trifunović,	716	Z. Vujić,	742
M.S. Trtica,	537	I. Vukanac	654
T.M. Trtić-Petrović,	326	N. Vukelić,	510
Ts. Tzacheva,	207	Z. Vukmirović,	621
H. Uji-i,	108	V. Vukojević	258, 350
J. Ullschmied,	469	Z. Vuković,	156, 168, 588
D. Uskoković	498, 516, 519	Ch. Wagner,	716
V. Vasić	359, 401, 695	S.T. Wellinghoff,	479
G. Vasile,	87	E.K.L. Yeow,	108
Lj. Vasiljević	745	M. Yoshimura	489, 492
D. Vasiljević-Radović,	528	J. Zakrzewska	111, 561
B.Z. Veličković,	748	S.D. Zarić	689, 692, 704
N. Veličković,	413, 425	B. Zarić,	344, 416, 422
S. Veličković,	117, 504	M. Zečević,	329
M. Veljković,	117, 504	Z. Zheleva,	198, 513
D. Veselinović,	639, 642	S. Zlatanovic-Milošević,	440
D. Vilotić	84	S. Zlatanović,	61
S. Vladimirov,	353	M. Zloh,	347
V.V. Volkov	365	J. Zvezdanović,	410
M. Voslař,	238	V.D. Živanović,	546, 549
S. Vranješ,	445, 460	D. Živković,	52, 55
S.D. Vranješ-Đurić,	431	Ž. Živković	55
M.M. Vrvic	192	A.M. Žujić,	633, 666
V. Vučić,	344, 422		

Participating Institutions

Advanced Technological School, 8 Hajduk Veljkova St, Šabac, Serbia	555
AG Festkörperspektroskopie, Ruhr-Universität-Bochum, Germany	75
Boreskov Institute of Catalysis SB RAS, pr. Lavrentieva, 5, Novosibirsk, 630090, Russia	144
Center for Multidisciplinary Studies, University of Belgrade, Kneza Višeslava 1, Belgrade, Serbia	279, 341, 350, 362, 733, 552
Centre for Multidisciplinary Studies, Laboratory of Biophysics, University of Belgrade, 29. Novembra 142, Belgrade, Serbia;	105
Centrohem, Karadorđeva 129, 22300 Stara Pazova, Serbia.	579, 582
Charles University in Prague, Department of Analytical Chemistry, UNESCO Laboratory of Environmental Electrochemistry, 128 43 Prague 2, Czech Republic	285
Chemical Industry HIPOL, 25250 Odžaci, Serbia	138
CIS Institute, Belgrade, Serbia	591
Copper Institute, Zeleni bulevar 35, 19210 Bor, Serbia	52
Dániel Berzsenyi Lutheran Lyceum, H-9400 Sopron, Széchenyi tér 11, Hungary	707
Ecole Polytechnique Palaiseau, LULI, France	469
Eko-Lab, Industrijska zona bb, P. Skela, Belgrade, Serbia	642
European Organization for Nuclear Research, CERN, Geneva, Switzerland	445
Faculty of Agriculture, University of Belgrade, Nemanjina 6, P. O. Box 127, Belgrade-Zemun, Serbia	174, 189, 371, 392, 648, 680, 745, 757
Faculty of Agronomy, University of Kragujevac, Kragujevac, Serbia	147, 150
Faculty of Biological Sciences, Institute of Botany and Botanic Garden, University of Belgrade, Takovska 43, Belgrade, Serbia	621
Faculty of Chemistry, University of Belgrade, Studentski trg 12, P.O. Box 157, 11000 Belgrade, Serbia	49, 111, 174, 189, 192, 195, 320, 332, 359, 368, 377, 392, 510, 522, 579, 627, 630, 689, 692, 695, 698, 701, 704, 710, 713, 716
Faculty of Electronic Engineering, Department of Microelectronics University of Niš, 18000 Niš, PO Box 73, Serbia	489, 492, 495
Faculty of Forestry, University of Belgrade, Kneza Višeslava 1, 11000 Belgrade, Serbia	84, 585

Faculty of Geography, University of Belgrade, Studentski Trg 4/III, Belgrade, Serbia	663
Faculty of Mathematics and Natural Sciences, University of Kragujevac, Radoja Domanovica 12, Kragujevac, Serbia	440
Faculty of Mathematics, University of Belgrade, Studentski trg 16, Belgrade, Serbia	368
Faculty of Mechanical Eng., University of Belgrade, 27. marta 80, 11000 Belgrade, Serbia	213
Faculty of Medicine, University of Niš, Bulevar dr Zorana Đinđića 81, 18000 Niš, Serbia	516, 719
Faculty of Medicine, Department of Chemistry, University of Niš, Bulevar dr Zorana Đinđića 81, 18000 Niš, Serbia,	754
Faculty of Medicine, Department of Pharmacy, University of Niš, Bulevar dr Zorana Đinđića 81, 18000 Niš, Serbia	114, 177, 722
Faculty of Mining and Geology, University of Belgrad, Đušina 7, 11000 Belgrade, Serbia	180, 320, 531, 543, 555
Faculty of Mining and Geology, Department of Mineral Processing, 7 Đušina St., 11000 Belgrade, Serbia	201
Faculty of Mining and Geology, Studentski trg 12-16, 11000 Belgrade, Serbia	525
Faculty of Natural Sciences and Mathematics, Department of Chemistry, University of Niš, Višegradska 33, P.O.Box 224, 18000 Niš, Serbia	114
Faculty of Natural Sciences and Mathematics, Department of Chemistry, University of Niš, Višegradska 33, P.O.Box 224, 18000 Niš, Serbia	177
Faculty of Pharmacy, University of Belgrade, Vojvode Stepe 450, Belgrade, Serbia	252, 713, 739, 742
Faculty of Pharmacy, Institute of Analytical Chemistry, Vojvode Stepe 450, P.O.Box 146, 11000 Belgrade, Serbia	329
Faculty of Pharmacy, Institute of Pharmaceutical Chemistry and Drug Analysis, Vojvode Stepe 450, P.O.Box 146, 11000 Belgrade, Serbia	329, 353
Faculty of Pharmacy, Institute of Physical Chemistry, Vojvode Stepe 450, P.O.Box 146, Belgrade	258, 329

Faculty of Physical Chemistry, University of Belgrade, Studentski trg 12-16, P.O. Box 137, 11000 Belgrade, Serbia	49, 81, 93, 99, 96, 102, 105, 111, 174, 186, 189, 204, 252, 258, 261, 264, 276, 317, 320, 323, 332, 335, 341, 350, 362, 463, 501, 507, 510, 516, 531, 543, 573, 579, 582, 639, 642, 648, 651, 677, 680, 683, 733
Faculty of Physics, Beograd, POB 368, Serbia	599
Faculty of Science Skopje, Institute of Chemistry, POBox 162, 1001 Skopje, Macedonia	67
Faculty of Science, University of Kragujevac, Kragujevac, Serbia	147, 150
Faculty of Science, Department of Chemistry, University of Kragujevac, 34000 Kragujevac, Serbia	716
Faculty of Science, Niš, Serbia	594
Faculty of Science, Department of Chemistry, Višegradska 33, Niš	404, 754
Faculty of Science, Mladena Stojanovića 2, Banja Luka, BIH	585
Faculty of Sciences, Department of Chemistry, University of Novi Sad, Trg D. Obradovića 3, Novi Sad, Serbia	290, 657, 763
Faculty of Technical Sciences, 21000 Novi Sad, Serbia	159
Faculty of Technology, Zvornik, University of East Sarajevo, Bosnia & Herzegovina	745, 757
Faculty of Technology and Metallurgy, 4 Karnegijeva St., 11000 Belgrade, Serbia	204, 213, 296, 534, 546, 549, 591
Faculty of Technology and Metallurgy, Department of Inorganic Chemical Technology, University of Belgrade, Karnegijeva 4, Belgrade, Serbia	730
Faculty of Technology, University of Nish, Leskovac, Serbia	410
Faculty of Technology, Bulevar Cara Lazara 1, 21000 Novi Sad, Serbia	159, 383, 386, 389
Faculty of Technology, University of Nish, Bulevar Oslobođenja 124, 16000 Leskovac, Serbia	404, 407, 719, 722
Foundation of Research and Technology Hellas, Institute of Chemical Engineering and High Temperature Processes, FORTH-ICE/HT, PO Box 1414, GR-26504 Rion, Achaïas, Patras, Greece	304

High School of Technics and Technology, Kosančićeva 22, Kruševac	323, 683
High School of Technology, 15000 Šabac, Serbia	713
Holding Institute of General and Physical Chemistry, Studenski trg 12/V P.O. Box 551, Belgrade, Serbia	61, 90, 111, 150, 174, 213, 252, 261, 276, 335, 371, 374, 377, 380, 392, 440, 522, 561,
Imperial College London, Faculty of Medicine, Hammersmith Hospital, Ducane Road, London W12 0NN, UK	347
Institut de Recherches sur la Catalyse CNRS, 2 Av. A Einstein, 69626 Villeurbanne, France	123, 680
Institut National Agronomique, 78850 Thiverval-Grignon, France	105
Institute for Chemistry, Technology and Metallurgy, Njegoševa 12, Belgrade,	630, 713
Institute for Chemistry, Technology and Metallurgy, Center for Catalysis and Chemical Engineering, Njegoševa 12, Belgrade	156, 162, 165, 168, 171, 180, 204, 207, 210, 252, 264, 317, 320, 510, 588, 591,
Institute for Chemistry, Technology and Metallurgy, Center for Chemistry, Njegoševa 12, Belgrade	174, 332, 585, 588, 624, 654, 716
Institute for Chemistry, Technology and Metallurgy, Department of Electrochemistry, P.O. Box 815, Belgrade	332, 698,
Institute for Chemistry, Technology and Metallurgy, Institute of Microelectronic Technologies and Single Crystals, Njegoševa 12, Belgrade, Serbia.	528, 671
Institute for Technology of Nuclear and Other Mineral Raw Materials 86 F. d'Esperey St. Belgrade, Serbia, Serbia	486, 546, 549, 645
Institute for the Application of Nuclear Energy, INEP, Banatska 31B, Zemun	454, 639, 651
Institute of Catalysis, Bulgarian Academy of Sciences, Acad. G. Bonchev St., Block 11, 1113 Sofia, Bulgaria,	165, 171, 198, 207, 210, 230, 513, 564, 567
Institute of Chemical Technology, Center for Nonlinear Dynamics of Chemical and Biological Systems, Prague, Technická 5, 166 28 Prague 6, Czech Republic	273
Institute of Chemical Technology, Department of Chemical Engineering, Prague, Technická 5, 166 28 Prague 6, Czech Republic.	238, 246, 249
Institute of Macromolecular Chemistry, Academy of Sciences of the Czech Republic, Heyrovsky Sq. 2, 162 06 Prague 6, Czech Republic.	582

Institute of Meat Hygiene and Technology, Kačanskog 13, 11000 Belgrade, Serbia	660
Institute of Nuclear Chemistry and Technology & Department of Chemical and Process Engineering, University of Technology, Warsaw, Poland	38
Institute of Nuclear Sciences Vinca, 11001 Beograd, P.O. Box 522, Serbia	58, 344, 401, 416, 422, 428, 448, 451, 454, 463, 472, 504, 510, 519, 537, 585, 588, 594, 607, 624, 633, 654, 657, 663, 666, 695, 748,
Institute of Nuclear Sciences Vinca, Chemical Dynamics Laboratory, Vinča Institute of Nuclear Sciences, 11001 Belgrade, P.O.Box 522, Serbia	457
Institute of Nuclear Sciences Vinca, Department of Atomic Physics P.O. Box 522, Belgrade, Serbia.	507
Institute of Nuclear Sciences Vinca, Department of Physical Chemistry, P.O. Box 522, Serbia	81, 117, 335, 356, 359, 374, 457, 507, 639, 733,
Institute of Nuclear Sciences Vinca, Department of Theoretical Physics and Physics of Condensed Matter 020/2, P. O. Box 522, Belgrade	264, 267, 516, 570, 573, 692, 701
Institute of Nuclear Sciences Vinca, Laboratory for Molecular Biology and Endocrinology, P.O. Box 522, Belgrade, Serbia	395, 398, 413, 419, 425, 437,
Institute of Nuclear Sciences Vinca, Laboratory for Radiochemistry and Physics, Serbia	353, 498
Institute of Nuclear Sciences Vinca, Laboratory for Radioisotopes, P.O. Box 522, Belgrade, Serbia	431, 434, 445, 457, 460
Institute of Nuclear Sciences Vinca, Laboratory of Material Sciences, Institute for Nuclear Sciences Vinča, Belgrade, Serbia	501, 525, 534, 540
Institute of Nuclear Sciences Vinca, Laboratory of Nuclear Physics, Belgrade, Serbia	501
Institute of Nuclear Sciences Vinca, Laboratory of Physics, P.O. Box 522, Belgrade, Serbia	326
Institute of Oncology and Radiology of Serbia	463
Institute of Physical Chemistry, BAS, Sofia, Bulgaria	207
Institute of Physical Chemistry, Polish Academy of Sciences Kasprzaka 44/52, 01-224 Warsaw, Poland	15

Institute of Physical Chemistry, "Ilie Murgulescu" Bucharest, Romania	153
Institute of Physics, P.O. Box 57, University of Belgrade, Zemun, Pregrevica 118, Serbia	84, 90, 624, 627
Institute of Physics, Environmental Physics Laboratory, University of Belgrade, Zemun, Pregrevica 118, Serbia,	621
Institute of Problems of Chemical Physics RAS, 1 prosp. Akad. Semenova, 142432 Chernogolovka, Moscow Region, Russia	674
Institute of Technical Science of the Serbian Academy of Sciences and Arts, Knez Mihailova 35/IV, Belgrade, Serbia	498, 516, 519
Instituto de Catalis y Petroleoquimica, CSIC, Cantoblanco, 28049 Madrid, Spain	564
Istituto Nazionale di Fisica Nucleare, LNS, Catania, Italy	448, 451
Joint Institute for Nuclear Research, 141980 Dubna, Russia	627
Karolinska Institute, Department of Clinical Neuroscience, Stockholm, Sweden	258, 350
Katholieke Universiteit Leuven, Department of Chemistry, Celestijnenlaan 200 F, 3001 Heverlee, Belgium	108
Faculty of Tehnology, Laboratory for General Chemistry, University of Niš, P.O. Box 79, 16000 Leskovac, Serbia.	751
Laboratory for Geochemistry, Cosmochemistry & Astrochemistry, University of Niš, P.O. Box 224, 18000 Niš, Serbia.	727, 748, 751
Lawrence Livermore National Laboratory, University of California, Energy and Environment Directorate, Livermore, California 94550, USA	730
Limerick University, Limerick, Ireland	144
Maize Institute "Zemun Polje" Laboratory of Biophysics, Belgrade, Serbia	276
Martin-Luther-Universität Halle-Wittenberg, Institut für Anorganische Chemie, Kurt-Mothes-Straße 2, D-06120 Halle, Germany	716
Max-Planck Institut für kohlenforschung, Kaiser-Wilhelm Platz-1, Mülheim an der Ruhr, Germany	304
Max-Planck Institute for Iron Research, Max-Planck Str. 1, 40237 Düsseldorf, Germany.	58
Military Medical Academy, Crnotravska 17, 11000 Belgrade	651
Mining and Metallurgy Faculty, University of Pristina, 38220 Kosovska Mitrovica, Serbia	55

Moscow State University Lomonosov, Moscow, Russia	276
Moscow State University M.V. Lomonosov, Laboratory of Molecular Spectroscopy, Department of Chemistry, 1 Leninskie gory, 119992 Moscow, Russia,	674
Moscow State University Lomonosov, Faculty of Chemistry, Moscow, 119899, Russia	132
Moscow State University Lomonosov, Chemical Department, Moscow, Russia	144
Moscow State University, M.V.Lomonosov, Department of Biophysics, Moscow Russia	365
Nanyang Technological University, Division of Chemistry and Biological Chemistry, 1 Nanyang Walk, Block 5, Level 3, Singapore 637616	108
National Research and Development Institute for Industrial Ecology-ECOIND, 90-92 Panduri St., 050663 Bucharest – 5, Romania	87, 636
NCSR “Demokritos”, Institute of Radioisotopes and Radiodiagnostic Products, POB 60228, 15310 Agia Paraskevi, Athens, Greece	434, 460
NIS – Oil Refinery, Pančevo, Serbia	519
Nova Gorica Polytechnic, Laboratory for Environmental Research, Vipavska 13, Nova Gorica, Slovenia	401
Osaka University, ILE, 2-6 Yamadaoka, Suita City, Osaka 565-0871, Japan	469
Otto-von-Guericke University, Universitätsplatz 2, 39106 Magdeburg, Germany	273
PALS Research Centre, Za Slovankou 3, 18221 Prague 8, Czech Republic	469
Penn State Berks, Reading, PA 19610, U.S.A.	255
Permanent Representation of the Republic of Serbia to the OPCW, The Hague, The Netherlands	615
Pharmaceutical and Chemical Industry „Zdravlje”, Vljakova 199, 16000 Leskovac, Serbia	719, 722
Polish Academy of Sciences, Institute of Physical Chemistry, Warsaw, Poland	270
Rice University, Chemistry Department MS60, 6100 Main St., Houston, TX 77005, USA	698
School of Electrical Engineering, University of Belgrade, King Alexander's Boulevard 73, P.O. Box 35-54, Belgrade, Serbia	733

School of Medicine, University of Belgrade, Višegradska 26, Belgrade,	374, 401
School of Medicine, Department of Chemistry, University of Belgrade, Visegradska 26, Belgrade	192
Semenov Institute of Chemical Physics RAS, Moscow, Russia	144
Southwest Research Institute, Division of Chemistry and Chemical Engineering, 6220 Culebra Road, San Antonio, Texas, USA 78238	479
Technic faculty, "Mihajlo Pupin" Đ. Đakovića bb, 23000 Zrenjanin	642
Technical Faculty Bor, University of Belgrade, VJ 12, 19210 Bor, Serbia	52, 55
Technical Faculty Čačak, University of Kragujevac	543
Texas A&M University, Department of Soil and Crop Science, Cereal Quality Laboratory, College Station, Texas 77843-2474	377
The Maize Research Institute „Zemun Polje”, Serbia	365
Tigar, Pirot	594
Tokai University, School of Science, Department of Physics, 1117 Kitakaname, Hiratsuka 259-1292, Japan.	3
Tokyo Institute of Technology, Materials and Structure Laboratory, Center for Materials Design, Yokohama 226-8503, Japan	489, 492
Topchiev Institute of Petrochemical Synthesis RAS, Moscow, Russia	144
Umeå University, Department of Medical Biochemistry and Biophysics, Umeå, 90781 Sweden	23
Università degli Studi di Milano, Via Celoria 16, 20133 Milano, Italy	469
Università di Bologna, Dipartimento di Chimica 'G. Ciamician', Via Selmi, 2, Bologna, Italy	255
Università di Firenze, Dipartimento di Chimica, Via della Lastruccia 3, 50019 Sesto Fiorentino (FI), Italy	31
Università di Milano Bicocca, Dipartimento di Fisica "G. Occhialini", Piazza. Della Scienza 3, 20126 Milano, Italy	469
Universite Catholique de Louvain, Unite de Catalyse et Chimie de Matériaux Divises, Place Croix de Sud, 2/17, 1348 Louvain-la-Neuve, Belgium	567
Université de Pau et des Pays de l'Adour, Laboratoire de Physico-Chimie Moléculaire, 2, Av. P. Angot, 64053 Pau Cedex 9, France	123
Université Libre de Bruxelles, Faculté des Sciences Appliqués, CP165/63, Av. F. Roosevelt 50, 1050 Bruxelles, Belgium	219

University of Athens, Department of Chemistry, Laboratory of Analytical Chemistry, Environmental Analysis Group, Panepistimioupoli, 15771 Zografos, Athens, Greece.	736
University of Cantabria, Group of Inorganic Chemistry, E-39005 Santander, Spain	183
University of Catania, Institute of Radiology and Radiation Oncology, Italy	451
University of Essex, Wivenhoe Park, Colchester, CO4 3SQ, UK	469
University of Hamburg, Institute of Biochemistry and Molecular Biology, Martin-Luther-King-Pl. 6, Hamburg, Germany	440
University of London, The School of Pharmacy, Department of Pharmaceutical and Biological Chemistry, 29/39 Brunswick Square, London, UK	347
University of London, The School of Pharmacy, Department of Pharmaceutics, 29/39 Brunswick Square, London, UK	347
University of Miami, Department of Chemistry, 1301 Memorial Drive, Cox Science Center, Coral Gables, FL 33146, U.S.A.	11
University of Oxford, Physical and Theoretical Chemistry, South Parks Road, Oxford OX1 3QZ, United Kingdom.	314
University of Patras, Physical Chemistry Laboratory, 26504 Patras, Greece.	736
University of Plovdiv, Department of Physical Chemistry, 4000 Plovdiv, Bulgaria	198, 513
University of Texas Health Science Center, Restorative Dentistry, 7703 Floyd Curl, San Antonio, Texas, USA 78284	479
University of West Hungary, Institute for Chemistry, H-9400 Sopron, Bajcsy-Zs. u. 4., Hungary	707
Uppsala University, The Ångström Laboratory, Materials Chemistry, Box 538, S-751 21 Uppsala, Sweden	67
Varta Microbattery GmbH, Daimlerstrasse 1, 73479 Ellwangen, Germany	311
Zorka EXA, 1 Hajduk Veljkova St, Šabac, Serbia,	555

CIP - Каталогизација у публикацији
Народна библиотека Србије, Београд

544(082)

621.35(082)

543.42(082)

**INTERNATIONAL Conference on Fundamental and
Applied Aspects of Physical Chemistry (8 ;
2006 ; Beograd)**

Physical Chemistry 2006 : proceedings of
the 8th International Conference on
Fundamental and Applied Aspects of Physical
Chemistry, [September 26-29, 2006,
Belgrade, Serbia].

Vol. 1 / [organized by The Society of
Physical Chemists of Serbia ;
editor A.[Ankica] Antić-Jovanović]. –
Belgrade : The Society of Physical Chemists
of Serbia, 2006 (Belgrade :
Jovan). - X, 442 str. : ilustr. ; 24 cm

Tiraž 250. - Str. VII: Preface / Editor. –
Bibliografija uz svaki rad. - Abstracts.

ISBN 86-82139-26-X

1. Antić-Jovanović, Ankica 2. The
Society of Physical Chemists of Serbia
(Beograd)

a) Физичка хемија - Зборници b)
Електрохемијско инжењерство - Зборници
c) Спектроскопија - Зборници
COBISS.SR-ID 133423628